AD A135 157 AERODYNAMICS OF VORTICAL TYPE FLOWS IN THREE DIMENSIONS: CONFERENCE PROCE..(U) ADVISORY GROUP FOR AEROSPACE RESEARCH AND DEVELOPMENT NEUILLY.. JUL 83 1/6

UNCLASSIFIED AGARD-CP-342 F/G 20/4 NL

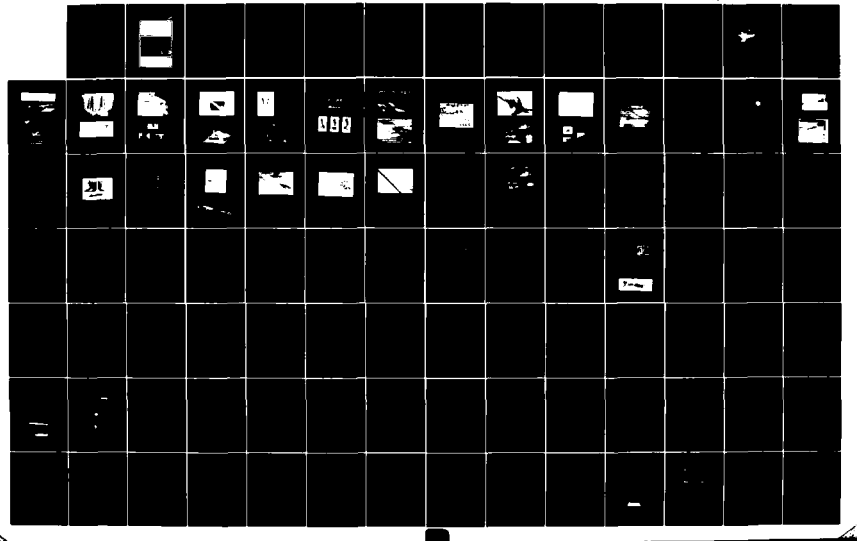

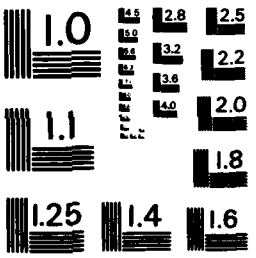

AGARD-CP-342

ADVISORY GROUP FOR AEROSPACE RESEARCH & DEVELOPMENT

AGARD CONFERENCE PROCEEDINGS No. 342

Aerodynamics of Vortical Type Flows in Three Dimensions

COMPONENT PART NOTICE

THIS PAPER IS A COMPONENT PART OF THE FOLLOWING COMPILATION REPORT:

(TITLE): Aerodynamics of Vortical Type Flows in Three Dimensions: Conference Proceedings Held at Rotterdam, Netherlands on 25-28 April 1983.

(SOURCE): Advisory Group for Aerospace Research and Development, Neuilly-sur-Seine, (France).

TO ORDER THE COMPLETE COMPILATION REPORT USE AD-A135 157.

THE COMPONENT PART IS PROVIDED HERE TO ALLOW USERS ACCESS TO INDIVIDUALLY AUTHORED SECTIONS OF PROCEEDINGS, ANNALS, SYMPOSIA, ETC. HOWEVER, THE COMPONENT SHOULD BE CONSIDERED WITHIN THE CONTEXT OF THE OVERALL COMPILATION REPORT AND NOT AS A STAND-ALONE TECHNICAL REPORT.

THE FOLLOWING COMPONENT PART NUMBERS COMPRISE THE COMPILATION REPORT:

AD#:	TITLE:
P002 242	On Issues Concerning Flow Separation and Vortical Flows in Three Dimensions.
P002 243	The Vortex Skeleton Model for Three-Dimensional Steady Flows.
P002 244	On the Structure of the Turbulent Vortex.
P002 245	Instabilities in Trailing Vortices: Flow Visualization Using Hot-Wire Anemometry.
P002 246	On the Generation and Subsequent Development of Spiral Vortex Flow over a Swept-Back Wing.
P002 247	An Experimental Investigation of the Vortex Flow over Delta and Double-Delta Wings at Low Speed.
P002 248	Laser Velocimetry Study of Compressibility Effects on the Flow Field of a Delta Wing.
P002 249	Recent Studies at NASA-Langley of Vortical Flows Interacting with Neighboring Surfaces.
P002 250	Experimental Investigation of Forebody and Wind Leading-Edge Vortex Interactions at High Angles of Attack.
P002 251	Some Results from a Programme of Research into the Structure of Vortex Flow Fields Around Missile Shapes.
P002 252	Predicting Aerodynamic Characteristics of Vortical Flows on Three-Dimensional Configurations Using a Surface-Singularity Panel Method.
P002 253	Separation and Vortical-Type Flow Around a Prolate Spheroid - Evaluation of Relevant Parameters.
P002 254	On the Generation of Vortical Flow at Hypersonic Speeds over Elliptical Cones.
P002 255	Viscous Three-Dimensional Flow Separations from High-Wing Propeller-Turbine Nacelle Models.
P002 256	Theoretical Modelling of Three-Dimensional Vortex Flows in Aerodynamics.
P002 257	Computational Vortex Flow Aerodynamics.
P002 258	Vortex Flow Simulations Past Wings Using the Euler-Equations.

COMPONENT PART NOTICE (CON'T)

AD#:		TITLE:
	P002 259	Numerical Solutions of the Euler Equations Simulating Vortex Flows Around Wings.
	P002 260	The Treatment of Convected Vortices in Compressible Potential Flow.
	P002 261	Vortex Stability and Breakdown.
	P002 262	The Break-Up Mechanism of a Streamwise Directed Vortex.
	P002 263	Vortex Breakdown: A Two-Stage Transition.
	P002 264	A Contribution to the Problem of Vortex Breakdown.
	P002 265	Numerical Simulation of Vortex Breakdown by the Vortex-Filament Method.
	P002 266	Waves on Vortex Cores and Their Relation to Vortex Breakdown.
	P002 267	Vortical Flow Management for Improved Configuration Aerodynamics - Recent Experiences.
	P002 268	The Effects of Wing Tip Devices on the Performance of the BAe (British Aerospace) Jetstream.
	P002 269	The Effect of Wing Tip Devices on the Far-Field Wake of a Paris Aircraft.
	P002 270	Boundary Layer Segmentation on Sharp Highly Swept Leading Edges and Its Effects on Secondary Vortices.
	P002 271	Augmentation of Fighter-Aircraft Performance by Spanwise Blowing over the Wing Leading Edge.

AGARD-CP-342

NORTH ATLANTIC TREATY ORGANIZATION

ADVISORY GROUP FOR AEROSPACE RESEARCH AND DEVELOPMENT

(ORGANISATION DU TRAITE DE L'ATLANTIQUE NORD)

AGARD Conference Proceedings No.342

AERODYNAMICS OF VORTICAL TYPE FLOWS IN THREE DIMENSIONS

Papers presented and Discussions held at the Fluid Dynamics Panel Symposium at the Atlanta Hotel in Rotterdam, Netherlands, 25–28 April 1983.

THE MISSION OF AGARD

The mission of AGARD is to bring together the leading personalities of the NATO nations in the fields of science and technology relating to aerospace for the following purposes:

- Exchanging of scientific and technical information;
- Continuously stimulating advances in the aerospace sciences relevant to strengthening the common defence posture;
- Improving the co-operation among member nations in aerospace research and development;
- Providing scientific and technical advice and assistance to the North Atlantic Military Committee in the field of aerospace research and development;
- Rendering scientific and technical assistance, as requested, to other NATO bodies and to member nations in connection with research and development problems in the aerospace field;
- Providing assistance to member nations for the purpose of increasing their scientific and technical potential;
- Recommending effective ways for the member nations to use their research and development capabilities for the common benefit of the NATO community.

The highest authority within AGARD is the National Delegates Board consisting of officially appointed senior representatives from each member nation. The mission of AGARD is carried out through the Panels which are composed of experts appointed by the National Delegates, the Consultant and Exchange Programme and the Aerospace Applications Studies Programme. The results of AGARD work are reported to the member nations and the NATO Authorities through the AGARD series of publications of which this is one.

Participation in AGARD activities is by invitation only and is normally limited to citizens of the NATO nations.

Published July 1983

ISBN 92-835-0334-1

Printed by Specialised Printing Services Limited
40 Chigwell Lane, Loughton, Essex IG10 3TZ

EXECUTIVE SUMMARY

Vortical flows are an inevitable feature of almost all flow fields of aeronautical interest. For example, they arise from leading and trailing edges of wings, from bodies at high angles of attack and are always evident in separated flows. They can have major effects on the loading of surfaces with which they interact. They are sometimes stable and well ordered and their effects can then be beneficient and exploitable, but when unstable their effects are generally adverse. To expand the flight envelopes and controllability of modern aircraft we need to improve considerably our understanding of such flows as they are at the root of many important design problems. The aim of the Symposium was therefore to reveal the current state of our understanding and to provide useful guidelines for future research.

The Symposium was divided into five sessions with the following topic headings: Fundamental Generation and Structure of Vortical Flows, Interaction of Vortical Flows with Surfaces, Modelling and Computing, Stability and Breakdown of Vortical Flows, Control and Exploitation of Vortical Flows. A final but regrettably brief period was devoted to a review of main impressions of the Symposium presented by J.H.B.Smith followed by a general discussion.

The papers showed that in all the main areas of interest considerable progress has been made in recent years, but much remains to be done. We have a good topological basis for describing separated flows and the associated vortical flow regions; the computation of inviscid models (e.g. panel methods, Euler equation solutions, convected vortex element methods) is developing well; and practical forms of control and exploitation have been successfully demonstrated. Our understanding of interaction effects has made good progress as a result of some well planned experimental work coupled with comparisons with theory. The stability and breakdown of vortical flows is an important subject of much complexity and a lively source of controversy, but the main qualitative features are becoming understood.

However, much research remains to be done and the main problem areas appear to be:

1) The inclusion of viscous effects and associated effects of scale in the theoretical models, - in particular secondary separations need to be modelled realistically.

2) The need to eliminate the dependence of current models on some prior knowledge of the separation line positions.

3) The need for more sets of good data for comparison with the predictions of theoretical methods.

4) The need for criteria for breakdown relevant to the main types of vortical flow that occur on aircraft.

5) Current knowledge of dynamic effects is very inadequate and needs expanding.

6) The effects of stores and store pylons on vortical flows are not well understood.

7) The use of boundary layer control for vortical flows is very promising and further work is needed.

A.D.YOUNG,
Symposium Chairman.
July 1983.

AGARD FLUID DYNAMICS PANEL

M. l'Ing. en Chef B.Monnerie
Chef de la Division d'Aerodynamique Appliquée
ONERA
29 Avenue de la Division Leclerc
92320 Châtillon, France

Dr L.Roberts
Joint Institute for Aeronautics and Acoustics
Department of Aeronautics and Astronautics
Stanford University
Stanford
California 94305, USA

PROGRAM COMMITTEE MEMBERS

Professor A.D.Young (Chairman)
Queen Mary College, Aeronautics Dept
Mile End Road
London E1 4N6, UK

Professor Dr Ing. K.Gersten
Insitut für Thermo und Fluiddynamik
Ruhr-Universität Bochum
Postfach 102148
D-4630 Bochum 1, FRG

Professor J.J.Ginoux
Director
Von Kármán Institute for Fluid Dynamics
Chaussée de Waterloo 72
DB-1640 Rhode-Saint-Genèse, Belgium

Professor Dr Ir. J.L. van Ingen
Department of Aerospace Engineering
Delft University of Technology
Kluyverweg 1
2629 HS Delft, Netherlands

Dr W.J.McCroskey N202A-1
Senior Staff Scientist
Ames Research Center
Moffett Field
CA 94035, USA

Professor H.Nørstrud
Division of Aero- and Gas Dynamics
The University of Trondheim
N-7034 Trondheim-NTH, Norway

Professor M.Onorato
Politecnico di Torino
Istituto di Meccanica Applicata all
Macchine, Aerodinamica e Gasdinamica
Corso Duca degli Abruzzi 24
10129 Torino, Italy

M. l'Ing. en Chef C.Thery
Institut Franco-allemand de Recherches
de Saint-Louis
12 rue de l'Industrie
Boite Postale 301
68301 Saint-Louis, France

CONTENTS

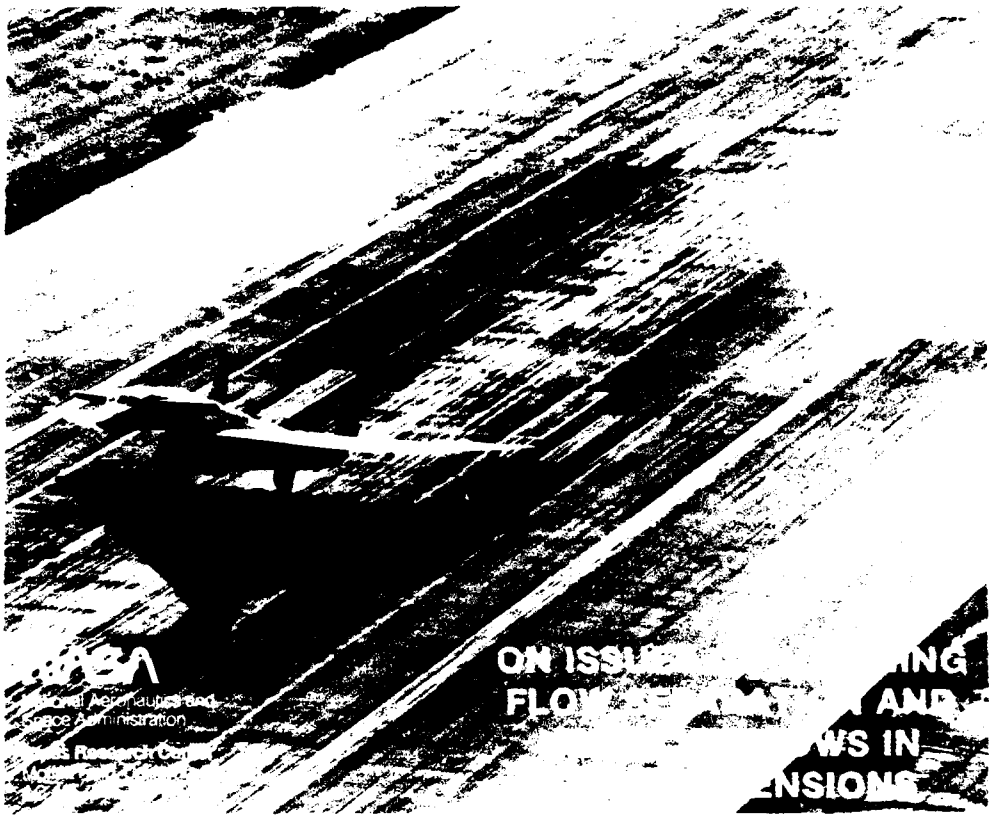

David J. Peake
Research Assistant to Center Director

and

Murray Tobak
Research Scientist

NASA Ames Research Center
Moffett Field, California 94035, U.S.A.

SUMMARY

This review provides an illustrated introduction laying the knowledge base for vortical flows about three-dimensional configurations that are of typical interest to aerodynamicists and researchers in fluid mechanics.

The paper then compiles a list of ten issues, again in illustrative format, that the authors deem important to the understanding of complex vortical flows. These issues and our responses to them provide, it is hoped, a skeletal framework on which to hang the ensuing conference proceedings.

1.0 INTRODUCTION

About typical flight vehicles, three-dimensional (3D) flow separations emanating from separation lines oblique to the general flow direction tend to roll up into tightly coiling vortex motions. One readily familiar example is the trailing-vortex system behind a high-aspect-ratio lifting wing, where the separation lines occur at the wing tips and extend around and along the trailing edges. Even on this simple configuration, when flaps are deflected the ensuing vortical wake is very complex because of a multitude of additional separations located at the side edges of the flap components.

Associated with the use of a large sweep angle on a wing, often coupled with a leading-edge extension, 3D vortical flows generated ahead of the trailing edge, at or near the leading edge itself, have become increasingly evident. Such leeside flows are usually well-ordered structurally. As a result, designers of combat aircraft and missiles have sought to exploit these axial vortex motions to good effect in meeting speed and maneuver requirements.

At this time, our understanding of such flows remains essentially qualitative. For particular configurations like the slender wing, flow separations are controlled in the sense that separation lines are fixed at the sharp leading edges, and from the results of many experiments we now possess a fine knowledge of the flow field. In fact, the study of this flow example over the last thirty years has allowed us to extrapolate our findings and appreciate the physics of 3D separations materializing on many other bodies at high angles of attack. Two phenomena significantly restricting the use of vortical flows, however, are the readiness of leeward vortices to develop asymmetrically (particularly those from slender forebodies), or to develop spiral or axisymmetric modes of breakdown. A direct result of vortex breakdown is aerodynamic buffet, where the intensity builds up as the vortex breakdown point moves forward from the trailing edge (as angle of attack increases further) and affects a significant surface area of the wing.

Asymmetry and breakdown are frequently encountered together when a fighter airplane flies under conditions of high angle of attack with sideslip. When the vortical flow is antisymmetric, large side forces and yawing moments may be generated. These moments may be unsteady, and they may be larger than counteracting moments available from the maximum deflections of the control surfaces. Moreover, there may be additional constraints of low observable technology and V/STOL (or STOVL) capability imposed, whereby propulsion-system inlets may be immersed in the leeside vortical wake causing a major impact on the distortion levels in the internal-flow ducting. The control of the development of the leeward vortex wake is hence crucial to flying capably at very high angles of attack under controllable and stable conditions.

Other specialized vehicles, such as rotorcraft, are flying with parts of the airframe immersed in heavily interacting vortical flow fields from the rotor, throughout the entire flight envelope. One concept under development, the tilt-rotor aircraft, utilizes an innovative propulsion system that combines the benefits of high-speed forward flight (with the rotor axes pivoting to near horizontal) with V/STOL capability (the rotor axes close to vertical). In the flight transitional phase of rotating the thrust vector, the vortical wakes from the rotors may have a large impact on tail surfaces, if improperly positioned.

The following photographs (Figs. 1-22) vividly illustrate these introductory remarks.

3-D FLOW SEPARATIONS AND ENSUING VORTICAL MOTIONS OCCUR ON ALL LOW-ASPECT RATIO VEHICLES AT CRUISE . . .

F1

. . . WHEN MANEUVERING . . .

F2

F3

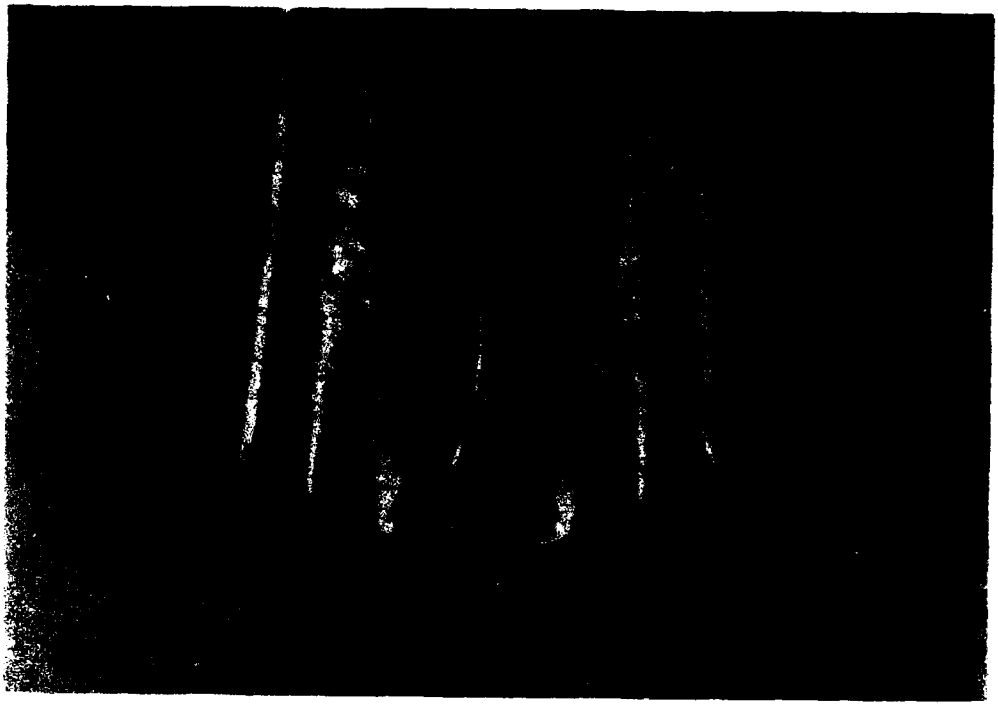

F4

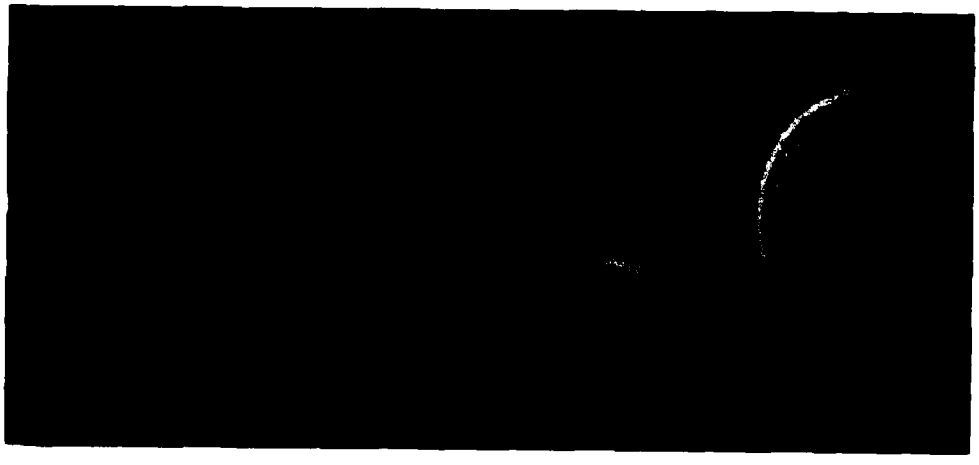

PRODUCING A COMPLEX VORTICAL WAKE

F5

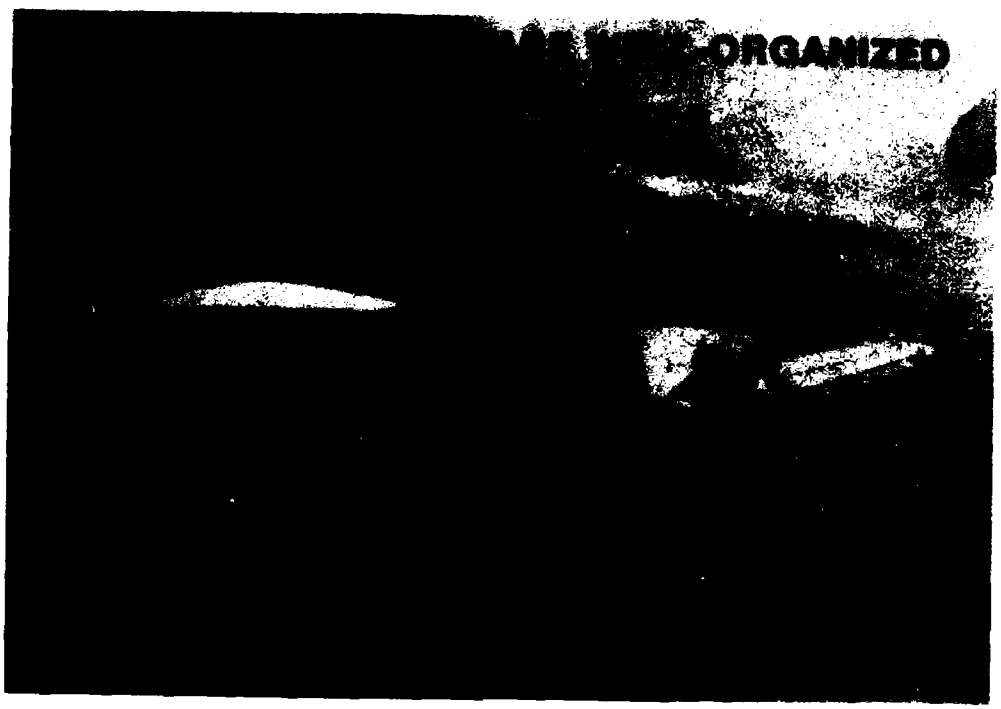

F6

ROLLED UP AND STEADY IN THE MEAN . . .

(a) SIDE ELEVATION

(b) PLAN VIEW

(c) CROSS FLOW

F7

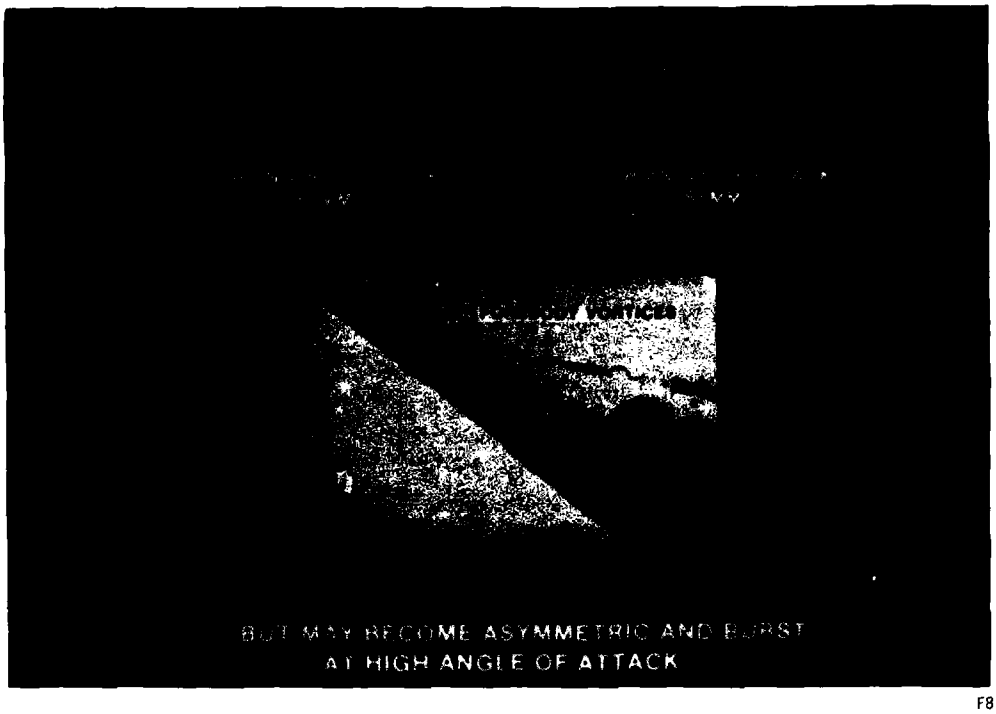

F8

F9

SUBSTANTIAL YAWING MOMENTS RESULT

F10

... CAN PROVIDE UNSTABLE BREAKS IN YAWING MOMENT DATA

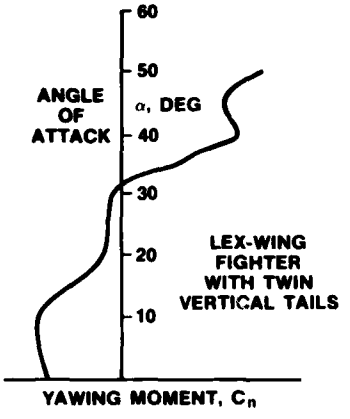

F11

POSITION OF VERTICAL FIN(S) INFLUENCES VORTEX BURST POSITION UNDER COMBINED ANGLE-OF-ATTACK AND SIDESLIP CONDITIONS

F12

PREFER FIXING SEPARATION LINES AT SALIENT EDGES FOR CONTROLLED SEPARATION AND PREDICTABLE FORCE AND MOMENT CHARACTERISTICS . . .

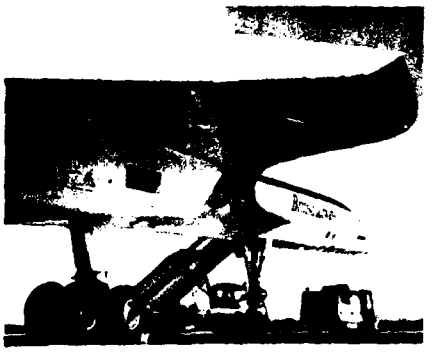

F13

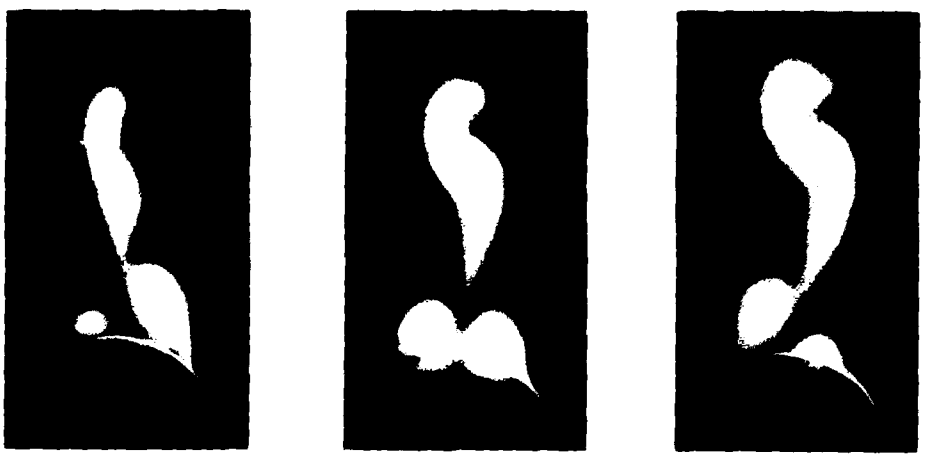

CONE, α/θ_C = 3.3, C_μ ≈ 0.003, M_∞ = 0.6
CROSS-SECTION VIEWED FROM DOWNSTREAM

. . . OR ACTIVELY CONTROL ORIENTATION OF LEESIDE VORTICES BY BLOWING

F14

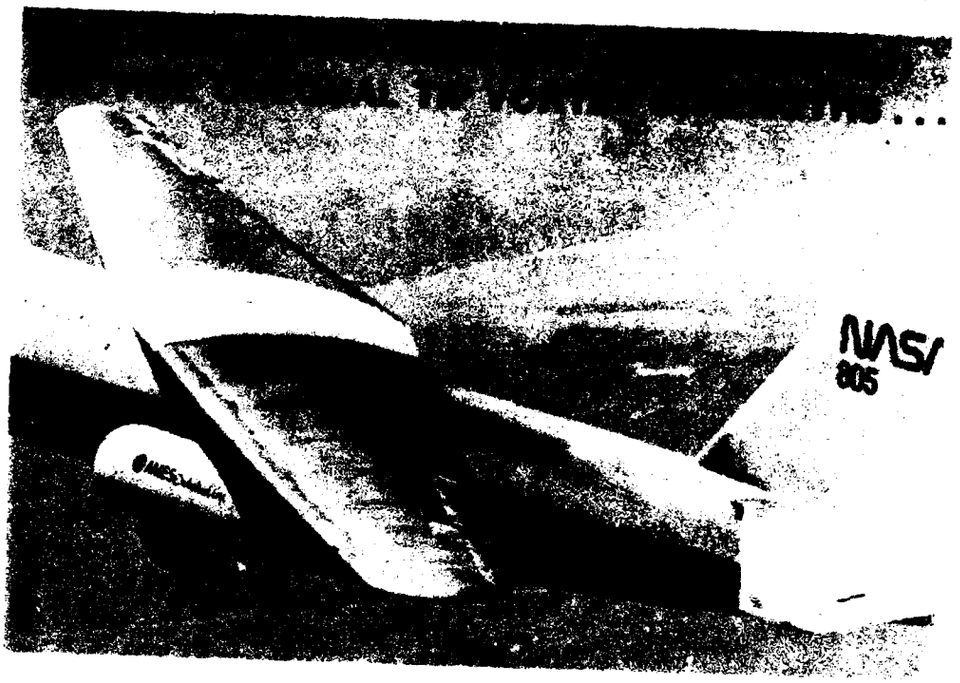

F15

F16

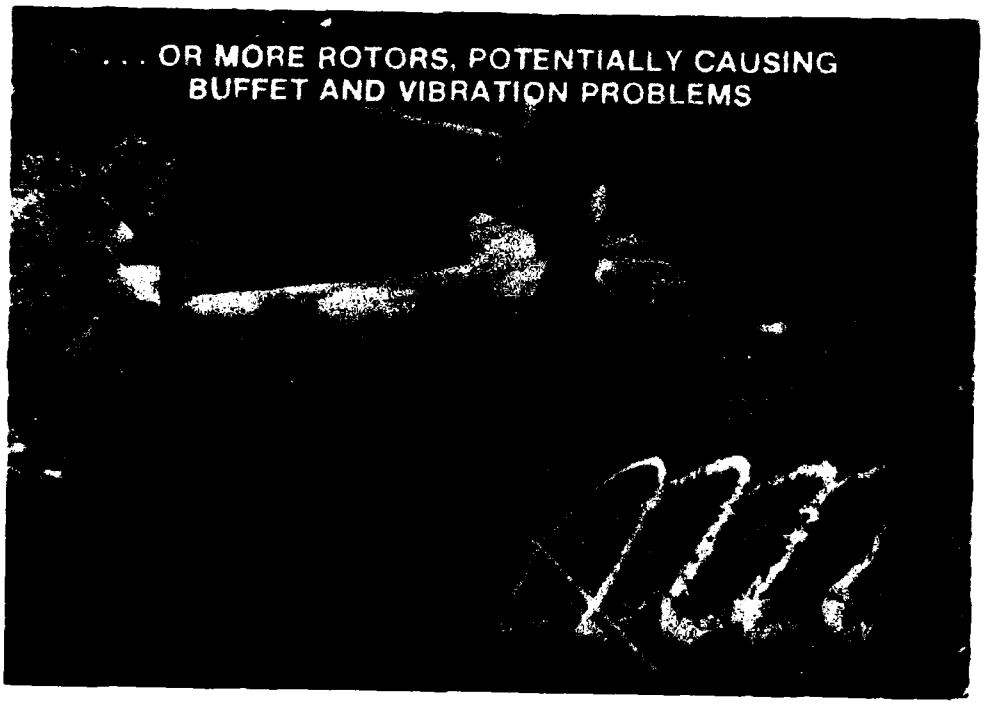
. . . OR MORE ROTORS, POTENTIALLY CAUSING
BUFFET AND VIBRATION PROBLEMS

F17

WITH VORTICES GENERATED FROM VARIOUS SHARPLY-SWEPT EDGES . . .

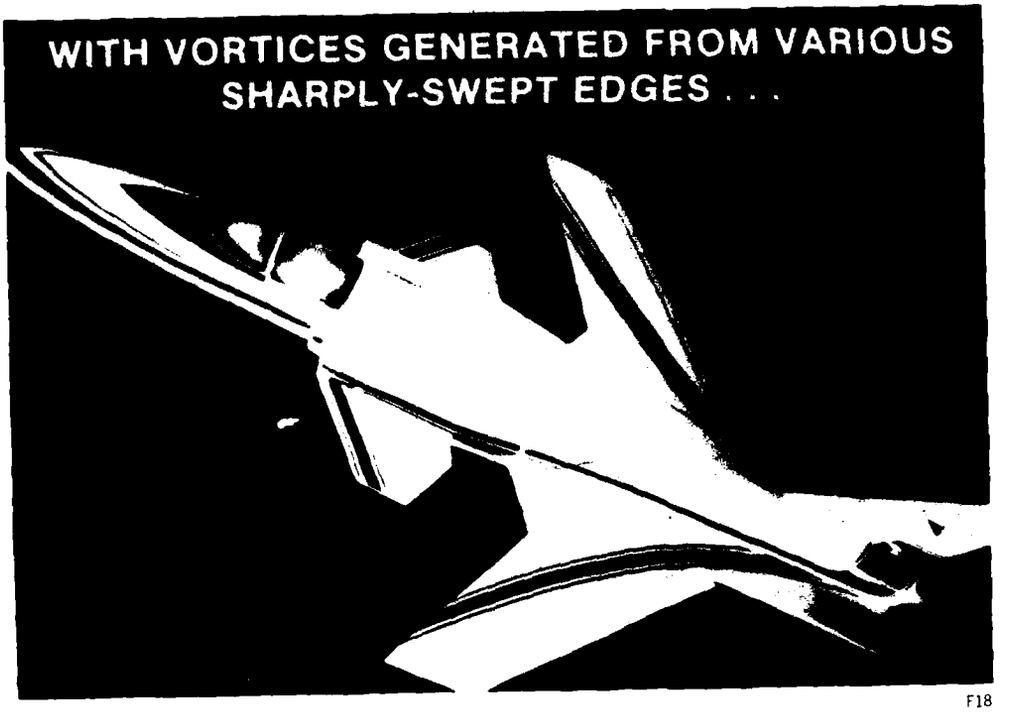

F18

F19

MANDATORY TO ADOPT RATIONAL BASE
TO UNDERSTAND FLOW STRUCTURE

F21

HYPOTHESIZE MATHEMATICAL FRAMEWORK OF CONTINUOUS VECTOR FIELDS (E.G., STREAMLINES IN FLOW AND SKIN-FRICTION LINES ON BODY) IN ASSOCIATION WITH LIMITED NUMBER OF (ZERO VELOCITY OR ZERO SKIN-FRICTION) ANALYTIC SINGULAR POINTS

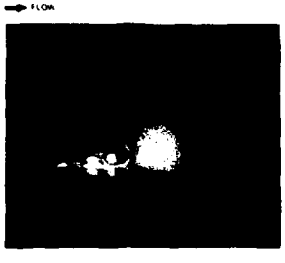

SMOKE FLOW
ABOUT OBSTACLE

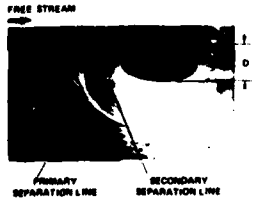

WATER TUNNEL

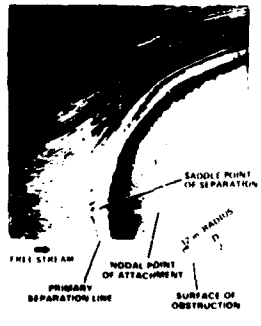

WIND TUNNEL

F22

ISSUES

Having presented a foundation for where vortical flows are important in aerodynamic design, we now present some pertinent issues concerning our knowledge and understanding of 3D, viscous vortical flows. For instance:

1. Do we have an unambiguous definition of separation in three dimensions?

2. Do we understand the structure and mechanisms of separation and the ensuing coiled-up vortical motions?

3. Is it possible to formulate a principle that will distinguish between the scale of vital and unimportant organized vortical structures?

4. Can we exploit the well-organized vortex motions for significant benefit when they are stable?

5. Do we understand the instability mechanisms leading to vortex breakdown and leeside wake asymmetries at high angles of attack?

6. Do we understand the implications of vortices interacting with local flow fields about the wing and tail surfaces?

7. Can we exercise control over these interacting vortical flow fields?

8. Can we use the Navier-Stokes equations, assumed to govern fluid motion, to compute vortical flows about complex aerodynamic configurations at high angles of attack?

9. If not, with appropriate simplifications of the Navier-Stokes equations, and with our current understanding of modelling turbulence, are we able to compute vortical flows about chosen aerodynamic components at high Reynolds numbers?

10. Can modelling the vortical flows by essentially inviscid approaches provide us with satisfactory insight into the flow physics?

Let us now attempt to address each of these issues in turn. In so doing, we hope to provide some responses that will provoke thoughtful reflection and spark additional needed research, both experimental and computational, in using 3D vortical flows to maximum benefit in rational aerodynamic design. Strong consideration must be given to understanding the mean and fluctuating 3D flow structure and how the vortices can be controlled actively or passively.

ISSUES

- DO WE HAVE AN UNAMBIGUOUS DEFINITION OF SEPARATION IN THREE DIMENSIONS? YES — IF A SEPARATION LINE IS CONSIDERED ALWAYS TO EMANATE FROM A SADDLE POINT.

F23

Complications arise, however, because flow configurations exist where the conditions for 3D separation appear to be present: skin-friction lines on the body surface converge onto a particular line and, in cross-flow planes, streamlines corresponding to trajectories of the velocity components in these crossflow planes roll up around what appear to be vortex cores. But within the limits of numerical or experimental resolution, the particular skin-friction line on which others converge, does not appear to emanate from a saddle point. Frequently, it appears to emerge from the region of the attachment node (i.e., stagnation point) or the nose of the body. An appropriate example is offered for consideration in Fig. 24, where both primary and secondary separation lines on the leeside of a missile body, obtained on a surface oil-flow pattern, can be considered continuously traceable to the stagnation point. Nevertheless, the eruption of fluid away from the body is confined to those areas downstream of which we first picture the very rapid convergence of skin friction lines, i.e., on the cylindrical afterbody.

Indeed, the question of an adequate, yet convincing, description of 3D separated flow arises with especial poignancy when one asks how 3D separated flow patterns originate and how they succeed one another as the relevant parameters of the problem (e.g., angle of attack, Mach number, and Reynolds number) are varied. In a past essay (Refs. 1 and 2) we proposed to answer this question by placing an extension of a hypothesis of Legendre (Ref. 3) that skin-friction lines comprise a continuous vector field, wherein the singular points of the field can be categorized mathematically, within a framework broad enough to include the notions of topological structure and structural stability coupled with arguments from bifurcation theory. From this rational framework emerged the concepts of local and global separation (again, see Refs. 1 and 2) wherein a separation line was considered as starting at a nodal singular point or a saddle singular point, respectively. The local concept, in fact, implies that when the separation line appears, no new singular points form on the surface or in the flow field to alter the topology. Conversely, the development of a global separation line is connected categorically with the appearance of a new saddle/node pair on the surface and a new 3D singular (zero-velocity) point in the external flow.

Upon admitting, however, that no computational or wind-tunnel experiments of which we are aware give incontrovertible evidence in support of the absence (or the presence) of saddle singular points originating at lines of local separation (in contrast to clear evidence of a saddle/node pair commencing at a global horseshoe shaped separation line), we may perhaps offer an inference from a knowledge of the structure of the external flow in the case of local separation.

Matters are clarified if we accept the existence of a coiling vortical motion downstream (we use Fig. 24 once more to aid the discussion), where the 3D separation lines are pronounced. There, a particular streamline in the external flow is along the axis of the core of the rolled-up fluid. Just as in the case of a global separation, we can form a stream surface which includes this particular streamline in the external flow and the skin-friction line on the surface which has become the line of separation. We can then trace the paths of these two particular lines upstream, and it is clear that the core streamline will be in close proximity to the surface as the nose is approached. The question of the origin of the local separation then reduces to the behavior of the stream surface in the immediate vicinity of the nodal point of attachment at the nose. The problem of resolving the flow detail at the nose forces us to consider two alternative possibilities: either the core streamline passes upstream to infinity, in which case the separation is indeed local; or it terminates in a focal singular point in the flow or on the surface, in which case the line of separation would originate at a saddle point and the separation is global. We argue that inasmuch as we have been able to single out these lines, each must have a special property, which we suggest manifests itself by origination at focal and saddle singular points.

We are suggesting, then, that if a coiling vortex-type flow is admitted downstream, the core streamline must emanate from an upstream singular point, no matter how obscured the singular point may be by a lack of

LOCAL SEPARATION ON A MISSILE BODY

$M_\infty = 2.3$

(a) SIDE ELEVATION, $R_{L_\infty} \sim 10 \times 10^6$, $R_D = 1.3 \times 10^6$

LENGTH, L = 38.2 cm (15 in.); D = 5.0 cm (1.97 in.)

S_1 = PRIMARY SEPARATION OF BOUNDARY LAYER DEVELOPING FROM WINDWARD GENERATOR

S_2 = SECONDARY SEPARATION

A_1 = PRIMARY ATTACHMENT LINE

A_2 = SECONDARY ATTACHMENT

$M_\infty = 2.3$

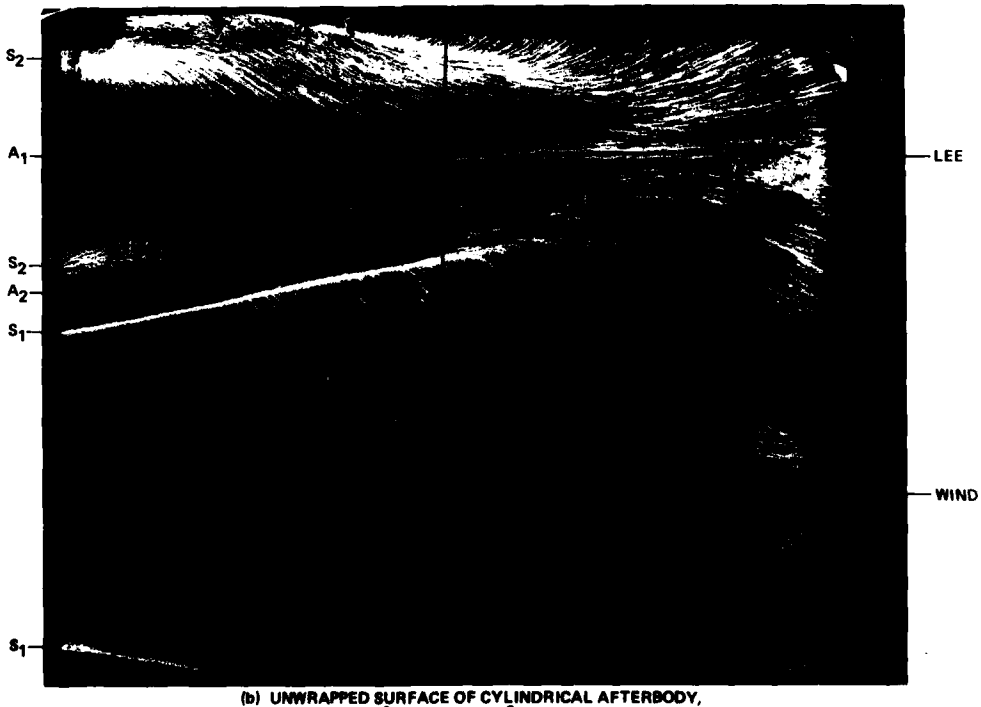

(b) UNWRAPPED SURFACE OF CYLINDRICAL AFTERBODY, $R_{L_\infty} \sim 10 \times 10^6$, $R_D = 1.3 \times 10^6$

F24

resolution in numerical and wind-tunnel experiments. Under these circumstances, we must allow a combination of saddle/node singular points (see Fig. 25) in the stagnation region at the nose not unlike the choice of patterns proposed very much earlier by Legendre (Ref. 3) and Lighhill (Ref. 4). This argument, if acceptable, would lead us to favor the second alternative, which suggests that all 3D separations where coiling vortex motions exist are global events (see also Legendre, Ref. 16).

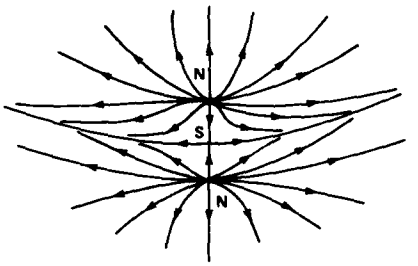

LIGHTHILL 1963

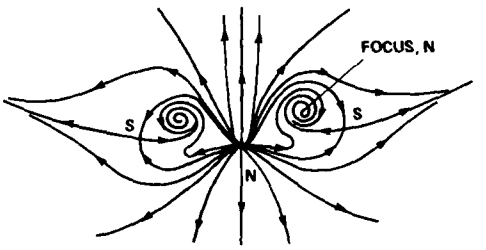

LEGENDRE 1972

F25

ORIGINS OF GLOBAL SEPARATION

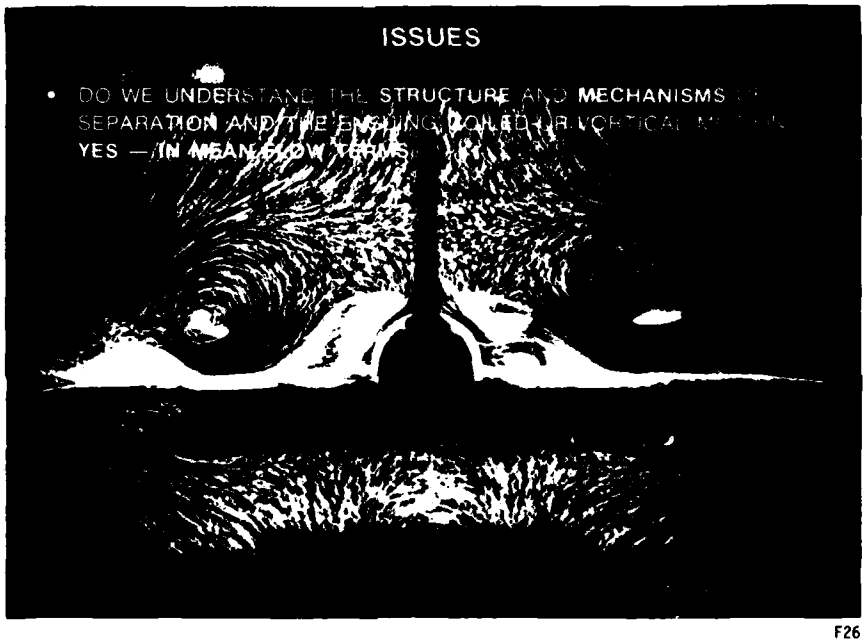

F26

We have a good understanding in mean-flow terms in that we know how to draw topological structures of separated flows and we can envision how the structures manage to undergo topological changes with variations of the governing parameters (e.g., angle of attack). We do not yet have a firm grasp of the relation between structural features and physical quantities such as, e.g., surface pressures, turbulence quantities, etc. We do not yet know how to predict conditions for the emergence of singular points or for their subsequent changes in number and form.

ISSUES

- IS IT POSSIBLE TO FORMULATE A PRINCIPLE THAT WILL DISTINGUISH BETWEEN THE SCALE OF **VITAL** AND **UNIMPORTANT** ORGANIZED VORTICAL STRUCTURES? **UNKNOWN AT THIS TIME**

FLOW BEHIND CAMBERED DELTA WING AT M_∞ = 1.68

F27

One of the several processes of transition is frequently characterized by the appearance of arrays of vortices with axes slightly skewed from the local external flow direction when the body is at low angle of attack. In Fig. 27, where a cambered slender wing is shown at 1° angle of attack, we see a row of near-circular, small black patches behind the inner part of the wing; with increasing angle of attack, the row of patches disappears. Maltby, in Ref. 6, considers that these patches represent a row of streamwise vortices in the boundary layer that are caused by an instability of the 3D shear flow in the region of the cambered, swept leading edge. It has also been inferred by McDevitt and Mellenthin in Ref. 7 that these vortices exist on cones at high Mach number; some of their representative results are shown in Fig. 28. This figure illustrates an oil-film study on a 10° half-angle cone at 5° angle of attack with a transitional attached boundary layer immersed in a Mach 7.4 airstream. In the laminar region of the flow near the cone apex and on the windward side, the delicate pattern of the skin-friction lines has a distinctively different appearance and direction from that farther back on the leeside. This regular pattern of leeward streak lines (separation lines?) is thought to be indicative of the existence of streamwise vortices entrained within the boundary layer. Clearly, the presence of the vortices substantially alters the appearance and the direction of the local skin-friction line pattern reflecting the interaction between the vortices and the mean crossflow.

Another example is depicted in Fig. 29, where similar evidence of small-scale streamwise vortices immersed within the boundary layer on a hemisphere cylinder in transonic flow is shown. It is unclear, however, whether small-scale vortices of this type are the precursors to 3D separation, whether they are modifiers, whether their effect is relatively minor, or whether all or some of these conditions apply. In hypersonic flow, we might expect that these arrays of vortices could influence the heat transfer to the body – at high and low Mach numbers, the answer is that we do not understand the physical processes that are underway. This scenario is similar to the modelling question in turbulent flows, resembling also the phase transition phenomena in chemistry and physics. Advanced concepts are definitely required so that modelled equations average out the small-scale structures and, at the same time, give the correct bifurcation behavior at the appropriate critical Reynolds number(s).

EVIDENCE OF VORTICAL STRUCTURES ON CONE AT ANGLE OF ATTACK

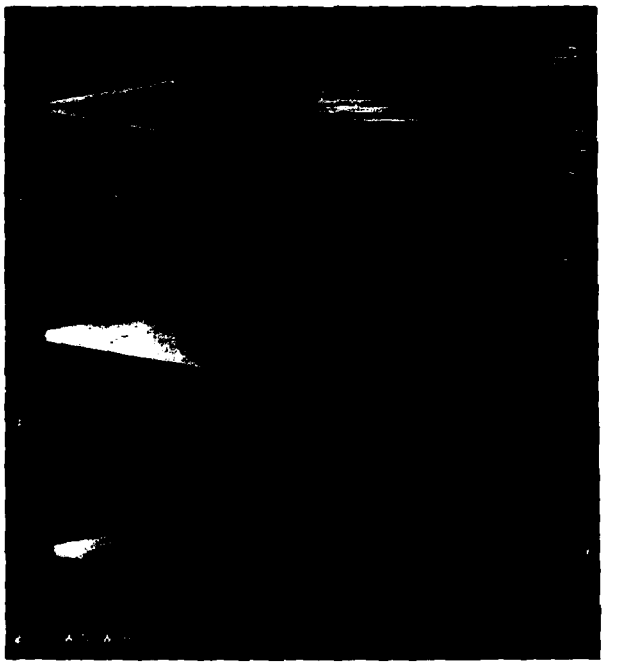

OIL-FILM STUDY ON A 10° SEMI-ANGLE CONE AT $\alpha = 5°$, $M_\infty = 7.4$, $R_{L_\infty} = 3 \times 10^6$, $T_T = 1050°K$, (McDEVITT AND MELLENTHIN 1969)

F28

EVIDENCE OF VORTICAL STRUCTURES ON HEMISPHERE-CYLINDER AT ANGLE OF ATTACK

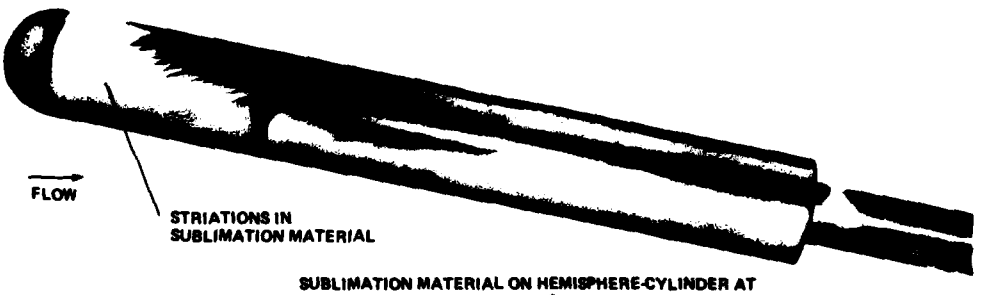

SUBLIMATION MATERIAL ON HEMISPHERE-CYLINDER AT $\alpha = 19°$, $M_\infty = 1.2$, $R_{L_\infty} = 4.9 \times 10^6$, $L = 7.5\,D$, $D = 2.6$ in.

F29

ISSUES

- CAN WE EXPLOIT THE **WELL-ORGANIZED** VORTEX MOTIONS FOR SIGNIFICANT BENEFIT WHEN THEY ARE STABLE? **YES**

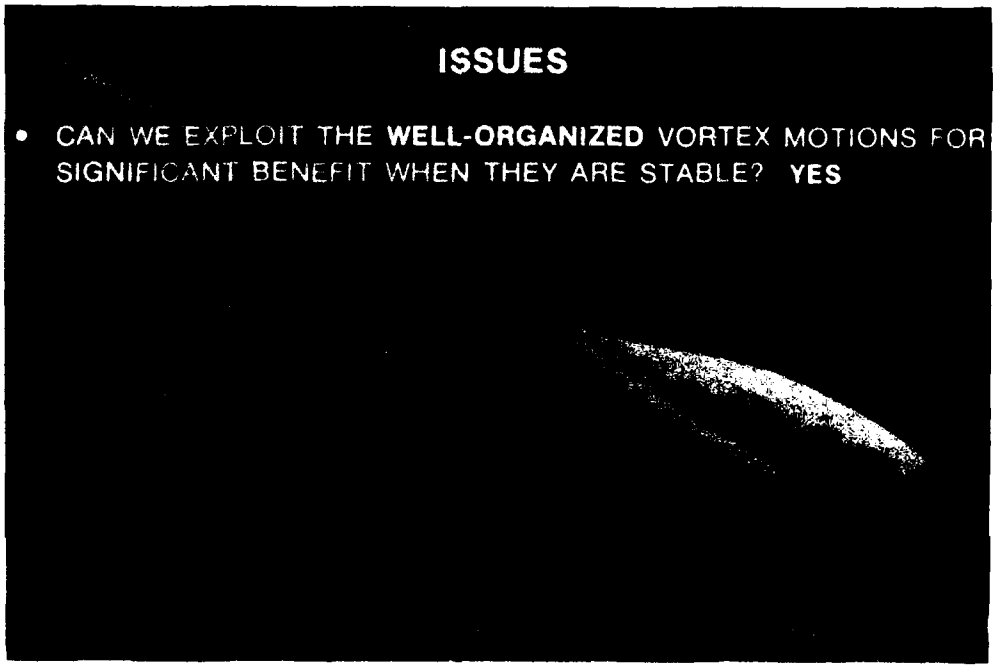

F30

When a 3D boundary layer detaches from the surface it will, almost without exception, leave along a swept separation line, rolling up in the process into a well-organized nominally steady vortical motion. The underlying mechanism appears to be independent of both Reynolds number and Mach number, although under laminar conditions the flow features are normally more exaggerated. Hence, the overall details of many flows of practical interest can be determined in a water-tunnel facility, in which aircraft and missile designers can make changes to configurations quickly and cheaply.

It is clear that when the leeside 3D separated flow fields are symmetric and stable, whether from the forebody or from other sharply swept edges farther downstream, the suction pressures induced by the coiling vortex motions can add substantial nonlinear components to the normal force as angle of attack is increased.

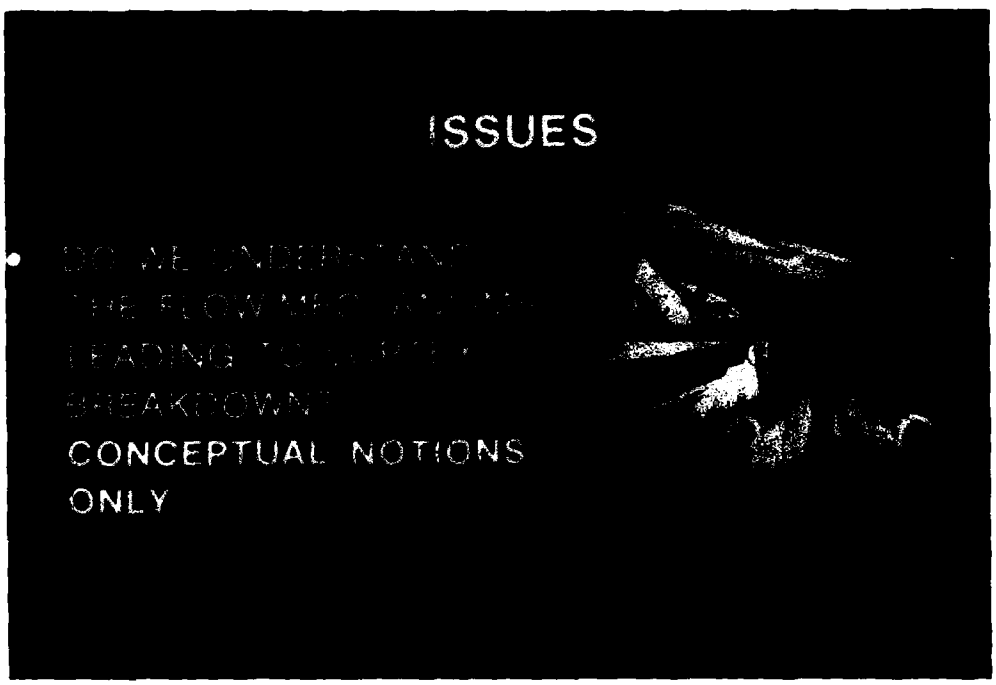

F31

The enhancement to the lift on a body provided by leeside streaming vortical motions is eventually limited when breakdown of the vortices occurs over the body. Currently, there is no theory available to predict the effect of vortex breakdown on the lift of an aerodynamic configuration. According to Wedemeyer (Ref. 8), explanations for vortex breakdown can essentially be divided into two categories: those that relate breakdown to an instability mechanism and those that do not. The two forms of vortex breakdown, called the bubble (axisymmetric) form and the spiral form, are frequently assumed to be different phenomena, although the bubble form is rarely found about a moving aircraft. Based on experimental observations, the bubble form appears to be the result of a change in topology only rather than related to a flow instability; to the contrary, the spiral form of breakdown is considered to be initiated by an instability resulting from an amplification of spiral perturbations.

All theories predict vortex breakdown to occur within the experimentally observed range of swirl angles and the sensitivity of breakdown to the severity of axial pressure gradients. No theory, however, yields the flow detail in the breakdown zone, nor an accurate location of breakdown to compare with experimental results.

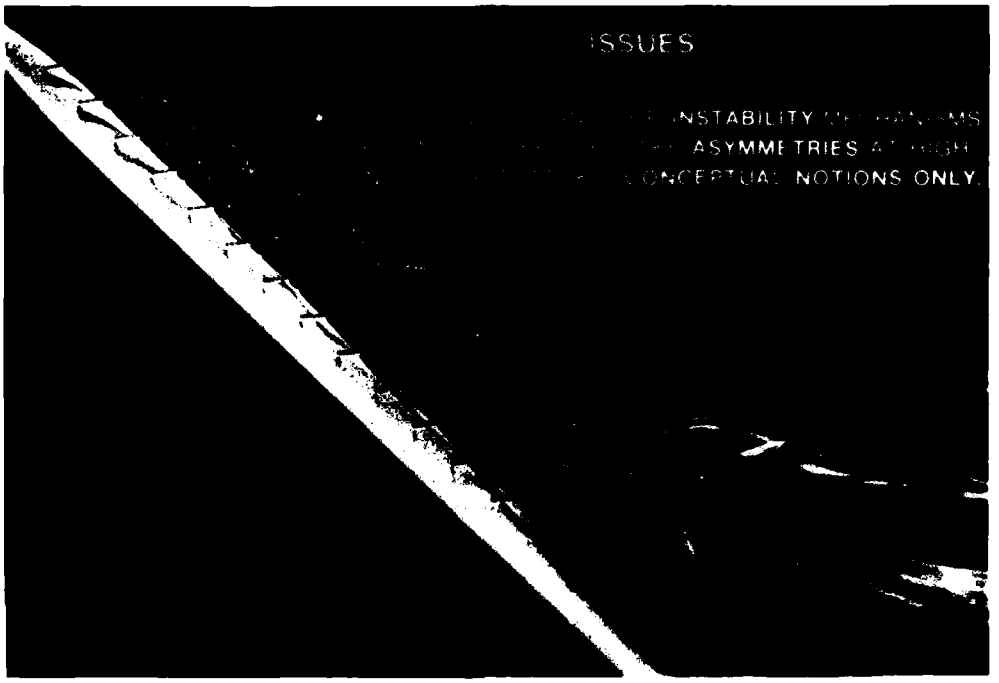

F32

Hypotheses have been advanced to explain the phenomenon based on the use of the impulsive flow analogy and the stability of the flow past a 2D circular cylinder. Details of the assumptions in these hypotheses are explained in Ref. 9. A typical flow topology in cross-section is depicted on Fig. 33, illustrating the conceptual side-to-side structural development of the subsonic flow about a slender forebody of nose semi-apex angle, θ_c.

Let us assume an asymmetric disturbance to originate at the nose, of the same rotation, say, as the port side primary vortex. If this disturbance amplifies in the vicinity of the enclosing saddle point as a consequence of instability of the inflexional velocity profiles, there will be an effective increase in the vorticity of the port-side primary vortex. This vortex will enlarge slightly and move away from the surface as shown in Fig. 33(a). As the relative incidence increases up to 3.2, the feeding shear layer continues to stretch, as shown in Fig. 33(b). At a relative incidence of 3.3, in conjunction with the appearance of gross unsteadiness of the secondary vortices, the elongated shear layer itself passes through a shedding stage, as shown in Fig. 33(c), until at a relative incidence of 3.4 there is definitive evidence of a third spiral vortex motion, as shown in Fig. 33(d). In order that the two vortices of the same rotational direction be able to coexist in tandem on the left-hand side, the rules of topology (Ref. 10) instruct us that a new saddle point must be inserted between them, as shown in Fig. 33(c). As the relative incidence increases still further, the starboard-side primary vortex begins to grow, as shown in Fig. 33(d) and (e), resulting eventually in the repetition of the shedding process for the opposite side; these incidences at which shedding occurs correspond with the maximum induced side loads. Note that the one crossflow streamline emanating from the enclosing saddle point to the body at A1 as shown, for example, in Fig. 33(e), always partitions the left- and right-hand sides of the wake. Except during the shedding process, each flow field is composed of well-organized spiral vortex motions.

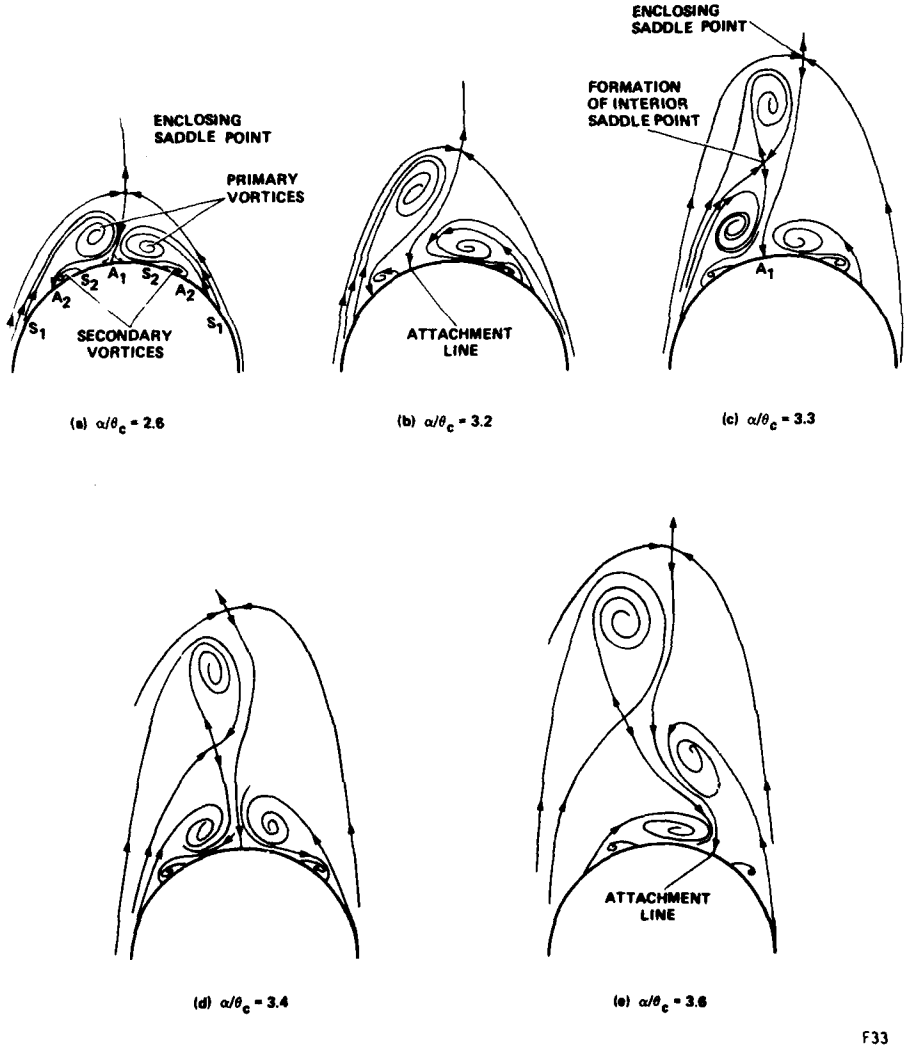

(a) $\alpha/\theta_c = 2.6$

(b) $\alpha/\theta_c = 3.2$

(c) $\alpha/\theta_c = 3.3$

(d) $\alpha/\theta_c = 3.4$

(e) $\alpha/\theta_c = 3.6$

F33

CONCEPTUAL DEVELOPMENT OF ASYMMETRIC LEESIDE VORTEX WAKE STRUCTURE

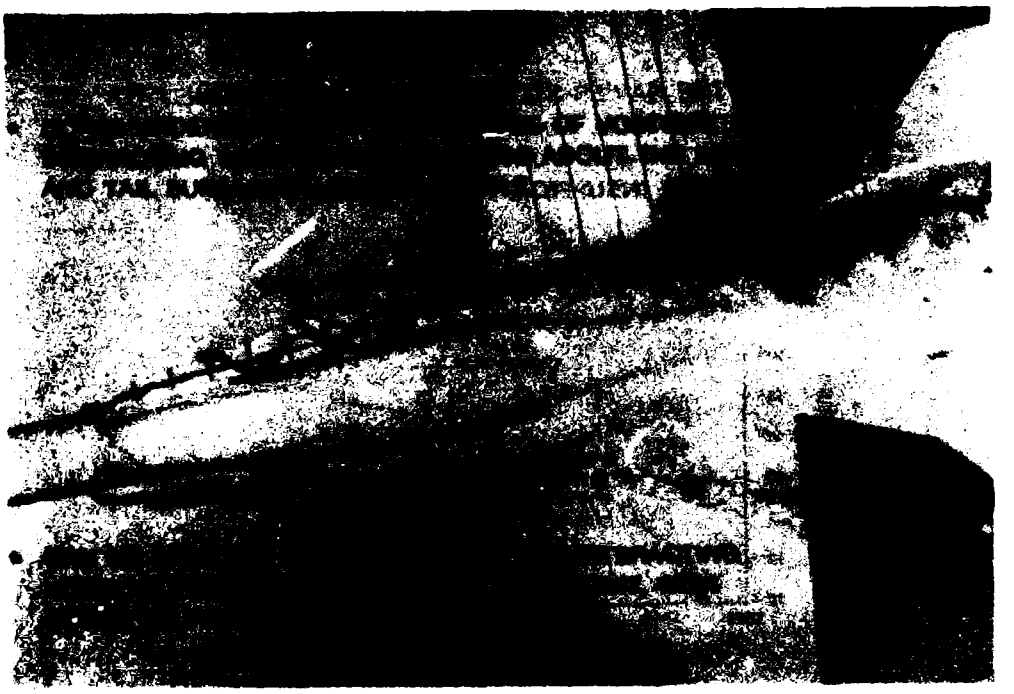

F34

The leading-edge extension, or LEX as it is commonly called, offers the advantage that induced lift, provided by the vortices from the sharply swept edges, can be used beneficially to extend combat-maneuvering capabilities. These benefits can include an elevation in maximum lift that is now available at a higher angle of attack, an improved steadiness in rolling-moment performance, and lower root-mean-square wing-root bending moments, as representative examples. It also appears that in transonic flow, the vortex from the LEX avoids the necessity for the formation of the usual forward branch of the wing shock pattern by providing a "soft" boundary for the flow turning inboard over the leading edge, instead of the "stiff" boundary given by the fuselage side. A substantial discussion by Skow and Erickson on modern fighter-aircraft design for high-angle-of-attack maneuvering is available in Ref. 11.

At low angles of attack, the vortex emanating from a LEX will pass over the wing close to the surface, and farther downstream it will be adjacent to both horizontal and vertical tail surfaces. Wing-flap deflection will, of course, cause a significant downwash to be exerted on the vortex and readjust the position of the vortex relative to the tail. Moreover, the pressure field imposed by the tail may promote vortex breakdown; this may be a significant problem under sideslip conditions. The overall outcome is that both lift characteristics and longitudinal stability can be affected by vortex interaction with the tail surfaces.

At high angles of attack, the horizontal tails have less effect on vortex behavior due to the dominance of the wing pressure field. Several of our current fighter aircraft feature twin vertical-tail arrangements to maintain directional stability in the extended angle-of-attack range attainable with wings that include leading-edge extensions. Improper placement of the vertical tails can promote premature vortex breakdown and thereby limit the maximum lift obtainable, influencing both the longitudinal- and lateral-directional stability levels.

The sharp edge of the LEX fixes the 3D separation line there so that there is controlled flow separation about this component. Tailoring the camber and the sweepback of the LEX will clearly influence the position of the ensuing vortex. Small strakes on the forebody can be beneficial to forcing symmetric vortices to exist at higher angles of attack, but may cause strong effects on the lateral stability. Usually, it is preferable to reshape the cross-section of the forebody into a shark-like snout (see Ref. 11). Control of the orientation of forebody vortices can be implemented by tiny amounts of normal or tangential blowing, emerging into the flow from one orifice asymmetrically disposed with respect to the leeward meridian and initially beneath the vortex that grows rapidly away from the surface. This technique has the ability not only to return the asymmetric flow to a near-symmetric one as the blowing momentum increases but is powerful enough to produce a further movement of the forebody vortices to provide sideforce in the opposite sense to that given by the initial asymmetry. Asymmetric blowing can hence be used as a means of direct sideforce control to prevent departure of a fighter into a spin condition.

ISSUES

- CAN WE USE THE NAVIER-STOKES EQUATIONS, ASSUMED TO GOVERN FLUID MOTION, TO **COMPUTE** VORTICAL FLOWS ABOUT COMPLEX AERODYNAMIC CONFIGURATIONS AT HIGH ANGLES OF ATTACK? **NOT YET; INSUFFICIENT COMPUTING POWER**

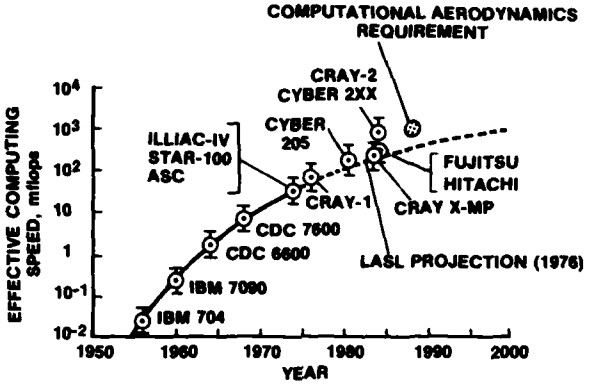

F35

ISSUES

- WITH APPROPRIATE SIMPLIFICATIONS OF THE NAVIER-STOKES EQUATIONS, AND WITH OUR **CURRENT** UNDERSTANDING OF MODELLING TURBULENCE, ARE WE ABLE TO COMPUTE VORTICAL FLOWS ABOUT CHOSEN **AERODYNAMIC** COMPONENTS? **YES, BUT FOR SIMPLE SHAPES ONLY.**

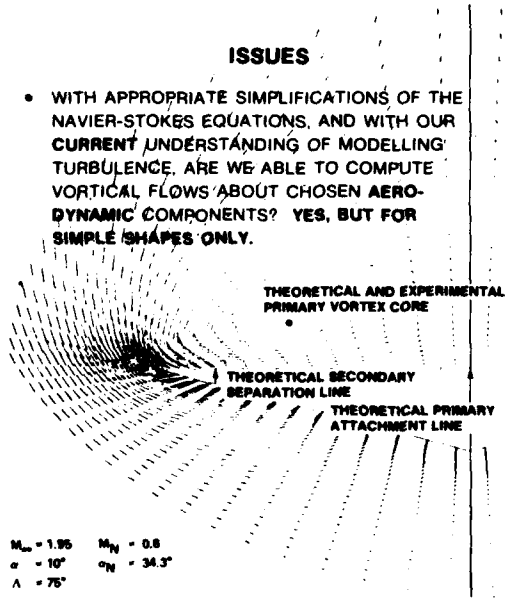

F36

At least one additional order of magnitude in effective computing speed is required for us to be able to come near to analyzing numerically the entire flow about a real aerodynamic vehicle. Nevertheless, some intriguing and impressive results are being and have been obtained from computations of laminar flow fields about simple 3D aerodynamic components using approximate forms of the Navier-Stokes equations (see the review in Ref. 10). Moreover, the potential exists for obtaining satisfactory answers in turbulent flow once appropriate turbulence models can be found. Unfortunately, even these simple shapes must be surrounded with relatively coarse computational meshes; otherwise, the available computer storage on our largest machines becomes saturated. With our present capabilities, we arrive at an impasse. On the one hand, the singular points in the flow and on the body surface usually have simple, fundamental forms and their types, number, and placement, practically characterize a real separated flow. On the other hand, it is just in the vicinity of these singular points that a finite-difference scheme requires inordinately fine mesh spacing to capture their behavior. Even supposing that sufficient computer storage were available for the mesh to be tightened, computation costs would be increased, perhaps to an unacceptable degree. As a way out, we suggest that it may be possible to make a useful advance in the computation of 3D separated flows if finite-difference methods could be combined with a separate treatment (perhaps involving analytic or finite-element methods) of the singular points, thereby obtaining an adequate resolution in the vicinity of the singular points and avoiding very fine meshes.

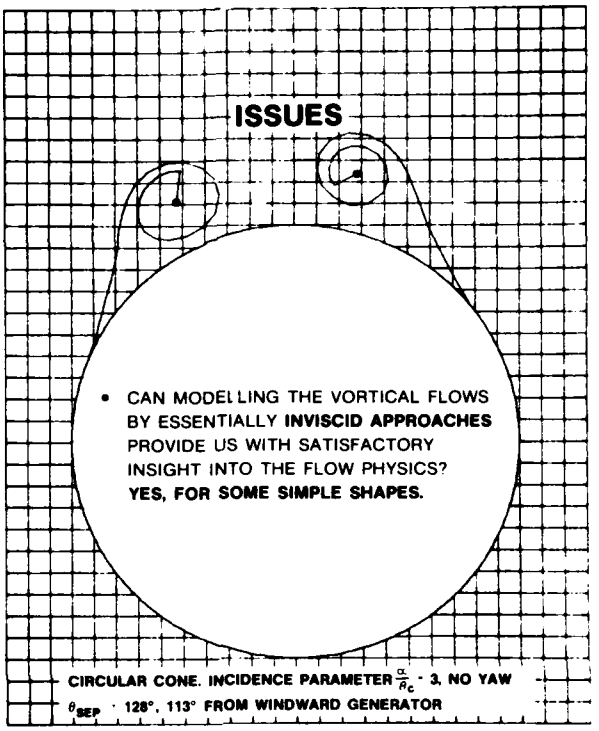

F37

On wings with sharply swept leading edges, 3D separation occurs at the salient edges, being virtually independent of the oncoming boundary-layer properties at the high Reynolds numbers of interest to us. In the limit of infinite Reynolds number – or, for practical purposes, at high enough Reynolds numbers – the coiled viscous shear layer may be modeled approximately by an inviscid-flow vortex sheet. In other words, we adopt a viewpoint similar to that underlying the use of the Kutta-Joukowsky condition for determining flow at the trailing edge in inviscid wing theory. We say that viscosity causes the separation; the location is determined by the edge geometry, after which the flow may be modelled as an inviscid flow. The local behavior of a vortex sheet as it leaves the vicinity of a salient edge is tangential to either the top or underside of the edge, depending on the sign of the shed vorticity and on whether the external mean flow is directed inboard or outboard. In the region of the vortex external to the core, the axial velocity does not change substantially. and we may describe it to a satisfactory degree of approximation by ignoring diffusion (i.e., viscous) effects there. Diffusion is only important in the inner part of the vortex core where there are substantial velocity gradients. For a 3D core growing in space, the swirling fluid is drawn into the core, acquiring a high axial velocity as it escapes along the axis. Reynolds number does not appear to have a significant effect on the development of the large-scale structure of the flow, whereas the core center diminishes as Reynolds number increases. In numerical calculations of incompressible flows about swept edges there seems to be a qualified but free choice available as to whether the vortex sheet should be represented as collections of isolated vortices, as line vortices, or as a continuous sheet. Particular mathematical or numerical difficulties in the stability of the roll-up process have been overcome.

On bodies, the separation location is unknown a priori. We must attempt to calculate its position by 3D boundary-layer theory, which requires an appropriate external flow, or map its position from experimental surface oil-flow visualization. In the former, an iteration between the boundary layer and inviscid flow is required, with a guessed separation-line position, followed by subsequent correction of the inviscid pressure distribution. Once the separation line is supplied, an inviscid vortex sheet model of the separated flow can be invoked (in incompressible flow at least) on which the following boundary conditions will be adequate to determine it completely. The sheet must leave the surface tangentially along the separation line. It is an open vortex sheet in the sense that fluid at the same total pressure wets the vortex sheet on either side. Both pressure and velocity are continuous across the sheet, which is a stream surface. The velocity on the upstream side of the sheet provides the convective component to remove the vorticity from the surface.

On the downstream side of the sheet, replacing the Kutta condition for separation at a sharp edge is the requirement that the velocity be directed downstream tangentially to the separation line. On the upstream side of the separation line, the surface streamlines of the inviscid model are inclined to the separation line but are, of course, still tangential to the wall. The vortex sheet model may be used on simple shapes, such as pointed right-circular and elliptic cones, for which the separation lines are along generators and the coordinate geometry presents few difficulties. On more complex configurations the solution eludes us, for

boundary-layer calculations have not usually been successful in providing separation-line positions, particularly when separation starts some distance back from the nose. Moreover, we still do not have a suitable flow model for the breakaway dividing surface, under conditions where neither conical nor slender body flows exist.

There has been some recent success in numerically solving the Euler equations in which vortex flows around wings of high sweepback angle have been simulated. It appears that if the computed results are to be realistic, the edge must be relatively sharp to ensure that the development of the "shear layer" is virtually insensitive to Reynolds number. This is the only possible way to represent a separated flow field by the Euler equations in which there is artificial viscosity in the numerical scheme.

CONCLUDING REMARKS

A study of the issues involved in the understanding of complex vortical flows leads us to the following remarks:

- We have an unambiguous definition of separation in three dimensions if a separation line is construed to emanate always from a saddle point even in cases where the origin is obscured by lack of resolution.
- The structure and mechanism of separation and the ensuing coiled-up vortical motions are understood in mean-flow terms.
- We are unable at this time to formulate a principle that will distinguish between the scale of vital and unimportant organized vortical structures.
- We are able to exploit the well-organized vortex motions for significant benefit when they are stable.
- We have only conceptual notions to understand the instability mechanisms leading to vortex breakdown and leeside wake asymmetries at high angles of attack.
- We are unable to predict the implications of vortices interacting with local flow fields about the wing and tail surfaces, although we can exercise control over these interacting flow fields to some extent with active or passive control.
- With appropriate simplifications of the Navier-Stokes equations, and with our current understanding of turbulence modelling, we are able to compute vortical flows about chosen aerodynamic components at high Reynolds numbers, but only for very simple shapes.
- Modelling of vortical flows by essentially inviscid approaches can provide us with insight into the flow physics, but our understanding extends only to simple shapes.

REFERENCES

1. Tobak, M. and Peake, D. J., "Topology of Three-Dimensional Separated Flows," Ann. Rev. Fluid Mech., Vol. 14, 1982, pp. 61-85.

2. Peake, D. J. and Tobak, M., "Three-Dimensional Separation and Reattachment," Paper No. 1, AGARD LS-121, 1982.

3. Legendre, R., "Séparation de l'Écoulement Laminaire Tridimensionnel," Rech. Aéro., No. 54, 1956, pp. 3-8.

4. Lighthill, M. J., "Attachment and Separation in Three-Dimensional Flow," in Laminar Boundary Layers, Chap. II, Sec. 2.6, ed. L. Rosenhead, Oxford Univ. Press, 1963, pp. 72-82.

5. Legendre, R., "La Condition de Joukowski en Écoulement Tridimensionnel," Rech. Aérosp., No. 5, 1972, pp. 24-48.

6. Maltby, R. L., "Flow Visualization in Wind Tunnels Using Indicators," AGARDograph No. 70, April 1962.

7. McDevitt, J. B. and Mellenthin, J. A., "Upwash Patterns on Ablating and Non-Ablating Cones at Hypersonic Speeds," NASA TN D-5346, July 1969.

8. Wedemeyer, E., "Vortex Breakdown," Paper No. 9, AGARD LS-121, Dec. 1982.

9. Skow, A. and Peake, D. J., "Control of the Forebody Vortex Orientation by Asymmetric Air Injection: Part A — Application to Enhance Departure Spin Recovery of Fighter Aircraft; Part B — Details of the Flow Structure," Paper No. 10, AGARD LS-121, Dec. 1982.

10. Peake, D. J. and Tobak, M., "Three-Dimensional Interactions and Vortical Flows with Emphasis on High Speeds," AGARDograph No. AG-252, July 1980.

11. Skow, A. and Erickson, G. E., "Modern Fighter Aircraft Design for High Angle-of-Attack Maneuvering," Paper No. 4, AGARD LS-121, Dec. 1982.

12. Peake, D. J. and Tobak, M., "Three-Dimensional Flows about Simple Components at Angle of Attack," Paper No. 2, AGARD LS-121, Dec. 1982.

13. Kutler, P., "A Perspective of Theoretical and Applied Computational Fluid Dynamics," AIAA Paper 83-0037, Jan. 1983.

14. Vigneron, Y. C., Rakich, J. V., and Tannehill, J. C., "Calculation of Supersonic Viscous Flow over Delta Wings with Sharp Subsonic Leading Edges," AIAA Paper 78-1137, July 1978.

15. Fiddes, S. P. and Smith, J. H. B., "Calculations of Asymmetric Separated Flow Past Circular Cones at Large Angles of Incidence," Paper No. 14, AGARD CP-336, 1982.

16. Legendre, R., "Évolution Régulière ou Catastrophique d'Écoulements Permanents Dépendant de Paramètres," Rech. Aérosp., No. 4, 1982, pp. 225-232.

ACKNOWLEDGEMENTS

Frontispiece	Ames-Dryden
F1	Ames-Dryden
F2	Reference 10
F3	Ames-Dryden
F4	Ames-Dryden
F5	Boeing (J. Crowder)
F6	Ames-Dryden
F7	Reference 10 (H. Werlé)
F8, F9	Reference 11
F10, F11, F12	Reference 11
F13, F14	References 9, 10
F15	Ames-Dryden
F16	Ames-North
F17	Ames-North/H. Werlé
F18	Ames-Dryden
F19	Reference 11
F20	Reference 10 (Northrop)
F21	Reference 10
F22	Ames-Dryden
F23	Reference 10 (R. Sedney and C. Kitchens)
F24	Reference 10 (S. Boersen)
F25	References 4 and 5
F26	Reference 10 (H. Werlé)
F27	Reference 6
F28	Reference 7
F29	Reference 12
F30	Reference 11
F31	Ames-North/H. Werlé
F32	Reference 10 (M. Fiechter)
F33	Reference 9
F34	Reference 11
F35	Reference 13
F36	Reference 14
F37	Reference 15

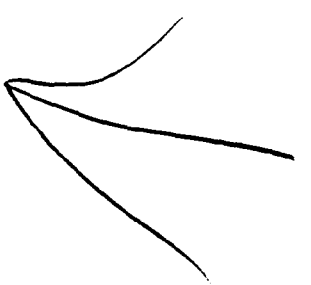

THE VORTEX SKELETON MODEL FOR THREE-DIMENSIONAL STEADY FLOWS

H.G. Hornung

DFVLR Institute for Experimental Fluid Mechanics
D-3400 Göttingen, Bunsenstraße 10, Germany

SUMMARY

The work of Hornung and Perry (1982) is reviewed in which the essential concepts of two-dimensional separation were extended to three-dimensional steady flow, and the vortex skeleton model and electromagnetic analogy were introduced. The model is extended to give a simple topological rule by which the vortex skeleton of a flow can be established from the structure of the wall streamline pattern. The important question of the occurrence of smoothly starting separation without zeros in the wall shear stress, is examined in the light of a new local solution of the Navier-Stokes and continuity equations.

1. INTRODUCTION

Consider steady, incompressible, viscous flow over a simply connected body. Let the flow be uniform at large distances from the body, and let the Reynolds number be large. Vorticity is generated in such a flow by viscous friction mainly in the thin boundary layer at the body surface (wall). This vorticity can be carried away from the wall by viscous diffusion or by convection. At large Reynolds number the latter mechanism is the one that is responsible for carrying vorticity to distances of one ore more characteristic body lengths from the wall.

The distribution of vorticity in the flow field around a body is very important to the aerodynamicist. If it is known, the forces on the body may be determined fairly accurately by a relatively crude inviscid model of the flow. This model can be simplified further if the vorticity concentrates into "ropes" of high vorticity within a relatively small distance from the body. A very descriptive illustration of how this may occur behind a wing was given by Lanchester (1907), see Fig.1. If this occurs, the distribution of vorticity may be represented approximately by a relatively small number of discrete vortices, whose locations and strengths must, of course, be known.

It is not surprising therefore, that a great deal of effort has been invested in the study of the process by which vorticity is transported into the flow field ("separation") and how the vorticity behaves after leaving the surface. An excellent compendium of the work on this subject has been given by Peake and Tobak (1980) (see also Tobak and Peake, 1982). An example of sophisticated numerical work in the latter field is to be found in Saffman (1982) and a description of the field is given by Lugt (1979).

For a calculation of the forces on a body from the disposition of discrete vortices, it is necessary to know their strengths and shapes. An even more basic requirement is the knowledge of the number of vortices which occur and their topological structure. In particular, changes from one to another topological structure of the flow field around the same body are of considerable importance, for example, such as arise in the problems of missile aerodynamics. Such transitions cannot at present be accurately predicted theoretically, and only in relatively simple cases have they been mapped out experimentally. (An example for the case of thick delta wings is given by Szodruch, 1977, see also Szodruch 1980).

The aim of the present paper is not to study the exact geometric modelling of flow fields, but to find a model which will reproduce the topological structure of three-dimensional, steady flows. It should be emphasized that our concern is not merely with the topological structure of the *wall* streamlines (integral curves of the wall shear stress) but with that of the complete three-dimensional flow field. A terminology has been given by Hornung and Perry (1982) which allows the qualitative features of such flow fields to be described unambiguously. This work is briefly reviewed and extended to allow some of the features of the spatial topology of a flow field to be determined systematically from a knowledge of the qualitative features of the wall streamline field. In addition, the question of the occurrence of a gradually beginning three-dimensional separation (i.e. without points at which the wall shear stress is zero) is examined in some detail.

2. TWO- AND THREE-DIMENSIONAL SEPARATION

The essential feature of steady, two-dimensional separated flow is that there exist two half-saddle points in the streamline pattern. They occur on the wall and are joined by one and the same streamline, see Fig.2. The half-saddle points are called separation and reattachment point respectively and the special streamline joining them is sometimes referred to as a separatrix. It separates a region of closed streamlines from the remainder of the flow field. A few accompanying features are that the wall shear stress is zero at the two half-saddle points, and that backflow occurs at the wall between them.

Separation is by no means so easy to describe in three-dimensional flow. The questions that arise are: What is the equivalent of a saddle point in three dimensions? What is the meaning of backflow in three dimensions? The wall shear stress is now a vector. Which component needs to be zero at separation, if any? Finally, what is the equivalent of a separatrix?

The last of these questions gives a clue as to how one might start in extending the concepts of two-dimensional separation to the spatial situation. In two-dimensional flow a stream*line* is able to separate two regions of the space. In three dimensions a *surface* is needed for this purpose. To find the logical extension of the two-dimensional concept of a separatrix to three-dimensional flow, it is therefore necessary to look for a particular stream*surface*. A streamsurface in a given flow field is defined by those streamlines which pass through a given curve in the three-dimensional space. (The concept "streamsurface" is probably more familiar in the form "streamtube", where the defining curve is closed.)

A stream*surface* in a given three-dimensional flow field is only uniquely determined by its defining *curve* if it does not bifurcate anywhere, just as, analogously, a stream*line* in a given two-dimensional flow field may only be uniquely defined by a *point* if it does not bifurcate anywhere. Stream*lines* in two-dimensional flow bifurcate at saddle or half-saddle *points*, i.e. for example at the separation or reattachment point. The logical extension to three dimensions of the separation and reattachment points of two-dimensional flow is therefore to be sought in *streamsurface bifurcation lines* on the wall.

An example of how streamsurface bifurcations may occur in three-dimensional flow is shown qualitatively in Fig.3. From the bifurcation line PQ on the wall, the streamsurface S_1 emerges and rolls up into a vortex. At the same time the streamsurface S_2 divides at the streamsurface bifurcation line P'Q' on the wall. The streamsurfaces S_1 and S_2 respectively emerge from and flow into the three-dimensional analogues of half-saddle points (i.e. streamsurface bifurcation lines) and are therefore the logical extensions of the separatrices of two-dimensional flow. They are the free sheets of the streamsurface bifurcations. The significant difference from the two-dimensional case is that these special streamsurfaces do not in general, form closed regions of the space, i.e. S_1 and S_2 are not the same streamsurface.

These concepts and their implications are discussed at greater length and with mathematical support by Hornung and Perry (1982). Among other results, their work shows that the concept "strength of separation" becomes meaningful in three-dimensional flow, and that complicated topological structures of steady, three-dimensional flow fields may be described unambiguously by the types and disposition of their bifurcation lines and free sheets. They proceed to classify a number of frequently occurring flow configurations.

One of the questions that arose is whether it is necessary for a streamsurface bifurcation line to start at a point where the wall shear stress is zero, or whether it can start gradually, without a zero-shear point. An often-observed example of the former case is shown in the sketch of Fig.4 in which a negative streamsurface bifurcation starts from a saddle in the wall streamline pattern. This pattern also shows a positive bifurcation line starting smoothly, without a zero in the wall shear stress. (The notation "positive" means that the streamsurface divides into two in the direction of flow and vice versa.) Experiments certainly suggest that both smooth and zero-shear beginnings of bifurcation lines are possible. This question is examined in more detail in section 4.

3. THE VORTEX SKELETON MODEL

While the qualitative features of the structure of a steady three-dimensional flow may be described unambiguously by the bifurcating streamsurfaces of the flow, such descriptions become extremely cumbersome except for the simplest configurations. If only the qualitative features are to be described, an equally effective and much simpler method consists of representing the flow field by a finite number of discrete vortices in a uniform flow. The validity of this model depends on the assumption that any distributed vorticity that may be present does not alter the spatial topology of the flow.

In order to illustrate the two methods, a number of frequently observed flow situations are presented in Fig.'s 5,6,7 and 8 taken from Hornung and Perry (1982). Fig.5 shows simple U-shaped separation by means of the bifurcating streamsurfaces that occur. Figures 6,7 and 8 show the flow structure that sometimes occurs at sting-body junctions using both methods. This last example makes the superiority of the vortex skeleton method particularly clear. Only six discrete vortices are needed (see Fig.8) to present the topology of the flow field, in which a total of 18 free sheets of 12 streamsurface bifurcations occur. (Bifurcations that occur in the flow field, i.e. not at the wall, generally have four free sheets.) Clearly, it becomes extremely difficult to present the latter in a sketch, see Fig.7, while the presentation of the vortex skeleton of Fig.8 is relatively simple and provides corresponding information.

The assumption that all the vorticity of the flow is concentrated into discrete vortices is, of course, incorrect. However, the aim here is to represent only the topology of the flow correctly. This means, for example, that the number and connectivity of the nodes, saddles and bifurcation lines of the wall streamline pattern are

to be correctly reproduced. It turns out that, whenever a pair of such critical points (node and saddle) occurs on the wall, it is associated with a concentration of vorticity in the vicinity. For example, in the U-shaped separation of Fig.5, one such node-saddle pair occurs in the wall streamline pattern (A, F). This is associated with the vortex formed by the rolling up of the streamsurface S_1. The converse is not necessarily the case, i.e. a vortex may be so weak and distant from the wall that it does not cause a saddle-node pair to occur on the wall. However, since our interest is in the vorticity that is spilt into the flow from the boundary layer, such vortices need not concern us. A more important way in which a vortex might occur without a saddle-node pair on the wall is through a gradually starting negative streamsurface bifurcation, similar to that proposed schematically in Fig.3. Supposing for the present (see also section 4) that such smoothly starting bifurcations are possible, it is a relatively simple matter to establish the following topological rule:

The minimum number of discrete vortices required to represent the spatial topology of uniform flow over a simply connected body is given by the equality limit of the inequality

$$V \geqslant P + S, \qquad (1)$$

where V is the number of vortices, P is the number of saddle-node pairs in the wall streamline pattern, and S is the number of those negative streamsurface bifurcations in the wall streamline pattern which do not start at a saddle point.

Consider, for example, the flow of Fig.6. The wall streamline pattern contains six saddle-node pairs and all negative streamsurface bifurcations on the wall start from saddle points. Thus, P = 6, S = 0, so that six vortices are needed to present the topological structure of the flow, see Fig.8. The fact that the body is chopped off at front and back means only that, were it closed, two additional nodes (e.g. front and rear stagnation point) would occur in the wall streamline pattern. The vortex skeleton model of a particular flow, for which the wall streamline pattern is known, can thus be established systematically by arranging the number of vortices prescribed by the rule (1) appropriately.

A large amount of distributed vorticity always resides in the boundary layer near the wall. However, the presence of this distributed vorticity does not introduce topological features such as nodes, saddles or bifurcation lines in the wall streamline pattern except through the formation of a vortex, i.e. by distributed vorticity concentrating into discrete bundles. Thus, the topological structure of the wall streamlines is not affected by the distributed vorticity in the boundary layer, but is correctly reproduced by the vortex skeleton model with the assumption that the flow outside the vortex cores is irrotational. The exact shape of the wall streamlines is, of course, influenced by the distributed vorticity, but their topological structure is not.

Such a model can be simulated directly by the electromagnetic analogy, in which the vortices are replaced by wires carrying electric current, so that the induced magnetic field corresponds to the velocity. The uniform flow field can be simulated by a current-carrying solenoid coil generating a uniform magnetic field within itself. Solid surfaces, at which the velocity must be tangential in the fluid mechanical analogue, can be simulated for a plane wall by the method of images, i.e. by introducing a mirror image of the vortex system on the opposite side of the "wall". In order to show the wall streamlines, for example, iron filings may be scattered on it and exposed to the magnetic field. The electric current carried by a wire corresponds to the strength of the simulated vortex.

In order to illustrate the use of the method, Fig.9 shows sketches of six types of symmetrical wall streamline patterns occurring in separated flows, together with their simulation by the electromagnetic analogy. In each case the topological rule, equation (1), is satisfied. In Fig.9f the two vortices have to disperse into "boundary-layer vorticity" at their leading end. In the electromagnetic analogy this has been achieved by joining the two wires with a copper plate parallel to and near the surface. It could also be achieved by joining the two wires at their upstream end with a wire which is far from the wall. Such connections (far from the surface or with distributed currents) are disregarded in counting the number of vortices for the purpose of equation (1). I.e. V = 2 for Fig.9f.

In some of these simulations the experiment was embedded in an overall field which converges near the wall in order to simulate the situation on the lee side of a slender body. This was achieved by two additional vortices flanking the region of interest. Equation (1) is not violated by this step because of the inequality sign which allows for such weaker or more distant vortices.

4. GRADUALLY STARTING SEPARATION

In this section the question is examined as to whether it is possible for a negative streamsurface bifurcation line to start forming gradually at a wall, without the wall shear stress becoming zero anywhere. It is necessary to discuss this question because this kind of separation is certainly observed experimentally (see e.g. Kreplin, Vollmers, and Meier, 1982) as well as numerically (see e.g. Wang, 1982) while at the same time it has been the cause for some dispute (see e.g. Wang, 1981).

In order to illustrate the fact that experiment certainly suggests that this is so, consider the two surface oil flow pictures of Fig.10. Fig.10a shows two negative bifurcation lines issuing from two saddle points of the wall streamline pattern, i.e. from points where the wall shear stress is zero. On the other hand, Fig.10b shows two negative bifurcation lines which start smoothly, without a saddle. Similar effects may, of course, also be produced by the electromagnetic analogy (see Fig.9).

The transition from the flow type of Fig.10a to that of Fig.10b may be imagined as follows: Consider a vortical node and a saddle in the wall streamline pattern to be embedded in a region, in which the wall shear stress falls smoothly in the flow direction. Let them be separated by a distance d. Consider the magnitude T of the wall shear stress. Fig.11a gives a sketch of the wall streamlines in such a situation. Fig.'s 11b and c show how this pattern is expected to change as the distance d is reduced to zero. At the same time these figures show profiles of T along the lines joining the critical points. Fig.11d shows how this process may be extrapolated to the case where the shear stress no longer quite reaches the value zero and the bifurcation line starts smoothly.

A method by which the flow in the vicinity of critical points or bifurcation lines may be studied theoretically, is to seek local solutions of the Navier-Stokes and continuity equations by expanding the velocity vector in a Taylor series in terms of the position vector, see Perry and Fairlie (1974), Hornung and Perry (1982). Usually, only the first term in this series is retained, as the number of terms in each component increases rapidly with each new vector term. Such solutions give asymptotic approximations which converge within a region of validity $r < R$ around the point $r = 0$, see Fig.12, the error being of the next higher order in $r = \sqrt{x^2 + y^2 + z^2}$ than the last retained term.

Recently Perry (1983) obtained such a solution to a particular degenerate case which has the following form:

$$\begin{aligned} u &= -exy^2z + 0(r^5) \\ v &= fyz + gz^2 + ex^2yz + 0(r^5) \\ w &= -fz^2/2 - ex^2z^2/2 + ey^2z^2/2 + 0(r^5) \\ p/\mu &= -ex^2z + ey^2z + 2gy - fz + p_o/\mu + 0(r^4), \end{aligned} \tag{2}$$

where u, v, w are the x, y, z - components of velocity p and μ are pressure and viscosity and e, f, g and p_o are constants. For a particular choice of the constants e, f and g, namely $e > 0$, $f < 0$, $g = 0$, this solution is sketched in Fig.13. As can be seen this has the character of almost two-dimensional separation. A feature of equation (2) is that the inertia terms in the Navier-Stokes equation are unimportant to this approximation, the pressure being determined entirely by the viscous terms.

At first glance, the flow of Fig.13 does not seem to have any relevance to our problem. However, it may be seen with a little imagination, that superposition of a plane shear flow of the form

$$u = kz \tag{3}$$

will produce a wall streamline pattern similar in character to that to be expected near the beginning of a negative bifurcation line. Naturally, one cannot just superpose solutions in this nonlinear system of differential equations. Indeed, it turns out that the term in (3) causes an additional term in u to become necessary, which, this time, arises from the inertia terms. The new form of u is thus:

$$u = -exy^2z + kz - kfz^4/(24\nu) + 0(r^5), \tag{4}$$

where ν is the kinematic viscosity. The other components of velocity and the pressure are not affected by these additional terms. The solution (2) with u replaced by (4) represents an asymptotic approximation satisfying the Navier-Stokes and continuity equation and the no-slip conditior at $z = 0$, to the stated accuracy.

Choosing $f < 0$, $e > 0$, $k > 0$ and setting $g = 0$, $a^2 = -f/e$, $b^3 = k/e$, the equation for the wall streamlines becomes ($z = 0$)

$$\frac{dy}{dx} = \frac{v}{u} = \frac{y\,(x^3 - a^3)}{b^3 - xy^3}. \tag{5}$$

This pattern has two critical points (which are vortical nodes in the parameter range of interest here, namely if $b^3/a^3 < 16$) at

$$(x, y) = (a, \pm\sqrt{b^3/a}). \tag{6}$$

These lie outside the range of validity of the solution. The solution of equation (5) with $a = 0.5$, $b = 0.5$, is presented in Fig.14. As can be seen, the nature of this solution is like that expected for a gradually beginning bifurcation. Of course, this local solution does not only give the wall streamlines, but the whole three-dimensional flow field near the beginning bifurcation. It gives mathematical support to the

supposition made in section 3, that negative streamsurface bifurcations may begin smoothly. The wall shear stress is not zero anywhere in this solution.

5. CONCLUSIONS

The work of Hornung and Perry (1982) has been reviewed, in which the essential concepts of two-dimensional separation had been extended logically to three-dimensional steady flow, and the vortex skeleton model and electromagnetic analogy had been introduced. A simple topological rule has been given, by which the minimum number of vortices necessary to represent a flow over a simply connected body with a given wall streamline pattern may be determined. It has been shown that the electromagnetic analogy is usually sufficiently accurate to represent the topological structure of a flow pattern, distributed vorticity being unable to introduce topological features such as nodes, saddles or bifurcations. Finally a local solution of the Navier-Stokes and continuity equations has been obtained, by extending a solution given by Perry (1983), which has all the features of a gradually beginning streamsurface bifurcation, with everywhere finite wall shear stress.

6. ACKNOWLEDGEMENTS

Most of this work has resulted from joint work and discussions with Dr.A.E. Perry of the University of Melbourne. The only reason why he is not a co-author is that my production of the manuscript has been too slow for us to communicate about it between Germany and Australia. I would also like to thank Dr. Bippes, Dr. Dallmann and Professor E. Becker for many fruitful discussions.

7. REFERENCES

Bippes, H. to be published, 1983

Hornung, H. and Perry, A.E., "Streamsurface Bifurcation, Vortex Skeletons and Separation", DFVLR IB 222-82 A 25, 1982

Kreplin, H.-P., Vollmers, H. and Meier, H.U., "Measurements of the Wall Shear Stress on an Inclined Prolate Spheroid", ZFW Vol.6, 1982, pp. 248-252

Lanchester, F.W., "Aerodynamics", London, 1907, Fig.86

Lugt, H.J., "Wirbelströmung in Natur und Technik", Braun, Karlsruhe, 1979

Peake, D.I. and Tobak, M., "Three-Dimensional Interactions and Vortical Flows with Emphasis on High Speeds", AGARD-AG-252, 1980

Perry, A.E. to be published, 1983

Perry, A.E. and Fairlie, B.D., "Critical Points in Flow Patterns", Advances in Geophysics B 18, 1974

Saffman, P.G., "Structure and Stability of Streets of Finite Vortices", in "Vortex Motion" ed. H.G. Hornung and E.-A. Müller, Vieweg, Braunschweig, 1982, p.142

Szodruch, J., "Leeseiten-Strömung bei schlanken Deltaflügeln endlicher Dicke", Institut für Luft- und Raumfahrt, TU Berlin, Rept. 23, 1977

Szodruch, J., "Experimental Study of Viscous Leeside Flow over a Slender Delta Wing", NASA TM 21248, 1980

Tobak, M. and Peake, D.I., "Topology of Three-Dimensional Separated Flows", Annual Reviews of Fluid Mechanics Vol. 14, 1982, pp. 61-85

Wang, K.C., "New Developments about Open Separation" AE & EM TR-82-02, San Diego State University, 1982

Wang, K.C., "On the Current Controversy about Unsteady Separation" in "Numerical and Physical Aspects of Aerodynamic Flows", ed. Tuncer Cebeci (1981) pp. 280-367

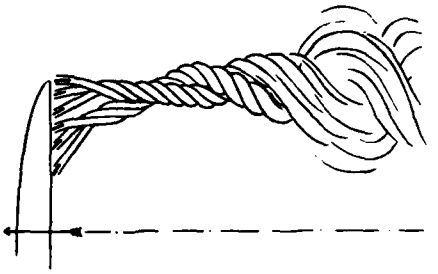

Fig.1: Lanchester's (1907) sketch of vorticity being concentrated into a vortex rope behind a wing.

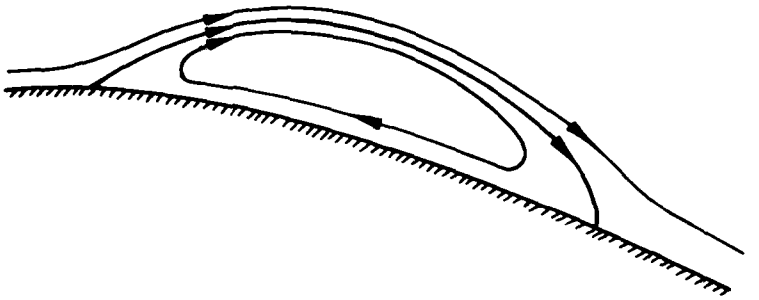

Fig.2: In two-dimensional, steady-flow separation, two half-saddle points occur at the wall. They are joined by a streamline which separates a region of closed streamlines from the rest of the flow field.

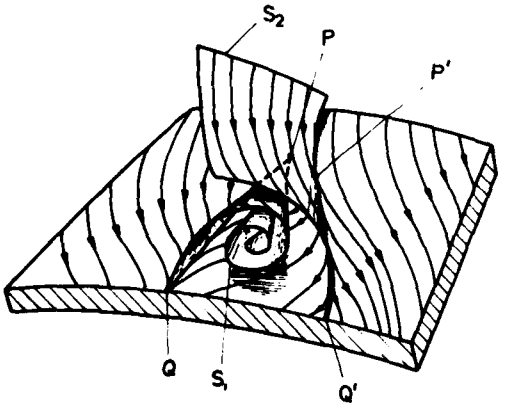

Fig.3: Example of three-dimensional separation. The free sheet S_1 of the negative streamsurface bifurcation line PQ is not the same as the free sheet S_2 of the accompanying positive bifurcation line P'Q'.

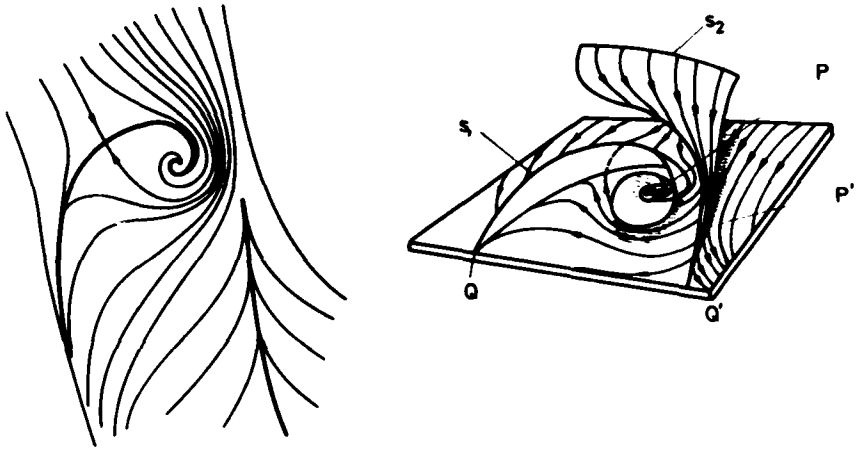

Fig.4: Example of three-dimensional separation in which the negative streamsurface bifurcation starts from a saddle point in the wall streamline pattern. At the same time the accompanying positive bifurcation line P'Q' starts without a critical point a) wall streamline pattern, b) perspective sketch.

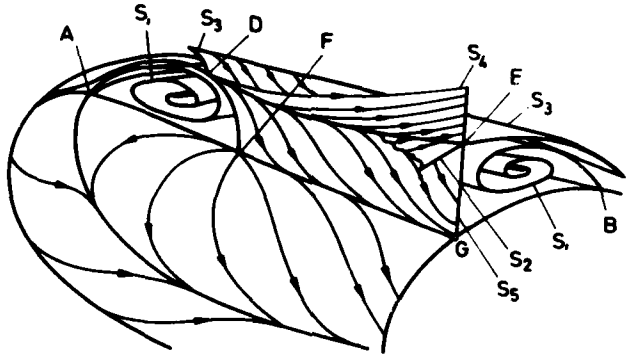

Fig.5: Simple U-shaped separation, port side showing wall streamline pattern, starboard side showing perspective sketch. Apart from a negative bifurcation AB, a double free bifurcation DE and a positive bifurcation FG occur. Of the five free sheets S_1 is the only one that rolls up into a vortex.

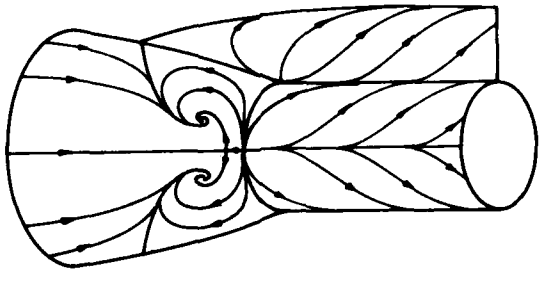

Fig.6: Wall streamline pattern and one of the free sheets of the separation pattern sometimes observed at sting-body junctions of axisymmetric bodies at zero incidence.

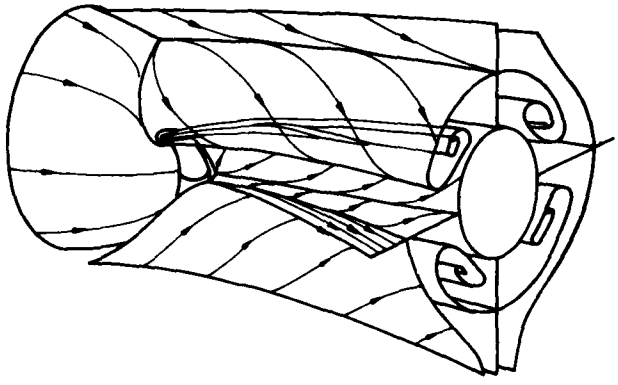

Fig.7: It becomes extremely difficult to sketch the 12 bifurcation lines and their 18 free sheets in the case of "sting-body" separation.

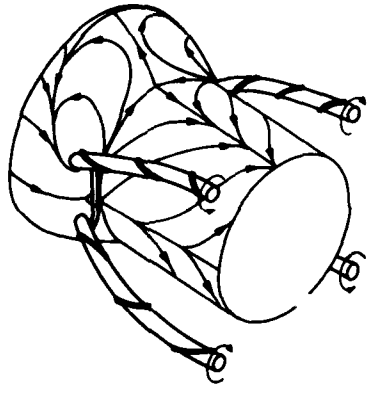

Fig.8: Equivalent information as that of Fig.7 can be conveyed more easily and more effectively with a presentation of the vortex skeleton of the flow, shown here together with the wall streamline pattern.

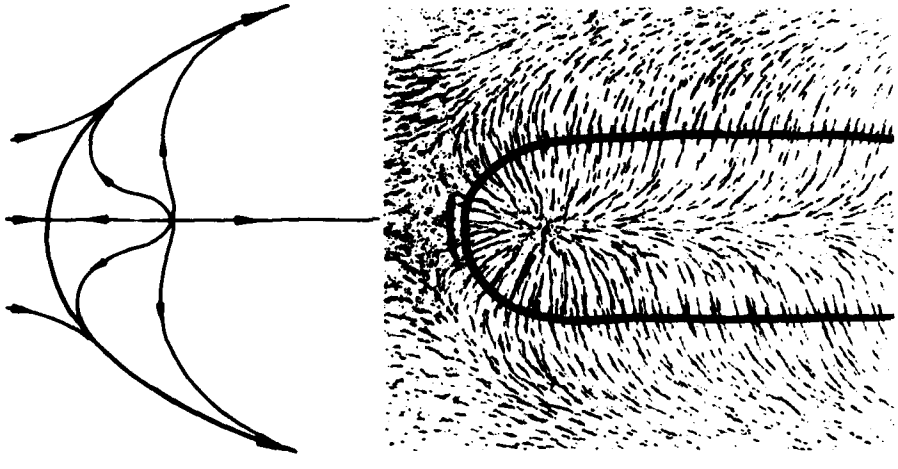

Fig.9a: Wall streamline pattern for simple U-shaped separation, sketch and electromagnetic simulation. One saddle-node pair occurs, all negative bifurcations start at saddles, i.e. P=1, S=0. Hence $V \geq 1$. One vortex only is needed in the skeleton.

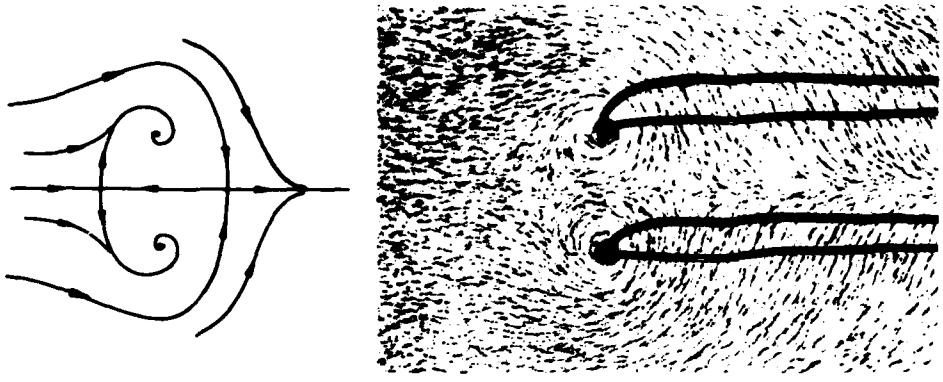

Fig.9b: Owl-face pattern of the first kind. P=2, S=0 so that V⩾2. The two vortex-wires cast shadows onto the wall. Only two wires were used.

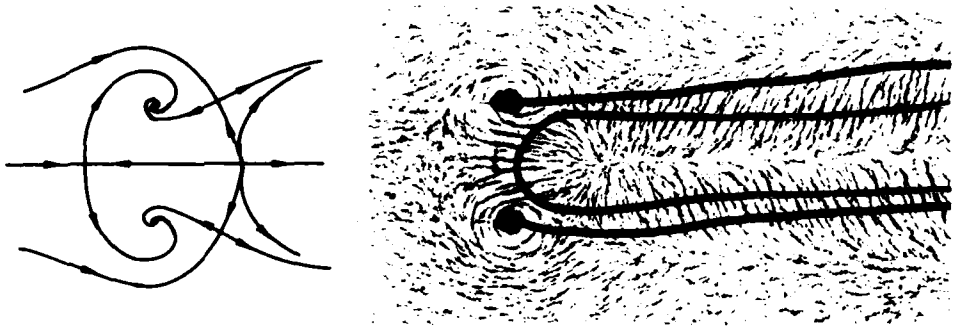

Fig.9c: Owl-face pattern of the second kind. P=3, S=0. so that V⩾3.

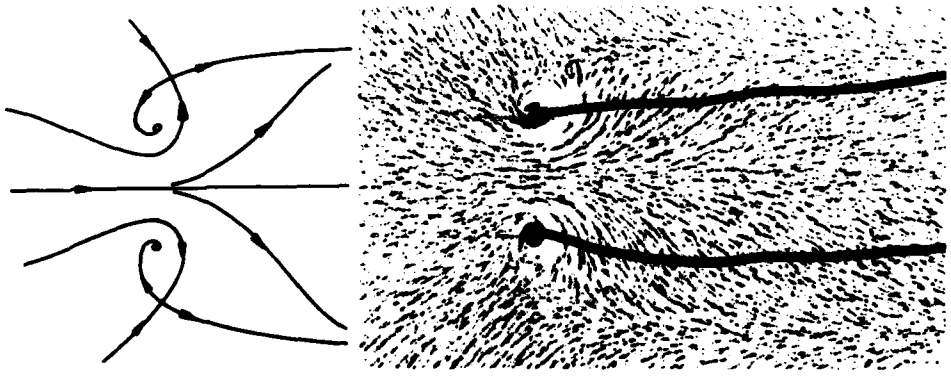

Fig.9d: Owl-face pattern of the third kind (Werlé-Legendre separation). P=2, S=0, so that V⩾2.

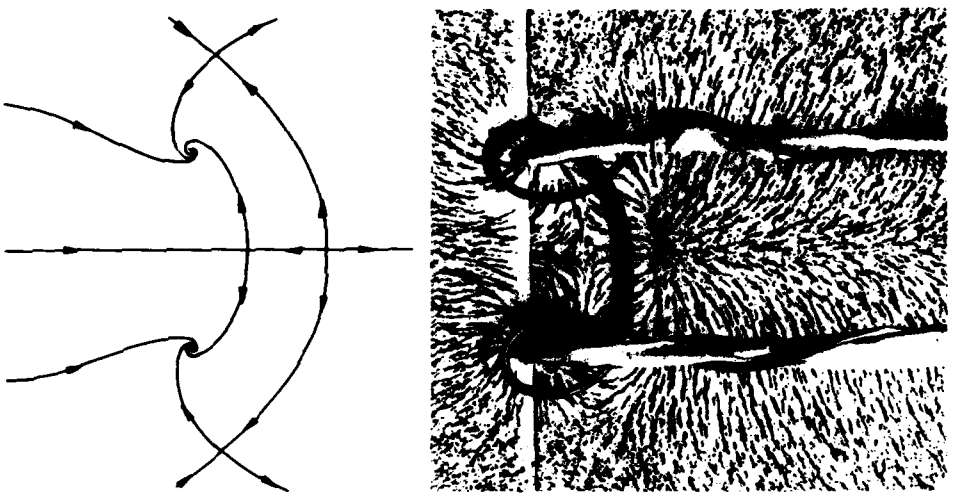

Fig.9e: Owl-face pattern of the fourth kind. P=3, S=0, so that V⩾3.

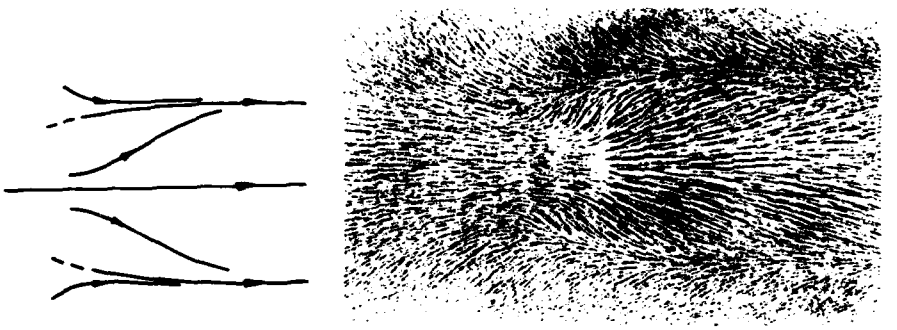

Fig.9f: Separation with two smoothly-beginning negative bifurcation lines. No critical points occur on the bifurcation lines. P=0, S=2, i.e. V⩾2.

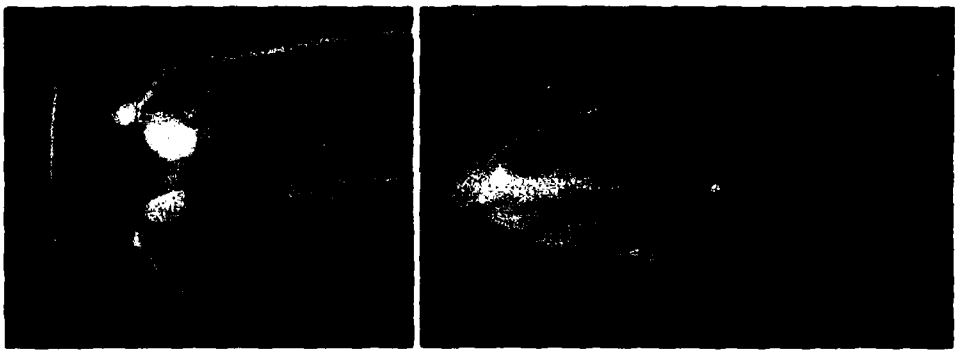

Fig.10: Examples of surface oil flow visualization photographs showing bifurcation lines starting with and without a point of zero wall shear stress. From Bippes (1983), and Kreplin, Vollmers and Meier (1982) respectively.

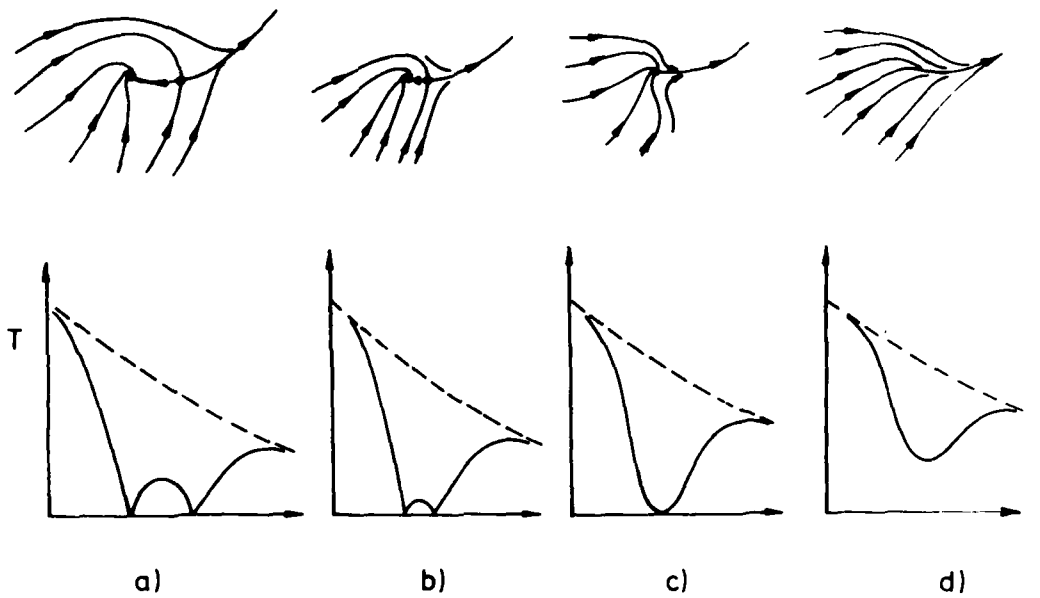

Fig.11: Bifurcation line starting from a saddle-node pair: As the distance between the saddle and node is reduced to zero (a-c) the degenerate case c) results, where the magnitude of the wall shear stress, T, just reaches zero. Fig.11d) shows that, when this process is extrapolated, the smoothly starting bifurcation line results, in which T does not reach zero any more.

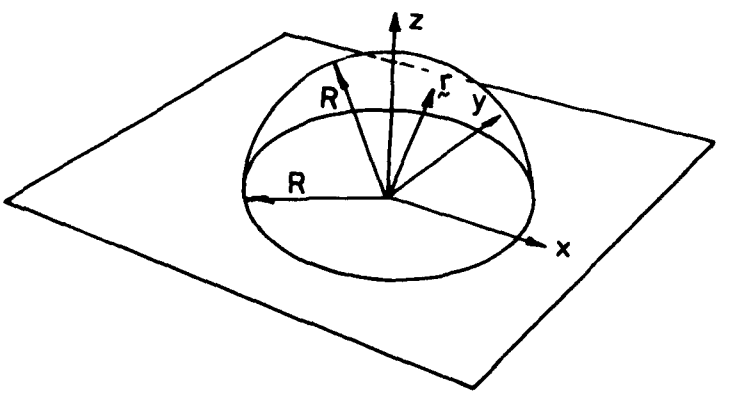

Fig.12: Local cartesian coordinate system illustrating region of convergence.

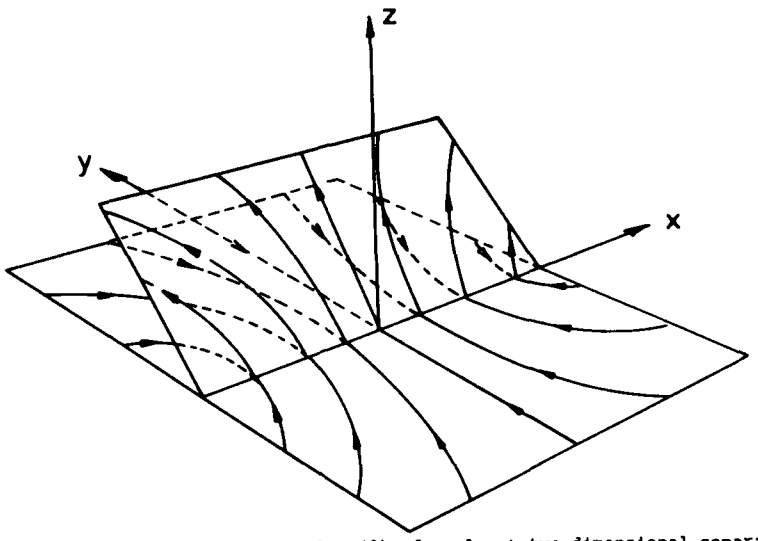

Fig.13: Perry's (1983) solution equation (2), for almost two-dimensional separation. The plane z=0 is the wall. The streamlines in the plane of symmetry (x=0) are those of two-dimensional separation.

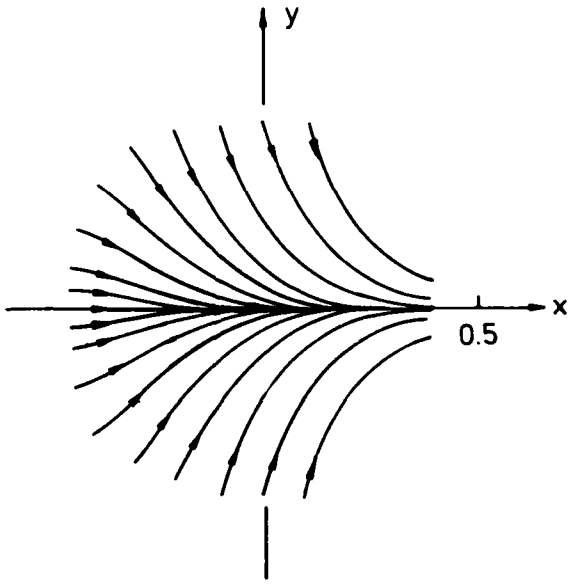

Fig.14: Wall streamlines near the beginning of a smoothly starting negative bifurcation line; numerical integration of equation (5) with a=0.5, b=0.5.

ON THE STRUCTURE OF THE TURBULENT VORTEX

by

Leonard Roberts
Joint Institute for Aeronautics and Acoustic
Durand Bldg Room 269
Stanford University
Stanford, CA 94305
USA

SUMMARY

This paper provides an analysis that describes the trailing vortex generated by a lifting surface, the structure of its turbulent core and the influence of axial flow within the vortex on its initial persistence and on its subsequent decay. Similarity solutions of the turbulent diffusion equation are given in closed form and results are expressed in sufficiently simple terms that the influence of the lifting surface parameters on the length of persistence and the rate of decay of the vortex can be evaluated readily.

SYMBOLS

A	wing reference area
AR	aspect ratio b^2/A
b	aircraft wing span
b_1	distance between vortices
C_D	induced drag coefficient
C_L	lift coefficient
c	$2\pi r/k^2\Gamma_1$
d	characteristic length of vortex persistence
e	wing lifting efficiency, $C_L^2/\pi ARC_D$
G	$= \frac{\Gamma}{\Gamma_1}$
k	constant, 0.06
l	outer edge of turbulent core
Re	$Ub/\nu AR$
r	distance in radial direction
s	lift distribution parameter, $\int_0^1 \frac{\Gamma}{\Gamma_1} dY$
S	$=\sinh(4s^2/e - 11/12)$
V	velocity function
V^*	maximum value of V
v_θ	circumferential velocity
x	distance in axial direction
$\bar{x}$	x/d
Y	$=y/(b/2)$
y	distance in spanwise direction
z	$=r/r_1(x)$
z^*	$(\frac{4}{3}log\frac{1}{c})^{\frac{1}{3}}$
Γ	circulation
ϵ	coefficient of eddy viscosity
ν	coefficient of kinetic viscosity
ρ	density

1. INTRODUCTION

The structure of the wake vortex generated by a lifting surface such as an aircraft wing or a rotor blade has been the subject of much previous study, both theoretical and experimental (see for example ref. 1-4). The trailing vortex, after its initial formation is known to comprise two phases, namely (1) a region of persistence for long distances compared to the wing span and (2) a region of decay in which the circumferential velocity is reduced, and the vortex diffuses radially with increasing distance (fig. 1). In this regard it is of particular interest to understand the structure of the vortex in sufficient detail to predict the velocity distribution in the vortex, to explain the initial persistence, and characterize its subsequent rate of decay in terms of the aerodynamic properties of the lifting surface.

2. ANALYSIS

The Potential Flow

The potential flow due to a vortex pair has been analyzed by Spreiter and Sachs (ref 1). In their approach the vortices are considered as a pair of rotating cylinders around which a potential flow exists in the plane normal to the axis of the vortices. The relevant expressions which relate the characteristics of the wing to those of the vortex pair are derived here, for completeness, as follows.

The lift is expressed as

$$L = \frac{1}{2}\rho U^2 C_L A = \rho U b \Gamma_1 \int_0^1 G dY. \tag{1}$$

where Γ_1 is the circulation at the root, $G = \frac{\Gamma}{\Gamma_1}$ is the spanwise distribution of lift, and $Y = \frac{2y}{b}$ is the dimensionless spanwise distance.

The integral in equation (1) is denoted by

$$\int_0^1 G dY = s \tag{2}$$

s is a parameter which characterizes the lift distribution.

The vortex sheet behind the wing rolls into a cylindrical vortex, the inner part of the cylinder containing the vorticity shed from the tip and the outer part containing that shed from the root; thus Γ_1 is the strength of the vortex at its outer edge r_1.

From equation (1), Γ_1 may be written

$$\Gamma_1 = U \frac{b}{2} \frac{C_L}{AR} \cdot \frac{1}{s} \tag{3}$$

where the aspect ratio is $AR = b^2/A$.

Following further the Spreiter-Sachs analysis, the induced drag is related to the rate of formation of rotational kinetic energy in the wake. This relationship is written

$$D = \frac{1}{2}\rho U^2 C_D A = \int\int \frac{1}{2}\rho v_\theta^2 dS' \tag{4}$$

where the integral is performed over the entire plane normal to the direction of flow.

Equations (1) and (4) can be combined to given an expression which relates the energy integral to the wing efficiency

$$\int\int \left(\frac{v_\theta}{\Gamma_1}\right)^2 dS' = \frac{4s^2}{e} \tag{5}$$

where $e = \frac{C_L^2}{\pi AR C_D}$ is the wing efficiency factor.

The integral in equation 5 has contributions from the potential flow outside the vortex pair and from the vortex pair itself; thus

$$\int\int \left(\frac{v_\theta}{\Gamma_1}\right)^2 dS' = \left[\int\int \left(\frac{v_\theta}{\Gamma_1}\right)^2 dS'\right]_{pot} + \frac{1}{\pi}\int_0^{r_1} \left(\frac{\Gamma}{\Gamma_1}\right)^2 \frac{dr}{r} \tag{6}$$

where the substitution $v_\theta = \frac{\Gamma}{2\pi r}$ has been made within the vortex pair.

The contribution from the potential flow is evaluated in closed form and may be written

$$\left[\int\int \left(\frac{v_\theta}{\Gamma_1}\right)^2 dS'\right]_{pot} = \frac{1}{\pi}\sinh^{-1}\frac{b_1}{2r_1} \tag{7}$$

where b_1 is the separation distance between the vortices. The contribution from the vortex pair must be evaluated from the radial distribution of $\frac{\Gamma}{\Gamma_1} = G$ within the vortex. This contribution is found by solving the turbulent flow equations and, as seen later, gives

$$\int_0^r \left(\frac{\Gamma}{\Gamma_1}\right)^2 \frac{dr}{r} = \frac{11}{12} \tag{8}$$

Substitution of (6), (7), and (8) into (5) gives an expression for r_1,

$$r_1 = \frac{b_1}{2} S^{-1} \tag{9}$$

where $S = \sinh(4s^2/e - 11/12)$

The relationship (9) between the vortex radius r_1 and the separation distance b_1 will hold even when r_1 varies with the distance x along the vortex since the flux of rotational energy must be constant and equal to the induced drag at all values of x.

A determination of the separation distance b_1 between the vortices requires that an additional condition be prescribed. It is assumed that the centroid of vorticity is conserved during the roll-up process and thus the initial spanwise separation of the vortex is given by

$$\frac{b_1(0)}{2} = \frac{b}{2}\int_0^1 Y dG = \frac{b}{2}s$$

(after integration by parts).

The initial radius of the vortex is

$$r_1(0) = \frac{b}{2} s S^{-1} \tag{10}$$

The initial vortex radius $r_1(0)$ and the circulation Γ_1, given by equation (3) are important parameters in the description of the turbulent core of the vortex as seen in the following analysis.

The Turbulent Vortex Core

For any location x downstream of the lifting surface the characteristics of the vortex will be influenced by turbulence and, to a lesser degree, by kinematic viscosity. There will exist a core within which the circumferential velocity will differ from that given by the potential flow (fig. 2). This vortex core flow can be described by a differential equation expressing the transport of angular momentum as follows:

$$u\frac{\delta G}{\delta x} + v\frac{\delta G}{\delta r} = \frac{r\delta}{\delta r}\left[(\nu + \epsilon)\frac{1}{r}\frac{\delta G}{\delta r}\right] \tag{11}$$

where ν is the kinematic viscosity and ϵ is a turbulent eddy viscosity.

The eddy viscosity for vortex flows has been investigated by Hoffman and Joubert (ref 5) and a model formulated in a way analogous to the traditional mixing length theory of Prandtl. A dimensional analysis suggests that the eddy viscosity is related to the circumferential shear stress through the relationship

$$\epsilon = k\left(\frac{\tau}{\rho}\right)^{\frac{1}{2}} r$$

where

$$\frac{\tau}{\rho} = \epsilon\left(\frac{\delta v_\theta}{\delta r} + \frac{v_\theta}{r}\right)$$

which may be combined to give

$$\epsilon = k^2 r \frac{\delta}{\delta r}(r v_\theta) = \frac{k^2 \Gamma_1}{2\pi} r \frac{\delta G}{\delta r} \tag{12}$$

where the constant k must be determined experimentally. The value $k = 0.06$ appears to fit the experimental data.

When equation (12) is substituted into equation (11) the result is written

$$u\frac{\delta G}{\delta x}+v\frac{\delta G}{\delta r}=\frac{k^2\Gamma_1}{2\pi}r\frac{\delta}{\delta r}\left[\left(c+r\frac{\delta G}{\delta r}\right)\frac{1}{r}\frac{\delta G}{\delta r}\right] \tag{13}$$

where

$$c=\frac{2\pi\nu}{k^2\Gamma_1}=\frac{4\pi}{k^2}\frac{\nu AR}{Ub}\frac{1}{C_{L\alpha}}$$

(substituting for Γ_1 from equation (3)).

The quantity c is seen to vary inversely with the Reynolds number $\frac{U}{\nu}\frac{b}{AR}$ based on a characteristic chord length, $\frac{b}{AR}$. For a typical aircraft wing c is of the order of 10^{-2} or 10^{-3} and the effects of kinematic viscosity on the overall wake characteristics are negligible. However, in the region close to the center of the vortex (where $r\frac{\delta G}{\delta r}<c$) the effect of viscosity will change the local velocity gradients significantly, creating a "laminar sub-core".

Equation 13 must be solved for the distribution $G(r)$ subject to appropriate boundary conditions, and using suitable approximate expressions for u and v, the convective velocity components. Two cases are considered here corresponding to the region of persistence, where the vortex remains tightly rolled, and the region of decay where the vortex increases its radius and decreases its circumferential velocity with distance along the vortex.

(1) Region of Persistence: Immediately behind the wing it is to be expected that the axial velocity u in the vortex core will be less than the free stream value, U but must accelerate to this value in a distance d say. The velocity components along and normal to the centerline of the vortex may be approximated as

$$\frac{u}{U}=\frac{x}{d},\quad \frac{v}{U}=-\frac{1}{2}\frac{r}{d}\quad for\ \ x<d$$

satisfying the equation of continuity.

The accelerating flow along the axis (see fig. 3a) causes a radial inflow which in turn convects vorticity inward to balance the outward diffusion by turbulence. This causes the vortex to remain tightly rolled until the axial velocity returns to its free-stream value and the inflow ceases.

(2)Region of Decay: At far distance behind the wing where the axial velocity has recovered to the free stream value

$$\frac{u}{U}=1,\frac{v}{U}=0\quad \text{for}\ \ x>d.$$

Here (see fig. 3b) there is no radial inflow but radial diffusion is balanced by axial convection resulting in a spreading of the vortex and as will be seen, a decay in the circumferential velocity, with distance along the vortex.

Approximate Solutions

For both of these regions simple approximate solutions for G can be obtained from equation (11). First it is convenient to define dimensionless variables

$$\bar{x}=\frac{x}{d},\ z=\frac{r}{r_1(x)};\ \frac{u}{U}=\bar{x}^n,\ \frac{r_1(x)}{r_1(1)}=\bar{x}^m$$

and seek self similar solutions of the form $G=G(z)$

The resulting ordinary differential equation, derived from equation 13, is written

$$\left[(c+zG')\frac{G'}{z}\right]'+4\beta^2G'=0 \tag{14}$$

where

$$\beta^2=\frac{1}{4}\left[\frac{\pi U r_1^2(1)}{k^2\Gamma_1 d}\right]\frac{d}{d\bar{x}}\left[\left(\frac{r_1(\bar{x})}{r_1(1)}\right)^2\frac{u(\bar{x})}{U}\right] \tag{15}$$

and the prime denotes differentiation with respect to z.

Since β must be independent of $\bar{x}$ for similarity to hold, the exponents m and n in the expressions for $r_1(\bar{x})$ and $u(\bar{x})$ respectively must satisfy the relation $2m+n=1$, thus giving from equation (15).

$$\beta^2=\frac{1}{4}\pi U r_1^2(1)/k^2\Gamma_1 d \tag{15a}$$

Since $m = \frac{1-n}{2}$, it can be seen that in the region of persistence $\left(\frac{x}{d} < 1, \frac{u}{U} = \frac{x}{d}, n = 1\right)$ the corresponding value of m is $m = 0$, so that $r_1(x) = r_1(1) = r_1(0)$. Similarly, in the region of decay $\left(\frac{x}{d} > 1, \frac{u}{U} = 1, n = 0\right)$ the value of m is $m = \frac{1}{2}$, so that $r_1(x) = r_1(1)\left(\frac{x}{d}\right)^{\frac{1}{2}}$.

In order to obtain the solution, $G(z)$, equation (14) must be solved subject to the boundary conditions $G(1) = 1, G'(1) = 0$ (assuming that the core merges with the potential solution ($G \equiv 1$),) and $G(0) = 0$ giving zero circumferential velocity at the center of the vortex.

Equation 14 is nonlinear; however an approximate solution can be found in two steps: since c is a small parameter the solution G for $c = 0$ is found valid except for a small region near the center of the vortex where $zG' < c$, and an improved solution, using the approximation $c + zG' = c + z\dot{G}'$, is then found from the resulting linear equation.

Thus, with $c = 0$, equation 14 becomes

$$\left[\dot{G}'\dot{G}'\right]' + 4\beta^2\dot{G}' = 0 \tag{14a}$$

and a solution satisfying the boundary conditions is determined as

$$\begin{aligned} 1 - \dot{G} &= (1 - z)^2 \\ \beta &= 1 \end{aligned} \tag{16}$$

The term $(c + zG')$ is now approximated as

$$c + zG' \approx c + z\dot{G}' \approx 2(1 - z)(z + \frac{c}{2})$$

so that equation 14, with $\beta = 1$, becomes

$$\left[(1 - z)(z + \frac{c}{2})\frac{G'}{z}\right]' + 2G' = 0 \tag{14b}$$

Which has the improved solution

$$\begin{aligned} 1 - G &= (1 - z)^2\left(1 + \frac{2z}{c}\right)^c \\ \beta &= 1 \end{aligned} \tag{16a}$$

Equation 16 closely approximates equation (16a) for small values of c except for $z = 0(c)$, corresponding to a 'laminar subcore' at the center of the vortex.

All of the relevant characteristics of the vortex can now be determined using equation (16a), i.e., the length of persistence, the radius of the turbulent core, the radius of the laminar sub-core, the velocity profiles and the variation of vortex size and velocity with distance x along the axis.

First the integral of equation 8 can now be evaluated using the approximate solution $\dot{G} = 1 - (1 - z)^2$ giving

$$\int_0^{r_1}\left(\frac{\Gamma}{\Gamma_1}\right)^2\frac{dr}{r} = \int_0^1 \dot{G}^2\frac{dz}{z} = \frac{11}{12}$$

thus verifying equation 8.

The characteristic distance of persistence, d is found from 15a, with $\beta = 1$, as

$$d = \frac{\pi}{4}\frac{U}{k^2\Gamma_1}r_1^2(0) \tag{17}$$

The same result, expressed in terms of the aerodynamic parameters of the wing (b, C_L, and AR) is written

$$d = \frac{\pi}{8k^2}\frac{AR}{C_L}s^3S^{-2}b \tag{17a}$$

The radius of the turbulent core r_1 is determined as

$$\begin{aligned} r_1 &= r_1(0) \qquad \text{for} \frac{x}{d} < 1 \\ r_1(0)\left(\frac{x}{d}\right)^{\frac{1}{2}} &\qquad \text{for} \frac{x}{d} > 1 \end{aligned} \tag{18}$$

corresponding to the region of persistence and decay respectively.

Alternatively, in terms of the wing parameters

$$\begin{aligned} r_1 &= sS^{-1}\frac{b}{2} \qquad \text{for } \frac{x}{d} < 1 \\ &= \left(\frac{8k^2}{\pi}\cdot\frac{C_L}{AR}\right)^{\frac{1}{2}} s^{-\frac{1}{2}}\left(\frac{x}{b}\right)^{\frac{1}{2}}\frac{b}{2} \qquad \text{for } \frac{x}{d} > 1 \end{aligned} \tag{18a}$$

with d given by equation 17a.

The circumferential velocity v_θ is determined from $v_\theta = \frac{\Gamma}{2\pi r}$ as

$$\begin{aligned} v_\theta &= \frac{\Gamma_1}{2\pi r_1(0)}V(z), \qquad \frac{x}{d} < 1 \\ &= \frac{\Gamma_1}{2\pi r_1(0)}V(z)\left(\frac{x}{d}\right)^{-\frac{1}{2}}, \qquad \frac{x}{d} > 1 \end{aligned} \tag{19}$$

where

$$\begin{aligned} V(z) = \frac{G}{z} &= \frac{1-(1-z)^2\left(1+\frac{2z}{c}\right)^c}{z}, \qquad z < 1 \\ V(z) &= \frac{1}{z} \qquad z > 1 \end{aligned} \tag{20}$$

with $z = \frac{r}{r_1(x)}$ and $r_1(x)$ given by equation (18), d by equation (17).

Alternatively

$$\begin{aligned} v_\theta &= \frac{1}{2\pi}\frac{C_L}{AR}s^{-2}SV(z)U \qquad \text{for } \frac{x}{d} < 1 \\ &= \frac{1}{2}(8\pi k^2)^{-\frac{1}{2}}\left(\frac{C_L}{AR}\right)^{\frac{1}{2}} s^{-\frac{1}{2}}\left(\frac{x}{b}\right)^{-\frac{1}{2}}V(z)U \qquad \text{for } \frac{x}{d} > 1 \end{aligned} \tag{19a}$$

with d given by equation (17a). The variation of v_θ with $\frac{x}{d}$ is shown in fig. 4.

The velocity profile $V(z)$ represented by equation 20 has the following characteristics (described in fig. 5):

(a) For $z \ll c, V(z) \approx \frac{2z}{c}$ giving a linear variation with slope $\frac{2}{c}$ near the center of the vortex corresponding to the laminar subcore,

(b) For $c \ll z < 1; V(z) = 2 - z$ corresponding to the turbulent core,

(c) For $z > 1; V(z) = \frac{1}{z}$ corresponding to the potential vortex.

The maximum circumferential velocity is found by differentiation of $V(z)$. For $c \ll 1$ it can be shown that the maximum occurs at $z = z^* = \left(\frac{c}{2}\log\frac{1}{c}\right)^{\frac{1}{2}}$ and has the value

$$V^* = 2 - 2\left(\frac{c}{2}\log\frac{1}{c}\right)^{\frac{1}{2}} \tag{20a}$$

For most purposes, the limiting case $c = 0$ corresponding to infinitely large Reynolds number, can be taken giving

$$V^* = 2 \text{ at } z = 0$$

3. RESULTS AND DISCUSSION

The analysis has provided approximate closed-form solutions that describe the structure of the turbulent vortex pair generated by a lifting surface. Two regions of the wake are identified; a region of persistence followed by a region of decay. The initial persistence of the wake is associated with an acceleration of the flow along the axis of the vortex causing a radial inflow which counteracts the outward radial diffusion. When the axial velocity recovers to the free stream value the inflow ceases and the vortex starts to decay.

In the interest of brevity the results discussed here will be primarily for the case of an elliptically loaded wing with brief mention of the influence of inboard and outboard loading which may be determined when the quantities s and $e = \frac{C_D}{\pi AR C_L^2}$ are known. The general expressions for the quantities of interest are given in equations (17)-(20) which reduce to the simpler forms discussed below with $s = \frac{\pi}{4}$ and $e = 1$ corresponding to elliptic loading.

The length of persistence d for a wing of elliptic loading is given by

$$d = 10.4\frac{AR}{C_L}b$$

and shows that the length of persistence varies directly as the product of the span and the aspect ratio and inversely as the lift coefficient. For a typical large transport aircraft in a high lift configuration (b=200ft, AR=7 and C_L=1) the length of persistence is approximately 14,000ft (2.65 miles). On the other hand for a typical fighter aircraft (b=50ft, A =1, C_L=2) the length of persistence is only 250ft.

Considering now a description of the vortex, in the persistence region, the radius of the turbulent core r_1, where the flow departs from the potential vortex is given by

$$r_1 = .175b$$

independent of aspect ratio and lift coefficient. The laminar subcore radius, taken as the location of maximum velocity depends on the Reynolds number and (for elliptical loading) is:

$$r^* = .175\left(\frac{c}{2}\log\frac{1}{c}\right)^{\frac{1}{2}}b$$

where $c = \frac{4\times10^4}{Re}$, $Re = \frac{Ub}{\nu AR}$. For $Re = 10^7$, $c = .004$ the value of r^* is

$$r^* = .018b$$

thus, for a transport aircraft of 200ft span, the maximum velocity occurs near the center of the core at a radius of 3.6ft.

The maximum velocity is given (again for elliptic loading) by

$$v_\theta^* = 1.16\frac{C_L}{AR}U$$

Thus for the transport aircraft ($AR = 7, C_L = 1$) and U=300ft/sec the maximum velocity near the center of the vortex is 50ft/sec; for a fighter aircraft, ($AR = 1, C_L = 2$ and $U = 300$ft/sec) however, the maximum velocity would be 700ft/sec (ignoring compressibility effects).

In the decay region, i.e. for $x > 10.4\frac{AR}{C_L}b$, the radius of the turbulent core and the subcore grows as $\left(\frac{x}{d}\right)^{\frac{1}{2}}$,i.e.,

$$r_1(x) = .175\left(\frac{x}{d}\right)^{\frac{1}{2}}b = .054\left(\frac{C_L}{AR}\right)^{\frac{1}{2}}\left(\frac{x}{b}\right)^{\frac{1}{2}}b$$

and

$$r^*(x) = .054\left(\frac{C_L}{AR}\right)^{\frac{1}{2}}\left(\frac{c}{2}\log\frac{1}{c}\right)^{\frac{1}{2}}\left(\frac{x}{b}\right)^{\frac{1}{2}}b$$

For the transport aircraft given in the previous example the turbulent core extends to a radius of 70ft at a distance of 10.6 miles behind the aircraft and the radius r^*, at which the maximum velocity occurs, is approximately 7ft. The velocity v_θ^* at this point is 25ft/sec. For the fighter aircraft the velocity rate of decay with distance is greater (since the velocity reduces by a factor of 2 in a distance $x = 5d$, and d is only 250ft in this case).

From the general equation for d (equation 17a) and v_θ (equation 19a) it can be inferred that configurations which have smaller values of v_θ on the vortex wake (small C_L, large AR, large s) also have larger distances of persistence, (and those configurations having higher values of v_θ have smaller distance of persistence). Moreover, from 19a it can be seen that in the decay region the only dependence on the span distribution parameter s is $v_\theta \sim s^{-\frac{1}{2}}$, a relatively weak dependence which suggests that the reduction of the high velocities in the far wake through tailoring of the span distribution of lift is not a very promising technique.

Although comparison with experiments is not made in this paper it has been found that the general trends are reasonably well represented by the analysis given here. The dependence of persistence on the axial flow at the center of the vortex probably deserves further analysis, however, including the influence of promoting decay through mass injection thereby permitting the axial flow to recover earlier to free stream conditions.

Finally, application of the solutions given here to rotor wakes also deserves mention. In this regard the effects of Reynolds number on the behavior of the velocity v_θ near the axis of the vortex may be much more important, particularly in a proper description of the interaction of the vortex with a following blade. In this situation the effects of viscosity in the laminar subcore play an essential role in eliminating the singularity in the velocity gradient thereby permitting a realistic calculation of the vortex-blade interaction including the acoustic field so generated.

REFERENCES

1. Spreiter, J. R. and Sachs, A. H.: The rolling up of the trailing vortex sheet and its effect on the downwash behind wings, Journal of the Aeronautical Sciences, vol. 18, no.1, January 1951, pp 21-32.

2. Squire, H. B.: The growth of a vortex in turbulent flow, Aeronautical Quarterly, vol. 16, 1965, pp 302-306.

3. Iversen, J. D.: Correlation of turbulent trailing vortex decay data, AIAA Journal of Aircraft, May 1976.

4. Roberts, L.: Persistence and Decay of Wake Vorticity; AGARD Conference on Flight/Ground Testing Facilities Correlation, 1975.

5. Hoffman, E. R. and Joubert, P. N.: Turbulent line vortices, Journal of Fluid Mechanics, vol. 16, 1963, pp. 395-411.

6. Corsiglia, V. R., Schwind, R. G., and Chigier, N. A.: Rapid scanning, three dimensional hot wire anemometor surveys of wing tip vortices, AIAA Journal of Aircraft, vol. 10 no. 12, December 1973, pp 752-757.

7. Donaldson, C. DuP.: Calculation of turbulent shear flow, for atmospheric and vortex motions, AIAA Journal, vol. 10, 1972, pp. 4-12.

8. Tung, C., Pucci, C. S., Caradonna, F. X., and Morse, H. A.: The structure of trailing vortices generated by model rotor modes, NASA TM 81316.

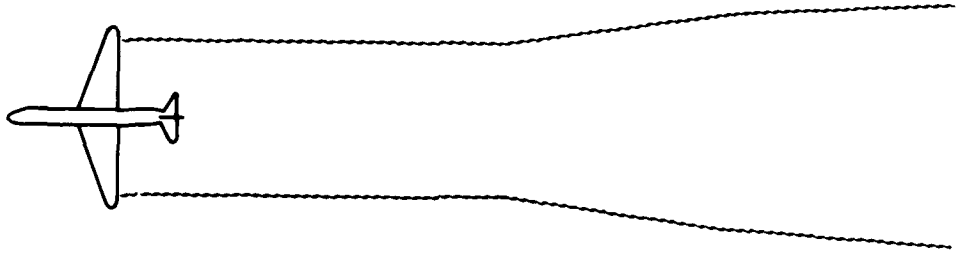

Persistence

Vortex scale and velocity unchanged with distance behind the aircraft

Decay

Vortex radius increases, and velocity decreases, with distance behind the aircraft

Fig.1 Trailing vortex flow

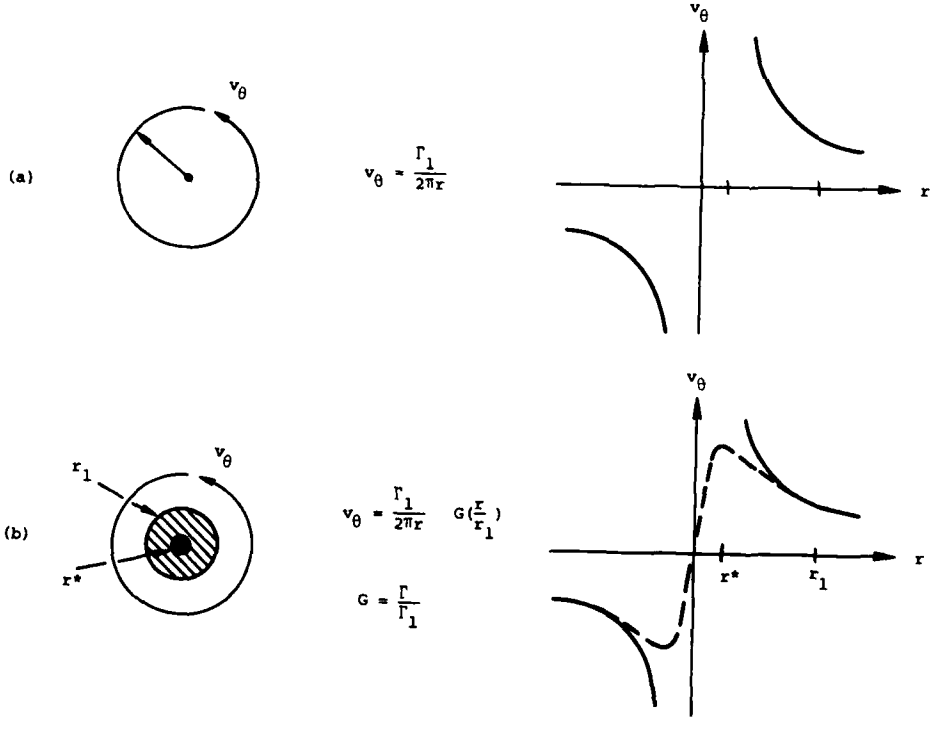

Fig.2 Vortex structure: (a) Potential flow, (b) Turbulent flow, (r_1 = radius of turbulent core, r^* = radius of laminar subcore)

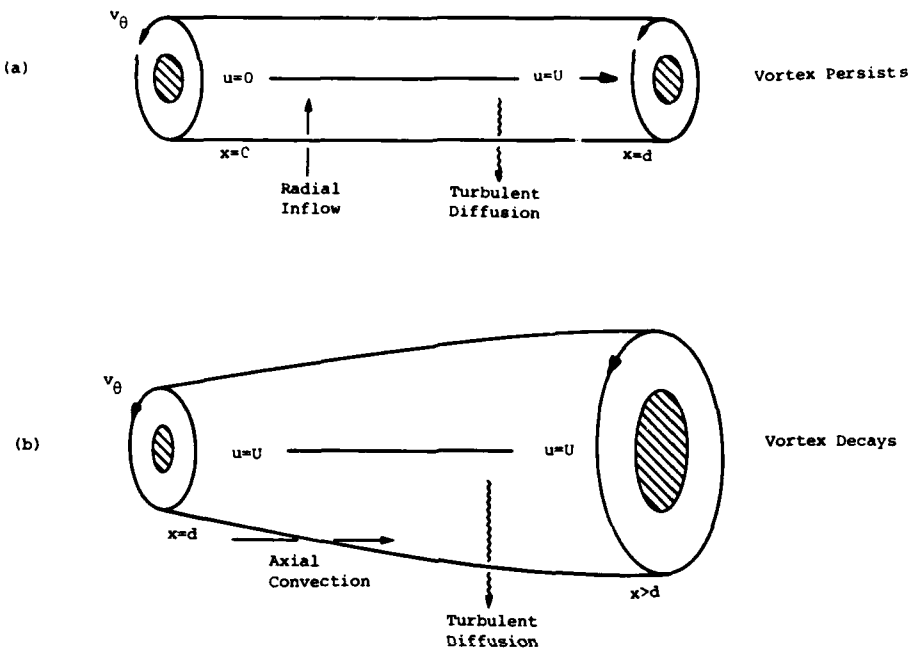

Fig.3 Effect of axial flow on the vortex. (a) Accelerating axial flow, (b) Constant velocity axial flow

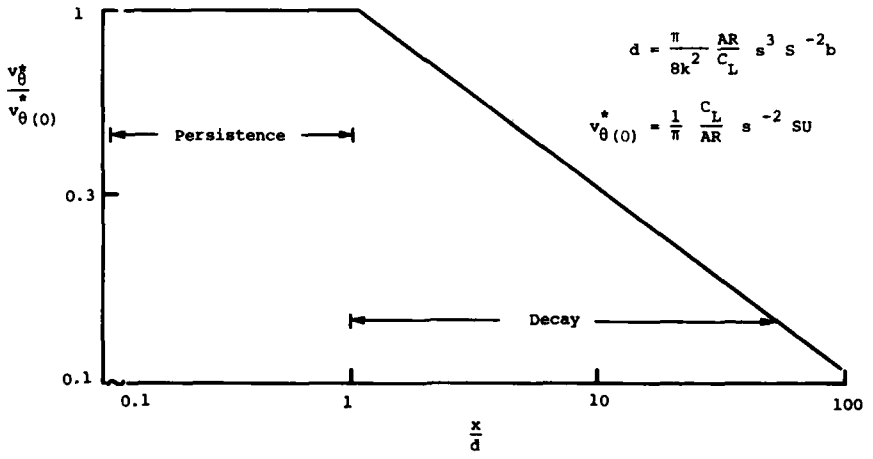

Fig.4 Variation of maximum circumferential velocity with distance behind an aircraft

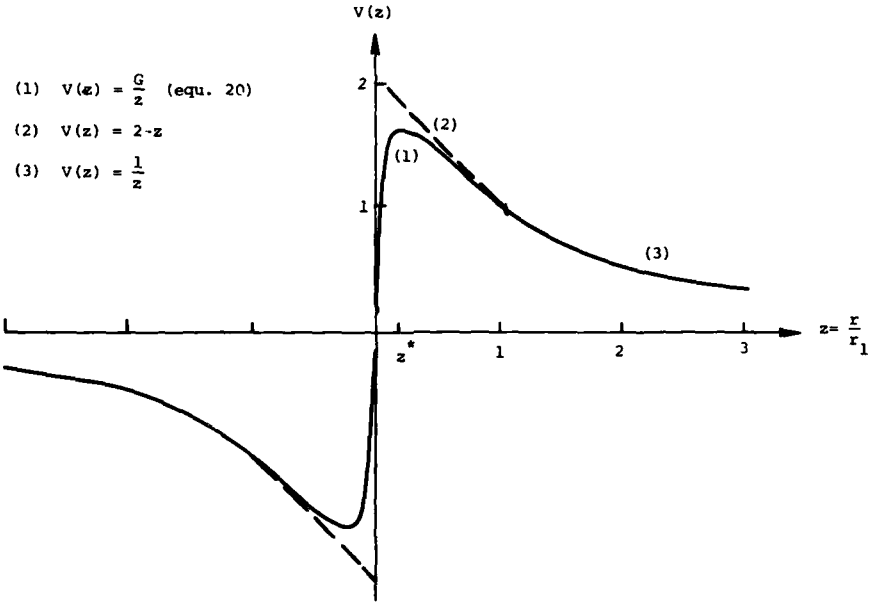

Fig.5 Radial profiles of circumferential velocity

INSTABILITIES IN TRAILING VORTICES: FLOW VISUALIZATION USING HOT-WIRE ANEMOMETRY

C. Strange* and J.K. Harvey

Department of Aeronautics
Imperial College, London SW7 2BY, England

SUMMARY

It is noted that trailing vortices often break up after the formation of disc shaped disturbances. Reference is made to a flow visualisation experiment performed by Fackrell in which similar strongly dissipative disturbances were produced in the laboratory. Details of the origin and development of this instability are discussed. To obtain quantitative information on this phenomenon an experiment using hot wire anemometry and a conditional sampling technique was set up. Data are presented on a solitary wave-like disturbance which was found on the outer edge of the core and convected downstream at about the same velocity as the ambient fluid. The perturbation flow field associated with this disturbance is not axi-symmetric.

INTRODUCTION

Trailing vortices are formed when the shear layers shed from a wing roll up into two cores of high vorticity in which no trace of the separate turns of the shear layers can be found. The cores have appreciable axial velocity components and are usually turbulent. They are quasi-cylindrical, i.e. the fluid moves in spirals around the axis and variations in the axial direction are very small compared with variations in the radial direction. Such a concentrated vortex structure would be very enduring if simple diffusion were the only form of decay but there is much evidence to suggest that the vortices undergo large-scale instabilities long before they are destroyed by diffusion.

It cannot be claimed that the initial rolling up process in which these vortices are formed is as yet fully understood. The problems encountered in attempting an analysis of this process can be seen in a paper by Spreiter and Sacks (1951) who deal with both subsonic and supersonic flow and are mainly concerned with determining the proper vortex distribution to be used for calculating downwash. Their results show that the degree of rolling up of the vortex sheet is dependent on the distance behind the wing and on the lift coefficient, span loading and aspect ratio of the wing. For low aspect ratio wings the vortex sheet is shown to become rolled up into two trailing vortices within a chord length of the trailing edge. When fully formed the vortices are found to have an axial flow within their core. Batchelor (1964) attempted to account for this in an analysis of the rolling up process, concluding that it is a consequence of the highly three-dimensional nature of the flow close to the wing. The magnitude and radial distribution of the axial velocity within the vortices vary widely depending on the shape of the wing, the value on the centre line being possibly several times that of the free stream. Batchelor also considered the effects of viscosity on this axial flow far downstream. It is evident that the effect of viscous decay is to increase the pressure in the core and hence produce axial deceleration, in this way the induced drag on the wing, associated with the generation of the trailing vortex, is gradually manifested as an ordinary wake with an axial velocity defect.

MECHANISMS LEADING TO THE DECAY OF TRAILING VORTICES

Real trailing vortices are probably turbulent far downstream, whereas Batchelor's analysis is for a laminar vortex. A simple approach would be to replace the kinematic viscosity, ν, by an eddy viscosity, ν_T, in order to apply this work to turbulent vortices. Indeed this sort of representation has been used by Squire (1954) in proposing a model of a turbulent vortex, in which the effect of turbulence is to produce an eddy viscosity of uniform strength, proportional to the circulation around circuits distant from the core. When this model is used to predict the decay of a trailing vortex, the general predictions agree fairly well with experimental results. However, Owen (1970) points out that, unless some mechanism is used to extract energy from the main flow, the turbulence, confined to the core, will suffer a rapid decay. Owen's model of the turbulent vortex sets out to create such a mechanism.

Numerous attempts have been made to model the turbulent decay of vortices since Owen's paper. However, there is a large body of experimental evidence available, including the present report, which suggests that the vortex undergoes some form of large scale instability which rapidly accelerates its decay. The vortex thus dies long before it would have done if turbulence within a quasi-cylindrically structured flow had been the primary dissipative mechanism. The turbulent flow predictions can therefore be considered to apply to a 'mid-period' vortex. The development during this phase is likely to be responsible for the changes in the velocity distributions within the vortex that trigger at least some ofthe instabilities that have been observed. An exception to this is the instability attributed to Crow (1970) which is very commonly seen in photographs of condensation trails (see Figure 1) and which does not appear to be strongly influenced by the structure of the core.

Crow used a lengthy and involved argument to find the mode favoured by the instability. From this he concluded that the vortices distort into symmetric waves of length

* Present address: Department of Aeronautical Engineering,
Queen Mary College, London.

8.4 times the vortex spacing (b), confined to fixed planes inclined at 48° to the horizontal. The instability grows by a factor e in a time = $9.4(A_R/C_L)(b/U)$ (U = velocity of aircraft) which is 26 times longer than the time given by Spreiter and Sacks for the vortex sheet behind an elliptically loaded wing to become rolled up, i.e. $0.36(A_R/C_L)(b/U)$. So the growth of the instability is slow compared to the initial rolling up. Figure 1 shows clearly this type of gently wavy instability in the condensation trails that mark the path of the trailing vortices behind an aircraft at high altitude. It is interesting to note that in this photograph there are two other types of periodic disturbances evident; ring-like disturbances on the core of the upper vortex and helical ones on the lower. These are not often seen.

Crow suggests that normally the vortex cores remain essentially unchanged but become more and more wavy, until they meet at the nearest points, where they break apart to form vortex rings. The evidence is that this sometimes happens but often another mechanism that can be seen clearly in Figure 2 appears simultaneously with the Crow instability. This second instability grows rapidly and appears to take a dominant role in bringing about the vortex disintegration. A series of 'discs' or 'knobs' appear along both vortices. At first sight they seem to be akin to what is described a 'vortex' breakdown', observations of which have been made in confined swirling flow experiments by Harvey (1962) and Sarpkaya (1970) and on low aspect ratio wings, e.g. Lambourne and Bryer (1962). In this phenomenon there is an abrupt deceleration of the flow along the axis of rotation. The deceleration and consequent expansion of the stream surfaces, appears as if a solid object had been encountered but the breakdown occurs far from any solid surfaces. In many cases the deceleration is enough to cause a stagnation point on the axis followed by a region of reversed axial flow. When the breakdown occurs near a wing its position is linked to the pressure field set up by the wing and it remains stationary with respect to the wing. In contrast, the 'disc' or 'knobs' refered to above appear to move only slowly with respect to still air and thus, as far as the wing generating the vortices is concerned, are convected downstream at about the speed of the aircraft. In a flow visualisation experiment by Fackrell (1970) a towing tank was used to enable the long term growth of trailing vortices to be observed and, in particular, make it practical to study the development of any disturbance that move slowly with respect to the ambient fluid. Fackrell's experiments were done in water at Imperial College and photographs taken from his report which was not widely publicised are reproduced as Figure 3 in this paper. They show the development of an instability into a disc-like disturbance which closely resembled the phenomenon commonly seen in condensation trails and illustrated in Figure 2.

In this experiment the core of one trailing vortex was made visible with dye ejected from the wing. His observations are of particular interest in that they show how these disturbances are initiated. In Figure 3 several of Fackrell's photographs are reproduced. In Figure 3(a) a small U-shaped vortex can be seen which forms wrapped around the outside of the core. Just before the emergence of this U-shaped vortex Fackrell noted that the dye in the main vortex core changed and took on a longitudinally striated appearance, possibly indicating the onset of some instability. The U-shaped vortex is quickly stretched because of the variations in swirl velocity to become the pair of contra rotating "quasi-ring" vortices seen on the left in Figure 3(b). The rings move apart leaving a much thinner and less energetic core behind. It would seem that much of the vorticity which lay originally in the trailing vortex axial direction has been rotated into the circumferential direction. Figure 3(b) shows on the right another ring which had originated beyond the field of view of the earlier photograph. This ring and the nearer of the first pair approach each other and the sequence of photographs 3(c) to (e) illustrate how this mechanism sweeps up dye and finally leads to the formation of a 'disc' shaped cloud closely resembling the features seen in Figure 2. This process is highly turbulent and very dissipative. The 'break-downs' occurred far downstream of the wing and they moved only slowly with respect to the ambient find. There was no meaningful correlation between the formation of these vortex rings and the Crow instabilities which were also noted.

While flow visualisation experiments are extremely valuable in developing an understanding of the physics of a flow, quantitative measurements cannot usually be obtained from them. Thus an experiment complementing Fackrell's work has been undertaken.

CONDITIONAL SAMPLING OBSERVATIONS OF A VORTEX INSTABILITY

In this study of one possible instability of aircraft trailing vortices, the flow far behind a delta wing in a low speed wind tunnel was examined for a disturbance which moved roughly with the outer flow velocity.

In an attempt to artificially age the vortices the first experiments were conducted with a 1.6 m chord delta wing placed upstream of the contraction of the wind tunnel. This was an interim measure pending the completion of the 8.53 m working section in which all subsequent experiments were carried out. Cross-wire surveys, examples of which are shown in Figure 4, taken within the vortex cores, showed that the fluctuating velocity components remain fairly constant. However their product uv or uw appears to have large bursts at irregular intervals. The velocity coordinate system is u, v, w; u is in the same direction as U_∞, v is radial and w is the azimuthal velocity component. The wing Reynolds number, Re_y, based on the centre-line chord was 1.65×10^6. The magnitude of the bursts was typically 10-12 times that of the rest of the uv or uw signal and varied in size according to the position in the vortex. The best position for obtaining these

bursts was that of the edge of the core of the vortex, the bursts being more pronounced in the trace of the uw signal.

In an attempt to study the structure of the vortex at the occurrence of such a burst a conditional sampling technique was employed. A cross-wire positioned on the edge of the core of the vortex under study was used to generate a trigger signal from the product of the fluctuating velocities. The high magnitude of uw at 'burst' ($f(t+r_n)$) was used to start a data recording system. The actual point at which triggering occurred was determined by uw exceeding a threshold value and it was designated the centre of a data record $f(t)$. For each $f(t+r_n)$ signal, a fresh $f(t)$ was superimposed on the average of previously recorded signals using a digital technique. This was necessary since each individual record had high levels of noise due to turbulence superimposed on any coherent structure.

With this conditional sampling technique a "general picture" of the structure of the disturbance was obtained by traversing a single hot-wire horizontally through the centre of one of the vortices. In Figure 5 it can be seen that the structured disturbance varied in shape for different positions throughout the vortex. Placing the single wire at three downstream positions relative to the trigger probe, the speed at which the disturbances travelled was calculated to be approximately that of the surrounding undisturbed flow, see Figure 6. Observations made some distance away from the vortices confirmed that the disturbance was restricted only to the vicinity of the core.

Greater detail of the disturbance was obtained by replacing the single wire with a cross-wire; measurements of the fluctuating velocities were in both cases, taken using the negative peak of the uw trigger signal. The wave-like disturbance was found to be present in all velocity components throughout the range of radial coordinates of -2.11a to 2.63a, where a is the core radius. The core diameter is defined as the distance between the maxima in swirl velocity amplitude.

The amplitude of the disturbance was greatest within and just outside the core of the vortex and the region of rapid change from positive to negative peak extended about 20 cm. The overall disturbance was about 1 m long and it occurred at random intervals. It did not appear to be linked with the Crow instability for which the most unstable long wave would have a length of 2 m. Figure 7 shows a vector plot of the disturbance constructed from the hot wire surveys. This shows a structured perturbation flow which is completely asymmetrical. Axisymmetry had been assumed implicitly in setting up this experiment. This is not correct and a full three-dimensional investigation would be needed to determine the physical nature of this flow.

These experiments were repeated with a similar smaller 0.71 m chord delta wing mounted at an angle of incidence of -12.5° at the beginning of the 8.53m working section. Velocity measurements were again taken with a cross-wire using the conditional sampling technique triggered mostly from the negative peak of the uw triggering signal; a few measurements were also taken using the positive peak. The measuring cross-wire was traversed horizontally through the core of one of the vortices and positioned such that it lay parallel to the local streamlines of the flow. The measuring station was 21 vortex spacings downstream of the trailing edge of the wing and the wing Reynolds number, Re_w, was 1.18×10^6. Very similar disturbances to ones discovered previously were found in the streamwise component fluctuating velocity. The separation of the vortices was 262 mm, thus the wavelength of the maximally unstable Crow instability would be 2.2 m. As can be seen from Figure 8 the disturbance began to form at -1.93 core radii (a) from the centre of the vortex and increased in amplitude until the -0.67 a position, by the next position (-0.33a) the disturbance had begun to decay and at the centre of the vortex it had died out completely. Only a very weak reappearance was seen on the other side of the core at +2.07. Had the wave been generated by 'snaking' of the vortex past the fixed probe (for example, due to a Crow instability) an asymmetrical pattern about the vortex centre would have been expected. A few positions in the vortex were studied using the positive peak of the uw trigger signal in the conditional sampling technique. The positively triggered disturbance, see figure 9, appeared to be a reversed and inverted image of the negatively triggered disturbance. Compare the -1.1a position in Figure 8 with the -1.43a position in Figure 9. For completeness measurements of the mean azimuthal velocity and the turbulence intensities for this vortex are shown in Figures 10 and 11.

It is appreciated that great care has to be exercised in interpreting conditionally sampled data since the results can only be at best the envelope of a series of events which may differ markedly from each other. The effect of 'jitter' on the triggering will further distort the result. Even so, it is felt that these experiments establish that a structured disturbance existed on the edge of vortex core which moved at a constant speed equal or nearly equal to that of the freestream. The disturbance was of a solitary wave type and not axisymmetric. This is of some importance since most of the theoretical studies of vortex instability have, for obvious reasons, assumed symmetry about the axis.

CONCLUDING REMARKS

The type of breakdown observed in Fackrell's and the present experiments is different from that commonly referred to as 'Vortex Breakdown' as the disturbance does not emanate from the vortex axis and exhibits marked asymmetry (see Figure 8). The toroidal vortices, seen in Fackrell's experiment, around the core are strongly reminiscent of those observed by Taylor (1923) in the unstable flow between two rotating cylinders. The

possibility of a trailing vortex becoming unstable in the Rayleigh sense (1917) has already been suggested by Govindaraju and Saffman (1971) and Donaldson and Sullivan (1971) who have predicted that an overshoot in the radial circulation distribution could develop as a result of turbulent transport. It is difficult to be certain that their results are truly representative of the real flows since their flow models are open to criticism, nevertheless an argument based on this overshoot concept appears to agree well with these observations which themselves show a close similiarity to the breakdown seen in condensation trails. The association between toroidal vortices and the Rayleigh criterion for instability is well established but the mechanism leading to their formation has remained obscure. If a quasi-cylindrical vortex becomes unstable, for example, due to a circulation overshoot mechanism discussed above, the core will then no longer maintain its true axi-symmetry. If its edge is distorted away from the axis its rate of rotation will be reduced as, for example, demonstrated by Batchelor (1967) who considered a sinusoidal perturbation to a core boundary. If one now considers bundles of vortex filaments from the edge of the core, these will revolve about the vortex axis less rapidly at the site of the instability. They will become distorted into the U-shape vortex shown in Figure 3 and eventually, after much attendant stretching, into quasi-vortex rings as argued earlier. Fackrell's experiments showed this happening in some instances. However, many of his observations, in common with the present wind tunnel studies, pointed strongly to asymmetries developing, although a final flow exhibiting the 'disc like' phenomenon usually evolved. While the very considerable value of theoretical studies of axisymmetric instabilities on vortices is appreciated, it is suggested that attention should be focussed on analysing possible flow patterns in which such symmetry is not assumed.

REFERENCES

Batchelor, G.K. 1967 An Introduction to Fluid Dynamics, Cambridge University Press.

Batchelor, G.K. 1964 Axial Flow in Trailing Line Vortices, JFM 20, 4, 645-58.

Crow, S.C. 1970 Stability Theory for a Pair of Trailing Vortices, AIAA 8,12.

Donaldson, C. du P. and Sullivan, R.D. 1971 Decay of an Isolated Vortex. 'Aircraft Wake Turbulence and its Detection', Ed. J. Olson, A. Goldberg and M. Rogers, Plenum Press, N.Y. pp389-412.

Fackrell, J.E. 1970 Some Observations of a Trailing Vortex, M.Sc. Thesis, Imperial College, London.

Graham, J.A.H., Newman, B.G. and Phillips, W.R. 1974 Turbulent Trailing Vortex with Central Jet or Wake. ICAS Paper No. 74-40.

Govindaraju, S.P. and Saffman, P.G. 1971 Flow in Turbulent Trailing Vortex. Phy. Flu., 14, October 1971, pp2074-80.

Harvey, J.K. 1962 Some Observations of the Vortex Breakdown Phenomenon. JFM 14, 585-592.

Lamb, H. 1932 'Hydrodynamics', Cambridge University Press.

Lambourne, N.C. and Bryer, D.W. 1962 The Bursting of Leading Edge Vortices - Some Observations and Discussion of the Phenomenon. ARC R&M 3282.

Owen, P.R. 1970 The Decay of a Turbulent Trailing Vortex. Aero Quarterly, Vol. 21.

Rayleigh, Lord 1917 On the Dynamics of Revolving Fluids, Proc. Roy. Soc. London A 93, pp148-154.

Sarpkaya, T. 1970 An Experimental Investigation of the Vortex-Breakdown Phenomenon, United States Naval Postgraduate School, NPS-59SL0071A.

Spreiter, J.R. and Sacks, A.M. 1951 The Rolling up of the Trailing Vortex Sheet and its Effects of the Downwash behind Wings, J. Aero. Sci. 18, 1, 21-32.

Squire, H.B. 1954 The Growth of a Vortex in Turbulent Flow, British ARC 16666 F.M. 2053.

Taylor, G.I. 1923 Stability of Viscous Liquid Contained between Two Rotating Cylinders. Phil. Trans. Roy. Soc. A 223, pp289-343.

ACKNOWLEDGEMENT

This work was undertaken while receiving support from the Ministry of Defence under Contract AT/2037/0158 SRA.

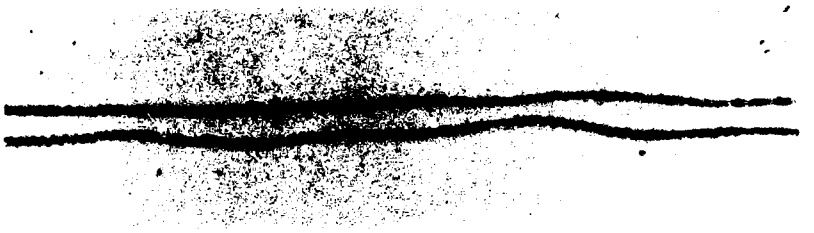

Fig.1 Condensation trails behind a wide-bodied jet showing the Crow instability and helical and ring-like disturbances (RAE Bedford).

Fig.2 Condensation trails behind a wide-bodied jet showing disc-like disturbances (RAE Bedford).

(a)

(b)

Fig.3(i) Flow visualization of a trailing vortex (Fackrell) Series I (a and b).

(c)

(d)

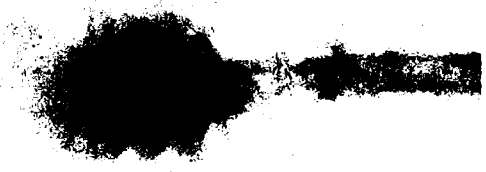

(e)

Fig.3(ii) Flow visualization of a trailing vortex (Packrell) Series II (c-e)

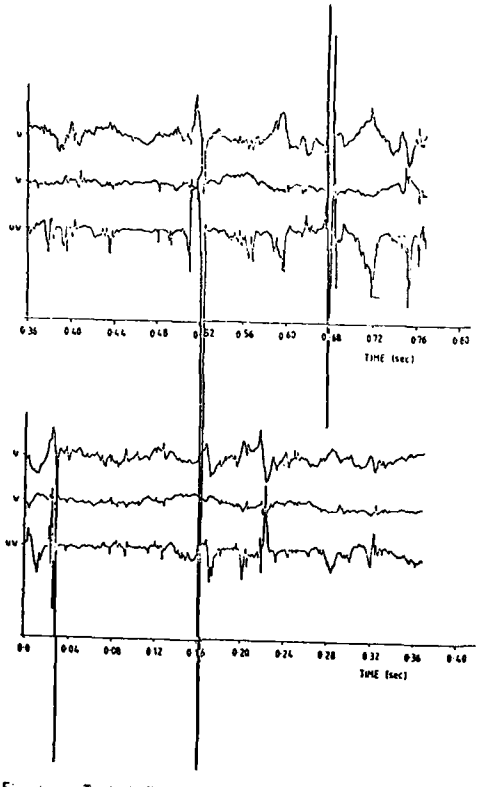

Fig. 4 Typical fluctuating velocity components and their instantaneous product.

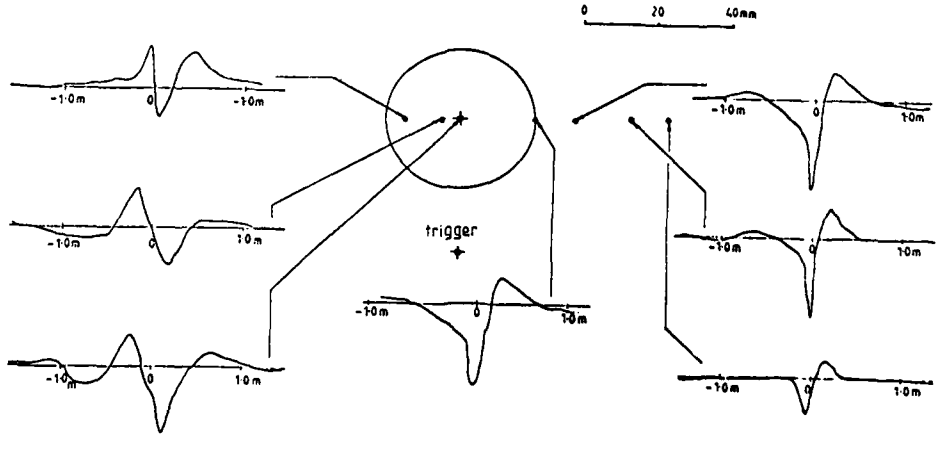

Fig. 5 The structured disturbance at positions through the centre of the vortex - a horizontal traverse with a single hot wire.

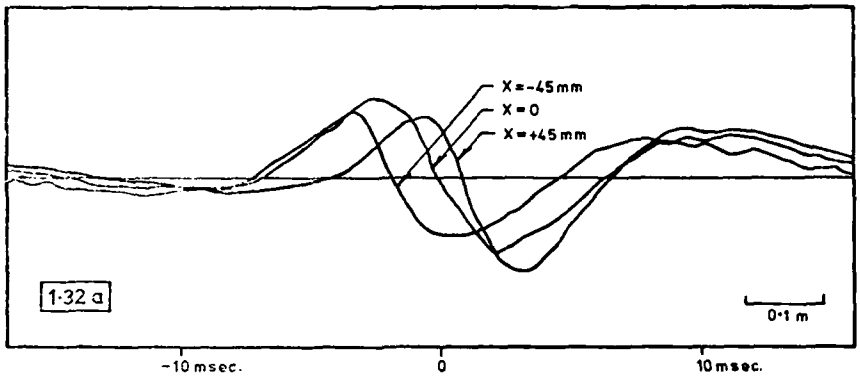

X is the distance moved by the measuring hot-wire relative to the trigger cross-wire.

Fig. 6 Determination of the speed at which the structured disturbance travelled; the disturbance at three downstream positions.

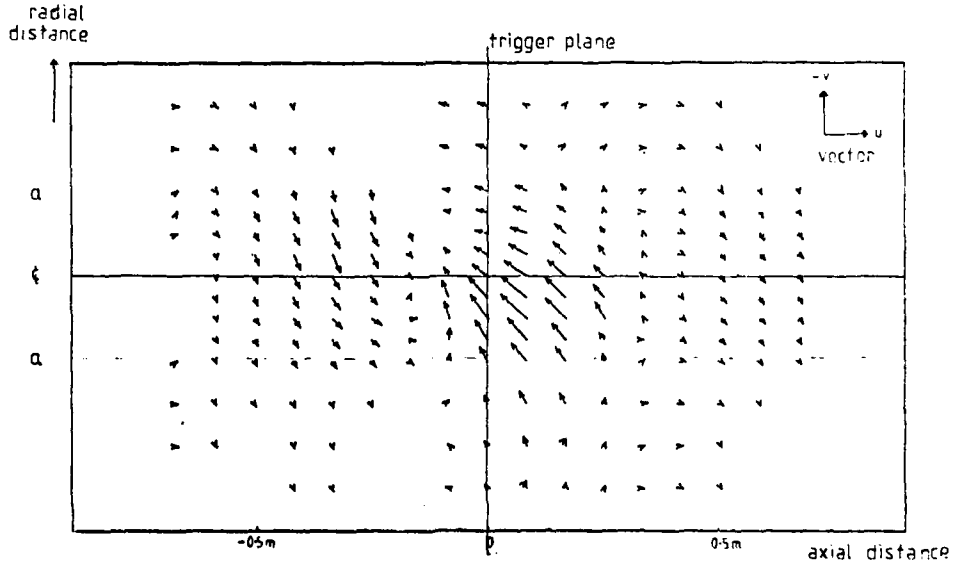

Fig. 7 Perturbations in the UV plane at various positions in the vortex. (a = core radius).

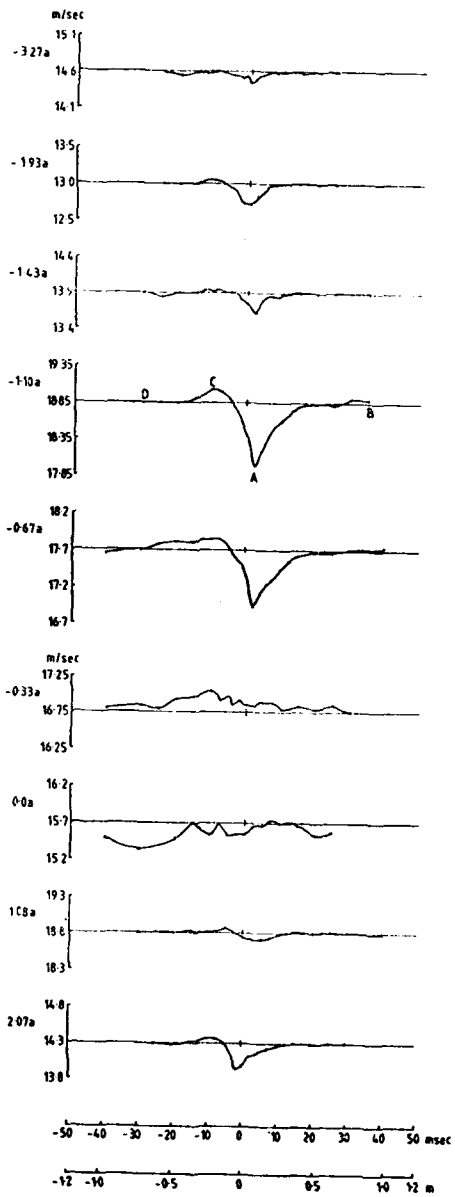

Fig. 8 Velocity profiles obtained using conditional sampling technique.

Streamwise component, U_s, over a timescale of 100 msec, triggering on the negative peak of the uw signal. (U_s - U_r plane)

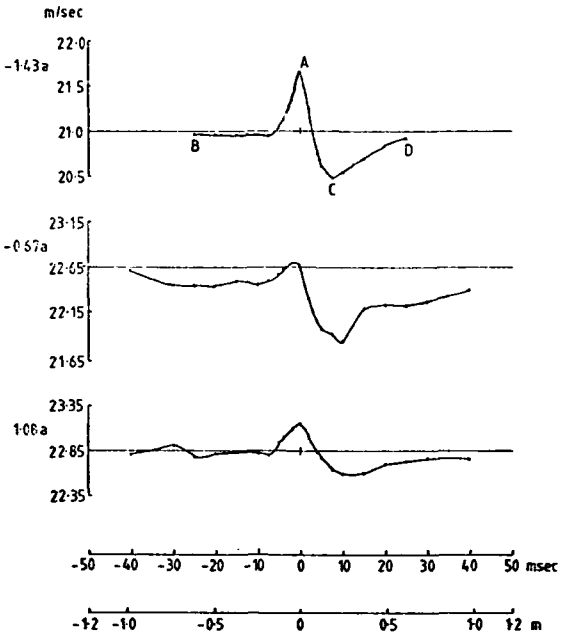

Fig. 9 Velocity profiles obtained using conditional sampling technique.
Streamwise component, U_s over a timescale of 100 msec, triggering on the positive peak of the uv signal. ($U_s - U_t$ plane)

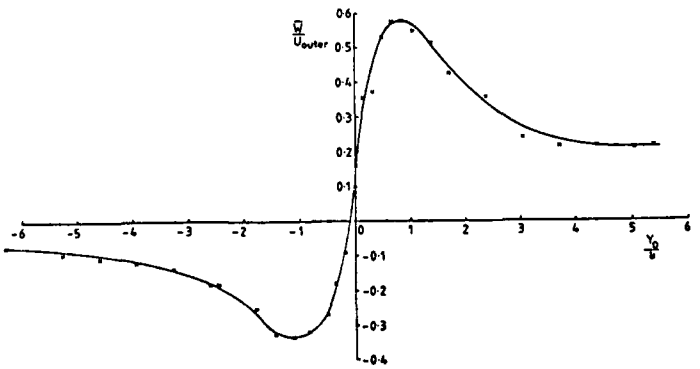

Fig. 10a Azimuthal velocity profile of the vortex under study.

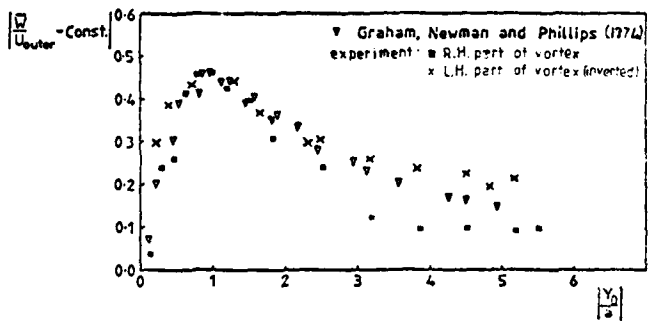

Fig. 10b Azimuthal velocity profile of the vortex under study.

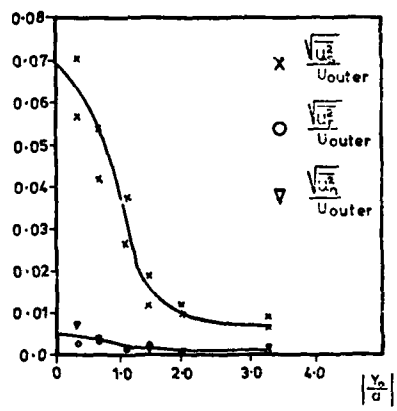

Fig.11 Turbulence intensity levels

INTERACTION ENTRE UNE ONDE DE CHOC ET UNE STRUCTURE TOURBILLONNAIRE ENROULEE

par

J. DELERY et E. HOROWITZ

Office National d'Etudes et de Recherches Aérospatiales (ONERA)

92320 CHATILLON - FRANCE

RESUME

L'interaction entre une structure tourbillonnaire enroulée (vortex) et une onde de choc normale à l'axe de la structure a été étudiée sur les deux plans : expérimental et théorique. Des mesures systématiques effectuées pour quatre valeurs du nombre de Mach comprises entre 1,6 et 2,28 ont permis de caractériser l'effet du choc pour les interactions sans éclatement. Elles ont également conduit à la définition d'une limite d'éclatement en fonction des deux paramètres : intensité du choc, taux de rotation du vortex. Deux configurations dont une éclatée, ont été analysées plus finement au vélocimètre laser. Pour un éclatement, la structure moyenne de l'écoulement méridien inclut un "bulbe de recirculation" fermé situé sur l'axe du vortex. Une modélisation a été développée à partir des équations d'Euler stationnaires. Tant que le vortex n'éclate pas, elle donne une description fidèle des phénomènes et prédit même une limite d'éclatement en bon accord avec l'expérience.

INTERACTION BETWEEN A SHOCK-WAVE AND A VORTEX FLOW

SUMMARY

The interaction between a vortex and a shock-wave normal to the streamwise axis of the vortex has been studied both experimentally and theoretically. Measurements have been made for four values of the upstream Mach number ranging from 1.6 to 2.28. They allowed the characterization of the shock effect on the vortical flow structure when breakdown does not occur. They also led to the definition of a breakdown limit function of the two parameters : normal shock strength - vortex swirl/ratio Two flow configurations associated respectively with interaction without and with vortex bursting have been carefully probed by using a two-color LDV system. When breakdown occurs, the mean meridian motion comprises a "recirculating bubble" near the axis of the structure. A flow model has been developed in the framework of the Euler equations. As long as the vortex does not burst, the calculations thus made give a faithfull description of flow phenomena. They also predict a limit for vortex breakdown which agrees satisfactorily with experiment.

1 - INTRODUCTION -

L'interaction entre une onde de choc et une structure tourbillonnaire enroulée est susceptible de se produire sur un avion de combat évoluant à grande incidence et en transsonique élevé lorsque, par exemple, le tourbillon généré par un canard traverse un choc prenant naissance près du bord de fuite de l'aile. Un tel phénomène est également concevable sur un avion supersonique où il peut arriver que le tourbillon engendré par une surface portante soit "avalé" par une prise d'air placée plus en aval. Le problème de mécanique des fluides qui se pose dans ces circonstances peut se formuler schématiquement dans les termes suivants : que se passe-t-il quand une structure tourbillonnaire organisée autour d'un axe Ω_x, sensiblement aligné avec le courant principal, traverse une onde de choc perpendiculaire à Ω_x ? Et plus précisément, le saut de pression résultant du choc ne peut-il pas déstabiliser l'écoulement et provoquer l'éclatement de la structure ? Ce dernier point est extrêmement important pour les applications puisque l'aile au-dessus de laquelle l'éclatement survient subit une chute brutale de portance, le plus souvent de manière dissymétrique, c'est-à-dire, qu'en général, l'éclatement ne se produit ni en même temps, ni à des endroits identiques sur chacune des ailes de l'avion. D'où l'apparition de moments importants qui peuvent rendre le contrôle de l'appareil délicat. Dans le cas de la prise d'air, l'éclatement, qui se manifeste par la formation d'un écoulement fortement fluctuant et très dissipatif, entraîne une perte d'efficacité et peut amorcer des instabilités de fonctionnement du groupe propulseur.

A notre connaissance, le problème de l'interaction, tel qu'il est formulé ci-dessus, a été très peu étudié et il est, de ce fait, fort mal connu, [1, 2, 3]. En conséquence, dans le cadre d'une première approche à caractère surtout fondamental, on est tout naturellement conduit à définir des configurations d'étude schématiques où les paramètres d'influence pris en compte sont en nombre réduit. Ainsi (voir fig.1), le choc sera normal à l'axe Ω_x matérialisant la direction de l'écoulement principal amont supposé uniforme à l'extérieur de la structure tourbillonnaire. L'intensité du choc sera donc uniquement définie par le nombre de Mach M_∞ sur sa face amont.

L'enroulement tourbillonnaire, que nous désignerons également par le nom de "vortex" dans ce qui suit, est supposé présenter une symétrie de révolution autour de l'axe Ω_x. Il s'agit évidemment d'une shématisation, les tourbillons créés expérimentalement n'étant jamais parfaitement de révolution. Toutefois, les mesures effectuées ont montré que les supposer axisymétriques est une approximation raisonnable. La "force" ou intensité du vortex sera caractérisée, en première approximation, par le taux de rotation $\mathcal{T}$. Le paramètre $\mathcal{T}$ est défini comme le rapport de la vitesse tangentielle maximale V_{θ_M} à la vitesse axiale périphérique locale V_{x_e} (voir fig.1).

En fait, c'est dans un souci de simplification que seulement deux paramètres seront évoqués dans ce qui va suivre. Dans la réalité la situation est plus complexe. Le comportement du tourbillon, vis-à-vis de l'éclatement notamment, dépend de la forme locale des distributions de vitesse longitudinale et tangen-

tielle (tant que le vortex n'est pas éclaté, la composante radiale V_r est généralement très faible et joue un rôle secondaire). Ainsi le profil axial $V_z(r)$ peut comporter soit un déficit ($V_{z_0}/V_{z_e} < 1$), soit un excès ($V_{z_0}/V_{z_e} > 1$) de vitesse sur l'axe selon son mode de génération et plus généralement selon son histoire antérieurement à sa rencontre avec un choc. Il pourra en résulter des interactions de nature très différente. L'étude qui va être présentée ici est limitée au cas $V_{z_0}/V_{z_e} \neq 1$. Ses objectifs étaient les suivants :

- analyser le comportement d'un écoulement tourbillonnaire quand il est soumis à l'action d'une onde de choc,
- définir une limite d'éclatement, c'est-à-dire préciser, pour chaque intensité du choc, la valeur limite du taux de rotation au-delà de laquelle la discontinuité de pression provoque l'éclatement du vortex.

Cette étude s'inscrit dans un programme de recherche plus général que l'ONERA consacre aux écoulements tourbillonnaires. En particulier, le problème de l'éclatement en écoulement incompressible est l'objet d'une autre communication à ce même symposium [4].

Dans ce qui suit, sera d'abord présentée une analyse expérimentale des phénomènes mettant notamment en jeu la vélocimétrie laser. Ensuite, une modélisation dans le cadre des équations d'Euler sera exposée.

2 - ETUDE EXPERIMENTALE -

2.1 - Montage d'essai et techniques de mesure -

La partie expérimentale de l'étude a été exécutée dans une soufflerie supersonique à retour (soufflerie S5Ch de l'ONERA) fonctionnant en continu. Sa veine bidimensionnelle a une largeur de 300 mm. Elle peut être aménagée soit en tuyère complète (la section d'essai est alors de 300 x 300 mm^2), soit en demi-tuyère (section égale à 300 x 150 mm^2). Des nombres de Mach M_∞ différents sont réalisés par changement des blocs tuyère Pour les présents essais, les conditions génératrices de l'écoulement amont étaient les suivantes :

- pression p_{i_∞} = 53 kPa,
- température absolue : T_{i_∞} = 300 K.

Un choc normal est créé au moyen d'un dispositif en forme de prise d'air bidimensionnelle monté dans la partie de la veine où l'écoulement supersonique est uniforme (fig.2).Un obstructeur mobile placé en aval provoque le blocage de l'écoulement sortant de la prise d'air. Le débit capté peut ainsi être ajusté de façon telle que le choc droit se place juste en amont du plan d'entrée de la prise d'air (la distance de détachement était voisine de 5 mm dans toutes les configurations testées).

Le vortex est engendré par une aile dont l'incidence est réglable de manière à pouvoir faire varier le taux de rotation. Ce "générateur de tourbillon" peut être placé :

a) dans la partie supersonique de la tuyère, position qui donne, au niveau du choc, le taux de rotation le plus élevé à incidence fixée. La contrepartie de cette disposition est la formation inévitable d'ondes perturbatrices assez intenses pour altérer gravement le phénomène à analyser ;

b) dans la partie subsonique de la tuyère, c'est-à-dire en amont du col. L'avantage évident de ce montage est l'absence de toute perturbation gênante. En revanche, il ne permet pas de réaliser des taux de rotation $\mathcal{T}$ élevé. En effet, $\mathcal{T}$ qui peut être initialement important juste en aval de l'aile, diminue ensuite fortement en raison de l'accélération de l'écoulement au cours de la détente dans la tuyère. Ceci s'explique par le fait, démontré à la fois par le calcul et par l'expérience, qu'un vortex soumis à une accélération voit sa composante de vitesse axiale croître alors que sa composante tangentielle demeure pratiquement invariante. Il en résulte une diminution du taux de rotation qui, en conséquence, ne pourra avoir au niveau du choc des valeurs aussi élevées qu'avec la disposition précédente.

Les résultats présentés ici ont été obtenus avec l'aile placée en subsonique, la pureté de l'écoulement à analyser étant un critère déterminant pour une étude à caractère fondamental. La limitation du taux de rotation n'était d'ailleurs pas vraiment une gêne dans la mesure où les valeurs de $\mathcal{T}$ réalisées étaient quand même suffisantes pour obtenir des interactions avec éclatement.

En fait, deux montages expérimentaux conçus tous deux selon le principe b ont été réalisés. Le premier, représenté schématiquement figure 2a, a servi pour les explorations à la sonde de pression dont les objectifs essentiels étaient :

a) de qualifier le dispositif d'essai adopté et de définir la structure des tourbillons générés par l'aile (contrôle de la symétrie et détermination du taux de rotation en fonction de l'incidence et du nombre de Mach M_∞).

b) de déterminer la limite l'écoulement en fonction de $\mathcal{T}$ et de M_∞ .

Pour ce montage, la veine était équipée en demi-tuyère. Le "générateur de choc" a une section d'entrée de 100 mm de haut et de 200 mm de large. Il est muni de bords d'attaque aigus et équipé de fenêtres latérales afin de permettre l'observation (éventuelle) du phénomène. Le générateur de vortex est une demi-aile delta montée sur la paroi inférieure de la veine. Ses caractéristiques géométriques principales sont les suivantes : envergure de 62,5 mm ; corde à l'emplanture de 310 mm ; flèche égale à 75°.

Ce premier montage s'est révélé inadapté pour les mesures par vélocimétrie laser en raison :

a) des trop faibles dimensions des fenêtres d'observation ;

b) de la hauteur insuffisante de la prise d'air dont les parois haute et basse trop rapprochées risquaient de produire un effet de confinement gênant, spécialement quand le vortex éclate.

Un deuxième montage (voir fig. 2b) a donc dû être réalisé. Il utilise la tuyère complète dans laquelle il a été possible d'installer une prise d'air de section 184 x 184 mm^2. Les fenêtres d'observation sont sensiblement plus grandes. Le vortex est ici généré par une demi-aile type "Concorde" de 100 mm d'envergure et ayant une corde à l'emplanture de 260 mm.

Dans une première étape de l'étude, les champs de vitesse moyenne et de pression ont été mesurés à l'aide d'une sonde anémo-clinométrique conique comportant cinq orifices de pression et dont le diamètre était de 1,5 mm [5]. La sonde est tenue par un explorateur dont le déplacement est commandé par un mini-ordinateur selon un trajet pré-programmé [6].

L'analyse fine de configurations typiques a été exécutée au moyen d'un Vélocimètre Laser développé par la Direction de la Physique de l'ONERA [7]. Il s'agit d'un appareil bidirectionnel mesurant simultanément deux composantes du vecteur vitesse ; la figure 3 en donne le schéma de principe. La source est un laser à Argon ionisé pouvant émettre une puissance maximale toutes raies de 15 W. Les rayonnements bleu (longueur d'onde $\lambda = 0{,}4880\ \mu m$) et vert ($\lambda = 0{,}5145\ \mu m$) sont focalisés pour interférer dans un volume de mesure dont le diamètre utile est d'environ $400\ \mu m$. Les deux systèmes de franges sont inclinés à $\pm$ 45° par rapport à l'horizontale. Afin de permettre au système de détecter l'orientation du vecteur vitesse mesuré, les faisceaux traversent des modulateurs acousto-optiques (cellules de Bragg).

Le vélocimètre fonctionne selon le mode diffusion directe de manière à bénéficier d'un rapport signal/bruit maximal, ce qui est essentiel pour la mesure des vitesses élevées. Les fréquences Doppler sont mesurées par des compteurs DISA 55L connectés à un mini-ordinateur par l'intermédiaire d'un "numérisateur simultané". Cet appareil contrôle la simultanéité des mesures effectuées sur les voies verte et bleue de manière à ne permettre l'acquisition que s'il s'agit bien de la même particule qui vient de traverser le volume de mesure.

Pour la plupart des explorations, il était procédé à l'acquisition de 500 couples de valeurs des composantes de la vitesse en chaque point de mesure. Afin d'obtenir une meilleure résolution, les histogrammes à deux dimensions présentés paragraphe 2.2.3 ont été établis sur des échantillons de 6000 couples.

L'écoulement était ensemencé par de la fumée d'encens émise dans la chambre de tranquillisation de la soufflerie.

Pour les deux parties de l'étude expérimentale, les points de mesure sont repérés dans un système d'axes orthogonaux $Oxyz$ dont l'origine est dans le plan d'entrée de la prise d'air. L'axe Ox est horizontal et sensiblement parallèle à l'axe du vortex, Oy est l'axe transversal et Oz est vertical. Les résultats exploités seront présentés dans un système de coordonnées cylindriques où, pour se conformer à l'usage le plus courant, r désignera la distance radiale depuis l'axe du vortex et Z la coordonnée longitudinale.

2.2 - Présentation des résultats -

2.2.1 - Remarque préliminaire -

Dans une première partie seront analysés les résultats obtenus à partir des mesures à la sonde de pression. Compte tenu des limitations de cet instrument, l'accent a été mis alors sur l'examen d'interactions dont l'intensité est en-deçà de la limite d'éclatement. Cette étude a permis de dégager l'influence des principaux paramètres (taux de rotation, intensité du choc) sur les modifications subies par la structure d'ensemble du vortex. Les mesures ont été effectuées pour quatre valeurs du nombre de Mach M_∞ : 1,6 ; 1,75 ; 2 et 2,28. L'interprétation d'explorations pratiquées sur des configurations éclatées a également permis de définir une limite d'éclatement en fonction de τ et de M_∞.

La seconde partie de l'étude a porté sur une analyse plus fine du phénomène au moyen de la vélocimétrie laser. Les mesures ont été exécutées sur deux configurations à même valeur du nombre de Mach : $M_\infty = 2{,}28$. l'une correspond à une interaction sans éclatement, l'autre à une interaction avec éclatement.

2.2.2 - Interactions sans éclatement. Limite d'éclatement -

Des mesures préliminaires ont d'abord servi à caractériser la structure de l'écoulement tourbillonnaire au moment où il va aborder l'onde de choc. Les deux paramètres variables sont M_∞ et l'incidence α de l'aile. La figure 4 montre les champs de la composante de vitesse dans un plan perpendiculaire à l'axe horizontal Ox et situé à 70 mm en amont du plan d'entrée de la prise d'air. L'axe Ox étant très sensiblement parallèle à l'axe du vortex, les vecteurs représentés s'identifient pratiquement avec la composante tangentielle V_θ. Les cartographies mettent en évidence une structure régulière présentant une assez bonne symétrie de révolution, ce qui justifie l'hypothèse d'un vortex axisymétrique faite dans les exploitations ultérieures. Le rayon r_M de la structure (r_M est conventionnellement défini comme la distance radiale à laquelle V_θ est maximale) est une fonction croissante de l'incidence α mais varie assez peu avec M_∞. Pour fixer les ordres de grandeur, $r_M = 20$ mm pour $\alpha = 20°$. La figure 5 donne l'évolution du taux de rotation : $\tau = V_{\theta M}/V_{Ze}$ en fonction de α (le vortex n'étant pas parfaitement de révolution, $V_{\theta M}$ est ici une moyenne évaluée à partir de deux explorations pratiquées selon des axes y et $\bar{y}$ passant par le centre de la structure). D'une manière générale, τ augmente d'abord de façon quasi-linéaire avec α. Puis les courbes s'infléchissent et τ diminue rapidement : cette décroissance correspond très vraisemblablement à un éclatement du tourbillon au niveau de l'aile. Le taux de rotation maximal réalisable diminue avec le nombre de Mach en raison de l'effet d'accélération de plus en plus grand dont on sait qu'il affecte presque uniquement la composante axiale V_{Ze} (voir § 1 ci-dessus). De 0,35 pour $M_\infty = 1{,}75$, τ_M passe à 0,22 pour $M_\infty = 2{,}28$. Le comportement de τ à $M_\infty = 1{,}6$, qui semble contredire cette tendance, résulte en fait d'un montage différent de l'aile qui se trouvait dans une zone à plus basse vitesse.

Examinons maintenant l'influence du choc. La figure 6 montre des cartographies dans des plans yz situés de part et d'autre du choc pour deux valeurs de M_∞ ($M_\infty = 1{,}6$ et $M_\infty = 2$) et des taux de rotation "modérés" ($\tau = 0{,}3$ et $\tau = 0{,}23$ respectivement). Dans ces conditions, la structure générale du vortex ne se trouve pas fondamentalement modifiée par la traversée du choc; l'écoulement conserve une allure régulière. En particulier le rayon r_M n'augmente que très légèrement au cours de l'interaction. De même, ainsi que le montre la figure 7, la composante tangentielle $V_{\theta M}$ demeure pratiquement invariante, du moins tant que le vortex n'éclate pas. On assiste alors à un "effondrement" des vitesses de rotation comme cela sera précisé par les mesures au vélocimètre laser (voir aussi la réf. [4] pour l'étude de l'éclatement en incompressible). La quasi-invariance du profil des vitesses tangentielles en l'absence d'éclatement est un comportement prévisible puisque V_θ est contenue dans le plan du choc.

Les altérations les plus sensibles affectent la composante axiale V_z qui est perpendiculaire au choc. Sur la figure 8 sont portées les évolutions en fonction de τ et pour les quatre nombres de Mach étudiés des grandeurs suivantes :

a) composante axiale à la périphérie du vortex : V_{z_e}

b) composante axiale sur l'axe du vortex : V_{z_0}

Ces résultats sont relatifs à une section située à environ 60 mm en aval du choc (x = 55 mm).

On constate que V_{z_e} subit une discontinuité égale au saut de vitesse théorique à travers un choc normal dans la très grande majorité des cas. Les valeurs plus élevées de V_{z_e} observées à M_∞ = 2 et M_∞ = 2,28 pour $\tau > 0{,}2$ sont une conséquence de l'éclatement du vortex qui se produit alors. En effet, l'éclatement se traduit par une forte dilatation du noyau dissipatif (voir § 2.2.3 ci-dessous) d'où un effet d'obstruction (ou de déplacement) qui entraîne une accélération de l'écoulement externe potentiel confiné dans la prise d'air.

En amont du choc, la composante sur l'axe V_{z_0} est généralement un peu supérieure à V_{z_e}. Cette légère survitesse croît avec le taux de rotation, ce qui est une conséquence de la dépression plus grande qui se crée au centre du vortex quand les vitesses tangentielles augmentent. L'amplitude de la discontinuité subie par V_{z_0} est d'autant plus grande que τ est plus élevé, la zone centrale du tourbillon étant soumise, au travers du choc à un ralentissement plus important que la périphérie. Ce phénomène est également observé quand le vortex est soumis à une compression étalée. Il s'explique alors très simplement en considérant l'équation pour l'équilibre radial [8].

La quasi-invariance de V_θ jointe à la décroissance notable de V_z entraîne une forte augmentation du taux de rotation (voir fig. 9). La traversée du choc a donc comme conséquence importante d'accroître la "fragilité" du vortex vis-à-vis d'un éventuel éclatement. C'est en effet un résultat bien connu que la stabilité d'un enroulement tourbillonnaire diminue quand l'intensité relative du mouvement de rotation augmente (pour une revue des nombreux travaux consacrés au problème de l'éclatement des tourbillons, voir la référence [9] où l'on trouvera une importante bibliographie sur cette question). L'éclatement se produit le plus souvent quand l'angle d'hélice $\gamma = \mathrm{Arctg}\,(V_\theta/V_z)$ atteint localement une valeur voisine de 50° (alors $V_\theta \simeq 1{,}2\ V_z$). La traversée du choc augmente partout l'angle d'hélice et plus particulièrement dans la zone centrale du vortex où se produit le plus fort ralentissement de la composante axiale. On conçoit donc qu'un état puisse être atteint, à une certaine intensité du choc, où localement γ est proche de la valeur critique de 50°, d'où un brusque éclatement de la structure.

Ainsi qu'il a déjà été souligné, la sonde de pression est inadéquate pour explorer un tourbillon éclaté où l'*orientation du vecteur vitesse* varie considérablement. On peut néanmoins utiliser ce moyen pour faire la démarcation entre des configurations éclatées et des configurations non éclatées. Ainsi, la figure 10 montre deux cartographies, en amont et en aval du choc, pour M_∞ = 2 et τ = 0,27. Les croix portées sur le tracé aval signifient qu'en ces points les indications de la sonde n'étaient pas exploitables : ce qui correspond à une situation où le module de V_z est très petit, V_z ayant même éventuellement changé de signe. Une telle cartographie peut être associée à un état éclaté avec une bonne certitude. L'interprétation de cartes analogues établies systématiquement en faisant varier progressivement l'incidence de l'aile a permis de définir, pour chaque valeur de M_∞ , un taux de rotation limite au-delà duquel le tourbillon est éclaté. Il est ainsi possible de tracer dans le plan (M_∞ , τ) une courbe frontière séparant les interactions sans éclatement des interactions avec éclatement. Cette courbe est donnée figure 11 : elle représente une limite pour le cas où le profil axial est quasi-uniforme. Si la distribution axiale comporte un déficit (profil du type "sillage") on doit s'attendre à une plus grande fragilité du vortex ; et la courbe frontière sera décalée vers le bas. Le contraire sera évidemment vrai si la distribution présente un excès de vitesse (profil du type "jet").

L'allure générale de la courbe de la figure 11 confirme le fait intuitif que le saut de pression nécessaire pour faire éclater le vortex doit être d'autant plus élevé que le taux de rotation est plus faible.

La limite d'éclatement à M_∞ = 2,28 a également été déterminée au vélocimètre laser qui est un moyen d'analyse beaucoup plus fiable. Le point obtenu (voir fig. 11) confirme parfaitement le résultat donné par la sonde de pression.

2.2.3 - *Analyses fines au vélocimètre laser* -

Cette étude plus approfondie de la structure de l'écoulement tourbillonnaire a été effectuée pour une seule valeur de l'intensité de l'onde de choc correspondant à M_∞ = 2,28. Deux configurations ont été retenues : pour la première, l'interaction s'effectue sans éclatement, pour la seconde le choc fait éclater le vortex.

Les écoulements ont été explorés à différentes abscisses x situées pour la plupart en aval du choc. La procédure expérimentale était la suivante : d'abord repérage du centre ω du vortex, puis exécution de deux explorations selon des lignes en "croix" passant par ω , l'une selon la direction horizontale y , l'autre selon la direction verticale y . Le vélocimètre laser mesurait les composantes de vitesse contenues dans le plan vertical, c'est-à-dire V_z et V_y . Il est à noter que dans l'hypothèse où le vortex est axisymétrique (ce qui est assez bien vérifié expérimentalement), l'exploration selon l'axe transversal y donne directement les composantes dites axiale V_z et tangentielle V_θ .

Par la suite, nous ne parlerons donc que de V_z et V_θ .

Les distributions des vitesses moyennes V_z et V_θ en amont du choc sont représentées figure 12. Dans le cas présent, les deux profils axiaux, en fait pratiquement identiques, présentent un léger déficit de vitesse sur l'axe (environ 4 %). Dans les essais précédents (voir § 2.2.2 ci-dessus), V_{z_0} était un peu supérieure à V_{z_e} . La différence provient vraisemblablement de l'emploi d'ailes de formes différentes. Les profils tangentiels ont une allure classique, caractéristique d'un tourbillon "visqueux", avec un noyau central où la rotation est du type corps solide (loi de vitesse en $V_\theta = k_1 r$) et une évolution externe qui tend vers le tourbillon potentiel (en $V_\theta = k_2 / r$). Pour le vortex le moins intense (incidence de

l'aile $\alpha = 10°$), le taux de rotation vaut 0,11 ; à l'incidence $\alpha = 22,5°$ correspond la valeur $\mathcal{C} = 0,17$. Le second cas, comme nous le verrons, donne bien lieu à une interaction avec éclatement, ce qui est conforme au résultat de la figure 11 selon lequel à $M_\infty = 2,28$ le $\mathcal{C}$ limite vaut 0,15.

Les figures 13 ($\alpha = 10°$) et 14 ($\alpha = 22,5°$) montrent certaines des distributions V_z et V_θ mesurées en aval de l'onde de choc qui se positionne à environ 5 mm en amont du plan d'entrée de la prise d'air. On notera immédiatement les différences les plus marquantes entre les deux champs de vitesse :

a) pour $\alpha = 10°$, les profils aval sont assez peu modifiés quant à leur forme. Seule la composante axiale a été fortement ralentie par le choc.

b) Pour $\alpha = 22,5°$, apparaît une région où V_z est négative dénotant l'existence d'un "bulbe" qui est l'indice le plus caractéristique de l'éclatement. Egalement, les profils tangentiels sont sensiblement affectés : le mouvement de rotation est assez fortement ralenti et, en conséquence, le vortex s'est dilaté.

Ces comportements sont précisés par les figures 15 et 16 où sont tracées les évolutions de certaines grandeurs caractéristiques : vitesses axiales à la périphérie (V_{z_e}) et au centre (V_{z_0}), vitesse tangentielle maximale (V_{θ_M}) et rayon du noyau "visqueux" (r_M).

Les résultats obtenus ici confirment ceux de la première partie de l'étude, à savoir :

a) pour les interactions avec ou sans éclatement, la composante V_{z_e} subit une discontinuité en accord avec un choc droit à $M_\infty = 2,28$. La vitesse V_{z_0} est plus fortement ralentie ; elle devient même négative pour le vortex éclaté.

b) si le tourbillon n'éclate pas, la composante tangentielle demeure pratiquement invariante à la traversée du choc ; de même que le rayon r_M qui ne se dilate que très légèrement.

c) quand l'éclatement se produit, en revanche, V_{θ_M} diminue notablement, $V_{\theta_M}/V_{z_\infty}$ passant de 0,17 à 0,12. Corrélativement, r_M croît de 25 mm à près de 50 mm.

La figure 17 donne les évolutions de V_{z_0} et V_{θ_M} rapportées à la composante locale périphérique V_{z_e}. Ces tracés mettent bien en évidence l'accentuation très importante du "trou" de vitesse sur l'axe ainsi que la croissance du taux de rotation. Les effets cumulatifs de ces deux tendances auront pour conséquence de "fragiliser" le vortex, à moins que le choc soit suffisamment intense pour le faire éclater immédiatement.

Les distributions de pression statique et de pression génératrice sont tracées figures 18 et 19. Elles ont été calculées à partir de l'équation pour l'équilibre radial écrite sous la forme (approximation d'un écoulement quasi-cylindrique) :

$$(1) \qquad \frac{\partial p}{\partial r} = \rho \frac{V_\theta^2}{r}$$

et en supposant l'enthalpie génératrice partout constante.

L'écoulement tourbillonnaire se caractérise par l'existence d'un déficit de pression génératrice qui est d'autant plus prononcé que les vitesses de rotation sont (relativement) plus élevées. En aval du choc, ce déficit tend à s'amoindrir.

Les distributions radiales de pression statique permettent de fournir une explication du ralentissement de plus en plus fort que subit la composante axiale V_z quand on se rapproche de l'axe. Nous considérons le cas non éclaté. En amont du choc, compte tenu des vitesses V_z et V_θ mesurées à la périphérie du vortex, où l'écoulement est isentropique, la pression statique p_e est ici telle que $p_e/p_{i_0} = 0,0695$. D'où, d'après l'équation pour l'équilibre radial, la valeur sur l'axe $(p_s)_1 = 0,0584\ p_{i_0}$. Sur l'axe de la structure, le choc doit être normal, le nombre de Mach sur sa face amont y est égal à 2,24 ; d'où une pression $(p_0)_2$ immédiatement en aval telle que : $(p_0)_2 = 0,332\ p_{i_0}$. Par ailleurs, les équations du choc normal appliquées à la périphérie avec $M_\infty = 2,28$ et la condition d'équilibre radial écrite pour la première section de mesure située en aval du choc donnent sur l'axe la valeur suivante : $p_0 = 0,382\ p_{i_0}$.
Il y a donc incompatibilité entre la pression juste derrière le choc et la pression imposée par la périphérie, via l'équilibre radial. Il doit donc probablement exister une zone d'étendue très réduite où, dans la région centrale, l'écoulement axial se ralentit afin que la pression, initialement trop faible, s'ajuste avec celle imposée par l'équilibre radial en aval de l'interaction. Ce mécanisme demanderait bien sûr à être confirmé par des mesures plus fines dans le voisinage immédiat de l'onde de choc.

La structure générale de l'écoulement peut être "visualisée" en dessinant les pseudo-lignes de courant associées à l'écoulement méridien moyen. Il est à remarquer que de telles lignes sont en fait fictives puisqu'elles sont associées à un écoulement moyen au sens de la turbulence statistique (décomposition de Reynolds). Dans la réalité, l'écoulement peut être fortement fluctuant et sa structure instantanée beaucoup plus complexe que celle mise en évidence ici (voir en particulier les références [10-11]). De telles lignes sont définies comme des iso-débit q_m avec :

$$q_m = 2\pi \int_0^r \rho V_z \eta\, d\eta$$

La masse spécifique ρ a été calculée par l'équation d'état où la pression p était évaluée comme indiqué plus haut (éq. 1) et la température T en supposant la température génératrice partout constante.

Les figures 20 et 21 représentent ces "lignes de courant" pour les deux configurations analysées (la position du choc n'est qu'indicative, sa forme exacte n'ayant pas été déterminée). Lorsque le tourbillon n'éclate pas, les iso-débit demeurent quasiment cylindriques : on observe seulement une légère dilatation près de l'axe et une légère contraction des zones périphériques. Quand le vortex est éclaté, les "lignes de courant" sont nettement plus déformées. Une forte dilatation se produit dans la région centrale avec formation d'un "bulbe de recirculation" où le débit q_m prend des valeurs négatives.

Les aspects turbulents du phénomène n'ont été que peu étudiés, la taille relativement réduite des échantillons (500 particules) entraînant une trop grande incertitude statistique, surtout sur les corrélations croisées. Néanmoins, les présents essais permettent d'obtenir des renseignements significatifs sur l'évolution des taux de fluctuation de chacune des composantes V_z et V_θ .

La figure 22 donne les profils des valeurs efficaces σ_{V_z} et σ_{V_θ} des fluctuations de V_z et V_θ . Dans le cas non éclaté, les distributions de σ_{V_z} et σ_{V_θ} sont pratiquement confondues et présentent un maximum de faible amplitude situé sur l'axe. Lorsque le tourbillon est éclaté les niveaux de fluctuation augmentent fortement. Alors σ_{V_z} est maximal en dehors de l'axe, en un point qui coïncide sensiblement avec le point d'inflexion des profils de V_z . Le maximum de σ_{V_θ} reste sur l'axe de la structure. La figure 23 montre les évolutions en fonction de la distance axiale de certains niveaux caractéristiques :

a) fluctuation $(\sigma_{V_z})_M / U_\infty$ maximale ;

b) fluctuation $(\sigma_{V_z})_0 / U_\infty$ sur l'axe ;

c) fluctuation $(\sigma_{V_\theta})_0 / U_\infty$ sur l'axe, qui est également le niveau maximal.

En amont du choc, les taux de fluctuation sont compris entre 0,03 et 0,04. Ces niveaux relativement élevés pour ce genre d'écoulement, traduisent en fait une fluctuation d'ensemble de la structure tourbillonnaire.

En l'absence d'éclatement, les différents taux, n'augmentent que modérément à la traversée du choc. (le maximum maximorun est voisin de 0,05). En revanche, quand le vortex éclate les taux de fluctuation (normalisés par U_∞)dépassent largement 0,10. Ainsi $(\sigma_{V_z})_M / U_\infty$ atteint 0,15, ce qui correspond à une intensité $(\sigma_{V_z})_M / V_{Ze}$ = 0,43 si on normalise par la vitesse périphérique locale.

La figure 24 montre des histogrammes à deux dimensions des valeurs instantanées de V_z et V_θ . Ils ont été construits pour une station située à Z = 17 mm, c'est-à-dire à environ 22 mm en aval du choc et sont relatifs à la configuration éclatée. Les trois histogrammes représentés sont associés à des points situés respectivement près de l'axe, là où la vitesse V_z est négative, à l'ordonnée r_M , où la vitesse tangentielle est maximale, et près de la périphérie du vortex.

3 - *MODELISATION DE L'INTERACTION* -

L'interaction choc-vortex est ici modélisée par un écoulement stationnaire de fluide parfait (c'est-à-dire non visqueux) régi par les équations d'Euler. Une telle approche est très certainement justifiée tant que le tourbillon n'éclate pas. Le phénomène s'apparente alors à un processus d'"interaction rapide" dont l'échelle longitudinale (selon l'axe Z) est du même ordre ou plus petite qu'une échelle transversale caractéristique (par exemple, le rayon r_M du noyau visqueux ou une épaisseur attachée au profil axial, si ce dernier n'est pas uniforme).

Dans ces conditions, les forces de viscosité (aussi bien turbulentes que laminaires) ont une action négligeable comparée à celle résultant des forces de pression et des termes d'inertie. La viscosité n'intervient que dans la mesure où elle a créé du rotationnel. En conséquence, l'écoulement abordant le choc a une entropie variable d'une ligne de courant à l'autre, ce qui se manifeste par un "creux" de pression génératrice dans la région centrale du tourbillon (l'enthalpie d'arrêt est elle pratiquement uniforme si le nombre de Mach M_∞ est modéré).

Une telle analyse est classique pour décrire l'interaction entre une couche limite et une onde de pression concentrée (onde de choc ou détente de Prandtl-Meyer). Il est alors démontré que la plus grande partie de la couche limite se comporte comme en écoulement rotationnel non visqueux [12]. Les calculs exécutés selon ce schéma sont très bien recoupés par l'expérience, surtout en turbulent où l'échelle longitudinale est extrêmement réduite [13-14-15]. Il faut toutefois noter que, dans le cas de la couche limite, la viscosité doit forcément intervenir à proximité de la paroi, ce qui pose de délicats problèmes de principe dont la solution a exigé l'introduction de modèles "multi-couches" [12,16]. Une telle difficulté n'existe pas pour le vortex et il y a tout lieu de penser que le modèle rotationnel non visqueux est en mesure de décrire les phénomènes avec une excellente précision tant qu'il n'y a pas éclatement. Quand le tourbillon éclate une approche fluide parfait stationnaire devient discutable (comme dans le cas de la couche limite décollée) en raison du plus grand rôle joué par la viscosité surtout sous forme de corrélations turbulentes résultant des fortes fluctuations qui naissent alors. Il est cependant loisible d'estimer que le schéma non visqueux demeure valable jusqu'à l'apparition de l'éclatement. Dans cette optique, ce peut être un moyen "économique" pour prédire l'apparition de l'éclatement sous l'effet d'un choc, à l'instar de l'utilisation des modèles de couche limite multi-couches pour définir le décollement naissant [17-18].

L'écoulement tourbillonnaire étant supposé de révolution ($\partial/\partial\theta = 0$) les équations d'Euler s'écrivent sous la forme suivante :

- continuité :

$$\frac{\partial \rho}{\partial t} + \frac{\partial(\rho V_z)}{\partial Z} + \frac{\partial(\rho V_r)}{\partial r} + \frac{\rho V_r}{r} = 0$$

- quantité de mouvement :
  . axiale :

$$\frac{\partial}{\partial t}(\rho V_z) + \frac{\partial}{\partial Z}(\rho V_z^2 + p) + \frac{\partial}{\partial r}(\rho V_z V_r) + \rho \frac{V_z V_r}{r} = 0$$

  . radiale :

$$\frac{\partial}{\partial t}(\rho V_r) + \frac{\partial}{\partial Z}(\rho V_z V_r) + \frac{\partial}{\partial r}(\rho V_r^2 + p) + \rho \frac{V_r^2 - V_\theta^2}{r} = 0$$

  . tangentielle :

$$\frac{\partial}{\partial t}(\rho V_\theta) + \frac{\partial}{\partial Z}(\rho V_z V_\theta) + \frac{\partial}{\partial r}(\rho V_r V_\theta) + 2\rho \frac{V_r V_\theta}{r} = 0$$

Une solution stationnaire du système ci-dessus est recherchée via une méthode pseudo-instationnaire où l'enthalpie d'arrêt est supposée constante en permanence sur chaque ligne de courant [19] (dans l'application présente elle est prise constante dans tout le champ). Une telle condition n'est satisfaite que pour une solution stationnaire ; il s'agit donc d'un artifice qui permet d'"économiser" la résolution de l'équation de l'énergie. En contrepartie, la phase instationnaire du calcul est dépourvue de signification physique.

La technique de résolution numérique utilise un schéma prédicteur-correcteur explicite. Le domaine de calcul est représenté figure 25. Il est composé d'une partie amont à section constante BC suivie d'un évasement CD jusqu'à une nouvelle portion cylindrique. La partie terminale du domaine est de forme convergente-divergente de manière à constituer un col en E.

Les conditions aux limites du problème sont les suivantes :

a) glissement sur la paroi BCDEF ;

b) symétrie sur l'axe de révolution AG ;

c) sur la frontière amont AB, où l'écoulement est supersonique, il faut imposer les distributions de vitesse $V_z(r)$ et $V_\theta(r)$ (V_r est supposée nulle) ainsi que celle de la pression p (où, ce qui est équivalent, le profil de pression génératrice) ;

d) le calcul est conduit de façon telle que le col E est amorcé, l'écoulement étant partout supersonique sur FG : donc aucune condition n'est à imposer le long de FG.

La section du col E est définie (par tâtonnement) de manière que le blocage ainsi créé impose une onde de choc située dans la zone évolutive CD où elle peut occuper une position stable en raison de la divergence. La modélisation par un dispositif à second col (qui reflète d'ailleurs, en la schématisant, la réalité expérimentale) permet d'avoir un problème mathématiquement bien posé où les frontières amont et aval du domaine de calcul sont toutes deux supersoniques.

Pour les cas de calcul présentés ici les conditions imposées sur AB sont les suivantes :

a) le profil axial $V_z(r)$ est uniforme, ce qui correspond sensiblement à la situation des expériences décrites au paragraphe précédent.

b) Le profil tangentiel $V_\theta(r)$ est donné par la formule :

$$(2) \qquad V_\theta(r) = \frac{K}{r}\left[1 - \exp\left(-\frac{r^2}{r_H^2}\right)\right]$$

Le coefficient K fixe le taux de rotation du vortex et r_H (même définition que plus haut) sa "concentration". Le rayon r_H est choisi de façon à ajuster au mieux le profil (2) avec les distributions expérimentales.

c) La pression statique est déterminée d'après (2) en intégrant l'équation pour l'équilibre radial.

La figure 25 présente un exemple de maillage utilisé. Des resserrements denses sont prévus près de l'axe ainsi que dans la région du choc.

A titre d'illustration, les figures 26 et 27 donnent des résultats de calcul sous forme de lignes iso-vitesse axiale. Ils sont relatifs à des taux de rotation de 0,22 et 0,55 pour $M_\infty = 1,4$ et de 0,105 et 0,265 pour $M_\infty = 2$ Aux valeurs de τ les plus élevées, les tracés révèlent l'existence d'une "zone de recirculation" où V_z est à contre courant de l'écoulement principal. La formation d'un "décollement" au sein d'un écoulement de fluide parfait s'explique par la présence d'une zone centrale où l'entropie est plus élevée (la "bosse" d'entropie étant d'autant plus haute que le taux de rotation est plus grand) : là, il peut arriver que les particules fluides aient une pression génératrice insuffisante pour surmonter le saut de pression imposé par le choc. Elles sont alors refoulées vers l'amont et piégées dans un "bulbe" de recirculation.

Un balayage systématique en valeurs de M_∞ et τ a ainsi permis de déterminer une limite théorique d'apparition de l'éclatement. Celle-ci est définie comme la situation (M_∞ , τ) où, pour la première fois, existe un point où V_z est ralentie jusqu'à la valeur zéro. La courbe obtenue de cette façon est tracée figure 28. On constate qu'elle est en bon accord avec l'expérience.

La résolution des équations d'Euler, beaucoup plus économique que celle des équations de Navier-Stokes complètes, apparaît donc comme un moyen adéquat pour prédire la limite d'éclatement. Cet "outil" théorique peut ainsi être employé pour procéder à un examen de l'influence de la forme des distributions de vitesses axiale et tangentielle.

4 - CONCLUSION -

L'interaction entre une structure tourbillonnaire enroulée (ou vortex) et une onde de choc normale à l'axe longitudinale de cette structure a été étudiée à la fois sur le plan expérimental et sur le plan théorique.

Une première série de mesures à la sonde de pression anémoclinométrique exécutée pour quatre valeurs du nombre de Mach : M_∞ = 1,60 - 1,75 - 2 et 2,28, a permis :

a) de qualifier l'écoulement au moment où il va aborder l'onde de choc ;

b) de préciser, en l'absence d'éclatement, les modifications de structure que le vortex subit à la traversée du choc. L'influence du taux de rotation est mise en évidence.

c) de définir une limite d'éclatement en fonction des deux paramètres : intensité du choc - taux de rotation. Le résultat obtenu montre un accroissement de la "fragilité" du vortex quand ses vitesses de rotation augmentent.

L'étude a été complétée par une analyse du champ (mesure des grandeurs moyennes et fluctuantes) au vélocimètre laser. Deux configurations (à $M_\infty = 2{,}28$) ont été explorées en détail : l'une est une interaction sans éclatement, l'autre correspond à une situation où le choc fait éclater le vortex Dans ce dernier cas, les mesures mettent en évidence une structure moyenne dont l'écoulement méridien inclut un "bulbe de recirculation" fermé situé sur l'axe du vortex. L'éclatement s'accompagne d'un très fort accroissement des fluctuations de vitesse.

Une modélisation de l'interaction a été développée à partir des équations d'Euler stationnaires (le phénomène est assimilé à un processus d'interaction rapide où les effets visqueux jouent un rôle négligeable). En l'absence d'éclatement, le calcul donne une description fidèle de l'écoulement. La théorie permet aussi de prédire une limite d'éclatement qui, pour les cas traités, est en bon accord avec l'expérience.

5 - NOTATIONS UTILISEES -

Symboles

M : nombre de Mach

p : pression statique

p_i : pression génératrice

q_m : débit massique

r : distance à l'axe de la structure tourbillonnaire

T : température statique absolue

T_i : température génératrice absolue

U : vitesse longitudinale extérieure au vortex, en amont de l'onde de choc

V_r : composante de vitesse radiale

V_z : composante de vitesse longitudinale

V_θ : composante de vitesse tangentielle

$Oxyz$: trièdre "mesure", O est au centre de la section d'entrée de la prise d'air, Ox est l'axe horizontal longitudinal, Oy est l'axe horizontal transverse, Oz est vertical.

Ω_z : axe longitudinal du vortex, supposé de révolution . Ω est dans le plan d'entrée de la prise d'air.

α : incidence de l'aile générant le vortex

γ : angle d'hélice $\gamma = Arctg\ (V_\theta / V_z)$

θ : coordonnée angulaire

ρ : masse spécifique

σ_{V_z} : valeur efficace de la fluctuation de V_z.

σ_{V_θ} : valeur efficace de la fluctuation de V_θ

τ : taux de rotation $(\tau = V_{\theta_M} / V_{z_e})$

ω : centre local du vortex

Ω : origine de l'axe longitudinal du vortex.

Indices

e : caractérise les conditions à la périphérie du vortex

0 : caractérise les conditions au centre du vortex

M : caractérise les conditions au point de vitesse tangentielle maximale

∞ : caractérise les conditions à l'extérieur du vortex en amont du choc.

6 - REFERENCES -

[1] PEAKE, J.D et TOBAK, M. -
"Three dimensional interactions and vortical flows with emphasis on high speeds"
AGARDograph No 252 (1980).

[2] CRAVEN, A.H. et ALEXANDER, A.J. -
"An investigation of vortex breakdown at Mach 2" The College of Aeronautics, Department of Aerodynamics; CoA Note Aero 158 (1963).

[3] ZATOLOKA, V.V., IVANYUSHKIN, A.K. et NIKOLAYEV, A.V. -
"Interference of vortexes with shocks in airscoc -. Dissipation of Vortexes "Fluid Mechanics, Soviet Research, Vol.7, No.4, pp.153-158 (1978) En anglais.

[4] SOLIGNAC, J.L. et LEUCHTER, O. -
"Etudes expérimentales d'écoulements tourbillonnaires soumis à des effets de gradient de pression adverse"
AGARD Symposium on "Aerodynamics of vortical type flows in three dimensions", Rotterdam, Netherlands, 25-28 April 1983.

[5] GAILLARD, R. et HOORELBEKE, J.-
"Utilisation de sondes de pression anémoclinométriques miniaturisées fonctionnant dans le domaine 0,2 M 2,6 et dans une large plage d'incidence (40°)"
ONERA - RT n° 67/1865 AN (à paraître).

[6] GAILLARD, R -
"Etat actuel des systèmes d'acquisition spécifiques de la soufflerie S5Ch"
ONERA - RT n° 66/1865 AN (Juillet 1982).

[7] BOUTIER, A -
"Two dimensional laser velocimeter 20 H61"
ONERA data sheet 1981-4 (1981).

[8] HALL, M.G. -
"Vortex breakdown" Annual Review of Fluid Mechanics, vol.4 pp. 195-218 (1972).

[9] WEDEMEYER,E -
"Vortex breakdown" in"High Angle of Attack Aerodynamics",
AGARD-VKI Lecture Series 121 (1982).

[10] SARPKAYA, T.
"On stationary and travelling vortex breakdowns"
J.Fluid Mech. vol. 45, pp.545-559 (1971).

[11] WERLÉ, H. -
"Sur l'éclatement des tourbillons"
ONERA - NT 175 (1971).

[12] LIGHTHILL, M.J. -
"On boundary layers and upstream influence. II Supersonic flows without separation"
Proc. Roy. Soc., A 217, pp.478-507 (1953).

[13] CARRIERE, P. et SIRIEIX, M. -
"Facteurs d'influence du recollement d'un écoulement supersonique ".
10è Congrès International de Mécanique Appliquée, Stresa, Italie (1960).

[14] DELERY, J. et MASURE, B -
"Action d'une variation brusque de pression sur une couche limite turbulente et application aux prises d'air hypersoniques".
La Recherche Aérospatiale, No 129, pp. 3 - 12 (1969).

[15] ROSE, W.C, MURPHY, J.C et WATSON, E.C -
"Interaction of an oblique shock-wave with a turbulent boundary-layer" .
AIAA Journal, vol.6, No 9, pp.1792 - 1793 (1968).

[16] STEWARTSON, K et WILLIAMS, P.G. -
"Self induced separation" Proc. Roy. Soc., A 312, pp.181-206 (1969).

[17] INGER, G.R.
"Transonic shock/ turbulent boundary-layer interaction and incipient separation on curved surfaces"
AIAA Paper 81-1244 (1981).

[18] BOHNING, R. et ZIEREP, J. -
"Normal shock/turbulent boundary-layer interaction at a curved wall".
AGARD CP - 291 (1981)

[19] VIVIAND, H. et VEUILLOT, J.P. -
"Méthodes pseudo-instationnaires pour le calcul d'écoulements transsoniques"
ONERA - Publication No 1978-4 (1978).

REMERCIEMENTS

Les auteurs tiennent à remercier l'équipe de la soufflerie S5 qui, sous la responsabilité de M.J.HOORELBEKE, a assuré la conduite des essais ainsi que MM. C.d'HUMIERES et D.SOULEVANT qui avaient la charge des mesures au vélocimètre Laser.

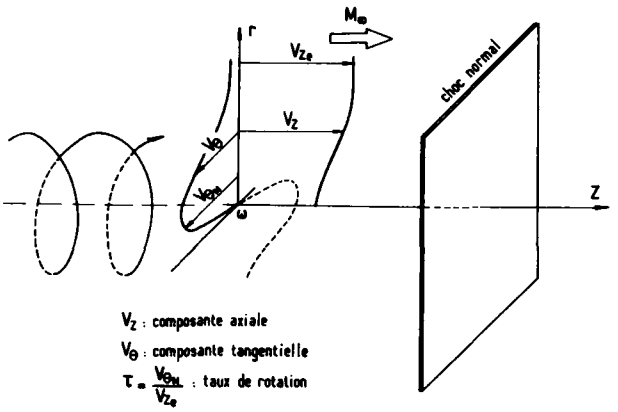

Fig. 1 SCHEMATISATION DU PHENOMENE ETUDIE

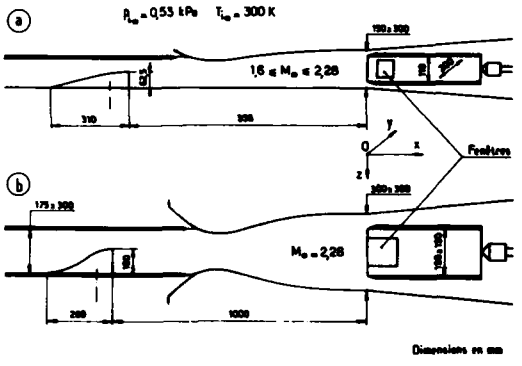

Fig. 2 MONTAGES EXPERIMENTAUX

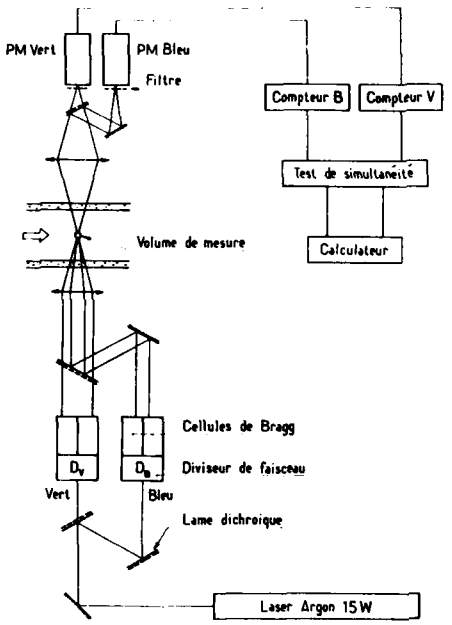

Fig. 3 SCHEMA DE PRINCIPE DU VELOCIMETRE LASER

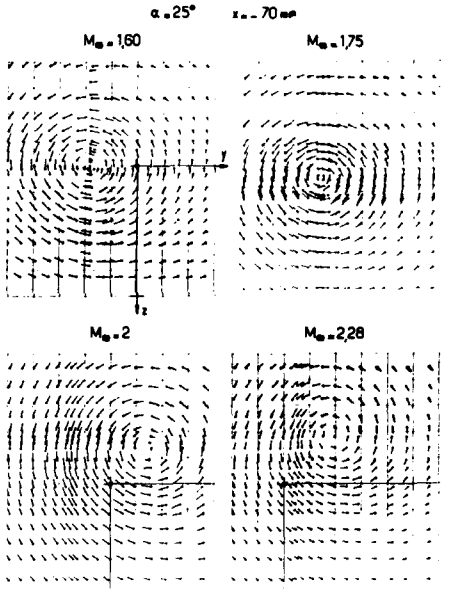

Fig. 4 CARTOGRAPHIES DU CHAMP TANGENTIEL EN AMONT DU CHOC

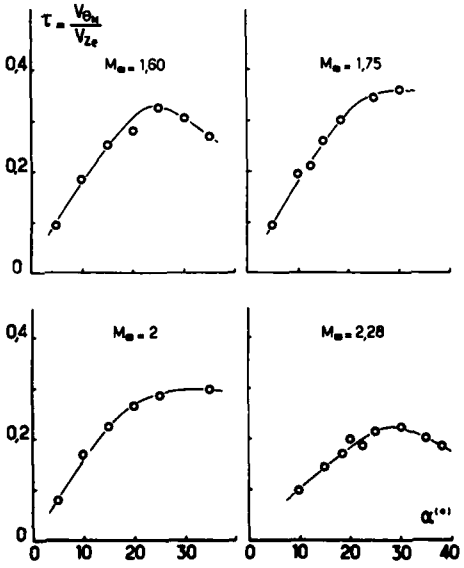

Fig. 5 TAUX DE ROTATION EN AMONT DU CHOC
(α : incidence de l'aile)

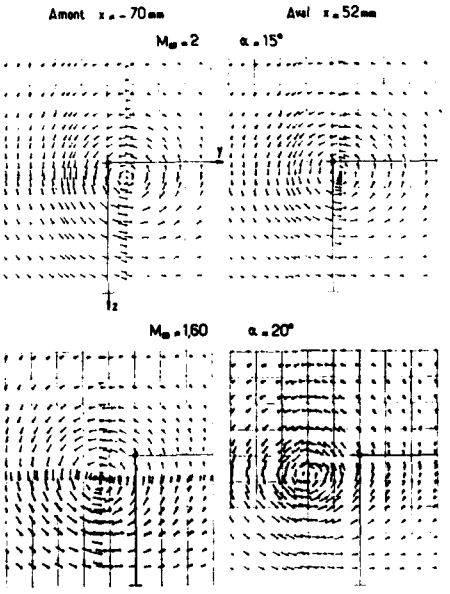

Fig. 6 CARTOGRAPHIES DU CHAMP TANGENTIEL EN AMONT ET EN AVAL DU CHOC

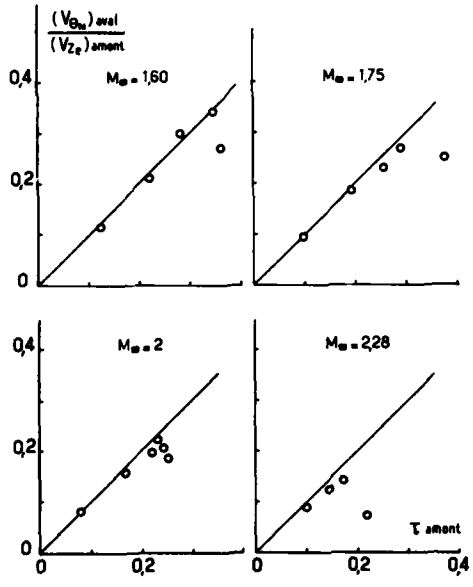

Fig. 7 INFLUENCE DU CHOC SUR LA COMPOSANTE TANGENTIELLE MAXIMALE

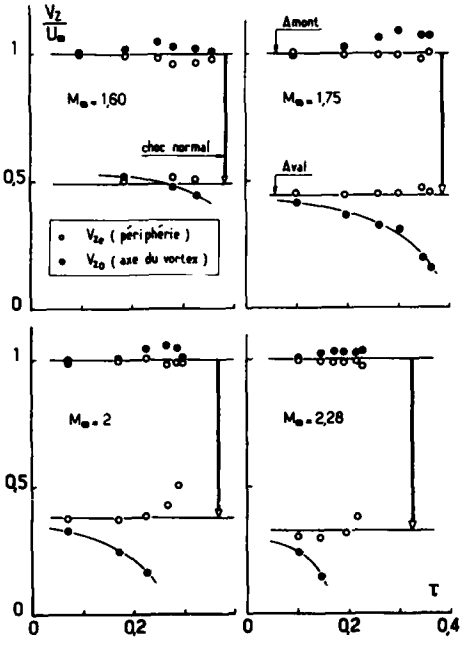

Fig. 8 INFLUENCE DU CHOC SUR LA COMPOSANTE AXIALE

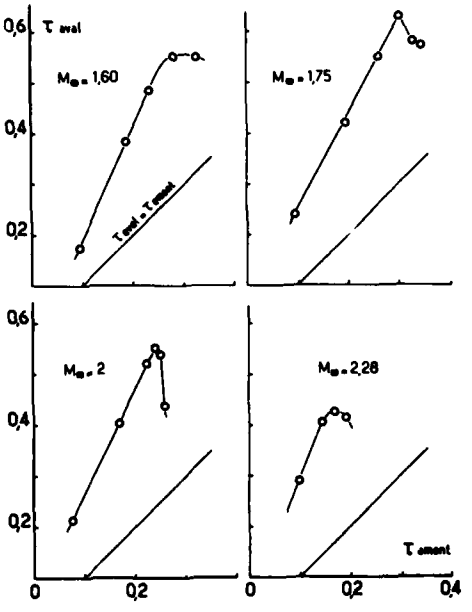

Fig. 9 INFLUENCE DU CHOC SUR LE TAUX DE ROTATION

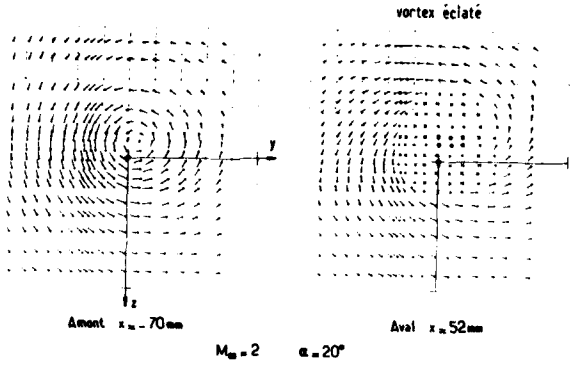

Fig. 10 CARTOGRAPHIES DU CHAMP TANGENTIEL EN AMONT ET EN AVAL DU CHOC

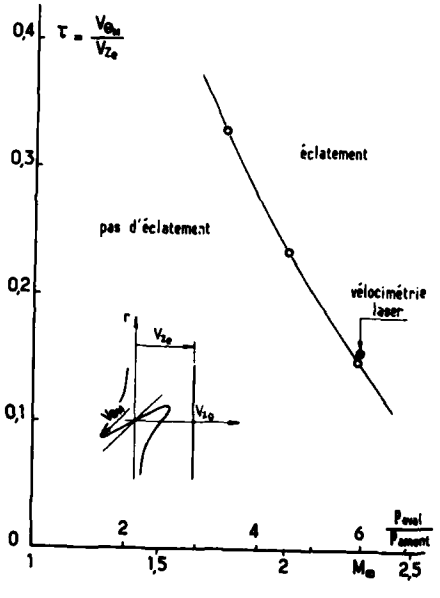

Fig. 11 TAUX DE ROTATION LIMITE EN FONCTION DE L'INTENSITE DU CHOC POUR $V_{z_0} \approx V_{z_\infty}$

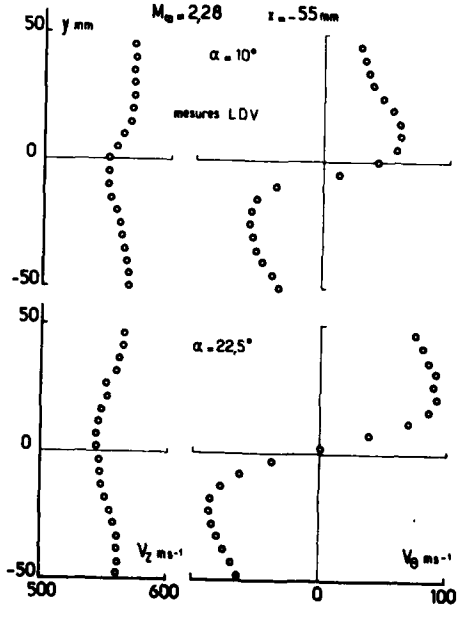

Fig. 12 PROFILS AXIAUX ET TANGENTIELS EN AMONT DE L'ONDE DE CHOC

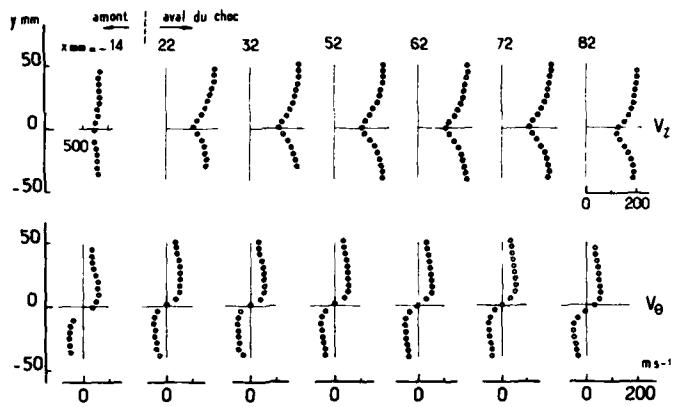

Fig. 13 PROFILS AXIAL ET TANGENTIEL _ Vortex non éclaté _ ($\alpha = 10°$)

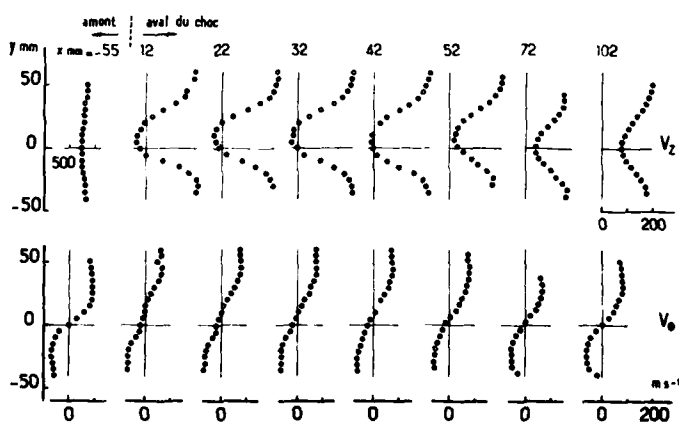

Fig. 14 PROFILS AXIAL ET TANGENTIEL _ Vortex éclaté _ ($\alpha = 22,5°$)

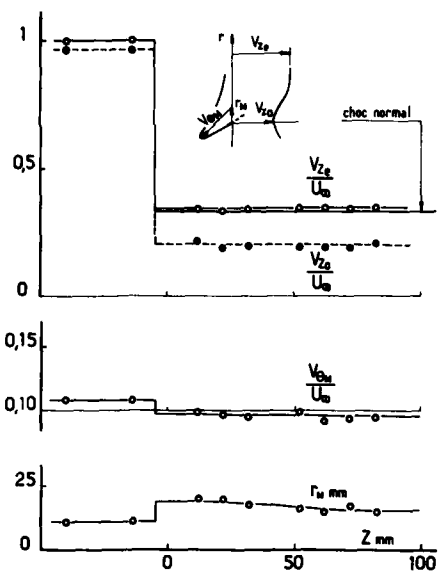

Fig. 15 EFFET DU CHOC
SUR CERTAINES GRANDEURS CARACTERISTIQUES
Vortex non éclaté _ α = 10°

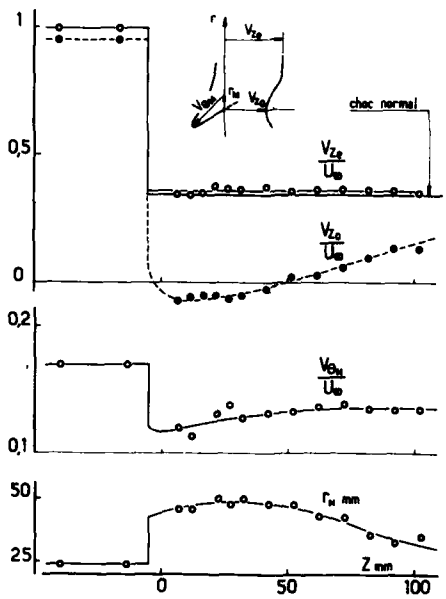

Fig. 16 EFFET DU CHOC
SUR CERTAINES GRANDEURS CARACTERISTIQUES
Vortex éclaté _ α = 22,5°

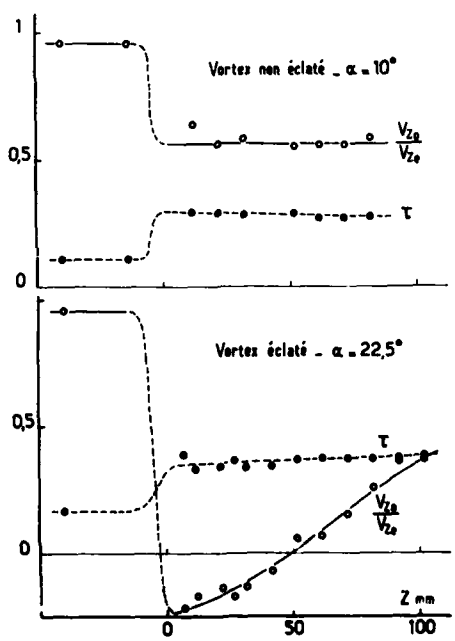

Fig. 17 EFFET DU CHOC SUR LA VITESSE SUR L'AXE
ET LE TAUX DE ROTATION

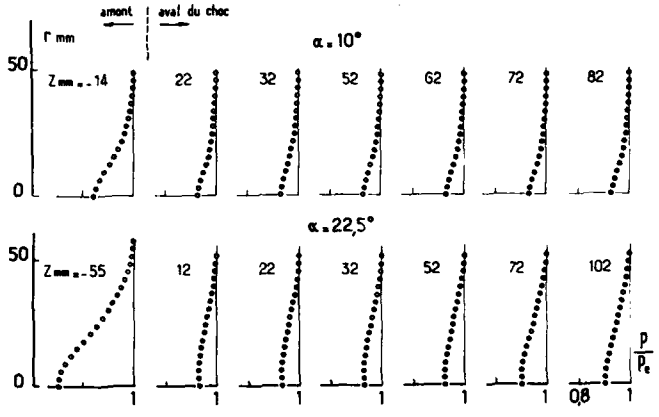

Fig. 18 DISTRIBUTIONS DE PRESSION STATIQUE

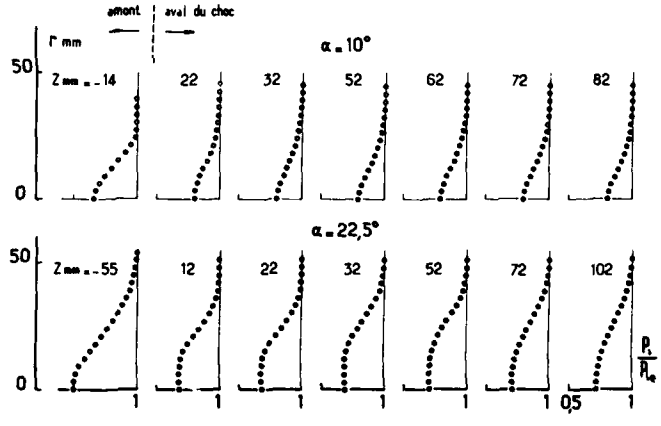

Fig. 19 DISTRIBUTIONS DE PRESSION GENERATRICE

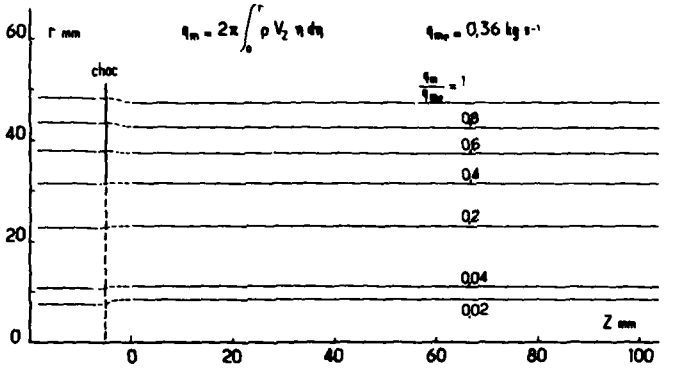

Fig. 20 LIGNES DE COURANT DE L'ECOULEMENT MERIDIEN MOYEN
Vortex non éclaté . $\alpha = 10°$

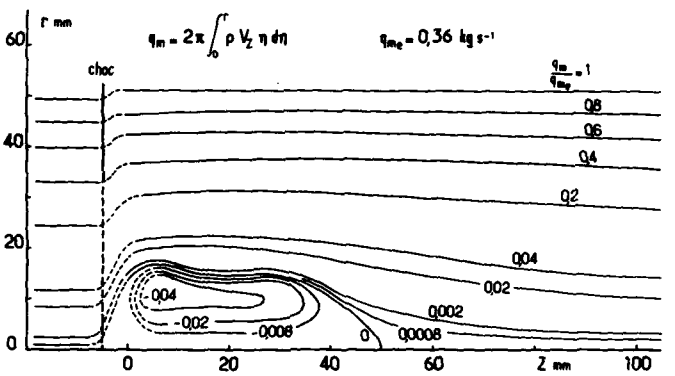

Fig. 21 LIGNES DE COURANT DE L'ECOULEMENT MERIDIEN MOYEN
Vortex éclaté . $\alpha = 22,5°$

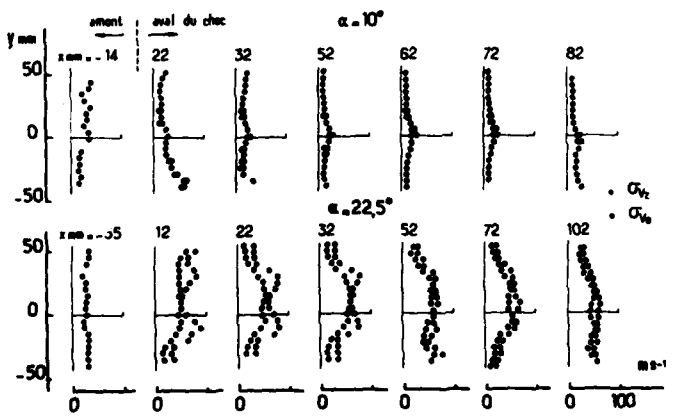

Fig. 22 VALEURS EFFICACES DES FLUCTUATIONS DE V_z ET V_θ

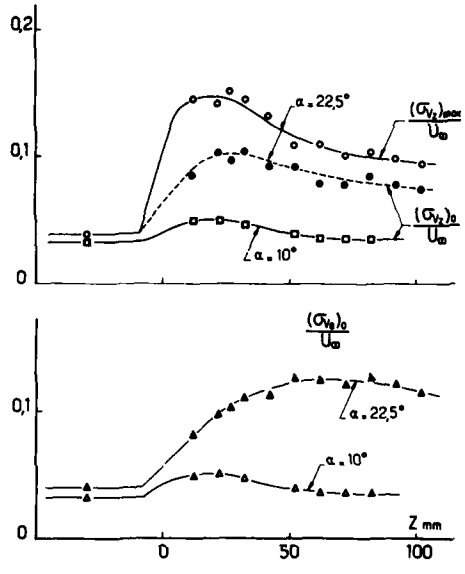

Fig. 23 EFFET DU CHOC
SUR DES NIVEAUX DE FLUCTUATION CARACTERISTIQUES

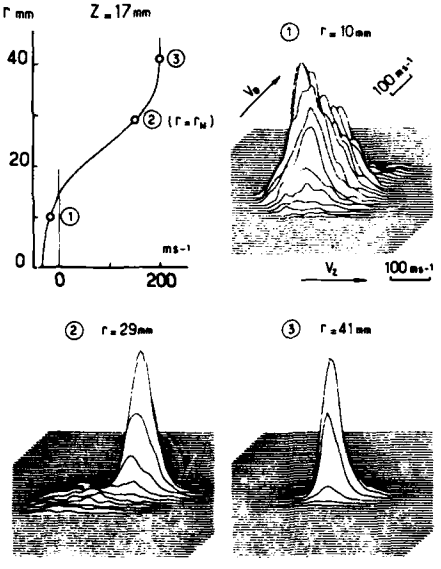

Fig. 24 HISTOGRAMMES DES VITESSES V_Z ET V_θ

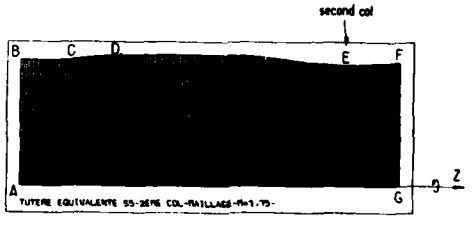

Fig. 25 DOMAINE DE CALCUL ET MAILLAGE

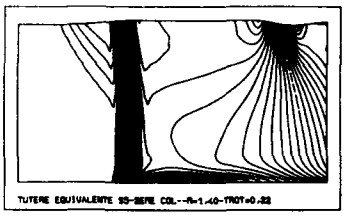

τ = 0,22

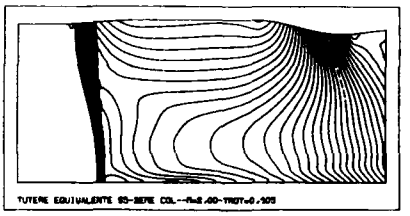

τ = 0,105

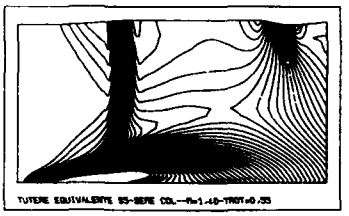

τ = 0,55

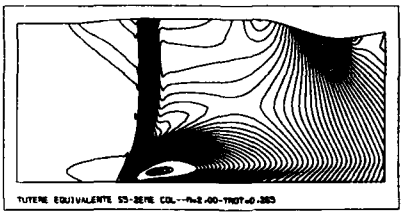

τ = 0,265

Fig. 26 LIGNES ISO-VITESSE AXIALE $M_\infty = 1,4$

Fig. 27 LIGNES ISO-VITESSE AXIALE $M_\infty = 2$

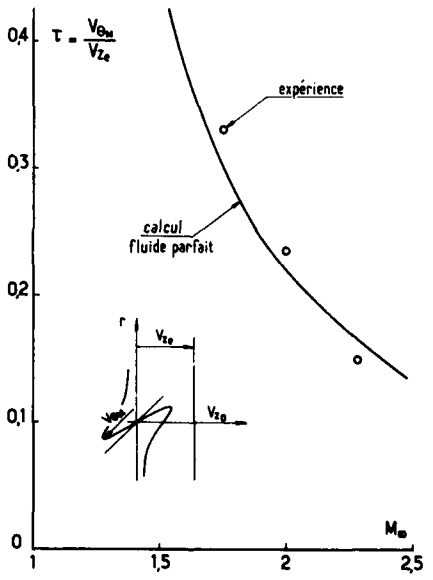

Fig. 28 LIMITE D'ECLATEMENT CALCULEE
$V_{Z_e} = V_{Z_s}$

'ON THE GENERATION AND SUBSEQUENT DEVELOPMENT OF SPIRAL VORTEX FLOW OVER A SWEPT-BACK WING'

by

D.I.A. Poll

Aerodynamics Division, College of Aeronautics,
Cranfield Institute of Technology, Cranfield,
Bedfordshire, MK43 OAL, England

SUMMARY

An experimental investigation has been performed to study the formation and development of spiral vortex flow over a swept-back wing. An aerofoil section with three alternative leading edge shapes was tested at sweep angles ranging from 0° to 56° for unit Reynolds number of 1×10^6/m and 2×10^6/m. The principal diagnostic tool was the surface oil-flow visualisation technique supplemented by pressure distribution measurements in certain cases. No spiral vortex flow was observed for sweep angles of 0° and 15° but at higher sweep angles the oil-flows indicated that there were three different mechanisms for the formation of spiral vortices. The angle of incidence at the onset of vortex flow, and the mechanism responsible for its formation, were found to depend upon the sweep angle, the leading edge shape and the Reynolds number. It was also noted that the larger the leading edge radius the greater the dependence upon Reynolds number. However comparison with other work suggests that Reynolds number, incidence and sweep angle alone are insufficient to determine the type of spiral vortex flow occuring on a given wing.

NOTATION

C	normal to leading edge chord	x	distance measured along C
C_o	streamwise chord	y	distance measured normal to C
Cp	pressure coefficient $(p-p_\infty)/\frac{1}{2}\rho_\infty Q_\infty^2$	α	streamwise incidence
p	static pressure	ν	kinematic viscosity
Q_∞	free-stream speed	ρ	leading edge radius in the x, y plane
R	streamwise Reynolds number $Q_\infty C_o/\nu$	ρ_∞	free-stream density

1. INTRODUCTION

For many years sweep-back has been applied to wings to delay the onset of compressibility effects. However sweep-back can also radically alter other aerodynamic characteristics of a wing. In particular it may have an important effect on the generation of lift at high angles of incidence. For an unswept wing the 'stall' usually sets an upper limit on the useful lifting performance. This phenomenon is characterised by the separation of the upper surface boundary layer at some point between the leading and trailing edges. The vortex sheet which issues from the point of separation is displaced from the corresponding sheet shed from the lower surface at the trailing edge by a distance which is of order the aerofoil chord length and these vortex sheets form the upper and lower boundaries of an unsteady wake. The application of sweep, however, offers this stalled flow an extra degree of freedom in so far as the addition of a spanwise component of velocity may lead to a rolling up of the upper surface sheet into a single spiral vortex. If this vortex is strong and located close to the upper surface then its pressure field can considerably extend the useful lifting range of the wing although there is, of course, a substantial drag penalty.

Whilst the benefits of encouraging spiral vortex flow for the improvement of high incidence performance have been exploited to some degree; for example by the use of strakes, our basic understanding of the physical processes is still generally poor. This is despite the fact that the conceptual ground rules for vortex sheet separation and associated phenomena were formulated 30 years ago by Küchemann[1] and Maskell[2]. In particular for a given aerofoil section, sweep angle and Reynolds number it is not possible to predict with any degree of accuracy the angle of incidence at which spiral vortex flow is established.

The object of the present experiment was to investigate in a systematic way, the combination of sweep angle, Reynolds number and incidence necessary for the onset of spiral vortex flow for a family of aerofoil sections having different leading edge radii. Of special interest was the way in which the establishment of the spiral vortex flow was affected by Reynolds number since there is very little swept wing data available from tests in which the chord Reynolds number was greater than 10^6. In addition, the development of the spiral vortex flow and its influence on the wing pressure distribution were investigated up to the highest incidences available with the tunnel/model combination.

2. THE EXPERIMENTAL ARRANGEMENT

The tests were carried out on a wing of rectangular planform which was mounted as a 'half model' in the College of Aeronautics 2.44 m x 1.83 m low-speed wind-tunnel - see figure 1. This basic panel had a taper ratio of 1.0 and a nominal chord length of 0.762 m measured in the normal to leading edge direction. In all the configurations considered the semi-span was fixed at 75% of the tunnel width and triangular end pieces were added so that the wing always had a streamwise tip section. This restriction on the semi-span was imposed in order that the variation of local angle of attack induced by the close proximity of the solid wind-tunnel walls be kept sufficiently small to avoid premature tip stalling - see reference 3. Tests were conducted at sweep angles of 0°, 15°, 30°, 45° and 56°. A summary of the variation of the planform characteristics with sweep angle is presented in Table 1.

The datum aerofoil section chosen for this investigation was RAE 101 with a 12% thickness to chord ratio when viewed in a plane drawn perpendicular to the leading edge. This is shown in figure 2. Despite the fact that the RAE aerofoil sections were developed 40 years ago this particular shape was chosen for two reasons. Firstly, the geometry is expressed in a convenient, explicit algebraic form (Goldstein and Richards[4]) which greatly simplified the design of the model and, secondly, the location of the maximum thickness is typical of that found on modern aft loaded aerofoil sections. In addition to the datum RAE 101 leading edge ($\rho/C = 0.012$) two additional leading edge sections were designed. These were based upon a general shape described by the function

$$y = (a + bx + cx^2 + dx^3)^{\frac{1}{2}},$$

for

$$x_o \leqslant x < 0.1,$$

where a, b, c, d are constants and x_o is the value of x at which y = 0. For the present purposes three of the four constraints necessary to determine the values of the constants were provided by equating the displacement, slope and curvature of the nose profile to those of the basic RAE 101 section at an x of 0.1. The final constraint was provided by specifying the value of the leading edge radius. This is equivalent to fixing the value of x_o because the leading edge radius is a function of x_o only. Since only two alternative profiles were to be made, extreme values were chosen for the leading edge radii. In the first case ρ/C was fixed at 0.0003. This small value was chosen so that results could be compared directly with the large body of data which exists for slender delta wings with 'sharp' leading edges. For the second case ρ/C was chosen to be 0.03. Leading edges with this degree of bluntness are sometimes found on the more modern super-critical class of aerofoil sections. The three leading edge profiles are compared in figure 3.

The major part of the experimental work consisted of a comprehensive surface oil-flow visualisation investigation. This was conducted for the parameter ranges indicated in Table 2. A total of 250 combinations of sweep, incidence, Reynolds number and leading edge radius were examined and 107 of the patterns were photographed. In a subsequent exercise sets of pressure tappings were drilled at three spanwise stations corresponding to root, mid-span and tip. Each set consisted of 51 holes distributed over the upper and lower surfaces of the wing. Using the oil-flow results as a guide, pressure distributions were recorded for 46 configurations which were believed to exhibit features of interest.

3. RESULTS

Sharp leading edge ($\rho/C = 0.0003$)

a) Zero Sweep

At zero incidence the flow was attached right to the trailing edge with boundary layer transition occuring at approximately 50% chord except at the root and tip where turbulent wedges emanated from the leading edge. As incidence was increased beyond zero degrees the upper surface laminar boundary layer separated close to the leading edge. The resulting free shear-layer rapidly underwent a transition to turbulence which resulted in flow re-attachment to form a bubble structure. However, since the root and tip stations supported turbulent wedges the lines of separation and re-attachment met at these locations thereby closing the bubble at its spanwise extremities. Over the mid-part of the span the chordwise distance between the position of separation and the position of re-attachment increased rapidly with increasing incidence. This was due almost entirely to aft movements of the re-attachment line and this behaviour indicates that the bubble structure was of the 'long' type. The downstream end of the bubble reached the trailing edge at the mid-span location at an incidence of 12°. The corresponding surface oil-flow pattern and pressure distributions are presented in figure 4. These pressure distributions show that the closer the re-attachment line was to the leading edge (root and tip regions) the lower the minimum pressure. It should also be noted that the point of minimum pressure always lay within the bubble region. At incidences beyond 12° the lifting performance deteriorated rapidly, the flow over the wing became very unsteady and the pressure over the upper surface became almost constant, except in regions very close to the tip.

AD A135 157 AERODYNAMICS OF VORTICAL TYPE FLOWS IN THREE DIMENSIONS: CONFERENCE PROCE..(U) ADVISORY GROUP FOR AEROSPACE RESEARCH AND DEVELOPMENT NEUILLY.. JUL 83 AGARD-CP-342 2/6

UNCLASSIFIED F/G 20/4 NL

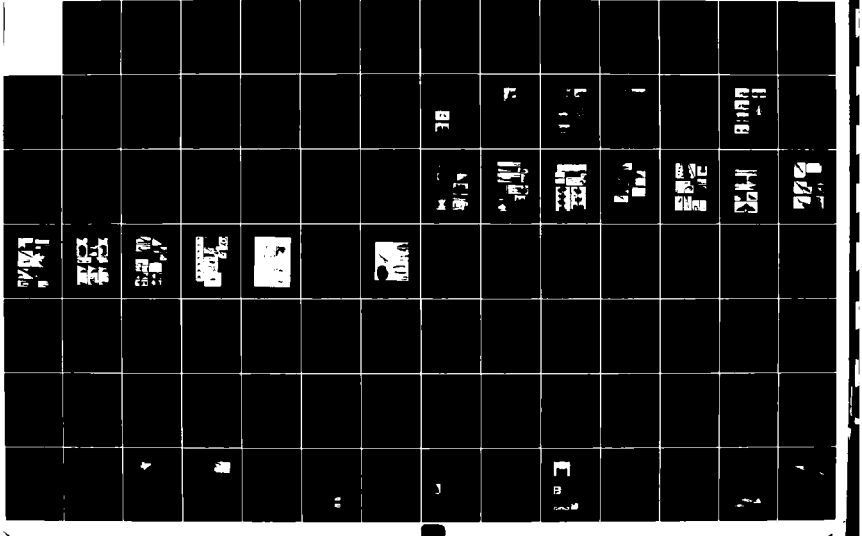

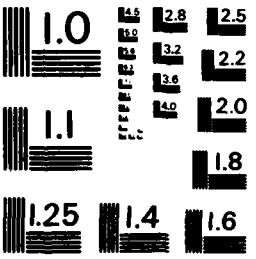

b) 15° Sweep

The development of the flow with incidence as determined by the surface oil-flow visualisation was virtually the same as the zero sweep case. Stalling occurred at an incidence of approximately 12° as the downstream end of the long bubble passed the trailing edge at the mid-span point. There was no identifiable spiral vortex flow developed at this sweep angle.

c) 30° Sweep

With 30° of sweep significant three-dimensional effects were noted in the oil-flow patterns even at low angles of attack. At an incidence of 3.5° the quasi two-dimensional long bubble structure was no longer observed. Instead the oil-flow revealed the presence of the fully three-dimensional vortex sheet structure sketched in figure 5. In this case it appears that the sheet which left the wing surface along the primary separation line at the leading edge was rolling up to form a strong vortex which lay very close to the wing. This vortex drew free-stream fluid down towards the surface to attach along the line shown. On one side of this attachment line the flow travelled towards the trailing edge and reached it without separating. However, on the other side the flow was towards the leading edge. Initially this reversed flow experienced a favourable pressure gradient but having passed beneath the vortex core an adverse pressure gradient was encountered and the flow separated as indicated. The sheet of vorticity emanating from this secondary separation line then became entrained into the vortex in the manner shown in the figure. The modest amount of pressure recovery attained by this flow suggests that, for the Reynolds number range considered in this experiment, the boundary layer was in the laminar state at the point of secondary separation. For incidences up to 9° a clear attachment line structure was observed. In each case the origin lay close to the leading edge at the root station and the line was straight almost up to the tip. The extrapolated attachment line met the tip at a chordwise station which increased with increasing incidence e.g. at 5° the line met the tip station at an x/C of approximately 0.06 whilst at 7° it was 0.10 - see figure 6. Beyond 9° incidence the vortex burst over the wing. This modification to the vortex induced pressure field caused the attachment line to terminate part way across the span as shown in figure 7. One interesting consequence of this was that the inboard flow near the secondary separation line was from root to tip whilst the outboard flow was from tip to root. Therefore a 'blob' of oil formed on the leading edge at approximately the same spanwise location as the vortex burst. Further increases in incidence simply drove the vortex burst (and the oil blob) towards the apex of the wing with the limiting position being reached at approximately 20° incidence. Beyond 20° there was considerable flow unsteadiness.

d) 45° Sweep

Up until 8° incidence the flow was similar to that found with 30° of sweep. However, as the vortex burst developed beyond 8° the attachment line became highly curved as shown in figure 8. This indicates that the vortex was turning to align itself with the free stream and that it crossed the trailing edge somewhere between the mid-span and tip locations. The appearance of a separation line out near the tip also suggests that the flow along the trailing edge had passed underneath the vortex. As incidence was increased further the secondary separation line moved away from the leading edge and joined the tip separation line to form a continuous structure running from the wing apex to the trailing edge - see figure 9. In this case the pressure distribution clearly indicates that in the vicinity of the root the boundary layer was turbulent at secondary separation and the location of the vortex burst is shown by a kink in the secondary separation line. This steady flow pattern was found at all incidences up to the highest available i.e. 25°.

e) 56° Sweep

Once again at the low incidences (7°) the surface oil-flow patterns showed a qualitively similar behaviour to those found at 30° and 45° sweep. At an incidence of 7° the vortex core passed over the trailing edge causing a separation of the spanwise flow near the tip station. Figure 10 shows the surface flow patterns and pressure distributions for 11° incidence where a continuous attachment line and continuous secondary separation line ran from the leading edge at the root to the trailing edge out near the tip. The pressure distributions show that the vortex was strong and that the boundary layer flow was probably turbulent at the secondary separation line. There was no kink in the separation line to suggest vortex bursting. This steady flow was obtained at all incidences up to the maximum of 20°. The peak suctions induced by the vortex occurred at approximately 14° incidence for all spanwise stations.

The tests described above were conducted with a wind speed of approximately 30 m/sec. In order to examine the effect of Reynolds number many of the configurations were also tested at 15 m/sec. In the case of the sharp leading edge the surface oil-flow patterns showed no significant variation for the Reynolds number range 0.75×10^6 to 3.0×10^6.

RAE 101 leading edge (ρ/C = 0.012)

a) Zero Sweep

For angles of incidence less than 6° the flow was attached from leading to trailing edges. Transition was clearly visible in the surface oil-flow and the transition front on the upper surface was observed to move forward as the angle of incidence was increased. At 7° a bubble was formed close to the leading edge which extended from the root to within 0.46 m of the tip. Further increases in incidence caused the outboard end of the bubble to move closer to the tip but the chordwise extent of the bubble was hardly altered. The absence of chordwise length variation with incidence indicates that the bubble was of the 'short' type. At a Reynolds number of 8×10^5 the wing stalled at about 14°. When the Reynolds number was increased to 1.5×10^6 the stall began at 16°. The stall was produced by a separation of the turbulent boundary layer downstream from the short bubble. Unsteady reversing flow was observed from the trailing edge right up to the bubble but there was a small region of attached flow maintained at the tip. The surface pressure distributions showed large suctions developing close to the leading edge. At the incidences just below the stall the peak suctions (C_p of order -7) were occuring over the mid-span region with reduced suctions being found towards both root and tip.

b) 15° Sweep

As in the case of zero sweep there was attached transition and no bubble structure formed until 7° incidence. At 7° incidence a short bubble formed over the mid-span section of the wing - where the pressure measurements indicated that the loading near the leading edge was largest. As incidence was increased further the bubble spread rapidly in the spanwise direction towards both root and tip. A full span bubble was observed at 10°. Once again the stall angle was found to be Reynolds number dependent. At the highest Reynolds number (1.5×10^6) the flow was separated from the bubble to the trailing edge at 16° incidence, although there were some small regions of attached flow in the vicinity of the root and tip. By 18° incidence the flow was unsteady and reversing right from root to tip with only small patches of short bubble structure remaining.

c) 30° Sweep

In this case the short bubble formed in the mid-span region at about 6°. At 7° the outboard end of the bubble had reached the tip whilst the inboard end was still some 0.43 m from the root. As incidence was increased the inboard end of the bubble moved closer to the root with the movement being essentially complete by 12°. At this incidence there was spanwise flow at the trailing edge with a small region of reverse flow at the tip - see figure 11. Going from 13° to 14° incidence caused the outboard flow to collapse as shown in figure 12 leaving the root as the most highly loaded portion of the wing. The movement of the oil over the outboard sections suggested that the vortex sheet leaving the primary separation line was rolling up to form a part-span spiral vortex - see Black[5]. However, at this sweep angle the vortex was only capable of inducing relatively weak flows at the aerofoil surface. Increasing the incidence to higher values simply caused the spanwise extent of the attached root flow to contract with a corresponding increase in the general level of unsteadiness in the separated flow. Flow patternsobtained at Reynolds numbers of 8.7×10^5 and 1.7×10^6 showed very similar qualitative behaviour.

d) 45° Sweep

For a Reynolds number of 2.1×10^6 a short leading edge bubble formed at the tip at 4° incidence. Increasing the incidence caused the upstream end of the bubble to move closer to the root. At 12° incidence the bubble was still 0.2 m from the root with the oil-flow indicating predominantly spanwise flow with a region of reversed flow at the trailing edge over the outer part of the wing. When the incidence was raised to 14° the flow in the vicinity of the tip collapsed to form a part-span vortex with the characteristic oil-blob 'eye' located close to the leading edge and 0.89 m from the tip. The corresponding oil-flow and surface pressure distribution are given in figure 13. As the incidence was increased further the part-span vortex origin moved along the leading edge towards the root and a line of secondary separation developed as shown in figure 14. A similar flow field was observed up to the maximum incidence available (24°).

Tests at the lower Reynolds number (1×10^6) revealed that for incidences below 12° the surface oil-flow patterns were indistinguishable from those observed at a Reynolds number of 2.1×10^6. However, at 13° the surface flow changed abruptly to the type sketched in figure 15. In this case the short bubble structure did not form. Instead the shear layer eminating from the primary separation line appeared to be rolling up to form a strong spiral vortex which caused free-stream air to attach at some downstream station with a secondary separation line forming between this attachment line and the primary separation line. The structure of this flow appears to be qualitatively similar to that found on the sharp leading edge at the same incidence and sweep angle - see figure 9. Further increases in incidence did not change the basic features of the pattern but beyond 14° the secondary separation line crossed the trailing edge rather than the tip and beyond 16° the attachment line structure did not extend right to the trailing edge.

e) 56^{o} Sweep

At incidences below 10^{o} the development of the surface flows were very similar to that observed at 45^{o} of sweep and the same results were observed at Reynolds numbers of 1.4×10^{6} and 2.7×10^{6}. The surface oil-flow pattern and pressure distributions for 10^{o} incidence are shown in figure 16. At the higher Reynolds number increasing the incidence to 11^{o} resulted in a modification in the tip flow as shown in figure 17. Here there was a full span short bubble structure but on the outer part of the wing the flow separated just downstream from the bubble re-attachment line. The shear layer originating at this secondary separation line apparaently rolled up to form a vortex which was sufficiently strong to induce the free-stream fluid to form a secondary attachment line as shown. Finally flow from the secondary attachment line was observed to separate along a tertiary separation line which was formed close to the trailing edge. Further increases in incidence at this high Reynolds number caused the flow features described above to move across the wing towards the root station - see figure 18. At the lower Reynolds number the short leading edge bubble was not found at incidences beyond 10^{o}. Instead the three-dimensional vortex structure previously observed at the low Reynolds number with 45^{o} sweep was found again as shown in figure 19. This pattern was observed at incidences up to the maximum available (18^{o}).

Blunt leading edge ($\rho/C = 0.03$)

a) Zero Sweep

At zero incidence the flow was attached from leading to trailing edges with boundary layer transition occuring at an x/C of 0.35. For this leading edge shape a 'short' separation bubble formed at very low incidence - it was clearly visible at only 2^{o}. The stall appeared to be due to the 'bursting' of the short leading edge bubble and the angle of incidence at which the stall took place varied between 12^{o} and 15^{o} for the Reynolds number range available in the test.

b) 15^{o} Sweep

The flow patterns produced were qualitatively similar to those found at zero sweep except that a small spanwise flow component developed in the vicinity of the trailing edge. At a Reynolds number of 1.6×10^{6} the aerofoil stalled at 15^{o} incidence due to bursting of the leading edge separation bubble.

c) 30^{o} Sweep

Up until 14^{o} incidence the development of the flow was very similar to that found at 15^{o} sweep although there was much more cross-flow towards the trailing edge. At a Reynolds number of 1.7×10^{6} the flow over the outer portion of the wing collapsed at 15^{o} to form a part-span vortex as shown in figure 20. In this case, however, the oil-blob 'eye' structure was very large and was centred at an x/C of 0.23. Flow patterns observed at incidences up to 24^{o} were quantitatively similar with the centre of the 'eye' moving slowly towards the root and towards the mid-chord position as incidence increased. In all cases there was general unsteadiness in the separated part of the flow. At the lower Reynolds number of 9×10^{5} the flow over the outer part of the wing also collapsed at 15^{o} incidence. However, as may be seen in figure 21, there were significant differences in the surface oil-flow patterns. Firstly, in the region near the root, there was no short bubble formed. Instead the three-dimensional separation/separation/attachment structure was found. Secondly, the part-span vortex was eminating from a location which was closer to the leading edge as indicated by the position of a much smaller oil-blob 'eye'. Further increases in incidence simply caused the part-span vortex origin to move along the leading edge towards the root.

d) 45^{o} Sweep

At zero incidence the flow was attached everywhere with transition located at 50% chord. As before a short leading edge bubble formed at very low incidence. For a Reynolds number of 2.1×10^{6} there was attached flow downstream of the bubble until an incidence of 14^{o} was reached. At this incidence a secondary separation line was forming out near the tip at an x/C of about 0.5. This flow is shown in figure 22. Increasing the incidence at this Reynolds number caused the separation line to increase in length and move closer to the leading edge bubble. At 20^{o} incidence the leading edge bubble failed to close at the tip and a part-span vortex was formed at the junction between the two flow regions. Further increases in incidence caused the origin of the part-span vortex to move towards the root as indicated in figure 23. When the Reynolds number was reduced to 1×10^{6} the short leading edge bubble failed to form at an incidence of 10^{o} and, as in previous cases, the fully three-dimensional spiral vortex flow was observed - see figure 24. By 14^{o} incidence the attachment line was crossing the trailing edge at about the mid-span position and the secondary separation had moved further away from the leading edge. Beyond 14^{o} incidence the attachment line did not reach the trailing edge, suggesting that a vortex burst was taking place over the wing. At 24^{o} there was no longer any attachment line structure discernable in the oil-flow pattern.

e) 56^{o} Sweep

For incidences below 10^{o} the flow was similar to that observed in the 45^{o} sweep case. At 0^{o} the flow was wholly attached with transition taking place at 40% chord. A short leading-edge bubble formed at 2^{o} and, at a Reynolds number of 2.7×10^{6}, this flow persisted until an incidence of 12^{o}. The oil-flow pattern observed at 12^{o} incidence is sketched in figure 25. Beyond 12^{o} a secondary separation developed parallel to and approximately 0.02 m downstream of the bubble re-attachment line in the immediate vicinity of the tip. The vortex sheet springing from this separation line appeared to roll up to form a strong spiral vortex whose axis was almost aligned with the undisturbed free-stream direction. The oil-flow produced at an incidence of 15^{o} is sketched in figure 26 where the influence of the spiral vortex on the tip region of the wing is clearly visible. As the incidence was increased the starting point for the secondary separation moved along the leading edge towards the root with a tertiary separation developing behind the secondary separation. Figure 27 shows the oil-flow obtained at the maximum incidence available which was 19^{o}. At the lower Reynolds number of 1.4×10^{6} the short bubble structure failed to form at 7^{o} incidence and once again the three-dimensional spiral vortex flow was observed. The flow exhibited features similar to those found at other sweep angles and with other leading edge radii. Figure 28 shows the pattern observed at 11^{o}. This type of flow was found to exist up to the maximum incidence attainable (19^{o}).

4. DISCUSSION

At the lowest unit Reynolds number (1×10^{6}/m) none of the three sections tested exhibited spiral vortex flow at either 0^{o} or 15^{o} sweep. However at 30^{o} sweep, and above, all the sections produced the type of three-dimensional spiral vortex flow which is sketched in figure 5 - see for example figures 10, 15 and 24. In each case the shear layer which leaves the surface at the primary separation line rolls up to form a spiral vortex. This vortex, which has its origin in the wing root apex, produces a new line of attachment at some station further back along the chord. The attachment line also has its origin in the wing root apex and the flow patterns over the inboard portion of the various wing sections are very similar in appearance to those produced by the near conical spiral vortex flows generated when thin delta wings are placed at incidence to an oncoming flow. There is also a strong similarity between the present flow patterns and the patterns observed by Sutton[6] in his study of flow attachment downstream of separation from a swept salient edge. The combination of sweep and incidence necessary for the establishment of this 'conical' type of spiral vortex flow are presented in figure 29. In each case the 'critical'value for the streamwise incidence decreases as the angle of sweep-back is increased. It is also apparent that there is a strong dependence upon leading edge radius. As might be expected the section with the 'sharp' leading edge exhibits the spiral vortex flow at the lowest incidence - less than 4^{o} for all the sweep angles considered. However it is particularly interesting to note that the highest critical incidences are found on the section with the intermediate leading edge radius (1.2%C). The precise reason for this behaviour is not known at present but it seems likely that progress towards an understanding of this phenomenon will require much more detailed knowledge of the flow processes taking place in the free shear-layer immediately downstream of the line of primary separation.

When the unit Reynolds number was increased to 2×10^{6}/m there was still no spiral vortex flow found at 0^{o} and 15^{o} sweep. However, at sweep angles beyond 15^{o} a variety of spiral vortex flow was observed. With the 'sharp' leading edge wing section the behaviour was precisely the same as that found at the lower Reynolds number with the 'conical' spiral vortex flow appearing at the same angles of incidence. For 30^{o} of sweep both the rounded leading edge sections exhibited a similar behaviour in so far as part-span vortices were generated when the short leading-edge bubble failed to close on the more highly loaded outer part of the wing - see figures 12 and 20. At 45^{o} of sweep the RAE 101 nose (1.2%C) also produced a part-span vortex by this same mechanism - as shown in figure 13. However for the blunt nosed section at this sweep angle the flow downstream of the short bubble separated close to the bubble on the outer part of the wing and it would appear that the rolling up of the shear layer leaving the surface along this line of secondary separation produced the spiral vortex flow. This situation is illustrated in figure 23 where it can also be seen that the short bubble does not close on the outer part of the wing. A very similar situation occured with the RAE 101 nose at 56^{o} of sweep as shown in figure 18. However for the blunt nose at 56^{o} of sweep the part-span vortex was fed from the shear layer leaving the secondary separation line whilst a full-span short bubble structure was retained up to the highest incidence investigated. This is shown in figure 27. A summary of the combinations of sweep angle and incidence necessary for the onset of spiral vortex flow is presented in figure 30. As was the case for the lower Reynolds number tests the 'critical' incidence decreases with increasing sweep angle. However at the high Reynolds numbers the section with the largest leading edge radius also had the largest critical incidence. By comparing figures 29 and 30 it may be tentatively concluded that the larger the leading edge radius the stronger the dependence of 'critical' incidence upon Reynolds number.

With regard to Reynolds number dependence it is interesting to note that in the present tests no part-span vortices were observed at the lower unit Reynolds number. However Black[5] produced a part-span vortex on a wing with a leading edge sweep of 44^{o} at a Reynolds number of 0.5×10^{6}. In the present tests there was no part-span vortex found at 45^{o} of sweep with a Reynolds number of 1.1×10^{6}. Similarly Dickmann[7] observed

part-span vortices on a wing with an NACA 0012 section laid normal to the leading edge for sweep angles between 20° and 50° at Reynolds numbers from 0.35×10^6 to 0.51×10^6. Therefore it is necessary to conclude that Reynolds number is not, in itself, sufficient to determine the type of spiral vortex flow produced in a given situation. This supports the notion that the type of flow which emerges is determined by the processes such as transition, entrainment etc., which take place in the free shear-layer immediately downstream of the primary separation line. If this is the case then future work in this area should include measurements of those quantities which are known to affect the development of free shear-layers such as free-stream turbulence levels, turbulence spectra and tunnel acoustic disturbance levels.

Finally it is appropriate to point out an additional feature which was clearly visible in some of the photographs of the surface oil-flows. In reference 6 Sutton has noted that in some cases a shear-layer issuing from a swept separation line becomes very sensitive to small surface imperfections ahead of the separation line. The effect of an imperfection is to produce a local shedding of vorticity in the form of a small trailing vortex which is approximately aligned with the free-stream direction. In the present series of tests imperfections were occasionally introduced by the formation of small agglomerations of titanium dioxide powder during the surface oil-flow visualisation process. These sources of disturbance produced trailing vortices on the sharp leading edge section at 56° sweep, 5° incidence and a Reynolds number of 2.7×10^6. No such vortices were found for the RAE 101 nose. However, for the blunt nosed section at the high unit Reynolds number, disturbances were clearly visible at 45° sweep when the incidence was greater than 17° and at 56° sweep when the incidence was greater than 12°.

5. CONCLUSIONS

The investigation has revealed that for sweep angles in excess of 15° there are at least three different ways in which a spiral vortex flow can be generated over a swept-back wing. These are:-

a) A full-span vortex can be formed by a rolling up of the shear layer which leaves the aerofoil surface at the primary separation line. This type of vortex flow is very similar in appearance to the flows generated on sharp edged thin delta wings at incidence.

b) A part-span vortex can be formed when conditions are such that the shear layer from the primary separation re-attaches to form a short bubble on the inboard portion of the wing but fails to re-attach on the more heavily loaded outboard sections. That part of the shear layer which does not re-attach rolls up to form the vortex.

c) A part-span vortex can be formed when the boundary layer flow downstream of a short separation bubble leaves the surface close to the bubble along a line of secondary separation. This secondary separation line forms first in the vicinity of the tip where the loading is highest and the resulting free shear-layer rolls up to form the vortex.

In the present tests type (a) was observed for all the sections tested when the unit Reynolds number was 1×10^6/m. When the unit Reynolds number was increased to 2×10^6/m the section with the sharp leading edge continued to generate type (a) whilst the two rounded sections produced type (b) at 30° sweep and type (c) at 56° sweep. In general it was found that the incidence necessary for the onset of spiral vortex flow depended strongly upon leading edge radius and that dependence upon Reynolds number increased with increasing leading edge radius. For a given leading edge radius and unit Reynolds number the critical incidence decreased with increasing sweep angle.

With regard to Reynolds number dependence, comparisons with other work show that Reynolds number, sweep and incidence are insufficient in themselves to determine the type of flow which will occur on a given aerofoil section. It is suggested that future experimental work should include measurements of the wind-tunnel disturbance environment.

REFERENCES

1. Küchemann, D. — Types of flow on swept wings - with special reference to free boundaries and vortex sheets. RAE TN Aero 2234, March, 1953.

2. Maskell, E.C. — Flow separation in three dimensions RAE Report Aero 2565, November, 1955.

3. Pope, A. Harpur, J.J. — Low-speed Wind Tunnel Testing John Wiley and Sons Inc.

4. Goldstein, S. Richards, E.J. — Approximate two-dimensional aerofoil theory, Part III. Approximate designs of symmetrical aerofoils for specified pressure distributions. ARC CP 70, 1952.

5. Black, J. Flow studies of the leading edge stall on a swept-back wing at high incidence. Journal of the Royal Aeronautical Society, Vol. 60, pp. 51-60, January, 1956.

6. Sutton, E.P. Experiments on a flow with swept separation and re-attachment of a boundary layer. Proceedings of the IUTAM Symposium on Three-Dimensional Turbulent Boundary Layers, Berlin, March, 1982, Springer-Verlag.

7. Dickmann, C.C. Flow over swept wings. M.Sc. Thesis, Department of Aerodynamics, College of Aeronautics, September 1976.

ACKNOWLEDGEMENTS

The experimental pressure distributions contained in this paper were measured by Mr. D.J. Paisley. Financial support for the work was provided by the Procurement Executive of the Ministry of Defence.

sweep angle	0	15°	30°	45°	56°
semi-span (m)	1.83	1.83	1.83	1.83	1.83
streamwise chord (m)	0.76	0.79	0.88	1.08	1.36
taper ratio	1.00	1.00	1.00	1.00	1.00
aspect ratio	4.80	4.64	4.16	3.39	2.68

Table 1. A summary of the planform characteristics

leading edge radii (r/Cx100)	0.03, 1.2, 3.0
sweep angles (degrees)	0, 15, 30, 45, 56
streamwise incidence (degrees)	continuously variable from 0 to 36 x cos Λ
streamwise Reynolds number	0.75 x 10^6 to 3.0 x 10^6
free-stream Mach number	0.1

Table 2. The range of parameters covered in the tests.

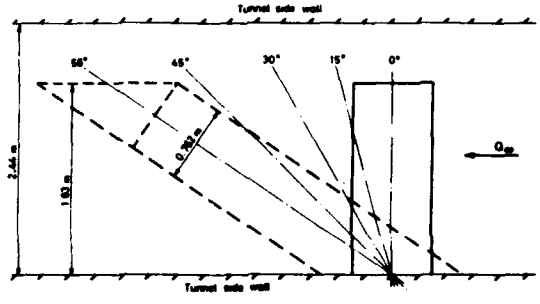

Figure 1. Plan view of the variation sweep wing in the 2.44 m x 1.83 m low speed wind tunnel.

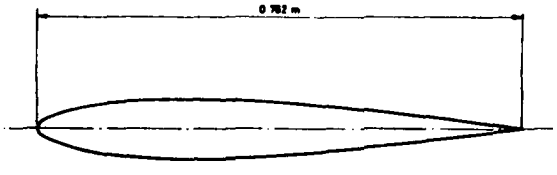

Figure 2. RAE 101 aerofoil section with t/c of 12%

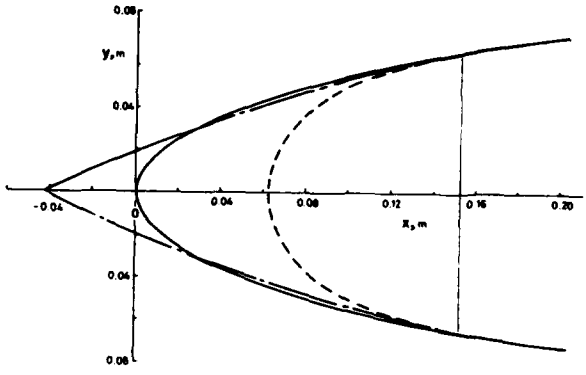

Figure 3. The various nose geometries considered in the investigation.

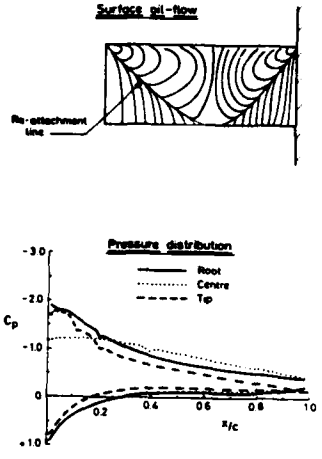

Figure 4. Leading edge radius = 0.03 % C, sweep = 0°, incidence = 12°, Reynolds No. = 1.5×10^6

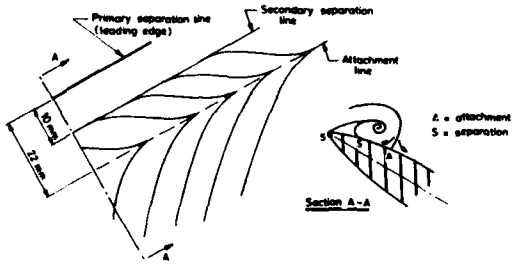

Figure 5. The flow close to the sharp leading edge, sweep = 30°, incidence = 4°, Reynolds No. = 1.7×10^6

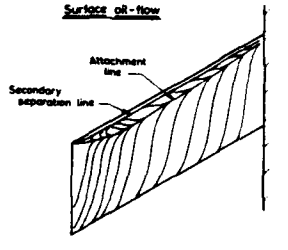

Figure 6. Leading edge radius = 0.03 % C, sweep = 30°, incidence = 7°, Reynolds No. = 1.7×10^6

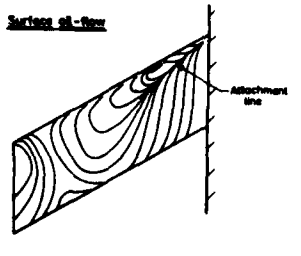

Figure 7. Leading edge radius = 0.03 % C, sweep = 30°, incidence = 10°, Reynolds No. = 1.7×10^6

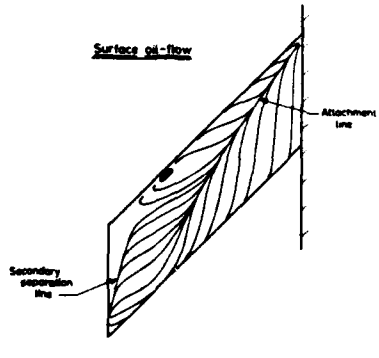

Figure 8. Leading edge radius = 0.03 % C, sweep = 45°, incidence = 11°, Reynolds No. = 2.1×10^6

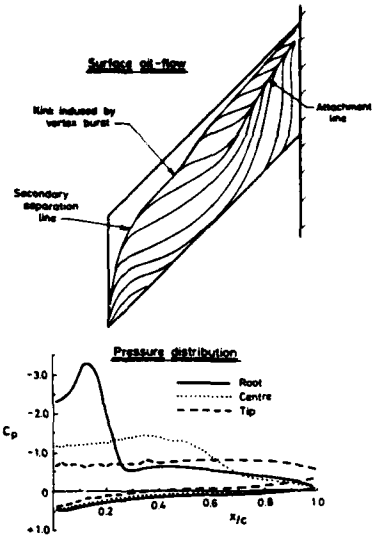

Figure 9. Leading edge radius = 0.03 % C, sweep = 45° incidence = 14° Reynolds No. = 2.1×10^6

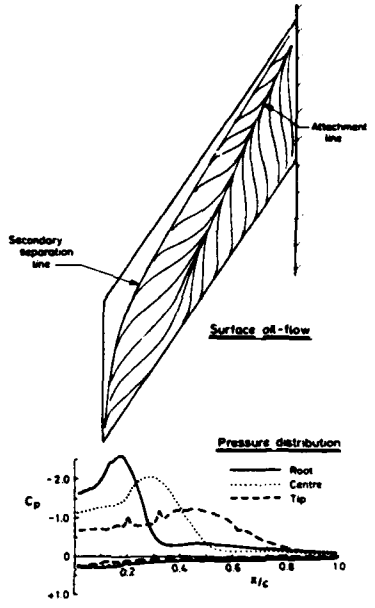

Figure 10. Leading edge radius = 0.03 % C, sweep = 56°, incidence = 11°, Reynolds No. = 2.7×10^6

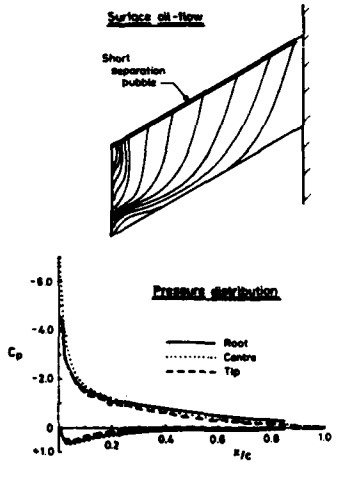

Figure 11. Leading edge radius = 1.20 % C, sweep = 30°, incidence = 12°, Reynolds No. = 1.7×10^6

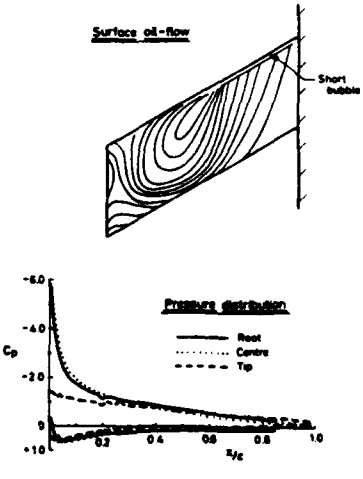

Figure 12. Leading edge radius = 1.20 % C, sweep = 30°, incidence = 14°, Reynolds No. = 1.7×10^6

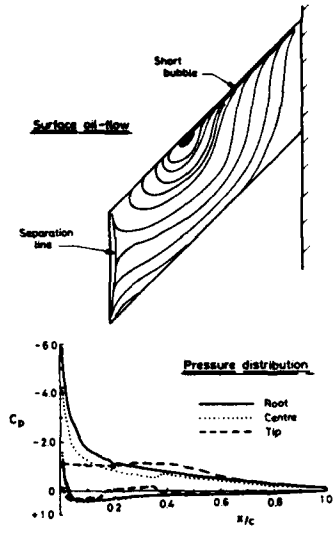

Figure 13. Leading edge radius = 1.20 % C, sweep = 45° incidence = 14°, Reynolds No. = 2.1 x 10^6

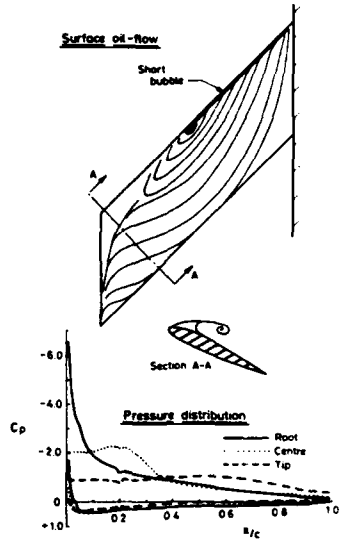

Figure 14. Leading edge radius = 1.20 % C, sweep = 45°, incidence = 16°, Reynolds No = 2.1 x 10^6

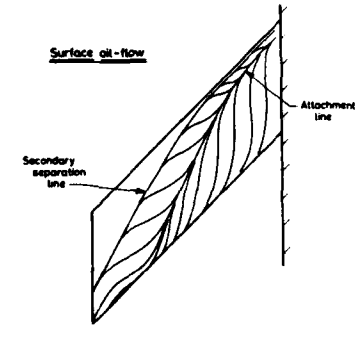

Figure 15. Leading edge radius = 1.20 % C, sweep = 45°, incidence = 13°, Reynolds No. = 1.1 x 10^6

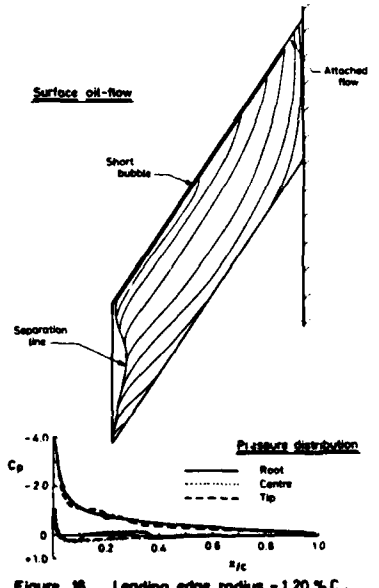

Figure 16. Leading edge radius = 1.20 % C, sweep = 56°, incidence = 10°, Reynolds No. = 2.7 x 10^6

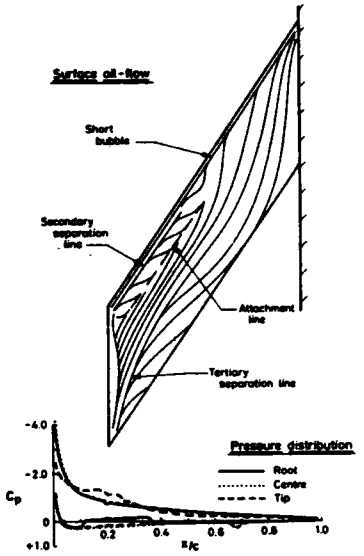

Figure 17. Leading edge radius = 1.20 % C, sweep = 56°, incidence = 11°, Reynolds No. = 2.7×10^6

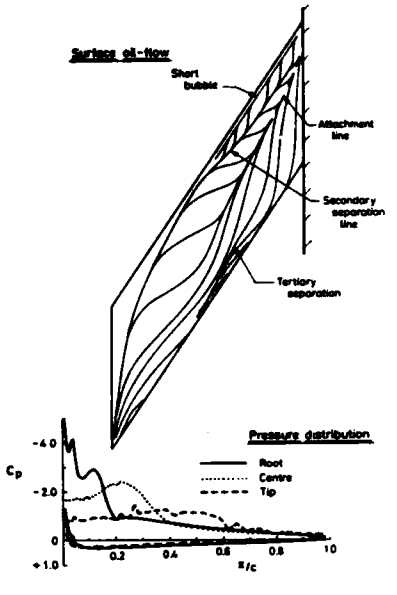

Figure 18. Leading edge radius = 1.20 % C, sweep = 56°, incidence = 16°, Reynolds No = 2.7×10^6

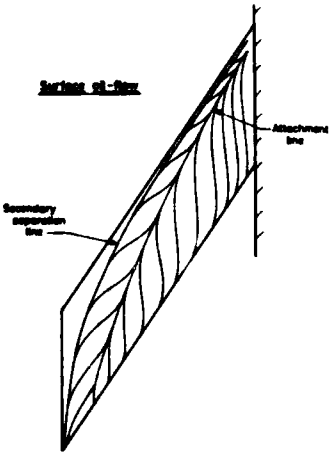

Figure 19. Leading edge radius = 1.20 % C, sweep = 56°, incidence = 10°, Reynolds No. = 1.4×10^6

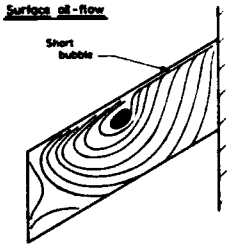

Figure 20. Leading edge radius = 3.0 % C, sweep = 30°, incidence = 15°, Reynolds No. = 1.7×10^6

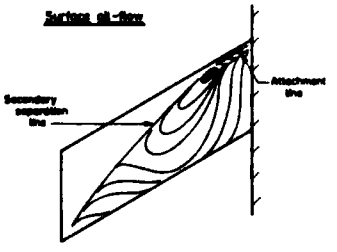

Figure 21. Leading edge radius = 3.0 % C, sweep = 30°, incidence = 15°, Reynolds No. = 0.9×10^6

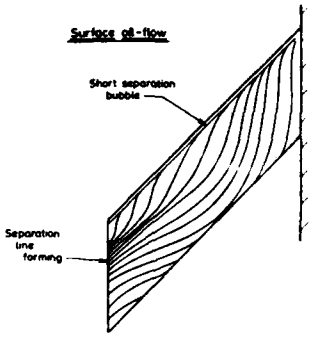

Figure 22. Leading edge radius = 3.0 % C, sweep = 45°, incidence = 14°, Reynolds No. = 2.1×10^6

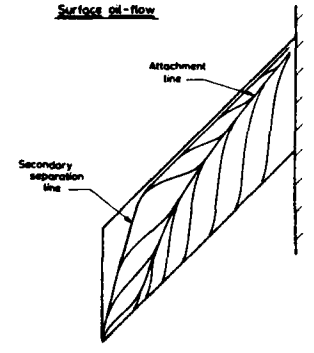

Figure 24. Leading edge radius = 3.0 % C, sweep = 45°, incidence = 10°, Reynolds No. = 1.0×10^6

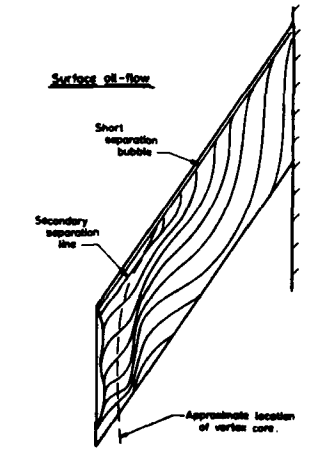

Figure 26. Leading edge radius = 3.0 % C, sweep = 56°, incidence = 15°, Reynolds No. = 2.7×10^6

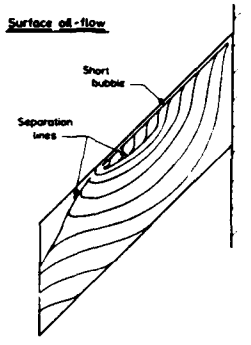

Figure 23. Leading edge radius = 3.0 % C, sweep = 45°, incidence = 23°, Reynolds No. = 2.1×10^6

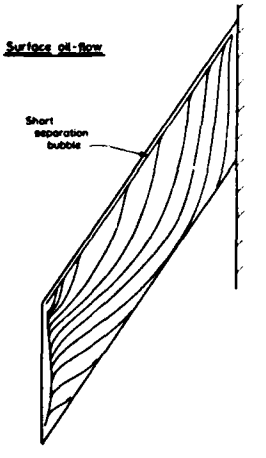

Figure 25. Leading edge radius = 3.0 % C, sweep = 56°, incidence = 12°, Reynolds No. = 2.7×10^6

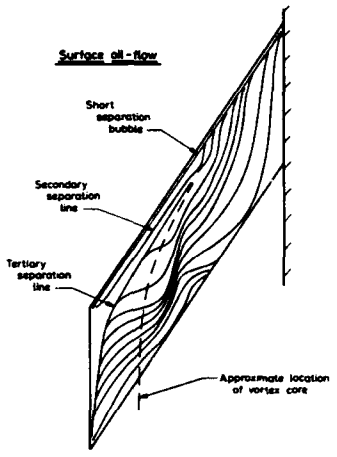

Figure 27. Leading edge radius = 3.0 % C, sweep = 56°, incidence = 19°, Reynolds No. = 2.7×10^6

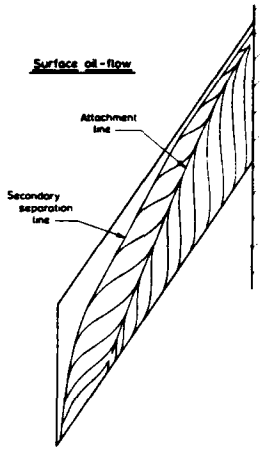

Figure 28. Leading edge radius = 3.0 % C, sweep = 56°, incidence = 11°, Reynolds No. = 1.4×10^6

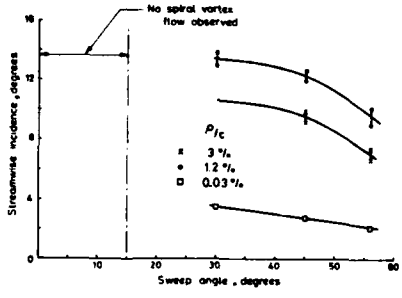

Figure 29. Approximate location of the boundary between attached flow and spiral vortex flow at a unit Reynolds No. of 1.0×10^6/m

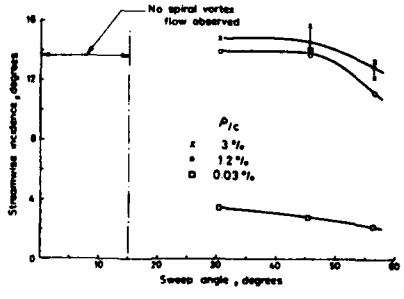

Figure 30. Approximate location of the boundary between attached flow and spiral vortex flow at a unit Reynolds No. of 2.0×10^6/m

AN EXPERIMENTAL INVESTIGATION OF THE VORTEX FLOW OVER DELTA AND DOUBLE-DELTA WINGS AT LOW SPEED

by
N.G. Verhaagen*
Delft University of Technology
Department of Aerospace Engineering
Kluyverweg 1, 2629 HS Delft
the Netherlands

SUMMARY

A wind-tunnel investigation was performed to study, by employing a laserlight-sheet and oil-flow visualization technique, the flow above and behind a sharp-edged 76 deg. delta wing and two sharp-edged double-delta wing models (76/60 and 76/40 deg., kink at midchord). In addition, balance measurements were performed to determine lift, drag and pitching moment. The tests were carried out for angles of attack from 5 to 25 deg. and at a free-stream velocity of 30 m/sec, corresponding to a Reynolds number of 1.4×10^6, based on centerline chord.
Above both double-delta wings a single-branched strake vortex is formed fed by vorticity from the strake leading edge. Downstream of the leading-edge kink a wing vortex is formed which is conjectured to be single-branched at about 5 deg. angle of attack and double branched at angles of 10 deg., and beyond. The flow pattern downstream of the trailing edge of the 76/60 deg. double-delta wing has been observed to be similar to that behind the delta wing. Above the 76/40 deg. double-delta wing breakdown of both the wing and strake vortices took place ahead of the trailing edge.

SYMBOLS

AR	aspect ratio, $\frac{b^2}{S}$
b	wing span, m
C_D	drag coefficient, drag/$q_o S$
C_L	lift coefficient, lift/$q_o S$
C_{L_α}	slope of lift curve, $\frac{dC_L}{d\alpha}$
C_M	pitching-moment coefficient, pitching-moment/$q_o S c_o$ referenced to $x = 0.5c_o$ position
c_o	centerline chord, m
p_o	free-stream static pressure, N/m^2
p_t	total pressure, N/m^2
q_o	free-stream dynamic pressure, N/m^2
Re	Reynolds number, $\frac{U_o c_o}{\nu}$
S	wing area, m^2
s	local wing semi-span, m
T.E.	trailing edge
t	wing thickness, m
U_o	free-stream velocity, m/sec
u,w	velocity components parallel, and normal to vortex axis, m/sec
x,y,z	coordinates of wing-axes system, origin in apex (see fig. 1), m
α	angle of attack, deg
α_o	angle of attack at zero lift
Λ_w	wing leading-edge sweep angle, deg
ν	kinematic viscosity, m^2/sec

* Research Associate

1. INTRODUCTION

Thin slender wings with highly swept and relatively sharp leading edges are of increasing importance for several modern aircraft. By applying sharp leading edges the primary line of separation remains fixed at these edges. As a consequence, within a wide range of angles of attack and sideslip a steady and stable separation-induced vortex flow is formed which is more of less independent of Reynolds number. The research into this phenomenon of three-dimensional separated flow has especially been activated by the fact that the slender-wing concept has been applied for supersonic aircraft as a means to minimize wave drag. Most of the experimental work has been concentrated on sharp-edged slender delta wings. Investigations by Earnshaw (ref. 1), Hummel (refs.2 and 3) and many others have helped to obtain a good insight into the topology of the vortex flow over such wings and have formed a basis for the development of a physically correct model for various computational methods.

The National Aerospace Laboratory (NLR) and the Department of Aerospace Engineering of the Delft University of Technology (DUT) in the Netherlands conduct a collaborative research program with the objective to develop a free-vortex-sheet high-order panel method to predict the aerodynamic characteristics of slender, sharp-edged wing configurations with controlled separation. The theoretical development of the computational method is performed at NLR by Hoeijmakers and Vaatstra (refs. 4 and 5), while the experimental investigations are carried out at DUT by Verhaagen et al. In ref. 5 it is demonstrated that with the present NLR method a satisfactory prediction is obtained for the pressure distribution and normal force of a slender sharp-edged delta wing of unit aspect ratio. In addition, the shape of the wake behind such a wing is very well predicted. At present the free-vortex-sheet method is extended to the case of the strake-wing configuration. Such a configuration is employed for several current military aircraft in order to extend their high-angle-of-attack maneuvering performance. The highly swept and sharp-edged strake forms an additional lifting surface above which a stable vortex is formed. This strake vortex persists over the main wing and induces a strong lateral velocity field which energizes the boundary layer on its leeward surface. As a consequence, a well-organized flow is maintained over the main wing. A limit to the favourable effects induced by the strake vortex is reached once the angle of attack attains values where vortex breakdown occurs ahead of the trailing edge. For the flow about strake-wing configurations no physically correct mathematical model is available at present. Experimental investigations by Luckring (ref. 6), Liu et al. (ref. 7), and in particular Brennenstuhl and Hummel (ref. 8) have been valuable in obtaining a first insight into the interaction and the structure of the vortices above such configurations. However, little is still known about such fundamental aspects as the position and shape of the free shear layers, the strength of the vortices, etc. In an attempt to provide more data on these and other characteristics of the complicated vortex flow above strake-wing configurations the DUT is carrying out an experimental investigation of the flow over three simple sharp-edged wind-tunnel models at low speed (fig. 1). As basic model a 76 deg. swept delta wing (model I) was chosen featuring a stable and near-conical vortex flow. The other two models are double-delta wing models, i.e. simplified strake-wing configurations, with 76/60 and 76/40 deg. leading-edge sweep for model II and III, respectively. Model II is more or less representative for high-speed aircraft, while model III is representative for several current highly-maneuverable aircraft. In the model development phase it was theorized that model II would exhibit two vortex systems, namely a strake vortex system fed by vorticity from the strake leading edge, and a wing vortex system fed by vorticity from the wing leading edge. This model thus would be suited to study the interaction of both vortex systems. For model III it was expected that at low angle of attack only the strake vortex system would be present over the model and that, because of the reduced sweep angle of the wing leading edge, the flow over the outboard panel would be attached. A wing vortex is expected to form only at sufficient high angle of attack.

At present, balance measurements and flow-visualization tests have been performed. Some first tests results have been reported earlier in ref. 5. In the present paper, after describing the experimental setup, the results of the flow-visualization tests are given. These results are used to determine the shape and position of the free shear layers, and to construct the conjectured topology of the vortex flow in cross-flow planes. Finally, results of balance measurements are presented. The investigation will be described in greater detail in ref. 9.

2. EXPERIMENTAL SETUP

2.1. Wind tunnel and test conditions

The investigation was carried out in the low-speed wind tunnel of the Department of Aerospace Engineering of the DUT. The wind tunnel has an octagonal test section, 1.25 m high x 1.80 m wide, and a turbulence level of about 0.05% at the speed of 30 m/sec used in the present investigation. The Reynolds number was 1.4×10^6, based on centerline chord.

2.2. Models

The geometry of the three models is given in fig. 1. The models are made out of flat Duraluminium plate. The leading and trailing edges have a thickness of 0.2 mm. These edges were chamfered on the windward side of the model only in order to leave the leeward side flat. The models have a centerline chord length of 0.667 m and a maximum thickness to centerline chord ratio of 0.03. In the wind tunnel each model was suspended at the $x = 0.75c_0$ position through a streamlined strut connected to a six-component balance system. In order to avoid interference between the vortex flow over the model and the strut, the models were mounted with their leeward side facing downwards. The suspension allowed angles of attack between minus and plus 25 deg.

2.3. Flow visualization

To obtain an indication of the lateral position and the breakdown point of the leading-edge vortices smoke was injected into the flow upstream of the model. The smoke (small paraffin oil droplets) is sucked into the core of the vortices and forms smoke trails. These trails were visualized by illuminating the leeward side of the model with two 1000 Watt lamps.

To study the crossflow structure of the leading-edge vortices a laserlight-sheet technique was used. A schematic view of the setup used for this technique is given in fig. 2. The cross-section of the vortices was illuminated by a thin sheet of intense light produced by a 5-Watt argon-ion laser in conjuction with

an optical system. The laser was mounted on a traversing platform enabling a translation in free-stream direction. Through this, the streamwise development of the vortex flow could be visualized. The flow patterns have been photographed at 15, 20 and 25 deg. angle of attack by a remotely-controlled camera positioned in the diffusor of the wind tunnel. In addition, the flow pattern from 10 to 25 deg. angle of attack has been recorded on video tape from the same position.
The boundary-layer flow direction on the leeward side of the model was visualized by means of an oil-flow technique.

2.4. Force and moment measurements

Balance measurements were performed for angles of attack from -5 to +25 deg. Lift and drag are referred to the wind-axis system. For position reference the body-axes system xyz is used indicated in fig. 1. The pitching moment was taken relative to the $x = 0.5c_o$ point.
Corrections were applied for aerodynamic interference between strut and model, and for deflection of the strut under aerodynamic loads. As far as tunnel-sidewall corrections are concerned, the angle of attack and the aerodynamic coefficients were also corrected for blockage and lift effects following methods discussed by Rogers and Garner in chapter 3 and 5 of ref. 10. Although developed for attached flow conditions, Karou (ref. 11) has shown that these correction methods can be successfully applied for flows with strong leading-edge vortices.

3. RESULTS OF FLOW FIELD INVESTIGATION

3.1. Delta wing model I

3.1.1. Vortex flow characteristics

The crossflow over model I is clearly visualized by the laserlight-sheet technique. In fig. 3 results are shown at $x = 0.75c_o$ and $1.25c_o$ for an angle of attack of 20 deg. From the leading edge a free shear layer can be seen to depart formed by the merging of the boundary layers from the windward and leeward surface of the wing. Under the influence of the vorticity contained in it the shear layer rolls up in a spiral fashion to form the so-called rotational core. In fig. 4 the velocity and pressure distribution along a traverse through the vortex center is presented measured by Verhaagen and vanderSnoek (ref. 12) on a slender delta wing (AR = 1) having a biconvex cross-section. The shear layer is characterized by a jump in the direction of the velocity vector and by a reduction of the total pressure. Through viscous forces, the thickness of the shear layer increases with increasing distance to the leading-edge.
Inside the rotational core no longer a shear layer can be detected because viscous diffusion has smoothed out completely the jumps in the direction of the velocity. The vorticity inside the core is distributed continuously. The region in the center of the core is called the viscous subcore and is characterized by large gradients of velocity and pressure. Axial velocities have been recorded there of more than twice the free-stream velocity. Because of the high circumferential velocity inside the subcore smoke particles entering this region are immediately centrifuged out of it, which explains why this region shows up as a black spot in laserlight-sheet flow photographs.
The secondary vortices could not be visualized with the laserlight-sheet technique since these vortices are too weak and close to the wing surface. Their presence, however, is clearly evidenced in the oil-flow pattern on the leeward surface of the model (fig. 5). On this surface the near-conical vortex flow generates a pattern which is characterized by attachment, secondary separation and tertiary separation points located on rays through the apex. At the $x = 0.85c_o$ chordwise position the secondary separation lines move outboard due to the transition from laminar to turbulent of the boundary layer underneath the primary vortex.
A short distance downstream of the trailing edge a concentrated trailing vortex is formed at the approximately $y = 0.70$ b/2 spanwise position. Although the trailing vortex has the same direction of rotation as the secondary vortex, observations by Hummel (ref. 3) show that these are separate vortices. Downstream of the trailing edge the (more outboard) secondary vortex decays rapidly, while the trailing vortex, on the contrary, increases in strength and is moved upwards around the stronger primary vortex. The trailing vortex is a double-branched vortex, because one shear layer is connected to the wake, the other one to the primary vortex.
The crossflow above and behind the model was observed from 10 to 25 deg. angle of attack. From the observations it can be concluded that, as might be expected, the crossflow structure remains topologically the same with increasing angle of attack. The position of the leading-edge vortex core has been determined from laserlight-sheet photographs. The coordinates, made dimensionless by the centerline chord c_o or by the local semi-span s, are presented in fig. 6.

3.1.2. Crossflow plane topology

In a penetrating study of three-dimensional-flow phenomena Peake and Tobak (ref. 13) provide a tool for the construction of the topology of surfaceflow and crossflow patterns. Based on studies of Lighthill (ref. 14) and Legendre (ref. 15), they suggest that surface oil-flow streaks are representative of skin-friction lines and that the pattern formed by the skin-friction lines can be considered as a continuous vector field in which singular points (nodes, foci and saddle points) occur at points on the surface where surface vorticity and skin friction become identically zero. The number and type of singular points on the surface obey simple topological laws. Hunt et al. (ref. 16) have shown that in conjunction with the skin-friction lines pattern it is possible to construct the characteristics of the external flow field. This consists of a continuous vector field (streamlines) with a finite number of singular points embedded in the flow at which velocity equals zero. The crossflow-plane streamlines are not the projection of the three-dimensional streamlines into the crossflow plane, but are the streamlines produced by the crossflow velocity vector field. Just as the singular points on the surface, those in the external flow satisfy topological rules. For the streamlines on a two-dimensional plane cutting a three-dimensional body ref. 13 gives the following relation (topological rule no. 3):

$$(\Sigma_N + \tfrac{1}{2}\Sigma_{N'}) - (\Sigma_S + \tfrac{1}{2}(\Sigma_{S'_a} + \Sigma_{S'_s})) = -1,$$

where

Σ_N = number of nodes in the external flow

$\Sigma_{N'}$ = number of half-nodes on the model surface

Σ_S = number of saddle points in the external flow

$\Sigma_{S'_a}$ = number of half-saddle points of attachment on the model surface

$\Sigma_{S'_s}$ = number of half-saddle points of separation on the model surface

From the flow visualization results of model I (figs. 3 and 5), the postulated streamline pattern in a crossflow plane has been deduced and sketched in fig. 7. Consistent with the skin-friction line pattern of fig. 5, this figure shows a symmetrically arranged crossflow with primary and secondary separation. Within the external flow there are five singular points, namely four nodes and one saddle point. On the leeward surface the points of attachment and separation form seven half-saddle points, on the windward surface there is another half-saddle point (of attachment). As indicated in fig. 7, this streamline pattern is in accordance with topological rule no. 3 of ref. 13.
The origin of the vortices in the vicinity of the apex is still not well understood. In this region the skin-friction line pattern usually lacks sufficient resolution to be of much help. Theoreticians have postulated some patterns by magnifying the apex region to such an extent that the edges may be considered to be round. The flow near the apex may then assumed to be similar with the flow near a round-nosed wing. An overview and detailed description of physically possible skin-friction line patterns for such a case is given also in ref. 13.

3.2. Double-delta wing model II

3.2.1. Streamwise development of the vortex flow at α = 20 deg.

In fig. 8 the results are shown of the visualization of the vortex flow above and behind model II for an angle of attack of 20 deg.
Above the forward half (strake) of this model (fig. 8a) the flow is similar to the flow above the forward half of a slender delta wing. The flow is nearly conical and dominated by two near-conical leading-edge vortices. The shear layers which emanate from the strake leading edges roll-up into the so-called strake vortices. Downstream of the leading-edge kink an additional vortex, the wing vortex, is formed. In the pictures of fig. 8 this vortex can be seen to whirl around the strake vortex. But, through mutual induction, also the strake vortex is forced into a whirling motion. The wing vortex is a double-branched vortex, because one shear layer is connected to the wing leading edge and the other one to the strake vortex. Presumably all vorticity in the shear layers is of the same sign. The wing vortex is continuously fed with vorticity from the wing leading edge as well as from the shear layer between wing and strake vortex. As a consequence it will increase in strength with distance to the kink. At some distance of the kink the amount of vorticity fed into the strake vortex will gradually diminish. Consequently, the strength of this vortex will become constant or even reduce because vorticity is "stolen" by the wing vortex. Detailed measurements of the flow field downstream of the leading-edge kink have been carried out by Brennenstuhl and Hummel (ref. 8). As model they used a thin flat-plate 80/60 deg. swept double-delta wing, the leading-edge kink being at the midchord position. From the velocity and total-pressure distribution measured in the $x = 0.75c_o$ crossflow plane at an angle of attack of 12 deg. the wing vortex appeared to be of about the same size as the strake vortex. They found, however, that in this plane the wing vortex was already stronger than the strake vortex. The core of the wing vortex remains visible up to the trailing edge. Downstream of the trailing edge the wing and strake vortex have merged into one single vortex (fig. 8i). Exactly like the flow behind model I, here too a trailing vortex is formed. As a result a flow pattern is obtained which resembles much the one behind the delta wing model (fig. 3b).
For model II vortex breakdown was observed at 25 deg. angle of attack, namely downstream of the trailing edge at $x = 1.5c_o$. For a 60 deg. swept delta wing vortex breakdown has been observed at the trailing edge at an angle of attack as low as 13 deg. (ref. 17), which demonstrates that the flow over the wing is stabilized considerably by adding the strakes.

3.2.2. The vortex flow at various angles of attack

In order to study the development of the flow with angle of attack, the crossflow above and behind the model has been observed for angles from 10 to 25 deg.. Apart from differences in the cross-sectional dimensions, in this range of angles of attack no topological changes in the crossflow structure have been noted. The position of the strake and wing vortex core has been determined from laserlight-sheet photographs. The coordinates of the cores, made dimensionless by the centerline chord c_o or by the local semi-span s, are presented in figs. 9 and 10 for the strake and wing vortex, separately. As can be seen in these figures, increasing the angle of attack results in general in an inboard and upward displacement of the vortices.

3.2.3. Leeward-surface flow pattern

In fig. 11 sketches are presented of the oil-flow pattern on the leeward surface of model II for 5 to 25 deg. angle of attack.
Above the strake the near-conical vortex flow induces the well-known skin-friction line pattern which is also formed above a slender delta wing. The pattern changes little with the angle of attack and is characterized by straight attachment and separation lines.
Downstream of the leading-edge kink the changes with angle of attack are larger. At 5 deg. angle of attack (fig. 11a), the attachment and secondary-separation lines of the strake and wing vortices remain clearly distinguishable up to the trailing edge. For this angle the strake and wing vortices apparently remain too weak and too far apart to induce a whirling motion. Between the strake and the wing vortex the skin-friction line pattern shows evidence of a secondary vortex. Outboard of the wing vortex there are also clear markings of secondary separation from the leading-edge kink up to about $x = 0.80c_o$. At an angle of 10 deg., the wing and strake vortex have been observed to whirl about each other. The stronger wing vortex displaces the strake vortex in a downward and spanwise direction. As a consequence, at some distance from the leading-edge kink the secondary-separation line of this vortex can be seen to move outwards (fig. 11b).

Upstream of the inflexion point of this separation line the integral-sign shaped skin-friction line regions of the strake and wing vortices are visible separately. Downstream of the inflexion point these regions have merged to one region on each wing half. Outboard of the secondary-separation line there are markings of a secondary vortex. In the range of angles of attack from 10 to 25 deg. the following changes can be identified in the skin-friction line pattern. An increasing angle of attack leads to:
- an increase of the distance between attachment and secondary-separation line due to increase in the strength of the vortices,
- an upstream displacement of the inflexion-point in the secondary-separation line.

3.2.4. Flow structure in crossflow plane

Based on the flow visualization results the position of the vortex cores as well as the conjectured shape and position of the free shear layers are presented in fig. 12 for 20 deg. angle of attack (the scale of the figure on the right-hand side is larger than the scale of the figure on the left-hand side). Since the crossflow structure showed no essential changes from 10 to 25 deg. angle of attack, this figure is considered to be representative for the crossflow in this range of angles of attack.
The streamline pattern in a crossflow plane of the strake is assumed to be similar to the pattern sketched in fig. 7 for delta wing model I.
The position of the shear layers as well as the conjectured streamline pattern of the crossflow plane at $x = 0.625c_o$ has been sketched in fig. 13 for one wing half.This streamline pattern is entirely topological, the sizes of the vortices are not meant to indicate their relative strength. Consistent with the flow visualization results, a strake, wing and secondary vortex has been drawn. This pattern yields 6 nodes for the entire crossflow ($\Sigma_N = 6$). Between the wing and strake vortex a saddle point is hypothesized. On the wing surface there is an equal number of half-saddle points of attachment and of separation. This streamline pattern satisfies topological rule no. 3 of ref. 13.
At 20 deg. angle of attack an attachment line is located at the centerline of the wing leeward surface (fig. 11d). At 15 deg. and below, two attachment lines can be detected near the centerline (figs. 11a to c). This indicates that the central part of the wing surface is affected by attached streamwise flow.
In the crossflow streamline pattern at high angles of attack a saddle-point has been conjectured above the wing centerline (fig. 13). With decreasing angle of attack this saddle point approaches and eventually coincides with the half-saddle point of attachment at the centerline of the leeward surface. Based on the surface oil-flow patterns, at 15 deg. and below both saddle points are replaced by a half-saddle point of separation (at the wing centerline) and two half-saddle points of attachment.
The crossflow pattern for 5 deg. angle of attack has been sketched in fig. 14. At this low angle the strake and wing vortices do not whirl about each other and between these vortices there is evidence of secondary separation. It is conjectured here that the wing vortex is no longer connected to the strake vortex, both vortices are assumed to be single branched.
The flow on the windward side of the models has not *been visualized* during the present investigation. It may be possible that at low angles of attack the streamline pattern on this side of the model is different from the one sketched in fig. 14. At very low angles of attack it can namely be expected that the central part of the wing surface is affected by streamwise attached flow, while near the leading edges the flow is directed outwards. This would result in a half node at the wing centerline and a half-saddle point of attachment on each wing half. More evidence about this will be obtained in a future investigation.
In fig. 12 a rather complicated shape for the free shear layer of the strake vortex is conjectured downstream of the $x = 0.8125c_o$ chordwise station. Here, the laserlight-sheet flow pictures lack sufficient resolution to be of much help. Near the trailing edge it is presumed that through viscous diffusion a region of continuously distributed vorticity is formed which encompasses the inner loops of the free shear layer of both the wing and strake vortex.
It should be remarked here, that although the visualization of the flow has been of great help to obtain a first insight into the complicated structure of the flow over model II, further experimental investigation of the pressure and velocity distribution in crossflow planes is needed to support, correct and extend the flow topology conjectured above.

3.3. Double-delta wing model III

3.3.1. Streamwise development of the vortex flow at $\alpha = 20$ deg.

In fig. 15 the results of the laserlight-sheet visualization of the flow over model III are shown for an angle of attack of 20 deg.
Above the strake (fig. 15a) the two shear layers are visible which emanate from the strake leading edges. At a short distance downstream of the kink (figs. 15b and c) the crossflow structure is quite similar to that above model II (figs. 8b and c). Because of the reduced leading-edge sweep the wing vortex above model III, however, is weaker and farther apart from the strake vortex. As a consequence, there is less interaction between both vortices. The wing vortex is again a double-branched vortex embedded in the shear layer from the wing leading edge. An important difference with the flow over model II is that now the wing and strake vortices break down above the model at about $x = 0.70c_o$ and $0.74c_o$, respectively (figs. 16 and 17). Downstream of the vortex breakdown point the vortex core expands radially and becomes highly turbulent. Hummel (ref. 2) and Anders (ref. 18) have measured a considerable reduction of the flow velocity in the core downstream of the bursting point. Even reverse axial flow was observed. At constant angle of attack the vortex-breakdown point above model III not always remained at the same x-position, but was observed to fluctuate within a region of about 5 per cent c_o. Due to this instability the breakdown of the wing or of the strake vortex not always took place at the same location above the right and left wing-half. At high velocity and angle of attack the vortex breakdown gave rise to high-frequent vibrations in model III and its suspension. To avoid this, the free-stream velocity for this model had to be reduced to 30 m/sec. Subsequently, this was the velocity chosen for all three models used for the present investigation.

3.3.2. Vortex flow at various angles of attack

Identical to the other two models, from 10 to 25 deg. angle of attack no significant changes with angle of attack have been observed in the structure of the crossflow. A few observations were also made at 5 deg. angle of attack. At this angle the vortices are weak and very close to the surface of the model. For this

situation the laserlight-sheet technique does not provide sufficient resolution to indicate whether the wing vortex is still connected to the shear layer of the strake vortex. It can be imagined that the distance between these vortices is so large that no interaction will take place.
The average breakdown position of both the strake and wing vortex is presented in fig. 17. In general, the wing vortex breaks down earlier than the strake vortex. The breakdown of the strake vortex might possibly be induced by disturbances due to the breakdown of the wing vortex further upstream. The distance between the breakdown points of both vortices decreases with increasing angle of attack.

From the laserlight-sheet photographs the position of the vortex cores has been determined. The coordinates of the vortex cores, made dimensionless by the centerline chord c_o or by the local semi-span s, are presented in figs. 18 and 19 for the strake and wing vortex, respectively. Increasing the angle of attack displaces the vortices inboard and upwards. The wing vortex is affected most.

3.3.3. Leeward-surface flow pattern

The surface oil-flow pattern at the leeward side of model III has been sketched in fig. 20 for angles of attack from 5 to 25 degs. Just like the other two models the forward half of model III shows clear evidence of a nearly conical flow. Downstream of the leading-edge kink, at 5 and 10 deg. angle of attack (figs. 20a and b), the strake and wing vortices can individually be distinguished from the kink up to the trailing edge. Since, compared to the higher swept model II, the strake and wing vortices are weaker and at a greater distance from each other, these vortices remain individually distinguishable up to a larger angle of attack than was the case for model II. At 5 deg. angle of attack secondary separation of these vortices is clearly marked up to approximately the $x = 0.70c_o$ chordwise station, and up to the trailing edge at 10 deg.. At 15 deg. (fig. 20c) after a short distance downstream of the kink the integral-sign shaped line-pattern induced by the strake vortex becomes tangent to the integral-sign shaped line-pattern induced by the wing vortex. This indicates that between these two vortices no adverse pressure gradient is present in a spanwise direction to cause secondary separation. Downstream of the $x = 0.73c_o$ chordwise station vortex breakdown occurs of first the wing vortex and then the strake vortex (fig. 17). Both vortices eventually merge into one single vortex with a big turbulent core. This vortex induces long integral-sign shaped lines in a lateral direction and is responsible for the outboard shift of the secondary-separation line towards the leading edge. From 15 deg. angle of attack (figs. 20c to e), the region between attachment and secondary-separation line widens with increasing angle of attack due to upstream movement of the vortex breakdown. At 15, 20 and 25 deg. angle of attack, just outboard of the secondary separation line there is a region where oil-flow is accumulated. This region moves upstream with increasing angle of attack and is largest and clearest at 20 deg. It is conjectured here that this region consists of a saddle-point/focus combination, sketched on a larger scale in fig. 20d, and that it is connected with the occurence of vortex bursting.

3.3.4. Flow structure in crossflow plane

In fig. 21 the position of the vortex cores and the free shear layers are presented for 20 deg. angle of attack. This figure is based on the flow visualization results of figs. 15 and 20.
Above the strake the crossflow streamline pattern is assumed to be similar to that above the delta wing model (fig. 7).
At low angles of attack a single-branched strake and wing vortex with secondary separation is conjectured yielding a crossflow streamline pattern similar to fig. 14. From 10 deg. angle of attack the strake and wing vortices have been observed to be connected to each other. At 10 deg. both vortices still induce a separate secondary vortex. In fig. 22a the crossflow streamline pattern for this angle has been drawn. From 15 to 25 deg. angle of attack only one secondary vortex can be identified on each wing half (fig. 20c to e) so that a streamline pattern is obtained as sketched in fig. 22b. Both patterns presented in fig. 22 satisfy the third topological rule of ref. 13.

4. FORCE AND MOMENT COEFFICIENTS

The lift, drag and pitching-moment coefficients of the three models used for the present investigation are presented in figs. 23a to c. At zero angle of attack the lift has a negative value because the models are not symmetric with respect to the z = 0 plane (fig. 1) and effectively have slight negative camber. Since the aspect ratio of model II and III is larger than that of model I, these models exhibit a larger lift curve slope at the zero-lift angle of attack. It is evident from fig. 23a that model II produces more non-linear lift than model III because of the stronger wing vortices and because a larger part of the wing is affected by vortex flow. For model III vortex breakdown of both the strake and wing vortex (fig. 17) causes the reduction of its lift curve slope at about 13 deg. angle of attack. The influence of vortex breakdown is also visible on the drag curve (fig. 23b). The pitching moment in fig. 23c is taken relative to the $x = 0.5c_o$ position. Both double-delta wing models exhibit a larger pitch-down moment than the delta wing. Vortex breakdown on model III reduces the moment coefficient because of the reduced effectiveness of the vortex flow on the rear part of its wing.

5. CONCLUSIONS

- Insight into the vortex flow about sharp-edged delta and double-delta wing models has been obtained using both a laserlight-sheet and an oil-flow visualization technique.
- The present investigation indicates that the flow above the double-delta wings at 5 deg. angle of attack consists of single-branched strake and wing vortices. From 10 to 25 deg. angle of attack, the flow consists of single-branched strake vortices and of double-branched wing vortices which are embedded in the shear layer from the leading edge. In this range of angles of attack the flow pattern downstream of the 76/60 deg. double-delta wing is similar to that behind a simple delta wing. Above the 76/40 deg. double-delta wing breakdown of the wing and strake vortices takes place ahead of the trailing edge.
- To support further investigation of the vortex flow detailed measurements of the pressure and velocity distribution of the flow fields about these models will be needed.

REFERENCES

1. Earnshaw, P.B. — An experimental investigation of the structure of a leading-edge vortex. ARC R&M 3281, 1961.

2. Hummel, D. — Untersuchungen über das Aufplatzen der Wirbel an schlanken Deltaflügeln. ZFW 13 (1965), Heft 5.

3. Hummel, D. — On the vortex formation over a slender wing at large angle of incidence. AGARD-CP-247, Paper 14, 1979.

4. Hoeijmakers, H.W.M.; Bennekers, B. — A computational method for the calculation of the flow about wings with leading-edge vortices. AGARD-CP-247, Paper 25, 1979.

5. Hoeijmakers, H.W.M.; Vaatstra, W.; Verhaagen, N.G. — On the vortex flow over delta and double-delta wings. AIAA Paper 82-0949, 1982.

6. Luckring, J.M. — Flow visualization studies of a general research fighter model employing a strake-wing concept at subsonic speeds. NASA TM 80057, 1979.

7. Liu, M.J. et al — Flow patterns and aerodynamic characteristics of a wing-strake configuration. J. Aircraft 17, 5, 1980.

8. Brennenstuhl, U.; Hummel, D. — Vortex formation over double-delta wings. ICAS Paper-82-6.6.3, 1982.

9. Verhaagen, N.G. — An experimental investigation of the vortex flow over delta and double-delta wings at low speed. Rep. LR-372, Dept. of Aerospace Engineering, Delft University of Technology, to be published in 1983.

10. Garner, H.C.; Rogers, E.W.E. — Subsonic wind-tunnel wall corrections. AGARDograph 109, 1966.

11. Karou, A. — Separated vortex flow over slender wings between side walls; theoretical and experimental investigation. Rep. LR-300, Dept. of Aerospace Engineering, Delft University of Technology, 1980.

12. Verhaagen, N.C.; Snoek, L. van der — An experimental investigation of the entrainment into a leading-edge vortex. Rep. LR-332, Dept. of Aerospace Engineering, Delft University of Technology, 1981.

13. Peake, D.J.; Tobak, M. — Three-dimensional interactions and vortical flows with emphasis on high speeds. AGARDograph no. 252, 1980.

14. Lighthill, M.J. — Attachment and separation in three-dimensional flow. Laminar Boundary Layers, L. Rosenhead, ed., Oxford Univ. Press, 1963.

15. Legendre, R. — Lignes du courant d'un écoulement permanent: décollement et séparation. Rech. Aérosp. 1977-6.

16. Hunt, J.C.R.; Abell, C.J.; Peterka, J.A.; Woo, H. — Kinematical studies of the flows around free or surface-mounted obstacles; applying topology to flow visualization. J. Fluid Mech. (1978), Vol. 86, part 1.

17. Earnshaw, P.B.; Lawford, J.A. — Low-speed wind-tunnel experiments on a series of sharp-edged delta wings. ARC R&M 3424, 1966.

18. Anders, K. — Measurements of velocity distributions in delta wing vortices using laser doppler velocimetry. VKI Project Rep. 1981-03, 1981.

ACKNOWLEDGEMENT

The author is indebted to the personnel of the low-speed wind-tunnel laboratory for their assistance during the preparation and performance of the present investigation. The author further gratefully acknowledges the Audio-Visual Center of the DUT for their assistance of filming the laserlight-sheet investigation.

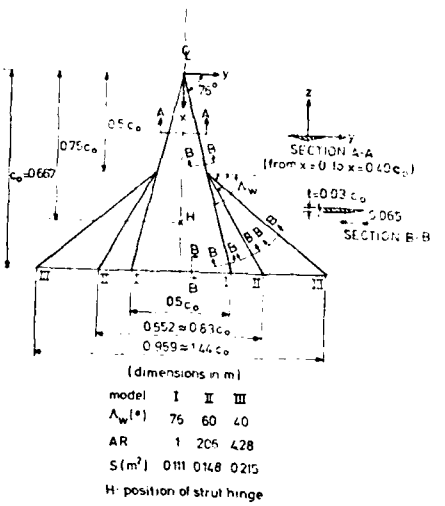

Fig. 1. Geometrical data of wind-tunnel models

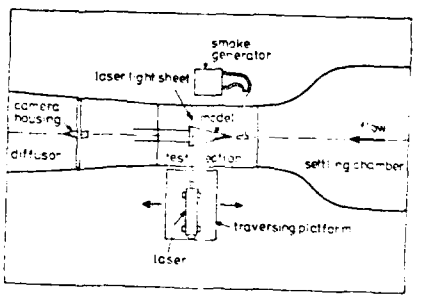

Fig. 2. Schematic of laserlight-sheet setup

a. $x = 0.75c_o$

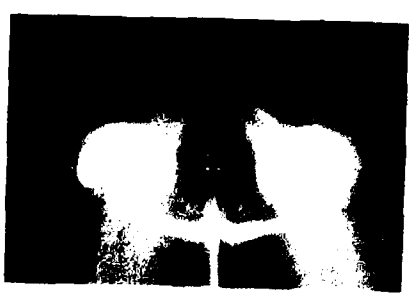

b. $x = 1.25c_o$

Fig. 3. Flow over model I at $\alpha = 20^o$

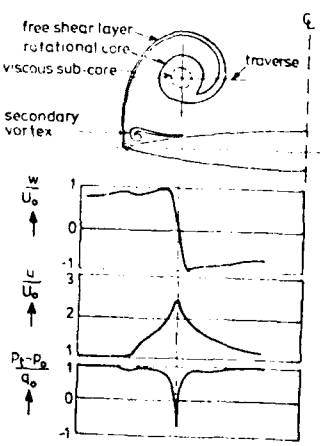

Fig. 4. Horizontal traverse of vertical and axial velocity, and total pressure through the axis of a leading-edge vortex (ref. 12)

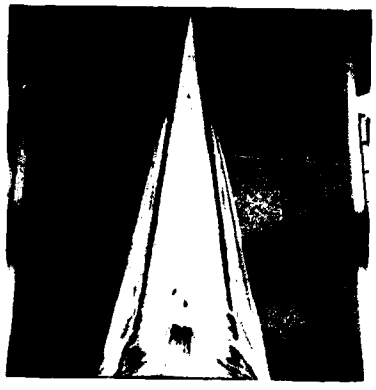

Fig. 5. Oil-flow pattern on leeward side of model I ($\alpha = 20^{o}$)

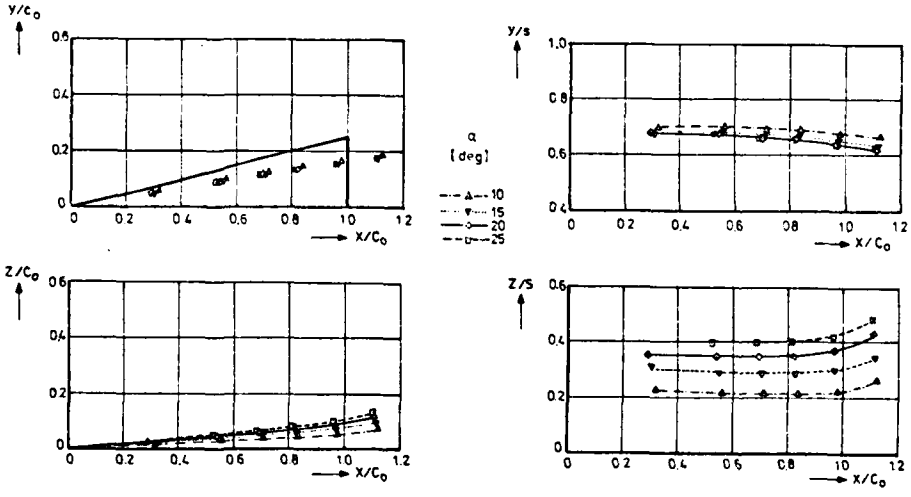

Fig. 6: Position of vortex on model I

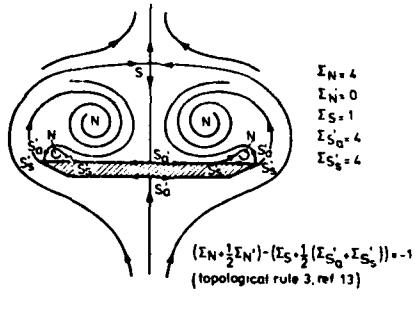

Fig. 7: Crossflow streamlines about model I at $\alpha = 20^{o}$

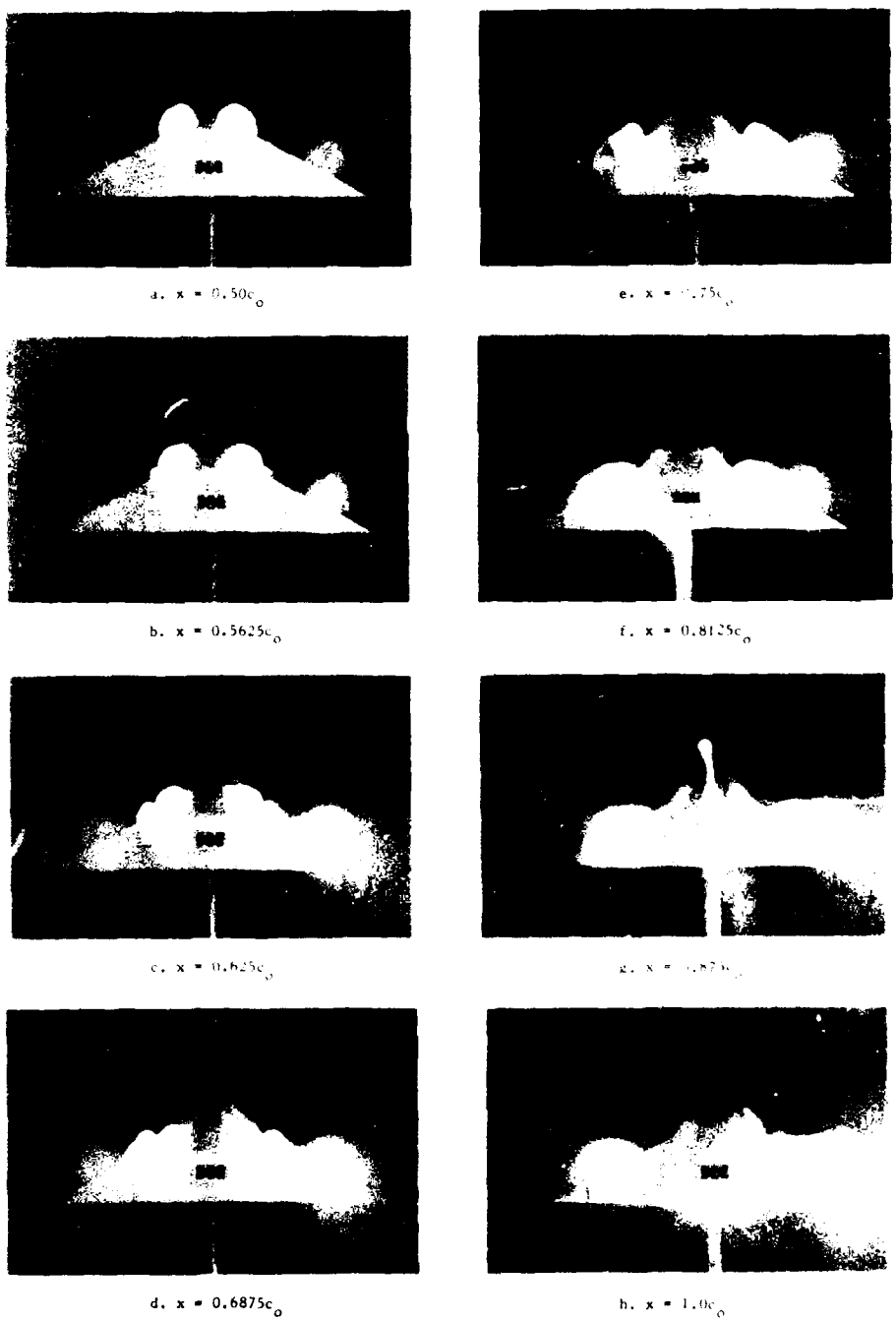

a. $x = 0.50c_o$

e. $x = 0.75c_o$

b. $x = 0.5625c_o$

f. $x = 0.8125c_o$

c. $x = 0.625c_o$

g. $x = 0.875c_o$

d. $x = 0.6875c_o$

h. $x = 1.0c_o$

Fig. 8. Flow about model II at $\alpha = 20^o$.

i. $x = 1.125c_o$ k. $x = 1.25c_o$

Fig. 8. Continued

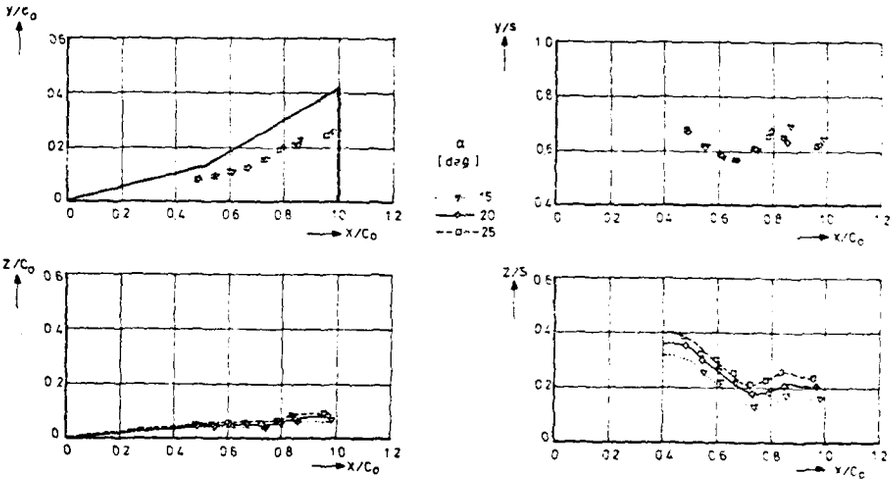

Fig. 9. Position of strake vortex on model II

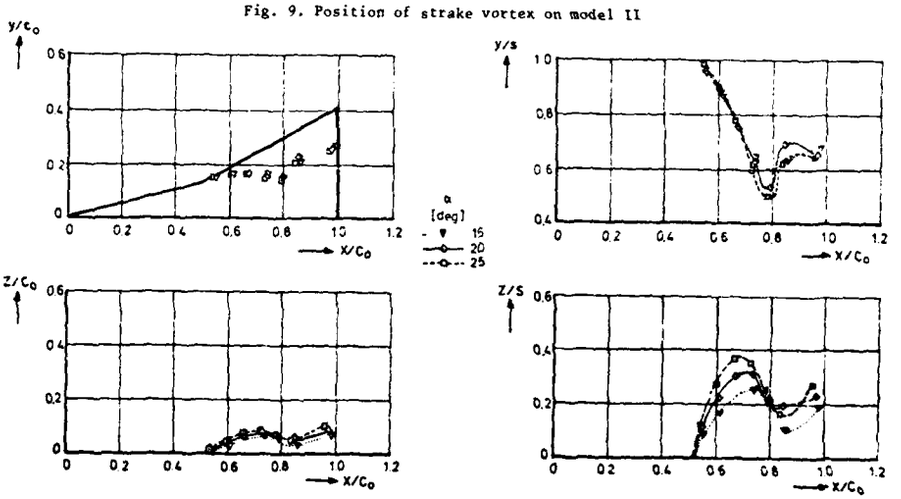

Fig. 10. Position of wing vortex on model II

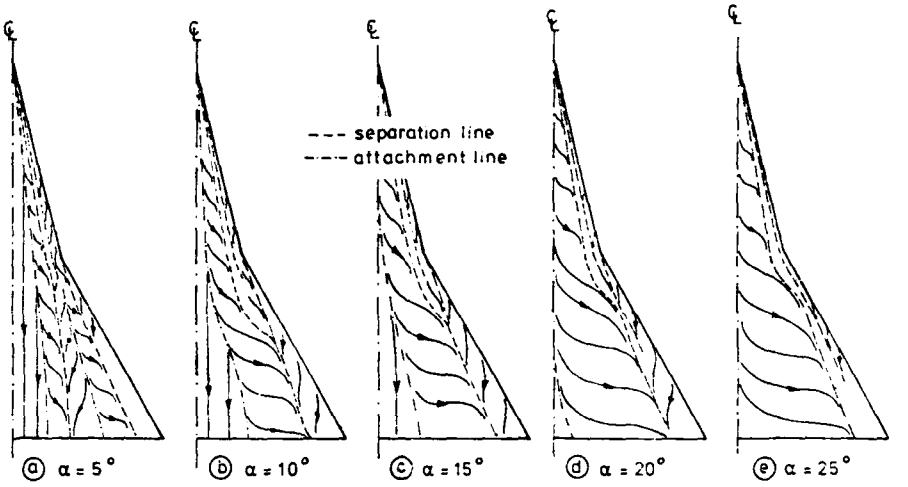

Fig. 11. Leeward-surface flow patterns of model II

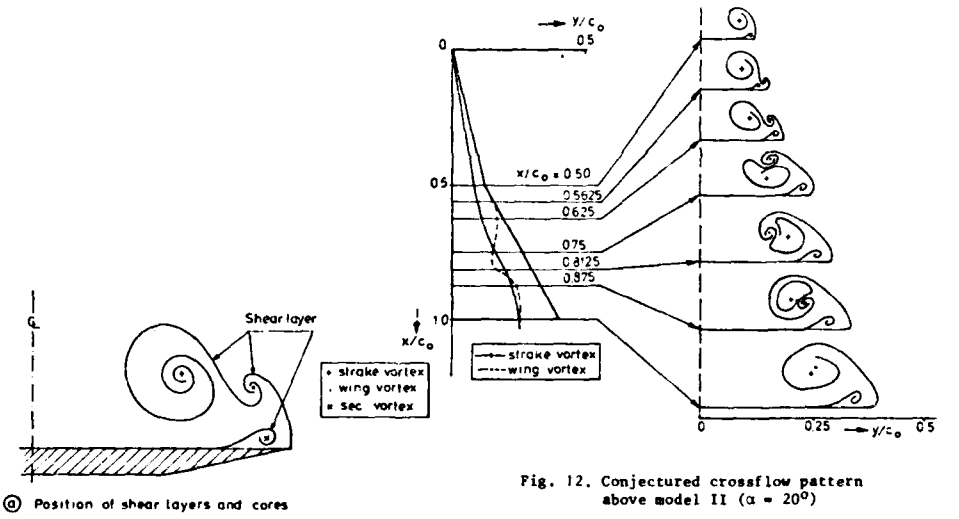

Fig. 12. Conjectured crossflow pattern above model II (α = 20°)

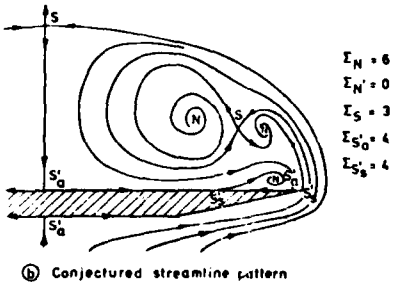

Fig. 13. Crossflow at x = 0.625c_o (α = 20°) model II

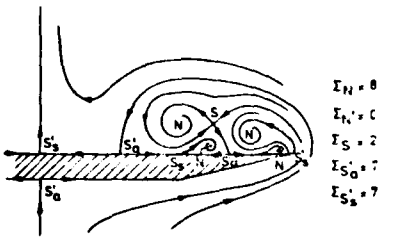

Fig. 14. Conjectured crossflow streamline pattern at x = 0.625c_o (α = 5°) model II

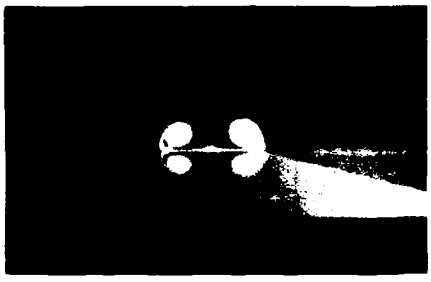

a. $x = 0.5c_o$

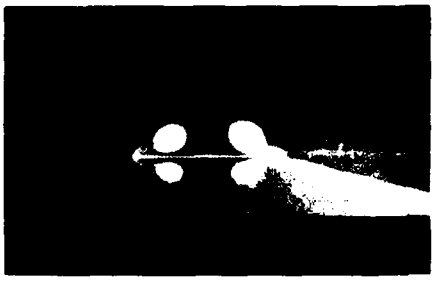

b. $x = 0.5625c_o$

c. $x = 0.625c_o$

d. $x = 0.75c_o$

Fig. 15. Flow about Model III at $\alpha = 20^o$

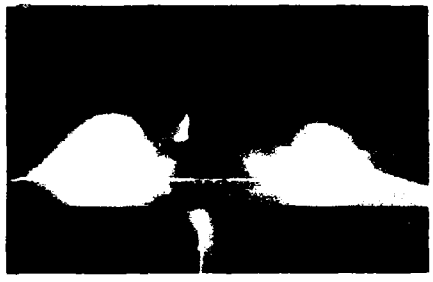

e. $x = 0.8125c_o$

Fig. 15. Continued

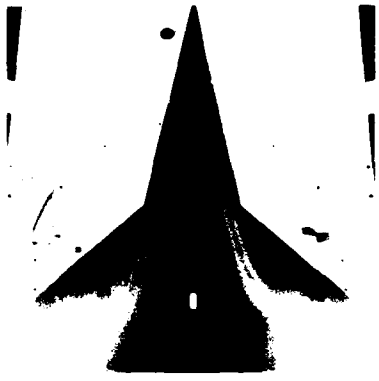

Fig. 16. Vortex smoke trails on leeward side of model III at $\alpha = 20^o$

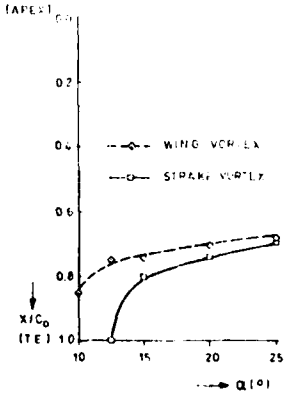

Fig. 17. Vortex-breakdown positions on Model III

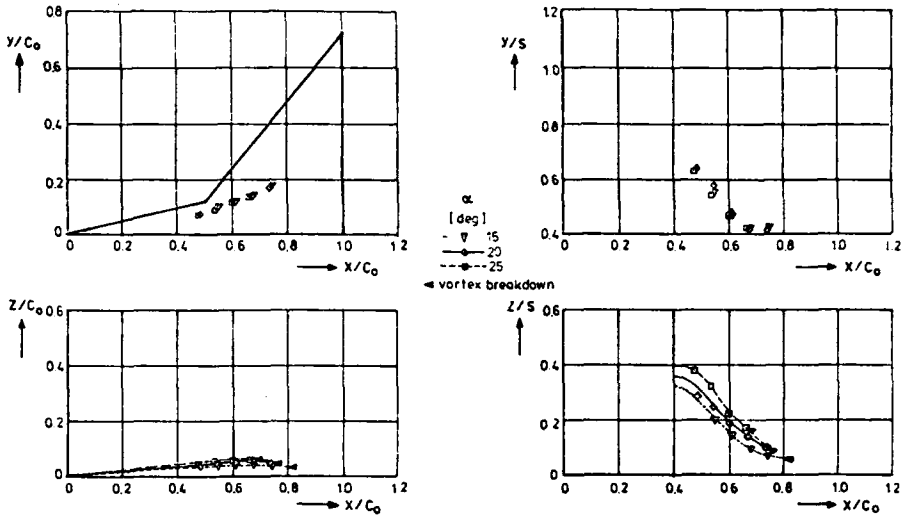

Fig. 18. Position of strake vortex on model III

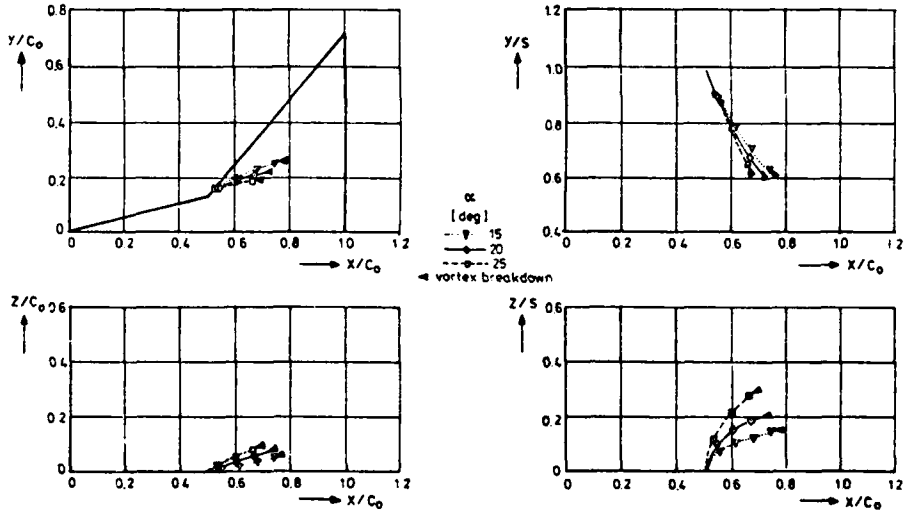

Fig. 19. Position of wing vortex on model III

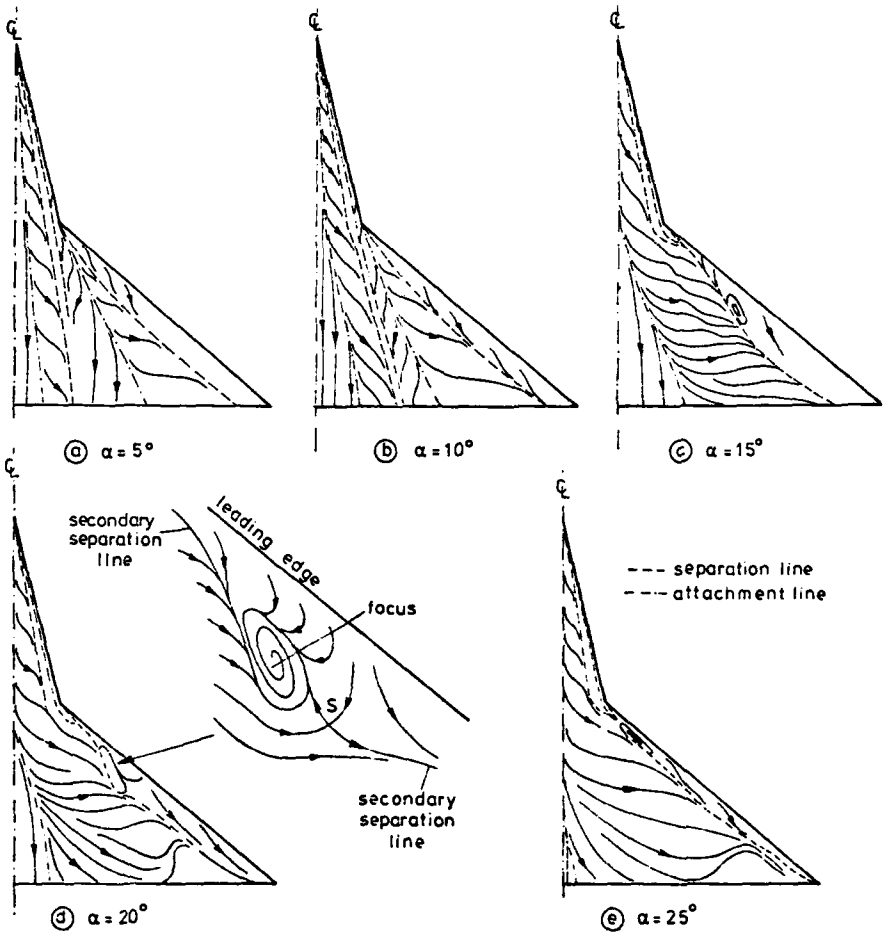

Fig. 20. Leeward-surface flow patterns of model III

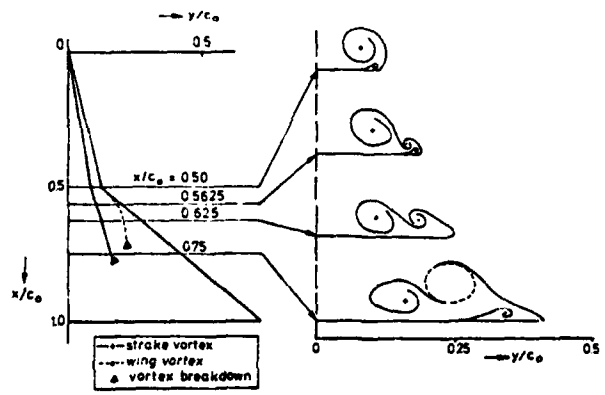

Fig. 21. Conjectured crossflow pattern above model III (α = 20°)

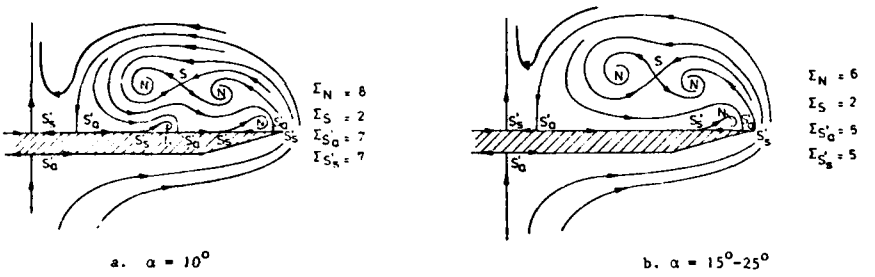

a. $\alpha = 10^\circ$ b. $\alpha = 15^\circ$–25°

Fig. 22. Conjectured crossflow streamlines about model III

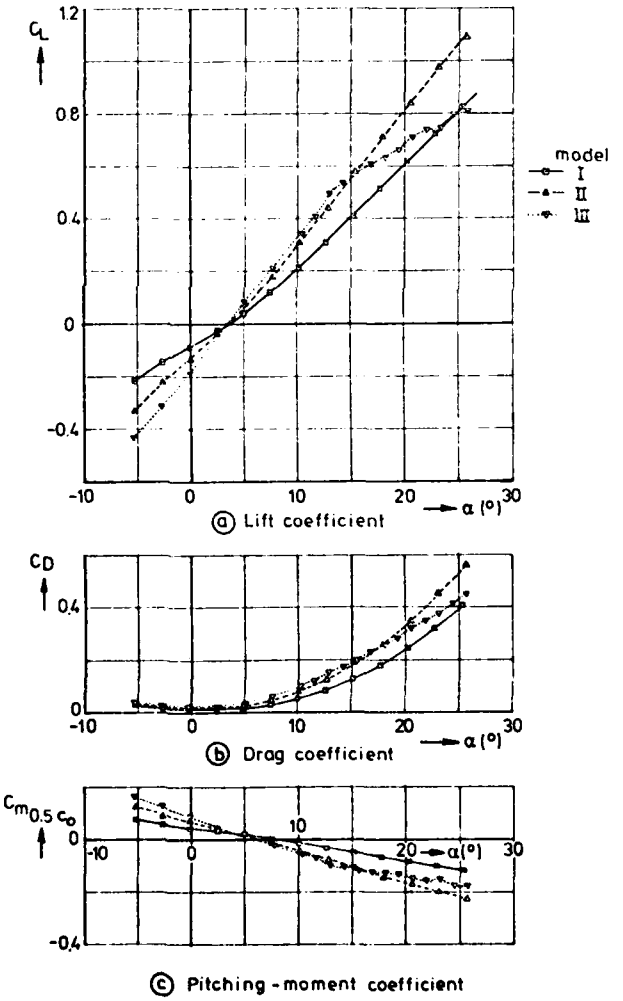

Fig. 23. Force and moment coefficients

VISUALISATION DES ECOULEMENTS TOURBILLONNAIRES TRIDIMENSIONNELS

par

H. WERLÉ

Office National d'Etudes et de Recherches Aérospatiales (O.N.E.R.A)
92320 CHATILLON - FRANCE

RESUME

Pour l'étude des écoulements tridimensionnels à caractère tourbillonnaire, la visualisation s'avère non seulement utile, mais bien souvent indispensable pour permettre de comprendre des phénomènes généralement complexes, pour compléter ou limiter les mesures effectuées en soufflerie parfois délicates à interpréter, enfin pour guider les calculs numériques en leur fournissant les éléments physiques de contrôle.

Que ce soit au cours d'une recherche fondamentale ou d'une étude à caractère appliqué, une visualisation aérodynamique ou hydrodynamique peut dans ces conditions fournir le schéma tourbillonnaire qui caractérise le phénomène, ainsi que son évolution en fonction des paramètres définissant l'écoulement, l'attitude et la forme géométrique du modèle.

Cet exposé tente de passer en revue les principaux types de tourbillons concentrés que l'on peut observer ainsi en régime permanent ou en écoulement instationnaire, tels qu'ils ont pu être visualisés en tunnel hydrodynamique, en soufflerie, et même en vol.

VISUALIZATION OF VORTICAL TYPE FLOWS IN THREE DIMENSIONS

SUMMARY

For the study of the three-dimensional vortex flows, visualization is not only useful , but often indispensable for understanding generally complex phenomena, for completing or limiting the measurments in wind tunnels (at times difficult to interpret) and finally for guiding the numerical calculations with physical control elements.

In both fundamental research and applied studies, one aerodynamic or hydrodynamic visualization can, under these conditions, give the vortical flow patterns, which characterize the phenomenon, as well as the evolution as a function of the parameters defining the flow, the position and the geometrical shape of the model.

This paper attempts to give a review of the principal types of concentrated vortices, which have been observed in steady or unstedy flows, as visualized in water, windtunnel and even in flight.

1 - INTRODUCTION -

Il est indéniable que les écoulements tourbillonnaires ne sont pas seulement une curiosité scientifique, dont le côté esthétique ne manque pas de fasciner la plupart d'entre nous, mais représentent un des phénomènes essentiels de la dynamique des fluides. Leur importance dépasse le cadre aérospatial qui nous intéresse et déborde même les limites de la mécanique des fluides que peut contrôler l'être humain, car c'est l'atmosphère terrestre toute entière qui subit leurs lois et parfois leurs contraintes (fig.1a-c) [1].

La formation des zones tourbillonnaires, leurs effets et instabilités, et jusqu'à leur désorganisation plus ou moins rapide font depuis longtemps l'objet de nombreuses études qui se poursuivent à notre époque avec la mise en oeuvre de moyens théoriques et expérimentaux sans cesse plus nombreux, puissants et rafinés. La visualisation, qui permet une observation directe des phénomènes, a souvent été un des premiers procédés utilisé pour aborder de telles études. C'est d'ailleurs bien souvent la nature elle-même qui, visualisant ses propres tourbillons, a suggéré à l'homme l'emploi de traceurs : poussières ou feuilles mortes virevoltant dans le vent ou flottant sur l'eau, fumées, condensations d'humidité et même nuages dans le ciel ; ces traceurs ont très vite attiré l'attention sur les zones tourbillonnaires : trombes se déplaçant à la surface terrestre, malstrom (fig.1c) se produisant dans l'eau, etc. A notre époque, des vues prises par satellite ont confirmé l'importance des cyclones (fig. 1b) et des sillages tourbillonnaires (fig.1a), phénomènes tridimensionnels qui sont à l'échelle de notre planète et contre lesquels l'homme reste impuissant.

Dans son activité propre, l'homme n'a pas manqué d'être à l'origine de phénomènes tourbillonnaires du même type, et parfois moins souhaitables (champignon atomique), il en est ainsi avec les sillages de ses constructions fixes (ponts, immeubles, tours, cheminées, torchères....) et avec les décollements sur ses structures mobiles (véhicules, sous-marins, avions, hélicoptères, engins,....).

Dans le domaine aérospatial qui nous concerne, la visualisation est devenue une discipline à part entière avec la création d'installations d'essais spécifiques aussi bien dans l'air que dans l'eau. Elle a donné naissance à une grande variété de méthodes qu'il n'est pas possible de passer en revue dans le cadre de cet exposé. Enfin son champ d'application ne cesse de s'étendre dans toutes les directions : des modèles les plus simples (ex.cylindre) aux maquettes les plus complexes (ex.hélicoptère), de la surface du modèle jusqu'à son sillage lointain, des angles d'attaque faibles aux plus élevés, du vol au point fixe au vol hypersonique,etc...

Quand l'aérodynamique s'aventure dans ces conditions extrêmes ou difficiles, il importe que la manoeuvrabilité des avions, le contrôle des engins, la sécurité du vol, la réduction des nuisances soient assurées. La visualisation peut alors souvent apporter son aide efficace à l'analyse des phénomènes tourbillonnaires

qui caractérisent ces cas limites.

Il n'est pas possible de faire ici une synthèse complète sur un sujet aussi vaste, aussi le présent exposé va se limiter au domaine incompressible. Il commence par un bref rappel des techniques expérimentales mises en jeu, avec la description de quelques installations types consacrées essentiellement à la visualisation, et des méthodes de visualisation par traceurs qui y sont pratiquées. Le lecteur intéressé trouvera dans une récente Lectures Series AGARD [2] une revue plus détaillée et plus complète sur ce sujet avec de nombreuses références.

La suite de l'exposé tente d'analyser à l'aide d'exemples variés * les principaux types de tourbillons que l'on peut observer dans les écoulements tridimensionnels.

2 - RAPPELS CONCERNANT LES TECHNIQUES EXPERIMENTALES -

2.1 - Essais dans l'air -

Dans le cadre de leur activité normalement consacrée aux mesures (efforts, pression etc...), la plupart des souffleries classiques effectuent aussi des visualisations d'écoulement. Les méthodes qu'elles utilisent [3] ont fait l'objet de mises à jour récentes [4], parmi lesquelles on note plus particulièrement celle de T.MUELLER [5], qui a l'Université de Notre Dame dispose d'installations particulièrement adaptées à la visualisation à l'aide de fumée (souffleries à grand coefficient de contraction et à faible taux de turbulence, rampes d'émissions de fumée, etc....).

Les fumées généralement blanches sont obtenues à l'aide de générateurs ou de "smoke wire" à partir de titanium tetrachloride (J.K.HARVEY : fig.5m), de kérosène (fig.11a), de vapeur d'huile [6](fig. 11e) ou d'eau condensée par de l'azote liquide [7](fig.5an). Une visualisation tomographique des écoulements peut alors être réalisée à l'aide d'un éclairage par faisceau laser plan [8], permettant d'obtenir par exemple des coupes transversales (fig.5a) ou longitudinales (fig.5n) du noyau du tourbillon d'extrados d'une aile delta mince avec incidence. Sous l'effet de forces centrifuges, l'axe du noyau en amont de son éclatement reste vide de fumée et apparaît en noir sur les clichés. Grâce à un laser impulsionnel (durée : 15 ns), ce procédé peut être utilisé même en régime instationnaire et fait apparaître présentement la structure du noyau éclaté (fig.5n).

Dans la pratique, une bonne visualisation de phénomènes tourbillonnaires tridimensionnels reste toujours délicate, que l'on procède avec une rampe d'émission de fumée amont créant son propre sillage ou que la fumée soit émise directement à partir du modèle. D'autre part, ce procédé reste ponctuel et ne peut couvrir l'ensemble du champ aérodynamique.

D'autres types de visualisation peuvent être brièvement rappelés ici :

- les écoulements pariétaux [9] visualisés par des émissions continues de liquide coloré à la surface des maquettes ou par des enduits visqueux déposés avant chaque essai (fig.5b).

- une méthode originale, celle du Dr. CROWDER de BOEING [10] traduit en points lumineux de différentes couleurs un sondage de pression totale effectué dans un plan transversal derrière le modèle et fait apparaître ainsi sans traceurs le sillage tourbillonnaire d'une aile munie de volets de courbure (fig.3c).

Un autre type d'installation fonctionnant dans l'air est le remarquable canal de la NASA à Langley (fig. lef). Il s'agit d'une tranchée rectiligne couverte longue de 550 m dans laquelle se déplace une maquette suspendue à une balance et entraînée par un chariot jusqu'à une vitesse de 30 m/s en palier. Dans ce canal (section : 5,5m x 4,3 m),la visualisation peut être assurée par un rideau de fumée dense, émis préalablement et couvrant la totalité du champ étudié. Cette installation permet, comme on le verra plus loin, de simuler correctement le sol et d'étudier le sillage lointain du modèle.

Il reste enfin à mentionner les visualisations faites au cours d'essais en vol, le plus souvent loin du sol et nécessitant alors un émetteur de fumée haubanné et de grande hauteur (fig.1d). Ce dernier assure une distribution de fumée avant et pendant le passage de l'avion, mais généralement perturbée par la présence du vent.

Enfin, les avions expérimentaux sont rarement équipés d'émetteurs de fumée, et cherchent le plus souvent à profiter de la condensation de l'humidité atmosphérique pour obtenir une visualisation des tourbillons (fig.6fg).

2.2 - Essais dans l'eau -

Comme pour les essais dans l'air, on peut distinguer les mêmes types d'installations :

- les bassins à surface libre généralement sans circulation d'eau et dans lesquels se déplace la maquette entraînée par un chariot, comme celui de la D.F.V.L.R./AVA à Göttingen [11](fig.1g);

- les tunnels hydrodynamiques, l'équivalent des souffleries, pour lesquels il existe de nombreuses variantes suivant la disposition verticale ou horizontale de la veine, la fermeture ou non du circuit, le mode de motorisation etc.. (voir [2]).

Rappelons ici que les 3 tunnels équipant le nouveau laboratoire hydrodynamique de l'ONERA [12](fig.12a) sont verticaux en circuit ouvert et fonctionnent par vidange sous l'effet de la gravité.

Pour assurer la visualisation des écoulements dans l'eau, on utilise le plus souvent des traceurs [13,14] liquides ou gazeux :

*)quelques exemples ont été groupés dans le film ONERA 1071 présenté en cours de séance .

- colorants ordinaires ou fluorescents, de mêmes densité et viscosité que l'eau, émis à partir des maquettes, ou encore à l'aide d'une rampe amont qui introduit inévitablement son propre sillage ; à l'ONERA, nous avons adopté depuis quelque temps le rhodorsil dilué, émulsion blanche et stable qui se mélange facilement à l'eau et aux différents colorants, grâce auxquels on peut distinguer le sens de l'enroulement des filets des tourbillons (fig. 12 et 13).

D'autre part, les circuits d'émission sont contrôlés individuellement par des robinets assurant un réglage précis du débit du colorant à chaque instant ; dans ces conditions, un arrêt progressif des émissions permet d'obtenir des visualisations pariétales (par exemple fig.9n). Dans le cas des écoulements tourbillonnaires, la difficulté principale réside surtout dans le choix de la bonne position des orifices d'émission devant visualiser l'axe et les filets hélicoïdaux des tourbillons (fig. 2ac) et si possible convenir pour toute une gamme d'incidences et de nombres de Reynolds d'essai ;

- bulles d'air en suspension dans l'eau et obtenues à l'aide d'un agent émulsionnant introduit au moment du remplissage du réservoir (procédé ONERA). Eclairées par un faisceau plan de faible épaisseur, les bulles d'air précisent l'allure de l'écoulement dans une tranche longitudinale (fig.2b) ou transversale et située au bord de fuite du modèle (fig.2e) ou en aval de ce dernier (fig.2f). Sur certaines maquettes, elles permettent aussi de visualiser l'écoulement pariétal (fig.5c). Notons ici que contrairement à ce que l'on observe pour la fumée dans l'air, les bulles d'air contenues dans le noyau d'un tourbillon intense tendent, sous l'effet des forces centripètes, à venir s'accumuler le long de l'axe qu'elles visualisent ainsi (fig.2d) jusqu'au point d'éclatement (fig.6e);

- bulle d'hydrogène obtenues par électrolyse [15] et utilisées notamment quand on veut éviter toute pollution dans un bassin sans circulation d'eau (fig.7ab), ou lorsque l'on veut limiter la visualisation au seul phénomène étudié, soit par exemple à la nappe enroulée en "cornet" au-dessus d'une aile delta en incidence (fig.5fgh).

Il reste à mentionner ici quelques cuves spécialement conçues pour l'étude des tourbillons, disposant d'un convergent annulaire à aubes produisant un courant hélicoïdal de pas réglable dans une veine circulaire. Ce courant représente le noyau et peut être soumis à un gradient de pression antagoniste, la visualisation étant assurée par des émissions de colorant [16 - 21](fig.6a).

3 - *PRINCIPAUX TYPES DE TOURBILLONS OBSERVES* -

3.1 - *Tourbillons marginaux* -

Le cas classique [22 - 23] du tourbillon marginal qui se développe le long du saumon d'extrémité d'une aile rectangulaire isolée en incidence est illustré par les visualisations (fig.2a-f) obtenues au tunnel ONERA TH2 dans le cas d'un profil NACA 0012 placé à 12°,5 d'incidence :

- à faible Reynolds, les colorants (fig.2a) mettent en évidence la structure hélicoïdale des filets constituant le noyau du tourbillon, tandis que les bulles d'air (fig.2b) précisent ses dimensions et même la pente des filets hélicoïdaux dans une coupe longitudinale passant par l'axe du tourbillon, ainsi que la trajectoire du noyau, qui, en l'absence de gradient antagoniste, reste organisé loin derrière la voilure;

- à Reynolds élevé, si la structure hélicoïdale des filets ne peut être décelée qu'au voisinage de l'origine du tourbillon en raison de la rapide diffusion du colorant, on note que le colorant qui alimente l'axe du tourbillon, demeure cependant plus dense que dans le reste du noyau turbulent (fig.2c). Dans ce noyau, les bulles d'air les plus grosses s'accumulent sur l'axe (fig.2d) sous l'effet des forces centripètes et on les retrouve dans les coupes transversales (fig.2ef).

Ces coupes peuvent être rapprochées de celles obtenues à l'aide de fumée au canal aérodynamique de la NASA derrière une maquette de monoplan en incidence (fig.2g). Enfin une comparaison avec un avion réel évoluant près du sol peut être faite grâce à une visualisation inattendue obtenue avec un monoplan agricole commençant une vaporisation d'insecticide (fig.2h) [1]. Un deuxième exemple est celui d'un petit avion de la NASA traversant un rideau de fumée (fig.2 ij). Sur toutes ces visualisations, la fumée précise au passage de l'avion la position de l'axe du noyau et l'enroulement de la nappe marginale.

Mais le tourbillon d'extrémité d'une aile d'avion, et plus particulièrement quand il s'agit de celle d'un avion de transport en configuration d'atterrissage, n'est généralement seul : en effet, chaque extrémité libre de volet de courbure braqué donne naissance à son propre tourbillon marginal et des interactions se produisent entre tous ces tourbillons, dont on retrouve la trace dans le sillage.

Un premier exemple de ce type obtenu au tunnel ONERA TH1 concerne une maquette de l'Airbus (fig.3a) et son propre sillage (fig.3b), dont on retrouve l'exacte image dans les sondages de pression totale derrière une configuration similaire chez BOEING (procédé du Dr.CROWDER) [10](fig.3c).

Les visualisations par fumée obtenues au canal de la NASA (Langley) avec une maquette de BOEING 747 confirment le schéma tourbillonnaire multiple du proche sillage (fig.3d), mais révèle en outre son évolution à l'aval, caractérisée par un mouvement de rotation des différents tourbillons issus de chaque aile (fig.3efg) et leur concentration finale en deux gros tourbillons contrarotatifs (fig.3 hij). On sait que la formation et la persistance de gros tourbillons de ce type présente un véritable danger dans les aéroports à trafic intense.

3.2 - *Tourbillons d'ailes en flèche* -

Alors que l'écoulement qui décolle sur une aile de faible flèche (Φ = 30°) placée à 20° d'incidence ne présente pas de caractère tourbillonnaire organisé en dehors de son tourbillon marginal (fig.4a), sur une aile en flèche accentuée (Φ = 60°) comme l'aile cylindrique équipée d'un profil symétrique ONERA D, aile qui a fait l'objet d'une étude systématique à l'ONERA [24], le décollement d'extrados présente une structure tourbillonnaire organisée, dont l'origine se situe près de l'apex (fig.4d). Cette structure rejoint celle fournie par un calcul des lignes d'émission basé sur la méthode des tourbillons ponctuels [26](fig.4e).

Les coupes transversales visualisées par bulles d'air (fig.4bc) révèlent, outre les tourbillons principal et secondaires de bord d'attaque, la présence d'un tourbillon se formant le long du bord de fuite lui aussi en flèche accentuée. De telles visualisations ont permis de dégager le schéma précis et complet de l'écoulement [25].

Une deuxième comparaison calcul-expérience a été effectuée avec cette même aile en présence d'un plan canard de même forme en plan et placé à la même incidence (fig.4 fghi) ; cette configuration donne lieu à des interactions entre les tourbillons. De telles interactions peuvent être bénéfiques lorsqu'elles contribuent à retarder le décrochement et à maintenir sur le modèle un écoulement tourbillonnaire organisé. Dans le cas d'un avion évoluant à incidence élevée, ces tourbillons fournissent un supplément de portance, et donc de manoeuvrabilité. De telles études d'interaction tourbillonnaire entre fuselage, strake, aile, prise d'air, etc.. sont effectuées systématiquement autour d'avions de chasse à l'aide de visualisations obtenues au tunnel vertical de NORTHROP [27-28].

Au cas du décollement libre sur l'aile épaisse examiné ci-dessus peut être opposé le décollement fixé au bord d'attaque aigu d'une aile delta (Φ = 75°), cas classique pour lequel les visualisations avaient contribué à mettre en lumière dès 1952 [29] l'enroulement en cornet de la nappe qui se détache le long du bord d'attaque aigu de l'aile. Cet exemple donne ici l'occasion de comparer et recouper des visualisations obtenues par différents procédés aussi bien en soufflerie (fig.5abmn) qu'au tunnel ONERA TH1 (fig.5c-1)[30]. Ces visualisations montrent en outre le phénomène d'éclatement [31]qui désorganise ces tourbillons aux incidences élevées (fig.5 j-n), et en particulier la structure généralement spirale du noyau éclaté (fig.5jn).

Peu sensible aux effets du nombre de Reynolds, le phénomène d'éclatement remonte d'aval en amont, quand l'incidence de l'aile croît (fig.13bb') ou sous l'effet d'un gradient de pression antagoniste.

3.3 - *Eclatement de tourbillon* -

Il existe plusieurs types d'éclatement de tourbillon [32], comme par exemple l'éclatement du type bulbe (fig.6a), et un certain nombre de chercheurs ont étudié systématiquement ce phénomène au sein d'un écoulement hélicoïdal réglable traversant une veine circulaire en présence d'un gradient antagoniste [16 - 21].

Dans les tunnels ONERA, ce phénomène a été étudié en soumettant soit les deux tourbillons d'une aile delta entière (fig.13bb'), soit un tourbillon marginal isolé au sein d'un écoulement sensiblement uniforme à un gradient antagoniste créé par un obstacle ou une prise d'air placée sur la trajectoire du noyau (fig.6b-e). Que ce soit en régime laminaire (fig.12c) ou en régime turbulent (fig.12d), l'éclatement observé est du type spirale, sauf dans des conditions particulières, pour lesquelles apparaît un éclatement du type bulbe (écoulement laminaire et à faible Reynolds, etc.).

L'éclatement en spirale a été observé en vol sur l'avion DOUGLAS F5D [33] (fig.6fg) et ces essais en vol ont à leur tour été recoupés par des visualisations au tunnel ONERA TH1 (fig.6h).

3.4 - *Tourbillons de corps fuselés* -

Les corps ogivo-cylindriques lisses représentant des missiles, les fuselages isolés et les ellipsoïdes de révolution allongés constituent une autre classe de modèles souvent étudiés à l'heure actuelle, notamment dans le cas des grands angles d'attaque .

Comme le rappellent les visualisations obtenues au canal du DFVLR à Göttingen [34] et dans les tunnels ONERA [35], le décollement libre sur les bords arrondis d'un corps cylindrique lisse perd la structure tourbillonnaire symétrique et relativement stable qu'il présente aux incidences moyennes (fig.7ac) pour devenir le siège de tourbillons asymétriques moins stables mais stationnaires dès que l'incidence se situe entre 35° et 60° (fig.7bd), tout en conservant leur symétrie près de la pointe avant (fig.7e et 13a). Les essais précisent en outre les effets d'une variation du nombre de Reynolds et l'influence de la forme du nez : les premiers tourbillons se fixent au nez pointu de l'ogive et au contraire restent séparés par un bulbe de décollement médian sur un nez arrondi (fig.7f et 13a'). Ce résultat recoupe ceux d'une étude de l'influence de la forme du nez sur le décollement tourbillonnaire observé autour d'ogives de révolution aux incidences élevées [36-37]:

- ogive pointue avec des tourbillons issus de l'apex (fig.8n),
- ogive à nez arrondi avec des tourbillons faisant leur jonction dans un bulbe décollé médian (fig.8m),
- enfin, dans le cas d'un nez profilé comme celui d'un ellipsoïde de révolution allongé, les deux tourbillons se trouvent d'abord séparés par un couloir médian sain non décollé (fig.8 fg), puis se rejoignent en aval (fig.8 hi).

Les émissions de colorant plus ou moins pariétales (fig.8g et 13e) faites sur le nez du modèle montrent que les tourbillons principaux se forment à la suite d'un cisaillement accentué de la couche limite amont, mais ne permettent pas de distinguer les singularités classiques caractérisant l'origine d'un tourbillon (foyer) [38, 39].

Pour cette raison, ce type de décollement est généralement qualifié de décollement ouvert, non sans faire l'objet de polémiques [40]. Quand le nombre de Reynolds croît (fig.8jkl) ou lorsque l'incidence diminue (fig.8de et 8a-c),les tourbillons se forment plus en aval avec des noyaux plus réduits, mais la structure du décollement reste inchangée. De telles visualisations complètent les mesures effectuées en soufflerie sur ce même type de maquette aussi bien à l'ONERA qu'au DFVLR [41].

3.5 - *Tourbillons de corps aplatis* -

L'étude du décollement tridimensionnel libre a été poursuivie dans les tunnels ONERA avec des ellipsoïdes de forme plus aplatie (fig.13c et d), qui s'apparentent au cas d'une aile plus ou moins élancée.

Dans le cas de l'ellipsoïde circulaire qui peut être examiné en détail sur le fig.9, les différentes vues révèlent l'évolution du décollement d'extrados en fonction de l'incidence et du nombre de Reynolds

et permettent de distinguer les différents cas suivants :

- tourbillons marginaux séparés par un large couloir d'écoulement sain (fig.9 e-h)
- tourbillons perturbés par un large décollement médian (fig.9a-d et 13e),
- tourbillons séparés par un bulbe de bord d'attaque médian à caractère mixte laminaire-turbulent et plus ou moins étendu (fig.9cj et fig.9k)
- tourbillons marginaux séparés par un bulbe laminaire (fig.9mn) et généralement suivi d'un décollement médian arrière (fig.13d).

3.6 - *Tourbillons autour de cylindres* -

Au cas précédent du décollement libre sur un ellipsoïde circulaire en incidence peut être confronté celui du décollement se produisant au culot incliné d'un cylindre sans incidence (fig.10a-f) : ce décollement fixé le long du bord aigu du culot (fig.10a) est le siège de deux tourbillons symétriques issus de points de convergence spirale (fig.10b) situés de part et d'autre d'un bulbe décollé médian fixé au bord avant du culot (fig. 10c). Ces tourbillons relativement stables se développent jusqu'au bord aval du culot (fig.de) et viennent constituer le sillage tourbillonnaire du modèle (fig.10f). Ce type d'écoulement concerne directement l'étude aérodynamique des véhicules terrestres [42].

L'exemple du cylindre droit illustré par les fig.10g-n évoque le cas des structures fixes soumises au vent ou au courant (tour, cheminée, pile de pont, etc...). Comme on le sait, l'écoulement autour d'un tel cylindre n'est véritablement plan qu'en dehors de son sillage (fig.10h) ou du voisinage des panneaux entre lesquels il est monté (fig.10g). On observe devant le cylindre un décollement de la couche limite du panneau avec formation de tourbillons principaux et secondaires comportant une structure tridimensionnelle. Alimentés par une mince couche de courant, ces tourbillons s'incurvent en fer à cheval de part et d'autre du cylindre et évacuent vers l'aval le débit capté [43]. Même en régime laminaire (fig.11ki), les tourbillons de Bénard Karman qui se forment assez loin dans le sillage, finissent, quand la vitesse augmente, par produire des effets instationnaires sur ces tourbillons en fer à cheval (fig.10ij). A vitesse élevée (fig.10mn), l'écoulement le long du panneau devient turbulent et plus instationnaire, mais conserve finalement sa même structure moyenne [44].

3.7 - *Tourbillons en régime instationnaire* -

Pour évoquer les écoulements tourbillonnaires instationnaires, les visualisations retenues dans cet exposé ne concernent que le cas des tourbillons marginaux se formant au bout des pales d'un rotor d'hélicoptère. Le lecteur intéressé pourra trouver dans [2,45] de nombreux exemples d'autres types de tourbillons instationnaires visualisés par les mêmes moyens.

La figure 11 dévoile les différents aspects des phénomènes tourbillonnaires se produisant autour d'un rotor tripale isolé, d'abord au point fixe où les tourbillons hélicoïdaux se déplacent à la frontière du flux du rotor (fig.11a-d), puis en vol d'avancement où les tourbillons de forme en plan cycloïdale sont emportés par le courant (fig.11 e-g).

Ces recoupements effectués entre des essais dans l'air et dans l'eau [6] ont permis de comparer les trajectoires des tourbillons et de préciser les effets de certains paramètres. Ces essais, qui se poursuivent actuellement dans les tunnels ONERA, mettent en jeu une maquette motorisée d'hélicoptère complet avec simulation des prises d'air et sorties de gaz, aussi bien en vol d'avancement (fig.11h) qu'en vol stationnaire (fig.12b) [12].

CONCLUSION -

En régime stationnaire comme en régime instationnaire, les visualisations obtenues en tunnel, en soufflerie ou en vol apportent une contribution évidente à la connaissance des écoulements tourbillonnaires tridimensionnels, qu'il s'agisse d'une étude fondamentale ou d'aérodynamique appliquée.

Puissent-elles aider aussi bien les théoriciens que les expérimentateurs à mieux interpréter leurs propres résultats et à guider ainsi leurs recherches dans ce domaine.

REMERCIEMENTS -

L'auteur tient à témoigner sa gratitude à G.C. GREENE, NASA Research Center (Langley), J.JCORNISH III LOCKHEED Georgia Cie (Marietta) pour leur contribution en photographies, films et documents relatifs à leurs travaux récents. Pour quelques clichés et informations extraits de leurs publications, mes remerciements vont aussi à K.HARTMANN DFVLR (Göttingen), J.P.CROWDER BOEING (Seattle) J.K.HARVEY Imperial College UK ainsi qu'à mes collègues de l'ONERA trop nombreux pour pouvoir les citer.

REFERENCES *voir pages 18 et 20*

a

Fig. 1 – Phenomènes tourbillonnaires naturels et installations d'essais.

a, b, et c de la ref. [7].

Sillage tourbillonnaire d'une île vu d'un satellite (tourbillons alternés)

b

Cyclone au-dessus du Golfe du Mexique (tourbillon-trombe)

Maëlstrom à la surface de l'eau (tourbillon-puits)

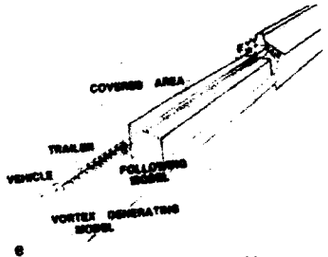

c

Schéma du canal de la NASA

Emetteur de fumée pour les essais en vol loin du sol (NASA Langley).

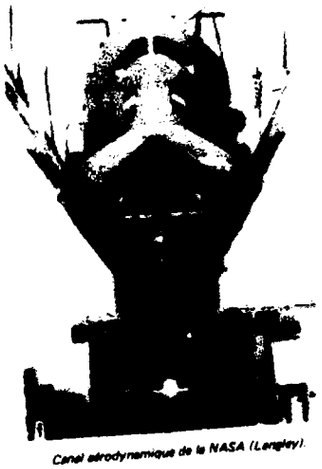

Canal aérodynamique de la NASA (Langley).

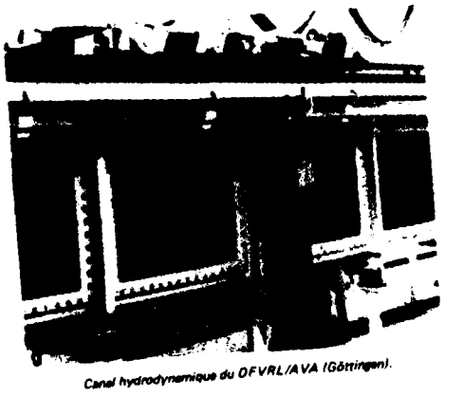

Canal hydrodynamique du DFVRL/AVA (Göttingen).

Fig 2 Tourbillon marginal d'une aile droite

Profil NACA 0012 α 12 5 $Re_c \sim 0.5\ 10^6$ (a, b) ou $2\ 10^6$ (e f)

Essai au tunnel ONERA TH2 d'une aile seule ; visualisation par colorant (a, c) ou bulles d'air (b, d, e, f).

Essai au canal NASA d'un monoplan (visualisation par fumée).

Monoplan en vol près du sol (avec vaporisation d'insecticide) voir [1].

Essai en vol d'un monoplan près du sol (NASA Langley), visualisation par fumée

Fig. 3 – Avions de transport.

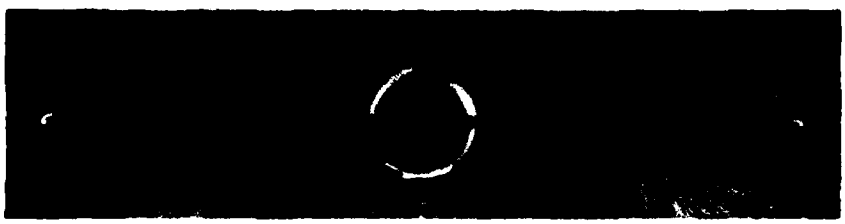

Essai au tunnel ONERA TH1 de l'airbus ; $\alpha = 2°,5 - 6a_b \simeq 10^6$. (maquette au 1/2 50ème sans simulation des réacteurs).

Essai à la soufflerie Boeing d'une maquette d'avion de transport ($\alpha \simeq 3°$) – Méthode du D^r Crowder (sondage de pression totale).

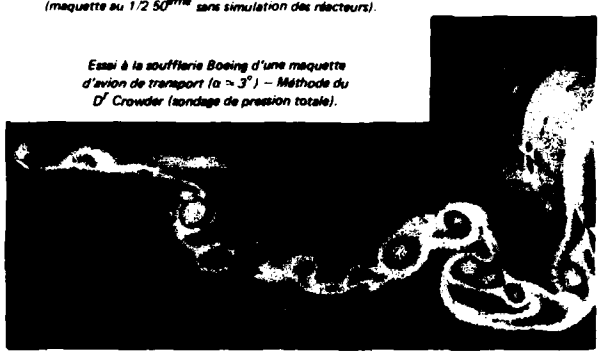

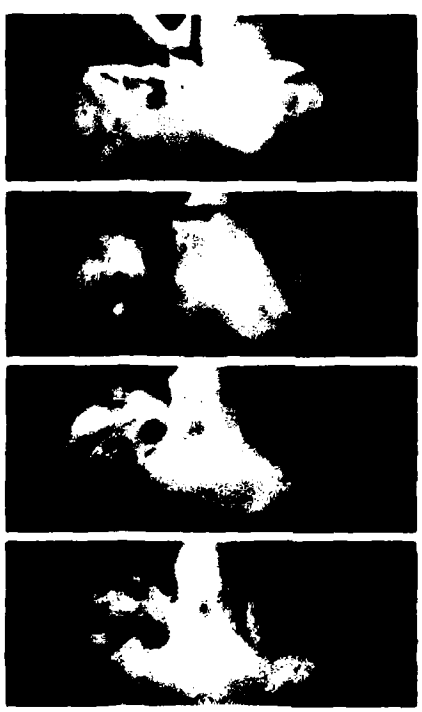

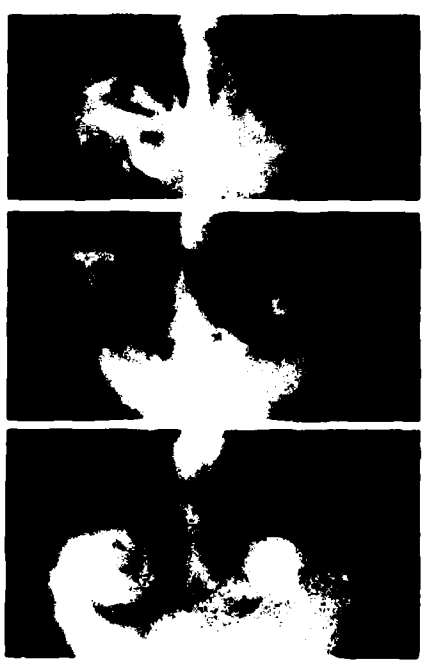

Essai au canal NASA (Langley) d'une maquette du Boeing 747 en configuration d'atterrissage (V ≈ 30 m/s).

Fig. 4 – Aile rectangulaire en flèche.

Essai au tunnel ONERA TH1
$\alpha = 20°$ – $Re_c > 10^4$ – Profil ONERA D

Aile seule à faible flèche ($\zeta = 30°$).

a-e, f et g : coupes transversales.

Aile seule à flèche élevée ($\zeta = 60°$)

Aile ($\zeta = 60°$) avec plan canard de même forme en plan

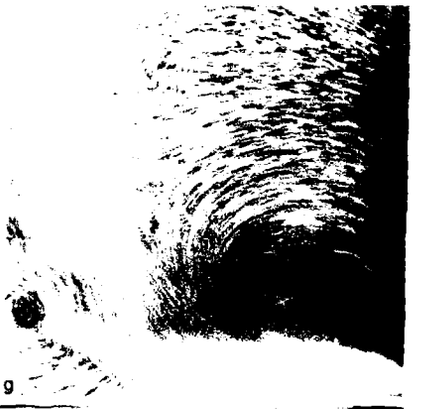

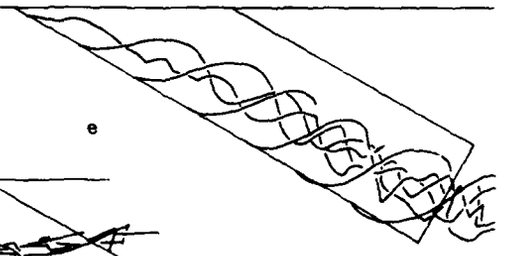

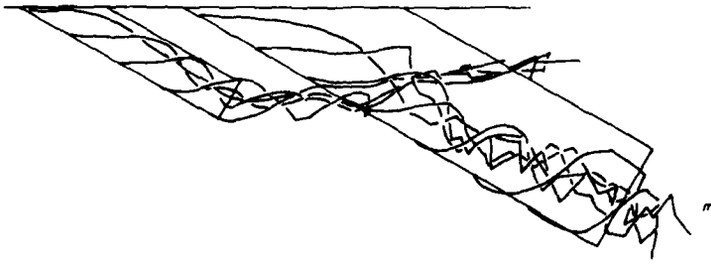

$\alpha = 19°$.

Calcul des lignes d'émission ; méthode des tourbillons ponctuels avec séparation au bord d'attaque.

Fig. 5 – Ailes delta minces.

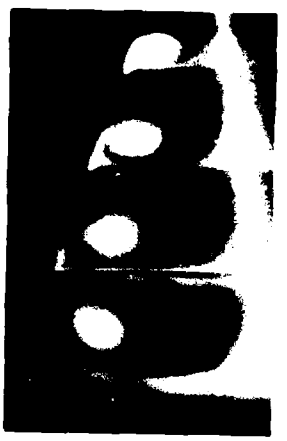

Soufflerie ONERA S2L Ch ($\alpha = 15°$) ; coupes visualisées par fumées - plan laser.

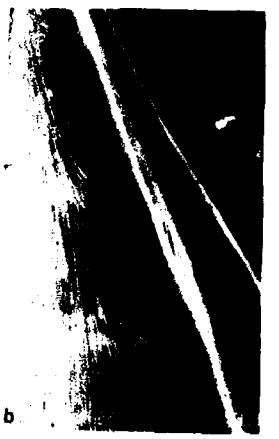

b

Soufflerie ONERA S1 MA ($\alpha = 14°$) ; visualisation par enduit visqueux.

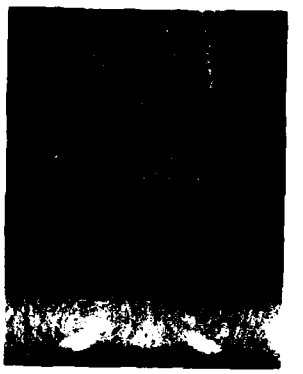

Tunnel ONERA TH1
$\varphi = 75° - \alpha = 15°$
$Re_c \geq 2.10^4$.

Visualisation par bulles d'hydrogène (électrolyse) ; coupes situées à la mi-corde (d, g, k) ou au bord de fuite (e, h, l).

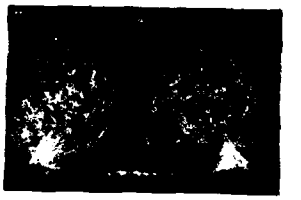

$\alpha = 30°$.
Visualisation par bulles d'air.

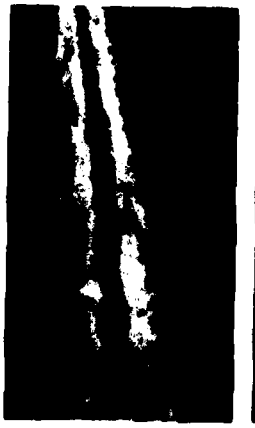

Éclatement de tourbillons visualisé par fumée ; soufflerie (J. Harvey) [3] ; soufflerie ONERA S2L Ch (plan laser).

$\alpha = 20°$

Visualisation par émissions de colorant.

$\alpha = 30°$

Fig. 6 – Éclatement de tourbillon

a

Éclatement du type bulbe précédant l'éclatement du type spirale d'un écoulement hélicoïdal dans la veine circulaire d'une cuve à eau (T. Sarpkaya et al.) [16 · 21].

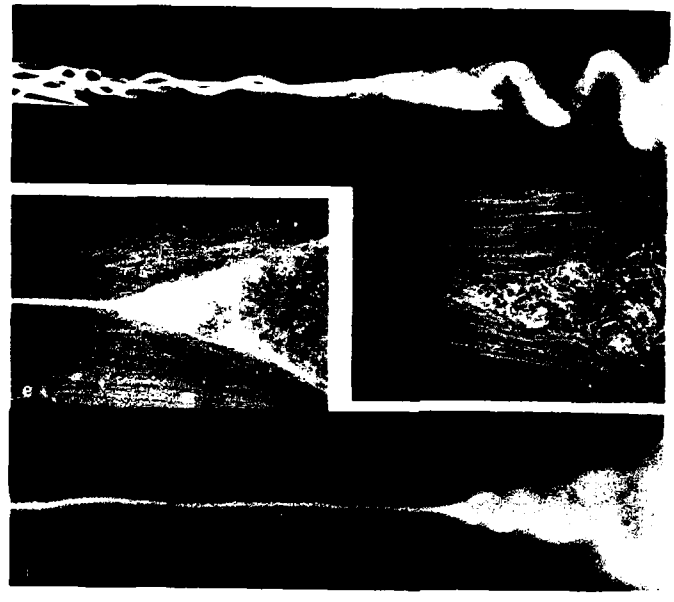

Éclatement du type spirale d'un tourbillon marginal isolé soumis à un gradient de pression antagoniste. (Voir Fig. 6b-d).

En régime laminaire ($\mathcal{R}e_c \sim 0{,}5.10^5$).

En régime turbulent ($\mathcal{R}e_c \sim 2.10^5$).

Avion expérimental Douglas F5D

Essai en vol (NASA AMES), visualisation par condensation de l'humidité atmosphérique.

Essai au tunnel ONERA TH1, maquette au 1/72,5ème, $\alpha = 15°$ – $\mathcal{R}e \simeq 10^6$. Visualisation par colorant.

Fig. 7 - Fuselages cylindriques.

Essai au canal du DFVRL AVA (Göttingen) Dr Hartmann

Ogivo-cylindre à nez pointu (L = 15 D) ; visualisation par bulles d'hydrogène (électrolyse).

$\alpha = 30° - Re_D > 0{,}5.10^6$

$\alpha = 55° - Re_D > 10^5$

$\alpha = 20°$

Essai au tunnel ONERA TH2 $Re_D > 0{,}5.10^6$. Visualisation par colorants (e, f) ou bulles d'air (c, d).

Ogivo-cylindre à nez pointu (L = 15 D).

$\alpha = 50°$

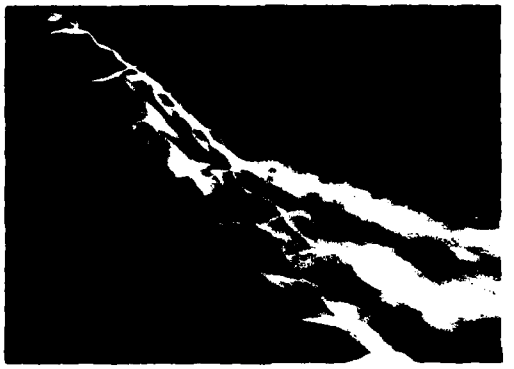

Ogivo-cylindre à nez arrondi (L = 14 D).

Coupes transversales arrières.

Fig. 8 – Ellipsoïde et ogives de révolution.

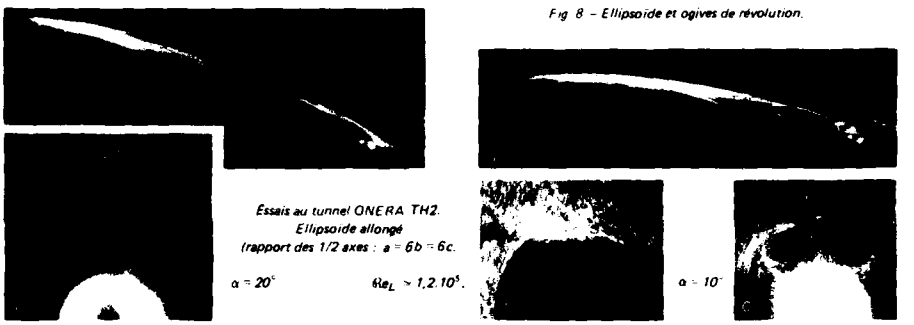

Essais au tunnel ONERA TH2.
Ellipsoïde allongé
(rapport des 1/2 axes : a = 6b = 6c.

$\alpha = 20°$ $\quad Re_L \sim 1,2.10^5$.

$\alpha = 10°$

$\alpha = 30°$
$Re_L \sim 1,2.10^5$

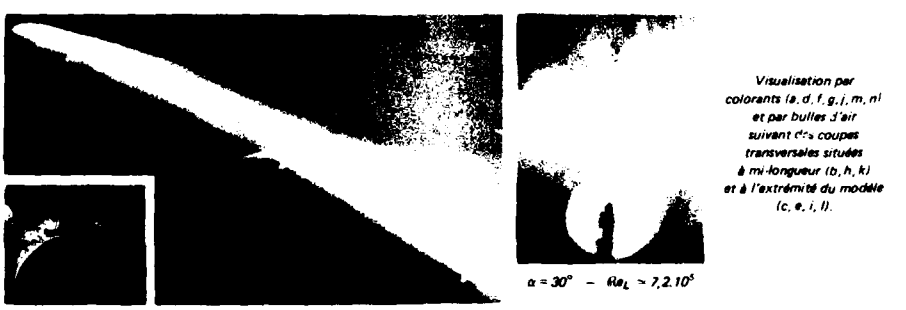

Visualisation par colorants (a, d, f, g, j, m, n) et par bulles d'air suivant des coupes transversales situées à mi-longueur (b, h, k) et à l'extrémité du modèle (c, e, i, l).

$\alpha = 30° \quad Re_L \sim 7,2.10^5$

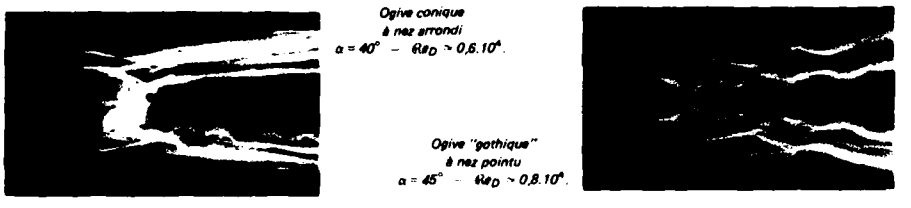

Ogive conique
à nez arrondi
$\alpha = 40° \quad Re_D \sim 0,8.10^6$.

Ogive "gothique"
à nez pointu
$\alpha = 45° \quad Re_D \sim 0,8.10^6$.

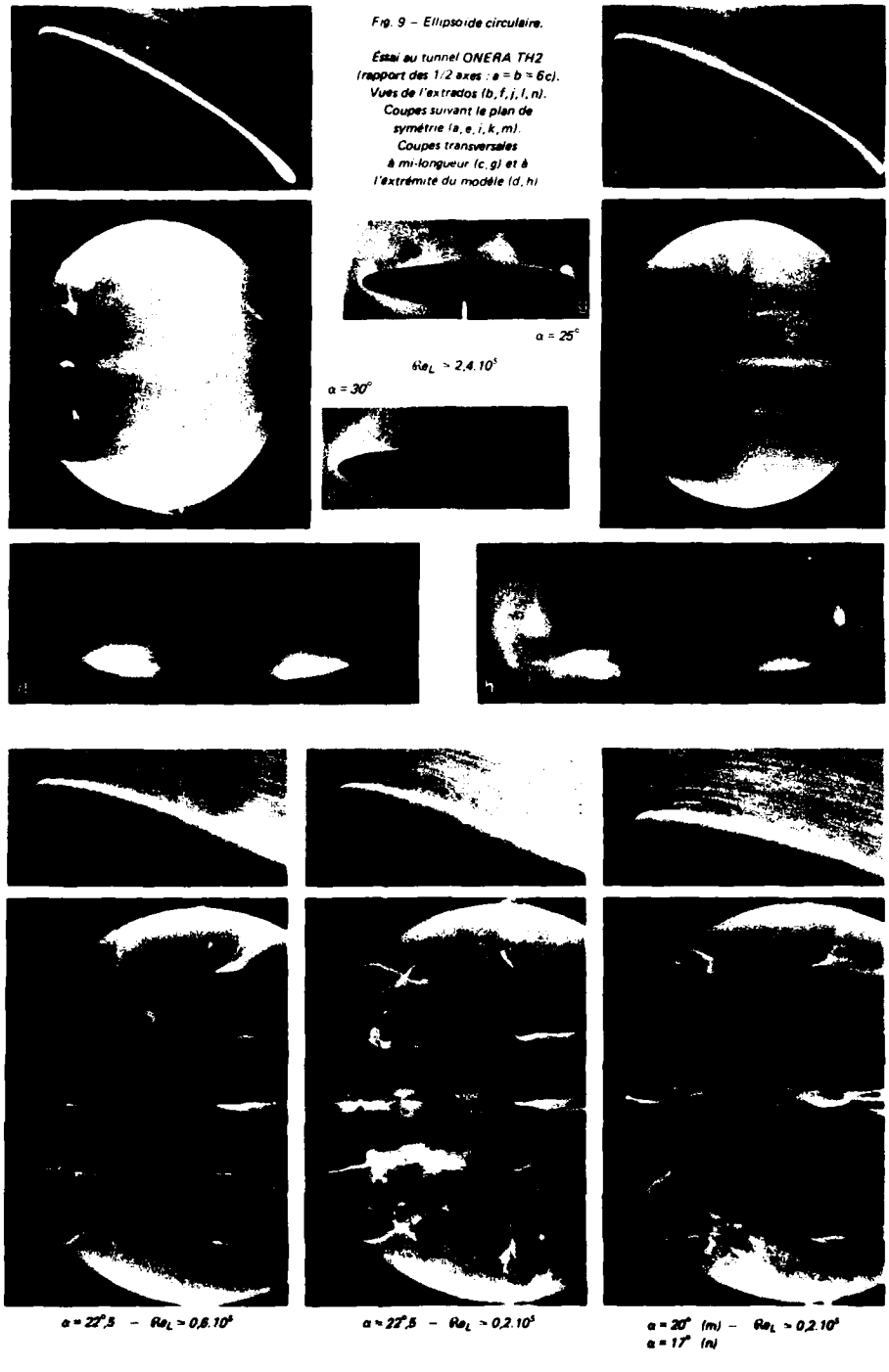

Fig. 9 – Ellipsoïde circulaire.

Essai au tunnel ONERA TH2 (rapport des 1/2 axes : a = b = 6c). Vues de l'extrados (b, f, j, l, n). Coupes suivant le plan de symétrie (a, e, i, k, m). Coupes transversales à mi-longueur (c, g) et à l'extrémité du modèle (d, h)

$\alpha = 25°$

$\theta Re_L \simeq 2,4.10^5$

$\alpha = 30°$

$\alpha = 22°,5 \quad - \quad \theta Re_L \simeq 0,8.10^5$

$\alpha = 22°,5 \quad - \quad \theta Re_L \simeq 0,2.10^5$

$\alpha = 20°$ (m) – $\theta Re_L \simeq 0,2.10^5$
$\alpha = 17°$ (n)

Fig. 10 – Cylindres.

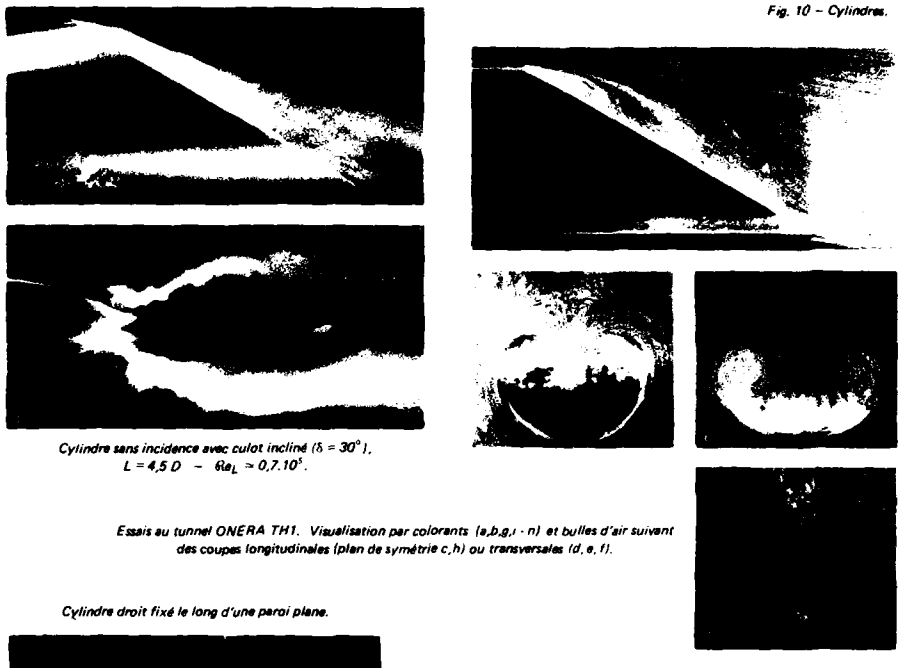

Cylindre sans incidence avec culot incliné ($\delta = 30°$),
$L = 4{,}5\ D$ – $\mathcal{R}e_L \simeq 0{,}7.10^5$.

Essais au tunnel ONERA TH1. Visualisation par colorants (a,b,g,i · n) et bulles d'air suivant des coupes longitudinales (plan de symétrie c,h) ou transversales (d, e, f).

Cylindre droit fixé le long d'une paroi plane.

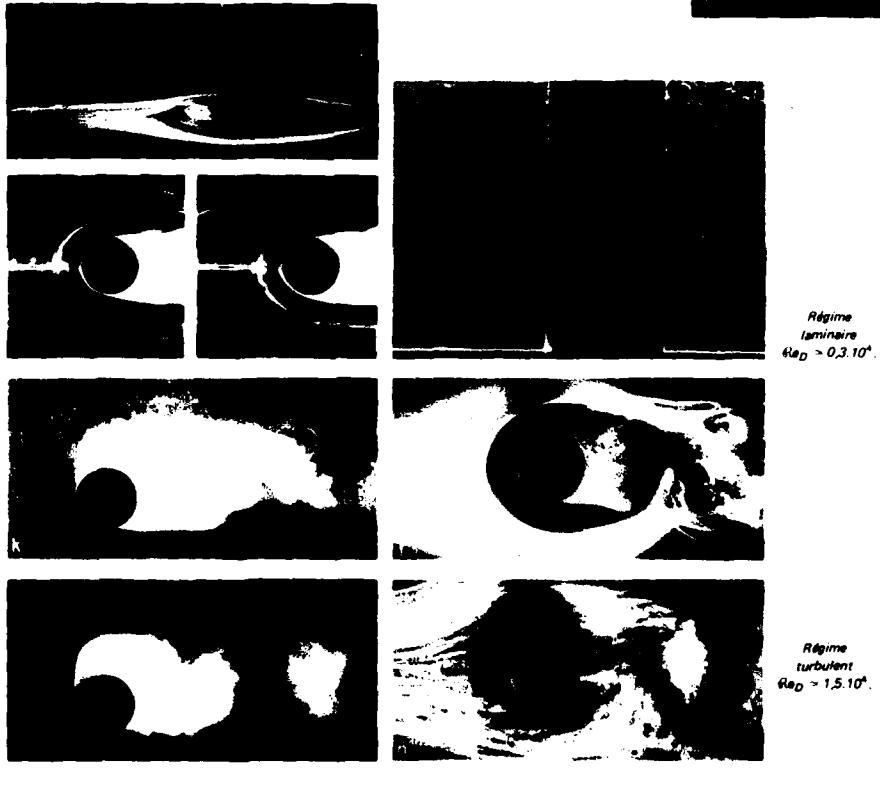

Régime laminaire
$\mathcal{R}e_D \simeq 0{,}3.10^4$.

Régime turbulent
*$\mathcal{R}e_D \simeq 1{,}5.10^4$.

Essais au banc S2 de l'Aérospatiale (Bourget); rotor tripale type 330 au point fixe. Visualisation par fumée.

Essai au tunnel ONERA TH3 ; rotor tripale au point fixe.

$\lambda = 0{,}3$.
Essai à la soufflerie ONERA S1MA ; rotor tripale en vol d'avancement.

Visualisation par fumée (volutes à l'aval du rotor).

Essai au tunnel ONERA TH1 ; rotor tripale en vol d'avancement $\lambda = 0{,}3$.

Visualisation par colorant (c, d, f, g, h).

Visualisation par bulles d'air suivant une coupe diamétrale (b)

Essais au tunnel ONERA TH2 ; hélicoptère complet motorisé en vol d'avancement $\lambda = 0{,}35$.

Fig. 11 – Rotors.

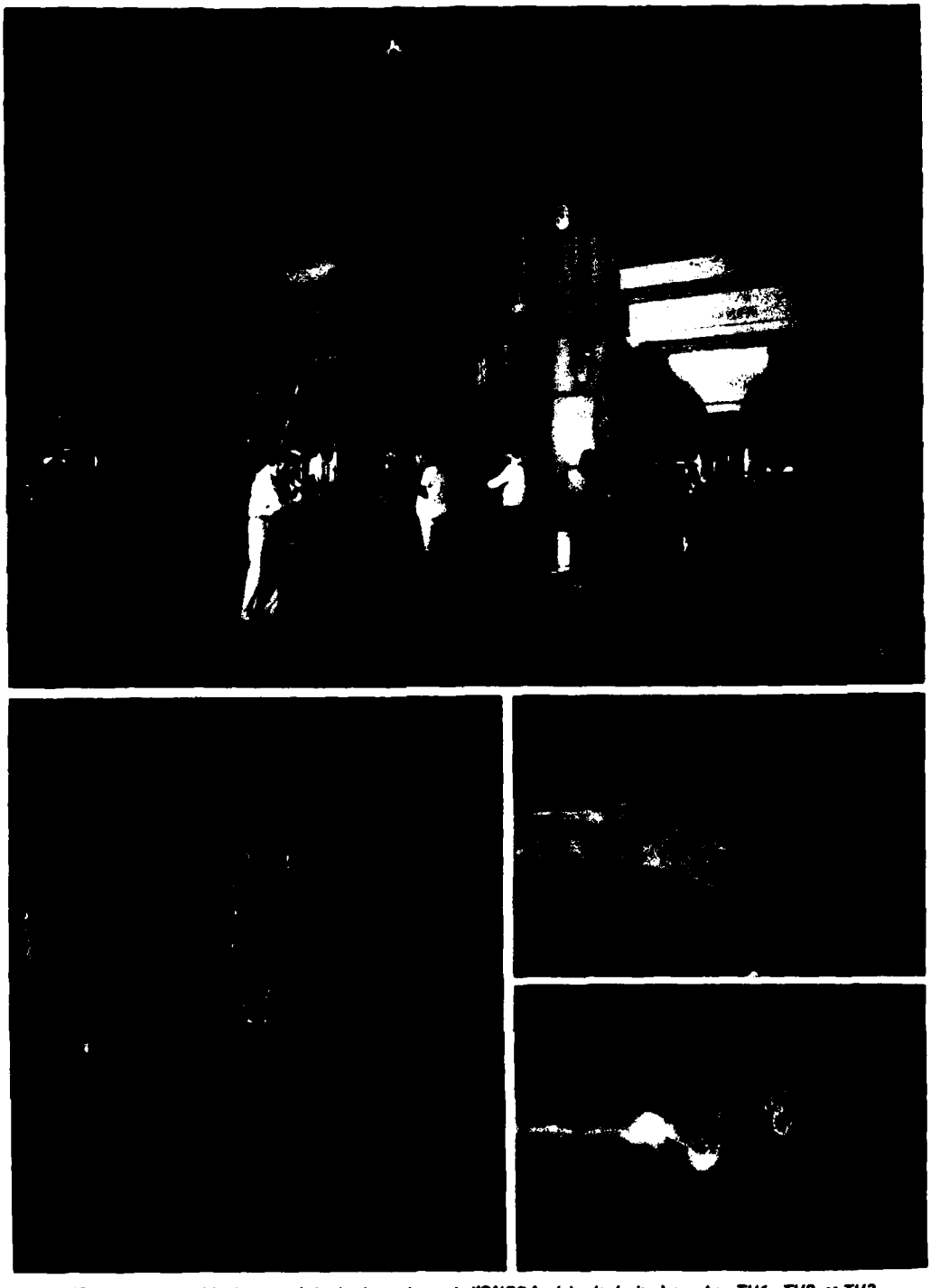

Fig. 12 – Vue d'ensemble des tunnels hydrodynamiques de l'ONERA. (a) : de droite à gauche . TH1, TH2 et TH3. Écoulement au point fixe (TH3) autour d'une maquette motorisée d'hélicoptère (b). Éclatement d'un noyau tourbillonnaire (TH2) en régime laminaire (c) ou turbulent (d).

REFERENCES

[1] CORNISH III J.J.(Oct.1982) Vortex Flows - Eighth quick-Goethert Lecture Series - Univ. of Tennessee Space Inst.Tullahoma.

[2] WERLÉ H. (Mars 1982) - Flow Visualization Techniques for the study of high incidence aerodynamics AGARD-VKI Lecture Series 121.

[3] MALTBY R.L.(1962)- Flow visualization in wind tunnels using indicators AGARDograph 70.

[4] MERZKIRCH W. (1974) - Flow Visualization Academic Press Inc.New-York.

[5] MUELLER T.J. (1981) - Flow Visualization by direct injection short Course of Fluid Mechan. Measur. Univ. Minnesota.

[6] WERLÉ H. et ARMAND Cl. (1969) - Mesures et Visualisations Instationnaires sur les rotors VIe Colloque AFITAE - ONERA TP 777.

[7] BISPLINGHOFF R.L., and al(1976)- Water fog generation system for subsonic flow visualization AIAA Journal Vol 14 n°8.

[8] PHILBERT M, BEAUPOIL R. et FALENI J.P. (1979) Application d'un dispositif d'éclairage laminaire à la visualisation des écoulements aérodynamiques en soufflerie par émission de fumée. Rech.Aerosp. 1979-3.

[9] WERLÉ H., LAVERRE J. et SOULIER Ch.(1977) - Techniques de visualisations d'écoulements pariétaux - ONERA T.P 1977-86.

[10] CROWDER J.P. (Octobre 1980) - Quick and easy flow field surveys. Astronautics and Aeronautics p.38.

[11] BIPPES H.and COLAK-ANTIC P. (1973) - Der Wasserschleppkanal der DFVLR Z.F.W. 21 p. 113.120.

[12] WERLÉ H. et GALLON M. (1982) - Le nouveau laboratoire de visualisation hydrodynamique de la Direction de l'Aérodynamique Rech. Aerosp. 1982-5 p. 289-311.

[13] WERLÉ H. (1973) - Hydrodynamic flow visualization Annual Review of Fluid Mechanics vol.5.

[14] WERLÉ H. (1974) - Méthodes de visualisation hydrodynamique des écoulements dans Techniques de mesure dans les écoulements Edition EYROLLES.

[15] SCHRAUB F., KLINE S., HENRY J., RUNSTADLER P., LITTEL A. (1964) Stanford Univ.Rep. MD 12

[16] HARVEY J.K (Déc.1962) Some observations of the vortex breakdown phenomenon J.of Fluid Mech.vol.14 Part.4.

[17] KIRKPATRICK D.L.I (May 1964) - Experimental investigation of the breakdown of a vortex in a tule RAE T.N.Aero 2963.

[18] CHANAUD R.C (1965) Observations of oscillatory motion in certain swirling flows J.Fluid Mech.Vol.21 part.1.

[19] SARPKAYA R.(1971) On stationary and travellling vortex breakdowns J. Fluid Mechanics vol. 45 part 3 pp 545-559

[20] LEIBOVICH S. (1978) The structure of vortex breakdown Annual Review Fluid Mech. n° 10 p. 221-246.

[21] ESCUDIER M.P. et ZEHNDER N. (Février 1982) Vortex-Flow Regimes J.Fluid Mech.vol.115 p 105-121.

[22] VALENSI J. (1938) Application de la méthode des filets de fumée à l'étude des champs aérodynamiques P.S.T Min.Air n° 178.

[23] CHARTIER Ch. (1942) - Etude expérimentale du sillage des ailes. Publ. S.T. Min.Air n° 226.

[24] SCHMITT V. et MANIE F. (1979) - Ecoulements subsoniques et transsoniques sur une aile à flèche variable Rech. Aerosp.1979-4

[25] MIRANDE J., SCHMITT V. et WERLÉ H. (1978) - Système tourbillonnaire présent à l'extrados d'une aile en flèche à grande incidence AGARD CP n° 247 mémoire n° 12.

[26] REHBACH C. (1977) - Calcul numérique d'écoulements tridimensionnels instationnaires avec nappes tourbillonnaires. Rech. Aerosp. 1977-5.

[27] ERICKSON G.E. (July 1979) - Water tunnel Flow Visualization : insight into complex three dimensional Flow-Fields AIAA paper n° 79-1530.

[28] ERICKSON G.E. (May 1982) - Water Tunnel Flow Visualization and Wind tunnel data Analysis of the F/A-18 NASA 16617.

[29] ROY M. (1952) Caractères de l'écoulement autour d'une aile en flèche accentuée CR Ac. Sc. t 234 p.2501-2503. et LEGENDRE R. (1952) Ecoulement au voisinage de la pointe avant d'une aile à forte flèche aux incidences moyennes Rech.Aeron.n° 30-31.

Fig. 13 – Décollements tourbillonnaires aux grandes incidences TH2 – $Re_L \cong 10^5$
(visualisation à l'aide de colorants).

– ogive cylindre lisse ($\alpha = 50°$) à nez pointu (a) ou arrondi (a').
– aile delta mince ($\varphi = 75°$) placée à $\alpha = 40°$ (b) ou 30° (b').
– ellipsoïde de révolution aplati à $\alpha = 25°$ (c).
– ellipsoïde de révolution allongé à $\alpha = 30°$ (e).
– ellipsoïde de forme intermédiaire à $\alpha = 30°$ (d).

[30] WERLÉ H. (1961) Etude physique des phénomènes tourbillonnaires au tunnel hydrodynamique ATMA (session 1961) n° 1311 .

[31] WERLÉ H. (1971) Sur l'éclatement des tourbillons ONERA NOTE TECHNIQUE 175.

[32] LAMBOURNE N.C. and BRYER D.W (1961) British A.R.C.R. and M. n° 3281

[33] ROLLS St., KOENIG D. and DRINKWATER III Fr. (1965) Flight investigation of the aerodynamic properties of an ogee wing. NASA T.N.D. 3071.

[34] BIPPES H.V (1980) Visualization of flow separation and separated flows with the aid of hydrogen bubbles Intern. Symp.BOCHUM

[35] WERLÉ H. (1979) Tourbillons de corps fuselés aux incidences élevées. L'Aeron. et l'Astron.1979-6 p.3-22

[36] WERLÉ H. (1962) Le décollement sous les corps de révolution à basse vitesse. Rech. Aéron. n° 90.

[37] PEAKE D.J. and TOBAK M. (1980) Three-dimensional Interactions and vortical flows with emphasis on hight speeds AGARD AG 252.

[38] LEGENDRE R. (1965) Lignes de courant d'un écoulement continu Rech.Aerosp. n° 105. p.3-9.

[39] PEAKE D.J. and TOBAK M. (March 1982) Three dimensional separation and reattachment AGARD VKI Lecture Series n° 121.

[40] WANG K.C. { (janv.1983) On the disputes about open Separation AIAA-83-0296 ; (July 1982) New Developments about open Separation San Diego State Univ.AE & EM.TR 82-02

[41] KREPLIN H.P. , VOLLMERS H., MEIER H.U. (1982) Measurements of the wall shear stress on an inclined prolate spheroïd Z.F.W.6 Heft.4 p.248-252.

[42] CHOMETON F. et FONTANET P.(1979) Ecoulements tridimensionnels décollés autour de véhicules terrestres 16ème Colloque d'Aérody.Appl.

[43] THWAITES B. (1960) Ed. Incompressible Aerodynamics.Oxford Univ.Press.

[44] WERLÉ H.(1980) Transition et décollement : visualisations au tunnel hydrodynamique de l'ONERA Rech. Aérosp.1980-5 p.331-345.

[45] WERLÉ H.(1971) Visualisation hydrodynamique d'écoulements instationnaires ONERA Note Technique n° 180.

LASER VELOCIMETRY STUDY OF COMPRESSIBILITY EFFECTS ON THE FLOW FIELD OF A DELTA WING

by

G. Vorropoulos and J.F. Wendt
von Karman Institute for Fluid Dynamics
Chaussée de Waterloo, 72
B - 1640 Rhode Saint Genèse, Belgium

SUMMARY

Compressibility effects on the lee-side vortical flow field of a delta wing at incidence were studied using laser doppler velocimetry. The tests covered the Mach number range from 0.18 to 0.80; both axial and circumferential velocity components were measured. It was found that the axial velocity excess observed at low Mach numbers became an axial velocity deficit at Mach numbers above 0.6. Strong asymmetry was observed in the circumferential velocity distribution at the higher Mach numbers. A flow picture including an embedded shock wave is proposed as physical explanation of the observed compressibility effects.

LIST OF SYMBOLS

AR	aspect ratio of delta wing
C_p	pressure coefficient
C_p^*	critical pressure coefficient
d_p	particle diameter
M_∞	free stream Mach number
M_n	free stream Mach number component normal to the wing leading edge
M_e	Mach number at the vortex outer edge (Ref. 20)
r	distance of seeding particle from vortex axis
Re	Reynolds number
Re_p	particle Reynolds number
S	model semispan
t	time
u	axial velocity of fluid
U_e	axial velocity at the vortex outer edge (Refs. 8,20)
$\bar{V}$	fluid velocity vecto
V_e	circumferential velocity at the vortex outer edge (Ref. 8,20)
V_∞	component of the free stream velocity parallel to the vortex axis
v, v_p	fluid and particle circumferential velocities respectively
w, w_p	fluid and particle radial velocities respectively
(x,y,z)	coordinate system used in our tests (Fig. 7)
(Y_a, Z_a)	location of vortex axis on the cross flow plane
Y_0	defined in text (page 5) and figure 7
α	wing incidence
α_n	leading edge incidence
$(\Delta x, \Delta y, \Delta z)$	probe volume dimensions
θ	defined in text
μ	viscosity coefficient
$\xi = \frac{r}{x}$	conical coordinates of a point inside a conical vortex
ξ_0	conical coordinate of a point at the conical vortex outer edge
ρ_p	particle density
τ_v	$d_p^2 \rho_p / 18\mu$
ω	fluid angular velocity

1. INTRODUCTION

The symmetric vortical flow over delta wings in the low speed regime has been extensively studied, both experimentally (e.g. Refs. 1,2,3,4) and theoretically (Refs. 5,6,7,8). Several investigators have studied modifications to the lee-side vortex flow arising when the Mach number increases. Stanbrook and Squire (Refs. 9,10,11) observed, in a test series on delta wings of aspect ratio 1.86 at incidence and in the Mach number range from 0.7

to 2.0, that as M_∞ increases the vortex sheet is flattened and the vortex axis approaches the wing surface. They observed a conical shock above the vortex sheet for $M_\infty > 1.75$. Following these observations, Stanbrook and Squire proposed to classify the flow field above a delta wing into three regions, depending on the leading edge incidence, α_n, and the Mach number, M_n, normal to the leading edge. These flow regions are shown in figure 1; they are characterized as follows :

Region A : For subsonic and transonic M_n, the flow still exhibits the characteristics of a leading edge separation. For supersonic free stream Mach numbers, a detached shock exists upstream of the wing leading edges.

Region B : The detached shock approaches the wing leading edges and supersonic expansions occur which are terminated by inboard shock waves. The shocks may cause separation of the upper surface boundary layer and possibly separation vortices.

Region C : This type of flow is similar to that of region B, with the exception that the bow shock is now attached to the leading edges.

Transition from the separated flow of region A to the attached flow of region B occurs smoothly. The flattening of the vortex sheet, and the existence of a conical shock above it, are associated with this transition process. Gaudet and Winter (Ref. 12) and Monnerie and Werlé (Ref. 13) scanned the lee-side vortex with a five hole conical head probe and a pitot probe, respectively, for the case of supersonic free stream Mach numbers and values of α_n and M_n corresponding to region A, figure 1. They expressed doubts about the validity of their results due to interference of the probe with the vortex. Nevertheless, Gaudet and Winter (Ref. 12) tentatively concluded that the local Mach number decreased towards the vortex axis. Monnerie and Werlé (Ref. 13) detected a centerline shock, when the wing incidence was so large that the outer surfaces of the vortices were very close to each other, forming effectively a supersonic nozzle. Stahl et al. (Ref. 14) observed that, as the Mach number increased, for constant wing incidence and Reynolds number, the spanwise suction was reduced (Fig. 2). The pressure distributions became flatter at M_∞ exceeding 0.8 and showed some signs of secondary separations.

The compressible leading edge vortex has been studied theoretically by Brown (Ref. 20); the assumptions imposed were :

- The vortex core is geometrically slender.
- The flow field is inviscid, rotational, homoentropic, conical, steady and axially symmetric.

The continuity, momentum and energy equations are reduced to a system of ordinary differential equations, which can be solved under the following boundary conditions :

- The radial velocity is zero on the axis.
- The axial and circumferential velocity components as well as the density are prescribed at the outer edge of the vortex.

Thus, the problem is identical to that solved by Hall (Ref. 8) for incompressible flow.

Brown found that as the Mach number increases, the ratio of the axial velocity at the core to the U_e velocity decreases (Fig. 3). It was also found that the compressibility drastically changes the behaviour of the circumferential velocity. At $M_e = 0$ the circumferential velocity increases towards the vortex axis, whereas for the cases $M_e = 0.95$ and 1.6 this velocity component decreases towards the axis (Fig. 3). No experimental validation of Brown's model has been reported to date.

The objective of the present research was to investigate compressibility effects on delta wing vortices for subsonic free stream Mach numbers. To avoid the effects of an intrusive measurement technique, laser doppler velocimetry (LDV) was selected. Emphasis was placed on the behaviour of the axial velocity component, since measurements and theory at low speed (eg. Refs. 1,7) have shown that, depending on the wing aspect ratio and incidence, the axial velocity could attain values two or three times larger than the free stream velocity. Measurements of the tangential component were also accomplished in this study, to aid in the development of the understanding of the flow field structure.

2. EXPERIMENTAL SET-UP

The experiments were carried out in the VKI S-1 continuous transonic wind tunnel, which was equipped with a slotted-wall test section. The model was a flat plate, sharp-edged delta wing of aspect ratio two with a chord length of 150 mm (Fig. 4). It was fixed by a strut support to a continuous incidence mechanism.

The LDV system (Fig. 5) consisted of :

Transmitting optics : A Spectra-Physics Argon-Ion laser (mod 164A) produced a beam of 1.8 Watt maximum power at $\lambda = 5145\text{Å}$. The beam was divided by an OEI beam splitter into two beams, the intensity of which was equalized by means of a Spectra-Physics polarizer. An OEI beam spacer was used to reduce the beam separation distance to 1.. mm. A 350 mm focal length lens provided a fringe spacing, d_f, of 11.8 μm. For the measurements of the circumferential velocity, OEI Bragg cells were included in the transmitting optics.

Receiving optics : The light scattered by particles crossing the probe volume was collected by a TEMRON zoom lens and was sent to an RCA 4526 photomultiplier tube powered by a TSI 9165 power supply. A 200 μm pinhole was placed between the zoom lens and the photomultiplier to reduce the optical noise. The receiving optical unit was oriented at a 15° off-axis angle (with respect to the transmitting optics axis) to reduce the probe volume length as seen

by the photomultiplier. Thus the effective probe volume dimensions which define the spatial resolution of the velocimeter were $\Delta x = \Delta y = 0.2$ mm and $\Delta z = 2$ mm (Fig. 5). The number of fringes observed was 20.

Processing electronics : The signal of the output of the photomultiplier was processed by a TSI 1990A counter. The counter output was connected to a PDP 11/34 mini computer via the VKI data acquisition system for storage and further processing of the velocity data. For these tests the LDV set-up was operated in the forward scatter mode for maximum scattered light intensity. Therefore, the transmitting and receiving optics were placed on either side of the tunnel, Schlieren windows providing optical access to the test section. The LDV system was supported on a programmable table which could move along three mutually perpendicular axes with a preselected step size.

Seeding : A Norgren microfog lubricator provided a mist of fine oil droplets; their size distribution was measured with an OEI Parco isokinetic sampling probe; the result is shown in figure 6. The mean droplet diameter was found to be 0.45 µm ± 0.05 µm. Seeding was introduced through a perforated tube 2 m upstream of the test section (in the tunnel reservoir).

3. TEST PROGRAM

A fixed model incidence of 10° corresponding to a blockage ratio of 1.2% was chosen to ensure that the flow field was stable and that the vortex rotational velocity was not excessively large considering the expected behaviour of the seed particles (see section 4).

The measured velocity components (see Fig. 7) were :

(1) The component parallel to the vortex axis, which will be referred to as the axial velocity, u.

(2) The component normal to the plane defined by the two vortex axes and which will be referred to as the circumferential velocity, v.

Separate tests, with the appropriate fringe orientation for each, were required for the measurement of these two components. Due to flow symmetry, velocity measurements were carried out only in one vortex. The support table was moved in such a way that the probe volume traversed horizontally the vortex center along a direction normal to the vortex axis. These traverses were carried out at several chordwise stations ranging from 30% to 80% of the chord length.

The vortex axis location was determined as follows : at a given chordwise station the cross flow plane was scanned with the LDV. The vortex axis was defined as the region of minimum LDV data rate and minimum LDV signal-to-noise ratio. This location corresponded to the maximum or minimum (depending on M_∞) of the axial velocity, as will be seen later, and to the sign reversal of the circumferential velocity. In addition, the spanwise location of the vortex axis was identical to that of the suction maximum as determined by the pressure distribution measurements of Muylaert (Ref. 19) using the same wing. The position of the vortex axis was determined with an accuracy of 0.7% of the trailing edge semispan (i.e., ± 0.5 mm) in the vertical direction and of 1.3% of the trailing edge semispan (i.e., ± 1 mm) in the horizontal direction. Table 1 summarizes the test conditions. The Reynolds number was 3.4×10^5 and was kept constant within 5% throughout the tests

M_∞	Measured component	Chordwise stations
0.18	axial	30%,40%,50%,60%,70%,80%
0.80	axial	30%,40%,50%,60%,70%,80%
0.42	axial	50%
0.60	axial	50%
0.71	axial	50%
0.18	circumferential	50%
0.80	circumferential	50%

TABLE 1

4. PARTICLE BEHAVIOUR

A laser velocimeter measures the velocity of particles entrained in the fluid. The measured quantity coincides with the fluid velocity only if the seeding particles accurately follow the flow. The particles may be said to follow the flow if they have the same velocity as the fluid within a prescribed tolerance. In a high speed vortex, however, large centrifugal forces act on the particle which, if their mass is large enough, would tend to move outward in the radial direction and thus would acquire velocities different than those of the vortex. The problem was therefore to determine whether or not the 0.45 µm mean diameter oil droplets produced by the Norgren microfog lubricator seeding system would follow the strong vortical flow under investigation. Maximum particle lag would be expected in the region of the vortex subcore, which rotates as a solid body. From a preliminary test series on the same wing (Refs. 15,16) it was found that the angular velocity of the flow in the vortex subcore was approximately 30.000 rad/s at $M_\infty = 0.8$.

A theoretical study was undertaken to predict particle motion in two and three dimensional vortices. Considering a forced vortex rotating with an angular velocity ω and assuming Stokes drag (i.e., $Re_p < 1$) and spherical particles, the equations of motion are:

$$\frac{dw_p}{dt} - \frac{v_p^2}{r} = \frac{1}{\tau_v}(w-w_p) \tag{1}$$

$$\frac{dv_p}{dt} + \frac{w_p v_p}{r} = \frac{1}{\tau_v}(v-v_p) \tag{2}$$

where w and v are the fluid radial and circumferential velocities and w_p and v_p the particle radial and circumferential velocities (for a forced vortex w = 0 and $v = \omega r$, where ω is the angular velocity and r the distance of the fluid particle with velocity v from the vortex axis). The parameter τ_v is such that its product with ω gives the ratio of the centrifugal force acting on the particle to the Stokes drag force; i.e. :

$$\omega\tau_v = \frac{\pi(d_p^3/6)\rho_p\omega^2 r}{3\pi d_p \mu \omega r} \tag{3}$$

where d_p is the particle diameter, ρ_p its density, r the radial distance of the particle from the vortex axis and μ the viscosity coefficient.

Equations (1) and (2) were numerically solved, using as initial conditions the particle position at t = 0 and the assumption that particles initially follow the flow. Typical results are shown in figure 8 for the case of ω = 30000 rad/s. It can be seen that the particle radial velocity increases rapidly with increasing particle diameter whereas the particle circumferential velocity remains constant and is less than 1% inferior to that of the fluid for particle diameters less than 1 μm. Above that value, the particle circumferential velocity decreases.

These calculations were extended to a three dimensional vortex using Hall's model (Ref. 8). The analytical solution of Hall was obtained under the assumptions of a conical slender vortex; of an inviscid, rotational, steady, axisymmetric and incompressible flow field; of known axial and circumferential velocities as well as static pressure on the outer edge of the vortex and of zero radial velocity on the axis. It is important to note that the particle motion in a direction parallel to the vortex axis is not influenced by the centrifugal force field. This is due to the fact that the equation for a particle motion parallel to the vortex axis is uncoupled from the equations of motion in a vortex cross flow plane (containing the centrifugal force term), if $Re_p < 1$ (i.e., if Stokes drag law is applicable)(Ref. 17). This has been confirmed by solving numerically the motion equation of a particle in a vortex described by Hall's model. The parameters of Hall's model were given values such that the rotational speed close to the axis of this vortex roughly corresponded to that observed in our preliminary tests (Ref. 15). Figure 9 shows the velocity distributions of the hypothetical vortex used in these computations. In figure 10, based on these velocity distributions, the variation of the quantities v_p/v, u_p/u and $w_p/|\bar{V}|$ versus the angle θ is shown (θ is the angular distance from the projection of the particle positions at a time t onto a plane normal to the vortex axis to the projection onto the same plane of its initial position (at t=0)) and u and u_p are the axial velocities of the fluid and particle respectively and $|\bar{V}|$ is the total fluid velocity. It was assumed in these calculations that the particle was released at a position corresponding to the outer edge of the vortex subcore, with initial velocity components equal to those of the local fluid velocity. It can be seen that for a particle whose diameter d_p is 0.50 μm (i.e., close to the mean particle diameter in our tests) the ratio $w_p/|\bar{V}|$ attains rapidly a maximum value of 3% close to the axis and then decreases continuously. It can also be seen that this particle has circumferential and axial velocity components only slightly different (less than 0.5%) from those of the fluid. For d_p = 1.0 μm, the maximum value of $w_p/|\bar{V}|$ is 14% and the particle follows the axial and circumferential velocity components within 1% after one revolution. The particle Reynolds number was always less than unity for particle diameters less than 1 μm.

Our results closely corresponded to the theoretical and experimental results of Mazumder (Ref. 18), who found that the latex particles of diameter of 0.5 μm followed within 0.5% an oscillating, one dimensional flow, of frequency 32.2 kHz. Thus we conclude that the velocity of the oil droplets embedded in the rapidly rotating flow of this experiment could be equated to the fluid velocity.

5. RESULTS AND DISCUSSIONS

In figure 11 the spanwise distribution of the axial velocity on a traverse through the vortex core at the 50% chord is shown for M_∞ equal to 0.18 and 0.80. The accuracy in the measured velocities was estimated at ± 1% away from the vortex axis and ± 3% close to the vortex axis. For the case of M_∞ = 0.18, the axial velocity distribution is similar to that observed by other investigators of the low speed, delta wing flow field (e.g., Refs. 1,2). Inboard of the leading edge the axial velocity, u, increases reaching a maximum value of approximately 1.3 V_∞ where V_∞ is the free stream velocity component parallel to the vortex axis. This maximum value is found at approximately 60% of the local semispan which corresponds to the location of minimum data rate and signal-to-noise ratio.

Inboard of this location, u decreases and finally attains a value close to V_∞ near the wing centerline. A slight vortex asymmetry is observed, which has been previously noticed (Ref. 2).

At $M_\infty = 0.80$, a dramatic change in the axial velocity distribution is observed. Instead of an "excess" in u ($u > V_\infty$) as observed at $M_\infty = 0.18$, a "deficit" in u($u < V_\infty$) now characterizes the core region of the velocity distribution. The axial velocity decreases inboard of the leading edge and reaches a minimum, again at 60% of the local semispan. The minimum value of u occurs at the same location (i.e., on the vortex axis) as the maximum in u for the case of $M_\infty = 0.18$. Further inboard of the vortex subcore, at $M_\infty = 0.80$, the axial velocity abruptly increases to a value of 1.1 V_∞ and then slowly decreases towards the centerline. Thus it can be said that at $M_\infty = 0.80$, the vortex exhibits a rather unexpected behaviour, i.e., an axial velocity deficit and a pronounced asymmetry in u about its axis.

To examine the transition in the spanwise axial velocity distribution from $M_\infty = 0.18$ to $M_\infty = 0.80$, similar spanwise axial velocity measurements were performed at the 50% chordwise station for Mach numbers of 0.42, 0.60 and 0.71. Results are shown in figures 12, 13 and 14. At $M_\infty = 0.42$ the excess in axial velocity is similar to that observed at $M_\infty = 0.18$. The maximum value in u is slightly less than that at $M_\infty = 0.18$, but this may be due to the small number of data points in the region of the vortex core. At $M_\infty = 0.60$ and 0.71, a deficit in axial velocity and an asymmetric distribution with an abrupt increase in u inboard of the vortex subcore characterize the vortex. Thus, a transition from an axial velocity excess to a deficit occurs between $M_\infty = 0.42$ and $M_\infty = 0.60$.

In table 2 we present the location of the vortex axis as a function of Mach number for the 50% chordwise station.

M_∞	Z_a/Y_0	Y_a/Y_0
0.18	.13 ± 0.01	.63 ± 0.05
0.42	.10 ± 0.01	.63 ± 0.05
0.60	.10 ± 0.01	.63 ± 0.05
0.71	.10 ± 0.01	.63 ± 0.05
0.80	.10 ± 0.01	.63 ± 0.05

TABLE 2

Z_a and Y_a are the coordinates of the vortex axis and Y_0 is the length AB of figure 7. It can be seen that the spanwise location of the vortex remained constant (within the measurement accuracy) for the Mach number range of the tests. On the other hand for $M_\infty > 0.42$ the vortex axis moved towards the wing surface.

Further tests were performed at $M_\infty = 0.18$ and 0.80 to examine the conicity of the vortex. To that end, axial velocity measurements were carried out across the vortex axis for chordwise stations of 30%, 40%, 60%, 70% and 80% of the chord length. The results are plotted in figures 15 and 16. Inspection of these figures reveals that :

- The deficit in axial velocity, u, is present at all spanwise profiles for $M_\infty = 0.80$, in contrast to an excess for $M_\infty = 0.18$.

- The departure from conicity is characterized by a reduction in u maxima (for the case $M_\infty = 0.18$) for chordwise stations downstream of the 50% station. For the case of $M_\infty = 0.80$, the axial velocity gradients along the spanwise direction are decreased downstream of mid chord and there is a tendency for the axial velocity distribution to become more symmetric. This departure from conicity is due to the presence of the trailing edge downstream of which the vortex tends to become parallel to the free stream.

In figures 17 and 18 are plotted the equal axial velocity lines as measured during several traverses of the cross flow plane at the 50% chordwise station and for $M_\infty = 0.18$ and 0.80. Both figures show characteristics of the vortex structure. It is again noted that although compressibility did not affect the spanwise location of the vortex axis, its vertical distance from the wing surface decreases with increasing Mach number. A region is observed in figure 18 with large spanwise axial velocity gradients just inboard of the vortex axis.

The investigation was extended to the measurement of the spanwise distribution of the circumferential velocity component. Only two tests were performed at $M_\infty = 0.18$ and 0.80 at the 50% chordwise station. The results are shown in figure 19. Inspection of figure 19 shows that at $M_\infty = 0.18$ the circumferential velocity component, v, increases inboard of the leading edge up to a point where a sudden drop and then a recovery occur characteristic of the existence of a vortex sheet. Further inboard, v increases towards the vortex axis, where a change in its sign occurs. The location of this sign change is the same as that of the maximum in the axial velocity discussed earlier. The maximum value of v was approximately 0.6 V_∞. The spanwise behaviour of the circumferential velocity, v, at $M_\infty = 0.80$ is shown in figure 19. Again, as at low speed, v increases inboard of the leading edge and then decreases suddenly, again showing the presence of a vortex sheet. Following this drop, there is a recovery in v, which,

however, attains smaller values (0.2 V_∞ approximately) than in the low Mach number case. The circumferential velocity, v, slightly increases near the vortex axis, where a sign reversal is noted. Inboard of the axis v reaches again 60% of V_∞ and then decreases towards the wing centerline.

Our results are not in agreement with Brown's theoretical prediction of the compressible vortex flow (Ref. 20) which was discussed in section 1. An excess in axial velocity is always predicted by this model in contrast to what was found as a result of the present investigation.

The observed compressibility effects on the leading edge vortex velocity field leads us to present the following hypothesis on the flow field structure : At a sufficiently high value of M_∞ (for an AR = 2 wing, between M_∞ = 0.42 and M_∞ = 0.60), local supersonic flow regions develop in the lee side vortical flow. These supersonic flow regions are more likely to occur inboard of the vortex axis, where the flow is accelerated towards the wing surface. Their existence is established by the pressure measurements of Muylaert (Ref. 19) on the same wing, an example of which is shown in figure 20 for M_∞ = 0.79. The value of the critical pressure coefficient, C_p^*, (i.e., the value of C_p for a local Mach number of 1) at this value of M_∞, is -0.43. It is exceeded (in absolute value) in a region around the suction maximum, covering 30% to 40% of the local semispan for all chordwise stations. It should also be noted that for M_∞ = 0.60, C_p^* = -1.29 which is very close to Muylaert's (Ref. 21) measured value of C_p at the suction maximum (-1.20 upstream of the 50% chordwise station). The supersonic flow, having to pass through a "throat" formed by the vortex sheet and the wing surface (Fig. 19) is compressed and a conical shock wave is formed beneath the vortex as sketched in figure 21. The existence of this shock cannot be directly shown from the surface pressure measurements, since the spanwise pressure distribution is a result of both the vortical flow and the shock. However, the observed compressibility effects in the vortex structure (i.e., deficit in axial velocity and asymmetry in both the axial and the tangential velocities) can be considered as consequences of this shock wave. It can be argued that the low circumferential velocities, v, observed outboard of the vortex axis are due to the presence of this shock wave which produces an abrupt reduction in the velocity component normal to the shock as shown in figure 21, where this component becomes, after a 90° turn, the measured circumferential velocity, v. Due to the strong coupling between velocity components and pressure gradients in the Navier-Stokes equations describing the vortex, there is a marked change in the vortex structure, which results in the axial velocity deficit and the presence of strong spanwise axial velocity gradients. The exact cause of this change cannot be fully understood without a further theoretical investigation of the compressible vortex. Our conclusion of an embedded shock wave could also explain the flattening of the pressure distributions with increasing M_∞ measured by Stahl et al., (Ref. 14) as well as by Muylaert (Ref. 19). The shock interacts with the upper surface boundary layer, causing a secondary separation. Furthermore, the observed decrease in circumferential component at M_∞ = 0.80 results in a loss in vortex circulation and consequently (Ref. 6) the vortex is closer to the wing surface than at low speed, in agreement with our observations of vortex axis position. It should be recalled that the approach of the vortex axis to the wing surface for increasing M_∞ has been observed also by Stanbrook and Squire (Ref. 9). If the distance of the vortex axis from the wing surface decreases with increasing M_∞, but its spanwise location is constant, then obviously the vortex sheet will appear to flatten with increasing M_∞. We can therefore propose the following modification of the Stanbrook-Squire diagram, shown in figure 22 : Inside their region A, there exists a flow sub-region A_1 which is characterized by the existence of an embedded conical shock wave beneath the vortex. In this region, the vortex flow is modified by the shock which represents the first effect of compressibility on the delta wing lee side flow. In other words sub-region A_1 is the intermediate step for the transition of the separated flow of region A to the attached flow of region B.

6. CONCLUSIONS

An experimental investigation of the lee-side vortical flow about a delta wing at incidence for Mach numbers up to 0.80, has been carried out using laser doppler velocimetry. It was found that the axial velocity excess, observed at low speed becomes a deficit for $M_\infty > 0.60$. Furthermore, asymmetries were found in the distributions of both the axial and the circumferential velocity for M_∞ = 0.80. These results suggest the appearance of a conical shock wave below the primary vortex as being the main flow feature responsible for the observed compressibility effects.

REFERENCES

1. MARSDEN, D.J.; SIMPSON, R.W.; RAINBIRD, W.J.: The flow over delta wings at low speed with leading edge separations. Cranfield College of Aeronautics, Rep CoA 114, 1957.

2. EARNSHAW, P.B.: An experimental investigation of the structure of the leading edge vortex. ARC R&M 3281, 1962.

3. HUMMEL, D.: On the vortex formation over a slender wing at large angles of incidence. in High Angle-of-Attack Aerodynamics, AGARD CP 247, 1978.

4. POISSON-QUINTON, Ph. & WERLE, H.: Water tunnel visualization of vortex flow. Astronautics and Aeronautics, Vol. 5, No. 6, June 1967, pp 64-67.

5. LEGENDRE, R.: Ecoulement au voisinage de la pointe avant d'une aile a forte flèche aux incidences moyennes. ONERA Recherche Aerospatiale, N° 30, 1952.

6. BROWN, C. & MICHAEL, E.: Effect of leading edge separation on the lift of delta wings. J. Aeronautical Sciences, Vol. 21, No. 10, October 1954, pp 690-694.

7. MANGLER, K. & SMITH, J.H.B.: A theory on the flow past a slender delta wing with leading edge separation. Proc. Roy. Soc., Vol. A251, 1959.

8. HALL, M.G.: A theory for the core of a leading edge vortex. J. Fluid Mechanics, Vol. 11, 1961, pp 209-228.

9. STANBROOK, A. & SQUIRE, L.C.: Possible types of flow at swept leading edges. Aeronautical Quart., Vol. 15, Part 1, 1964, p 72.

10. SQUIRE, L.C.; JONES, J.G.; STANBROOK, A.: An experimental investigation of the characteristics of some plane and cambered 65° delta wings at Mach numbers from 0.7 to 2.0. ARC R&M 3305, 1961.

11. SQUIRE, L.C.: Flow regimes over delta wings at supersonic and hypersonic speeds. Aeronautical Quart., Vol. 27, Part 1, 1976, p. 1.

12. GAUDET, L. & WINTER, K.G.: Preliminary measurements of the flow field on the lee side of a delta wing of unit aspect ratio at a Mach number of 2.6 and an incidence of 15°. RAE TN Aero 2787, 1961.

13. MONNERIE, B. & WERLE, H.: Etude de l'écoulement supersonique et hypersonique, autour d'une aile élancée en incidence. in: Hypersonic Boundary Layers and Flow Fields, AGARD CP 30, 1968.

14. STAHL, W.; HARTMANN, K.; SCHNEIDER, W.: Force and pressure measurements on a slender delta wing at transonic speeds and varying Reynolds numbers. in: Facilities and Techniques for Aerodynamic Testing at Transonic Speeds and High Reynolds Number, AGARD CP 83, 1971.

15. VORROPOULOS, G. & WENDT, J.F.: Preliminary results of LDV surveys in the compressible leading edge vortex of a delta wing. VKI TN 137, 1982.

16. WENDT, J.F.: Compressibility effects on flows around simple components. in: High Angle-of-Attack Aerodynamics, AGARD LS 121, 1982.

17. RUDINGER, G.: Fundamentals of gas particle flow. in: Gas Solid Suspensions. VKI LS 90, 1976.

18. MAZUMDER, N.K. & KIRSCH, .: Flow tracing fidelity of scattering aerosol in LDV. J. Applied Optics, Vol. 14, No. 4, April 1971.

19. MUYLAERT, J.: Vortex bursting on slender delta wings in transonic flow and its influence on missile aerodynamic characteristics. DGLR Vortrag Nr. 81-047 Jahrestagung der DGLR, Aachen 1981. Also VKI PR 1980-21.

20. BROWN, S.N.: The compressible inviscid leading edge vortex. J. Fluid Mechanics, Vol. 22, Part 1, 1965, pp 17-32.

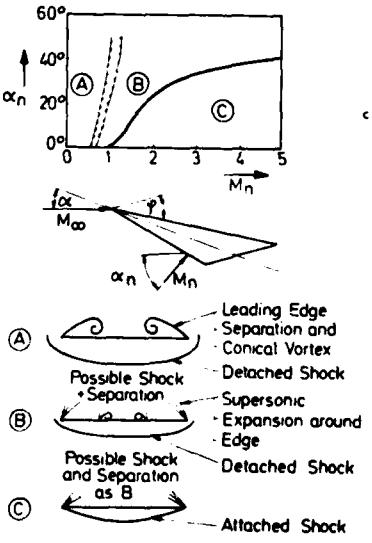

Fig. 1 - Flow regimes about a delta wing at high speed, following Stanbrook and Squire (Ref. 9)

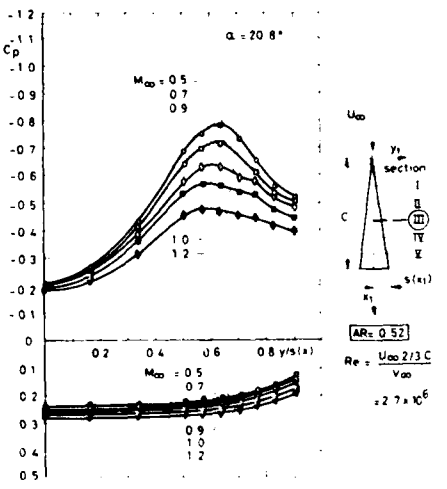

Fig. 2 - Spanwise suction distribution on delta wing at constant incidence and Reynolds number for varying Mach numbers (Ref. 14)

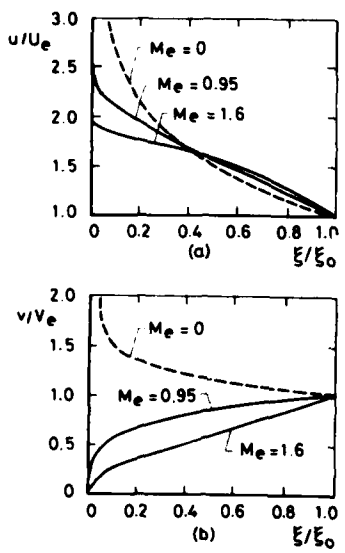

Fig. 3 - Axial (u) and tangential (v) velocity distributions in a compressible vortex for various Mach numbers according to Brown (Ref. 20)

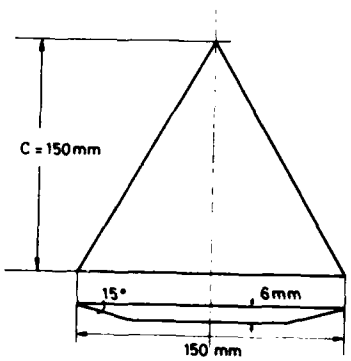

Fig. 4 - Delta wing model used in the present tests

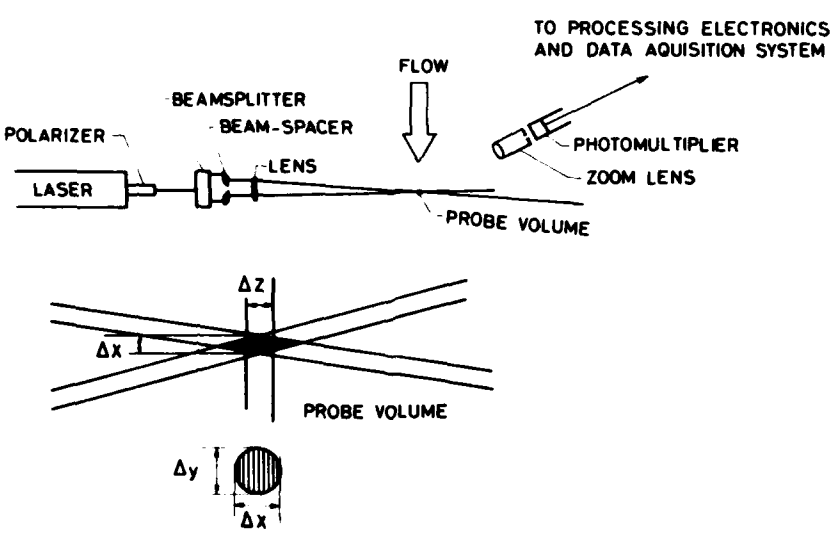

Fig. 5 - Schematic of LDV system used during this study

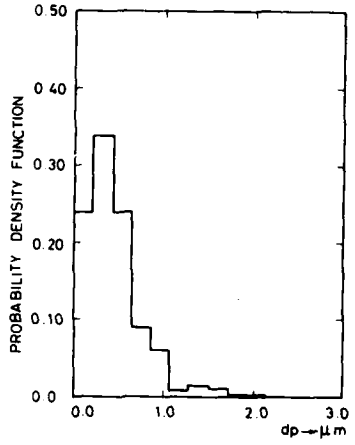

Fig. 6 - Measured diameter distribution for the seeding oil particles

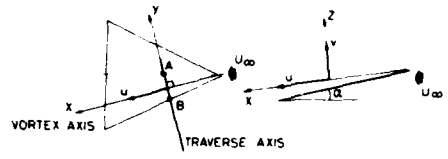

Fig. 7 - Coordinates system associated to the vortex and measured velocity components u and v (AB = Y_2)

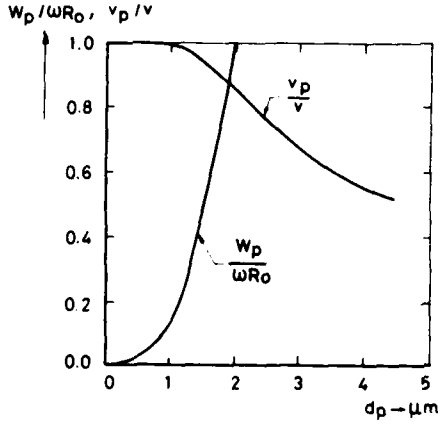

Fig. 8 - Dependence of the particle radial (w_p) and tangential (v_p) velocity on the particle diameter ($\rho_p=10^3$ kg/m^3) for the case of a forced vortex (ω=30000 rad/s)

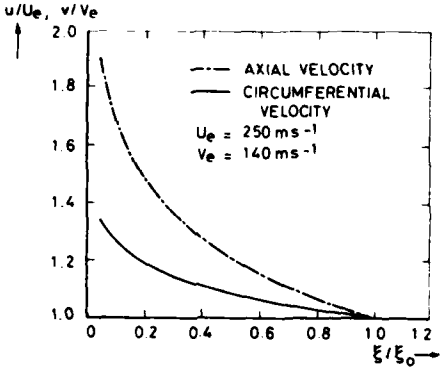

Fig. 9 - Axial and tangential velocity distributions in the Hall's vortex used as test case for the study of three dimensional particle behaviour

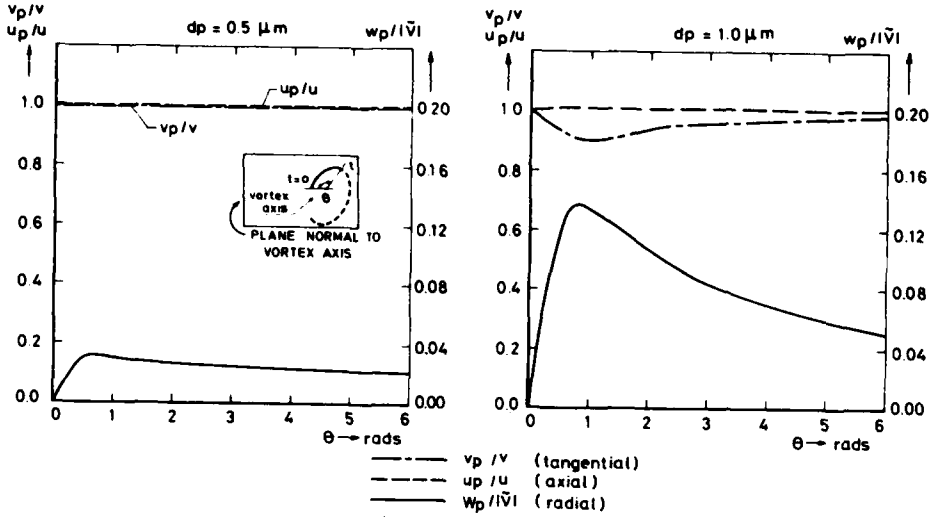

Fig. 10 - Variation of v_p/v, u_p/u and $w_p/|\bar{V}|$ with θ for a particle released in a Hall's vortex ($\rho_p=10^3$ kg/m^3)

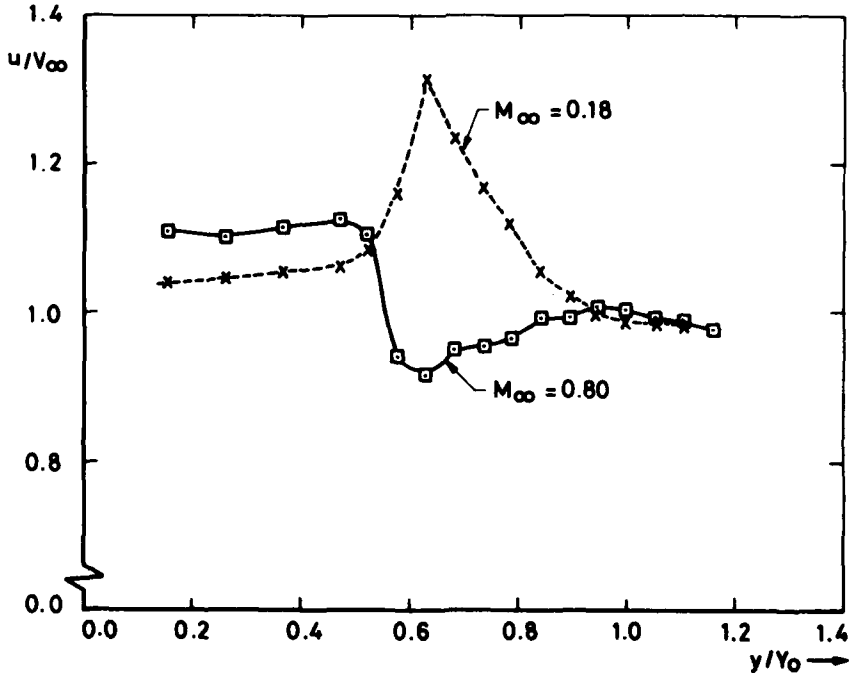

Fig. 11 - Axial velocity distributions for M_∞ = 0.18 and 0.80 at the 50% chordwise station

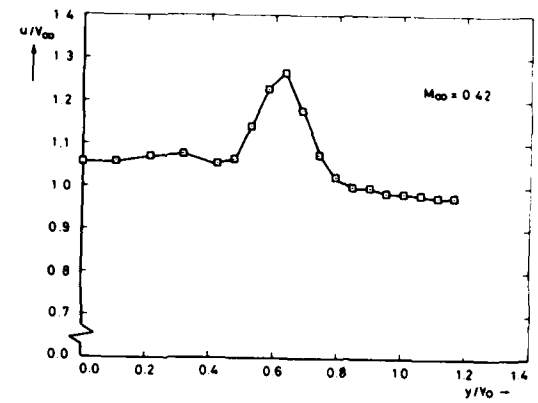

Fig. 12 - Axial velocity distribution for M_∞ = 0.42 at the 50% chordwise station

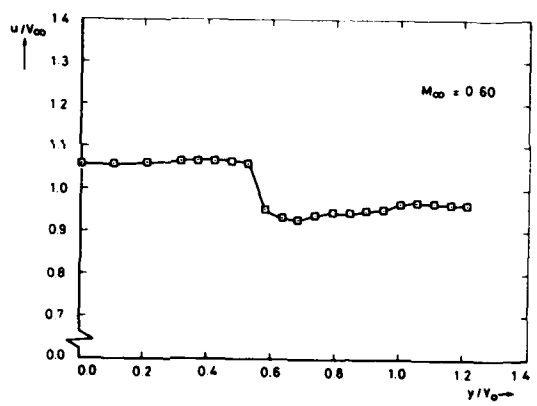

Fig. 13 - Axial velocity distribution for M_∞ = 0.60 at the 50% chordwise station

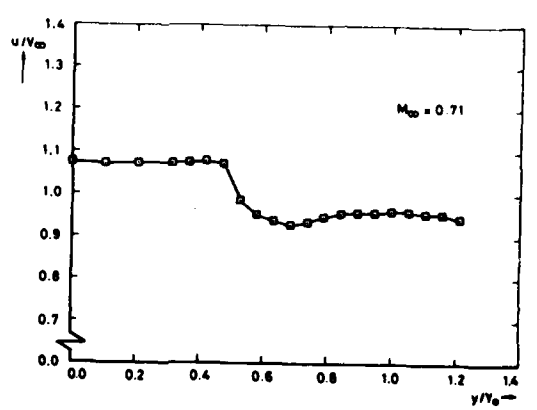

Fig. 14 - Axial velocity distribution for M_∞ = 0.71 at the 50% chordwise station

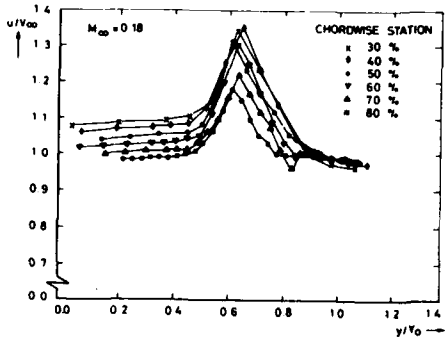

Fig. 15 - Axial velocity distributions for M_∞ = 0.18 at various chordwise stations

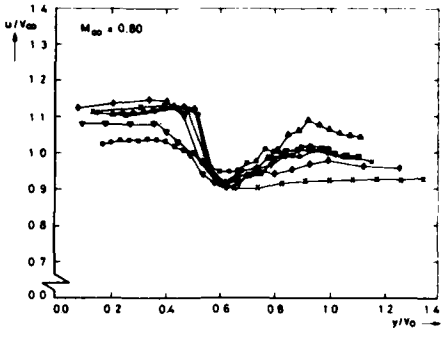

Fig. 16 - Axial velocity distribution for M = 0.80 at various chordwise stations (the same symbols as in Fig. 15 were used)

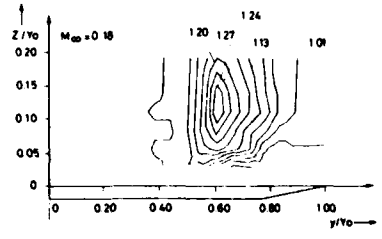

Fig. 17 - Lines of equal values of u/V_∞ for M_∞ = 0.18 at the 50% chordwise station (not to scale)

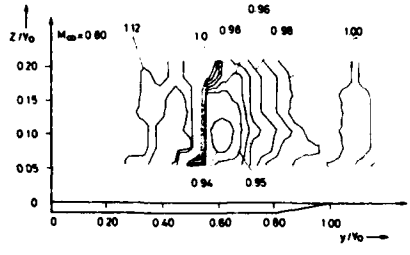

Fig. 18 - Lines of equal values of u/V_∞ for M_∞ = 0.80 at the 50% chordwise station (not to scale)

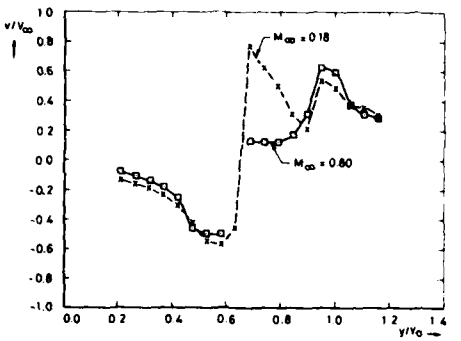

Fig. 19 - Tangential velocity distributions for M_∞ = 0.18 and 0.80 at the 50% chordwise station

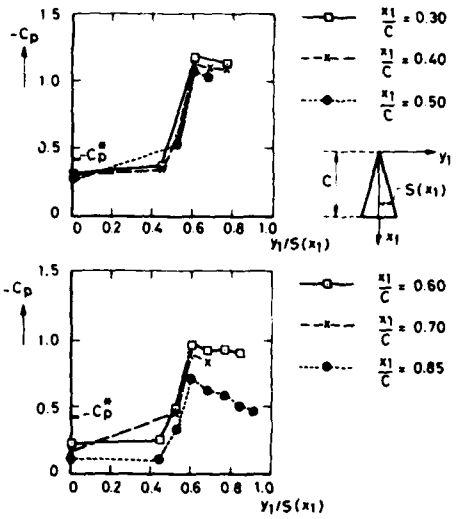

Fig. 20 - Spanwise pressure distributions on the upper side of the delta wing of this study at α = 10° and M_∞ = 0.79 at various chordwise stations (Ref. 19)

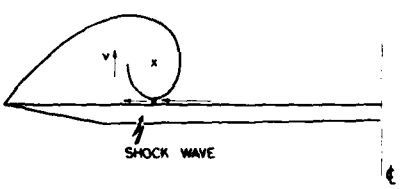

Fig. 21 - Assumed location of the conical shock wave

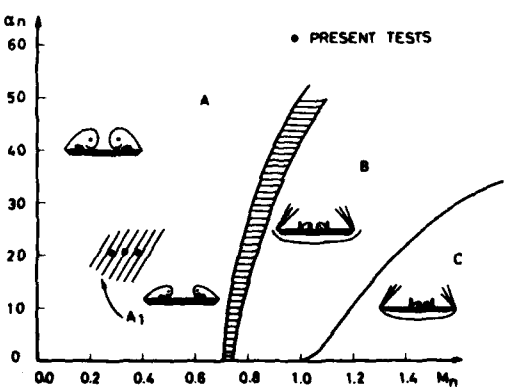

Fig. 22 - Proposed modification of the Stanbrook-Squire diagram

RECENT STUDIES AT NASA-LANGLEY OF VORTICAL FLOWS INTERACTING WITH NEIGHBORING SURFACES

John E. Lamar
Aeronautical Research Scientist

James F. Campbell
Assistant Head, NTF Aerodynamics Branch

NASA Langley Research Center
Mail Stop 294
Hampton, Virginia 23665

SUMMARY

Leading-edge vortical flows, which occur near and interact with neighboring surfaces, are of great interest in a variety of civil and military aircraft applications. This paper summarizes recent work in this area conducted or sponsored by NASA Langley Research Center since the 1978 AGARD Conference on "High Angle of Attack Aerodynamics." In particular, the cumulative results of a number of theoretical and experimental studies are discussed. These studies have been carried out so as to gain a better understanding of, and be better able to utilize, this kind of flow. Much of the effort has been spent in improving the lift-to-drag ratio and pitch characteristics for wings in this flow; however, some effort has also been expended to examine the unsteady and lateral characteristics. Though much research has been accomplished, much remains to be done in order for these vortical flows to be treated with the same degree of confidence in the design of an aerospace vehicle as is currently done with attached flows.

LIST OF SYMBOLS

A	aspect ratio
b	span
C_D	drag coefficient, $\frac{\text{drag}}{q_\infty S_{ref}}$
ΔC_D	drag-due-to-lift, $\frac{\text{drag-due-to-lift}}{q_\infty S_{ref}}$
C_L	lift coefficient, $\frac{\text{lift}}{q_\infty S_{ref}}$
C_{NL}	longitudinal load distribution coefficient
C_N	normal force coefficient, $\frac{\text{normal force}}{q_\infty S_{ref}}$
C_S	leading-edge suction force coefficient, $\frac{\text{leading-edge suction force}}{q_\infty S_{ref}}$, illustrated on figures 2 and 4 as operating only on one side
C_T	leading-edge thrust coefficient, $\frac{\text{leading-edge thrust}}{q_\infty S_{ref}}$, illustrated on figures 2 and 4 as operating only on one side
C_l	rolling moment coefficient, $\frac{\text{rolling moment}}{q_\infty S_{ref} b}$
C_{l_p}	damping-in-roll parameter, $\frac{\partial C_l}{\partial (pb/2V_\infty)}$, per radian
C_{l_β}	roll due to sideslip, $\frac{\partial C_l}{\partial \beta}$, per degree
C_m	pitching moment coefficient, $\frac{\text{pitching moment}}{q_\infty S_{ref} \bar{c}}$
ΔC_m	incremental pitching moment coefficient
C_n	yawing moment coefficient, $\frac{\text{yawing moment}}{q_\infty S_{ref} b}$
C_{n_β}	yaw due to sideslip, $\frac{\partial C_n}{\partial \beta}$, per degree
C_p	pressure coefficient, $\frac{p - p_\infty}{q_\infty}$

ΔC_p	lifting pressure coefficient, $\frac{p_\ell - p_u}{q_\infty}$
C_μ	inlet momentum coefficient, $\frac{\dot{m} V_I}{g\, q_\infty\, S_{ref}}$
c	streamwise chord
c_f	flap chord measured normal to wing leading edge
$\bar{c}$	reference chord, mean aerodynamic chord primarily used
$c_{\ell,v}$	section vortex lift coefficient, $\frac{\text{section vortex lift}}{q_\infty\, c}$
c_n	section normal force coefficient, $\frac{\text{section normal force}}{q_\infty c}$
c_R	section profile nose drag coefficient, $\frac{\text{profile nose drag}}{q_\infty c}$
c_s	section leading-edge suction force coefficient, $\frac{\text{section suction force}}{q_\infty\, c}$
c_t	section thrust coefficient, $\frac{\text{section thrust}}{q_\infty\, c}$
D	diameter of the pumped vortex suction apparatus
d	distance of flap hinge-line from wing leading edge
$\hat{e}$	unit edge vector
$\hat{F}$	force vector
g	acceleration due to gravity
h	vertical distance between inlet centerline of the pumped vortex suction apparatus and wing chord plane
L/D	lift-drag ratio, $\frac{C_L}{C_D}$
ℓ	distance along the leading edge from apex to centroid of spanwise suction distribution inboard of its peak value, see figure 10
M	Mach number
$\dot{m}$	mass flow rate
$\hat{n}$	unit normal vector
p	pressure; also, roll rate, rad/sec
q	dynamic pressure
$R_{\bar{c}}$	Reynolds number based on $\bar{c}$
r	streamwise distance from the leading edge to vortex action point, identified with the rotated suction force; also leading-edge radius normal to edge
S_{ref}	reference area, usually projection of wing with LE and TE extended to centerline
s	distance along surface; also, local semispan
t/c	maximum thickness ratio
V	velocity
$\hat{V}$	total velocity vector
X,Y,Z	coordinate axes centered at the leading edge apex
x,y,z	distance from the coordinate origin; x positive downstream, y positive toward right wing, z positive upward
x/c	fractional distance along the local chord
x/c_r	fractional distance along the root chord
y_c	centroidal location of the suction distribution existing between its inboard origination point and the peak value, see figure 10
y/s	fraction of local semispan

α	angle of attack, degrees
β	angle of sideslip, degrees
Δ	jump in quantity across singularity surface, or jump in quantity between two networks
δ	flap deflection angle in plane normal to hinge-line, positive downward, degrees
δ_Γ	strake anhedral angle, positive downward, degrees
η	fraction of wing semispan
η_s	fraction of strake semispan
Λ	leading-edge sweep angle, degrees
Λ_h	hinge-line sweep angle, degrees
λ	wing taper ratio, $\frac{c_t}{c_r}$
$\vec{\zeta}$	surface vorticity vector
ρ	density of fluid
ϕ	perturbation velocity potential
ω	oscillation frequency

Subscripts

a	attainable
BD	vortex breakdown
I	inlet of pumped vortex suction apparatus
av	average
d	design
exp	experimental
h	hinge-line
l	lower
max	maximum
N	normal
p	potential or attached flow
r	root; also residual
ref	reference
s	separation
t	tip; also, theory
tot	total
u	upper
V	vortex
vac	vacuum
xx,yy,zz	second partial derivative with respect to x,y,z, respectively
z	z-component
o	value at $C_L = 0$
1	first order expansion in perturbation quantities
2	second order expansion in perturbation quantities
∞	freestream

Abbreviations

AD	analytically designed
BL	butt line
FVS	Free Vortex Sheet
LE	leading edge
LEE	leading-edge extension
MS	model station
QVLM	Quasi-Vortex Lattice Method
R.F.	Related Flow
SA	Suction Analogy
SE	side edge
SF	Separated Flow
3-D	three-dimensional
TE	trailing edge
VL	Vortex Lift
VLM	Vortex Lattice Method
VORCAM	Vortex Flow Aerodynamics for Cambered Wing (Lan)

INTRODUCTION

Leading-edge vortex flows occur naturally on many aircraft types during all or portions of their flight envelopes. The interaction of this flow with a neighboring surface may be favorable or unfavorable, depending upon the part of the airplane involved, its geometry and orientation. If the interaction is unfavorable, then the designer must try to eliminate or work around the problem; however, if it is favorable, then the designer has at his disposal another useful flow to utilize in his design and trade studies. Examples of such favorable interactions are found on the Concorde and F-16. The Concorde was designed to have vortex flow under all flight conditions (ref. 1), whereas, the F-16 mainly develops vortex flow during maneuver (ref. 2), as seen in figure 1.

There has been a considerable effort expended by many researchers to understand this flow for about 40 years (ref. 3) with the aid of both experimental and theoretical guidance. One of the early efforts was associated with the NACA-Langley test, conducted in 1946, of a thick 60-degree diamond wing having a round leading edge, designated the DM-1 glider by its German builders. A qualitative understanding was provided by the theoretician S. Katzoff (ref. 4) regarding the type of flow this vehicle should develop, whereupon the experimenters Wilson and Lovell (ref. 5) set about to achieve it. Their approach was to add a device to the leading-edge which would generate a stable vortex system, energize the upper surface flow, and produce an increase in the maximum lift. They were successful. Since then, leading-edge vortex flows have come under increased scrutiny in the principal aerodynamic facilities throughout the world. In particular, the development, structure, and interactions with neighboring surfaces of vortex flows, as well as attempts to model portions of their character theoretically, have been documented in various separate reports and conference proceedings, such as references 6, 7, and 8. Among the more familiar names associated with the experimental work are Lambourne and Bryer (ref. 9), Peckham (ref. 10), and Squire (ref. 11) of the U.K., Werle (ref. 12) of France, Hummel (ref. 13) of the F.R.G., and Skow and Erickson (ref. 14), Manro (ref. 15), Chambers (ref. 16), and Rao (ref. 17) of the U.S.A. Some of the more familiar names associated with the theoretical work are Brown and Michael (ref. 18), Levinsky and Wei (ref. 19), Polhamus (ref. 20), Mook and Maddox (ref. 21), Brune, et al. (ref. 22), and Kandil (ref. 23) of the U.S.A., Gersten (ref. 24) of the F.R.G., Legendre (ref. 25), and Rehbach (ref. 26) of France, Kuchemann (ref. 27), Mangler and Smith (ref. 28), and Hall (ref. 29) of the U.K., Hoeijmakers and Bennekers (ref. 30) of the Netherlands, and Belotserkovskii (ref. 31) of the USSR. This list is not intended to be complete. Other significant contributors in vortex flow aerodynamics have invited or chosen papers in this symposium.

At the 1978 AGARD meeting in Norway in which high angle-of-attack aerodynamics was the focus, several of the preceding methods were discussed in the paper by Lamar and Luckring (ref. 32) of the NASA-Langley Research Center. It is the intent of this paper to review the vortex-flow-aerodynamics research undertaken or sponsored by NASA-Langley since the 1978 conference and provide specific details in order to highlight the extent of the effort (see fig. 1). The breadth of the research activity covers theory

extensions, validations and applications, with configuration design being a particular goal. In addition, an ambitious experimental effort has been undertaken, across a broad front, to ascertain the phenomenological aspects of certain new and novel configurational and flow augmentation concepts which are not fully modeled by existing theories. Finally, an assessment of the future needs in this area of work is provided for interested researchers to consider.

THEORETICAL METHODS EXTENDED

In this chapter, the four theoretical methods, (one conical- and three non-conical-flow types) discussed in reference 32 have been reexamined from the viewpoint of determining the extensions needed to yield improved analysis and/or design capability. These methods are shown in figure 2. The conical-flow method is based on Smith's model (ref. 33), and the non-conical-flow methods are based on the suction analogy model of Polhamus (ref. 20), the free-vortex filament model of Mehrotra and Lan (ref. 34) and the Free Vortex Sheet model of Johnson, et al. (ref. 35). The extensions to each will now be discussed in that order.

CONICAL-FLOW EXTENSIONS

Conical-flow theories continue to be of use, primarily in providing a datum from which to judge non-conical effects. In order to compare Smith's conical-flow theory to the Free Vortex Sheet theory, Luckring (ref. 36) extended the Smith formulation (fig. 3) to include the trigonometric effects of the α variation, important at high α, in the boundary conditions (except for one term associated with the free sheet) and evaluated the pressure with the full isentropic expression. The omitted free sheet boundary condition could not be readily implemented in the referenced study. These modifications have led to a method called the modified conical flow. In addition, research is under way to estimate secondary vortex separation with the Smith conical flow.

SUCTION ANALOGY EXTENSIONS

Due to the ease of use and generally acceptable overall estimates of forces and moments, the Polhamus suction analogy continues to be heavily utilized by research and developmental engineers. Furthermore, because of its success, ways have been sought and found to extend its usefulness even to heretofore unmodeled areas. Figure 4 shows the general categories of analysis and design, as well as specific details, associated with these extensions which have occurred primarily in the last 4-5 years. (It should be pointed out that the suction analogy is not associated with any particular potential flow method. However, at Langley, there is one which has been coupled with the suction analogy to produce a greater wealth of generated results and accompanying reports, and therefore it is more commonly known, i.e., the VLM-SA code by Lamar and Gloss (ref. 37).)

Analysis

This section deals with the technology items or extensions in which most of the recent research activity has been centered. There is a further delineation by flow type, steady or unsteady, with the steady ones being considered first.

Steady Flow

By far the most progress in extending the suction analogy concept in steady flow has been centered in treating (1) more complex geometries, i.e., cranked and cambered wings, (2) more realistic flow situations, i.e., vortex core movement and breakdown, initiation of separation wings with round leading-edges, and (3) supersonic speeds. These will be discussed in order.

Complex geometries.- Figure 5 shows the manner in which vortex flows on complex configurations can be represented using the suction analogy and augmented vortex flow concepts at both high and low values of α. This figure, based on one presented in reference 32, shows the modeling employed in the VLM-SA which continues to be used for estimating the aerodynamic characteristics of strake-wing configurations, as demonstrated in reference 38.

Cambered wings.- Vortex flows and their effects on cambered wings are of increasing importance due to emphasis on vortex flow control devices, such as deflected flaps, in the wing leading-edge region. Extensions have been made to the Langley VLM-SA method to account for these cambered wing effects (ref. 39). Other methods have also been extended, including two by Lan, one which uses his QVLM method as a potential flow base (ref. 40) and the other which uses the original linearized aerodynamics of Woodward (ref. 41) as above. The latter method is called VORCAM (ref. 42).

Vortex action point.- Lan has also modeled the effect of the center of the vortex, called herein the vortex action point, moving inboard/downstream with α in reference 43. This is physically correct and not accounted for in original suction analogy modeling schemes. In these earlier schemes, the vortex was assumed to remain along the leading edge regardless of the α value, and is represented by the suction force being rotated normal to the surface and applied at the edge, as depicted in figure 4. The vortex action point movement produces no aerodynamic effects for a planar wing, but for a cambered/twisted wing there will be differences. They are associated with the local

mean-camber slope varying along the chord, thereby causing the local contributions to lift and drag, calculated from the suction force, to differ from earlier results. This can be understood by examining the right-hand sketch in figure 6, taken from reference 43.

Lan's concept was derived by comparing measured vertical velocites present near the wing leading edge with those associated with potential flow. The difference is attributed to the action of the vortex system and its magnitude based on data for one wing at one value of α and was determined to be $V_\infty/2$. From this concept he developed a streamwise flow model which has the characteristics outlined in the left and center sketches of this figure. The basic assumption is that the exchange of linear momentum into and out of a control surface of length $2r$ would be just balanced by the section leading-edge suction force. Physically, it says that the force required to keep the control surface from moving away from the wing, due to the linear momentum exchange, is just balanced by an additional force on the wing. These forces are both caused by a suction pressure present above the wing and leads to $r = c_s c$. The sketch at the right shows the reorientation of the suction force due to the movement of the vortex action point.

Round LE simulation.- For a round leading-edge wing, not all of the suction force is converted into an additional lift when the flow separates. Some of it remains as a "residual" suction force that acts in the plane of the leading edge. Polhamus showed for uncambered wings in the late 1960's (published with permission later by Kulfan in ref. 44) that there was experimental evidence to demonstrate the sum of the residual leading-edge suction and vortex normal force to be essentially the same as the theoretical value of the thin-wing leading-edge suction. Figure 7 shows one example prepared by Polhamus from the data of reference 45 for an $A = 1$ delta with a round leading edge and $t/c = 0.10$, which supports the preceding statement. The sketch on the left illustrates the forces involved, and the equation at the bottom shows the algebraic relationship. Henderson, in reference 46, later demonstrated experimentally that there was evidence to render this statement true over a wide Reynolds number range.

The two main methods of simulating the effect of round leading edges use this Polhamus concept as a basis for determining the vortex forces; however, they differ widely in the basic assumptions and computational procedures. Kulfan (ref. 44) uses a theoretical procedure for determining the vortex normal force, then employs the equation in figure 7 to find the residual suction; whereas, Carlson, et al. (refs. 46 and 47) use empirical formulas to determine the residual suction at supersonic and subsonic speeds, then employ this equation to determine the vortex normal force.

Kulfan's procedure, developed in a Boeing research effort, is depicted in figure 8. It is based on the assumptions that (1) the airfoil nose section is parabolic and (2) separation begins wherever the local value of theoretical leading-edge suction exceeds the parabolic nose drag value, c_R. The vortex and its associated normal force are assumed to occur when the local angle-of-attack exceeds that required for local separation, α_s, and to be proportional to $\sin^2(\alpha - \alpha_s)$.

Carlson assumes that the thrust at the leading edge is limited by the amount of pressure that can be attained there. An example of how the limiting pressure can reduce the leading-edge thrust to its "attainable" value is shown on figure 9. Here the limiting pressure is vacuum and its impact can be clearly seen with increasing α or theoretical section thrust coefficient, c_t. (Note, if the limiting pressure were ∞, $\frac{c_{t,a}}{c_t}$ would be 1.00 for all values of c_t.) By analyzing airfoil data, Carlson correlated the experimental residual thrust with normal Mach number, airfoil thickness and leading-edge radius ratios, and limiting pressure. The proper values for limiting pressure were determined empirically from an airfoil data base that covered a wide range of Mach and Reynolds numbers. This procedure is extended to wings by using simple sweep theory.

α_{BD} criteria.- Lan in reference 49 has developed a correlation between the centroid of the inboard portion of the leading-edge suction distribution and the onset of vortex breakdown at the wing trailing edge for a variety of simple planforms. Figure 10 shows the y centroidal location, y_c, projected to the wing leading edge. From that, the distance along the edge, ℓ, is normalized by wing semispan to provide the data in a format which can be represented by a least-square averaged curve, as shown at the right. This curve has been expressed as a unique function of ℓ.

Further, Lan used the delta wing data of Wentz (ref. 50) to develop an equation for the progressive forward movement of vortex breakdown point on the wing in terms of the α above that for α_{BD} at the trailing edge. He has applied these ideas to determine, in particular, the higher α longitudinal and lateral aerodynamics characteristics of wings in reference 49.

Supersonic speeds.- The suction analogy has been extended to supersonic speeds by Lan in reference 43 by using the original Woodward linearized aerodynamics as a base in order to produce a program called VORCAM (ref. 42). In addition, a means of accounting for the α delay for sharp-edged wings developing supersonic vortex lift has been formulated and incorporated into this code.

Unsteady Flow

Lan in reference 51 has extended the suction analogy to unsteady flow by coupling the Unsteady QVLM method (ref. 52) with the idea of "vortex lag." Vortex lag is associated with the phase lag angle that exists between the wing motion and the buildup of the vortex strength at the leading edge. Lan determined the phase lag angle and with that was able to estimate the unsteady suction force, and hence the vortex flow aerodynamics.

Design

Two kinds of design capabilities are considered herein, as shown on the right of figure 4. The first is associated with developing the proper mean camber surface to utilize vortex flows for a fixed planform, and the second is associated with developing the appropriate planform shape. The latter effort is generally associated with obtaining a planform which will generate a stable leading-edge vortex flow. (The idea for using these flows in a design mode is not new, i.e., refs. 53 and 54.)

Mean Camber

There are two ways in which mean camber solutions have been obtained recently for wings developing vortex flows: manual- and numerical-optimization. Both are seen on this figure to involve a number of iterations between the optimization (manual or numerical) and analysis module.

Manual optimization.- A cranked planform selected for a joint NASA-General Dynamics study was the first configuration to be optimized manually (parametrically) in which both the vortex-flow aerodynamics and the structural constraints, associated with the wing box, were taken into account. For this wing, called the Pre-Scamp, additional assumptions were made regarding the leading-edge vortex system. It was assumed that at each spanwise station only one vortex system would be present and that it would be of a small diameter, not be shed inboard of the tip, and only begin to come into being on the upper surface as the design C_L is approached. The design conditions sought for the cranked wing, shown in figure 11, were $C_{L,d} = 0.5$ and $M_d = 0.9$. In addition, a rooftop ΔC_p distribution (uniform to $x/c = 0.7$, decreasing thereafter linearly to zero at the trailing edge) was initially specified along the chord. It should be noted further that the resulting initial solution for the span load from the VLM attached-flow-design code (ref. 55) was elliptical, in keeping with minimum induced drag considerations.

The preceding conditions led to the smooth onflow incidence distribution for the "wing box." The term "wing box" incidence refers to the inclination of the center portion of the wing chord; for this study it is assumed to lie between 15 and 75 percent of the local wing chord. An extreme variation of structural box twist from the side of the fuselage to the tip, shown in reference 56, was required for the smooth onflow initial solution, which would be impractical for any real aircraft configuration. In order to provide a more practical design from structural and aerodynamic standpoints, a different box incidence distribution was used. Here the structural box remains at an essentially constant incidence and is only twisted over the outermost 15 percent of the semispan.

The camber ahead of the wing box (15-percent chord) was represented by five equal-semispan, cambered, leading-edge flap segments whose deflection angles were adjusted parametrically while monitoring the VLM-SA drag level. Though these levels were optimistic, they were considered reliable in estimating the proper trend of lowering drag with flap deflection angle. After a set of angles was obtained about the 15-percent chord line which produced a minimum drag value, the resulting camber was smoothed and the process was repeated about the 2.5-percent chord line. These smoothed camber lines are shown in reference 56 where they are designated as the final designed camber.

In order to apply this camber to the wing, two things were done. The first was to shift the local camber distribution vertically to provide a constant elevation along the wing midchord. The second was to match the fuselage incidence to the final inboard wing incidence to provide an even wing-fuselage juncture. (Note that $C_{L,d}$ occurs at an α of 9.4^0.) Photographs of the designed wing mounted on an existing fighter fuselage appear on figure 11.

For the final camber, the VLM-SA code indicated that $C_{L,d}$ occurred at a wing slightly larger than that required for smooth onflow all across the span. If this flow characteristic is obtained in the actual test, then the model should enable a large amount of the available leading-edge suction to be recovered at the design point. Use of the leading-edge vortex to recover suction also provides the mechanism for reattaching the flow aft of the shoulder of the forward camber.

Comparisons between the wind-tunnel data for this designed wing and estimates made with the VLM-SA method are shown in the next chapter.

Numerical optimization.- Numerically optimized solutions using VLM-SA and the optimizer CONMIN (ref. 57) were shown in reference 32. Since then, Chang and Lan (ref. 58) have coupled the VORCAM program with the CONMIN optimizer to determine mean

camber shapes at both subsonic and supersonic speeds. This method allows for the introduction of geometrical constraints, such as twist and camber progression, into the problem along with the necessary aerodynamic ones. Solutions are sought that yield minimum drag without violating any of the constraints.

Planform

Figure 4 shows there to be two types of planform shapes which are considered herein; that of the strake and vortex flap. Both are associated with the wing and either enhance or control the wing leading-edge flow, as appropriate.

Strakes.- Reference 59 describes a correlation that was found to exist between the stability of the leading-edge vortex system and the leading-edge suction distribution. Those distributions which were roughly triangular and had high peaks near the tip developed stable vortex systems. This may be interpreted in a physical sense for separated flows, with the aid of the leading-edge suction analogy, in that they are more stable for shapes which have higher levels of separation induced vorticity near the tip.

However, to take advantage of this correlation for planform design, a simplification of the flow field was necessary in order to be able to solve the problem efficiently for the planform variables in terms of the leading-edge suction distribution. The assumptions employed in going from 3-D potential flow to the simplified flow field, called "Related Flow," are given in figure 12. Note further the other assumptions which specifically impact the resulting planform. It is intended that these shapes would be used for strakes which would carry their isolated-planform performance characteristics from "Related Flow" over to the 3-D integration with a wing-body configuration. A typical resulting shape is gothic, as indicated in this figure.

Vortex flaps.- In the Pre-Scamp study, the planform was fixed and only the camber was altered to take advantage of the leading-edge vortex. However, if this constraint is relaxed and a leading-edge hinged flap or variable camber device is used, the combination of planform and camber variability is very powerful in being able to optimize the configuration over a wide range of flight conditions. This is the idea behind the vortex flap, a special kind of leading-edge flap, and it encompasses the principles presented thus far in the design section.

FREE VORTEX FILAMENT EXTENSIONS

The addition of free vortex filaments by Mehrotra and Lan (ref. 34) to the QVLM of Lan (ref. 40) produced the QVLM-SF. This method uses discrete vortex filaments which emanate from the wing leading edge and bend back over the wing to represent a diffused vortex system, as illustrated in figures 13 and 14. This system can be used to represent either a full- or part-span leading-edge separation.

Pao and Lan, in reference 60, have extended the QVLM-SF method by introducing a concentrated vortex core model, allowing for side-edge vortex separation, and permitting the modeling of cranked wings with two vortex systems. Figure 14 shows the vortex filament differences in the two different QVLM-SF methods. Pao's model starts out with Mehrotra's model but after two iterations the free vortex filaments are merged into the concentrated core. An additional consequence of using the concentrated core model is the reduced cost associated with solving an analytically simpler problem.

FREE VORTEX SHEET EXTENSIONS

Near Wake

The Free Vortex Sheet (FVS) theory continues to be extended to more complex flow regimes and geometries, as illustrated in figure 15. The governing equation and boundary conditions for this theory are illustrated in figure 16 (taken from ref. 36). They are based on higher-order panel technology and differ from attached flow methods by virtue of the more complicated boundary conditions. The chief difference is associated with the free sheet having to simultaneously satisfy both the no-load and no-flow boundary conditions; this renders the subject problem nonlinear. A second difference is associated with the near wake boundary condition. This condition needs to be satisfied to second order accuracy in order to obtain correct results. The effect of this near-wake model (fig. 17) is to decrease the wing loads near the trailing edge which will impact total normal force, pitching moment, and root bending moment. The higher order near wake is physically more realistic than the lower order formulation and generally agrees better with experiment.

Multiple Abutment

A recently developed version allows for the multiple abutment of network edges and the resulting correct treatment of multiple vortices. This capability must be used in modeling strake-wing or cranked-wing vortex flows where the inboard vortex tears away from the leading edge and persists downstream over a lifting surface. See figure 18 taken from reference 61.)

VALIDATION/APPLICATION OF THEORETICAL METHODS

With the theoretical methods of interest now established, the purpose of this chapter is to show comparisons with additional or new data, taken from critically designed experiments, in order to validate the non-conical flow solutions beyond those of reference 32. These experimental data are not necessarily associated with analytically designed models, but are for configurations at appropriate attitudes to generate the dominate vortex flow field modeled by the respective theories. By using this comparison process, a range of validity of the methods can be partially established. It can only be established partially because of the large investment needed in personnel and computer resources to examine the entire range of geometrical and flow options available for any particular method.

The validation and application comparisons are outlined in figure 19. They are seen to include forces and moments, surface pressures, and vortex core location. Specific examples for simple and complex geometries will be shown and others cited.

FORCE AND MOMENT-LONGITUDINAL

Delta Wings

The effects estimated for delta wings include: wings with round leading edges, compressibility, spanwise camber, and vortex flaps. They are discussed in order.

Round Leading Edge

Two different suction analogy extensions were outlined in the last chapter to estimate the vortex flow aerodynamic characteristics on round-edged wings. The concept/method of Kulfan has been used herein and the results are shown in figures 20 and 21 for the same 60^0 delta wing having an NACA-0012 airfoil.

Figure 20 shows three different theoretical curves for the round-edged wing; one each by Lan and Lamar, and the original method by Kulfan. Lan and Lamar have taken Kulfan's concept and implemented it for the round-edged wing in undocumented versions of the QVLM-SA and VLM-SA codes, respectively. The mathematical basis for their formulations is slightly different from Kulfan's and rests on the work reported by Robinson and Laurmann in reference 62. A comparison is offered in figure 20 between the three methods.

As can be seen for this 60^0 delta at $\alpha = 15^0$, the thin sharp airfoil vortex lift distributions agree well. However, this is not true for the round-edged NACA- 0012 airfoil. Here the QVLM-SA and VLM-SA methods differ significantly from that of Kulfan, at inboard locations, indicating marked differences in the computed separation angles.

The C_L data from reference 63 is shown at the right of figure 20 for this wing. It is interesting to note that excellent agreement with the data is obtained by Kulfan's method; whereas, the other two methods yield similar but somewhat higher values. However, there are more flow features involved than just the one cited, as can be seen on figure 21.

Here, the QVLM-SA method of Lan, incorporating the round-edge effect and his vortex breakdown criteria, is used to estimate the data in reference 49. When both effects are used, good agreement is obtained between the theoretical and the experimental results of reference 63. Hence, by reflecting on the comparisons shown in figure 20 for C_L, somehow the numerical results obtained by Kulfan have not only the round leading-edge effect, but that of vortex breakdown as well. Since Kulfan did not model vortex breakdown, his results are striking in light of the preceding results by Lan. This whole area of round leading-edge modeling requires further study. The pitching moment data are seen to be less sensitive to these additional effects due to the delay in vortex formation and low α_{BD} keeping the wing load center forward.

Compressibility Effects

The differences in the aerodynamic results obtained with Smith's conical flow model and the FVS method should go to zero as $M_\infty \to 1$, due to the reduction in the governing equation and the diminished effect of the trailing-edge Kutta condition in the FVS method. However, it is shown in figure 22 (ref. 36) that this does not occur. A study of the compressibility effects from this figure for the FVS theory and the data of reference 64 showed a good correlation of normal force and pitching moment coefficients to exist. For this slender wing and angle of attack, the vortex flow force increments were large, compared with the attached flow results from reference 37, and the FVS theory agreed well with the modified conical flow theory in the limit as $M_\infty \to 1$.

Spanwise Camber

Solutions for delta wings with spanwise camber have been obtained for both subsonic and supersonic speeds using a variety of methods in order to assist the validating process.

Subsonic speed.- Reference 65 compares the data from the seven spanwise cambered wings tested by Squire (ref. 11) with converged results from the QVLM-SP, FVS, and

VLM-SA methods. Converged solutions were difficult to obtain with the QVLM-SF and FVS methods, so primarily the VLM-SA method was used. The results reported in reference 65 showed the VLM-SA to estimate the C_L and ΔC_D well, and even C_m at values of C_L up to 0.5. Above C_L of 0.5, the C_m data were, in general more positive than the VLM-SA estimates, and better predicted by the FVS converged solutions.

Supersonic speed.- Figure 23, taken from reference 43, shows an example of the comparisons made with the VORCAM code and data (ref. 66). These results for a delta wing having a conical leading-edge flap tested at $M_\infty = 1.4$ highlight an important feature of this code: its ability to model geometries and Mach numbers of continuing interest. Furthermore, its vortex flow modeling leads to slightly better agreement with the C_L and C_D data than the attached flow solution assuming full leading-edge suction.

Lower Surface Vortex Flap

Figure 24 (from ref. 67) presents a comparison of the experimental force and moment data obtained by Rao and the VLM-SA and FVS theoretical predictions obtained by Frink. The resulting comparisons are shown at an $\alpha = 14^0$ and $M_\infty = 0.3$ so as to summarize the effect of flap deflection on the coefficients. Note in the sketch on the right of figure 24, that there are differences in the experimental and theoretical geometries. In particular, the geometry used for the theoretical calculations is a wing-alone configuration where the cylindrical fuselage has been omitted and the flap hinge line and trailing edge are extended to the centerline. (The resulting area is used for reference herein.) Also note that there is additional area in the apex region of the flap on the theoretical geometry. These modifications were necessary to obtain solution deflections up to 20^0. Quantitatively, the two theories are showing an overestimation of lift and drag for flap deflections from 0^0 to 30^0 measured normal to the hinge line. These overestimations initially are surprising because the VLM-SA generally underpredicts drag on cambered configurations since the suction analogy prescribes the rotated suction vector to be applied at the leading edge. (These VLM-SA calculations were performed without the use of the vortex action point feature.) However, the excellent qualitative correlation of lift and drag suggests the differences may be a result of the variance in geometry. The moment coefficients are not estimated as well as the forces but the FVS theory exhibits the qualitative behavior of the data.

Other Vortex Flaps

Other vortex flap arrangements have been studied with the FVS method. Some involve a lower flap mounted on a round-edged wing, whereas others include the upper and apex vortex flaps attached to round- or sharp-edged wings. (See the next chapter.) The FVS solutions for these other arrangements have had varying degrees of success, which are dependent upon the extent of the unmodeled flow regions. These regions typically occur near round leading edges and in cavities.

The upper vortex flap modeling done by Reddy in reference 61, produced a generally successful comparison for the C_L data obtained by Rao (ref. 68) in the low α range; however, unmodeled flow features caused the higher α results to differ. Regarding the apex flap, Buter in reference 69 generated remarkable results for a delta wing with this device. Though the quantitative agreement with data was not good, the FVS method did capture the qualitative aerodynamic features of this flap.

Arrow Wing

The FVS method has been used at Langley by Schoonover to predict steady-state vortex-flow pressure distributions on a highly-swept aircraft wing at various angles of attack (ref. 36). The panel layout for this arrow wing is shown on the left side of figure 25 and was determined by him to be one which would facilitate convergence and increase the "resolution of the vortex-induced pressures near the wing apex." The resulting non-linear loading increments (due to the vortex) were then incorporated by the Douglas Aircraft Company into an unsteady loads analysis to enhance their prediction of the structural responses of such wings to blast loads caused by a nearby nuclear detonation. The results, when compared to attached flow theory and experimental data obtained on a rocket sled (ref. 70) and shown on the right side of figure 25, indicated that inclusion of these theoretical vortex-induced loading increments resulted in a substantial improvement in their capability to predict blast-induced gust loadings with α.

Cranked Wings

Pre-Scamp wing

The cranked-wing model of figure 26 had its camber and twist designed using the VLM-SA theory for a $C_{L,d}$ of 0.50 and M_d of 0.90 in a manual-optimization mode. This process is described in references 56 and 4. The tests were, however, conducted at $M_\infty = 0.85$ due to wind-tunnel power limitations, and it is the data from these tests which also appear in figure 26. From this figure, it can be seen that the lift data are well predicted by the VLM-SA for angles of attack up to 12 degrees, and that using

vortex flow one is able to achieve $C_{L,d}$ at a lower value of α than with potential flow alone. The figure also shows data for both the planar and vortex-flow-designed wing drag polars in comparison with two theoretical curves. As expected, over most of the C_L range the planar wing data follow the upper or zero edge-force curve which includes the full theoretical vortex lift. The designed wing data are generally much lower than the planar wing data and approach the lower bound polar in the C_L range from about 0.35 to 0.45, even though the wing is thin (maximum thickness ratio is 3.2 percent) and the leading edge is sharp. This off-design feature is an attractive benefit of designing with vortex flows. Furthermore, at the design C_L the data reach a level equivalent to 77 percent of full leading-edge suction. This large value of equivalent suction is remarkable for such a slender wing, particularly at this high Mach number maneuver condition. It should be noted that this highly effective suction level includes the penalty associated with outboard aft separation. Hence, with additional tailoring this penalty could be reduced.

Strake-wing

Another kind of cranked wing is the strake-wing configuration. Reference 71 presented a summary of results from some 15 strake-wing-body combinations; since then, some 17 other combinations have been tested. This last group differs in the strake portion of the configuration. Some of the strakes were designed analytically, using the method described previously, and some designed empirically.

Typical lift and pitching moment characteristics for these combinations, AD 19 depicted, are shown in figure 27. The drag data are not given since their variation is just $C_{D,o} + C_L \tan \alpha$ for these thin unwarped lifting surfaces. From reference 38 it was determined that in general for this and the other configurations, the C_L data are better estimated by the High α theory. Though better estimated, there may be an α range below the α for $C_{L,max}$ for which the C_L data are underpredicted. This is most likely associated with the High α theory not accounting for any vortex lift from the wing. A further evidence of this deletion is seen in the C_m versus C_L results, where the theory shows the center of pressure to be ahead of the data. The potential-flow curve is added to the C_L versus α plot for reference in figure 27. Component data for the strake-forebody and wing-afterbody were also obtained from the wind-tunnel results and are reported in reference 38.

Series

Other cranked wing studies have been performed using a group of double delta models with $\Lambda_{LE} = 80^0/65^0$ and published as reference 72. A typical comparison between theory and experiment for this cranked wing (fig. 28) shows the VLM-SA High α theory to estimate the longitudinal aerodynamic characteristics well. (Refer to figure 5 for a geometrical definition of the theory terms.) At the higher values of C_L the C_m data show a slight pitch-up tendency associated with a lack of complete flow reattachment of the vortex in the notched trailing-edge region.

SURFACE PRESSURES

Delta Wings

The FVS method has been used to estimate the surface pressures of a large number of delta wings. Many of these comparisons with data appear in the literature, e.g., references 65 and 73.

74-Degree

Recently a 74^0 delta has been added to this list (ref. 67). The agreement with data is generally good except when the effects of the secondary vortex become sufficiently large to alter the effects of the primary vortex. This typically occurs at the higher angles of attack near the leading edge and results in an inflection (or flat region) in the pressures between the primary vortex pressure peak and the leading edge. The effect of this secondary vortex is to displace the primary vortex inboard and reduce the magnitude of its suction peak. The secondary vortex is not modeled but is inherent in the viscous surface flow as noted.

Lower Surface Vortex Flap

A correlation of experimental and FVS theoretical pressures at a moderate value of α are shown in figure 29, taken from reference 67, for the same 74^0 delta vortex flap configuration described in figure 24. The spanwise upper surface pressures at the chord station indicated on the sketch are shown in figure 29 for flap deflections of 0^0, 10^0, and 20^0. The spanwise coordinate is nondimensionalized by the local hinge semispan, $(s)_h$, so that pressures acting on the flap surface correspond to $y/(s)_h > 1$ and on the wing surface to $y/(s)_h < 1$. As can be seen, the experimental pressures measured by Rao are estimated quite well by the FVS theory, even near the leading edge, and particularly

so for deflections of 0^0 and 10^0. For a 20^0 deflection, the theory overpredicts the suction peak but its general spanwise position is in good agreement with the data. Over the range of deflections presented, the general character of the data is well predicted by the theory. Both theory and experiment exhibit an outward shift in suction peak location and a corresponding rise in peak level with increasing flap deflection along with a decrease in suction just inboard of the hinge line.

It should be pointed out that Frink uses these flap pressures to calculate hinge moments for both attached and separated flow. The conclusion of the study was that vortex flaps developing separated flow probably present no more of a load or actuation problem than those developing attached flow.

Cropped Delta

Comparisons of theoretical and experimental spanwise pressure distributions are presented in figure 30 for a 63.4^0 cropped delta at two longitudinal locations (ref. 36). Compared to attached-flow theory and conical-flow theory (which has no trailing edge Kutta condition), the FVS theory provides a substantially improved estimate of the experimental pressures. However, the FVS theory generally predicts vortex-induced pressure peaks which are somewhat higher in magnitude and displaced outboard, when compared with experimental data. This is similar to the experience with the delta wings.

Arrow Wings

The FVS method has recently been applied by Manro (ref. 74) to a series of NASA/Boeing arrow wings having the same planform but differing in their mean-camber warp. These wings were of $A = 1.65$, $\Lambda = 71.2^0$, $\lambda = 0.10$ and had flat, twisted, and cambered/twisted mean-camber surfaces (see fig. 31), and were designed in part to be able to assess and estimate aeroelastic effects on this class of wing. Other features of these wings that made them useful configurations with which to apply the FVS method were the round- and sharp-leading edges, leading- and trailing-edge flaps, and pressure instrumented outboard fins (not shown). (Previous reports have dealt with estimates of this extensive subsonic, transonic, and supersonic data base by various methods including linear panel, higher ordered panel, suction analogy, conical flow, and transonic flow, which are referenced in reference 74.) The comparisons made by Manro showed the FVS method to generally predict the pressures well and to adequately reflect the changes due to wing warp.

Other nonlinear techniques that account for the effect of vortex flow have been applied to this data set. They are semi-empirical (ref. 75) and a combinational technique (ref. 76). These have met with varying degrees of success, with the semi-empirical technique of Wery and Kulfan (ref. 75) generating the better agreement.

Cranked Wings

Converged solutions for both the QVLM-SF/Two Vortex Model method of Pao and the FVS method are used to estimate the lift/pitching moment, and surface pressures on cranked wings, and the results are shown on figures 32 and 33, respectively. Figure 32, taken from reference 60, shows two different cranked wings and their lifting pressures across the span or along a constant x/c line for the aft wing. In general, the QVLM-SF method yields good agreement with the lift data of references 72, 77, and 78, and captures a portion of the experimental lifting pressure variation. The pressures do show at least two humps indicative of the dual vortex system present behind the leadng-edge crank.

The FVS method, figure 33, taken from reference 61, shows the aerodynamic consequences of the various LE vortex modeling techniques highlighted on figure 18 in comparison with the data of reference 72. In particular, the lift seems better modeled by a single vortex all along the edge, whereas the pitching moment is better modeled by the two vortex system. The single vortex passing over the wing has the smallest overall range of good agreement. Though no data comparison is made for the local surface pressures, it is useful to understand the wide variation in the C_p distribution which results from the different models. Note especially the one large hump associated with the single vortex modeling along the leading edge and the two humps associated with the others. The multiple humps for the two vortex system is expected, whereas that for the single vortex over wing is not. However, when it is understood that the high suction peak near y/s of 1.0 for the single vortex model (long-and-short dashed line) is associated with attached flow and not vortex action, then it makes sense. Furthermore, note that the lower surface pressures for this model have the same characteristic behavior near the edge as do those for the upper surface.

The conclusions from this study are that converged solutions for lift are probably easier to get with the QVLM-SF/Two Vortex Model; whereas, if converged solutions can be obtained with the FVS method employing multiple vortex systems then the pitching moment and surface pressures will most likely be in better agreement with data.

VORTEX CORE LOCATION

As part of a validation program for the FVS theory, four swept (63.4^0) pressure-instrumented wings (delta, cropped delta, cropped arrow, and cropped diamond) have been fabricated and have been or are to be tested. During the test of the cropped delta

wing, the vortex-core trajectory was rendered visible due to the naturally occurring condensation in the wind tunnel. That event was photographed and is compared with the theoretical solution for the core trajectory in figure 34, taken from reference 36. The side-by-side comparison shown was made possible by projecting the theoretical path onto the planform. The conclusion of the comparison is that the theory is seen to give a core trajectory consistent with the observed one. This is a very encouraging result, particularly since the predicted core location crosses the side-edge slightly upstream of the experimental location, which is consistent with the effect of the secondary vortex. (See the discussion regarding surface pressures.)

MOMENTS DUE TO LATERAL MOTION

Steady

The QVLM-SA method, with allowance for leading-edge vortex breakdown, has been applied to a cropped delta wing in reference 49 to determine the lateral aerodynamic characteristics. Figure 35 shows the agreement with the data of reference 79 to be remarkable. Reference 49 points out that the inclusion of the side-edge vortex terms is important to get this good agreement. (The steps noted in the theory curves are due to the vortex breakdown criteria affecting each side of the model differently at α with $\beta \neq 0$, i.e., dependent upon the local flow conditions present.)

Unsteady

Figure 36 shows results obtained by applying the unsteady suction analogy (ref. 51) to the prediction of oscillatory roll damping for a gothic wing. Shown are experimental and theoretical data for C_{l_p} versus α for reduced frequencies of $k = 0.75$ and 1.20. The theory and experimental data of reference 80 agree quite well primarily due to an appropriate modeling of the vortex lag and convective effects. Note the reduction in roll damping at high angles of attack shown in figure 36. This feature offers a possible explanation of the wing rock phenomenon encountered by slender wing geometries operating at those attitudes.

REYNOLDS NUMBER EFFECTS

The comparisons presented in this chapter have been made with data at small Reynolds number. Furthermore, they have primarily highlighted sharp-edged wings for which the dominant primary vortex flow is essentially Reynolds number insensitive. That Reynolds number does play a role in the actual flow field is well known and has been compiled by Smith (ref. 33) for delta wing models, and Dee and Nicholas (ref. 81) for the Fairey Delta-2 aircraft. More recent flight evidence is shown in figure 37 for the round-edged F-111 TACT airplane (ref. 82). In particular, this figure shows that at the lower $R_{\bar{c}}$, the leading-edge flow has separated and the vortex is present, whereas at the higher $R_{\bar{c}}$, the leading-edge flow remains attached, suppressing the vortex.

These effects are not fully modeled by existing methods and, hence, provide opportunity for future comparisons as the techniques are improved.

VORTEX CONTROL DEVICES

Generally, the validation and application of vortex theories have been successful when the vortices are stable and well behaved. As the vortex changes character, due to breakdown, or the vortex pair becoming asymmetric, theoretical calculations of the flow fields interacting with neighboring surfaces are very difficult to obtain. This problem is compounded because these phenomena are sensitive to a large number of configuration and flow-field variables. For example, the effect of wing leading-edge sweep on the angles of attack for breakdown or asymmetry is shown in figure 38 for sharp-edge delta wings at low speeds. This chapter discusses a variety of vortex control devices that enhance aircraft performance in two areas of vortex flow. An outline of this research effort is shown in figure 39. The first area is to utilize the stable vortex flow at low-to-moderate α. An example of this was the previously mentioned Pre-Scamp research model which successfully used wing camber to control the vortex position for drag reduction benefits. The second area delays the onset of vortex breakdown or asymmetry by using various wing and body vortex control devices, including body shaping. Concepts and selected data are presented to highlight the aerodynamic benefits achieved with particular devices in both of the angle-of-attack regions.

ENHANCED WING LOW-TO-MODERATE α CHARACTERISTICS

Three vortex flow control concepts are discussed which enhance wing low-to-moderate α characteristics. These are vortex flaps, vortex generators, and leading-edge extensions.

Vortex Flaps

The vortex flap effort was an outgrowth of the slender-wing vortex-design study described in figure 26, which demonstrated that simple leading-edge and trailing-edge flaps could approximate the transonic maneuver drag benefits of the fixed Pre-Scamp design (ref. 56). During the last four years, vortex flaps have undergone extensive

experimental testing to build the data base using generic research and fighter models, while a parallel effort has been underway to mature the vortex theories to calculate details of the vortex flap flow field.

Types

Flow patterns are shown in figure 40 for three types of vortex flaps under active consideration--lower surface, upper surface, and apex. The lower-surface flap is similar to conventional leading-edge flaps on current fighters in that both are articulated to improve the maneuver drag polar. The conventional flaps, such as those on the F-16, help to keep the leading-edge flow attached. The lower surface flap promotes a separated vortex with flow reattachment at the flap hinge-line and smooth, attached flow on the wing's upper surface. With these desired flow conditions, the vortex-induced suction pressures act on the forward-facing flap surface, which leads to good drag efficiency at the cruise, maneuver, and climb-out lift conditions.

Folding, hinged, and tabbed are three categories of the lower-surface flap that have been investigated. The folding flap (refs. 83, 84, 85, and 86) deploys from the lower surface of the wing and uses the added flap area to improve L/D, in addition to the natural aerodynamic gain. The hinged flap (refs. 87 and 88) is exposed to the flow throughout the flight envelope and changes deflection angle to optimize flap performance. The tabbed flap (refs. 89 and 90) has a small retractable tab at the flap leading edge which helps control the vortex formation along the leading edge for a variety of upwash conditions. The tab is shown in the sketch as it would be integrated with the folding flap, although it is also applicable to the hinged flap.

The upper surface flap was developed by Rao (ref. 68) as a variation of the lower surface arrangements. This flap generates a stable two-vortex system, a leading-edge vortex on the flap, and an inboard vortex over the wing. The unique features of the flap concept are its ability to increase lift at low α and to increase L/D and roll control at moderate α.

The upper surface flap and apex flap are both forced-vortex concepts with the objective of using vortex flows to improve the lift capability of slender wings at low α. The apex flap is deflected (up) about a transverse hinge-line and generates vortices which shed over the wing inducing a suction effect and a lift increase (ref. 69). In addition, Rao (ref. 17) shows that the vortex lift and long pitching moment arm of the apex flap combine to make it a powerful trim device, permitting the trailing-edge flaps to be fully utilized at low α's.

Of the three flap types, the most research attention has been focused on the lower surface flaps. The next three figures give a perspective of the various vortex flap geometries that have been investigated, and a sample of wing performance data to illustrate the effect of hinge-line location and sweep.

Shape, Size, Segmentation

The characteristics associated with some of the lower-surface flap geometry changes are depicted in figure 41. Rao (refs. 17, 83, and 84) demonstrated that reducing the length inboard improves flap efficiency. In addition, shaping the flap inboard improves the vortex formation while shaping outboard promotes vortex flow reattachment at the hinge line, both of which reduce drag and delay pitch-up. Increasing flap size was shown by Rao (ref. 83) and Schoonover (ref. 86) to delay the inboard movement of the vortex, which combines with the increased flap frontal area to reduce drag.

In recent studies on an arrow-wing configuration (ref. 91) and a cropped-delta wing model (ref. 92), Rao demonstrated that flap segmentation is an effective technique to reduce the flap area while still achieving the same L/D as without segmentation. The flap segments generate multiple vortices that remain closer to the leading edge, improving the efficiency of the vortex flow in the tip region, which delays tip stall and improves the longitudinal stability characteristics.

Hinge-Line Location

The effect of hinge-line location on L/D is shown in figure 42 for a 74^0 delta wing (ref. 93). The configuration has the full-span vortex flap with hinge-line attachment simulated to occur at various positions behind the lower-surface leading edge. The resulting data were obtained to evaluate the effect of hinge-line location on the aerodynamic performance for a Krueger-like flap arrangement. A leading-edge radius was used to assure a smooth surface for reattachment of the vortex flow and to minimize leading-edge separation effects on the upper surface. The basic wing data are shown for reference. The deflection angle was constant, $\delta_{LE} = 45^0$, and the L/D data presented in this figure are based on the actual projected area rather than a fixed reference area to take out the added-on area effect for the C_L.

From figure 42, the flap-on data show that with the hinge-line located at the leading edge, the largest L/D values result throughout the C_L range, and that as the hinge line is moved aft there is a progressive decrease in the aerodynamic efficiency. This decrease is caused by combinational changes in wing upwash, vortex strength, and the increase of negative lift associated with the vortex being confined behind and

underneath the leading-edge. Compared to the flap-off data, the vortex flaps appear to be an efficient way to utilize vortex lift for $C_L > 0.15$.

Hinge-Line Sweep and Deflection Angle

Frink, et al. (ref. 87) recently performed a subsonic experiment in the Langley Research Center 7- by 10-Foot High Speed Tunnel to evaluate the effects of wing sweep on vortex flap effectiveness. A sample of the data is shown in figure 43. The research was conducted for a family of planar delta wings with $\Lambda = 50^0$, 58^0, 66^0, and 74^0, having constant chord vortex flaps, and mounted on a general research fighter fuselage. A constant chord flap, of course, implies that $\Lambda = \Lambda_h$. The effect of Λ_h on L/D is shown for a maneuver value of $C_L = 0.6$ with $\delta_{LE} = 0^0$ and 40^0. The conclusion is that increasing sweep decreases L/D for a given flap deflection, while increasing flap deflection increases L/D for any sweep; the flap deflection effectiveness being greater at the lower sweeps.

Vortex Generators

Vortex generators are also used to enhance aircraft low-to-moderate α characteristics, and are depicted in figure 44. The generators that have been investigated are the pylon, fence, and slot. These are fixed devices at the leading edge (refs. 94, 95, 96, and 97), and are generally used with round-edge wings. Each device generates a vortex that flows streamwise over the upper surface of the wing and splits the primary leading-edge vortex into segments. This change in wing flow field results in a drag reduction due to improved leading-edge suction, and a slight lift loss due to the suppression of the leading-edge vortex. A significant feature of the vortex generators is their ability to improve longitudinal stability. The devices delay the inboard movement of the tip vortex, which increases tip vortex lift and delays pitch-up, compared to a wing without the devices.

Leading-Edge Extension (LEE)

The last vortex flow control concept to be discussed for enhancing wing low-to-moderate α characteristics concerns the application of a leading-edge extension (LEE) to the outboard portion of a transonic wing. The intent is to improve the drag polar by energizing the wing flow in the tip region at the higher α values with vortex action. This investigation, illustrated in figure 45, is intriguing because it involves the interaction of a vortical flow over the outboard panel of a fighter wing designed for attached supercritical flow. The early and advanced designs depicted in the figure are maneuver configurations developed by Mann, et al. (ref. 98) using transonic methodology.

In an effort to alleviate the shock-induced flow separation that eventually occurs in the wing-tip region as lift increases, the attached flow design was supplemented with a sharp LEE on the outer wing panel. Pressure measurements reported in reference 98 indicated that there was less flow separation on the outer panel with the LEE, which corresponds to the drag reduction obtained at high C_L. Further research of this vortex control concept is necessary in order to fully understand the implications of combining vortical flows with supercritical attached flows for maneuver wing designs.

ENHANCED WING-BODY HIGH α CHARACTERISTICS

Five different vortex flow concepts are discussed for enhancing this flow and its aerodynamic benefits to high angles of attack. Four of these employ fixed geometrical pieces, whereas, the other uses a fluid. In particular, they are the leading edge extension (LEE), discussed earlier, the raked tip, the strake applied to a wing, jet augmentation, and fuselage forebody shape.

Leading-Edge Extension (LEE)

This LEE was applied to a thick round-edge, 60^0 diamond shape, low-speed glider called the DM-1. The problem to be solved with this device, shown in figure 46, was to energize the flow on the leeward side of the wing so as to generate a $C_{L,max}$ value closer to that measured on thin sharp-edged wings. (Note that this device was successful as seen by the organized flow at $\alpha = 18.9^0$.) This figure, developed from reference 5, shows the final placement of the LEE to be inboard. In this location the device not only increases $C_{L,max}$ but generates less drag as well. The lower drag is associated with low surface pressures acting between the LEE and the maximum thickness line of the wing section which produce a thrust.

An ideal arrangement would be for the LEE to be mounted to a thick round-edge wing along the pseudo-stagnation stream surface which is associated with smooth onflow at the attached flow design condition. For flight attitudes above that for smooth onflow, which would occur for take-off, landing, and maneuver, a vortex would be generated in the region between it and the upper surface. This would energize the leeward surface flow and produce the lower pressures needed for drag reduction.

Raked Tip

An in-plane extension or retraction of the side-edge of a cropped delta wing, caused by pivoting a portion of the wing about the tip leading edge, has led to a raked-tip device for enhancing the high α lateral characteristics. This patented device (ref. 99) was first discussed in reference 100. Its purpose is to modulate the strength of the vortex system and the associated reattachment area so that significant amounts of rolling moment can be generated at attitudes where other devices, such as ailerons, are known to be ineffective. The concept works best when the raked tips of a wing move in the same direction during deployment. The device has been found to generate essentially a linear growth rate of rolling moment with either increasing α or tip rake angle. Furthermore, its deployment produced either no or a proverse yawing moment.

Strakes

The general longitudinal aerodynamic effects of adding a strake to a wing-body are well known, but are repeated on figure 47 for completeness. In particular, strakes organize the wing flow field to a higher value of α, i.e., increase wing α_{BD}, which leads to an increase in C_L. This in turn loads up the strake more at the higher values of α and leads to a larger nose-up pitching moment when this vortex system breaks down. Also, on this figure are highlighted two experimental studies. The first is to determine the effect of strake shape on the strake vortex system with emphasis on its α_{BD} characteristics; and the second is the effect of strakes on lifting surfaces which interact.

Strake-Wing-Body

The photograph on the left of figure 47 shows a typical strake-wing-body in the strake effectiveness study. Reference 101 reported that, for a range of analytically and empirically designed strakes, those which developed a higher value of the section leading-edge-suction force at their spanwise extremity generally had the higher values of α_{BD} at the wing trailing edge. (It was also pointed out in reference 38 that the maximum value of the additional lifting surface efficiency factor and α_{BD} at the wing trailing edge have the same variation with the ratio of strake-exposed-area to wing-reference-area.)

Space-Jet

The other photographs show a "Space-Jet" concept (configuration of ref. 102). It is conceived of as being a possible follow-on to the Space Shuttle, in which the inventors, Jackson, et al. (ref. 103) envisioned using vortex lift to help this turbo-jet-powered vehicle take off horizontally. However, the resulting closely spaced interacting vortical flow systems were determined not to interact favorably, and to be potentially beyond current modeling capability.

Forward-Swept Wing Application

Strakes have also been used on swept forward wings in an attempt to improve the wing-root flow field by Huffman and Fox (ref. 104) at $M_\infty = 0.3$. These low-speed results showed that the effect of the strake was to increase the configurational C_L and aerodynamic efficiency.

Hinged Strakes

An alternate approach for improving usable lift at high α is to utilize variable strake geometry as a lifting and control device. Moss (ref. 105) evaluated variable incidence and camber, while Rao and Huffman (ref. 106) studied the effects of anhedral on a hinged-strake concept. The hinged strakes are articulated to suppress the strake vortices, and thus eliminate or soften the vortex-breakdown effect. The hinged strakes, which are structurally separate from the wing, are attached to the fuselage through longitudinal hinges. The effect of hinged strakes on high α aerodynamic characteristics is shown in figure 48 for a wing-body-vertical tail configuration. With respect to the strake-off configuration, the addition of the planar-strake ($\delta_T = 0^0$) leads to the characteristic vortex breakdown condition evidenced by a peak in C_L accompanied by pitch-up. Note also the opposite lateral-directional behavior as α approaches 30^0 due to the asymmetric breakdown of the strake vortices being different from that of the basic configuration. Deflecting the strakes to 30^0 anhedral greatly alleviates these vortex breakdown effects. In his current paper for this conference, Rao (ref. 17) presents additional data analysis to show that horizontal-tail effectiveness is increased by symmetric deflections of the strakes, and that large rolling moments occur due to asymmetric deflections that become larger than conventional ailerons at high α.

Jet-Augmented Concepts

Another approach for favorably effecting high α aerodynamic performance is to use jet flows to augment and control the wing vortex. Three jet-augmented vortex concepts are under investigation and are shown in figure 49. These concepts are the fluid strake, spanwise blowing, and pumped vortex. Their function is to delay vortex breakdown and organize the wing upper-surface flow field to yield the desired

aerodynamic benefits by the addition of energy to the system.

Fluid Strake

The fluid strake concept (refs. 107 and 108) uses a jet sheet formed by blowing through a series of small in-line orifices located symmetrically on the sides of the fuselage ahead of the wing. The intent is to create the effect of a "fluid" strake that can be activated to obtain the high α benefits of a solid strake, such as those discussed in figures 47 and 48. (Note this may be done either symmetrically or antisymmetrically, depending upon the individual blowing rates.) The jet sheet generates a stable vortex flow over the wing, which increases $C_{L,max}$ and improves the drag polar and vertical tail effectiveness at high α. The lift augmentation of the fluid strake is comparable to that obtained with spanwise blowing.

Spanwise Blowing

This concept energizes the leading-edge vortex by blowing a jet spanwise over the upper surface of a wing in a direction approximately parallel to the leading edge. Pressure data obtained by Campbell (ref. 109) demonstrated that full vortex lift could be achieved at inboard wing stations with relatively small blowing rates, but progressively higher values are required to obtain full vortex-lift levels at the more outboard span stations. Research by Erickson and Campbell (ref. 110) and Staudacher, et al. (ref. 111) on fighter models showed that spanwise blowing increases lift, improves the drag polar, and linearizes pitching moment at moderate-to-high α. Spanwise blowing has significant effects on lateral-directional aerodynamics, which appear to be configuration dependent. Both rudder and aileron effectiveness are improved by spanwise blowing (ref. 111). Furthermore, it results in more stable roll damping and, as demonstrated in a free-flight experiment (ref. 112), helps eliminate wing rock.

Pumped Vortex

Building on the work of Hummel (ref. 113), Taylor, et al. (ref. 114) investigated a pumped-vortex concept and showed the criticality of the location of the suction device used to pump the vortex downstream. Using an injector drive system, they were able to significantly increase the axial flow in the vortex which stabilizes the system to a higher value of α. The effects of the suction device on the lift characteristics for a blended delta model are shown in figure 50, which indicates that increasing C_μ increases C_L at moderate α and increases $C_{L,max}$. The augmented lift levels obtained here are higher than those obtained in Hummel's suction experiment because of the much higher C_μ values used for this test. These larger values induce higher velocities over the wing upper surface which even increases the potential flow lift contributions.

Fuselage Forebody Shape

At higher angles of attack, beyond that for wing vortex or strake vortex breakdown, the effect of the aircraft forebody shape becomes increasingly important in establishing the aerodynamic characteristics. This results from the tendency of the forebody crossflow to be asymmetrical, and is associated with the fineness ratio and cross-sectional shape of the forward part of the aircraft body. Original work documented by Edwards (ref. 115) of Northrop on the F-5 produced the shark nose (F-5F), and provided an example of how the high α asymmetry can be reduced by proper shaping. (See also the work by Erickson in ref. 116.) More recently, a systematic forebody/length experimental study has been done at Langley by Carr and Gilbert (ref. 117) on a high-performance fighter-type model at low Reynolds number to uncover some of these high α aerodynamic interactions associated with the geometrical components. (This work builds on an earlier study by Grafton, et al. (ref. 118)).

FUTURE NEEDS

Though much work has been done to theoretically model the effects of, validate and apply the resulting methods to, and generate an extensive experimental data base for vortex flows interacting with neighboring surfaces, there are still gaps in this technology area. These gaps are expressed as future needs and reflect the authors' views as to where research attention should be focused in both the near and far term. The needs are highlighted in figures 51 and 52 and subsequent paragraphs.

For relatively sharp edges, inviscid modeling will continue to provide useful predictions of the complete surface pressure distributions that are required for many aerodynamic and structural design problems. The biggest challenges lay in incorporating the effects of viscosity both in the surface boundary layer and in the shed vortex core system. This is important in order to determine the onset and effects of (1) the development of a primary vortex on round edges, (2) the secondary, etc. vortices, (3) vortex breakdown in the cores, and (4) asymmetrical vortex shedding at higher values of α. A step in this direction can be made by incorporating three-dimensional boundary-layer effects and separation criteria in inviscid prediction methods; this will allow calculations of the Reynolds number sensitive flow on rounded leading-edge wings and fuselages. In addition, more extensive use needs to be made of the Euler codes (see for example, the one used in ref. 119) in order to determine how well they predict the

separated vortex flow onset and effects associated with wings/bodies with or without thickness. It should be determined if Euler codes have unique capabilities to accurately predict the interaction processes associated with shocks and vortex flows, multiple vortex systems, and augmented vortex flows, so that configurational trade studies can be made to take advantage of these types of flows. These promising codes, and the associated computing equipment, need to be matured so that they may be used in a design mode. Design activities for thick wings developing vortical flows should be considered a goal. Furthermore, reliable methods need to be established for predicting the incremental aeroelastic effects of slender wings at subsonic, transonic, and supersonic speeds. In addition, the higher order panel codes need to be used or extended to estimate the effects of vortex flow on configurations in unsteady motion.

Current capabilities of existing codes need to be examined to determine the useful flight and configurational bounds. In particular, the Free Vortex Sheet theory needs to be fully validated for configurations having thickness and a fuselage, and parallel-nonplanar or intersecting lifting surfaces with interacting vortical flows. Furthermore, design activity, using available analysis tools, needs to be undertaken to take advantage of the leading edge extension and vortex flap configurational opportunities. Additional strakes should be designed for specific needs to see if the technology is sufficient.

A data base should be generated to determine the effects of wing leading-edge radius, thickness, camber, planform, and vortex augmentation on the angle-of-attack boundaries for vortex breakdown and asymmetry. Also, key experiments necessary for the more thorough understanding and modeling of off-surface flow features for wings and bodies, as well as that on the surface, should be made. In addition, similar studies need to be undertaken and documented for multiple, nonplanar lifting surfaces developing interferring vortical flows under steady and unsteady conditions. Furthermore, bridging the gap between the low Reynolds number wind-tunnel data and flight results with a high Reynolds number facility, such as the Langley National Transonic Facility, is encouraged. This is or particular importance in order to set the stage for application of variable geometry vortex flow control devices in flight.

CONCLUDING REMARKS

The recent research activity of vortical flows interacting with neighboring surfaces, conducted or sponsored by NASA-Langley, has been reviewed. Theoretical capabilities have been validated to determine the overall force, moment, and surface pressures on a variety of planforms in steady flow. Unsteady flow capability and effect of sideslip have also been demonstrated on a more limited basis. The simple theoretical methods employing the suction analogy continue to be useful and have been extended to include the effects of vortex breakdown, round leading-edge modeling, and supersonic flight. The Free Vortex Sheet method continues to be among the better methods for predicting surface pressures and moments, even on wings having vortex flaps.

An extensive experimental data base has been identified which is dedicated to enhancing the wing low-to-moderate angle-of-attack or high angle-of-attack characteristics through the appropriate use of a vortex-flow control device. These devices include vortex flaps, vortex generators, leading-edge extensions, strakes, raked tips, and jet augmentation.

Though much has been done, it will be necessary in the future to improve the theoretical tools by including the effects of viscosity and unsteady flow, develop and extend other codes, extend the geometrical shapes and parameters considered so as to enlarge the data base, and to use a high Reynolds number facility, such as the National Transonic Facility at Langley, to gain confidence in variable geometry vortex flow control devices, so that early, successful flight demonstrations can be conducted.

REFERENCES

1. Morgan, M., Sir: A New Shape in the Sky. Aeronautical Journal, pp. 1-18, Jan. 1972.

2. Smith, C. W.; Ralston, J. N.; and Mann, H. W.: Aerodynamic Characteristics of Forebody and Nose Strakes Based On F-16 Wind-Tunnel Test Experience, Volume I: Summary and Analysis. NASA CR-3053, July 1979.

3. Matoi, T. K.: On the Development of a Unified Theory for Vortex Flow Phenomena for Aeronautical Applications. Contract No. N00014-57-A-0204-0085, MIT, April 1975. (Available from DTIC as AD-A012 399.)

4. Lamar, J. E.: The Use of Linearized-Aerodynamics and Vortex-Flow Methods in Aircraft Design. AIAA Paper No. 82-1384, 1982.

5. Wilson, H. A.; and Lovell, J. C.: Full-Scale Investigation of the Maximum Lift Flow Characteristics of an Airplane Having Approximately Triangular Plan Form. NACA RM L6K20, Nov. 1946.

6. Three-Dimensional and Unsteady Separation at High Reynolds Numbers. AGARD LS-94, 1978.

7. Missile Aerodynamics. AGARD LS-98, 1979.

8. High Angle of Attack Aerodynamics. AGARD CP-247, 1978.

9. Lambourne, N. C.; and Bryer, D. W.: Some Measurements in the Vortex Flow Generated by a Sharp Leading Edge Having 65 Degrees Sweep. A.R.C. Tech. Rept., C.P. 477, 1960.

10. Peckham, D. H.: Low-Speed Wind-Tunnel Tests on a Series of Uncambered Slender Pointed Wings with Sharp Edges. British A.R.C.-R.&M. No. 3161, 1961.

11. Squire, L. C.: Camber Effects on the Nonlinear Lift of Slender Wings with Sharp Leading Edges. ARC C.P. No. 924, Ministry of Technology (London), 1967.

12. Werlé, H.: Sur l'éclatement des tourbillons. ONERA N.T. 175, 1971.

13. Hummel, D.: Zur Umstromung Scharfkantiger schlanker Deltaflügel bei großen Anstellwinkeln. Z. Flugwiss.,Vol. 15, pp. 376-385, 1967.

14. Skow, A. M.; and Erickson, G. E.: Modern Fighter Aircraft Design for High-Angle-of-Attack Maneuvering. High Angle-of-Attack Aerodynamics, AGARD LS 121. Mar. 1982.

15. Manro, M. E.: Transonic Pressure Measurements and Comparison of Theory to Experiment for Three Arrow-Wing Configurations. Vol. I: Experimental Data Report-Basic Data and Effect of Wing Shape. NASA CR 165701, Nov. 1981.

16. Chambers, J. R.: Overview of Stall/Spin Technology. AIAA Paper No. 80-1580, 1980.

17. Rao, D. M.: Vortical Flow Management for Improved Configuration Aerodynamics-Recent Experiences. AGARD Symposium on Aerodynamics of Vortical Type Flows in Three Dimensions, Paper No. 30, 1983.

18. Brown, C. E.; and Michael, W. H.: On Slender Delta Wings with Leading Edge Separation. Journal of Aeronautical Sciences, Vol. 21, pp. 690-694, Oct. 1954.

19. Levinsky, E. S.; and Wei, M. H. Y.: Nonlinear Lift and Pressure Distribution on Slender Conical Bodies with Strakes at Low Speeds. NASA CR 1202, Oct. 1968.

20. Polhamus, E. C.: Predictions of Vortex-Lift Characteristics by a Leading-Edge Suction Analogy. J. Aircraft, Vol. 8, No. 4, pp. 193-199, April 1971.

21. Mook, D. T.; and Maddox, S. A.: Extension of a Vortex-Lattice Method to Include the Effects of Leading-Edge Separation. J. Aircraft, Vol. 11, No. 2, pp. 127-128, Feb. 1974.

22. Brune, G. W.; Weber, J. A.; Johnson, F. T.; Lu, P.; and Rubbert, P. E.: A Three-Dimensional Solution of Flows Over Wings with Leading-Edge Vortex Separation. NASA CR-132709, 197[illegible].

23. Kandil, O. A.: State of the Art of Nonlinear Discrete-Vortex Methods for Steady and Unsteady High Angle of Attack Aerodynamics. High Angle of Attack Aerodynamics, AGARD CP-247, Paper 005, Jan. 1979.

24. Gersten, K.: Calculation of Non-Linear Aerodynamic Stability Derivative of Aeroplanes. AGARD Rep. 342, April 1961.

25. Legendre, R.: Écoulement au voisinage de la pointe avant d'une aile a forte fleche aux incidences moyennes, Rech. Aero. 35, 1953.

26. Rehbach, C.: Numerical Investigation of Leading-Edge Vortex for Low-Aspect Ratio Thin Wings.AIAA Journal, Vol. 14, pp. 253-255, 1976.

27. Küchemann, D.: A Nonlinear Lifting Surface Theory for Wings of Small Aspect Ratio with Edge Separations. RAE Report Aero 2540, ARC 17769, 1955.

28. Mangler, K. W.; and Smith, J. H. B.: A Theory of Flow Past Slender Delta Wings with Leading-Edge Separation. Rept. Aero-2593, Royal Aircraft Establishment, Farnborough, England, 1957; also Proceedings of the Royal Society, London, A. 251, p. 200, May 1959.

29. Hall, M. G.: Vortex Breakdown. Ann. Rev. Fl. Mech., Vol. 4, pp. 195-218, 1972.

30. Hoeijmakers, H. W. M.; and Bennekers, B.: A Computational Method for the Calculation of the Flow about Wings with Leading-Edge Vortices. High Angle of Attack Aerodynamics, Paper No. 25, AGARD CP-247, Jan. 1979.

31. Belotserkovskii, S. M. (J. W. Palmer, transl.): Calculation of the Flow About Wings of Arbitrary Planform at a Wide Range of Angle of Attack. Libr. Transl. No. 1433, Brit. R.A.E., Feb. 1970.

32. Lamar, J. E.; and Luckring, J. M.: Recent Theoretical Developments and Experimental Studies Pertinent to Vortex Flow Aerodynamics-With a View Towards Design. High Angle of Attack Aerodynamics, AGARD CP-247, Paper No. 24, Jan. 1979.

33. Smith, J. H. B.: Improved Calculations of Leading-Edge Separation from Slender Delta Wings. R.A.E. - T.R. No. 66070, March 1966.

34. Mehrotra, S. C.; and Lan, C. E.: A Theoretical Investigation of the Aerodynamics of Low-Aspect-Ratio Wings with Partial Leading-Edge Separation. NASA CR-145304, Jan. 1978.

35. Johnson, F. T.; Lu, P. Tinoco, E. N.; and Epton, M. A.: An Improved Panel Method for the Solution of Three-Dimensional Leading-Edge Vortex Flows. Volume I.- Theory Document. NASA CR-3278, July 1980.

36. Luckring, J. M.; Schoonover, W. E., Jr.; and Frink, N. T.: Recent Advances in Applying Free Vortex Sheet Theory for the Estimation of Vortex Flow Aerodynamics. AIAA Paper No. 82-0095, 1982.

37. Lamar, J. E.; and Gloss, B. B.: Subsonic Aerodynamic Characteristics on Interacting Lifting Surfaces with Separated Flow Around Sharp Edges Predicted by Vortex-Lattice Method. NASA TN D-7921, Sept. 1975.

38. Lamar, J. E.; and Frink, N. T.: Aerodynamic Features of Designed Strake-Wing Configurations. J. Aircraft, Vol. 19, No. 8, pp. 639-646, Aug. 1982.

39. Lamar, J. E.; and Herbert, H. E.: Production Version of the Extended NASA-Langley Vortex Lattice FORTRAN Computer Program - Volume I.- User's Guide. NASA TM-83303, April 1982.

40. Lan, C. E.: A Quasi-Vortex-Lattice Method in Thin Wing Theory. J. Aircraft, Vol. 11, No. 9, pp. 518-527, Sept. 1974.

41. Woodward, F. A.; Tinoco, E. N.; and Larsen, J. W.: Analysis and Design of Supersonic Wing-Body Combinations, Including Flow Properties in the Near Field. Part I - Theory and Application. NASA CR-73106, Aug. 1967.

42. Lan, C. E.; and Chang, J. F.: VORCAM - A Computer Program for Calculating Vortex Lift Effect of Cambered Wings by the Suction Analogy. NASA CR-165800, Nov. 1981.

43. Lan, C. E.; Chang, J. F.: Calculation of Vortex Lift for Cambered Wings by the Suction Analogy. NASA CR-3449, July 1981.

44. Kulfan, R. M.: Wing Airfoil Shape Effects on the Development of Leading-Edge Vortices. AIAA Paper No. 79-1675, 1979.

45. Berndt, S. B.: Three Component Mesurement and Flow Investigation of Plane Delta Wings at Low Speeds and Zero Yaw. KTH-Aero TN 4, June 1948.

46. Henderson, W. P.: Effects of Wing Leading-Edge Radius and Reynolds Number on Longitudinal Aerodynamic Characteristics of Highly Swept Wing-Body Configurations at Subsonic Speeds. NASA TN D-8361, Dec. 1976.

47. Carlson, H. W.; and Mack, R. J.: Studies of Leading-Edge Thrust Phenomena. AIAA Paper No. 80-0325, 1980.

48. Carlson, H. W.; and Walkley, K. B.: A Computer Program for Wing Subsonic Aerodynamic Performance Estimates Including Attainable Thrust and Vortex Lift Effects. NASA CR-3515, March 1982.

49. Lan, C. E.; and Hsu, C. H.: Effects of Vortex Breakdown on Longitudinal and Lateral-Directional Aerodynamics of Slender Wings by the Suction Analogy. AIAA Paper No. 82-1385, 1982.

50. Wentz, W. H., Jr.; and Kohlman, D. L.: Wind-Tunnel Investigation of Vortex Breakdown on Slender Sharp-Edged Wings. NASA CR-98737, 1968.

51. Lan, C. E.: The Unsteady Suction Analogy and Applications. AIAA Paper No. 81-1875, 1981.

52. Lan, C. E.: The Unsteady Quasi-Vortex-Lattice Method with Applications to Animal Propulsion. Journal of Fluid Mechanics, Vol. 93, Part 4, p. 747, 1979.

53. Smith, J. H. B.: Attempted Design of a Slender Wing with Leading-Edge Separation. RAE T.R.-71079, April 1971.

54. Kuchemann, D.: On the Possibility of Designing Wings that Combine Vortex Flows with Classical Aerofoil Flows. RAE T.M. Aero 1363, Oct. 1971.

55. Lamar, J. E.: A Vortex-Lattice Method for the Mean Camber Shapes of Trimmed Noncoplanar Planforms with Minimum Vortex Drag. NASA TN D-8090, 1976.

56. Lamar, J. E.; Schemensky, R. T.; and Reddy, C. S.: Development of a Vortex-Lift Design Procedure and Application to a Slender Maneuver-Wing Configuration. J. Aircraft, Vol. 18, No. 12, pp. 259-266, April 1981.

57. Vanderplaats, G. N.: CONMIN - A FORTRAN Program for Constrained Function Minimization - User's Manual. NASA TM X-62282, 1973.

58. Chang, J. F.; and Lan, C. E.: Design of Wings with Vortex Separated Flow. Technical Report CRINC-FRL-426-3, Jan. 1983.

59. Frink, N. T.; and Lamar, J. E.: Water Tunnel Investigation of the Effect of Strake Design Variables on Strake Vortex-Breakdown Characteristics. NASA TP 1676, Aug. 1980.

60. Pao, J. L.; and Lan, C. E.: A Vortex-Filament and Core Model for Wings with Edge Vortex Separation. NASA CR-165847, Feb. 1982.

61. Reddy, C. S.: Aerodynamic Performance of Slender Wing with Separated Flows. Old Dominion University Research Foundation, Dept. of Mech. Eng. and Mechanics, Technical Report for the period ending August 31, 1981.

62. Robinson, A.; and Laurmann, J. A.: Wing Theory. Cambridge at the University Press, p. 323, 1956.

63. Jaquet, B. N.; and Bower, J. D.: Low-Speed Static-Stability and Rolling Characteristics of Low-Aspect-Ratio Wings of Triangular and Modified Triangular Planforms. NACA RN-L8L29, Dec. 1948.

64. Stahl, W.; Hartmann, K.; and Schneider, W.: Force and Pressure Measurements on a Slender Delta Wing at Transonic Speeds and Varying Reynolds Numbers. AGARD CP No. 83, Paper No. 9, April 1971.

65. Reddy, C. S.: Theoretical Study of Aeodynamic Characteristics of Wings Having Vortex Flow. NASA CR-159184, Nov. 1979.

66. Igglesden, M. S.: Wind-Tunnel Measurements of the Lift-Dependent Drag of Thin Conically Cambered Slender Delta Wings at Mach Numbers of 1.4 and 1.8. RAE, TN No. Aero. 2677, April 1960.

67. Frink, N. T.: Analytical Study of Vortex Flaps on Highly Swept Delta Wings. ICAS 82-6.7.2, 1982.

68. Rao, D. M.: Upper Vortex Flap - A Versatile Surface for Highly Swept Wings. ICAS 82-6.7.1., 1982.

69. Buter, T. A.; and Rao, D. M.: Experimental and Computational Investigation of an Apex Flap Concept on a 74^0 Delta Wing. NASA CR-166080, April 1983.

70. Zartarian, G.; Reutenik, J. R.; and Smiley, R. G.: Measurements of Blast Pressures on a Rigid 65^0 Sweptback Wing at Mach 0.76 from Rocket Propelled Sled Tests. Volume III--Correlation with the Doublet-Lattice Method in VIBRA-6. DNA 4400F3, Dec. 1977.

71. Luckring, J. M.: Aerodynamics of Strake-Wing Interactions. J. Aircraft, Vol. 16, No. 11, pp. 756-762, Nov. 1979.

72. Lamar, J. E.: Analysis and Design of Strake-Wing Configurations. J. Aircraft, Vol. 17, No. 1, pp. 20-27, Jan. 1980.

73. Johnson, F. T.; and Tinoco, E. N.: Recent Advances in the Solution of Three-Dimensional Flows over Wing with Leading Edge Vortex Separation. AIAA Paper No. 79-0282, 1979.

74. Manro, M. E.: Aeroelastic Loads Prediction for an Arrow Wing. Task III - Evaluation of the Boeing Three-Dimensional Leading-Edge Vortex Core. NASA CR-3642, Jan. 1983.

75. Wery, A. C.; and Kulfan, R. M.: Aeroelastic Loads Prediction for an Arrow Wing. Task II - Evaluation of Semi-Empirical Methods. NASA CR-3641, Jan. 1983.

76. Borland, C. J.: Aeroelastic Loads Prediction for an Arrow Wing. Task I - Evaluation of R. P. White's Method. NASA CR-3640, Jan. 1983.

77. White, R. P., Jr.: Prediction and Measurement of the Aerodynamic Forces and Pressure Distributions of Wing-Tail Configurations at Very High Angle of Attack. AGARD CP-247, Oct. 1978.

78. White, R. P., Jr.: An Experimental Investigation of Vortex Flow Control for High Lift Generation. ONR CR-212-223-2, Dec. 1975.

79. Tosti, L. P.: Low-Speed Static Stability and Damping-in-Roll Characteristics of Some Swept and Unswept Low-Aspect-Ratio Wings. NACA TN-1468, Oct. 1947.

80. Owen, T. B.: Low-Speed Wind-Tunnel Measurements of Oscillatory Rolling Derivatives on a Sharp-Edged Slender Wing. Effects of Frequency Parameter and of Ground. British Aeronautical Research Council, Reports and Memoranda No. 3617, 1968.

81. Dee, F. W.; and Nicholas, O. P.: Flight Determination of Wing Flow Patterns and Buffet Boundaries for the Fairey Delta-2 Aircraft at Mach Numbers Between 0.4 and 1.3, and Comparison with Wind-Tunnel Results. RAE R. and M. No. 3482, Sept. 1964.

82. Polhamus, E. C.; and Gloss, B. B.: Configuration Aerodynamics. High Reynolds Number Research - 1980. NASA CP-2183, pp. 217-234, Dec. 1980.

83. Rao, D. M.: Leading-Edge Vortex Flap Experiments on a 74-Deg. Delta Wing. NASA CR-159161, Nov. 1979.

84. Rao, D. M.: Leading-Edge Vortex Flaps for Enhanced Subsonic Aerodynamics of Slender Wings. ICAS 80-13.5, 1980.

85. Smith, C. W.; Campbell, J. F.; and Huffman, J. K.: Experimental Results of a Leading Edge Vortex Flap on a Highly Swept Cranked Wing. Tactical Aircraft Research and Technology. NASA CP-2162, 1980.

86. Schoonover, W. E., Jr.; and Ohlson, W. E.: Wind-Tunnel Investigation of Vortex Flaps on a Highly Swept Interceptor Configuration. ICAS 82-6.7.3, 1982.

87. Frink, N. T.; Huffman, J. K.; and Johnson, T. D, Jr.: Vortex Flow Reattachment Line and Subsonic Aerodynamic Data for Vortex Flaps on 50^0 to 74^0 Delta Wings on Common Fuselage. NASA TM-84618, 1983.

88. Grantz A. C.; and Marchman, J. F., III: Trailing Edge Flap Influence on Leading-Edge Vortex Flap Aerodynamics. J. Aircraft, Vol. 20, No. 2, pp. 165-169, Feb. 1983.

89. Runyan, L. J.; Middleton, W. D.; and Paulson, J. A.: Wind Tunnel Test Results of a New Leading Edge Flap Design for Highly Swept Wings - A Vortex Flap. Supersonic Cruise Research '79 - Part 1, NASA CP-2108, pp. 131-147, Nov. 1980.

90. Yip, L. P.; and Murri, D. G.: Effects of Vortex Flaps on the Low-Speed Aerodynamic Characteristics of an Arrow Wing. NASA TP-1914, Nov. 1981.

91. Rao, D. M.: Exploratory Subsonic Investigation of Vortex-Flap Concept on Arrow Wing Configuration. Supersonic Cruise Research '79 - Part 1, NASA CP-2108, pp. 117-129, Nov. 1980.

92. Rao, D. M.: Segmented Vortex Flaps. AIAA Paper No. 83-0424, 1983.

93. Lamar, J. E.; and Campbell, J. F.: Design Related Study of Transonic Maneuvering Slender Wings Having Vortex Flaps. Tactical Aircraft Research and Technology, Vol. 1, NASA CP-2162 Part 2, pp. 543-562, 1980.

94. Johnson, T. D.; and Rao, D. M.: Experimental Study of Delta Wing Leading-Edge Devices for Drag Reduction at High Lift. NASA CR-165846, Feb. 1982.

95. Tingas, S. A.; and Rao, D. M.: Subsonic Balance and Pressure Investigation of a 60-Degree Delta Wing with Leading-Edge Devices. NASA CR-165923, May 1982.

96. Rao, D. M.; and Johnson, T. D.: Investigation of Delta Wing Leading-Edge Devices. J. Aircraft, Vol. 18, No. 3, pp. 161-167, March 1981.

97. Rao, D. M.; and Johnson, T. D.: Alleviation of the Subsonic Pitch-Up of Delta Wings. AIAA Paper No. 82-0129, 1982.

98. Mann, M. J.; Mercer, C. E.; and Campbell, R. L.: Supercritical Maneuvering Fighter Configuration Wind-Tunnel Investigation at Mach Numbers of 0.60 to 0.95. NASA TM-84513, Sept. 1982.

99. Lamar, J. E.: Vortex-Lift Roll-Control Device. U.S. Patent 4,132,375, Jan. 1979.

100. Lamar, J. E.: Prediction of Vortex Flow Characteristics of Wings at Subsonic and Supersonic Speeds. J. Aircraft, Vol. 13, No. 7, pp. 490-494, July 1976.

101. Lamar, J. E.; and Frink, N. T.: Experimental and Analytical Study of the Longitudinal Aerodynamic Characteristics of Analytically and Empirically Designed Strake-Wing Configurations at Subcritical Speeds. NASA TP 1803, June 1981.

102. Small, W. J.; Riebe, G. D.; and Taylor, A. H.: Aerodynamics of a Turbojet-Boosted Launch Vehicle Concept. Journal of Spacecraft and Rockets, Vol. 18, No. 1, pp. 36-43, Jan.-Feb. 1981.

103. Jackson, L. R.; Weidner, J. P.; Small, W. J.; and Martin, J. A.: Orbiter/Launch System. U.S. Patent 4,265,416, May 1981.

104. Huffman, J. K.; and Fox, C. H.: Subsonic Longitudinal and Lateral-Directional Static Aerodynamic Characteristics for a Model with Swept Back and Swept Forward Wings. NASA TM-74093, 1978.

105. Moss, G. F.: Some UK Research Studies of the Use of Wing-Body Strakes on Combat Aircraft Configurations at High Angles of Attack. AGARD CP-No. 247, Paper No. 4, Oct. 1978.

106. Rao, D. M.; and Huffman, J. K.: Hinged Strakes for Enhanced Maneuverability at High Angles of Attack. J. Aircraft, Vol. 19, No. 4, April 1982.

107. Huffman, J. K.; Fox, C. H., Jr.; and Ziegler, H.: Subsonic Longitudinal and Lateral-Directional Static Aerodynamic Characteristics of a General Research Fighter Configuration Employing a Jet Sheet Vortex Generator. NASA TM-74049, Jan. 1978.

108. Ziegler, H.; and Wooler, P. T.: Aereodynamic Characteristics of a Jet Sheet Vortex Generator. NASA CR-158904, June 1978.

109. Campbell, J. F.: Augmentation of Vortex Lift by Spanwise Blowing. J. Aircraft Vol. 13, No. 9, pp. 727-732, Sept. 1980.

110. Erickson. G. E.; and Campbell, J. F.: Improvement of Maneuver Aerodynamics by Spanwise Blowing. NASA TP 1065, Dec. 1977.

111. Staudacher, W.; et al.: Aerodynamic Characteristics of a Fighter-Type Configuration During and Beyond Stall. AGARD CP No. 247, Paper No. 8, Oct. 1978.

112. Anglin, E. L.; and Satran D.: Effects of Spanwise Blowing on Two Fighter Airplane Configurations. J. Aircraft, Vol. 17, No. 12, pp. 883-889, Dec. 1980.

113. Hummel, D.: Study of the Flow Around Sharp-edged Slender Delta Wings with Large Angles of Attack. NASA TT F-15, 107, Sept. 1973.

114. Taylor, A. H.; Jackson, L. R.; and Huffman, J. K.: Vortex Lift Augmentation by Suction on a 60^0Swept Gothic Wing. AIAA Paper No. 82-0231, 1982.

115. Edwards, O. R.: Northrop F-5F Shark Nose Development. NASA CR-158936, Oct. 1978.

116. Erickson, G. E.: Water Tunnel Flow Visualization and Wind Tunnel Data Analysis of the F/A-18. NASA CR-165859, May 1982.

117. Carr, P. C.; Gilbert, W. P.: Effects of Fuselage Forebody Geometry on Low-Speed Lateral-Directional Characteristics of Twin-Tail Fighter Model at High Angles of Attack. NASA TP-1592, Dec. 1979

118. Grafton S. B.; Chambers, J. R.; and Coe, P. L., Jr.: Wind-Tunnel Free-Flight Investigation of a Model of a Spin-Resistant Fighter Configuraton. NASA TN D-7716, June 1974.

119. Hitzel, S. M.; and Schmidt W.: Slender Wings with Leading-Edge Vortex Separation - A Challenge for Panel-Methods and Euler-Codes. AIAA Paper No. 83-0562, 1983.

- THEORETICAL METHODS EXTENDED - DESIGN APPLICATION
- VALIDATION AND APPLICATION OF THEORETICAL METHODS
- VORTEX CONTROL DEVICES
- FUTURE NEEDS
- CONCLUDING REMARKS

Fig. 1.- Recent studies at NASA-Langley of vortical flows interacting with neighboring surfaces.

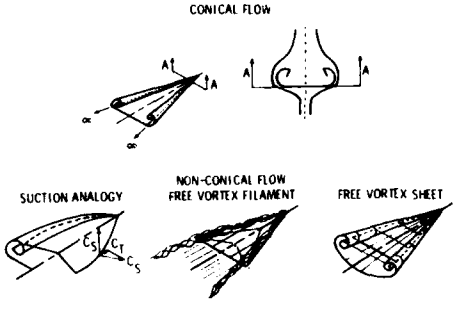

Fig. 2.- Theoretical methods extended.

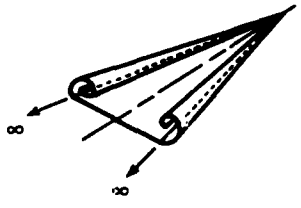

- TRIGONOMETRIC TERMS INVOLVING α INCLUDED
- PRESSURES EVALUATED WITH FULL ISENTROPIC EXPRESSION
- SECONDARY VORTEX SEPARATION LINE STUDY DeJARNETTE NCSU

Fig. 3.- Conical flow extensions.

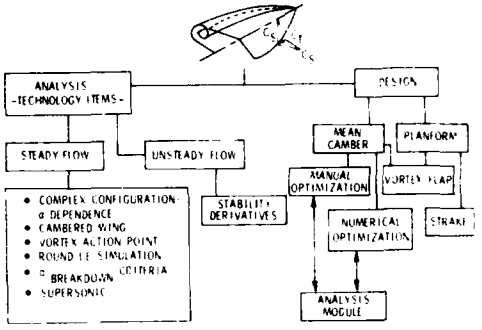

Fig. 4.- Suction analogy extensions; SA.

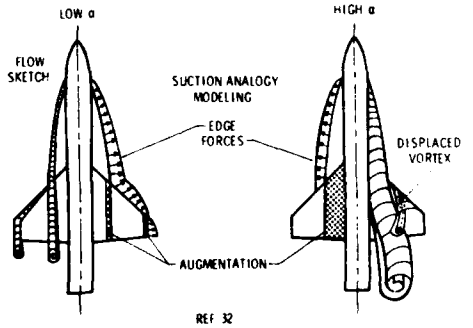

Fig. 5.- Effect of α on vortex flow models for complex configurations; VLM-SA/Lamar, Luckring.

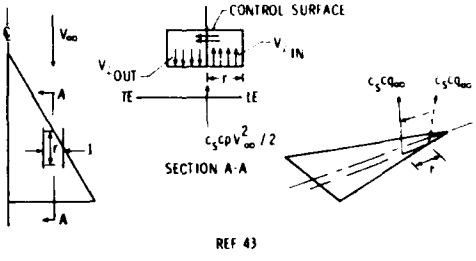

Fig. 6.- Vortex action point concept; Lan.

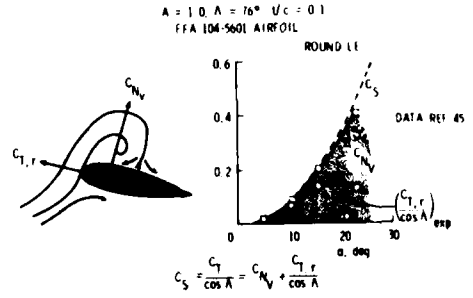

Fig. 7.- Relationship between vortex normal force and residual thrust.

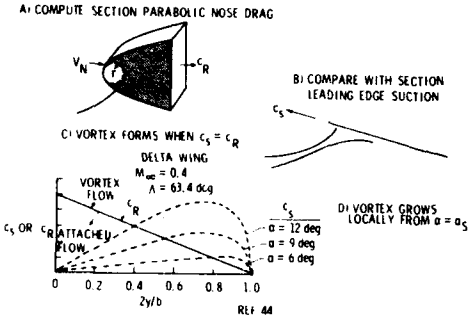

Fig. 8.- Kulfan's method of predicting vortex normal force.

Fig. 11.- Designed transonic-maneuver wing on fuselage; 3/4 front view, VLM-SA.

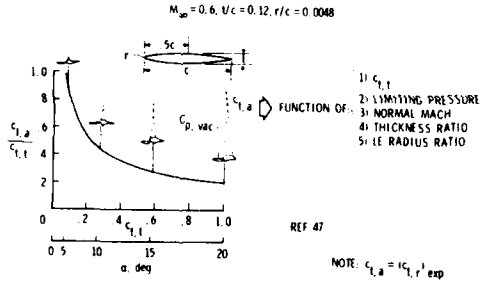

Fig. 9.- Carlson's method for predicting residual thrust.

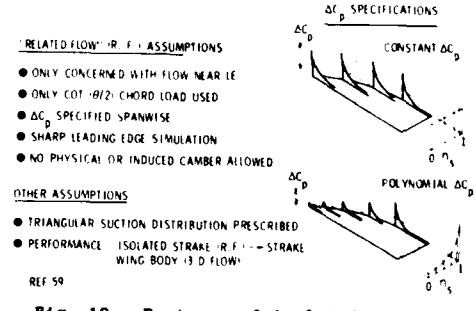

Fig. 12.- Features of isolated strake design process.

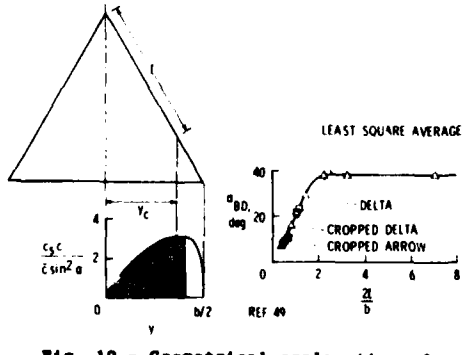

Fig. 10.- Geometrical explanation of Lan's α_{BD} criteria.

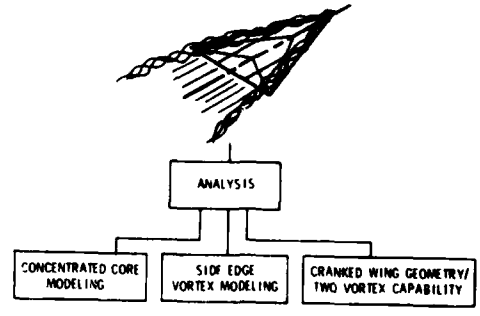

Fig. 13.- Free vortex filament extensions; QVLM-SF/Pao.

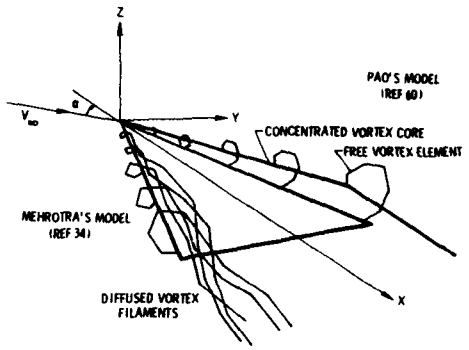

Fig. 14.- Concentrated core modeling.

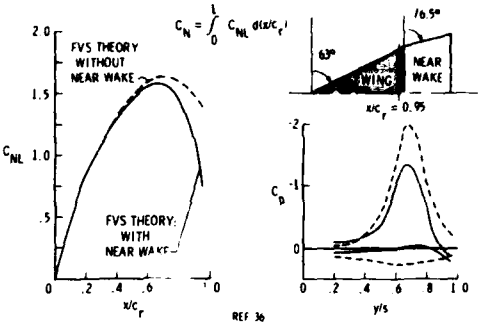

Fig. 17.- Effect of near wake model on load distributions; A = 2.04, $\alpha = 20^0$, $M_\infty = 0.3$

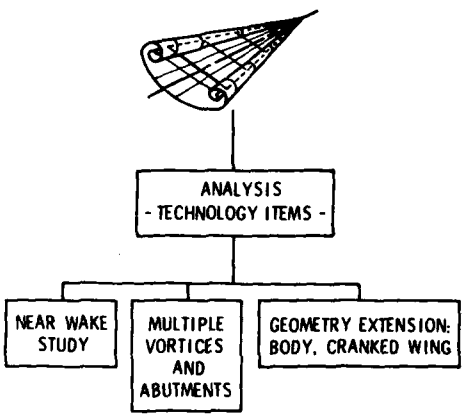

Fig. 15.- Free vortex sheet extensions; FVS.

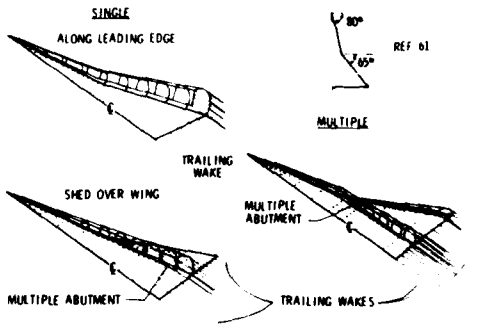

Fig. 18.- Cranked wing leading edge vortex modeling; A = 1.60, $M_\infty = 0$, FVS.

- FORCE AND MOMENT - LONGITUDINAL
- SURFACE PRESSURES
- VORTEX CORE LOCATION
- MOMENTS DUE TO LATERAL MOTION
- REYNOLDS NUMBER EFFECTS

Fig. 19.- Validation/application of theoretical methods.

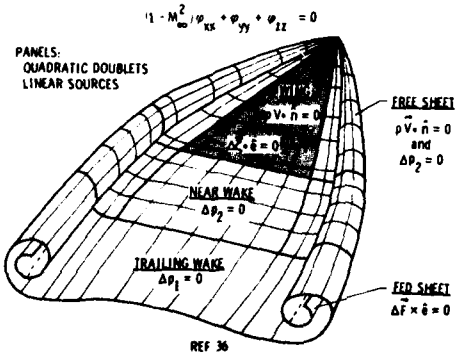

Fig. 16.- Theoretical formulation-panel method-FVS.

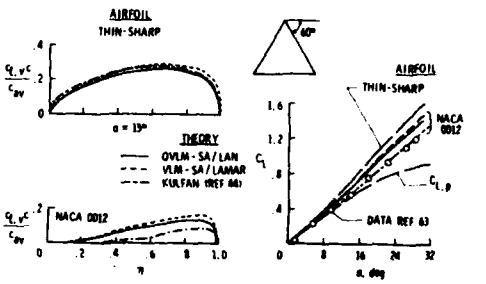

Fig. 20.- Effect of round LE modeling on vortex lift, A = 2.31, $M_\infty = 0$.

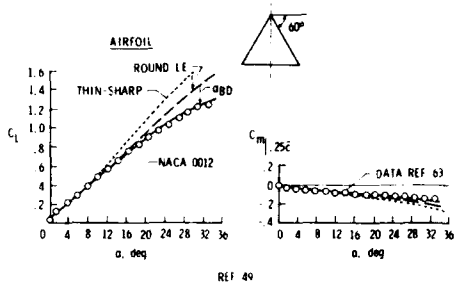

Fig. 21.- Longitudinal aerodynamic characteristics of 60^0 delta with round LE; A = 2.31, M_∞ = 0, QVLM-SA.

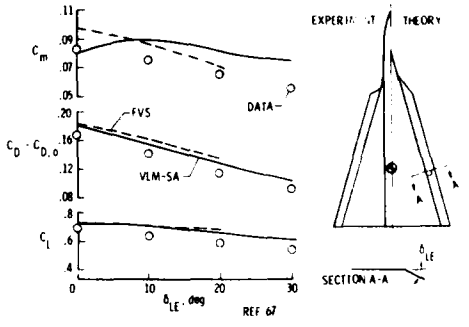

Fig. 24.- Longitudinal aerodynamic characteristics of 74^0 delta with deflectable constant-chord vortex flap; $\alpha = 14^0$, $M_\infty = 0.3$.

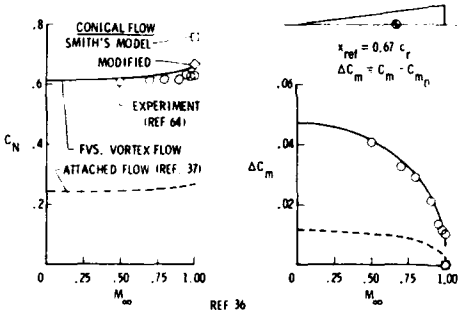

Fig. 22.- Compressibility effects on forces and moments; A = 0.516 delta, $\alpha = 20.8^0$.

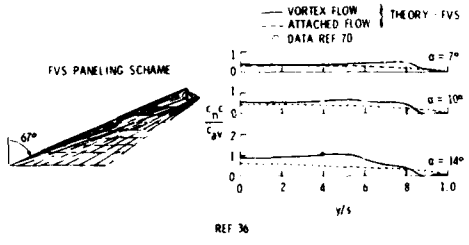

Fig. 25.- Span load distribution for arrow wing; A = 2.43, $\Lambda = 67^0$, $\lambda = 0.37$, $M_\infty = 0.76$.

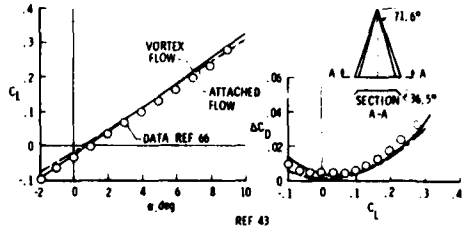

Fig. 23.- Longitudinal aerodynamic characteristics of delta wing with conical LE flap; A = 1.333, M_∞ = 1.4, VORCAM/Lan.

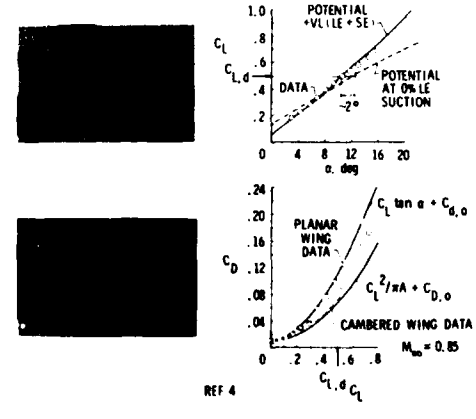

Fig. 26.- Longitudinal aerodynamic characteristics for designed transonic-maneuver wing; A = 1.383, $\Lambda_{LE} = 76.6^0/66.6^0$, $C_{L,d} = 0.50$, $M_d = 0.90$, VLM-SA.

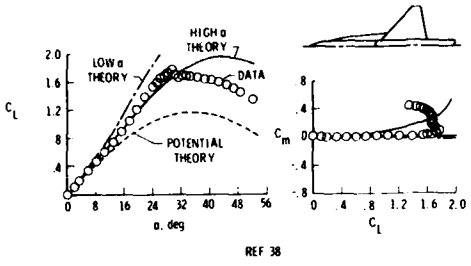

Fig. 27.- Longitudinal aerodynamic characteristics for AD 19 strake-wing-body configuration; wing A = 2.5, $\Lambda = 44^0$, $\lambda = 0.2$, $M_\infty = 0.2$.

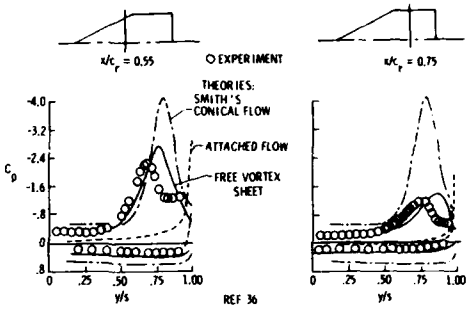

Fig. 30.- Spanwise pressure distribution on cropped delta wing; $\Lambda = 63^0$, $\lambda = 0.4$, $\alpha = 20^0$, $M_\infty = 0.3$.

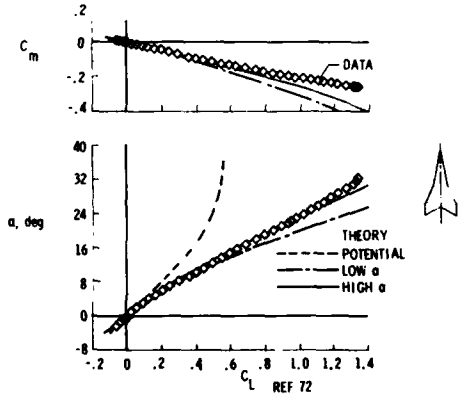

Fig. 28.- Longitudinal aerodynamic characteristics for cranked wing; A = 1.10, $\Lambda_{LE} = 80^0/65^0$, $M_\infty = 0$, VLM-SA.

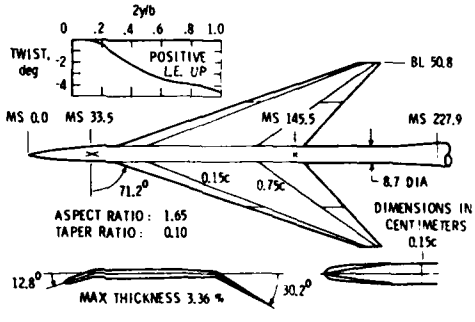

Fig. 31.- NASA/Boeing arrow wing general arrangement and characteristics.

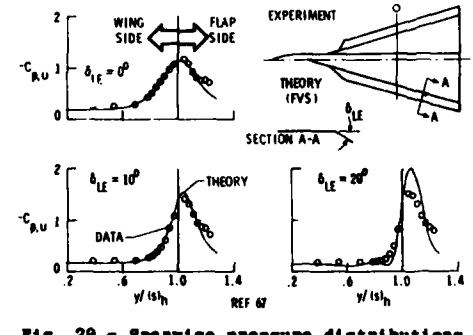

Fig. 29.- Spanwise pressure distributions on 74^0 delta with constant-chord vortex flap; $\alpha = 14^0$, $M_\infty = 0.3$.

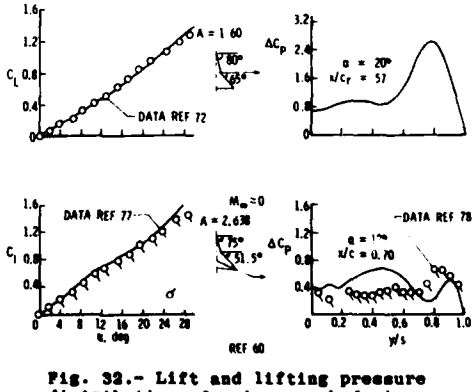

Fig. 32.- Lift and lifting pressure distributions for two cranked wings; $M_\infty = 0$, QVLM-SF/two vortex model.

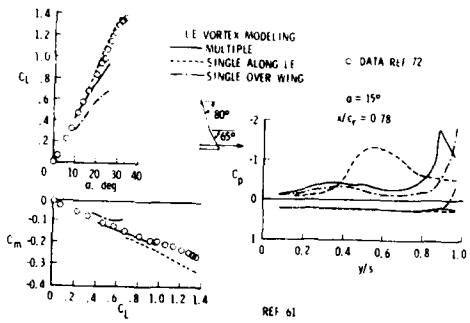

Fig. 33.- Longitudinal aerodynamic characteristics and surface pressures on cranked wing; A = 1.60, M_∞ = 0, FVS.

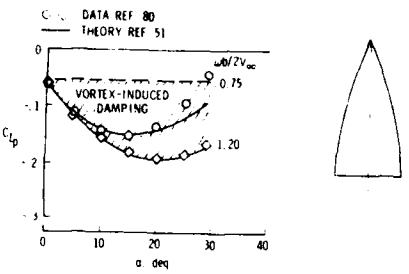

Fig. 36.- Oscillatory roll damping for gothic wing; A = 0.75, M_∞ = 0, Unsteady SA/Lan.

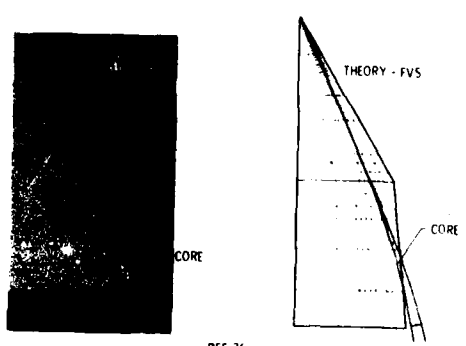

Fig. 34.- Vortex core trajectory; A = 63°, λ = 0.4, α = 20°, M_∞ = 0.3.

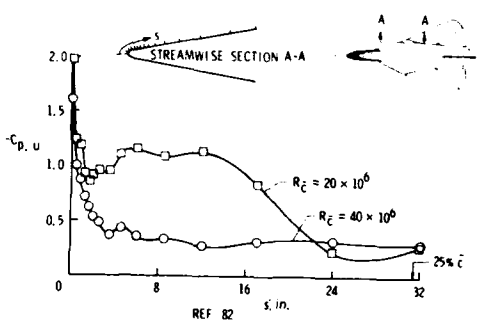

Fig. 37.- Effect of Reynolds number on vortex flow development--F-111 TACT flight experiment-; α = 6°, M_∞ = 0.6.

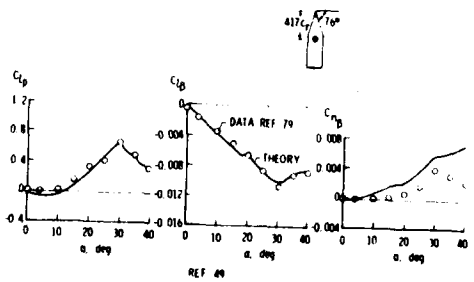

Fig. 35.- Stability derivatives for cropped delta; A = 0.333, λ = 0.5, β = 5°, M_∞ = 0, QVLM-SA.

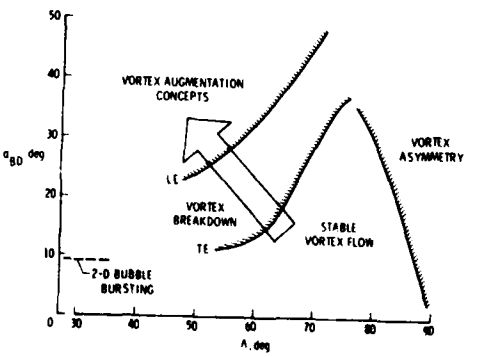

Fig. 38.- LE vortex breakdown trends for sharp-edge deltas; M_∞ = 0.

- ENHANCED WING LOW - TO - MODERATE α CHARACTERISTICS
  - VORTEX FLAPS
  - VORTEX GENERATORS
  - LEADING EDGE EXTENSION FOR TRANSONIC FIGHTER
- ENHANCED WING-BODY HIGH α CHARACTERISTICS
  - LEADING - EDGE EXTENSION FOR LOW SPEED GLIDER
  - RAKED TIP
  - STRAKES
  - JET AUGMENTATION
  - FUSELAGE FOREBODY SHAPING

Fig. 39.- Vortex control devices.

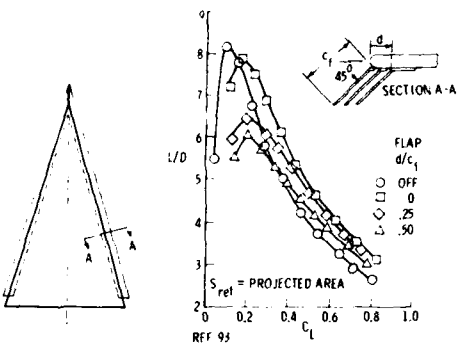

Fig. 42.- Effect of hinge-line location on maneuver L/D; 74°delta, M_∞ = 0.2.

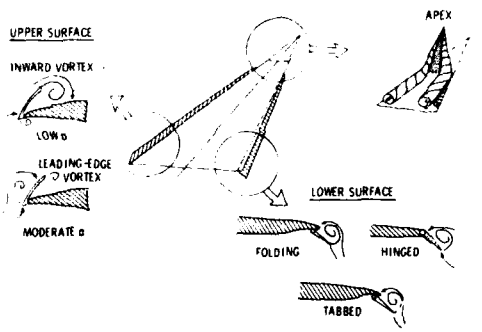

Fig. 40.- Types of vortex flaps--flow patterns-.

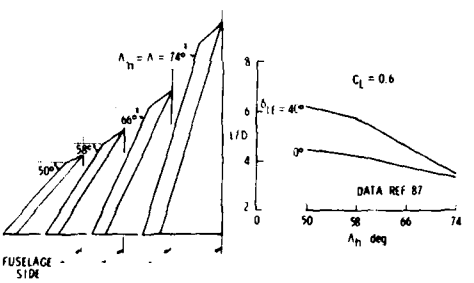

Fig. 43.- Effect of hinge-line sweep and vortex flap deflection angle on wing performance; M_∞ = 0.3.

Fig. 41.- Characteristics of various vortex flap geometries--lower surface-.

Fig. 44.- Vortex generators.

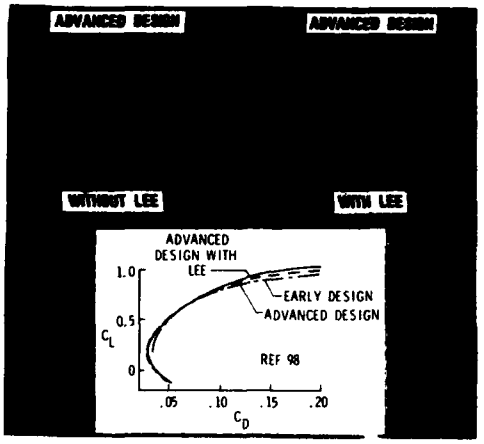

Fig. 45.- Effect of Leading-Edge Extension (LEE) on drag polar for a thin transonic fighter; A = 3.28, $\Lambda = 45^0$, $\lambda = 0.21$, $M_\infty = 0.85$.

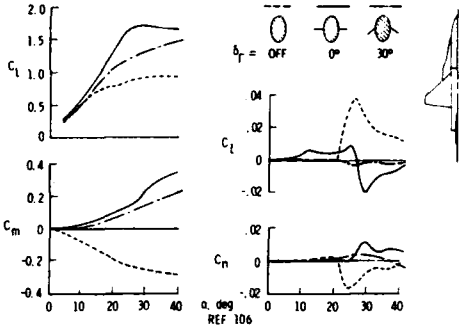

Fig. 48.- Effect of hinged-strake on high α aerodynamic characteristics; wing A = 2.5, $\Lambda = 44^0$, $\beta = 0^0$, $M_\infty = 0.30$.

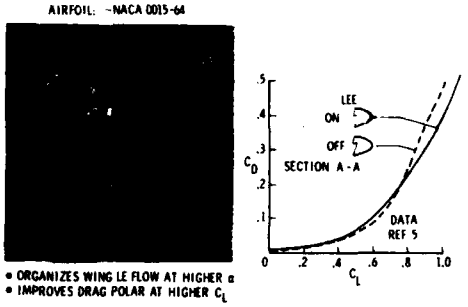

Fig. 46.- Effect of LEE on drag polar for thick low-speed glider (DM-1); A = 1.80, $\Lambda = 60^0$, $M_\infty = 0$.

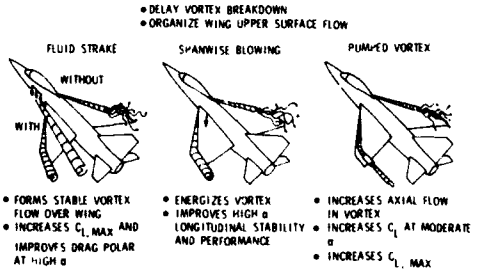

Fig. 49.- Jet-augmented vortex concepts.

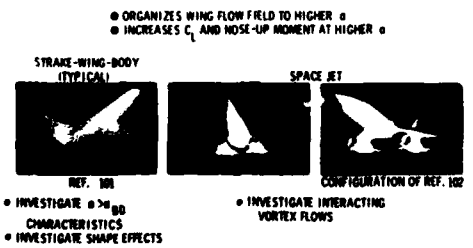

Fig. 47.- Use of strake.

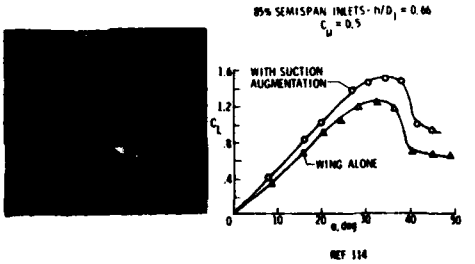

Fig. 50.- Effect of pumped vortex on blended-delta lift characteristics; $M_\infty = 0.15$.

- THEORETICAL EXTENSIONS/VALIDATIONS WITH VORTEX FLOWS
  - INCORPORATE VISCOUS EFFECTS
    - VORTEX ONSET - ROUND LE
    - ASYMMETRICAL SHEDDING
    - SECONDARY VORTEX
    - VORTEX BREAKDOWN
  - ESTABLISH UNIQUE EULER CODE CAPABILITIES
    - SHOCK AND VORTEX INTERACTION
    - MULTIPLE SYSTEMS
    - THICK WINGS
  - EXTEND HIGHER ORDERED CODES TO INCLUDE UNSTEADY MOTIONS WITH VORTEX FLOW
  - VALIDATE FVS METHOD
    - THICKNESS AND FUSELAGE EFFECTS
    - MULTIPLE OR INTERFERING LIFTING SURFACES

Fig. 51.- Future needs, (1).

- THEORETICAL EXTENSIONS/VALIDATIONS WITH VORTEX FLOWS
  - DESIGN ACTIVITY
    - THICK WING
    - LEADING-EDGE EXTENSIONS AND VORTEX FLAPS
- EXTEND VORTEX CONTROL DATA BASE TO INCLUDE
  - EFFECT OF WING SECTION SHAPE, PLANFORM AND VORTEX AUGMENTATION ON BREAKDOWN AND ASYMMETRY
  - OFF SURFACE FLOW DATA
  - CONFIGURATION AND MOTION EXTENSIONS
  - HIGH REYNOLDS NUMBER TESTING

Fig. 52.- Future needs, (2).

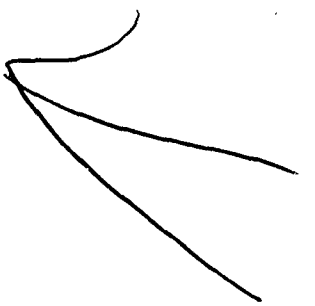

EXPERIMENTAL INVESTIGATION OF FOREBODY AND WING LEADING-EDGE VORTEX INTERACTIONS AT HIGH ANGLES OF ATTACK*

by
Gary E. Erickson, Senior Engineer
Aerodynamics Research Department
3812/82
Northrop Corporation, Aircraft Division
One Northrop Avenue
Hawthorne, California 90250
USA
and
William P. Gilbert, Assistant Head
Flight Dynamics Branch
Mail Stop 355
NASA Langley Research Center
Hampton, Virginia 23665
USA

SUMMARY

An experimental investigation was conducted to assess the vortex flow-field interactions on an advanced, twin-jet fighter aircraft configuration at high angles of attack. Flow-field surveys were conducted on a small-scale model in the Northrop 0.41- by 0.60-meter water tunnel and, where appropriate, the qualitative observations were correlated with low-speed wind tunnel data trends obtained on a large-scale model of the advanced fighter in the NASA Langley Research Center 30- by 60-foot (9.1- by 18.3-meter) facility. Emphasis was placed on understanding the interactions of the forebody and LEX-wing vortical flows, defining the effects on rolling moment variation with sideslip, and identifying modifications to control or regulate the vortex interactions at high angles of attack.

The water tunnel flow visualization results and wind tunnel data trend analysis revealed the potential for strong interactions between the forebody and LEX vortices at high angles of attack. In particular, the forebody flow development near the nose could be controlled by means of carefully-positioned radome strakes. The resultant strake-induced flow-field changes were amplified downstream by the more powerful LEX vortical motions with subsequent large effects on wing flow separation characteristics.

SYMBOLS

C_l – Rolling Moment Coefficient

C_{l_β} – Lateral Stability Parameter ($\partial C_l / \partial \beta$)

C_L – Lift Coefficient

C_n – Yawing Moment Coefficient

C_Y – Side Force Coefficient

$Re_{\bar{c}}$ – Reynolds Number Based on Mean Aerodynamic Chord

V_∞ – Free-Stream Speed, Meters/Second

α – Angle of Attack, Degrees

β – Angle of Sideslip, Degrees

δ_n – Leading-Edge Flap Deflection, Degrees

ϕ – Forebody Strake Radial Position, Degrees

INTRODUCTION

Current and future fighter aircraft with the requirement for subsonic-transonic maneuver capability are characterized at moderate-to-high angles of attack by organized flow separation in the form of concentrated vortices shed from slender fuselage forebodies, wings, canards, and wing leading-edge extensions (LEXs). These vortical motions induce highly-nonlinear longitudinal and lateral-directional characteristics. Contributing to the complexity of the three-dimensional flow-field are vortex trajectory asymmetries, vortex breakdown and breakdown asymmetries, and interactions of multiple vortices. Current fighters and designs for future fighter aircraft are, and will be, operating at increasing angles of attack above maximum lift, where such nonlinear flow-fields exist. Obtaining a working understanding of the principal fluid-dynamic phenomena is a necessity for developing aircraft designs having desirable stability and control characteristics. A primary objective of this study is to improve this understanding.

* This work was performed for NASA Langley Research Center under NASA Contract NAS1-16617, Mr. William P. Gilbert, NASA Technical Monitor. Contract results are documented in NASA CR-163899, May 1982.

This paper will discuss (1) representative results obtained in detailed water tunnel flow visualization studies of a small-scale model of a current, twin-engine advanced fighter configuration, and (2) correlations of the qualitative flow-field observations with low-speed wind tunnel data trends obtained on a large-scale model of the same fighter.

The paper will commence with a brief discussion of the confidence with which a water tunnel was utilized in the present investigation. A discourse on uncoupled and coupled forebody and LEX-wing vortex flows will be presented along with factors contributing to vortex interaction. The advanced fighter model and associated model changes will be described, and this will be followed by discussions of flow-field results obtained on the baseline model and the model with forebody geometry modifications. The paper will conclude with a presentation of Northrop low-speed wind tunnel test results on advanced fighter models that support the main findings of the present investigation.

I. WATER TUNNEL UTILITY IN THE STUDY OF VORTICAL MOTIONS AT HIGH ANGLES OF ATTACK

The complex vortex interactions on LEX-wing fighter configurations at high angles of attack are not well understood due to the difficulty, using present-day wind tunnel flow visualization techniques, in visualizing in a vivid manner highly-three-dimensional vortical motions. For the present study, the Northrop water tunnel facility was selected to provide the required detailed visualization of the vortex flow-field.

At the angles of attack of primary interest (30 to 40 degrees), significant regions of organized flow separation are developed on the slender forebody and LEX surfaces regardless of Reynolds number value. The dominant vortical flow is shed from the sharp edges of the leading-edge extensions and, consequently, the overall behavior of the LEX vortices is relatively insensitive to Reynolds number. Consideration of these factors led to the hypothesis that the water tunnel operating at low speed would provide valid qualitative information regarding the fundamental vortex flow behavior including the vortex interactions at higher Reynolds number conditions.

Support of the above hypothesis and a detailed account of the application of water tunnels to the understanding of high angle-of-attack vortex flows are provided in a United States Air Force-funded study conducted by Northrop. Results are documented in References 1 and 2.

II. UNCOUPLED AND COUPLED FOREBODY AND LEX VORTEX FLOWS

Uncoupled Vortex Flows. Figure 1 presents a flight photograph of a current fighter aircraft configuration. The water tunnel photograph in Figure 2 illustrates the vortex flows about a small-scale model of this fighter configuration near stall angle of attack. The forebody and LEX vortex systems are essentially uncoupled at high attitudes. One reason for this is that the LEX vortex under steady flow conditions* cannot persist to angles of attack in excess of 30 degrees due to LEX area limitations. Additional factors contributing to absence of strong forebody and LEX vortex interaction are related to the LEX surface location in relation to the fuselage forebody and include: (1) low wing position, and (2) aft and outboard LEX positioning dictated by the side-mounted engine inlets. Consequently, this type configuration is characterized by two specific angle-of-attack regimes within which either the LEX vortices or forebody vortices are dominant.

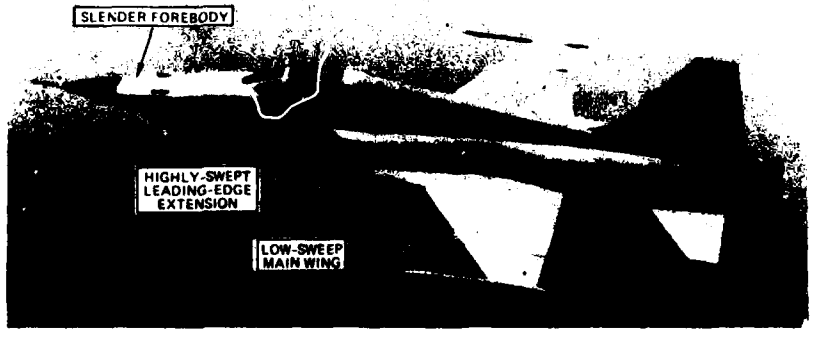

FIGURE 1. FLIGHT PHOTOGRAPH OF CURRENT FIGHTER AIRCRAFT

* Under dynamic flow conditions, the LEX vortices can persist to much nigher angles of attack (see Reference 3, for example).

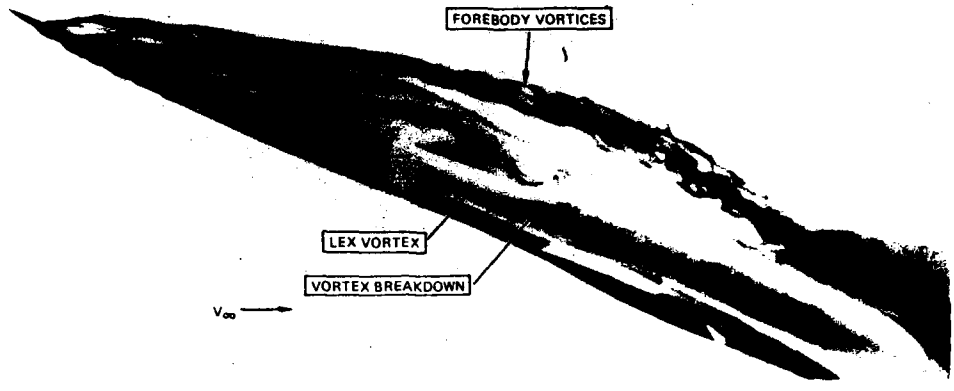

FIGURE 2. UNCOUPLED FOREBODY AND LEX VORTEX FLOWS

The forebody vortices, which dominate at high angles of attack, can shed asymmetrically at zero sideslip if the forebody is sufficiently slender. This flow asymmetry, depicted in Figure 3, is not related to any influence of the LEX-wing flow-field but, instead, is due in large part to an apparent inviscid hydrodynamic instability phenomenon (see Reference 4). The forebody primary vortex orientation can be tailored by means of forebody shaping, a case in point being Northrop's new F-20A Tigershark forebody design. Wind tunnel and flight test results documented in Reference 5 showed that forebody geometry changes influenced primarily the yawing moment and side force characteristics with a lesser effect on rolling moment. The data suggest, therefore, only a weak interaction between the forebody and wing flow-fields.

Coupled Vortex Flows. The vortex flow-field at high angles of attack is more complex on advanced fighter aircraft that are characterized by large LEXs in proximity to the fuselage forebody as illustrated in the flight photograph in Figure 4. Such configurations can develop strong flow interactions throughout the extended angle of attack range owing to the persistence of the vortical motions and their proximity to one another. An example of the strong coupling of forebody and LEX vortices on a scale model of the aircraft shown in Figure 4 is provided by the water tunnel photograph in Figure 5. The flow-field is characterized by symmetric forebody vortex shedding at zero sideslip and entrainment of this vortex pair by the dominant LEX vortical flows. It will be shown in the following sections that this multiple-vortex interaction can be very sensitive to geometric sideslip. Furthermore, modulation of the forebody vortex orientation in sideslip can, under certain conditions, influence the wing stall behavior and, hence, rolling moment characteristics.

III. TEST CONFIGURATIONS

The twin-jet, advanced fighter configuration is illustrated in Figure 6. Water tunnel flow-field surveys were conducted on a 0.025-scale model in the Northrop 0.41- by 0.60-meter facility at a free-stream speed of 0.1 meter per second corresponding to a Reynolds number of approximately 10^4 based on mean aerodynamic chord. The model forebody was instrumented with six flush dye orifices in each of two longitudinal rows positioned on either side of the bottom meridian with mirror image orifice positions on the forebody upper surface. Each LEX was instrumented with three external dye ports suitably positioned on the lower surface near the leading edge to depict the vortex core and vortex roll-up. Suction tubes were applied to the model exhaust nozzles to provide inlet suction to simulate a realistic inlet mass flow ratio. Leading- and trailing-edge flaps were deflected 35 degrees and 0 degrees, respectively. This configuration is referred to as the baseline model.

Low-speed wind tunnel tests were conducted by NASA on a 0.16-scale model of the fighter configuration in Figure 6 in the Langley 30- by 60-foot (9.1- by 18.3-meter) facility. Tests were conducted at a free stream speed of approximately 28 meters per second corresponding to a Reynolds number of 1.1 (10^6) based on mean aerodynamic chord.

Water tunnel and wind tunnel results will also be presented for the configuration with forebody strakes mounted 40 degrees above the maximum half breadth (MHB) and strakes mounted along the MHB. The strakes are depicted in Figure 7.

AD A135 157 AERODYNAMICS OF VORTICAL TYPE FLOWS IN THREE DIMENSIONS: CONFERENCE PROCE..(U) ADVISORY GROUP FOR AEROSPACE RESEARCH AND DEVELOPMENT NEUILLY.. JUL 83

UNCLASSIFIED AGARD-CP-342 F/G 20/4 NL

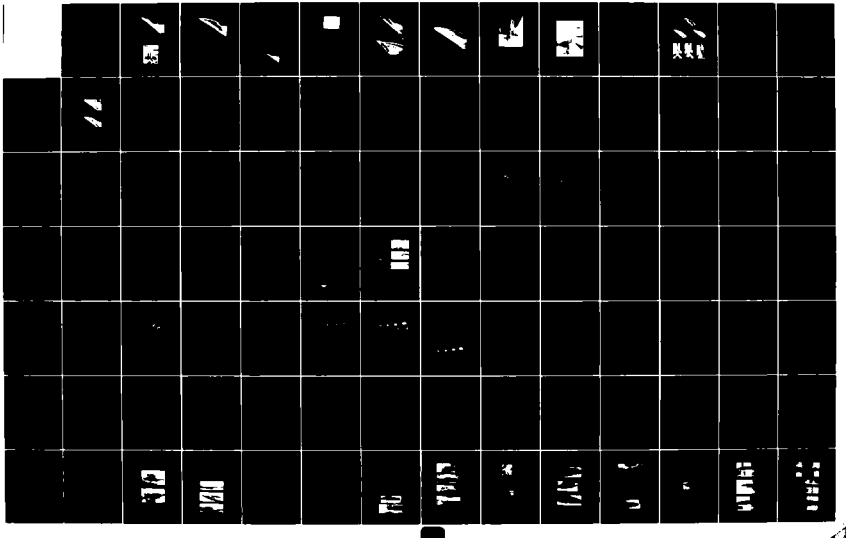

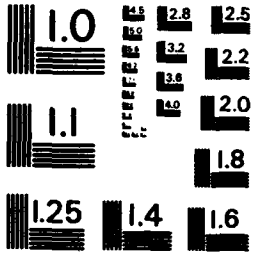

MICROCOPY RESOLUTION TEST CHART
NATIONAL BUREAU OF STANDARDS - 1963 - A

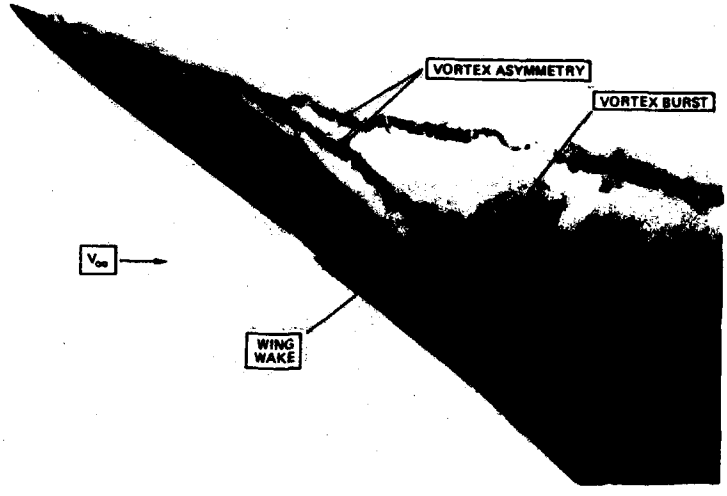

FIGURE 3. FOREBODY VORTEX FLOW ASYMMETRY AT ZERO SIDESLIP

FIGURE 4. FLIGHT PHOTOGRAPH OF AN ADVANCED FIGHTER AIRCRAFT WITH CLOSELY-COUPLED FOREBODY AND LEX

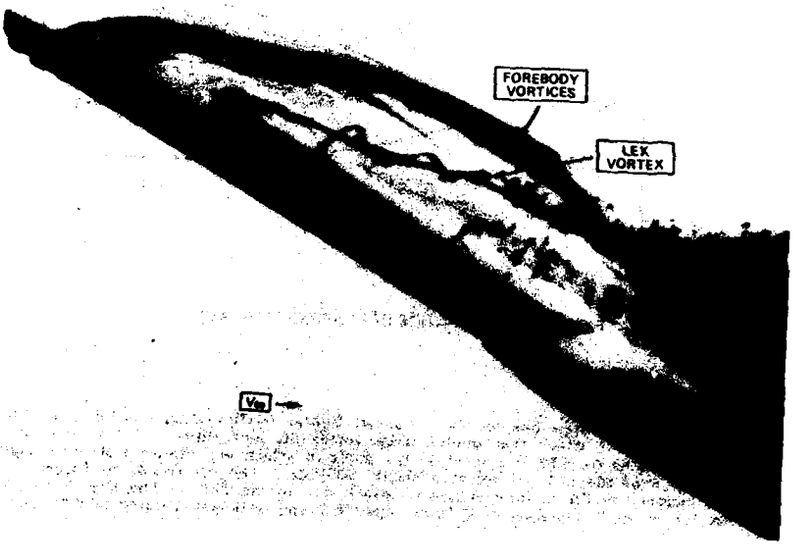

FIGURE 5. STRONG COUPLING OF FOREBODY AND LEX VORTEX FLOWS

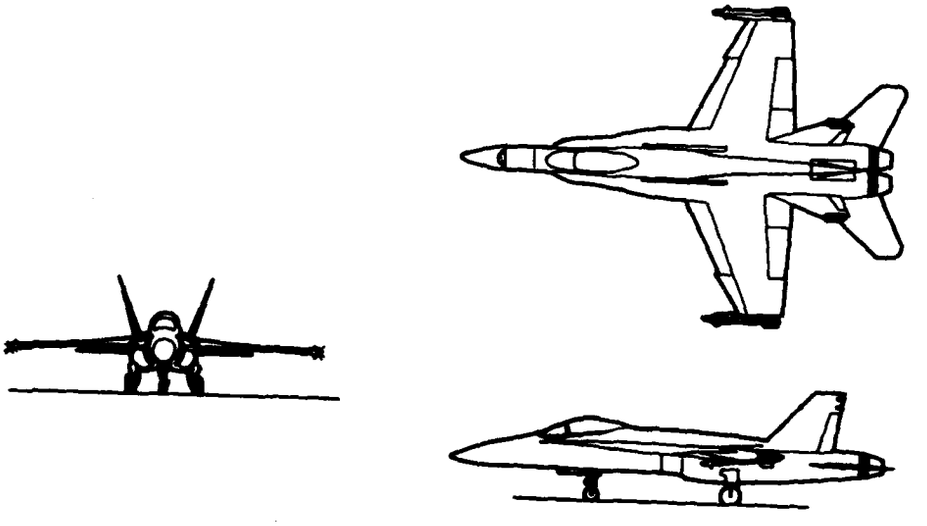

FIGURE 6. BASELINE MODEL DESCRIPTION

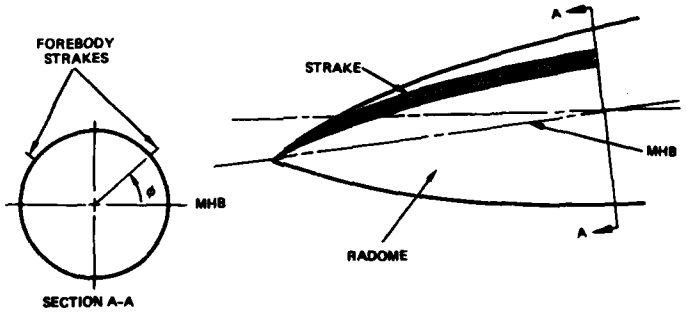

FIGURE 7. ILLUSTRATION OF FOREBODY STRAKES

IV. BASELINE RESULTS

The wing leading-edge extensions on the advanced fighter configuration develop powerful vortices at moderate-to-high angles of attack that induce large vortex-lift increments. The water tunnel photograph in Figure 8 illustrates the LEX vortex at a high angle of attack and Figure 9 shows a flight photograph from Reference 6 of the LEX vortex at a similar attitude. The lift trends in Figure 10 reveal a nearly 50 percent increase in lift at high angles of attack due to the LEXs. The significant increase in maximum lift results in high instantaneous turn capability and efficient landing/takeoff performance. Although LEX vortex breakdown has advanced far upstream on the wing at angles of attack from 30 to 40 degrees, the nonlinear vortex-induced lift effects remain significant. It is of interest to note that in full-scale flight tests pilots have detected a sudden increase in external noise intensity at these high angles of attack where vortex breakdown occurs.

The LEX vortex flow-field alters the wing spanwise lift distribution. Disturbance to the vortex behavior due to sideslip, for example, can promote potentially-large changes in the spanwise lift distributions on the upwind and downwind wing panels. Consequently, in the design of an efficient leading-edge extension, one strives for high maximum lift concurrent with minimization of the sensitivity of vortex breakdown to sideslip variations. At moderate-to-high angles of attack where the outboard wing sections are stalled, the aircraft can, in effect, be regarded as a slender wing-body configuration. It is well-established (see References 7 and 8) that such configurations exhibit a lateral sensitivity at high angles of attack due to asymmetric leading-edge vortex breakdown effects. This vortex breakdown sensitivity due-to-sideslip in the 30- to 40-degree angle of attack range can be influenced by the manner in which the forebody vortices interact with the LEX vortex flows, as described below.

Figure 11 shows the pair of concentrated, symmetric forebody vortices developed on the LEX-wing fighter configuration at high angle of attack and zero sideslip and the entrainment of this vortex system into the low-pressure region induced by the LEX vortices. For comparison, the water tunnel photograph in Figure 12 shows a highly-asymmetric forebody vortex pattern on the same model with LEXs removed. In the latter case, forebody vortex interaction with the wing flow-field is negligible. This example is purely academic, however, as the aircraft could not achieve this high angle of attack without the benefit of vortex lift.

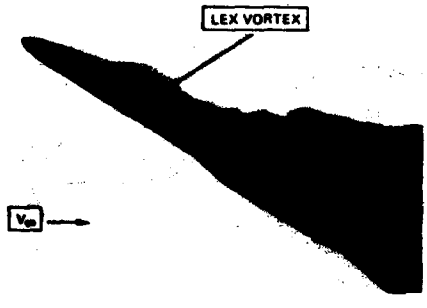

FIGURE 8. ADVANCED FIGHTER AIRCRAFT LEX VORTEX FLOW (WATER TUNNEL)

FIGURE 9. ADVANCED FIGHTER AIRCRAFT LEX VORTEX FLOW (FLIGHT)
(FROM REFERENCE 6)

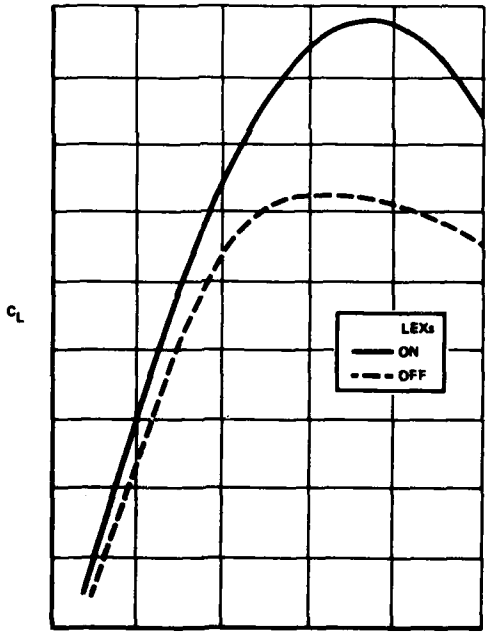

FIGURE 10. LEX EFFECT ON LIFT

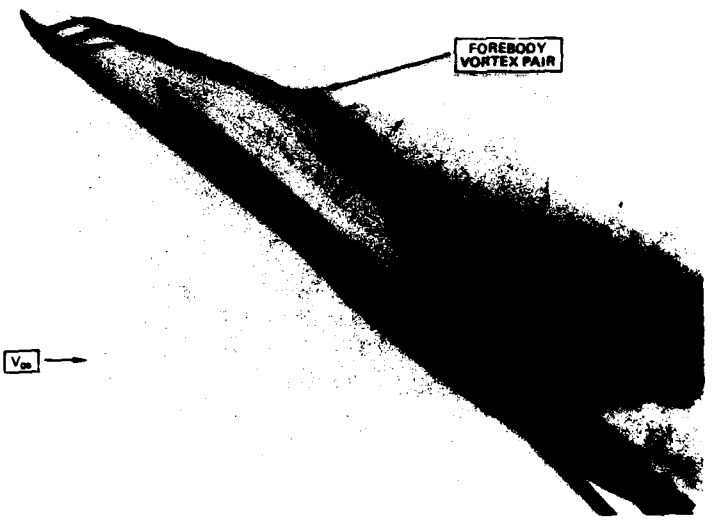

FIGURE 11. CONCENTRATED, SYMMETRIC FOREBODY VORTEX PAIR AT HIGH ANGLE OF ATTACK

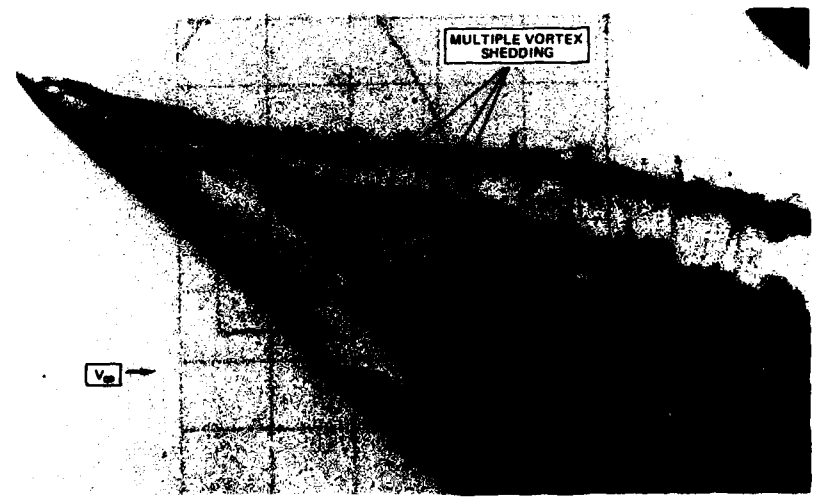

FIGURE 12. ASYMMETRIC FOREBODY VORTEX SHEDDING WITH LEXs OFF

As a result of the coupling of the forebody-LEX vortical motions, small sideslip changes can promote large asymmetries in the forebody vortex pattern. This is illustrated in Figure 13. The downwind body vortex is strongly entrained into the downwind LEX vortex whereas the upwind body vortex "shears" away from the fuselage with no apparent influence on the downstream flow behavior. This flow pattern was very repeatable.

Previous Northrop and NASA studies (References 9 and 10) of the fighter aircraft shown previously in Figure 1 indicated that the manner in which the forebody vortices orient themselves in sideslip can be correlated with the level of directional stability exhibited by the aircraft at high angles of attack. The vortex flow situation is illustrated in the water tunnel photograph in Figure 14. It is hypothesized that this type of correlation can be extended to the LEX-wing fighter in the present study. With the support of limited flow visualization and wind tunnel data trend comparisons, it will be shown that the forebody vortex orientation in the 30- to 40-degree angle of attack range is an indicator of the lateral stability exhibited by the advanced fighter configuration owing to the coupled nature of the forebody and LEX-wing flow-fields.

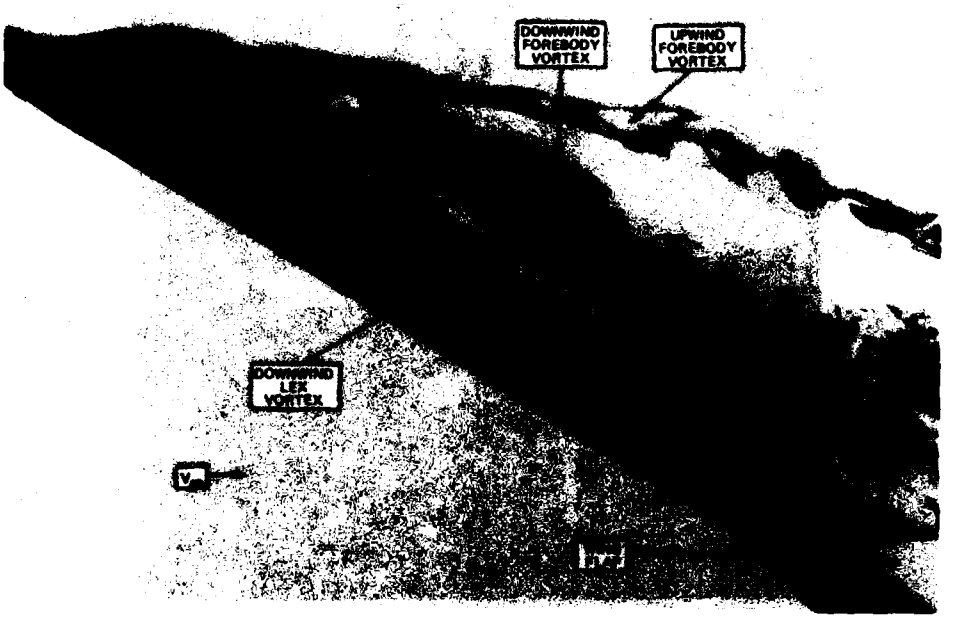

FIGURE 13. ASYMMETRIC FOREBODY VORTEX ORIENTATION DUE TO SIDESLIP

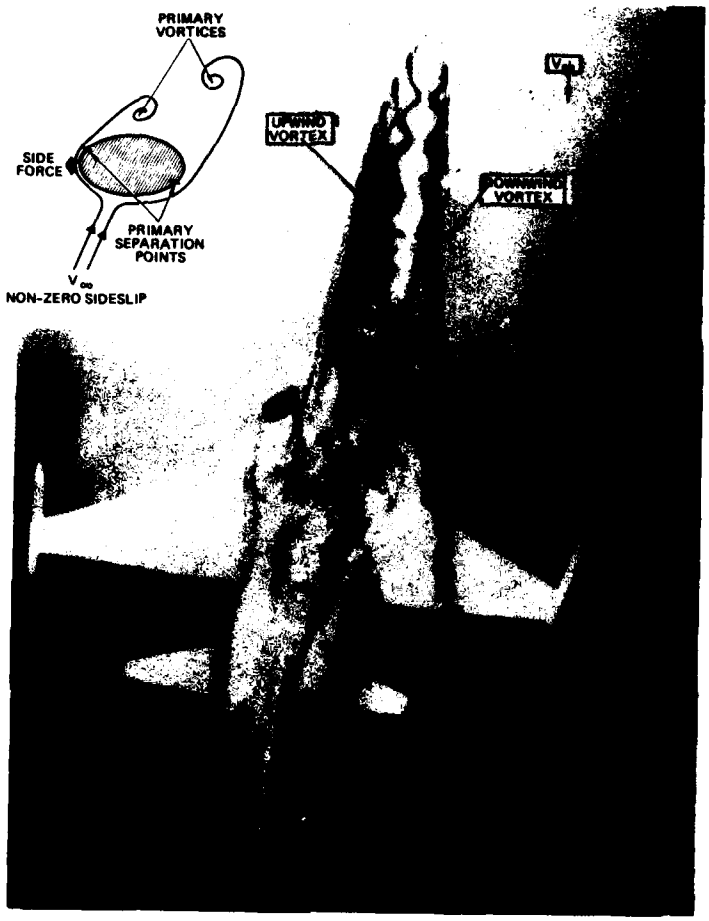

FIGURE 14. FOREBODY VORTEX ORIENTATION IN SIDESLIP ON UNCOUPLED FOREBODY AND LEX CONFIGURATION

Figure 15 illustrates the interactive behavior of the multiple vortices generated on the LEX-wing fighter configuration in sideslip. The body vortex orientation is opposite to the flow situation shown previously in Figure 14. The manner in which the forebody vortices are oriented is consistent with the low levels of lateral stability exhibited in the low-speed wind tunnel data in Figure 16. There is, however, no direct evidence to indicate that the forebody vortices strongly affect the baseline lateral stability trends. However, results in the next section will show conclusively that the forebody vortex orientation can be modulated in such a manner as to significantly modify the wing stall behavior.

V. FOREBODY MODIFICATIONS

Forebody Strakes. The sensitivity of the wing flow separation characteristics to changes in the forebody geometry was vividly demonstrated in water tunnel studies of forebody strakes symmetrically-deployed on the advanced fighter model.

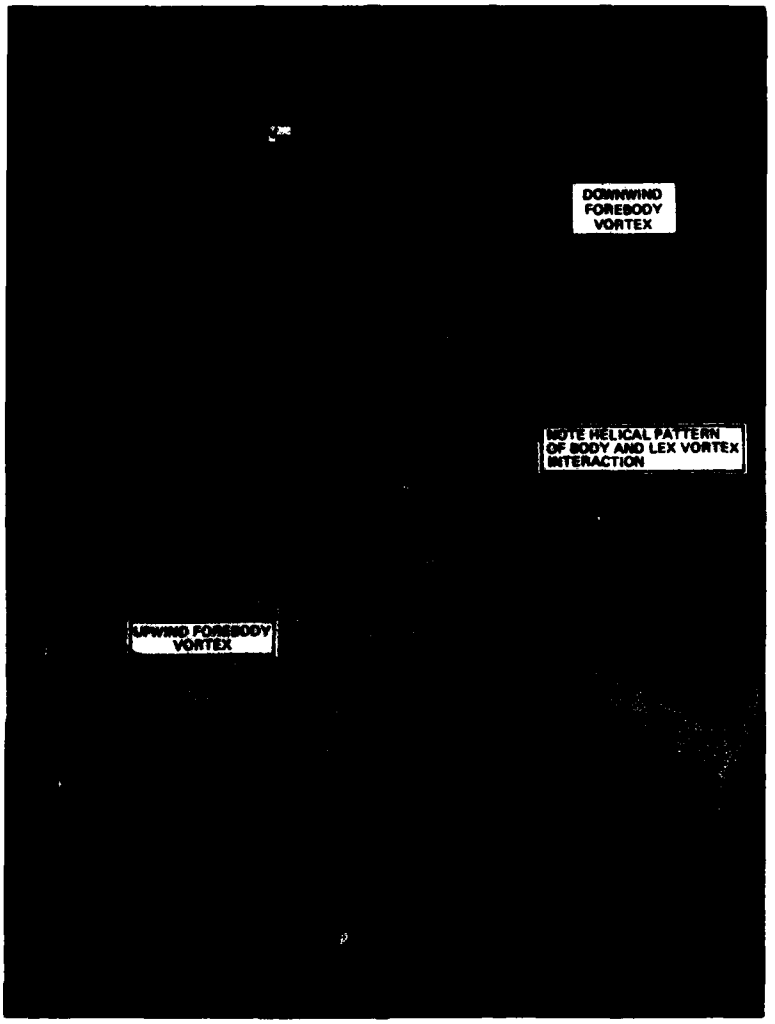

FIGURE 16. MULTIPLE VORTEX INTERACTION ON COUPLED FOREBODY AND LEX CONFIGURATION

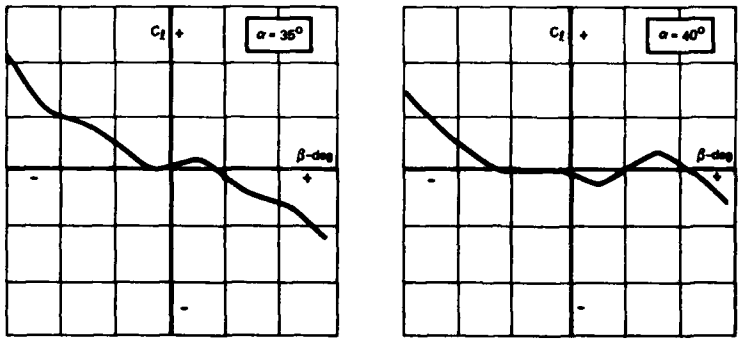

FIGURE 16. ROLLING MOMENT VARIATION WITH SIDESLIP – BASELINE MODEL

Strakes located 40 degrees above the maximum half-breadth (MHB) were nearly coincident with the primary boundary layer separation lines along the radome at angles of attack of approximately 35- to 40-degrees. *In* sideslip, the strakes (1) promoted symmetric boundary layer separation in this region, and (2) developed a pair of concentrated vortices that were observed to "feed" directly into the primary forebody vortex system. As a consequence, the forebody vortices were resistant to asymmetric orientation in sideslip. This effect is illustrated in the water tunnel photographs in Figure 17. At small sideslip angles the body vortex system was actually biased towards the upwind side (see Figure 17). The downwind forebody vortex would periodically pass underneath the upwind body vortical flow. This flow situation is consistent with smoke flow visualization conducted by NASA researchers in the Langley 30- by 60-foot wind tunnel on the 0.16-scale model. The strake effects on the forebody-LEX vortex interactions resulted in powerful vortex-induced downwash and sidewash on the upwind wing panel, thereby delaying complete wing stall to angles of attack in excess of 40 degrees. The vortex flow situation as observed in the water tunnel is sketched in Figure 18 which depicts a transverse cut at approximately wing mid-chord. For comparison, the baseline model forebody vortex patterns are also shown.

The lateral aerodynamics determined in low-speed wind tunnel tests are consistent with the flow-field observations. The forebody strakes promote a highly stable variation of rolling moment with sideslip at angles of attack from 30- to 40-degrees as shown in Figure 19. In addition, full-scale flight tests confirmed the increased lateral stability promoted by the radome strakes.

Consistent with results documented in Reference 9, the beneficial effects in roll are accompanied by unstable yawing moment increments, as shown in Figure 19. Additional disadvantages associated with forebody strakes include possible degradation of radar performance and ingestion of the strake vortices into engine inlets at low angles of attack. The strakes also induced undesirable lateral oscillations as described below.

In contrast, strakes mounted along the MHB promote large, stable yawing moment increments at the expense of favorable forebody – LEX vortex effects on rolling moment characteristics. This is illustrated in the low-speed wind tunnel data in Figure 20. Figure 21 presents water tunnel photographs of the corresponding strake effects on forebody and LEX vortex interactions. It is evident that strakes symmetrically-deployed at the MHB disrupt the forebody vortices, thereby uncoupling the forebody and LEX-wing flow-fields.

Free-to-roll tests conducted in the Langley wind tunnel revealed a modest wing rock (amplitude ±10 degrees) when strakes were deployed on the large-scale model at 40 degrees above the MHB. In contrast, the baseline model was free of any lateral oscillations. These results are consistent with the unsteady forebody vortices observed in the water tunnel and wind tunnel on the respective models with strakes installed and the steady vortex patterns developed on the baseline models. Furthermore, full-scale flight tests confirmed the development of strake-induced lateral oscillations, which would degrade the flying qualities of the aircraft.

VI. SUPPORTIVE WIND TUNNEL DATA

Lateral sensitivity at high angles of attack is an inherent characteristic of any slender wing fighter configuration that develops large amounts of vortex-induced lift. Low-speed wind tunnel data trends corresponding to two LEX-wing fighters are shown in Figure 22. Results show highly-nonlinear rolling moment variations with sideslip due to asymmetric LEX vortex breakdown.

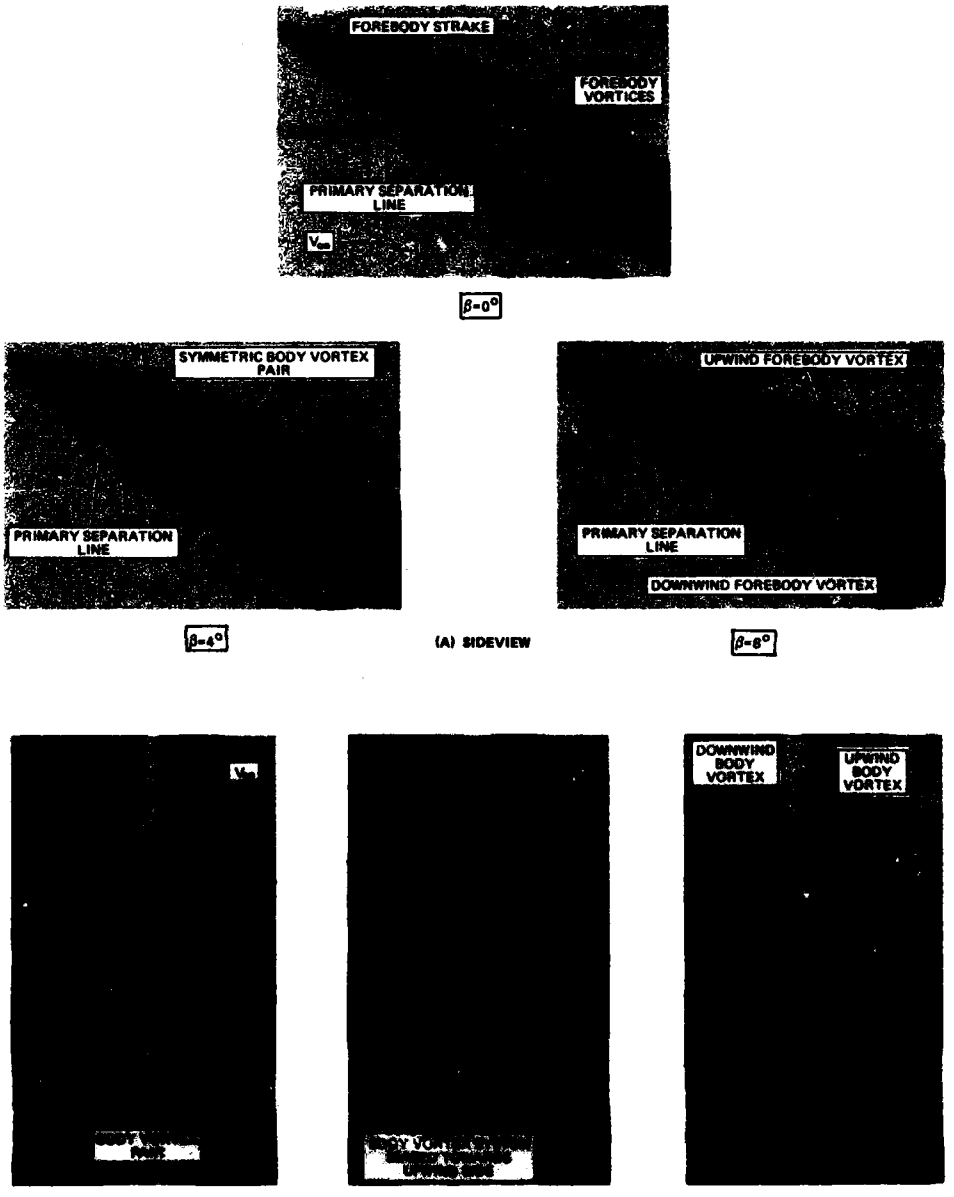

FIGURE 17. FOREBODY VORTEX BEHAVIOR WITH STRAKES INSTALLED; α = 35 DEGREES

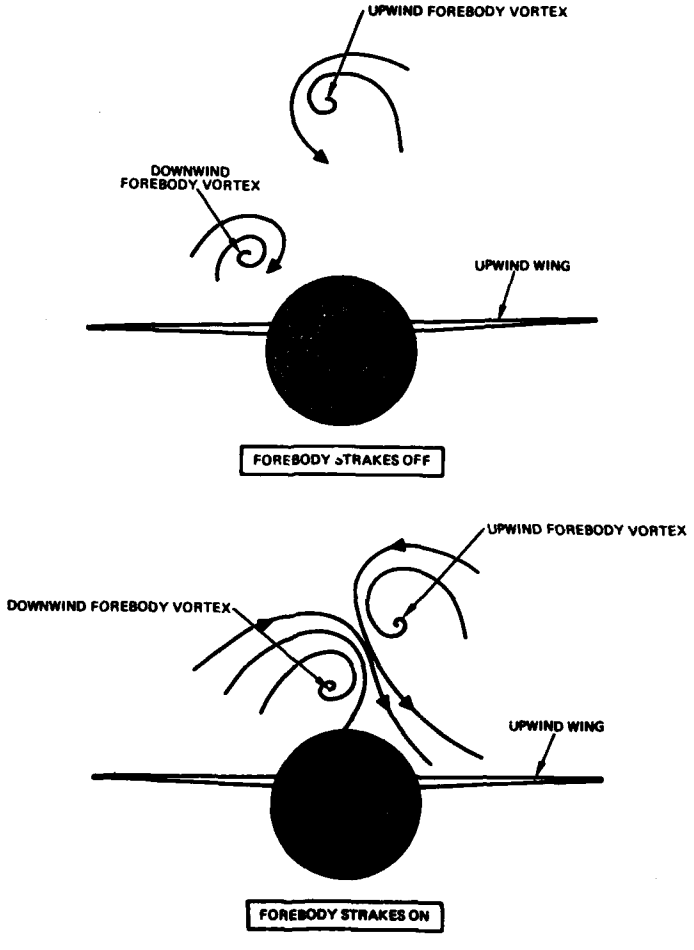

FIGURE 18. SKETCH OF FOREBODY STRAKE EFFECT ON BODY VORTEX PATTERNS

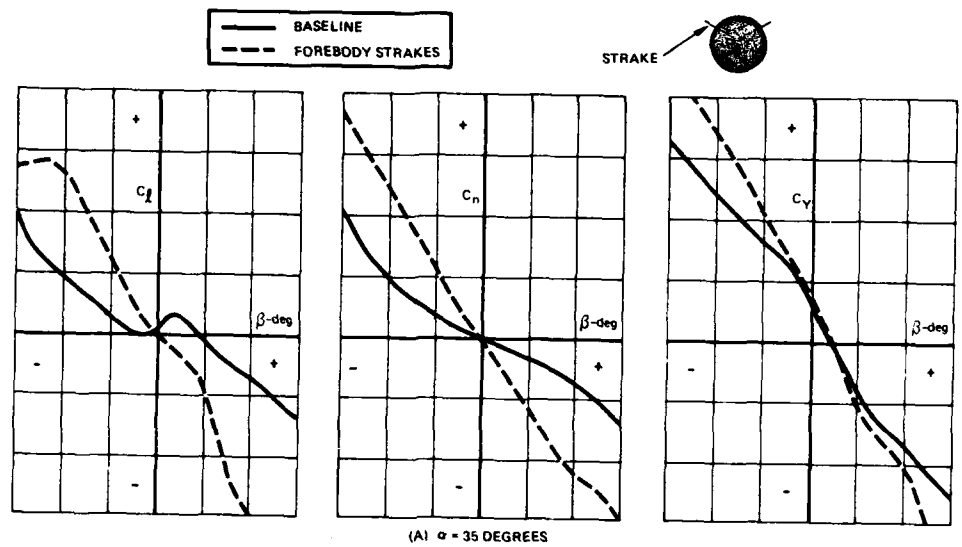

(A) α = 35 DEGREES

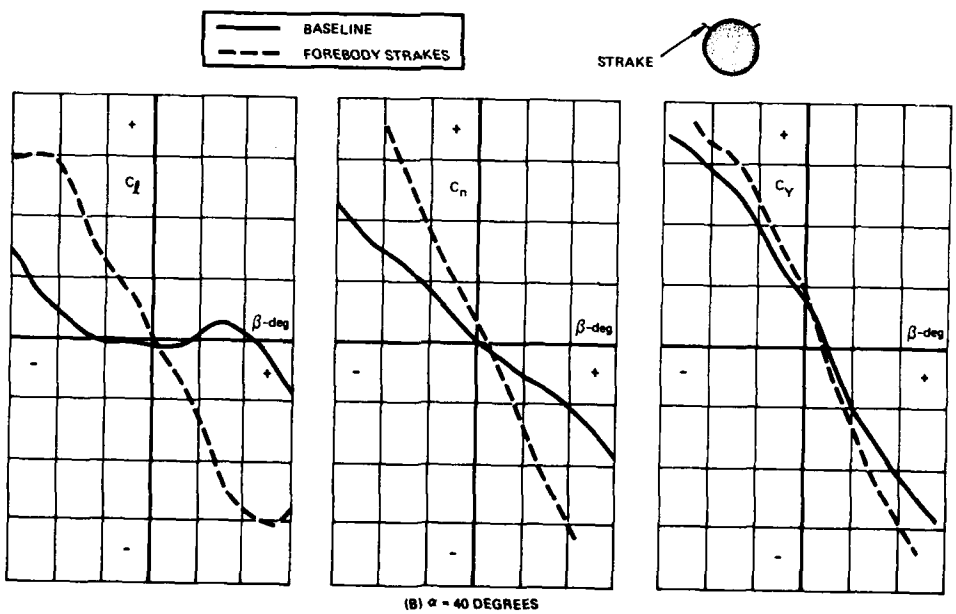

(B) α = 40 DEGREES

FIGURE 19. EFFECT OF FOREBODY STRAKES ON ROLLING MOMENT, YAWING MOMENT, AND SIDE FORCE COEFFICIENT VARIATION WITH SIDESLIP

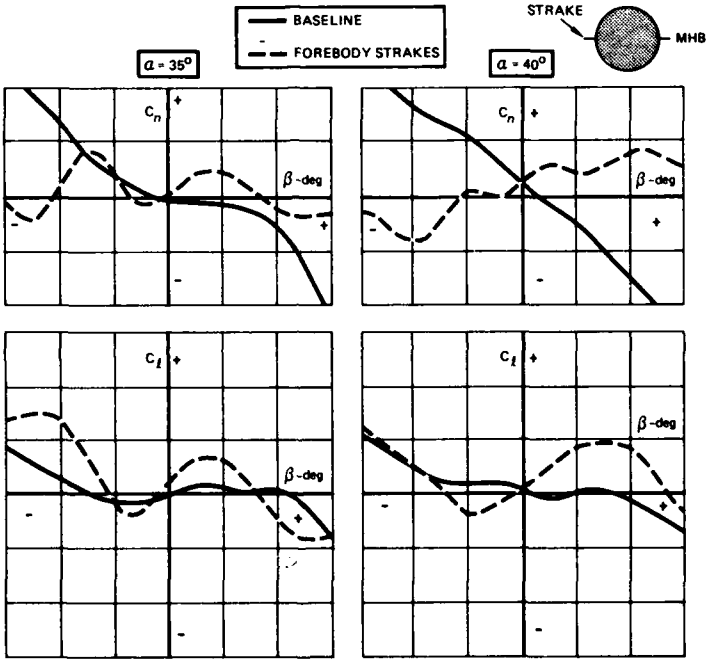

FIGURE 20. EFFECT OF FOREBODY STRAKES AT THE MAXIMUM HALF BREADTH ON ROLLING MOMENT AND YAWING MOMENT VARIATION WITH SIDESLIP, δ_n = 25 DEGREES.

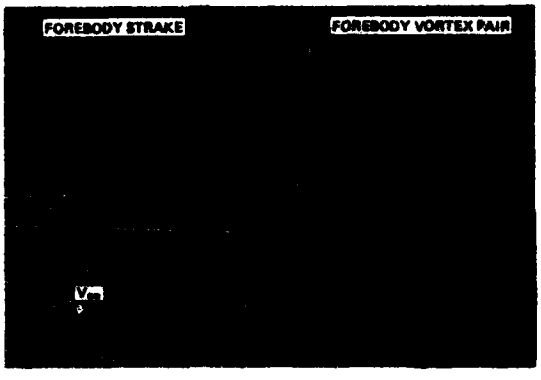

β=0°

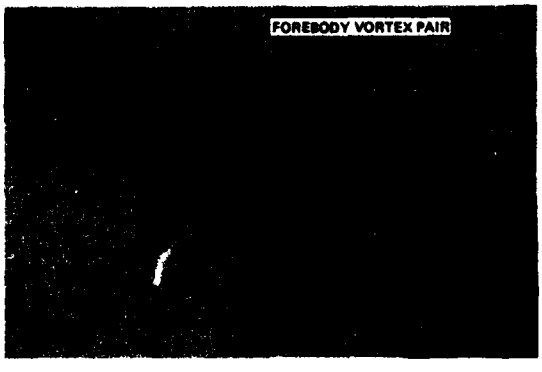

β=4°

FIGURE 21. FOREBODY VORTEX FLOW BEHAVIOR WITH STRAKES AT MHB; α = 35 DEGREES

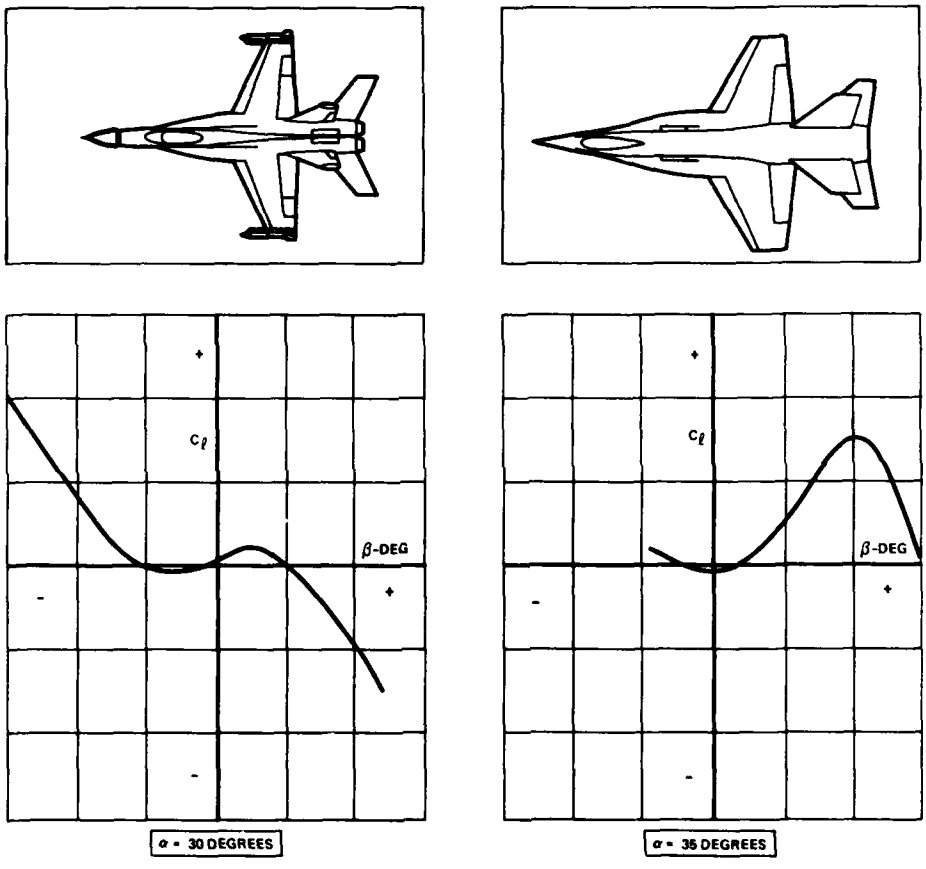

FIGURE 22. ROLLING MOMENT VARIATION WITH SIDESLIP FOR LEX-WING FIGHTER CONFIGURATIONS; δ_n = 25 DEGREES

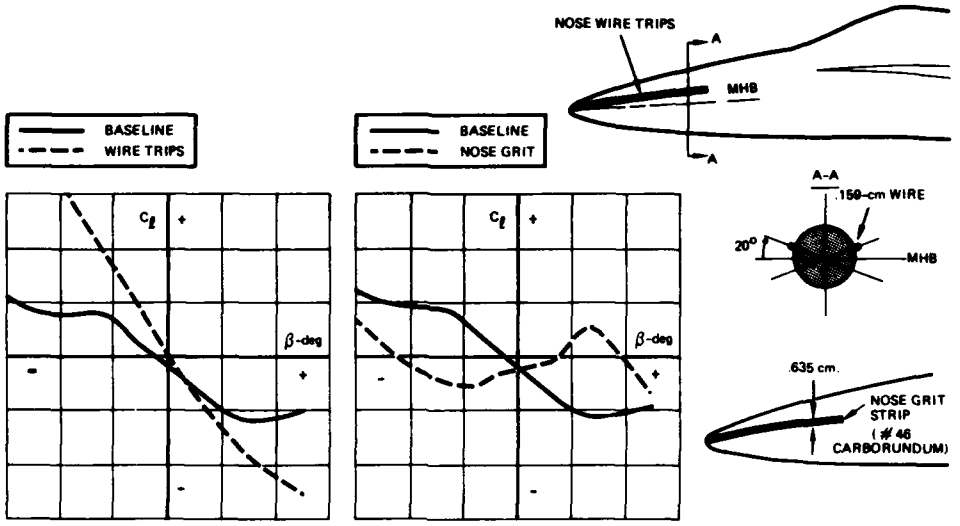

FIGURE 23. EFFECTS OF NOSE GRIT AND NOSE WIRE TRIPS ON ROLLING MOMENT VARIATION WITH SIDESLIP; δ_n = 25 DEGREES ; $Re_{\bar{c}}$ = 1.6 (10^6); α = 35 DEGREES.

Strong coupling of forebody and LEX vortex flows at high angles of attack has been evident in Northrop low-speed wind tunnel tests of advanced fighter configurations. Figure 23 presents rolling moment variations with sideslip for a slender fighter model. The data indicate that flow-field changes associated with the addition of surface roughness or wire trips to the fuselage forebody propagate downstream to affect the wing aerodynamics. The effects of grit and wire trips on rolling moment variation with sideslip are opposite. The phenomenological aspects of the respective forebody-LEX vortex interactions, however, are not well-understood at the present time.

Recent tests in the Northrop low-speed wind tunnel have indicated that acceptable levels of lateral stability can be achieved by manipulation of the forebody slenderness. Figure 24 presents the effect of forebody fineness ratio on the minimum value of the static lateral stability parameter, C_{l_β}. With the aid of water tunnel flow visualization tests, it was determined that increased forebody slenderness displaced the forebody vortices away from the LEX-wing flow-field, thereby reducing an unfavorable coupling mechanism that existed at lower fineness ratios.

VII. CONCLUSIONS

Advanced fighter configurations with slender forebodies and highly-swept wing leading-edge extensions develop powerful vortices on the forebody and LEX surfaces at moderate-to-high angles of attack. On closely-coupled forebody-LEX configurations the flow field is characterized by strong interactions between the multiple vortices. Furthermore, the global flow-field becomes more complex in sideslip because of the asymmetric manner in which the forebody vortices interact with the LEX vortical motions.

Water tunnel flow visualization studies, low-speed wind tunnel tests, and full-scale flight investigations have shown that under certain conditions the extent to which flow separation occurs on the wings is related to the forebody vortex flow development. Symmetrically-deployed radome strakes can modulate the forebody vortex interaction with the LEX-wing flow-field to reduce wing flow separation in sideslip and, hence, improve lateral stability at high angles of attack. Concurrent with this, however, are offsetting penalties such as yaw instability and lateral oscillations. Further research is needed to better understand these stability trades and to identify better forebody designs.

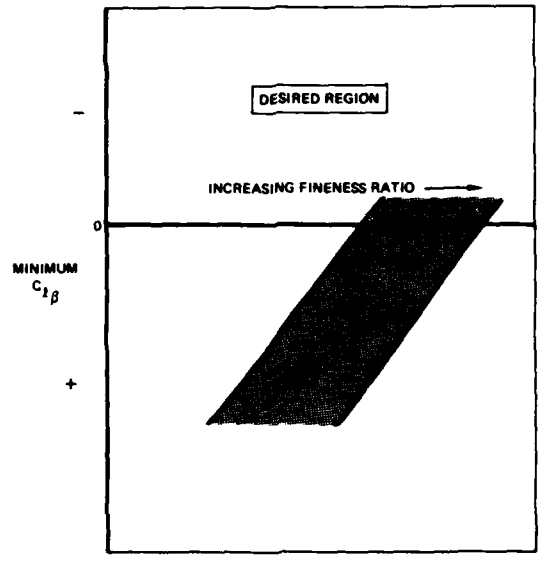

FIGURE 24. EFFECT OF FOREBODY FINENESS RATIO ON MINIMUM C_{l_β} OF ADVANCED LEX-WING FIGHTER CONFIGURATIONS

VIII. ACKNOWLEDGEMENTS

The authors gratefully acknowledge the support and contributions of the following individuals:

Mr. A.M. Skow, Manager, Northrop F-20 Aerosciences

Dr. B.L. Hunt, Manager, Northrop Aerosciences Research

Mr. H.A. Gerhardt, Manager, Northrop Aerodynamics Research

Mr. D.J. Lorincz, Senior Engineer, Northrop Advanced Design

Mr. J.L. Johnson, Head, NASA Langley Flight Dynamics Branch

Mr. J.R. Chambers, Assistant Head, NASA Langley Low Speed Aerodynamics Division

References

1. Erickson, G.E., "Vortex Flow Correlation," AFWAL-TR-80-3143, January 1981.

2. Erickson, G.E., "Vortex Flow Correlation," ICAS Paper No. 82-6.6.1, August 1982.

3. Ericsson, L.E., and Reding, J.P., "Unsteady Aerodynamics of Slender Delta Wings at Large Angles of Attack," J. of Aircraft, Vol. 12, No. 9, September 1975.

4. Keener, E.R., and Chapman, G.T., "Similarity in the Vortex Asymmetries Over Slender Bodies and Wings," AIAA Journal, Vol. 15, No. 9, September 1976.

5. Skow, A.M., Titiriga, A., and Moore, W.A., "Forebody/Wing Vortex Interactions and Their Influence on Departure Resistance," AGARD CP-247, October 1978.

6. Aviation Week and Space Technology, Vol. 114, No. 25, June 22, 1981, pg. 18.

7. Johnson, J.L., Grafton, S.B., and Yip, L.P., "Exploratory Investigation of the Effects of Vortex Bursting on the High Angle-of-Attack Lateral-Directional Stability Characteristics of Highly-Swept Wings," AIAA Paper No. 80-0463, 1980.

8. Küchemann, D., The Aerodynamic Design of Aircraft, Pergamon Press, 1978.

9. Grafton, S.B., Chambers, J.R., and Coe, P.L., Jr., "Wind Tunnel Free-Flight Investigation of a Model of a Spin-Resistant Fighter Configuration," NASA TN D-7716, June 1974.

10. Skow, A.M., and Titiriga, A., Jr., "A Survey of Analytical and Experimental Techniques to Predict Aircraft Dynamic Characteristics at High Angles of Attack," AGARD CP-235, May 1978.

SOME RESULTS FROM A PROGRAMME OF RESEARCH INTO THE STRUCTURE OF VORTEX FLOW FIELDS AROUND MISSILE SHAPES

by

T R Byram and A Petersen

Procurement Executive, Ministry of Defence, Royal Aircraft Establishment, Aerodynamic Department, Bedford MK41 6AE, UK

S T Kitson

Aerodynamics Research Department, British Aerospace PLC, Dynamics Group, Bristol Division, PO Box 5, Filton, Bristol BS12 7QW, UK

SUMMARY

Wind tunnel tests have been performed to measure the leeside flow field of a generalised missile model at an angle of attack of 14° and freestream Mach numbers of 0.7 and 1.8. Flow field data are presented for a station towards the rear of the model showing the flow structure for the body alone and the effects of mounting a cruciform set of delta fins near to the nose and near to the base. The data presented include vector plots of the components of velocity in the cross flow plane, the distributions of local total pressure, local Mach number and vorticity. The presence of the set of forward mounted fins and its roll orientation has been found to have a significant effect on the development of the body vortices. Fins mounted towards the rear of the body were found to disrupt the body vortex feeding region but had little effect on the vortex centres unless these lay in or very close to the plane of the fins.

LIST OF SYMBOLS

d	body diameter
H	total, or stagnation, pressure of freestream
M	Mach number of freestream
r	radial position measured from body axis
V	velocity of freestream
v	velocity component along Oy
w	velocity component along Oz
x,y,z	position coordinates; origin O at body nose with x measured aft along body axis, y positive to starboard, z positive to leeward (upwards). Oxz plane coincident with angle of attack plane. (See also Fig 1).
Γ	circulation evaluated round a contour by a line integral of the components of velocity in the crossflow plane, v and w. Positive anti-clockwise looking forward.
γ	non-dimensional circulation ($\gamma = \Gamma/\pi dV\sin\sigma$)
λ	model roll angle, positive starboard tip down, fins horizontal and vertical at $\lambda = 0°$.
$\bar{\xi}$	vorticity component parallel to the body axis ($\bar{\xi} = \frac{\partial w}{\partial y} - \frac{\partial v}{\partial z}$)
ξ	non-dimensionl vorticity component ($\xi = \bar{\xi}(d/V\sin\sigma)$)
σ	model angle of attack

SUBSCRIPT

L	local value of a quantity; eg H_L, local stagnation pressure.

1 INTRODUCTION

The flow fields around manoeuvring missiles are dominated by the presence of vortices generated by various parts of the missile airframe. The interaction of these vortex flows with the missile components, in particular lifting surfaces, can give rise to non-linear aerodynamic forces and moments. Even at moderate angles of attack of 20° or less this can result in a severe loss of stability, or control problems which current

aerodynamic prediction methods may be unable to predict accurately. As a step towards improving the aerodynamic prediction capabilities in these areas a comprehensive series of experiments are being performed in the RAE 8 ft x 8 ft Wind Tunnel.

The first set of experiments measured overall and fin-panel forces and moments for an axisymmetric body fitted with various cruciform fin arrangements. These experiments are being followed by measurements of the flow fields around the same model, including the body alone and the body with forward or aft mounted fins. Some of the force and moment data have been presented in Ref 1 together with the results of an approximate panel load estimation method using data derived from the preliminary flow field surveys. Also presented in Ref 1 are a limited number of plots illustrating flow field structure. Ref 2 tabulates all the flow field data obtained to date and presents vector plots of the cross flow velocity fields.

The present paper presents only that portion of the available flow field data which shows the effects of adding fins in either a forward or aft position to an axisymmetric body at an angle of attack of 14° for freestream Mach numbers of 0.7 and 1.8. The data are presented chiefly in the form of vector plots showing the components of flow field velocity in the cross flow plane, together with contour plots showing the local total pressure and vorticity distributions. Additional information is given for some of the flow fields in the form of local Mach number distributions (contours), and topographical or "relief" plots of local total pressure and vorticity distributions.

2 MISSILE MODEL AND FLOW SURVEY EQUIPMENT

The model used in the flow field experiments is illustrated in Fig 1. Overall length of the body is 13 calibres(d) including the 1.5d tangent ogive nose which is spherically blunted by a radius of 0.05d. A cruciform set of delta fins set at zero incidence with respect to the body can be carried in either a forward or rear location; as shown. The fins have an exposed semi-span of 1d with a leading edge sweep angle of 45°, and a double wedge section with a thickness to chord ratio of 0.1.

Flow surveys are performed using a set of five-hole yawmeters which have been calibrated at 11 Mach numbers from 0.4 to 2.0 and for angles of attack up to 39°. The yawmeters are carried on a purpose built traversing rig mounted coaxially with the model; a three-view drawing of the arrangement is shown in Fig 2. The traversing rig houses an axial drive to which various extension stings can be added to place the yawmeters at any desired axial location along the model. Data are obtained throughout the chosen cross flow plane (ie a plane normal to the body axis) by using a combination of the radial drive built into the traversing rig and by rolling the entire traversing rig around the model. The data acqusition, including traverse movement, is computer assisted. At supersonic speeds an array of four yawmeters (illustrated) is used while at subsonic speeds a single yawmeter is used in order to minimise interference. An important feature of the test facilities is the on-line production of a flow field display in the form of a vector plot of the cross flow velocities. This is achieved by using a small graphics computer with a simplified data reduction program employing approximate polynominal fits to the calibration data. This facility allows the on-line identification of interesting areas of the flow field, ensures adequate data coverage, and provides a check on data quality.

3 TEST PROGRAMME AND PRESENTATION OF RESULTS

The full range of cases that have been investigated to date is shown in Table 1. The flow survey cases presented in this paper (marked with an asterisk in Table 1) are restricted to a body angle of attack (α) of 14° and freestream Mach numbers (M) of 0.7 and 1.8; the Reynolds number was kept constant throughout at 0.62×10^6, based on body diameter. The data presented here illustrate the body alone flow fields at the rear hinge position (11.5d from the nose) together with the changes in the flow fields resulting from adding a cruciform set of delta fins at both the forward and rear locations.

For the case of body plus forward mounted fins(as in a canard-control arrangement) flow surveys are presented for model roll angles (λ) of 0° and -45°(see Fig 1). With fins mounted at the rear location, such as would occur with a rear-controlled missile, flow surveys were performed for three model roll angles, λ = 0°, -45° and -72°. The surveys were performed in this case in a plane 12.2d from the nose which placed the yawmeters 0.34d behind the trailing edges of the fins. For all the "symmetrical" configurations (λ = 0° and -45°) only the starboard leeside quadrant was investigated, but for the rear mounted fins at λ = -72° both leeside quadrants were surveyed. In the latter case the model roll angle was chosen so that one of the leeward fins lay close to the body vortex centre. The radial extent of the flow surveys was determined by the capabilities of the traversing rig. At subsonic speeds (using a single yawmeter) the coverage was from an inner radius of 0.575d to an outer radius of 1.5d, the corresponding distances at supersonic speeds (rake of 4 yawmeters) were 0.55d and 2.3d.

After completion of the wind-tunnel tests the data are processed by a "table look-up" program which employs the full calibration data base to derive the final flow field results as presented in this paper. The accuracy of the final results is estimated to be: yawmeter pitch and yaw angles to ±0.3°, local Mach number to ±0.01 and local total pressure to ±1.5%. Positional accuracy in the cross flow plane is better than ±0.002d.

The data presented in this paper mainly comprise vectorial representations of the velocity components in the cross flow plane (henceforth referred to as vector plots), and contour plots of the local total pressure. For some of the flow fields the distribution of vorticity has also been presented as contour plots. Additional representations of some of the flow fields have been made in the form of local Mach number distributions (contours) and topographical or "relief" plots of local total pressure and vorticity distributions. The cross flow velocity vector lengths are scaled to the freestream cross flow component ($V\sin\alpha$), shown on the plots springing from the body axis, while the local total pressure and Mach number are presented as ratios of the corresponding freestream values. The values of vorticity have been presented in non-dimensional form as shown in the list of symbols. Finally, in order to maintain clarity of presentation some of the available data have been omitted from some of the vector plots.

4 DISCUSSION OF RESULTS

4.1 ADDITION OF THE FORWARD MOUNTED FINS TO THE BODY ALONE

The structure of the body alone flow field and the effect of adding forward mounted fins at roll angles of 0° and -45° are illustrated in Figs 3 to 8. Data are presented for a station 11.5d aft of the nose at α = 14° for M = 0.7 and 1.8. The vortex flows presented here for the body alone are similar to those found by other investigators and reported in Refs 3 to 11.

4.1.1 Results for M = 0.7

The cross flow velocity field of the body alone is shown in Fig3(a). A well developed body vortex is readily apparent together with its feeding sheet, resulting from the separation of the body boundary layer. (The innermost radial position of the yawmeter is 0.575d and does not allow the position of the separation line to be estimated). At this angle of attack (α = 14°) the flow field is symmetrical and a good indication of this is shown by the alignment of the cross flow velocity vectors along the vertical meridian. Additional data (not shown) have been recorded in the left hand side of the cross flow plane which confirm this symmetry.

Fig 3(b) shows the corresponding distribution of total pressure. The vortex is shown as a nearly circular region of low total pressure, the centre of which appears to provide a good indication of the location of the centre of the vortex. This position, marked by a dot in a circle, has also been shown on the vector plot in Fig 3(a). The feeding sheet shows up as a fairly diffuse feature and the term "feeding region" is probably more appropriate. It should be noted that whilst a contour value of H_L/H = 1.0 has been included, its position should be regarded with some caution as it is in a region of low total pressure gradient.

The distribution of vorticity has been derived and is displayed in its non-dimensional form (ξ) in Fig 3(c). The vortex centre derived from the total pressure plot has been plotted in Fig 3(c) and lies in the centre of the area of maximum vorticity. The region of vorticity (for clarity delineated arbitrarily by the contour ξ = 1) can be seen to cover an area comparable to that experiencing a loss in total pressure. It would be difficult to define the extent of a core region for the body vortex since the vorticity and the total pressure losses are spread over a large region in the lee of the body. However, a contour ξ = 10 would approximately mark the outer boundary of the area of higher vorticity gradient. This occurs at a radius of about 0.12d and is comparable to the size of the region of higher total pressure gradient. The distribution of vorticity illustrates the diffuse nature of the feeding region which shows a marked reduction in the levels of vorticity and vorticity gradients as distance from the body increases. The circulation of the body vortex (excluding most of the feeding region) has been determined for the arbitrarily chosen contour ξ = 5 shown in Fig 3(c). This does not include all the body vortex vorticity but avoids difficulties of separating the main body vortex from the feeding region. The value obtained in this way was γ = 0.28. (The rate at which vorticity is convected from the body via the feeding region is important, but is beyond the scope of the present paper).

The effect of adding the fins at the forward location for λ = 0° is illustrated in Fig 4 (fins horizontal and vertical). The strong vortex structure of the body alone is absent, leaving only a very weak recirculating region. What was the body vortex feeding region now passes out of the upper boundary of the surveyed area as a relatively thick shear layer separating the essentially freestream outer flow from a body lee side flow which is approximately parallel to the body axis. The forward fins seem to be preventing the rolling up of the feeding region to form a normal body vortex system. It is possible that the trailing wake from the fins is the cause, but a more extensive survey would be required to establish that this was so, as the tip vortex does not lie within the presently surveyed area.

At λ = -45° the addition of forward fins ('X' orientation) produces the flow shown in the vector plot of Fig 5(a). The body vortex has been considerably weakened, but is still present. The vortex shed by the forward starboard windward fin is present in the top right of the survey field. This feature is made clearer in Fig 5(b) in which the uniform cross flow velocity of the freestream has been removed from the measured flow so that the datum flow direction (null vector) is in the freestream direction. A symmetrical vortex will appear as a symmetrical region of circulating flow if the axis of

the vortex has no velocity component relative to the chosen datum flow direction. For this reason, and because the body vortex is following a path nearly parallel to the body axis, the body vortex is more easily seen in Fig 5(a) in which the datum flow direction is parallel to the body axis. The fin vortex is following a path more nearly aligned to the freestream direction and so is better seen in Fig 5(b).

Fig 5(c) is a contour plot of the distribution of total pressure. The body vortex is shown as a fairly weak feature, both in comparison to the fin vortex and to the body vortex for the body alone (Fig 3(b)). Compared to the latter case, the location of the body vortex has been rotated slightly to windward and moved closer to the body, presumably under the influence of the fin vortices. The corresponding vorticity distribution is shown in Fig 5(d) and superimposed are the vortex centres determined from the distribution of total pressure of Fig 5(c). The total pressure and vorticity distributions indicate a possible link between the fin tip vortex and the body vortex. The body vortex for the body alone case, Fig 3(c), is considerably stronger than the fin tip vortex seen in Fig 5(d). An approximate determination of the strength of the main part of the tip vortex has been made by employing the contour $\xi = 5$ and a value of $\gamma = 0.14$ was derived. This compares with the body alone vortex strength of $\gamma = 0.28$ and illustrates the importance of the body vortex in determining missile aerodynamic characteristics.

The distribution of local Mach number shown in Fig 5(e) is also a useful indicator of flow structure and, for this relatively complex flow field, presents an almost identical picture to the total pressure plot of Fig 5(c), including the location of the vortex centres. Note the decreased Mach number in the vortical regions and the increase in local Mach number round the shoulder of the body.

4.1.2 Results for M = 1.8

The body alone flow field is shown in Fig 6(a). One of the main differences compared to $M = 0.7$ is that the body vortex is positioned about 75% further from the body surface, however its angular location from the vertical meridian is virtually unchanged. The corresponding variation of total pressure in the survey plane is presented in Fig 6(b). Qualitatively this is very similar to that pertaining at $M = 0.7$ but the maximum loss in total pressure is about four times as large, and the overall area of reduced total pressure is greater. The distribution of vorticity presented in Fig 6(c) shows higher maximum levels than for $M = 0.7$ but the qualitative features, such as the more diffuse nature of the vorticity in the feeding region as the distance from the body increases, are very much the same. The circulation of the body vortex has been calculated for the contour $\xi = 5$ shown in Fig 6(c) and yields a value of $\gamma = 0.35$ which compares with $\gamma = 0.28$ at $M = 0.7$. In spite of the increased vortex strength there is only a slight increase in the size of the vortex core region. Inspection of the distribution of total pressure and vorticity for $M = 1.8$ implies a central core region of about 0.15d radius (0.12d at $M = 0.7$); but, as at $M = 0.7$, there is no clearly defined boundary and these dimensions are therefore only approximate.

A further feature of the flow field for $M = 1.8$ (and not so readily seen at $M = 0.7$) is what is probably the result of a secondary boundary layer separation, shown in Fig 6(b) by the trough in total pressure at a roll angle of about 30° from the vertical meridian, and in Fig 6(c) as a region of negative vorticity. The vector plot of Fig 6(a) shows the presence of a small vortex region corresponding to the negative contours in Fig 6(c). However, the two groups of vectors in the innermost row which indicate strong flows towards the body are possibly artifacts of the experimental technique since the yawmeter was very close to the model surface and in a region which may have been especially sensitive to disturbance at supersonic speeds due to shockwave-boundary layer interaction.

The changes in vortex strength and location between $M = 0.7$ and $M = 1.8$ can be compared with the general trends presented in Fig 5 of Ref 12 (which presents a compilation of experimental data on body-vortex characteristics). The increased vortex strength at $M = 1.8$ is in general agreement with the results of Ref 12, as is the change in the horizontal location of the vortex. The experimental data presented in Ref 12 are not sufficiently comprehensive to describe the effects of Mach number on vortex vertical location, but the vortex locations obtained from the data herein lie within the spread of data in Ref 12.

When forward fins at $\lambda = 0°$ were added to the body for $M = 1.8$ the flow field was modified to that shown in Fig 7. The location of the body vortex has been altered significantly, moving closer to the body and being rotated to windward. Evaluation of the circulation around the contour $\xi = 5$ seen in Fig 7(b) shows that the body vortex has been reduced in strength from $\gamma = 0.35$ for the body alone to $\gamma = 0.24$ with the fins present. The primary boundary layer separation on the body still feeds the body vortex, and there is still evidence for the presence of a secondary boundary layer separation. Therefore, although the flow has been considerably altered by the presence of the forward fins, the basic flow structure is still generally similar to the body alone case. This is in marked contrast to the case for $M = 0.7$ where the formation of the body vortex was entirely prevented.

Fig 7(b) shows an area of vorticity lying above the body vortex. This vorticity probably originates from the starboard fin and can be loosely described as the fin tip

vortex. Two vortex centres are implied by the data, the stronger of the two being near to the edge of the surveyed area. The vector plot of Fig 7(c) shows the cross flow velocity vectors relative to the freestream direction, and reveals the presence of the double tip vortex. Figs 7(d) and 7(e) respectively present relief plots of the total pressure and vorticity distributions, and provide a useful adjunct to the contour plots. Fig 7(d) illustrates the total pressure losses associated with the various vortex structures and shows a "valley" connecting the body vortex and feeding region with the fin tip vortex region. The vector plot of Fig 7(c) shows that fluid from the fin vortex region is flowing towards the body vortex. Therefore the fin wake is the probable source of the total pressure "valley". The relief plot of vorticity (Fig 7(e)) shows the relative strengths of the vortex regions well. Whereas a connecting feature between the two main vortex regions was seen in Fig7(d), no strong link between these areas is apparent in the vorticity distributions, although there are indications that some vorticity may be present in this region, see Fig 7(b). The rapid reduction in the level of vorticity in the feeding region with increasing distance from the body surface is clearly shown.

With the forward fins at $\lambda = -45°$ the results shown in Fig 8 were obtained. The estimated positions of the total pressure minima are shown; for the body vortex a circle-dot symbol has been used, while the vortex from the starboard windward fin (labelled as 'FIN') is shown by a cross. The position of the maximum vorticity for the fin vortex is shown by a dot in a triangle. Note that the total pressure and vorticity centres for the fin vortex do not coincide for this case. While this may be due to experimental inaccuracies it is not thought to be so, and the result is probably genuine. Also shown by Figs 8(a) and 8(b) is a region of vorticity associated with a total pressure loss, and marked 'A'. In comparison with the case for $\lambda = 0°$ the body vortex is more diffuse with lower values of total pressure loss and lower maximum vorticity. For $\lambda = 0°$ the maximum vorticity of the body vortex was approximately in the centre of the area enclosed by the $\xi = 1$ contour, while for $\lambda = -45°$ this is no longer so, and the body vortex is therefore less symmetrical. The body vortex centre defined by the total pressure minimum and vorticity maximum is close to, but slightly outboard of the position found for $\lambda = 0°$.

The vorticity contours for the fin vortex show a lobe extending towards the body vortex region, with a small matching lobe extending from the latter as if to link the two regions together. Another such, but weaker, affinity is suggested between feature 'A' and the body vortex. These linking areas can also be seen in the total pressure contour plot, where that associated with 'A' is the more pronounced. It seems possible that 'A' and the associated linking feature may represent the presence of fluid from the wake of the forward leeward fin.

Vector plots are shown in Fig 8(c), relative to the body axis as measured, and Fig 8(d), relative to the freestream (by subtracting the uniform cross flow component of the freestream flow). Also shown in these figures are the vortex 'centres' derived from total pressure and vorticity distributions, as described above. The alignment of the flow vectors gives a visual impression of the position of the body vortex centre, and is different for each of the figures. The perceived position that is closest to that derived from the total pressure and vorticity distributions is for the vector plot of Fig 8(d). This implies that the vortex is, at the survey station, tending to follow the freestream direction rather than tracking parallel with the body axis. If this is so, it is an interesting result and warrants further investigation. The fin tip vortex centre as determined from the vorticity distribution is coincident with the perceived vortex centre of Fig 8(d). The axis of this vortex must therefore also be lying close to the freestream direction. Returning to the linking features connecting the fin vortex and region 'A' to the body vortex; Fig 8(d) shows a region of approximately streamwise velocity (null vectors) in between the fin vortex and the body vortex, and a downward flow from region 'A' to the body vortex. It seems therefore that there may be a slow 'diffusion' of vorticity across the gap between the body vortex and the fin vortex, and that fluid from the wake of the leeward fin is being drawn into the body vortex.

Comparison of the body vortex strengths for $\lambda = 0°$ and $-45°$ on a consistent basis is difficult because of the much more intimate linking of the feeding region and the body vortex for the latter case. However, an arbitrary contour based on $\xi = 5$ has been selected as shown in Fig 8(b) and the estimate obtained is $\gamma = 0.22$, which compares with $\gamma = 0.24$ obtained for $\lambda = 0°$ and $\gamma = 0.35$ for the body alone. The strength of the fin vortex has been estimated for the $\xi = 5$ contour and the value $\gamma = 0.07$ was found. This is half the value for the similar case at $M = 0.7$. (This result differs strikingly from that which would be obtained from a simple horseshoe vortex model. From a knowledge of the fin panel loads as given in Ref 1 the ratio of the non-dimensional vortex strengths for these two Mach numbers would be predicted as 0.8, rather than the value of 0.5 measured).

The results of Section 4.1 have shown that mounting a set of fins near the nose of the model has a marked effect on the body vortex development downstream and that changes in the roll orientation of the fins are important. Data are presently available for one axial station only and further measurements at additional locations along the body will be necessary in order to define the flow field development.

4.2 ADDITION OF REAR MOUNTED FINS TO THE BODY ALONE

The delta fins were mounted on the body alone at x/d = 11.5 and flow surveys were performed at x/d = 12.2, placing the yawmeter tips in a plane 0.34d aft of the fin trailing edges. To allow true comparisons to be made some flow measurements were also performed for the body alone at x/d = 12.2 but are not presented here due to lack of space. These results were very similar to those presented for x/d = 11.5, to which reference can be made for qualitative comparisons.

4.2.1 Results for M = 0.7

The flow surveys with the fins present are shown in Fig 9 for λ = 0°, -45° and -72°. Total pressure distributions are given for all the cases, and for λ = -72° the vector plot is also shown. Vorticity distributions are not given since these results were not available at the time of preparing this paper, and are expected to be of limited value because the data are insufficiently closely spaced. The total pressure plots of Figs 9(a) to (c) show the change in conditions as the starboard fin approaches the body vortex. On each plot is shown the position of the minimum total pressure within the body vortex centre for x/d = 12.2 on the body alone. The effect of the fins on the body vortex will be discussed first, followed by some observations concerning the fin wakes.

For λ = 0° the vertical fin lies inbetween the pair of body vortices but a comparison with Fig 3(b) for the body alone shows that the centre of the starboard vortex (say within the contour H_L/H = 0.925) is little affected, and its location is little changed. The root of the horizontal fin has altered conditions at the body side and the feeding region has been attenuated. For λ = -45° the feeding region is cut by the fin, although vestiges of it remain. The central part of the body vortex is still largely unaffected. Finally, in Figs 9(c) and (d) we see the case where the starboard body vortex region is cut through by the fin. The flow downstream of this fin is the combination of the body vortex flow and the fin wake flow. Therefore the term "body vortex" strictly should not be applied to this starboard side vortex, which has clearly been intimately mixed with the fin wake. The interaction of the vortex and fin would be expected to result in the fin wake containing elements of streamwise vorticity of opposite sign to the body vortex, thus partially cancelling the vortex. The fin wake will also be deficient in total pressure which will contribute to the deficit already present in the body vortex. The measured flow appears to be consistent with these considerations, with the vortex appearing weaker and more diffuse, and with a larger central area of reduced total pressure. Nevertheless, the centre of the vortex region lies approximately in the same location as for λ = 0° and -45°, despite the interaction with the fin. The starboard feeding region for λ = -72° is attenuated in comparison with the body alone case. This is due to the presence of a fin panel lying at a roll angle of 18° below the horizontal meridian. The port body vortex and port fin would be expected to exhibit a state part way between the λ = 0° and -45° cases for the starboard side, and this is indeed the case.

It is worth noting some features of the fin wakes. For λ = 0° the horizontal fin wake is extensive and contains three regions of total pressure minima, one near to the fin root, and two more pronounced areas centred at 50% and 75% exposed semi-span respectively. The latter two regions appear to suggest a vortex shed at part span, probably generated by the inboard portion of the swept leading edge, and another vortex shed nearer to the tip. The minimum near to the body is possibly due to a separation in the fin root region. The results of Ref 1 show that for this case the fin panel is operating well into the non-linear normal force region, tending to confirm the present observations on the fin wake. As the fin is rolled to leeward the effective angle of attack is reduced, and the effective leading edge sweep is increased. The changes in the fin wake can be followed for the fins rolled to leeward by 18° (port-fin), 45° (starboard fin), and 72° (starboard fin); and trivially, 90° in Fig 9(a) for the vertical fin. The fin wake progressively becomes a less prominent feature as the fin is rolled to leeward, but some form of multi-vortex wake structure seems to be maintained at least up to λ = -45°. For the latter case there seems to be a large double tip vortex region and a further vortex at about 50% exposed semispan, and a low energy region near to the fin-body junction.

4.2.2 Results for M = 1.8

Total pressure distributions and vector plots are presented in Fig 10. As for M = 0.7, the position of the minimum total pressure in the body vortex for the body alone at x/d = 12.2 is superimposed on the plots. No distributions of vorticity have been included for the reasons given in Section 4.2.1.

Figs 10(a) to (c) show the total pressure distributions in the same order as those previously presented for M = 0.7. The presence of the fins has the same general consequences that were seen for M = 0.7 but with differences of detail, some of which are now discussed. For λ = -72° (Figs 10(c) and (f)) the starboard body vortex has moved, compared to the body alone case, by rather more than at M = 0.7; but the deviation is still relatively small, about 0.05d. The structure of the centre of the body vortex is not affected to the same degree by the close approach of the fin as it was at M = 0.7. The central region (say within the H_L/H = 0.7 contour) is about the same size, although the peak total pressure deficit is slightly smaller than for the body alone. The vector

plot of Fig 10(f) shows that the velocity distribution in the central region is also less affected than for M = 0.7. However, it should be noted that the body vortices are positioned slightly differently with respect to the fin for the two test Mach numbers. For M = 0.7 the nominal vortex position lies within the fin outline, while for M = 1.8 it is just to leeward of it. The sensitivity of the vortex to its position relative to the fin for small separation distances is not known, but this could be important. The movement of the starboard vortex (from the position it occupied in the body alone case) for $\lambda = -72°$ largely accounts for the asymmetrical flow in the vicinity of the leeward meridian. There was some asymmetry present at M = 0.7, but not quite to the same degree. At M = 1.8 the feeding region is a more pronounced feature of the flow than it was for M = 0.7, and therefore appears more persistent in the former case, particularly for $\lambda = -45°$.

The vector plots, when examined in conjunction with the total pressure plots, reveal some interesting regions. These are identified by sudden large changes between adjacent velocity vectors which correlate with features in the total pressure plots. These regions are identified by dotted lines on the total pressure plots, and by dot-cross lines on the vector plots, and appear in Figs 10(a), (b), (d) and (e) for $\lambda = 0°$ and $-45°$. The feature indicated for $\lambda = -45°$ probably indicates the presence of a shock wave, as is further suggested by the static pressure distribution (not shown). The explanation of the feature indicated for $\lambda = 0°$ is not so readily found, but it too may have a shock wave associated with it. This feature is also present above the starboard windward fin (lying at a roll angle of 18° below the horizontal meridian) for $\lambda = -72°$, and can be seen in Figs 10(c) and (f). It may also be present in an attenuated form above the port leeward fin for the same case. It is possible that the wakes shed from the fins contain more than one region of concentrated vorticity, as they did for M = 0.7, although the fins have nominally supersonic leading edges. There is some similarity in the fin wakes for M = 0.7 and 1.8 in that a feature exists at about 50% exposed semispan.

The results presented in Section 4.2 have an important bearing on missile prediction methods for vortex-fin interference load. It appears that it may be an acceptable approximation to employ the vortex flow that would obtain in the absence of the fin to such calculations, without the necessity of considering mutual interference effects and possible consequent changes in vortex position or structure. However, the feeding regions may have a significant effect on nearby fin panels, and these are disrupted by the presence of the fins. The importance of this effect on fin panel loading has yet to be established.

5 CONCLUSIONS

A series of wind-tunnel tests have been performed to measure the leeside flow field of a generalised missile model. Flow field data have been presented for a station towards the rear of the model for a body angle of attack of 14° and freestream Mach numbers of 0.7 and 1.8. The structure of the body alone flow fields has been investigated together with the modifying effects of mounting a cruciform set of delta fins in either a forward or rear location. For the body alone, well developed body vortices were evident for both M = 0.7 and M = 1.8.

The fins mounted in the forward position had a profound effect on the body vortex development as measured near the rear of the body. The effect achieved depended on model roll angle and Mach number. For M = 0.7 the body vortex development was heavily suppressed, particularly for the case of a horizontally mounted fin where the feeding region no longer rolled up into a vortex, but extended to leeward as a shear layer. For M = 1.8 the body vortex development was attenuated by the addition of the fins but still remained significant, although the vortex structure and position were altered.

For the aft mounted fins the main effect on the body vortex flow in cases where the body vortex did not impinge on a fin was the blocking or cutting of the feeding region. For the cases where the fins cut through or near to the centre of a body vortex, the vortex was still identifiable, and was approximately in the same location as for the body alone case. For M = 0.7 the body vortex was more diffuse, and the net vorticity was reduced by the fin; while at M = 1.8 there was less effect on the vortex. However, the nominal vortex locations relative to the fin chordal plane were not quite the same at the two test Mach numbers.

These results show that missile aerodynamic prediction methods for complete missile airframes currently do not represent correctly the effect of forward surfaces on the body vortex development. However, the assumption that the vortex-fin interference for aft surfaces can be calculated by ignoring possible profound effects of the fin on the vortex position or structure does not appear unreasonable, at least for fins of the same order of size as those investigated here.

The cases examined here are part of a continuing research programme into the development of vortex flows commonly present around missile airframes. Much scope exists for further study in order to provide the necessary material with which to improve missile aerodynamic prediction methods.

REFERENCES

1 A Petersen, T R Byram. Comparison of some panel load measurements for forward and aft-mounted fin panels on an axisymmetric body, 1982. AGARD CPP-336, Paper No 16.

2 S T Kitson. Reduction and presentation of results from RAE flow survey tests, 1982. BAe DG Report BT 13461.

3 L H Jorgensen, E W Perkins. Investigation of some wake vortex characteristics of an inclined ogive-cylinder body at Mach number 2, 1958. NACA Report 1371.

4 F R Grosche. Wind tunnel investigation of the vortex system near an inclined body of revolution with and without wings, 1971. AGARD CP-71-71.

5 W L Oberkampf, T J Bartel. Supersonic flow measurements in the body vortex wake of an ogive nose cylinder, 1978. AFATL-TR-78-127.

6 J F Mello. Investigation of normal force distributions and wake vortex characteristics of bodies of revolution at supersonic speeds, March 1959. J Aero Sci, Vol 26, pp 155-168.

7 B E Tinling, C Q Allen. An investigation of the normal force and vortex wake characteristics of an ogive-cylinder body at subsonic speeds, 1962. NASA TN D-1297.

8 D J Raney. Measurement of the cross flow around an inclined body at a Mach number of 1.91, 1955. RAE Tech Note No Aero 2357.

9 W C Ragsdale. Flow field measurements around an ogive-cylinder at angles of attack up to 15° for Mach number 3.5 and 4, 1972. NOLTR 72-198.

10 K A Fellows(Mrs). Flow survey above a body of revolution at transonic speeds, 1977. ARA Model Test Note M116/1.

11 J R Deane, M H Tovey(Miss). Vortex dominated flow fields. Analysis of ARA flow survey data, 1978. BAe Report ST 20963.

12 M R Mendenhall, J N Nielsen. Effect of symmetrical vortex shedding on the longitudinal aerodynamic characteristics of wing-body-tail combinations, 1975. NASA CR-2473.

ACKNOWLEDGEMENTS

The experiments were carried out with the assistance of the staff of the RAE Bedford 8 ft x 8 ft Wind Tunnel. Many people were involved but the efforts of S O Lineham, P J Haynes and M N Cripps were of particular value. Assistance with data computation was given by A Odell of RAE Bedford.

CONFIGURATION		ANGLE OF INCIDENCE, α (DEGREES)	AXIAL POSN IN CALIBRES FROM NOSE	MODEL ROLL ANGLE λ(DEGREES)	FREESTREAM MACH NUMBER
BODY ALONE	B	14·0	3·5	0	0·7, 1·8
	B	14·0	11·5	0	0·7*, 1·8*
	B	20·0	3·5	0, -45	0·7
				0	1·8
	B	20·0	11·5	0	0·7, 1·8
BODY PLUS 10 × 10 FORWARD DELTA FINS	BC_{IF}	14·0	11·5	0	0·7*, 1·8*
	BC_{IF}	14·0	11·5	-45	0·7*, 1·8*
	BC_{IF}	20·0	11·5	0	1·8
BODY ALONE	B	14·0	12·2	0, -45	0·7, 1·8
BODY PLUS 10 × 10 REAR DELTA FINS	BC_{IR}	14·0	12·2	0, -45, -72	0·7*, 1·8*

Reynolds number = 0·62 × 10^6 throughout (based on body diameter)

* Cases presented in this paper

Table 1 Range of configurations examined to date showing flow conditions and location of flow survey planes.

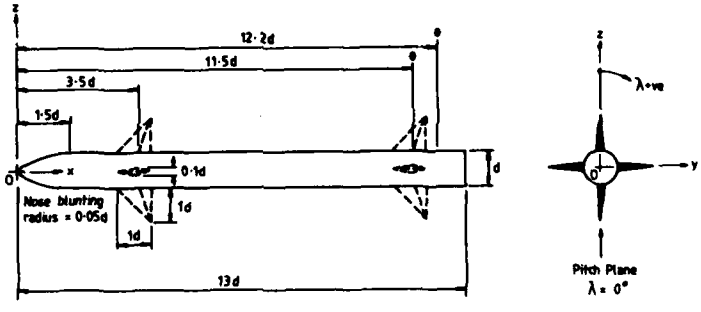

* Flow survey planes

Fig 1 Model dimensions and location of flow survey planes.

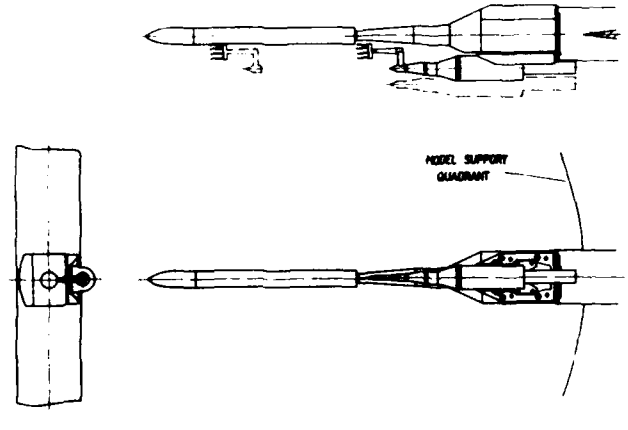

Fig 2 Model with flow survey traverse rig.

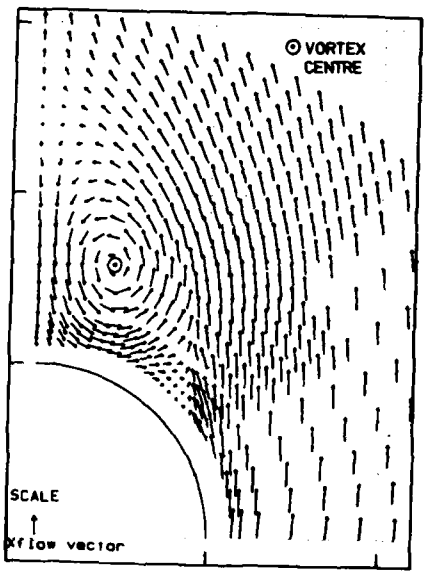

(a) Cross flow velocity vectors.

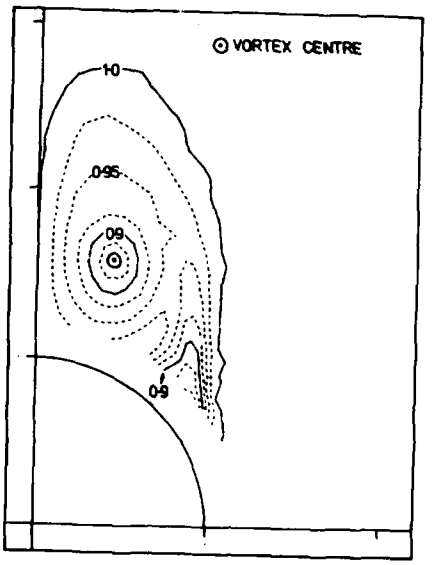

(b) Distribution of total pressure, H_t/H.

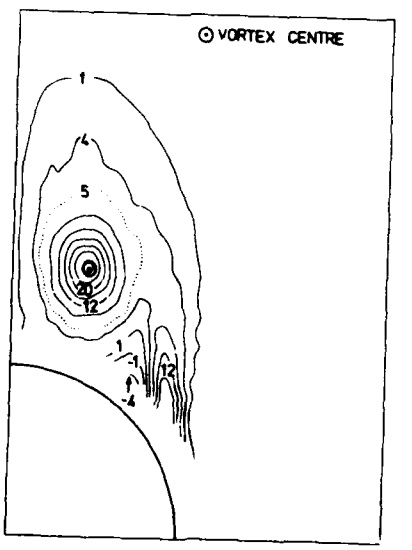

(c) Distribution of non-dimensional vorticity, ξ.

Fig 3 Flow survey for body alone. $M = 0.7$, $\alpha = 14°$, $x/d = 11.5$.

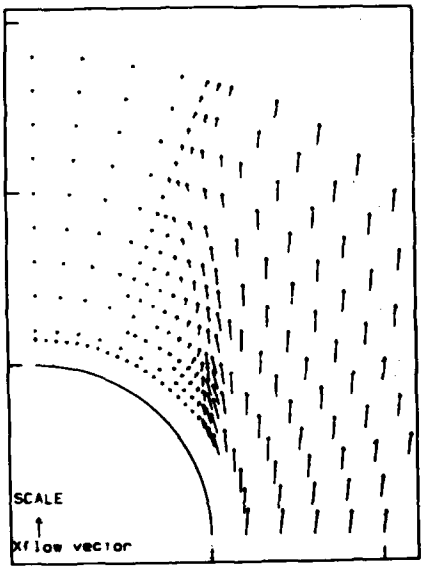

(a) Cross flow velocity vectors.

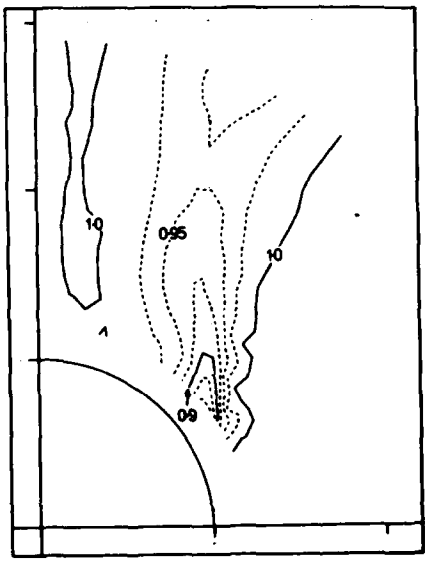

(b) Distribution of total pressure, H_L/H.

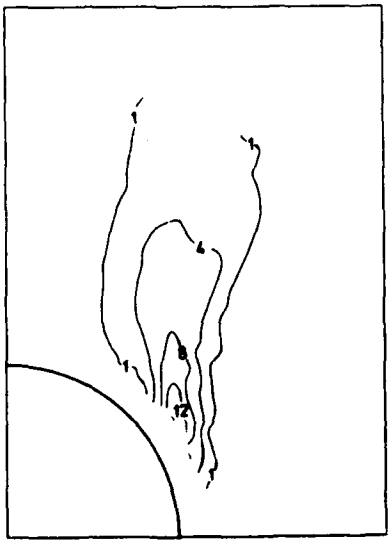

(c) Distribution of non-dimensional vorticity, ξ.

Fig 4 Flow survey for body plus forward mounted fins at $\lambda = 0°$. $M = 0.7$, $\sigma = 14°$, $x/d = 11.5$.

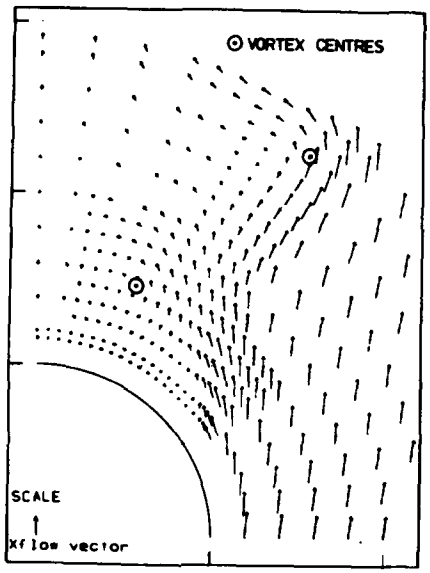

(a) Cross flow velocity vectors.

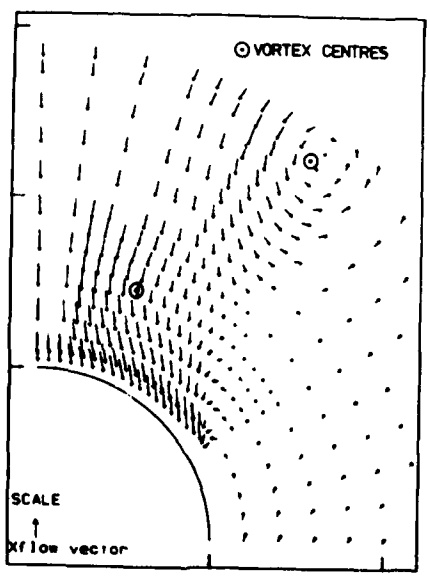

(b) Modified cross flow velocity vectors (the cross flow component of the freestream has been subtracted).

Fig 5 Flow survey for body plus forward mounted fins at $\lambda = -45°$, $M = 0.7$, $\alpha = 14°$, $x/d = 11.5$.

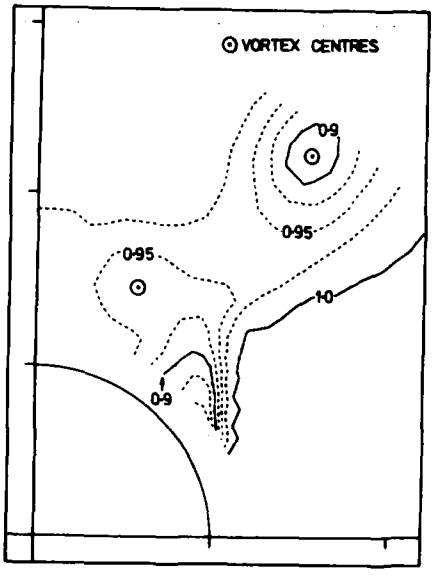

(c) Distribution of total pressure, H_L/H.

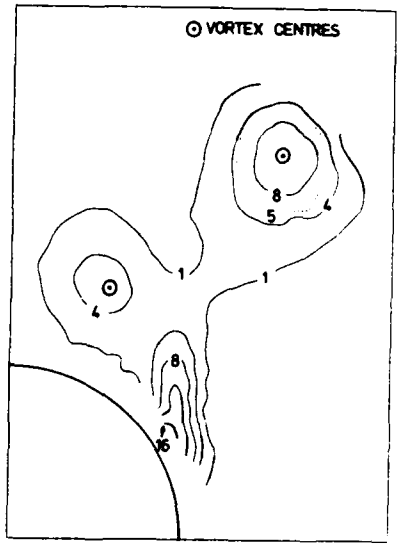

(d) Distribution of non-dimensional vorticity, ξ.

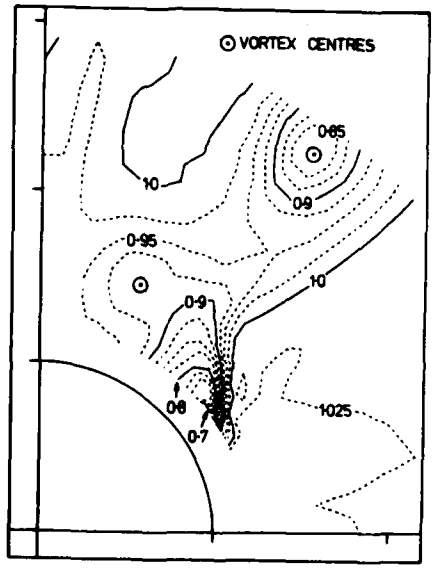

(e) Distribution of local Mach number, M_L/M.

Fig 5 Concluded.

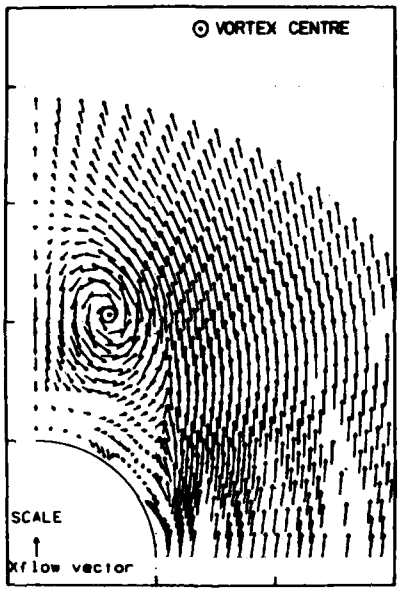

(a) Cross flow velocity vectors.

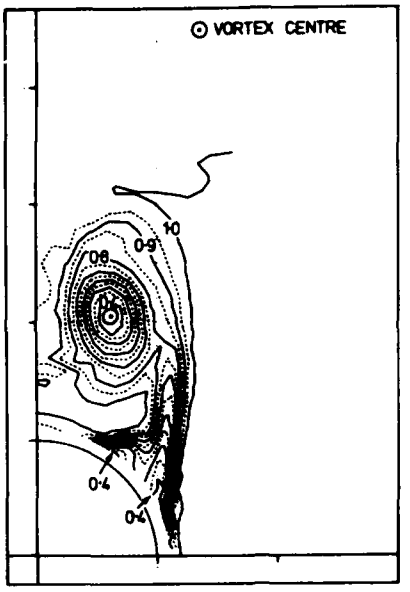

(b) Distribution of total pressure, H_L/H.

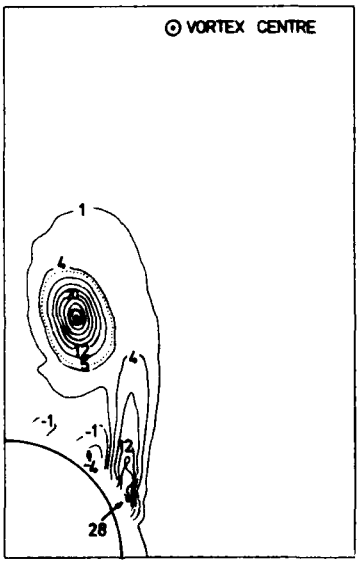

(c) Distribution of non-dimensional vorticity, ξ.

Fig 6 Flow survey for body alone. $M = 1.8$, $\alpha = 14°$, $x/d = 11.5$.

(a) Distribution of total pressure, H_L/H.

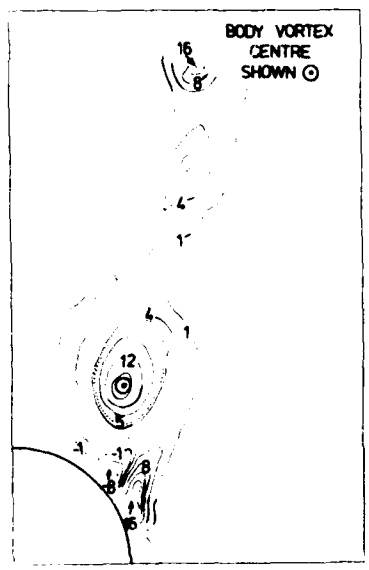

(b) Distribution of non-dimensional vorticity, ξ.

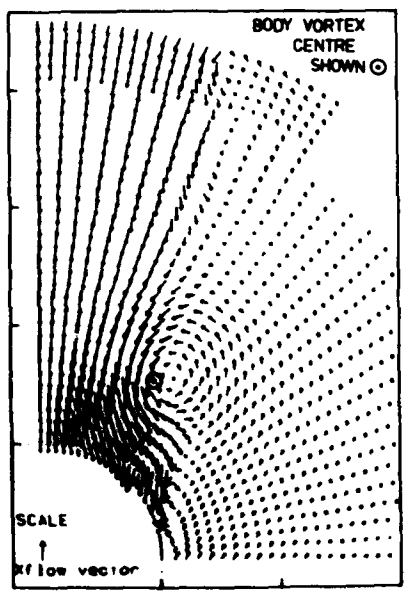

(c) Modified cross flow velocity vectors (the cross flow component of the freestream has been subtracted).

Fig 7 Flow survey for body plus forward mounted fins at $\lambda = 0°$. $M = 1.8$, $\sigma = 14°$, $x/d = 11.5$.

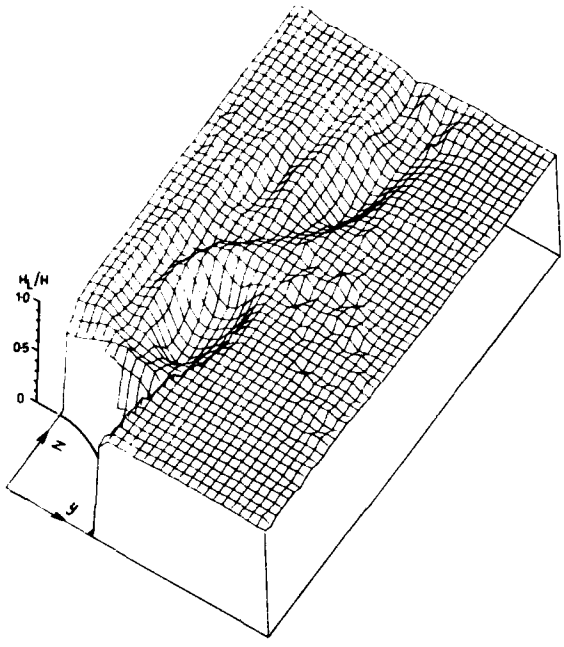

(d) Distribution of total pressure, H_L/H.

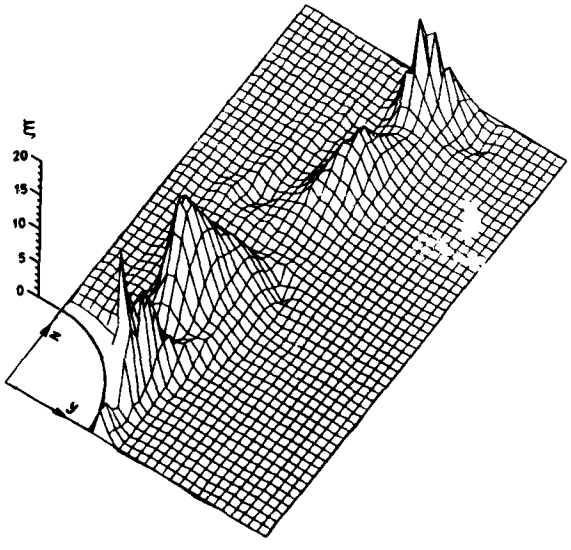

(e) Distribution of non-dimensional vorticity, ξ.

Fig 7 Concluded.

(a) Distribution of total pressure, H_L/H.

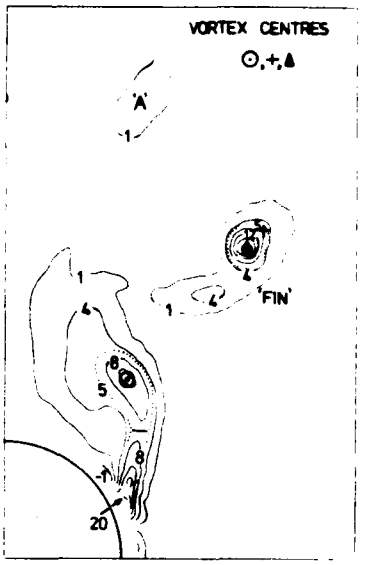

(b) Distribution of non-dimensional vorticity, ξ.

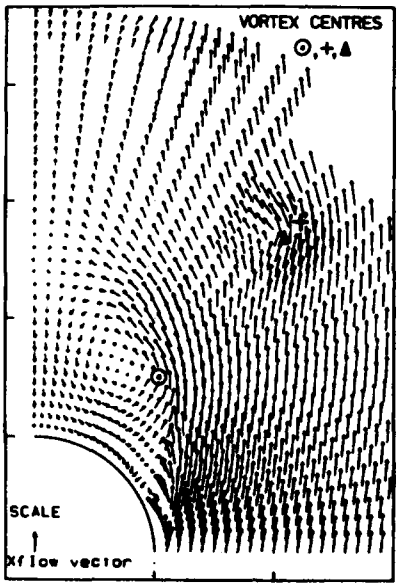

(c) Cross flow velocity vectors.

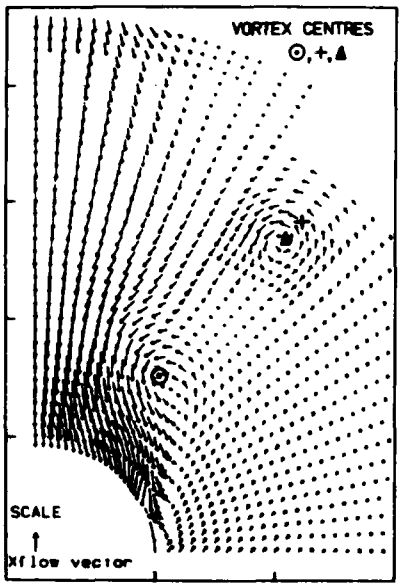

(d) Modified cross flow velocity vectors (the cross flow component of the freestream has been subtracted).

Fig 8 Flow survey for body plus forward mounted fins at $\lambda = -45°$. $M = 1.8$, $\alpha = 14°$, $x/d = 11.5$.

(a) Distribution of total pressure, H_L/H. $\lambda = 0°$.

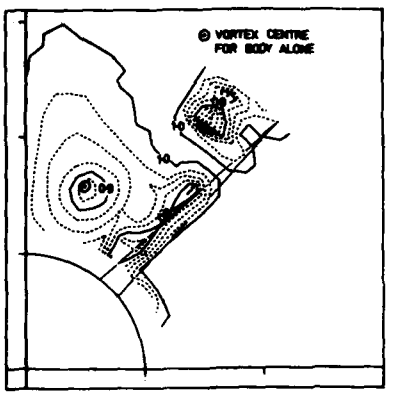

(b) Distribution of total pressure, H_L/H. $\lambda = -45°$.

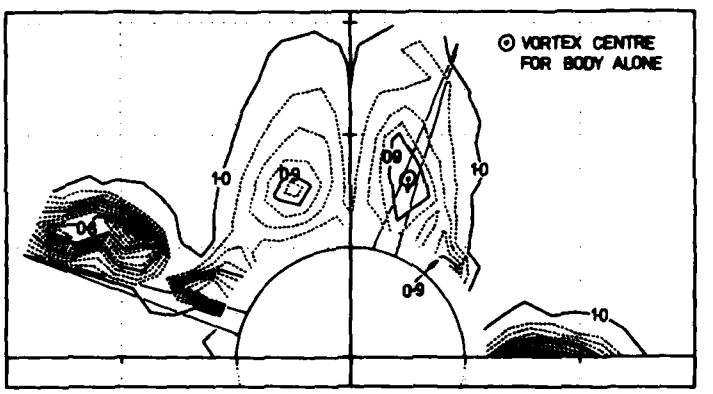

(c) Distribution of total pressure, H_L/H. $\lambda = -72°$.

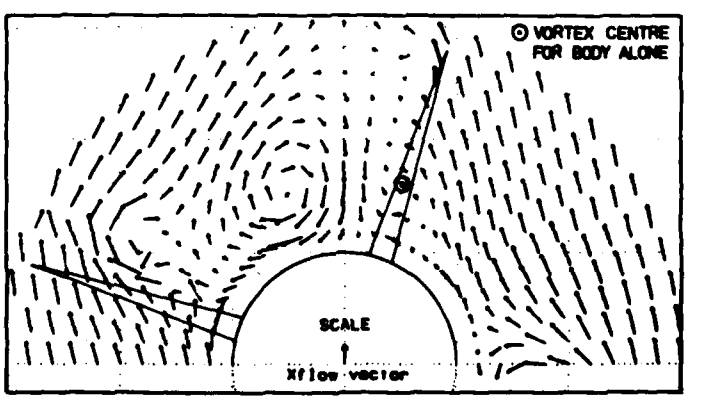

(d) Cross flow velocity vectors. $\lambda = -72°$.

Fig 9 Flow survey downstream of rear mounted fins. $M = 0.7$, $\alpha = 14°$, $x/d = 12.2$.

(a) Distribution of total pressure, H_L/H. $\lambda = 0°$.

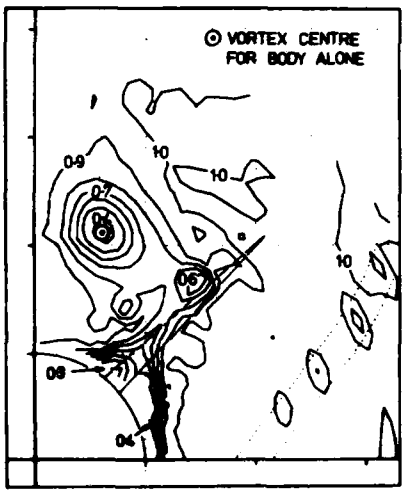

(b) Distribution of total pressure, H_L/H. $\lambda = -45°$.

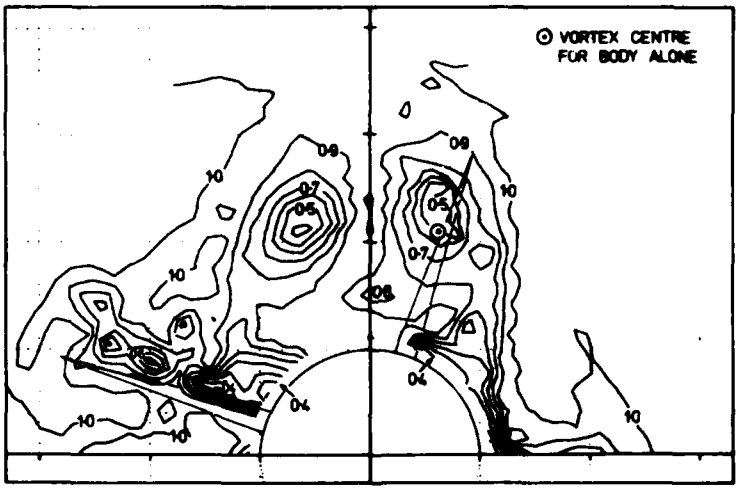

(c) Distribution of total pressure, H_L/H. $\lambda = -72°$.

Fig 10 Flow survey downstream of rear mounted fins. $M = 1.8$, $\sigma = 14°$, $x/d = 12.2$.

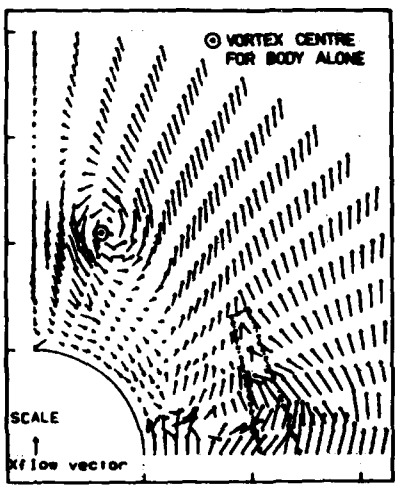

(d) Cross flow velocity vectors.
$\lambda = 0°$.

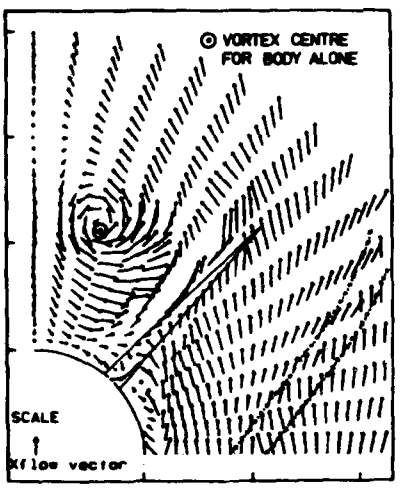

(e) Cross flow velocity vectors.
$\lambda = -45°$.

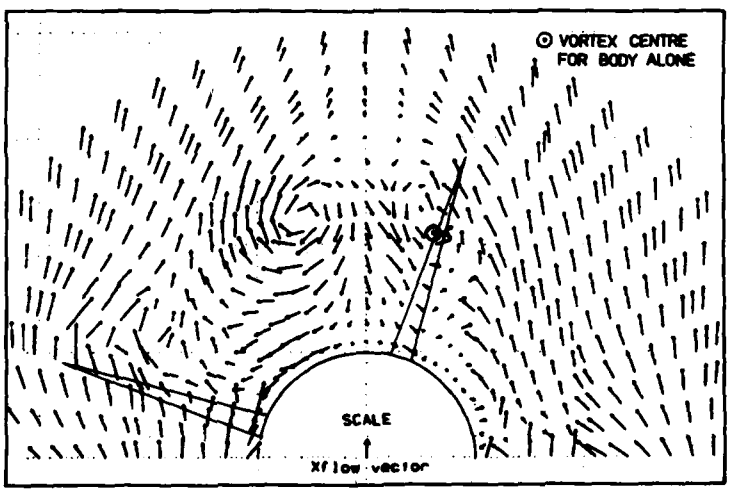

(f) Cross flow velocity vectors.
$\lambda = -72°$.

Fig 10 Concluded.

PREDICTING AERODYNAMIC CHARACTERISTICS OF VORTICAL FLOWS ON THREE-DIMENSIONAL CONFIGURATIONS USING A SURFACE-SINGULARITY PANEL METHOD

B. Maskew
Analytical Methods, Inc.
P.O. Box 3786
Bellevue, Washington 98052
U.S.A.

SUMMARY

A general low-order surface-singularity panel method is used to predict the aerodynamic characteristics of a problem where a wing-tip vortex from one wing closely interacts with an aft mounted wing in a low Reynolds Number flow; i.e., 125,000. Non-linear effects due to wake roll-up and the influence of the two wings on the vortex path are included in the calculation by using a coupled iterative wake relaxation scheme. The interaction also affects the wing pressures and boundary layer characteristics: these effects are also considered using coupled integral boundary layer codes and preliminary calculations using free vortex sheet separation modelling are included. Calculated results are compared with water tunnel experimental data with generally remarkably good agreement.

INTRODUCTION

The vortical flow regions that exist near a vehicle generating lift have varying degrees of non-linear interaction with the vehicle's surface, depending on the form of the configuration. Through their effects on the integrated forces and moments, these vortical flows can strongly influence the performance and stability characteristics of a vehicle. Only in the simplest case of the treatment of wing-tip vortices on a conventional transport aircraft with high aspect ratio wings operating at low lift coefficients can the non-linear effects be ignored. For the most part, predicting the aerodynamic characteristics of modern high-performance vehicles requires the non-linear effects of vortical flows to be included in the modelling (e.g., see reviews in Refs. 1 and 2). The present paper concerns the application of a surface singularity panel method, program VSAERO (for Vortex Separation AERODynamics (3)), to configurations with vortical flows at subsonic speeds. Iterative procedures are used for the non-linear effects of vortex wake location and for surface boundary layer development. Emphasis is placed on practical, cost-effective engineering solutions for the short-term treatment of problems, rather than an elegant mathematical modelling for the longer term.

The VSAERO code is basically a low-order panel method developed specifically for application to complete aircraft configurations operating in low-speed, high-lift conditions. The program gives comparable accuracy to higher-order formulations (see Ref. 3) but at a considerably lower computing cost. This fact, plus its inherent versatility and ease of use--both of which stem from its simple basis--make the method an attractive, practical tool for treating non-linear problems requiring iterative solution techniques; e.g., problems of vortex/surface interaction with wake deformation and viscous/potential flow effects included. Furthermore, the method has also proven practical for the treatment of unsteady problems using a time-stepping approach (4) and to modelling problems with extensive separation (5).

At the outset, justification for using the simple model approach for the non-linear vortical flow calculations was based partly on the concept of prescribed separation lines (6). This followed from the increasing tendency towards the use of controlled vortex separation using sharp-edged strakes, trips, etc. (1) and (2). Here, the designer aims to exploit the favorable aspects of vortex/surface interaction; e.g., the creative integration of the vortex low pressure zone in a region which enhances lift and thrust while also stabilizing surface flows. With this approach, stable vortical flow structures are obtained over a wide range of conditions. Calculation of vortex/surface interaction when the line of separation is fixed is therefore inherently more amenable to theoretical treatment (1) than is the case where the vortex separation is more by "accident"; e.g., separation from smooth rounded surfaces. In the latter case, the vortical flow pattern can change markedly with small changes in vehicle attitude and this can lead to poor stability characteristics. Although undesirable, this latter type of flow probably cannot be completely eliminated and so still needs some consideration. Also, situations exist where largely uncontrolled vortex/surface encounters occur, such as in the case of a helicopter rotor blade-tip vortex interacting with a following blade, or in the case of a wing in the presence of a canard vortex under off-design conditions. From these points of view, the scope of the VSAERO vortical flow calculations has been extended to try to locate and model separation boundaries in addition to including boundary layer displacement effects. These aspects, which are included in the present paper, are useful even when exploiting "controlled" vortex separation; it is important that the designer should know when and where vortex separation is likely to occur so that the applied vortex devices serve mainly as a "trigger" and a stabilising agent for the phenomenon.

There are a number of aspects of vortical flow interaction that are of concern for a practical prediction method both as regards modelling and also for the numerical behavior:

(i) the condition at the separation line--how are the singularity values transferred from the solid boundary onto the free vortex sheets and how does this relate to a Kutta condition?

(ii) How does the newly formed vortical structure interact with the local (i.e., generating) surface? For example, vortices at the wing leading- and tip-edges and also flap edges.

(iii) How does the essentially fully developed vortex core and wake interact with downstream surfaces; e.g., canard/wing or body/fin problems?

(iv) What happens to the vortex core structure as it passes through downstream pressure gradients? For example, questions on vortex breakdown.

The present paper is largely concerned with item (iii). For this case we examine the vortex wake from one wing interacting with an aft located second wing. In recent years this problem has received considerable attention in relation to aircraft wake-vortex hazard; e.g., Reference 7.

Earlier calculations of vortex/wing interaction considered a straight onset vortex passing over a wing (e.g., Refs. 8, 9 and 10). Patel and Hancock (9) warned of the need to complement such calculations with experimental work since the non-linear aspects of modifying the wing boundary layer and the effect of the wing on the path of the vortex were not included. The present method has been developed to include these aspects in the computation and has already shown very good results in applications to a number of aircraft configurations, some of which had strong vortex interactions (e.g., Ref. 11). In addition, several exploratory calculations have been performed on the basic problem of a wing in the presence of an oncoming vortex wake; these calculations were of the nature of numerical experiments whose main purpose was to explore the behavior of the program. A case in which an oncoming wake actually intersected a downstream wing was reported in Ref. 12 in relation to helicopter application. This situation has also been encountered in a canard/wing configuration. Reference 6 discusses a case where the edge vortex of the oncoming wake passed over the aft wing. In both cases, the roll-up of the wake and the track of the edge vortex were calculated under the influence of the complete two-wing configuration. This second case also included preliminary surface streamline and boundary layer calculations. The present paper continues the vortex-wing interaction investigation and compares the calculated results with experimental data from a water tunnel (13).

METHOD DESCRIPTION

The whole flow field is regarded as a potential flow with regions of viscous domination confined to infinitely thin boundary layers and free shear layers and to vortex cores of small diameter. The basic formulation of the VSAERO panel method by way of Green's Theorem is described in Reference 3. For completeness, a brief overview of the method is presented here before describing more details of the wake relaxation procedure. The outline of the complete iterative procedure--including that for the viscous/potential iteration--is shown in Figure 1.

The surface of the configuration is approximated by a set of flat quadrilateral panels of uniform source and doublet singularities. The panel source values are determined by the local external Neumann boundary condition while the panel doublet values are solved from a set of simultaneous linear equations specifying explicitly the internal Dirichlet boundary condition that the total velocity potential on the interior surface of each panel shall be equal to the free-stream velocity potential there (i.e., the condition of zero perturbation potential inside the volume). This particular formulation gives a doublet/source combination which is just one of an infinite set (other forms were considered earlier for VSAERO (3)). The present formulation was used earlier by Johnson and Rubbert (14) but in a higher-order method. The low-order formulation in VSAERO gives an equation identical to that given by Morino (15) who used a direct application of Green's Theorem in the external flow field.

In VSAERO, the wake surfaces (i.e., the free shear layers) are represented by flat quadrilateral panels of uniform doublet singularities. The wake panel strengths are determined by the conditions at the separation line. The piecewise constant singularity distribution gives a discrete vortex-line model for simple wakes. The initial vortex-line geometry is normally prescribed; alternatively, a simple preprocessor is being coupled to the program to generate the initial wake structure for complex configurations (6). In subsequent solutions, vortex lines are relocated along calculated mean streamlines in an iterative procedure, Figure 1.

Within the program the geometry of each vortex line is described in a system of vertical cross-flow planes called Wake-Grid-Planes, Figure 2. The wake-grid-planes are given x-station locations in the program input; more dense spacing is used in regions where large curvature is expected in the wake lines.

A wake panel is normally bounded by two consecutive wake-grid planes and by two neighboring vortex lines, Figure 2. A regular wing wake has its panels arranged in columns starting at the upstream separation panel. On this type of wake all the panels down a column have the same doublet strength determined by the jump in velocity potential across the separation line. The jump in doublet strength from one column to the next is the strength of the streamwise vortex at the common boundary.

Another type of wake is used to enclose large regions of separation (5). This has a linear doublet distribution in the streamwise direction (representing uniform vorticity with tangential vector in the cross-flow direction). In the cross-flow direction the wake doublet distribution is still piecewise constant. This separation model is still under development, particularly for the more general vortical type of separation.

During the wake relaxation iterative procedure the wake panel streamwise edges (i.e., vortex segments) are repositioned into calculated local mean flow directions. The panel corners are maintained in the wake-grid planes. The local velocity vector is calculated at the set of corner points in each wake-grid plane in turn and the local average vector used to move across each wake-grid-plane interval. When moving from one plane to the next, an initial velocity is first predicted at the next wake-grid plane using a linear extrapolation of two previously calculated upstream velocities (if available). The average direction across the new interval is then used to relocate the next point on the wake line. At this time a new velocity is calculated at the new point by summing all contributions from the singularity panels and onset flow. A corrected point is then obtained. The calculation normally proceeds through this predictor/corrector cycle for one more pass; however, more cycles can be requested if necessary. All wake lines intersecting a wake-grid plane are treated together; i.e., the velocities are evaluated for all points in that plane before moving the lines over. All wake points in the downstream wake-grid planes are simultaneously moved over by the movement vector for their respective wake line. The wake-grid-plane scheme is very effective for regular forward flight but has drawbacks for situations where the local flow deviates from the general onset flow direction by a large angle. (A more general scheme is being considered as an alternative module for such cases.)

When the wake shape iteration cycles are complete the program--using the latest potential flow solution--computes inviscid surface streamlines (i.e., external to the boundary layer). This routine, which is based on a second-order surface stream function formulation, was developed and coupled to the VSAERO program by T.S. Vaidyanathan. The procedure is described in Reference 16. The location of a point on each streamline is selected by the user who is, therefore, responsible for ensuring that a family of streamlines adquately covers the regions of interest.

Integral boundary layer calculations are then performed along each computed streamline using boundary layer codes assembled earlier by F.A. Dvorak and described in Reference 17. At this time the essentially two-dimensional integral methods are preferred in keeping with the practical approach and low computing times. The integral methods coupled in the VSAERO program at this time include the effects of surface curvature and streamline convergence/divergence under the assumption of local axisymmetric flow. However, they can be expected to break down in regions of large cross flow; e.g., near a vortical separation line. (An alternative infinite swept-wing boundary layer code with cross flow model is also coupled with the VSAERO program but this was not used in the present work.)

For laminar flow the method is basically that of Thwaites (18) with an adaptation by Curle (19). Transition is based on Granville's (20) procedure. Conditions for laminar separation and turbulent reattachment or catastrophic separation are based on empirical relationships from measurements by Gaster (21) and others. The turbulent boundary layer development calculation is the Nash and Hicks (22) method.

The boundary layer module is fully coupled with the VSAERO inviscid code in an outer viscous/potential iteration loop, Figure 1. In further iterations, the displacement effect of the boundary layer is modelled in the potential flow calculation using the source transpiration technique; i.e., the boundary layer displacement term appears in the external Neumann boundary condition equation as a local non-zero normal velocity component and is thereby related directly to source singularities in this formulation. The boundary layer calculation also provides a separation point on each streamline, thereby defining a boundary of separation for a family of streamlines. The criterion for separation is currently a vanishingly small skin friction coefficient (in the direction of the external streamline). Although not strictly correct, particularly in regions of strong cross flow, the procedure has given surprisingly good guidance for the onset of separation for a wide range of practical problems. Given the location of separation lines, later calculations can be performed in which the separated flow zone is enclosed within free-vortex sheets which then form part of the overall vortex/wake structure of the problem.

VORTEX/WING ENCOUNTER

Configuration Description

The general layout of the model used in the water tunnel experiment in Reference 13 is shown in Figure 3. Basically, a vertical wing with a NACA 0015 section set at 10° to the onset flow is placed ahead of a horizontal wing with a NACA 0012 section. The tip of the forward wing is level with the quarter-chord line of the aft wing. The forward wing has a chord of 2 inches and the aft wing, 4 inches. The distance between the two quarter-chord lines is 8 inches. The quarter-chord lines form the pivot axes for the two wings. For the calculations, the rear wing is considered at three setting angles, 8°, 12° and 16°. The rear wing is mounted between the water tunnel walls, with the tunnel 8.4 inches wide and 12 inches deep. The Reynolds Number of the flow based on the aft wing chord is 125,000.

For the present calculations, the tunnel surfaces are not panelled; instead, pseudo two-dimensional conditions are represented for the aft wing by extending its wing tips, giving an aspect ratio of about 8, Figure 4. The forward wing has been given a span of 12 inches so that its center section coincides with the tunnel roof location; it has 8 panels around the chord, 9 panels vertically and a 3 x 4 panel array closing the bottom tip edge. Panel size distributions are weighted towards the leading edge and towards the bottom tip edge using equal angle increments in a simple cosine formula.

The rear wing is panelled in three parts: the two parts outside the tunnel wall location each have 16 panels chordwise and 3 panels spanwise. The wing "inside" the tunnel has 32 panels chordwise with density increasing towards the leading edge. The spanwise panel arrangement has a central zone with 12 columns equally spaced and two outer zones of 3 panel columns increasing in size away from the wing center. This central piece of the wing--which corresponds with the actual wing in the experiment--was declared a separate component in the present program in order to obtain the force and moment acting on it for comparison with the experimental data.

The calculations start with the wake lines preceeding straight back parallel to the onset flow, Figure 5. This figure also shows the location of the wake-grid planes. The figure does not show the downstream part of the wake where the wake-grid planes are located at ever widening intervals. Notice that in the starting condition shown in Figure 5, the vortex lines actually pass through the aft wing. This is not a recommended practice in general, but was employed here as part of the checkout of the behavior of the calculations. This is considered further in the 12° case below.

Wing Alone

Preliminary runs were made with the aft wing alone at 8°, 12° and 16° angle of attack. The main objective was to make sure that the flow was essentially parallel at the tunnel wall location; however, the calculation of the basic flow condition was also of interest. The calculations included a second pass through the viscous/potential iteration cycle bringing in the effect of boundary layer displacement but not modelling separation at this time. The calculated flow conditions (upper surface) are summarised below.

(i) 8°:- Laminar separation with turbulent reattachment occurred near the leading edge and the turbulent boundary layer remained attached back to the trailing edge.

(ii) 12°:- Again, laminar separation with turbulent reattachment occurred near the leading edge, and turbulent separation occurred at about 85% of the chord. Figure 6 shows a plan view of the calculated streamlines and separation zone. Normally, further viscous/potential flow iterations would be performed for this case using the separated flow model.

(iii) 16°:- Catastrophic laminar separation occurred from near the leading edge over the full span.

As far as the extent of separation is concerned, the above results are essentially confirmed by experimental observations with the forward wing at 0° and using hydrogen bubble flow visualization. However, force and moment data (13), not shown here, indicate a significant loss in lift curve slope after about 8°. Certainly, from past experience with this type of calculation, modelling the separated flow in the 12° case would be expected to move the predicted separation forward.

Two-Wings

With the forward wing in place and set at 10°, the calculations were performed over three wake-shape iterations; i.e., three complete potential flow calculations were performed, the first with the prescribed wake in Figure 5 and then with two calculated shapes. (Convergence of the results will be discussed later under the 12° case.) Surface streamline and boundary layer calculations were then carried out.

A typical calculation takes about 160 C.P. secs. on the CRAY computer and requires 163,000 memory words; this calculation involves a total of 756 surface panels (i.e., 756 unknowns), 33 wake columns with about 400 wake panels, 15 on-body streamlines--each with a boundary layer calculation--and 450 off-body velocity calculations.

Calculations were performed for aft wing incidences of 8°, 12° and 16°. Photographs of the experimental flow field (using hydrogen bubble visualization) for these angles were provided by C. Tung. These are shown in Figure 7(a), (b) and (c), respectively.

Aft Wing at 8°

A general view of the final calculated wake shape for the 8° case is shown in Figure 8(a); only the "real part" of the aft wing is plotted. Figure 8(b) shows a side view of this. The computation of the roll-up of the tip vortex lines is clearly affected by the presence of the aft wing; there is a tendency for the rate of roll-up to decrease in the acceleration zone ahead of the wing and then to increase again in the recovery zone towards the wing trailing edge. This behavior is very plausible and merits further investigation in the future in relation to the implied helix angle in the roll-up and the connection between this and the onset of vortex breakdown.

The dotted line in Figure 8(b) indicates the locus of computed centroid of vorticity for the vortex lines involved directly with the tip roll-up. This locus is in remarkably good agreement with points representing the path of the vortex core in the experiment. These points were measured from the flow field photograph (Figure 7(a)). The small vertical shift in the vortex path is due to tip-edge separation occurring ahead of the trailing edge. This tip-edge vortex formation was not modelled in the present calculation.

After the third wake shape solution, a family of inviscid surface streamlines was calculated on the aft wing and boundary layer calculations were performed. Figure 9 shows a plan view of these streamlines, each of which is stopped at the point of calculated separation. Whereas the wing-alone case remained fully attached, we now see a region of turbulent separation on the left side of the wing brought on by the increased loading on the upwash side of the vortex. It is difficult to positively confirm this feature from the flow field photograph, Figure 7(a), at this time. The thickness of the region highlighted by the bubbles and located beneath the vortex has certainly thickened slightly relative to the wing-alone case (13).

A calculated velocity survey conducted in a vertical plane just behind the wing, Figure 10, gives the impression that the vortex roll-up has been flattened slightly by its interaction with the aft wing.

The computed force and moment coefficients for the aft wing at 8° are compared with experimental measurements in Figure 11 and show remarkably good agreement.

Aft Wing at 16°

With the aft wing set at 16°, the streamline/boundary layer calculations--performed after the wake-shape iterations--gave essentially the same result as for the case with wing alone; i.e., laminar separation along the entire leading edge, except in this case there was a small zone just on the downwash side of the vortex where turbulent reattachment was predicted (i.e., under the slight alleviation of the leading-edge suction peaks). However, turbulent separation occurred within 10 to 15% back from the leading edge. Although these tendencies seem plausible, such flow details have not been obtained from the experiment at this time.

The trajectories of the calculated wake lines for the above case are shown in side view in Figure 12. The locus of the calculated vorticity centroid for this initial solution follows closely the experimental vortex track (transferred from Figure 7(c)) ahead of the aft wing. The calculated path shows a slightly larger upswing just before the leading edge--this is consistent with the larger level of circulation, see Figure 11, in the initial calculation which has attached flow. Due to this additional circulation, the computed vorticity centroid locus is pulled quickly down over the upper surface of the wing, whereas the experimental vortex path passes more freely higher above the surface.

A second calculation was performed in which the predicted separation zone was enclosed within free vortex sheets (5). Initially, there was some conflict between the two wakes as they were relaxed simultaneously--the initial wake lines from the front wing (Figure 5) actually pass inside the rear separated wake. The calculated wake shape after the third solution is shown inset in Figure 12. Another pass should be performed in this case. A better approach would probably be to first relax the oncoming wake while holding the aft wing wakes rigid, then releasing the latter in the third pass. In any event, this calculation was not pursued to a complete convergence at this time. Also, there were indications (see below) that the vorticity separation model may require further ingredients for these highly three-dimensional situations where considerable vortex sheet stretching can occur.

Even though this calculation is incomplete at this stage, the track of the calculated vorticity centroid shows a plausible change relative to the attached flow solution, showing a smaller upswing ahead of the wing leading edge and passing more freely above the wing. In fact, the track over the wing now runs approximately parallel to the experimental vortex path except it is too low. The reason for the latter discrepancy is not clear at this stage, especially since the computed lift coefficient--and also the drag coefficient--are now in close agreement with the experimental measurements, Figure 11. The pitching moment coefficient also is in reasonably good agreement with the experiment. All three quantities show quite large changes due to including the separation model, Figure 11.

A chordwise pressure distribution computed on the aft wing close to the vortex passage location is shown in Figure 13(a). Pressure coefficients inside the separation zone (i.e., almost the entire upper surface) include the term for the jump in total pressure relative to free stream (5). Although the distribution is in good shape on the whole, the small hump in the upper surface distribution is a matter for concern. The main contribution to this is a chordwise velocity increment rather than a spanwise component which might then have been attributed to the passing vortex. The chordwise velocities are strongly influenced by the separated vortex sheet model, which at this station is strongly influenced by the oncoming vortex. Examination of the separation model formulation in this situation has indicated a possible weakness due to the vortex sheet stretching; model refinements are therefore being planned.

Figure 13(b) shows the chordwise plot of surface velocity magnitude corresponding to the pressure coefficient distribution above. This indicates an almost converged solution for the separated flow model--the present calculation was based on inner and outer velocity magnitudes of 0.05 and 1.3, respectively, for the velocity shear across the vortex sheets. These values determine the wake vorticity level and, hence, the magnitude of the total pressure difference between the onset flow and the separated flow. The computed velocity values at both ends of the separated zone are very close to the above values, Figure 13(b).

Aft Wing at 12°

The convergence of the wake-relaxation iteration was examined for the 12° case. Figure 14 compares the computed wake-line shapes for the second- and third-wake solutions. The recovery from the initial "bad" setup (Figure 5) is clearly very rapid for the basic attached flow case. Also, there is very little change in the geometry between the second and third wakes. Comparisons of wing pressure distributions (not shown here) also confirm the convergence of the solution.

In the third wake-shape iteration it is interesting to compare the spanwise velocity components, Vy, calculated along three spanwise cuts through the aft wing. Figure 15 shows the upper and lower Vy distributions at chordwise stations, x/c $\approx$ 0.0, 0.25 and 0.9. Near the leading edge, the spanwise flow induced by the vortex is obviously almost the same on the upper and lower surfaces--these have just "entered" the circulatory velocity field around the vortex. The spanwise velocity component, therefore, has peaks on both surfaces. At the quarter-chord station, however, the lower surface has almost "forgotten" that the vortex is present and by the 90% chord station on the lower surface there is essentially no trace left of the vortex effect. On the upper surface, the spanwise velocity peak first increases from the leading edge to the quarter-chord station, then decreases towards the trailing edge. In the meantime, the effective base width of the Vy peak grows steadily as we proceed across the wing chord.

The calculated locus of vorticity centroid for the tip vortex lines is in remarkably good agreement, Figure 16, with the track of the experimental vortex taken from Figure 7(b). As it passes over the aft wing, the latter appears to cover a wider zone than was the case at 8° and 16°; real-time observation in the experiment suggests an unsteadiness in the vortex path rather than a broader vortical region (13). The calculated vorticity locus seems to favor the lower edge of the region--this would be consistent with the fully attached assumption of the calculation and perhaps an intermittent separation in the experiment caused by the mutual interaction between the vortex path and the extent of separation; i.e., a low vortex path may induce separation causing the vortex to move up, at which time the decreased interaction may allow a reattachment or at least a reduced extent of separation--and this would bring the vortex back down again.

The streamline/boundary layer calculations for the 12° case do, in fact, indicate an interesting situation, Figure 17. The calculations predict a catastrophic laminar separation from the leading edge over the entire upwash side of the oncoming vortex; elsewhere, the laminar separation is followed by turbulent reattachment and eventual separation occurs well back on the upper surface. In comparison with Figure 6, the present upwash-side separation is clearly vortex induced.

The perturbation to the wing pressure distributions due to the presence of the vortex is illustrated in Figure 18, which compares the chordwise pressure distributions at spanwise stations, y = -1, 0 and +1; i.e., proceeding from the upwash side to the downwash side through the vortex location. These locations represent horizontal offsets from the projected vortex position of approximately the height of the vortex above the surface at the quarter-chord line. The main differences in the computed pressure coefficients occur on the wing upper surface forward of the quarter-chord location. The suction peak varies from -5.9 through -4.9 to -3.3 as we proceed from the upwash to the downwash side.

These calculations, of course, represent the first pass of an iterative solution; i.e., the separation has not been modelled at this stage. Initial attempts at modelling the part-span separation have so far met with mixed success. Certainly, sectional lift, drag and pitching moments calculated at sections both on the upwash and on the downwash side of the vortex have values closely related to the total experimetnal values: however, in the region of the predicted edge of the part-span separation, the interaction between the onset vortex and the open end of the separation model are clearly very strong, and, as mentioned for the 16° case, the separation model does not at this stage include adequate representation for vortex sheet stretching--which in this case is a serious omission. The planned refinements in the model, therefore, are absolutely essential for

further treatment of this case. Another factor that must also be considered for the present case is the jump in total pressure that is essential for calculating separated zone pressures at the end close to the tunnel wall location; near the onset vortex location, however, the side of the separated zone is essentially open to the free air and, consequently, has the same total pressure as the onset flow. A model of the total pressure variation between these two extremes must be considered in future refinements. In the meantime, further information on the actual vortical flow pattern in the experiment, including surface flow visualization, would be a very beneficial guide to any modelling improvements.

CONCLUSIONS

Program VSAERO, a low-order panel method with coupled iterative routines for representing non-linear effects due to wake shape and boundary layer growth, has been applied to a simple vortex/wing encounter problem with very encouraging results and with very reasonable computing costs.

(i) Vortex wake trajectory calculations converged rapidly in the two-wing situation with attached flow wakes, even though the initial wake lines cut through the aft wing.

(ii) With separated flow wakes included in the model, some minor numerical problems occurred in the interaction between these and the oncoming vortex. A simple cure for this seems to be to delay the aft wake relaxation until the forward wake is in position.

(iii) Computed vorticity centroid loci agreed fairly well with the experimental vortex track for the 8° and 12° aft wing cases, but was somewhat below--but parallel--to the experimental track over the massive separation for the 16° case.

(iv) Computed force and moment coefficients were in good agreement with measured data for the 8° case and also for the 16° case with initial separation modelling.

(v) Further refinement in the separation model vortex sheets, e.g., allowing the vorticity level to vary with distance, would improve some details of the vortex/wing calculation with full-span separation. Such changes are absolutely essential for the part-span separation model which also needs additional treatment for the probable vortical separation under the vortex.

(vi) Finally, it should be emphasized that these conditions were at very low Reynolds Number, 125,000. Similar calculations performed earlier at higher Reynolds Number gave quite different separation characteristics; in other words, some caution is needed if attempting to relate the results of vortex/surface interaction to conditions at a different Reynolds Number.

REFERENCES

1. Smith, J.H.B., "Inviscid Fluid Models Based on Rolled Up Vortex Sheets for Three-Dimensional Separation at High Reynolds Number", AGARD LS 94, (Three-Dimensional and Unsteady Separation at High Reynolds Numbers), May 1978.

2. Peake, D.J. and Tobak, M., "Three-Dimensional Interactions and Vortical Flows with Emphasis on High Speeds", NASA TM 81169, March 1980.

3. Maskew, B., "Prediction of Subsonic Aerodynamic Characteristics--A Case for Low-Order Panel Methods", Paper 81-0252, Presented at the AIAA 19th Aerospace Sciences Meeting, St. Louis, MO, January 12-15, 1981.

4. Maskew, B., "Influence of Rotor Blade Tip Shape on Tip Vortex Shedding--An Unsteady Inviscid Analysis", Paper 80-6 in Proceedings of the 36th Annual Forum of the American Helicopter Society, May 1980.

5. Maskew, B., Rao, B.M. and Dvorak, F.A., "Prediction of Aerodynamic Characteristics for Wings with Extensive Separations", Paper No. 31 in Computation of Viscous-Inviscid Interactions, AGARD-CPP-291, September 1980.

6. Maskew, B. and Rao, B.M., "Calculation of Vortex Flows on Complex Configurations", Paper 6.2.3, in ICAS Proceedings 1982, held in Seattle, WA, U.S.A., August 22-27, 1982.

7. Rossow, V.J., Corsiglia, V.R., Schwind, R.J., Frick, J.K.D. and Lemmer, O.J., "Velocity and Rolling-Moment Measurements in the Wake of a Swept-Wing Model in the 40- by 80-foot Wind Tunnel", NASA TM X-62414, April 1975.

8. Johnson, W., "A Lifting-Surface Solution for Vortex-Induced Airloads", AIAA J., Vol. 9, No. 4, April 1971.

9. Patel, M.H. and Hancock, G.J., "Some Experimental Results of the Effect of a Streamwise Vortex on a Two-Dimensional Wing", Aeronautical J., April 1974, pp. 151-155.

10. McMillan, O.J., Schwind, R.G., Nielsen, J.N. and Dillenius, M.F.E., "Rolling Moments in a Trailing Vortex Flow Field", NASA CR-151961, February 1977.

11. Maskew, B., Strash, D., Nathman, J. and Dvorak, F.A., "Investigation to Advance Prediction Techniques of the Low-Speed Aerodynamics of V/STOL Aircraft", to be published as a NACA CR.

12. Clark, D.R. and Maskew, B., "Calculation of Rotor/Airframe Interference for Realistic Configurations", Paper No. 2.6, Presented at the 8th European Rotorcraft and Powered Lift Aircraft Forum, Aix-en-Provence, France, August 31 - September 2, 1982.

13. McAlister, K.W. and Tung, C., "Airfoil Interaction with an Impinging Vortex", to be published as a NASA TM.

14. Johnson, F.T. and Rubbert, P.E., "A General Panel Method for the Analysis and Design of Arbitrary Configurations in Subsonic Flows", NASA CR-3079, 1980.

15. Morino, L., Chen, L.-T., and Suci, E.O., "Steady and Oscillatory Subsonic and Supersonic Aerodynamics around Complex Configurations", AIAA J., Vol. 13, No. 3, March 1975.

16. Vaidyanathan, T.S., "A Flow Field Analysis Procedure Based Upon Velocity Potentials", to be presented at the AIAA Applied Aerodynamics Conference, Danvers, MA, July 13-15, 1983.

17. Dvorak, F.A., Maskew, B. and Woodward, F.A., "Investigation of Three-Dimensional Flow Separation on Fuselage Configurations", USAAMRDL-TR-77-4, March 1977.

18. Thwaites, B., "Approximate Calculation of the Laminar Boundary Layer", Aero. Quart., Vol. I, 1949.

19. Curle, H., "A Two-Parameter Method for Calculating the Two-Dimensional Incompressible Laminar Boundary Layer", J. R. Aero. Soc., Vol. 71, 1967.

20. Granville, P.S., "The Calculation of the Viscous Drag of Bodies of Revolution", David W. Taylor Model Basin Report 849, 1953.

21. Gaster, M., "The Structure and Behavior of Laminar Separation Bubbles", ARC 28-226, 1967.

22. Nash, J.F. and Hicks, J.G., "An Integral Method Including the Effect of Upstream History on the Turbulent Shear Stress", Proc. Computation of Turbulent Boundary Layers - 1968, AFOSR-IFP-Stanford Conference, Vol. 1, Stanford University Dept. Mech. Eng., Stanford, CA.

ACKNOWLEDGEMENTS

The basic VSAERO program was developed under Contract NAS2-8788 through NASA Ames Research Center. Extensions of the code to model the separated flow and vortex interactions were funded by the Office of Naval Research under Contracts N00014-78-C-0128 and N00014-82-C-0354. The present application of the code to compare with the experimental observations was performed under Army Research Office Contract DAAG29-81-C-0032. The author is grateful to C. Tung who supplied information and flow photographs on the water tunnel experiment.

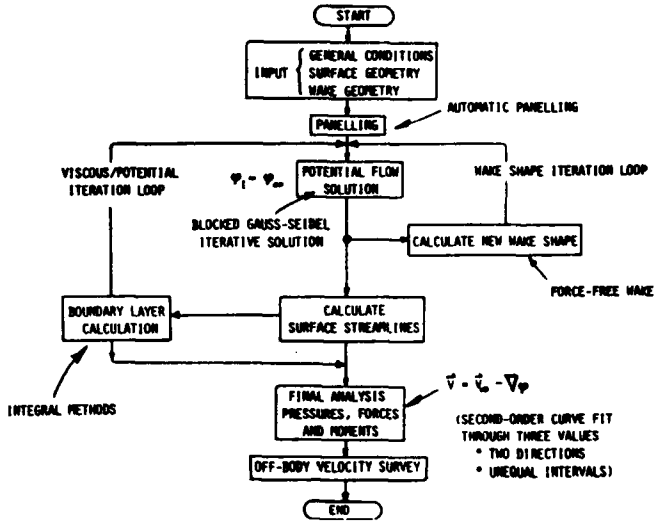

Fig. 1. VSAERO Method Outline.

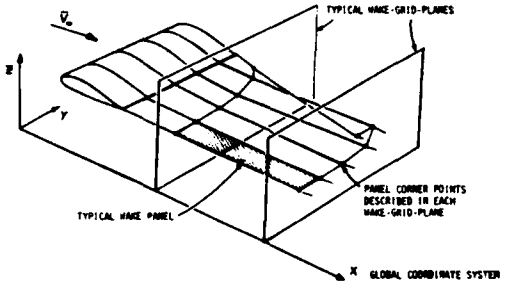

Fig. 2. Wake-Grid-Plane Scheme.

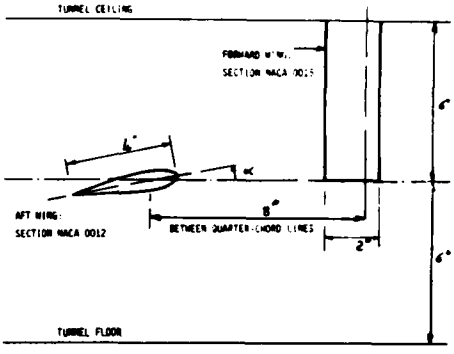

Fig. 3. Layout of the Model for the Vortex/Wing Encounter.

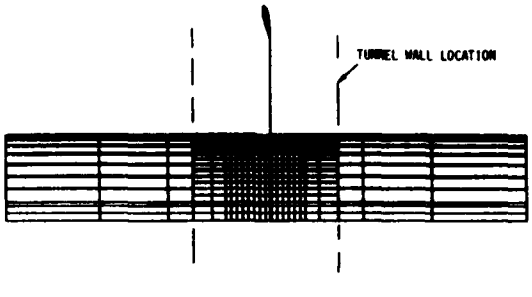

Fig. 4. Aft Wing Panel Arrangement for the Calculations.

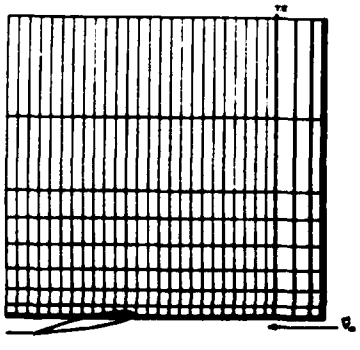

Fig. 5. Starting Condition for the Wake Calculations Showing Wake-Grid-Plane Locations.

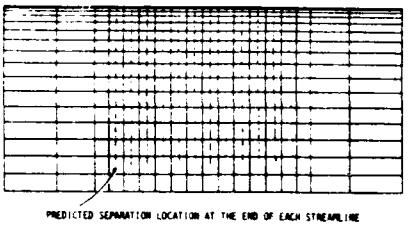

Fig. 6. Plan View of Calculated (External) Streamlines for the Wing Alone at 12° Incidence (First Iteration).

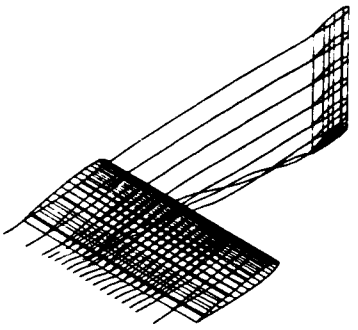

(a) General View.

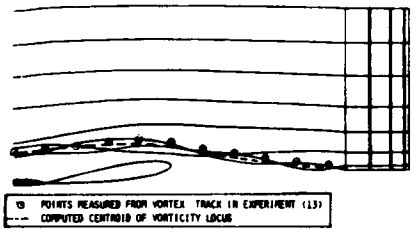

(b) Side View and Comparison with Experimental Vortex Track.

Fig. 8. Final Calculated Wake Configuration for the 8° Case.

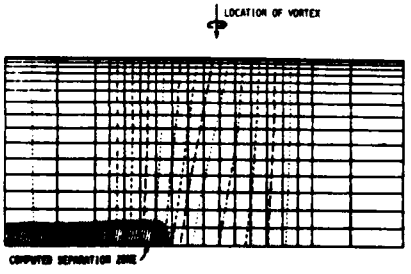

Fig. 9. Plan View of the Calculated (External) Streamlines for the Aft Wing at 8° in Presence of Vortex.

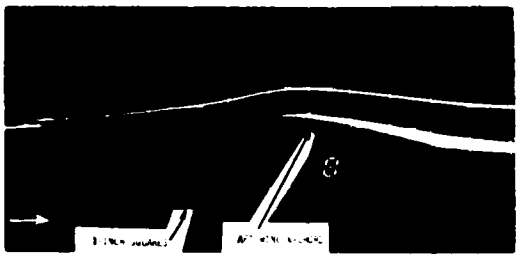

(a) α = 8°

(b) α = 12°

(c) α = 16°

Fig. 7. Side Views of Experimental Flow Field with the Forward Wing at 10°, From Ref. 13.

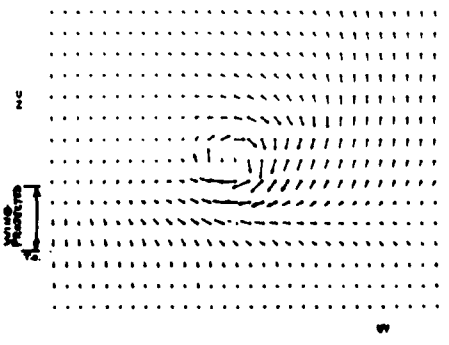

Fig. 10. Velocity Survey Calculated in a Vertical Plane just Downstream of the Aft Wing at 8° in Presence of Vortex.

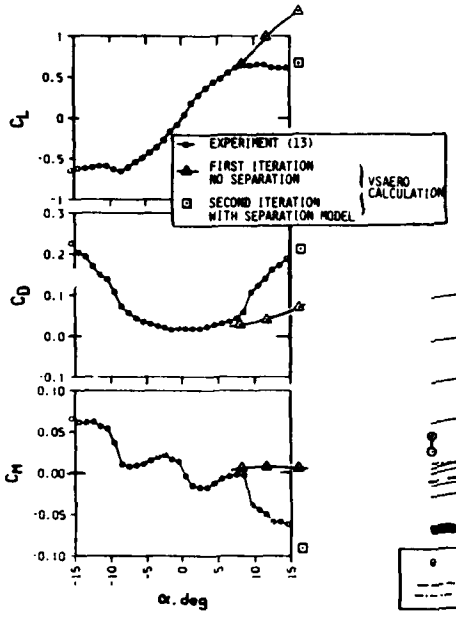

Fig. 11. Comparison of Calculated and Experimental Force and Moment Coefficients in Presence of Vortex.

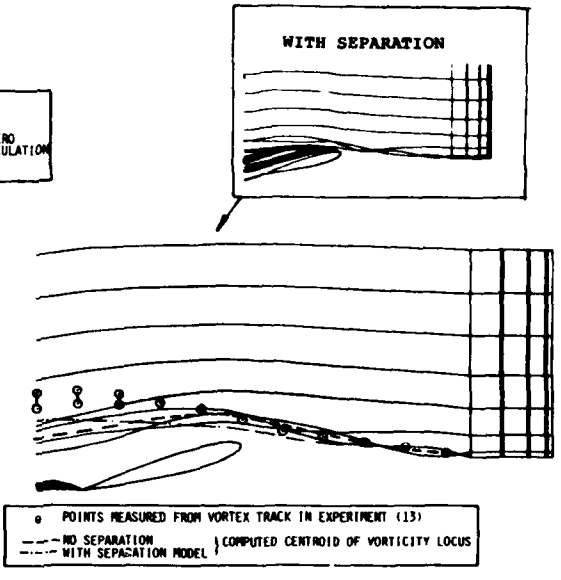

Fig. 12. Side View of Calculated Wake Configuration and Experimental Vortex Track with Aft Wing at 16°.

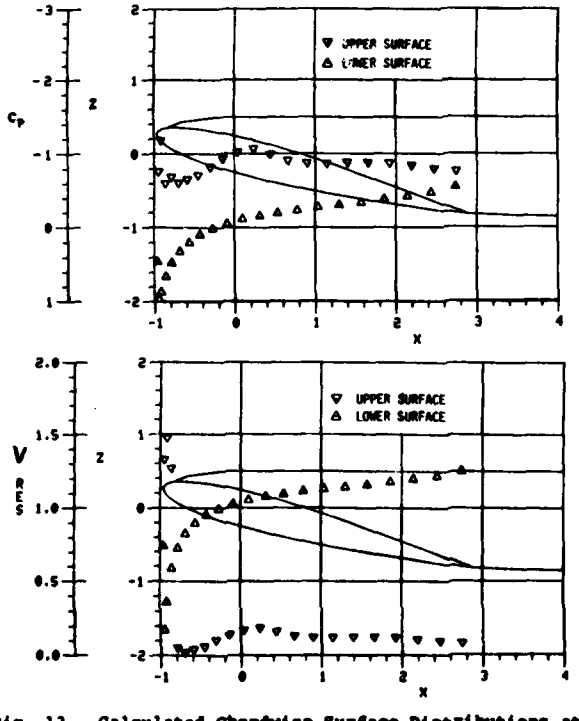

(a) Pressure Distribution.

(b) Resultant Velocity Magnitude.

Fig. 13. Calculated Chordwise Surface Distributions at y = 0 in the Aft Wing at 16° with Initial Separated Wake Model.

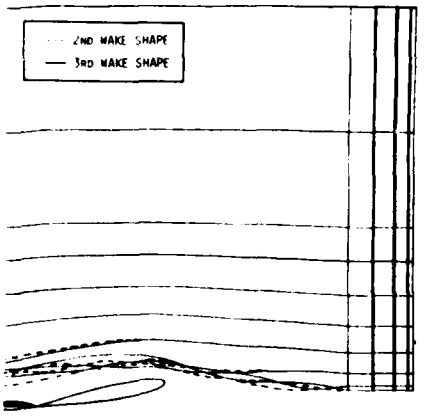

Fig. 14. Comparison of Second and Third Calculated Wake Shapes for Aft Wing at 12°.

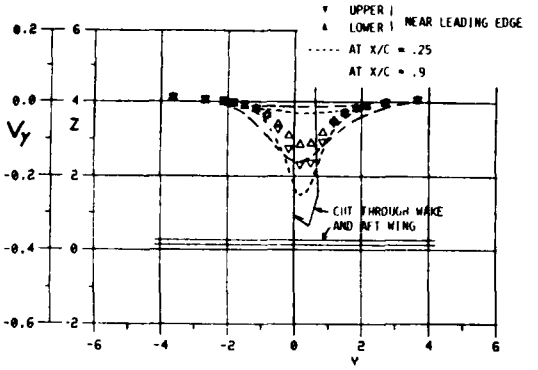

Fig. 15. Calculated Spanwise Distribution of Spanwise Velocity Component on Aft Wing at 12° in Presence of Vortex: Comparison at x/c = 0.0, 0.25 and 0.29.

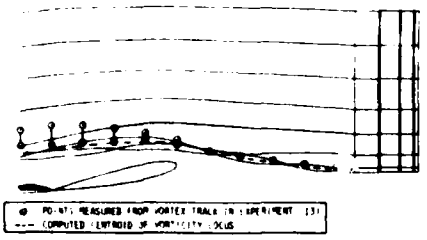

Fig. 16. Comparison of Computed Wake and Experimental Vortex Track for Aft Wing at 12°.

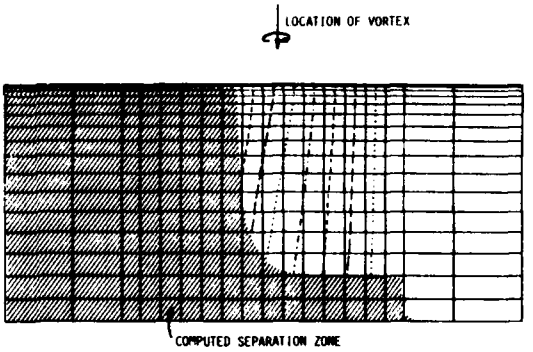

Fig. 17. Top View of Calculated Surface Streamlines on Aft Wing at 12° in Presence of Vortex and Showing Calculated Separation Zone (First Iteration).

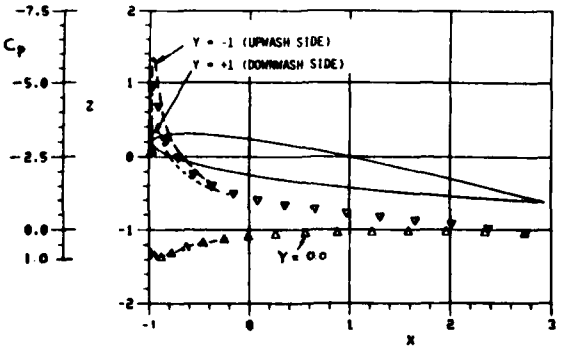

Fig. 18. Calculated Chordwise Pressure Distributions on the Aft Wing at 12° in Presence of Vortex. Comparisons for Three Spanwise Locations at y = -1.0, 0.0 and 1.0 (First Iteration).

SEPARATION AND VORTICAL-TYPE FLOW AROUND A PROLATE SPHEROID
- EVALUATION OF RELEVANT PARAMETERS -

by
H. Vollmers
DFVLR Institute for Theoretical Fluid Mechanics
H.-P. Kreplin, H.U. Meier
DFVLR Institute for Experimental Fluid Mechanics
D-3400 Göttingen, Bunsenstraße 10
Germany

SUMMARY

The definition of some special lines in a flow field is discussed and a criterion for the identification of axes of local rotation is given. A preferred direction is introduced in space using the local direction of the velocity. A surface is constructed locally such that at any point the surface is normal to the velocity field. For a (normalized) direction field of the velocity, the components of the gradient tensor on this surface can be regarded as being equivalent to the curvature tensor of the surface. The behaviour of the curvature is discussed ..e surface is partitioned into hyperbolic and elliptic regions by the sign of the Gaussian curvature. It is found that the special points are associated with regions of extremely steep variations of the Gaussian curvature. Experimental evidence to this effect is provided by measurements of wall shear stress vectors and velocity vectors in the flow field around an inclined prolate spheroid. The above procedure is shown to be a tool for revealing some properties of the vortex skeleton of a flow field. Several other parameters of the measured flow field are also evaluated and presented.

LIST OF SYMBOLS

a	semi major axis of the prolate spheroid
b	semi minor axis of the prolate spheroid
c^i	vector of curl, contravariant component
d_2	discriminant, Eq.(14)
d_3	discriminant, Eq.(9)
J	velocity gradient tensor, Eq.(15)
K	Gaussian curvature, Eqs.(13), (16)
M_K	kinematic vorticity number, Eq.(18)
M_D	dynamic vorticity number, Eq.(19)
p	pressure
U_∞	free stream velocity, Fig. 2
u^i	velocity vector
v^i	vector, three-dimensional
w^i	eigenvector
x^i	coordinate
x_0	coordinate along the axis of rotation of the model, Fig. 2
α	angle of incidence
$\beta^i{}_{i'}$	coordinate transformations, Eq.(11)
$\delta^i{}_j$	Kronecker delta
ϵ^{ijk}	permutation tensor
λ	eigenvalue
θ	angle
ρ	density
μ	dynamic viscosity
σ^α	vector, two-dimensional
τ^α	$= \mu\, u^\alpha\|_3$ wall shear stress vector
φ	angle of rotation of the spheroid, Fig. 2
$\|_i$	covariant differentiation

Indices:
range conventions (summation convention is applied):
Latin indices $i,j,k, \ldots = 1,2,3$
Greek indices $\alpha,\beta,\gamma, \ldots = 1,2$
The coordinate number 3 refers to the direction normal to the respective surface or wall.

1. INTRODUCTION

For the analysis and description of the phenomena of three-dimensional separation and vortical flow fields several concepts have been proposed, that are intuitive generalizations of ideas successfully used in two-dimensional or even planar flows. Such generalizations are of limited practical use, if they disregard the restrictions to which a two-dimensional flow field is subject but which are absent in a three-dimensional flow. For example an axis of rotation in a two-dimensional flow is perpendicular to the velocity field while the strain rate depends only on the two coordinates of the velocity field. So, for an application of two-dimensional concepts, it is generally necessary to introduce locally a preferred direction in three-dimensional space.

Successful developments of the description of flow fields with isolated singular points have been guided by the theory of ordinary autonomous differential equations of two degrees of freedom [1]. Together with topological rules [2] it is an effective tool for investigating the topological structure of a vector field with isolated singularities on a surface.

The location of isolated singularities is obviously related to points where the vector field vanishes. They are classified by the behaviour of the vector field in their neighbourhood. The two classes are nodal points (nodes, foci) which behave elliptically and saddle points having a hyperbolic behaviour. The respective indices are +1 and -1. The paths between these singularities are streamlines. This is the reason why the topology of limiting streamlines may sometimes easily be obtained from oil flow patterns.

Recently Hornung and Perry [3] proposed a generalization of this concept for the analysis of the vortex skeleton in a three-dimensional flow field. They used bifurcation lines instead of singular points. The concept was successful in clarifying the topology in sections through three-dimensional flow fields. However no stipulation was given for the determination of the location of the bifurcation lines from a given three-dimensional velocity vector field.

The aim of this paper is the discussion and use of kinematical relations and invariants for the description of separation and vortical flow fields.

2. THEORY

Several relations will be derived and discussed for the analysis of three-dimensional vortical flow fields. We shall restrict ourselves to incompressible fluids governed by the continuity equation and the stationary Navier-Stokes equations. In tensor notation we have

$$u^i|_i = 0 \tag{1}$$

$$\rho u^i|_j u^j = - p|^i + \mu u^i|^j{}_j. \tag{2}$$

At a wall where the no slip condition holds the left hand side of Eq.(2) vanishes:

$$p|^i = \mu u^i|^3{}_3. \tag{3}$$

The first derivates of the velocity component normal to the wall, $u^3|_i$, vanish, while the second and third derivatives may be related to the wall shear stress $\tau^\alpha = \mu u^\alpha|_3$ and the pressure p and their derivatives at the wall. Using derivatives of Eqs.(1) and (3) we get

$$\tau^\alpha|_\alpha + \mu u^3|_{33} = 0, \tag{4}$$

$$\tau^\alpha|_{\alpha\beta} + \mu u^3|_{33\beta} = 0, \tag{5}$$

$$p|^\alpha{}_\alpha = \mu u^\alpha|^3{}_{3\alpha} = - \mu u^3|^3{}_{33}. \tag{6}$$

So the first generally nonvanishing derivatives of the velocity field can be evaluated from data at the wall. Eq.(4) relates the derivative of the velocity component normal to the surface to the divergence of the wall shear stress obtained on the wall. Only the second and higher derivatives of the wall pressure field are related to the velocity component normal to the wall. Therefore wall pressure measurements are relatively insensitive to the phenomena of separation. Only "massive" separations are detected from wall pressure measurements.

2.1 A LOCAL ROTATION

A more exact description may be obtained from the identification of local rotations. Realising the fact that we may establish a nonvanishing curl of a vector field without what we intuitively call a vortex, as for instance in a Couette flow, we are stimulated to discuss the local quality of both those terms and their relations. The curl is a term well defined by spatial derivatives of a vector field. A vortex should be a locally rotating part of the fluid where in a cross section the streamline patterns look like centres or foci.

A local linear vector field may be represented by the vector of displacement $u_i|_j\, dx^j$ with the tensor $u_i|_j$ of the spatial derivatives of the velocity field. The symmetric part of this tensor, $(u_i|_j + u_j|_i)/2$, is the stress tensor and the components of the skew symmetric part, $(u_i|_j - u_j|_i)/2$, are related to the curl of a vector field by the permutation tensor $c^k = \varepsilon^{ijk}\, u_j|_i$. The vector $u^i|_j\, dx^j$ describes the displacement of $x^j + dx^j$ with respect to a certain (Lagrangian) frame of reference attached to the point x^j and participating locally in its translatory motion u^i. For the determination of a line element vector dx^j that has the same direction as the relative displacement $u^i|_j\, dx^j$ we obtain the eigenvalue problem

$$u^i|_j\, w^j = \lambda\, w^i, \tag{7}$$

where λ is an eigenvalue and w^i is an eigenvector.

The characteristic equation of Eq.(7) reads

$$\lambda^3 - u^i|_i\, \lambda^2 + (u^i|_i u^j|_j - u^i|_j u^j|_i)\, \lambda\, /\, 2 - \det(u^i|_j) = 0,$$

which reduces due to the conservation of mass in Eq.(1):

$$\lambda^3 - u^i|_j u^j|_i\, \lambda\, /\, 2 - \det(u^i|_j) = 0. \tag{8}$$

To distinguish the eigenvalues with nonvanishing imaginary part we introduce the discriminant

$$d_3 = (u^i|_j u^j|_i)^3/27 - (\det(u^i|_j))^2/4. \tag{9}$$

For values of $d_3 \geq 0$ Eq.(8) has only real roots and the principal axes of deformation have the direction of the eigenvectors. For a symmetric tensor $u_i|_j$ the eigenvectors are orthogonal and we may construct the well-known ellipsoid of principal stresses. If the values of d_3 become negative, Eq.(8) has only one real root. The corresponding eigenvector is the axis of a local rotational displacement that we may intuitively call a vortex. Thus we can localize a domain in a flow field where axes of local rotations may occur by distinguishing the complex eigenvalues of the velocity derivative tensor $u_i|_j$ by Eq.(9). The region occupied by a vortex may be larger than this domain.

The familiar structure of the streamlines like the pattern near foci or centres is realized if the observer looks parallel to the principal axis and a Galilean transformation is applied that locally cancels the components of the velocity vector normal to the principal axis. Though the principal axes are invariant with respect to Galilean transformations, the recognition of this intuitive structure of a local rotation is generally not invariant with respect to Galilean transformations. It is only if the principal axis is almost parallel to the local velocity vector that a local rotation is observed in the original frame of reference. The admissible angle of deviation depends on the ratio of the real eigenvalue to the absolute value of the complex eigenvalue. But also in this case the velocity vector at that point must vanish on a plane normal to the viewing axis. If the stress vanishes, i.e. the tensor $u_i|_j$ becomes purely skew symmetric, the curl is an eigenvector of Eq.(7).

As the flow is parallel to a wall, Eq.(8) may be specialized for the field of wall shear stresses in a frame of reference where the wall is at rest. If we accept the (nonvanishing) wall shear stress vector τ^α to represent the local translatory motion we obtain for $u^3|_\alpha = 0$:

$$(-\tau^\alpha|_\alpha - \lambda)\, (\lambda^2 - \tau^\alpha|_\alpha\, \lambda + \det(\tau^\alpha|_\beta)) = 0 \tag{10}$$

for the determination of eigenvalues λ. This means that an axis of local rotation may not be situated in the wall.

2.2 SOME SPECIAL POINTS IN A FLOW FIELD

For revealing the structure of the flow field we shall investigate the occurrence of of some special lines or surfaces. The theory of autonomous ordinary linear differential equations of two degrees of freedom is applied to two-dimensional vector fields which vanish at certain points. The behaviour of the equations in the neighbourhood of such points is investigated leading to the result that the different behaviours given in Fig. 1 can be distinguished by three parameters. The parameters are related to the tensor of the derivatives. They are the determinant, the trace, and the discriminant d_3 for complex eigenvalues. As the vector field vanishes, the local behaviour of the streamlines is described by the next higher nonvanishing differential of the streamline.

In order to obtain a similar situation as in Fig. 1 for a nonvanishing velocity field we shall investigate the differentials that only affect the motion perpendicular to the local velocity vector. We are looking for special lines and points where the differential vanishes. The variation of the investigated differential near that point ensures that the streamlines are governed by a higher order differential.

Although in principle there is no preference of a direction in space, we introduce the local velocity vector as a preferred direction for investigations of the velocity field in a fixed frame of reference. In this case an observer is moving with the local velocity field and looking only in the direction of the local velocity vector. The direction of the velocity vector has to be told to him by a second observer staying in some frame of reference.

For this purpose a base transformation $\beta^{i'}{}_{i}$ has to be applied locally to the velocity vector u^i such that it has only one component $u^{3'}$ different from zero in the new (dashed) base: $u^i = \beta^{i'}{}_{i}\, u^{i}$. The components of the two-dimensional gradient tensor $u_{\alpha'}|_{\beta'}$ can be evaluated from

$$u_{\alpha'}|_{\beta'} = \beta^{i}{}_{\alpha'}\, \beta^{j}{}_{\beta'}\, u_i|_j \tag{11}$$

with $\beta^{i'}{}_{i}\, \beta^{i}{}_{k'} = \delta^{i'}{}_{k'}$.

The field of velocity vectors u^i may be normalized, because only the direction v^i is necessary for the determination of a streamline. Then above transformation is almost equivalent to the construction of a surface whose tangential plane is everywhere locally perpendicular to the direction field v^i. If the equations of Mainardi-Codazzi, $v_i|_{kl} = v_i|_{lk}$, and Gauss are satisfied, the construction is uniquely defined for a given point of the surface and a nonvanishing velocity field. As the vectors of the direction field have unit length, i.e. $v^i v_i = v^{3'} = 1$, the above (symmetric) gradient tensor $v^{\alpha'}|_{\beta'}$ is the (negative) tensor of curvature of the surface. The invariants of the associated eigenvalue problem

$$(v^{\alpha'}|_{\beta'} - \lambda \delta^{\alpha'}|_{\beta'})\, v^{\beta'} = 0, \tag{12}$$

i.e. the trace $v^{\alpha'}|_{\alpha'}$ and the determinant $K = \det(v^{\alpha'}|_{\beta'})$ are also invariants of the surface. They are known respectively as (negative) mean curvature and Gaussian curvature. The eigenvalues λ are the principal curvatures of the surface. We have for the two eigenvalues λ_1 and λ_2 of Eq.(12) the trace

$$v^{\alpha'}|_{\alpha'} = \lambda_1 + \lambda_2,$$

the Gaussian curvature

$$K = \det(v^{\alpha'}|_{\beta'}) = \lambda_1\, \lambda_2, \tag{13}$$

and the discriminant for complex eigenvalues

$$d_2 = (v^{\alpha'}|_{\alpha'})^2/4 - \det(v^{\alpha'}|_{\beta'}). \tag{14}$$

If the value of d_2 becomes negative the construction of the surface is no longer unique. The moving observer will then see a local rotation.

The classification of points on this surface is obtained from the Gaussian curvature K. For nodes we have an elliptic behaviour with $K > 0$, and saddles occur in hyperbolic regions with $K < 0$. A parabolic behaviour is established for $K = 0$. The value $K = 0$ may be interpreted also in another way. The gradient tensor is singular and higher order derivatives may be involved. The first order derivative is no longer significant. These are the points we are looking for.

There exist regions where the behaviours classified by K may occur. In order to locate the very line, or point on the surface being used for revealing the topology of the flow field we require the displacement tensor $v^{\alpha'}|_{\beta'}$ to be singular. We are looking for points with $K = \det(v^{\alpha'}|_{\beta'}) = 0$. If we additionally have $v^{\alpha'}|_{\alpha'} = 0$, we are in the origin of the coordinate system of Fig. 1.

For distinguishing the regions the above construction of a surface is not necessary. Any given surface is possible. However, the arbitrary surface should be nowhere tangential to the velocity field in the domain under investigation for reasons of the recognition of variations of the parameters.

2.3 SPECIAL LINES AT THE WALL

The above construction may also be applied to the flow field at a wall. As the velocity vanishes at the wall, the observer is consequently looking in the direction of the wall shear stress because the translatory motion is parallel to the wall. By analogous proce-

dures as before a surface is constructed that is normal to the field of wall shear stress and the wall. In this case we have $v_\alpha|_3 = \sigma_\alpha$, $v_3|_3 = 0$ and $v^\alpha|_3 v_\alpha|_3 = 1$. Thus the three-dimensional gradient tensor for the vector field reads:

$$J = \begin{pmatrix} v_1|_{31} & v_1|_{32} & v_1|_{33} \\ v_2|_{31} & v_2|_{32} & v_2|_{33} \\ 0 & 0 & v_3|_{33} \end{pmatrix} \tag{15}$$

and the characteristic equation is analogous to Eq.(10). If the wall shear stress vector is aligned with the first coordinate, i.e. $v_2|_3 = 0$, the two-dimensional gradient tensor is the lower right part of the matrix in Eq.(15). The invariants are obtained from Eqs.(13) and (14). Using $\sigma^1\sigma_1 = 1$ and Eqs.(3) to (5) we get (disregarding the metric coefficients as multipliers)

$$v^3|_{33} = -\sigma^\alpha|_\alpha, \quad v^2|_{32} = \sigma^2|_2.$$

So we have the equations for the trace $v^\alpha|_{3\alpha} = -\sigma^1|_1$,

the determinant $\quad K = -\sigma^2|_2\,\sigma^\alpha|_\alpha$, (16)

and the discriminant $d_2 = (2\sigma^2|_2 + \sigma^1|_1)^2 \geq 0$. (17)

The last equation supports the conclusion from Eq.(10), that a local rotation cannot have an axis in a wall. We are looking for locations with extrem descent of the Gaussian curvature to the zero line. The sign of the divergence (at the wa l) of the wall shear stress may qualify - due to the Eq.(4) - the line as separation o reattachment. The magnitude of K and the steepness of K may be looked at as a measure for the strength of separation or reattachment. Looking parallel to the wall shear stress vector the moving observer will see an angle θ between the local displacement and the surface. It is given by $\tan\theta = -1 - \sigma^1|_1/\sigma^2|_2$.

3. EXPERIMENTAL RESULTS

For the experiment a sting-mounted prolate spheroid was used in the 3-meter Low Speed Wind Tunnel of the DFVLR Göttingen. The model was especially designed for investigations of three-dimensional boundary layers, the phenomena of boundary layer separation and vortical flows. For this purpose measurements of the pressure and wall shear stress vector at the surface and the velocity vector in a region around the body were carried out. The test set-up and the data reduction procedures have been described in Refs.[4] to [6].

The wall shear stress vectors have been measured by means of hot films in twelve cross-sections of the prolate spheroid. For further processing the data have been taken as an input of a two-dimensional approximation by spline functions, which allow an evaluation of the components of the vectors and their derivatives at any point in the considered domain. A result is given in Fig. 3, where limiting streamlines are shown, which have been obtained by an integration of the direction field of wall shear stress vectors. The most significant feature is the convergence of the lines which is interpreted as separation whereas their divergence is associated with attachment.

The velocity vectors have been measured with a pressure probe of 6 mm diameter. It is a direction probe that uses the pressure information from ten holes [6]. The velocity vector was measured at points of a conical surface that is normal to the model as indicated in Fig. 2. In Fig. 4 the velocity vectors at the first and the last surface are shown. The seven intermediate surfaces are indicated by dashed lines at the wall. The choice of conical surfaces had the advantages of using monoclinic coordinates of the surface and an easier application of spline routines, which were applied to the evaluation of the components and the derivatives in the three-dimensional field. Actually the contravariant components u^i of the velocity vector were processed in the spline routines. The field had been measured for a free stream velocity of $U_\infty = 45$ m/s ($Re = 2a\,U_\infty\,\rho/\mu = 7.2 \cdot 10^6$) and an angle of incidence of $\alpha = 29.5°$.

The drawings of results from the measurements of the velocity field are obtained in the following way. For reasons of a simpler evaluation of the metric coefficients the respective values of the presented functions perpendicular to the wall of the spheroid have been evaluated on conical surfaces, as shown in Fig. 2. This surface was then projected on a surface being normal to the x_0-axis. There are only slight distortions because the angles between the two surfaces are relatively small. The plot of the velocity vectors in Fig. 5 summarizes the basic information for the other results. (The observer is looking in the direction of $U_\infty \cdot \cos\alpha$.) The same spacing of the points, where the functions are evaluated,

is used throughout the next figures. As an estimation of errors of the measured values is difficult to obtain, at least the functions being evaluated from spatial derivatives should be looked at more qualitatively then quantitatively. An indication of the error of the spatial derivatives is given in Fig. 6, where lines of constant absolute values of the divergence of the velocity field are drawn.

A function based on spatial derivatives is the curl whose vector components normal to the axis x_0 are plotted in Fig. 7. In the given sections of the flow field the shear layer and the vortex are the most significant features of the drawing. They gradually depart from the surface with increasing x_0. The vertical components in the plane of symmetry at $\phi = 180°$ indicate also the magnitude of the error. The components of the curl in the plane of symmetry must vanish. The magnitude of the vector of curl in Fig. 8 also reveals the dominance of the curl in the vortices and the shear layers. In order to have a relation between the vector fields of curl and velocity, Fig. 9 shows the local relative angles between both vectors. In the main vortex on the given side of the prolate spheroid the curl and the velocity have opposite directions. For $x_0/2a = 0.7$ it is seen that in one of the smaller vortices both vector fields have the same direction.

Truesdell [7] proposed two measures for a characterization of a vortical flow field. These are one "kinematic vorticity number"

$$M_K = [(u_{i|j}-u_{j|i})(u^{i}{}_{|j}-u^{j}{}_{|i})/[(u_{i|j}+u_{j|i})(u^{i}{}_{|j}+u^{j}{}_{|i})]]^{1/2} \qquad (18)$$

which depends on some ratio of the skew symmetric part (curl) and the symmetric part (stress) of the deformation tensor, and the "dynamic vorticity number"

$$M_D = [(u^{i}u_{k}{}_{|i}-u^{i}u_{i}{}_{|k})\ (u^{j}u^{k}{}_{|j}-u^{j}u_{j}{}^{|k})/(u^{i}u_{i}{}_{|k}\ u^{j}u_{j}{}^{|k})]^{1/2} \qquad (19)$$

which measures the importance of the curl relative to the gradient of the velocity field for the left handside of the Navier-Stokes equations, Eq.(2). The meaning of the values had been extensively discussed in Ref. [7]. For this reason we only present results in Figs. 10 and 11 which were derived from the experiment.

The next figures show applications of some parameters discussed before. In Eq.(9) we introduced the discriminant d_3 for complex eigenvalues of the three-dimensional tensor of spatial derivatives. In Fig. 12 lines of $d_3 = 0$ are presented. Within the region $d_3 < 0$ axes of local rotations occur. In comparison to vector fields of velocity and curl of velocity in Figs. 5 and 7 the space in Fig. 12 is much more structured. The dominating feature occupies the region where the main vortex in Fig. 5 is seen, while the strong shear layer being indicted by the curl in Fig. 7 is less striking and not connected as Fig. 8 might have indicated. The smaller vortices in Fig. 5 near to the wall are clearly indicated. Some lines of constant relative angles between the real eigenvector, i.e. the principal axis of the local rotation, and the velocity vector and its curl are shown in Figs. 13 and 14, respectively. They indicate regions where the respective vectors are parallel or antiparallel. The regions are nearly the same as those shown in the figures before.

In Fig. 15 we answer the question as to whether an observer will see a local rotation if he is looking parallel to the local velocity vectors. Such regions are confined by the lines with $d_2 = 0$ of Eq.(14). They are approximately the same as those confined by $d_3 = 0$ of Eq.(9). Only parts of the shear layer have been excluded.

In Fig. 16 lines of constant values of the Gaussian curvature K are presented for surfaces that are normal to the local velocity vector at the point of evaluation. As the spatial resolution of the experiment is insufficient to admit an evaluation of the criteria of special lines only regions of extreme values of K are shown, which give an impression where higher order differentials are involved. In Fig. 15 the regions with positive values have the quality of foci or centres.

The spatial resolution is much better for the measurements of the wall shear stress vectors. In Fig. 17 the variation of K at the wall is displayed together with the magnitude of the wall shear stress and the divergence of the wall shear stress. A great variation of K is found in the region where the wall streamlines indicate separation and reattachment (cf. Fig. 3). Also points with $K = 0$ are found in that region. They are correlated to the lines of converging wall streamlines within the spatial resolution of the measurement.

REFERENCES:

[1] Oswatitsch, K., "Die Ablösebedingung von Grenzschichten", in: Grenzschichtforschung", H. Görtler (ed.), Springer Verlag, New York and Heidelberg, 1958, pp. 357 - 367.

[2] Tobak, M.; Peake, D.J., "Topology of Three-Dimensional Flows", Ann. Rev. Fluid Mech.14, 1982, pp. 61 - 85.

[3] Hornung, H.; Perry, A.E., "Streamsurface Bifurcation, Vortex Skeleton and Separation", DFVLR IB 222-82 A 25, 1982; see also this AGARD-CP.

[4] Kreplin, H.-P.; Vollmers, H.; Meier, H.U., "Measurements of the Wall Shear Stress on an Inclined Prolate Spheroid", Z. Flugwiss. Weltraumforschung 6, 1982, pp. 248 - 252.

[5] Meier, H.U.; Kreplin, H.-P., "Experimental Investigation of the Boundary Layer Transition and Separation on a Body of Revolution", Z. Flugwiss. Weltraumforschung 4, 1980, pp. 65 - 71.

[6] Meier, H.U.; Kreplin, H.-P.; Vollmers, H., "Development of Boundary Layers and Separation Patterns on a Body of Revolution at Incidence". In: Proceedings of the "Second Symposium on Numerical and Physical Aspects of Aerodynamics Flows", 17-20 January 1983, State University, Long Beach, California, U.S.A.

[7] Truesdell, C., "Two Measures of Vorticity", J. Rat. Mech. Anal. 2, 1953, pp. 173 - 217.

ACKNOWLEDGEMENT

The authors would like to thank Mr. Holler for his support in the data processing and several clarifying discussions.

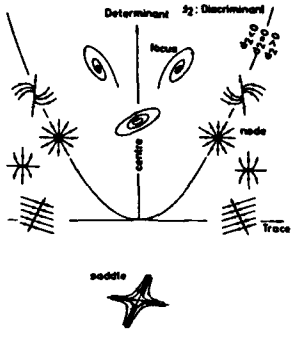

Fig. 1 Behaviour of autonomous ordinary differential equations of two degrees of freedom in different regions.

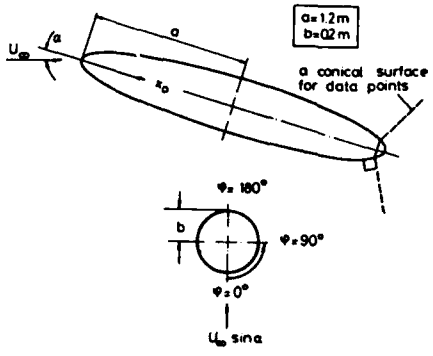

Fig. 2 Configuration of the model investigated.

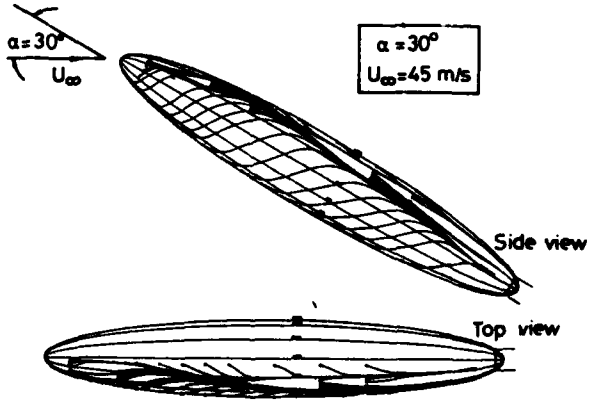

Fig. 3 Limiting streamlines on the inclined prolate spheroid.

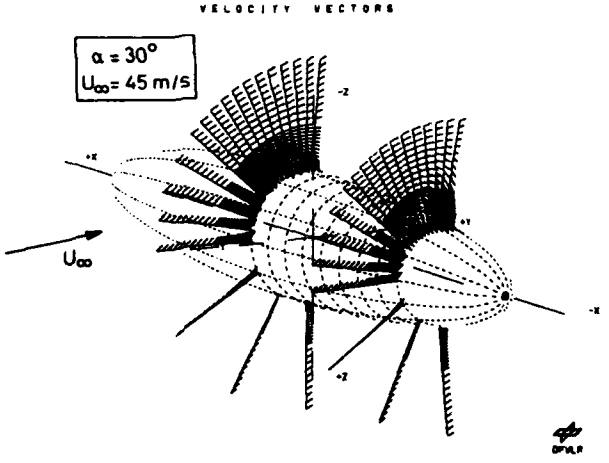

Fig. 4 Measured velocity vectors attached to conical surfaces. The intermediate surfaces are indicated by dashed lines at the wall.

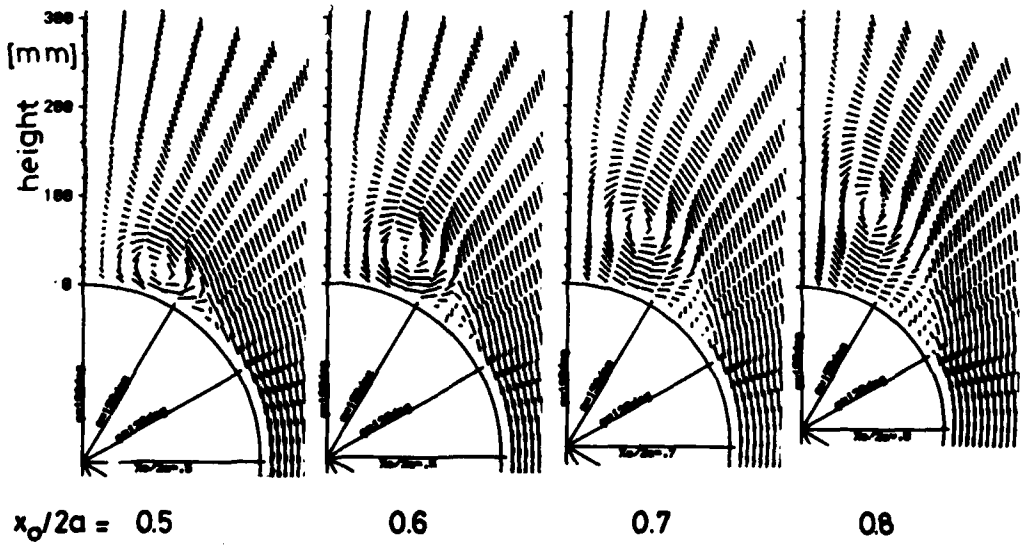

Fig. 5 Components of the velocity vector field that are normal to the main axis x_0 of the model at different sections (interpolated).

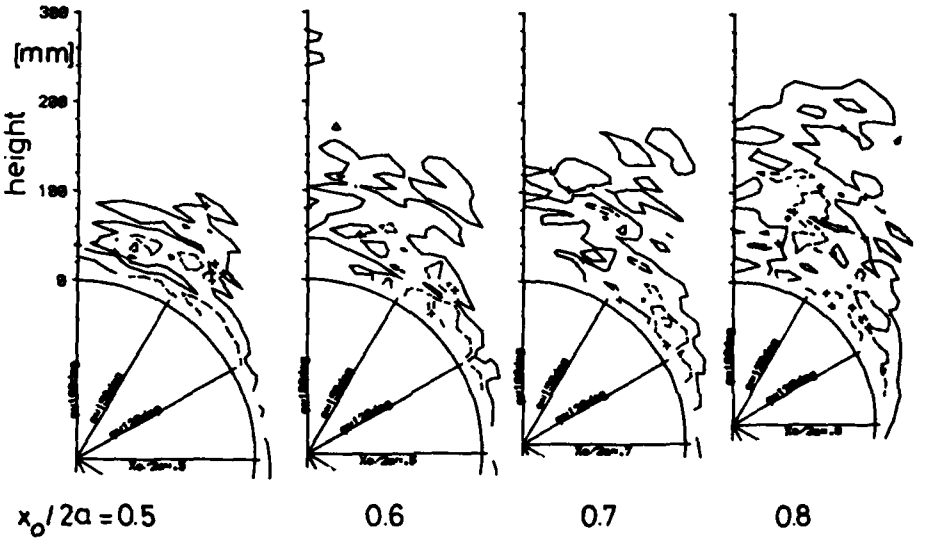

Fig. 6 Lines of constant absolute values of the divergence of the velocity field indicate the magnitude of the errors in the computed derivatives of the field. ——— 0.001, ------ 0.004 U_∞/mm.

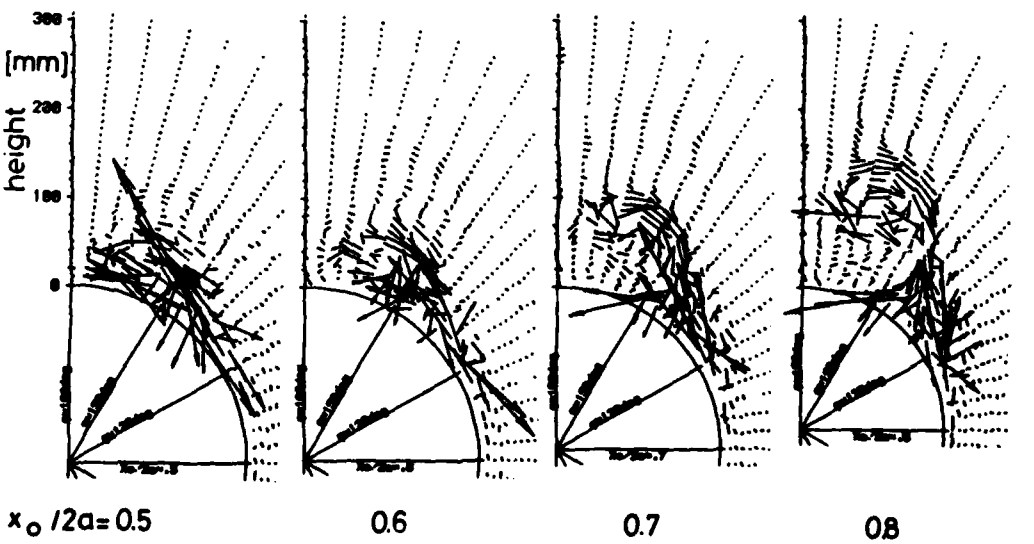

Fig. 7 Components of the curl of velocity normal to the main axis x_0 of the model.

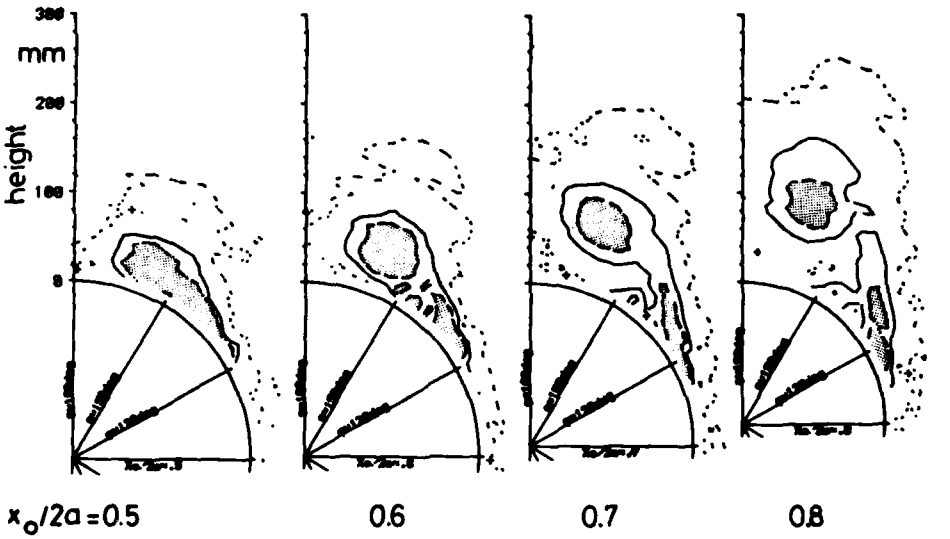

Fig. 8 Magnitude of the curl of velocity. ▒▒▒ > 0.025, —— 0.01, ----- 0.001 U_∞ /mm.

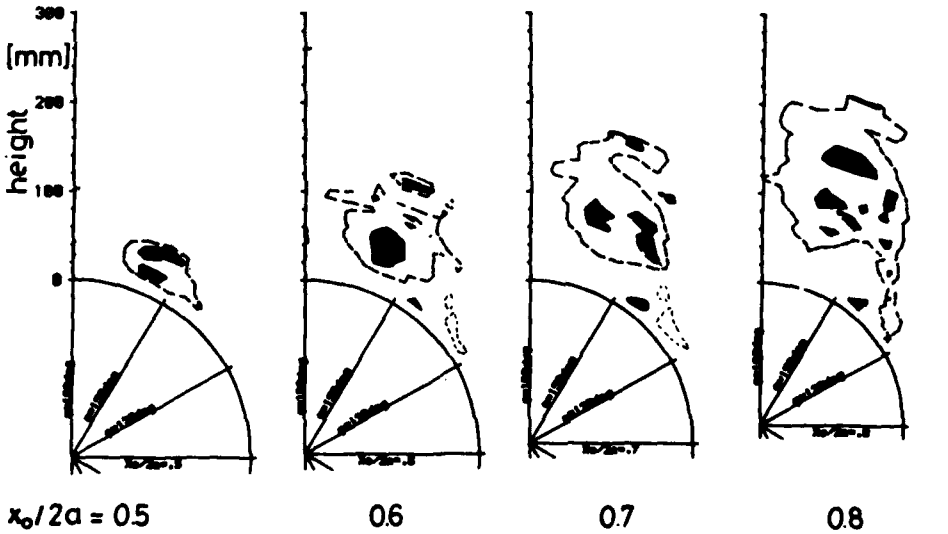

Fig. 9 Angle between the velocity vector and its curl. ▓▓▓ > 170°, ----- 150°, ▓▓▓ < 30°.

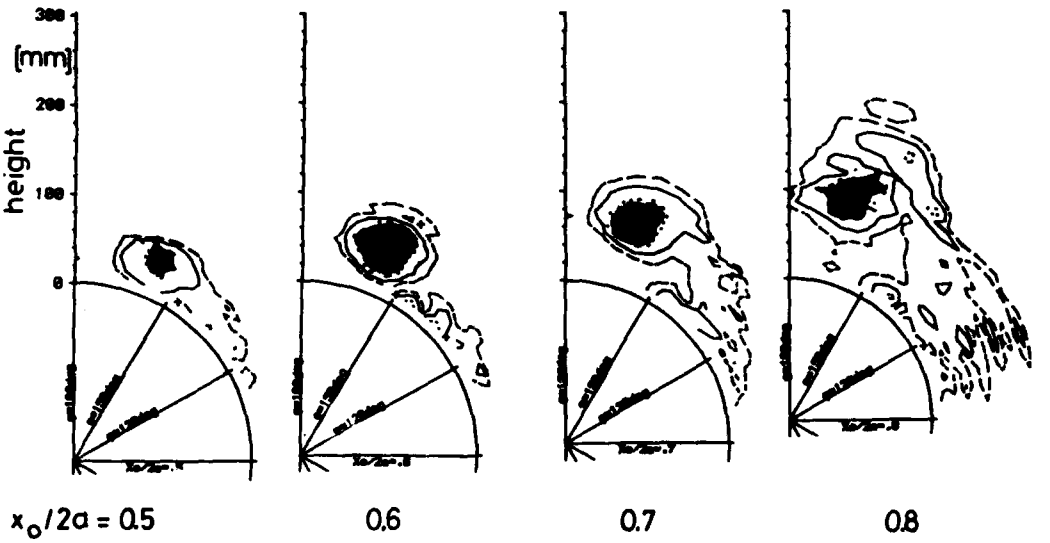

Fig. 10 Kinematic vorticity number M_K, Eq.(18). ▓▓ >2.0, ——— 1.0, ----- 0.5.

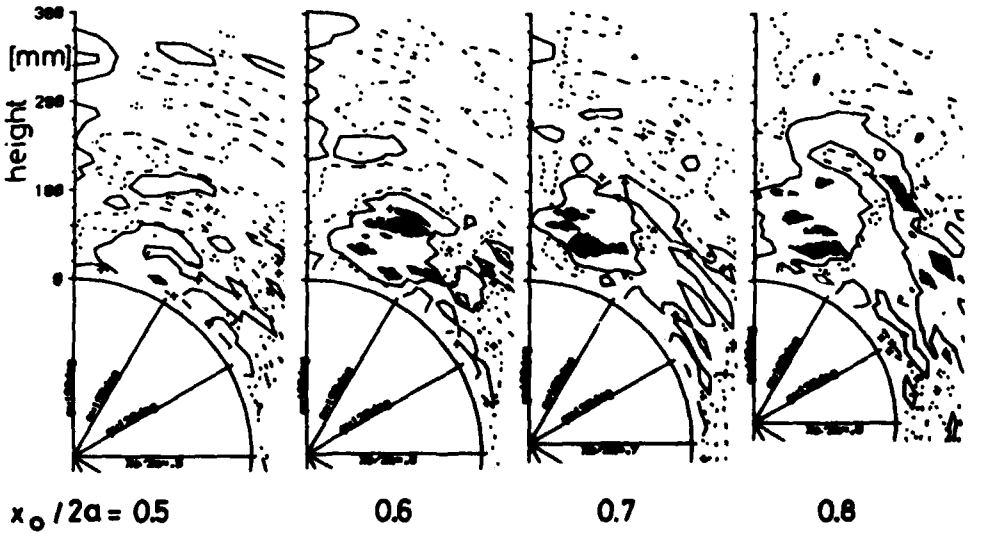

Fig. 11 Dynamic vorticity number M_D, Eq.(19) ▓▓ >4.0, ——— 1.0, ----- 0.4.

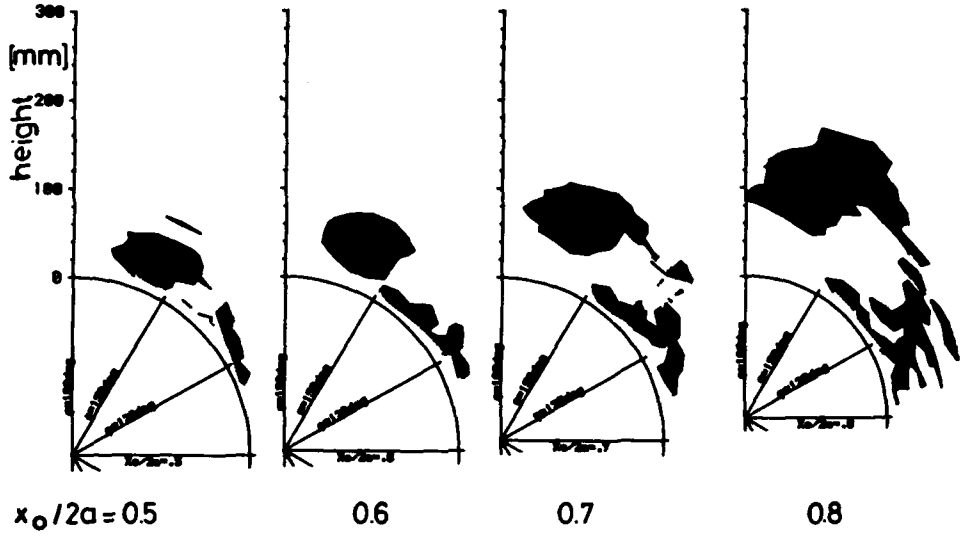

Fig. 12 Axes of local rotations occur in the shaded regions with complex eigenvalues of the displacement tensor. ($d_3 < 0$ from Eq.(9).)

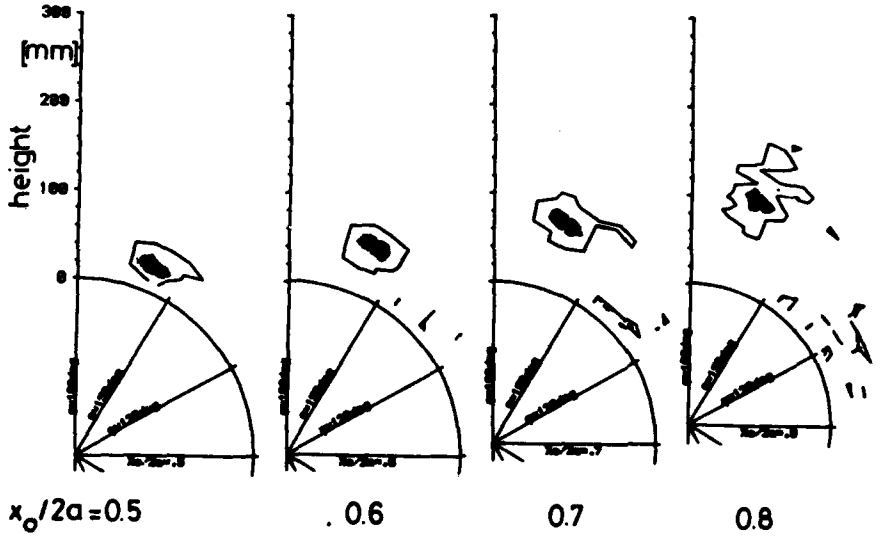

Fig. 13 Angle between the real eigenvector and the velocity vector in regions with $d_3 < 0$. The deviation from parallel or antiparallel arrangement is presented. ▓▓▓ <15°, ——30°.

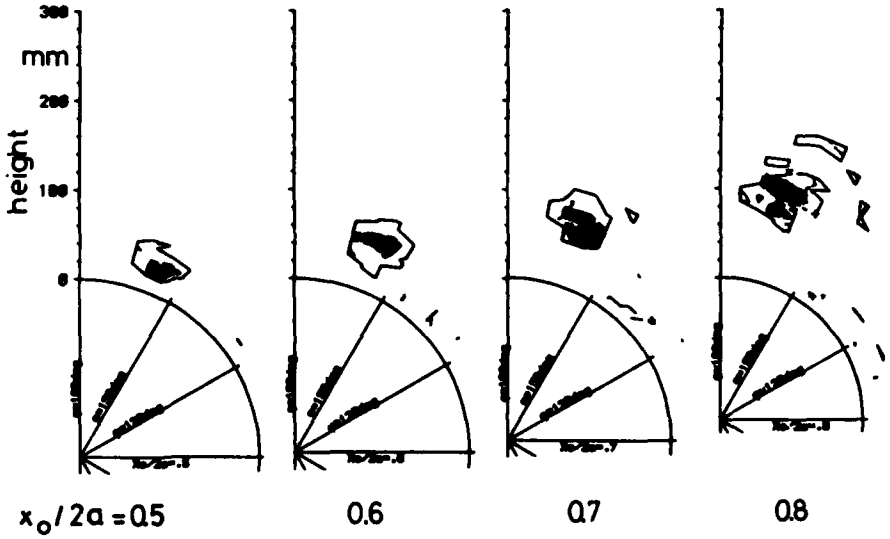

Fig. 14 Angle between the real eigenvector and the curl of velocity in regions with $d_3 < 0$. The deviation from parallel or antiparallel arrangement is presented. ▬ < 10°, ——— 0°.

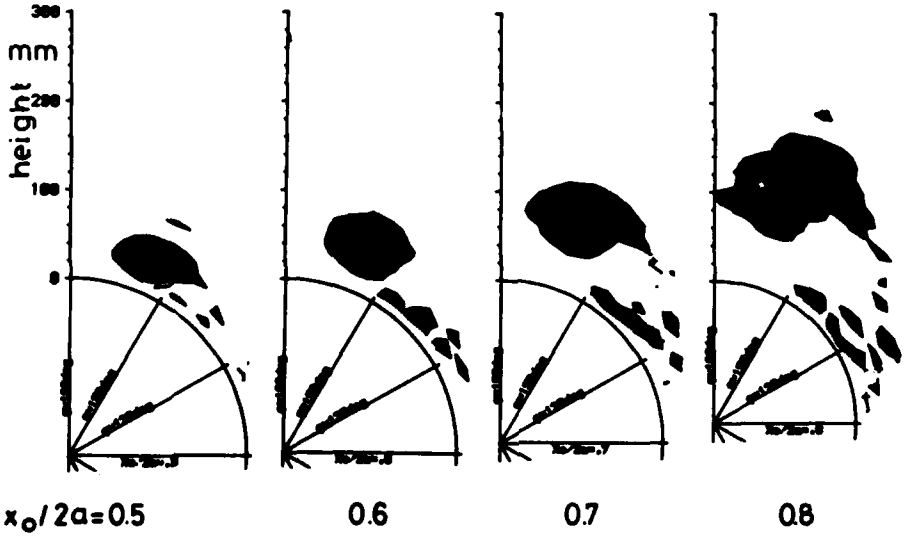

Fig. 15 Regions of $d_2 < 0$ from Eq.(14).

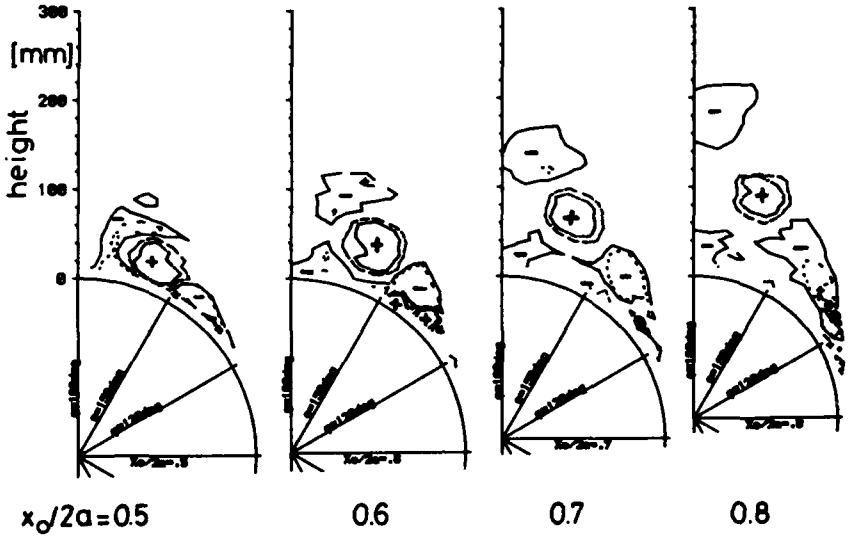

Fig. 16 Regions of extreme positive (+) and negative (-) values of the determinant K, Eq.(13).

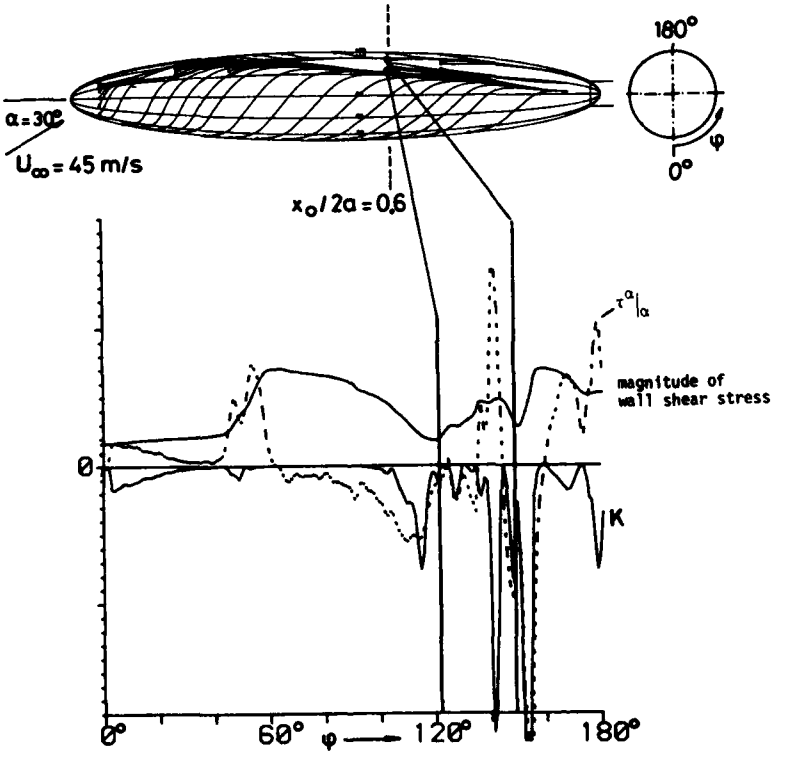

Fig. 17 Magnitude of the wall shear stress (———,>0), $\tau^\alpha|_{\alpha_{U_\infty}}$ (Eq.(4)) (-----), and K(Eq.(16)) (———),<0) for a free stream velocity U_∞ = 45 m/s and an angle of incidence α = 30°.

ON THE GENERATION OF VORTICAL FLOW AT HYPERSONIC SPEEDS OVER ELLIPTICAL CONES

Dr. Panajotis Evangelou
Ministry of National Defence
Defence Industry Directorate
Athens, Holargos, Greece

SUMMARY

A method for calculating the hypersonic slip flow around slender elliptic cones at slight angle of attack is developed. The governing equations are derived from the Navier-Stokes equations and the energy equation by an order of magnitude analysis. There results a system of partial nonlinear parabolic differential equations for the flow variables of the shock formation regime. The system is integrated by means of an explicit finite-difference scheme and the results so obtained are compared with experimental data. Finally the influence of the elliptic cross section geometry as well as the influence of the angle of attack on the flow field properties with particular attention on the cross flow are investigated.

SYMBOLS

C	Chapman-Rubesin factor = $(\mu_w \cdot T_\infty)/(\mu_\infty \cdot T_w)$
c	axis ratio of the elliptical cross section
ϵ	small quantity = $O(1/\sqrt{Re_{ref}})$
γ	ratio of specific heats
λ_∞	mean free molecular path
L_{ref}	reference length = $M_\infty^4 \gamma \ \mu_\infty / \rho_\infty u_\infty$
μ	viscosity coefficient
M	Mach number
p	static pressure
ρ	density
Re_{ref}	reference Reynolds number
Re_1	Reynolds number of the free stream per centimeter
χ_∞	shock boundary layer interaction parameter = $M_\infty^3 / \sqrt{Re_1 / C_\infty}$
ω	cone angles (see Fig. 2)

INDICES

∞	free stream
W	cone surface
1	per path length

1. INTRODUCTION

Extensive experiments in the hypersonic regime on Delta wings with sharp leading edges on circular cones and also on complete hypersonic bodies have demonstrated a three dimensional flow field with vortices on the lee side of these bodies. The results of the investigation on the triangular wing (Ref. 1) as well as on the circular cone (Ref. 2) indicated that the vortex formation takes place within the boundary layer and that the location of the vortex formation lies further downstream on the circular cone than on the Delta wing for the same angle of attack assuming comparable wing leading edge and cone angle. Since no leading edge separation of the flow field did occur on the triangular wing and the flow field around the Delta wing or the circular cone have consequently the same structure the different location of the vortex formation must be caused by the cross flow structure on the apex. This phenomenon can be explained due to the strong expansion of the flow around the leading edge of the wing which results in a stronger cross flow on the apex of the wing than on the apex of the circular cone. The above stated suggestion can be supported by the results of two other experimental investigations on Delta wings whereas the region of the vortex is further downstream removed by changing the geometry of the apex. For this reason the apex has been blunded (Ref. 3) and drooped (Ref. 4). Both apex modifications resulted in a change of the cross flow structure. It should be mentioned that on the apex no vortices can be expected as it has been indicated experimentally in (Ref. 1) and theoretically in (Ref. 5) as long as the shock/boundary layer interaction parameter is greater than 1. The basic aim of this study is to clarify the physical reasons for the differing vortex formation on a Delta wing and on a circular cone. Since no leading edge flow field separation must be taken into consideration for the reasons stated above the Delta wing or triangular plate and the circular cone can be considered as the extrema of a cone with elliptical cross section. Thus in this work the physical and geometrical conditions for the vortex formation on the lee side of hypersonic bodies will be theoretically investigated by means of an elliptical cone. The cross flow on the apex of this body will be affected by varying the axis ratio of the elliptical section and the angle of attack of the cone taking account of the free flow conditions. Concerning the results particular attention will be paid to the occurrence of an adverse pressure in azimuthal direction on the lee side as well as to the properties of the azimuthal

velocity whereas the azimuthal velocity profiles are expected to become gradually similar to the well known separation profiles.

2. THE PHYSICAL MODELL

Since the vortex generation will be theoretically investigated by considering the cross flow conditions in the vicinity of the apex the physical modell of the hypersonic flow field for zero or small angles of incidence will be strongly affected by the conditions on the surface (Ref. 5). The flow field modell along a generator line of the cone will then be basically similar to a two dimensional hypersonic flow field over a flat plate with a sharp leading edge at incidence (Fig. 1) (Ref. 6). Thus the flow field over a cone generator line at high Mach number and low Reynolds number can be distinguished between the shock formation region characterized by large pressure and temperature gradient normal to wall and the region of the viscous interaction with the frictionless but rotational flow field between shock and boundary layer. Thus this physical modell of the flow field is the basis of the present investigation. The flow field has been investigated only within the shock formation region. Since this flow modell is not suitable for the consideration of stagnation effects only small cone angles as well as angles of incidence can be considered. With increasing angle of attack a cross flow appears which will be considered in the mathematical modell. Furthermore simplifications concerning the physical behaviour of the medium have been made in order to reduce the computational time for the numerical calculations. Thus the effects which from experience do not influence the flow field substantially such as nonequilibrium and wall catalytical effects are not considered here. Furthermore the medium is assumed to be thermally and calorifically perfect gas.

3. THE MATHEMATICAL MODELL

In order to carry out the theoretical investigation a mathematical modell has been developed. Since the flow field has boundary layer properties the mathematical modell to be applied here has to deal with hypersonic three dimensional flow field similar to a boundary layer.

The Coordinate Transformation

Consequently a body fixed surface oriented coordinate system has been chosen here. The cone surface is covered with a grid of orthogonal coordinate lines Θ_1 or R, Θ_2 or φ. The third coordinate line Θ_3 or h coincides with the surface normal at each point. The coordinate ω_1 or φ is the penetration line between a sphere with the radius R and the cone to be considered here. The coordinate system R, φ, h (Fig. 2) is orthogonal on the cone surface and remains orthogonal all over the space around the cone because the coordinates R and φ are main curvature lines of the cone. It is worth mentioning that this coordinate system enables the investigation of cones with high ellipticity. The transformation equations from the surface oriented to the cartesian coordinate system are given in (Ref. 7). Since the coordinate φ occurs as a trigonometric function it is possible to put more computational points at the vicinity of vortex of the elliptical section where also large gradients of pressure are expected.

The Differential Equation System

The mathematical model has been developed on the basis of the three following basic equations, i.e. conservation of mass, conservation of momentum and conservation of energy. A system of partial non-linear differential equations of second order for the coordinate system already described has been derived from these basic equations and has consequently been made dimensionless using among other quantities a reference length in the order of magnitude of the shock formation region length. Details of the equation system in dimensionless form are given in (Ref. 7).

Type Definition of the Equation System - Initial and Boundary Conditions

While the pressure gradients in azimuthinal and in normal to surface momentum equations $\partial p/\partial\varphi$ and $\partial p/\partial h$ respectively have to be considered during the calculation because they are of the order of magnitude equal 1. The pressure gradient in R-direction can be neglected because it appears in the term

$$\frac{1}{\gamma M_\infty^2}\,\frac{\partial p}{\partial R} \longrightarrow O(\varepsilon^2)$$

This term is of higher order small compared with other terms. The so derived equation system of motion becomes parabolic and can be solved as an initial-boundary value problem. The initial and external boundary conditions are the free stream conditions (Ref. 7) whereas the initial conditions are assumed to be constant in the height. The Maxwell slip flow conditions have been applied to the cone surface (for details see Ref. 7).

Limitation Concerning the Cone Angle and Angle of Incidence

By means of an order of magnitude analysis the cone angles ω_1 and ω_2 as well as the angle of attack α can be estimated as

$$(\omega_1 + \alpha) \longrightarrow O(\varepsilon)$$

and

$$\omega_2 \longrightarrow O(\varepsilon)$$

As it will be stated below the above angles should be of the order of magnitude of 10 degrees.

Numerical Algorithm

The differential equation system has been solved by means of an algorithm based on a pure explicit finite difference method (Ref. 7). The step width in the R-direction has been controlled using the appropriate stability condition for a three dimensional explicit difference method. The boundary conditions have been taken into consideration by iteration (Ref. 8).

4. RESULTS

The Free Flow Conditions

The flow field calculations have been carried out on the basis of the following free flow parameters

free stream Mach number	$M_{\infty} = 7{,}95$
free stream Reynolds number per length	$Re_1 = 38456/cm$
free stream Prandtl number	$Pr_{\infty} = 0{,}7368$
mean free stream molecular path	$\lambda_{\infty} = 0{,}0003122$ cm

The reference length is

$$L_{ref} = 0{,}1454 \text{ cm}$$

and the reference Reynolds number

$$Re_{ref} = 88{,}48$$

The Quality of the Present Method

Within the present investigation no experiments have been carried out. In order to prove the quality of method presented here experimental results from the bibliography have been used. For this reason the wall pressure distributions for a cone with an axis ratio of the elliptical section c = 0,5 and for the angles of incidence $\alpha = 0^{\circ}$ and $\alpha = 4^{\circ}$ have been calculated and compared with experimental results on an elliptical cone with c = 0,5 and a Mach number of $M_{\infty} = 5{,}8$ which is too low to be considered here (Ref. 9). Since the shock boundary layer interaction parameter χ_{∞} is different only a qualitative comparison of the results of both investigations could be carried out (Fig. 3). A good qualitative agreement between the theoretical and experimental results has been achieved for both angles of attack $\alpha = 0^{\circ}$ and $\alpha = 4^{\circ}$ concerning the azimuthal pressure distributions. This conformity becomes better with decreasing shock/boundary layer interaction parameter χ_{∞} since the same paramter for the experiment is much smaller than 1.

The Influence of the Angle of Attack on the Cross Flow

The azimuthal pressure distribution on an elliptical cone with c = 0,5 for angles of attack from $\alpha = 0^{\circ}$ to $\alpha = 8^{\circ}$ has been calculated (Fig. 4). An increase of the pressure gradient occurs on the vertex of the elliptical cone - $\varphi = 90^{\circ}$ - with increasing angle of attack, also the wall pressure maximum is moving towards - $\varphi = 0^{\circ}$ - on the wind side. At the angle of incidence $\alpha = 8^{\circ}$ the maximum lies on the generator line $\varphi = 0^{\circ}$. This means that a strong cross flow occurs from the windward side to the lee side. This crossflow did not appear for an angle of incidence $\alpha \ll 4^{\circ}$. Furthermore a constant pressure is already built up between $\varphi = 150^{\circ}$ and $\varphi = 180^{\circ}$ with a slight increase between $\varphi = 160^{\circ}$ and $\varphi = 180^{\circ}$. This leads to the assumption that an adverse pressure is already built up although the shock/boundary layer interaction parameter is still quiet high. The already mentioned cross flow around the cone towards the lee side for $\alpha = 8^{\circ}$ results in a rotation of the near surface stream lines towards the lee side (Fig. 5). The rotation of the streamlines on the cone surface is defined as

$$\Theta_w = \arctan \left(\frac{v}{u}\right)_w$$

whereas v and u are the velocity components in φ- resp. R-direction. The rotation is positive in case the v-component shows from the windward side to the lee side of the cone or to the generator line $\varphi = 180^{\circ}$.

The Influence of the Axis Ratio of the Cross Section

The influence of the axis ratio of the elliptical section on the azimuthal pressure distribution on the cone surface has been investigated (Fig. 6).

For the cone with a high axis ratio c = 0,333 and for an angle of attack $\alpha = 4^{\circ}$ the pressure plateau between $\varphi = 150^{\circ}$ and $\varphi = 180^{\circ}$ already exists and a slight adverse pressure appears between $\varphi = 160^{\circ}$ and $\varphi = 180^{\circ}$. On the contrary on the cone with an axis ratio c = 0,5 the pressure gradient towards the x-z-plane still exists. Furthermore the gradient around the leading edge is stronger at a c = 0,333 than at a c = 0,5 which consequently leads to the occurance of a strong cross flow.

Flow Field Variables

Following this some variables of the flow field around the cone with an axis ratio $c = 0,5$ at an angle of incidence $\alpha = 8^{\circ}$ and with increasing distance from the apex i.e. with decreasing χ_{∞} will be discussed in detail. First the azimuthal velocity profiles at various stations φ and χ_{∞} will be considered (Fig. 7). As we expected the flow at the station $\varphi = 150^{\circ}$ decelarates near the surface with increasing distance from the apex while the flow accelerates at the wind side and at the vertex of the elliptical section. Also a stronger decrease of the slip flow appears at $\varphi = 90^{\circ}$ than elsewhere on the cone surface. The form of the cross flow profiles can be explained due to the shock formation above the cone surface (Fig. 8). As might be expected the formation of the shock on the lee side proceeds slower than on the windward side. It is worth noting that the shock has still a width and that this width corresponds with the indentation of the azimuthal velocity profiles. Finally the azimuthal wall pressure distribution at various distances from the apex of the cone has been calculated (Fig. 9). The increasing expansion around the leading edge of the elliptical cone with decreasing χ_{∞} strongly modifies the wall pressure distribution between $\varphi = 60^{\circ}$ and $\varphi = 100^{\circ}$ Furthermore the formation of the adverse pressure at $\varphi > 140^{\circ}$ has also been observed since a slight increase of the static pressure occurs in this region of the coordinate φ. Finally it is worth mentioning that a strong rotation of streamlines towards the lee side takes place in the vicinity of the vertex due to the expansion while the shock/boundary layer interaction parameter χ_{∞} decreases (Fig. 10).

CONCLUSIONS

The present investigation shows that for small angles of incidence of an elliptic cone - in contrast to the circular cone - the cross flow occurs only slowly or not at all whereas at moderate incidence and because of the large expansion around the ridgeline a marked cross flow occurs around the ridgeline. This expansion and thus the cross flow becomes more marked with increasing ellipticity of the conical section and with increasing incidence. No formation of vortices could be found within the shock formation region. This may be attributed to the large diffusion within this region. The slight increase in static pressure on the lee side with the advance of the calculation in the main flow direction leads to the assumption that an adverse pressure forms which would generally lead to the formation of a vortex in a three dimensional flow. Since this process occurs at large shock/boundary layer interaction parameter χ_{∞} and moderate angle of incidence it can be assumed that for an elliptic cone - in contrast to the circular cone - the vortex formation occurs at larger χ_{∞} and smaller α.

The present calculation method based on an explicit finite difference scheme is not suitable for calculations up to $\chi_{\infty} \approx 1$ because of the high computational time required. Therefore another method based on an implicit difference scheme should be developed.

REFERENCES

1) Rao, D.M., and Whitehead, A.H.Jr., "Lee Side Vortices on Delta Wings at Hypersonic Speeds," AIAA Journal, Vol. 10, Nov. 1972, No. 11, pp. 1458-1465.

2) Tracy, R.R., "Hypersonic Flow Over a Yawed Circular Cone," Cal. Inst. of Techn. CALCIT Memo., No. 69, 1963.

3) Whitehead, A.H.Jr., and Bertram, M.H., "Alleviation of Vortex-Induced Heating to the Lee Side of Slender Wings in Hypersonic Flow," AIAA Journal, Vol. 9, Sept. 1971, No. 9, pp. 1870-1872.

4) Rao, D.M., "Hypersonic Lee-Surface Heating Alleviation on Delta Wing by Apex Drooping," AIAA Journal, Vol. 9, Sept. 1971, No. 9, pp. 1875-1876.

5) Lin, T.C., and Rubin, S.G., "Viscous Flow Over a Cone at Moderate Incidence, I. Hypersonic Tip Region," Computers and Fluids, Vol. 1, 1973, pp. 37-57.

6) Hirschel, E.H., "Die Stroemung eines hochverduennten, dissoziierten Gases ueber eine ebene, vorne scharfe Platte," DLR-FB 70-60, Dez. 1970.

7) Evangelou, P., "Hypersonische Gleitstroemung um schwach angestellte schlanke elliptische Kegel," DFVLR-FB 79-21, 1979 or "Hyperson'c Slip Flow Around Slender Elliptical Cones at Slight Angle of Attack," ESA-TT-644, 1980, (Translation).

8) Rudman, S., and Rubin, S.G., "Hypersonic Viscous Flow Over Slender Bodies Having Sharp Leading Edges," RIBAL Rep. No. 1018, May 1967.

9) Chapkis, R.L., "Hypersonic Flow Over an Elliptic Cone, Theory and Experiment," J. Aerospace Sci., Vol. 28, Nov. 1961, No. 11, pp. 844-854.

* The investigation was performed in the Deutsche Forschungs- und Versuchsanstalt fuer Luft- und Raumfahrt e.V., 5 Koeln 90, West Germany.

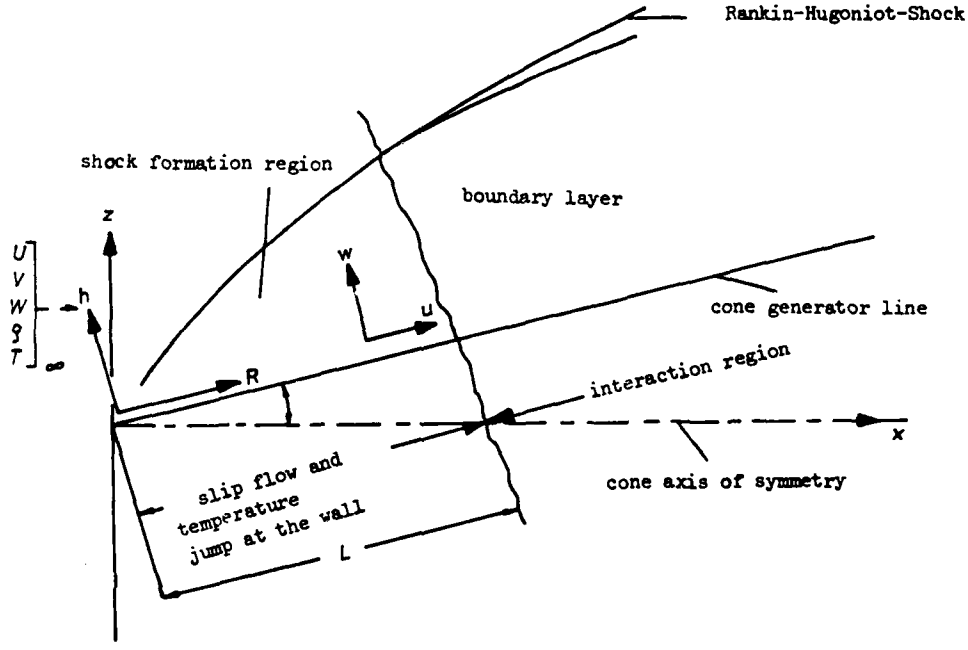

Fig.1 Sketch of the flow along a cone generator line

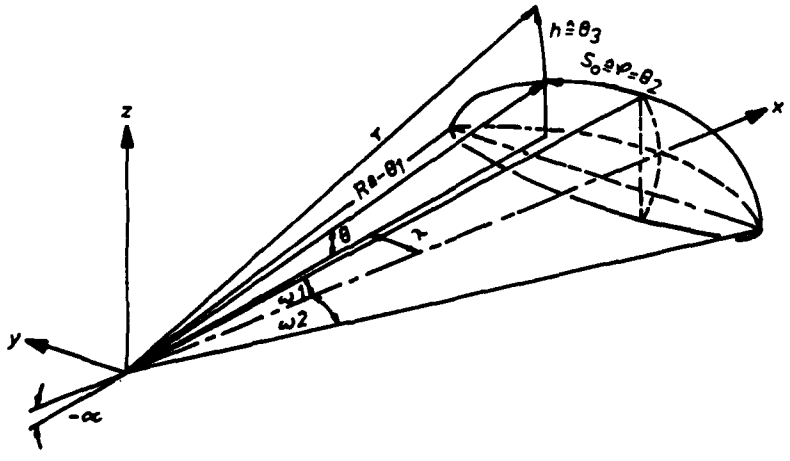

Fig.2 Cone geometry and the co-ordinate system employed R, ϕ, h

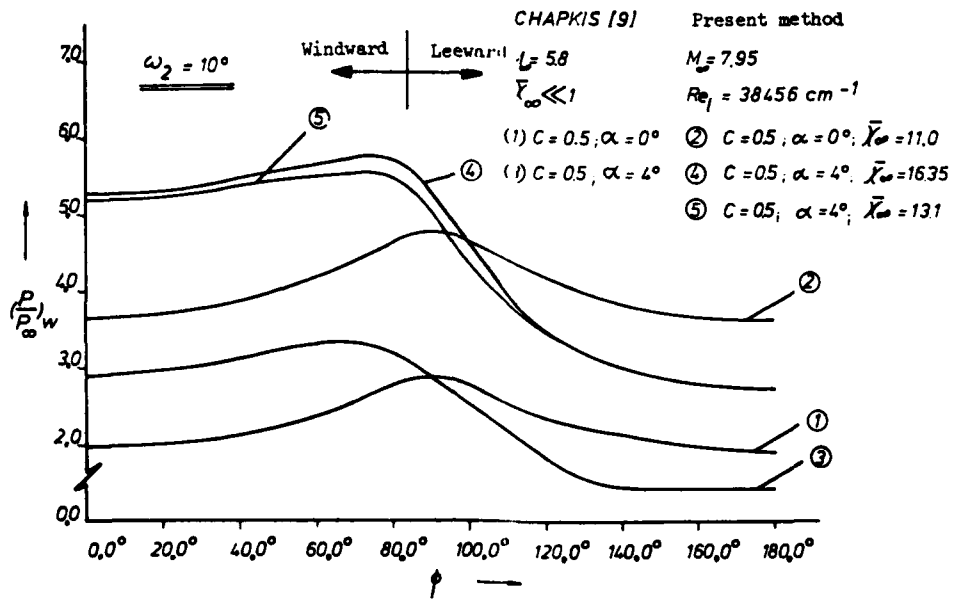

Fig.3 Azimuthal pressure distribution from theory and experiment above an elliptica

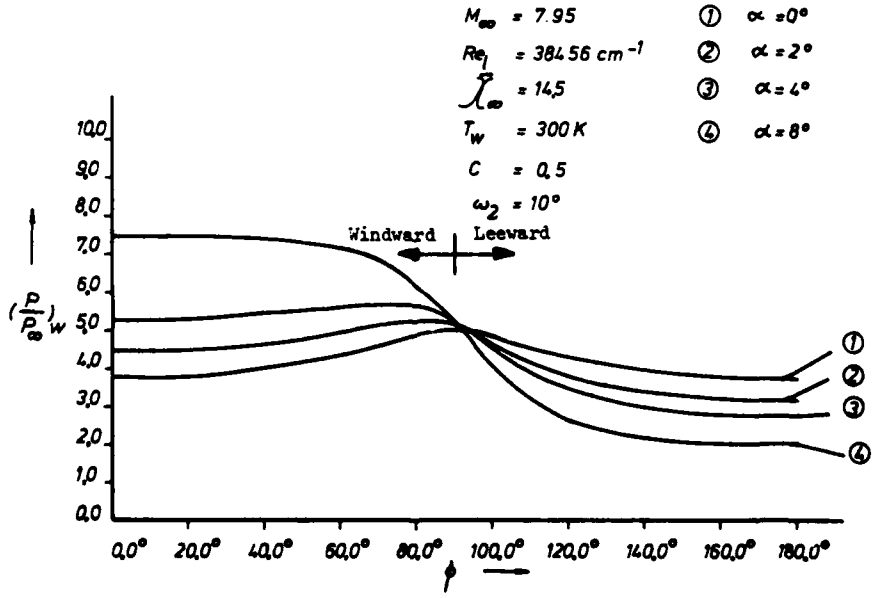

Fig.4 Azimuthal wall pressure distribution on an elliptical cone for various angles of incidence α

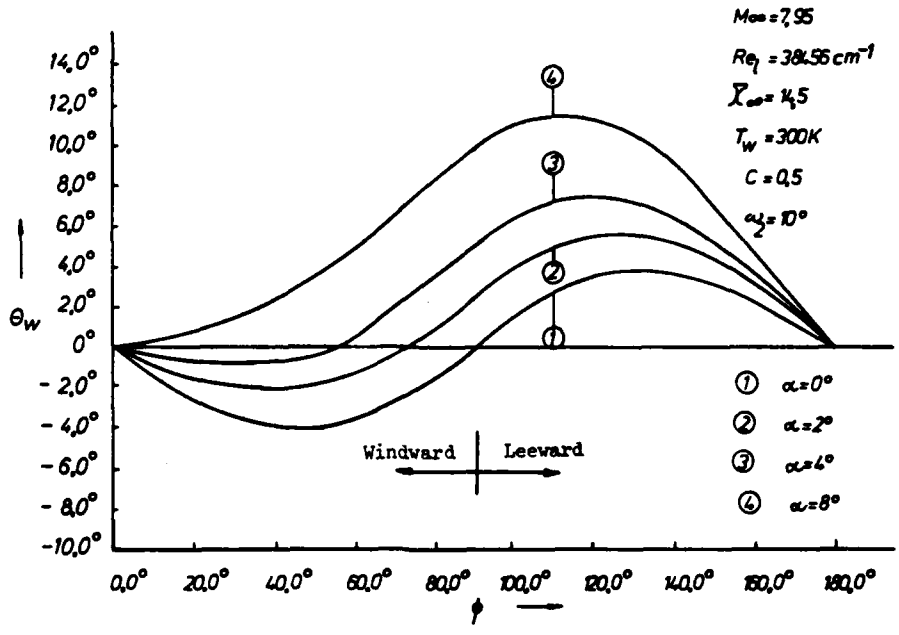

Fig.5 Wall streamline rotation Θ_w on an elliptical cone at various angles of incidence α

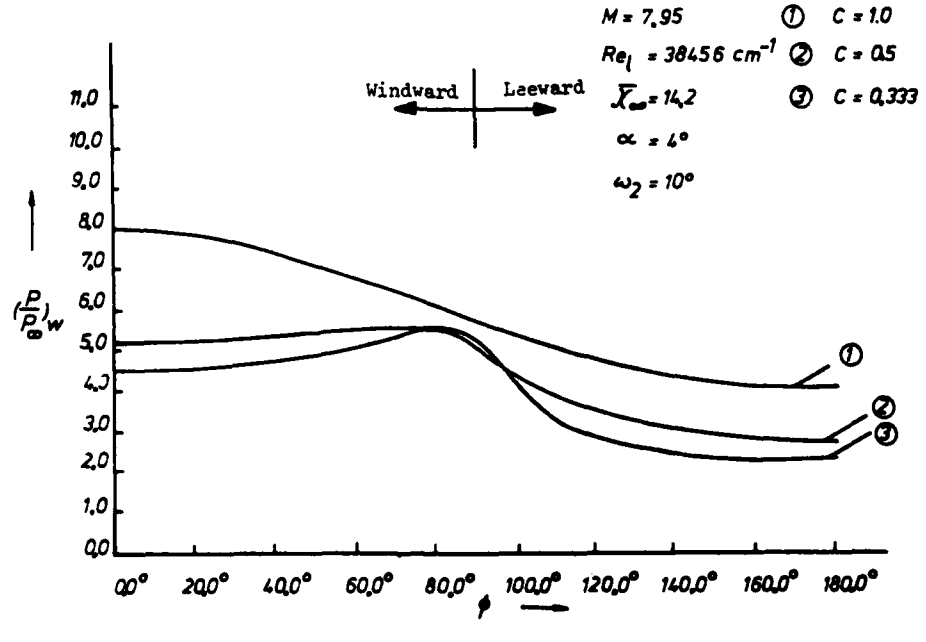

Fig.6 Azimuthal wall pressure distribution for various axis ratios

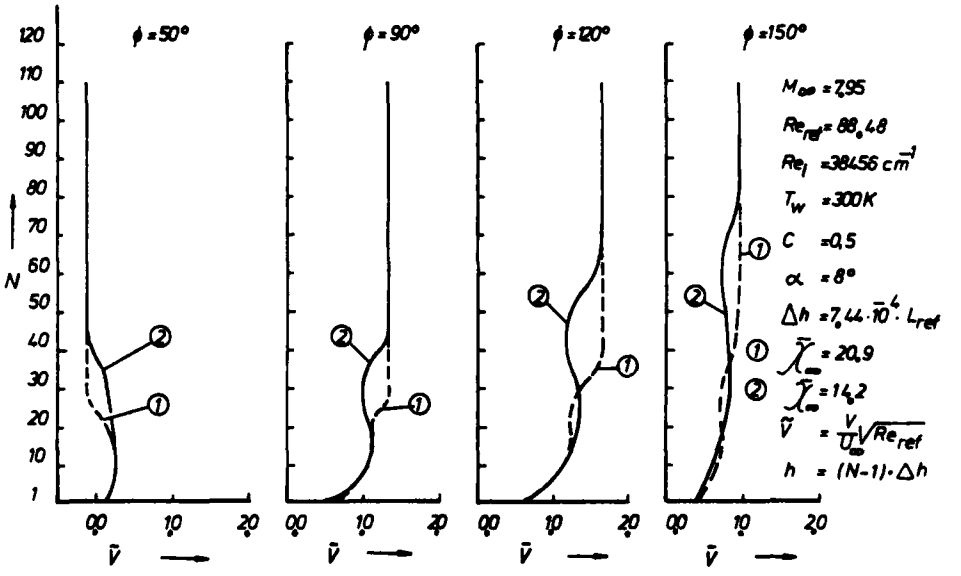

Fig.7 Tangential velocity profile for various ϕ and $\bar{\chi}_\infty$ values

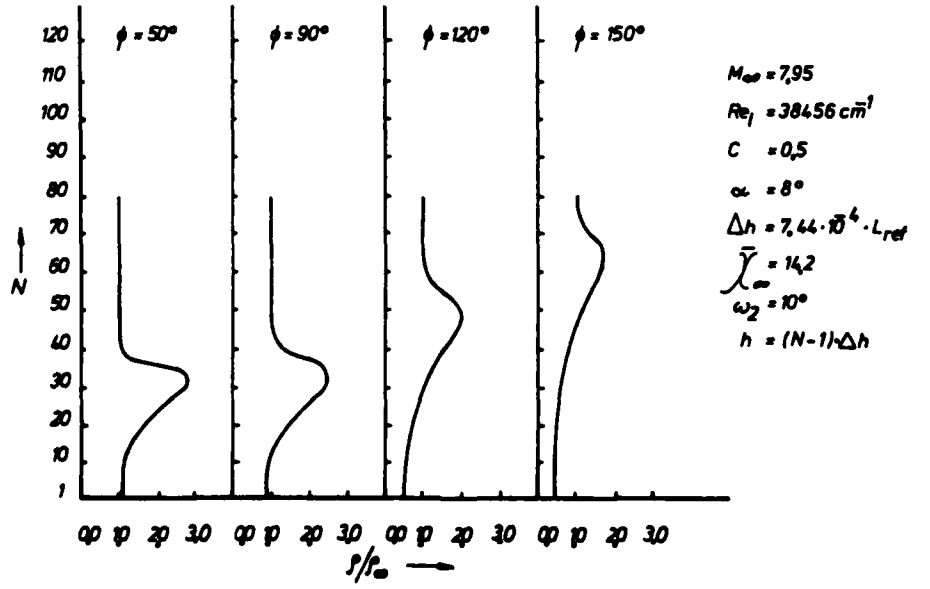

Fig.8 Density profile for various ϕ co-ordinates

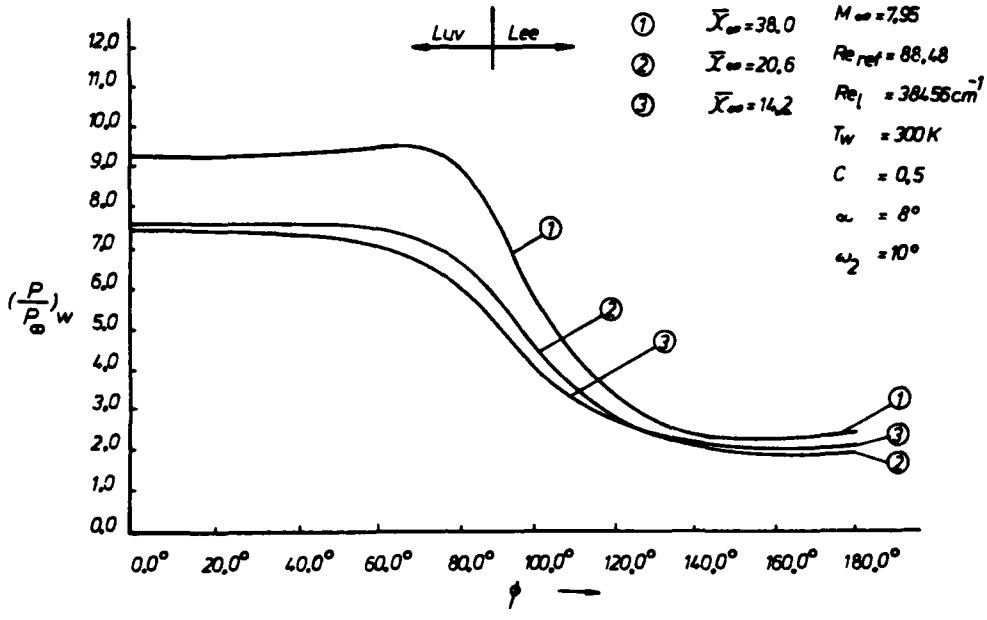

Fig.9 Azimuthal wall pressure distribution for various values of ϕ

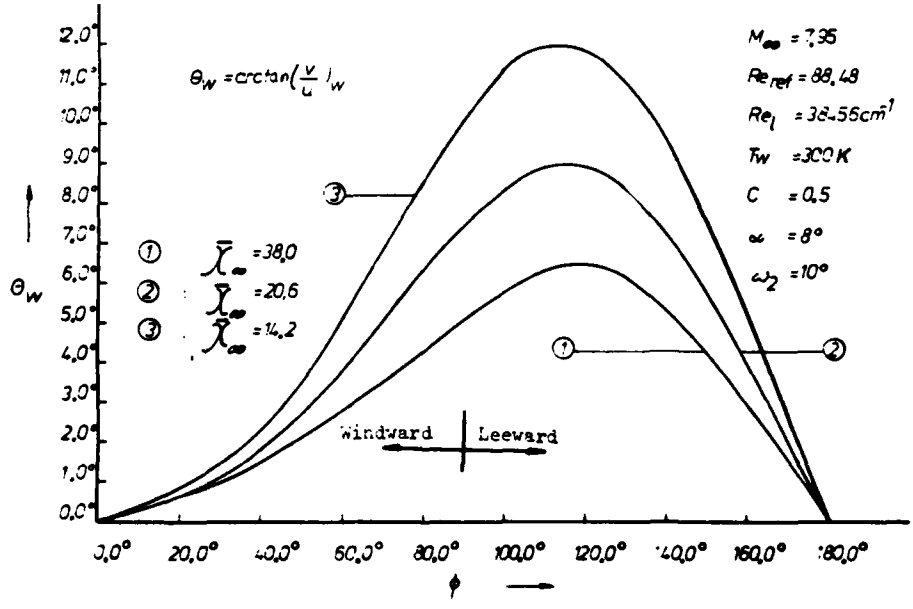

Fig.10 Rotation of the wall streamline for various χ_∞

VISCOUS THREE-DIMENSIONAL FLOW SEPARATIONS FROM HIGH-WING PROPELLER-TURBINE NACELLE MODELS

R.H. Wickens
Low Speed Aerodynamic Laboratory
National Aeronautical Establishment
National Research Council Canada
Ottawa, Canada K1A 0R6

SUMMARY

This paper describes an investigation of viscous three-dimensional flows on high-wing nacelle configurations which are typical of current commuter aircraft.

Flow visualization on two nacelle configurations was used to depict the viscous vortex separations in the underwing junction, the nacelle afterbody, and the wing upper surface over the central region. The surface shear stress patterns, although complex, were composed of combinations of elementary three-dimensional viscous flows and free vortices which stream downwind. A strong vortex flow was produced over the top of the wing by the use of leading edge extensions along the forward portion of the nacelle.

Observations were also made of the effects of a propeller slip-stream and the distortion of this propulsive flow by the mutual interference of the wing and nacelle.

SYMBOLS

A	aspect ratio $\frac{b^2}{S}$	V	flight speed
b, b_N	wing span, nacelle effective span	w	wake downwash
C_L	lift coefficient	y	spanwise location
C_D	drag coefficient	z	vertical location
e	wing efficiency factor	α	angle of attack
H	total pressure parameter $\frac{p_T - p_o}{\frac{1}{2}\rho V^2}$	α_{DW}	downwash angle (positive in negative lift direction)
p_T	total pressure	β_{SW}	sidewash angle (positive along starboard wing)
p_o	reference pressure	ϵ	wing streamtube deflection angle
S	wing area	θ	nacelle streamtube deflection angle

INTRODUCTION

This paper presents wind tunnel observations of various types of three-dimensional viscous flow separations on high-wing nacelle configurations which are representative of current propeller-turbine technology for commuter aircraft. These observations, in which flow visualization was used extensively, have dealt mainly with flows in the under-wing junction, along the top of the wing at high incidence, and on the nacelle afterbody. The models were unpowered, however, the effects of a propulsive streamtube, and slip-stream rotation were observed for certain cases.

Since most or all of the observed flows were of a three-dimensional vortical type, the surface shear stress patterns seen on the model surfaces reflected the presence of steady, rolled up vortex sheets which stream down-wind. In addition, schematic representation of the various viscous singularities with which these complex flows can sometimes be represented, are also presented. In some cases it was also possible to do wake traverses in order to locate the regions of vorticity or separation.

Interest in this subject stems from Research and Development in Canada, and elsewhere, of a new generation of propeller-driven commuter class aircraft. The DeHavilland Dash-7 and Dash-8, now under development, are current examples. These aircraft exploit the advantages of the propeller-turbine propulsion system and reflect the most recent advances in aerodynamic design. Aerodynamic refinement of both the airframe and engine is necessary for efficient flight, and much information, both theoretical and experimental is being applied to the development of these new types of aircraft. One area which is of particular importance is the engine nacelle, and its design and placement on the wing so as to produce the optimum integration of lift and thrust. A typical aircraft development program requires large amounts of wind tunnel testing and analysis of data, leading to a final, satisfactory design; however, the present research program was undertaken to explore certain aspects of the aerodynamic flow over idealized wing-nacelle configurations (Ref. 7).

NACELLE AERODYNAMIC CHARACTERISTICS

In a wing-high configuration, typical of many current aircraft types, the main factors in the design and sizing of the nacelle, are the engine choice and placement, and the location, size and retraction mode of the main undercarriage. Having satisfied these requirements, the aerodynamicist must now shape the external contours to produce smooth flow, and minimum drag increments. His choices are narrow however; for example, the width of the nacelle and its cross-sectional shape, and also the afterbody length and shape,

are important aerodynamic parameters but, these are essentially fixed by the retracted position of the main landing gear wheels, and the mode of efflux of the engine exhaust. The nacelle shape which evolves is usually somewhat functional, and may not represent the most efficient aerodynamic form, particularly in the vicinity of the wing, where interference flows are high, and separations are likely to occur.

Wing-nacelle interference and design has been the subject of a large amount of aerodynamic research and some of the more interesting and relevant conclusions have been summarized in References 1 to 10.

Early investigations on the subject showed that the measured drag of the wing-nacelle combination was considerably higher than the drag of the isolated wing, and that lift and lift distribution was also different, with a lift loss occurring over the nacelle. Assessment of complete aircraft configurations showed that for twin engined aircraft, the total nacelle drag could represent a large fraction of the total. It was these drag increments therefore, which were of concern to aircraft designers, and any improvements which might be gained, would be of significant benefit in the improvement of total aerodynamic efficiency.

The drag increment resulting from the addition of a nacelle to a wing is attributed to two main causes: the first results in an increase of overall induced drag due to the loss of lift. Part of this increase is also due to a reduced wing efficiency resulting from the non-uniform spanwise lift distribution over the nacelle. These distributions also result in the shedding of streamwise vorticity at the junction, which induces a non-uniform distribution of downwash along the wing span. These effects are different for different nacelle vertical locations. The centrally-mounted nacelle has the smallest drag increment. The underslung nacelle results in a larger loss of lift and higher induced drag increment, however, these can be alleviated by adjustments to the wing and afterbody length. The effects of engine nacelle vertical placement on nacelle drag are shown in Figure 1.

A second type of interference drag arises in the expanding corners of the nacelle-wing junction near the wing trailing edge. Experience has shown that if the nacelle terminates at or before the trailing edge, separation is likely, with a resulting increase in drag. This type of flow is particularly severe with the underslung nacelle, as Figure 2(a) shows, but can be avoided by extending the nacelle beyond the wing, or by expanding the mid-section contours near the trailing edge, thus allowing the development of a steady, more gradual type of separation.

The significant regions of the wing-nacelle configuration where aerodynamic flows are important are the nose portion, particularly where the nacelle merges with the wing; the mid-section where interference velocities are high, and viscous separations are likely to occur; and the afterbody, from which steady three-dimensional separations should originate. The main physical parameters which affect the overall wing nacelle performance have been found to be:

1. wing vertical location,
2. position of nacelle maximum thickness, and
3. afterbody length behind the wing trailing edge.

To a lesser extent, nacelle cross-sectional shape is also important, particularly on the upper shoulder, just ahead of the wing leading edge junction (for high wing configurations).

If turbulent breakdown in the expanding corner is avoided by extending the afterbody rearward, the separation tends to be more gradual, and takes place along lines of confluence which fix the point of departure of the surface flows. Lines of confluence are defined as streamwise edges (virtual or fixed) along which fluids of differing velocities and flow direction meet. They are natural origins for vortex sheets and are a desirable element of flow detachment from slender streamwise configurations. The sketch (below) shows possible lines of confluence along the afterbody of a nacelle. This type of flow separation is the mechanism whereby the abrupt spanwise lift gradients produce the required wing-body vortices. It results in further vortex shedding but is, however, a satisfactory alternative to complete separation. In this regard, also, cross-section shape is important; a sharp edge would act as a natural line of confluence.

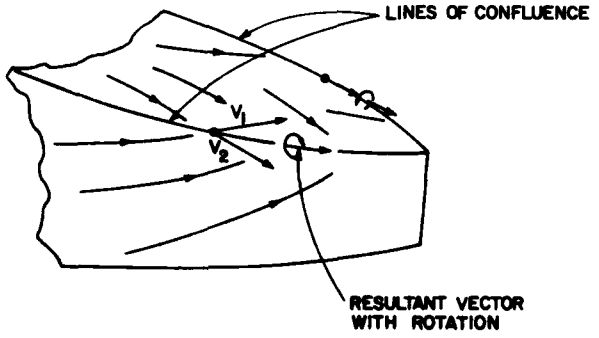

SKETCH (I)

The importance of the efficiency of nacelle design on the overall drag and performance of an actual aircraft was illustrated graphically in the wartime research and development of the Douglas A26 attack bomber. This aircraft, one of the most successful of its type in World War II, and still flying today in the fire-bombing role, was initially troubled by poor performance as a result of unacceptably high nacelle drag. Investigation revealed that the two engine nacelles contributed over 30% to the total airplane drag. This drag was composed of cooling flow momentum loss, and drag due to the external contour. Of this latter drag, 75% was due to flow over the mid- and aft-portions of the nacelle, and 25% due to the flow over the engine cowling. By making suitable changes to the cowling contours, and by adjusting the shape and exiting cooling flow over the afterbody, the nacelle drag was reduced, with a corresponding increase in aerodynamic cleanness (Ref. 11).

The method used to assess the drag increments of the A-26 nacelles was a pitot rake, positioned downstream of the nacelle afterbody, which rotated about the nacelle reference line. The local drag coefficients so determined were found to be sensitive to the separation which was occurring on the nacelle afterbody, and the extent to which it was sensitive to upstream conditions (i.e. cooling exit mass flow).

WING-BODY INTERFERENCE

Drag and Vortex Wake

The physical nature of the inviscid interference between a wing and a fuselage or nacelle produces alterations in the forces (i.e. lift and drag), the pressure distribution, and the flow in the wake. Although the changes in lift may be small, the increases in drag can be significant and where nacelles are present and may account for a significant fraction of the total airplane drag.

The main inviscid interference effects on the wing have been shown to result in a slight decrease in lift over the centre section due to the reaction of the wing vortex system with the body, and a further increase in induced drag as a result of the abrupt changes in lift distribution across the span. The influence of the body may also extend outwards along the span of the wing, resulting in further small changes in lift and drag, due to the flow displacement effects of the wing thickness and fuselage volume.

The body (nominally a non-lifting system) will also experience inviscid interference effects which produce both lift and drag forces; and are due to an effective incidence change on both fore and aft regions resulting from the induced upwash and downwash field of the wing. Incremental pressure forces will also be present on the body as a result of its own shed vorticity, which has been carried over from the wing.

In all of these interactions, which are the most prominent in the junction itself, viscous flows are present in the form of skewed boundary layers on the body and three-dimensional attachment and separation regions in the junction and elsewhere. These viscous separations appear as concentrations of vorticity which stream downwind and make their own contribution to induced drag.

The alterations of lift and lift distribution, and the resulting induced drag are reflected, in classical inviscid vortex models, by distributions of lift which are considerably different from, for example, the elliptically loaded wing.

The wake which, at a later stage, rolls up to form trailing vortices, is an essential element of the entire flow; vortices will therefore be present even in an inviscid flow. Classical theory assumes that vortex sheets representing the wing, or combinations of a wing and body, extends into the wake long distances downwind of the configuration, to the so-called Trefftz plane, and that the downwash resulting from this wake depends on the strength of the vorticity, and its distribution. Minimum drag for a given lift occurs when the wake vortex system, which has its own downward motion, moves without deformation, thus preserving the original shape of the cross-sectional flow as it left the lifting system. Thus the monoplane wing of minimum induced drag will have a drag polar of the form

$$C_{D_{i_W}} = \frac{C_L^2}{\pi A} \tag{1}$$

and a distribution of vorticity which is anti-symmetric and concentrated heavily near the wing tips.

The addition of a body changes both the downwash distribution and the drag polar.

Thus

$$C_{D_{i_{WB}}} = \frac{C_L^2}{\pi A\left[1 - \frac{R^2}{b^2}\right]^2} \tag{2}$$

and the induced drag is made somewhat higher by the addition of a wing at mid-height.

Moving the wing to the shoulder or high position changes both the spanwise load, and the drag, as shown by Pepper in Reference 14. Figure 3 shows, for the monoplane wing, and the wing body, with the wing at mid and high positions, the theoretical drag polars for minimum induced drag, and also the spanwise load distributions. The main difference between the mid and high wing location seems to be a reversal in the sign of the body lift, and hence the shed vorticity at the junction. The vortex sheets will roll up eventually to form concentrated vortex cores as shown. Figure 4 shows experimental spanwise lift distributions of wings on a cylindrical fuselage (Ref. 5).

A useful concept is the momentum streamtube (see sketch). This is an idealization which suggests that the trailing vortex wake and its circulating flows are contained within a descending cylindrical tube which streams downwind of the aircraft, and which contains all of the momentum associated with the production of lift. Thus for an aircraft flying at velocity V, the lift is

$$L = \rho V W_o S_m \tag{3}$$

where W_o is the bulk or average downward motion of the wake as a whole, and S_m is the cross-sectional area of the momentum streamtube, for the monoplane wing, or for various wing-body configurations in which the vortex sheets have not rolled up; the addition of a body results in a diminished streamtube, and less lift for a given downwash. The classical flow models have assumed that the fuselage or afterbody is infinitely long, and retains its influence for ever. In fact flow will separate from the after body in the form of oblique rolled-up vortex sheets which, in an inviscid flow must occur along physical or viscous lines of confluence as noted in Sketch (i). The resulting wake model which must now represent the aerodynamic flow from the wing-body configuration will have to include free vortices which have been shed from the afterbody, and perhaps also other regions of the airframe. In this regard, some of the purely viscous flows, such as those in the under wing junction could be looked on as free vortex separations which comprise an equivalent inviscid flow model. The result of this altered distribution and formation of wake vorticity will affect not only lift and drag, but also the streamtube size and motion and the concept of minimum induced drag.

Junction Flow

The main results of wing-body interference have been shown to be related to changes in lift and induced drag, with vortex flows originating over the central portion. Some of these characteristics can be estimated using classical wing theory without any detailed knowledge of what is occurring at the wing-body junction itself. Local flows in the junction are important, however, and

frequently lead to overall effects such as separation, which further increase drag. Even where disorganized separation does not occur, three-dimensional boundary layer separation does, with shedding of additional streamwise vortices.

Since the interference flows are always greatest in the junction between the wing and the body, the shaping of the intersection is important, and frequently results in elaborate fillets or contours which are meant to produce not only smooth flow, but also minimum pressure drag.

The main aerodynamic effects of wing-body interference at the junction can be divided into four main areas according to Reference 15.

(a) Displacement Effects

The displacement effect of wing-body interference has been shown to produce marked changes to the streamwise velocity distribution at the junction; these induced velocities result from the finite thickness of the wing, and the compound curvature of the intersection line. A symmetrical wing section at mid-height on a cylindrical body produces, along the junction, symmetrical velocity distributions, and results in no net lift on the combination. A similar, but asymmetric displacement effect occurs when the wing is set at an incidence relative to the body. In this case, a lift increment results which is related only to the asymmetry of the junction flows.

If the wing is lifted to the shoulder or high-wing location, the intersection lines are no longer symmetrical with respect to the cylinder. The resulting velocity distributions will also be asymmetric, and the wing-body junctions will thus generate lift, with the appropriate vorticity shed downstream.

(b) Lifting Effects

The lifting effects of wing-body interference as it alters total lift and lift distribution is fairly well described by lifting line theory and its extensions. In addition to these changes, however, velocity increments will also be induced along the junction intersection lines due to the vorticity distributions on both the wing and the body.

The placement of a lifting wing on a cylindrical body set at zero incidence, for example, produces alterations in the wing spanwise vorticity and a continuation of this vorticity over the body width. Thus velocity increments are produced on both the wing and the body as a result of their proximity.

Detailed calculations of such flows are discussed in References 15, 16 and 17 and these indicate that both chordwise and spanwise load distribution, and hence local velocities are changed considerably in the vicinity of the junction and beyond. This requires that, for the isolated wing loading to be maintained everywhere, the wing must be cambered and twisted. This type of wing warping is also alluded to by Hoerner (Ref. 3) and Reference 1, in relation to the induced drag of underslung nacelles. By adjusting the local wing loading at the nacelle location using a trailing edge flap, the lift increment of the configuration may be to zero with a corresponding reduction of induced drag.

If the body is also lifting, and the carry-over of vorticity from the wing implies this; then there will be a further interaction at the wing. If there is body incidence, then the resulting upwash at the wing will increase the loading generally, with corresponding increases in the velocity increments in the junction.

(c) Non-Symmetrical Wing Locations

The overall changes to lift and drag when the wing is lifted from mid- to shoulder height on a cylindrical body can be seen in the drag polars of Figures 3 and 4. The flow at the junction, due to both displacement and lift effects is also altered considerably. The displacement flows are now asymmetric, and result in lift, independent of incidence (Ref. 15).

Induced velocity increments due to lift are also changed in character when the wing is off-centre. The wing vorticity is carried over on to the body and within it in a much more complex way; the resulting velocity increments, for example, in the underwing junction, are in the present state of the art, of uncertain magnitude and accuracy (Ref. 15).

Measurement of wing lift distributions, such as those indicated by Figure 4 suggests that there are large concentrations of pressure near the wing leading edge junction. Figure 5 taken from Reference 8 shows pressure isobars on the upper surface of a high-wing body configuration at an angle of attack of 2.5°. The concentration of isobars near the leading edge junction indicates a local change of both lift and leading edge suction.

(d) Viscous Effects

The viscous flows result in a gradual development of three-dimensional boundary layers on the nacelle and wing. Boundary layer separation occurs along oblique separation lines in the junction and elsewhere, with trailing vortices shed downstream. These flows are particularly prominent on the nacelle, which has a short after body.

The assessment of viscous effects are mainly undeveloped, but are considered to be of equal (if not of more) importance in contributing to wing-body interference. Whereas lift interference can be calculated fairly accurately under some conditions, drag interference cannot be, and an inspection of any of the viscous flows which appear in the wing-body junctions or elsewhere shows why (Fig. 13).

The complexity of these flows precludes any accurate estimate of drag, however, the existence of steady rolled-up vortex sheets suggests that it may be attributable to induced effects. It is also noteworthy that the surface shear stress patterns (as in Fig. 24) of the viscous attachment regions in the junction and aft of the trailing edge, bear a resemblance to a source-like flow in which momentum is related to drag. These viscous losses arising from junction flows might be contained within a streamtube whose dimensions roughly encompass the frictional shear stress regions as estimated from surface observations and would be related the vortex flows within them.

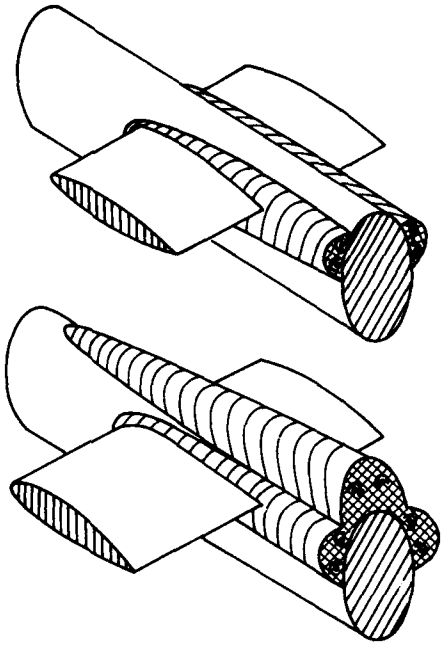

a) JUNCTION SEPARATIONS ONLY

b) JUNCTION AND FOREBODY SEPARATIONS

SKETCH (ii)

The nature and complexity of the viscous separations along the wing-body junction were also investigated in the NAE water tunnel using models which are typical of current nacelle designs. These flows are shown in Figure 6 and although at a very low Reynolds number, they correspond very closely with larger scale tests, and demonstrate the complex nature of the viscous effects near the wing root leading edge.

Propulsive Effects

An important element of the flow over the wing-nacelle configuration relates to the propulsive streamtube produced by a propeller. The slipstream is composed of mainly axial and rotational fluid motion induced by a helical vortex system which leaves the blades, and interacts with the wing and body. This interaction produces further changes in lift and drag, and is an essential design feature of aircraft designed for the STOL mode. Its effect is favourable in that it results in an altered span load distribution, reduced induced drag, and a favourable environment for the wing boundary layer outside the slipstream.

The aerodynamic loading on both the wing and the body, will also change, as will the junction flows and also the configuration of the wake vortex sheets. The propeller slipstream, initially cylindrical, will undergo considerable deformation, particularly on the under side of the wing, and will gradually merge with the wake vortex system of the nacelle. The flow downwind of the wing-nacelle will therefore be composed of both propulsive and vortical elements.

The propeller slipstream, particularly the flow rotation component, will have a major effect on the flow and pressure distribution at the wing leading edge junction and the concentration of vorticity which normally appears on a high-wing configuration (Fig. 5) will be enhanced on the up-going blade side, due to the local increase of incidence, and reduced on the down-going blade side, resulting in an overall increase of leading edge suction, and an asymmetric distribution of pressure. If LEX are installed, with vortex separations leaving the streamwise edges, then slipstream rotation may produce an asymmetric three-dimensional separation with free vortices of unequal strength streaming downwind.

The design of leading edge extensions for propeller-driven aircraft must conciliate the conflicting requirements at the leading edge for smooth flow and the development of maximum suction in the cruise and climb mode, with steady separated flow and vortex-induced lift during the landing approach.

The overall effect of a propulsive flow on a wing or wing-body can be assessed by the use of a simple two-stream momentum model as described in Reference 18. In this idealization, part of the lift and all of the thrust is derived by deflecting and energizing a streamtube of air which passes through the propulsion system. The remainder of the lift is generated by a wing or wing-body which is considered to deflect downward, a second streamtube. The sketch shown below is the vector diagram of the two-stream model.

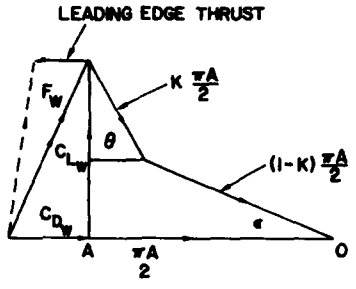

SKETCH (iii)

The vector OA is the approaching streamtube momentum of magnitude $\frac{\pi A}{2}$. If the wing or wing-body is unpowered, then the flow leaves the wing at downwash angle ϵ. If power is applied over part of the wing, it is assumed that a certain fraction of the department momentum $\frac{K\pi A}{2}$ leaves the wing at angle θ, while the remainder $(1 - K)\frac{\pi A}{2}$ leaves at angle ϵ. Thus the effective span of the powered lift streamtube is proportional to $\sqrt{K}$.

The vector F_w is the resultant force acting on the airframe, having components C_{L_W} and C_{D_W}. If the wing is immersed in a propeller slipstream, then the rotational components of the propulsive flow may enhance the leading edge suction on either side of the nacelle, resulting in a thrust or reduction of induced drag. The vector $\frac{RK\pi A}{2}(1 - \cos\theta)$ is that fraction of nacelle induced drag which is recovered at the leading edge.

Lift and drag coefficients (for small angles) are:

$$C_{L_W} = \left(\frac{\pi A}{2}\right)\epsilon\left[(1-K) + \frac{K\theta}{\epsilon}\right] \tag{4}$$

$$C_{D_W} = \left(\frac{\pi A}{4}\right)\epsilon^2\left[(1-K) + K(1-R)\left(\frac{\theta}{\epsilon}\right)^2\right] \tag{5}$$

This leads to a drag polar of the form:

$$C_{D_W} = \frac{(1-K) + K(1-R)\left(\frac{\theta}{\epsilon}\right)^2}{\left[(1-K) + K\frac{\theta}{\epsilon}\right]^2} \cdot \left(\frac{C_{L_W}}{\pi eA}\right)^2 \tag{6}$$

and wing efficiency factor is:

$$e = \frac{\left[(1-K) + K\frac{\theta}{\epsilon}\right]^2}{(1-K) + K(1-R)\left(\frac{\theta}{\epsilon}\right)^2} \tag{7}$$

Figure 7 shows e plotted against the ratio $\left(\frac{bn}{b}\right)$ for values of $\left(\frac{\theta}{\epsilon}\right)$ of 2, corresponding to a positive nacelle lift increment, and 0.5, corresponding to a negative nacelle lift increment. The effect of a 10% recovery of leading edge thrust is also shown.

These results show that when the combination of propulsive and interference effects are distributed uniformly across the span, $\left(\frac{\theta}{\epsilon} = 1\right)$, then wing efficiency factor is a maximum, and equal to unity. If the angles differ markedly, then e decreases, and as Figure 7(b) shows, reaches a minimum when the spanwise disturbance covers about 60% of the span. It appears, therefore, for high wing efficiency factors, that any spanwise disturbances should cover either a very small portion of the wing span, or a very large portion. In this regard, the negative lift increments produced by the presence of an unpowered nacelle result in a lower loss of wing efficiency than positive increments produced by powered lift. The effect of a leading edge thrust recovery factor R results in an increase of wing efficiency factor in both cases.

The two-stream flow model has assumed that all of the momentum associated with both propulsive and wing-body interactive effects are contained within the propulsive streamtube. Viscous effects, which are also encompassed within this region contribute indirectly in that they represent a portion of the flow which may be deflected with the general flow over the nacelle. They are, however, non-productive, resulting in a loss of momentum, and, specifically a loss of leading edge suction at the wing-nacelle junction.

WIND TUNNEL MODELS

The nacelles were mounted in the underwing position on a rectangular planform reflection plane model. The wing airfoil was the NACA 0015 and had an equivalent aspect ratio of 6.58, Figure 8 is a general arrangement showing the basic dimensions. The model was attached to the wind tunnel balance for the purpose of measuring lift and drag.

The basic proportions of the nacelles, relative to the wing chord, were chosen to be similar to those under consideration for commuter aircraft design studies. Two basic thickness distributions and cross-sections were chosen. The first (N-1) was based on the NACA standard body as described in Reference 8. A variation of this form, with the maximum thickness pushed back to 60% of wing chord, was tested since the data of Reference 1 indicated a favourable result when maximum thickness is close to the wing trailing edge. The afterbody terminated 0.65 wing chords behind the trailing edge in an ogival contour.

The second model (N-2) was elliptical in cross section and of more slender configuration. The fore and aft body lengths extend 1.2 and 0.8 wing chords beyond the wing leading and trailing edges; the after body terminated in a vertical trailing edge. Figure 8 shows the basic form of the two nacelles with relevant dimensions noted. On nacelle N-2, leading edge extensions (LEX) were fitted in order to encourage the formation of vortices over the top of the wing.

WIND TUNNEL TEST PROGRAM

Balance Data

Force measurements were made at a tunnel dynamic pressure of 40 psf ($Re = 1.2 \times 10^6$). The model was rotated through an angular range which brought the wing beyond stall, with lift, drag and moment recorded.

Lift and drag coefficients for the two configurations, including the isolated wing are presented in Figures 9(a) and 9(b). The main effect of adding a nacelle is to decrease $C_{L_{max}}$ and stalling angle. The lift and drag characteristics for the isolated wing in the linear range of lift implies a wing efficiency factor $e = 0.75$. The addition of a nacelle decreases e slightly, to a value of 0.6. Figure 10 shows, for nacelle N-3, the effects of adding the LEX, on maximum lift, and drag. There is evidently an increase in lift and a small increase in lift slope due to the presence of free vortices shed from the LEX. This is accompanied by a decrease in L/D at angles greater than 10 degrees.

Model pitching moments are also changed by the presence of a nacelle as seen in Figures 9 and 10. With the short nacelle (N-1) the pitching moment destabilizing (nose up); however Cm reverses sign over the α range from 4 to 14 degrees on the slender nacelle (N-2). The addition of leading edge extensions on nacelle N-2 reverses the sign of the pitching moment from nose down to nose up.

Flow Visualization

The medium for flow visualization was Titanium Dioxide suspended in a light machine oil. When illuminated by a strong light source, the T_iO_2 gave off a brilliant reflection, and the properties of the suspension were such that spreading took place in the form of streamwise ligaments when exposed to the frictional layer on the model surfaces.

Water tunnel flow visualization was done at very low Reynolds number using coherent filaments of Flouresceien, a commercial dye. In some instances at higher Reynolds number, a suspension of Aluminum particles enabled vortex flow fields to be visualized.

Downwind Flow Surveys — Powered Models

Downwind flow surveys using pitot tubes, or five-hole yawmeters were made behind two powered wing nacelle models. The first was a powered version of nacelle N-2 (Fig. 8); the power effects resulted in both axial and rotational velocity components over the nacelle and wing.

More extensive measurements (i.e. velocities, total pressure, flow direction) using five-hole probes were made behind a large-scale powered wing-nacelle model which was under investigation by DeHavilland Canada. The proportions of this model were, in general, similar to nacelle N-2.

The purpose of these flow surveys was to locate localized regions of separation, and centres of vortex activity; and also to explore the deformed slipstream downwind of the model.

Classification of Three-Dimensional Viscous Flows

Three-dimensional viscous flows, such as those depicted by the photographs of surface streamlines shown in this paper, appear to be of a very complex nature, as they reflect the combined action of skewed, separating boundary layers, and the action of rolled up vortex sheets lying just above the surface. These apparent complexities, however, can be separated into various combinations of relatively few simple singular flows, which act on the wetted surfaces, and satisfactorily describe the action of viscous separations and attachment. The anatomy of these singular flows has been thoroughly described in References 19 and 20. They are seen to occur regularly in the skin friction patterns of all three-dimensional attached and separated viscous flows, and are related either to regions of attachmentor of separation on the body. They are classified schematically, as in Figure 11.

The nodal point of attachment is shown in Figure 11(a) — the oncoming flow impinges on the nose of the body at a single point, and the surface streamlines radiate outward and rearward toward the leeward side.

If two adjacent nodes of attachment occur, as on the blunt surface of a windshield the streamlines divide between them and are redirected, by means of a saddle point, on either side of the line of symmetry.

If the onset flow impinges obliquely on a slender configuration, or along intersecting surfaces, then attachment is not at a single point or node, but along an oblique line of attachment. This type of flow can be seen along the windward surface of the nacelle (Fig. 12) or along the under wing junctions. Surface fluid always flows away from an oblique line of attachment toward separation lines, or the general flow.

Figure 11(d) and (e) shows various aspects of three-dimensional separation. Figure 3 is a nodal point of separation which would permit closure of the streamlines in an ideal flow. This does not occur in practice, as other modes of separation occur on the aft portions of a body.

The focus of separation, (Fig. 11(d)) is characterized as a surface flow in which the streamlines spiral inward toward a clearly defined centre. A vortex core rises from this centre, and streams downwind. The flow at the spiral focus has been interpreted (Ref. 19) as the termination point of bound vorticity which leaves the surface in a single concentrated filament. The spiral foci are clearly evident on the wing-nacelle models when separation occurs (Fig. 26) and on the windward side of a leading edge strake (Fig. 17). These flows are considered to be undesirable since they tend to detach randomly from the surface and are associated with buffetting and periodic flow separation.

Figure 11(e) shows an oblique line of separation, a flow which is characteristic of separation from slender wings and bodies. Boundary layer fluid approaches the line of confluence from both sides, and separates as a thin sheet which rolls up above it. If the vortex is strong enough, the surface shear stress lines may exhibit a point of inflexion in their curvatures. The attachment line depicted in Figure 11(e) along the plane of symmetry represents the presence of fluid which has been brought down on to the surface as a result of vortex action.

WING-NACELLE VISCOUS FLOW SEPARATIONS

This section presents observations on the main characteristics of the various types of three-dimensional flow separations which occurred on the wing-nacelle junction region. The comments are supported by photographs and interpretation of the surface shear stress patterns in the context of the elementary viscous singular flows described before. The interpretation of the surface flows and their synthesis into equivalent vortex flow models are somewhat subjective, and, as Reference 21 points out, notoriously ambiguous and open to question. Nevertheless, it is hoped that a clearer understanding of the steady separated vortex flows over the nacelle will result, and that this work may be useful as a point of departure for a more complete understanding of the aerodynamic flow over wing-nacelle configurations.

Attachment Flows

Regions of flow attachment are shown on the windward portions of nacelle N-2 at an angle of attack of 21 degrees (Fig. 12). In this flow, the node of attachment, at the nose of the spinner, develops into an oblique line of attachment along the ventral surface of the nacelle, and from which fluid flows along the sides of the nacelle, toward the wing junction and afterbody. The lateral deflection of the flow on either side of the centreline, particularly at the nose is severe, but diminishes over the mid-section and upswept afterbody.

Leading Edge Junction — No LEX

The flow near the leading edge, along the wing root junction, as depicted in the water tunnel photographs of Figure 6, represents the main viscous interaction between the nacelle and the wing. As these illustrations show, for a normal leading edge, the stagnation region between the wing and nacelle produces a sudden local separation which has resulted in a horseshoe-type vortex which wraps itself around the wing contour, and whose trailing arms stream downwind.

The surface shear stress pattern of Figure 13 show, at a Reynolds number of 1.2×10^6, a variety of viscous separation and attachment regions which are concentrated within a fairly narrow band along the underside of the wing. Details of this surface flow for nacelle N-2 are shown for angles of attack of 0,8 and 16 degrees.

On the basis of these flow patterns, it is possible to identify both primary and secondary oblique separation lines, nodes of attachment between them, and oblique lines of attachment lying along the sides of the nacelle. In the case of $\alpha = 16°$, it is also possible to identify the stagnation streamline which separates fluid which flows over the top of the wing, from that which traverses the length of the nacelle.

A schematic interpretation of the junction flow shows the probable origin and behaviour of the vortex filaments shed from the junction (Fig. 14). This vortex appears to remain coherent underneath the wing, but is apparently embedded in the boundary layer flow on the upper surface or, since there is little reason for its existence, probably dies out. No trace of it was discernible on the nacelle afterbody. The secondary vortex, although visible in the underwing junction, has apparently merged with the primary vortex on the wing upper surface.

Leading Edge Junction with Leading Edge Extensions (LEX)

In the normal wing junction geometry, the wing meets the nacelle squarely, the only relief afforded by the body curvature on the upper surface. The junction vortex is thus formed abruptly and the resulting flow is as that shown in Figure 6(c). In order to encourage a more gradual formation in the vortex and to change the stalling characteristics a leading edge strake or extension was placed on the top of the nacelle ahead of the wing leading edge. The strake configuration and dimensions are shown in Figure 8.

With this device fitted, free vorticity is shed along the streamwise edges as flow coming up from the ventral attachment line separates along the top of the nacelle. The vortex sheets roll up above the wing, producing downwash in the place of symmetry, and increased lift. At high incidences, these vortices become part of the separated, but steady flow on the wing upper surface.

The junction vortex system which originates on the strake windward edge exists, but exhibits an altered behaviour. The flow on the windward side of the strake, upwind of the stagnation streamline, leaves the swept edge, and rolls up immediately into a strong free vortex above the nacelle. Flow on the nacelle upper surface also flows toward this separation line.

Flow downwind of the stagnation streamline is directed along and underneath the nacelle as before. Between these two flows, on the strake itself, is a region of three-dimensional separation and attachment, similar to the normal leading edge situation, in which surface fluid flows along the underwing junction in one direction, and toward the swept edge of the strake in the other, a prominent node of attachment lies at the wing-nacelle junction. A primary vortex sheet leaves the separation line and, on the underside of the wing, gradually develops and rolls up underneath the wing as before. There is an impression that the junction vortex produced this way is somewhat weaker than its normal counterpart. The flow patterns, especially in the attachment region along the underwing junction do not exhibit a particularly strong three-dimensional effect. A secondary vortex separation is also present, and behaves in a similar fashion to the primary flow.

The other half of this horseshoe vortex is directed across the half-span of the strake, and leaves the edge together with flow from the attachment region, to roll up and become merged with the free vortex which by now is well developed above the nacelle surface.

The development of the strake/vortex flow appears in the surface shear stress patterns of Figure 15 and schematically in Figure 16.

There appears to be two ways in which the underwing vortex can develop. If the strake is suitably blended into the wing-nacelle junction, then the gradual separation process produces the attachment region on the windward surface, with vortices gradually developing as shown. If the strake is not properly designed, or simply consists of a thin plate normal to the nacelle surface, the stagnant fluid in the re-entrant corner appears to encourage the formation of a spiral focus, which acts as the origin of the underwind vortex (Fig. 17). This flow situation is undesirable because of its unsteady nature.

The photographs and schematic diagrams of Figures 15 and 16 show the two possible modes of flow and separation with the strake fitted.

Flow on the Wing-Nacelle Upper Surface — No LEX

The flow on the upper surface of the nacelle at angles below stall is composed mainly of fluid which has left the ventral attachment region, flowed around the sides of the nacelle and along the top of the wing. In addition, there are narrow regions of three-dimensional flow induced by each junction vortex as it streams over the top of the wing. The behaviour of the flow on the wing/nacelle upper surface is critically affected by angle of attack. The three-dimensional effects induced by the junction vortices become more prominent, and the unseparated flow between them is subject to rapid changes in velocity as judged from the streamline patterns of Figure 18 for nacelle N-1.

As incidence increases, new separation lines emerge, on the top of the nacelle at the wing leading edge. These evidently result from detachment of fluid along the top of the nacelle which does not enter the junction separation region. The vortices which are shed are depicted in the sketch as rotating inward, and will be the beginnings of the full-scale wing upper surface vortex flows which are prominent near and after stall. The junction vortex filaments, which branch away from these new vortices are probably eventually swallowed, and would not appear downstream. If flow separation is premature then the breakdown of the wing boundary layers produce undesirable aerodynamic characteristics, and this is reflected in both the surface shear stress patterns and the lift and drag characteristics.

With a more slender nacelle (N-2), as stall develops, it is possible to see more easily what happens to the junction vortex on the upper surface. Figures 19(a), (b), (c) show, for a wing with a normal leading edge, the gradual development of three-dimensional separation leading to prominent but unstable vortex flows for angles of attack of 0,16 and 20 degrees. The schematic interpretation of this process indicates that the junction separation lines may terminate at spiral foci on the wing upper surface near the leading edge. Separation appears to occur as a result of vortex filaments leaving these foci, but also from weak oblique separation lines which traverse the wing chord. These two flow separations presumably merge with one another.

Flow on the Wing Upper Surface — LEX Installed

With a strake fitted, the upper surface flow is dominated mainly by the vortices shed from its free edges, even at moderate angles of attack. Figure 21 shows for nacelle N-2 the upper surface flows at angles of attack of 0,8 and 16 degrees.

The flow is now more stable, and, in comparison with no LEX, at 8 degrees, composed entirely of three-dimensional flow over the centre section. The separation lines, which commence along the streamwise edges of the strake, continue across the wing chord to the trailing edge and begin to form the main vortex system which, at high lift coefficients, keeps the flow attached on the centre section. In this way the classical decrement of loading over the centre portion of a wing-body may have been "filled in" by the action of a favorable viscous separation. The lift curves of Figure 10(a) indicate a slight increase in lift.

The flow in the vicinity of these separation lines, particularly in the interior region, is notably three-dimensional, and exhibits many of the characteristics of the shear stress patterns seen on slender delta wings. At higher angles of attack ($\alpha > 16°$) outboard of the main separation lines, fluid is drawn to both primary and secondary separation lines which originate well beyond the physical dimensions of the nacelle. The schematic diagram of Figure 22(a) shows the main features of the vortex flow over the top of the wing, induced by leading edge extensions. Attachment takes place along the line of symmetry for $\alpha = 8°$. At higher angles of attack, when the vortex flows are stronger, two attachment lines lie on either side of the plane of symmetry.

There appears to be an alternate configuration of the upper surface vortex sheets which may occur at low angles of attack. In this situation, shown in Figure 23 the separation line which originates on the streamwise edge of the LEX does not continue on to the wing. Rather, the vortex sheet may detach at the wing/LEX junction, and both ends roll up, resulting in the formation of double branched cores over the wing. The resulting flow disturbance on the wing may be small. This conjecture has not, so far, been supported by direct observation, and as wing incidence increases; there is a greater likely hood of the vortex sheet "sticking" to the wing. The junction vortex, which does not appear on the wing upper surface with LEX installed, presumably rolls up with the free vortex sheet.

Afterbody Attachment and Separation

Another region where significant separation and reattachment occurs is just aft of the wing trailing edges, on either side of the nacelle afterbody. These attachment regions as seen in Figure 24 for nacelles N-2 and N-3 are slender formations of three-dimensional flow with a prominent node of attachment at the nose. Fluid apparently flows from the oblique attachment line located in the center of these regions to separation lines around the periphery. The sense of the shed vortices is uncertain; Reference 21 discusses a similar flow at the trailing edge of a two-dimensional wing-plate configuration at comparable Reynolds numbers. These trailing edge separation patterns were attributed to a continuation of the secondary vortex flows generated in the junction; thus the flow in the attachment region was weak, and the sense of the free vorticity was opposite to the primary junction vortices.

In the present situation, aft of the wing-nacelle, the reverse is true, in the author's opinion, since the attachment flows appear to be strong, and to suggest vorticity which is rotating in the same sense as the junction vortices.

The size of this attachment region appears to depend on the shape of the nacelle afterbody; the wider, more blunt-ended NACA nacelle (N-1) has significantly larger regions of disturbance, than does the more slender configuration (N-2). A schematic interpretation of the flow on the nacelle afterbodies is shown in Figure 25.

REYNOLDS NUMBER EFFECTS

The present tests were done at a fairly low Reynolds numbers, ranging from about 5000 in the water tunnel to 1.2×10^6 in the wind tunnel. The structure of the wing root junction flow contains not only primary vortices, but also secondary, and in some

instances, tertiary separations along the sides of the nacelle. This multiple vortex shedding tends to be a characteristic of three-dimensional protuberance flows at these low Reynolds numbers, but is found not to occur at the higher Reynolds numbers which correspond to full-scale flight. Thus in attempting to describe the staggering multiplicity of vortices which stream downwind of a wing-nacelle configuration, it should only be necessary to count the primary separations. The sketches in Figure 26 depict various combinations of vortices which should appear in cross flow planes downwind under different conditions of flight. If the upper surface flow is unseparated, with a normal leading edge, then a total of eight primary vortex cores stream from the junctions, and afterbody separations. If a LEX is installed, with vortices streaming from the swept edges, then additional vortices will appear above the wing bringing the vortex. If the propulsive streamtube also deforms and rolls up, as the wake survey's tend to suggest, then additional areas of vorticity will be present in the flow downwind.

EFFECTS OF A PROPELLER SLIPSTREAM

The effects of a propulsive streamtube, and slipstream rotation are shown in Figures 27 to 30.

The powered version of nacelle N-2 did not produce high thrust levels; the average value of the pressure rise behind the propeller corresponded to a total pressure coefficient $Cp_t = 1.1$. This did not result in large velocity increments, however, the slipstream rotation was quite large, and yawmeter measurements indicated a value of about 10 degrees at a radius corresponding to the maximum nacelle width.

Flow visualization indicated some of the changes caused by the slipstream. With LEX installed on nacelle N-2, at low model incidence ($\alpha = 4°$), the flow on the ventral surface was seen to reflect slipstream rotation, and the flow pattern on the wing upper surface was slightly skewed toward the downgoing (outer wing) blade side. At very high angles of attack, with separated flows over the wing surface, the slipstream tends to encourage a more symmetric flow formation that would otherwise occur. In the middle ranges of α there appeared to be no noticeable alteration in the flow patterns due to slipstream effects.

With a normal leading edge (no LEX) the slipstream rotation effects are present for angles of attack only greater than 16 degrees, in that the upper surface flow patterns were slightly skewed toward the outer wing.

A total pressure survey was also done behind the powered and unpowered versions of nacelle N-2 (LEX on), at mid chord, on the wing upper surface. At 16 degrees, (unpowered, Fig. 27(a)), just before stall, the isobars indicate the presence of two stable vortices, spaced 1/3 chord apart, and lying about 1/10 chord above the wing surface. At 20 degrees, well beyond $C_{L_{max}}$, the starboard or inner vortex has become incoherent with flow breakdown occurring over the wing (Fig. 27(c)).

Isobars for the powered nacelle, at angles of attack of 16 and 20 degrees are presented in Figure 27(b, and (d). Slipstream effects do not appear to produce any important changes in the appearance of the flow for these angles.

Further explorations of the nacelle-wing wake were made using five-hole yawmeters behind a more heavily loaded configuration. The model was similar in its proportions to nacelle N-2 although not of the same design. The test conditions were appropriate to a climb configuration, with a fairly high thrust coefficient, and flaps set at 15 degrees.

The measurement plane was three chords behind the aerodynamic centre, and the quantities shown in Figure 28 are sidewash and downwash angles, β_{sw}, α_{ow}, and total pressure H (Fig. 29).

Observations in the cross-flow plane showed that the propulsive streamtube of the propeller was grossly deformed by the mutual effects of the wing and the nacelle. In addition, as a result of viscous separation in the wing-body junction, and the roll-up of the propulsive streamtube, regions of concentrated vorticity were present in the flow.

The total pressure contours of Figure 29 trace out the configuration of the deformed slipstream, which in this case tends to form an "inverted T", a configuration which as been observed before (Ref. 22). The slipstream flowing over the top of the wing is evidently contracting, while that flowing over the bottom contains most of the really high pressure levels, and appears to be spreading laterally beyond the physical dimensions of the propeller.

It was difficult to identify precisely, any regions of vorticity, however, the downwash contours suggest vortex-like activity below the wing on the up-going blade side. The sense of rotation of the cross-flow appears to be clockwise, viewed from the rear, and is consistent with a vortex shed from the port wing body junction. Similarly, the sidewash angle contours indicate a similar type of rotation, also originating from the port side.

CONCLUSIONS

The aim of this paper has been to summarize some of the important problems in the integration of a wing and nacelle, for turbo-propeller aircraft, and to emphasize in particular, the viscous interations which occur.

The nacelle models were sized to represent current practice, and were mounted on a half-wing of aspect ratio approximately six. Balance measurements demonstrated the characteristic decrease of lift and increase in drag which occurs when an underslung nacelle is added to a wing. The addition of leading edge extensions (LEX) resulted in a slightly improved lift slope, higher $C_{L_{max}}$, and a gentle stall.

Flow visualization showed that steady three-dimensional separations with rolled-up vortex sheets played an important role in the development of good aerodynamic flow over the wing-nacelle configuration. These vortical flows occurred in three main regions of the nacelle; firstly at the wing-nacelle junction where a horse-shoe shaped separation line sweeps along the underwing junction, and over the top of the wing. A vortex sheet is shed from this line, and rolls up gradually along the length of the nacelle, bringing the oncoming fluid into the intersection. Secondary separations may also occur.

The second important region of three-dimensional separation and attachment lies aft of the wing trailing edge, on either side of the nacelle upper surface plane of symmetry. These flows consist of prominent regions of attachment bounded by streamwise separation lines which are shedding vortex sheets. Four trailing vortices are produced as a result of these separations. An accurate anatomy and origin of these separations is not understood at present.

The third important region of separation occurs at high angles of attack where the nacelle fore-body may separate and shed vorticity along the dorsal surface. These separation lines continue along the wing chord at low angles of attack, and begin to form the main vortex system which, at higher lift coefficients, keep the flow attached on the centre section and delays stall.

A leading edge extension, placed on the top of the nacelle at the wing leading edge modified the flow considerably. With this device fitted, the junction vortex, instead of being formed abruptly in the stagnation region between the wing and the nacelle, is now encouraged to separate more gradually along the streamwise edge of the LEX. The vortex sheet rolls up above the wing, producing downwash along the centreline, and increased lift. The separation lines, which had originated on the edges of the strake, continue across the chord to the trailing edge. The surface flow between them is not unlike that of a slender delta wing.

The effects of a propulsive flow on the wing-nacelle vortex characteristics were investigated by a flow survey using five-hole probes. This survey showed that the propeller slipstream was grossly deformed by the mutual effects of the wing and nacelle, and that as a result of separations in the wing-body junction, and roll up of the propeller streamtube, regions of concentrated vorticity were present in the flow.

REFERENCES

1. Smelt, R. et al — The Installation of an Engine Nacelle on a Wing, ARC R&M 2406, 1950.
2. Owen, E. Warden, R. Parkhurst, R.C. — Note on Wing-Nacelle Airscrew Interference, ARC R&M 2439, 1950.
3. Hoerner, S. — Aerodynamic Drag.
4. House, R.O. Wallace, A.R. — Wind Tunnel Investigation of the Effect of Interference on Lateral Stability Characteristics, etc. NACA Report 704, 1941.
5. Schlichting, H. — Report on the Special Field "Interference" to the Wind Tunnel Committee in February 1945, NACA TM 1347, May 1953.
6. Sandahl, C. Vollo, S. — Wind Tunnel Investigation of the Air Load Distribution on Two Combinations of Lifting Surfaces and Fuselage, NACA TN 1295, May 1947.
7. Wickens, R.H. — Observations of the Viscous Three-Dimensional Separations on Unpowered High-Wing Propeller Turbine Nacelle Models, NRC, NAE LTR-LA-258, February 1982.
8. McLellan, C. Cangelosi, J. — Effects of Nacelle Position on Wing-Nacelle Interference, NACA TN 1593, June 1948.
9. Becker, J. Leonard, L. — High-Speed Tests of a Model Twin-Engine Low Wing Transport Airplane, NACA R750, 1942.
10. Neely, R.H. Fairbanks, R.W. Conner, D.W. — Effects of Wing and Nacelle Modifications on the Drag and Wake Characteristics of a Bomber-Type Airplane Model, NACA ARR L5J05.
11. Johnston, F. Flawans, B. Danforth, E. — Flight Investigations of Factors Affecting the Carburetor Ram and Nacelle Drag of an A-26 Airplane, NACA MR L6F21.
12. Kayten, G. Koven, W. — Comparison of Wind-Tunnel and Flight Measurements fo Stability and Central Characteristics of a Douglas A-26 Airplane, NACA ARR L5H11a, March 1946.
13. Ashworth, C. — Pressure Distribution Measurements on Various Surfaces of a 0.2375-scale Model of the Douglas XA-26 Airplane in the 9-Foot Pressure Tunnel, NACA MR 90, October 1943.
14. Pepper, P. — Minimum Induced Drag in Wing-Fuselage Interference, NACA TN 812, September 1941.
15. Kuchemann, D. — Aerodynamic Design of Aircraft, Pergamon, 1978.
16. Weber, J. — Interference Problems on Wing-Fuselage Combinations, Part I – Lifting Unswept Wing Attached to Cylindrical Fuselage at Zero Incidence in Mid-Wing Position, ARC CP 1331.
17. Weber, J. Joyce, M. — Interference Problems on Wing-Fuselage Combinations, Part II – Symmetrical Unswept Wing at Zero Incidence Attached to a Cylindrical Fuselage at Zero Incidence in Mid-Wing Position, ARC CP 1332.
18. Templin, R.J. — A Momentum Rule for Aircraft Performance in the V/STOL Transition Regime, NRC, LR-470, January 1967.
19. Peake, D.J. Tobak, M. — Three-Dimensional Interactions and Vortical Flows with Emphasis on High Speeds, AGARD AG 252.

20. Maskell, E.C. Flow Separation in Three Dimensions, Report Aero 2565, November 1955.

21. *Young, A.D* Some Special Boundary Layer Problems, 20th Ludwig Prandtl Memorial Lecture, May 1977, ZFW Band 1, Heft 6, *November* 1977.

22. Wickens, R.H. The Aerodynamic Characteristics and Trailing Vortex Wake of Propeller V/STOL Configurations, Canadian *Aeronautics and Space Institute Journal, Vol. 21, No. 3, March 1975.*

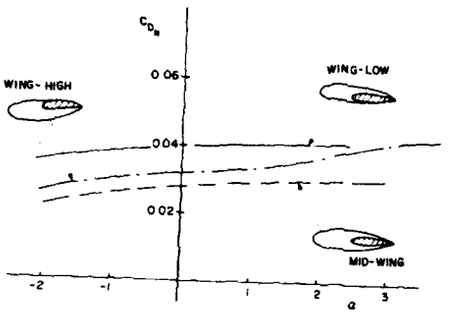

FIG 1 EFFECT OF NACELLE VERTICAL POSITION ON NACELLE DRAG (REF 9)

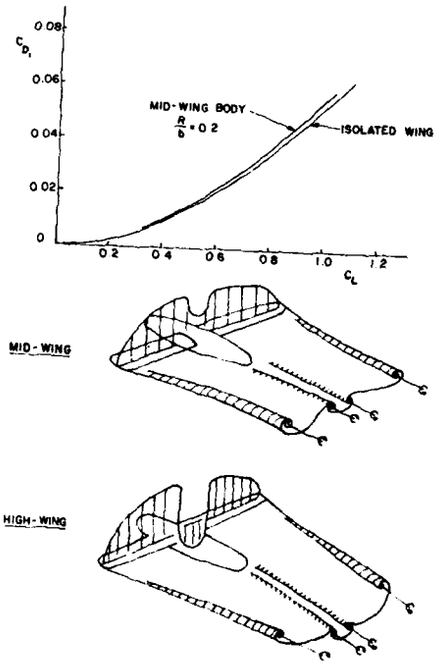

FIG 3 INDUCED DRAG AND LIFT DISTRIBUTION FOR WING BODY CONFIGURATIONS

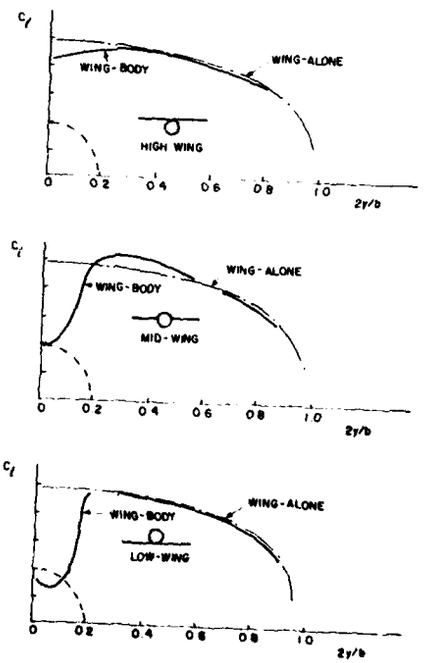

FIG 4 SPANWISE LOAD DISTRIBUTIONS OF WING BODY CONFIGURATIONS

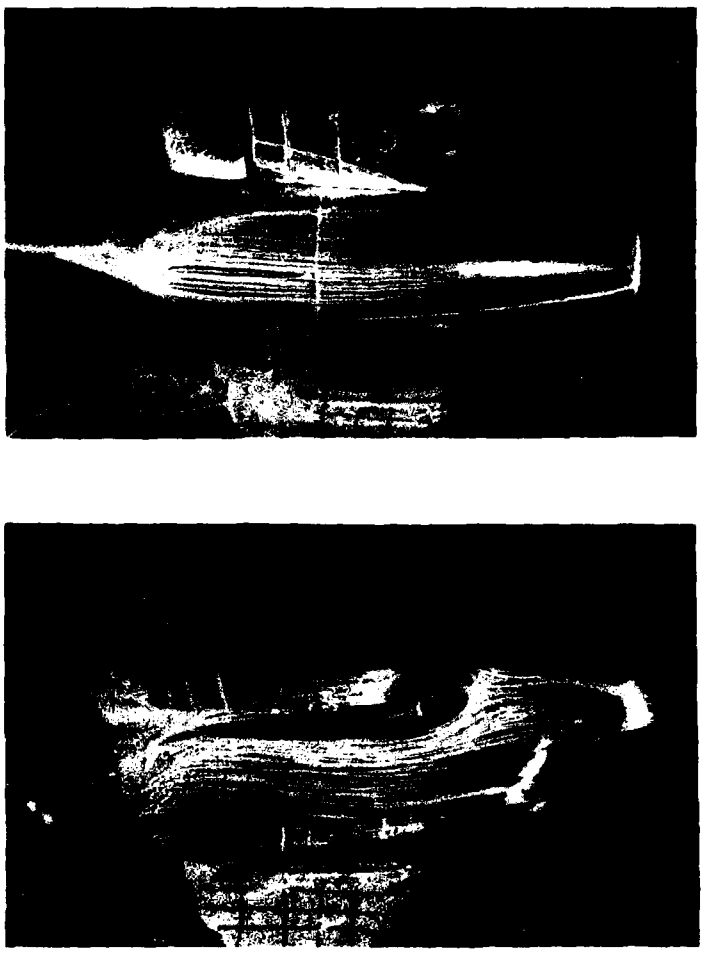

FIG. 2: TURBULENT SEPARATION IN EXPANDING CORNER – UNDERSLUNG NACELLES

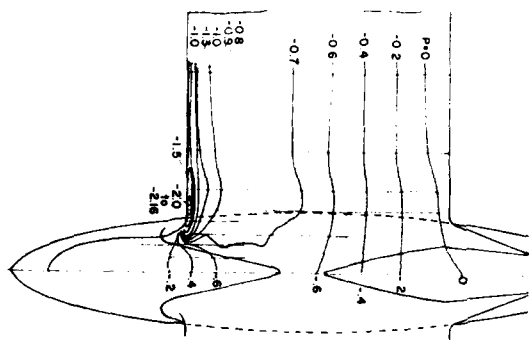

FIG. 5: ISOBARS ON WING UPPER SURFACE OF HIGH-WING MODEL, SHOWING SUCTION CONCENTRATION AT THE WING ROOT JUNCTION $\alpha = 2.5°$, M = 0.6 (REF. 8)

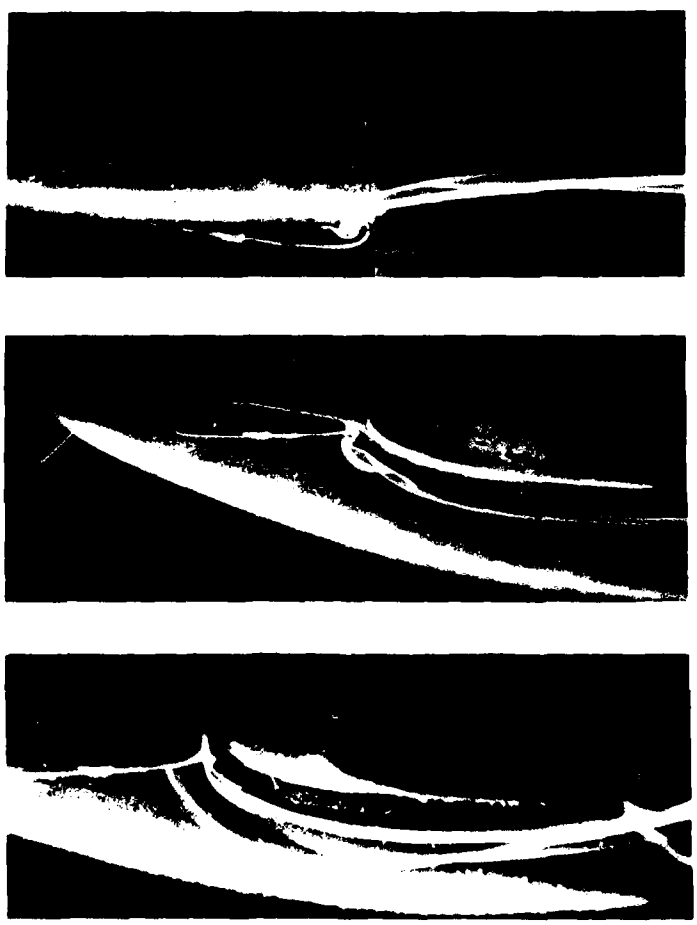

FIG. 6: VORTEX FLOWS IN THE WING ROOT JUNCTION

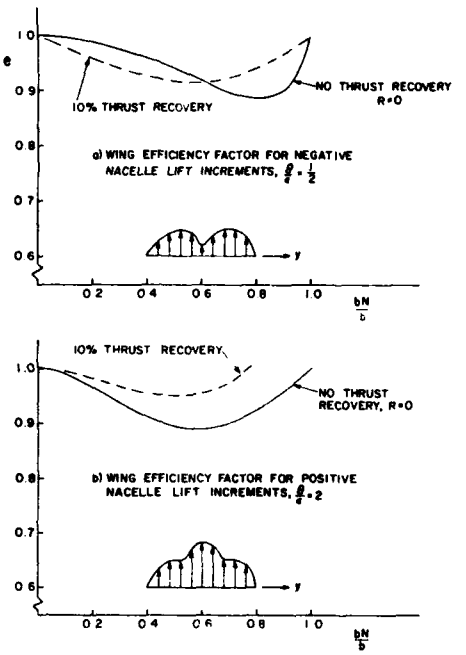

FIG. 7: WING EFFICIENCY FACTOR FOR POWERED LIFT AIRCRAFT

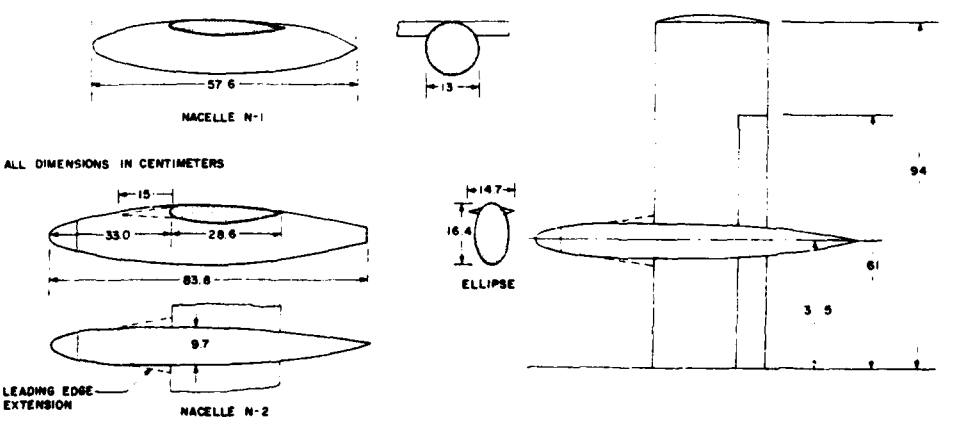

FIG. 8: GENERAL ARRANGEMENT OF HALF-MODEL CONFIGURATION

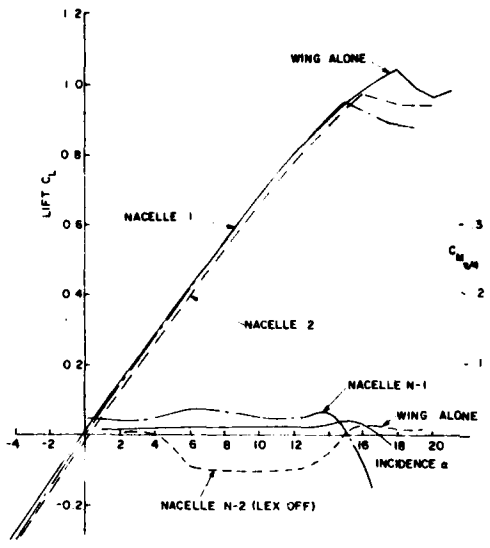

FIG. 9(a): LIFT AND MOMENT CHARACTERISTICS UNPOWERED WING NACELLE MODELS

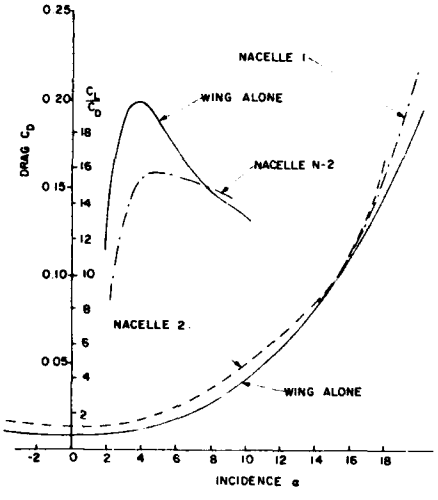

FIG. 9(b): DRAG AND L/D FOR UNPOWERED WING NACELLE MODELS

FIG. 9 LIFT AND MOMENT CHARACTERISTICS UNPOWERED WING-NACELLE MODELS

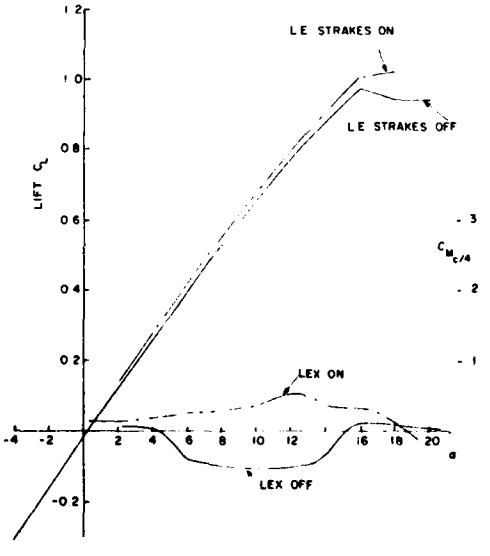

FIG. 10(a): EFFECT OF LEADING EDGE EXTENSIONS ON LIFT AND MOMENT – NACELLE 2

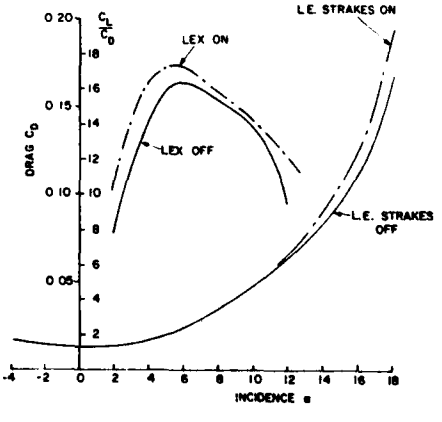

FIG. 10(b): EFFECT OF LEADING EDGE EXTENSIONS ON DRAG AND L/D

FIG. 10 EFFECT OF LEADING EDGE EXTENSIONS ON LIFT AND MOMENT – NACELLE 2

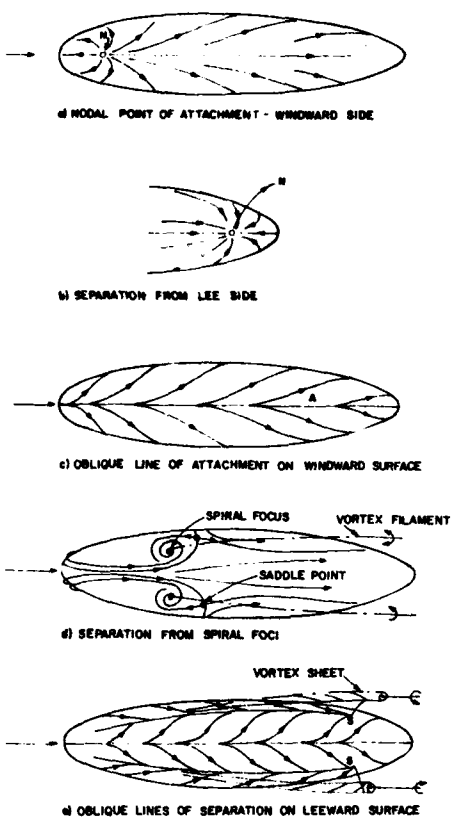

FIG. 11: CLASSIFICATION OF VISCOUS FLOWS

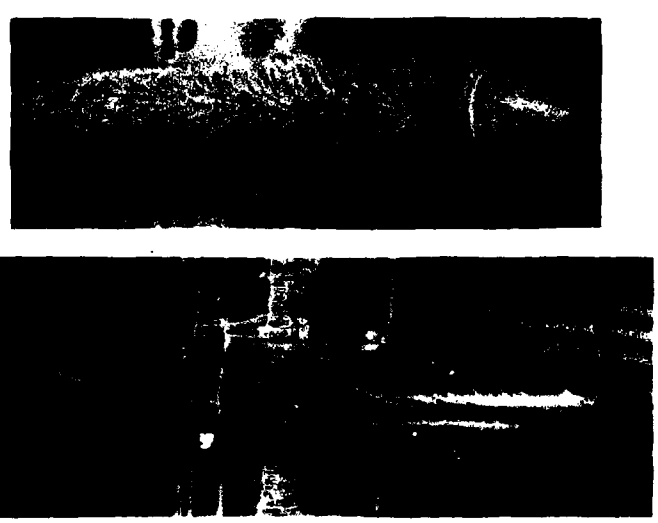

FIG. 12: ATTACHMENT FLOWS ON NACELLE N-2 FOREBODY – $\alpha = 20°$

a) N-2 $\alpha = 0$

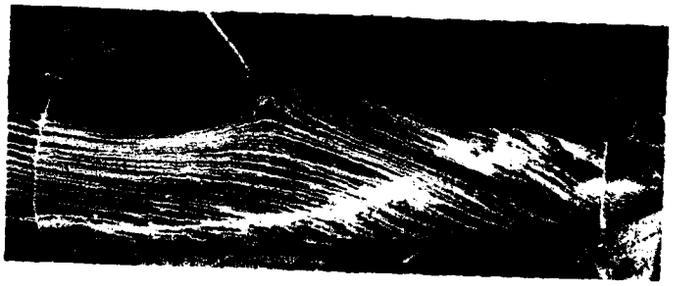

b) N-2 $\alpha = 8°$

c) N-2 $\alpha = 16°$

d) N-1 $\alpha = 16°$

FIG. 13: SEPARATION AND ATTACHMENT IN THE WING-ROOT JUNCTION – NO LEADING EDGE EXTENSION

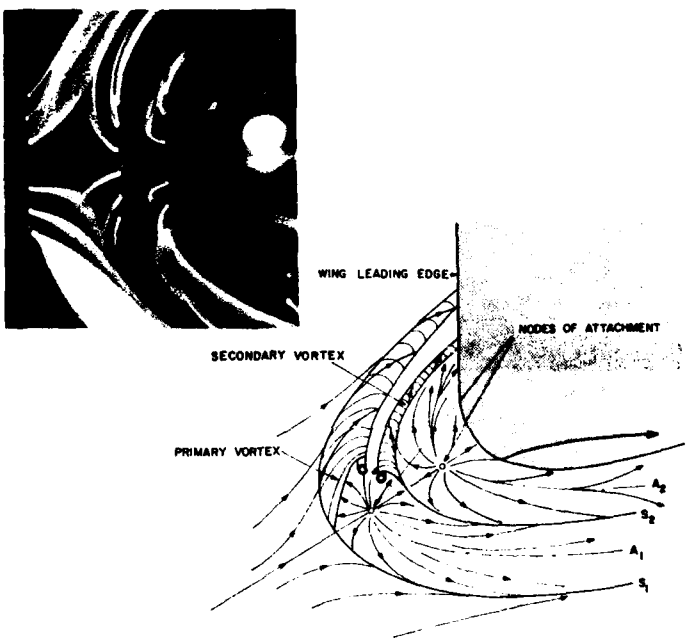

FIG. 14: FLOW IN THE WING-BODY JUNCTION – NO LEADING EDGE EXTENSION

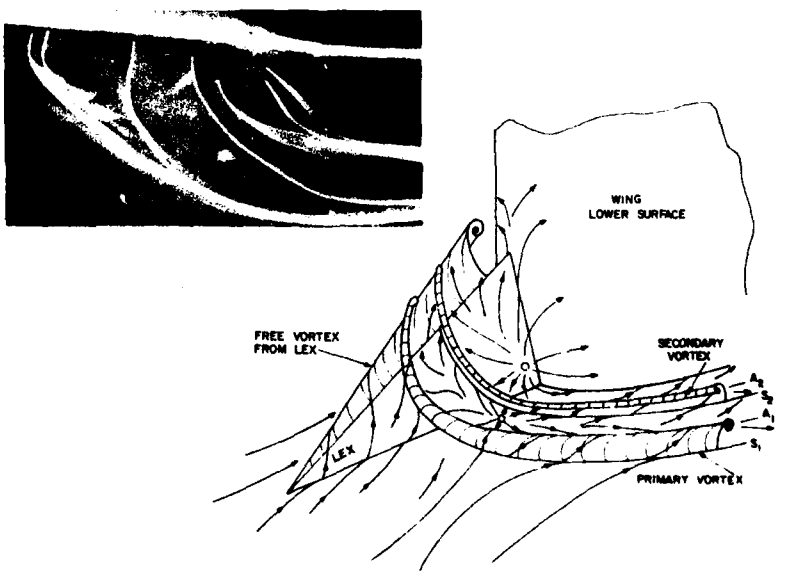

FIG. 16: VISCOUS VORTEX SEPARATION ON WINDWARD SURFACE OF LEADING EDGE EXTENSION

a) N-2 α = 8°

b) N-2 α = 8°

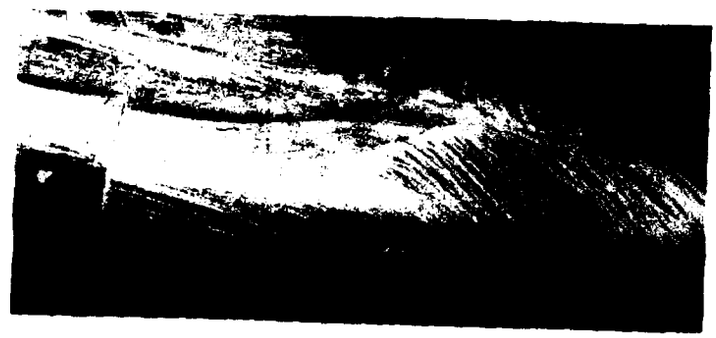

c) N-2 α = 16°

FIG. 15: SEPARATION AND ATTACHMENT IN THE WING-ROOT JUNCTION – WITH LEADING EDGE EXTENSION

FIG. 17(a): UNDER-WING VORTEX SHED FROM SPIRAL FOCUS IN WING-ROOT JUNCTION

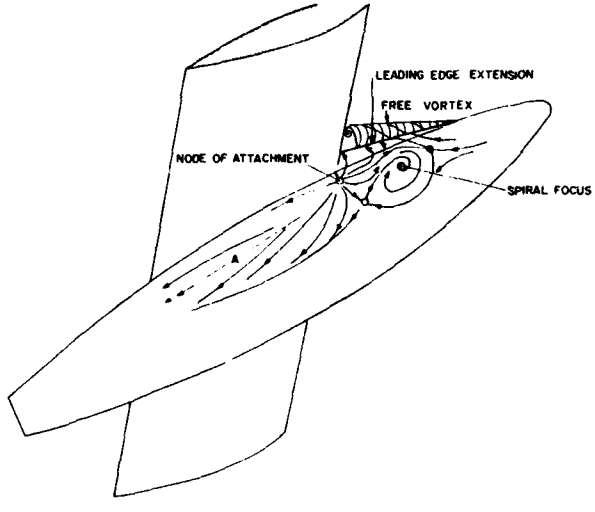

FIG. 17(b): JUNCTION FLOW WITH LEADING EDGE EXTENSION – VORTEX FILAMENT ISSUING FROM SPIRAL FOCUS

FIG. 18(a): FLOW ON NACELLE UPPER SURFACE – NO LEADING EDGE EXTENSION, NACELLE N-1, $\alpha = 16°$

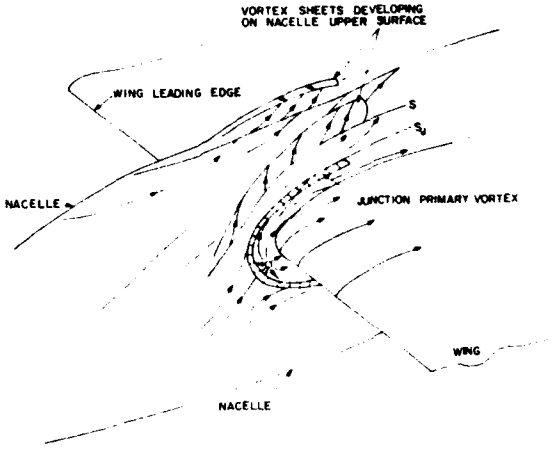

FIG. 18(b): DEVELOPMENT OF THREE-DIMENSIONAL VORTEX SHEETS ON NACELLE UPPER SURFACE AT ANGLES BELOW STALL – NO LEADING EDGE EXTENSION

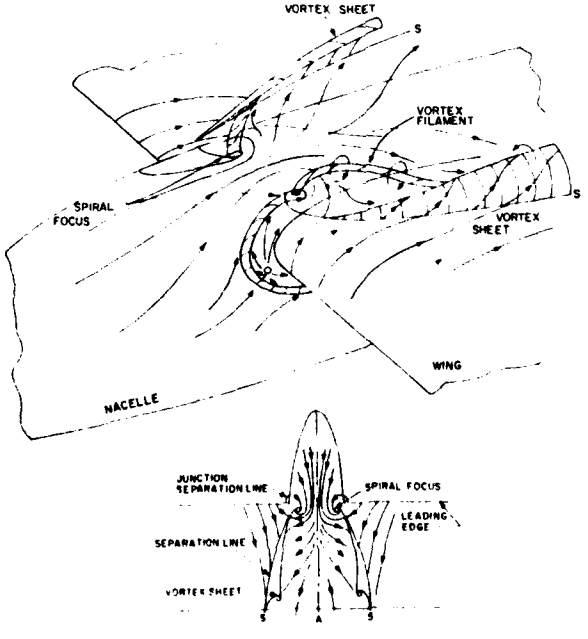

FIG. 20: DEVELOPMENT OF WING UPPER SURFACE VORTEX FLOWS – NO LEADING EDGE EXTENSION

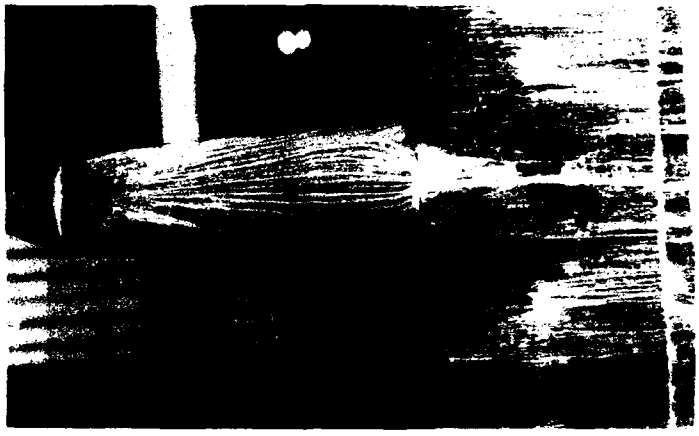

a) $\alpha = 0°$

b) $\alpha = 20°$

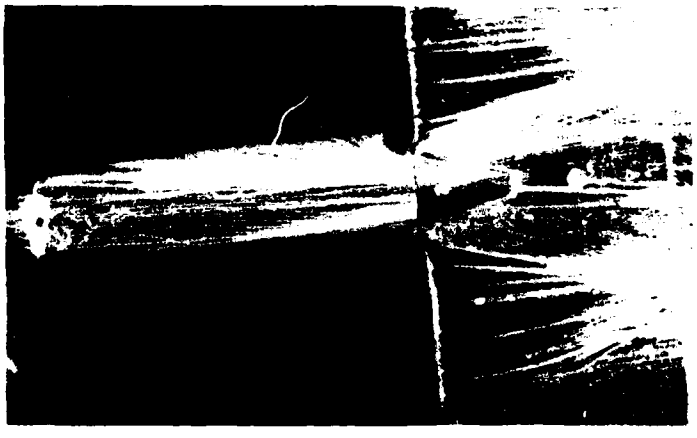

c) $\alpha = 16°$

FIG. 19: WING UPPER SURFACE FLOW – NO LEADING EDGE EXTENSION

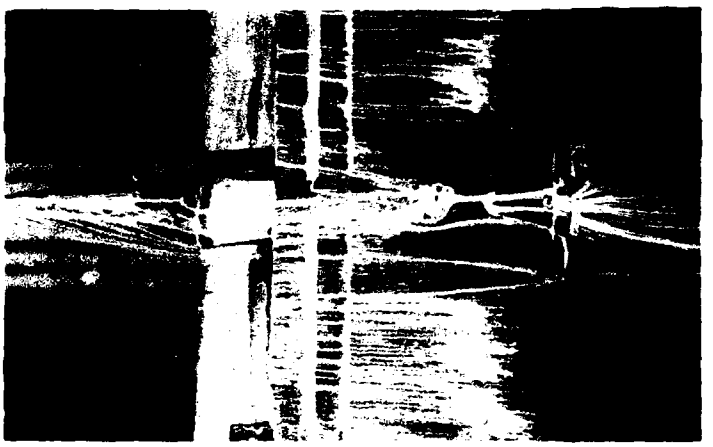

a) $\alpha = 0$ NACELLE N-2

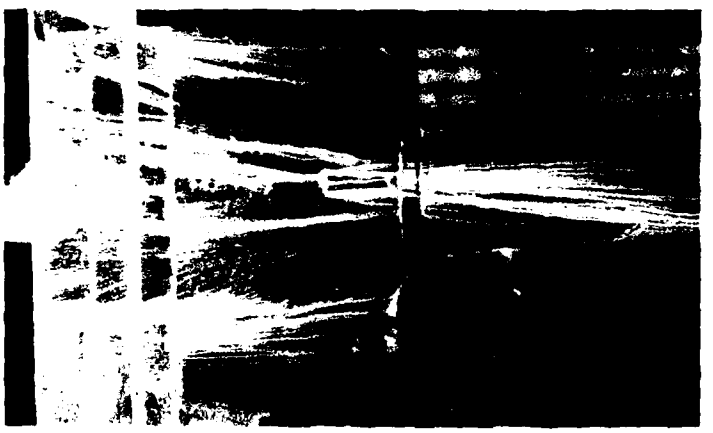

b) $\alpha = 8°$ NACELLE N-2

c) $\alpha = 16°$ NACELLE N-2

FIG. 21: FLOW ON THE WING UPPER SURFACE – LEADING EDGE EXTENSION ON

AD A135 157 AERODYNAMICS OF VORTICAL TYPE FLOWS IN THREE DIMENSIONS: CONFERENCE PROCE..(U) ADVISORY GROUP FOR AEROSPACE RESEARCH AND DEVELOPMENT NEUILLY.. JUL 83

UNCLASSIFIED AGARD-CP-342 F/G 20/4 4/6 NL

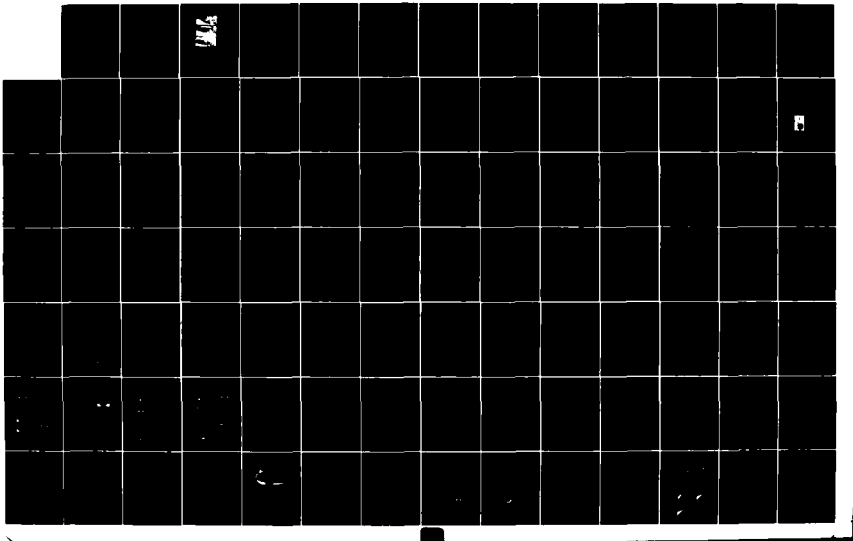

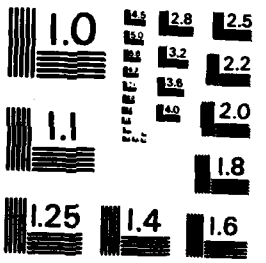

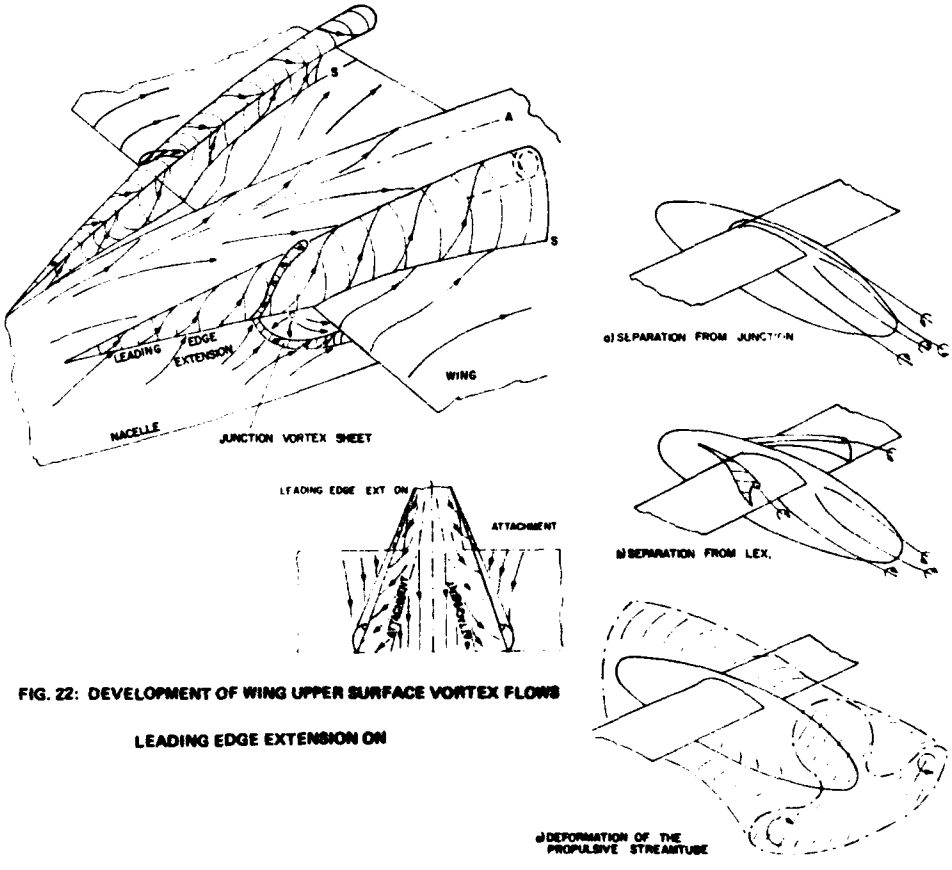

FIG. 22: DEVELOPMENT OF WING UPPER SURFACE VORTEX FLOWS

LEADING EDGE EXTENSION ON

FIG. 26: WAKE-VORTEX SYSTEMS FOR WING-NACELLE CONFIGURATIONS

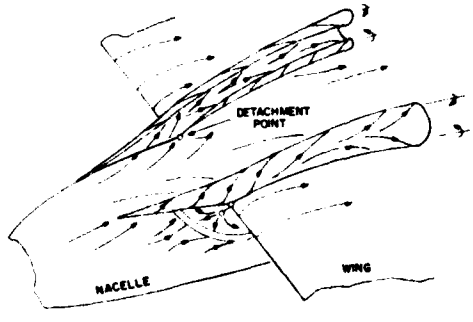

FIG. 23: DETACHMENT OF WING VORTEX SHEETS WITH FORMATION OF DOUBLE-BRANCHED CORES – LEADING EDGE EXTENSION ON

a) NACELLE N-1 $\alpha = 8°$

b) NACELLE N-2 $\alpha = 0°$

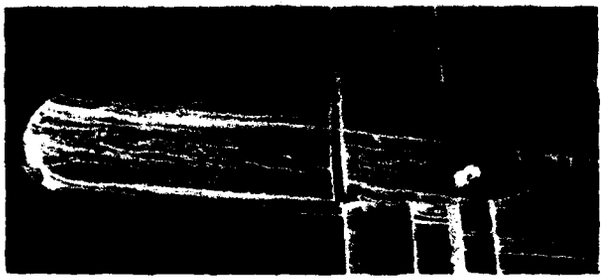

c) SEPARATION FROM
LINE OF CONFLUENCE $\alpha = 0°$

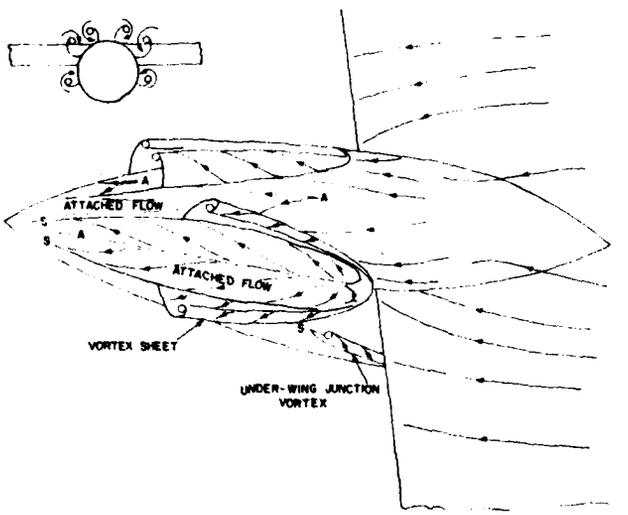

FIG. 24 SEPARATION AND ATTACHMENT FROM NACELLE AFTERBODIES

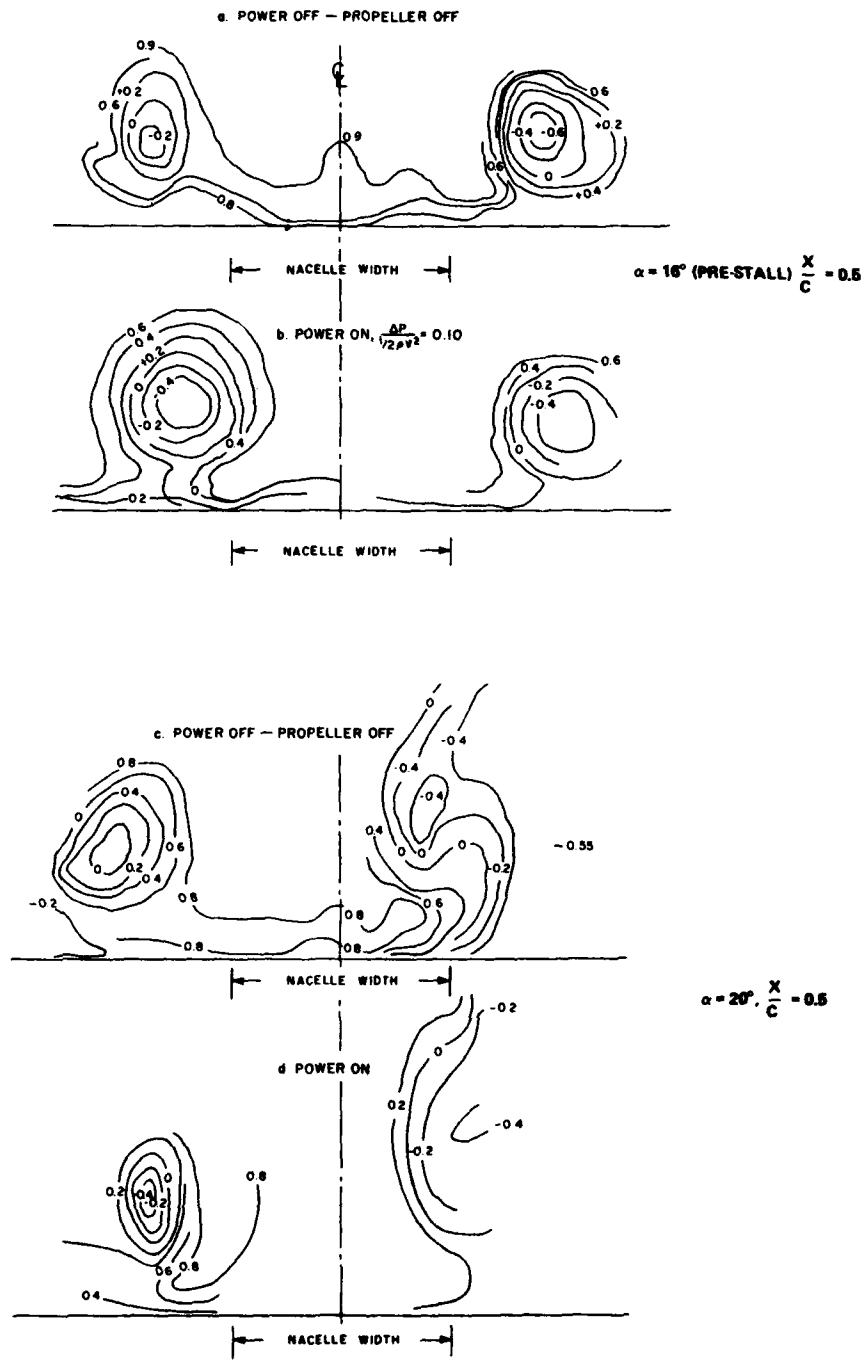

FIG. 27: TOTAL PRESSURE SURVEY C_{p_T} ON WING UPPER SURFACE NACELLE N-2 (LEX ON)

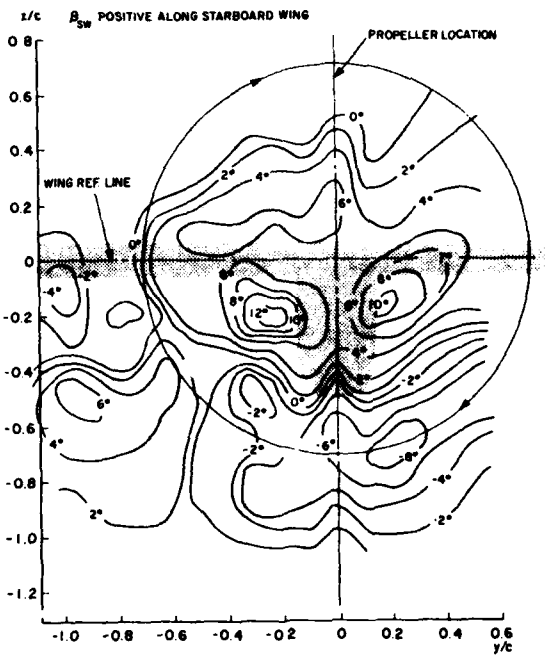

FIG. 28(a): SIDEWASH ANGLE DOWNWIND OF QUASI-2-D POWERED WING-NACELLE MODEL

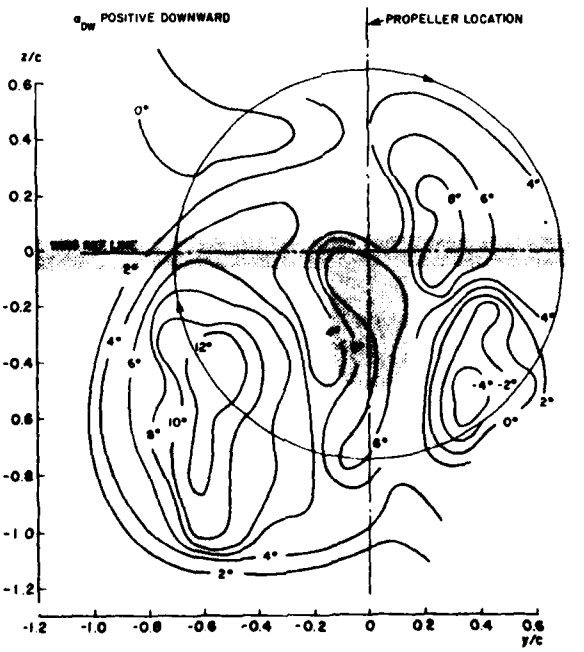

FIG. 28(b): DOWNWASH ANGLE DOWNWIND OF QUASI-2-D POWERED WING-NACELLE MODEL

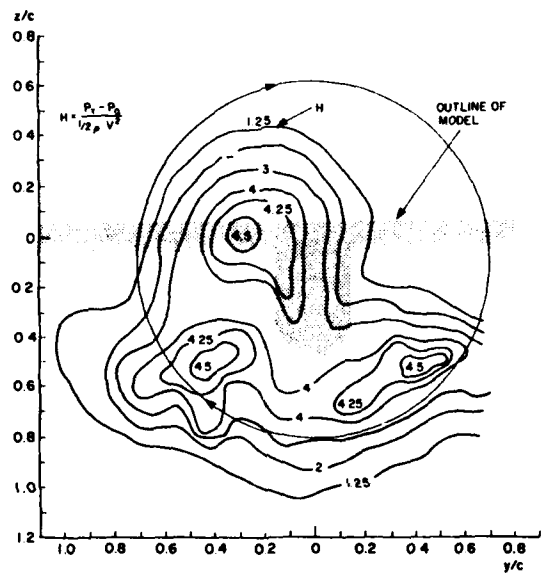

FIG. 29: TOTAL PRESSURE H, DOWNWIND OF QUASI-2-D POWERED WING-NACELLE MODEL

THEORETICAL MODELLING OF THREE-DIMENSIONAL VORTEX FLOWS IN AERODYNAMICS

by

J. H. B. Smith
Aerodynamics Department,
Royal Aircraft Establishment,
Farnborough, Hampshire, UK

SUMMARY

A unified account is presented of the various inviscid models used to represent three-dimensional vortex flows in aerodynamics; essentially those relying on vortex sheets and line-vortices. Recent developments in extending the scope, accuracy, and stability of these models are described. An evaluation of their relative strengths and weaknesses suggests that the different models all have continuing roles to play. It is claimed that vortex modelling has come of age, in the sense that we can now learn about the real world from the behaviour of models, after decades of trying to make the models conform with reality.

1 INTRODUCTION

To set the sort of model to be discussed in perspective, it is helpful to recall the usual hierarchy of flow models, together with the assumptions about the fluid and the flow which give rise to them. The first model, the Navier-Stokes equations, depends on assumptions about the nature of the fluid. Flow at large Reynolds numbers involves turbulence, and the mean motion is then modelled by the time-averaged Navier-Stokes equations, involving Reynolds stress terms. To represent these Reynolds stresses in terms of the mean motion and its history, one or more turbulence models are required. In the flow of a uniform stream past a body at a large Reynolds number, both turbulent motion and the large shears which make molecular viscosity important are confined to thin boundary layers on the body and to the wake which arises from the separation of these boundary layers from the surface of the body. Outside the boundary layers and wake the flow behaves as if the fluid were inviscid.

For most flows of importance to aerodynamics, the wakes are thin, in the sense that their thickness reduces as Reynolds number increases. The effects of turbulence and viscosity can then be modelled by the theory of thin shear layers, provided there is an appropriate model for the interaction between the external flow and the thin shear layers. A thin shear layer affects the external flow in two ways: through a displacement effect, requiring a difference in normal velocity between its opposite surfaces; and through a vortex effect, requiring a difference in tangential velocity between its opposite surfaces. As the Reynolds number tends to infinity, the displacement effect dies away, but the vortex effect remains. The shear layers become vortex sheets in the limit. This leads to an inviscid model of the flow, which is governed by the Euler equations. However, in general, the formulation of the problem for the Euler equations must include a specification of the lines on the body from which the vortex sheets arise, the separation lines.

A symmetrical wing at zero incidence sheds no vortex wake, so it is not necessary to specify a separation line. When the wing is placed at incidence the assumption that separation takes place from the sharp trailing-edge is automatically made. In reality, separation also takes place from the tip, spreading forward from the trailing-edge as the angle of incidence increases, at a rate depending on the design of the tip. For a wing with a highly-swept sharp leading-edge, a similar separation takes place from the leading edge.

We may expect that, for most bodies of practical interest to aerodynamicists, the limit of the real flow as the Reynolds number tends to infinity will be an inviscid flow with embedded vortex sheets. In this limit, it seems likely that the positions of the separation lines are determined, though not necessarily uniquely. The same flow representation may also be used as a model of the flow at large, but finite, Reynolds numbers, though then the positions of the separation lines must be supplied to the model from outside it. The assumptions leading to this model are, first, large Reynolds number and, second, the sort of thin wake flow which is naturally associated with aerodynamically efficient shapes.

For shock-free flows past bodies immersed in a uniform stream, the inviscid flow can be represented by a potential function, and the same representation can be extended to model flows with weak shock waves. From this point, at which the flow is described by a potential function everywhere outside the body and outside the vortex sheets, the various treatments to be discussed in this paper diverge. To order the discussion, we reserve the word 'model' to describe an approximation to the vortex sheet, and introduce the word 'framework' to describe a treatment of the potential flow in which the vortex sheet is embedded. Then the models of the vortex sheet to be considered are the classical rigid-wake model of a trailing vortex sheet, the Mangler-Smith model[1] for a rolled-up core, the multiple line-vortex model, and the single line-vortex model. The possible frameworks are the full nonlinear potential formulation, the nonlinear transonic small

perturbation approximation, the linear small perturbation (Prandtl-Glauert) approximations for subsonic and supersonic flows, and the slender-body approximation. To illustrate the independent aspects of model and framework, a two-dimensional presentation is useful:

Framework \ Model	Rigid wake	Rolled-up core	Multiple line-vortex	Single line-vortex
Full potential	Jameson			
TSP	Albone			
P - G, M < 1	Multhopp	F.T. Johnson, *et al*[2]	Rehbach[3]	Nangia and Hancock[4]
P - G, M > 1	D. Cohen			
Slender-body	R.T. Jones	Mangler and Smith[1]	Sacks, *et al*[5]	Brown and Michael[6]

In this table the names have been introduced for illustrative purposes only. The classical rigid-wake model has, of course, been used in all the frameworks; but the other vortex models have only been used to a significant extent in the subsonic Prandtl-Glauert framework, which includes the important special case of incompressible flow, and the slender-body framework.

A further point is worth clarifying at this stage, even though it is of greater significance for Dr Hoeijmaker's paper[7] which follows. This concerns the mathematical nature of the problems to which the various frameworks give rise, and how these can be modified by particular geometries. The discussion is restricted to steady flow. To illustrate the point, consider a purely supersonic flow and ignore the complexities of the vortex models. Both the full potential and the supersonic Prandtl-Glauert frameworks lead to hyperbolic problems. However, for the flow past a conical shape, the problem can be reformulated in conical variables, yielding an equation in only two variables which changes type from elliptic near the free-stream direction to hyperbolic at a large inclination to it. The presence of vortex sheets of conical form does not change the type of the problem in this case, though of course the presence of boundaries of unspecified shape does make it more complex. In the slender-body framework, the solution splits into an axial flow perturbation depending only on the distribution of cross-sectional area, and a cross-flow perturbation. The problem for the cross-flow is governed by Laplace's equation and is therefore always elliptic. Without the complication of the vortex sheets, each of the two-dimensional cross-flow problems is independent of the others and can be solved in isolation. With vortex sheets each cross-flow problem depends on the solution upstream. In this respect the problem takes on a quasi-parabolic character, with the streamwise coupling represented by ordinary, rather than partial, differential equations, because the circulation is concentrated in sheets, not diffused as vorticity. In the particular case of a conical body shape, for which a conical vortex configuration is sought, the quasi-parabolic behaviour is eliminated. A single elliptic problem with unknown boundaries then emerges. The other effect of introducing a vortex representation which goes beyond the rigid planar wake is to introduce an essential nonlinearity into the problem. The governing differential equations for the Prandtl-Glauert and slender-body frameworks are linear, but the condition of continuity of pressure across a vortex sheet is nonlinear.

In view of the large amount of work in this field using the slender-body framework, it is worth recalling the relationship between it and the theory of incompressible two-dimensional flow. There is an exact correspondence between the cross-flow component of a slender-body solution and an unsteady two-dimensional flow in which the body is growing, moving, and deforming in time in the same way as the cross-section of the three-dimensional body is changing in the streamwise direction. When vortex sheets are present, the separation lines must also be specified in the same way. There is no direct relationship between the viscous effects in the two- and three-dimensional flows. A consequence of this correspondence is that the classical treatment of the roll-up of a three-dimensional wake, treating it as a time-dependent problem, is just a slender-body approximation to the three-dimensional flow.

2 MODELS OF VORTEX SHEETS

The flat wake behind an elliptically-loaded wing is in equilibrium, in the classical treatment just referred to. The equilibrium is unstable, but even the existence of a simple equilibrium configuration makes this an exceptional case. In general, the equilibrium shape of a vortex sheet involves the rolling up of its free edges into a spiral form, the spiral containing an infinitely large number of turns about its axis. We shall be concerned with the representation of such spiral sheets. For a conventional, tail-aft, configuration, the rolling up of the vortex wake is of relatively little importance to the aircraft itself (though it may be very significant for a lighter, following aircraft) because it takes place well downstream of the wing and well outboard of the tail. Rolling up is of greater importance for a canard lay-out and is a dominant feature of flows involving leading-edge separation from strakes and delta wings. It is also becoming clear that the behaviour of rolled-up vortex sheets can explain many aspects of the aerodynamics of the noses of aircraft and missiles at large angles of attack.

To represent an infinite spiral in a numerical calculation would present considerable difficulties. The simplest way out is that adopted by Mangler and Smith[1]. It is simply to represent the inner turns of the vortex sheet by a single line-vortex, at least as far as the effects of the inner turns on the rest of the flow field are concerned. A few turns on the outside of the spiral can then be represented explicitly in a numerical treatment. An essential feature of flows of this kind is that circulation* is being convected along the sheet. Some simplified representation is therefore needed of the convection of circulation from the free edge of the outer part of the sheet to the line-vortex representing its core. In the existing model, used both in the slender-body and the subsonic Prandtl-Glauert frameworks, this convection process is represented as occurring entirely in the cross-flow plane, which is not very different from a plane normal to the line-vortex. As a result, a discontinuity of pressure appears across the cut connecting the free edge of the sheet to the vortex, a discontinuity whose magnitude depends on the streamwise coordinate only. To obtain a force-free system, the force which arises from this pressure difference in each cross-flow plane is balanced by the local force on the line-vortex which arises from its inclination to the local flow direction. Since the force arising from the pressure difference scales on the product of the circulation of the line-vortex and its distance from the free edge of the sheet, it will tend to zero as the extent of the properly-modelled outer part of the sheet increases. In fact, for most purposes, it is enough to include explicitly about half a turn of the sheet on a delta wing[8].

Because this model has often been applied to flows which are conical, it is often thought of as being restricted to conical flows. In fact it has been used for non-conical flows in the frameworks of slender-body theory[9,10] and of the fuller Prandtl-Glauert treatment for subsonic flow[2,11]. The boundary conditions to be applied on the properly-represented outer part of the sheet are that the pressure is continuous across the sheet and that the sheet forms part of a three-dimensional stream surface. These are exactly equivalent to the requirement that the circulation is convected with the mean of the velocity vectors on the two sides of the sheet. An additional Kutta condition is usually needed at the separation line. For flows without lateral symmetry it is also necessary to fix the overall circulation about the cross-section of the configuration to be zero; a condition which follows from the application of Kelvin's theorem to a closed contour which is convected from upstream to surround the configuration.

This model, implemented in the slender-body framework, has been shown to give a useful qualitative picture of the effects of planform, thickness, cross-sectional and lengthwise camber, side-slip, roll, and oscillations in pitch and heave for simple flows over sharp-edged wings, involving only a single pair of leading-edge vortices. It has also been implemented, with much greater difficulty, in the subsonic Prandtl-Glauert framework; and has been shown to give reliable quantitative predictions of lift, pitching moment and pressure distribution. For a discussion of these results and more complete lists of references, see previous reviews[8,12]. For these simple flows, the major weaknesses arise from the absence of any representation of secondary separation or vortex breakdown.

An important special case of this vortex-sheet model, which significantly pre-dates it, is obtained by omitting the explicit representation of the outer turns of the spiral sheet, so that the cut extends from the line-vortex to its associated separation line. This was used by Brown and Michael[6], following earlier work by Legendre[13]. The same model was applied to represent vortices shed from inclined cones and cylinders by Bryson[14], still within the framework of slender-body theory, and it has also been implemented in the subsonic Prandtl-Glauert framework[4,15]. It will be referred to as the (single) line-vortex model. Again it is not confined to conical flow, though the curvature of the line-vortex then presents a mathematical difficulty.

The self-induced velocity of a curved line-vortex is infinite and directed normal to itself. This is obviously non-physical and indicates that the model is over-simplified. The same difficulty arises with the core representation in the vortex-sheet model. It can be resolved by considering the vortex core to have a finite cross-sectional area, based on the geometry in the cross-flow plane, and a continuous distribution of vorticity, based on one of the asymptotic solutions[1,16-18] for the inner part of a vortex. The self-induced velocity is then finite, and can be calculated[19], and could, in principle, be included in the model. In the slender-body framework the self-induced velocity is of the same order as other neglected quantities and there is no mathematical reason to include it.

Another omitted effect in the representation of the whole or part of the spiral sheet by a line-vortex is that of the circumferential component of the vorticity vector. This component has the effect of accelerating the flow along the axis of the vortex, often very appreciably, producing an associated inflow as required by continuity. It is possible to represent the effect of this inflow on the outer flow by combining a line-sink with the line-vortex. This approach has been discussed by Hoeijmakers[20] and Verhaagen[21], but it is necessary to take considerable care over the definition of

---

* The term 'circulation' is here used in a slight extension of its usual meaning. Conventionally, circulation is a property of a closed contour. However, in a potential flow with embedded vortex sheets, the circulation about all closed contours which intersect one sheet only, and that sheet at one and the same point, is the same, so that it can be regarded as a local property of the sheet. It is just the jump in potential across the sheet. It seems better to extend the use of 'circulation' in this way rather than use 'vorticity' in senses which may be confusing.

entrainment if their results are to be interpreted correctly. It again appears that, in the slender-body framework, the strength of the line-sinks is of the same order as the other neglected quantities.

In view of these complexities, it is not surprising that other, apparently more straightforward, approaches have been made to the modelling of the infinitely rolled-up sheet. The most popular of these is the representation of the sheet by a large number of line-vortices. The basis of this may be seen by drawing on the sheet a family of spiral curves which are lines of constant circulation, or constant jump in potential. As mentioned above, these will also be streamlines of the mean flow. The spiral curves cut the sheet into ribbons, and, if the circulation in each ribbon is condensed into a line-vortex, a multiple line-vortex model is obtained. The condition to be satisfied is simply that each line-vortex should be aligned with the local flow direction along the whole of its length.

The question of the self-induced velocity of the curved line-vortex arises again. This time the line-vortex represents, not a core of finite area, but a ribbon of the sheet, and a different approach is needed. Since a plane element of sheet has no self-induced velocity, no local contribution from the ribbon is required. A plausible procedure would be to omit from the range of Biot-Savart integral for the self-induced velocity of a line-vortex at a point P an interval surrounding P of the same length as the distance between the adjacent line-vortices. In the published calculations using this multi-vortex model, the curved line-vortices are replaced by segments of straight lines. The velocity is either calculated at the mid-point of the segment, where it is finite, or at the end, where it is presumably necessary to neglect the infinite contributions of the two segments which meet there.

The multi-vortex model is most naturally used to describe separation from the edge of a wing which is also represented by a set of line-vortices, as in a vortex-lattice or vortex-ring model of the wing. The Kutta condition is then just that the vortices run off the edge into the sheet, with continuity of circulation. If the wing is represented by a continuous load distribution, as in slender-body theory, for instance, there is some arbitrariness about where the vortices representing the sheet are to be introduced, and a similar difficulty arises in modelling separation from a smooth surface. This arbitrariness affects the circulation of the vortices through the Kutta condition.

There are three basic difficulties which affect calculations with the multi-vortex model, though the last only arises in the slender-body framework. The first is that a large number of line-vortices are needed to obtain an accurate solution. The evidence for this comes from the calculations by Sacks, *et al*[5] in the slender-body framework, where they were able to use a large number of vortices. A slight generalization of their estimate of the number of vortices needed for a converged solution is:

$$30 + 300A/\alpha \quad , \tag{1}$$

where A is the aspect ratio and α is the angle of incidence in degrees. The largest value of A/α covered in their calculations is 0.2. There seems no reason why fewer vortices would be needed in another framework.

The second difficulty concerns the shape of the line-vortices. These should follow the streamlines and these, as we know from many visualization experiments, are helices, with the pitch of the helix becoming smaller the nearer the streamline lies to the axis of the vortex. It follows that a line-vortex starting near the apex of a delta wing should follow a helix of very small pitch, and such a helix requires very many elements to describe it with any realism. The more vortices are introduced, to meet the first difficulty, the closer to the apex the first starts, so increasing the second difficulty. The solution must be to represent the inner part of the sheet separately, probably by a line-vortex of growing circulation, as in the vortex-sheet model.

In the slender-body framework, a third difficulty arises because of the quasi-parabolic nature of the problem referred to above. The shapes of the line-vortices are found by integrating ordinary differential equations in the streamwise direction. As a result of the basic instability of this process and of the close approach of neighbouring vortices, the shapes of the vortices become chaotic, as Sacks, *et al* found[5]. This situation has since been studied in the exactly analogous planar unsteady problem, where the onset of chaos has been postponed in two ways. Moore[22] has used an explicit core representation, as suggested above for other reasons; and Fink and Soh[23] have redistributed the vortices along the sheet at the end of each time step. Recent work[24] with a multi-vortex formulation which overcomes some of these difficulties will be described later.

3 RECENT DEVELOPMENTS IN THE MODELS

Four recent developments will be outlined. Two of these relate to the adaptation of models generally applied to separation from salient edges to the representation of separation from smooth surfaces; and two arise from the need to represent more complicated flow patterns than those on a delta wing.

Let us consider first the extension of the vortex-sheet model to describe separation from smooth surfaces, as reported by Fiddes[25] for the case of the slender elliptic cone at incidence. The first point to realize is that the sheet must leave the surface tangentially[26]. There are then two possible types of behaviour of the flow normal to the separation line[26,27]. With the downstream side of the separation line defined as the side

towards which the vortex sheet departs, these behaviours are: either the vortex sheet has infinite curvature and the pressure gradient upstream of the separation line is infinitely adverse; or both the sheet curvature and the upstream pressure gradient are finite. The form of the singularity in both the curvature and pressure gradient is the inverse square root of the distance from the separation line. To represent this behaviour in a calculation is not trivial, and the problem has been attempted so far only in the slender-body framework. Clearly, curved elements, or panels, are needed to represent the sheet, and the base element apparently needs infinite curvature at one end. An ingenious use of conformal mappings[25,28] avoids the need for such a special element, and an existing form[1] can be used.

From the point of view of the inviscid modelling, the outstanding question concerns the Kutta condition. Since all the velocities are finite in the attached flow, and the pressure is continuous everywhere, it is not clear that any further condition is required. However, a further condition on the numerical solution is useful. In the exact inviscid solution, the fact that both the body surface and the vortex sheet are stream surfaces implies that the velocity vector on the surface on the downstream side of the separation line must be parallel to the separation line. This will not naturally emerge from a numerical solution, in which the stream surface condition is enforced by setting the normal component of the velocity to zero. It is therefore helpful to require, as a form of Kutta condition, that the surface velocity is along the separation line on its downstream side.

From the point of view of modelling the real viscous flow, the outstanding question is the determination of the separation line. For boundary layers which are laminar upstream of separation, Fiddes describes an approach which is both rational mathematically, and reasonably successful in reproducing the observations on circular cones. The approach rests on the asymptotic theory of laminar separation for large Reynolds number which was put forward by Sychev[29] and completed by F.T. Smith[30]. The essential points are: (i) at infinite Reynolds number, separation must be smooth, *ie* the singular behaviour in sheet curvature and upstream pressure must not occur; (ii) at finite Reynolds number, the separation line is displaced downstream from the position of smooth separation until there is a balance between the strength of the singular behaviour and the level of skin friction upstream of separation.

The use of this approach, with the vortex sheet model and a laminar boundary layer calculation, makes it possible to calculate the position of the separation line as a function of Reynolds number. Fig 1 shows how the predicted movement of the separation line with Reynolds number compares with that observed by Rainbird, *et al*[31] in a water-tunnel experiment on a circular cone. The trend is well predicted, and the difference in actual position is small compared with the displacement of the separation line from its position for infinite Reynolds number. There is, of course, no reason to expect that the line along which the vortex sheet leaves the surface in the model should agree exactly with any particular observed feature of the real flow. It is surprising that the asymptotic treatment is as successful as it appears to be, relying as it does on a leading term which is of order $R^{-1/8}$.

The inviscid model can be assessed independently by using it with a measured position of the separation line. Fig 2 shows a cross-section of the calculated vortex configuration, with the separation line at the observed, laminar position; and the observed position of the core of the vortex for comparison. The vortex is at about the right distance from the surface, but not far enough round from the separation line. The same sort of discrepancy arises in wing flows, and is usually attributed to the failure to represent secondary separation in the model. A further comparison is shown in Fig 3. To give some idea of the shape of the real vortex, contours of total pressure measured by Rainbird[32] around a circular cone in a wind tunnel are shown, with the calculated vortex configuration superimposed. The observed position of the turbulent separation line was used in the calculation. The model is clearly producing the correct qualitative behaviour.

It seems perfectly feasible to extend this work to non-conical slender bodies of general cross-sectional shape, and, with rather more effort, to implement the model in the subsonic Prandtl-Glauert framework. However, to produce a similar method capable of predicting turbulent separation demands a new insight.

Compared with this substantial achievement, the second advance to be reported is a minor one. What it provides is an improvement in the Kutta condition for use with the single line-vortex model. The standard boundary condition, introduced by Bryson[14], is that the velocity at the separation line is parallel to it. This forces the separating stream surface to leave the body in a direction normal to the body, whereas, if the sheet were represented, it would leave tangentially. The improvement is achieved by writing the Kutta condition for the sheet model, that the velocity on the downstream side is parallel to the separation line, entirely in terms of the mean velocity and the rate at which circulation is being shed. These are quantities which also appear in the simpler line-vortex model and so the revised form of the Kutta condition can be taken over immediately. For the simple example of separation from a body of revolution at incidence, with the separation line lying along a meridian, the condition becomes

$$v = \sqrt{\frac{U}{2}\frac{dr}{dx}} \qquad (2)$$

where v is the circumferential component of the velocity, U is the undisturbed speed, and $d\Gamma/dx$ is the axial rate of growth of the circulation. Compared with the original form of the condition, *ie* v = 0, equation (2) clearly allows the vortex to be weaker if its position is unchanged. The general expression corresponding to (2) is given in Ref 12. An illustration of the effect of the different forms of Kutta condition is given in Fig 4 for conical flow. The curves drawn are all cross-sections of conical stream surfaces, of which the body surface forms one. At the top is sketched a vortex sheet solution, in which the sheet leaves the body tangentially along the separation line, S , to form the surface of separation. On the left, the flow corresponds to a line-vortex solution with the original Kutta condition: the separation line is a singular point for the family of curves shown and the separation surface leaves the body there in the normal direction. On the right, the flow corresponds to a line-vortex solution with the revised Kutta condition: the specified separation line, S , is no longer singular and the separation surface follows further round the body before leaving it, again in the normal direction. Neighbouring conical stream surfaces are now more like those in the vortex sheet solution shown at the top.

Calculations[33,34] for conical bodies using the revised Kutta condition do show smaller circulation, lower peak suction, lower lift, and vortices lying further inboard. These changes tend to improve the relationship with experimental observations. There is a lower bound on the angle of incidence for which the line-vortex model has solutions in which the vortex lies near the separation line. This bound is unrealistically high in relation to experiment and to the vortex-sheet model's predictions[25]; unfortunately the use of (2) does not lower the bound.

We now turn to the improvements aimed at the treatment of more complicated vortex configurations, in particular, configurations which involve more than one axis about which rolling-up occurs. Hoeijmakers and Vaatstra[35,36], using the vortex sheet model in time-dependent planar problems, equivalent to the slender-body framework, have introduced a very useful feature. Where, in the course of the evolution of the vortex sheet, a kink begins to form in the shape, a short segment of the sheet is removed. The circulation about this segment is concentrated into a line-vortex, which is inserted in place of the segment, and connected by cuts to the free edges of the sheet, leaving the velocity potential single-valued once more. Circulation convected off the free edges of the sheet is added to the circulation of the line-vortex. The system of a line-vortex with two cuts represents an infinitely rolled-up, double-branched core of the sheet, which we can imagine as growing from a point on the vortex sheet at which a singularity has appeared. The spontaneous emergence of singularities in the evolution of vortex sheets has recently been discussed by Moore[37] in a proper mathematical context. It appears that by identifying and treating these kinks or singularities an orderly evolution of the vortex configuration can be computed for longer times, or further downstream, than would otherwise be possible. No doubt Dr Hoeijmakers will show some results in his own paper[7].

One of the configurations for which this sort of extra freedom is needed is the double-delta wing, or the swept-wing with strake. If the inboard and outboard portions of the leading-edge have almost the same angle of sweep and the angle of incidence is not too small, a vortex sheet will form along the whole leading-edge and roll-up into a single spiral core, just as if the planform were smoothly curved. The local disturbance to the sheet produced by the kink in the edge is quickly smoothed out. This flow should present no difficulty to any of the models.

If the kink is larger, the disturbance it causes to the smooth growth of the sheet will result in the formation of a second centre of roll-up, as sketched in Fig 5. This situation has been made visible by Verhaagen, whose photographs are published in Ref 36. The circulation shed from the outboard leading-edge cannot be convected past the newly-formed outboard core, so the circulation of the inboard part of the sheet remains constant, or may even reduce if the outboard core becomes strong enough to convect circulation back towards itself. The outboard core continues to grow on the circulation shed from the leading-edge, and will eventually dominate, and perhaps swallow, the inboard core, if the wing extends far enough. The surface sketched in Fig 5 is a stream surface, but not necessarily a proper vortex sheet everywhere. The jump in tangential velocity may decay to zero near the points of inflexion in the curves which connect the two cores, since both cores are convecting circulation away from the inflexion points.

If the kink is larger, or the incidence smaller, part of the stream surface connecting the two cores is likely to collapse onto the surface of the wing, as sketched in Fig 6. The structure of the outboard vortex is now of the familiar leading-edge vortex type, though it is worth noting that its initial growth from the kink is not conical, even in the slender-body framework. The inboard core is shown as connected to the wing surface by a stream surface springing from the line AB. This is not meant to suggest that the boundary layer on the wing separates along AB, though it might do so. However, there must be a surface streamline such as AB which forms a boundary between the surface streamlines which are swept outboard beneath the inboard core and the surface streamlines which attach to the upper surface of the wing after passing above the outboard core. Fig 7 shows a sketch of the surface streamline pattern which would be associated with the flow structure of Fig 6. AC and DE are attachment lines from which boundary layers grow. These boundary layers may collide along AB and, if they do, circulation may be shed from AB. There is some evidence[38] that this does happen on practical configurations, but interpretation of the limited experimental information is complicated by the presence of a secondary vortex formed on the forward part of the wing. For simplicity, secondary separation has been ignored in Figs 5 to 7, and the streamlines sketched in Fig 7 may be regarded either as the surface streamline of the inviscid flow or as the limiting streamlines of the real flow.

The stream surface through AB is drawn as simply as possible in Fig 6, intersecting the wing normally. This implies that there is no shedding of circulation along AB. Part of the stream surface will then no longer be a vortex sheet, as suggested in Fig 8a. It is then likely that a second centre of roll-up will form, as in Fig 8b. On the other hand, if circulation is being shed from AB, the cross-section of the sheet will resemble Fig 8c or 8d, depending on the sign of the shed circulation. Resolving these details seems unlikely to be important.

If the flow near the kink is as sketched in Fig 6, there is still a question about its downstream development. The inboard vortex is moving slightly outboard, under the influence of its image vortex in the wing, while the outboard vortex is growing in size and strength. Will the outboard vortex capture the inboard one? We return to this question later.

As the sequence of reductions in the sweep of the outboard wing and reductions in the angle of incidence continues, the separation on the outboard leading-edge is eventually suppressed. The flow structure then resembles that of Figs 6 and 8, with the outboard vortex removed. The corresponding surface streamline pattern is sketched in Fig 9. The line AB now forms a boundary between the flow swept outboard under the vortex from the attachment line DE and the flow coming inboard from the leading-edge AC. Again there is the possibility of separation from AB and again the real flow is complicated by secondary separation on the strake. Ref 38 provides data on a flow of this kind also.

If a calculation method is to tell us which of these flow patterns actually occurs on a particular wing at a particular angle of incidence, then it must clearly be a flexible one. It may well be that Hoeijmakers technique of representing double-branched spirals provides the needed flexibility, but an alternative approach is to turn to the multiple line-vortex model.

Peace[24] has implemented a multi-vortex model, in the slender-body framework, which incorporates two improvements over the original approach of Sacks, *et al*[5]. The first of these is to allow the circulation of the vortex which was shed most recently to increase along its length. Each vortex can then start with zero circulation, at a point actually on the leading-edge of the wing; instead of starting with its ultimate strength at a point near the leading-edge. Moreover, the Kutta condition can be satisfied at every point of the leading-edge, through the continuously varying strength of the most recently shed vortex. The first vortex can be shed from the apex of a delta wing, so that near the apex the model is just the single line-vortex model. As soon as the second vortex is introduced at the leading-edge, the first vortex is no longer fed with circulation and convects with the local flow. The second vortex grows in circulation, so as to satisfy the Kutta condition; and follows a path which is determined by the condition of zero overall force on it and the cut which joins it to the leading-edge. When the third vortex is introduced, the second is shed, and so on.

The second improvement is to form a strong core vortex by successively amalgamating vortices with the first one to be shed. This is the approach successfully used by Moore[22] to delay the onset of chaos in evolutionary multi-vortex calculations. The usual technique is to replace the two vortices with one, of the same total circulation, placed at their 'centroid of circulation'. This introduces a minor discontinuity into the evolutionary process, which may trigger a potential instability. Peace avoids this by transferring the circulation, and moving the vortices, gradually, again making use of a condition of zero overall force. Two minor details of the technique are worth noting. The initial growth of each new vortex is given by an asymptotic expansion, with the numerical integration process taking over when the vortex is a short distance from the leading-edge. To avoid a multiplicity of weak vortices with a random distribution of signs being formed, vortex formation is suppressed over any length of the leading-edge for which the Kutta condition is approximately satisfied by the existing vortices. This is important in the case of a wing with lengthwise camber, to be considered later.

The new method has three significant advantages. Many vortices can be shed, to represent the flow accurately, without necessarily inducing a chaotic development. Greater smoothness in the streamwise development of the flow is achieved, though weak fluctuations remain. The overall accuracy is greater, because the flow near the apex is better represented.

Before giving an example of the capability of the method for a wing flow, we note that the technique of allowing each new vortex to grow from the separation line cannot be applied to separation from smooth surfaces. There is no asymptotic solution for the initial growth of such a vortex from a finite point, as pointed out by Bryson[14].

To illustrate the capability of this multi-vortex technique, we show the results, taken from Ref 24, of applying it to a double-delta configuration like those discussed above. The planform is defined by the equations

$$s(x) = \begin{cases} 0.1x & \text{for} \quad 0 \leq x \leq 10 \\ 1 + 0.4(x - 10) & \text{for} \quad 10 \leq x \leq 20, \end{cases} \qquad (3)$$

for the local semi-span, $s(x)$, of the wing. This corresponds to a semi-angle of 5.7° at the apex and a kink in the leading-edge of 16.1°. In Fig 10 results are shown for an angle of incidence of 5.7°. Cross-sections of the calculated vortex configuration are shown for three streamwise stations, the first at the kink. This shows the usual

pattern expected of a conical vortex sheet solution for an incidence equal to the semi-apex angle. Further downstream, the vortices being shed roll-up into a new core close to the leading-edge, leaving those shed upstream to convect as a group. The last vortex shed upstream of the kink just fails to be caught up in the rotating group. The numbers beside the groups of vortices indicate the total circulation in the group, as a value of Γ/U . The value of 0.48 at the kink station compares well with that of 0.47 given by the sheet model[39] ($\Gamma/KUs = G + g = 4.7$, $K = 0.1$, $s = 1$, in the notation of Ref 39). The circulation of the outboard group grows quickly, owing to the lower sweep of the outboard leading-edge. There is no indication of any appreciable interaction between the groups of vortices at this angle of incidence.

Fig 11 shows the vortex configuration for the same cross-sections on the same planform, for an angle of incidence of 10.3°, nearly twice as large as before. Again at $x = 10$ we have the expected behaviour for a delta wing - at this incidence Ref 39 gives $\Gamma/U = 0.98$ - with a larger size and circulation corresponding to the increased incidence. Again the newly shed vortices downstream of the kink roll up in a separate group, which is also larger and stronger than before. However, at this incidence, the inboard group of vortices moves fast enough laterally, under the influence of its image in the wing, to interact significantly with the outboard group. At $x = 17.5$ the inboard group is just being broken up by the interaction. By $x = 20$, not reproduced here, the orderly structure has been disrupted, with the capture of several individual inboard vortices by the outboard group. It should be pointed out that many more individual line-vortices are involved in the calculation than appear in the final downstream section, because many of them have been amalgamated in the cores.

4 RELATIVE ADVANTAGES OF THE DIFFERENT MODELS

As a starting point for a comparison of the advantages of the three different models of rolled-up vortex sheets, it is helpful to describe the features which belong particularly to one of them. The remaining, shared, features are then discussed; and an overall view is formed.

The particular advantage of the single line-vortex model is its simplicity. When implemented in the slender-body framework, the model is simple enough for exact analysis to be possible. For instance, the equations governing the Bryson model[14] of separated flow over a circular cone at incidence have been reduced to a polynomial of the 18th degree, so that all solutions can be found[34]. After the obviously non-physical solutions have been rejected, a branch additional to that found by Bryson remains, and may be of physical significance. When lateral asymmetry is allowed in the Bryson model further solutions are found[40]. An asymptotic analysis of the equations is possible, for large values of the incidence parameter α/δ (best thought of as arising from small values of the cone semi-angle, δ). This confirms the physically realistic asymmetric solutions which had been found numerically; and reveals a second branch, which turns out to be non-physical.

In the case of wing problems, asymptotic expansions of the line-vortex model for small values of the circulation have proved useful. In particular they have shed light on the difficulty in finding solutions of the vortex-sheet model in two cases. The first of these is the flat-plate delta wing, for which it has proved impossible to find vortex sheet solutions which spring from the leading-edge at very small values of the incidence parameter, α/A , where A is the aspect ratio. Barsby[41] found solutions in which the sheet springs from the upper surface, just inboard of the edge. Examination of the line-vortex model shows that it, too, predicts a separation stream surface springing from the upper surface, rather than the leading-edge, when α/A is small. Asymptotic analysis shows the same situation arising on wings with non-zero thickness[42]. The second case, also discovered by Barsby[43], is of a thin delta wing with conical camber. For such a wing, the flow is attached all along the leading-edge for a particular angle of incidence, α_s . Solutions of the sheet model could be found for $\alpha < \alpha_s$, but not for a significant range of angles of incidence below α_s , for which a vortex would be expected to lie below the wing. Examination of the asymptotic expansion of the line-vortex model showed that the analytic behaviour of the solution for the cambered wing is quite different from that for the plane wing; and that no solution could be found for angles of incidence just below α_s .

The numerical work involved in applying the line-vortex model is also much lighter than it is for the vortex sheet and multi-vortex models. This would be useless unless the solutions obtained had some value. One way in which the solutions are of value is in pointing the way to existence and uniqueness properties of more complex models. Examples of this 'structural similarity' between the models, additional to those mentioned above, are given below. Levinski and Wei[44] calculated flows past cones with conical strakes in the slender-body framework and found multiple solutions for a certain range of angles of incidence. The same behaviour arises for both the line-vortex model and the vortex-sheet model, though the ranges of incidence are not the same for the two models. For a delta wing with lengthwise camber, placed at an overall angle of incidence such that the local geometric incidence falls to zero at some lengthwise station, both the vortex sheet model[9] and the line-vortex model produce unphysical results before the station of zero local incidence is reached. For laterally symmetric flow past a circular cone at incidence, there are no solutions to the line-vortex model with the vortex close to the separation line if

$$\alpha/\delta < 1.5 \operatorname{cosec} \theta_s \quad , \qquad (4)$$

where θ_s is the elevation of the separation line above the horizontal*. Solutions of the vortex sheet model have been found below this limit[25], but there still appears to be a lower bound below which solutions cannot be found. When the restriction to lateral symmetry is removed, families of asymmetric solutions have been found for the line-vortex[40] and vortex-sheet[28] models. In fact, the solutions for the line-vortex model were used to find the vortex-sheet solutions.

It must be said that much of the simplicity of the line-vortex model is lost when the slender-body framework is replaced by the Prandtl-Glauert framework. Although the vortex circulation and path can still be described simply, the need to model the wake more completely than in treatments of attached flow, in order to satisfy the Kutta condition at the trailing-edge, introduces a considerable complexity[4,15]. The model has not proved popular in this framework.

The particular advantage of the multiple line-vortex model is its flexibility. In principle, circulation is shed from the separation line and convected with the local flow. In the slender-body framework, techniques following that description have been implemented and solutions, of a kind, are always obtained. The problem of the delta wing with lengthwise camber mentioned above illustrates this advantage of the multi-vortex model very clearly. Both the vortex-sheet model and the single line-vortex model break down because they are not sufficiently flexible to represent the change from shedding circulation towards the upper surface over the forward part to shedding it towards the lower surface over the rearward part. Peace[24] has treated the problem using his multi-vortex model to obtain the results shown in Fig 12. The planform of the wing is defined by the local semi-span

$$s(x) = 0.25x \quad . \tag{4a}$$

The apex region of the wing is at a uniform positive incidence, given by

$$\frac{\partial z}{\partial x} = -0.2 \qquad \text{for} \quad 0 \leqslant x \leqslant 1. \tag{4b}$$

Further aft, the local incidence reduces smoothly, passing through zero at x = 2, after which it is negative:

$$\frac{\partial z}{\partial x} = -0.2(2 - x) \qquad \text{for} \quad x \geqslant 1. \tag{4c}$$

Fig 12 shows sections through the vortex configuration for four stations, all downstream of the conical flow region. Note that only the region near the leading-edge is illustrated at each station. At x = 1.4, the multi-vortex configuration, shown by the circles, agrees quite well with Clark's sheet solution[9], shown by the line and cross. By x = 1.8 no further positive vortices have been shed, as indicated by the unchanged figure for the circulation above the wing, but a single negative vortex, represented by a solid circle, has just been shed towards the lower surface. The geometric incidence is still positive at this station. Clark's solution also shows negative circulation being shed, but the shape of the sheet has begun to look unrealistic, and the solution could not be extended further downstream. The multi-vortex solution will go further: by x = 2.2 a rolled-up system of negative vortices has formed below the wing, though its strength is still weak compared with the upper surface vortex, now reduced to a core by the operation of the amalgamation algorithm. By x = 2.6, the negative system is stronger than the positive one. Note how the interaction between the systems has drawn both of them outboard of the leading-edge. Not surprisingly, the orderly structure is disrupted in a relatively short further distance downstream, before the local incidence reaches a negative value as large as the positive value at the apex.

Further evidence of the flexibility of the multi-vortex method is provided by the calculations for the double-delta wing shown in Figs 10 and 11 and discussed above. Many calculations of time-dependent planar flows and of the evolution of trailing vortex wakes show the same flexibility. Hoeijmaker's recent work[35,36] has made the vortex-sheet model more flexible, while Peace's use of an amalgamation algorithm has made the multi-vortex model rather less flexible. The two models are perhaps moving towards a common capability, but the multi-vortex model is still the more flexible.

When the multi-vortex model is implemented in the Prandtl-Glauert framework for steady, subsonic flow, the problem becomes elliptic. The simple idea of shedding and convecting circulation no longer applies, since what is shed downstream affects the flow upstream. Considerable ingenuity may then be needed to obtain solutions for flows with a simple structure, as Rehbach[45] and Schröder[46] found for the case of the delta wing. The difficulty is presumably that the flexibility of the model is not yet matched by a corresponding flexibility in the numerical schemes available to solve the large number of nonlinear simultaneous equations to which the model gives rise. It would seem worth trying to exploit the existence of slender-body techniques: either to provide an initial guess for the Newton-Raphson method, as Forrester, *et al*[2] do; or as a step in an iterative method, as Jepps[47] has proposed.

For unsteady incompressible flow, the problem is again an evolutionary one and the flexibility of the multi-vortex model reappears[48,49,50]. Unfortunately, the tendency for the motion of the vortices to become chaotic also reappears. It seems that neither steady nor truly periodic solutions have been produced as a result of evolutionary calculations, and, in their absence, it is hard to assess the accuracy of the calculations.

---

* NB this is a different definition of θ_s from that in Fig 1.

The particular advantage of the vortex-sheet model lies in the greater realism with which it describes separation from a line on a smooth surface. As indicated earlier, the theory used by Fiddes[25] to calculate the position of laminar separation on a cone requires the strength of the singular behaviour of the inviscid solution at the separation line. This can only be found from a vortex-sheet model. Even if it is not intended to predict the position of the separation line, it still seems unlikely that reasonable accuracy can be obtained without treating the inviscid flow near the separation line adequately. The sketches of Fig 4 show the sort of qualitative difference that can arise. As an extreme example of the quantitative differences between the predictions of the vortex-sheet model and the predictions of the single line-vortex model, we have Fig 18, which is discussed in detail later. The discrepancy is far greater than that for flows over wings.

The common advantage of the vortex-sheet and multi-vortex models over the line-vortex model is that they both offer a closer approximation to the infinite Reynolds number limit of the real flow. As would be expected, they almost always give closer agreement with measurements at finite Reynolds number. As between these two models, the remaining advantages are less clear cut. In the terminology of panel methods, the sheet model is a higher-order method. Consequently it gives greater accuracy for a similar number of elements, with the ability to predict a smooth behaviour of the flow. On the other hand, the programming effort involved in the sheet method is greater, and computing time for the same member of elements should also be greater. At present no comparison can be made on the basis of computing time for the same accuracy, but the multi-vortex method must involve more storage space. If it is desired for some reason to represent many turns of a rolled-up configuration, the vortex-sheet model has an advantage, because a multi-vortex calculation is likely to be disrupted by vortices from adjacent turns pairing-off and rotating round one another.

A large potential advantage of a multi-vortex model in the subsonic Prandtl-Glauert framework is that it might well predict vortex breakdown. In fact Aparimov, *et al*[51] claim that the failure of their multi-vortex model to converge at a large angle of incidence is related to vortex breakdown in the real flow. Rehbach, aiming particularly at the calculation of unsteady incompressible flow, has introduced[52] a Lagrangian model based on the vorticity equation, which has some resemblance to a multi-vortex model. The outcome is a set of streak-lines which spring from the separation line, in a direct simulation of Werlé's famous dye-lines. Rehbach also claims[53] that the disorganization of the calculated streak-lines near the axis of the vortex corresponds to vortex breakdown. It should also be possible to predict at least the initial occurrence of vortex breakdown using the vortex-sheet model in combination with a technique like that of Hall[54] for calculating the flow in an axisymmetric core of distributed vorticity. By averaging the predictions of the vortex-sheet model in the circumferential direction, the inward flow of mass and circulation to the core and the pressure distribution along it could be obtained. These are the boundary conditions required for the core calculation, which would in turn supply a displacement effect along the axis of the vortex in the sheet model. So far as the prediction of breakdown is concerned, it cannot be said that either model has the demonstrated capability, nor that either is incapable. It may well be that a direct attack on the Euler equations, like the one Rizzi is going to describe[55], will provide the best approach to the problem.

In summary, if a method of useful accuracy is required, the choice is between the vortex-sheet and multi-vortex models. For separation from smooth surfaces, the sheet model is preferable. If the same program is required to calculate very different vortex structures with minimal changes, the multi-vortex model is preferable. The line-vortex model has a useful role to play in initial investigations and in suggesting the underlying structure of families of solutions of the more realistic models.

5 WHY MODELLING?

Since these models all lead to such complexities and still fall short of a proper description of the behaviour of the fluid, we must ask whether it is worthwhile pursuing them further. After all, solutions of the Navier-Stokes equations and the Euler equations by field methods are becoming available and must eventually become the accepted methods for making quantitative predictions about vortex flows. Nonetheless, I believe it is worth continuing with modelling techniques. In support of this view, I have first some very general remarks, which can conveniently be put as quotations, and then an account of how modelling has recently helped with a particularly intractable problem.

To start with, here is a quotation from a lecture[56] given by James Lighthill to the Royal Aeronautical Society, when he was Director of the RAE. He is speaking of the role of mathematics in generating physical ideas.

"Examples of this mathematically generated kind of physical idea, which I have already mentioned, are trailing vorticity, boundary layer, dynamic stability and Nyquist diagram.

The value of physical ideas in practical work, of course, is their elasticity. Provided that they are sound ideas, such as those thrown up as the genuinely appropriate physical description of the mathematical solution of some well defined class of problem, they usually show a splendid capacity to stand up to distortions of the problem, and indeed to radical changes and complications in its conditions, and still give the right guidance about what needs to be done. In other words, a well designed physical idea has wide elastic limits, and will tolerate being pulled and twisted about, and go on giving good service in suggesting the right experiment, or the way out of such and such a

difficulty, or in giving someone a feeling that he is not just dismally accumulating a confused mass of experimental data, but there is some thread running through them which gives them meaning and interest. Naturally, then, these ideas are much in demand, and when we come to a new kind of problem, where we are short of physical ideas because none of the old ones that we are accustomed to seems to give any help in solving it, then we can only hope that someone will come along with a mathematical treatment of some appropriately simplified, although possibly also generalised case, and interpret its solution by introducing a new animal into the zoo of useful aeronautical concepts, preferably a well-behaved beast, which all of us will in due course be able to ride as to the manner born, probably ignoring, if we are not mathematicians, what kinds of technique were used to lick him into shape."

Lighthill went on to discuss the role of mathematics in getting actual answers.

Now for a quotation from the final section of Dietrich Küchemann's book[57] on the aerodynamic design of aircraft.

"Above all, it is such conceptual frameworks which enable us to formulate intelligent ways of modifying and controlling our part of human endeavours. Ideas and concepts come out of the mind, not out of computers or wind tunnels. If there is one overriding purpose throughout these notes, above all others, it is to demonstrate the continued need for conceptual frameworks and for understanding the physics of airflows in any work on aerodynamic design."

Finally, because I have not found a better way to express the idea since, a quotation from a previous AGARD paper[58] of my own.

"The philosophical argument naturally concerns ends rather than means. If our aim is to reproduce our bit of the real world in a computer, then the solution of the Navier-Stokes equations is a possible approach, at least for laminar flows. We may hope to obtain more precise information, more quickly and more cheaply than by making measurements in real fluids, and this is well worth doing. However, as scientists we wish to understand things, and as engineers we wish to alter things. In both of these processes the acquisition of data needs to be accompanied by the growth of conceptual frameworks which can account for the data we already have and show us where more is needed. It is such conceptual frameworks which enable us to formulate intelligent ways of modifying and controlling our bit of the universe. They are built of models, some far-reaching and all-embracing, but some quite special. I do not see the need for special models disappearing in our field. In particular, I expect the distinction between the external inviscid flow and the boundary layer, on which the science of aerodynamics has been built, to continue, supplemented locally by special models of separation phenomena."

These quotations put the abstract case for modelling very clearly, but they do not provide much in the way of illustration. It is therefore appropriate to turn to a description of some recent work with two of the models that have formed the basic theme of this paper, work that has significantly increased our understanding of some baffling observations. These observations are of the lack of expected symmetry in flows past bodies at large angles of incidence, leading to very significant out-of-plane forces on missiles and to large yawing moments on aircraft[59]. The work is that described by Fiddes[28] at the Trondheim meeting last year, using first the line-vortex model and then the vortex-sheet model, and in each case showing the existence of a second family of solutions which produce large out-of-plane forces on circular cones. I shall conclude by suggesting that the simplifications implicit in the models have actually helped to bring about the increased understanding.

Both models are implemented in the framework of slender-body theory and applied to flow past circular cones at incidence. The line-vortex model is then simply the one which was devised by Bryson[14]: the only change is that the port and starboard vortices are allowed to lie asymmetrically about the incidence plane and to have different circulations, and that the separation lines are also allowed to be asymmetrically placed. The model is entirely inviscid, so the positions of the separation lines must be supplied to it. The separation lines are supposed to be generators of the cone. The entire geometry is then conical, so, since slender-body theory is used, the existence of a conical flow solution is to be expected. This means that the solution sought depends on three parameters: the angular positions of the two separation lines round the circumference of the cone, and an incidence parameter, α/δ, which is the ratio of the angle of incidence, α, to the semi-apex angle of the cone, δ. The entire flow field can be written down in terms of these three parameters and six unknown quantities: the two coordinates and the circulation of each of the two vortices. Six conditions are available to determine these six unknowns: a Kutta condition at each separation line, and the vanishing of the two cross-flow components of the overall force on the combination of each vortex and the cut which joins it to the appropriate separation line. The original form of the Kutta condition is retained.

The equations expressing the two Kutta conditions are linear in the two circulations and so can be solved for them. The expressions which result can be substituted into the remaining four equations, which are then extremely nonlinear in the four coordinates of the vortices. A generalized Newton-Raphson technique is used to solve these equations. The results are most easily understood by concentrating on the case in which the two separation lines are placed symmetrically with respect to the incidence plane, so that the solutions depend only on the separation line position and the incidence parameter. Fig 13a&b shows the variation of the two coordinates of the starboard

vortex, as the incidence parameter increases, for separation lines which are $\theta_s = 56^\circ$ round from the 'horizontal' plane through the axis of the cone. The coordinates are referred to horizontal and vertical axes in the cross-flow plane, with origin on the cone axis. For small values of the incidence parameter, no solutions have been found. For values above the limit of 1.81, given by equation 4), Bryson's symmetric solutions appear. No others have been found until the point B on the symmetric solution curve is reached. Here the solution, as a function of α/δ, bifurcates in the classical manner, with the Jacobian matrix becoming singular. Two further solution branches exist for larger values of α/δ and these are mirror images in the incidence plane. It is only the intersection at B in Fig 13 which represents a bifurcation; at the other intersections only one of the two coordinates agrees.

It is easier to appreciate the solutions when the loci of the vortices are plotted in the cross-flow plane for varying values of the incidence parameter. Fig 14 shows the symmetric solution and one of the asymmetric solutions for values of α/δ between 3 and 10, and a rather earlier separation position, $\theta_s = 40^\circ$. It is necessary to check that the flow on the surface of the cone does actually converge towards the postulated separation lines, since the equations are equally well satisfied by attaching flows. It turns out that the solutions are physically sensible for values of α/δ up to a value rather greater than the largest in Fig 14. Since the slender-body framework assumes the incidence is small, such large values of α/δ would be irrelevant for practical configurations.

Fig 15 shows the asymmetry in the circulation of the vortices, the strength of each being referred to the strength of the vortices in the symmetric solution for the same value of α/δ. The range of values of α/δ does not extend downward as far as the bifurcation point, so the curves do not start with a common value of unity, as they should. In view of the very different loci shown in Fig 14, it is somewhat surprising that the circulations of the asymmetric vortices are not more different from one another and from those of the symmetric vortices. It is well known that slender-body theory tends to overpredict lifting forces and the line-vortex model also tends to overpredict the nonlinear contributions. Therefore, to make a comparison with force measurements, the ratio, C_Y/C_N, of side force to normal force is presented in Fig 16. The separation lines are still symmetrically placed at the arbitrarily selected value, $\theta_s = 40^\circ$. The theoretical curve needs no explanation, since it arises directly from the asymmetric solutions described. The experimental points are taken from the measurements by Keener, *et al*[60]. Each point represents the largest value of C_Y/C_N measured at that particular angle of incidence, so the roll angle and Reynolds number may be different for the different points. The agreement with observation is striking in view of the simplicity of the model and the framework.

It is clear that asymmetric effects comparable with those observed can be produced by an entirely inviscid mechanism, separation having been fixed symmetrically in the calculations. To make it clear that this mechanism is the relevant one, a further step is needed. As explained above, the model allows the positions of the separation lines to be chosen freely, but so far the results presented have been for separation lines placed symmetrically about the incidence plane. Solutions for asymmetrically placed separation lines can be obtained by proceeding in small steps from either a symmetric solution or an asymmetric solution with symmetric separation lines. Obviously all the solutions obtained in this way are asymmetric, but they fall into two distinct families: the first family derives from solutions which are symmetric when the separation lines are symmetric; the second derives from solutions which are asymmetric when the separation lines are symmetric. The importance of the second family can be confirmed by examining the level of side force produced by the first family. Fig 17 shows typical values of the ratio of side force to normal force that correspond to solutions of the first family, for an incidence parameter of 3.5. For this value of the incidence parameter, Fig 16 shows the experimental value is 0.75, so the calculated values in Fig 17 are smaller by an order of magnitude. The abscissa in the figure is the degree of asymmetry in separation line position, and the curves are drawn for fixed positions of one of the separation lines. It is concluded that the second, globally asymmetric, family of solutions is needed to produce the observed results on cones, and that it is capable of generating side forces of the right order.

The vortex-sheet model has subsequently been applied to the same configuration, in the same framework. This offers two advantages: an increase in accuracy, and the possibility of extending the calculation to the prediction of laminar separation, as previously demonstrated[25] for the symmetrical case. So far, however, the vortex-sheet model has been used with specified separation lines, in the same way as the line-vortex model. The asymmetric solutions of the line-vortex model were only found after a long search, but it was hoped that they would provide a good starting point from which to seek solutions of the vortex-sheet model. In fact, the search for sheet solutions took even longer.

Fig 18 shows one of those found, with, on the left, the symmetric solutions for the same incidence parameter and separation line position. For comparison, the positions of the line-vortices in the corresponding solutions for the simpler model are shown by solid circles. For the symmetric solutions on the left, the difference between the core positions for the two models is not much greater than that familiar from solutions for delta wings, and of a similar form. However, the asymmetric solutions on the right seem scarcely related. This may be a rather extreme example - the starboard line-vortex has moved initially downwards and outboard from the bifurcation point - but the differences between the asymmetric vortex positions predicted by the two models are generally large. This explains why it was hard to find the vortex-sheet solutions, but indicates that the effort was probably worthwhile. The starboard sheet in the asymmetric solution is very similar

in appearance, and, in turns out, in structure, to the symmetric sheets; but the port sheet is quite different. In shape it is like the conical trailing vortex sheet calculated by Jones[61], and its structure is also similar in that only a small part of the total circulation lies in the core, with the bulk of it on the sheet. Fig 19 shows a vapour-screen photograph due to Peake, *et al*[62] of the flow over a circular cone at a similar value of the incidence parameter, in which the vortices are visible as dark regions. There is clearly a remarkable resemblance between the calculated solution and the visualisation of the flow.

Ref 28 also includes a comparison of the forces predicted by the vortex-sheet model with those measured in some unpublished work by Mundell at RAE. The positions of the straight, laminar separation lines were measured along with the forces, with the flow tripped at the apex by a tiny protuberance. Great care was taken to ensure that measured forces arose from a region of approximately conical flow. The live portion of the model is a circular cone of 10° semi-apex-angle, with a length of 292 mm. Forces were measured over a range of Reynolds numbers in a low-speed wind tunnel, for a continuously-varying roll angle. The values chosen for comparison correspond to the largest Reynolds number for which the boundary layer at separation is wholly laminar, and to the roll angle for which the side force is greatest. At an angle of incidence of 36°, the observed separation lines lay in the 'horizontal' reference plane on one side and 14° above it on the other side. (It is worth noting in passing that this degree of asymmetry in the separation line position is small compared with the range considered in Fig 17.) Any calculated solution with these separation lines must be asymmetric; but there is again a distinction between a first family of solutions which derive from a symmetric solution and a second family whose members derive from solutions which are asymmetric even when their separation lines are symmetric. The solutions from the first and second families, for the experimental value of the incidence parameter and measured separation positions, are illustrated in Fig 20. The table below shows some details of these solutions and a comparison of the forces.

		First family	Second family	Experiment
Total circulation	left	-13.7	-13.9	
	right	16.0	14.0	
$\frac{\text{Core circulation}}{\text{Total circulation}}$	left	0.64	0.80	
	right	0.60	0.25	
C_Y/δ^2		-1.5	-19.7	-17.6
C_N/δ^2		36.8	36.8	27.0

The table shows first that the circulations of all the vortices are similar, despite the very different shapes of those in the second family solution. However, the different shapes are accompanied by a difference of structure: most of the left-hand vortex circulation is in its core, and most of the right-hand vortex circulation is on the sheet. The force coefficients are based on the plan area of the cone; each is divided by δ^2 to bring it to a similarity form. The side force in the first family is smaller than that measured by an order of magnitude, but the second family prediction is close, considering it is based on slender-body theory. The normal force is almost the same for the two solutions and much larger than the measurement. The discrepancy is not surprising, since the slender-body framework relies on the angle of incidence, 36° in the experiment, being small. There can be little doubt that the solution from the second family corresponds to the experimental situation.

The success of this work in explaining the origin of the large side forces measured on circular cones at angles of incidence greater than the apex angle is very significant, but it is only the first step in the process of explaining the observations of side force on practical aircraft and missile shapes. For instance, in a conical flow the local side force coefficient is the same along the whole length of the cone, whereas the oscillatory variation of the local side force along the length of an ogive-cylinder is well known. Moreover, a significant level of side force arises on an ogive-cylinder at angles of incidence too small in relation to its apex angle for the second family of solutions to exist at the apex. However, the work has identified one mechanism which must exert an important influence on the aerodynamics of slender pointed bodies. Before it there was only conjecture about the origin of out-of-plane force. After it, one origin is clear.

I think this is the first time that vortex modelling, in the sense used in this paper, has actually told us something we did not know before. After decades of trailing behind experimental observation and measurement, models have at least repaid our efforts by telling us something about the real world.

Obviously we should be trying to overcome the limitations of models, and much of this paper has been devoted to efforts to do so. However, there is a sense in which the very limitations of the models used can contribute to the clarity of the outcome. It is the need to supply the separation lines to the inviscid model which forces the isolation of the large-scale asymmetry of the second family from the small-scale asymmetry of the first family. It is the consideration of conical flow which concentrates attention on

the flow at the apex of the body. It is the use of the simplest possible model which reduces the behaviour of the solution from being that of a three-dimensional continuum, as is the case when the steady Euler or Navier-Stokes equations are solved, to a dependence on four numbers, the coordinates of the line-vortices; and so makes it possible to contemplate a systematic search for solutions.

It is too much to hope that second family solutions, even with a more appealing name, will ever come to figure alongside 'boundary layer' and 'trailing vortex' in a list of concepts given by mathematics to aeronautics, but they do encourage us to keep modelling.

REFERENCES

1 K.W. Mangler, J.H.B. Smith: "A theory of the flow past a slender delta wing with leading-edge separation." Proc. Roy. Soc. Lond. A, 251, 200-17 (1959); also Report Aero 2593 (1957)

2 F.T. Johnson, P. Lu, E.N. Tinoco, M.A. Epton: "An improved panel method for the solution of three-dimensional vortex flows: Vol.1 - Theory document." NASA CR-3278 (1980)

3 C. Rehbach: "Numerical investigation of leading-edge vortex for low aspect ratio thin wings." AIAA J, 14, 253-5 (1976)

4 R.K. Nangia, G.J. Hancock: "A theoretical investigation for delta wings with leading-edge separation at low speeds." ARC CP 1086 (1968)

5 A.H. Sacks, R.E. Lundberg, C.W. Hanson: "A theoretical investigation of the aerodynamics of slender wing-body combinations exhibiting leading-edge separati ." NASA CR-719 (1967)

6 C.E. Brown, W.H. Michael: "Effect of leading-edge separation on the lift of a delta wing." J. Aero. Sci. 21, 690-4 and 706 (1954)

7 H.W.M. Hoeijmakers: "Computational vortex flow aerodynamics." In AGARD FDP Symposium 'Aerodynamics of vortical type flow in three dimensions' (1983)

8 J.H.B. Smith: "Achievements and problems in modelling highly-swept flow separations." In 'Numerical methods in aeronautical fluid dynamics' (ed. P.L. Roe), Academic Press (1982)

9 R.W. Clark: "Non-conical flow past slender wings with leading-edge vortex sheets." ARC R & M 3814 (1976)

10 I.P. Jones: "Leading-edge separation from a slender rolling wing-body combination." RAE Technical Report 80039 (1980)

11 E.N. Tinoco, P. Lu, F.T. Johnson: "An improved panel method for the solution of three-dimensional vortex flows: Vol.2 - Users' guide." NASA CR-3279 (1980)

12 J.H.B. Smith: In 'Three-dimensional and unsteady separation at high Reynolds numbers', AGARD-LS-94 (1978)

13 R. Legendre: "Écoulement au voisinage de la pointe avant d'une aile à forte flèche aux incidences moyennes." Rech. Aero. Nos.30, 31 and 35 (1953)

14 A.E. Bryson: "Symmetrical vortex formation on circular cylinders and cones." J. Appl. Mech. (ASME), 26, 643-8 (1959)

15 T.K. Matoi, E.E. Covert, S.E. Widnall: "A three-dimensional lifting-surface theory with leading-edge vortices." US Office of Naval Research ONR-CR-215-230-2 (1975)

16 M.G. Hall: "A theory for the core of a leading-edge vortex." J. Fluid Mech. 11, 209-28 (1961)

17 S.N. Brown: "The compressible inviscid leading-edge vortex." J. Fluid. Mech. 22, 17-32 (1965)

18 K.W. Mangler, J. Weber: "The flow field near the centre of a rolled-up vortex sheet." J. Fluid Mech. 30, 177-96 (1967)

19 D.W. Moore, P.G. Saffman: "The motion of a vortex filament with axial flow." Phil. Trans. Roy. Soc. Lond. A, 272, 403-29 (1972)

20 H.W.M. Hoeijmakers, W. Vaatstra: "A higher-order panel method for the computation of the flow about slender delta wings with leading-edge vortex separation." NLR MP 81053U (1981)

21 N.G. Verhaagen, L. van der Snoek: "An experimental investigation into the entrainment into a leading-edge vortex." Delft Univ. of Techn. Report LR-332 (1981)

22 D.W. Moore: "A numerical study of the roll-up of a finite vortex sheet." J. Fluid Mech. 63, 225-35 (1974)

23 P.T. Fink, W.K. Soh: "A new approach to roll-up calculations of vortex sheets." Proc. Roy. Soc. Lond. A, 362, 195-209 (1978)

24 A.J. Peace: "A multi-vortex model of leading-edge vortex flows." To appear in Int. J. of Numerical Methods in Fluids (1983)

25 S.P. Fiddes: "A theory of the separated flow past a slender elliptic cone at incidence." Paper 30 in 'Computation of viscous-inviscid interactions', AGARD CP 291 (1980)

26 J.H.B. Smith: "Behaviour of a vortex sheet separating from a smooth surface." RAE Technical Report 77058 (1977)

27 F.T. Smith: "Three-dimensional viscous and inviscid separation of a vortex sheet from a smooth non-slender body." RAE Technical Report 78095 (1978)

28 S.P. Fiddes, J.H.B. Smith: "Calculations of asymmetric separated flow past circular cones at large angles of incidence." Paper 14 in 'Missile aerodynamics', AGARD CP 336 (1982)

29 V.V. Sychev: "On laminar separation." Izv. Ak. Nauk Mekh. Zh. Gaza, No.3, 47-59 (1972); Trans. in Fluid Dynamics, Plenum, March 1974, 407-417

30 F.T. Smith: "The laminar separation of an incompressible fluid streaming past a smooth surface." Proc. Roy. Soc. Lond. A, 356, 443-63 (1977)

31 W.J. Rainbird, R.S. Crabbe, L.S. Jurewicz: "A water-tunnel investigation of flow separation about circular cones at incidence." NRC (Canada) Aeron. Rep. LR 385 (1963)

32 W.J. Rainbird: "The external flow field about yawed circular cones." Paper 19 in AGARD CP 30 (1968)

33 R.K. Nangia: "A study of slender conical thick wings and bodies with variation of flow separation point." Bristol Univ., Dept of Aero. Eng., Grant No.AFOSR-77-3243 (1978)

34 K. Moore: "Line-vortex models of separated flow past a circular cone at incidence." RAE Technical Memorandum Aero 1917 (1981)

35 H.W.M. Hoeijmakers, W. Vaatstra: "A higher-order panel method applied to vortex sheet roll up." AIAA Paper 82-0096 (1982)

36 H.W.M. Hoeijmakers, W. Vaatstra: "On the vortex flow over delta and double-delta wings." AIAA Paper 82-0949 (1982)

37 D.W. Moore: "The spontaneous appearance of a singularity in the shape of an evolving vortex sheet." Proc. Roy. Soc. Lond. A, 365, 105-19 (1979)

38 P.J. Butterworth: "Flow measurements in the wake of a wing fitted with a leading-edge root extension (strake)." RAE Technical Report 79120 (1979)

39 J.H.B. Smith: "Improved calculations of leading-edge separation from slender, thin, delta wings." Proc. Roy. Soc. Lond. A, 306, 67-90 (1968); RAE Technical Report 66070 (1966)

40 D.E. Dyer, S.P. Fiddes, J.H.B. Smith: "Asymmetric vortex formation from cones at incidence - a simple inviscid model." Aeronautical Quarterly 33, 293-312, November 1982; also RAE Technical Report 81130 (1981)

41 J.E. Barsby: "Separated flow past a slender delta wing at low incidence." Aeronautical Quarterly 24, 120-8 (1973)

42 R.W. Clark, J.H.B. Smith, C.W. Thompson: "Some series-expansion solutions for slender wings with leading-edge separation." ARC R & M 3785 (1975)

43 J.E. Barsby: "Flow past conically cambered slender delta wings with leading-edge separation." ARC R & M 3748 (1972)

44 E.S. Levinsky, M.H.Y. Wei: "Non-linear lift and pressure distribution on slender conical bodies with strakes at low speeds." NASA CR-1202 (1968)

45 C. Rehbach: "Étude numérique de nappes tourbillonnaires issues d'une ligne de décollement près du bord d'attaque." Rech. Aero., No.6, 325-30 (1973)

46 W. Schröder: "Berechnung der nichtlinearen Beiwerte von Flügeln mit kleinem und mittlerem Seitenverhältnis nach dem Wirbelleiterverfahren in inkompressibler Strömung." DFVLR-78-26 (1978); Trans. as ESA-TT-585

47 S.A. Jepps: "The computation of vortex flows by panel methods." VKI Lecture Series 5, Computational Fluid Dynamics (1978)

48 S.M. Belotserkovskii, M.I. Nisht: "Unsteady nonlinear theory for a thin wing of arbitrary planform." Izv. Ak. Nauk Mekh. Zh. Gaza, No.4, 100-8 (1974); Trans. in Fluid Dynamics, 9, 583-9

49 E.H. Atta, O.A. Kandil, D.T. Mook, A.H. Nayfeh: "Unsteady aerodynamic loads on arbitrary wings including wing-tip and leading-edge separation." AIAA Paper 77-156 (1977)

50 O.A. Kandil, E.H. Atta, A.H. Nayfeh: "Three-dimensional steady and unsteady asymmetric flow past wings of arbitrary planforms." NASA CR-145235 (1977)

51 V.A. Aparimov, S.M. Belotserkovskii, M.I. Nisht, O.N. Sokolova: "On the mathematical simulation in an ideal fluid of separated flow past a wing and the destruction of the vortex sheet." Dokl. Ak. Nauk SSSR, 227, 820-3 (1976); Trans. in Sov. Phys. Dokl., 21, 4, 181-3

52 C. Rehbach: "Calcul numérique d'écoulement tridimensionels instationnaires avec nappes tourbillonnaires." Rech. Aero. 1977-5, 289-98 (1977)

53 C. Rehbach: "Calcul instationnaire de nappes tourbillonnaires émises par des surfaces portantes fortement inclinées." Paper 14 in 'High angle of attack aerodynamics', AGARD CP 247 (1978)

54 M.G. Hall: "A numerical method for solving the equations for a vortex core." RAE Technical Report 65106 (1965)

55 A. Rizzi: "Numerical solution of Euler equations simulation of three-dimensional vortex flow." In AGARD FDP Symposium 'Aerodynamics of vortical type flow in three dimensions' (1983)

56 M.J. Lighthill: "Mathematics in aeronautics." J. Roy. Aeron. Soc. 64, 375-84 (1960)

57 D. Küchemann: "The aerodynamic design of aircraft." page 513, Pergamon (1978)

58 J.H.B. Smith: "A review of separation in steady three-dimensional flow." Paper 31 in 'Flow separation', AGARD CP 168 (1975)

59 B.L. Hunt: "Asymmetric vortex forces and wakes on slender bodies." AIAA Paper 82-1336 (1982)

60 E.R. Keener, G.T. Chapman, L. Cohen, J.T. Taleghani: "Side-forces on forebodies at high angles of attack and Mach numbers from 0.1 to 0.7; two tangent ogives, paraboloid and cone." NASA TM X-3438 (1977)

61 I.P. Jones: "Flow separation from yawed delta wings." Computers & Fluids 3, 155-77 (1975)

62 D.J. Peake, F.K. Owen, D.A. Johnson: "Control of forebody vortex orientation to alleviate side-forces." AIAA Paper 80-0183 (1980)

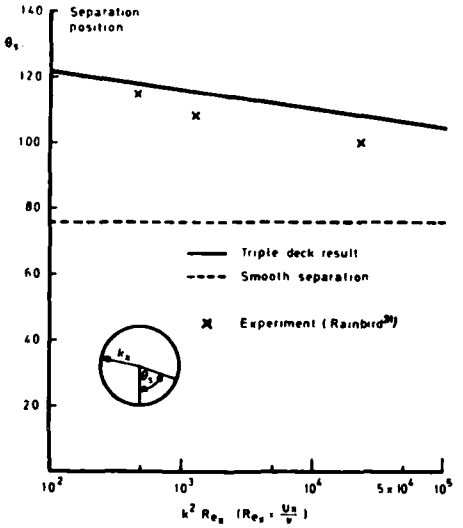

Fig 1 Variation of laminar separation position on a circular cone with a scaled Reynolds number (Fiddes[25])

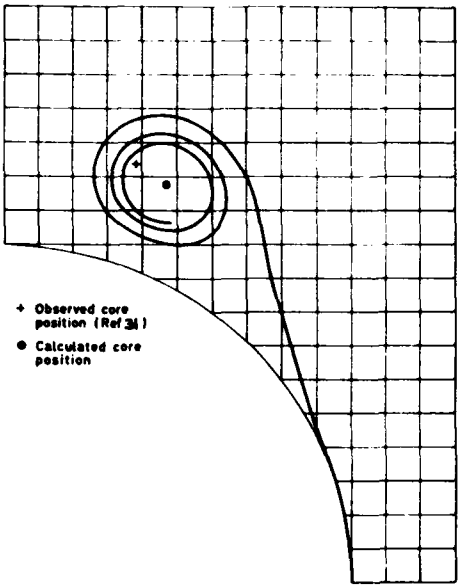

Fig 2 Observed core position on a circular cone compared with vortex-sheet calculation for same, laminar, separation position (Fiddes[25])

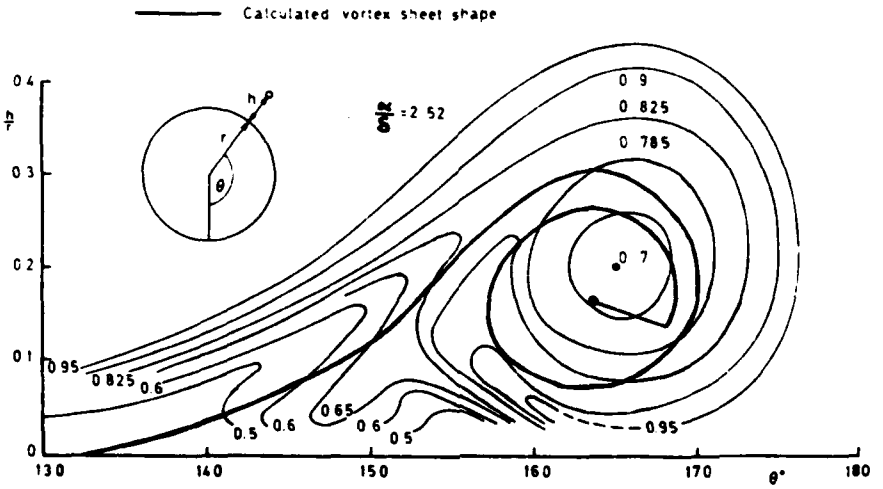

Fig 3 Observed contours of total pressure on circular cone[32] compared with vortex sheet calculation for same, turbulent, separation position (Fiddes[25])

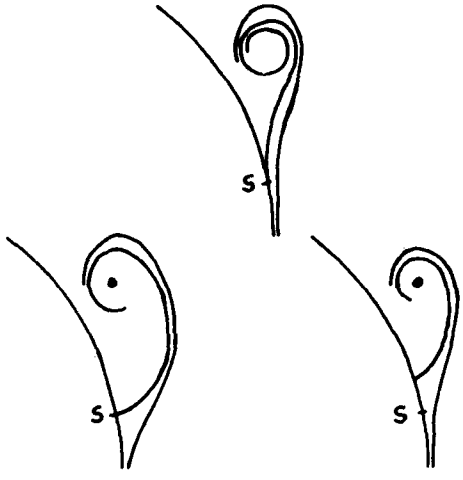

Fig 4 Effect of different Kutta conditions on conical streamline patterns (sketch only)

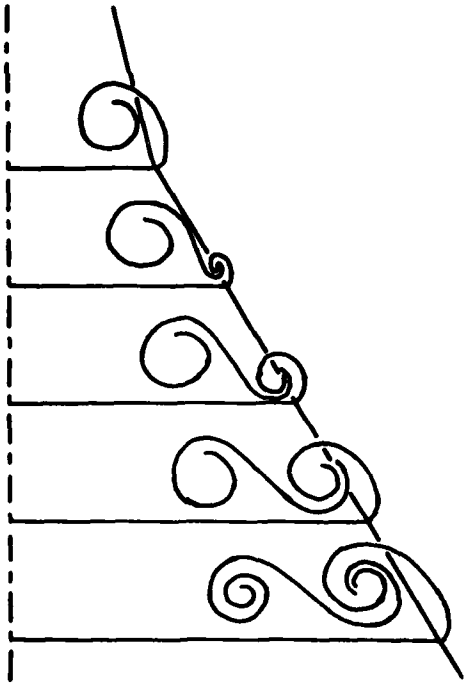

Fig 5 Shape of vortex sheet on double-delta wing with small change in sweep-back angle (sketch)

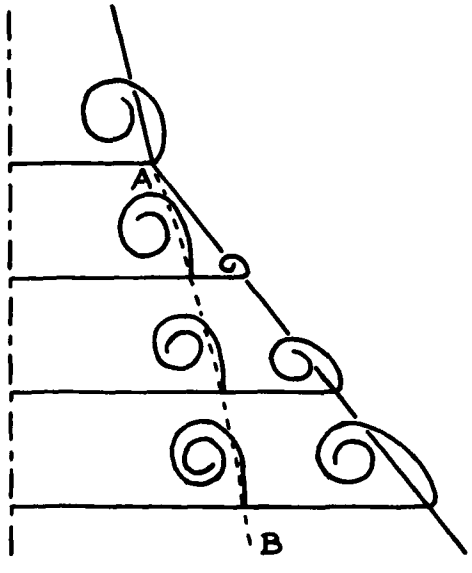

Fig 6 Shape of vortex sheet on double-delta wing with moderate change in sweep-back angle (sketch)

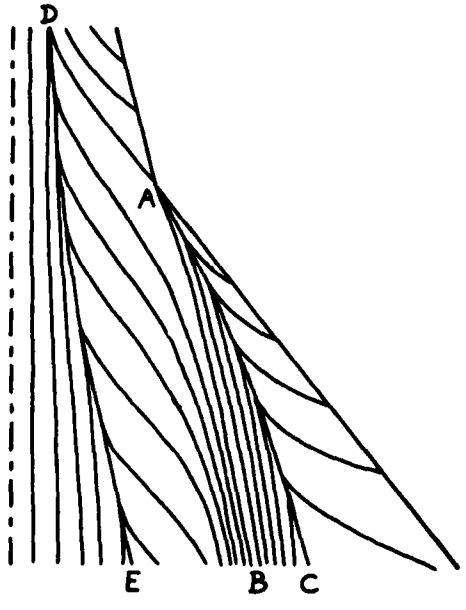

Fig 7 Surface streamline pattern on double-delta wing with moderate change in sweep-back angle (sketch)

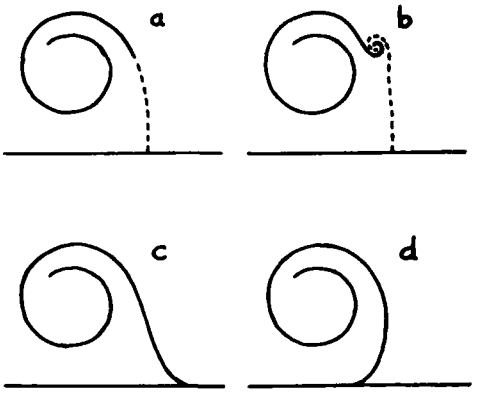

Fig 8 Possible forms for inboard vortex sheet (———) and stream surface (-----) (sketch)

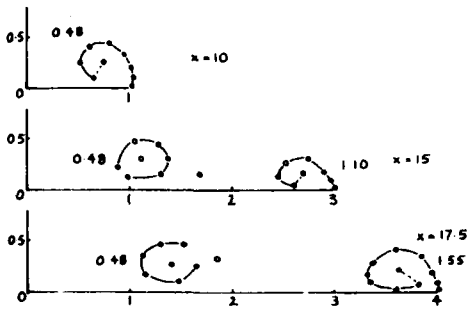

Fig 10 Calculated vortex configuration on double-delta wing at low incidence (Peace[24])

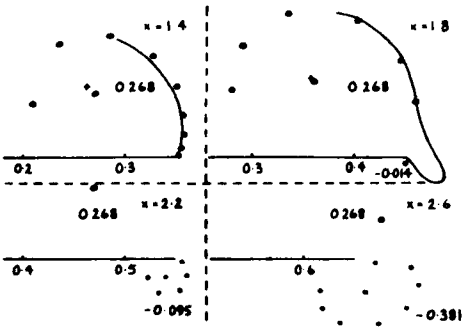

Fig 12 Calculated vortex configuration on delta wing with lengthwise camber (———, + Clark[9]; ○,● Peace[24])

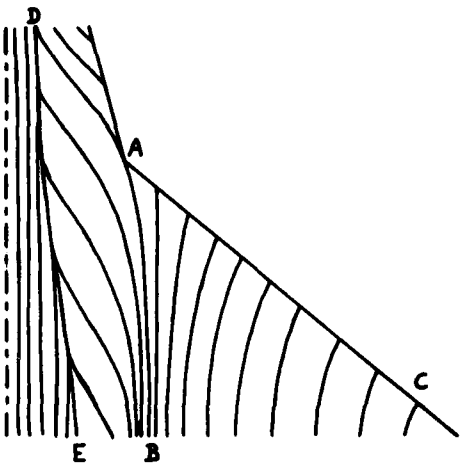

Fig 9 Surface streamline pattern on double-delta wing with attached flow on outboard panel (sketch)

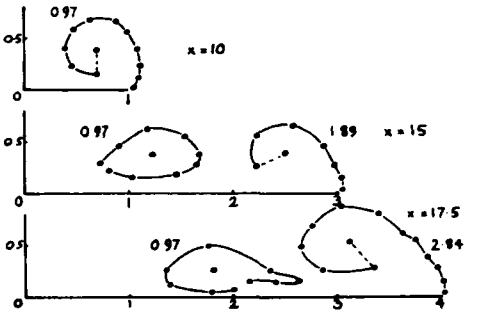

Fig 11 Calculated vortex configuration on double-delta wing at higher incidence (Peace[24])

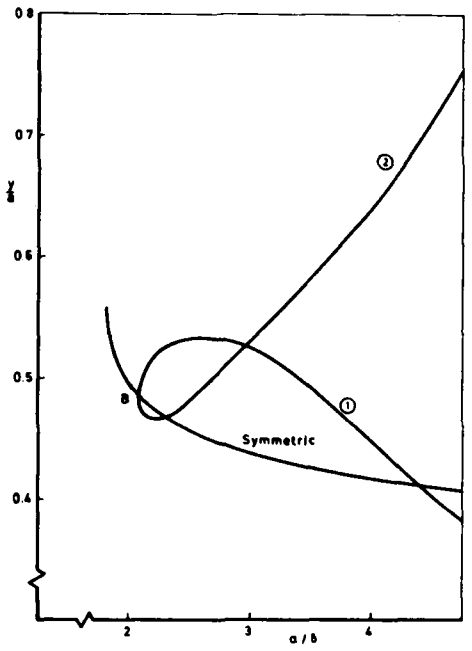

Fig 13a Bifurcation of line-vortex solutions for circular cone[40]
(a) lateral position of vortices

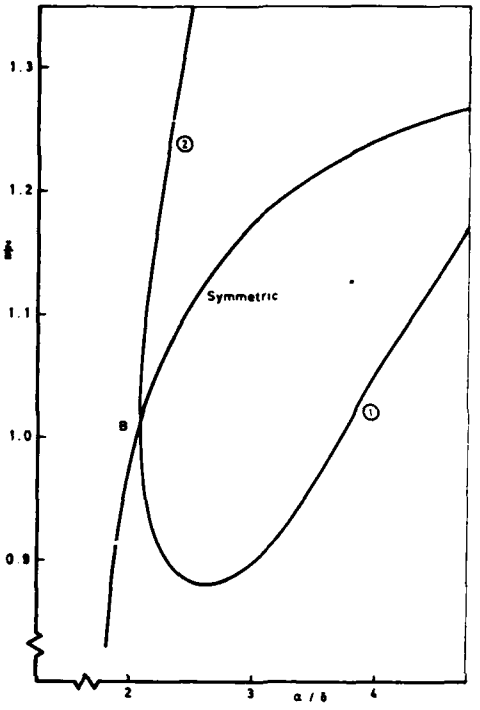

Fig 13b Bifurcation of line-vortex solutions for circular cone[40]

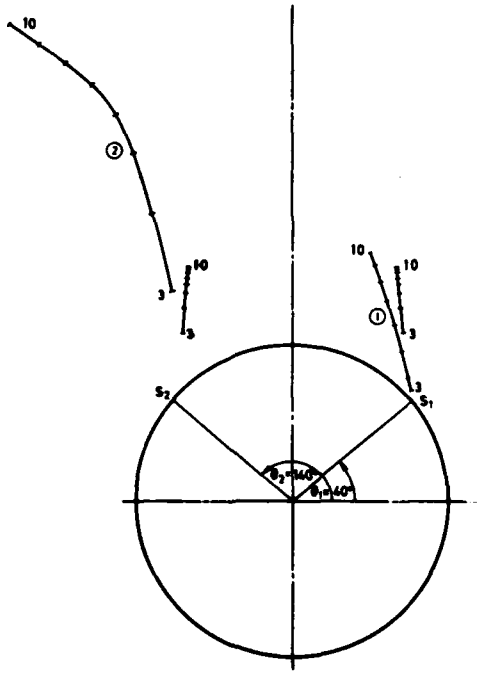

Fig 14 Variation with incidence parameter of vortex positions for symmetric separation lines on circular cone[40]

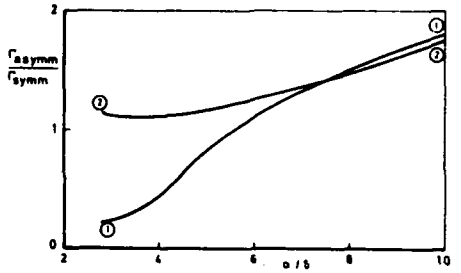

Fig 15 Circulations of asymmetric vortices referred to symmetric values for circular cone[40]

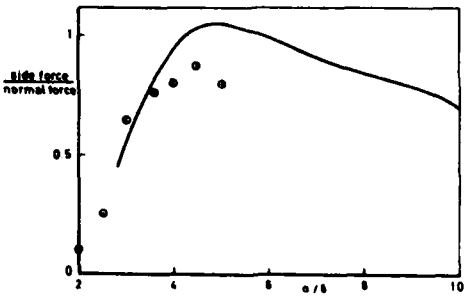

Fig 16 Ratio of side to normal force on circular cone; theory[40] and measurement[60]

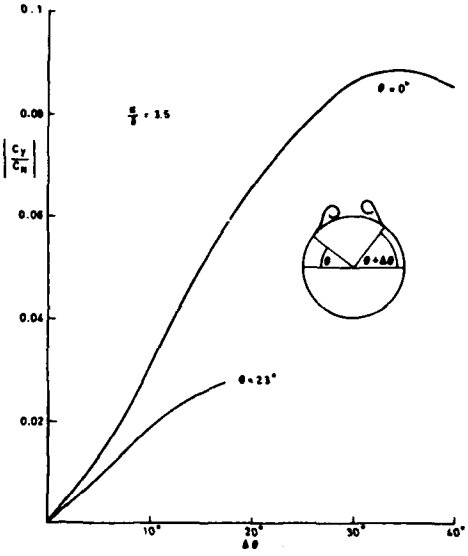

Fig 17 Effect on side force of asymmetry in separation line position for first family of line-vortex solutions[28]

(b) $\alpha/\theta_c = 3.2$

Fig 19 Shadowgraph of vortex configuration on circular cone, from behind the base (Peake, *et al*[62])

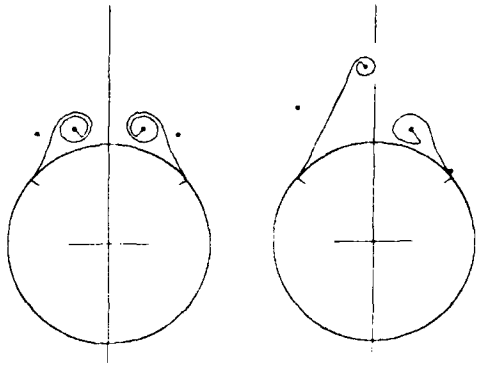

Fig 18 Symmetric and asymmetric solutions with symmetric separation lines; vortex sheet[28] and line-vortex[40] solutions

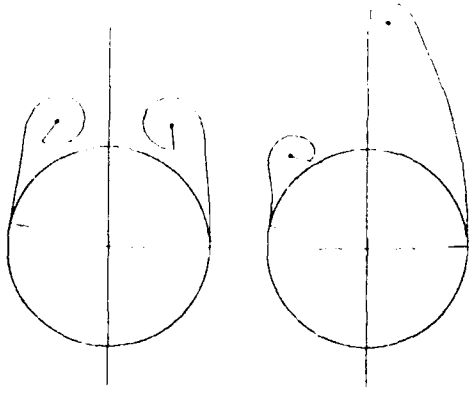

Fig 20 First (left) and second (right) family solutions for observed, laminar, separation lines[28]

COMPUTATIONAL VORTEX FLOW AERODYNAMICS

H.W.M. Hoeijmakers+
National Aerospace Laboratory NLR
Anthony Fokkerweg 2
1059 CM AMSTERDAM
The Netherlands

SUMMARY

A review is presented of computational methods for the determination of the characteristics of vortical type flows occurring in aircraft aerodynamics. The review covers primarily computational methods for computing the downstream development of vortex wakes and methods for computing the characteristics of configurations with leading-edge and strake vortices. The various computational methods in use at present are discussed in some detail. The possibilities and limitations of the methods are indicated and results of different methods are compared and discussed.

Prospects for improving existing computational methods and promising new developments are identified.

1. INTRODUCTION

In aerodynamics vortical type of flows usually arise from some form of flow separation (Refs 1, 2). The relatively large-aspect-ratio wings of subsonic and transonic transport aircraft are designed such that boundary-layer type of separation occurs in relatively small regions only. For this type of configurations vortical-type flows occur primarily in the tip region of wings, deployed flaps, extended slats and in the wake. In the rolling-up wake the trailing vorticity becomes concentrated into two or more vortex cores. Usually the details of the wake have only a minor influence on the pressure distribution on the generating airplane itself, leading to a simplified treatment in classical wing theory (e.g. Ref. 3), panel methods for linearized flow (e.g. Ref. 4) and current computational transonic potential flow methods (e.g. Ref. 5). However, the strong and persistent trailing vortex system of large transport aircraft has proven to form a possible hazard for other air traffic, which has resulted in the present stringent rules imposed on air traffic involving large planes. The most important vortex flow problems for large-ratio wings are formed by the interaction of the rolling-up wake of an extended slat with the flow over the main wing component, the interaction of the wake of the wing with the flow about deployed flaps and to a lesser extent the flow near the wing tip and the interaction of the wake of the wing and the flow about the tail. In off-design conditions boundary-layer separation may result into a complicated and usually unsteady vortical flow pattern which may be related to the occurrence of buffet.

Vortex flow associated with flow separation from leading, side and trailing edges plays an important role in the high-angle-of-attack aerodynamics of various modern fighter aircraft (e.g. Ref. 6). Examples are aircraft designed for high speed employing the slender-wing concept with highly swept and aerodynamically sharp leading edges and aircraft designed for maneuvering employing the strake-wing concept or the close-coupled canard concept. For these configurations the introduction of sharp edges results in a flow structure that is "controlled", i.e. steady and stable and maintainable within a wide range of Reynolds number, Mach number, angle of attack, etc. The pressure distribution associated with the vortex flow is such that the convential type of ("uncontrolled") boundary-layer type of separation is delayed to a higher angle of attack. Moreover the lift increases more rapidly with angle of attack than in absence of vortex flows, resulting in a substantial increase in lift capability. A limit to the favourable effects is reached when large-scale vortex breakdown occurs above the wing. Since the attached flow theories commonly used in present-day design procedures are inadequate to predict the characteristics of configurations employing vortex flow, the design of these configurations has been almost entirely empirical. In these circumstances the resulting aircraft geometry is inevitable the result of extensive and costly cut-and-try type of wind-tunnel tests, including measurement of detailed surface pressure distributions. If the vortex lift capabilities of slender-wing, strake-wing and canard-wing configurations are to be fully understood and utilized a detailed knowledge and adequate mathematical modeling of this type of flow is required. It is in this area that computational methods, able to predict the detailed structure of the flow field, can make a major contribution. This contribution consists in reducing the number of configurations to be considered for wind-tunnel testing and by guiding the designer, possibly with the aid of an automated optimization procedure, towards a more optimal design. (See reference 7 for a general discussion of applying computational aerodynamics in design and reference 8 specific for a possible role in high-angle-of-attack aerodynamics.)

Another fascinating flow problem is the vortex flow associated with flow separation from smooth slender bodies, pertinent to aircraft noses and missiles (Refs 2 and 6). At low incidences the flow separates symmetrically and a symmetric flow pattern occurs. At higher incidences the flow may still separate nearly symmetrically (or forced to do so), however, the flow may lock into an asymmetric flow pattern or even switch occasionally from one asymmetric pattern to another one (Ref. 9). This asymmetric flow pattern is accompanied by lateral forces of the same order of magnitude as the normal force, which especially in case of a switching pattern may cause guidance and control problems. Prediction methods for these vortex flows will necessarily also have to exhibit multiple possible solutions. In contrast to vortex flow associated with separation from leading, side and trailing edges of lifting components the smooth-surface (primary) separation position is not known a priori and has to be determined as part of the solution. Since the separation position depends amongst others on Reynolds number, such a prediction method has to account in one way or another for viscous effects.

Still another class of configurations where vortical flow effects are of great importance, but will not be considered in the present paper, are helicopters and also wind turbines and propellers. Here there is a strong interaction of the (often transonic) flow about a blade with the rolling-up wake of the preceding blades (e.g. Refs 10, 11, 12). Also in the present paper confined vortex flows and geophysical vortex flows (tornado's) will not be discussed.

+ Research Engineer, Fluid Dynamics Division

It is the purpose of the present paper to review computational methods for vortex wakes and computational methods in the prediction of the flow about configurations that generate a vortical type of flow and that to a certain extent exploit this vortex flow profitably. The characteristics feature of the latter flow is its strong nonlinearity; due to vortical effects the airloads increase nonlinearly as the angle of attack is increased. As the Mach number is increased from low subsonic to transonic and supersonic also strong nonlinear compressibility effects (shock waves) will occur and in general a strong coupling between both types of nonlinearities may occur (e.g. Ref. 13). While the development and use of computational methods for either one of these nonlinearities has been quite extensive the development of methods for the coupled effects of these nonlinearities has only recently attracted increased attention. In the present paper only computational methods for configurations with vortex flow associated with separation from the leading, side and trailing edges will be discussed. However, it is noted that for configurations with vortex flow associated with separation from the smooth surface the same type of computational methods can be used if the separation lines are specified and relatively highly swept. As a matter of fact, at present such methods are used in conjunction with a method that models the separation process, i.e. determines the line of separation. Especially in missile aerodynamics a number of advanced engineering methods have been developed that employ this concept.

Computational methods for the flow about oscillating configurations have not yet been developed to the same extent as the methods for steady flow. Although some of the steady flow methods discussed here have been extended to the case of oscillating configurations these will not be considered here.

The various methods will be discussed primarily with a view toward three-dimensional subsonic steady flow applications. The present review is meant to give some insight into the weaknesses, strengths and prospects of the different methods.

Recent other reviews of methods for the computation of vortical type of flows that also provide additional background have been presented by Smith (Refs 14 and 15), Saffman & Baker (Ref. 16) and Leonard (Ref. 17).

In Chapter 2 computational methods will be discussed for computing vortex wakes, where in general the interaction of the vortex flow with the generating configuration is weak. In Chapter 3 methods are discussed for configurations with vortex flow separation from leading and side edges where a strong interaction takes place between vortex flow and the configuration. In Chapter 4 the methods are summarized and possible improvements are indicated. The final chapter contains conclusions regarding the existing computational methods, their prospects for future improvements and extensions.

2. VORTEX WAKES

In this chapter computational methods are discussed for computing the development of the wake shed at the trailing edge of wings. For transport type aircraft in cruise condition the precise shape of the wake has in general only a small effect on the lift and on the pressure distribution on the wing. It is therefore general practice in most current computational methods for transport type aircraft to assume a rigid wake of some suitable shape. It has been demonstrated that the differences between the pressure distribution computed assuming a rigid wake and the one computed with a "relaxed" wake are confined to the trailing edge and tip regions. This suggests then that in order to include more accurate boundary layer corrections, for which the pressure at the trailing edge is rather important, a more accurate description of the wake in this region is necessary. This is also true for transport type aircraft in landing or take-off configuration and also for fighter aircraft, where in general there is a stronger interaction.

In this chapter first a qualitative description of the flow will be given, followed by a description of various computational methods.

2.1 Description of the flow

At the trailing edge of a wing of finite span at angle of attack vorticity is shed due to a difference in direction of the flow velocity on upper and lower surface at the trailing edge. If the Reynolds number is large, convection dominates diffusion and the vorticity remains within a thin free shear layer. The characteristic feature of a free shear layer is that under influence of the velocity induced by its own vorticity the shear layer tends to roll-up into vortex cores (see Fig. 1). At free edges of a shear layer usually a single-branched spiral vortex (the tip vortex) is formed, while depending on the shed vorticity distribution, at initially smooth portions of the layer one or more double-branched vortex cores may be formed. In downstream direction vorticity is continuously fed into the vortex cores, resulting into a growth of the vortex cores both in strength and usually also in dimension and resulting into an extensive stretching of the shear layer in the cross-flow plane.

Further downstream of the wing the roll-up process will be completed and most of the vorticity is contained within the cores. As this stage interaction between and merging of cores with vorticity of the same or opposite sign may occur followed by viscous diffusion and decay. Alternatively complicated longitudinal instabilities may be triggered before the merging or decay process has started, resuling in a break-up of the trailing vortex system.

In the present paper only the initial roll-up will be discussed. For a discussion of methods for computing the later stages of development of vortex wakes the reader is referred to e.g. references 18 and 19. During the initial roll-up process, for the high Reynolds numbers pertinent to aircraft aerodynamics, the flow may be considered to be a potential flow with embedded regions of rotational flow of infinitesimal extent (vortex sheets) and regions of rotational flow of finite extent (vortex cores). The vortex sheets model the (stretching) thin shear layers, while the vortex cores model rolled-up regions. The latter may be thought of as created by the mixing of subsequent loops of the spiraling shear layer where viscous diffusion has smeared out the large velocity gradients across the shear layer (see Refs 20, 21 and 22). Subsequently a distinct shear layer cannot be observed anymore, only a region of continuously distributed vorticity remains. In this region viscous forces can be ignored again, except for a region near the center of the core where velocity gradients are large and a viscous subcore is formed. Alternatively, for the limiting case of infinite Reynolds number the core consists of a tightly wound vortex sheet of infinite angular extent, which in this view also represents an inviscid core of rotational flow of finite extent (Fig. 2). The wake vortex problem of current practical interest occurs at landing speeds, where in first approximation the flow is assumed incompressible.

2.2 Two-dimensional time-dependent methods

Under the assumption that the trailing vortex sheet is only mildly curved in streamwise direction and that no direct influence is felt of the upstream wing, the original three-dimensional steady problem is reduced to a two-dimensional time-dependent problem in the cross-flow (Trefftz) plane. This is accomplished by replacing the streamwise coordinate x (see Fig. 1) by $U_\infty \tau$, where τ is a time-like coordinate. The resulting problem is an initial-value problem describing the motion of a two-dimensional vortex sheet as it is convected with its own induced velocity in subsequent cross-flow planes. The initial conditions of the problem are the shape of the trailing (or shedding) edge and the distribution of the streamwise component of the vorticity at this edge. The latter is proportional to the spanwise derivative of the wing loading. The time-dependent analog of the vortex wake roll-up problem is a classical problem in aerodynamics and has been studied by a large number of researchers. It can be expressed as

$$\vec{u}(\vec{x}(t;\tau)) = \frac{d\vec{x}}{d\tau} = -\frac{1}{2\pi}\vec{e}_x \times \left(\int_C \frac{d\rho}{dt'} \frac{\vec{x}(t)-\vec{x}(t')}{|\vec{x}(t)-\vec{x}(t')|^2}\, dt' - \left[\rho(t') \frac{\vec{x}(t)-\vec{x}(t')}{|\vec{x}(t)-\vec{x}(t')|^2} \right]_{t'=0}^{t'=T} \right) \qquad (2.1)$$

where the vorticity distribution is expressed in terms of the doublet distribution $\rho(t)$ and $\vec{x}(t;\tau)$ is the description of the sheet C in terms of its arc length t, $t\in[0,T]$. This equation expresses that $\rho(t)$ is convected as conserved quantity. In equation (2.1) it is assumed that $\rho(t)$ and C are continuous or alternatively can be broken up into continuous parts. In the latter case one has to sum the contribution of each continuous part. In this section first computational methods will be described used for computing vortex wake roll-up, followed by the comparison of numerical results of these methods (Figs 7-9).

Discrete-vortex approximation

In the past there have been a large number of attempts to model vortex sheet motion by replacing the continuous vortex sheet by a finite number of vortices, or, equivalently, the doublet sheet by segments carrying a piecewise constant doublet distribution (see Fig. 3a). Equation (2.1) is then reduced to

$$\frac{d\vec{x}_i}{d\tau} = \frac{1}{2\pi}\vec{e}_x \times \sum_{\substack{j=1 \\ j\neq i}}^{N} \Delta\rho_j \frac{\vec{x}_i-\vec{x}_j}{|\vec{x}_i-\vec{x}_j|^2} \quad , \; i = 1(1)N \qquad (2.2)$$

where $\Delta\rho_j$ is the strength of the discrete vortex at $\vec{x}_j$. The first one to attempt this approach was Rosenhead (Ref. 23) in studying the nonlinear Kelvin-Helmholtz instability of a two-dimensional periodic vortex sheet of constant strength. Westwater (Ref. 24) was the first to apply this approximation to vortex wake roll-up. He computed the evolution of the wake behind an elliptically loaded wing using only 20 vortices and carrying out 33 time steps by hand, resulting into a relatively smooth roll-up. With the advent of powerful computers Westwater's case was reconsidered using more vortices and smaller time steps. It appeared, however, that because of the singular behaviour of the induced velocity this approach inevitably leads to chaotic motion of the vortices in the region of the (single-branched) spiral. In this region the identity of the sheet is lost. Different approaches have been attempted to regularize the velocity field induced by the discrete-vortex approximation. The first one is to introduce a finite ("viscous") core for the discrete vortices in which the velocity induced by the vortex is modified to remain finite (Refs 25 and 26). The artificial viscosity introduced in this way depends on more or less arbitrary parameters such as core size and core velocity distribution. A second approach is to use a process of amalgamation in which vortices are combined if they approach each other too closely and also if due to the stretching of the sheet the vortices represent a too large part of a turn of the spiralling sheet (Moore, Ref. 27). In the latter case this results into a representation for the core region. A third alternative approach is to use the so-called subvortex technique (Maskew, Ref. 28) where a vortex is divided into subvortices whenever it is approached too closely. However, all these concepts result into chaos at some stage in the computation. These numerical problems stem from the circumstance that the sheet stretches considerably as it rolls up. This implies that a particular discrete vortex has to represent a portion of the sheet that increases in length as the computation progresses. In the highly rolled-up regions, where the stretching is largest, this rapidly leads to an inadequate representation of the spiraling sheet. The technique of periodically redistributing the discrete vortices as introduced by Fink & Soh (Ref. 29) has been the most successful in producing smooth vortex-sheet roll-up with more discrete vortices and over longer periods than had been reported previously. However, recent investigations by Baker (Ref. 30) into the stability of the rediscretization technique for the case of the wake behind a ring wing, where a double-branched spiral is formed, demonstrate that this method eventually end into chaos as well. In applying a rediscretization technique in addition to an amalgamation procedure for double-branched spirals Bromilow & Clements (Ref. 31) succeeded in computing a smooth development of the nonlinear Kelvin-Helmholtz instability.

Although it must be noted here that the matter of existence and uniqueness of solutions for the continuous initial-value problem has not yet been fully resolved (e.g. Moore, Ref. 32), it appears that there may be a fundamental difference between continuous vortex sheets and its discretization as an assembly of point vortices. This latter question is discussed to some length by Moore (Ref. 33).

"Cloud-in-cell" method

The computational effort required for the discrete-vortex method using N vortices is $O(N^2)$ per time step. In order to reduce this computing time the "cloud-in-cell" method (Ref. 34) may be used. In this method, the Lagrangian treatment of the vorticity field is retained, but the velocity field is obtained from solving the Poisson equation on a fixed rectangular and equidistant Eulerian mesh. The latter can be accomplished efficiently by use of a fast Poisson solver. In incompressible and inviscid flow the Euler equations are expressed as

$$\vec{\nabla}.\vec{u} = 0 \qquad (2.3a)$$

$$\frac{\partial\vec{\omega}}{\partial t} + (\vec{u}.\vec{\nabla})\vec{\omega} = (\vec{\nabla}.\vec{\omega})\vec{u} \qquad (2.3b)$$

$$\vec{\omega} = \vec{\nabla}\times\vec{u} \qquad (2.3c)$$

For two-dimensional flow these equations can be written in terms of the stream function ψ and the vorticity

$\vec{\omega} = \omega\vec{e}_x$ as:

$$\frac{\partial\omega}{\partial t} + \vec{u}.\vec{\nabla}\omega = 0 \qquad (2.3d)$$

$$\nabla^2\psi = -\omega \qquad (2.3e)$$

where $\vec{u} = (0, v, w) = (0, \frac{\partial\psi}{\partial y}, -\frac{\partial\psi}{\partial z})$. Note that in two dimensions there is no counterpart for the three-dimensional vorticity stretching term $(\vec{\omega}.\vec{\nabla})\vec{u}$. The vorticity transport equation (2.3d) is accounted for by a Lagrangian treatment, i.e. moving the N discrete vortices with the local velocity. The vorticity ω in equation (2.3e) is obtained by redistributing the discrete vortices over the nearest four corner points (see Fig. 4), usually employing some area-weighting scheme. With appropriate far-field boundary conditions, equation (2.3e) is then solved in M $\log_2$ M operations where M is the number of grid points. The velocity at the cell corners is obtained from the computed ψ's at these grid points by finite-difference expressions. Finally the velocity at the position of the discrete vortices is obtained by interpolation from the velocity at the nearest cell corners. In general M will by O(N) and possibly much larger, so that also accounting for the time spent in computing the far-field boundary conditions, the saving may turn out to be disappointing in practice. The "cloud-in-cell" method has as advantage that for the velocity field calculation each singular discrete vortex is effectively distributed over a mesh cell resulting in a continuous vorticity distribution (see Fig. 4). The artificial viscosity effectively introduced in this way is mesh dependent. In addition, the mixed Lagrangian/Eulerian description retains the desirable feature that the vortex wake remains compact and is not diffused, as would be the case if the vorticity transport equation was treated in an Eulerian fashion also. Baker (Refs 35, 36) has applied the "cloud-in-cell" method to cases of vortex wake roll-up, using of the order of 2000 vortices and a grid size of 129x129. The computed results show that, although the many small-scale instabilities introduced by the grid destroy the definition of the sheet, the large-scale vortex structures appear to emerge consistently. However, the method has the same deficiencies as all discrete vortex methods, namely that (i) at locations where the sheet is stretched the representation of the vortex sheet becomes rapidly inaccurate, (ii) in regions of roll-up the vortices get clustered close together and the definition of the sheet is lost and (iii) because of a discrete form of Kelvin-Helmholtz instability small-scale grid dependent structures appear which relevance to the large-scale roll-up process is difficult to assess.

Finally it is noted that Murman & Stremel (Ref. 37) have modified the stream-function/vorticity formulation into a velocity-potential/vorticity formulation in order to try to establish a link with modern compressible potential flow calculations. In the latter codes the wake is treated as a planar internal surface of the mesh. By tracking the wake in the Lagrangian frame and distributing it to the Eulerian frame for the potential calculation, the wake is permitted to float through the mesh. In this way the topologically quite impossible requirement to fit the mesh to the nonplanar rolling-up wake is eliminated. In some sense the wake is "captured" rather than "fitted". Thus far no application of this concept to a three-dimensional problem has been reported.

Panel methods

Employing a more accurate method than the discrete-vortex method for computing the induced velocity field will to a large extent exclude the appearance of spurious numerical effects. A method which serves this purpose is the panel method. In this method the sheet is divided into a large number of segments. On these panels both $\rho(t)$ and $\vec{x}(t)$ are approximated by piecewise polynomial representations. The Cauchy-Principal-Value integral in equation (2.1) is evaluated such that the correct behaviour of the induced velocity is ascertained at points near the sheet.

Mokry & Rainbird (Ref. 38) employing a first-order panel method (straight segments, panel-wise constant $\frac{d\rho}{dt}$) obtained promising results. The second-order panel method (curved segments, panel-wise constant $\frac{d^2\rho}{dt^2}$) developed at NLR (Ref. 39) is capable to describe complicated vortex sheet motion in a reliable and stable manner. In the following the most important features of this method, designated VOR2DT, are described.

(i) Vortex cores. In the method vortex sheets and vortex cores are identified explicitly as such during the computation. The model used for single-branched vortex cores is depicted in figure 3b. In this model the influence of the tightly rolled-up inner portion of the sheet (Fig. 2a) on the outer flow field is represented by an isolated line vortex at the center of vorticity of the spiral. The vortex is connected to the remainder of the sheet by a cut (feeding sheet). Such a representation has been used by Smith (Ref. 40) for the case of a leading-edge vortex above a slender delta wing and by Pullin (Ref. 41) in his study of similarity solutions for rolled-up vortex sheets. For a double-branched vortex core (Fig. 2) a similar model is derived by representing the highly rolled-up inner region by an isolated line vortex connected to the remainder of the sheet by cuts (Fig. 5). Such a model has been used also by Pullin & Phillips (Ref. 42) for an investigation into the generalization of Kaden's problem of the roll-up of a semi-infinite vortex sheet.

(ii) Rediscretization. The representation of the sheet by panels is chosen such that the spatial discretization error is uniform along the sheet and remains the same as the roll-up proceeds. This is accomplished by a rediscretization technique based on an adaptive curvature-dependent panel scheme. In this scheme the panel size Δt is computed as

$$\Delta t = \text{Min}\{\Delta_{max}, R\theta_{max}\} \qquad (2.4)$$

where Δ_{max} is the basic panel size and $R\theta_{max}$ spans an arc of θ_{max} radians of a circle with radius R equal to the average radius of curvature of the panel. The basic panel size Δ_{max} is chosen such that the desired degree of accuracy is ensured in regions of relatively small curvature. Its choice is primarily governed by the desired accuracy for the panelwise representation of the doublet distribution. The second parameter θ_{max} then ensures that at highly curved parts of the sheet the panel size is reduced and the overall accuracy is maintained. During the roll-up process the sheet tends to wrap around the vortex cores, considerably stretching in the process, resulting in an increasing number of loops as the computation progresses. A solution to this problem is to specify the maximum angular extent of the rolling-up sheet, i.e. the attitude of the cut(s) is held fixed in time. Any part of the sheet stretched beyond this point is cut off and its vorticity is dumped into the core. In this manner the vortex cores are allowed to grow in strength in downstream direction, which also resembles reality.

(iii) Singular doublet distribution. At $\tau = 0$ the doublet distribution will behave like $\rho(t) \sim \sqrt{\epsilon}$ near the wing tip, ϵ being the distance from the tip. If a panel method is used to compute the velocity field

induced by a doublet distribution with such singular behaviour large errors appear near the wing tip and no smooth roll-up can be expected. In view of this Pullin's (Ref. 41) self-similar solution for the initial roll-up is used to provide the initial value for the present method. This solution, in which the single-branched tip vortex is already present, is regular and can be handled by the panel method. Finally note that the "cloud-in-cell" technique can equally well be formulated for vortex sheets discretized by piecewise continuous vortex sheet segments as used in panel methods.

Vortex layer and finite core methods

The representation of the inner portion of vortex cores by an isolated vortex connected to the sheet by cuts, is only valid near the center of the core where the spiralling sheet is more or less of circular shape. In downstream direction the relative dimension of the rolled-up region increases and in general it becomes less circular in appearance. In the case of the above model the ellipticity of the rolled-up region should be represented by an increasing number of loops of the vortex sheet. A more appropriate model is the finite-core model depicted in figure 3c. Here the inner portion of the rolld-up region is represented by a region of distributed vorticity. The vorticity distribution and the shape of the inviscid rotational core follow from solving Euler's equations (Eqs 2.3a-c) within this region. The outer portion of the rolled-up region is represented by a vortex sheet as before. Note that an essential feature of the model will be to allow for feeding vorticity into the core.

Equations (2.3a) and (2.3c) are satisfied exactly by writing the velocity at $\vec{x}_o$ as

$$\vec{u}(\vec{x}_o) = \vec{u}_s(\vec{x}_o) + \frac{1}{2\pi}\vec{e}_x \times \iint_{S_c} \omega(\vec{x})\,\frac{\vec{r}}{|\vec{r}|^2}\,dS_c \qquad (2.5)$$

where $\vec{u}_s(\vec{x}_o)$ is the velocity due to the vorticity on the sheet, S_c denotes the rotational core and $\vec{r} = \vec{x}_s - \vec{x}$. The vorticity-transport equation, equation (2.3b) can then be solved by a finite-difference method. Huberson (Ref. 43) discretizes equation (2.5) using the discrete-vortex method for the sheet and a piecewise constant vorticity distribution on a rectangular equidistant Cartesian mesh. Special measures are taken to preclude a rapid diffusion of the rotational region due to the numerical viscosity, i.e. the truncated terms in the discretized version of equation (2.3b).

Portnoy (Refs 44, 45) considers a related method in which the total vortex sheet is replaced by a vortex layer of finite thickness. Moore (Ref. 46) derived the equation of motion for a vortex layer of small but finite thickness which applies only to the not rolled-up portion of the vortex layer. In references 45 and 46 the wake cross-section is divided into triangular elements, each carrying a constant vorticity distribution. The elements are convected with the self-induced velocity field (Lagrangian formulation). Since the area of region with constant vorticity is an invariant of the motion, the area of each element will remain constant even though its shape may change quite extremely. The main difficulty of the method lies in the choice of the shape of the initial cross-section. In references 45 and 46 the initial wake has an elliptic cross-section, which, at least for wings with an elliptic loading near the tip seems unrealistic. In the examples shown this is apparent by the thinning of the layer into a sheet rolling up in the same fashion as described for the vortex sheet methods. However, although some numerical instabilities are present, in the case of non-elliptic loading double-branched vortex cores evolve as regions of distributed vorticity.

Zabusky (Ref. 47) considers the problem of the interaction between isolated regions of distributed but constant vorticity. In this case the velocity induced by the cores (see Eq. 2.5) can be reduced to a contour integral,

$$\vec{u}(\vec{x}_o) = \sum_i \frac{\omega_i}{2\pi} \int_{\partial S_{c_i}} \ell n|\vec{r}|\,d\vec{l} \qquad (2.6)$$

where the summation is over all cores, ∂S_c denotes the boundary of the cores and $d\vec{l}$ is directed along ∂S_c. For a stretching contour similar rediscretization procedures are required as for the case of an evolving vortex sheet. Although it is expected that the vorticity distribution of vortex cores produced by the roll-up of a vortex layer is far from being uniform, the method of "contour dynamics" may be useful for studying the final stages of inviscid roll-up. In that case almost all vorticity is contained within a number of relatively closely spaced vortex cores which begin to interact and merge.

Weston & Liu (Ref. 48) consider the Navier-Stokes equations in vorticity/stream function formulation, i.e. equation (2.3d-e) with the vorticity transport equation replaced by

$$\frac{\partial \omega}{\partial t} + \vec{u}.\vec{\nabla}\omega = \nu\nabla^2\omega \qquad (2.7)$$

where ν is the kinematic viscosity. The Poisson equation, equation (2.3e) is solved on a subdomain D1 embedded in a larger computational domain D. The boundary conditions on the boundary of D1 and the velocity throughout D-D1 are computed by a far-field expansion of

$$\psi(\vec{x}_o) = -\frac{1}{2\pi}\iint_{-\infty}^{\infty} \omega(\vec{x})\,\ell n|\vec{r}|\,dS \qquad (2.8)$$

Assuming that the vorticity distribution is confined to a relatively small area, the far-field expansion is truncated at the third moments of the vorticity distribution. Some of these moments are invariants of the motion, which can be used to reduce computing time, or to monitor the accuracy of the method. Employing a fast Poisson solver in the domain D1 to obtain ψ the velocity in D1 is obtained by taking partial derivatives of ψ. Subsequently the vorticity distribution is advanced in time by integration of equation (2.7) using a Dufort-Frankel scheme. Compared to the methods using standard boundary conditions (e.g. Ref. 18) a two orders of magnitude reduction in computing time is achieved. Then the resulting computer resources requirements are comparable to the ones of the vortex sheet methods. Weston & Liu apply the method starting at the trailing edge of the wing. Note that it would be more appropriate to start the viscous computation with the results of one of the described methods for inviscid roll-up.

Comparison of computational results

The three cases for which results of different methods are compared are depicted in figure 6. The

first one is the classical case of the elliptically loaded wing. In figure 7a, b and c results are shown for different methods at $\tau = 1.0$, 2.0 and 4.0 respectively. It is shown (e.g. Fig. 7c) that the discrete-vortex method results into instabilities as the number of vortices is increased, and the discretization becomes rather coarse in regions where the sheet is stretched considerably. The rediscretization technique of Fink & Soh (Fig. 7a) solves these problems to some extent, especially if during the roll-up process the number of vortices is increased such that the distance between the equidistant vortices remains the same. The "cloud-in-cell" method results in unrealistic behaviour near the center of the spiral (Fig. 7a). The results of the panel method show a smooth roll-up behaviour. The results of the finite-core method and vortex-layer method are quite similar to the vortex sheet methods. However, as is clear from figure 7b the choice of elliptic cross-section as initial shape in references 44 and 45 does not result into a core region with distributed vorticity as would be expected and as is the case for the method of Huberson and that of Weston & Liu.

The second case considered is the wake behind a ringwing or nacelle (Fig. 8). This case is of interest because initially both the geometry and the doublet distribution are non-singular. It is clearly shown in figure 8a that after some time ($\tau \approx 1.5$) a vortex structure evolves which resembles the tip vortex of the preceding case. The discrete-vortex method of Fink & Soh (Fig. 8a) results into instabilities in the region where the now double-branched vortex develops, while the panel method result shows a smooth roll-up behaviour. Results for longer times are shown in figure 8b. The cloud-in-cell method produces a number of (grid dependent) sub-scale structures. In the panel method results also long-wave (compared to the panel size) instabilities occur. Apparently, aside from the global structure, the details of the computed shapes depend on the amount of inherent smoothing applied. In the VOR2DT panel method the smoothing is controlled by the basic panel width Δ_{max}. This is clearly demonstrated in figure 8c which shows results for $\tau = 1.77$ with $\Delta_{max} = 0.1$, 0.05 and 0.025. Depending on Δ_{max} the first vortex has not yet developed or has developed further. As Δ_{max} is reduced further more waves appear that eventually will develop into vortices. Generally disturbances with a wave length of less than a few times Δ_{max} will be smoothed. This, more or less fortuitously resembles reality, where it has been observed that in shear layers regular small-scale structures with a length scale less than a few times the shear-layer thickness do not amplify into well-defined rotational cores but are smoothed out. The results presented here also suggest that the initial value problem for the inviscid evolution of a ring wing vortex sheet is ill-posed, i.e. that the vortex sheet is inherently unstable.

The last case concerns the wake of a transport aircraft with deployed part-span flaps during landing or take-off (Fig. 6). In this case the vorticity $-\rho'(t)$ changes sign, resulting in counter-rotating vortex cores. In figure 9a results are compared of the "cloud-in-cell" method and the panel method VOR2DT. Although the many small-scale structures in the results of Baker (Ref. 36) make it difficult to identify the sheet, the global structure agrees reasonably well with that of the panel method. Finally figure 9b compares the result of the VOR2DT panel method computation and the vortex-layer method of reference 48 for a longer time ($\tau = 1.0$). In both results the vortex cores have approximately the same elliptical appearance, dimension and position in space, suggesting that vorticity diffusion effects in the method of reference 48 have been small.

2.3 Methods for three-dimensional flow

Computing the development of a wake by means of the 2D time-dependent analogy provides basic insight into the development of quite general wakes as well as a useful test for mathematical models and numerical schemes. However, it suffers from a number of severe limitations if wakes of real aircraft are to be computed. The main limitation is that the influence of the upstream wing is neglected. For instance, unless some other (3D) method provides the $\tau = 0$ initial conditions, i.e. shape and shed vorticity distribution of the wake in some plane downstream of the trailing edge, a meaningfull 2D-time dependent calculation would be impossible for wings with swept trailing edges. A second severe limitation is that the interaction of the rolling-up wake with nearby parts of the configuration cannot be accounted for. The latter includes the interaction of wing and tailplane, slat and wing, wing and deployed part-span flap, etc. A further noteworthy point is that the formation of the wing-tip vortex usually starts already upstream of the trailing edge. In case of a swept-back wing tip or a sharply-edged tip the flow may separate all along the tip. In case of a rounded tip the situation is more complicated. Here the flow at the wing tip may partly be attached but downstream of some (Reynolds number dependent) position be separated. In either case there is a relatively strong interaction between the rolling-up shear layer from the tip and the flow around the tip. In most spanwise load distributions obtained in experiments this is apparent as a relatively small region of increased loading, the details of which depend on the geometry of the wing tip. Thus clearly a fully three-dimensional method is necessary for early stages of vortex-wake roll-up. In the present section cases are considered with a relatively weak interaction between the rolling-up wake and the generating configuration. Cases with a strong interaction will be considered in the next chapter

2.3.1 Potential flow methods

It follows from the description of the high-Reynolds number flow (section 2.1) that if the location of the separation lines are known the flow may be assumed irrotational with embedded regions of rotational flow. These regions are either of infinitesimal extent, i.e. vortex sheets, or of small but finite extent, i.e. vortex cores. Assuming subsonic subcritical (linear compressible) flow, the flow is governed by the Prandtl-Glauert equation for the perturbation velocity potential $\varphi(\vec{x})$

$$\beta^2 \frac{\partial^2\varphi}{\partial x^2} + \frac{\partial^2\varphi}{\partial y^2} + \frac{\partial^2\varphi}{\partial z^2} = 0 \quad , \quad \beta^2 = 1 - M_\infty^2 \tag{2.9a}$$

The velocity is given by $\vec{u} = \vec{U}_\infty + \vec{\nabla}\varphi$ with $\vec{U}_\infty = U_\infty \vec{e}_x$. Employing Green's third identity the solution of equation (2.9a) is expressed as the velocity field induced by a source distribution $q(\vec{x})$ on S_w and a doublet distribution $\mu(\vec{x})$ on $S_w + S_v$:

$$\vec{u}(\vec{x}_o) = \vec{U}_\infty + \frac{1}{4\pi} \iint_{S_w} q(\vec{x}) \frac{[B](\vec{r})}{|[B]\vec{r}|^3} dS(\vec{x}) + \frac{\beta^2}{4\pi} \iint_{S_w+S_v} \vec{\gamma}(\vec{x}) \times \frac{\vec{r}}{|[B]\vec{r}|^3} dS(\vec{x}) - \frac{\beta^2}{4\pi} \int_{\partial(S_w+S_v)} \mu(\vec{x}) \frac{\vec{r} \times d\vec{\ell}(\vec{x})}{|[B]\vec{r}|^3} \tag{2.9b}$$

where $\vec{r} = \vec{x}_o - \vec{x}$, $B = \begin{pmatrix} 1 & 0 & 0 \\ 0 & \beta & 0 \\ 0 & 0 & \beta \end{pmatrix}$, $\vec{\gamma} = -\vec{n} \times \vec{\nabla}\mu$ is the surface vorticity vector and $\vec{n}$ the unit normal. Across the singularity distribution the velocity is discontinuous. This discontinuity can be expressed as

$$\Delta\vec{u}(\vec{x}_o \in S) = q(\vec{x}_o) \frac{\vec{n}}{\beta^2 |[B^{-1}]\vec{n}|^2} + \vec{\gamma}(\vec{x}_o) \times \frac{[B^{-1}]([B^{-1}]\vec{n})}{|[B^{-1}]\vec{n}|^2} \tag{2.9c}$$

The pressure coefficient follows from Bernouilli's equation as:

$$c_p = \frac{p - p_\infty}{\frac{1}{2}\rho_\infty U_\infty^2} = \frac{2}{\gamma M_\infty^2} \left[\left\{ 1 + \frac{\gamma-1}{2} M_\infty^2 \left(1 - \frac{|\vec{u}|^2}{U_\infty^2} \right) \right\}^{\frac{\gamma}{\gamma-1}} - 1 \right] \tag{2.9d}$$

which is the so-called isentropic formula. The second-order accurate approximation (in terms of the perturbation velocity $\vec{\nabla}\varphi$) to the isentropic formula is:

$$c_{p_2} = - \left(2 \vec{U}_\infty \cdot \vec{\nabla}\varphi + |\vec{\nabla}\varphi|^2 - M_\infty^2 \frac{(\vec{U}_\infty \cdot \vec{\nabla}\varphi)^2}{U_\infty^2} \right) / U_\infty^2 \tag{2.9e}$$

The boundary conditions that apply on the configuration and vortex wake are (Fig. 10):
(i) Zero normal velocity on the solid surface S_w and on the vortex sheet S_v, i.e.

$$\vec{u} \cdot \vec{n} = 0 \quad \text{on } S_v \text{ and } S_w \tag{2.9f}$$

Note that this condition implies that according to equation (2.9c) thin wings as well as vortex sheets have to carry a source distribution of strength $\beta^2 \vec{\gamma} \times \vec{n} \cdot [B^{-1}]([B^{-1}]\vec{n})$, which is nonzero for $M_\infty \neq 0$.
(ii) Zero pressure jump across the vortex-sheet S_v, i.e.

$$\Delta C_p = C_p^+ - C_p^- = 0 \quad \text{on } S_v \tag{2.9g}$$

In incompressible flow it follows from Bernouilli's equation (2.9e) and equation (2.9c) that the zero pressure jump can be written as

$$\vec{\gamma} \times \vec{n} \cdot \vec{u} = 0 \quad \text{on } S_v \tag{2.9h}$$

where $\vec{u}$ is to be taken as the average velocity, i.e. $\frac{1}{2}(\vec{u}^+ + \vec{u}^-)$ on S_v. This condition implies that vortex lines and streamlines are parallel in incompressible flow. As far as vortex wakes is concerned incompressible flow will be assumed in the remainder of this chapter.

The unknowns of the problem are the singularity distributions on the configuration and on the wake as well as for the unknown geometry of the wake. Because of the nonlinearity associated with the unknown geometry an iterative solution procedure has to be employed. For the case of weak interaction considered here, a convenient procedure is obtained by fixing the geometry of the wake and its singularity distribution, choosing some degenerate form of the boundary conditions on the vortex sheet (i.e. the Kutta condition) and solving the resulting linear problem for the singularity distribution on the wing. Subsequently the wake is relaxed such that a better approximation to the true boundary conditions is obtained, followed by solving again a linear problem for the singularity distribution on the wing but taking into account the latest geometry of the wake.

Vortex-lattice methods

The extension of the discrete-vortex method to three dimensions is the vortex-lattice method. This method has found wide application for computing the attached flow loading of lifting surfaces. In the vortex-lattice method the lifting surface is divided into elements. Each element carries a line vortex along its ¼-chord line connected to line vortices trailing to infinity downstream along the side edges of the element. In this way a horse-shoe vortex is associated with each element. The strength of the vortices are determined by imposing the zero-normal velocity condition (Eq. 2.9f) at the midpoint of the ¾-chord line of the elements. Butter & Hancock (Ref. 49) were amongst the first to attempt to relax the line vortices downstream of the trailing edge comprising the wake. Also Hedman (Ref. 50), Rom & Zorea (Ref. 51) and Mattei & Santoro (Ref. 52) developed a computational procedure to relax the wake using a vortex lattice method. In some of these cases the strength of the vortices were not updated from the values obtained for the planar initial wake. The vortex-lattice method developed by Rehbach (Refs 53, 54) includes the effect of separation from the wing tip. The flow separation from the tip is simulated by letting the streamwise trailing vortices nearest to the tip also free to align with the local velocity. Maskew (Ref. 55, 56) developed a vortex-lattice type of method in which on the wing vortex rings are used instead of horse-shoe vortices. Both representations are equivalent to piecewise constant doublet distributions, the former on the element spanned by the horse-shoe vortex, the latter on the element spanned by the vortex ring. In Maskew's method the last vortex ring, closed be a vortex segment at infinity downstream, is again a horse-shoe vortex. Examples computed include the vortex wake of a wing-flap-tail plane configuration, indicating the development of a strong flap side-edge vortex similar to the one considered before (Fig. 9). Suciu & Morino (Ref. 57) developed a similar method and compute the three-dimensional development of the wake behind rectangular wings. For the relatively small number of elements used in all applications reported realistic results could be obtained. However, increasing the number of elements usually results into numerical instabilities of the same kind as encountered when using the discrete-vortex methods of the preceding section.

Panel methods

In panel methods (e.g. see Ref. 4) the wing is represented more accurately by singularity distributions on the surface of the wing. In most current first-order panel methods the wake is represented by discrete trailing vortices, often forming the continuation of the lift generating internal vortex lattice or vortex sheet on the wing camber surface. If the wake is not relaxed the Kutta condition is applied on the wake, just downstream of the trailing edge. If the trailing-edge angle is finite the Mangler and Smith criterion (Ref. 58) is sometimes used to determine whether the wake leaves the wing tangentially to the

lower surface or tangentially to the upper surface. This criterion, based on purely inviscid arguments, implies that at a backward swept trailing edge the wake is usually tangent to the upper surface of the wing. Using this criterion to fix the initial direction of the line vortices, Labrujère & de Vries (Refs 59, 60), using the NLR panel method, computed the downstream development of the wake behind a AR = 5 swept wing (Fig. 11a) and compared numerical results with results of experiment (Fig. 11b). The correlation is satisfactory, although in the tip region numerical problems occur, even for the coarse spanwise panel scheme used. In the comparison with experiment it also appeared that the vortex wake in the real viscous flow tends to leave the wing tangentially to the lower surface, in contradiction with the Mangler and Smith criterion. In the wake relaxation method developed at British Aerospace, the Mangler & Smith criterion is not enforced and the method embodies a number of further improvements (Jepps, Ref. 61). In the region where the sheet rolls-up into the tip vortex an amalgamation procedure, like the one developed by Moore (Ref. 27) in two dimensions, has been developed resulting into a better representation of the tip vortex. A second improvement is that a procedure is employed, analogous to Maskev's subvortex technique (Ref. 28), to compute the near-field influence of a vortex sheet represented by a discrete vortex more accurately.

Although it is possible to obtain results for weakly interacting wakes employing the methods described above, the consistency and accuracy of these results may be questionably. Improvement upon this situation may be obtained using a more accurate description of the vortex sheets (e.g. using a higher-order panel method) and the explicit introduction of vortex core models (single and double-branched) for highly rolled-up regions. This is particularly required for cases of closely coupled lifting components where there is a relatively strong interaction between the rolling-up vortex wakes and the flow about the individual components.

2.3.2 Euler equation methods

Finite difference methods for the Euler equations or Navier Stokes equations have the advantage that regions with vorticity are "captured" rather than "fitted" as in the panel method approach. One of the drawbacks is that an adequate spatial mesh system is required. The development of computational methods for solving Euler's equations has been motivated by the need to compute transonic flows involving strong shocks. The Euler equations, however, also allow for rotational effects and allow the modeling of separated flow in cases of convection dominated flows. In this view the Euler equations (2.3a-c) admit "weak" solutions with both shock waves and vortex sheets. There are, however, some fundamental differences between shock waves and vortex sheets, which have strong implications for their numerical treatment. (i) Across shockwaves there is a convective mass transfer, across vortex sheets there is none. (ii) For shockwaves uniqueness is provided by the entropy condition, for vortex sheets there appears to be no such condition. (iii) The strength of the shockwave is determined by its shape and the conditions on one side of the shock, for vortex sheets the jumps are arbitrary, except in static pressure and velocity normal to the sheet. (iv) The thickness of the shockwave is independent of the dissipation, while the width of the vortex sheet is proportional to the dissipation. The latter implies that, since in the flow regime of present interest the dissipation due to the physical viscosity is much smaller than the artificial dissipation introduced by the numerical scheme, the accurate capture of vortex sheet discontinuities is much more difficult than the capture of shockwaves.

A further point that arises is the Kutta condition. In the immediate neighbourhood of sharp edges or other locations of flow separation the local flow is dominated by viscous forces. It should be expected that one or more additional conditions (i.e. Kutta conditions) have to be provided in order to obtain physically relevant solutions of the Euler equations. If the auxiliary Kutta conditions are not provided artificial viscosity effects will determine both position of the separation point and the solution at this point. It is obvious that these artificial viscosity effects are not the same as those provoked by the physical viscosity, but they may possibly be similar at sharp edges. Especially in cases of separation from a smooth surface, like a wing tip or a slender body, the location of the separation point and the amount of vorticity shed into the field at this point and thus the global flow pattern are strongly coupled, necessitating auxiliar (Kutta) conditions for the Euler equations to properly account for real viscous effects.

At least three different numerical approaches to solve the Euler equations can be found. The first one applies in the supersonic flow regime only. In case of steady supersonic flow the method consists of marching from a sharp nose or apex downstream. In this case near the nose or apex a starting solution is required, usually provided by a known solution for a cone. The spatial marching procedure is reasonable efficient and often applied in high-angle-of-attack aerodynamics of missile configurations (e.g. Refs 62 and 63 for a recent review). In all cases a Kutta condition is required to obtain consistent results.

The second approach is to use a time-marching procedure to asymptotically approach a steady-state solution to the time-dependent Euler equations. Using such a pseudo-time dependent approach solutions have been obtained in the transonic and low supersonic flow regime. It is suggested (Refs 64-67) that as long as shocks appear in the transient solutions no explicit Kutta condition is required. It is argued in references 64-67 that initially the inviscid compressible flow accelerates through an expansion fan around the edge, up to the point where a shock is needed to prevent the flow to expand to vacuum. The resulting strong shock will produce rotational flow downstream of the shock. Subsequently this vorticity will persist modify the flow field such that the flow decelerates until a steady state is attained, presumably without a shock and with the flow smoothly separating at the sharp edge. For a rounded edge like a wing tip this same purely inviscid mechanism will make the flow separate, at least as long as at the free stream Mach number considered the curvature is sufficiently large. In any other case a Kutta condition will have to be applied. The precise details of above sketched inviscid flow separation mechanism are still unclear. Also the question whether during the transient solutions sufficient vorticity can be produced to obtain the right type of separated flow is still unanswered.

A more plausible explanation for the vorticity generation in the Euler method is that the numerical scheme effectively adds a vorticity production term to the right-hand side of equation (2.3b). In the solution process vorticity will be produced depending on the magnitude of this term, i.e. the "artificial" viscosity and the magnitude of the gradients of the solution. If this speculation is correct, vorticity will certainly be produced at sharp edges, but also at all other places where gradients are sufficiently large.

Computational results of Euler codes for the flow about wings do show a qualitatively correct circulatory velocity pattern near the wing tip. This is illustrated in results obtained by Rizzi (Refs 64, 66, 67) for the ONERA M6 wing at $M = 0.84$ and $\alpha = 3^{\circ}$, using a finite-volume procedure, an internal temporally dissipative damping and local time stepping. Also results obtained by Chattot (Ref. 68) for the ONERA

AFV-D wing at M = 0.84 and α = 4°, using a MacCormack finite difference scheme reveal the qualitatively correct flow near the wing tip and in the wake immediate downstream of the trailing edge.

The third approach due to Rehbach (Refs 69-71) applies to incompressible flow only. The Euler equations are expressed as in equation (2.3a-c). Employing Green's identity results in the following expression for the velocity at $\vec{x}_o$

$$\vec{u}(\vec{x}_o) = \vec{U}_\infty - \frac{1}{4\pi} \iint_S \vec{\gamma}(\vec{x}) \times \frac{\vec{r}}{|\vec{r}|^3} dS(\vec{x}) + \frac{1}{4\pi} \iiint_V \vec{\omega}(\vec{x}) \times \frac{\vec{r}}{|\vec{r}|^3} dV(\vec{x}) \qquad (2.10)$$

where $\vec{r} = \vec{x} - \vec{x}_o$, $\vec{\gamma}(\vec{x})$ denotes the vorticity distribution on the surface of the configuration $S(\vec{x})$ and $\vec{\omega}(\vec{x})$ the vorticity in the field $V(\vec{x})$ surrounding the configuration. The surface integral is discretized using the vortex-lattice method. The volume integral is discretized by dividing the field that contains vorticity into cells of constant $\vec{\omega}dV$. The approach followed is a time dependent one, starting impulsively from rest. At each time step in the computation new "vorticity particles" of strength $\vec{\omega}\Delta V$ are shed into the flow field from separation lines, here sharp edges, employing a certain vortex shedding mechanism. During the subsequent time steps the volume of the particles is kept constant irrespective of their distortion and the rate of change of the total vorticity $\vec{\omega}\Delta V$ contained in the particle is given by the integral form of the vorticity transport equation (2.3b):

$$\frac{D}{Dt} \iiint_{\Delta V} \vec{\omega}(\vec{x}) dV(\vec{x}) = \iiint_{\Delta V} (\vec{\omega}(\vec{x}) dV(\vec{x}) . \vec{\nabla}) \vec{u}(\vec{x}) \qquad (2.11)$$

When the "vorticity particles" have been positioned in their new position the surface vorticity distribution, represented by the vortex lattice, is recomputed by imposing the zero normal velocity condition. It is emphasized here that Rehbach's approach does not require the construction of a spatial grid. The other two methods require a spatial grid covering the entire space around the configuration. Furthermore the vorticity production process is contained in the vortex shedding mechanism employed. The latter is derived from Kutta-condition type considerations.

3. VORTEX FLOW FROM LEADING AND SIDE EDGES

In this chapter computational methods are considered for computing the flow about configurations with leading-edge and side-edge vortex sheets. For these configurations the rolling-up vortex sheet is always in the near proximity of the surface and a strong interaction takes place between the vortex sheet and the flow field. This results in a complicated flow pattern and typically a nonlinear dependence of the lift on angle of attack is observed. In this chapter a qualitative description of the flow is given first, followed by a description of current computational methods for slender highly swept wings and strake-wing configurations.

3.1 Description of the flow

The low-speed high-angle-of-attack flow about slender wings with leading-edge vortex separation has been described extensively in the literature. Based upon primarily experimental investigations by amongst others Legendre (Ref. 72), Earnshaw (Ref. 73), Wentz & McMahon (Ref. 74), Fink & Taylor (Ref. 75) and Hummel (Ref. 76) the topology of the high-Reynolds number flow about these wings is well-established. At moderate to high angles of attack the flow separates at the leading edge resulting in a free shear layer emanating from the edge. This free shear layer rolls up in a spiral fashion to form the so-called (single-branched) leading-edge vortex (Fig. 12). It has been observed in experiments that the adverse pressure gradient in the region just outboard of the lateral position of the center of the primary vortex core causes a secondary separation, resulting in a secondary vortex core with vorticity of opposite sense to that of the primary core. In the downstream direction the trailing-edge vortex core is continually fed with vorticity from the leading edge, so that it is increasing in strength as well as in overall dimension. Downstream of the trailing edge of the wing vorticity from the shear layer continues to be fed into the core. In addition, the vorticity in the wake that is of opposite sense to that in the leading-edge vortex starts to roll-up in a (double-branched) so-called trailing-edge vortex. This phenomenon has been observed experimentally by Maltby (Ref. 77) and more recently by Hummel (Ref. 67). As a result of the strong interaction of leading-edge vortex core and the flow above the slender wing upper surface large vortex lift increments are produced. It has been observed that a stable ("controlled") vortex flow pattern persists up to angles of attack as high as 25 to 30 degrees.

The vortex flow above strake-wing configurations is more complex. Investigations by amongst others Lamar & Luckring (Ref. 78), Luckring (Refs 79 and 80) and Brennenstuhl & Hummel (Refs 81 and 82) have provided valuable insight into the vortex layer structure above strake-wing configurations. In reference 83 additional topological information has been acquired employing a laserlight-sheet flow visualization technique. From these investigations it follows that above a strake-wing configuration the (single-branched) leading-edge vortex originating at the leading edge of the strake continues above the wing. The vortex modifies the wing flow field considerable, inducing additional favourable effects. In case of sufficiently (depending on leading-edge sharpness, angle of attack, etc.) swept wing leading edges the flow separates also at the wing leading edge and downstream of the kink the shear layer emanating from the strake leading edge is continued as the shear layer emanating from the wing leading edge (see Fig. 13). In this shear layer the so-called (double-branched) wing vortex develops. This vortex starts at the kink and loops around the strake vortex. At some point downstream of the kink the two cores (with distributed vorticity of the same sign) merge into one core. At smaller sweep angles the flow does not separate at the wing leading edge. In this case the flow picture is not completely clear. Most investigators assume that the shear layer detaches (tears) at the kink (as proposed in Ref. 1, p. 254) resulting in the flow pattern sketched in figure 14. In this case the "free end" of the shear layer will roll-up into another (single-branched) vortex core. It might possibly also be hypothesized that downstream of the kink the strake leading-edge shear layer continues onto the wing upper surface, now emanating from some separation line. More detailed experimental investigation will be needed to clarify details of the flow structure for this case. A limit to the favourable effects induced by the vortex flow is reached when large-scale vortex breakdown

occurs above the wing. Vortex breakdown manifests itself as an abrupt increase in the cross-sectional area and turbulence level of the vortex core, at the higher incidences accompanied by an asymmetric flow pattern. The mechanism underlying vortex breakdown is still unclear (e.g. Hall, Ref. 84). However, it is observed that with increasing angle of attack vortex breakdown progresses in upstream direction and that it occurs in regions where there is an increase in the pressure along the core (e.g. Erickson Ref. 85). Furthermore the phenomenon depends only weakly on Reynolds number. Part of the increase in core dimension may possibly be explained as the response of the inviscid outer part of the rotational core to a pressure rise. Although it is recognized that vortex flow is of importance at transonic and supersonic speed (e.g. Klopfer & Nielsen, Ref. 86), in the present paper the emphasis will be on the case of vortex flow at low speed. As for the case of the vortex wake, the flow about configurations with leading-edge vortex separation may then be considered potential flow with embedded regions of rotational flow, i.e. vortex sheets, single and double-branched vortex cores (see Fig. 2). In incompressible flow, the mathematical model of this flow has already been described in Section 2.3, i.e. equations (2.9a-h) for the potential flow and e.g. equations (2.3a-c) for the rotational regions.

3.2 Conical-flow methods

Observation of the flow over the forward 75 % of slender delta wings suggests that even at subsonic speeds the flow is nearly conical, except possibly in the region very near the apex. Subsonic conical flow is only applicable to wings with highly-swept straight leading edges, for which also slender body theory is appropriate. Conical flow implies that the velocity is constant on rays from the apex and that the geometry scales linearly in downstream direction. Consequently the number of independent variables is reduced to two. Exploiting the slenderness of the configuration then results into a two-dimensional problem in the cross-flow plane (Fig. 15). The surface of the configuration (not necessarily infinitesimal thin) and vortex sheet is expressed as

$$\vec{x}(s,t) = s\,\vec{e}_x + as\,\vec{Y}(t) \tag{3.1a}$$

where $a = \cot \Lambda$, s is a surface coordinate in downstream direction, t is the arc length in the cross-flow plane s = constant, and $\vec{Y}(t) = (0, Y(t), Z(t))$ is a vector in this plane. The position of the core (Fig. 15), here modeled by an isolated line vortex/feeding sheet combination (Smith, Ref. 40), is written as

$$\vec{x}_v(s) = s\,\vec{e}_x + as\,\vec{Y}_v \tag{3.1b}$$

where $\vec{Y}_v$ is the dimensionless vortex position in the cross-flow plane. Legendre (Ref. 72) and Brown & Michael (Ref. 87) model the complete sheet by the feeding sheet/isolated vortex combination. Then by conformally mapping the wing geometry onto the plane of symmetry the boundary condition on the solid surface is satisfied automatically. The remaining three unknowns, i.e. $\vec{Y}_v = (0, Y_v, Z_v)$ and the strength of the vortex, are determined by imposing the Kutta condition at the leading edge and the condition that the model of the rolled-up sheet carries no force (Ref. 87). Smith (Refs 40, 88), Barsby (Refs 89, 90) and others have improved upon this method by including a sheet of finite extent as shown in figure 15. In the transformed plane the sheet is discretized in N straight segments (panels) each carrying constant vorticity. Expressing the geometry in terms of polar coordinates centered at the vortex position, this introduces an additional 2N unknowns, determined by imposing conditions (2.9f) and (2.9g) at N points. The resulting 2N+3 nonlinear equations, for as many unknowns, are solved by an iterative procedure. The range of body shapes that can be dealt with is limited to cases where a suitable (set of) conformal transformations can be devised.

In the conical flow method developed at NLR (Refs 83, 91), designated VORCON, the full problem is solved using a second-order panel method in the physical plane, allowing arbitrary cross-sections to be treated in a routine manner. Compatibility with the fully three-dimensional case is maintained by deriving the equations for the limiting case of slender conical flow directly from the three-dimensional formulation described already in equations (2.9a-h). This involves expressing the conical doublet distribution as $\mu(s,t) = as\rho(t)$, substitution of equations (3.1a-b) into equation (2.9b), subsequent integration with respect to s from 0 to ∞ followed by an expansion for small a and truncation of terms of order a^2 and higher (Ref. 91). In the method the wing is divided into NPW panels, the vortex sheet into NPV panels. The functions $Y(t)$, $Z(t)$ and $\rho(t)$ are approximated by piecewise quadratic spline-type representations, resulting with the unknown vortex position into NPW+3NPV+2 unknown parameters. A formulation in terms of polar coordinates centered at the vortex position (as used in Ref. 40) would result in NPW+2NPV+2 unknowns. However, the present arc-length formulation is preferred since it has no restriction on the cross-sectional shape of the vortex sheet to be described. An additional advantage is that the length of the sheet remains constant throughout the iterative procedure. A system of as many nonlinear equations for as many unknown parameters is obtained by imposing the boundary condition(s) at the panel midpoints, the condition that t is the arc length along the sheet and the "Brown & Michael" type of force condition at $\vec{Y}_v$.

Note that in contrast with Smith (Ref. 40) in VORCON the Kutta condition is satisfied implicitly. It is argued that applying the $\Delta C_p = 0$ condition at NPV points on the sheet implies that to consistent order of approximation $\Delta C_p = 0$ all along the sheet up to the leading edge. Since furthermore the doublet distribution and geometry are continuous to consistent order any Kutta condition is satisfied implicitly. The (full Newton) iterative solution procedure requires an initial guess, such that the procedure converges towards the solution. For this purpose it has been proven possible to devise a continuation process, in most cases resulting in a rapid quadratic convergence. One such process is to start with obtaining a solution for a short sheet, for which the initial guess is not that critical and, to use this solution to extend the sheet. A second continuation process consists of employing the solution already obtained for a value of the conical similarity parameter $A(= a/a$ in Refs 40, 88-90 and $\tan\alpha/a$ in Ref. 91) as initial guess for a neighbouring value of A. In VORCON both continuation processes have been automated, providing rapid convergence of the full Newton procedure employed.

Figure 16a shows the solution obtained for a delta wing of unit aspect ratio ($a = 0.25$) obtained by Smith (Ref. 40) for $\alpha = 13^\circ$ and by the VORCON code for $\alpha = 14^\circ$, both for a rather long vortex sheet. Except near the leading edge the solutions are almost identical. The computed pressure distributions (see Fig. 16b) show the characteristic suction peak underneath the rolled-up vortex sheet. There are some differences in the location and height of the suction peak, presumably due to slight differences in the formulation (approximation of $\tan\alpha$ by α, etc. in Ref. 40). On the lower surface the two computational results are

nearly identical. At the leading edge the pressure on the upper and lower surface become equal to the pressure on the vortex sheet.

In figure 16c the vortex sheet geometry computed by Barsby (Ref. 90) is compared with the result obtained with VORCON, for a AR = 1.0 delta wing at $\alpha \approx 1.4^{\circ}$. Note that the vortex sheet is confined to the last 10 % of the wing semi span. This solution though interesting from a computational point of view has little physical meaning since at such low incidence the free shear layer will be completely embedded within the boundary layer.

Finally figure 16d shows the geometry of the vortex sheet computed for a conically cambered wing at incidences both above and below the incidence for attached flow α_o. VORCON and Barsby's (Ref. 89) method yield quite similar results. It should be noted here that computing solutions at incidences near the incidence for α_o can be carried out employing the continuation process described in a rather routine manner. The panel method approach is easily extended to cases with thickness. Cases with thickness like the ones treated in for instance reference 88 can be treated in a routine manner by using a sequence of solutions for neighbouring geometries. In the VORCON method one surface of the wing and the vortex sheet are modeled by a doublet distribution while the remaining wing surface is modeled by a (linearly varying) source distribution. The latter also serves the purpose of providing the net source strength required to account for the downstream growth of the cross-sectional area.

Conical flow methods are not restricted to symmetric problems. For instance Jones (Ref. 92) using Smith's approach considers the problem of a delta wing at side slip. Also it should be possible to compute the asymmetric solutions observed in experiments with very slender symmetric delta wings at very high angle of attack in symmetric flow. Conical flow methods can be employed advantageously for
(i) investigation of the influence of the choice of parameters in the computational method such as sheet length, panel scheme, etc. in greater detail and at less expense than possible for a fully three-dimensional flow method.
(ii) obtaining a first insight in the influence of changing the cross-sectional geometry for design purposes.
(iii) constructing a reasonable initial guess for the full three-dimensional method.
(iv) Testing improved mathematical models and various numerical schemes.

For reasons of computational costs often a relatively short sheet is used in three-dimensional methods. If the rolled-up region is represented by the axi-symmetric isolated vortex model the examples considered in figure 16 show that in combination with a short sheet this representation of the rolled up vortex sheet may not always be accurate. It appears that the development of improved vortex core models or for instance finite-difference methods based on the Euler equations could advantageously start for conical flow, where ample numerical solutions for less advanced mathematical models already exist. In this respect the development of a model for the entrainment of flow into the vortex core (eg. Ref. 1, p. 365) as preliminary investigated in reference 91 might provide a starting point.

3.3 Methods for non-conical slender configurations

The extension of the conical flow model to treat the flow about slender non-conical configurations, still within the limitations of slender-body theory, is quite straightforward. In each cross-flow plane a solution is found of Laplace's equation in two dimensions, satisfying appropriate boundary conditions in this plane. The variation of the geometry in axial direction enters only through the boundary conditions. The derivatives in axial direction are approximated using finite differences Smith (Ref. 93) extended the Brown & Michael model to treat plane wings with curved leading edges. Sacks, Lundberg & Hanson (Ref. 94) treated wing-body configurations employing a discrete vortex technique to represent the leading-edge vortex sheet. Later Fink & Soh (Ref. 95) applied their rediscretization technique to regularize the results of the discrete-vortex simulation of leading-edge vortex flow. Quite recently Rao & Maskew (Refs 96, 97) employed the discrete-vortex method regularized by means of the sub-vortex technique, rediscretization and amalgamation as introduced by Moore (Ref. 27), to compute the flow about wings with curved leading edges and wings with thickness. The basic difficulty with the slender-body discrete vortex technique is that at subsequent cross-flow planes new discrete vortices must be shed to account for the increasing strength of the leading-edge vortex sheet. Obtaining the strength and position of the newly shed vortex from Kutta-condition type of considerations differs for each method and inevitably involves some empiricism. In figure 17 results of the above methods obtained for a delta wing are compared with conical flow methods, showing that similar results are obtained. Jones (Ref. 98) and Clark (Ref. 99) have extended Smith's (Ref. 40) vortex-sheet model to curved leading edges and to non-flat wings. As also demonstrated by Rao & Maskew (Refs 96, 97) realistic results can be obtained for wings with curved leading edges. Clark's (Ref. 99) result for a streamwise cambered delta wing indicates that for non-flat wings quite nontrivial vortex-sheet shapes may be expected, possibly involving a double-branched vortex core.

Since in each cross-flow plane only a two-dimensional problem is solved, comparable to the one two-dimensional problem solved in conical flow methods, the methods for nonconical slender bodies also provide a relatively inexpensive tool for preliminary investigation of the fully three-dimensional case and in addition can provide a reasonable and cost-effective initial guess for the three-dimensional solution of such configurations. The major drawback of the method, inherent to slender-body theory, is that the trailing-edge Kutta condition is not accounted for.

Downstream of the trailing edge of the slender wing the time-dependent analogy described in the preceding chapter can be applied. The initial values are the shape of the wing and vortex sheet together with the streamwise vorticity distribution in the trailing edge cross-flow plane. Employing as input the vortex-sheet shape and vorticity distribution computed by a method for conical flow or those computed by a non-conical slender-body method will result in a good initial guess for the fully three-dimensinal method.

In figure 18 computed wake shapes are compared with experimental data obtained by Hummel (Ref. 76). The VOR2DT computational procedure has been discussed in the preceding section, the initial solution was obtained from the VORCON conical flow program. The result due to Jeppe (Ref. 100) is obtained by the basic (Westwater-type) discrete-vortex method, using a guess for the shape of the vortex sheet at the trailing edge and no core representation. The result due to Kandil (Ref. 101) is obtained using a three-dimensional nonlinear vortex-lattice method with an amalgamation procedure. Both discrete-vortex methods show some tendency of the wake to form the double-branched vortex, but presumably the number of vortices is insufficient to obtain more detail. If the number of vortices is increased numerical problems are to be expected. The VOR2DT result is in rather close agreement with Hummel's (Ref. 76) experimental data. Note that compared with Hummel's result all three computational results have about the same difference in the downward displacement of the wake near the plane of symmetry. This difference is possibly attributable to wind-

tunnel wall interference.

Jepps (Ref. 61) has developed the so-called hybrid method in which the two-dimensional cross-flow plane onset velocity field is supplied by a three-dimensional panel method calculation applied to the configuration with position and strength of vortex sheets specified. The new position and strength of the vortex sheets in each cross-flow plane is then computed using the slender-body approach. The latter involves the solution of a set of two-dimensional flow problems, which is accomplished employing a two-dimensional panel method. Subsequently the three-dimensional panel method provides the new cross-flow plane onset flow. It is suggested that solving a set of (much) simpler and smaller two-dimensional problems instead of the full three-dimensional problem results in an easy to use as well as cost-effective computational procedure. Thusfar the method has been applied using the simple Brown & Michael model only.

3.4 Methods for three-dimensional flow

In order to account for the upstream effects of trailing edge, wake and changes in geometry methods are required that within the limitations of the mathematical model employed solve the complete three-dimensional problem. The model of the flow for the case of a delta wing is depicted schematically in figure 19. In essence it is the extension to three dimensions of Smith's (Ref. 40) vortex-sheet model for conical flow. The same type of model also applies to more general slender configurations, as long as the flow separates all along the leading (or side) edge. In this section various computational methods developed to treat the fully three-dimensional problem are discussed, more or less in order of their sophistication of the numerical approach.

3.4.1 The leading-edge suction analogy of Polhamus

The most widely used method for predicting the characteristics of configurations employing vortex flow is the so-called "Polhamus suction analogy" (Ref. 102). The analogy is based on the assumption that the vortex lift effect can be predicted utilizing the edge suction forces. In classical lifting surface (attached flow) theory a suction force occurs at leading and side-edges. This force acts normal to the local leading edge and lies in the plane of the wing. The magnitude of the suction force depends on the amplitude of the singular part of the loading as the edge is approched. On a three-dimensional wing the normal force found from integration of the net pressure distribution and the suction force combine to yield the lift, side force and induced drag of the wing. If the flow separates at the edge the suction force is lost. The analogy is based on the conjecture that in the latter case the suction force is recovered as a force rotated through 90 deg to act in the direction of the normal force (Fig. 20). This implies that the aerodynamic forces and moments on configurations with vortex flow can be computed by utilizing any conventional linear attached flow method. The magnitude of th suction force follows then from the behaviour of the loading near the edge. The method has been applied to a variety of configurations in subsonic and in supersonic flow. In general the correlation of computed forces, and to a lesser extent moments, with experimental data is very good. With a vortex-lattice method as attached flow solver Lamar and his co-workers (Refs 78, 102-106) have developed the method towards a very useful engineering tool both for analysis and design. Purvis (Ref. 107) employs a mode-function type of approach for the attached flow theory, where the amplitude of the suction forces is directly related to the amplitude of the singular mode functions. Larson (Ref. 108) derived a set of semi-empirical analytical formulas that for rectangular wings represent the nonlinear forces and pitching moment as computed by the vortex-lattice method/suction analogy procedure. However, it is noted that the case of the interaction of a vortex with parts of the configuration not near the edge, requires special modeling. An example of this is the strake-wing configuration, for which a so-called augmented vortex-lift concept has been developed (Ref. 79, 109). Also the occurrence of vortex breakdown, which is one of the prime considerations in strake design, has been considered to some depth by Lamar & Frink (Refs 110, 111) in connection with the suction analogy. Kulfan (Ref. 112) has developed a concept for treating rounded leading edges, where only a "partial recovery" of the suction force is achieved. The major drawback of the methods, using the suction analogy is that the pressure and velocity distribution cannot be predicted and that new situations, e.g. the encounter of a canard vortex with a wing, require the development of new empirical concepts.

3.4.2 Vortex-lattice methods

The basic vortex lattice method has already been described in the preceding chapter. In case of separation from the leading or side edge discrete line vortices trail from these edges. These vortices form the discrete representation of the rolling-up vortex sheet. The boundary conditions on the sheet are satisfied by aligning the vortices in local flow direction, while simultaneously their strength follows from satisfying the stream surface condition on the wing. It appears that reasonable results can already be obtained for the forces and moments by fixing the line vortices at an angle of $\alpha/2$ (Gersten, Ref. 113). Belotserkovskii (Refs 114, 115) considered separation from side-edges of low-aspect ratio wings, using the vortex-lattice method and relaxing the line vortices emanating from the side edges. Rehbach (116) applied the (nonlinear) vortex-lattice method to the case of a slender delta wing. The solution was obtained by starting with the solution for a rectangular wing with side-edge separation and gradually decreasing the sweep of the side edge until the delta wing is obtained, the new position and strength of the vortex sheet being computed after each change. In reference 117 the same geometry perturbation procedure is applied to obtain solutions for a flat ogee wing, a flat gothic wing and two chordwise cambered delta wings. Correlation of computed vortex-sheet shapes with water-tunnel flow visualization is good, however, it is stated that although overall force and moments are predicted satisfactorily the computed pressure distribution compares poorly with experimental data. Schröder (Ref. 118) developed a method for computing the characteristics of wings in the presence of rolling-up vortex sheets from side and leading edges, quite similar to Rehbach's method. Several improvements were implemented and reasonable results have been obtained for various wings. However, no converged solution could be obtained for the delta wing In Rehbach's method the vortex core is not explicitly modeled. This is also the case for the earlier nonlinear vortex-lattice method developed by Kandil et al. (e.g. Refs 119-121). A result of this method, modified to include an amalgamation procedure (Refs 101, 122) for the core of the leading-edge vortex, was already shown in figure 18. From a perusal of published results of nonlinear vortex-lattice methods it must be concluded that employing a discrete vortex representation for vortex sheets is apparently a too crude approximation. Difficulties like the ones encountered in the two-dimensional time-dependent analogy

(close encounter with other vortex or with wing, rapid stretching, etc.) appear in the three-dimensional case in the same form. In addition there is the problem of the singular behaviour of the self-induced velocity of a discrete curved vortex. However, reasonable results for overall forces can be obtained if the number of free line vortices is kept small. In this respect it is interesting to note that satisfactory results for forces and moments have also been obtained by Mangia & Hancock (Ref. 123) who modeled the core only (i.e. a three-dimensional version of the model of Brown & Michael). They held the wake-vortex sheet at a fixed position but allowed for the adjustment of the vorticity distribution on the wake. The latter implies that the trailing-edge Kutta condition can be satisfied (i.e. $\Delta C_p = 0$) and also that downstream of the trailing edge the core is still being fed with vorticity and thus keeps on growing in strength.

3.4.3 Panel methods

A number of the numerical problems, obviously associated with discrete vortex methods, can be overcome by employing a panel-method type of approximation, thereby eliminating the singular velocity field associated with a discrete line vortex. In this approach the configuration as well as the vortex sheets are divided into panels. The geometry of each panel as well as the singularity distribution(s) on it are approximated by local (surface spline-type) representations. There have been some attempts (Refs 124-126) to improve upon the vortex-lattice approach by incorporating some ingredients of the panel method approach. If this hybrid approach will be successful is not yet completely clear.

Boeing's LEV method

The panel method developed at Boeing by Johnson et al. (Refs 127-132) is the most sophisticated panel method for computing the subsonic subcritical flow about configurations with free vortex sheets. The model used in the latest improved version (Refs 128-132) is reproduced in figure 21a. The model consists of the wing surface, the leading-edge vortex sheet, the so-called fed (feeding) sheet, a near wake and a trailing (far) wake. The zero-normal velocity condition (Eq. 2.9f) is replaced by the zero normal mass-flux boundary condition

$$\rho\vec{u}.\vec{n} = 0 \tag{3.2a}$$

Expansion of $\rho\vec{u}$ assuming small perturbations, i.e. $\rho = \rho_\infty(1 - M_\infty^2\vec{U}_\infty.\vec{\nabla}\varphi/U_\infty^2)$ and writing $\vec{u} = \vec{U}_\infty+\vec{\nabla}\varphi$ results with $\vec{U}_\infty = U_\infty\vec{e}_x$ into the linearized mass-flux boundary condition:

$$\rho_\infty[\vec{U}_\infty + \beta^2[B^{-1}]([B^{-1}]\vec{\nabla}\varphi)].\vec{n} = 0 \tag{3.2b}$$

where terms of order $|\vec{\nabla}\varphi|^2$ have been neglected. Note that this condition implies that at the surface the normal-velocity component is not zero. It may be verified using equation (2.9c) that this linearized total mass-flux vector experiences a jump of

$$\Delta\rho\vec{u} = \frac{[B^{-1}]([B^{-1}]\vec{n})}{|[B^{-1}]\vec{n}|^2}\,q + \frac{[B]([B]\vec{\gamma})\times\vec{n}}{\beta^2|[B^{-1}]\vec{n}|^2} \tag{3.2c}$$

which implies that for this quantity there is no normal jump associated with a doublet distribution, i.e. no source distribution is required to nullify such a jump and only a doublet distribution can be used to model the (thin) wing and the vortex sheets. On the vortex sheets the zero pressure jump conditions (Eq. (2.9g)) is imposed employing the second-order pressure formula (2.9e). In the method the position of the wake (i.e. the vortex sheet downstream of the trailing edge) is held fixed, analogous to Mangia & Hancock (Ref. 123). On the near wake only the zero pressure jump condition is applied. This furnishes the doublet distribution the freedom to adjust in lateral direction. On the trailing (far) wake, directed in free-stream direction, the doublet distribution is constant in streamwise direction. This is equivalent to prescribing the zero pressure jump condition (2.9g) to first-order accuracy. At the leading and trailing edges the Kutta-type condition is applied that the component of the surface vorticity vector along the edge is continuous across the edge. Finally it is required that there is no resultant force in the plane normal to the model of the vortex core.

In the computer code, designated LEV code, the configuration and vortex sheets are divided into panels. Each panel is flat and carries a quadratically varying doublet distribution given by

$$\mu(s,t) = \mu^* + (s-s^*)\mu_s^* + (t-t^*)\mu_t^* + \tfrac{1}{2}(s-s^*)^2\mu_{ss}^* + (s-s^*)(t-t^*)\mu_{st}^* + \tfrac{1}{2}(t-t^*)^2\mu_{tt}^* \tag{3.3}$$

where (s,t) are local surface coordinates and μ^*, μ_s^*, μ_t^*, etc. are quantities at the panel center (s^*, t^*). Panel midpoints are chosen as collocation points. The main difficulty lies in constructing for the mixed analysis/design type of condition on the vortex sheet a numerically stable scheme for expressing μ^*, μ_s^*, μ_t^*, etc. in terms of the unknown singularity parameters. The singularity parameters correspond to doublet values at panel centers, panel corner points or panel-edge midpoints depending on whether the panel is on the solid surface, the vortex sheet, the near or far wake or the feeding sheet.

In the earlier version of the method (Ref. 127) μ^*, μ_s^*, μ_t^*, etc. were defined by fitting a quadratic through the singularity parameters in an immediate neighbourhood of the panel. Subsequently the induced velocity (aerodynamic influence coefficients) were computed by the discretized version of equation (2.9b). Since neither the doublet distribution nor the geometry is continuous across panel edges the last (discrete line vortex) integral in equation (2.9b) cannot be discarded. In the earlier method these discrete vortices caused a great deal of spurious effects. The starting point for the formulation of the improved method (Refs 128-131) is to enforce strict continuity of both doublet distribution and geometry, so that the discrete-vortex integral can be discarded everywhere except at panel edges corresponding to the leading-edge vortex core. Geometric continuity is warranted by describing each panel by a hyperboloidal surface, completely determined by its four corner points. Continuity of the doublet distribution is guaranteed by choosing a nine-parameter polynomial expression involving function values at the four corner points, the four panel-edge midpoints and the panel center. These nine doublet values are expressed in terms of the unknown singularity parameters by a weighted least-squares fit through (16) neighbouring singularity parameters. Although the piecewise surface integration in equation (2.9b) over the hyperboloidal panels carrying any polynomial distribution can be performed in closed form without further approximation (Morino, Ref. 133), this has apparently been overlooked. Instead a presumably rather costly numerical

approximation to these integrals was developed. However, it was found that the original flat panel approximation along with the quadratic approximation to the nine-parameter polynomial doublet distribution (i.e. equation (3.3)) agreed well with the strict continuous formulation Subsequently the original flat panel/quadratic doublet distribution formulation was reinstated, omitting the discrete edge vortices. In effect this is equivalent to first considering geometry and μ to be continuous, omitting the last term in equation (2.9b), followed by discretization of the remaining doublet (vorticity) integral.

Note, however, that now the numerical scheme to express μ^*, μ_s^*, μ_t^*, etc. in terms of the singularity parameters involves the intermediate step of expressing μ^*, μ_s^*, μ_t^*, etc. in terms of the nine doublet parameters of the panel considered. This appears to introduce sufficient smoothing for providing stability in most cases.

Figure 21b displays the kinematics of the free and fed sheet. The degrees of freedom are the panel orientation angles θ, the scale factor λ for the total vortex system and the scale factor ν for the feeding sheet. Note that the attitude of the feeding sheet is fixed with respect to the last panel.

The system of nonlinear equations arising from application of the boundary conditions is solved using a quasi-Newton procedure with controlled stepsize. It must be realized that the Jacobian matrix involves the computation of the derivative of the aerodynamic influence coefficients with respect to the unknown geometry parameters and is rather computationally expensive. Also because the scheme used to express the doublet distribution on a panel in terms of the unknown singularity parameters involves geometry, derivatives of these expressions with respect to the geometric unknowns are necessary. To reduce computational expense the Jacobian is not recomputed at each iteration. To what extent the then computed Jacobian is approximate is not extensively described. However, clearly one should compare the computational effort of obtaining a more accurate Jacobian with the computational cost of executing more iterations with a less accurate but less expensive approximation to the Jacobian. It appears that still some instability is present in the method, leading to problems in cases where the initial guess is too far off (Ref. 132). In such cases a no-panel-twist condition is added and a least-squares solution procedure is used to obtain a solution.

The NLR VORSEP method

The three-dimensional flow method developed at NLR (Refs 83, 134) is based on the same model as Boeing's method. However, the numerical implementation differs in a number of points. The method is intended to solve for the flow about slender wings of general shape and planform with leading-edge vortex flow. In the method, designated VORSEP, the problem is solved in the rectangular computational domain depicted in figure 22a. In the computational domain the wing is mapped onto the square $(s,t)\in([0,1],[0,1])$, the leading-edge vortex sheet on the region $(s,t)\in([1,T],[0,1])$, the near wake on $s\in[1, S_s]$ and the far wake on $s\in[S_s,\infty]$. In contrast with Boeing's method the near wake is free to move to a position where both the zero normal velocity boundary condition and the zero pressure jump condition are satisfied. In the VORSEP method no explicit Kutta condition is applied, rather it is assumed that application of $\Delta C_p = 0$ on the sheet and near wake in conjunction with the assumption that in all of the rectangular domain $(s,t)\in([0,S_s],[0,T])$ both doublet distribution and geometry are continuous and have continuous first derivatives imply zero pressure jump, finite flow, etc. at the leading and trailing edge. The computational domain is subdivided into rectangular panels and panelwise quadratic representations for the unknown bivariate functions $\mu(s,t)$ and $\underline{x}(s,t)$ as given in equation (3.3) are defined. Taking (s^*,t^*) as the panel midpoint μ_s^*, μ_t^*, etc. are approximated by second-order accurate finite difference type expressions, involving function values at neighbouring midpoints (Fig. 22b). Because the computational domain is rectangular and globally defined the latter expressions are relatively simple. Across panel edges both geometry and doublet distribution are discontinuous in function value and their derivatives. However, because the discontinuities are small of higher order they are neglected. In the preliminary version of the program (Ref. 134) central differences were chosen, but it turned out that for the mixed analysis/design type of boundary conditions on the sheet and near wake this choice resulted into instabilities. In the subsequent development it was found that numerical stability could be achieved by a central difference scheme for the second derivatives and a one-sided second-order accurate scheme for the first derivatives. The panel midpoints are taken as the collocation points and the number of unknowns equals the number of boundary conditions (Fig. 22b).

The velocity induced by the doublet distribution is computed from equation (2.9b), omitting the last line integral because of the assumed continuity, in closed form to second-order accuracy employing a small-curvature expansion. For collocation points in the far field of a panel an appropriate second-order accurate far-field expansion is used. The system of nonlinear equations is solved using a quasi-Newton procedure. In this procedure the Jacobian matrix is stripped and the gradient matrix equation has, similar to the finite difference molecule, a four block-diagonal form, which can be solved very efficiently. All the derivatives and in particular those of the induced velocity with respect to the geometric parameters are obtained from closed form expressions, avoiding the very expensive numerical differentiation. In the present quasi-Newton process the residue decreases by an order of magnitude or more in each interation, no step-size control is necessary and the solution is usually obtained in 5 or 6 iterations, recomputing the Jacobian matrix during each iteration. The initial guess for starting the iterative procedure is obtained from the conical flow method VORCON and the wake roll-up method VOR2DT described earlier. Furthermore continuation procedures are used to extend already obtained solutions to solutions with a longer or shorter vortex sheet or near wake. Also continuation to neighbouring angles of attack is often used. Divergence of the iterative procedure becomes usually apparent first on the last strip of the near wake (the sheet crossing itself, etc.). Although set up originally for incompressible flow it could easily be extended to linear compressible flow.

Examples of application

In figure 23a vortex sheet shapes computed by the VORSEP panel method, are shown for an AR = 1 delta wing (76 deg sweep) at α = 20 degrees. As far as the geometry is concerned the solution is conical up to 80-90 % of the wing chord. In the VORSEP method the near wake is not fixed, but the trailing-edge vortex (see Fig. 18) is not modeled explicitly. However, it does show up in the present result as a dent in the shape of the sheet. Results of further computations with the VORSEP method using a finer paneled near wake are presented in figure 23b. In both cases the near wake contains 6 strips but for the sake of reducing the computational effort the length of the vortex sheet has been shortened. The results indicate that the details of the trailing vortex roll-up become apparent as the discretization in the near wake is refined. Fortunately, however, the influence of the near wake discretization on the leading-edge vortex sheet geometry, lift and pitching moment and pressure distribution is rather small. That the geometry is conical

almost up to the trailing edge is demonstrated in figure 23c where the conical solution is compared with the three-dimensional solution. However, the doublet distribution, which in case of conical flow increases linearly in downstream direction, deviates from the conical solution obviously at the trailing edge where the Kutta condition is satisfied, but also near the apex. This is also found in the pressure distribution on the delta wing (Fig. 23d), which shows that on the upper surface the pressure increases monotonically towards the trailing edge. On the lower wing surface the three-dimensional pressure distribution agrees better with the conical flow solution. In figure 24 the solution obtained for the AR = 1.0 delta wing at α = 20 degrees as obtained by the LEV code (Ref. 131) and as obtained by the VORSEP code are compared. The vortex sheet computed by the LEV code appears to be less curved near the leading edge. The vortex core computed by the LEV code is further inboard than the one computed by VORSEP. Correspondingly the suction peak is shifted slightly in inboard direction. This shift is probably more than might be expected from the difference in sheet length used in the computation. The upper wing surface suction peaks and correspondingly the lift coefficient computed by the LEV code for the 60 wing-panel case is lower than computed by VORSEP for the 100 wing panel case. In general there is a trend for the lift to increase slightly with the angular extent of the vortex sheet, at least until the angular extent of the sheet is 2π or greater. This effect is caused by the vorticity in the additional portion of the sheet being closer to the wing upper surface in the case of the longer sheet than in the case of the shorter sheet where this additional vorticity resides in the vortex core further away from the wing surface. This is illustrated for the LEV code in reference 131 for the case of the AR = 0.25 delta wing and for the VORSEP code in figure 25 for the case of the AR = 1.0 delta wing, both at 20 degrees incidence. This effect will be more pronounced for higher incidences and lower aspect ratios where the vortex core is relatively further away from wing. The shape of the fixed near wake to be chosen for the LEV code has a rather large influence on the convergence characteristics of this method (see Ref. 129). The example considered for the VORSEP code with its "relaxed" near wake is the migration of the solution for the AR = 1.0 delta wing at α = 20 degrees, to the solution for the same wing at α = 17.5 degrees (Fig. 26). The convergence of the quasi-Newton procedure is satisfactory for this case. Quite apparent in the VORSEP result is that keeping the arc length of the sheet fixed results in an increased roll-up.

Comparison of computed results with experimental data demonstrates that panel methods have the potential to predict detailed characteristics of the vortex flow. Figure 27a compares computed vortex locations with experimental data (Ref. 83). The position of the vortices is excellently predicted by VORCON/VOR2DT. The position of the leading-edge vortex core as predicted by VORSEP is satisfactory and it may be verified that the location of the dent in the vortex sheet in figure 23 corresponds with the shown position of the trailing-edge vortex. In figure 27b the computed pressure distribution is compared with experimental data of references 135 and 136. Though the agreement of computed and measured pressure distributions is quite satisfactory, this figure shows one of the main difficulties in comparing computed and experimental vortex flow results. It concerns the secondary separation just outboard of the lateral position of the leading-edge vortex. The effect of the secondary separation depends on the status (laminar or turbulent) of the boundary layer on the wing upper surface. Especially in the case of a laminar boundary layer the experimentally found suction peak is generally lower than the one computed and in some cases the secondary vortex core induces a second suction peak between the leading-edge vortex and the leading edge. In case of the experiment of reference 136 the boundary layer was fully turbulent, while in reference 135 transition took place at 60 % root chord. In both experiments secondary separation effects are evident. Note that VORSEP correctly predicts the upper surface pressure increase towards the trailing edge and also that the conical flow method VORCON gives a good prediction up to 50 % root chord. The effect of secondary separation is much more apparent in the laminar flow case considered in figure 27c. It is the case of the 70 degrees swept delta wing at 14 degrees incidence. The suction peaks predicted by the VORSEP code are not attained in the experiment of Marsden et al. (Ref. 137). The computational results of the (early version of the) LEV code show that the measured pressure distribution is predicted quite satisfactorily. However, it appears that the 30 wing panels used are insufficient to resolve the suction peaks. This is also indicated by the computational results for the same wing at lower incidence presented in reference 127 where suction peaks even lower than measured are predicted. In general, for wings with turbulent boundary layers, as shown in figure 27b, correlation is better than for the laminar boundary layer case shown in figure 27c. In figure 28 vortex sheet shapes are compared computed with the Rehbach (Ref. 116) vortex lattice method, the conical flow method VORCON and the three-dimensional panel method VORSEP. It appears that compared to the panel methods the vortex lattice method predicts a vortex system that extents more inboard and upward. Figure 29 shows the vortex sheet geometry computed by VORSEP for a wing with a Concorde type ogee planform. Comparing this result with the result of Maskew's (Ref. 97) quasi three-dimensional discrete vortex method again shows that the latter method predicts a vortex system of a rather flatter overall appearance.

The LEV code has been applied to a variety of other cases, including arrow wings (Ref. 128), cambered wings (Refs 128, 129), leading-edge vortex flaps (Refs 132, 138, 139) and double-delta wings (Ref. 140). In the latter case it is assumed that the flow separates all along the leading edge, but the double-branched wing vortex (see Fig. 13) is not modeled explicitly. With the LEV code such a two vortex system can be handled, but an earlier attempt failed (Ref. 141). Results for a double-delta wing of the VORSEP code with its one-vortex system capability are presented in figure 30. Comparison of the vortex sheet shapes shown in figure 30a with the flow visualization results of reference 83 show that the shape of the sheet is correct, but the second vortex is not resolved for the rather coarse panel scheme employed. Note the tendency of the near wake to form a double-branched trailing vortex. The computed pressure distribution on the aft portion of the wing is shown in figure 30b. The extension of the panel method to configurations like the double-delta and the strake wing with explicit modeling of the two-vortex system seems rather straightforward (Ref. 83). Application of the LEV code to low-aspect ratio rectangular wings has been reported in reference 131. Maskew (Refs 96, 97) applied the time-stepping two-dimensional discrete-vortex method to a low-aspect ratio bent plate. In this case a double-branched vortex, formed at the kink, develops in the vortex sheet attached to the side edge quite realistically.

3.4.4 Euler equation methods

Methods for solving the Euler equations have been discussed in section 2.3.2 in connection with wake roll-up. These methods apply equally well to cases with extensive vortex flow over the wing. The main advantage over the panel method approach where the vortex sheets and cores are "fitted", is that no a priori knowledge is required about the topology of the flow field. Complex vortex flow structures will be "captured" automatically. One of the first applications of the Euler equation method to delta wings was presented by Eriksson & Rizzi (Refs 66, 142). In figure 31 their solution for the 70 degrees swept delta

wing at 15 degrees incidence is shown for $M_\infty = 0.7$ and compared with experiment and the incompressible VORSEP result. It appears that the suction peak on the upper surface is too far outboard in both computed results. In addition the height of the suction peak computed by the Euler method is even lower than found in the experiment, possibly indicating that in the computational result the amount of vorticity contained in the region representing the rolled-up vortex sheet is lower than in the experiment. This is also suggested by a comparison with the result of the VORSEP code for incompressible flow. In the comparison it is assumed the influence of compressibility is small (e.g. Luckring Ref. 132) and results only in slightly lower suction levels on the wing upper surface as well as a slight reduction in the cross-sectional dimension, i.e. a flattening of the rotational region. A further anomaly is the second, sharp, suction peak right at the leading edge. Such a suction peak has not been found in panel method type of computations and it appears to be a spurious numerical effect possibly indicating that the Kutta condition is not yet fully satisfied. In the M = 0.9 case presented in reference 66 this effect even dominates the solution over the forward half of the wing.

The method developed by Schmidt (Ref. 65) and Hitzel (Ref. 143) for solving the Euler equations has been applied to the case of the arrow-wing-body combination. It is shown in reference 143 that the computed pressure distribution agrees excellently with the experimental data of reference 144. In Hitzel's results for the sharp leading edge there is no evidence of a sharp secondary suction peak at the leading edge. No direct comparison is made with results of a panel method code. An earlier application of the LEV code to the same configuration, in absence of the body, has been shown to yield a load distribution also in excellent agreement with experimental data (Ref. 127). However, seen in the light of the LEV code results for the AR = 1.46 delta wing this may fortuitously be attributed to a coarse panel scheme in combination with a short vortex sheet.

It has been noted that in the solution of the Euler equations for the flow about slender wings there is some evidence that a phenomenon resembling secondary separation (Refs 66, 142) and vortex breakdown occur (Ref. 143). Whether these are true effects of the solution and not spurious numerical effects associated with the particular discretization used, will have to be investigated by means of computations on finer meshes.

Results of Rehbach's incompressible method are presented in references 68, 71 and 145. It concerns the high-angle-of-attack flow about rectangular wings, delta wings, a cruciform wing and a swept back wing. However, since no pressure distributions are presented a thorough assessment of this method is not possible here.

4. DISCUSSION

In this chapter the development of computational methods for vortex wakes and for configurations with "controlled" vortex flow are summarized and discussed. Possible extensions and improvements of existing methods as well as promising new developments are indicated.

Vortex wake roll-up - 2D time dependent

The most widely used method for this problem is the discrete-vortex method. In spite of various attempts to "regularize" the singular velocity field associated with a discrete vortex the method eventually appears to result in numerical problems as vortex sheet cross-over and loss of the identity of the sheet. The latter also occurs in the "cloud-in-cell" method, where in addition spurious small-scale structures may influence the evolution of the regular large-scale structures. In the panel method the sheet is modeled more accurately and if one accounts for the stretching of the sheet (redistribution, adaptive panel scheme) it has been demonstrated using the VOR2DT code that consistent results can be obtained. A necessary prerequisite to obtain results for longer times is the explicit representation of highly rolled-up regions by a vortex core model. For relatively compact nearly circular rolled-up regions the (axi-symmetric) isolated vortex/feeding sheet(s) model provides a sufficiently accurate model for the inner most turns. For rolled-up regions of larger cross-sectional area a relatively large extent of vortex sheet is required before the isolated vortex model forms a valid approximation for the remaining inner turns. In these cases a core model consisting of a finite region with continuously distributed vorticity is a more appropriate model of reality. The development of methods for the evolution of a wake consisting of rotational flow regions of infinitesimal extent (sheets) and of finite extent (cores) has only just started. It provides a fruitful area for extension of the current method, bridging to some extent the gap between panel methods and finite-difference methods for the Euler equations. Especially the interaction between the region of rotational flow with the vortex sheet(s) and the feeding of vorticity into this region requires further investigation. The results of the inviscid roll-up computation may be regarded as the appropriate initial value for a computational method for the later stages of the wake development where viscous effects become important.

Vortex wakes - 3D

Unfortunately the methods developed thusfar employ the vortex-lattice approach. Most of the methods experience the same kind of numerical problems as their its two-dimensional counter parts. The three-dimensional higher-order panel method presently under development at various institutes, provides a good opportunity to develop a more consistent method for the interaction of rolling-up wakes with nearby components of the configuration. Since the problem is nonlinear in terms of the wake geometry it will involve a number of panel method computations with the latest position of the wake. This means that the computational cost will be a multiple of the cost of the conventional panel method computation with a fixed wake geometry and might be quite substantial. In the panel method approach the topology of the wake has to be known a priori, i.e. the vortex system is fitted into the solution.

For a large number of practical configurations the topology of the wake is known or may possibly be derived from preliminary two-dimensional time-dependent computations. In more complex cases a vortex sheet "capturing" method is required to resolve the interaction. A further severe limitation of panel methods is that they are restricted to subcritical flow, i.e. flows without shock waves. The current transonic potential flow methods that account for these effects assume a simple geometry of the wake, usually the wake surface coincides with a plane of the spatial grid. Since in most cases it would be an almost impossible task to account for a "relaxing" wake in the grid generation process, the wake must be left free to "float" through a fixed grid. The investigation into this partly Lagrangian formulation has only recently started. An alternative to account for nonlinear compressibility effects, presently under development at

NLR, is to employ a panel method in which the surface singularity distribution is supplemented with a spatial source distribution in those regions of the 3D space where nonlinear compressibility effects are of importance. In this way the wake roll-up and interaction can be treated by the panel method as in the case of linear potential flow and in addition the spatial grid is only required in relatively small parts of 3D space. However, much effort is required to reduce the prohibitive N^2 dependence of the computational cost of the panel method approach. A further extension of the method is to add a spatial vorticity distribution to model well-developed vortex cores more accurately. Such an integral equation formulation (e.g. Ref. 146) would also be required in the case of a close-coupled canard where on the wing there is a strong interaction between nonlinear compressibility effects and rotational effects.

Computational methods for the Euler equations allow for nonlinear compressible as well as for rotational flow without explicitly knowing the topology of these regions. Although it is generally recognized that "capturing" vortex sheets and cores is more difficult than "capturing" shock waves, these methods are presently applied with apparent success to cases with vortex flow as the flow near wing tips and the flow about slender wings. The computational cost of these methods may be quite acceptable when use is made of the vectorial computing power of current super computers.

Leading-edge vortex flow - Slender configurations

The conical flow methods like the VORCON panel method yield good results for arbitrary cross-sections with or without thickness at low computational expense. The extension of such methods to nonconical slender configurations such as for instance arbitrarily shaped strakes appears to be straightforward. In addition to providing a relatively inexpensive tool for preliminary investigations it results also in a better initial guess for the solution of the fully three-dimensional flow about nonconical geometries.

The improvement of for instance the vortex core model from the isolated vortex/feeding sheet combination to a core with distributed vorticity might perhaps conveniently first be studied for the case of quasi-3D flow, where computer resources requirements are modest.

Leading-edge vortex flow - 3D configurations

Methods based on Polhamus' suction analogy are widely used, because an excellent correlation of predicted and measured forces and moments is obtained and quite importantly also because it only requires an update of the conventional well-established attached flow lifting surface methods. Unfortunately the Polhamus suction analogy does not supply the detailed pressure distribution on the configuration and the extension to for instance strake-wing and canard-wing configurations requires the development of additional (empirical) concepts. Panel methods developed for the flow about wings with leading-edge vortex flow have proven to be capable of computing the detailed pressure distribution. The major problem in applying the free-vortex-sheet panel method is to specify such an initial guess that convergence of the iterative procedure for solving the geometry of the vortex sheet and the doublet distribution is warranted. Also the computer resources requirements for the method are of the order of a multiple of the conventional panel method with a fixed wake. In this respect it is interesting to note that a recent preliminary study with a "vectorized" version of the VOR2DT panel code on the CRAY-1S computer indicates that a substantial reduction in computing time can be realized by vectorization of the computation of the influence integrals. Thusfar the method has been applied to wings with a single vortex system only, but extension to (strake-wing) configurations with a two-vortex system is straightforward. In the current methods the model of the vortex core is still the simple isolated vortex/feeding sheet model. Improvement of this model to a distributed vorticity model is required to account adequately for the flow at high angles of attack, for the flow about not so slender wings and for the flow about strake-wing configurations. In addition the modeling of the onset of vortex breakdown (e.g. Wilson, Ref. 147 for an earlier attempt), especially important for strake-wing design, should be investigated further.

From the comparison of computed results with experimental data it is clear that secondary separation effects are often quite important. Modeling of secondary separation on a delta wing by a vortex sheet has been reported earlier (see Smith, Ref. 15). The location of the separation line will have to be specified, or ideally have to be found as part of the solution. The latter undoubtedly will involve a strongly coupled viscous-inviscid interaction of the external flow with the boundary layer on the wing upper surface. This problem is closely related to the problem of vortex flow separation from the smooth surface of slender bodies (e.g. Fiddes, Ref. 148) and has not yet been considered extensively for wings or other three-dimensional configurations.

In panel methods linear compressibility effects can be accounted for by applying the Göthert transformation, i.e. solving the Prandtl-Glauert equation. This equation is valid for small perturbations to the main free stream, but certainly this assumption will be violated inside the vortex cores where both axial and circumferential velocities become large. If the normal velocity condition is applied the vortex sheet in addition to the doublet distribution must also carry a source distribution of strength related to the doublet distribution (section 2.3). This may seem a severe complication. However, employing the close correspondence between the velocity induced by a source distribution and the velocity induced by a doublet distribution (Ref. 149) results in little additional computational effort. In the mass-flux formulation the source distribution is not required, but for large perturbations the mass-flux boundary condition tends more rapidly to irrealistic results than the conventional velocity boundary condition.

Nonlinear compressibility effects as well as the ability to capture vortex sheets and rotational regions are included in the methods that solve the Euler equations. The latter implies that no a priori knowledge is required about the often complex topology of the vortical flow. It has been claimed that these methods also model secondary vortex separation and vortex breakdown. In the real flow secondary vortex separation depends on the Reynolds number, vortex breakdown has been reported to depend only weakly on Reynolds number. Whether the Euler equations can truly simulate these effects will require further investigation. If the vorticity production in the Euler methods is governed by "artificial" viscosity, it may be speculated that underneath the primary vortex, where gradients are large, "secondary separation" type of effects may occur in the form of the generation of vorticity of sense opposite to that of the primary vortex. However, comparing figures 27c and 31 and also considering Hitzel's (Ref. 143) results does not support this conjecture.

In the panel method and also in Rehbach's incompressible Euler method (Refs 69-71), bot not requiring a spatial grid, vorticity is produced only at predetermined locations. In this respect it would be very interesting and instructive to compare detailed results of Euler equation method and panel method computations for, say, a unit-aspect-ratio wing at 20 degrees incidence. In order to validate the computational methods described detailed experimental data from flow field surveys would be very valuable. Also exploratory flow field investigations (e.g. (Ref. 83) that reveal the structure of the vortical flow field are

indispensable especially for methods that "fit" the vortical regions.

The reported computational cost or computing times involved in running a Euler code are either modest (on a vector computer) or rather extreme, but undoubtedly further improvements are possible. It must be concluded that the Euler method is very attractive for cases with a complex vortex flow topology, but it remains to be seen whether for subsonic flow it will be more efficient than the (future) panel method in cases for which the topology of the vortex flow is known.

5. CONCLUSIONS

In the last few years considerable progress has been made in the development of computational methods for the prediction of the detailed aerodynamic characteristics of configurations with vortex flow. It has been demonstrated that for slender wings with a simple one-vortex system satisfactory results can be obtained employing panel methods. The extension to configurations with a more complex but a priori known well-defined vortex system appears to be relatively straightforward. A more accurate modeling of vortex cores will lead to a further enhancement of the usefulness of the panel method approach. The main limitation of the panel method approach is that the topology of the vortex flow must be known in advance.

It is not widely recognized that properties familiar in the context of finite-difference and finite-volume methods like stability, smoothing, dissipation, dispersion, etc. apply equally well to panel methods. The effects of these properties on the solution are not well understood.

Computing the flow about configurations with extensive vortex flow employing methods for solving Euler's equations with vortex sheet capturing capability appears very promising. It appears that also in the case of Euler methods the topology of the vortex flow structure must be known in advance if a grid is to be constructed with sufficient resolution at the right locations. Some of the questions raised with respect to the use of the Euler equations for vortex flow may be answered by an in depth comparison of computational results of panel method and Euler method.

There are good prospects for a substantial reduction in the computational resources requirements for both panel methods and Euler methods when employing the vectorial computing power of current super computers.

The development of computational methods for configurations with vortex flow is approaching a level that is useful for design purposes.

ACKNOWLEDGEMENTS

The NLR methods described in this paper have been developed partly under contract for the Scientific Research Division of the Directorate of Materiel Royal Netherlands Air Force, RNLAF. The author gratefully acknowledges the collegial collaboration with Mr. W. Vaatstra and the fruitful cooperation in vortex flow investigation with Mr. N.G. Verhaagen of the Delft University of Technology.

REFERENCES

1. Küchemann, D.: The Aerodynamic Design of Aircraft. Pergamon Press (1978).
2. Peake, D.J. and Tobak, M.: Three-dimensional Interactions and Vortical Flows with Emphasis on High Speeds. NASA TM 81169 (1980), also AGARDograph 252 (1980).
3. Ashley, H. and Landahl, M.T.: Aerodynamics of Wings and Bodies. Adison-Wesley Publ. Co. Inc. (1965).
4. Sytsma, H.A., Hewitt, B.L. and Rubbert, P.E.: A Comparison of Panel Methods for Subsonic Flow computation. AGARD-AG-241 (1979).
5. Holst, T.L., Slooff, J.W., Yoshihara, H. and Ballhaus Jr., W.F.: Applied Computational Transonic Aerodynamics. AGARDograph 266 (1982).
6. Skow, A.M. and Erickson, G.E.: Modern Fighter Aircraft Design for High-Angle-of-Attack Maneuvering. AGARD-LSP-121 (1982).
7. Ballhaus Jr., W.F.: Computational Aerodynamics and Design. Proc. of 8th Int. Conf. on Num. Meth. in Fluid Dynamics, Aachen, Lecture Notes in Physics No. 170, Springer Verlag (1982).
8. Hunt, B.: The Role of Computational Fluid Dynamics in High-Angle-of-Attack Aerodynamics. AGARD-LSP-121 (1982).
9. Ericsson, L.E. and Reding, J.P.: Steady and Unsteady Vortex-Induced Asymmetric Loads on Slender Vehicles. J. of Spacecraft, 18 pp. 97-109 (1981).
10. Pouradier, J.M. and Horowitz, E.: Aerodynamic Study of a Hovering Rotor. Vertica 5 (1981) pp. 301-315.
11. Miller, R.H.: A Simplified Approach to the Free Wake Analysis of a Hovering Rotor. Vertica 6 (1982) pp. 89-95.
12. Summa, J.M. and Maskew, B.: New Methods for the Calculation of Hover Airloads. Presented at 5th European Rotorcraft and Powered Lift Aircraft Forum, Amsterdam, The Netherlands, Sept. 4-7 1979.
13. Szodruch, J. and Ganzer, U.: On the Lee-Side Flow for Slender Delta Wings at High Angle of Attack. AGARD-CP-247 (1979).
14. Smith, J.H.B.: Inviscid Fluid Models, Based on Rolled-Up Vortex Sheets, for Three-Dimensional Separation at High Reynolds Number. AGARD VKI Lecture Series 94 (1978).
15. Smith, J.H.B.: Vortical Flows and Their Computation. VKI Lecture Series LS-1980-5 (1980). Also RAE TM Aero 1866.
16. Saffman, P.G. and Baker, G.R.: Vortex Interactions. Ann. Rev. Fluid Mech. No.11 (1979), pp. 95-122.
17. Leonard, A.: Vortex Methods for Flow Simulation. Review article J. of Comp. Physics, 37 (1980), pp. 289-335.
18. Steger, J.L. and Kutler, P.: Implicit Finite-Difference Procedures for the Computation of Vortex Wakes. AIAA Journal 15, No.4 (1977), pp. 581-590.
19. Bilanin, A.J., Teske, M.E., Donaldson, C. duP. and Williamson, G.G.: Vortex Interactions and Decay in Aircraft Wakes. NASA CR-2870 (1977).
20. Maskell, E.C.: Some Recent Developments in the Study of Edge Vortices. Proc. 3rd ICAS Congr. Stockholm (1962).

21. Guiraud, J.P. and Zeytounian, R.Kh.: A Double-Scale Investigation of the Asymptotic Structure of Rolled-Up Vortex Sheets. JFM, 79 (1977) pp. 93-112.
22. Guiraud, J.P. and Zeytounian, R.Kh.: A Note on the Viscous Diffusion of Rolled Vortex Sheets. JFM, 90 (1979) pp. 197-201.
23. Rosenhead, L.: The Formation of Vortices from a Surface of Discontinuity. Proc. Roy. Soc. Lond., A 134 (1931), pp. 170-192.
24. Westwater, F.L.: Rolling-Up of the Surface of Discontinuity behind an Aerofoil of Finite Span. ARC, R&M No.1962 (1935).
25. Chorin, A.J. and Bernard, P.S.: Discretization of a Vortex Sheet, With an Example of Roll-Up. J. of Comp. Physics, 13 (1973), pp. 423-429.
26. Kuwahara, K. and Takami, H.: Numerical Studies of Two-Dimensional Vortex Motion by a System of Vortices. J. of Phys. Soc. of Japan, 34 (1973), pp. 247-253.
27. Moore, D.W.: A Numerical Study of the Roll-Up of a Finite Vortex Sheet. JFM, 63 (1974), pp. 225-235.
28. Maskew, B.: Subvortex Technique for the Close Approach to a Discretized Vortex Sheet. J. Aircraft, 14, 2 (1977), pp. 188-193.
29. Fink, P.T. and Soh, W.K.: A New Approach to Roll-Up Calculations of Vortex Sheets. Proc. Roy. Soc. Lond. A 362 (1978), pp. 195-209.
30. Baker, G.R.: A Test of the Method of Fink & Soh for Following Vortex-Sheet Motion. JFM, 100 (1980), pp. 209-220.
31. Bromilow, I.G. and Clements, R.R.: Some Techniques for Extending the Application of the Discrete Vortex Method of Flow Simulation. Aeron. Quarterly, 33 (1982), pp. 73-89.
32. Moore, D.W.: The Spontaneous Appearance of a Singularity in the Shape of an Evolving Vortex Sheet. Proc. Roy. Soc. Lond., A 365 (1979), pp. 105-119.
33. Moore, D.W.: On the Point Vortex Method. SIAM J. Sci. Stat. Comput., 2, No.1 (1981), pp. 65-84.
34. Christiansen, J.P.: Numerical Simulation of Hydrodynamics by the Method of Point Vortices. J. Comp. Physics, 13 (1973), pp. 363-379.
35. Baker, G.R.: Studies in Vortex Motion. PhD. thesis California Institute of Technology (1977).
36. Baker, G.R.: The "Cloud in Cell" Technique Applied to the Roll Up of Vortex Sheets. J. of Comp. Physics, 31 (1979), pp. 76-95.
37. Murman, E.M. and Stremel, P.M.: A Vortex Wake Capturing Method for Potential Flow Calculations. AIAA Paper 82-0947 (1982).
38. Mokry, M. and Rainbird, W.J.: Calculation of Vortex Sheet Roll-Up in a Rectangular Wind Tunnel. J. of Aircraft, 12, 9 (1975), pp. 750-752.
39. Hoeijmakers, H.W.M. and Vaatstra, W.: A Higher-Order Panel Method Applied to Vortex Sheet Roll-Up. AIAA Paper 82-0096 (1982). Also AIAA Journal 21, No.4 (1983), pp. 516-523.
40. Smith, J.H.B.: Improved Calculations of Leading-Edge Separation from Slender, Thin, Delta Wings. Proc. Roy. Soc. Lond., A 306 (1968), pp. 67-90. Also RAE TR 66070 (1966).
41. Pullin, D.I.: The Large-Scale Structure of Unsteady Self-Similar Rolled-Up Vortex Sheets. JFM, 88 (1978), pp. 401-430.
42. Pullin, D.I. and Phillips, W.R.C.: On a Generalization of Kaden's Problem. JFM, 104 (1981), pp. 45-53.
43. Huberson, S.: Numerical Computation of Flows with Rolled-Up Vortex Sheets. Rech. Aérosp. No.1980-3, Engl. ed. (1980), pp. 57-63.
44. Portnoy, H.: The Initial Roll-Up of a Thick, Two-Dimensional Wake Behind a Wing of Finite Span. Aeron. J., Oct. 1976, (1976), pp. 442-447.
45. Portnoy, H.: Thick, Two-Dimensional Wake Roll-Up Behind a Wing of Finite Span-Extended Calculations. Aeron. J. Oct. 1977, (1977), pp. 460-463.
46. Moore, D.W.: The Equation of Motion of a Vortex Layer of Small Thickness. Studies in Appl. Math., 58 (1978), pp. 119-140.
47. Zabusky, N.J., Hughes, M.H. and Roberts, K.V.: Contour Dynamics for the Euler Equations in Two Dimensions. J. of Comp. Physics 30, (1979), pp. 96-106.
48. Weston, R.P. and Liu, C.H.: Approximate Boundary Condition Procedure for the Two-Dimensional Numerical Solution of Vortex Wakes. AIAA Paper 82-0951 (1982).
49. Butter, D.J. and Hancock, G.J.: A Numerical Method for Calculating the Trailing Vortex System behind a Swept Wing at Low Speed. The Aeron. J. of the Roy. Aeron. Soc., Vol. 75 (1971), pp. 564-568.
50. Hedman, S.G.: Computation of Vortex Models for Wings at High Angle of Attack in Incompressible Flow. FFA Technical Note AU-653 (1973).
51. Rom, J. and Zorea, C.: The Calculation of the Lift Distribution on the Near Vortex Wake Behind Low Aspect Ratio Wings in Subsonic Flow. TAE Rep. No.168 (1973). (See also TAE Rep. No.199 (1974).)
52. Mattei, A. and Santoro, E.: Numerical Computations of Wake Vortices behind Lifting Surfaces. ICAS Paper 74-28 (1974).
53. Rehbach, C.: Etude Numérique de L'influence de la Forme de L'extrémité d'une Aile sur L'enroulement de la Nappe Tourbillonaire. La Rech. Aerosp. No.1971-6, pp. 367-368.
54. Rehbach, C.: Calcul D'écoulements autour D'ailes sans Epaisseur avec Nappes Tourbillonnaires Evolutives. La Rech. Aerosp. No.1973-2 pp. 53-61.
55. Maskew, B.: The Calculation of Potential Flow Aerodynamic Characteristics of Combined Lifting Surfaces with Relaxed Wakes. Hawker Sideley Aviation Limited, Note No. YAD 3192 (1973).
56. Maskew, B.: A Quadrilateral Vortex Method Applied to Configurations with High Circulation. NASA-SP-405 (1976), pp. 163-186.
57. Suciu, E.O. and Morino, L.: Nonlinear Steady Incompressible Lifting-Surface Analysis with Wake Roll-Up. AIAA Journal Vol. 15, May 1977, pp. 54-58.
58. Mangler, K.W. and Smith, J.H.B.: Behavior of the Vortex Sheet at the Trailing edge of a Lifting Wing. RAE TR 69049 (1969).
59. Labrujère, Th.E. and de Vries, O.: The Deformation of a Vortex Sheet behind a Swept Back Wing, Comparison of Measurements and Calculations. NLR MP 74014 U (1974).
60. Labrujère, Th.E. and de Vries, O.: Evaluation of a Potential Theoretical Model of the Wake behind a Wing via Comparison of Measurements and Calculations. NLR TR 74063 U (1974).
61. Jeppe, S.A.: The Computation of Vortex Flows by Panel Methods. VKI Lecture Series 1978-4 (1978).
62. Klopfer, G.H. and Nielsen, J.N.: Computational Fluid Dynamic Applications to Missile Aerodynamics. AGARD-CP-336 (1982).
63. Nielsen, J.N.: Nonlinear Flow Phenomena at High Angles of Attack and Recent Advances in their Prediction. AGARD-CP-336 (1982).

64. Rizzi, A. and Eriksson, L.E.: Transfinite Mesh Generation and Dampled Euler Equation Algorithm for Transonic Flow about Wing-Body Configurations. AIAA Paper 81-0999 (1981).
65. Schmidt, W., Jameson, A. and Whitfield, D.: Finite Volume Solution for the Euler Equation for Transonic Flow over Airfoils and Wings Including Viscous Effects. AIAA Paper 81-1265 (1981).
66. Eriksson, L.E. and Rizzi, A.: Computation of Vortex Flow Around Wings Using the Euler Equations. Proc. 4th GAMM Conf. on Num. Meth. in Fl. Mech., ed. H. Viviand, Vieweg Verlag, Paris (1981) pp. 87-105.
67. Rizzi, A.: Dampled Euler-Equation Method to Compute Transonic Flow Around Wing-Body Combinations. AIAA Journal, Vol. 20, No.10, Oct. 1982, pp. 1321-1328.
68. Chattot, J.J., Boschiero, M. and Koeck, C.: Methodes Numeriques de Prediction de L'Aerodynamique des Missiles. AGARD-CP-336 (1982).
69. Rehbach, C.: Calcul Numérique D'écoulements Tridimensionnels Instationnaires avec Nappes Tourbillonnaires. La Rech. Aérosp. No.1977-5 (1977), pp. 289-298.
70. Rehbach, C.: Numerical Calculation of Three-Dimensional Unsteady Flows with Vortex Sheets. AIAA Paper 78-111 (1978).
71. Rehbach, C.: Calcul Instationnaire de Nappes Tourbillonnaires Emises par des Surfaces Portantes Fortement Inclinées. AGARD Cp-247 (1979).
72. Legendre, R.: Ecoulement au Voisinage de la Pointe Avant d'une Aile à Forte Flèche aux Incidences Moyennes. La Rech. Aéro. Vol.30 (1952), pp. 3-8; Vol.31 (1952), pp. 3-6 and Vol.35 (1952), pp. 7-8.
73. Earnshaw, P.B.: An Experimental Investigation of the Structure of a Leading-Edge Vortex. R&M No.3281 (1962).
74. Wentz, W.H. and McMahon, M.C.: An Experimental Investigation of the Flow Fields about Delta and Double-Delta Wings at Low Speeds. NASA CR 521 (1966).
75. Fink, P.T. and Taylor, J.: Some Early Experiments on Vortex Separation. R&M No.3489 (1967).
76. Hummel, D.: On the Vortex Formation over a Slender Wing at Large Incidence. AGARD-CP-247 (1979).
77. Maltby, R.L.: Flow Visualization in Wind Tunnels Using Indicators. AGARDograph No.70 (1962).
78. Lamar, J.E. and Luckring, J.M.: Recent Theoretical Developments and Experimental Studies Pertinent to Vortex-Flow Aerodynamics. With a View towards Design. AGARD-CP-247 (1979).
79. Luckring, J.M.: Aerodynamics of Strake-Wing Interactions. J. Aircraft, Vol. 16, No.11 (1979) pp. 756-762.
80. Luckring, J.M.: Flow Visualization Studies of a General Research Fighter Model Employing a Strake-Wing Concept at Subsonic Speed. NASA TM 80057 (1979).
81. Brennenstuhl, U. and Hummel, D.: Untersuchungen über die Wirbelbildung an Flügeln mit geknickten Vorderkanten. ZFW, Vol.5 (1981) pp. 375-381 (see also ZFW, Vol.6 (1982), pp. 239-247).
82. Brennenstuhl, U. and Hummel, D.: Vortex Formulation over Double-Delta Wings. ICAS Paper 82-6.6.3 (1982).
83. Hoeijmakers, H.W.M., Vaatstra, W. and Verhaagen, N.G.: On the Vortex Flow over Delta and Double-Delta Wings. AIAA Paper 82-0949 (1982).
84. Hall, M.G.: Vortex Breakdown. Annual Review of Fluid Mechanics, Vol.4 (1972), pp. 195-218.
85. Erickson, G.E.: Water Tunnel-Studies of Leading-Edge Vortices. J. Aircraft, Vol.19, No.6 (1982), pp. 442-448. (See also AIAA Paper 80-1423 (1980).)
86. Klopfer, G.H. and Nielsen, J.N.: Euler Solutions for Wing and Wing-Body Combination at Supersonic Speeds with Leading-Edge Separation. AIAA Paper 80-0126 (1980).
87. Brown, C.E. and Michael, W.H.: Effect of Leading-Edge Separation on the Lift of a Delta Wing. J. of Aeron. Sciences, Vol.21 (1954), pp. 690-694.
88. Smith, J.H.B.: Calculations of the Flow over Thick, Conical Slender Wings with Leading-Edge Separation. RAE TR 71057 (1971).
89. Barsby, J.E.: Flow Past Conically-Cambered Slender Delta Wings with Leading-Edge Separation. RAE TR 72179 (1972).
90. Barsby, J.E.: Separated Flow Past a Slender Delta Wing at Incidence. Aeron. Quarterly, May 1973, pp. 120-128.
91. Hoeijmakers, H.W.M. and Vaatstra, W.: A Higher-Order Panel Method for the Computation of the Flow about Slender Delta Wings with Leading-Edge Vortex Separation. Proc. 4th GAMM Conf. on Num. Meth. in Fl. Mech., ed. H. Viviand, Vieweg Verlag, Paris (1981), pp. 137-149. Also NLR MP 81053 U.
92. Jones, I.P.: Flow Separation from Yawed Delta Wings. Computer & Fluids, Vol. 3 (1975), pp. 155-177.
93. Smith, J.H.B.: A Theory of the Separated Flow from the Curved Leading Edge of a Slender Wing. ARC R & M No.3116 (1959).
94. Sacks, A.H., Lundberg, R.E. and Hanson, Ch.W.: A Theoretical Investigation of the Aerodynamics of Slender Wing-Body Combinations Exhibiting Leading-Edge Separation. NASA CR-719 (1967).
95. Fink, P.T. and Soh, W.K.: Calculation of Vortex Sheets in Unsteady Flow and Applications in Ship Hydrodynamics. Proc. 10th Symposium on Naval Hydrodynamics, Cambridge, Mass. (1974), pp. 463-491.
96. Rao, B.M. and Maskew, B.: Flows with Leading-Edge Vortex Separation. NASA CR 165858 (1982).
97. Maskew, B. and Rao, B.M.: Calculation of Vortex Flows on Complex Configurations. ICAS Paper 82-6.2.3 (1982).
98. Jones, I.P.: Leading-Edge Separation from Non-Conical Slender Wings at Incidence. Proc. 4th Int. Conf. on Num. Meth. in Fl. Dyn., Lecture Notes in Physics, Vol.35 (1974).
99. Clark, R.W.: Non-Conical Flow past Slender Wings with Leading-Edge Vortex Sheets. RAE TR 76037 (1976).
100. Jepps, S.A.: Theoretical Calculations of the Wake behind a Delta Wing with Leading-Edge Separation. BAC. Rep. Ae/A/583 (1978).
101. Kandil, O.A.: Numerical Prediction of Vortex Cores from the Leading and Trailing Edges of Delta Wings. ICAS Paper 14.2 (1980).
102. Polhamus, E.C.: A Concept of the Vortex Lift of Sharp-Edge Delta Wings Based on a Leading-Edge Suction Analogy. NASA TN D-3767 (1966).
103. Lamar, J.E. and Gloss, B.B.: Subsonic Aerodynamic Characteristics of Interacting Lifting Surfaces With Separated Flow Around Sharp Edges Predicted by a Vortex-Lattice Method. NASA TN D-7921 (1975).
104. Lamar, J.E.: Subsonic Vortex-Flow Design Study for Slender Wings. J. Aircraft, Vol. 15, No.9 (1978), pp. 611-617.
105. Lamar, J.E., Schemensky, R.T. and Reddy, C.S.: Development of a Vortex-Lift Design Procedure and Application to a Slender Maneuver-Wing Configuration. J. Aircraft, Vol. 18, No.4 (1981), pp. 259-266.
106. Lamar, J.E.: The Use of Linearized-Aerodynamics and Vortex-Flow Methods in Aircraft Design. AIAA Paper 82-1384 (1982).

107. Purvis, J.W.: Analytical Prediction of Vortex Lift. J. Aircraft Vol.18, No.4 (1981), pp. 225-230.
108. Larson, E.S.: Incompressible Symmetric Flow Characteristics of Sharp-Edged Rectangular Wings. J. Aircraft, Vol.19, No.6 (1982), pp. 508-510.
109. Lamar, J.E.: Analysis and Design of Strake-Wing Configurations. J. Aircraft, Vol.17, No.1 (1980), pp. 20-27.
110. Frink, N.T. and Lamar, J.E.: Analysis of Strake Vortex Breakdown Characteristics in Relation to Design Features. J. Aircraft, Vol. 18, No.4 (1981), pp. 252-258.
111. Lamar, J.E. and Frink, N.T.: Aerodynamic Features of Designed Strake-Wing Configurations, J. Aircraft, Vol.19, No.8 (1982), pp. 639-646.
112. Kulfan, R.M.: Wing Airfoil Shape Effects on the Development of Leading-Edge Vortices. AIAA Paper 79-1675.
113. Gersten, K.: Nichlineare Tragflächentheorie insbesondere für Tragflügel mit kleinem Seitenverhältnis. Ing. Arch. Vol.30 (1961), pp. 431-452. Also AGARD Rept. 342 (1961).
114. Belotserkovskii, S.M.: Calculation of the Flow about Wings of Arbitrary Planform at a Wide Range of Angles of Attack. RAE Lib. Transl. 1433 (1968).
115. Aparinov, V.A., Belotserkovskii, S.M., Nisht, M.I. and Sokolova, O.N.: Mathematical Modeling of the Detached Flow around a Wing in an Ideal Fluid and Break-Up of the Vortex Sheet. Sov. Phys. Dokl. Vol.21, No.4 (1976), pp. 181-183.
116. Rehbach, C.: Etude Numérique de Nappes Tourbillonnaires Issues d'une Ligne de Décollement près du Bord d'Attaque. Rech. Aérosp. No.1973-6 (1973), pp. 325-330.
117. Rehbach, C.: Numerical Investigation of Leading-Edge Vortex for Low-Aspect Ratio Thin Wings. AIAA Journal, Vol.14, No.2 (1976), pp. 253-255.
118. Schröder, W.: Berechnung der nichtlinearen Beiwerte von Flügeln mit kleinem und mittlerem Seiten-Verhältnis nach dem Wirbelleiterverfahren in inkompressibler Strömung. DFVLR FB 78-26 (1978).
119. Kandil, O.A., Mook, D.T. and Nayfeh, A.H.: Nonlinear Prediction of Aerodynamic Loads on Lifting Surfaces. J. Aircraft, Vol.13, No.1 (1976), pp. 22-28.
120. Atta, E.H., Kandil, O.A., Mook, D.T. and Nayfeh, A.H.: Nonlinear, Unsteady Aerodynamics Loads on Rectangular and Delta Wings. AIAA Paper 77-157 (1977).
121. Kandil, O.A.: State of Art of Nonlinear Discrete-Vortex Methods for Steady and Unsteady High Angle of Attack Aerodynamics. AGARD CP-247 (1979).
122. Kandil, O.A. and Balakrishnan, L.: Recent Improvements in the prediction of Leading and Trailing Edge Vortex Cores of Delta Wings. AIAA Paper 81-1263.
123. Mangia, R.K. and Hancock, G.J.: A Theoretical Investigation for Delta Wings with Leading-Edge Vortex Separation at Low Speeds. ARC C.P. No.1086 (1970).
124. Kandil, O.A., Chu, L.C. and Yates Jr., E.C.: Hybrid Vortex Method for Lifting Surfaces with Free Vortex Flow, AIAA Paper 80-0070 (1980).
125. Yen, A., Mook, D.T., Nayfeh, A.H.: A Continuous-Vorticity Panel Method for Lifting Surfaces. AIAA Paper 81-1895 (1981).
126. Kandil, O.A., Chu, L.C. and Tureaud, T.: Steady and Unsteady Nonlinear Hybrid Vortex Method for Lifting Surfaces at Large Angles of Attack. AIAA Paper 82-0351 (1982).
127. Weber, J.A., Brune, G.W., Johnson, F.T., Lu, P. and Rubbert, P.E.: Three-Dimensional Solution of Flows over Wings with Leading-Edge Vortex Separation. AIAA Journal, Vol.14, No.4 (1976), pp. 519-525. Also AIAA Paper 75-866 (1975).
128. Johnson, F.T., Lu, P., Brune, G.W. and Weber, J.A.: An Improved Method for the Prediction of Completely Three-Dimensional Aerodynamic Load Distributions on Configurations With Leading-Edge Vortex Separation. AIAA Paper 76-417 (1976).
129. Tinoco, E.N. and Yoshihara, H.: Subcritical Drag Minimization for Highly Swept Wings with Leading-Edge Vortices. AGARD CP-247 (1979).
130. Johnson, F.T., Tinoco, E.N., Lu, P. and Epton, M.A.: Three-Dimensional Flow over Wings with Leading-Edge Vortex Separation. AIAA Journal, Vol.18, No.4 (1980), pp. 367-380. Also Paper 79-0282 (1979).
131. Johnson, F.T., Lu, P., Tinoco, E.N. and Epton, M.A.: An Improved Method for the Solution of Three-Dimensional Leading-Edge Vortex Flows. Volume I - Theory Document, NASA CR 3278. Volume II - User's Guide and Programmer's Document (1980).
132. Luckring, J.M., Schoonover Jr., W.E. and Frink, N.T.: Recent Advances in Applying Free Vortex Sheet Theory for the Estimation of Vortex Flow Aerodynamics. AIAA Paper 82-0095 (1982).
133. Morino, L., Chen, L.T. and Suciu, E.O.: Steady and Oscillatory Subsonic and Supersonic Aerodynamics around Complex Configurations. AIAA Journal, Vol.13, No.3 (1975), pp. 368-374.
134. Hoeijmakers, H.W.M. and Bennekers, B.: A Computational Model for the Calculation of the Flow about Wings with Leading-Edge Vortices. AGARD CP-247 (1979).
135. Verhaagen, N.G.: Measurement of the Pressure Distribution on a Biconvex Delta Wing of Aspect Ratio 1. Unpubl. Rep. Dep. Aero. Eng. Delft University of Technology (1979).
136. Hummel, D. and Redeker, G.: Experimentelle Bestimmung der gebundene Wirbellinien sowie des Strömungs-Verlaufs in der Umgebung der Hinterkante eines schlanken Deltaflügels. Abh. Braunschweig. Wiss. Ges., Vol.22 (1972), pp. 273-290.
137. Marsden, D.J., Simpson, R.W. and Rainbird, W.J.: The Flow over Delta Wings at Low Speeds with Leading-Edge Separation. Cranfield College of Aeronautics Rep. No.114 (1957).
138. Reddy, C.S.: Effect of Leading-Edge Vortex Flaps on Aerodynamic Performance of Delta Wings. J. Aircraft, Vol.18, No.9 (1981), pp. 796-798.
139. Frink, N.T.: Analytical Study of Vortex Flaps on Highly Swept Delta Wings. ICAS Paper 82-6.7.2 (1982).
140. Reddy, C.S.: Effect of Sweep Angles on Aerodynamic Performance of Double Arrow Wing - An Analytical Study. J. Aircraft, Vol.18, No.8 (1981), pp. 702-703.
141. Kuhlman, J.M.: Analytical Study of Separated Vortex Flow on Highly Swept Wings. NASA CR 3022 (1978).
142. Rizzi, A.: Vector Coding the Finite-Volume Procedure for the CYBER 205. In Lecture Series Notes 1983-04, VKI (1983).
143. Hitzel, S.M. and Schmidt, W.: Slender Wings with Leading-Edge Vortex Separation. A Challenge for Panel Methods and Euler Codes. AIAA Paper 83-0562 (1983).
144. Manro, M.E. Manning, K.J.R., Hallstaff, Th.H. and Rogers, J.T.: Transonic Pressure Measurements and Comparison of Theory to Experiment for an Arrow-Wing Configuration-Summary Report. NASA CR-2610 (1975).
145. Brocard, Y. and Manie, F.: Etudes des Caractéristiques de L'écoulement Tourbillonnaire sur une Aile en Fleche. ONERA T.P. No.1979-147 (1979).
146. ElRefaee, M.M., Wu, J.C. and Lekoudis, S.G.: Solutions of the Compressible Navier-Stokes Equations Using the Integral Method. AIAA Journal, Vol. 20, No.3 (1982), pp. 356-362.

147. Wilson, J.D.: Calculations of Vortex Breakdown Locations for Flow over Delta Wings. J. Aircraft, Vol. 14, No.10 (1977), pp. 1020-1022.
148. Fiddes, S.P.: A Theory of the Separated Flow Past a Slender Elliptic Cone at Incidence, AGARD CP-291 (1980).
149. Hoeijmakers, H.W.M.: A Panel Method for the Prediction of Aerodynamic Characteristics of Complex Configurations in Linearized Subsonic or Supersonic Flow. AGARD CP-336 (1982). Also NLR MP 82040 U.

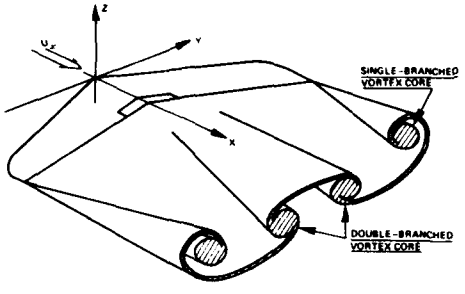

Fig. 1 Downstream development of a vortex wake

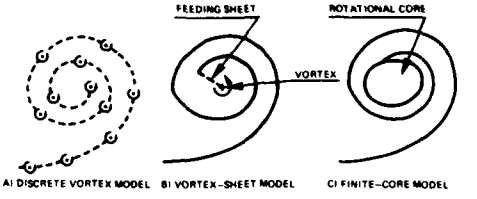

Fig. 3 Vortex sheet models; Single-branched spiral

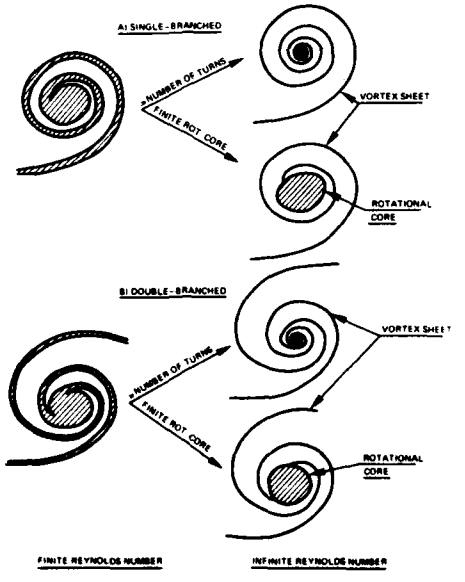

Fig. 2 Vortex-core models; Infinite number of turns or rotational core

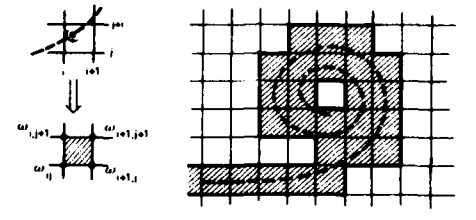

Fig. 4 "Cloud-in-cell" method

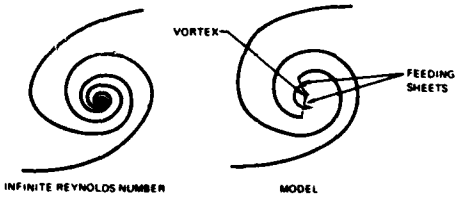

Fig. 5 Vortex sheet model; double-branched vortex core

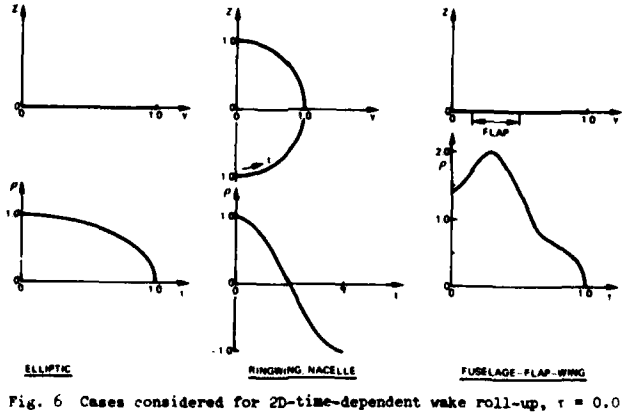

Fig. 6 Cases considered for 2D-time-dependent wake roll-up, $\tau = 0.0$

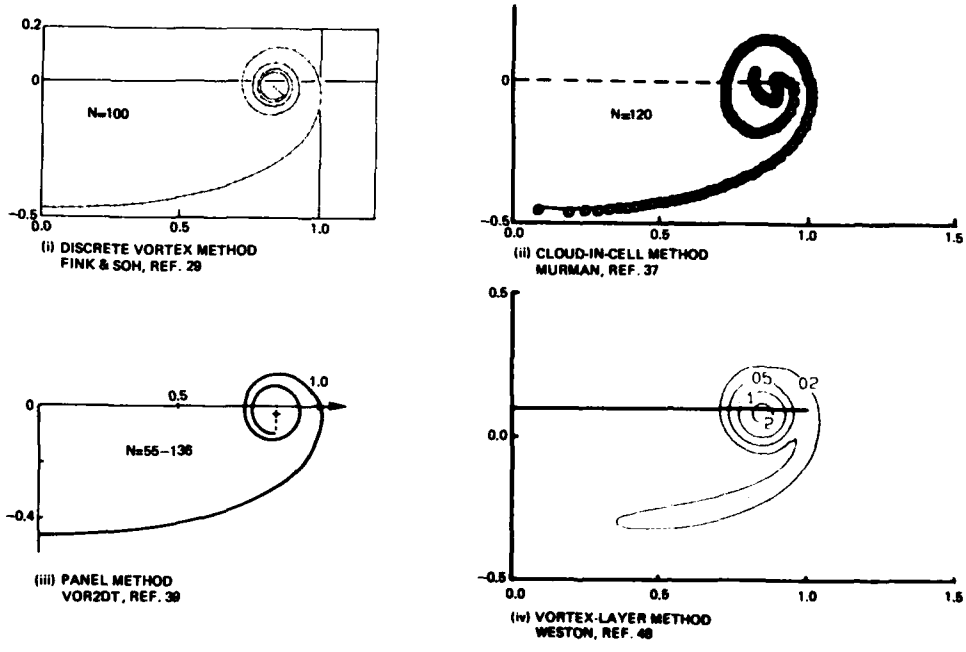

Fig. 7a Wake behind elliptically loaded wing, $\tau \approx 1.0$

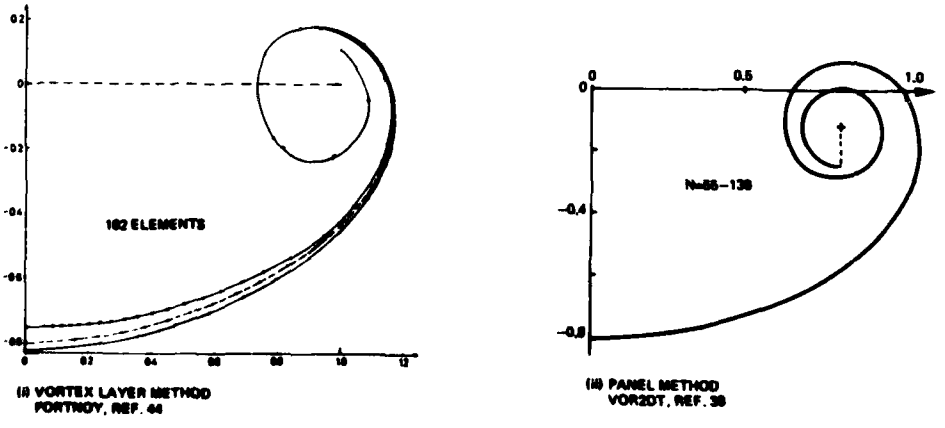

Fig. 7b Wake behind elliptically loaded wing, $\tau \approx 2.0$

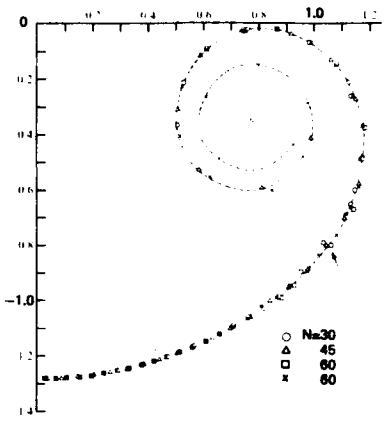

(i) DISCRETE VORTEX METHOD
MOORE, REF. 27

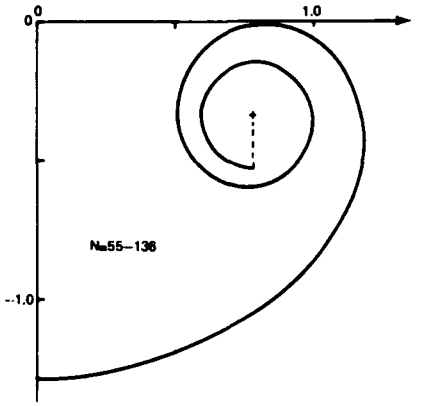

(ii) PANEL METHOD
VOR2DT, REF. 39

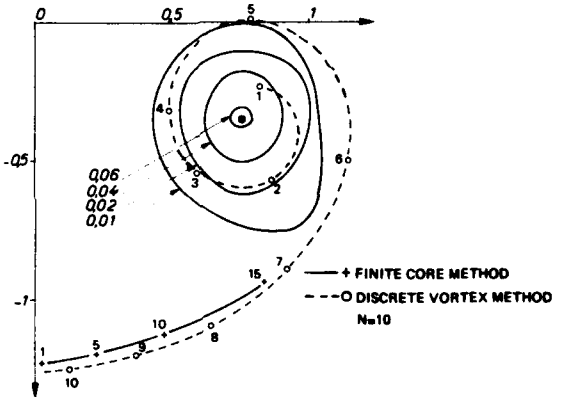

(iii) FINITE CORE METHOD
HUBERSON, REF. 43

Fig. 7c Wake behind elliptically loaded wing, $\tau \approx 4.0$

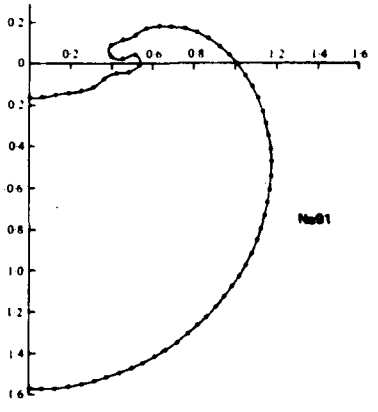

(i) DISCRETE VORTEX METHOD
BAKER, REF. 30

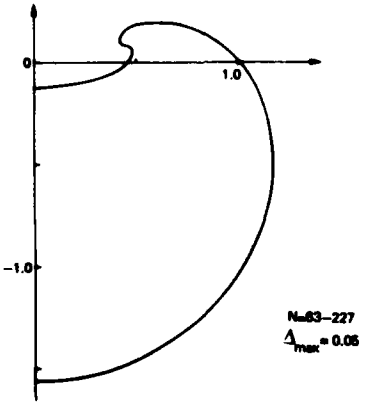

(ii) PANEL METHOD
VOR2DT, REF. 39

Fig. 8a Wake behind ring wing, $\tau \approx 1.5$

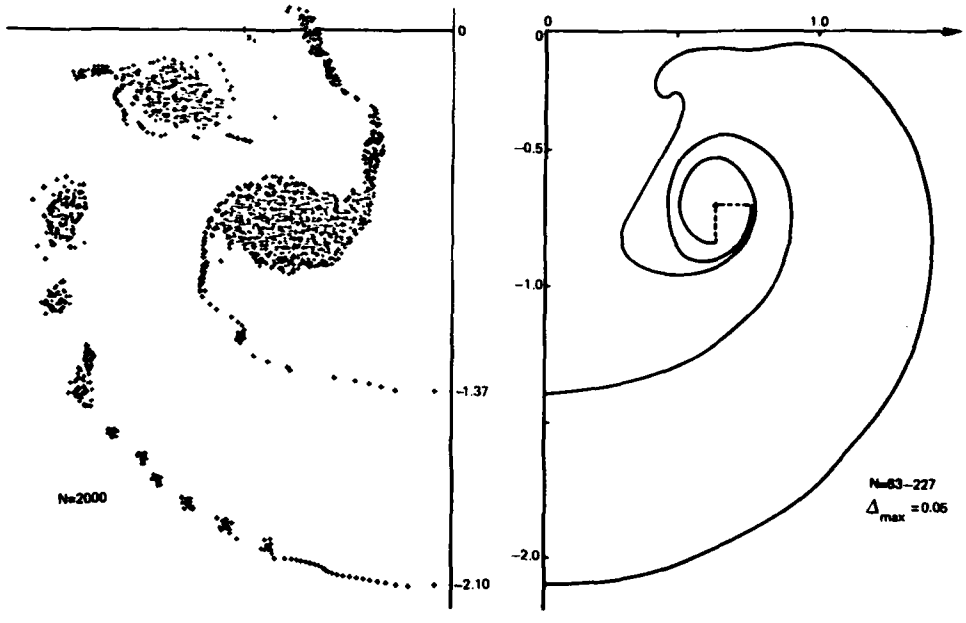

(i) CLOUD-IN-CELL METHOD
BAKER, REF. 35

(ii) PANEL METHOD
VOR2DT, REF. 39

Fig. 8b Wake behind ring wing, $\tau \approx 3.69$

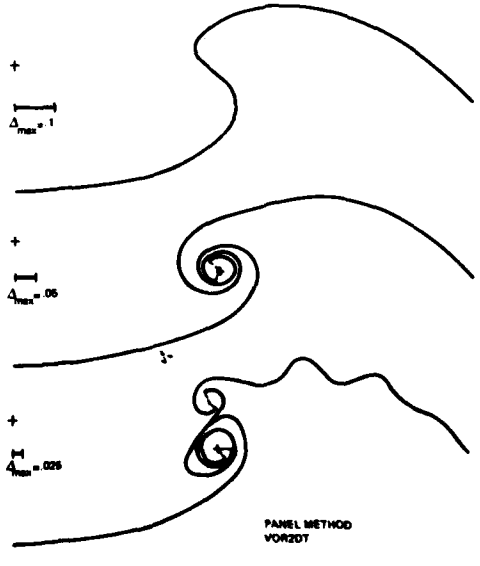

Fig. 8c Wake behind ring wing, $\tau \approx 1.77$

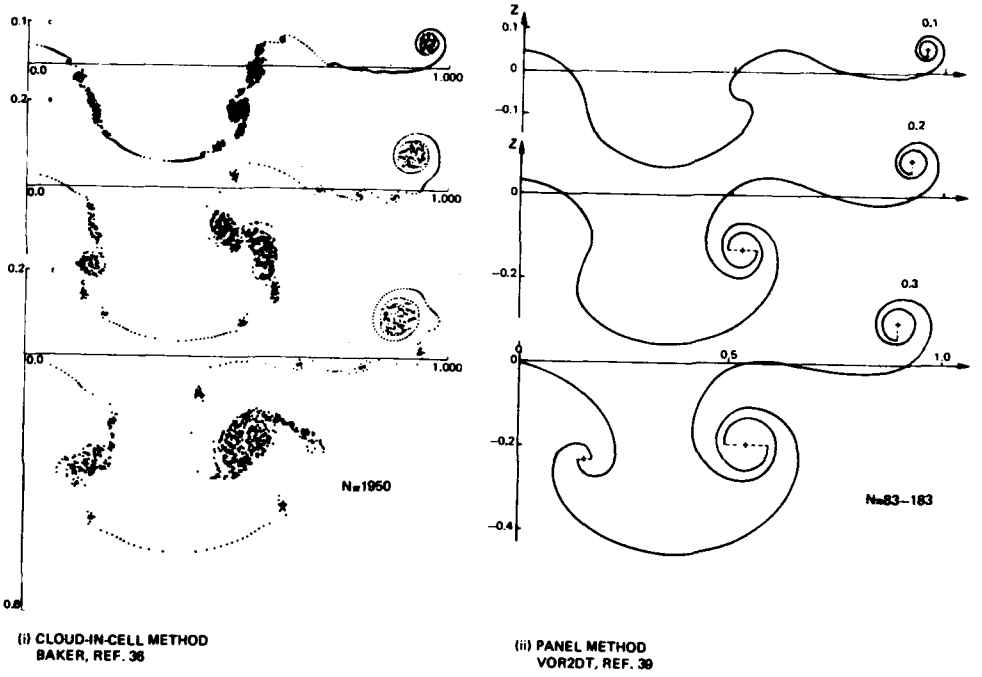

(i) CLOUD-IN-CELL METHOD
BAKER, REF. 36

(ii) PANEL METHOD
VOR2DT, REF. 39

Fig. 9a Wake behind wing-body with deployed flap

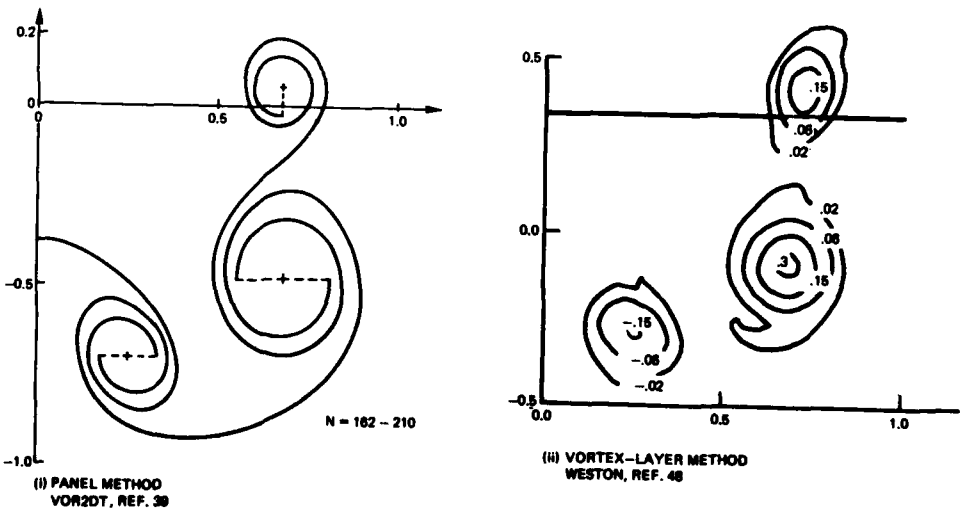

(i) PANEL METHOD
VOR2DT, REF. 39

(ii) VORTEX–LAYER METHOD
WESTON, REF. 48

Fig. 9b Wake behind wing-body with deployed flap, $\tau \approx 1.0$

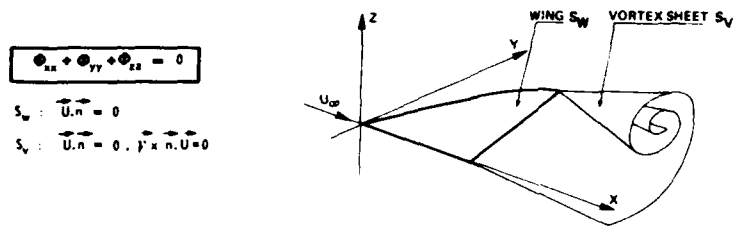

Fig. 10 Vortex sheet model 3D vortex wake

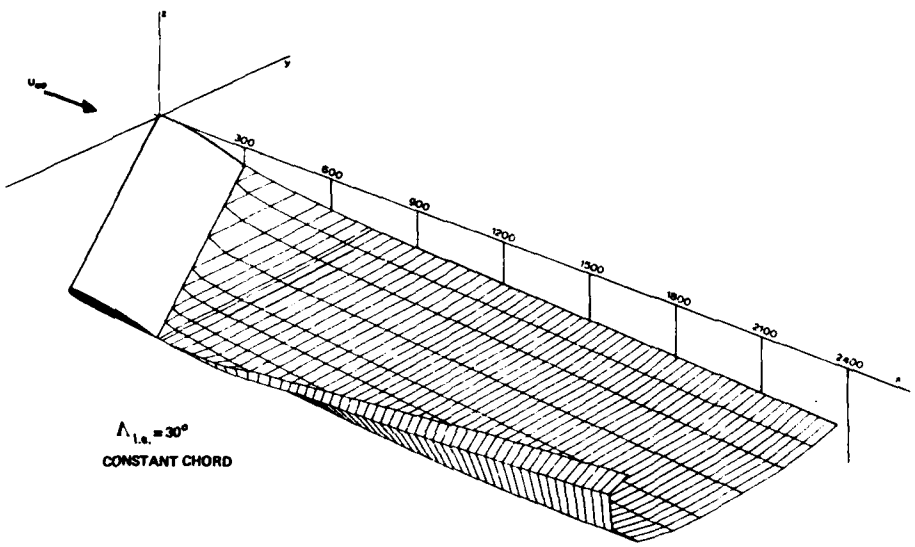

Fig. 11a Vortex wake behind AR = 5.0 swept wing, C_L = 0.82 (Ref. 60)

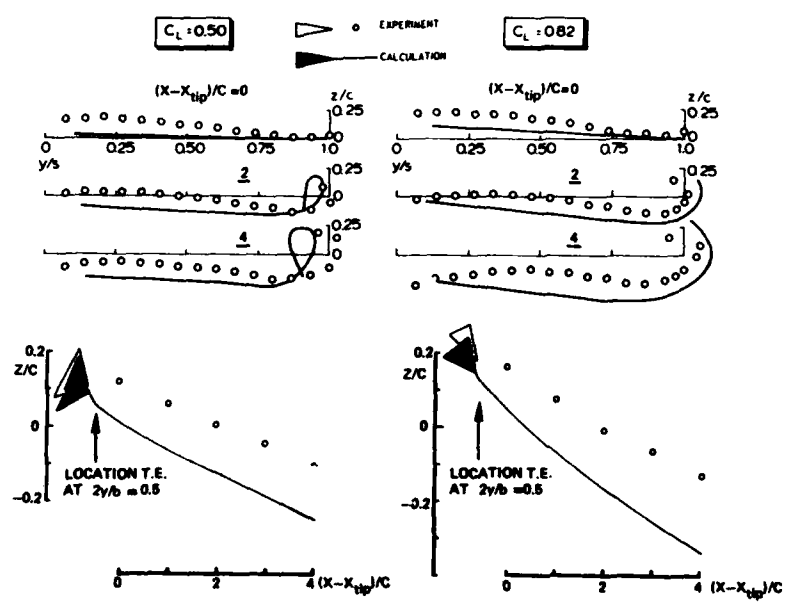

Fig. 11b Computed and measured vortex wake geometry behind AR = 5.0 swept wing (Ref. 60)

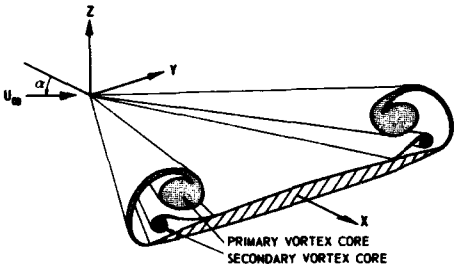

Fig. 12 Vortex flow about delta wing

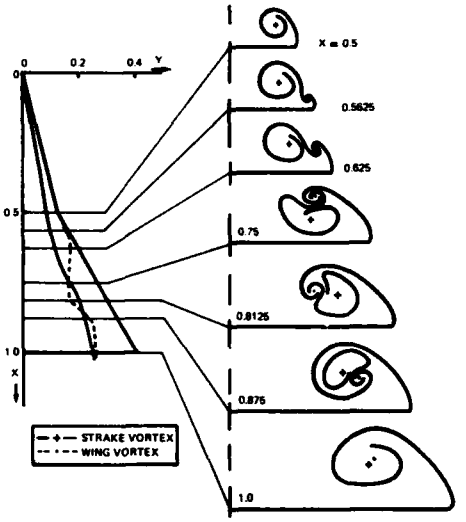

Fig. 13 Flow pattern above 76°/60° double-delta wing (Ref. 83)

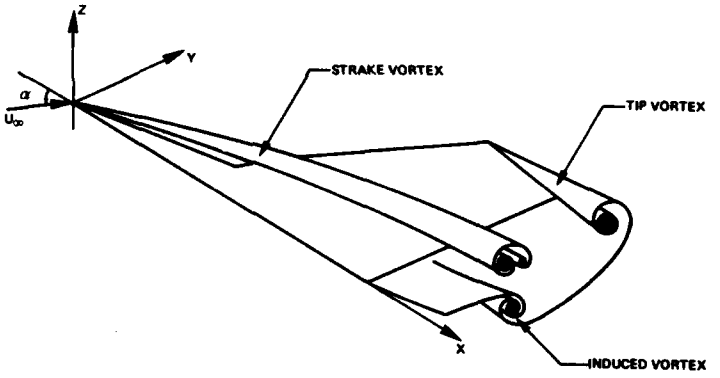

Fig. 14 Conceptual view strake-wing vortex flow after Küchemann (Ref. 1)

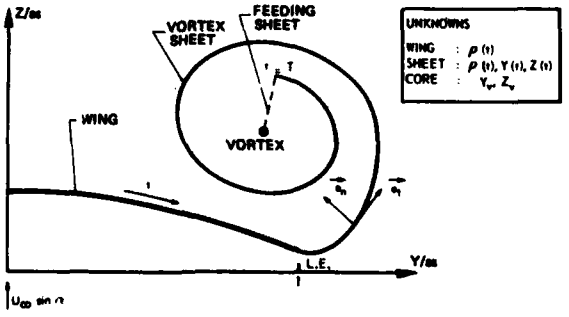

Fig. 15 Conical flow problem

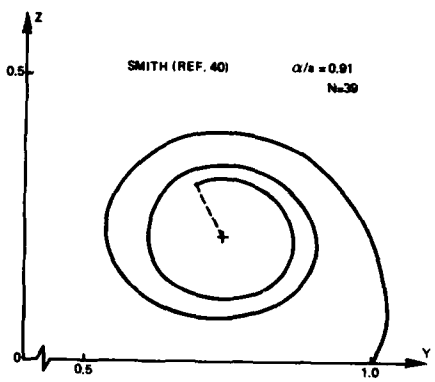

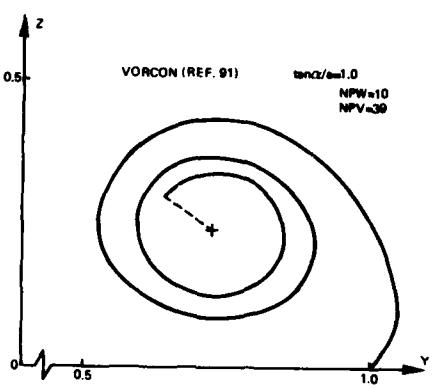

Fig. 16a Flat delta wing, AR = 1.0, $\alpha \approx 14$ deg

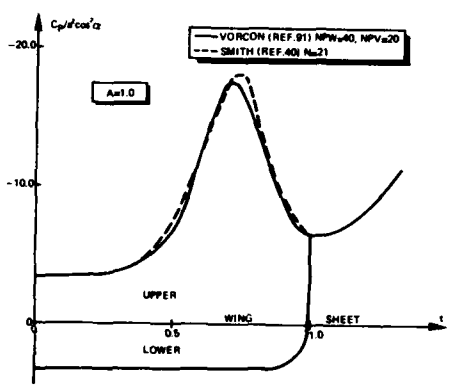

Fig. 16b Flat delta wing, A = 1.0. Computed conical pressure distribution

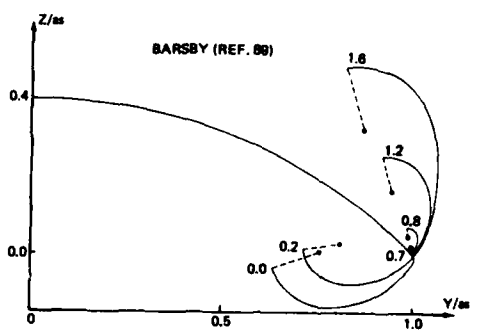

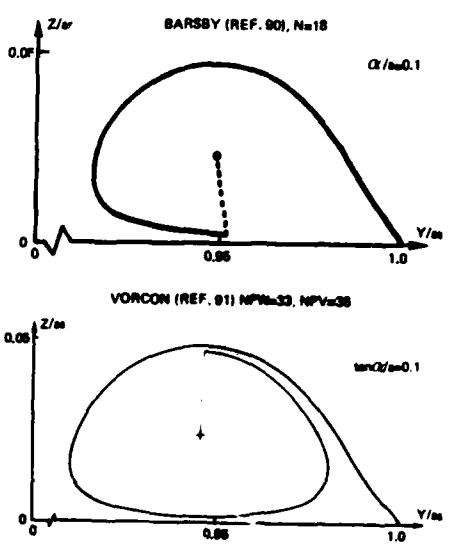

Fig. 16c Flat delta wing, AR = 1.0, $\alpha \approx 1.4$ deg

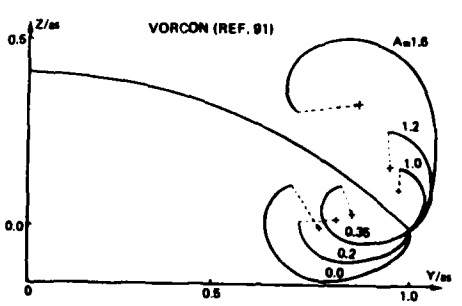

Fig. 16d Conically cambered delta wing

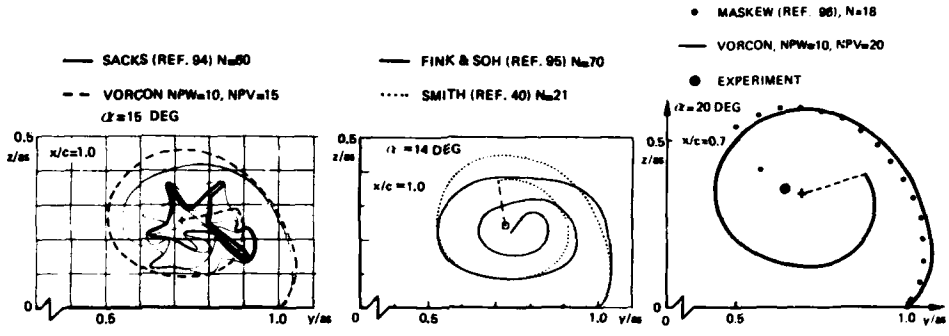

Fig. 17 Results of slender-body discrete-vortex methods compared with conical flow methods. Flat delta wing, AR = 1.0

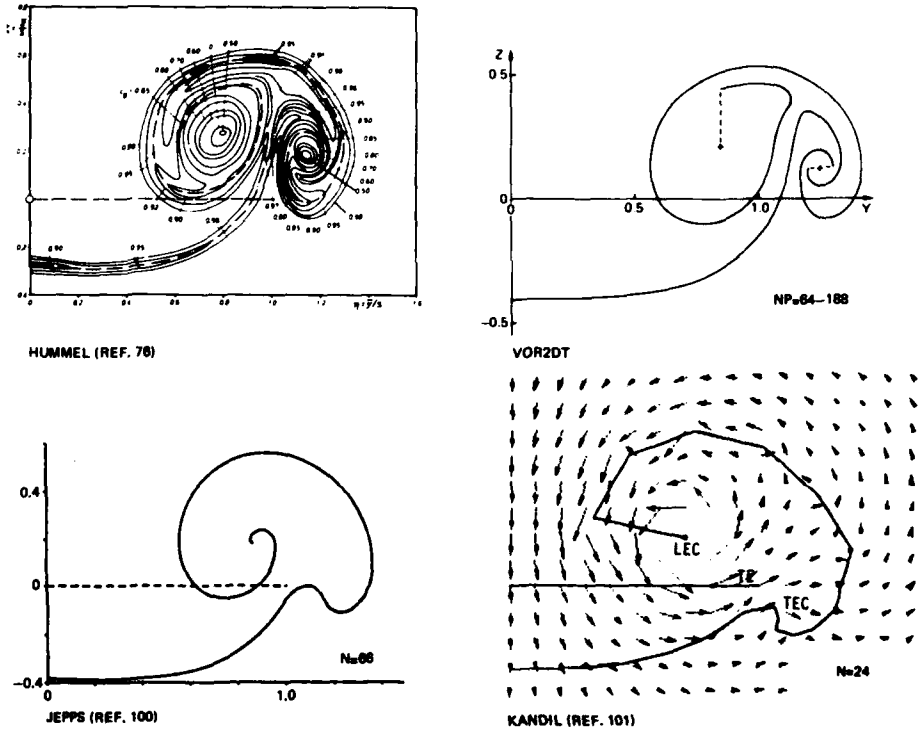

Fig. 18 Vortex wake at 1.067 half spans behind AR = 1.0 delta wing at α = 20 deg

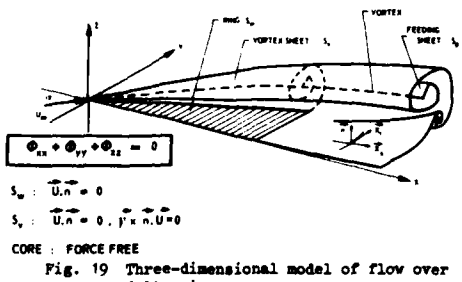

Fig. 19 Three-dimensional model of flow over delta wing

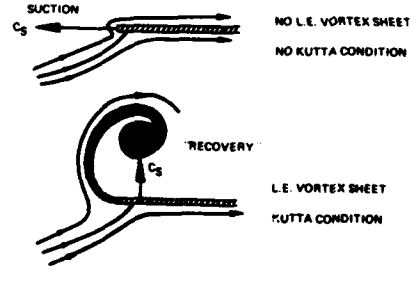

Fig. 20 Polhamus' leading-edge suction analogy

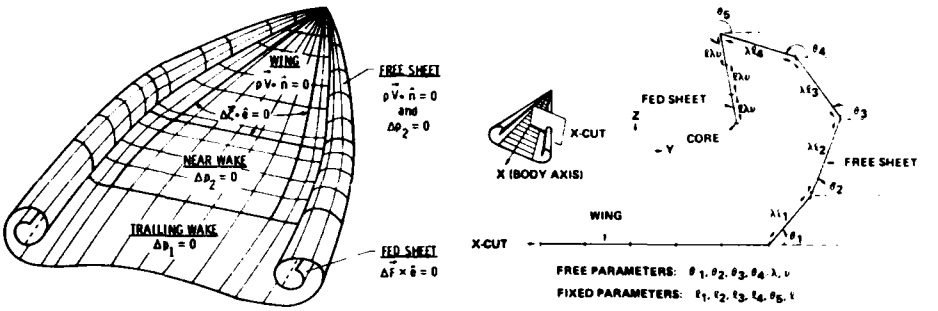

A) BOEING FREE VORTEX SHEET MODEL (REF. 132) B) FREE/FED SHEET KINEMATICS (REF. 131)

Fig. 21 Three-dimensional free-vortex-sheet method LEV (Ref. 131)

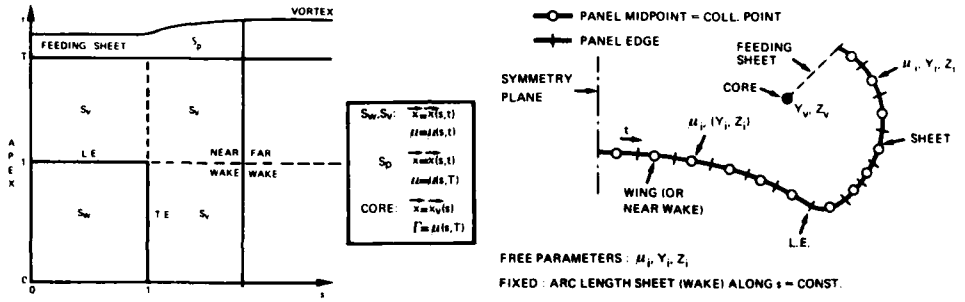

A) COMPUTATIONAL DOMAIN B) GEOMETRY IN PLANE S=CONST.

Fig. 22 Three-dimensional free-vortex-sheet method VORSEP (Ref. 134)

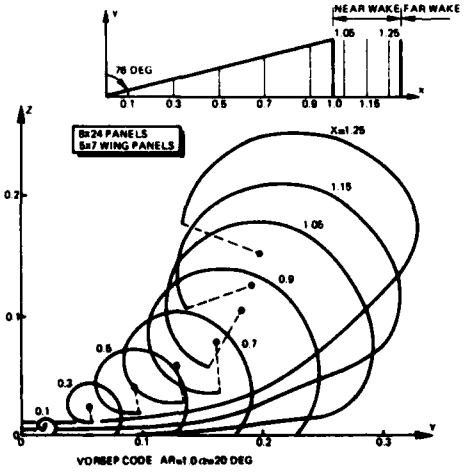

Fig. 23a Delta wing vortex sheet shapes computed with panel method VORSEP

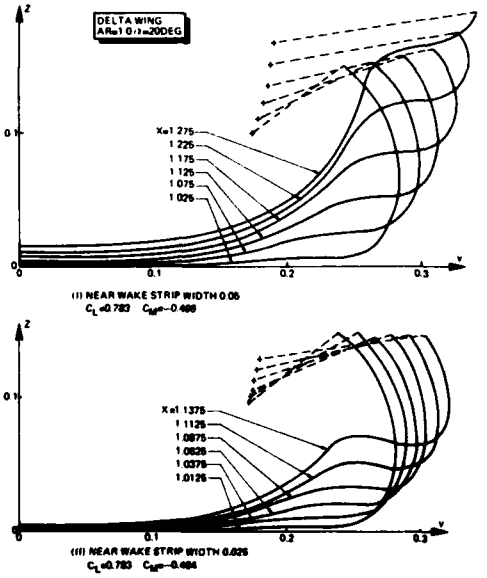

Fig. 23b VORSEP: Computed near wake shape, AR = 1.0 delta wing, α = 20 deg

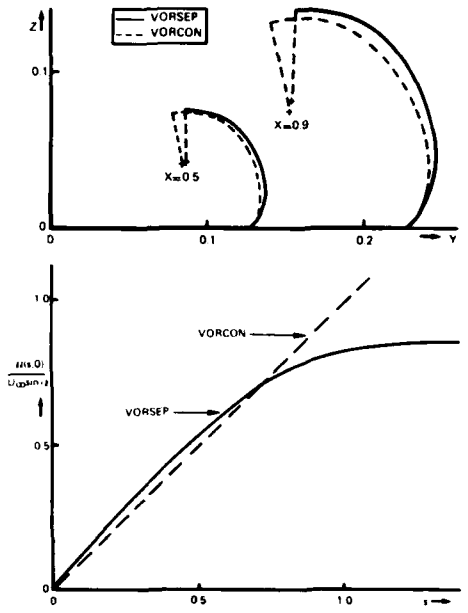

Fig. 23c Comparison of conical and 3D solution (Ref. 83)

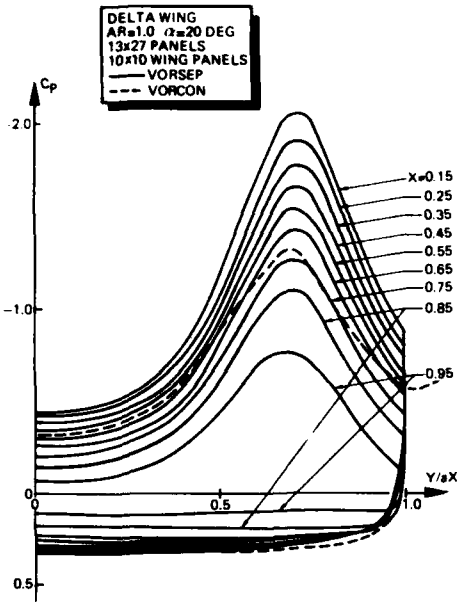

Fig. 23d Computed pressure distribution on delta wing

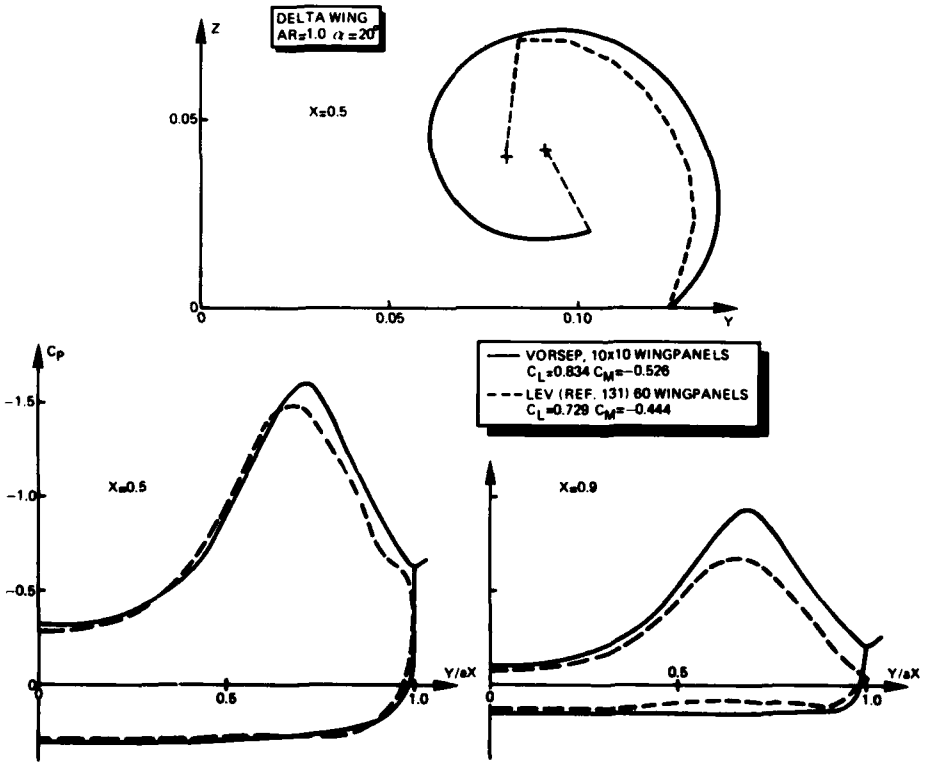

Fig. 24 Comparison of panel-method solutions

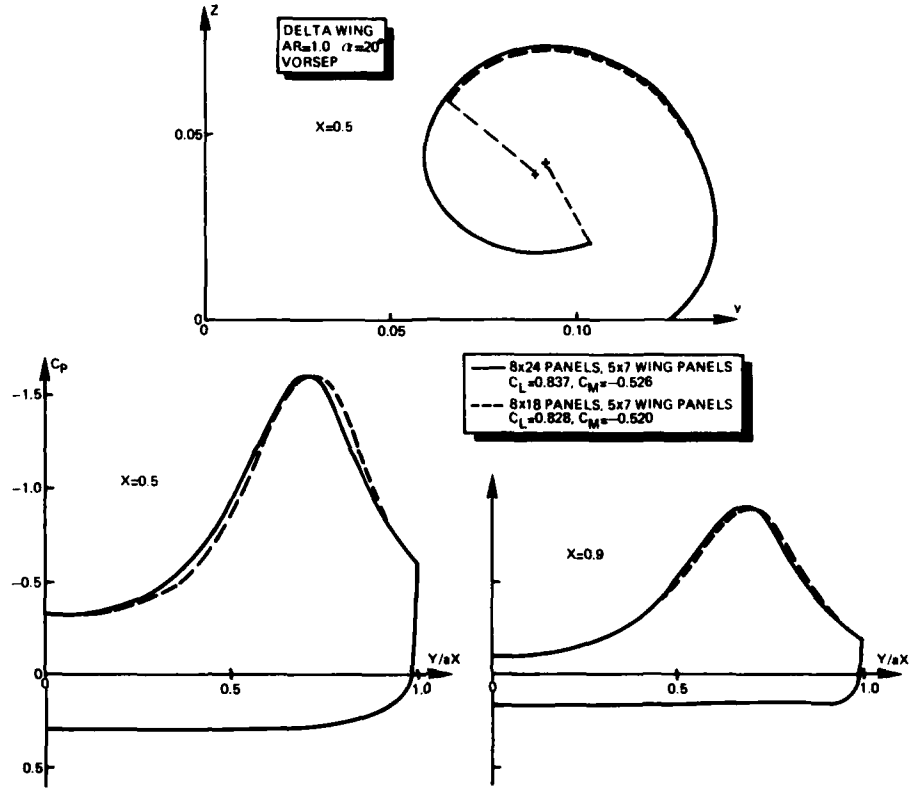

Fig. 25 Effect of variation in length of free vortex sheet

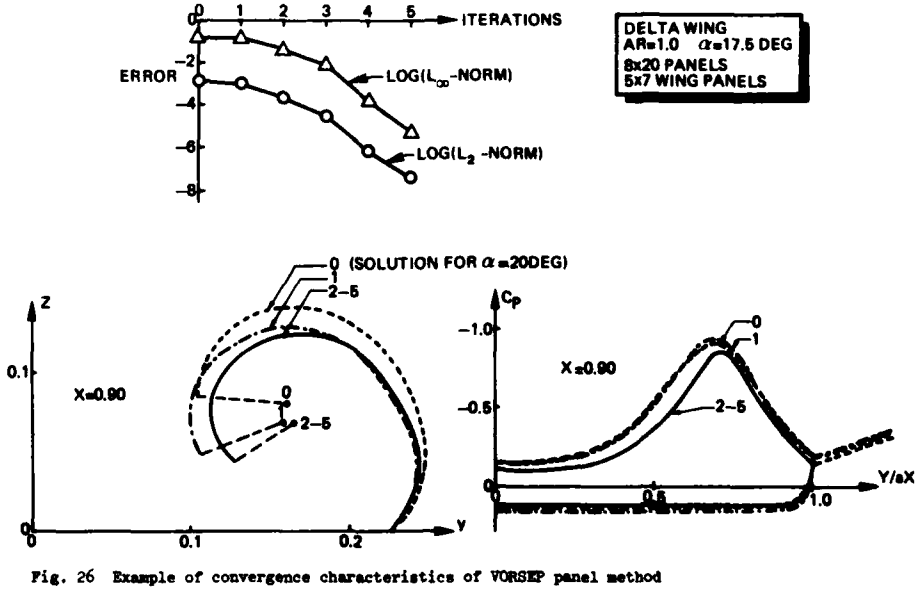

Fig. 26 Example of convergence characteristics of VORSEP panel method

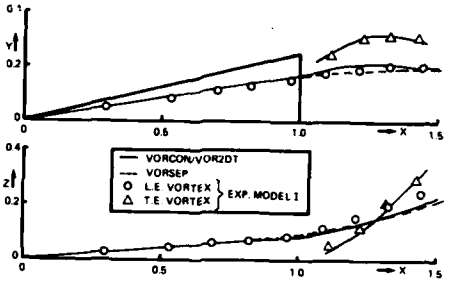

Fig. 27a Position of vortex cores above AR = 1.0 delta wing at α = 20 deg. Comparison with experiment (Ref. 83)

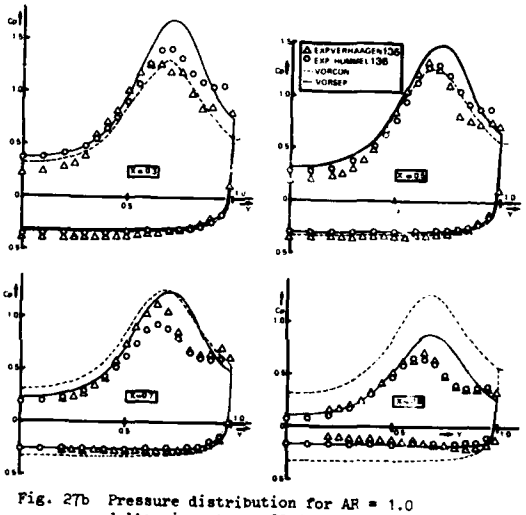

Fig. 27b Pressure distribution for AR = 1.0 delta wing at α = 20 deg. Comparison with turbulent flow experiment

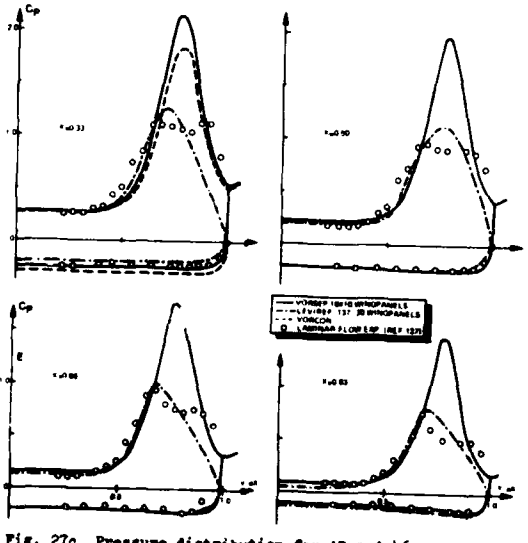

Fig. 27c Pressure distribution for AR = 1.46 delta wing at α = 14 deg. Comparison with laminar flow experiment

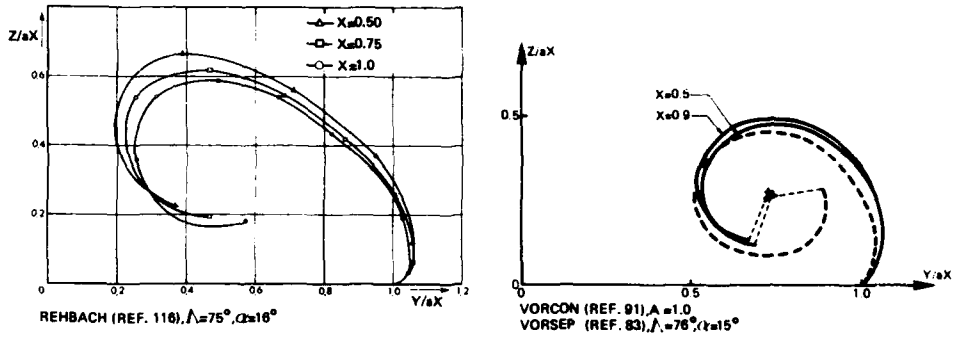

Fig. 28 Vortex-sheet geometry delta wing, comparison vortex lattice method and panel method

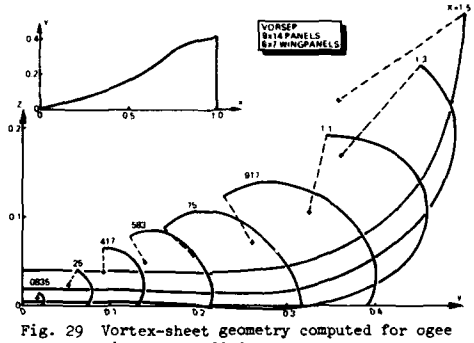

Fig. 29 Vortex-sheet geometry computed for ogee wing at α = 20 deg

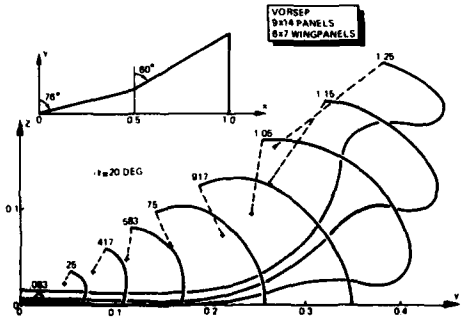

Fig. 30a Vortex sheet shape computed for double-delta wing at α = 20 deg

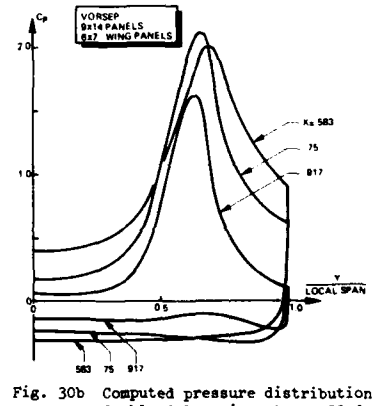

Fig. 30b Computed pressure distribution for double-delta wing at α = 20 deg

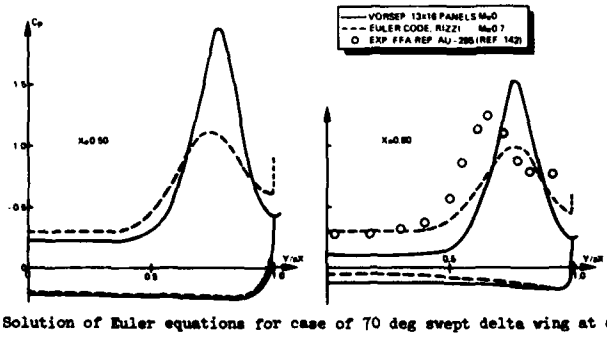

Fig. 31 Solution of Euler equations for case of 70 deg swept delta wing at α = 15 deg

VORTEX FLOW SIMULATIONS PAST WINGS USING THE EULER-EQUATIONS

Claus Weiland
Messerschmitt-Bölkow-Blohm GmbH
Ottobrunn, BRD

SUMMARY

Flow fields with vortex separation play an important role in the aerodynamics of missiles and for airplanes. Investigations carried out recently have shown that such flow fields can be computed by means of solutions of the Euler-equations. In the present paper results are presented for flow fields around delta-wings with freestream Machnumber larger than 1. The range of the angle of attack is up to $\alpha = 15°$. The Euler-equations are integrated by using a space-marching finite-difference method. The delta-wings have got sharp and blunted leading edges. At the sharp leading edge a condition is prescribed which produces a tangential discontinuity by means of which vorticity is introduced into the flow field. The formulation of the governing equations, the boundary conditions and the initial data is discussed. The results shown are the contours of the bow shock, the isobars, the lines of constant total pressure and the velocity vectors of the cross flow. The wave drag is determined by evaluating the integral relation for the momentum in an adequate surface in the flow field.

LIST OF SYMBOLS

A,B,C	matrices of the non-conservative Euler-equations	u,v,w	components of the velocity vector in (z,r,φ)-directions
a,b	constants	$\vec{v}$	velocity vector
c	speed of sound	W	drag force
D	Jacobi-determinant	X	solution vector of the non-conservative Euler-equations
e	total energy per volume	z,x,y	Cartesian coordinates
g	empirical coefficient	z,r,φ	cylindrical coordinates
h	enthalpy	α	angle of attack
H	vector of curvature terms of the quasi-conservative formulation	Γ	vector of curvature terms of the non-conservative formulation
J,K,L	Jacobian of the quasi-conservative Euler-equations	λ	stability parameter $0 < \lambda \leq 1$
L_1	total length of the delta wing (Fig. 2)	ρ	density
M	Machnumber	ψ	direction of the velocity at the sharp leading edge in the z,r,-plane ($\varphi = \pi/2$)
$\vec{n}$	$\hat{=}$ n normal vector	ω	$= \pi/2 - \epsilon$
p	static pressure	ε	sweep angle

1. INTRODUCTION

One of the aims of theoretical and particularly numerical fluid dynamics is the calculation of complete flow fields past missiles and aircraft shapes. Up to now we are far away from a general solution of the Navier-Stokes equations because of the problems of numerical mathematics (stable and fast algorithms for field points, compatible algorithms at the boundaries, grid generation), physical problems (stability of the flow, transition, turbulence), and bounds of performance of the computers available today (main memory, memory access, operation time of the functional units, etc.).

Nevertheless, in the last 2 decades considerable advances were achieved in integrating derivatives of the Navier-Stokes equations like the linearised potential equation, the full potential equation, the Euler-equations, the boundary-layer equations, the parabolized and thin-layer Navier-Stokes equations. These equations were solved for flows past more or less simple two-dimensional and three-dimensional configurations. It seems, that the calculation of flow fields with supersonic freestream Machnumbers ($M_\infty > 1$) is a relatively easy task compared to the calculation of subsonic and in particular transonic flow fields. This is due to the fact, that the formulation and the realization of the boundary conditions at inflow and outflow boundaries is simpler for supersonic flows than for subsonic- and transonic flows. In addition the potential equation and the Euler-equations are hyperbolic in space for supersonic flows and the theory for systems of quasilinear, hyperbolic partial differential equations in two and three dimensions is better developed than for quasilinear, elliptic problems. Because of the structure of the domain of dependence of hyperbolic problems (e.g.: steady inviscid supersonic flow fields), a space marching method can be applied whereby the expenses for the main memory of the computer are reduced by one space dimension.

The complete aerodynamical problem of flow field analysis is to determine the pressure distribution on the surface of a given configuration at given freestream values (Machnumber, Re-number, angle of attack, angle of yaw, etc.). All the relevant aerodynamical coefficients of forces and moments can be calculated by integrating the pressure distribution on the body surface. In some cases the distribution of temperature at the body surface is of special importance (missiles, space shuttle). When a complete field solution was found, the above mentioned quantities are part of the solution in the frame of the assumptions introduced.

A lot of effort have been spent in order to make it possible to calculate shocks with numerical methods. Two methods are available today: a) the "shock-fitting-technique" [1] and b) the "shock-capturing-technique" [2 ÷ 6]. The application of the shock-capturing technique - for embedded shocks usually employed - requires that the system of partial differential equations is formulated in such a manner that by integrating them over a region containing discontinuities, only integrable functions occur. It is also necessary for the prevention of expansion shocks that the numerical method contains artificial diffusion terms [6] (entropy condition).

Another kind of discontinuities in inviscid flow fields is given by vortex sheets. The transport of vorticity through a flow field is done by diffusion and by convection. It is known, that flow fields with vorticity can be calculated by using the Euler-equations which describe the convective transport. In recent years vortex flow calculations have been carried out by applying various numerical methods in order to integrate the Euler-equations: for problems of missile aerodynamic space-marching procedures in connection with a Kutta-condition are successfully employed [7 ÷ 9], a time-dependent method based on a finite volume procedure was used for the prediction of the flow past transonic and supersonic wings [10,11].

It was found by the last authors that along sharp and blunted leading edges of delta-wings vortex separation occured although no Kutta-condition was introduced. This is a surprising result and cannot be explained up to now [12].

In the present paper results are given from calculations of supersonic flow fields past delta-wings with blunt and sharp leading edges. A three-dimensional space-marching finite difference method based on the work in Refs. [13,17,18] is used.

The scope of the paper is to advance the understanding of Euler simulations of vortex flows.

2. CALCULATIONS OF FLOWS WITH VORTICITY USING THE EULER-EQUATIONS

Let us consider some of the effects and mechanisms which we encounter by the calculation of vortical type flows using a discrete numerical method.

a. Some sources of vorticity in a flow field are:
   α) shocks of varying strength
   β) intersecting shocks of different strength
   γ) no-slip condition at the walls [14,15]

b. Transport of vorticity by the Euler-equations through:
   α) convection (along streamlines)
   β) diffusion (normal to the streamlines) in solutions of discrete approximations of the Euler-equations due to the artificial diffusion terms

c. Introduction of vorticity in a discrete Euler solution by
   α) a. α) and a. β)
   β) a Kutta-like condition
   γ) initial and boundary conditions.

At sharp leading edges of wings the Euler-equations are undetermined. A tangential discontinuity is introduced there as a boundary condition which is similar to the Kutta-condition (c. β)) used at the trailing edge of profiles and wings. The vorticity produced by such discontinuities at sharp leading edges of delta wings is convective transported into the flow field and models the leeside vortices due to the artificial diffusive transport (b. β)).

3. THE GOVERNING EQUATIONS

The three-dimensional steady Euler-equations in a non-conservative formulation read for cylindrical coordinates (z,r,φ):

$$A\frac{\partial X}{\partial z} + B\frac{\partial X}{\partial r} + C\frac{\partial X}{\partial \varphi} + \Gamma = 0 \qquad (1)$$

where

$$X = \begin{Bmatrix} \rho \\ u \\ v \\ w \\ p \end{Bmatrix} \qquad \Gamma = \frac{1}{r}\begin{Bmatrix} \rho v \\ 0 \\ -w^2 \\ vw \\ c^2\rho v \end{Bmatrix}$$

$$A = \begin{Bmatrix} \rho & 0 & 0 & 0 & u \\ u & 0 & 0 & \rho^{-1} & 0 \\ 0 & u & 0 & 0 & 0 \\ 0 & 0 & u & 0 & 0 \\ c^2\rho & 0 & 0 & u & 0 \end{Bmatrix} \qquad B = \begin{Bmatrix} 0 & \rho & 0 & 0 & v \\ v & 0 & 0 & 0 & 0 \\ 0 & v & 0 & \rho^{-1} & 0 \\ 0 & 0 & v & 0 & 0 \\ 0 & c^2\rho & 0 & v & 0 \end{Bmatrix} \qquad C = \frac{1}{r}\begin{Bmatrix} 0 & 0 & \rho & 0 & w \\ w & 0 & 0 & 0 & 0 \\ 0 & w & 0 & 0 & 0 \\ 0 & 0 & w & \rho^{-1} & 0 \\ 0 & 0 & c^2\rho & w & 0 \end{Bmatrix}$$

For the calculation of strong and weak discontinuities (shocks and vortex sheets) using the capturing method it is necessary to use the governing equations in a conservative [2] or quasi-conservative [13,16] formulation, respectively.

The quasi-conservative formulation is given by:

$$J \frac{\partial U}{\partial z} + K \frac{\partial U}{\partial v} + L \frac{\partial U}{\partial \varphi} + H = 0 \qquad (2)$$

where $U^T = (\rho, \rho u, \rho v, \rho w, e)$ is the solution vector and $e = \frac{p}{\gamma-1} + \frac{1}{2} \cdot \frac{(\rho u)^2 + (\rho v)^2 + (\rho w)^2}{\rho}$ the total energy per volume.

The Jacobi-matrices J,K,L are lengthy and can be found in [13]. The correlation between the matrices A,B,C and J,K,L can conveniently be found from similarity transformations. We consider, for example, the first term of equation (2)

$$y = J \frac{\partial U}{\partial z}$$

and look at the vector $\partial/\partial z\, U$ as the components of a coordinate system. Let the linear transformation

$$y = f(\frac{\partial}{\partial z} U)$$

be given in this coordinate system. Then we obtain a transformation to another coordinate system by

$$\frac{\partial}{\partial z} U = T \frac{\partial}{\partial z} X \quad \text{and} \quad y = T \cdot \bar{y} \qquad (3)$$

From this it follows

$$\bar{y} = T^{-1} J T \frac{\partial}{\partial z} X$$

and $A = T^{-1} J \cdot T$

A similarity transformation does not change the characteristic equation of a matrix. Therefore J and A have the same eigenvalues. From equation (3) we obtain in a simple way the transformation matrix T:

$$\frac{\partial}{\partial z} \begin{Bmatrix} \rho \\ \rho u \\ \rho v \\ \rho w \\ e \end{Bmatrix} = \begin{Bmatrix} 1 & 0 & 0 & 0 & 0 \\ u & \rho & 0 & 0 & 0 \\ v & 0 & \rho & 0 & 0 \\ w & 0 & 0 & \rho & 0 \\ \frac{q^2}{2} & \rho u & \rho v & \rho w & \frac{1}{\gamma-1} \end{Bmatrix} \cdot \frac{\partial}{\partial z} \begin{Bmatrix} \rho \\ u \\ v \\ w \\ p \end{Bmatrix} = T \frac{\partial}{\partial z} \begin{Bmatrix} \rho \\ u \\ v \\ w \\ p \end{Bmatrix}$$

and the inverse:

$$T^{-1} = \begin{Bmatrix} 1 & 0 & 0 & 0 & 0 \\ -u/\rho & 1/\rho & 0 & 0 & 0 \\ -v/\rho & 0 & 1/\rho & 0 & 0 \\ -w/\rho & 0 & 0 & 1/\rho & 0 \\ \frac{\gamma-1}{2} q^2 & (\gamma-1)u & (\gamma-1)v & (\gamma-1)w & (\gamma-1) \end{Bmatrix} \qquad q^2 = u^2 + v^2 + w^2$$

4. THE BOUNDARY CONDITIONS

In this paper the flow past delta wings with blunt and sharp leading edges is considered. The flow field is computed between the bow shock and the body surface. The boundary conditions at the bow shock are given by the Rankine-Hugoniot equations. For large angles of attack and moderate freestream Machnumbers the bow shock surface on the leeward side turns into a Mach surface with continuous entropy across it. There, the prescribed boundary conditions are the freestream values and the characteristic direction-condition. At the body we have the condition that the normal component of the velocity-vector has to vanish. At the sharp leading edge the solution of the Euler-equations is indetermined [7,9]. A condition is introduced there, by means of which a tangential discontinuity is formed. We obtain

$$\begin{aligned} & w = 0 \\ & p = 0.5\,(p^+ + p^-) \\ & H = \frac{u^2 + v^2 + w^2}{2} + \frac{\gamma}{\gamma-1} \frac{p}{\rho} \\ (*) \quad & \tan\psi = 0.5\,((\tfrac{v}{u})^+ + (\tfrac{v}{u})^-) \\ (**) \quad & \tan\psi = \tan\omega\,(1+g) \qquad 0 < g < g_{max} \\ & \rho = 0.5\,(\rho^+ + \rho^-) \end{aligned} \qquad (4)$$

The direction of the velocity vector at the sharp leading edge can be determined by (*) or (**). Both equations have proved themselves to be conditionally useful. In (**) ω is the angle between the z-axis (marching-direction) and the leading edge, and g is an empirical quantity of the order of magnitude $O(g_{max}) = 1/4$.

5. THE ANALYTICAL FUNCTIONS FOR THE DESCRIPTION OF THE GRID

The frame of reference is given by the cylindrical coordinates (z,r,φ). A set of coordinates $\bar{z},\xi,\vartheta$ is chosen such that the physical space between the surface of the body contour and the surface of the initially unknown bow shock is transformed into a computational space having plane surfaces at his boundaries. In addition it is demanded that the origin p of a local polar coordinate system in planes $z = \text{const}$ can be defined by the two free functions x_0, y_0 (Fig. 1). In that way a proper resolution of the flow field in domain with strong curvature of the body contour is attained:

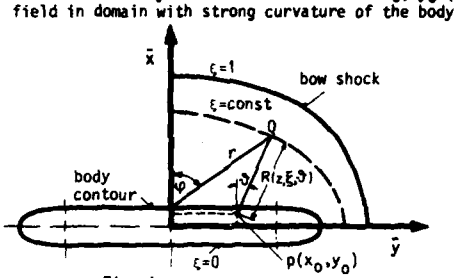

Fig. 1

$$
\begin{aligned}
z &= \bar{z}\\
y &= (\bar{x}^2+\bar{y}^2)^{1/2}\\
\varphi &= \arctan\frac{\bar{y}}{\bar{x}}\\
\bar{x}(\bar{z},\xi,\vartheta) &= x_0(\bar{z},\vartheta) + R(\bar{z},\xi,\vartheta)\cos\vartheta\\
\bar{y}(\bar{z},\xi,\vartheta) &= y_0(\bar{z},\vartheta) + R(\bar{z},\xi,\vartheta)\sin\vartheta\\
R(\bar{z},\xi,\vartheta) &= G(\bar{z},\vartheta) + \xi^n(F(\bar{z},\vartheta) - G(\bar{z},\vartheta))\\
R(\bar{z},1,\vartheta) &= F(\bar{z},\vartheta)\ ;\ R(\bar{z},0,\vartheta) = G(\bar{z},\vartheta)
\end{aligned}
\qquad (5)
$$

The functions $x_0(\bar{z},\vartheta)$ and $y_0(\bar{z},\vartheta)$ are problem-oriented and read for the delta wings considered here

$$
\begin{aligned}
x_0(\bar{z},\vartheta) &= 0\\
y_0(\bar{z},\vartheta) &= \text{const}\cdot\sin\vartheta\cdot\bar{z}
\end{aligned}
\qquad (6)
$$

6. THE NUMERICAL METHOD

The numerical method was derived from Ref. [17]. There it is employed for the solution of the Euler-equations in a non-conservative formulation. The extension of this method to the solution of the quasi-conservative formulated Euler-equations used here was carried out in Ref. [13]. Further extensions for more general geometries as considered here are discussed in [18]. To stabilize the method in critical flow regions (e.g. strong curvatures in the body contour) an explicit diffusion term of the kind $\partial/\partial\xi\ \Theta\ \partial U/\partial\xi$ with $\Theta = \lambda(|\bar{v}|+c)/(|\bar{v}|+c)_{max}$ was introduced.

The method itself is implicit and is solved in the direction between body and bow shock (ξ-coordinate) by a linear recurrence formula, and in the two remaining directions $(\bar{z},\vartheta)$ because of the quasi-linearity of the governing equations by an iteration process ($\bar{z}$ is the marching direction).

7. THE INITIAL CONDITION (STARTING SOLUTION)

The solution of a hyperbolic problem depends strongly on the initial conditions. This can be seen by considering the domain of dependence and the domain of influence of the flow. Therefore it is necessary to produce initial data as good as possible.

For the present solutions always a small part of the body near the apex is considered as conical and for this part a conical solution is provided. The cross-section of the body at the position where the calculation is to be started is considered as the basis of the cone. Along the cone the calculation using the marching-procedure is conducted until the conical solution is reached, i.e. the solution is independent on the marching coordinate. The Dillner-wing is taken as a sample case [19], Fig. 2. The equation describing the surface of the wing reads:

spanwise sections of biconvex circular arc with maximum thickness of 6%

$$
\left[z-\frac{1}{2}R(y)^{+}\right]^2 + \left[x \mp a\cdot R(y)^{-}\right]^2 = b^2(R(y)^{-})^2 \qquad (7)
$$

with $a = 4.1516$; $b = a + 0.03$

$$
R(y)^{\pm} = L \pm y\tan\varepsilon
$$

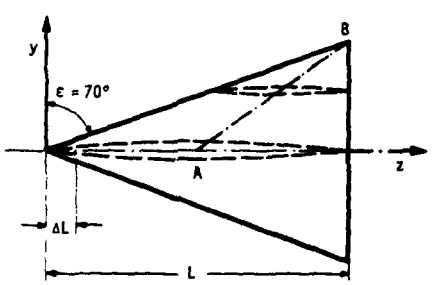

Fig. 2

The calculation is started at $\Delta L = 0.1\,L$. The equation for the Ersatz-nose cone having the basis of the cross-section surface at $z = \Delta L$ from equation (7) is given by

$$\left[\Delta L - \frac{1}{2}\left(L + \frac{\Delta L}{z}\cdot y\,\tan\varepsilon\right)\right]^2 + \left[\frac{\Delta L}{z}x \mp a\left(L - \frac{\Delta L}{z}\cdot y\,\tan\varepsilon\right)\right]^2 = b^2\left[L - \frac{\Delta L}{z}\cdot y\,\tan\varepsilon\right]^2 \qquad (8)$$

8. CALCULATION OF THE WAVE DRAG

For some of the cases in this paper the wave drag coefficient depending on the z-coordinate is evaluated. By considering the control surface plotted in Fig. 3, we can see that the wave drag of the body must be found in the surface 3 - 3'.

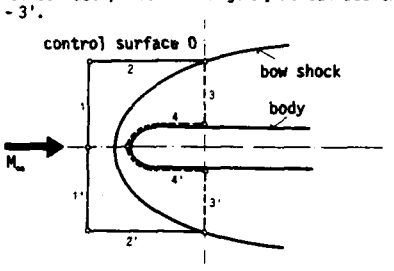

Fig. 3

The equation for the wave drag can be written as

$$W = \iint_0 \left[\rho\, v_n\,(u_\infty - u) + (p_\infty - p)\,n_z\right] d0 \qquad (9)$$

The accuracy of the field solution with respect to the numerical approximation can be checked by the application of an equation for the wave drag, consisting of eq. (9) and the energy equation.

We obtain

$$W = \frac{1}{u_\infty}\iint_0 \left[\rho\, v_n\left\{\frac{(u-u_\infty)^2 + v^2 + w^2}{2} - h - h_\infty\right\} + u_\infty\,(p_\infty - p)n_z\right] d0\,, \qquad (10)$$

where u_∞, p_∞, h_∞ are freestream values and n_z is the component of the normal vector in the z-direction of the control surface 0. The use of a body-fixed coordinate system and an angle of attack $\alpha > 0$ makes some changes necessary in the equations (9) and (10) [20]. During the computation of the flow past a conical body by means of a marching procedure the behaviour of the equations (9) and (10) can be studied. At the begin of the computation, when the flow variables are still far away from the conical solution, the values of the equations (9) and (10) differ strongly from each other. They converge to a common value only, if the conical solution is reached. This is due to the fact that the energy equation requires the conservation of the total enthalpy in the whole flow field which is not fulfilled at the starting position. For the coordinates z, ξ, ϑ we obtain for the integral eqs. (9) and (10)

$$\iint_0 Y\,d0 = \int_0^{2\pi}\int_0^1 Y\,D\,r\,d\xi\,d\vartheta \qquad (11)$$

Y is substituted by one of the integrands of eqs. (9) or (10) and D is the Jacobi-determinant. Eq. (11) is integrated by means of the trapezoidal formula.

9. RESULTS

In this chapter the results of flow field calculations past two delta-wings (Fig. 2, Fig. 4) are discussed. The delta-wing shown in Fig. 4 consists of a conical part of the length L_1 and a non-conical part of the length L_2, where for the non-conical part two cases are distinguished. Firstly, a blunted leading edge with an elliptic contour in the cross-section and secondly, a sharp leading edge.

The results presented are cross flow velocity vectors, the isobars, the lines of constant total pressure, and the contours of the bow shock in planes $z = \text{const}$. For the freestream Machnumber $M_\infty = 2.0$ and the angle of attack $\alpha = 10°$ the Figs. 5a,b (blunt leading edge) and the Figs. 6a,b (sharp leading edge) show the velocity vectors of the cross flow and the contour of the bow shock. From Fig. 5a (blunt leading edge) we can see, that the flow (up to $z = 2.2\,L_1$) has no tendency to separate in order to build up the leeside vortices known from the experiment. The blunted leading edge is completely flowed around. At the sharp leading edge (Figs. 6a,b), however, the flow separates due to the condition eqs. (4) implemented there. The Figs. 6a,b show the velocity vectors of the cross flow at $z = 2.88 \cdot L_1$. The number of grid points has been (17, 37) in the ξ,ϑ-directions.

Downstream of the conical part of the wing where the vortices are forming complicated vortex structures can be seen already for $\alpha = 10°$ which are strengthened for $\alpha = 15°$. In order to get more insight into this region the number of grid points in ϑ-direction was doubled. Fig. 7a ($z = 1.85\,L_1$) shows, how two small vortices and one large vortex are developing and further downstream (Fig. 7b; $z = 2.3\,L_1$) how they are merging. In Figs. 8a ($z = 4L_1$) and 9a ($z = 8L_1$) only one remaining strong vortex can be seen, which is

removed from the body surfaces. Fig. 8b shows the isobars in the cross flow plane, while in Fig. 9b the lines of constant total pressure are plotted.

In an inviscid flow with constant freestream values a profile in total pressure can occur either if the flow contains a curved shock or if a tangential discontinuity is enforced by a boundary condition. In this case (Fig. 9b) the position of the minimum of the total pressure is different from the position of the vortex core. This can not be explained in the sense of the above statement. On the windward side near the body surface we can also observe a weak decrease of total pressure due to the variation in the strength of the bow shock and hence conclude vorticity to be in that region. A small vortex seems to result near the plane of symmetry (Fig. 7c). In Fig. 10 the location of the center-line of the vortex is plotted which is taken from the cross-flow velocity vector plots. The center-line of the vortex is approximately a straight line which downstream removes from the body.

For freestream Machnumbers $M_\infty = 1.5$ and 2.0, and angles of attack $\alpha = 5°$ and 10°, flow fields around the Dillner-wing (Fig. 2) have been calculated. Fig. 11 shows some results in planes $z = \text{const}$ for $M_\infty = 1.5$ and $\alpha = 5°$. The grid used and the lines of total pressure are plotted at the positions $z = 0.1\,L_1$. The total pressure shows on the leeward side close to the leading edge a strongly changing profile and on the windward side near the body surface a weakly changing profile. The velocity vectors of the cross flow show at $z = 0.4\,L_1$ still no leeward side vortex. This is due to the displacement effect of the body, which posseses its local maximum of thickness along the line $\overline{AB}$ (Fig. 2). Only downstream of $z=0.5\,L_1$, where the thickness of the body decreases, vortices are exhibited by the plots of the cross-flow velocity vectors. The center of the completely developed vortex tends towards the leading edge ($z = 0.8\,L_1$). Furthermore a plot with isobars is shown at the position $z = 0.8\,L_1$. Lines of constant total pressure and velocity vectors of the cross flow are given at the position $z = 0.95\,L_1$ in the region where the vortex is fully developed. From the vector plot we can see, that the vortex lies close to the body surface due to the moderate angle of attack.

(Note: The reference length was changed for the representation of the velocity vectors in the cross flow plane $z = 0.95\,L_1$. Thereby a better resolution of the flow can be attained in the area where the vortex lies).

Fig. 12 shows some results for the freestream Machnumber $M_\infty = 2.0$ and the angle of attack $\alpha = 5°$. At the positions $z = 0.4\,L_1$, $z = 0.8\,L_1$, and $z = 0.95\,L_1$ a direct comparison with the results of Fig. 11 can be made. Due to the larger freestream Machnumber, compared with the before mentioned example, the strength of the bow shock has considerably increased. The physical domain between the body and the bow shock to be evaluated is much smaller than in the $M_\infty = 1.5$ case. In general we can say that the results shown in Figs. 11 and 12 are rather similar. The lines of constant total pressure at $z = 0.95\,L_1$ show a more pronounced minimum of the total pressure near the center of the vortex than in Fig. 11. At $z = 0.6\,L_1$ the velocity vectors of the cross flow indicates - due to the negative gradient of the function of the body contour with respect to the z-coordinate near the plane of symmetry - the onset of the vortex.

Fig. 13 shows the results for $M_\infty = 2.0$ and $\alpha = 10°$. A distinct vortex can already be seen at $z = 0.6\,L_1$. In the plane $z = 0.8\,L_1$ the velocity vectors of the cross flow show a vortex with a fully developed core. In this case the position of the local minimum of the total pressure agrees well with the position of the center of the vortex. Further downstream of the wing a decomposition of the core of the vortex is indicated ($z = 0.95\,L_1$). It may be that the artificial diffusion terms used here is causing this behaviour of the solution. The wave drag as function of the z-axis is plotted in Fig. 14 for the three calculated flow fields at the Dillner-wing. The wave drag was calculated using equations (9) and (10).

10. CONCLUDING REMARKS

In the preceding pages, a few calculations of flows around delta-wings with blunt and sharp leading edges have been discussed. The quasi-conservative Euler-equations are integrated by the use of a space marching finite difference procedure. The flows considered are always supersonic. The separation of the flow at the sharp leading edge of the wing is modeled by imposing a Kutta-like condition.

This paper describes a first step of a work to get more insight into the possibilities to calculate vortical type flows with numerical approximations of the Euler-equations. It shows that the numerical method used is able to predict the vortices on the leeward side of delta-wings. In a second step the amount of vorticity created by imposing a Kutta-condition will be investigated in more detail.

LITERATURE:

[1] MORETTI G.: On the Matter of Shock-Fitting. Lecture Notes in Physics 35, pp. 287-292. Springer, 1975.

[2] LAX P.D.: Weak Solutions of Nonlinear Hyperbolic Equations and Their Numerical Computations. Comm. Pure App. Math. 7 (1954), 159.

[3] LAX P.D., WENDROFF B.: Systems of Conservation Laws. Comm. Pure App. Math. 13 (1960), 217.

[4] McCORMACK R.W., PAULLAY A.J.: Computational Efficiency Achieved by Time Splitting of Finite Difference Operators. AIAA Paper No. 72-154, 1972.

[5] KUTLER P.: Computation of Three-Dimensional Inviscid Supersonic Flows. Short Course of v. Karman Institut, Rhode-Saint-Genese, Belgium, 1975.

[6] LAX P.D.: Hyperbolic Systems of Conservation Laws and the Mathematical Theory of Shock Waves. SIAM, Philadelphia, PA, 1972.

[7] NIELSEN J.N., KLOPFER G.H.: Basic Studies of Wing-Body Interference at High Angles of Attack and Supersonic Speeds. Report ONR-CR215-263-1, Oct. 1979.

[8] NIELSEN J.N.: Nonlinear Flow Phenomena at High Angles of Attack and Recent Advances in Their Prediction. AGARD-SP, 1982.

[9] MINAILOS A.N.: Calculation of Supersoric Flow Past Wings with Consideration of Tangential Discontinuities Shed from the Edges within the Scope of a Model Using a System of Euler-Equations. Fluid Dynamics, Vol.13, No.1, Sept. 1978, pp. 57-66.

[10] ERICSSON L.E., RIZZI A.: Computation of Vortex Flow Around Wings Using the Euler-Equations. Proc. of the IVth GAMM Conf. on Numerical Methods in Fluid Mechanics, Oct.1981, Vieweg Verlag.

[11] HITZEL S.M., SCHMIDT W.: Slender Wings with Leading-Edge Vortex Separation - A Challenge for Panel-Methods and Euler-Codes. AIAA Paper 83-0562, Jan. 1983.

[12] RIZZI A.: In: Recent Contributions to Fluid Mechanics (Ed. W.Haase), pp. 213-221, Springer Verlag, Berlin, 1982.

[13] WEILAND C.: Calculation of Three-Dimensional Stationary Supersonic Flow Fields by Applying the "Progonka" Process to a Conservative Formulation of the Governing Equations. J. of Comp. Phys. 29, No. 2, 1978.

[14] LIGHTHILL M.J.: Introduction: Boundary-Layer Theory. In: Laminar Boundary Layers, L.Rosenhead (ed.), Oxford at the Clarendon Press, 1963, pp. 46-88.

[15] HIRSCHEL E.H.: Considerations of the Vorticity Fields on Wings. In: Recent Contributions to Fluid Mechanics, W.Haase (ed.), Springer Verlag, 1982, pp. 129-137.

[16] WEILAND C.: Ober eine der klassischen Erhaltungssatzform äquivalenten Formulierung der Euler'schen Bewegungsgleichungen zur Berechnung eingebetteter Verdichtungsstöße (to be published).

[17] BABENKO K.I., VOSKRESENSKII G.P., LYUBIMOW A.N., RUSANOW V.V.: Three-Dimensional Flow of Ideal Gas Around Bodies. NASA TT F-380, 1966.

[18] WEILAND C.: Erfahrungen bei der Anwendung numerischer Verfahren zur Lösung nichtlinearer hyperbolischer Differentialgleichungssysteme. Lecture Notes in Math. 953, Springer Verlag, 1982.

[19] N.N.: FFA Report No. AU-295.

[20] WEILAND C.: Berechnung dreidimensionaler reibungsfreier Oberschallströmungsfelder um beliebige Flugzeugrümpfe. MBB/FE122/S/STY/S1, 1982.

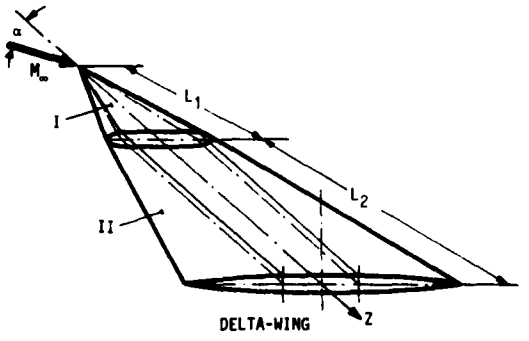

Fig. 4

FREESTREAM MACHNUMBER $M_\infty = 2.0$
ANGLE OF ATTACK $\alpha = 10°$
$Z = 2.20 \cdot L_1$

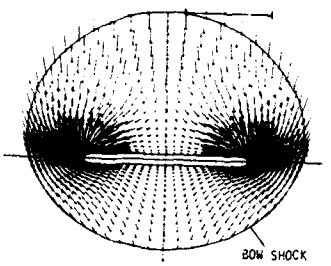

FIG. 5a CROSS FLOW VELOCITY VECTORS

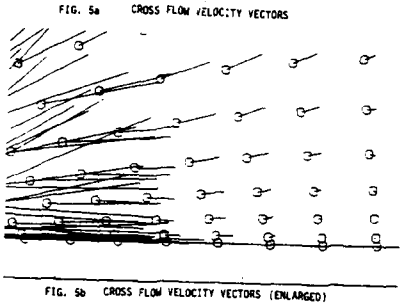

FIG. 5b CROSS FLOW VELOCITY VECTORS (ENLARGED)

FREESTREAM MACHNUMBER $M_\infty = 2.0$
ANGLE OF ATTACK $\alpha = 15°$
$Z = 1.86 \cdot L_1$

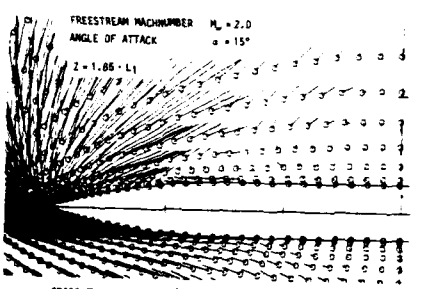

CROSS FLOW VELOCITY VECTORS (ENLARGED) FIG. 7a

$Z = 2.30 \cdot L_1$

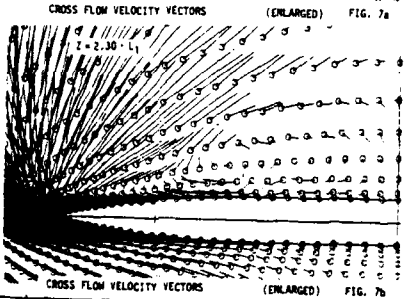

CROSS FLOW VELOCITY VECTORS (ENLARGED) FIG. 7b

$Z = 2.30 \cdot L_1$

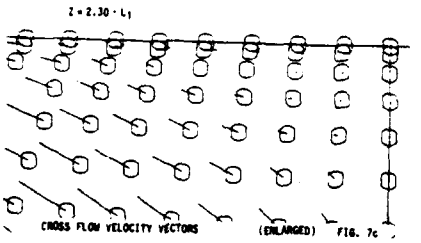

CROSS FLOW VELOCITY VECTORS (ENLARGED) FIG. 7c

FREESTREAM MACHNUMBER $M_\infty = 2.0$
ANGLE OF ATTACK $\alpha = 10°$
$Z = 2.88 \cdot L_1$

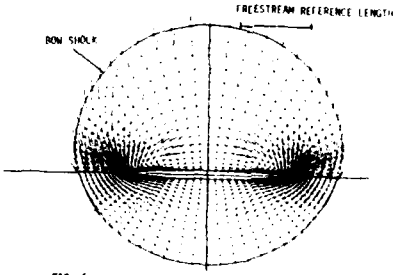

FIG. 6a CROSS FLOW VELOCITY VECTORS

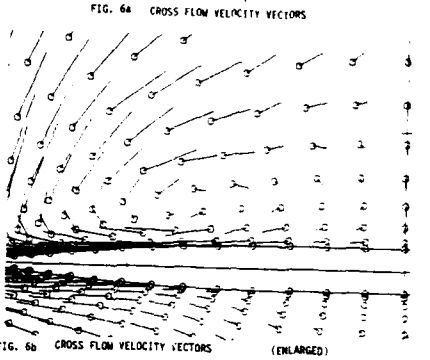

FIG. 6b CROSS FLOW VELOCITY VECTORS (ENLARGED)

FREESTREAM MACHNUMBER $M_\infty = 2.0$
ANGLE OF ATTACK $\alpha = 15°$
$Z = 4.0 \cdot L_1$

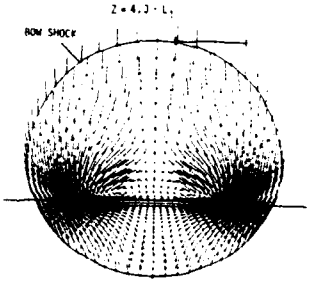

FIG. 8a CROSS FLOW VELOCITY VECTORS

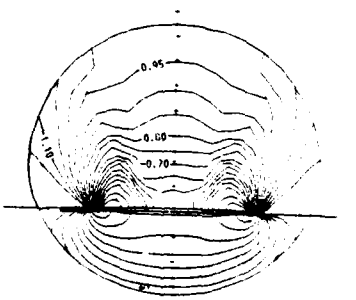

FIG. 8b ISOBARS

FREESTREAM MACHNUMBER $M_\infty = 2.0$
ANGLE OF ATTACK $\alpha = 15°$

$Z = 8.0 \cdot L_1$

FIG. 9b

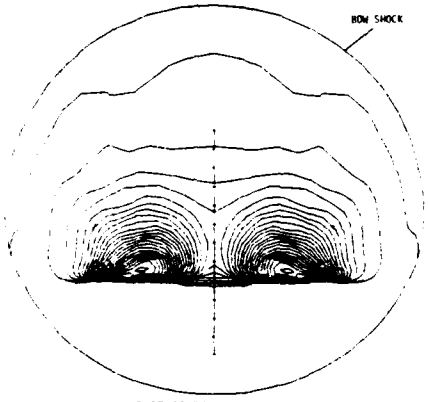

LINES OF CONST. TOTAL PRESSURE

FIG. 9a

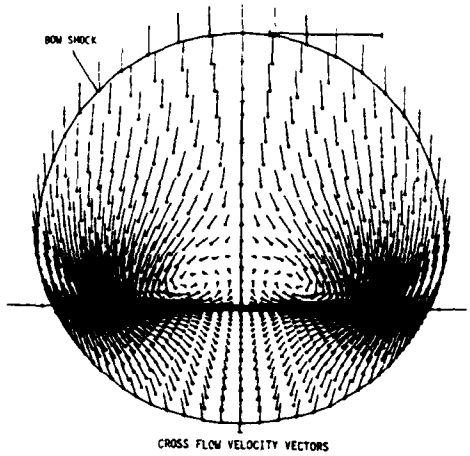

CROSS FLOW VELOCITY VECTORS

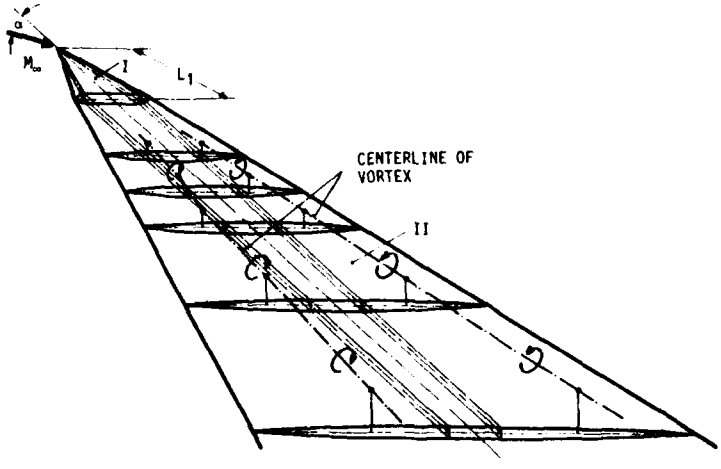

FIG. 10

FREESTREAM MACHNUMBER $M_\infty = 1.5$
ANGLE OF ATTACK $\alpha = 5°$
FIG. 11

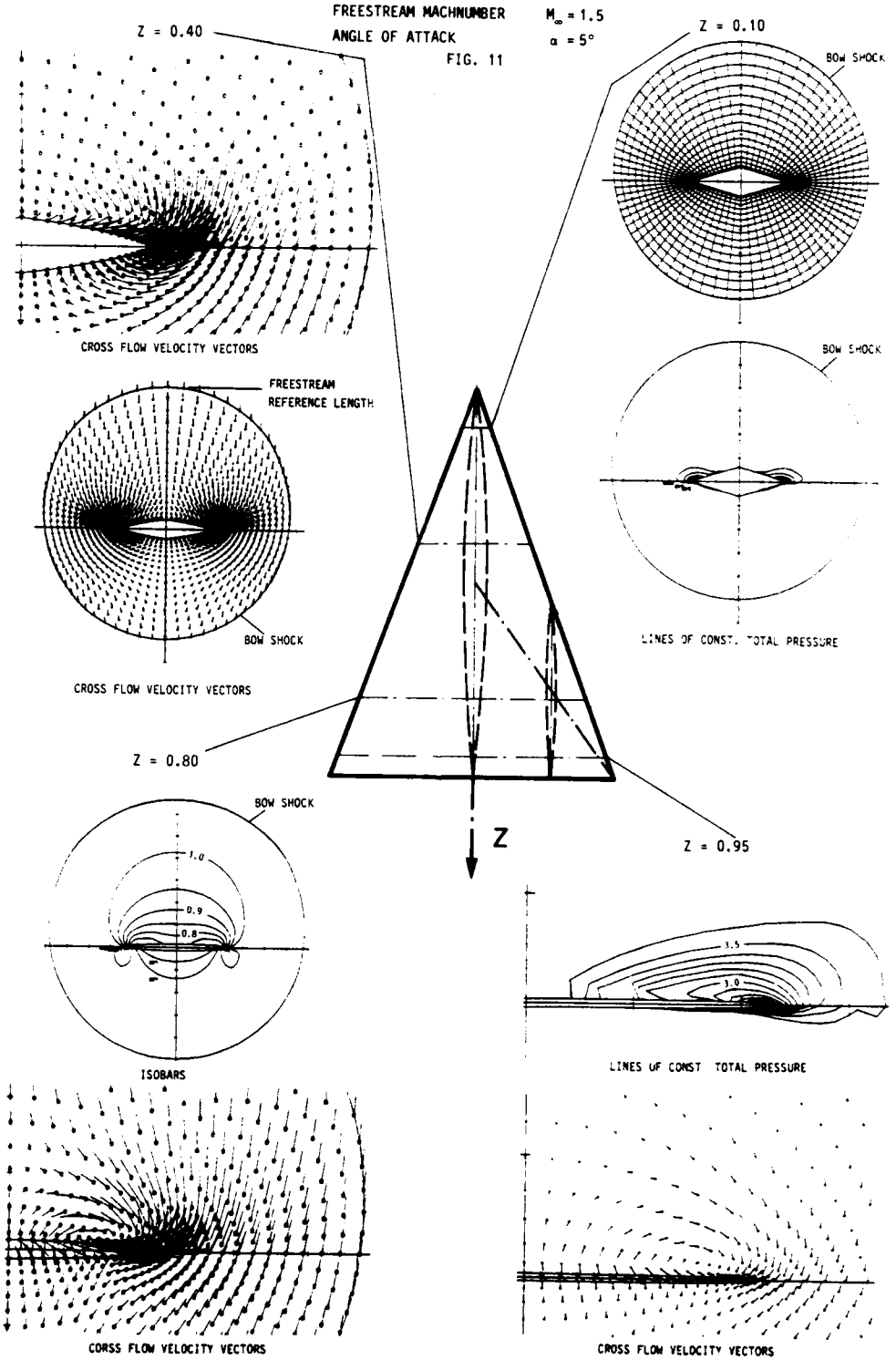

FREESTREAM MACHNUMBER $M_\infty = 2.0$

ANGLE OF ATTACK $\alpha \approx 5°$

FIG. 12

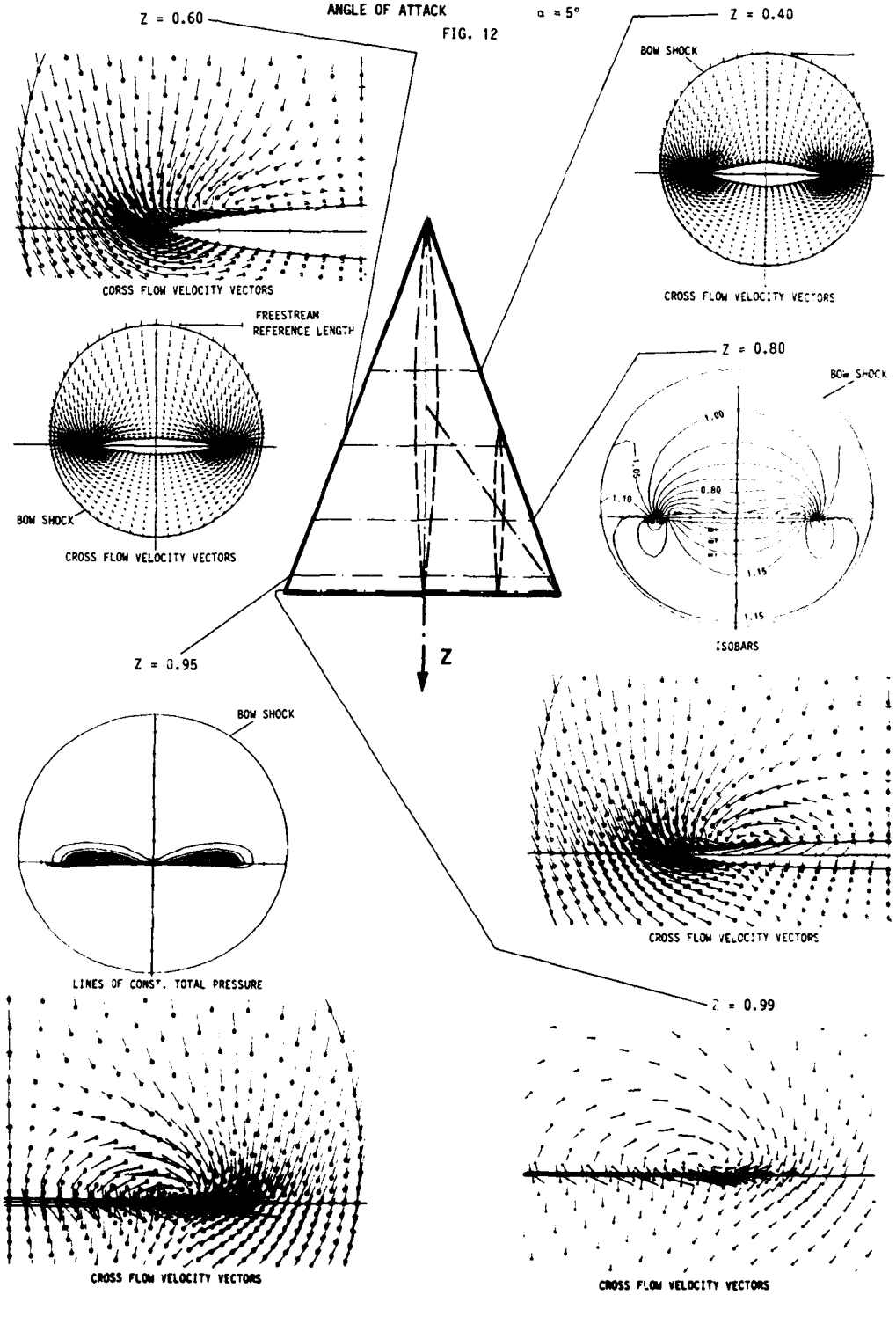

FREESTREAM MACHNUMBER $M_\infty = 2.0$

ANGLE OF ATTACK $\alpha = 10°$

FIG. 13

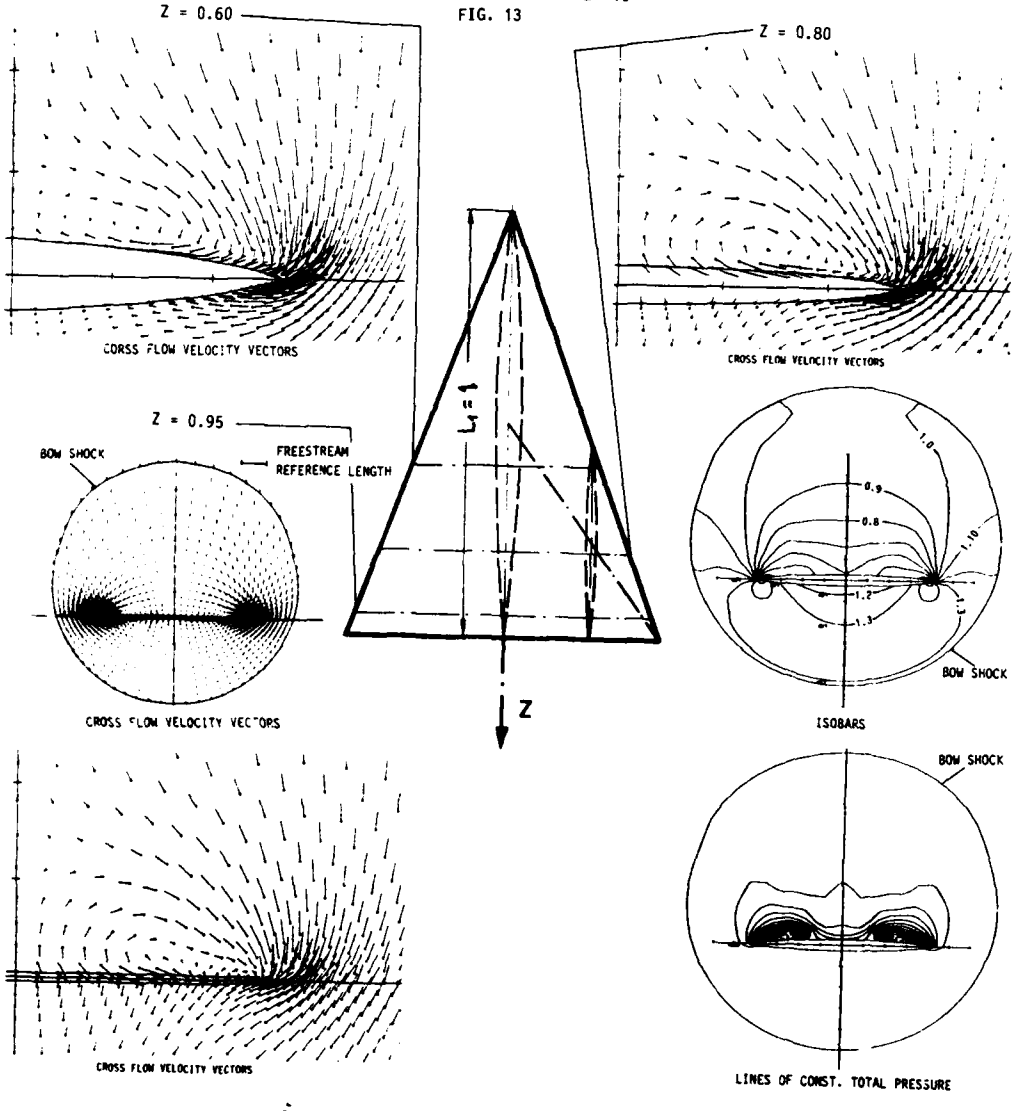

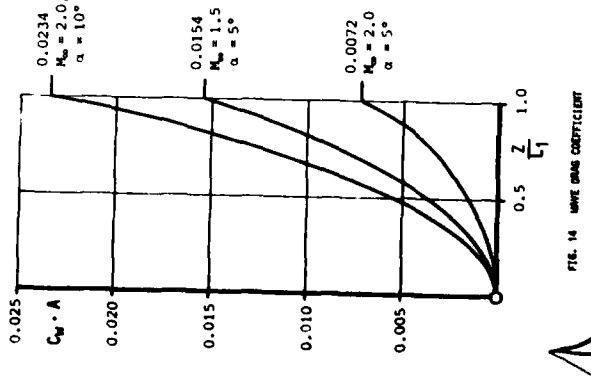

FIG. 14 WAVE DRAG COEFFICIENT

SIMULATION D'ECOULEMENTS TURBULENTS PAR UNE METHODE DE TOURBILLONS PONCTUELS

par

S. HUBERSON

Office National d'Etudes et de Recherches Aérospatiales (ONERA)
92320 CHATILLON - FRANCE

RESUME

On s'intéresse au calcul des écoulements turbulents de fluides parfaits incompressibles. La méthode de tourbillons ponctuels, étendue par Rehbach à la résolution de problèmes tridimensionnels, semble bien adaptée au calcul de l'évolution des grosses structures turbulentes. Les interactions avec les phénomènes correspondant aux échelles plus petites sont modélisées au moyen de l'introduction de plusieurs niveaux de discrétisation. Un algorithme numérique, indépendant du nombre de niveaux choisis est décrit, et son application à quelques écoulements plans est présentée.

SIMULATION OF TURBULENT FLOWS WITH A POINT VORTEX METHOD

SUMMARY

This paper deals with the computation of turbulent incompressible flows of an inviscid fluid. The point vortex method, extended by Rehbach to three-dimensional problems, is thought to be well-suited for the computation of the evolution of turbulent large eddies. The interaction with lower scales is modelized through the introduction of different hierarchies of vortices. A numerical algorithm, independent of the number of hierarchies, is presented, and applied to some examples of plan flows.

1 - INTRODUCTION-

La modélisation numérique d'écoulements réels, le plus souvent turbulents, comporte une étape essentielle : la discrétisation. Celle-ci consiste à établir une correspondance entre un système ayant un nombre infini de degrés de liberté et un système fini. Cette modélisation peut parfois s'avérer réalisable directement sans qu'il soit nécessaire de tenir compte de toute la finesse des phénomènes physiques. La méthode classique pour les écoulements turbulents consiste alors à écrire les équations pour les champs moyens et leur nature non linéaire introduit une moyenne de produit qui réapparaît à un ordre supérieur dans chaque équation, à mesure que l'on prend en compte des moments d'ordre plus élevés. Le découplage de ces équations n'est pas possible a priori puisqu'il reviendrait à réduire le nombre de degrés de liberté. On introduit donc des hypothèses de fermeture, spécifiques du nombre d'équations prises en compte et du type d'écoulement représenté. La résolution de ces équations complexes se fait en général par voie numérique et, la turbulence étant essentiellement un phénomène tourbillonnaire, les méthodes de type transport Lagrangien du tourbillon semblent fournir un modèle capable de calculer avec une certaine souplesse les écoulements incompressibles les plus généraux. Leur application à des écoulements turbulents a fait l'objet d'un grand nombre de travaux en particulier par Christiansen [1], et Aref et Siggia [2] pour des cas périodiques. Chorin [3] a également proposé une approche originale, mais qui semble poser des problèmes de précision (Milinazzo Saffman [4]). Le but de ce travail est de construire à partir d'idées physiques simples, un modèle ne constituant pas une méthode faisant appel à la résolution numérique des équations de Navier-Stokes, mais permettant d'aborder des comportements similaires à ceux induits par la turbulence. Ce modèle aura pour base la méthode particulaire de Rehbach [5] qui permet de calculer les écoulements tridimensionnels incompressibles de fluide parfait. Celle-ci présente l'intérêt de ne pas faire appel explicitement à la structure en filaments tourbillonnaires de l'écoulement et le principe de cet algorithme sera ici rappelé. On exposera ensuite les bases de la méthode numérique de résolution proposée et on essaiera de montrer en quel sens il s'agit d'une méthode de calcul d'écoulements turbulents. Enfin, quelques résultats seront présentés pour des écoulements bidimensionnels.

2 - LA METHODE DE REHBACH [5] -

L'écoulement d'un fluide parfait incompressible est régi par l'équation de Helmohltz pour le calcul de l'évolution dans le temps du tourbillon $\underset{\sim}{\omega}$ - rotation du champ de vitesse $\underset{\sim}{U}$, et l'équation de continuité :

$$\begin{cases} \dfrac{\partial \underset{\sim}{\omega}}{\partial t} + (\underset{\sim}{U}.\underset{\sim}{\nabla})\,\underset{\sim}{\omega} = (\underset{\sim}{\omega}.\underset{\sim}{\nabla})\,\underset{\sim}{U} & (2.a) \\ \underset{\sim}{\omega} = \underset{\sim}{\nabla} \wedge \underset{\sim}{U} & (2.b) \\ \underset{\sim}{\nabla}.\underset{\sim}{U} = 0 & (2.c) \end{cases}$$

avec :

$$\underset{\sim}{\nabla}^t = \left(\frac{\partial .}{\partial x}, \frac{\partial .}{\partial y}, \frac{\partial .}{\partial z}\right)$$

A partir des deux dernières équations de (2), on peut exprimer le champ de vitesse $\underset{\sim}{U}$ en fonction de $\underset{\sim}{\omega}$ par la formulation intégrale de Biot-Savart :

$$\underset{\sim}{U} = \frac{1}{2^{d-1}\pi} \iiint_{S_{sup}(\underset{\sim}{\omega})} \frac{\underset{\sim}{\omega}' \wedge (\underset{\sim}{x}' - \underset{\sim}{x})}{|\underset{\sim}{x}' - \underset{\sim}{x}|^d} \, dx' + \nabla\varphi\Big|_{\underset{\sim}{x}} \qquad (3)$$

où d est le dimension de l'espace, et φ est le potentiel des vitesses. Celui-ci est déterminé par les diverses conditions aux limites, en particulier à l'infini. La méthode particulaire a pour but de résoudre le système formé par les équations (2.a) et (3).

Le champ de tourbillon est discrétisé au moyen de particules tourbillonnaires et l'écoulement est alors décrit par deux champs de vecteurs discrets : le tourbillon $\underset{\sim}{\Omega}_i$ porté par chaque particule, et un vecteur position $\underset{\sim}{X}_i$ caractérisant la particule à chaque pas de temps. A l'instant initial, ces deux champs sont formés à l'aide de la relation :

$$\underset{\sim}{\Omega}_i = \iiint_{\mathcal{P}_i} \underset{\sim}{\omega} \, d\sigma \qquad (4.a)$$

$$\underset{\sim}{\Omega}_i \wedge \underset{\sim}{X}_i = \iiint_{\mathcal{P}_i} \underset{\sim}{\omega} \wedge \underset{\sim}{x} \, d\sigma \qquad (4.b)$$

l'indétermination sur le vecteur $\underset{\sim}{X}_i$ dansle cas d'écoulements tridimensionnels est levée au moyen d'une contrainte supplémentaire (minimisation de l'erreur sur la vitesse). Pour calculer l'évolution de ces deux champs de vecteurs, on utilise deux systèmes couplés d'équations différentielles obtenues en discrétisant (2.a) :

$$\frac{d\underset{\sim}{X}_i}{dt} = \overline{\underset{\sim}{U}}_i \qquad (5.a)$$

$$\frac{d\underset{\sim}{\Omega}_i}{dt} = \overline{(\underset{\sim}{\Omega}_i . \nabla)\underset{\sim}{U}}\Big|_i \qquad (5.b)$$

où $\overline{f}_i$ désigne une valeur représentative de la fonction f sur la particule $\mathcal{P}_i$ qui n'est pas, en général, la moyenne algébrique de f sur $\mathcal{P}_i$. Le champ de vitesse et son gradient sont calculés à partir de ($\underset{\sim}{\Omega}_i$, $\underset{\sim}{X}_i$) par des relations intégrales correspondant à (3) et à sa dérivée :

$$\overline{\underset{\sim}{U}(\underset{\sim}{X}_i)} = \overline{\underset{\sim}{U}}_i = \frac{1}{2^{d-1}\pi} \sum_{j \neq i} \frac{\underset{\sim}{\Omega}_j \wedge (\underset{\sim}{X}_j - \underset{\sim}{X}_i)}{|\underset{\sim}{X}_j - \underset{\sim}{X}_i|^d} + \nabla\varphi\Big|_{\underset{\sim}{X}_i} \qquad (6)$$

et pour $d = 3$:

$$\overline{(\underset{\sim}{\Omega}_i . \nabla)\underset{\sim}{U}}\Big|_i = \frac{3}{8\pi} \sum_{j \neq i} \frac{1}{|\underset{\sim}{X}_j - \underset{\sim}{X}_i|^5} \Big[\big((\underset{\sim}{X}_j - \underset{\sim}{X}_i).\underset{\sim}{\Omega}_i\big)(\underset{\sim}{X}_j - \underset{\sim}{X}_i) \wedge \underset{\sim}{\Omega}_j + \dots$$

$$\dots + \big(((\underset{\sim}{X}_j - \underset{\sim}{X}_i) \wedge \underset{\sim}{\Omega}_j).\underset{\sim}{\Omega}_i\big)(\underset{\sim}{X}_j - \underset{\sim}{X}_i)\Big] + (\underset{\sim}{\Omega}_i . \nabla)(\nabla\varphi\big|_{\underset{\sim}{X}_i}) \qquad (7)$$

Il est bien connu des utilisateurs des méthodes de tourbillons ponctuels que ces relations intégrales présentent des singularités, et donc des techniques de régularisation sont nécessaires. On utilise une une fonction régularisante qui peut être par exemple une gaussienne. Cette dernière présente l'intérêt d'être solution exacte de l'équation de diffusion par une source ponctuelle de tourbillon et on a dans (6) , pour les tourbillons tels que :

$$|\underset{\sim}{X}_j - \underset{\sim}{X}_i| < \varepsilon$$

$$\overline{\underset{\sim}{U}}_{ij} = \frac{1}{2^{d-1}\pi} \frac{\underset{\sim}{\Omega}_i \wedge (\underset{\sim}{X}_j - \underset{\sim}{X}_i)}{|\underset{\sim}{X}_j - \underset{\sim}{X}_i|^d} \exp\left(-|\underset{\sim}{X}_j - \underset{\sim}{X}_i|^2/4\nu t\right) \qquad (8)$$

où ε et ν sont des constantes à fixer. De nombreux calculs ont été réalisés par Rehbach [5-6] démontrant l'efficacité de la méthode. Enfin, l'analyse numérique de l'algorithme a été faite par différents auteurs : Cottet et Raviart [7] et aussi Maj a et Beale [8]. Il s'agit donc, à notre connaissance, de la seule méthode de tourbillons tridimensionnelle ayant fait l'objet d'une justification mathématique complète en ce qui concerne la convergence. Plus récemment cette méthode a été étendue par l'auteur à des obstacles en mouvement quelconque, et en particulier aux voilures tournantes. La figure 1 montre des lignes d'émission produites par un rotor monopale en vol stationnaire.

3 - UNE METHODE NUMERIQUE SIMPLIFIEE -

L'idée de base de la méthode proposée est la suivante : nous supposons que l'écoulement est représenté, comme cela a été décrit plus haut par un certain nombre de particules porteuses de tourbillon. A leur tour, ces particules peuvent être considérées comme formées par un système de taille plus petite. En reconduisant le procédé, on obtient une suite de systèmes emboités qui représentent assez bien l'image classique des écoulements turbulents. Nous allons voir dans ce qui suit comment un schéma peut être dérivé de l'analyse de la méthode des tourbillons ponctuels, et surtout comment des hypothèses physiques permettent de construire sur ces bases un algorithme numérique efficace.

Lors de la résolution numérique des équations (2.a) et (3), il est évident que l'étape la plus coûteuse est constituée par le calcul de la forme discrète de la relation (3). Sous la forme (6) elle nécessite un nombre d'opérations proportionnel au carré du nombre de tourbillons N_σ , ce qui devient vite une limitation sérieuse. On se trouve donc face au problème classique de choisir un nombre de tourbillons ponctuels qui soit le plus grand possible tout en restant compatible avec les capacités des moyens informatiques dont

on dispose. Ce nombre de particules détermine alors directement l'intervalle des échelles représentées dans le calcul. Un deuxième facteur intervenant sur celui-ci sera l'erreur de troncature commise dans l'étape de discrétisation. En un point donné, le calcul de l'intégrale (3) par la formule (6) contient une erreur qui peut être évaluée en fonction de la distance entre une particule $\mathcal{P}_i$ et le point de calcul. Supposons le domaine de calcul découpé en couches circulaires (bidimensionnelles) ou sphériques (tridimensionnelles) de rayons (r , $r+h$). La contribution de chaque couche $\mathcal{C}_i$ dans (3) peut être approchée en supposant que le tourbillon est réparti sur le cercle -ou la sphère- de rayon r_o contenu dans $\mathcal{C}_i$. On commet une erreur proportionnelle à h^2 / r_o , qui est maximum pour les premières couches.

On peut donc en déduire que la taille des échelles correctement représentées dépend essentiellement de l'erreur locale Ensuite, on constate que, quelle que soit la taille des particules, la méthode, au-delà d'une certaine distance ne permet plus de prendre en compte les petites échelles dont l'effet est alors noyé dans l'erreur globale. Ces conclusions amènent naturellement à l'idée que l'on peut au loin amalgamer un certain nombre de particules de façon à réduire le volume des calculs.

Pour réaliser ceci, il est nécessaire de faire choix d'une valeur h_o , plus petite échelle présente dans le calcul. On peut alors appauvrir le détail de l'écoulement au loin en prenant par exemple une suite de couches successives de rayons :

$$r_n \ , \ r_n + h_n \tag{9}$$

avec :

$$h_n = 2 h_{n-1} = 2^n h_o$$

$$r_n = \sum_{k=0}^{n-1} h_k$$

Par contre, le champ de vitesse devant être connu en tout point, il devient nécessaire de posséder partout dans le domaine de calcul des informations relatives à toutes les échelles, selon que le point de calcul est plus ou moins éloigné. Cette superposition à un instant t de toutes ces échelles rappelle la superposition dans un écoulement turbulent de toute une classe de nombres d'onde, et nous reviendrons sur ce point dans le chapitre suivant. Remarquons seulement ici que nous n'avons encore introduit aucune approximation supplémentaire dans (5) et que nous décrivons uniquement un modèle de calcul, sans souci de son éventuelle applicabilité. Si nous considérons maintenant une distribution de tourbillon $\omega_o(\underset{\sim}{x})$ on peut, étant donné une valeur h_n caractérisant par exemple l'arête d'une particule $\mathcal{P}_i$ initialement cubique définir une discrétisation de $\omega_o(\underset{\sim}{x})$ à partir des relations (4). On peut faire de même pour toutes valeurs de h_n prises dans la suite définie par (9). On introduit alors la condition supplémentaire qu'une discrétisation de rang $n+1$ constitue une subdivision de la discrétisation de rang n .

En d'autre terme, toute particule de la discrétisation $n+1$ est contenue dans une et une seule particule de rang n . On obtient ainsi une suite d'ensemble de particules (Ω_j^n , $\underset{\sim}{x}_j^n$) qui nous permettent de construire le champ de vitesse approché en $\underset{\sim}{x}_o$.

$$\underset{\sim}{U}(\underset{\sim}{x}_o) = \sum_n \sum_{j \in J(n, \underset{\sim}{x}_o)} \frac{\underset{\sim}{\Omega}_j^n \wedge (\underset{\sim}{x}_j^n - \underset{\sim}{x}_o)}{|\underset{\sim}{x}_j^n - \underset{\sim}{x}_o|} \tag{10}$$

où :

$$J(n, \underset{\sim}{x}_o) = \left\{ j \in J^n \Big/ \sum_{k=0}^{n-1} h_k < |\underset{\sim}{x}_j^n - \underset{\sim}{x}_o| < \sum_{k=0}^{n} h_k \text{ et } \mathcal{P}_j \notin \mathcal{P}_i, \forall i \in \bigcup_{m>n} J(m, x_o) \right\} \tag{11}$$

et J^n est l'ensemble des indices des particules de la discrétisation de rang n . On conçoit aisément que le calcul du champ de vitesse par (10) et (11) ne représente pas une économie puisque le nombre d'inconnues se trouve notablement augmenté cependant que son utilisation dans un problème d'évolution suppose une intégration des équations (2.a) et (3) pour chaque particule ! Nous allons voir maintenant comment on peut aboutir à l'économie de calcul recherchée en appliquant au système discrétisé quelques simplifications de nature physique.

4 - UN MODELE DE TURBULENCE -

Le modèle numérique que l'on vient d'établir fournit une représentation de l'écoulement très proche de l'image couramment admise des cascades de structures turbulentes -figure 2 - de plus, l'utilisation des tourbillons ponctuels amène que les structures correspondant aux petites échelles interagissent entre elles, et sont convectées avec leur vitesse propre relativement au déplacement d'ensemble des échelles supérieures. On peut remarquer, par ailleurs, que ces qualités sont dues principalement à la présence simultanée au sein de l'écoulement de toutes les discrétisations (Ω_j^n , $\underset{\sim}{x}_j^n$). Dans ce qui suit, et par analogie avec le langage habituel en turbulence, nous appellerons celles-ci "hiérarchies de rang n ". Nous allons maintenant introduire des simplifications supplémentaires de façon à former un modèle de l'écoulement pratiquement utilisable. L'idée la plus simple consiste à découpler le calcul de chaque structure à l'intérieur d'une hiérarchie, et à intégrer les équations (2.a) et (3) localement, comme si la structure évoluait en "bloc" . Supposons que les différentes hiérarchies soient construites selon le procédé décrit au paragraphe 3, chaque particule d'une hiérarchie n est mère d'un ensemble de particules de la hiérarchie $n+1$. On peut donc paramétrer une particule d'une hiérarchie n quelconque au moyen des indices correspondant à ses ancêtres dans les hiérarchies de rang inférieur à n :

$$\underset{\sim}{x}^n_{j_n, j_{n-1}, \dots, j_o} \qquad j_m \in J^m \tag{12}$$

En prenant pour origine, à l'intérieur d'une même structure ou système de particules, la particule mère représentant celle-ci, on peut écrire une nouvelle façon de caractériser une particule de rang n :

$$\underset{\sim}{x}^n_{j_n, j_{n-1}, \dots, j_o} = \underset{\sim}{x}^n_{j_n} + \sum_{i=0}^{n-1} \underset{\sim}{x}^i_{j_i} \tag{13}$$

Le déplacement de cette particule se trouve ainsi relié au déplacement de tous ses ancêtres, mais le calcul de ceux-ci par la formule (8) n'est plus envisageable. Nous allons donc introduire ici une hypothèse supplémentaire en supposant que chaquesystème de la hiérarchie n ne dépend dans son évolution que de lui-même et des hiérarchies de rang inférieur à n .

En d'autres termes, nous supposons que les structures d'une même échelle constituant un système, ou macro-structure, interagissent entre elles, mais n'ont pas d'interaction directe avec les structures de même échelle présentes dans d'autres macro-structures. On obtient ainsi un système d'équations différentielles permettant de calculer :

$$\frac{d\underset{\sim}{X}_i^n}{dt} = \sum_{\substack{i\neq j \\ i\in M(k,n-1)}} \frac{\underset{\sim}{\Omega}_i^n \wedge (\underset{\sim}{X}_i^n - \underset{\sim}{X}_j^n)}{2^{d-1}\pi\,|\underset{\sim}{X}_i^n - \underset{\sim}{X}_j^n|^d} \qquad (14)$$

où $M(k,n-1)$ est l'ensemble des indices des particules de la hiérarchie n qui, comme $(\underset{\sim}{\Omega}_j^n, \underset{\sim}{X}_j^n)$ ont pour mère la particule $(\underset{\sim}{\Omega}_k^{n-1}, \underset{\sim}{X}_k^{n-1})$. On forme de la même façon une équation pour $\underset{\sim}{\Omega}_j^n$ à partir de l'équation (7). En remarquant que $\underset{\sim}{\Omega}_j^n$ n'est plus cette fois une fluctuation du tourbillon, mais sa valeur locale.

On se trouve ainsi ramené à une succession de calculs élémentaires correspondant à autant d'applications de la méthode de tourbillons ponctuels. Si on suppose que toutes les structures composant une hiérarchie donnée sont composées du même nombre de particules, on a pour la hiérarchie ultime une population donnée par :

$$N^{n_0} = N^0 \prod_{i=1}^{n_0} m_i \qquad (15)$$

le nombre d'opérations étant proportionnel à :

$$N_{op} = (N^0)^2 + \sum_{n=1}^{n_0} \left(N^0 \prod_{i=1}^{n-1} m_i\right) m_n^2 \qquad (16)$$

et pour une méthode classique :

$$N_{op} = (N^0)^2 \prod_{i=1}^{n_0} m_i^2 \qquad (17)$$

L'introduction d'un plus ou moins grand nombre de hiérarchies dans le calcul se fait d'une façon très simple en exploitant le caractère récurrent du modèle. Chaque calcul pour une structure donnée correspondant à une application de la méthode des tourbillons ponctuels classique, il suffit de construire un algorithme de récurrence adaptable à un programme simple et pilotant celui-ci. Une des contraintes d'un tel calcul est qu'il faut alors ranger les informations relatives à toutes les particules sur un même vecteur de façon à automatiser la recherche d'indice. Il faut par ailleurs s'assurer que les relations (4) sont toujours vérifiées au sens où, si $(\underset{\sim}{\Omega}_j^n, \underset{\sim}{X}_j^n)$est particule mère des particules $(\underset{\sim}{\Omega}_i^{n+1}, \underset{\sim}{X}_i^{n+1})$, appartenant à $M(j,n)$, on a :

$$\sum_{M(j,n)} \underset{\sim}{\Omega}_i^{n+1} = \underset{\sim}{\Omega}_j^n \qquad (18)$$

$$\sum_{M(j,n)} \underset{\sim}{\Omega}_i^{n+1} \wedge \underset{\sim}{X}_i^{n+1} = 0. \qquad (19)$$

Ceci conduit donc, à chaque intégration de l'équation (2.a) pour toutes les particules d'un niveau $n+1$, à réactualiser le tourbillon et les positions des particules de la hiérarchie n. On complète l'algorithme en ce qui concerne la dépendance spatiale des différents niveaux d'approximation par la possibilité de rattacher une particule de niveau d'approximation $n+1$ à la particule dont elle est la plus proche, ce qui permet d'adapter au mieux les différentes discrétisations.

Il peut être intéressant de comparer la nature des termes obtenus dans l'équation du tourbillon avec leur analogue discret. La vérification des relations (18) et (19) représente l'action,sur le champ moyen de vitesse et de tourbillon,des petits mouvements que nous appellerons fluctuations de tourbillon d'échelles inférieures. En particulier, la relation (19) est une correction sur le barycentre de chaque cellule, et est donc tout à fait locale. Elle représente une forme discrète des fluctuations sur la déformation de chaque particule $\mathcal{P}_i$. La seconde étape quant à elle est une redistribution du tourbillon par l'effet des fluctuations de vitesse, mais son action sur les grosses structures ne devient effective que par l'application de la relation (18) qui entraîne à son tour la modification de (19). On peut écrire formellement des équations de transport correspondant à ces deux relations, en fonction du tourbillon moyen $\underset{\sim}{\Omega}$, et de la fluctuation locale $\underset{\sim}{\omega}$, avec pour la vitesse et la position des particules, les notations : $\underset{\sim}{U}$, $\underset{\sim}{u}$, $\underset{\sim}{X}$, $\underset{\sim}{x}$. On a :

$$\underset{\sim}{\Omega} \wedge \frac{d\underset{\sim}{x}}{dt} = \underset{\sim}{\Omega} \wedge \underset{\sim}{U} + \int_{\mathcal{P}_i} \underset{\sim}{\omega} \wedge \underset{\sim}{U} \, d\rho + \int_{\mathcal{P}_i} \underset{\sim}{\Omega} \wedge \underset{\sim}{u} \, d\rho + \int_{\mathcal{P}_i} \underset{\sim}{\omega} \wedge \underset{\sim}{u} \, d\rho + \int_{\partial\mathcal{P}_i} (\underset{\sim}{\omega} \wedge \underset{\sim}{x})(\underset{\sim}{u}\cdot\underset{\sim}{n}) \, d\rho \qquad (20)$$

$$\frac{d\underset{\sim}{\Omega}}{dt} = (\underset{\sim}{\Omega}\cdot\underset{\sim}{\nabla})\underset{\sim}{U} + \int_{\mathcal{P}_i} (\underset{\sim}{\omega}\cdot\underset{\sim}{\nabla})\underset{\sim}{u} \, d\rho + \int_{\mathcal{P}_i} \underset{\sim}{u}(\underset{\sim}{\Delta}\cdot\underset{\sim}{\omega}) \, d\rho + \int_{\partial\mathcal{P}_i} \underset{\sim}{\omega}(\underset{\sim}{u}\cdot\underset{\sim}{n}) \, d\rho \qquad (21)$$

avec :

$$\int_{\mathcal{P}_i} \underset{\sim}{\omega}\, d\sigma = \underset{\sim}{\Omega}$$

C'est-à-dire que si $\mathcal{P}_j$ est une particule contenue dans $\mathcal{P}_i$, on a avec les notations précédentes :

$$\Omega_j^n = \int_{\mathcal{P}_j} \left(\Omega_i^{n+1} / |\mathcal{P}_i| + \omega \right) d\sigma = \int_{\mathcal{P}_j} (\Omega + \omega)\, d\sigma \qquad (22)$$

Dans l'intégrale (20), le terme I est nul, et les deux termes II regroupés représentent l'effet des agitations des tourbillons d'un système sur la particule représentant celui-ci, et donc sont pris en compte dans l'étape de vérification des relations (18) et (19). Le terme III représente le fait qu'une particule ayant changé de système ne figure plus dans la relation (19). L'aspiration de celle-ci par une macro-structure voisine de celle dont elle faisait partie a pour effet de modifier la position de ces macro-structures. Les différents termes de l'équation (21) s'interprète de la même façon.

Il est possible d'étendre l'idée de la hiérarchie au pas de temps choisi dans la forme discrète de (2.a). En effet, le minimum pour ce pas de temps est lié à la discrétisation en espace par la classique condition de Courant, et peut être imposé par le niveau de discrétisation le plus fin. En fait, cette contrainte peut être en partie affaiblie pour les grosses structures, et remplacée par une formulation adaptée, et tenant compte de l'effectif par unité de volume -ou de surface- des systèmes de la hiérarchie concernée. Si on note $\overline{m(i)}$ ce nombre pour la hiérarchie i, la distance moyenne entre deux particules est donnée par $(\overline{m(i)})^{1/d}$, et on calcule le pas de temps Δt_i à partir du plus petit pas de temps utilisé par :

$$\Delta t_i = \prod_{k=i+1}^{i_0} \overline{m(k)}^{1/d} \qquad (23)$$

où i_0 est le nombre maximum de hiérarchies présentes dans le calcul. Cette prise en compte d'un pas de temps adapté à la taille des structures tourbillonnaires calculées peut aussi s'interpréter comme l'analogue discret d'une moyenne en temps sur les petites structures, leur action sur les grosses structures n'étant prise en compte qu'avec une échelle de temps propre à celles-ci. En outre, cette détermination du pas de temps permet un gain substantiel sur le nombre d'opérations à effectuer pour calculer l'évolution de l'écoulement pendant un intervalle de temps donné.

On a donc été amené à introduire des simplifications dans l'algorithme numérique qui peuvent se mettre sous forme d'hypothèses physiques admissibles sur la nature des écoulements turbulents. Les effets à grandes échelles sont calculés de façon exacte -aux termes de l'approximation numérique choisie- alors que les effets des petites échelles sont modélisés sous forme de corrections sur le champ moyen. On peut espérer par cette méthode atteindre des échelles suffisamment petites pour que les effets locaux de la turbulence puissent être modélisés facilement.

5 - EXEMPLES DE MISE EN OEUVRE NUMERIQUE -

Les exemples que nous présentons sont tous bidimensionnels. Cette restriction dont le but évident est de simplifier le programme de calcul n'est cependant pas trop gênante dans la mesure où la plupart des résultats de calculs disponibles correspondent à ce type d'écoulement. Pour construire une distribution initiale de tourbillon, nous supposons que celui-ci peut être représenté par une fonction de la forme :

$$\omega(x,y) = g(x) \cdot f_\delta(y) \qquad (24)$$

le support du tourbillon est alors discrétisé en pavés porteurs de tourbillon, donnés par les formules (4) et (20). Chaque pavé est lui-même ensuite redécoupé suivant le nombre de hiérarchies souhaité pour le calcul.

Le premier exemple présenté -figure 3- est relatif au problème de Kaden [9]. Il s'agit de calculer l'évolution d'une ligne portant une densité de tourbillon donnée par :

$$g(x) = Ux\,(a^2 - x^2)^{1/2} \qquad (25)$$

où U et a sont des vitesse et longueur caractéristiques. On traite ici le problème symétrique, c'est-à-dire que le support du tourbillon est fini et compris entre $-a$ et $+a$. Ce calcul correspond à un problème d'aérodynamique qui consiste à construire la nappe tourbillonnaire issue du bord de fuite d'une aile dont la charge est elliptique. L'analogie avec le calcul présenté est obtenue en supposant que la nappe est une petite perturbation d'un écoulement uniforme, et donc que la distance au bord de fuite de l'aile joue le rôle du temps. Nous avons étudié ce problème dans le cas où la nappe a une petite épaisseur ce qui peut représenter un effet de la viscosité. Pour ce calcul d'essais, nous avons choisi une répartition gaussienne correspondant à la diffusion visqueuse d'une densité linéique de tourbillon. On remarque sur la figure 3.2 des déferlements secondaires qui n'apparaissent pas sur 3.1 et qui peuvent être attribués à l'effet d'épaisseur alors que celui-ci n'intervient explicitement qu'au deuxième niveau de discrétisation.

Ce problème a été étudié par de nombreux auteurs pour le cas d'une nappe de discontinuité, et par Baker [10] pour le cas d'une nappe avec épaisseur faible. Celui-ci a utilisé la méthode de Christiansen [1] et on peut observer sur ces résultats des déferlements secondaires comparables à ceux que nous obtenons.

La figure 4 présente un calcul d'instabilité de type Kelvin-Helmholtz. Il s'agit là d'un problème périodique pour lequel la distribution initiale de tourbillon est donnée par :

$$\omega(x,y) = \sin(2\pi x/\lambda)\exp(-\alpha y^2) \qquad (26)$$

où λ est la période, et x la direction de périodicité. On peut calculer la vitesse induite au point (0,0) par une file de tourbillons de caractéristiques $(\Omega, X + k\lambda e_x)$, $k \in \mathbb{Z}$ et e_x étant un vecteur unitaire, on a :

$$U = \frac{\Omega}{2\pi\lambda} \frac{e^{-2y} - e^{2y}}{e^{-2y} + e^{2y} - 2 + 4\sin^2 x}$$

$$V = \frac{\Omega}{2\pi\lambda} \frac{-2\sin^2 x}{e^{-2y} + e^{2y} - 2 + 4\sin^2 x} \qquad (27)$$

Il faut remarquer que ces formules ne sont utilisées que pour le calcul de la première hiérarchie de tourbillons. En effet, on a fait l'hypothèse que l'écoulement interne d'une structure n'était pas influencé par ses voisines, et donc a fortiori par celle située à une distance $k\lambda$, $k \in \mathbb{Z}$. On peut comparer sur la figure (4) les effets obtenus pour 1, 2 et 3 hiérarchies présentes dans le calcul. On remarque en particulier qu'un plus grand nombre de niveaux accentue notablement le taux d'enroulement ce qui peut être obtenu aussi en augmentant le nombre de particules pour un niveau unique. Par ailleurs, on observe une dissymétrie marquée entre les deux coeurs tourbillonnaires qui est due à la superposition d'une perturbation à la distribution initiale de tourbillon, et est comparable à ce que l'on peut observer pour des écoulements turbulents.

6 - CONCLUSION -

Les résultats de quelques calculs préliminaires semblent indiquer de bonnes propriétés de la méthode pour représenter des écoulements turbulents. Une étude théorique récente de Chong, LIM et Perry [11-12-13], fondée sur un principe voisin, mais écrit dans l'espace des nombres d'ondes, nous permet d'espérer de bonnes performances de notre méthode pour les écoulements cisaillés type couche de mélange, et surtout pour modéliser le phénomène complexe du "bursting". Nous avons présenté l'algorithme de calcul dans le cadre plus général des écoulements tridimensionnels. L'une des caractéristiques intéressantes de la méthode semble être la modélisation directe de la déformation et de l'étirement des filaments tourbillonnaires. Il s'agit là d'un des mécanismes fondamentaux de la turbulence tridimensionnelle, et cet élément, allié aux bonnes propriétés observées dans les expérimentations numériques en écoulement plan doit nous permettre d'aborder maintenant les problèmes réellement tridimensionnels.

REMERCIEMENTS -

Je tiens à remercier ici Marc Lazareff, ingénieur à la Direction de l'Aérodynamique de l'ONERA, pour de nombreuses et fructueuses discussions qui sont à l'origine de ce travail.

REFERENCES -

[1] J.P. CHRISTIANSEN : Numerical Simulation of hydrodynamics by method of point vortices. J. of Comp. Phys. 13, p. 363, 1973.

[2] H. AREF et E.D. SIGGIA : "Point vortex simulation of the inverse cascade in two-dimensional turbulence" Phys. Fluids 24, p. 171 (1981).

[3] A.J. CHORIN : A numerical study of slightly viscous flow. J. Fluid Mech. 57, p. 21 (1973).

[4] MILIMAZZO et SAFFMAN : "The calculation of large Reynolds number two-dimensional flow using discrete vortices with random walk". J. Comp. Phys. 23, p. 380 (1977).

[5] C. REHBACH : "Calcul numérique d'écoulements tridimensionnels instationnaires avec nappes tourbillonnaires". La Rech. Aérosp. 1977-5, p. 289 (1977). English translation ESA-TT 459.

[6] C. REHBACH : "Calcul instationnaire de nappes tourbillonnaires émises par des surfaces portantes fortement inclinées". AGARD CP 247 n° 14 (1978).

[7] G.H. COTTET et P.A. RAVIART : "Particle methods for one-dimensional Vlassow-Poisson equation". (à paraître).

[8] A. MAJDA et T. BEALE : "Vortex Methods II : higher order accuracy in two and three dimensions" (Univ. Of California Berkeley report P.A.M. 54 (1981).

[9] KADEN : "Aufwicklung einer unstabilen unstetigkeits Flache". Ing. Archiv. 2 (1931) p. 140.

[10] BAKER : "The cloud in cell technique Applied to the Roll up of Vortex Sheets". J. of Comp. Phys. 31 p. 76 (1979).

[11] M.S. CHONG, T.T. LIM et A.E. PERRY : "Vortices in turbulence". Vortex motion, Colloquium 75th Anniversary of the aerodynamische Versuchsanstalt (1982).

[12] M.S. CHONG et A.E. PERRY : "A physical interpretation of the spectra of wall turbulence". Third. Symp. on Turbulent Shear flow. Univ. Of Calif. Davis Session I, p. 15 (1981).

[13] M.S. CHONG et A.E. PERRY : "On the mechanism of wall turbulence". J. Fluid Mech. 119, p. 173 (1982).

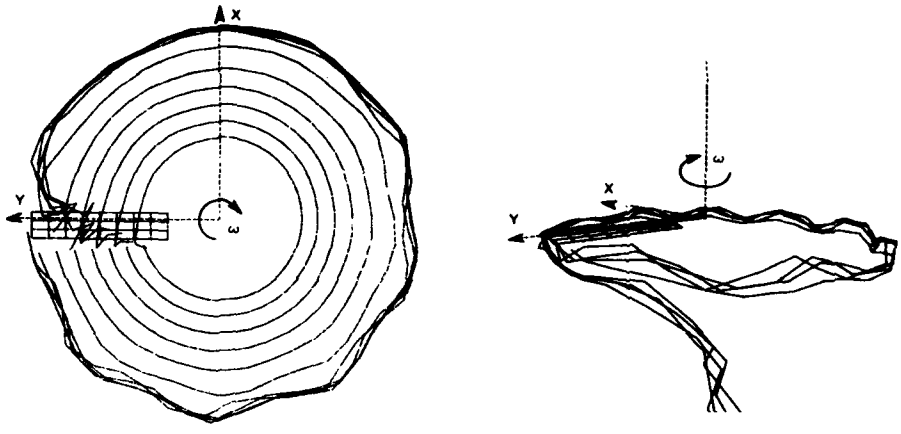

Fig. 1 – Calcul de l'écoulement sur un rotor monopale en vol stationnaire - lignes d'émission.

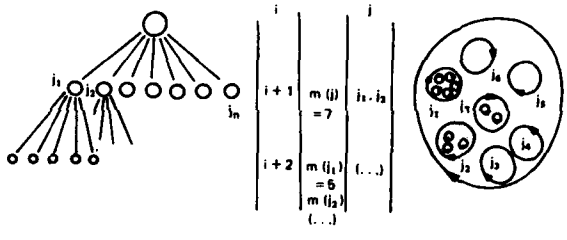

Fig. 2 – Représentation des structures tourbillonnaires sur trois hiérarchies.

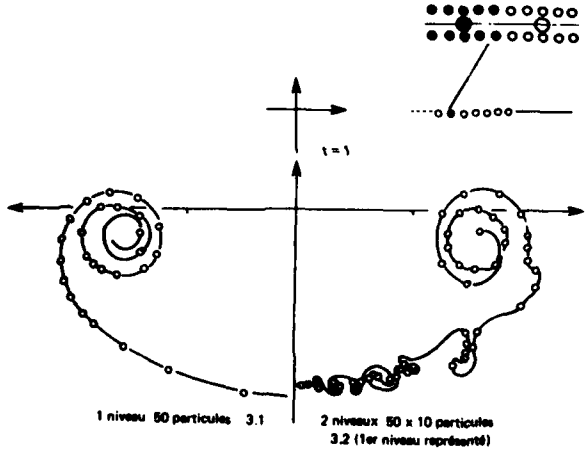

Fig. 3 – Problème de Kaden.

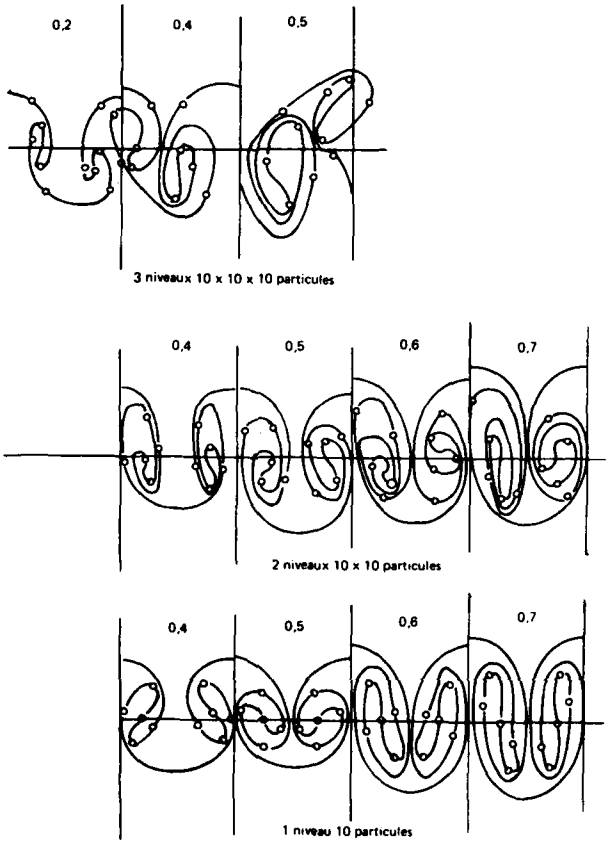

Fig. 4 – Problème de Kelvin-Helmholtz

NUMERICAL SOLUTIONS OF THE EULER EQUATIONS SIMULATING VORTEX FLOWS AROUND WINGS

by
Arthur Rizzi & Lars-Erik Eriksson
FFA The Aeronautical Research Institute of Sweden
S-161 11 BROMMA, Sweden
and
Wolfgang Schmidt & Stephan Hitzel
Dornier GmbH.
D-7990 FRIEDRICHSHAFEN, FRG

SUMMARY

The Euler equations have been established as an appropriate model for inviscid vortex flow. This paper demonstrates the range of this model's applicability by presentation of flowfields computed around a number of different wings with either sharp or rounded edges and at subsonic, transonic, and supersonic speeds. The emphasis here is on the physics of the flow model rather than the numerical aspects of the solution method. The results display both expected as well as unexpected vortex phenomena and they indicate the value of this computational tool. Particular attention is paid to the wake regions.

INTRODUCTION

Vortex phenomena prevail in the flow around all wings. The common numerical methods for the simulation of subsonic as well as transonic flow around wings incorporate classical wing theory into the computation of a velocity potential and, as part of the solution, solve for the vortex sheet which is positioned at a fixed spatial location trailing the wing. It is the inclusion of this sheet that enables an irrotational model to arrive at a realistic value for lift and induced drag. This potential theory fits well flow past relatively straight wings of high aspect ratio which can be regarded as essentially two-dimensional and irrotational (Fig. 1) in character over much of the span. The predominantly three-dimensional region near the tip, however, possesses a vortex structure more complex than the simplified trailing vortex sheet of the classical theory and rather similar in nature to the type found at the leading edge of a highly swept slender wing. This vortex tends to reduce the pressure directly under it which leads to local suction on the upper surface. A well-structured vortex phenomenon like this has a fundamental interest of its own and, with increasing sweep and decreasing aspect ratio, it also begins to assume much greater practical importance because it contributes to lift and drag. Since vortices are singular solutions to the potential equation, the usual potential methods for large aspect ratio wings cannot readily model this more detailed structure. For slender wings of low aspect ratio a number of potential methods (see Fig. 2 together with the discussion by Hitzel[1]) do allow the vortex sheet to roll up as a way to model the free-vortex layer in this type of flow. But these methods are limited by other restrictions, for example, thin wings of relatively simple geometry and incompressible subsonic flow. A mathematical model more general than the potential one and applicable throughout the entire transonic/supersonic speed range is the compressible Euler equations because flow with distributed vorticity is an admissible solution, and vortex structure can be captured in the computed field in a way very similar to the capturing of shock waves. Several three-dimensional flow examples have already been calculated, and the results support the initial feasibility of this approach. Indeed leading edge separation from a delta wing is obtained in these computed solutions even without the use of a Kutta condition. This brings us to the next stage of development and the subject of this paper - a study of the range of applicability and an assessment of the degree of realism exhibited by a number of newly-computed solutions to the Euler equations simulating vortex flows around wings.

OUTLINE OF METHOD

Development of a method to solve the 3D Euler equations was initiated by Dornier GmbH over 5 years ago and has continued since then as a cooperative effort by Dornier, FFA, and Professor A. Jameson at Princeton[2-5]. It is a time-dependent finite-volume approach that uses multistage explicit time integration schemes together with centered space differences to solve the compressible Euler equations

$$\frac{\partial}{\partial t} \int q_{ijk}\, dvol = - \iint \vec{B}\cdot\vec{D}\, da + \begin{matrix}\text{boundary conditions}\\ \text{and}\\ \text{artificial viscosity}\end{matrix} \qquad (1)$$

in each cell ijk of the mesh where $q_{ijk} = [\rho, \rho u, \rho v, \rho w]_{ijk}$ has elements of mass and Cartesian components of momentum and $\underline{H}(q)\cdot\underline{n} = [q\underline{V} + (0, \underline{e}_x, \underline{e}_y, \underline{e}_z)p]\cdot\underline{n}$ is the vector flux of q across the surrounding cell surfaces. Significant features of this approach are its integral conservation-law form, important for the correct capturing of shock waves and vortex sheets, its amenability to very general geometry without the need for a global coordinate transformation, and its toleration of mesh singularities because the flow equations are balanced only within the cells of the grid[6], and not at the nodal points. Different models for artificial viscosity, treatment of boundary conditions, as well as time integration schemes for Eq. (1) have all been investigated, but since these matters are of secondary interest to the present purpose we do not further elaborate on them here. What is worth commenting on, however, is that flows computed with the time-dependent Euler equations are found to separate from the leading edge of a sharp delta wing at angle of attack, and perhaps more surprisingly even from the smooth tip of a trapezoidal wing -- all without the use of a Kutta condition. Such observations of the solutions obtained by time-marching methods stand in contrast to those experienced with space-marching methods where evidently separated flow is computed only if a Kutta condition is enforced. This implies a fundamental difference in these two different numerical models of the Euler equations which can be argued from both the physical and mathematical point of view. There are grounds to believe that the inviscid mechanism that triggers separation involves the time-dependent compressibility aspect of the Euler equations[4], which of course is not included in the strictly steady equations. We can also see a major distinction in the mathematical behavior of these two systems by a comparison of their respective dependence on initial and boundary conditions. The largest disparity in sensitivity appears evidently in the respective boundary conditions on the wing surface. Without a Kutta condition the space-marching methods yield attached flow around even sharp edges, but give the entirely different result of separated flow as soon as a Kutta condition is set at just one point on the wing. Compare this to our experiment with three variations of the wing boundary condition (of which one included a Kutta condition) that showed a very minor effect on the solution of separated flow[7]. Such findings speak for a major difference between these two mathematical systems.

COMPUTED EXAMPLES

The grids around the trapezoidal and delta wings are 0-0 type generated by Eriksson's transfinite interpolation software package[8] whereas the grid around the arrow wing was constructed by the Dornier program[9].

ONERA M6 Wing $M_\infty = 0.84$ $\alpha = 3.06^\circ$

We choose to present results computed for this wing of intermediate aspect ratio to demonstrate the overall applicability of the method not only because it has become a standard test example but primarily because experiments have revealed the presence of a significant vortex above the wing tip. Flow expands from the high pressure of the lower surface around the tip, separates, and rolls up to form a tip vortex in much the same way as the leading edge vortex develops on a low aspect ratio delta wing. The situation is pictured schematically in Fig. 1. Inboard over most of the span the flow is expected to be irrotational and nearly two dimensional. This region of the flow has been simulated many times before and very accurately by potential flow methods. Our interest here is to focus on the tip region in order to determine whether or not the Euler-equation model is able to capture the rotational flow there with some degree of realism.

Containing 96×20×20 cells our grid is an 0-0 type that wraps smoothly around the tip with a cell density sufficient to resolve the details of the flow there. In order to grasp the nature of the results we must survey the computed solution by means of a series of contour maps not only on the wing surface itself but out in the field as well. An overall impression of the pressure field around the wing from root to tip is illustrated in Fig. 3 by isobar maps in 4 selected chordwise grid surfaces (nonplanar) that depict the familiar expansion/compression phenomenon near the leading and trailing edge as well as the formation of the lamda shock. These features are brought out even more distinctly by the isobar contours on the upper wing surface (Fig. 4) together with the usual sectional chordwise plots of C_p in Fig. 5. At the tip Fig. 4 further indicates by the coalescence of contour lines the stem of the lamda shock just aft of the leading edge as well as a local region of high compression at the trailing edge of the tip. Although novel for this type of wing, sectional spanwise plots of C_p are the best way to view this detail. Figure 6 contains three such sections (fore, mid, and aft chord) together with the usual experimental values plotted in this uncommon manner. Inboard, reflecting the two-dimensional character of the flow, the pressure varies only slowly with span until the tip approached. There locally in this intriguing region we see, and this is confirmed by the measurements, a small amount of negative lift being produced in section x/c = 0.28, which then changes to a positive contribution to lift in the next two sections x/c = 0.68 and 0.87. Similar to the pressure distribution on a delta wing, these figures lead

one to suspect separating vortex fl. A survey of the vorticity field by 4 contour maps (Fig. 7) of the vorticity magnitude $|\Omega| = |\text{curl } \underline{V}|$ in the field around the wing tip confirms the existence of rotational flow local to that region. The trace (Fig. 8) of these contours on the upper surface of the wing shows more clearly that the greatest amount and largest magnitude of vorticity is generated at the leading and trailing tip corners. Although curiously enough there is a small amount of vorticity along part of the leading as well as the trailing edge, the latter probably diffused upstream from the trailing vortex sheet. The leading edge vorticity is more difficult to explain. It is a region where the flow changes rapidly, gradients are large and, we believe, that this level of vorticity is an expression of the combined truncation error and artificial viscosity there. Of course the same reasoning holds at the tip, but the much higher magnitude and general physical character suggest that although the artificial viscosity may initially inject some vorticity it is the prevailing flow pattern that determines whether this initial amount is amplified or diminished.

The wake is another region of interest, and the behaviour of the trailing vortex is shown in Fig. 9 by 4 contour maps of $|\Omega|$ in surfaces that cut through the wake spanwise, one just 2% of the root chord behind the trailing edge and the others further downstream. In the first we see a small but clearly developed tip vortex and a rather strong vortex sheet spanning the trailing edge (a portion of the map is cut away to reveal the trailing edge for a position reference). As it moves downstream the vortex grows in size being fed by the decrease in vorticity across the trailing edge sheet. Also as expected the vortex sheet rises above the wing plane and the tip vortex drifts inboard. At the 150% station behind the trailing edge it is fully developed. Such wake phenomena are a good test of the numerical method. We remark that our artificial viscosity model does not unduly smear out the vortex sheet at the trailing edge. Although probably diffused on the rapidly expanding mesh, the vorticity contour is not at all distorted at the 450% station which is the station nearest to the downstream boundary, and an indication that our nonreflecting farfield boundary conditions are able to handle even this case of a vortex leaving the field.

Sharp-edged 70° Swept Delta Wing

We treat two cases of flow past a delta wing whose chordwise sections are 6% thick circular arcs and whose leading edge is swept 70° and is subsonic. In the first case the wing is immersed in a subsonic stream $M_\infty = 0.70$ and $\alpha = 15°$ and in the second a supersonic stream $M_\infty = 1.5$ and $\alpha = 15°$. The mesh used is an O-O type consisting of 65 nodes around the semispan section, 15 on both the upper and lower chord sections, and 21 from the wing outward to the far boundary. Because of the high angle of attack vortex flow is expected, and for the case $M_\infty = 0.7$, Fig. 10 presents contour lines of computed vorticity magnitude $|\Omega|$ in 3 selected spanwise grid surfaces (nonplanar) that clearly reveal the flow separating from the leading edge and rolling up to form a vortex over the upper surface of the wing. In a similar view, but this time for isobar contours, Fig. 11 shows the low pressure region centered about the core of the vortex. The presence of the vortex is felt as a pressure trough (suction peak in terms of C_p) in the isobars on the wing surface in Fig. 12 with the maximum depression located mid-chord and just inboard of the leading edge. The pressure measured experimentally in the 80% chord station indicates, however, that the maximum suction attained in the computations at the forward section should extend downstream to at least this station and be slightly further inboard. The overall agreement though is encouraging. Furthermore it is intriguing to take the middle-section plot of vorticity from Fig. 10 and examine it in an enlarged view in Fig. 13, where the curious structure in the vorticity field between the leading edge and the core of the primary vortex might suggest the presence of a secondary vortex.

The development of the wake is revealed by contour maps of $|\Omega|$ in a number of spanwise surfaces. The first (Fig. 14) is highly curved and cuts through the wake just behind the trailing edge. We see here two vortex phenomena, the vortex sheet from the leading edge that forms the primary vortex over the wing and the vortex sheet leaving the trailing edge that begins to roll up into a wake vortex. In the next view (5% behind the trailing edge) these two vortices interact and then merge (20%) into one oblong trailing vortex (125%).

The solution for the second flow past the delta wing $M_\infty = 1.5$ $\alpha = 15°$ is displayed in a similar series of figures. The vorticity magnitude contours (Fig. 15) indicate the presence of the primary vortex, but are more flattened than the corresponding ones for the flow with $M = 0.7$. The isobar contours (Fig. 16) also are different in that a much stronger expansion fan is centred at the sharp leading edge. The flow compresses in the windward side of the field and then expands around the leading edge. Isobar plots (Fig. 17) in the plane of symmetry depict a bow shock wave on the windward side very near the apex. Evidently the expansion around the leading edge is so strong that the bow wave disappears on the leeward side. A tail shock develops, however, at the upper trailing

edge. Isobars on the upper wing surface are given in Fig. 18 and show a low pressure trough under the primary vortex. At the 80% chord station the spanwise comparison of computed and measured pressure coefficient suggests that a good deal of realism is achieved by the numerical model. Contours of constant vorticity magnitude and Mach number (Fig 18) point out the rapid changes that take place along the leading and trailing edges.

Contour maps of Ω in a number of spanwise surfaces that slice through the wake are presented in Fig. 19 and are similar to those for the M= 0.7 case in the way that a double vortex system develops out of the leading edge vortices. But this case differs slightly in that these two distinct vortices persist above the wing further downstream (20%) before merging into a single vortex (125%).

Arrow Wing

Figure 20 gives a survey of the pressure distribution of the arrow wing configuration. Two different leading-edge-forms (sharp and round) and a subsonic and a transonic Mach-number are presented. The effect of compressibility is clearly shown by the reduced suction peak in comparison to Figs. 20a and b and the effect of the sharp leading-edge is represented by a considerably higher suction peak (Fig. 20c)= compared to the lower ones at the round leading-edges (Figs. 20a,b). The last ones also exhibit a smaller peak along the edge which can be seen from the experimental results too[10]. Also Figs. 21 allow a direct comparison with the experimental results. The semi-span separation is reproduced in Fig. 22 from the isobars of the arrow-wing with the round leading-edge exposed to 8 degrees angle of attack. The comparison of the computed results are very well in agreement with experimental results. As the leading-edge is not sufficiently sharp enough at 8 degrees angle of attack, the flow persists to separate from the front part as it is doing at higher incidence. At the lower incidence the typical isobar pattern for separation is visible only at the rear part of the wing, while at 16 degrees the same pattern is found everywhere along the leading-edge, as it is found more pronounced at very high incidence.

Figure 23 depicts the velocity-vectors for different crossflow-planes. Now it is easy to understand the good agreement of experimental and theoretical lift coefficients (Fig. 24). We finally note that even Hummels[11] trailing edge vortex is modelled by the procedure (Fig. 25).

CONCLUDING REMARKS

We have presented computed results for several cases of flow separating with a free shear layer at an aircraft edge. The comparison of these computations with measurements made experimentally as well as with what can be reasoned qualitatively about the physics of the flows serve to establish the realism that is obtained with this Euler-equation model. Even without the use of a Kutta condition the range of validity of the model includes cases where the flow separates from edges that are not strictly sharp. We believe, however, that if the computed results are to be realistic the local radius of curvature must be small in order that the shear-layer character and gross features of the real flow are by and large insensitive to Reynolds number and therefore possible to represent by inviscid equations that include a small amount of artificial viscosity.

References

1 Hitzel, S.M. and Schmidt, W.: Slender Wings with Leading-Edge Vortex Separation - A challenge for Panel-Methods and Euler-Codes, AIAA Paper No. 83-0562, 1983.

2 Jameson, A., Schmidt, W. and Turkel, E.: Numerical Solutions to the Euler Equation by Finite Volume Methods Using Runge-Kutta Time Stepping, AIAA Paper 81-1259, June 1981.

3 Rizzi, A. and Eriksson, L.E.: Transfinite Mesh Generation and Damped Euler Equation Algorithm for Transonic Flow Around Wing-Body Configuration, AIAA Paper 81-0999, June 1981.

4 Schmidt, W. and Jameson, A.: Recent Developments in Finite-Volume Time-Dependent Techniques For Two and Three Dimensional Transonic Flows, in Computational Fluid Dynamics, Lecture Series Notes 1982-04, VKI, Brussels, 1982.

5 Rizzi, A. and Eriksson, L.E.: Explicit Multistage Finite Volume Procedure to Solve the Euler Equations for Transonic Flow, in Computational Fluid Dynamics, Lecture Series Notes 1983-04, von Karman Inst., Brussels, 1983.

6 Eriksson, L.E.: A Study of Mesh Singularities and Their Effects on Numerical Errors, paper presented at Minisymposium on Analysis of Mesh Effects, SIAM Meeting, July 1982, to be published.

7 Eriksson, L.E. and Rizzi, A.: Computation of Vortex Flow Around Wings Using the Euler Equations, ed. H. Viviand, Proc. 4th GAMM Conf. Num. Meth., Vieweg Verlag, 1982.

8 Eriksson, L.E.: Practical Three-Dimensional Mesh Generation Using Transfinite Interpolation in Computational Fluid Dynamics, Lecture Series Notes 1983-04, von Karman Inst., Brussels, 1983.

9 Leicher, S., Fritz, W., Grashof, J. and Longo, J.: Mesh Generation Strategies for CFD on Complex Configurations, in 8th Conf. Num. Meth. Fluid Dynamics, ed. E. Krause, Lecture Notes in Physics 170, Springer, 1982.

10 Nanro, Manning, Hallstaff, Rogers: Transonic Pressure Measurements and Comparison of Theory to Experiment for an Arrow-Wing Configuration, NASA CR 2610, 1976.

11 Hummel: On the Vortex Formation Over a Slender Wing at Large Angles of Incidence, AGARD-CP-247, High Angle of Attack Aerodynamics, 1978.

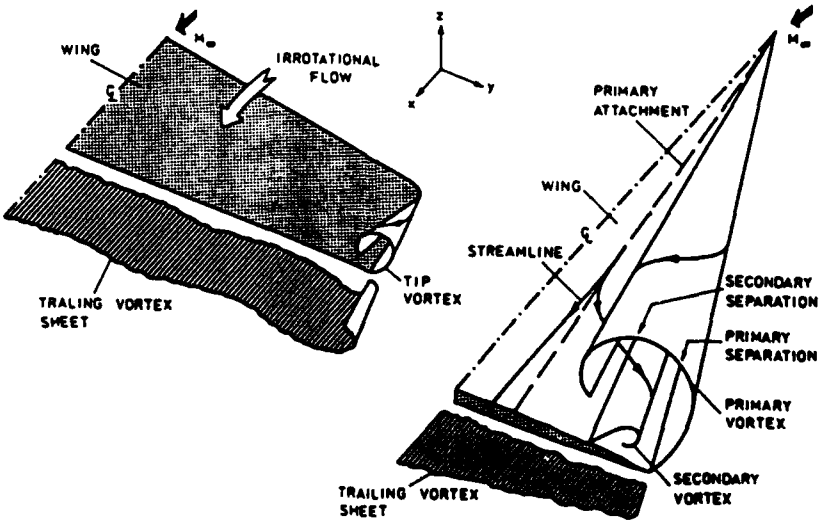

FIG. 1 GENERAL FEATURES OF THE FLOWS. A FREE SHEAR LAYER SEPARATES FROM THE TIP AND LEADING EDGE AND ROLLS UP INTO A VORTEX.

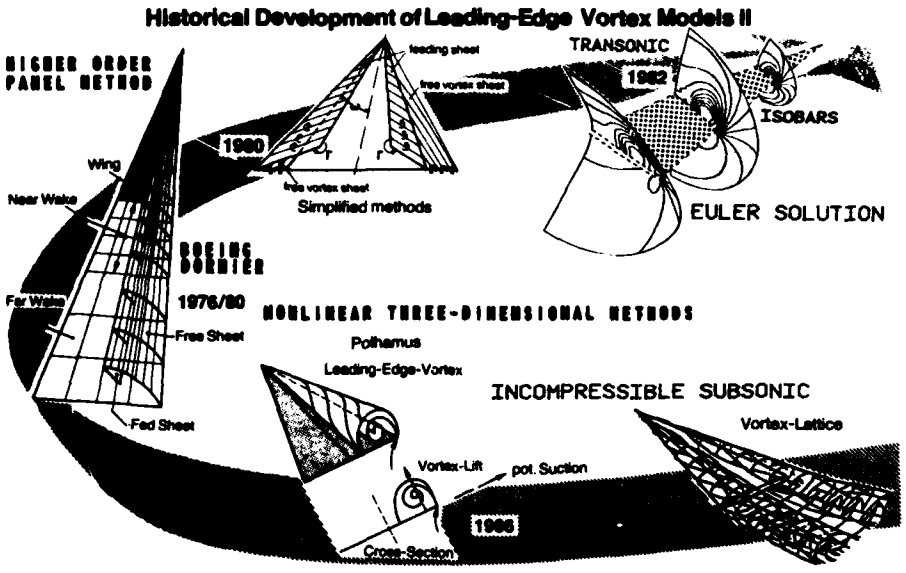

Fig. 2 Highlights of the historical evolution of leading-edge vortex models over the past 20 years, starting with incompressible subsonic flow and leading up to the present methods to solve numerically the compressible Euler equations for transonic flow.

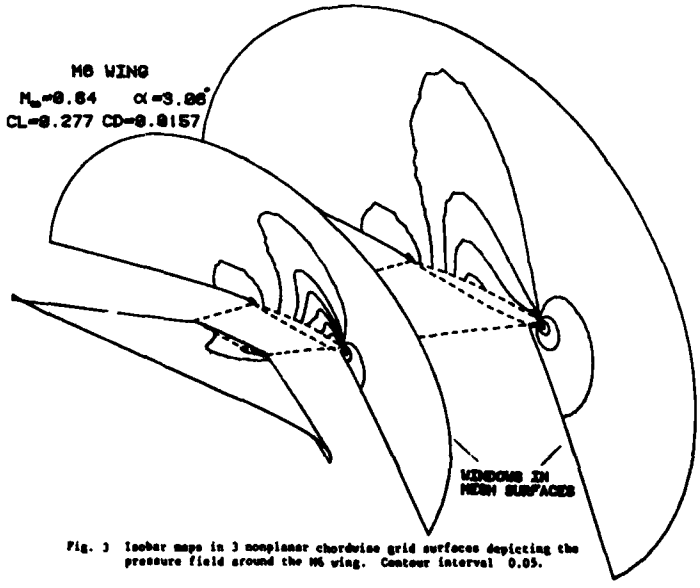

Fig. 3 Isobar maps in 3 nonplanar chordwise grid surfaces depicting the pressure field around the M6 wing. Contour interval 0.05.

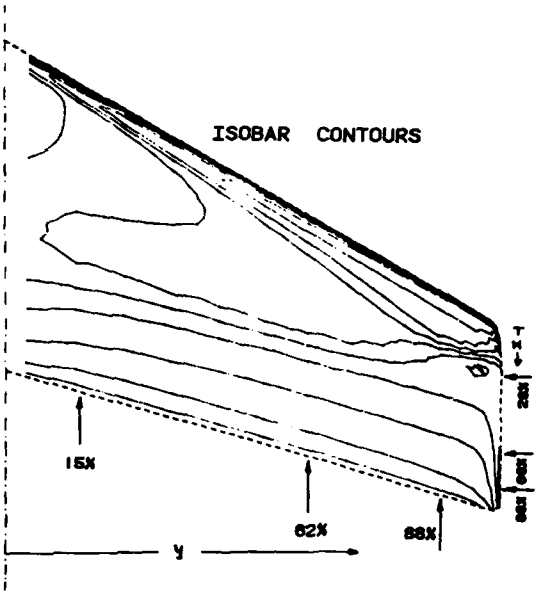

Fig. 4 Lines of constant pressure on the upper surface of the M6 wing. Percent stations indicate the location of the 3 chordwise and spanwise sectional plots displayed in Figs. 5 and 6. M_∞=0.84 α=3.06. Contour interval 0.05.

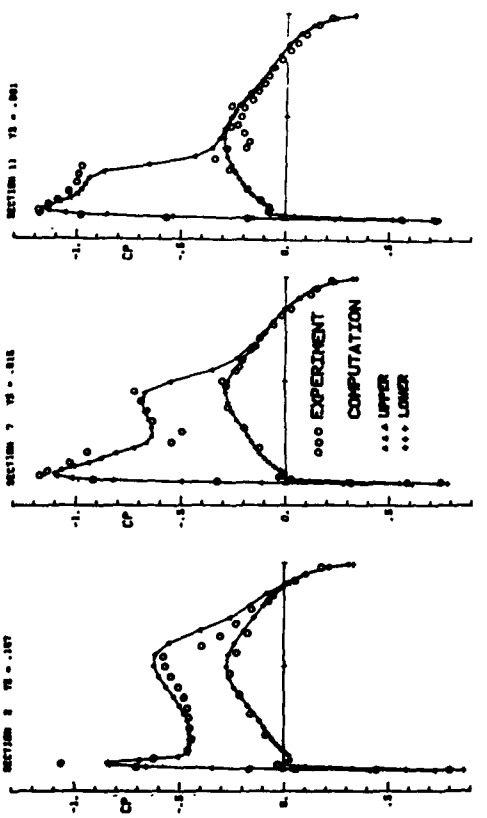

Fig. 5 Comparison of measured and computed C_p in three chordwise sections of the M6 wing (see Fig. 4). M_∞=0.84 α=3.06.

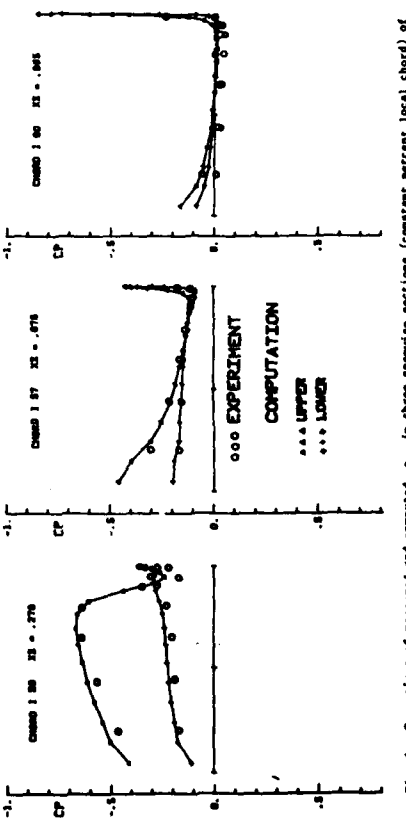

Fig. 6 Comparison of measured and computed C_p in three spanwise sections (constant percent local chord) of the M6 wing (see Fig. 4). M_∞=0.84 α=3.06.

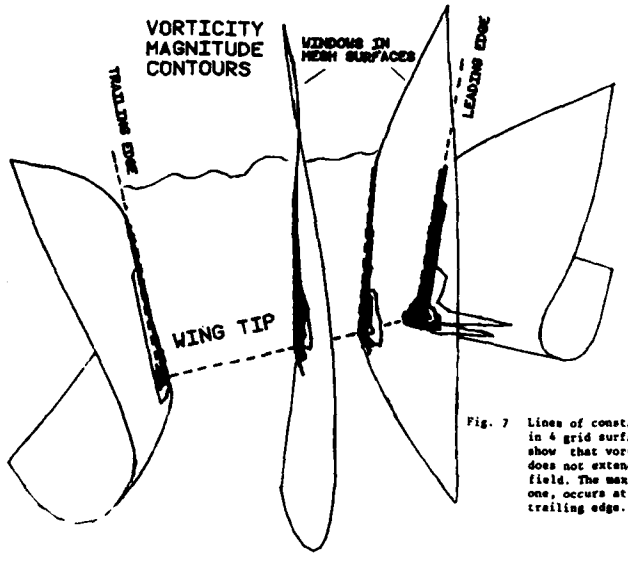

Fig. 7 Lines of constant vorticity magnitude $|\Omega|$ in 4 grid surfaces around the wing tip show that vorticity at these surfaces does not extend very far out into the field. The maximum value, normalized to one, occurs at the upper surface tip trailing edge. Contour interval 0.001.

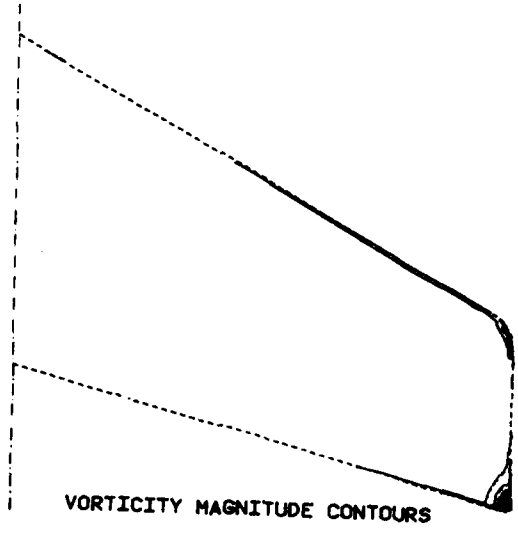

Fig. 8 Lines of constant vorticity magnitude $|\Omega|$ on the upper wing surface. The maximum value, normalized to one, occurs at the upper surface tip trailing edge. M6 wing M_∞=0.84 α=3.06 Contour interval 0.01.

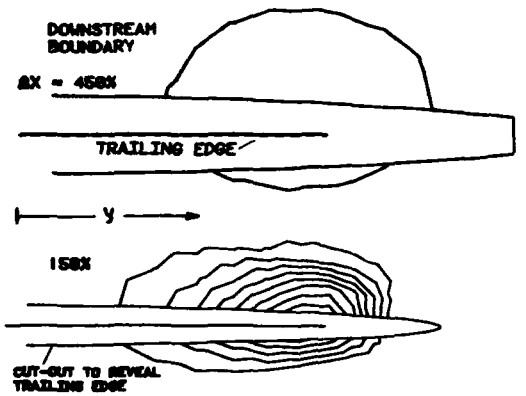

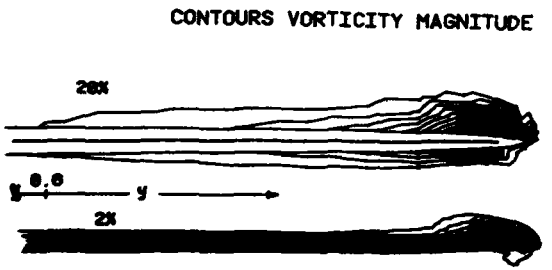

Fig. 9 The wake region behind the M6 wing revealed by constant vorticity magnitude contours plotted in 4 spanwise sections at distances in percent root chord behind the trailing edge. M_∞=0.84 α=3.06.

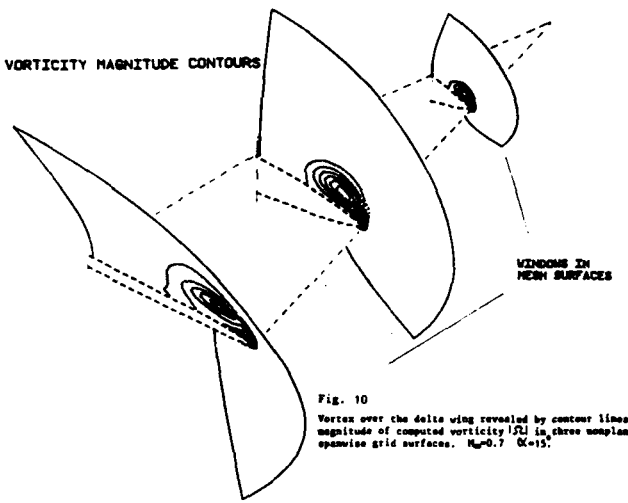

Fig. 10
Vortex over the delta wing revealed by contour lines of the magnitude of computed vorticity $|\Omega|$ in three nonplanar spanwise grid surfaces. M_∞=0.7 α=15°.

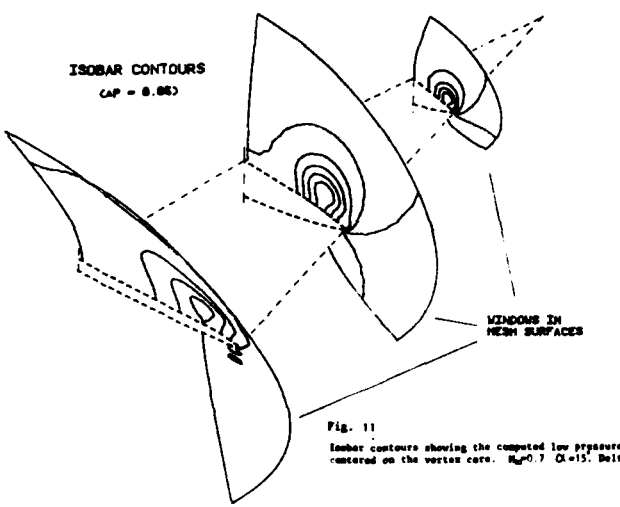

Fig. 11
Isobar contours showing the computed low pressure region centered on the vortex core. M_∞=0.7 α=15°. Delta wing.

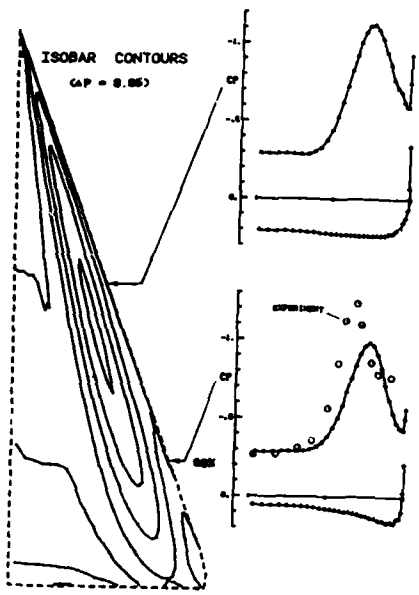

Fig. 12

Imprint of computed pressure trough given by isobar contours on wing surface together with two spanwise section plots of C_p of which one (88% chord) is compared with experimental values (FFA Report AU-295) M_∞=0.7 α=15°. Delta wing.

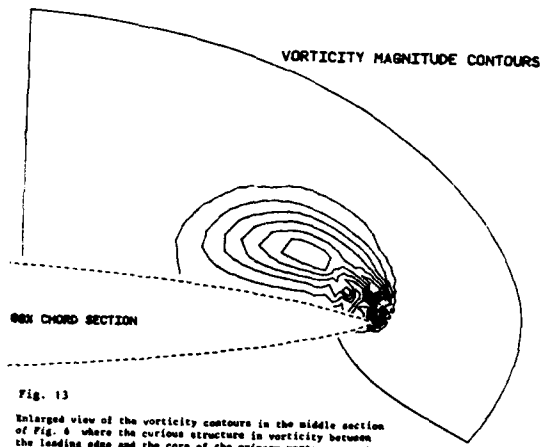

Fig. 13

Enlarged view of the vorticity contours in the middle section of Fig. 6 where the curious structure in vorticity between the leading edge and the core of the primary vortex suggests the presence of a secondary vortex. M_∞=0.7 α=15°.

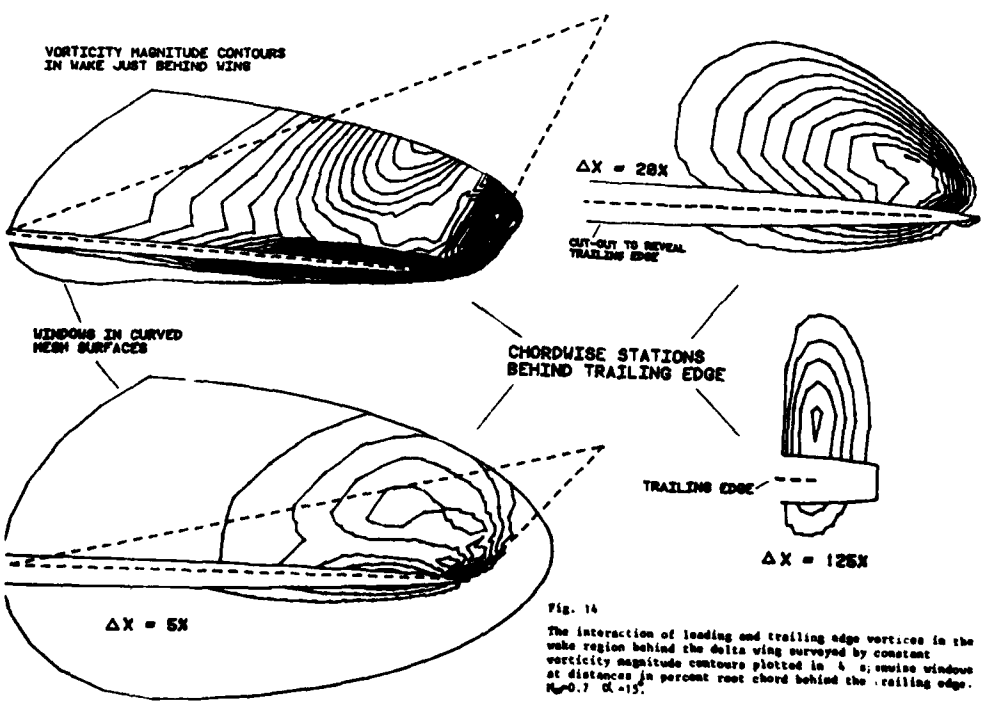

Fig. 14

The interaction of leading and trailing edge vortices in the wake region behind the delta wing surveyed by constant vorticity magnitude contours plotted in 4 spanwise windows at distances in percent root chord behind the trailing edge. M_∞=0.7 α=15°.

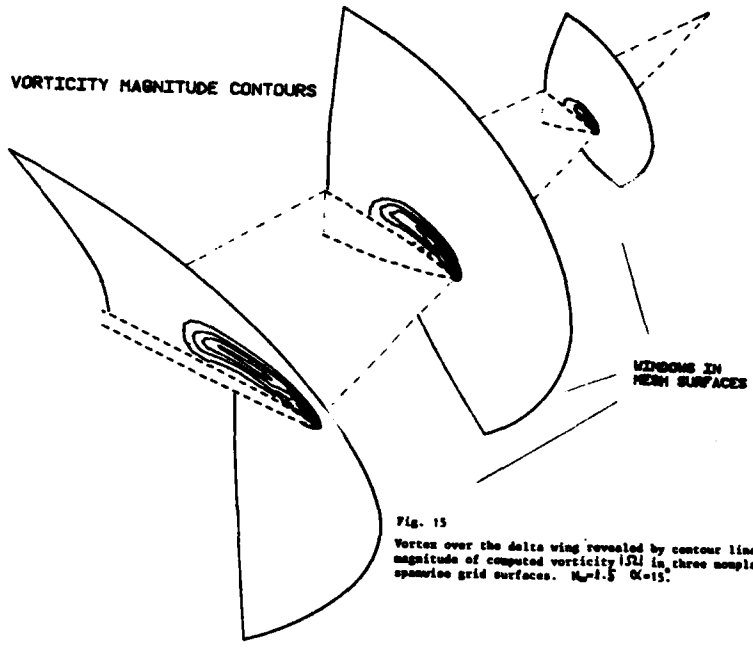

Fig. 15

Vortex over the delta wing revealed by contour lines of the magnitude of computed vorticity |Ω| in three nonplanar spanwise grid surfaces. M_∞=1.5 α=15°.

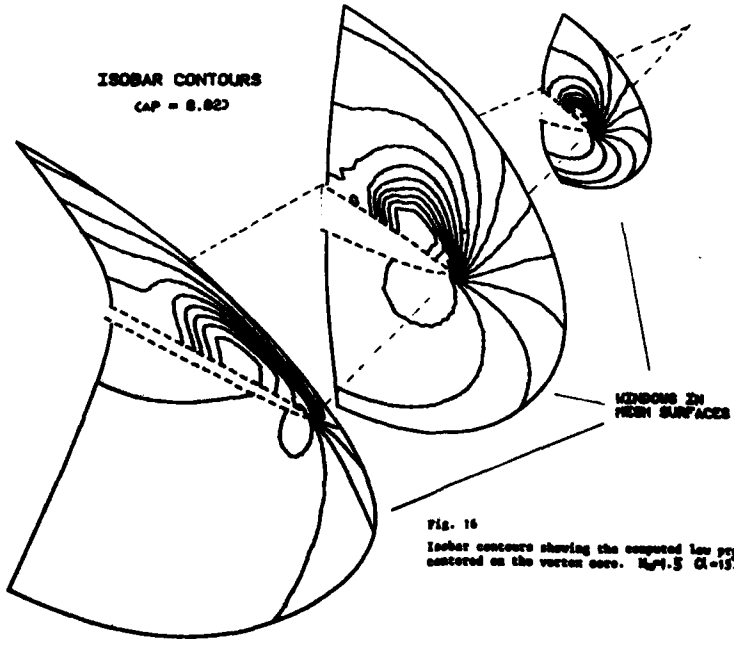

Fig. 16

Isobar contours showing the computed low pressure region centered on the vortex core. M_∞=1.5 α=15°. Delta wing.

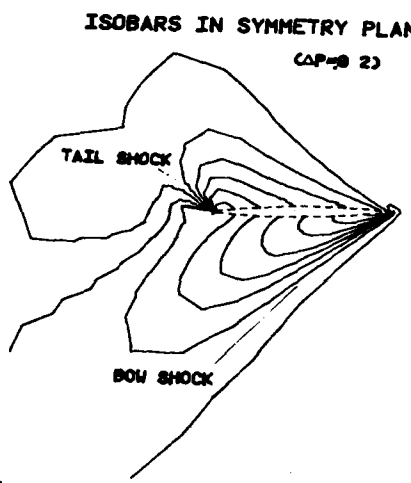

Fig. 17

Contours of isobars in the plane of symmetry of the delta wing showing the compression regions of the bow and tail shocks. M_∞=1.5 α=15°. Sweep 70°.

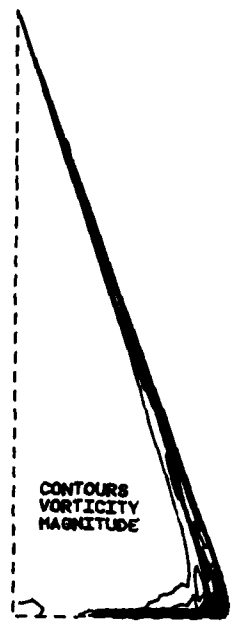

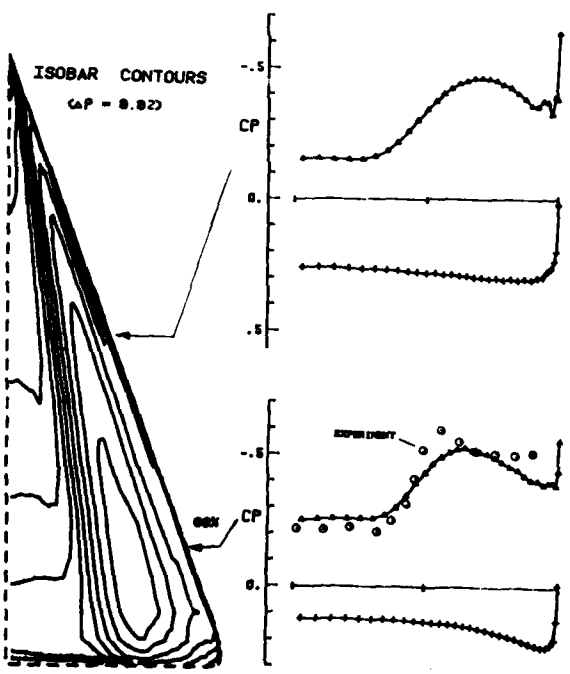

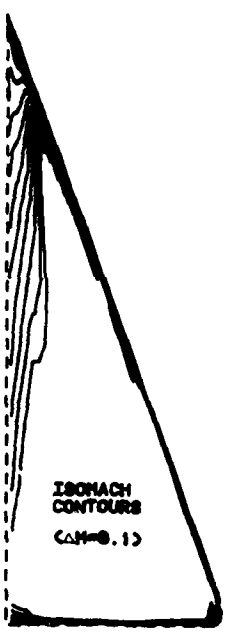

Fig. 18

Contours of constant vorticity magnitude, Mach number, and isobars on the wing surface together with two spanwise section plots of c_p of which one (80%) is compared with experimental values (FFA Report AU-295) M =1.5 α=15°. Delta wing.

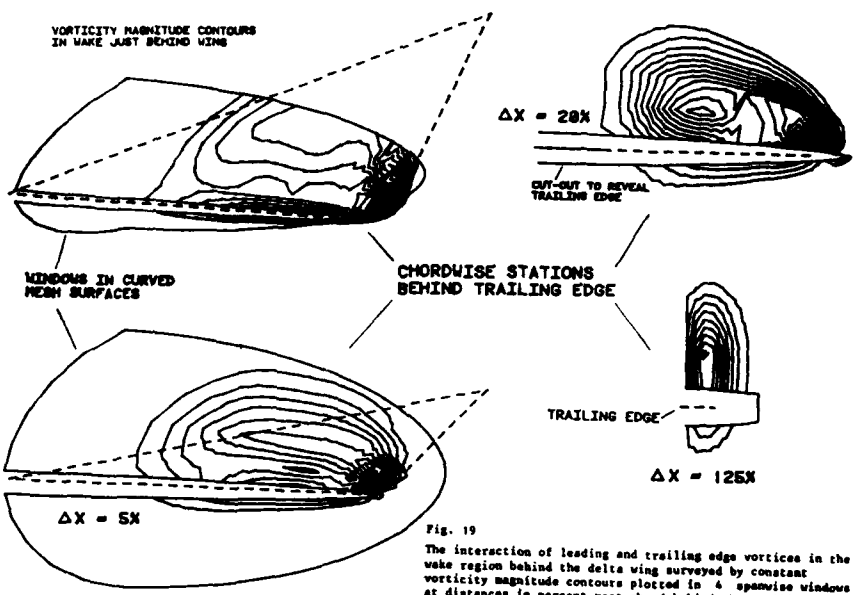

Fig. 19

The interaction of leading and trailing edge vortices in the wake region behind the delta wing surveyed by constant vorticity magnitude contours plotted in 4 spanwise windows at distances in percent root chord behind the trailing edge. M_∞=1.5 α=15°

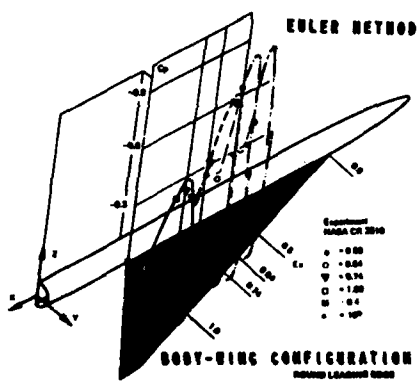

Fig. 20a

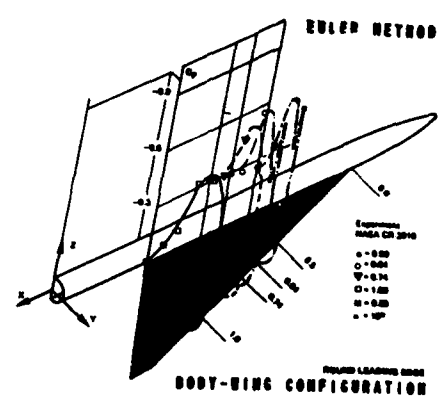

Fig. 20b

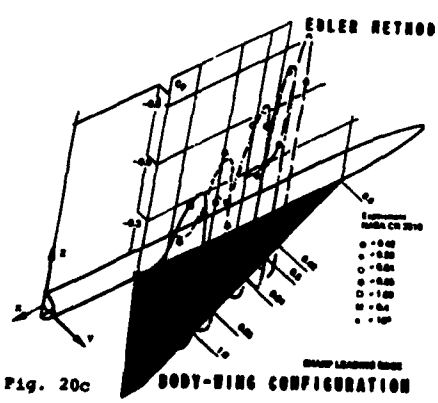

Fig. 20c

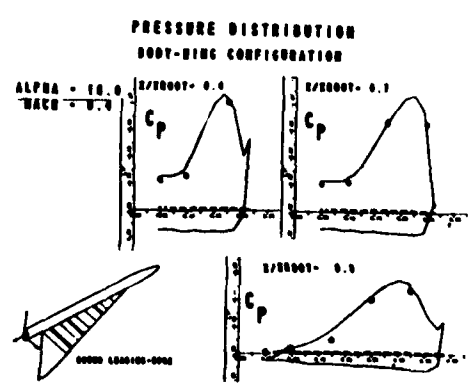

Fig. 21a

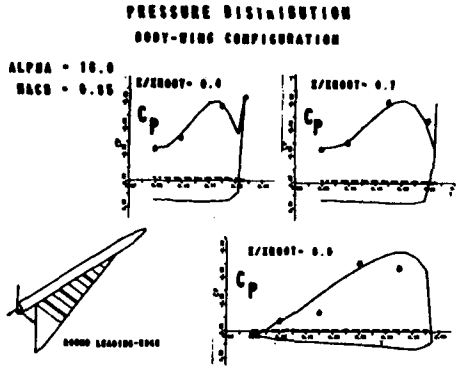

Fig. 21b

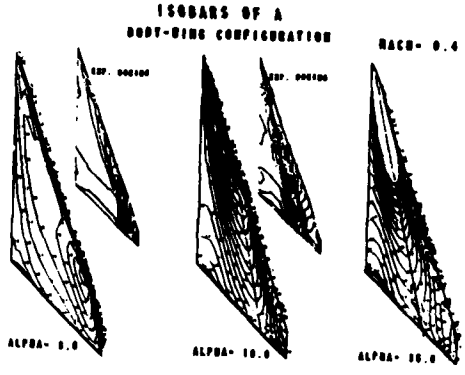

Fig. 22

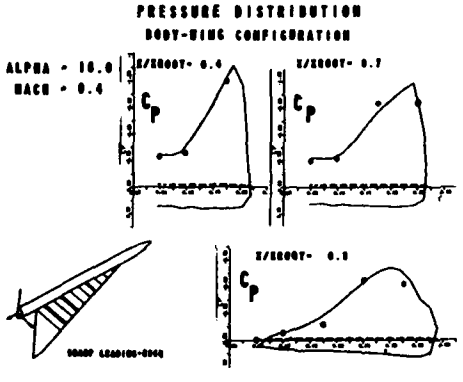

Fig. 21c

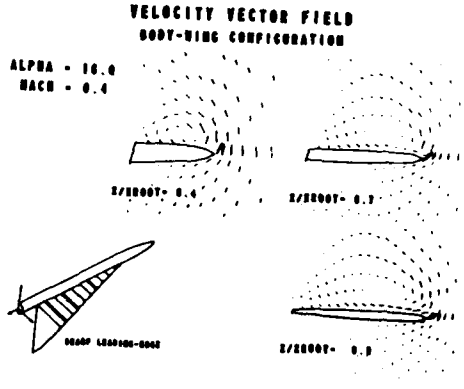

Fig. 23

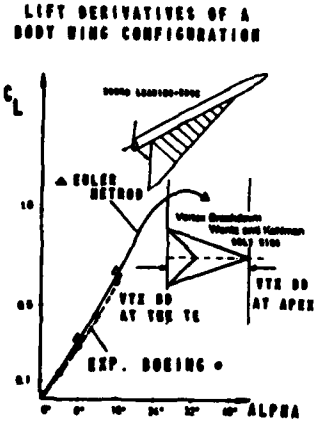

Fig. 24

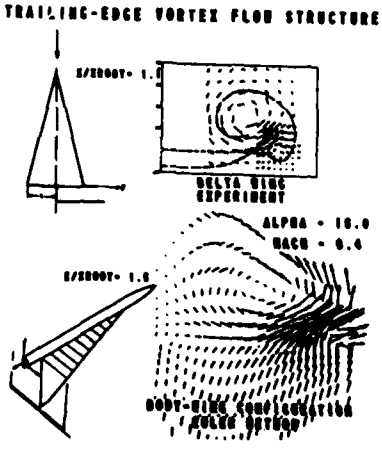

Fig. 25

THE TREATMENT OF CONVECTED VORTICES IN COMPRESSIBLE POTENTIAL FLOW

by

John Steinhoff, Associate Professor
K. Ramachandran, Research Assistant
K. Suryanarayanan, Research Assistant
University of Tennessee
Space Institute
Tullahoma, TN 37388 USA

SUMMARY

A method is described for incorporating line vortices into the three dimensional compressible Potential Flow equation. A modified Biot-Savart law is used to compute a vortical velocity field, which is added to the gradient of the potential to form a total velocity. A rapidly converging Approximate Factorization (AF2) scheme is then used to compute a potential such that the modified Potential Flow equation as well as the appropriate boundary conditions, based on total velocity, are satisfied. As part of a coupled iteration procedure, the positions of the line vortices are computed so that they convect with the total flow.

The method is used to compute the field due to a single line vortex convecting past a wing . This represents an approximation of the effect of a canard or other lifting surface ahead of the wing, which sheds a tip vortex. It can be seen that the flow field is substantially modified by the passage of the vortex.

Unlike Euler equation schemes, which could also be used to compute these flows, our solutions exhibit no numerical diffusion: The convected vortices retain their initial upstream width. Euler solutions, on the other hand, involve a vorticity which is numerically convected in an Eulerian frame and, unless extensive adaptive grid refinement is used they result in vortices which spread as they convect. Also, the Potential Flow method requires approximately two orders of magnitude less computing time and much less computer storage than the Euler methods.

1. INTRODUCTION

An important problem in computational aerodynamics consists of determining the effect of a vortex convecting past a lifting surface. Examples include vortices produced by the tip of a canard or by leading edge separation at a strake convecting past a wing, or tip vortices produced by a helicopter rotor blade convecting past another blade. These effects are especially important in transonic flow with shock waves, where the vortex can cause large movements of the shock and large changes in lift and drag.

Numerical methods for solving transonic flow problems, in the inviscid region exterior to boundary layers, usually involve either the Euler or the Potential Flow equations. The Euler equations can treat flow with vorticity, but concentrated vortex lines or sheets spread when convected due to numerical diffusion, even when moderate amounts of grid compression are used[1]. Besides this problem, which involves a grid that must adapt to the flow, Euler equations are expensive to solve, requiring about two orders of magnitude more computing time than Potential Flow solutions for the same problem.

In this paper we describe a method for incorporating vortices into the Potential Flow equations. It is conceptually and practically very similar to methods used to incorporate vortices into incompressible flow problems[2]. There, the basic flow is described by Laplace's equation and, because of the linearity, the velocity field due to a set of vortices can be added to the basic flow without the vortex. In problems such as ours the vortex trajectory depends on the total flow and, in general, an iterative procedure must be used to compute a steady solution where the vortices are convected with the flow, even in the incompressible case.

2. GOVERNING EQUATIONS

The basic method for compressible flow involves defining the total velocity to be the sum of the potential flow and that due to the convective vortices ($\vec{q}_v$), exactly as in the linear problem. Separating out the free-stream velocity, $\vec{q}_\infty$, we have,

$$\vec{q} = \begin{pmatrix} u \\ \cdot \\ w \end{pmatrix} = \vec{\nabla}\phi + \vec{q}_\infty + \vec{q}_v$$

The Potential Flow equation, which expresses conservation of mass for irrotational flow and is accurate

AD A135 157 AERODYNAMICS OF VORTICAL TYPE FLOWS IN THREE DIMENSIONS: CONFERENCE PROCE..(U) ADVISORY GROUP FOR AEROSPACE RESEARCH AND DEVELOPMENT NEUILLY.. JUL 83

UNCLASSIFIED AGARD-CP-342 F/G 20/4 NL

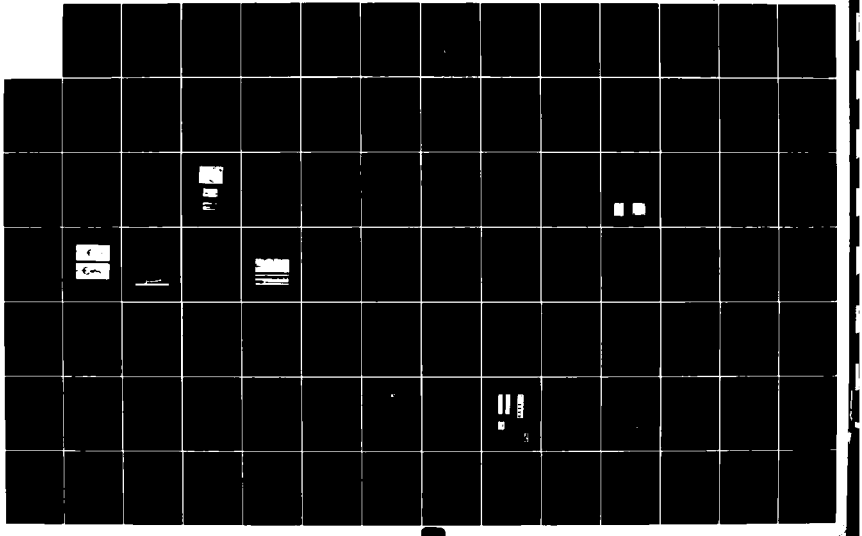

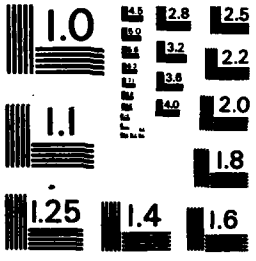

for regions outside of the vortices, is,

$$\partial_x(\rho u) + \partial_y(\rho v) + \partial_z(\rho w) = 0 \tag{1}$$

with the isentropic relation for density,

$$\rho = \left[1 - \left(\frac{\gamma-1}{2}\right) M_\infty^2 (1 - \vec{q}^2)\right]^{\frac{1}{\gamma-1}}$$

In this equation γ is the ratio of specific heats, M_∞ the free-stream Mach number, and the density, ρ, and velocity are normalized to unity at the sonic line.

The boundary conditions imposed on $\vec{q}$ are that it be tangent at material surfaces and approach $\vec{q}_\infty + \vec{q}_v$ in the far field. These will be enforced in the potential solver, which computes ϕ. There, the normal derivative,

$$\partial_n \phi = -(\vec{q}_\infty + \vec{q}_v)_n$$

on surfaces,

$$\partial_x \phi \to 0$$

on the donwstream boundary, where x is in the direction of the free-stream, and

$$\phi \to 0$$

on the other far field boundaries. In addition, for the results presented here, for flow past a wing, the trailing vortex sheet is computed by mapping to a grid surface and specifying a discontinuity in ϕ across it such that pressure and normal velocity are continuous. Since this main part is fairly flat, this treatment is efficient for the problems presently being treated. This sheet can also be described by a vortical velocity, $\vec{q}_v$. This modification will be included in the future.

For a given vorticity distribution, $\vec{\omega}$, $\vec{q}_v$ satisfies

$$\vec{\nabla} \times \vec{q}_v = \vec{\omega} \ . \tag{2}$$

The vorticity is determined by specifying an upstream distribution and convecting it with the flow. If the vorticity distribution is singular, concentrated in lines or sheets, it is further required to spread the distribution over several mesh points to avoid singularities in the flow. Unlike the increasing spreading of concentrated vorticity in Euler solutions, this spreading does not grow: The spread vorticity retains the same distribution when convected and does not diffuse.

In our scheme, we will not be interested in the flow in the interior of the spread vortex lines or sheets, which will be modeled. This is similar to the treatment of shocks in shock capturing methods, which use an artificial viscosity to spread disontinuities. This has been pointed out by Murman and Stremel[3], who are also developing methods for embedding vorticity in potential flow.

These equations only define $\vec{q}_v$ up to the gradient of a potential, ϕ_v. This arbitrariness will be used to simplify computation of $\vec{q}_v$. If different computations of $\vec{q}$ were made, with different ϕ_v, the converged results should be unique, although the final values of ϕ and $\vec{q}_v$ would be different.

Our scheme, then, involves the iterative use of three steps: First, a Potential Flow solver is used to compute ϕ with $\vec{q}_v$ fixed such that $\vec{q}$ satisfies the boundary conditions. Then, with ϕ and $\vec{q}_v$ fixed, a new vorticity distribution, $\vec{\omega}$, is computed by convection. Finally, a vortical velocity, $\vec{q}_v$, is computed from $\vec{\omega}$, with spreading if $\vec{\omega}$ is singular.

Murman and Stremel, in their scheme, also convect vorticies. They then redistribute vorticity among the neighboring node points of their computational mesh surrounding the vortex. Following this, they define a discontinuity in potential extending from each of these nodes. In this way the potential function can be used to include the effect of the vortices. Their published results concern the time-dependent movement of a set of vortices in two dimensions in free space, which approximates the cross-plane development of a vortex sheet behind a wing in incompressible flow. The extension of their method to compressible flow should not be too difficult. Tracing the discontinuities in three dimensions, however, may be somewhat complicated.

3. POTENTIAL FLOW SOLVER

3.1 Basic Formulation

The particular case described in this paper involves flow over a wing, although the technique is applicable to more general geometries. For this case, a Potential Flow solver using a rapidly converging "AFZ" factorization scheme, together with a finite volume discretization scheme is employed. These are described in Ref. [4] and [5].

First, a mapping is defined from physical (x, y, z) to computational (X, Y, Z) coordinates. A set of constant z computational planes are defined (see Figure 1). In each plane, inboard of the wingtip, a parabolic mapping is done about a singular line (dashed in the figure). This is followed by a shearing and stretching. The airfoil surface is thereby transformed to a segment of the computational boundary (X-Z plane) bounded by two lines representing the trailing edge, one representing the tip, and one the root.

If the transformations are represented by a Jacobian matrix H, eqn. (1) may be written in terms of transformed variables:

$$\frac{\partial}{\partial X}(\rho h U) + \frac{\partial}{\partial Y}(\rho h V) + \frac{\partial}{\partial Z}(\rho h W) = 0 \tag{3}$$

where U, V, and W are the contravariant velocities, and h is the transformation Jacobian, $h = \det(H)$. The Cartesian velocity components, in terms of the potential and added velocities are:

$$\vec{q} = \begin{pmatrix} u \\ v \\ w \end{pmatrix} = (H^{\dagger})^{-1} \begin{pmatrix} \phi_X \\ \phi_Y \\ \phi_Z \end{pmatrix} + \vec{q}_{\infty} + \vec{q}_{\bullet}$$

where only derivatives of the potential with respect to the computational coordinates are required. The contravariant velocities may be written in terms of the physical velocities.

$$\begin{pmatrix} U \\ V \\ W \end{pmatrix} = H^{-1} \begin{pmatrix} u \\ v \\ w \end{pmatrix}$$

Equation (3) is then written in discrete form. Conservation form artificial viscosity terms are added to (3) to provide numerical stability in the supersonic zones. Additional terms are added to the difference equations to prevent odd-even decoupling of the solution. The nonlinear equations to be solved have the form

$$\delta_X(\rho h U + P) + \delta_Y(\rho h V + Q) + \delta_Z(\rho h W + R) = 0$$

where P, Q and R are artificial viscosity terms and $\delta_X, \delta_Y, \delta_Z$ are second order accurate finite difference operators. Contravariant velocities U, V and W, are also computed using second order operators.

Two staggered grids are used; one for densities and velocities, another for the potential, the node coordinate values and the basic flux balance (see Fig. 2).

The formulation is completed by specification of the boundary conditions. The far field conditions have been described above. At the body surface, the condition that the normal velocity be zero is $V = 0$. For cases with lift, the Kutta condition is imposed by requiring that the velocity at the trailing edge be finite. This results in a trailing vortex sheet across which the potential has a jump proportional to the circulation. Treatment of the sheet is simplified by constraining it to lie in a plane ($Y = 0$) in the computational space. This excludes the effects of vortex sheet roll up. A flux balance is imposed across the sheet to ensure continuity of the normal velocity, V.

3.2 Solution Scheme

An AFZ approximate factorization scheme is used to rapidly converge to a solution. At each iteration equations are solved for a correction, $\delta\phi$:

$$[(\alpha_X - \delta_X A \delta_X)(\alpha_Y - \delta_Y B \delta_Y) - \alpha\omega C E_{\overline{Z}}]\delta\phi^n = \alpha\omega L\phi^n$$

$$\phi^{n+1} = \phi^n + \delta\phi^n$$

where ϕ^n is the latest approximation to the potential ϕ and $\delta\phi^n$ is the most recent correction. The operators α, α_X and α_Y are

$$\alpha = \alpha_0 + \alpha_1 \nabla_X + \alpha_2 \nabla_{\overline{Y}}$$
$$\alpha_X = \alpha - \nabla_X(a_3 U^2 \delta_{XX})$$
$$\alpha_Y = \alpha - \nabla_{\overline{Y}}(a_3 V^2 \delta_{YY})$$

where δ is the central difference operator, ∇_X is a backward or forward difference operator depending upon the sense of the local flow, $\nabla_{\overline{Y}}$ is the backward difference operator, and $E_{\overline{Z}}$ is the backward shift operator.

The factors α_1, α_2 and α_3 are non-zero in the supersonic zones where α becomes, approximately, a first-order up-wind difference operator. The coefficients A, B, and C are obtained from an expansion of (3) (see [5] for details) and have the form

$$A = \rho h(\widetilde{G}_{1,1} - U^2/a_2^2)$$
$$B = \rho h(\widetilde{G}_{2,2} - V^2/a^2)$$
$$C = \rho h(\widetilde{G}_{3,3} - W^2/a^2)$$

where G is the matrix $H^\dagger H$, $\widetilde{G}_{1,1}, \widetilde{G}_{2,2}, \widetilde{G}_{3,3}$ are the diagonal elements of the inverse of G, and a is the speed of sound.

The solution proceeds in the spanwise direction from one Z = constant plane to the next. At each Z-plane, the algorithm requires solution of

$$(\alpha_X - \delta_X A \delta_X)(\alpha_Y - \delta_Y B \delta_Y)\delta\phi^n = \alpha\omega[L\phi^n + CE_{\overline{Z}}\delta\phi^n]. \tag{4}$$

The correction $\delta\phi^n$ can be obtained by inverting the two operators on the left of (4), the first of which gives rise to a banded matrix with bandwidth of 5 and the second to one with a bandwidth of 4. The shift operator $E_{\overline{Z}}$ introduces a term on the right-hand side which utilizes the newly evaluted corrections in the previous span plane. The basic residual, $L\phi^n$, is evaluated from the previous approximation, ϕ^n, in all planes. This procdure is analogous to SLOR schemes where new values are determined in each column by using new values computed in the previous column and old values in the next. A modal analysis indicated that convergence of (4) should be rapid in the subsonic zone and when there are no extreme changes in the spanwise mesh spacing.

A sequence of values was employed for the parameters $\alpha_0, \alpha_1, \alpha_2$, and α_3. This had the effect of reducing the error components corresponding to a sequence of frequency ranges. Each factor was multiplied by a constant $b_\ell, \ell = 1, 2, \cdots, L_{\max}$. For the cases reported here, $b = [1, 1/2, 1/4, 1/8], L_{\max} = 4$.

The important computational features of the scheme are that it proceeds plane-by-plane in the direction of increasing Z and that the only three dimensional array stored is the potential, ϕ. In each plane the velocities are computed, the densities and residuals formed, and the factorized equations solved for a correction, $\delta\phi$ which is added to ϕ.

4. CONVECTION OF A LINE VORTEX PAST A WING

For this problem, a line vortex is assumed to originate upstream and convect past the wing in steady transonic flow. The vortex, then, follows a streamline with the vorticity vector parallel to the local velocity vector. A modified Biot-Savart law is used to simultaneously perform the necessary spreading and compute $\vec{q}_v$. Since this involves integration over the vortex line for each velocity computation, which must be done at each node point, if a large number of vortices were to be followed the $\vec{q}_v$ calculations could require much of the computing time. For these cases other methods of computing $\vec{q}_v$ are being investigated which will not have a significant impact on the total computing time. For the present case of a single vortex the scheme described here is entirely adequate.

The equation for $\vec{q}_v$, computed at point $\vec{r}$, is,

$$\vec{q}_v = \Gamma \int \frac{d\vec{\ell} \times (\vec{r} - \vec{r}_v(s))}{R^3} \tag{5}$$

where s is a parameter along the vortex, $\vec{r}_v(s)$ the vortex position, Γ the integrated strength or circulation and $d\vec{\ell}$ is a line element along the vortex. Also,

$$R = \max(|\vec{r} - \vec{r}_v(s)|, a)$$

where a is a constant. This results in solid body rotation for $|\vec{r} - \vec{r}_v| < a$ and the velocity due to a line vortex for $|\vec{r} - \vec{r}_v| > a$.

After computation of ϕ, a set of values of $\vec{r}_v$ must be computed along the vortex. For constant step size, Δs, the equation for $\vec{r}_v$ is

$$\vec{r}_v(s + \Delta s) = \vec{r}_v(s) + \Delta s \vec{q}(\vec{r}_v)$$

To generate this sequence of values of $\vec{r}_v$ it is necessary to determine which computational cell each vector is in and compute an interpolated value of $\vec{q}(\vec{r}_v)$ using values of $\vec{q}$ at corners of that cell. A simple test on z determines the plane, or k index of the cell. The other indices require tests on the cross products between vectors from the corners of the cell and $\vec{r}_v$ and vectors between adjacent corners. For example, if the current $\vec{r}_v(s)$ were in cell (i,j) a test that it had crossed into cell $(i+1, j)$ upon integration over one step

is that the cross product,

$$C(s) = (\bar{r}_{i+j} - \bar{r}_{i+1,j+1}) \times (\bar{r}_v(s) - \bar{r}_{i+1,j+1})$$

changes sign (becomes positive). Similar cross products are monitored for each of the other three sides. For these computations values of $\bar{r}$ averaged over neighboring constant z planes are used, since the mappings, and hence the coordinates may vary from plane-to-plane.

If the entire vortex were between two constant z planes, it could be integrated when the factorized scheme was being used to compute the velocities in those planes. Also, if it only crossed planes in the increasing z direction, it could be integrated in one complete factorization sweep. A special scheme is required to compute general vortex trajectories without requiring storage of any more velocities than the basic factorization scheme.

Once the set of $\bar{r}_v$'s are computed, the factorization scheme is used to update the potential. At each node point, when $\vec{\nabla}\phi$ is computed the summation over the vortex line elements defined by equation (5) is done to compute $\bar{q}_v$. Since the computation of the $\bar{r}_v$'s is inexpensive, it is done during each factorization sweep.

An important point is that the computation of $\bar{q}_v$ is considerably simplified by not enforcing tangency boundary conditions at material surfaces. This is exactly analagous to adding the free-stream velocity, $\bar{q}_\infty$, which also does not satisfy tangency conditions.

5. RESULTS

The first case computed involved a line vortex passing near a Lockheed swept wing at mid-span. The wing had a 1.5° angle of attack and .82 Mach number. In Figure 3 the solid line represents the $x - y$ projection of the center of a vortex with circulation .05. It also represents the new position of the streamline in the presence of the vortex. The computational grid is also plotted in the figure. This grid consists of $64 \times 8 \times 16$ cells. In Figure 4 the C_p distribution for a sequence of span stations is given with no vortex present. The same distributions are presented in Figure 5 in the presence of the vortex. It can be seen that the vortex has a significant effect. The C_p distributions at the station just inboard of midspan are presented in Figure 6. The lift was increased by 31% near midspan. Similar results were found over much of the wing and the total lift increased by 16% and the drag by 14%. In Figure 7, the decay of the average residual in the potential solver is plotted as a function of number of iterations, for solutions with and without a vortex. It can be seen that the vortex did not effect convergence very much.

The second case computed involved a more concentrated vortex passing very near a straight wing at mid-span. The wing had an NACA 0012 cross section with an aspect ratio of 8, at zero angle of attack and .72 Mach number. This case is similar to the one computed in Ref. 1 using the Euler equations. In Fig. 8 the dashed line represents the $x - y$ projection of a streamline for flow without a passing vortex. The solid line represents the center of a vortex with circulation .05 which coincides with the streamline upstream. It also represents the new position of the streamline in the presence of the vortex. The computational grid is also plotted in the figure. This grid consists of $128 \times 32 \times 32$ cells. The parabolic mapping was modified to maintain constant cell width near the wing. The $x - z$ projection of the two lines, together with the wing are plotted in Fig. 9. The width of the vortex is .05 chord. In Fig. 10 the C_p distribution for a sequence of span stations is given with no vortex present. The same distributions are presented in Fig. 11 in the presence of the vortex. It can be seen that the vortex has a significant effect. The C_p distributions just inboard of midspan are presented in Fig. 12. The span station inboard of the vortex developed a lift coefficient of +.11, and that outboard, -.07. (There were 16 span stations on the wing). Although the induced lift was significant at these span stations, there was almost complete cancellation over the entire wing and the total induced lift coefficient was only +.009.

6. CONCLUSION

A scheme has been presented for incorporating vortices into a steady transonic Potential Flow calculation. It allows the representation of a concentrated vortex without the numerical diffusion which would occur if the Euler equations were used. For one case, the convection of a single vortex past a wing in near transonic flow, the lift was increased by 16% and the drag by 14% when the vortex was included. Another case involved a concentrated vortex passing very near a wing. Even with grid refinement this presented a problem for an Euler scheme due to numerical diffusion, but did not for the Potential Flow method. The rapid convergence rate and low cost of the AFZ factorized Potential Flow solver was not significantly changed by the inclusion of the vortex.

7. REFERENCES

1) G. R. Srinivasan, W. J. Chyu and J. L. Steger, "Computation of Simple Three-Dimensional Wing-Vortex Interaction in Transonic Flow," AIAA paper 81-1206, June, 1981.

2) A. Leonard, "Vortex Methods for Flow Simulation," J. Comp. Phys., Vol. 37, 1980, pp. 289-335.

3) E. M. Murman and P. M. Stremel, "A Vortex Wake Capturing Method for Potential Flow Calculations," AIAA paper 82-0947, June, 1982.

4) J. Steinhoff and A. Jameson, "Application of Approximate Factorization to Three-Dimensional Transonic Potential Flow Calculations," Grumman Research Report, 1981. Also presented at AIAA 5th Computational Fluid Dynamics Conference, Palo Alto, Calif., June, 1981.

5) A. Jameson and D. Caughey, "A Finite-Volume Method for Transonic Potential Flow Calculations, Albuquerque, NM, June 1977, 35-54.

8. ACKNOWLEDGEMENT

The first author is grateful for the hospitality of NASA-Ames Research Center and the ASEE program while some of this work was being done.

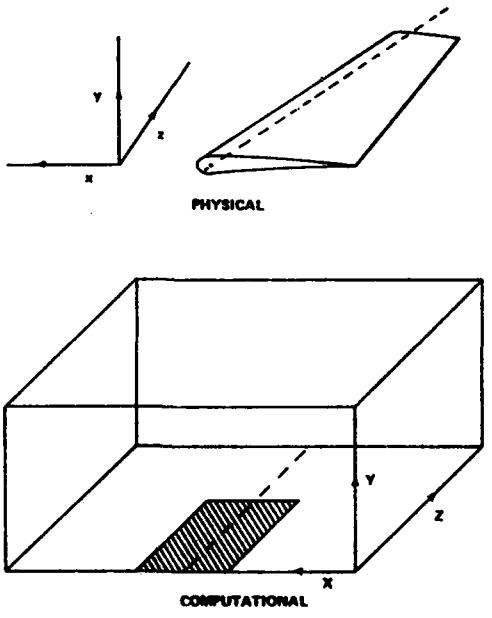

Fig. 1 Coordinate Systems

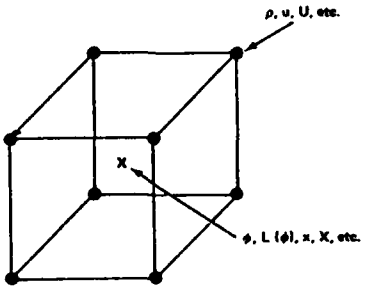

Figure 2 - Finite Volume Formulation

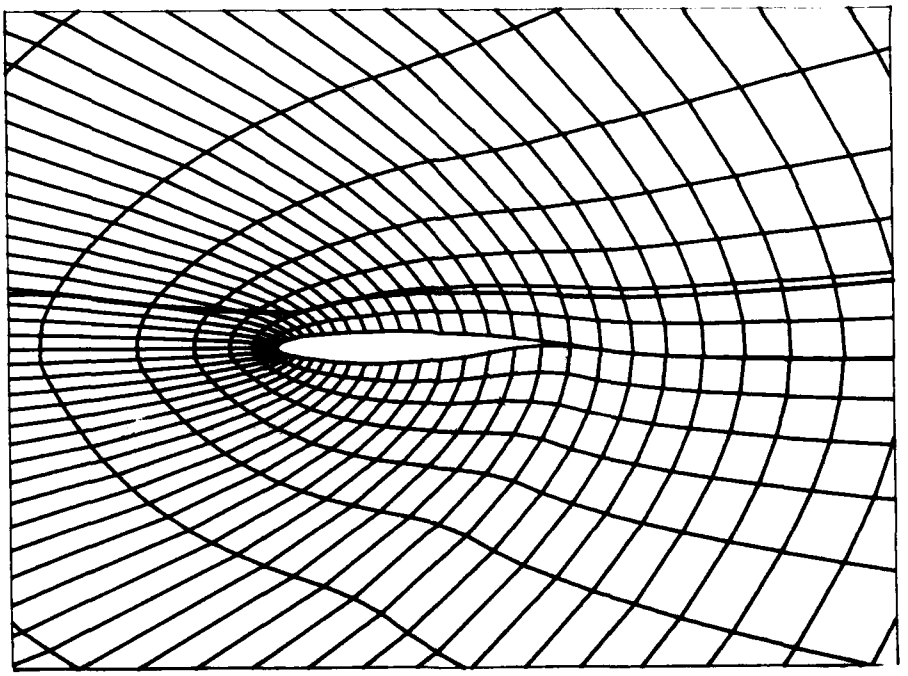

Figure 3 - Vortex Trajectory and Computational Grid

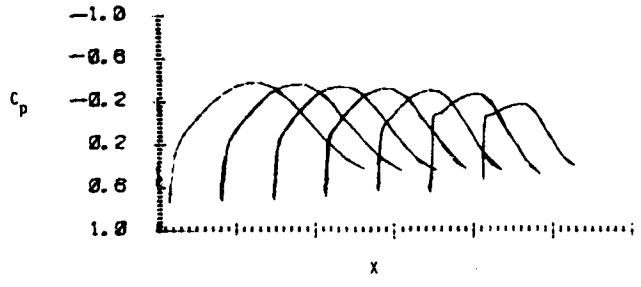

Figure 4a - C_p - Lower Surfaces - No Vortex

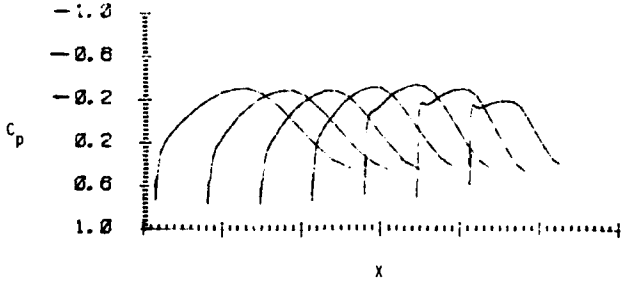

Figure 5a - C_p - Lower Surface - with Vortex

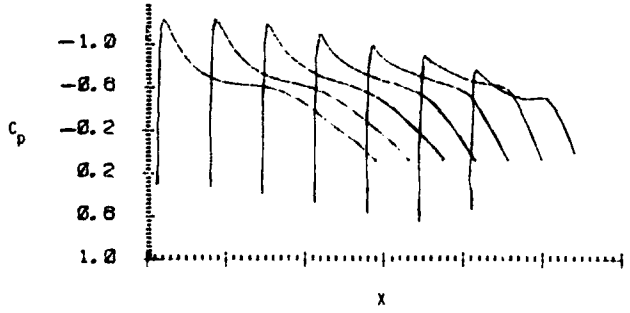

Figure 4b - C_p - Upper Surface - No Vortex

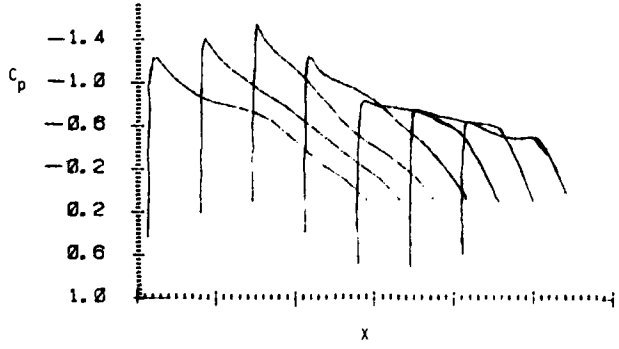

Figure 5b - C_p - Upper Surface - with Vortex

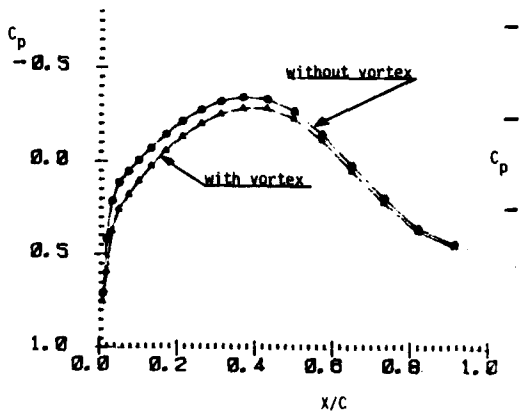

Figure 6a C_p - Lower Surface

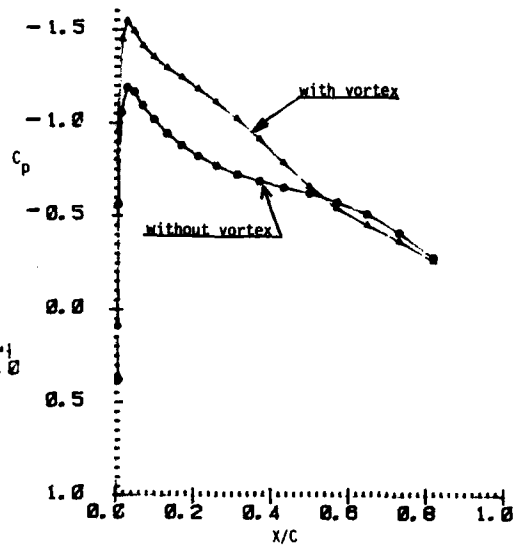

Figure 6b C_p - Upper Surface

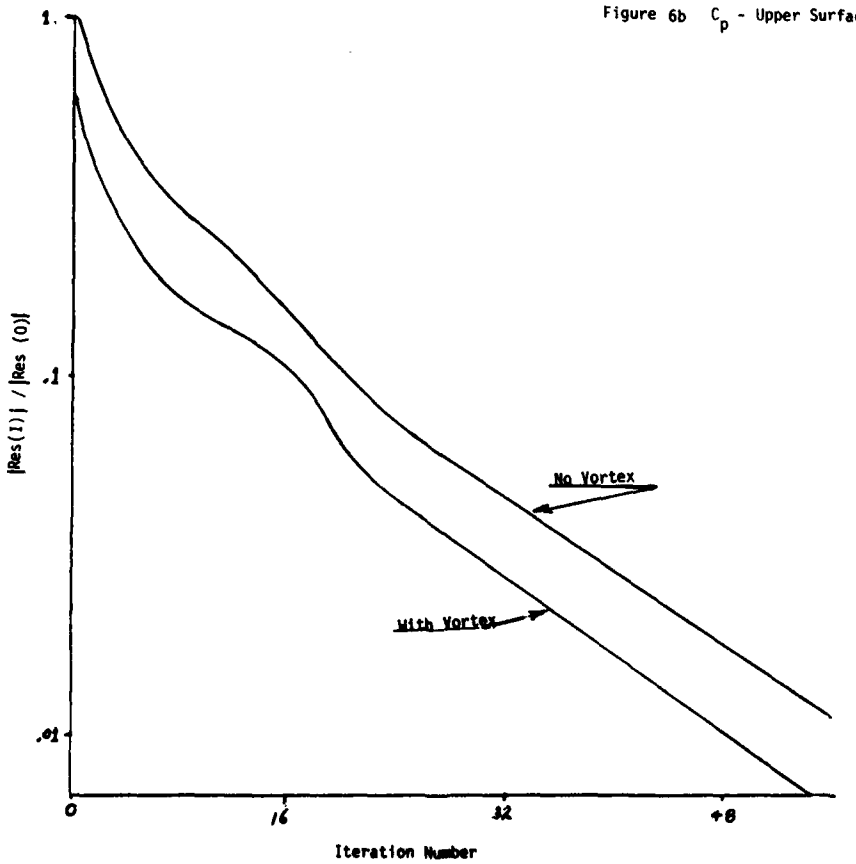

Figure 7 - Residual Decay

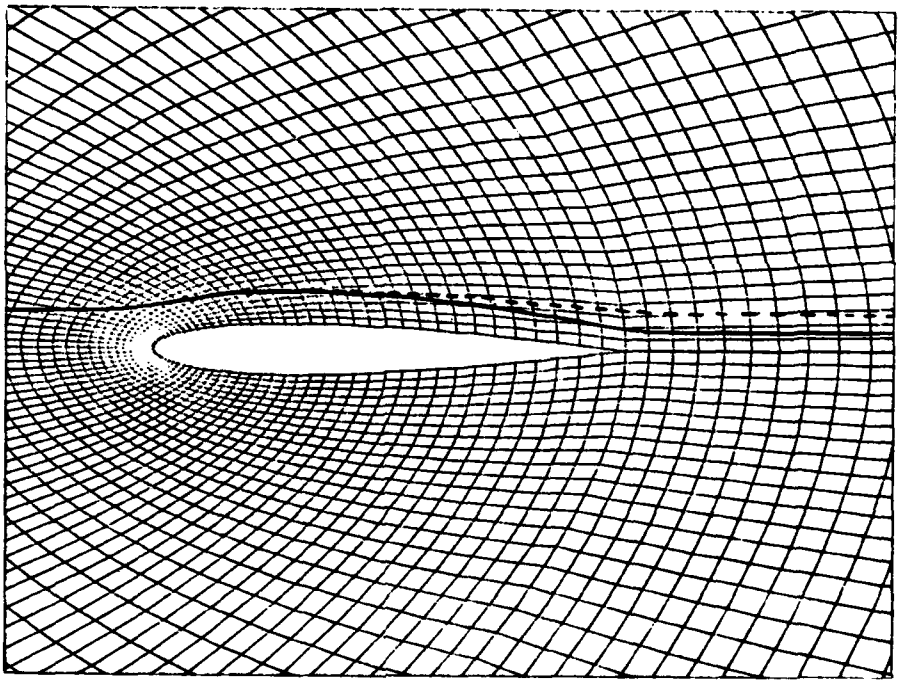

Figure 8 - Vortex and Streamline Trajectories

Vortex (——)

Streamline (- - -) (Without Vortex)

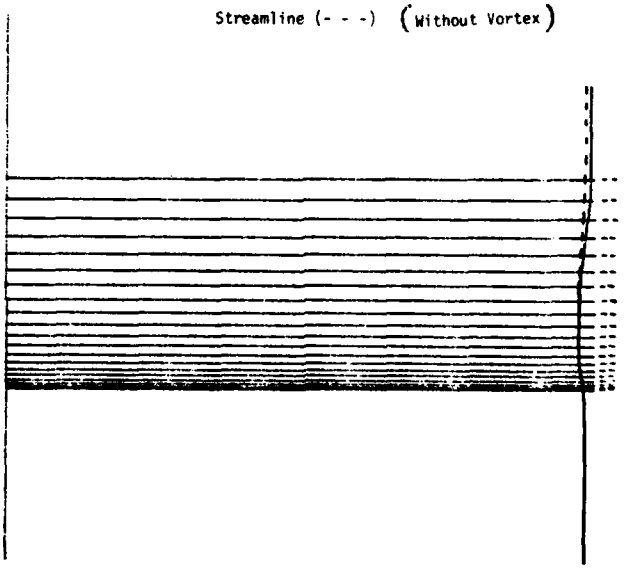

Figure 9 - Vortex and Streamline Trajectories

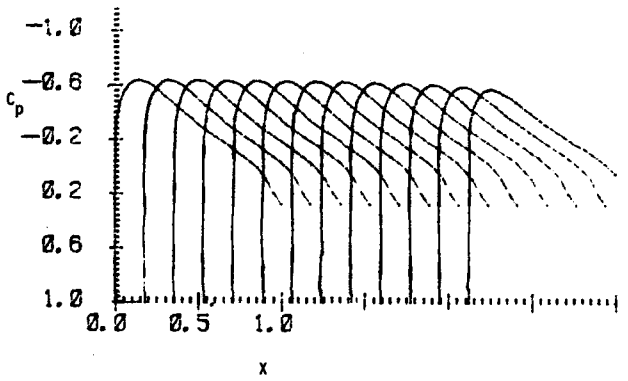

Figure 10 - C_p - No Vortex

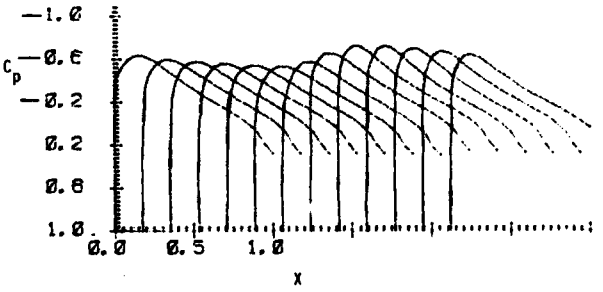

Figure 11a - C_p - Lower Surface - with Vortex

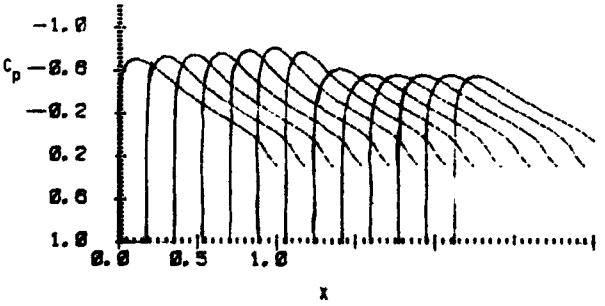

Figure 11b - C_p - Upper Surface - with Vortex

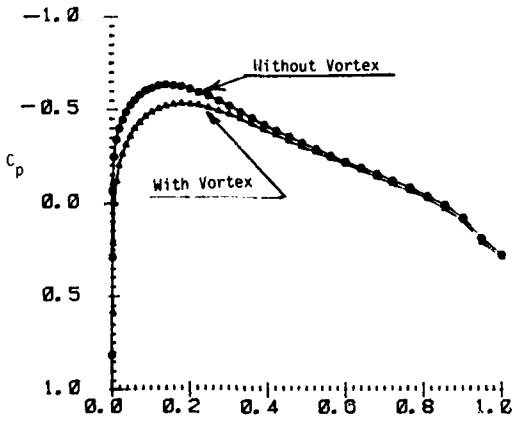

Figure 12a - C_p - Lower Surface

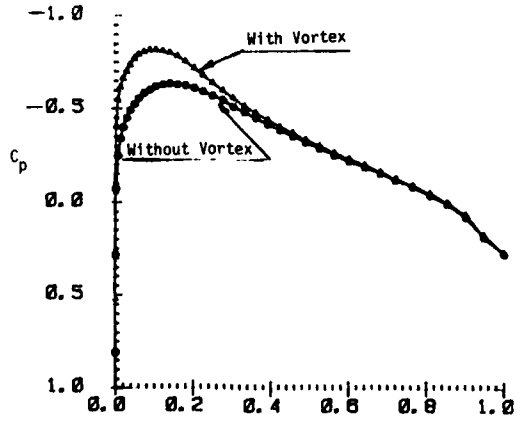

Figure 12b - C_p - Upper Surface

VORTEX STABILITY AND BREAKDOWN

by

Sidney Leibovich
Sibley School of Mechanical and Aerospace Engineering
Cornell University
Ithaca, New York 14853
U.S.A.

SUMMARY

Theoretical and experimental results, some quite recent, on the instability and breakdown of concentrated vortices at high Reynolds numbers are reviewed. Wave related theories of the vortex breakdown phenomenon are treated in some detail; these appear to provide a qualitative description of of the response of vortex breakdown to variations in swirl or flow rate, and Benjamin's criticality classification, a wave-based concept, is consistent with experimental data. Known general criteria for the stability or instability of inviscid columnar vortices are reviewed, together with numerical studies of an inviscid vortex model that provides an excellent analytical fit to measured velocity profiles in vortices that experience breakdown. A new analysis of experimental data on vortex breakdown flows sheds light on the interplay between criticality and instability. The flows sufficiently far upstream of breakdowns to be unaffected by them are supercritical and stable, but they are generally closer to marginal instability than they are to criticality. The wakes are both subcritical and unstable. A conceptual framework for vortex breakdown, incorporating nonlinear wave theory and instability to three-dimensional disturbances, is suggested based on information derived from the experimental studies.

1. INTRODUCTION

Vortex cores are fluid-mechanical waveguides capable of supporting dispersive waves, but complex instabilities may be engendered in them under conditions often realized in practical situations. In addition, as shown by Hall [1], substantial swirl velocities cause pressure gradients imposed at the edge of the vortex core to be amplified on the centerline, making the flow there highly sensitive to the environment in which the vortex resides. This sensitivity can result in large amplitude transitions of the flow structure, often leading to the formation of internal stagnation points and regions of reversed axial flow. Large amplitude disturbances result in the rapid decelerations known as "vortex breakdowns". The term as used here will refer to those disturbances leading to the development (in some frame of reference) of a stagnation point and flow reversal in a limited region. The phenomenon first attracted serious scientific interest when it was discovered to occur in the vortices formed above lifting surfaces with highly swept leading edges (Peckham & Atkinson, [2]), causing changes in the slopes of the lift, drag, and moment curves (Earnshaw & Lawford [3]; Hummel & Srinivasan, [4]).

This survey deals with vortex stability and breakdown in incompressible flows at high Reynolds numbers. The juxtaposition of the words "vortex stability" and "breakdown" in the title of this paper does not imply a causal relationship between the two varieties of events. A vortex can be unstable without breakdown, and it appears that axial flow reversals can be created in swirling flows without any sign of hydrodynamic instability to infinitesimal disturbances.

A breakdown event causes significant modifications of the vortex structure, however, and experiments at high Reynolds numbers reveal that the flow downstream of it is always "more" unstable than that upstream. Breakdown acts as a "switch" that marks the onset of transition to a turbulent flow downstream if the flow upstream is laminar, or transition to a flow with a higher level of turbulent fluctuations downstream if the vortex upstream of breakdown is already turbulent. With the possible exception of confined vortices at fairly low Reynolds numbers, the flow downstream of breakdown seems always to contain fluctuations that are not axially-symmetric, even if the flow upstream is axially-symmetric to a high degree of accuracy. The expansion of the vortex core in the wake of a breakdown event is due to the mixing associated with the instabilities and turbulence. Thus, whether instabilities are responsible for the existence of breakdown or not, they play an essential role in shaping the global structure of the flow, and therefore in determining the aerodynamic effects of breakdown.

An appreciation of the kinds of experimental arrangements that have been used to study the vortex breakdown phenomenon helps to place the experimental work into context. This survey therefore begins in section 2 with a brief discussion of the methods of formation of the vortices studied in the laboratory and arising in some cases of practical interest. This is followed in section 3 by descriptions of the two major types of vortex breakdown, the "bubble", which I shall call the B-type, or B-breakdown, and the "spiral" breakdown, which I will call the S-type, or S-breakdown. Both types are shown in Figure 1, a much reproduced photograph of both types appearing simultaneously in leading edge vortices above a delta wing taken from Lambourne & Bryer [5], and in the photographs of Figure 2 showing both forms in a tube. The question of the departure from axial-symmetry and whether or not it can be ignored is taken up in preliminary way in section 4.

Criteria for breakdown based on theoretical arguments that neglect all nonaxisymmetric phenomena are considered in section 5. The main unifying element, whether originally recognized or not, in all formulations of criteria for onset of breakdown in purely axisymmetric theories is the concept of critical flow. This condition was first introduced by Squire [6] in his wave criterion for breakdown,

enlarged and reinterpreted by Benjamin [7] in his theory of finite transitions between "conjugate" flow states, and shown by Ludwieg [8] and by Hall [9] to be common not only to the wave-based theories of Squire and of Benjamin, but also to earlier theories based upon ideas related to boundary layer separation. The finite amplitude wave theories of Benjamin [10] and Leibovich [11], and the transcritical theory of Leibovich & Randall [12] and Randall & Leibovich [13] are also centered around the criticality classification. The transcritical wave theory is outlined here, since I believe that it contains the germ of a comprehensive description of the phenomena; it serves as auseful vehicle to present speculations, to be found in section 7, on what a comprehensive description may turn out to be like.

The stability or instability of vortex cores at infinite Reynolds numbers is considered in section 6 partly from a theoretical point of view, and partly by reference to recent experiments. Ludwieg [14,15,16] advanced an explanation of vortex breakdown based upon hydrodyamic instability to three dimensional disturbances. This has not won acceptance, since the flows upstream are stable. Nevertheless, it appears as though instability may well be important in fixing the location of breakdown, and, of course, the properties of the wake. Instability to three-dimensional disturbances plays an important part in the conceptual framework for breakdown suggested in section 7, which arises from the analysis of experimental data summarized here.

Reviews of vortex breakdown are given by Hall [1], Hall [9], and Leibovich [17]. The reader should find them helpful; a recent general discussion by Legendre [18] will also be of interest.

2. VORTEX GENERATION

To address questions concerning modifications of the flow structure in vortices as some control parameter, such as angle of incidence, is varied, it is necessary to begin with some model of the vortex which may be expected to lead to a tractable analysis. This requires that the "vortex" be isolated from its surroundings in some consistent way. All models so abstracted for the purpose of analysis of stability or of breakdown have been axially-symmetric. This process of isolation leads to questions whose answers are not self-evident, particularly concerning the appropriate boundary conditions to impose on disturbances to the basic vortex flow model.

The problem of vortex breakdown first attracted serious scientific attention in the context of leading-edge vortices on highly swept leading edges, and the main aerodynamic interest probably continues to be in flows of this kind, or in trailing vortices; both are formed by the roll-up of a vortex sheet. Early on, it was recognized that detailed experimental data was in many ways more easily obtained on vortices confined to tubes, and the bulk of available data are for such cases.

Figure 3 is a sketch of a leading-edge vortex, and Figures 4 and 5 contain sketches of the two types of laboratory apparaus that have been used to study vortices confined to tubes. I shall discuss each of these in general terms.

Edge and Trailing Vortices

Experimental observation and measurement indicates that the vorticity in the separating boundary layer may be regarded as a vortex sheet as it leaves the separation line. As the sheet rolls up, its intersection with a plane normal to the lifting surface forms a spiral and the velocity profiles in the inner portion of the spiral appear to be nearly axially-symmetric. This axisymmetric "core" grows in radius in the downstream direction, and occupies the interior of a conical region. The circulation about this core increases, essentially linearly with distance along the axis, as vorticity is continuously wound into the core region. Axial speeds on the centerline increase with distance as well, due to the continuous drop in centerline pressure as the core vorticity increases.

Outside of the conical core, the flow is neither irrotational nor axially symmetric; in fact, the definition of the "core" is somewhat arbitrary. In their discussion of the incompletely rolled-up trailing vortex, for instance, Moore & Saffman [19] suggest a definition based upon the ratio of the distance between neighboring turns of the sheet to the distance from the center, using Kaden's [20] similarity model of roll-up. The core is considered to be axisymmetric for regions where this ratio remains less than an arbitrarily assigned value. In any event, the main requirement in isolating a vortical core presumably should be that the region abstracted contains most of the vorticity. Fortunately, it appears possible to define a core that is at the same time nearly axisymmetric, and this is an major simplifying feature. Its adoption, for example, permitted Hall [21] and Stewartson & Hall [22] to construct a successful theory for the leading-edge vortex at high Reynolds number. The theory represents the flow as rotational, inviscid, and conical except in a very slender, non-conical, viscous subcore.

It is important to note that the size of a vortical core formed by roll-up of a vortex sheet is independent of Reynolds number (although the radius of the *viscous subcore decreases* with increasing Reynolds number). The center of a leading-edge vortex is generally located on the order of a core diameter above the lifting surface, and the core diameter may not be negligibly small compared to the local semispan of the lifting surface. Should the core diameter increase by a substantial fraction, as it does in a vortex breakdown, there may be significant aerodynamic consequences.

Sufficiently far downstream of a lifting surface, its associated vortex sheet may be considered to be completely rolled up into two trailing vortices, each of constant circulation. The core of each is then naturally definable. If diffusion and mutual interactions are ignored and each trailing vortex is treated as if the other were not there, then the velocity field may be treated as columnar, with each streamline being a helix, and the flow outside the core as irrotational.

Vortex Generators with Tangential Jet Entry

Apparatus in which vortices are generated by jets directed tangent to the walls of a cylindrical cavity have been used in some laboratory experiments on vortex breakdown (Chanaud [23]; Escudier et

al [24]; Escudier & Zehnder [25]; Escudier et al [26]). At large Reynolds number, apparatus of this design, and in particular the slot entries used by Escudier's group, produce vortex cores with vorticity deriving mainly from the roll-up of a shear layer shed at the slot exit, as illustrated in Figure 4. Vorticity shed from separation of the end wall boundary layer is also entrained in the core, but this is probably a smaller effect except near the end wall itself. Thus some similarity in the structures of vortices produced this way to edge vortices in external aerodynamic flows is to be expected.

Velocity profiles measured by Escudier et al [26] are shown in Figure 6, alongside of data taken by Earnshaw [27] (figure shown is taken from Hall [21] in two mutually perpendicular traverses through a leading edge vortex over a delta wing model. Qualitative similarities are evident. In particular, in both sets of measurements, the azimuthal velocity component is nearly flat beyond the point of maximum swirling speed, although the swirl level in this flat stretch is larger for the leading edge vortex. The axial velocity component is associated with azimuthal vorticity throughout the flow region shown: there is no external irrotational flow.

Escudier et al [26] have found that the following model can be fitted to their data for the swirl component

$$V(r) = \Gamma_c/2\pi r)(1-\exp(-r^2/r_0^2) + \omega r/2 \qquad (1)$$

where Γ_c, r_0, and ω are constants for a profile at a fixed axial station; their profile constants have not been published, and no analytical fit has been suggested for the axial velocity component.

After leaving the vortex generation section, the flow enters a cylindrical exit tube. Presumably, the roll-up continues for at least some distance into the exit tube, but except for a sink of axial vorticity at the wall, all of the vorticity in the exit tube is convected from the swirl generator upstream. The core size in these vortices prior to any breakdown which may take place seems to be fixed by the roll-up process in the vortex generation section and varies weakly, if at all, with Reynolds number.

Vane Vortex Generators

The first experiments on vortex breakdown in tubes were conducted by Harvey [28], and one of the main motivations was the removal the asymmetries characteristic of leading edge vortices. Swirl was produced in the apparatus, previously used by Titchener & Taylor-Russell [29] for another purpose, by means of a radial inflow through a set of vanes. After aquiring swirl in passing the vanes, the radial flow is turned through an annular channel created by an outer curved wall and a centerbody, and exits axially into a cylindrical tube which serves as the test section. Since the flow accelerates through the turning section, the point of detachment is fixed at the tip of the centerbody. Sarpkaya [30,31,32] conducted experiments in a similar apparatus, but with conical test sections of generally small cone angles. Bellamy-Knights [33], Faler & Leibovich [34,35], and Garg & Leibovich [36] used apparatus modelled after Sarpkaya's.

Except for boundary layers on the centerbody and on the outer boundary, the flow in the vortex generator is essentially irrotational. In the test section, the flow is accurately irrotational in an annular region lying between a well-defined vortical core surrounding the tube centerline and the boundary layer on the outer wall. The vorticity in the core all derives from the boundary layer shed from the centerbody, and the circulation is constant for all circuits between the core and the wall boundary layer. The development of the vortex core by shedding of the centerbody boundary layer leads to a low centerline pressure and consequent formation of an axial jet just downstream that is confined to the vortex core.

Experimental data is well fitted by the analytical profiles for axial velocity W and swirl velocity V,

$$W = W_1 + W_2\exp(-\alpha r^2)$$
$$V = \lambda[1 - \exp(-\alpha r^2)]/r, \qquad (2)$$

where W_1, W_2, α, and λ are constants; these constants have been published for a number of experiments (Garg & Leibovich [36].

In this type of apparatus, the size of the core is determined by the thickness of the boundary layer shed by the centerbody, and decreases with an increase in Reynolds number. This core size dependence leads to a complicated coupling between the two control variables, flow rate (Reynolds number) and vane angle; an increase of either parameter leads to an increase in core vorticity.

3. VORTEX BREAKDOWN: DESCRIPTIVE SURVEY AND REMARKS

At large Reynolds numbers, breakdown assumes one of two characteristic geometric forms. In either form, a stagnation point appears on the vortex axis, followed by a limited region of reversed axial flow near the vortex centerline. A tracer released on the vortex axis upstream shows the B-breakdown to look much like a body of revolution placed in the flow; in the case of an S-breakdown, the tracer assumes a spiral or corkscrew shape that rotates about the vortex axis in the same sense as does fluid in the upstream vortex. In both forms the upstream approach flow has a jet-like axial velocity component with a centerline speed exceeding the axial velocity outside the core by a factor ranging up to three or even more. Deceleration of this strong axial jet to rest at an internal stagnation point is accomplished in an axial distance of one or two diameters of the upstream vortex core. Upstream of the deceleration interval, the presence of the breakdown is not evident to the eye, or in velocity measurements.

The stagnation point is followed by an axial interval of a very complicated nature which contains

one or more regions of flow reversal. The 'bubble' and the coherent corkscrew form are contained within a volume of whose radial extent is close to that of the upstream core radius, and both flow structures exhibit time periodic velocity fields that are not axially-symmetric. This zone typically has an axial extent of 1 to 3 diameters of the upstream vortex core. The flow downstream of the breakdown zone is wake-like and invariably turbulent with strong coherent periodic oscillations. The mean axial velocity deficit in this zone is reminiscent of the wake of a solid body of revolution, and the vortex core is greatly expanded.

Axial gradients in the approach flow upstream of the breakdown zone and in the wake downstream of it appear to be determined by globally imposed conditions, such as an overall (axial) pressure gradient, or the geometry of the container walls, or, if impressed forcing conditions are absent, by viscous decay. The axial scales of impressed forcing typically are much larger than the diameter of the vortex core; on these scales, the breakdown zone looks like a thin transition region joining the approach flow and the wake.

Measured values of the core expansion ratio (wake core diameter/approach flow core diameter) analyzed by Leibovich [17] (see Table 1 of section 5 below), using data from Garg & Leibovich [36], range from slightly over 1.5 to nearly 3. Expansions associated with the B-form were found to be significantly larger that those associated with the S-form.

Most of the information that is available concerning breakdown, including the very important qualitative information concerning onset, position, and type, have been obtained by flow visualization using smoke or dye as a tracer. In particular, the designations of different types of breakdown, the B and S forms, were made on the basis of their appearances in flow visualization experiments. Are these two forms really different, or just visual variants of the same flow state? Recognizing that care must be taken in the interpretation of streakline data, it might not be prudent to infer from the distinctive appearances of the B-form and the S-form as revealed by smoke or dye that these actually mark distinct flow disturbances. It might be argued, for example, that there are minor wiggles of the upstream dye or smoke feeder due to very slight disturbances near the stagnation point that are sometimes large enough to periodically deflect the tracers, leading to what we see as the S-form, while at other times they are too weak to have a noticeable effect, and we identify the disturbance as a B-form. This argument, while plausible based only on the shapes of the dye filament, is not correct; at least two pieces of evidence exist to show that the two forms are in fact distinct flow disturbances. One piece of evidence, the different core expansion ratios, has already been discussed. The second has to do with the upstream flow conditions which lead to either the B or the S-form.

Consider the flow in a conical tube apparatus of the Sarpkaya design at fixed flow rate (Reynolds number). For low values of swirl (i.e., small vane angle), the flow exhibits no unusual behavior. When the swirling speeds exceed a threshhold value, a large amplitude disturbance form appears in the test section. For a Reynolds number based on tube diameter of, say, 3000 or larger, the breakdown that first appears is of S-type, according to Sarpkaya [30], Faler & Leibovich [34], and Garg & Leibovich [36]. If the swirl level is further increased, the breakdown moves to a position farther upstream. Although there is vacillation in position, the breakdown appears to have a definite mean location that depends upon the swirl. As the swirl is further increased this process continues until, at a second critical value of the swirl, the S-form transforms into a B-form, and moves rapidly to a new equilibrium location several core diameters upstream of the previous mean position. (The metamorphosis is described by Sarpkaya [30] and by Faler & Leibovich [34]). Thus the transition to a B-form is associated with a discontinuity in the mean position versus swirl-level functional relationship, and this discontinuity is the clearest evidence that the two disturbance forms are truly distinct.

There are borderline ranges of swirl levels for which the B-form and the S-form spontaneously transform one into the other, each transition causing the location of the newly established breakdown to move rapidly to the mean axial location appropriate to its type. The response of a B-form to increases of swirl is similar to the S-form, the mean location moves upstream; furthermore, the spontaneous reversion to an S-form becomes increasingly rare and, as the swirl is increased beyond some level, this reversion no longer is observed to occur.

The location of breakdown has been measured as a function of volume flow rate Q (or a Reynolds number based upon Q) and swirl, measured in dimensionless form by the parameter $\Omega = \pi\Gamma D/4Q$ originally introduced by Sarpkaya [30]. Here Γ is the circulation about the vortex core, a quantity that can be inferred from the inlet data (for example, the vane angle and placement in a vane swirl generator), and D is a characteristic diameter of the apparatus. Measurements of this kind are presented by Sarpkaya [30-32], Faler & Leibovich [34], and Escudier & Zehnder [25]; a limited sample is also given by Garg & Leibovich [36]. Except for Escudier & Zehnder, who use a tangential jet swirl device, the experiments cited use vane swirl generation, and a typical compilation of results is shown in Figure 7. The dependence of the breakdown location with Re in these flows is probably not due to a viscous role in the breakdown mechanism, which appears to be essentially inviscid, and, although the point continues to be misinterpreted (cf. Escudier & Zehnder [25, pg.118], it certainly cannot be attributed to viscous wall effects (the discussion here excludes phenomena at Reynolds numbers so low as to allow frictional influences of the wall to penetrate to the vortex core). Rather, the breakdown location at fixed Ω and increasing (decreasing) Re varies primarily because of the increase (decrease) in peak swirl and core vorticity associated with a reduction (enlargement) in core diameter; recall that a vane-centerbody apparatus produces a vortex with a core diameter proportional to $Re^{-1/2}$.

Escudier & Zehnder [25] show that the simple rule $Re\Omega^3 R$ = constant, where R is a dimensionless parameter associated with the swirl generation section, correlates conditions for the occurrence of vortex breakdown at a fixed axial location in their apparatus. They also suggest that this result is applicable to other experimental data. For data apparatus using vane swirl generation, the correlation reduces to $Re\Omega^2$ = constant. Unfortunately, neither this result, nor any other functional relationship between Re and Ω, can possibly represent a universal criterion for the occurrence of breakdown at a fixed location, as Figure 7 indicates, simply because B and S breakdowns have

distinctly different locations as a function of Re and Ω in vane devices. In fact, as pointed out by Faler & Leibovich [34] and by Leibovich [17], the relevant dynamics in vortices scale with the vortex core diameter, and that it is likely to be more revealing to describe data using a Reynolds number based on that length.

The main characteristics of vortex breakdowns above delta wings at high incidences appear to agree with the findings described above for flows in tubes, although detailed structural information of the breakdowns that occur in the former cases is not available. Nevertheless, the appearance of the two main types, the B-form and the S-form are both well documented (Werle [37], Lambourne & Bryer [5], with the S-form predominating. Since this is the low swirl form of breakdown, this may merely imply that under conditions of aerodynamic interest, the swirl level is not high enough to render the B-breakdown the stable form. As the incidence is increased, and thereby the swirl level, an existing breakdown moves upstream like its tube counterpart (Elle [38]; Werle [37]; Earnshaw & Lawford [3]; Hummel & Srinivasan [4]).

It is interesting to note that the sense of the helical dye filament of the leading edge S-breakdown is opposed to the direction of rotation of the upstream vortex, although the apparent direction of rotation of the spiral, as a geometric form, agrees with it (Lambourne & Bryer [5]). Sarpkaya [30] and Faler & Leibovich [34] found the sense of the helix and its sense of rotation to agree with that in the approach flow in their experiments in vane-type devices. Escudier & Zehnder [26] found that the helix sense of S-breakdowns in their experiments agreed with the observations of Lambourne & Bryer. Since we have already argued that the flows generated by tangential jet entry devices are closer to leading edge vortices than they are to flows in vane devices, the latter agreement is perhaps to be expected. Actually, it is not clear that the helix sense has much significance. The helix marks a thin filament of fluid particles surrounding the upstream vortex axis. As Lambourne & Bryer [5] have shown, individual fluid particles in the streakline as it expands radially downstream of the stagnation point have virtually zero swirl velocity, consistent with the need to conserve angular momentum. The formation of a spiral structure is consistent with a nonaxisymmetric displacement of the dye filament of the form $\exp[i(\theta+\omega t)]$ in the neighborhood of the stagnation point, with each dyed fluid particle thereafter moving on a surface of revolution in an essentially fixed meridional plane until it passes into regions of turbulent flow. The sense of the helix is determined by the sign of ω. The 'rotation' of the geometric form is accomplished without rotation of its constituent parts.

4. REMARKS ON THE DEPARTURE FROM AXIAL SYMMETRY OF VORTEX BREAKDOWN

Approach flows which suffer breakdown can be made to have a high degree of axial symmetry, yet the flows in the breakdown zone and in the wake lose this symmetry. The loss of symmetry is associated with instability of the axisymmetric flow and presages transition to a turbulent wake. Thus asymmetry shapes the properties of the wake, and therefore the global flow, but is the loss of symmetry intrinsic and necessary for the formation of a stagnation point and consequently an essential element in the mechanism of breakdown? The answer is not known, nor of course could it be in the absence of a definitive identification of the breakdown mechanism. Nevertheless, a correct working hypothesis could help in the construction of a theory which, it is to be hoped, will eventually be constructed as a comprehensive explanation of the phenomenon. As will be seen in the next section, virtually all of the theoretical attempts that have been made adopt the view that nonaxisymmetric effects are incidental, and that the dominant mechanism of breakdown is axisymmetric; Benjamin [7] has most explicitly articulated this idea. In this section, I will give arguments that might be marshalled in support either side of the question.

If we adopt a cylindrical (r,θ,z) coordinate system, we may represent any flow variable by a Fourier series in the azimuth θ in the form

$$\sum_{n=-\infty}^{\infty} C_n(r,z,t)e^{-in\theta}.$$

Furthermore, if $C_n(r,z,t)$ are the Fourier coefficients of the axial velocity component, then $C_n(0,z,t) = 0$ for all nonzero integers n. Thus, the only disturbance to the axial velocity on the axis of symmetry is that associated with the axisymmetric ($n = 0$) Fourier component. Since the variation with z of this Fourier mode of the axial velocity must be large to describe the arrest of the axial jet of the approach flow, it is apparent that <u>any</u> vortex breakdown, be it of S or B type, must have a large axially-symmetric disturbances. Since the fluctuating velocities (indicative of the magnitude of the $n \neq 0$ Fourier components) are never more than a modest fraction of the axial jet in the approach flow, one could therefore assert that in this sense, the axisymmetric mode dominates the nonaxisymmetric modes. This is one argument in support of the position that nonaxisymmetric disturbances may play a secondary role in the mechanism of vortex breakdown.

A second argument is based upon the probable existence of exact, steady, axisymmetric solutions of the Navier-Stokes equations with reversed flow regimes that resemble vortex breakdown, and the known existence of physical flows with this characteristic. Laboratory experiments on flows in a closed cylindrical container, driven by a rotating lid, have been carried out by Vogel [39] and by Ronnenberg [40], and reveal the existence of a closed, steady, axially-symmetric region of reversed flow in a limited volume of fluid surrounding the axis of symmetry. Numerical solutions of the Navier-Stokes equations by Lugt & Haussling [41] successfully predict aspects of the observed flow. Of course, this is a flow dominated by wall friction; and the basic flow, as well as the flow reversal region singled out, is a recirculating one. Nevertheless, these numerical and experimental works show that 'ideal' axisymmetric solutions containing features broadly resembling the ones we are interested in here do exist and can be experimentally realized. More closely related, but perhaps less firmly established, are numerical solutions of the steady axisymmetric Navier-Stokes equations by Kopecky & Torrance [42] and by Grabowski & Berger [43] intended to simulate representative vortex breakdown flows. Although questions can be raised (Leibovich [17]) about the reliability of these solutions,

they constitute substantive evidence of the existence of exact steady, axisymmetric vortex breakdown solutions.

One can begin, taking the other side of the question, by accepting both of the points made above, that (a) the axially-symmetric Fourier component of vortex breakdown flows may be significantly larger than the nonaxisymmetric ones, and that (b) the Navier-Stokes equations may admit steady, axially-symmetric solutions with reversed flow regions. We will call the latter solutions of class A. The existence of such a class does not imply that the nearly axisymmetric flows observed in experiments, and admitted as point (a) here, need be close to any of the solutions of class A.

In fact, the sequence of successive transitions observed experimentally by Sarpkaya [30], Faler & Leibovich [34], Garg & Leibovich [36], and Escudier & Zehnder [25] as the swirl level is increased suggests that both S and B-forms of breakdown evolve from flows that are clearly not axially-symmetric. The first large amplitude disturbance arises as a steady, nonaxisymmetric bifurcation of a steady, axisymmetric flow (Faler & Leibovich [34]); sequential increases of the swirl beyond this first critical level lead to a sequence of nonaxisymmetric flows with (or so it seems) an increasing axisymmetric aspect, although nonaxisymmetric features are never lost. This suggests that the members of class A are unstable solutions of the Navier-Stokes equations, and the flows realized in experiment may or may not be close to them. The momentum transport created by the symmetry-breaking modes arising from the instabilities can cause the axially symmetric part of the motion to differ drastically from solutions belonging to A, even though the nonaxisymmetric modes remain much smaller that the axisymmetric one. The Taylor-Couette flow between coaxial rotating cylinders provides an example of this in a simpler and more extensively studied setting. In this case, the symmetry-breaking perturbations are the Taylor cells which are themselves steady and axisymmetric at modest supercritical Taylor numbers; the symmetry is broken by the appearance of axial coordinate z rather than the azimuth angle. Even when the cellular motion is weak compared to the mean flow, the z-averaged velocity profiles differ significantly from the exact stationary cylindrical solution of the Navier-Stokes equations.

In summary, although the matter remains somewhat uncertain, it appears that axially-symmetric "breakdowns" are admissible solutions of the Navier-Stokes equations, and these are physically realizable at sufficiently low Reynolds number in wall-dominated flows. On the other hand, maintenance of symmetry appears impossible at the high Reynolds numbers of aerodynamic interest, and the steady, axisymmetric solutions of the Navier-Stokes equations at high Reynolds numbers, assuming they exist, are unstable to non-axisymmetric perturbations. Furthermore, the long-range effects of breakdown arise because of these instabilities: without them, the breakdown disturbance would be a local imperfection, annealed by the flow. A step that would help to clarify the question and which seems feasible, *but only barely, is an investigation* of the stability of numerically generated flows of class A to three-dimensional disturbances. This involves a challenging nonseparable eigenvalue problem. (Nguyen [44], in a recent thesis, examined the viscous, spatial stability of solutions found by Grabowski & Berger [43], with the velocity profiles at each station treated as though the flow were columnar. Such an effort, though interesting and valuable, is incapable of treating what is likely to be the most significant region of instability, the breakdown zone itself.)

5. WAVE PROPAGATION AND THE CRITICALITY CRITERION

Viewed on scales much larger than the vortex core diameter, vortex breakdown appears to be a discontinuous transition between two flows with very different characteristics. In this sense, it is reminiscent of a shock wave in gasdynamics or its analog in free surface flows, the hydraulic jump.

Waves may propagate in all three of these physical systems. In hydraulic jumps, in gasdynamic shock waves, and (for all adequately documented observations) in vortex breakdowns, transition separates an upstream flow (the supersonic or supercritical region) incapable of supporting upstream propagating wavelets, from its downstream successor (the subsonic or subcritical region), which admits both upstream and downstream propagating wavelets. Furthermore, the three systems share a common sensitivity to conditions imposed downstream. The occurrence and position of a shock in a nozzle is controlled by the back pressure, and the occurrence and location of a hydraulic jump in a channel of variable width is controlled by backwater conditions. While it is more difficult to control "backwater" conditions in vortex breakdown experiments, the effects of changing pressure gradients (Sarpkaya [32]), insertion of solid objects on the vortex axis, and deflection of trailing-edge flaps (Lambourne & Bryer [5]) on the occurrence and location of vortex breakdown indicate that this phenomenon has a similar sensitivity to downstream conditions.

Like a free surface flow, a vortex core admits infinitesimal dispersive waves. If the wavelengths of wavy disturbances are small compared to the length scale on which the core characteristics change, then the waves may be treated approximately as if they were propagating on a columnar vortex. Let the velocity field in such a columnar vortex be (0,V(r),W(r)) in cylindrical (r,θ,z) coordinates. The radial velocity component of a wavelet has the form

$$u(r,\theta,z,t) = Au_0(r)\exp\{i[k(z-ct)-n\theta]\} + \text{c.c.} \qquad (4)$$

where $Au_0(r)$ is a complex amplitude (A being constant) describing the modal structure, c.c. stands for the complex conjugate of the preceding term, and $c = \omega/k$ is the phase speed of a wave of angular frequency ω in the z-direction. Other flow disturbance variables in the wave have a similar form.

The interpretation of supercriticality or subcriticality for vortex breakdown flows is based upon the wave propagation characteristics of the mean flows; this is the same as the instantaneous flow upstream, but the instantaneous downstream flow is replaced by its time-average, which is steady and axisymmetric. Furthermore, the classification, due to Benjamin [7], is based upon propagation of axisymmetric (n=0) wavelets. Flows are supercritical according to Benjamin if the minimum phase speed c is positive (where it is assumed that the basic flow axial velocity W(r) is everywhere positive), so that surfaces of constant phase cannot propagate upstream. It can be generally shown (see Leibovich

[45]) that if the flow is stable, there are two branches of the dispersion relation for axisymmetric waves, one corresponding to phase speeds $c_-(k)$ less than the minimum axial velocity of the basic flow, and one having phase speeds $c_+(k)$ greater than the maximum axial velocity.

Benjamin [7] showed that the general effect of increasing the level of swirl is to reduce the minimum value of c_-, so that increasing swirl in a supercritical flow drives it towards critical and if increased enough, the flow can be made subcritical. Since the medium is dispersive, the ability of perturbations to propagate upstream is determined by the group velocity $c_g = \partial\omega/\partial k$, not the phase velocity, and Benjamin's classification need not carry the interpretation given to it. Nevertheless, Leibovich [45] showed that Benjamin's criterion for supercriticality is always consistent with a definition based on group velocity; furthermore, since $c_g \to c$ as $k \to 0$, flows that are subcritical based upon a phase velocity criterion are also subcritical based upon the more fundamental group velocity criterion. Thus, Benjamin's classification based on phase velocities is coincident with a one based on group velocities, at least if consideration is restricted to axisymmetric modes.

It is not generally known whether the group velocity of nonaxisymmetric modes is directed downstream in supercritical flows as defined above. If not the concept of criticality is probably demolished. For the few special cases for which calculations have been made (Tsai & Widnall [46], for flow (2) with various profile constants determined by Garg [47]; and Leibovich & Ma [48], for the flow (2) with $W_2 = 0$ and $\alpha=1$), the classification remains intact.

Criticality Criterion of Onset

The wave propagation characteristics of a vortex core change with axial distance as the core evolves. This process is direct in a leading edge vortex, since then the core vorticity increases along with axis. In the case of tubes of variable area, the vortex properties are changed by the geometrical constraints. Squire [6] proposed that vortex breakdown first becomes possible when conditions in the vortex are critical. The model he used for his illustrative calculations was columnar and he did not discuss the evolution of core properties. Nevertheless he must have had in mind the evolving vortex, and presumably he intended to suggest that breakdown would occur somewhere near the spot where critical conditions arise. Thus, the presence of a downstream source of disturbance, such as a trailing edge of a wing, or a sudden change in tube area, would be communicated by waves propagating upstream through the subcritical section of the vortex waveguide, but would be unable to proceed further than the station at which critical conditions obtain.

Benjamin [7] criticized this conception, pointing out that the group velocity at criticality is positive in the downstream direction, so that in a columnar flow, disturbances cannot spread upstream from a disturbance source. Had Squire described the processes in an *evolving* vortex core, along the lines above, Benjamin's objection would not have seemed compelling.

As a first approximation, the location at which critical conditions occur in a vortex can be taken as an estimate of breakdown location. This may be refined by recognizing that the speed of a nonlinear wave increases linearly with its amplitude, so that a nonlinear wave can penetrate into the supercritical region of the vortex. Thus, a more general wave theory will locate a breakdown is somewhat upstream of the critical station. Further discussion of this point is deferred to the latter part of this section.

The critical condition for flows with given velocity profiles can be computed with little effort from a second-order ordinary differential equation. As an example, I have computed (using boundary conditions appropriate to unbounded domains, see Leibovich, 1970) the regions of supercritical and subcritical flow for a vortex model (2). The velocity profiles of the model may be given in rescaled form by

$$V(r) = q|\delta|r^{-1}[1 - \exp(-r^2)] \qquad \text{(a)}$$
$$W(r) = 1 + \delta \exp(-r^2) \qquad \text{(b)} \qquad (5)$$

where q is a positive constant, and $\delta > 0$ in an approach flow (jet) and $\delta < 0$ in a wake flow. As seen in (5b), the axial velocity tends to a constant as $r \to \infty$, and this speed has been used to normalize the velocities, while distances are normalized by the radial distance at which the axial vorticity e-folds once, a measure of the core size that turns out to be close to the radius of maximum swirl. The parameter q in (5a) was introduced by Lessen et al [49] in their treatment of the stability of this flow, and its value completely determines the inviscid stability characteristics. Consequently, q is retained in the description and I will call (5) the "Q-vortex" henceforth.

The results of the calculation are shown in Figure 8. Also shown there are regions of instability according to the theories summarized in section 6. I have also located on this plot the approach-wake transitions reported by Garg & Leibovich [36] and deduced from their Table 1. For convenience, the reprocessed data is compiled in Table 1, where the symbol A identifies approach flow and W the wake flow. The Reynolds number is given first with respect to the tube radius and, in parenthesis, with respect to the core diameter based on maximum swirl (as in Leibovich [17], Table 1). The core expansion ratio (Leibovich [17]) is also shown: the jump in q from higher values upstream to lower ones downstream is consistent with the mixing occurring in the wake, which causes an increase in core diameter and consequent reduction in peak core vorticity (hence a reduction in q)

Notice that all approach flows are supercritical. The "distance" from criticality is best measured by the Froude-like number N, introduced by Benjamin [7]

$$N = (c_+ + c_-)/(c_+ - c_-)$$

where c_+ and c_- are the greater and lesser values of the phase speed for waves of extreme

Reynolds number Breakdown type	A or W	δ	q	N	Core expansion ratio
(a) 11,480 (1920)	A	0.89	1.98	1.86	1.64
S	W	-0.72	1.45	0.60	
(b) 11,480 (1920)	A	1.58	1.59	1.32	2.45
B	W	-0.94	0.97	0.44	
(c) 14,100 (2812)	A	0.97	1.86	1.47	1.78
S	W	-0.94	1.43	0.57	
14,100 (2812)	A	1.4	1.62	1.37	1.97
B	W	-0.87	1.18	0.45	
20,160 (3348)	A	1.04	1.85	1.42	2.1
S	W	-0.82	1.38	0.46	
20,160 (3348)	A	1.48	1.64	1.32	2.76
B	W	-0.91	1.04	0.45	

Table 1. Data from refs.[17,36] with values of Froude number N appended. First Reynolds number is based on tube radius; number in parenthesis is based on core diameter [17]. A,W refer to data in approach or wake flows; B,S implies transition via bubble or spiral breakdown.

length. For prescribed values of δ and q, N may be found from the data in Figure 8. To find (c_+,c_-) for a noncritical flow with given (δ,q), relabel the abscissa, letting it be ξ; and let the positive branch of the continuous curve separating sub- and supercritcal regions be ξ_+, and the negative branch be ξ_-. Given q, two values $\xi_\pm(q)$ are defined, and

$$c_+ = \max(1 - \delta\xi_+,\ 1 - \delta\xi_-), \quad c_- = \min(1 - \delta\xi_+,\ 1 - \delta\xi_-)$$

In wake flows, $-1 < \delta \leq 0$, and $\xi_- < -1$. It is understood that flows with axial velocity reversals are excluded from the discussion.

Conjugate Flow States

For some applications, including aerodynamic ones, the details of the transition region are not as important as the position of breakdown and the general properties of the flow following it. A method of determining the wake properties from the approach flow, like shock jump conditions, may suffice.

Benjamin's [7] theory of conjugate flows, does not provide jump conditions, but it does aim at relating the downstream flow to the approach flow without considering the structure of the transition. The theory is cast in terms of steady, inviscid, and axisymmetric motion, which as is well known (cf. ref. [7]), is described by a single equation for the Stokes streamfunction, ψ. In cylindrical coordinates, the equation is

$$\psi_{rr} - r\,\psi_r + \psi_{zz} = r^2\,H'(\psi) - KK'(\psi), \tag{7}$$

where subscripts indicate partial derivatives. H is the total head and (except for a factor of 2π) K is the circulation; both are functions of ψ alone,

$$H = \frac{1}{\rho}\,p + \frac{1}{2}\,(u^2 + v^2 + w^2)$$
$$K = rv \tag{8}$$

where the (r,θ,z) velocity components are (u,v,w). The functional forms of H' and K may be determined if all streamlines intersect a plane z = constant upon which the pressure and velocity are known. These functions typically are highly nonlinear (and not Galilean invariant). For example, the vortex model (2) with $W_2 = 0$ has

$$H'(\psi) = \alpha\lambda^2\,e^{-\beta\psi}\,[1-e^{-\beta\psi}]$$
$$F = \lambda[1-e^{-\beta}]\ , \quad \beta = 2\alpha/W_1, \tag{9}$$

If $W_1 = 0$, in the same model,

$$H'(\psi) = 4\alpha^2\psi\{1 - \alpha q^2/\ln[1 - 2\alpha\psi/W_2]\} - 2\alpha W_2.$$
$$K = 2\alpha q\psi\ , \quad q = \lambda/W_2, \tag{10}$$

while Hall's [21] conical vortex model has

$$H'(\psi) = C\psi^{-1}$$
$$K(\psi) = \lambda\psi^{1/2} \qquad (11)$$

where C and λ are constants.

Benjamin [7] considers columnar solutions $\psi = \psi(r)$ in the cylinder $0 < r < a$. Assuming that a supercritical flow (0, V(r), W(r)) is prescribed, the corresponding functions H and K can be found, and the prescribed supercritical flow is obviously a solution of (7). Typically other solutions to (7) will exist, however, with the same functional forms for H and K; if so, then Benjamin shows that they are necessarily subcritical and have larger values of the momentum flux

$$S = 2\pi\int_0^a (p + \rho W^2)r\,dr,$$

which Benjamin calls the "flow force". These properties were placed on a rigorous mathematical footing by Fraenkel [50]. The defining supercritical flow and a second solution (assuming it exists) with S closest to the value of S of the defining flow are called a conjugate flow pair.

The conjugate flows do not represent an analog of a shock jump condition, however. Since momentum must be conserved, two flows in the same cylindrical space can be connected only if they have the same value of S (neglecting wall friction). This is possible only if energy is dissipated or radiated away by the (unsteady) formation of waves in a transition region that is outside the scope of the analysis. Benjamin [7] shows that the formation of waves leads to a reduction in S and his conception of idealized vortex breakdown is the transition between an upstream supercritical flow and a downstream flow consisting of the subcritical conjugate and a superposed wavetrain.

As in the theory of normal shocks, the level of supercriticality, measured by the Froude number N, at which a breakdown occurs cannot be specified, but Benjamin argues that slightly supercritical conditions are most dangerous for the occurence of "spontaneous" breakdown.

Hall [9] criticized Benjamin's theory on the grounds that it does not offer an advance of Squire's [6] simpler idea in providing a prediction of the occurrence and location of breakdown; and that the concept of reduction of S by waves is supported only by weakly nonlinear theory, whereas the perturbations occuring in breakdown are necessarily large. The most serious weakness of Benjamin's [7] theory in my view is that there is no clear way to relate it to experiments which, at high Reynolds numbers, always have unsteady, nonaxisymmetric wakes. The only conceivable way to relate the theory to experiment is to regard the streamfunction appearing in the theory as the streamfunction for the time-averaged flow in the wake, which is axially-symmetric and steady. If this is done, however, there is no need for the total pressure $H(\psi)$ in the wake to have the same functional form as it has in the supercritical defining flow upstream. The correspondence between the functions for H in the conjugate states can be destroyed simply by unsteadiness, and does not require energy dissipation. Thus to accept Benjamin's theory, which has provided such a wealth of useful concepts, requires an act of faith for which no scientific basis has yet been provided.

Nonlinear Wave Models

The linear long wave model of Squire's [6] leads to the critical condition. If the basic vortex flow forms a waveguide with slowly changing characteristics then, as outlined above, disturbances created downstream can penetrate upstream, the long waves coming to rest near the section of the vortex where critical conditions are reached. This picture of breakdown as a wave provides a simple conceptual framework that explains qualitative features concerning the location of breakdown and its movement in response to the variation of experimental control parameters.

Without accounting for finite wavelength, however, the region of wavy disturbances can have no beginning in a waveguide of fixed characteristics, the case explicitly treated by Squire, while if the waveguide varies, the long waves have a singularity at the critical station entirely analogous to that arising in linearized gasdynamics at the sonic condition.

The removal of these difficulties requires the inclusion of finite amplitude and finite wavelength effects and provides a wave model that is free of these inconsistencies. Furthermore, the enlarged wave theory shows that the position of breakdown, regarded as the location at which the wave is arrested, lies in the supercritical region of the waveguide and allows some structural information in the breakdown zone to be inferred.

Nonlinear wave theory is developed and applied to vortex breakdown in papers by Benjamin [10], Leibovich [11], Leibovich & Randall [12], and Randall & Leibovich [13]. The first two papers deal with columnar waveguides, while the second two deal with slowly varying vortex waveguides and provide a "transcritical" theory for the problem related, rather distantly, to transonic theory.

Benjamin [10] first showed that axially-symmetric solitary wave solutions are possible in a columnar vortex, that they are the only disturbances of permanent form that can arise in the absence of energy loss, and that they are stationary in a supercritical stream. Benjamin's paper is mainly concerned with infinite wavetrains of finite amplitude; the only example of a solitary wave presented leads to an acceleration of flow along the vortex axis rather that a deceleration as required for breakdown. Leibovich [11], in a further development of Benjamin's work, showed that axisymmetric waves of small but finite amplitude propagating on a columnar vortex have a Stokes streamfunction of the form

$$\psi = \Psi(r) - \varepsilon\phi_0(r)A(z,t), \tag{12}$$

where $\Psi(r)$ is the stramfunction of the unperturbed flow, ε is a small amplitude parameter, and $\phi_0(r)$ is the eigenfunction of a second order ordinary differential equation. The wave amplitude is governed by the Korteweg-deVries equation

$$A_t + c_0 A_z = \varepsilon\{\alpha A A_z + \beta A_{zzz}\}, \tag{13}$$

where c_0, the linear long wave speed, and the constants α and β are all functionals of the unperturbed flow field that may be computed. For radially unbounded flow with vorticity vanishing at distances large compared to the core radius, A is determined instead by an integrodifferential equation of the same form as (13), but with the term proportional to $\partial^3 A/\partial z^3$ replaced by

$$\kappa \frac{\partial^3}{\partial z^3} \int_{-\infty}^{\infty} \frac{A(\xi,t)d\xi}{[(z-\xi)^2 + \ell^2]^{1/2}} \tag{14}$$

where ℓ is the ratio of the core radius to the wavelength and κ is a constant (depending upon ℓ) that is fixed by the theory.

The Korteweg-deVries equation has solutions describing waves of permanent form, the "solitons", which evolve from initial conditions of rather general type; they are the solitary waves known since the nineteenth century. The soliton with unity as maximum value of the amplitude A propagates, in the notation used in equation (13), at a speed $c_0 - \varepsilon\alpha/3$ if $\varepsilon\alpha$ is positive, as it turns out to be in examples of realistic basic vortex flows. The dependence of wave speed on wave amplitude is again analogous to gasdynamics, but here the medium is dispersive and waves of permanent form can develop without dissipation. From this dependence, one concludes (Benjamin [10], Leibovich [11]) that the soliton is stationary if the flow upstream of it is supercritical. If the amplitude parameter ε is allowed to take any value, instead of the small ones for which the theory has asymptotic validity, then the soliton can create a stagnation point on the axis and axial flow reversal [11].

Being close to critical has no effect on waves in a cylindrical tube, but has a large effect on waves in a tube of variable area. Leibovich & Randall [12] showed that a different procedure is needed to find the structure of weakly nonlinear waves in nearly critical, or "transcritical" flow; their theory was applied to breakdown by Randall & Leibovich [13] when the deviation, g(z), of the tube area from its maximum value *is* small and changes slowly with z, so $(dg/dz)/g$ is small compared to the wavelength of the disturbance. The equation describing waves on a nearly critical flow in such a slowly varying waveguide is (in notation differing from the original)

$$A_t = \varepsilon\{\alpha A A_z + \beta A_{zzz} - \sigma(gA)_z - \nu A\}. \tag{15}$$

Here α, β, σ are again computed constants, and ν is a computed constant times an inverse Reynolds number based upon wavelength. Randall and I explored the consequences for breakdown ensuing from the adoption of (15) and the associated Stokes streamfunction and circulation

$$\psi = \Psi(r) + \phi_0(r)[g(z) - \varepsilon A(z,t)], \quad rv = K(\Psi) + \gamma_0[g(z) - \varepsilon A(z,t)],$$

where γ_0 is given in terms of ϕ_0, as a model for the flow without restriction to small ε. The presence of dissipation, represented here by ν, turns out to be important. Molecular diffusion, as assumed in Randall & Leibovich [13], is probably negligible as a source of dissipation in vortex breakdown at high Reynolds numbers, but I believe that another form of "apparent dissipation", to be explained in section 7, is significant and that ν should be based upon it.

Equation (15) has solutions resembling solitary waves. Assuming the tube diverges in the downstream direction, the area changes cause waves to amplify as they propagate upstream, and decay as they move downstream. The possible ultimate equilibrium position of a finite amplitude wave is closely estimated by the roots of the equation

$$\sigma dg/dz + 2\nu = 0. \tag{16}$$

In the problem that Randall and I considered (and which we thought was a reasonable model of Sarpkaya's [30] experiments, $\sigma > 0$. If ν is to represent dissipation, then $\nu > 0$, and the solutions must lie in a portion of the waveguide where $dg/dz < 0$, or where the tube is diverging. For problems of flow in an initially straight tube that flares out and then becomes straight again, there are two equilibrium points z_1 and $z_2 > z_1$. Only the upstream point is stable, however, in the sense that waves passing it in either direction experience a restoring tendency owing to the amplitude-speed behaviour of the waves.

If the wave is to be stationary at z_1, it must have a definite amplitude. Without loss of generality, the maximum value of A can be set at unity, and the condition that the wave be stationary at z_1 then fixes the amplitude parameter at

$$\varepsilon = 3g(z_1). \tag{17}$$

For the conditions obtaining in experiments containing vortex breakdown, the computed value of ε is not small and the resulting flow calculated contains a stagnation point. For the basic flow model selected as representative of Sarpkaya's experimental data, Randall and I found a streamline pattern containing a stagnation point and a recirculation bubble. The result was interesting because there are no adjustable constants in the theory; the fact that a reversed flow region exists is apparently the only possibility if the disturbance is to remain stationary! Furthermore, the core radius of the basic vortex and the radius of the 'bubble' of reversed flow are approximately the same, as observed in experiment.

Much has been made, mostly by me [10,17], of the fact that the sense of the swirl velocity reverses as one crosses a dividing streamline of a recirculation zone embedded in an inviscid swirling flow if the functional form of the circulation $K(\psi)$ (in the notation of equation (6)) is analytically continued from the outside of the closed streamline region where it is defined to the inside. This reversal, being impossible without an applied torque, was considered a serious weakness of the interior solutions found for the regions of reversed flow. I now believe that this qualitative inconsistency is easily removed. It has always been known (see Leibovich [51,17]) for discussions in the context of vortex breakdown) that a different functional form for $K(\psi)$ may be chosen for the interior. This cannot be done arbitrarily if the shape of the dividing streamline is to be maintained, because the interior and exterior pressures must balance on all points of the streamline, and an alteration of $K(\psi)$ alters the pressure distribution. Having found a dividing streamline using a single functional form for $K(\psi)$, however, one can maintain its shape by the replacement of $K(\psi)$ by $-K(\psi)$ in the interior; all dynamical balances are thereby unchanged and no swirl reversal then occurs.

6. INSTABILITY OF INVISCID COLUMNAR VORTICES

It is fortunate that great stretches of vortex flows, even those in which breakdown occurs, can be approximated as columnar, since the columnar vortex is analogous to the parallel model of two-dimensional basic flows. It is also fortunate that experimentally observed velocity profiles of vortices undergoing breakdown, at least in some carefully studied examples, can be fitted reasonably well by the analytically simple family of profiles given by equation (2) (the Q-vortex), and that some results are known about the stability of this family. The stability analysis of the Q-vortex is intricate and delicate and a complete characterization is not yet available. Nevertheless, I will review what is known about its stability, and then general criteria for stability and instability of columnar vortices. Attention will be restricted throughout to inviscid motions. Finally, I shall discuss the application of the results to the analysis of experimental data in vortices suffering breakdown.

Suppose the basic flow to be analyzed is described in cylindrical (r,θ,z) coordinates by the velocity vector

$$v = (0,V(r),W(r)).$$

If the flow is inviscid, the functional forms of V and W are arbitrary. The problem governing the linear inviscid temporal stability of columnar vortices to three dimensional disturbances of normal mode form $\exp[i(kz - n\theta - \omega t)]$ is the Howard-Gupta [52] eigenvalue problem

$$D[SD_* u] - \{1 + a(r)/n\gamma + b(r)/\gamma^2\}u = 0$$

$$u(R_1) = u(R_2) = 0,$$

where R_1 and R_2 are the boundaries, $0 < R_1 < R_2 < \infty$, $\mathcal{D}() \equiv d()/dr$, $D_*() \equiv D()+()/r$, and $a(r)$, $b(r)$, and $S(r)$ are prescribed functions of the basic flow, and of the assigned real wavenumbers k and n. The function γ is the (negative) Doppler-shifted frequency, and is given by

$$\gamma = k\cdot v - \omega, \quad k = (0,-n/r,k) \tag{19a,b}$$

where k is the wavenumber vector of the assumed normal mode, and the frequency ω is to be found as the eigenvalue. The function $S(r) = 1/(k\cdot k)$ is just a geometrical quantity. The functions $a(r)$ and $b(r)$ are given by

$$\begin{aligned} a(r) &\equiv nrD[Sr^{-1}D\gamma - nr^{-3}V], \\ b(r) &\equiv -2kr^{-2}VS[krD_*V + nDW]. \end{aligned} \tag{20}$$

The latter quantity plays an important role in the work to be described in this paper. It is of interest to note here that $b(r)$ has a simple kinematic interpretation. Let ζ be the vorticity vector of the basic flow and let $\Omega = (V/r)e_w$ be the angular velocity vector of a ring of fluid particles of radius r in the basic flow, where e_w is a unit vector in the direction of z-increasing, and let $e_n = k/(k\cdot k)$ be a unit vector normal to the wavefronts of the assumed normal mode disturbance. Then

$$b(r) = -2(e_w\cdot\Omega)(e_w\cdot\zeta). \tag{21}$$

Studies of the Q-Vortex Model

Lessen, Singh, and Paillet [49] investigated the stability of the flow with velocity vector v, given in cylindrical coordinates (r,θ,z) by

$$V = qr^{-1}[1-\exp(-r^2)]; \quad W = \exp(-r^2), \tag{22}$$

where r ranges from zero to infinity. There is no loss in generality if q is taken to be positive, and this will be assumed. This form serves (by a Galilean shift) as a model of flows with either jet-like or wake-like axial velocity components of model (2) or its equivalent, equation (5). The Galilean shift does not affect stability questions, nor therefore does the jet-like or wake-like character of the axial velocity profile: stability or instability is characterized only by the parameter q. Similarly, the stability of a columnar vortex with another set of profiles seems to depend upon the minimum value over r of the quantity

$$q = -rD_*V/DW$$

which is constant for the Q-vortex.

According to the results of numerical studies by Lessen et al [49] (supplemented by additional calculations by Duck & Foster [53], and by Leibovich & Stewartson [54]), the Q-vortex is unstable to three dimensional disturbances with normal modes of the form $\exp[i(kz-n\theta-\omega t)$ provided $q < q_1$. The precise value of q_1 (indeed, the existence of this upper bound) is unknown, but it is known to exceed 1.58. Modes with positive azimuthal wavenumbers n are found to be the most dangerous.

A plot of growth rate (ω_i = imag(ω)) against axial wavenumber (k) found by Lessen et al [49] for q = 0.8 is shown in Figure 9. Notice that the maximum growth rate increases with n, at least up to the largest value (6) of n considered. This makes one wonder if ω_i continues to increase with n indefinitely, or whether there is a most unstable wave at a particular value of n. If the former case holds, does ω_i approach a finite limit as $k \to \infty$, or does it increase without limit? These questions were considered by Leibovich & Stewartson [54]. They showed that, on energy stability grounds, ω_i cannot exceed the maximum value of the rate-of-strain, s, of the basic flow, where

$$s = [(rD\Omega)^2 + (DW)^2]^{1/2},$$

$\Omega \equiv V/r$ is the angular velocity of the basic flow. Furthermore, detailed considerations of the asymptotic behaviour obtaining as $n \to \infty$ revealed that ω_i approached a value $\omega_{\infty i}$ from below in the limit $n \to \infty$. Although originally derived for the Q-vortex, the result generalizes and holds for arbitrary profiles V(r) and W(r) and does not require that the flow be in a radially infinite region. The generalized value is

$$\omega_{\infty i} = \max[-VD\Omega(DW/s)^2[2 + J(r)]]^{1/2},$$
$$J(r) = 2(D\Omega)D(rV)/(DW)^2. \qquad (23)$$

The function J(r) is a local Richardson number, based upon the geometric mean of the angular velocity gradient $D\Omega$ and the circulation gradient D(rV), which should be compared to the Richardson number arising in the stability criterion of Howard & Gupta [52] (to be discussed in the next section), in which $D\Omega$ is replaced by Ω/r.

General Stability Criteria for Columnar Vortices and Further Results for the Q-Vortex

If the flow is inviscid, V and W can have arbitrarily prescribed functional forms. The special cases having W(r) = 0 will be referred to as "pure" vortices. Stability results of a general nature are as follows:

(i) (Rayleigh [55,56]; Synge [57]) A pure inviscid vortex is stable to infinitesimal axisymmetric perturbations if (Rayleigh) and only if (Synge)

$$\phi \equiv r^{-3}D(K^2) > 0, \qquad (24)$$

where $K(r) \equiv rV(r)$ as in previous sections of this paper.

Note that Synge's contribution, which is a sufficient condition for instability, is more definite than Rayleigh's, which is a sufficient condition for stability, since one cannot guarantee stability to nonaxisymmetric perturbations from Rayleigh's work.

(ii) (Rayleigh [55]; Fjortoft [58]) A necessary condition for the instability of a vortex to nonaxisymmetric two-dimensional disturbances is that the vorticity, $\zeta = r^{-1}D\Gamma$, have an extremum in the interior of the fluid (with the axis r = 0 considered a boundary point, if it is not excluded from the flow domain). This is the inflection point criterion applied to swirling flows. Thus, a vortex with monotonic vorticity is stable to two-dimensional disturbances.

This condition is strengthened by a refinement of Fjortoft's. A necessary condition for instability of a pure vortex to two-dimensional disturbances is that

$$[\Omega(r) - \Omega(r_1)](D\Gamma) < 0 \qquad (25)$$

in some region in the flow, where r_1 is a point at which $D\zeta = 0$.

As in parallel flows, this argument can be taken a step further (although we are not aware of it having been done in the literature) to virtually ensure instability if the angular velocity profile is monotonic, the vorticity ζ has a single extremum in the flow at $r = r_1$, and

$$[\Omega(r) - \Omega(r_1)](D\Gamma) < 0 \qquad (26)$$

throughout the flow. Then the equality holds only at $r=r_1$ and, by a well known argument due to Friedrichs, a regular neutral mode exists with $\omega = -n\Omega(r_1)$, where n is the azimuthal wavenumber of normal modes behaving like $\exp[-i(n\theta + \omega t)]$. An equally well known calculation of Tollmein's allows one to compute contiguous unstable modes, assuming they exist. Since the likelihood of a regular neutral mode being isolated is small, condition (26) provides a reasonable expectation that a flow of this kind is, in fact, unstable.

(iii) (Howard & Gupta [52]) In the presence of an axial velocity component, Howard & Gupta were able to generalize condition (24) to one of Richardson number type. They show that if

$$J \equiv \phi/(DW)^2 > 1/4, \qquad (27)$$

then the flow is stable to axially symmetric disturbances. For the Q-vortex, this guarantees stability to infinitesimal n=0 disturbances if q>0.403.

They also derived a semicircle theorem for axisymmetric perturbations which guarantees that unstable modes, if they exist, have critical layers. Barston [59] has produced a more flexible method of deriving semicircle theorems which is applicable to swirling flows with non-axisymmetric perturbations. No general conclusions concerning critical layers seem to emerged yet from that work, however.

(iv) (Maslowe & Stewartson, [60]) Swirling flow in a pipe or annulus of radius a is unstable if

$$V(a) \neq 0, \quad DW(a) \neq 0. \tag{28}$$

This result is obtained by generalizing the asymptotic analysis (as $n \to \infty$) of the problem a rigidly rotating Poiseulle flow in a pipe.

(v) (Leibovich & Stewartson [54]) A sufficient condition for the instability of a columnar vortex is

$$VDQ\left[DQDr + (DW^2\right] < 0. \tag{29}$$

This condition can be related to Rayleigh's mechanism of centrifugal instability, but here an axial velocity is permitted, and the perturbations are not restricted to axially-symmetric ones. This connection has already been made by Ludwieg [14], who derived it for flow in a narrow annular gap by ingenious physical reasoning. Ludwieg's derivation of (29) did not permit its status (necessary or sufficient for stability) to be determined, and an "improved" criterion derived mathematically by Ludwieg [15] for inviscid flows in a narrow annular gap is not applicable to general flows. We will now show that (29), which follows as a consequence of equation (23), analytically derived by Leibovich & Stewartson [54], is an indication of a centrifugal instability. First, we note that at each value of the radius, the basic flow has one principal axis of its rate-of-strain tensor which corresponds to zero rate-of-strain. This axis is tangent to the cylindrical surface r = constant and its direction is indicated by the vector $\underline{v}$ in figure 2. Positive values of the growth rate (23) are possible if, in the normal mode analysis, there is a radial position $r = r_0$ in the basic vortex for which (a) the coefficient $b(r_0)$, as given by equation (24), is positive, and for which the wavenumber vector $\underline{k}$ of the disturbance as given by (22b) is parallel to the principal axis corresponding to zero rate-of-strain of the basic flow. In a spiral coordinate system with one axis aligned with the direction of wave propagation, the flow field appears to be locally two-dimensional at $r=r_0$. Furthermore, if the basic flow vorticity and angular velocity are projected onto the direction of wave propagation, the function b(r) is the negative of Rayleigh's parameter. If the flow is locally a pure vortex and $b(r) > 0$, then the Rayleigh/Singh stability criterion is violated, and the flow is centrifugally unstable. This is the local picture at $r = r_0$ in the curvilinear coordinate system described; the existence of such an r_0 with $b(r_0) > 0$ is guaranteed when (29) is satisfied.

The criteria (i)-(v), to my knowledge, are the only general stability results available for inviscid, incompressible vortex flows with continuous velocity profiles. It is notable that most of them are restricted to either pure vortices or to axisymmetric disturbances. Detailed numerical studies of special cases in both inviscid and viscous flows indicate that axial velocity shears are destabilizing (Padley [61,62]; Mackrodt [63]; Maslowe [64]; Lessen et al. [49]; Lessen & Paillet [65]; Duck & Foster [53]; Foster and Duck [66] and that the most dangerous modes are not axially symmetric. The only definitive general results known to be applicable to these flows are (iv) and (v).

On the other hand, these results, both sufficient conditions for instability, are known from special cases not to be necessary for instability. For example, for the Q-vortex, criterion (29) is satisfied for $q < \sqrt{2}$ and is not satisfied for larger values of q, but it is known from numerical computations that the flow is unstable, at least for the smaller values of n, for values of q larger than $\sqrt{2}$. Furthermore, marginal instability of the inviscid flow is likely to be determined by the n = 1 mode, and will occcur at $q = q_1$; q_1, assuming that a finite value exists, is known to exceed 1.58.

When (29) is satisfied, the analysis of Leibovich & Stewartson [54] shows that inviscid modes with arbitrarily large azimuthal wavenumbers are excited. The numerical evidence for the vortex model (22) further shows that if an azimuthal mode n_1 is excited, then all modes with $0 < n < n_1$ are also excited. In such cases then, the satisfaction of criterion (29) implies that in the absence of viscosity an infinite number of modes simultaneously have a finite growth rate. This suggests that for large Reynolds number,(29) is a criterion for massive instability and transition to turbulence.

Application of Stability Results to Vortex Breakdown Flows

Garg & Leibovich [36] report experiments upstream and downstream of vortex breakdowns of both the B- and the S-forms to which I have already referred. In addition to mean flow measurements, they also report on an extensive set of measurements of power spectra that reveal strong low frequency periodic oscillations in the wakes of both breakdown forms; similar oscillations had been reported earlier by Faler & Leibovich [17] to occur in the interior of the recirculation zone of a B-form of breakdown. Because the mean velocity profiles in both the approach and wake flows can be fitted with good accuracy to the Q-vortex profiles, they were able to apply the results of Lessen et al [49] to show that the oscillation frequency in the wake agreed with the frequency of the n = 1 mode. The upstream measurement stations all were sufficiently far from the breakdown zone to ensure that the assumption of columnar flow w a good one. Traverses at several downstream stations were taken, and the mean data at the stations sufficiently far downstream were thought to be columnar to an acceptable approximation. Furthermore, the values of q in the wakes in all experiments performed were less than 1.58, therefore less than the critical value for instability to nonaxisymmetric disturbances. Improvements in the accuracy of the comparison between the frequencies of this experimental data base and the values from stability theory have been described by Tsai & Widnall [46]. Upstream of B-forms of breakdown, q was about 1.6; since we know that the critical value of q exceeds 1.58, the flows

upstream may be unstable according to stability theory; in any event they are at best marginally stable. (It should be noted at this point that, although Leibovich & Stewartson found instabilities at q = 1.58, the corresponding growth rates were very small.) The values of q in the wake of B-breakdowns were all less than $\sqrt{2}$, indicating strong instability, according to Leibovich & Stewartson [54].

Corresponding measurements for S-type breakdowns revealed significantly larger values of q upstream, indicating an approach flow with a higher degree of stability, while the mean flows in the wake were decidedly larger than values in the wake of B-breakdown, but grouped near $\sqrt{2}$, and therefore definitely unstable according to stability theory. One concludes that the approach and wake flows of B-breakdowns are less stable than those of S-breakdown. The core expansion is larger in B-breakdown than in S-breakdown, and since this is likely to be the consequence of turbulent mixing, this provides additional corroboration of the stability conclusions.

The jumps in q across the breakdowns in the Garg-Leibovich data base are summarized in Figure 8. It may be useful to emphasize that a larger q does not mean a larger swirl level; q is directly proportional to the peak swirl speed and inversely proportional to the axial velocity excess or deficit. The axial velocity excess or deficit is itself a strong function of swirl (see Faler & Leibovich [34, pg. 1387] for a brief discussion).

Escudier et al [26] analyzed their experimental measurements in terms of its instability and criticality. The experiments were conducted in an apparatus employing a slot-entry tangential-jet vortex generator, followed by a sudden contraction, their "exit tube", in which breakdown occured. They concluded that the flow was always both critical and unstable at the entrance to the exit tube, hence upstream of breakdown. These interesting conclusions are apparently based upon two distinct approaches. First, there was visual evidence of instability at the entrance to the exit tube. Second, q (assuming the flow to be a Q-vortex) and the state of criticality (apparently assuming the flow to be a Rankine vortex with uniform axial speed) were estimated at each axial station at which data was available. These indicated a rapid fall of q as the contraction was approached, with values falling below 1.5 (the value they used as a criterion for loss of stability) just upstream of the entrance to the exit tube. The value of q was estimated by the rule (appropriate for the Q-vortex) $q = 1.56\, V_{max}/W_2$, where V_{max} is the peak swirl speed, easily determined from the data.

The conclusions drawn by Escudier et al [26], in my view, are premature. It is not appropriate to apply a theory for columnar vortices to a region of flow with large axial gradients, as they have done, to arrive at the conclusion that q falls as the contraction is approached. Even if the flow were accurately columnar, they found it difficult fit the measured mean axial profile (which has a developing deceleration on the centerline, evidence of significant axial gradients) with that of a Q-vortex, and the stability characteristics of a columnar vortex coinciding with their measured profiles are likely to be very different from those of the Q-vortex. Furthermore, there is good reason to believe that a nonswirling flow would also exhibit an instability at the sharp-edged contraction that forms the entrance to the exit tube; that is, it seems likely that the instability observed is due to the design of the experimental apparatus, and not to the properties of the vortex.

7. NONAXISYMMETRIC MOTION IN S AND B BREAKDOWN

The theories described in section 5 make no distinction between S- and B-breakdown, yet there is a clear distinction between them. With fixed core radius, the S-breakdown is the low swirl form. This is seen from Figure 7 (where fixing the Reynolds number effectively fixes the size of the core), and from the data in Table 1, where the Froude number N is seen to be larger for S-breakdowns than for B-breakdowns in a vortex with the same core size. The discrimination between the two forms of breakdown is an important question yet to be addressed by theory.

One essential feature of S-breakdown is the presence of both $|n| = 1$ and $n = 0$ modes in its Fourier decomposition. The need for the $n = 0$ mode was explained in section 4. The $|n| = 1$ modes are needed to explain the corkscrew shape taken on by a streakline released on the vortex axis, since these are the only modes having a nonzero radial velocity component on the axis. Thus, a theoretical treatment of S-breakdown should include these modes as a minimal representation of the velocity field. Furthermore, because of the observations made in the previous section concerning the instability of the wake and the marginal stability of the approach flow in B-form breakdowns, it seems that the same minimal representation is required for <u>both</u> the B- and the S-forms of breakdown.

Because I believe the weakly nonlinear axisymmetric wave models have provided some insight into the B-breakdown, I would like to use similar perturbation ideas to briefly speculate about the role of the nonaxisymmetric flow features. Suppose a slowly varying axisymmetric basic flow is slightly perturbed and that to lowest order the perturbation consists of a superposition of $n = 0$ and $|n| = 1$ modes, with the axial velocity perturbation given to lowest order by

$$\varepsilon\, A(z,t)w_0(r) + \varepsilon_\theta[S(z,t)w_1(r)\exp i\left(\frac{kz-\omega t}{\delta}\right) e^{-i\theta} + \text{c.c.}]. \tag{30}$$

where ε, ε_θ, and δ are small parameters. If $\varepsilon_\theta = 0$, the form given describes the long axisymmetric waves discussed in section 5; the function S describes the amplitude modulation of the $|n| = 1$ (spiral) modes, and is allowed here to vary slowly compared to the length scale ($O(\delta/k)$) and time scale ($O(\delta/\omega)$) of these modes. If $\varepsilon = 0$, then solition solutions are possible (Leibovich & Ma [48]) and are described by the nonlinear Schroedinger equation

$$iS_t + \varepsilon_\theta^2 \alpha\, S_{zz} + \varepsilon_\theta^2 \beta\, S|S|^2 = 0 \tag{31}$$

The disturbances that emerge when both A and S are present will depend upon how they are coupled, and this will depend in a complex way upon the basic flow field. To fix ideas, think of the flow in a tube that is first cylindrical, then diverging. Assume infinite Reynolds number, and the existence of a basic axisymmetric flow. Assume furthermore that this flow is stable throughout, that it is supercritical at the beginning of the tube divergence, and that at the end, it is critical or only slightly supercritical. This picture is presumably what would be expected in the experiments conducted by Sarpkaya [30-32], and by my co-workers and me, if vortex breakdown had not occurred.

Now assume that a weak disturbance is introduced at the downstream end. The linear group velocities of the nonaxisymmetric disturbance modes are positive, under the assumptions adopted, so the nonaxisymmetric features will wash downstream. The linear group velocity of the axially-symmetric long wave components of the disturbance will be very small, but the speed of a long wave of finite amplitude may allow upstream propagation. Consider a disturbance that has made its way upstream. We may assume $S = 0$ since by assumption infinitesimal $n \neq 0$ modes are washed downstream; thus an equation like (15) is operative. As this axisymmetric disturbance moves upstream, it amplifies and its length decreases as a result of the area reduction it sees as it progresses. If the weakly nonlinear equation (15) holds throughout, and if dissipation can be ignored in it, then wave will pass right through the diverging section and continue to propagate upstream.

On the other hand, as its amplitude grows, the stability of the finite amplitude axisymmetric wave to $|n| \geq 1$ disturbances becomes increasingly suspect. In particular, if the basic flow is not far from marginal, and if the axisymmetric wave destablizes the flow to $|n| \geq 1$ modes, then a modest wave amplitude might be expected to lead to growth of three-dimensional disturbances, with linear growth rate proportional to $\epsilon - \epsilon_c$, where ϵ_c is the value of wave amplitude parameter corresponding to marginal instability to nonaxisymmetric perturbations. The presence of a coherent periodic signal in the spectra of disturbances measured by Singh & Oberoi [67] and by Garg and Leibovich [36] suggests that the nonaxisymmetric amplitude $S(z,t)$ grows out of this instability as a Hopf bifurcation (Iooss and Joseph [68]). This implies a saturation for the amplitude of the three-dimensional perturbations, with

$$|\epsilon_a S|^2 = O(\epsilon - \epsilon_c).$$

The gain in energy of the spiral mode comes at the expense of the axisymmetric mode. With $|S| \neq 0$, there is a feedback into the equation for A of a term of the form

$$-\gamma |S|^2 A \tag{32}$$

where γ is a coupling constant to be found as a functional of the basic flow. Thus, the self-excitation of the S mode in this scenario is made possible by virtue of presence of the A mode, and the transfer of energy to it from the A mode causes the dissipation of axisymmetric wave energy necessary to stabilize the position of the axisymmetric mode in the diverging part of the channel, since we may take

$$\nu = \gamma |S|^2 \tag{33}$$

in equation (15).

Thus, if (15) and (33) are adopted, the position and strength of breakdown are determined by the Froude number, N, of the basic flow, the imposed external forcing (represented in the example by wall tube slope function $g(z)$, and the energy density of the nonaxisymmetric motions, which depends upon how close the basic flow is to marginal instability.

This scenario is not yet supported by detailed calculation, but the conception seems plausible and provides at least a partial unification of the phenomena observed. The factors that distinguish between B-forms and S-forms of breakdown are not apparent. Recognizing from Fig.8 that the S-form appears under more stable and more highly supercritical conditions, it might be conjectured from inviscid theory, that the B-form may be unstable at higher values of q, and that the S-form emerges from the B-form as a secondary bifurcation.

8. CONCLUSION

Given a model describing the smooth streamwise evolution of a vortex core, the position of breakdown may be estimated by computing the Froude number N, the stability ratio q/q_c where q_c corresponds to the critical value of q. In the observations that can be documented, stationary vortex breakdown occurs in supercritical regions, N>1. The location seems to correlate better with the point at which the vortex reaches a marginally stable condition than it correlates with the point at which critical conditions are obtained.

A new conceptual framework is suggested based upon information derived from experimental studies of vortex breakdown. In the picture put forward, growth of axisymmetric modes occurs as a result of propagation in a variable vortex waveguide, and this wave loses stability to three-dimensional disturbances when it reaches a critical amplitude. Energy drain from the axisymmetric wave to the nonaxisymmetric modes serves to fix the possible equilibrium positions of the vortex breakdown, which is identified with a large amplitude a large amplitude axisymmetric wave and smaller amplitude superposed nonaxisymmetric wave modes.

REFERENCES

1. Hall, M.G., The structure of concentrated vortex cores, Prog. Aeronaut. Sci. 7, 1966, 53-110.

2. Peckham, D.H. & Atkinson, S.A., Aeronaut. Res. Counc., Preliminary results of low speed wind tunnel tests on a Gothic wing of aspect ratio 1.0, CP 508, 1957, 16pp.

3. Earnshaw, P.B. & Lawford, J.A., Aeronaut. Res. Counc., Low-speed wind-tunnel experiments on a series of shasrp-edged delta wings, R&M No. 3424, 1966, 47pp.

4. Hummel, D. & Srinivasan, P.S., Vortex breakdown effects on the low-speed aerodynamic characteristics of slender delta wings in symmetrical flow, J. Roy. Aero. Soc. 71, 1967, 319-322.

5. Lambourne, N.C. & Bryer, D.W., Aeronaut. Res. Counc., The bursting of leading edge vortices; some observations and discussion of the phenomenon, R&M No. 3282, 1961, 32pp.

6. Squire, H.B., Analysis of the "vortex breakdown" phenomenon, in Miszellaneen der Angewandten Mechanik, Berlin, Akademie-Verlag, 1960, 306-312.

7. Benjamin, T.B., Theory of the vortex breakdown phenomenon, J. Fluid Mech. 14, 1962, 593-629.

8. Ludwieg, H., Dtsch. Luft Raumfahrt, Vortex breakdown, Rep. 70-40, 1970.

9. Hall, M.G., Vortex breakdown, Ann. Rev. Fluid Mech. 4, 1972, 195-218.

10. Benjamin, T.B., Theory of the vortex breakdown phenomenon, J. Fluid Mech 14, 1962, 593-629.

11. Leibovich, S., Weakly nonlinear waves in rotating fluids, J. Fluid Mech. 42, 1970, 803-822.

12. Leibovich, S. & Randall, J.D., Amplification and decay of long nonlinear waves, J. Fluid Mech. 53, 481-493.

13. Randall, J.D. & Leibovich, S., The critical state: a trapped wave model of vortex breakdown, J. Fluid Mech. 53, 1973, 495-515.

14. Ludwieg, H., Stabilitat der Stroemung in einem zylindrischen Ringraum, Z. Flugwiss. 8, 1960, 135-140.

15. Ludwieg, H., Zur Erklarung der Instabilitat der uber angestellten Deltaflugeln auftretenden freien Wirbelkerne, Z. Flugwiss. 10, 1962, 242-249.

16. Ludwieg, H., Erklarung des Wirbelaufplatzens mit Hilfe der Stabilitatstheorie fur Stromungenmit schraubenlinienformigen Stromlinien, Z. Flugwiss. 13, 1965, 437-442.

17. Leibovich, S., The structure of vortex breakdown, Ann. Rev. Fluid Mech.10, 1978, 221-246.

18. Legendre, R., Remarques sur l'eclatement axisymetrique d'un tourbillon, La Rech. Aero. 1981, 295-302.

19. Moore, D.W. & Saffman, P.G., Axial flow in laminar trailing vortices, Proc. Roy. Soc. Lond. A333, 1973, 491-508.

20. Kaden, H., Aufwickling einer unstabilen unstetigkeitsflache, Ing. Arch. 2, 1931.

21. Hall, M.G., A theory for the core of a leading-edge vortex, J. Fluid Mech. 11, 1961, 209-228.

22. Stewartson, K. & Hall, M.G., The inner viscous solution for the core of a leading-edge vortex, J. Fluid Mech. 15, 1963, 306-318.

23. Chanaud, R.C., Observations of oscillatory motion in certain swirling flows, J. Fluid Mech. 21, 1965, 111-127.

24. Escudier, M.P., Bornstein, J. & Zehnder, N., Observations and LDA measurements of confined turbulent vortex flow, J. Fluid Mech. 98, 1980, 49-63.

25. Escudier, M.P. & Zehnder, N., Vortex-flow regimes, J. Fluid Mech. 115, 1982, 105-121.

26. Escudier, M.P., Bornstein, J. & Maxworthy, T., The dynamics of confined vortices, Proc. Roy. Soc. Lond. A 382, 1982, 335-360.

27. Earnshaw, P.B., Aeronaut. Res. Counc., An experimental investigation of the structure of a leading-edge vortex, Rep.no.22,876, 1961.

28. Harvey, J.K., Some observations of the vortex breakdown phenomenon, J. Fluid Mech. 14, 1962, 589-592.

29. Titchener, I.M. & Taylor-Russell, A.J., Aeronaut. Res. Counc., Experiments on the growth of vortices in turbulent flow, C.P.No. 316, 1957.

30. Sarpkaya, T., On stationary and travelling vortex breakdowns, J. Fluid Mech. 45, 1971, 545-559.

31. Sarpkaya, T., Vortex breakdown in swirling conical flows, AIAA J. 9, 1792-1799.

32. Sarpkaya, T., Effect of the adverse pressure gradient on vortex breakdown, AIAA J. 12, 1974, 602-607.

33. Bellamy-Knights, P.G., A note on vortex breakdown in a cylindrical tube, J. Fluids Eng. 98, 1976, 322-323.

34. Faler, J.H. & Leibovich, S., Disrupted states of vortex flow and vortex breakdown, Phys. Fluids 20, 1977, 1385-1400.

35. Faler, J.H. & Leibovich, S., An experimental map of the internal structure of a vortex breakdown, J. Fluid Mech. 86, 1978, 313-335.

36. Garg, A.K. & Leibovich, S., Spectral characteristics of vortex breakdown flowfields, Phys. Fluids 22, 1979, 2053-2064.

37. Werle, H., Sur l'eclatement des tourbi ons d'apex d'une aile delta aux faibles vitesses, La Rech. Aero. No. 74, 1960, 23-30.

38. Elle, B.J., Aeronaut.. Res. Counc., An investigation at low speed of the flow near the apex of thin delta wings with sharp leading edges, R&M No. 3176, 1958.

39. Vogel, H.U., Max-Planck Inst. fur Stromungsforschung, Goettingen, Bericht 6, 1968.

40. Ronnenberg, B., Max-Planck Inst. fur Stromungsforschung, Goettingen, Bericht 20,1977.

41. Lugt, H.J. & Haussling, H.J., Axisymmetric vortex breakdown in rotating fluid within a container, J. Appl. Mech., In press.

42. Kopecky, R.M. & Torrance, K.E., Initiation and structure of axisymmetric eddies in a rotating stream, Comput. Fluids 1, 289-300.

43. Grabowski, W.J. & Berger, S.A., Solutions of the Navier-Stokes equations for vortex breakdown, J. Fluid Mech. 75, 1976, 525-544.

44. Nguyen, T.T., Univ. Cal. Berkeley, An investigation of vortex breakdown from the point of view of hydrodynamic stability, Dissertation, 1980, 133pp.

45. Leibovich, S., Waves in parallel or swirling stratified shear flows, J. Fluid Mech. 93, 1979, 401-412.

46. Tsai, C-Y. & Widnall, S.E., Examination of group-velocity criterion for breakdown of vortex flow in a diverging duct, Phys. Fluids 23, 1980, 864-870.

47. Garg, A.K., Cornell Univ., Oscillatory behaviour in vortex breakdown flows: an experimental study using a laser Doppler anemometer, MS Thesis, 1977, 225pp.

48. Leibovich, S. & Ma, H.Y., Soliton propagation on vortex cores and the Hasimoto soliton, Phys. Fluids, In review.

49. Lessen, M., Singh, P.J. & Paillet, F., The stability of a trailing line vortex, J. Fluid Mech. 63, 1974, 753-763.

50. Fraenkel, L.E., On Benjamin's theory of conjugate vortx flows, J. Fluid Mech. 28, 1967, 85-96.

51. Leibovich, S., Axially-symmetric eddies embedded in a rotating stream, J. Fluid Mech. 32, 1968, 529-548.

52. Howard, L.N. & Gupta, A.S., On the hydrodynamic and hydromagnetic stability of swirling flows, J. Fluid Mech. 14, 1962, 463-476.

53. Duck, P.W. & Foster, M.R., The inviscid stability of a trailing line vortex, Z. angew. Math. Phys. 31, 1980, 523-530.

54. Leibovich, S. & Stewartson, K., A sufficient condition for the instability of columnar vortices, J. Fluid Mech. 126, 1983, 335-356.

55. Rayleigh, Lord, On the stability, or instability, of certain fluid motions, Proc. Lond. Math. Soc. 11, 1880, 57-70.

56. Rayleigh, Lord, On the dynamics of revolving fluids, Proc. Roy. Soc. Lond. A 93, 1916, 148-154.

57. Synge, J.L., The stability of heterogeneous liquids, Trans. Roy. Soc. Can. 27, 1933, 1-18.

58. Fjortoft, R., Application of integral theorems in deriving criteria of stability for laminar flows and for the baroclinic circular vortex, Geofys. Publikasjoner Oslo 17 (No.6), 1950, 1-52.

59. Barston, F.M. Circle theorem for inviscid steady flows. Int. J. Eng. Sci. 18, 1980, 477-89.

60. Maslowe, S.A. and Stewartson, K. On the linear inviscid stability of rotating Poiseuille flow. Phys. Fluids 25, 1982, 1517-23.

61. Padley, T.J., On the stability of rapidly rotating shear flows to non-axisymmetric disturbances, J. Fluid Mech. 31, 1968, 603-607.

62. Padley, T.J., On the instability of viscous flow in a rapidly rotating pipe, J. Fluid Mech. 35, 1969, 97-115.

63. Mackrodt, P.A., Stability of Hagen-Poiseuille flow with superimposed rigid rotation, J. Fluid Mech. 73, 1976, 153-164.

64. Maslowe, S.A., Instability of rigidly rotating flows to non-axisymmetric disturbances, J. Fluid Mech. 64, 1974, 303-317.

65. Lessen, M. & Paillet, F., The stability of a trailing line vortex. Part 2. Viscous theory, J. Fluid Mech. 63, 1974, 769-779.

66. Foster, M.R. & Duck, P.W., The inviscid stability of Long's vortex, Phys. Fluids 25, 1982, 1715-1718.

67. Singh, P.I. & Uberoi, M.S., Experiments on vortex stability, Phys. Fluids 19, 1976, 1858-1863.

68. Iooss, G. & Joseph, D.D., Elementary Stability and Bifurcation Theory, New York, Springer-Verlag, 1980.

ACKNOWLEDGEMENTS

This work was sponsored by the Fluid Mechanics Program of the National Science Foundation under Grant CME79-19817.

FIGURE CAPTIONS

1. Vortex breakdown in leading-edge vortices over a model delta wing, from [5]. The breakdown in the upper portion of the figure is a spiral, or S-type; the one in the lower portion is a bubble, or B-type.

2. Photographs of vortex breakdowns in a tube; from [34]. (a) B-type followed by S breakdown downstream. (b) S-type.

3. Sketch of a leading-edge vortex, taken from [21].

4. Tangential slot-entry swirl generation apparatus used in [23-26]. The rolling up of the shed vorticity layer is sketched as a spiral in the end-view on the left.

5. Swirl vane generation apparatus in perspective, from [28], with an inset showing details of the centerbody and turning section, from [34].

6. Top left figure is a measured axial velocity profile in the generation section in a slot-entry apparatus, taken from [26]; swirl profile is shown top right. Bottom left and right are axial and swirl velocity profiles in a leading-edge vortex measured by Earnshaw [27].

7. Plot of the position (abscissa) of breakdown as a function of Reynolds number Re and swirl lead Ω, from [34]. Positions marked 0 or 1 locate B-type breakdowns, while 2 locates S-breakdowns. Other designations (3-6) locate large amplitude disturbances that do not persist at high Reynolds number.

8. Parameter space for the Q-vortex, showing the regions of subcritical and supercritical flow, regions of stability to axisymmetric disturbances, and regions of instability to three-dimensional disturbances. Strong instability to three-dimensional disturbances is found for $q < \sqrt{2}$, and this region is shown. Also shown in the plot are the approach-wake transition for the three sets of data given in Table 1.

9. Growth rates as a function of wavenumber k for Q-vortex for $q = 0.8$ and for azimuthal wavenumbers 1 through 6, from ref. [49].

Figure 1

a

b

Figure 2

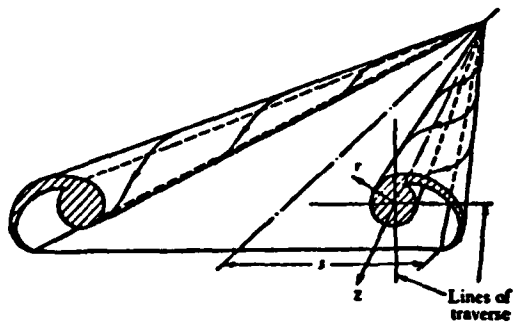

Figure 3

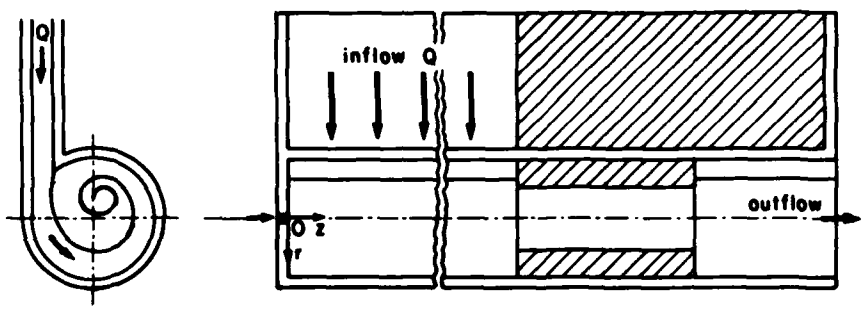

Figure 4

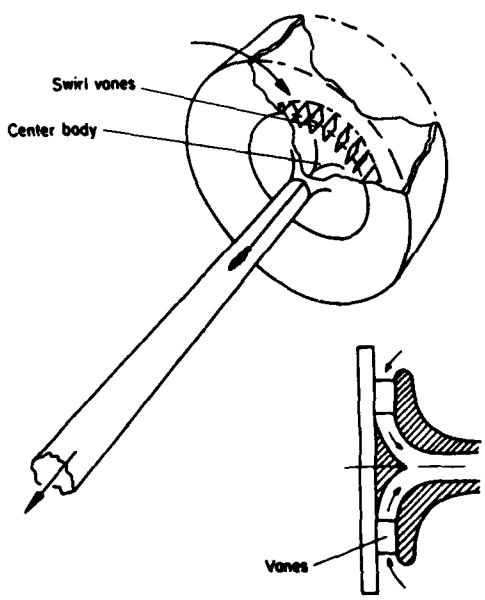

Figure 5

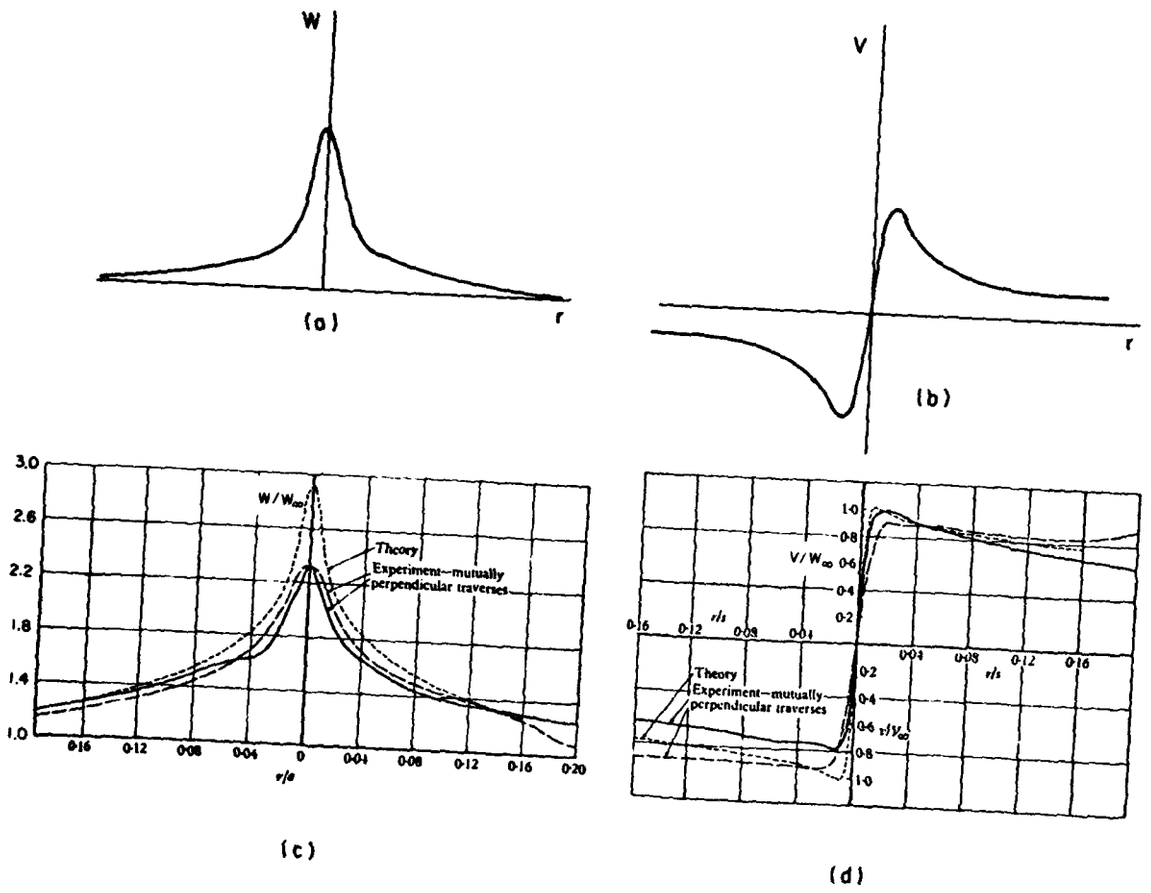
W
r
(a)
V
r
(b)
3.0
2.6
2.2
1.8
1.4
1.0
W/W∞
Theory
Experiment—mutually perpendicular traverses
0·16 0·12 0·08 0·04 0 0·04 0·08 0·12 0·16 0·20
r/a
(c)
1·0
0·8
V/W∞ 0·6
0·4
0·2
r/s
0·16 0·12 0·08 0·04
0·04 0·08 0·12 0·16
r/s
Theory
Experiment—mutually perpendicular traverses
0·2
0·4
0·6
0·8
1·0
r/½w∞
(d)

Figure 6

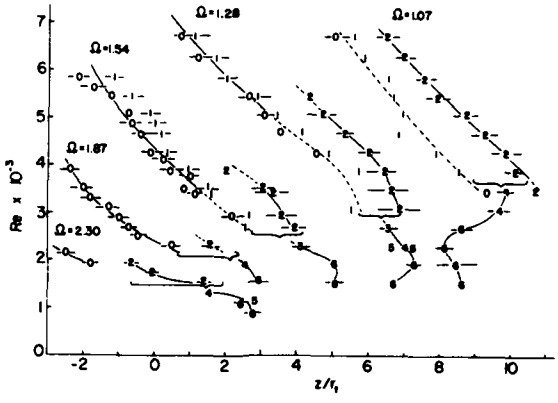

Figure 7

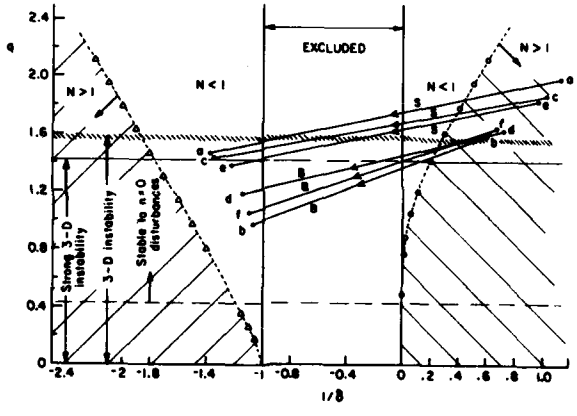

Figure 8

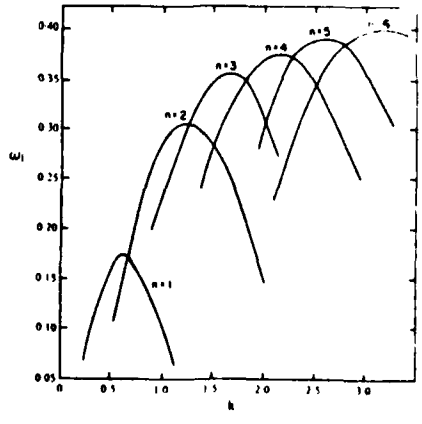

Figure 9

THE BREAK-UP MECHANISM OF A STREAMWISE DIRECTED VORTEX

by

Leif N. Persen
Full Professor
Institutt for mekanikk
Universitetet i Trondheim
N.T.H. 7034 Trondheim
Norway

Abstract.

The present paper considers the possible break-up mechanism of a vortex whith its axis paralell to the direction of the mean flow. Such streamwise directed vortices have been considered first of all by G.I. Taylor [1] in his famous investigation of the stability of the flow between two concentric cylinders. H. Görtler [2] has made his studies of streamwise directed vortices along a concave wall. In both these cases the vortices created seem to be very stable in the side-wise direction. However the G.I. Taylor vortices do not change in the direction of the mean flow, and thus do not exhibit any break-up mechanisms. In very many cases encountered under different flow conditions the break-up of a stream-wise directed vortex occurs after a certain distance downstream, and it is the purpose of this presentation to exhibit a possible mechanism whereby such a break-up can occur. This mechanism is inherent in the basic equations of the flow, and as such may also be exhibited on the equations of motion a non-viscous fluid.

List of symbols.

r, ϕ, z	cylindrical coordinates
v_r	radial velocity component
v_ϕ	tangential velocity component
v_z	axial velocity component
Ψ	stream function
ν	kinematic visocity
p	pressure
ρ	density of the fluid
C_1, C_2, C_3	constants of integration
Ω_o	initial angular velocity
ω_o	initial axial velocity
r_o	radius of reference
$\xi = r/r_o$	non dimensional radial coordinate
$\zeta = z/r_o$	non dimensional axial coordinate
κ, k	arbitrary constants
s	swirl parameter

1. The Non-Viscous Problem.

In the Taylor approach to his stability problem the characteristics of the streamwise directed vortex were independent of the coordinate in the direction of the axis of the vortex. One may point out that in this case a "feed-in" mechanism for energy is then needed to maintain the vortex. When the vortex is not being fed in some such way it may be expected that it will vary its characteristics with the axial coordinate. This effect may even be exhibited by a non-viscous problem. The Navier-Stokes' equations in cylindrical coordinates (r, ϕ, z) with no ϕ-dependence present will be:

$$\left.\begin{aligned} v_r\frac{\partial v_r}{\partial r} - \frac{v_\phi^2}{r} + v_z\frac{\partial v_r}{\partial r} &= -\frac{1}{\rho}\frac{\partial p}{\partial r} + \nu\left\{\frac{\partial^2 v_r}{\partial r^2} + \frac{1}{r}\frac{\partial v_r}{\partial r} - \frac{v}{r^2} + \frac{\partial^2 v_r}{\partial z^2}\right\} \\ v_r\frac{\partial v_\phi}{\partial r} + \frac{v_r v_\phi}{r} + v_z\frac{\partial v_\phi}{\partial z} &= \nu\left\{\frac{\partial^2 v_\phi}{\partial r^2} + \frac{1}{r}\frac{\partial v_\phi}{\partial r} - \frac{v_\phi}{r^2} + \frac{\partial^2 v_\phi}{\partial z^2}\right\} \\ v_r\frac{\partial v_z}{\partial r} + v_z\frac{\partial v_z}{\partial z} &= -\frac{1}{\rho}\frac{\partial p}{\partial z} + \nu\left\{\frac{\partial^2 v_z}{\partial r^2} + \frac{1}{r}\frac{\partial v_z}{\partial r} + \frac{\partial^2 v_z}{\partial z^2}\right\} \end{aligned}\right\} \qquad (1.1)$$

with the equation of continuity:

$$\frac{\partial}{\partial r}(rv_r) + \frac{\partial}{\partial z}(rv_z) = 0 \qquad (1.2)$$

This latter equation suggests the introduction of a streamfunction Ψ such that:

$$v_r = -\frac{1}{r}\frac{\partial \Psi}{\partial z} \quad , \quad v_z = \frac{1}{r}\frac{\partial \Psi}{\partial r} \qquad (1.3)$$

If the viscous terms are neglected the second equation (1.1) may be rearranged as follows:

$$rv_r\frac{\partial}{\partial r}(rv_\phi) + rv_z\frac{\partial}{\partial z}(rv_\phi) = 0 \qquad (1.4)$$

which in view of (1.3) may be formulated as:

$$\frac{\frac{\partial}{\partial r}(rv_\phi)}{\frac{\partial}{\partial z}(rv_\phi)} = \frac{\frac{\partial \Psi}{\partial r}}{\frac{\partial \Psi}{\partial z}} \qquad (1.5)$$

It is here not intended to seek a general solution to this problem, but rather to select a certain class of solutions and to work out specific cases. Thus the following expression is introduced:

$$rv_\phi = C_1\Psi \qquad (1.6)$$

where C_1 is a constant. This expression satisfies (1.5) and now only the two remaining equations of motion are to be considered. Neglecting again the influence of viscosity in the first and third equation of motion one may reformulate (1.1) as follows:

$$\left.\begin{aligned} v_z\left(\frac{\partial v_r}{\partial z} - \frac{\partial v_z}{\partial r}\right) - \frac{v_\phi}{r}\frac{\partial}{\partial r}(rv_\phi) &= -\frac{\partial}{\partial r}\left[\frac{p}{\rho} + \frac{1}{2}(v_r^2 + v_\phi^2 + v_z^2)\right] \\ -v_r\left(\frac{\partial v_r}{\partial z} - \frac{\partial v_z}{\partial r}\right) - \frac{v_\phi}{r}\frac{\partial}{\partial z}(rv_\phi) &= -\frac{\partial}{\partial r}\left[\frac{p}{\rho} + \frac{1}{2}(v_r^2 + v_\phi^2 + v_z^2)\right] \end{aligned}\right\} \qquad (1.7)$$

Stressing again the intention to seek only a special case, the following assumption is made:

$$\frac{p}{\rho} + \frac{1}{2}(v_r^2 + v_\phi^2 + v_z^2) = \frac{p_o}{\rho} + C_2\Psi \qquad (1.8)$$

where C_2 and p_o are constants. In view of (1.3) and (1.6) it is now easily verified that the two equations (1.7) are simultaneously, satisfied if:

$$\frac{\partial^2 \Psi}{\partial r^2} - \frac{1}{r}\frac{\partial \Psi}{\partial r} + \frac{\partial^2 \Psi}{\partial z^2} + C_1^2\Psi = C_2 r^2 \qquad (1.9)$$

In this way all equations are satisfied once Ψ is determined from (1.9).

The situation to be considered is given by the following boundary conditions:

$$\left.\begin{aligned} v_r(r,z): \quad & v_r(r_o,z) = 0 \\ v_\phi(r,z): \quad & v_\phi(r,0) = r\Omega_o \\ v_z(r,z): \quad & v_z(r,0) = w_o = \text{constant} \end{aligned}\right\} \qquad (1.10)$$

These conditions mean that the vortex is confined within a cylinderical surface of radius r_o and that no fluid leaves or enters this region through the cylinderical "walls". There is an axial flow which at $z = 0$ is evenly distributed over the circular crossection of the vortex. At the same location the entering fluid is rotating as a rigid body with the angular velocity Ω_o. The interest will be focused on the way this flow develops if and unspecified disturbance in the radial velocity at $z = 0$ is introduced.

A possible solution to this problem is given by:

$$\psi = \frac{C_2}{C_1^2} r^2 + C_3 r J_1(\kappa r) \sinh(kz) \tag{1.11}$$

where C_3 is an additional constant of integration whose physical significance will be explained subsequently. The boundary conditions (1.10) are now used to determine the constants of integration C_1, C_2 and C_3, and κ and k. The non-dimensional variables ξ and ζ are introduced:

$$\xi = r/r_o \ , \quad \zeta = z/r_o \tag{1.12}$$

It is further observed that the Bessel function $J_1(x)$ has zeros at $x = x_i$:

$$J_1(x_i) = 0 \quad (i = 1, 2, \ldots) \tag{1.13}$$

The two constants κ and k are coupled by the relation:

$$\kappa^2 = k^2 + C_1^2 \tag{1.14}$$

If the parameter s is introduced:

$$s = \frac{r_o \Omega_o}{w_o} \tag{1.15}$$

it is possible to write the solution in terms of the velocity components as follows:

$$\left.\begin{aligned} \frac{v_r}{w_o} &= \frac{C_3}{a w_o} J_1(x_1 \xi) \sqrt{x_1^2 - 4s^2} \cosh\left[\sqrt{x_1^2 - 4s^2}\ \zeta\right] \\ \frac{v_\phi}{w_o} &= s\left\{\xi + 2\frac{C_3}{a w_o} J_1(x_1 \xi) \sinh\left[\sqrt{x_1^2 - 4s^2}\ \zeta\right]\right\} \\ \frac{v_z}{w_o} &= 1 + \frac{C_3}{a w_o} x_1 J_o(x_1 \xi) \sinh\left[\sqrt{x_1^2 - 4s^2}\ \zeta\right] \end{aligned}\right\} \tag{1.16}$$

Here the first zero ($x_i = x_1$) of the Bessel function has been used. It is seen that the solution still contains an unknown parameter C_3/aw_o which may be chosen arbitrarily. It represents the magnitude of the velocity component v_r at $\zeta = 0$ which may be considered to represent the initial disturbance at this location. This disturbance is responsible for the further development of the velocity profiles downstreams. These velocity profiles have been plotted in Figs. 1a, 1b and 1c whereby the constants have been assigned the following values:

$$C_3/aw_o = 0.01 \ , \quad s = 1.5 \ , \quad x_1 = 3.8317 \tag{1.17}$$

Several interesting features are present in this solution. First it is noticed that if the parameter s in (1.15) is given a value greater than $x_1/2$, the hyperbolic sine will convert into a trigonometric sine and the flow field splits up into cells in the axial direction. One may conceive of this as one of several ways of break-up of a vortex. If however $s < x_1/2$ the development of the velocity profiles will occur exponentially, and another way of breaking up the vortex can be envisaged.

The development of the velocity profiles shows the following characteristics. The fluid near the axis of the vortex is rotating like a rigid body with an angular velocity that is increasing with increasing distance from the initial position. At the same time the axial velocity is increasing in magnitude at the centerline and decreasing at the "walls". Finally back-flow occurs. At that point the vortex may again be expected to become unstable.

The results exhibited here for a non-viscous fluid may have a bearing on the development of a stream-wise directed vortex in a viscous fluid just as Lord RAYLEIGH's criterion of an inviscid fluid was shown by Taylor , [1] to be a limiting case of the criterion for a viscous fluid.

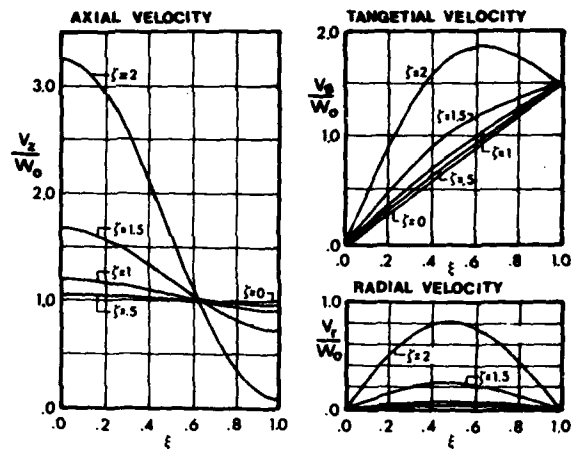

Fig.1 Velocity profiles at increasing downstream locations, ξ.

It was shown above that a development of cells in the axial direction could be demonstrated. This is an effect similar to G.I. Taylor's observation reproduced in Fig.2 where even in the case of rotating cylinders a tendency to formation of cells is visible. Since all experimental evidence to the author's knowledge indicate a final break-down of the vortex system, the mechanism may be as just demonstrated on this simple mathematical model.

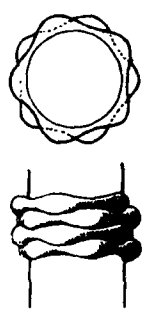

A final remark may be appropriate. The preceding deductions seem to be applicable only in cases where the vortex is confined to a cylinderical space, i.e. cases where the cross-wise dimension does not change with downstream distance. Such a situation is shown in Fig.3 where both the vortices and their break-up region is clearly visible. A similar situation is shown in Fig.4 where striations on a cone indicate the presense of streamwise directed vortices which are very stable in the sidewise direction and where the space occupied by the vortex increases in the cross-wise direction with increasing downstream distance. The break-up of these vortices seems to exhibit the same feature as demonstrated above.

Fig.2 Reproduction of Tylor's [1] original drawing showing the instability of the vortices.

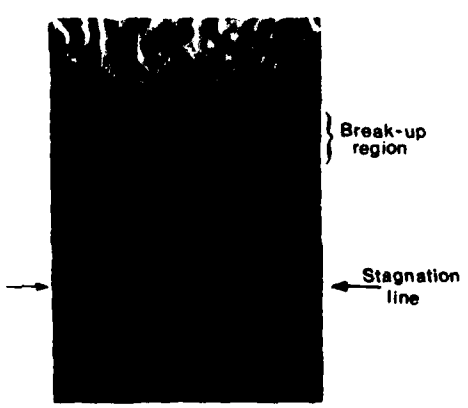

Fig.3 Streamwise directed vortices and their break-up in the region downstream of a stagnation line on a cylinder in crossflow.

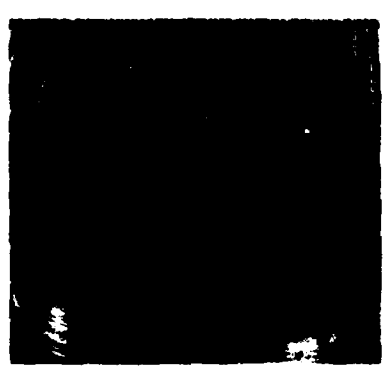

Fig.4 Striations on a cone in axial flow caused by streamwise directed vortices.

BIBLIOGRAPHY

[1] G.I. Taylor: "Stability of a Viscous Liquid contained between Two Rotating Cylinders", Roy.Soc.Proc., Series A, Vol. CCXXIII, A-612, 1923 p.289-343.

[2] H. Görtler: "Instabilität laminarer Grenzschichten an konkaven Wänden gegenüber gewissen dreidimensionalen Störungen", ZAMM, Vol.21, No.4, Aug. 1941.

VORTEX BREAKDOWN: A TWO-STAGE TRANSITION

M.P. Escudier and J.J. Keller
Brown Boveri Research Centre
CH-5405 Baden, Switzerland

SUMMARY

It is demonstrated that a large-scale isentropic transition between conjugate swirling flow states can occur with no change in the flow force and that both flow states are supercritical. It is argued that such a transition represents the first stage of vortex breakdown in a tube, the second stage being a non-isentropic transition in the nature of a hydraulic jump to the downstream subcritical state. The intermediate (supercritical) state consists of a zone of stagnant fluid surrounded by a region of potential flow. These two zones are separated by a layer of rotational fluid originating in the upstream vortex core. An outline is given of the analysis for an upstream flow modelled as a Rankine vortex. It is found that for any ratio of core-to-tube radii, breakdown (i.e. the first transition) occurs for a unique value of the swirl number $\Gamma/4\pi U$. In the limiting case of an infitesimally small core, the value is $\sqrt{2}$, compared with the critical value 2·405. It is argued that this limit cannot represent free breakdown, which in consequence must have a different character from the tube-flow breakdowns generally observed.

INTRODUCTION

Previous efforts to explain the phenomenon of vortex breakdown have been centred upon the concept of a single transition, either in the sense of Benjamin's [1] conjugate-state analysis or stability theories such as those of Ludwieg [2] and, most recently, Leibovich [3]. For the most part, these efforts have been limited to weak transitions. The experimental evidence reported by Harvey [4], Sarpkaya [5] and others [6,7], in contrast, shows breakdown to be invariably a strong perturbation of the flow, as has been emphasized by, for example, Hall [8] and Leibovich [9]. We present a new and simple approach to the problem of vortex breakdown in tube flow which yields a simple breakdown criterion and is consistent with the observed characteristics of the phenomenon.

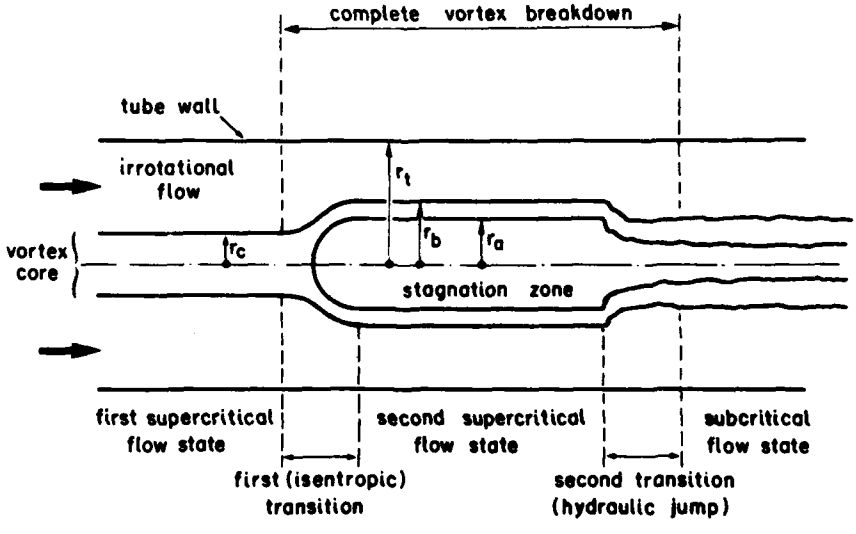

Figure 1. Schematic diagram illustrating the idealized process of vortex breakdown in a cylindrical tube.

The key features of the process of vortex breakdown in a tube are illustrated in figure 1. We propose that the transition may involve two stages, the first isentropic from the initial supercritical state to an intermediate state which is also supercritical. The second stage of the transition, to the downstream subcritical state, is non-isentropic, much like a hydraulic jump or shock wave. The crucial new idea here is that the first transition is both isentropic and also involves no change in the flow force even for a large-scale transition. The latter possibility has been overlooked until recently [10], most significantly by Benjamin [1]. A striking consequence of the analy-

sis is that for a given upstream vortex structure, breakdown occurs only for a unique value of the swirl number $\Gamma/\pi r_c U$ (an inverse Rossby number): e.g. $\sqrt{2}$ for a Rankine vortex with an infinitesimally small core radius r_c. Another prediction is that breakdown is also possible for a purely irrotational swirling flow: the example considered is that of flow in an annulus. Complete details of the analysis are given in two recent papers [10,11] and only the barest essentials are excerpted here to emphasize the principal assumptions and results. We also present the results of a number of experiments in support of the analysis and speculate on the nature of free vortex breakdown and on the real and apparent differences between the axisymmetric and spiral forms of breakdown.

VORTEX BREAKDOWN IN A CYLINDRICAL TUBE - ANALYSIS

A convenient model for the upstream flow state (1) (see figure 1) is the Rankine vortex:

$$v = \begin{cases} \Gamma r/2\pi r_c^2 & \text{if} \quad 0 < r < r_c \\ \Gamma/2\pi r & \text{if} \quad r_c < r < r_t \end{cases} \qquad (1)$$

$$w = \text{constant} = U$$

where v and w are the swirl and axial components of velocity, r_c is the core radius, r_t the tube radius and Γ the circulation. The intermediate state (2) is also assumed to be cylindrical with an inner stagnation region of radius r_a separated from the outer potential flow by a layer $r_a < r < r_b$ of rotational fluid originating in the upstream vortex core. The flow between these two states is assumed to be steady, incompressible, axisymmetric and inviscid. The equation governing the intermediate flow state is then [12]

$$\frac{d^2\phi}{dr^2} + \frac{1}{r}\frac{d\phi}{dr} - \frac{\phi}{r^2} = \begin{cases} -k^2\phi & \text{if} \quad r_a < r < r_b \\ 0 & \text{if} \quad r_b < r < r_t \end{cases} \qquad (2)$$

where $r\phi$ is the departure of the stream function from its upstream form and

$$k = \Gamma/\pi r_c^2 U \ . \qquad (3)$$

Specification of the intermediate state is completed by introducing appropriate matching conditions at r_a, r_b and r_t, i.e. constancy of the stream function on stream surfaces, continuity of the velocity across the interface $r = r_b$ and zero velocity at $r = r_a$. The solution of equation (2) and calculation of the distributions of v, w and the static pressure p (from $dp/dr = \rho v^2/r$) is then straightforward (see [10] - [12]).

To answer the question which pair of conjugate flow states corresponding to the preceding analysis is physically realistic, we must consider the momentum equation. We define first the flow force S by

$$S = 2\pi\int_0^{r_t}(\rho w^2 + p)r\,dr \qquad (4)$$

where ρ is the fluid density. Using the results already obtained, the flow force difference between the first and second flow states may be shown to be

$$\Delta S = \frac{\pi}{4}\rho U^2 k^2 r_c^2\left[-r_b^2 + \frac{1}{4}\left(\frac{r_b^4 - r_a^4}{r_c^2}\right) + \frac{3}{4}r_c^2 + \frac{1}{2}r_c^2\,\ell n\left(\frac{r_b^2}{r_c^2}\right)\right]. \qquad (5)$$

Since we are considering flow in a cylindrical tube, with no means of applying an external force to the flow, the <u>difference $\Delta S \equiv 0$</u>. The values of kr_c (= $\Gamma/\pi r_c U$) for which this identity is satisfied are plotted in figure 2 as a function of r_c/r_t together with the corresponding critical values of kr_c obtained from [1]

$$\frac{1}{2}\frac{kr_c\,J_0(kr_c)}{J_1(kr_c)} = \frac{-1}{(r_t/r_c)^2 - 1} \ . \qquad (6)$$

It is found that the upstream flow (for $\Delta S = 0$) is always supercritical (i.e. kr_c less than the critical value), as is the intermediate flow state which can be demonstrated on the basis of a variational principle [1,10]. As mentioned in the INTRODUCTION, this possibility of a non-trivial supercritical-supercritical transition was only recently recognized [10] and is suggested to be the key to understanding vortex breakdown. For the Rankine vortex, it turns out that for any value of r_c/r_t the first transition occurs for a unique value of kr_c. More generally it may be shown [10] that for given distributions of w(r) and v(r) the speed at which the vortex breakdown structure moves is unique. The subsequent transition to the downstream flow state must be dissipative, and can be treated essentially as a hydraulic jump.

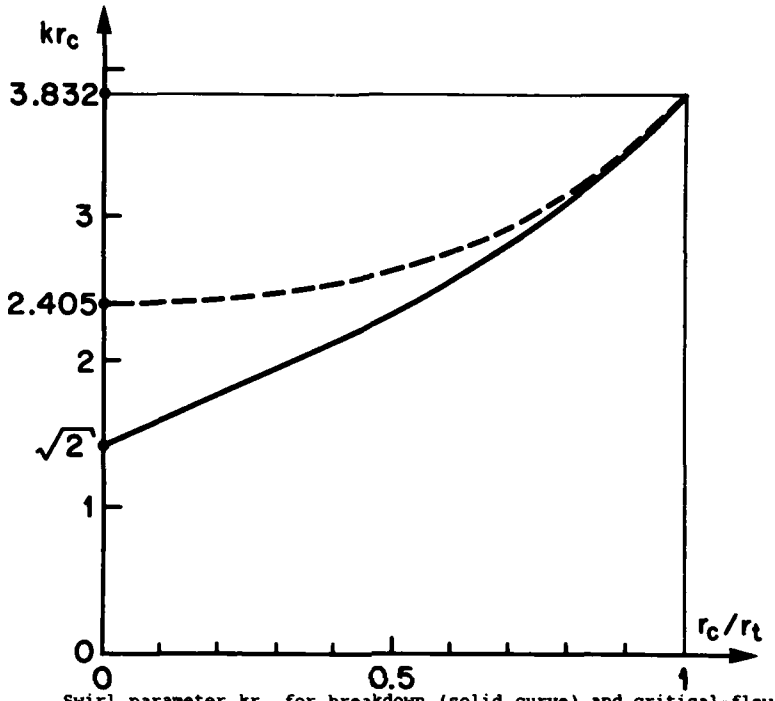

Figure 2. Swirl parameter kr_c for breakdown (solid curve) and critical-flow (broken curve) conditions as a function of normalized core radius.

A remarkable result of the analysis is that a non-trivial transition is predicted even for the asymptotic situation $r_c/r_t \to 0$. In this case

$$kr_c = \sqrt{2} \quad \text{for breakdown}$$
$$kr_c = 2{\cdot}405 \quad \text{for the critical state .} \qquad (7)$$

At first sight it might appear that the asymptote $r_c/r_t \to 0$ is relevant to the case of a free vortex ($r_t \to \infty$). However, an asymptotic analysis, which was the subject of [10], shows that this is not the case. In particular, it is found that for $r_c/r_t \to 0$, $r_c/r_b \to 0$ whereas for a free vortex it must be the case that r_c/r_b assumes a value different from zero. It has to be concluded that the free vortex represents a second type of transition compared to that which we have considered, and that this is a direct supercritical - subcritical transition necessarily involving dissipation. A corollary is that investigations of vortex breakdown in tubes are not directly representative of free-vortex breakdown.

Within the small-core approximation, the ideas contained here have been extended to the analysis of general vortex flow in a tube, including the possibility of area changes. In many circumstances it is possible and convenient to relate the actual flow to a fictitious reference Rankine vortex. An interesting result for flows with a strong overshoot in the axial velocity, as is produced by a strong area reduction, is that the critical and breakdown values of kr_c are proportional. This is suggested to be the main reason why Escudier and Zehnder [7] were able to make quite accurate predictions of breakdown on the basis of the criticality condition.

VORTEX BREAKDOWN IN A CYLINDRICAL TUBE - OBSERVATIONS

The two examples of axisymmetric vortex breakdown shown in figure 3 are typical of those reported by Harvey [4], Sarpkaya [5] and others [6,7]. Here advantage has been taken of the laser-induced fluorescence visualisation technique to reveal the inner structure of a breakdown bubble. Fluorescein dye has been injected on the tube axis into the upstream flow. The flow was illuminated by a rapidly oscillating Argon-ion laser beam sweeping through a diametral plane of the tube (further details of the experiment are given in [10] and [13]). Two features may be observed from figure 3 which support the interpretation of vortex breakdown proposed here. First, the fluid entering the bubble in each case clearly emanates from a region much smaller in radius than that of the bubble itself (and also much smaller in radius than the core), and the latter must therefore be a zone of essentially stagnant fluid. Secondly, the smooth appearance of

the bubble surface, even when the interior is turbulent, suggests that the first stage of the transition involves little dissipation. It may be remarked that the intermediate state may be masked by spreading of the shear layer at very low Reynolds numbers and by instability and roll up at higher Reynolds numbers.

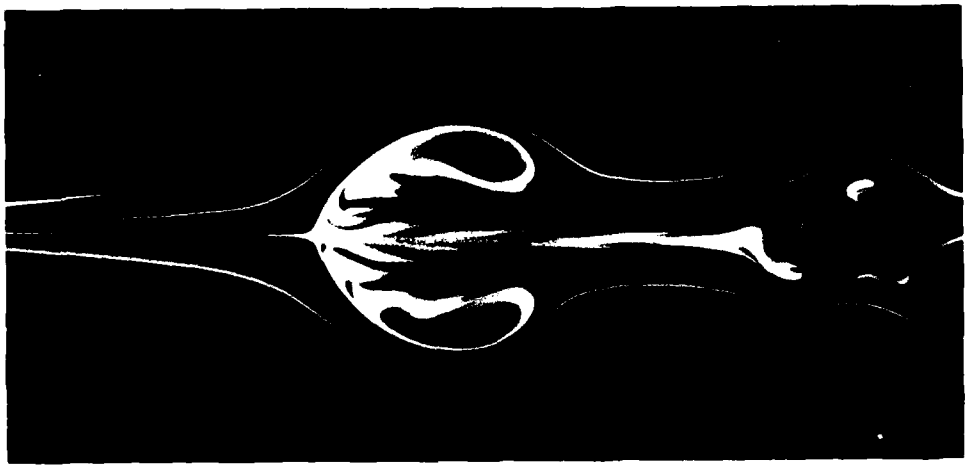

(a) $Ur_t/\nu = 575$

(b) $Ur_t/\nu = 1650$

Figure 3. Examples of vortex breakdown in a cylindrical tube. (Flow from left to right)

The internal structure which may be inferred from flow visualisation is confirmed by laser Doppler anemometry measurements: axial velocity profiles w(r;x) together with the corresponding streamline map for a low Reynolds number breakdown bubble are shown in figure 4. It may be noted that a consequence of the subcritical nature of the flow downstream of such a bubble is that the detailed structure of the bubble itself and the downstream flow are strongly influenced by the downstream geometry and conditions.

The problem of masking of the intermediate flow state, mentioned above, may be overcome by injecting air into the bubble as in the situation shown in figure 5. The smooth character of the first transition is again evident as is the more disturbed nature of the second (the hydraulic jump). The flow conditions are those under which a normal breakdown would occur in the absence of air injection.

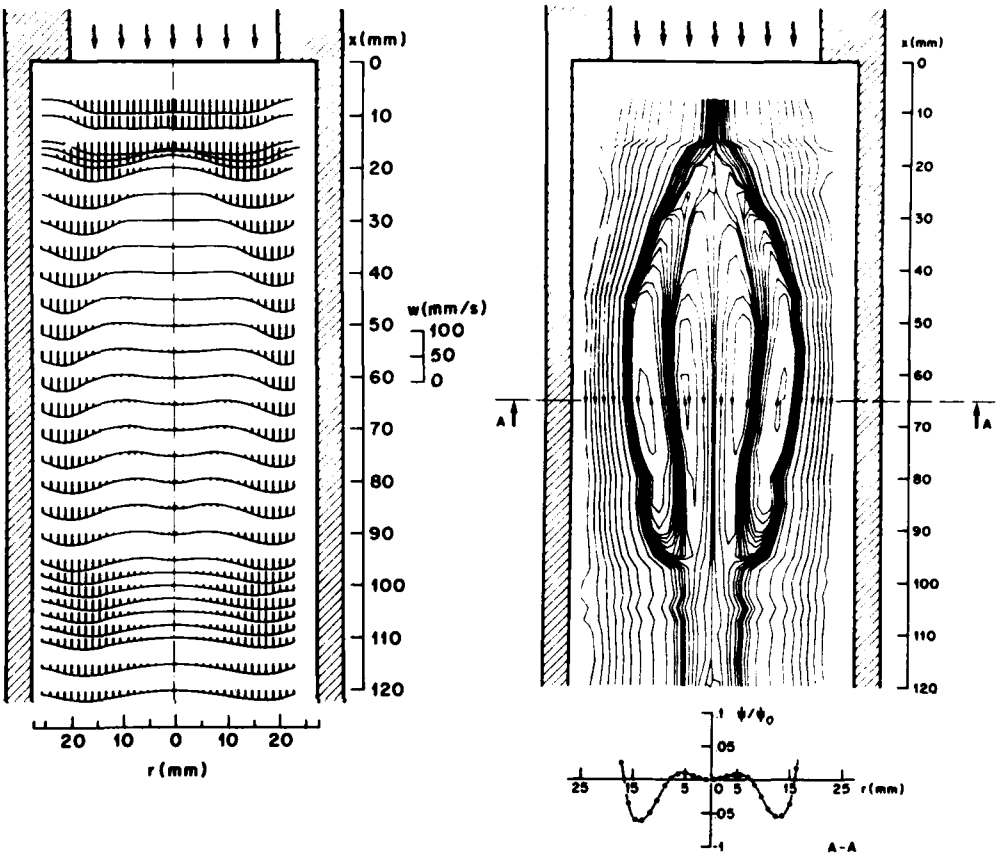

Figure 4. Measured axial velocity profiles w(r;x) and streamline map $\psi(r;x)$ for vortex breakdown in a cylindrical tube with $Ur_t/\nu = 265$.

Figure 5. An air-filled vortex-breakdown bubble. (Flow from left to right. Arrows indicate transition locations)

BREAKDOWN OF POTENTIAL FLOW IN AN ANNULUS - ANALYSIS

We consider here a swirling potential flow confined between concentric cylinders. The upstream flow state is defined by

$$\begin{aligned} v &= \Gamma/2\pi r \\ w &= U \end{aligned} \qquad r_c < r < r_t \tag{8}$$

i.e. we can imagine the viscous core in figure 1 to be replaced by a solid rod. The second or intermediate flow state is assumed to consist of an annulus of stagnant fluid of outer radius r_b surrounded by a potential vortex

i.e. $$\begin{aligned} v &= \Gamma/2\pi r \quad \text{and} \quad w = W \quad \text{if } r_b < r < r_t \\ v &= 0 \quad\quad\;\; \text{and} \quad w = 0 \quad \text{if } r_c < r < r_b \end{aligned} \tag{9}$$

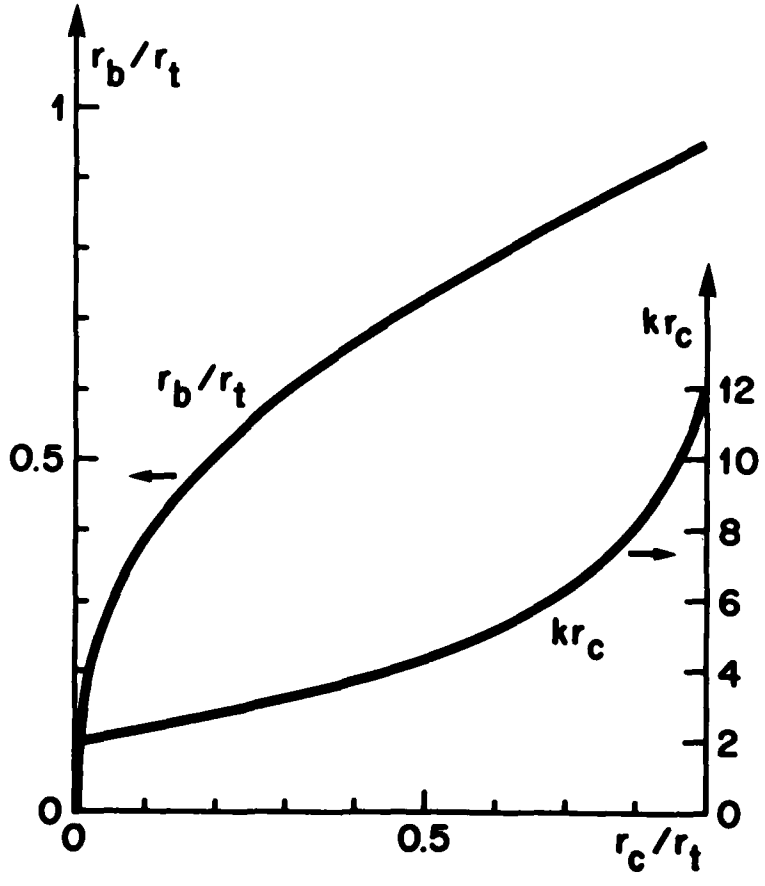

Figure 6. Normalized bubble radius and breakdown swirl parameter kr_c versus normalized inner radius for annular breakdown.

The assumption of an isentropic transition between these two flow states then leads to [10]

$$\left(\frac{r_t^2 - r_c^2}{r_t^2 - r_b^2}\right)^2 = \frac{1}{4}(kr_c)^2\left(1-\frac{r_c^2}{r_b^2}\right) \tag{10}$$

whilst for the flow-force difference we have

$$\Delta S = \frac{\pi}{2}\rho U^2 r_b^2\{[1-(\frac{r_c}{r_b})^2](\frac{r_t^2-r_c^2}{r_t^2-r_b^2})-\frac{1}{4}(kr_c)^2[1-(\frac{r_c}{r_b})^2+2(\frac{r_c}{r_b})^2 ln(\frac{r_c}{r_b})]\} \quad (11)$$

Setting $\Delta S = 0$ as before leads to kr_c and r_b/r_t as functions of r_c/r_t, as plotted in figure 6. In this case the criticality condition for the downstream flow [14] is

$$(kr_c)^2 = \frac{8r_b^4(r_t^2-r_c^2)^2}{r_c^2(r_t^2-r_b^2)^3} \quad (12)$$

and it is again found that this flow state is always supercritical.

BREAKDOWN OF POTENTIAL FLOW IN AN ANNULUS - OBSERVATIONS

Flow visualisation confirms the occurence of large-scale transitions for swirling flow in an annulus. In the first example (figure 7) multiple breakdowns are evident. Although the viscous core has been "replaced" by a solid rod, viscous influences are undoubtedly responsible for producing the conditions which allow successive breakdowns. The introduction of air into the breakdown region again produces a breakdown bubble similar to that predicted (figure 8). It is found that unless conditions closely match those corresponding to the analysis, air introduced into the flow either penetrates far upstream (kr_c too large) or is swept away (kr_c too small).

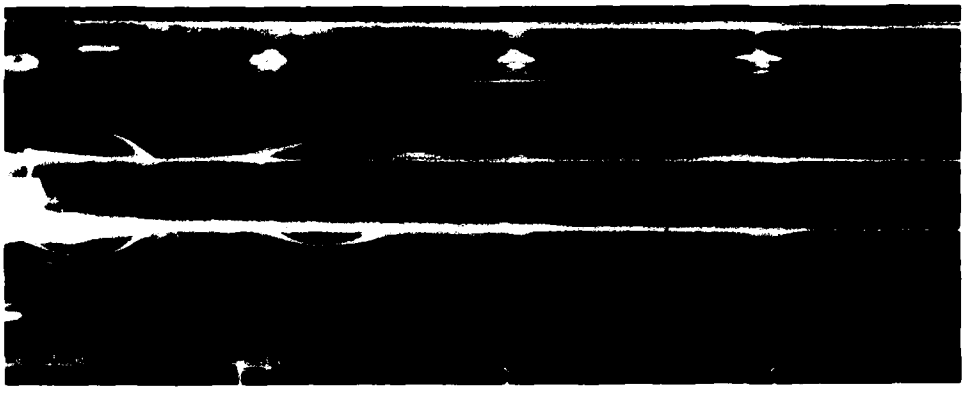

Figure 7. Successive annular breakdowns. (Flow from left to right)

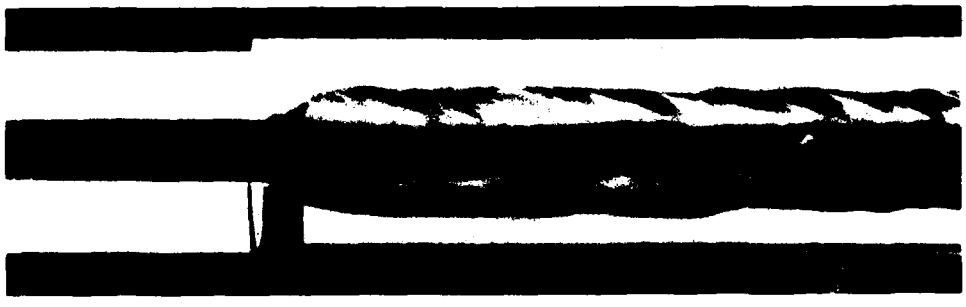

Figure 8. An air-filled annular breakdown. (Flow from left to right)

CONCLUDING REMARKS

The concept proposed here for the explanation of vortex breakdown has been worked out in detail using the Rankine vortex as a model for the upstream flow. The advantage of this formulation is that the equation for the stream function (2) is then linear both within the rotational layer ($r_a < r < r_b$) and also within the surrounding potential flow ($r_b < r < r_t$). As has been indicated, more complex flow situations can be analysed with reference to a fictitious reference Rankine vortex. Such an analysis has been carried out in [10] within the small-core approximation, a restriction which can also be dis-

pensed with as shown in [11]. Any more general analysis would evidently require numerical integration of the equation governing the stream function ψ (the Long [15]-Squire [16] equation) for a cylindrical flow

$$\frac{\partial^2\psi}{\partial r^2} - \frac{1}{r}\frac{\partial\psi}{\partial r} = \frac{r^2}{\rho}\frac{dH}{d\psi} - K\frac{dK}{d\psi} \qquad (13)$$

wherein H is the dynamic head and K = rv. Such an exercise would undoubtedly provide more accurate results for particular flows, but would be unlikely to contribute significantly to further understanding of the breakdown phenomenon.

We have already speculated that free-vortex breakdown represents a different type of transition to that for tube flow. By way of further speculation we suggest that there is no fundamental difference between the so-called spiral type of breakdown and the axisymmetric bubble type we consider here. The spiral character is suggested to be a consequence of azimuthal instability leading to roll up and detachment of the shear layer surrounding a bubble. This detachment process would then lead to a precessive motion of the near-stagnant interior fluid. Strong evidence in support of this point of view comes from the experiments of Escudier and Zehnder [7] who found the correlation of experimental breakdown data in terms of the simple criterion Γ^2/UvL = constant to be independent of the breakdown's appearance. It is also well known [8] that the spiral and axisymmetric breakdown forms are found in the same continuous range and are even interchangable under appropriate conditions. A further point is that were the spiral form inherently non-axisymmetric, the spiral would have to remain stationary, as is observed for the non-axisymmetric standing-wave patterns for hollow-core vortices [14].

REFERENCES

1. T.B.Benjamin. Theory of the vortex breakdown phenomenon. J. Fluid Mech. 14, 593-629 (1962).

2. H. Ludwieg. Zur Erklärung der Instabilität der über angestelllten Deltaflügeln auftretenden freien Wirbelkerne. Z. Flugwiss. 10, 242-249 (1962).

3. S. Leibovich. Wave propagation, instability, and breakdown of vortices. In "Vortex Flows", 50-67, Ed. Hornung and Müller, Vieweg (1982).

4. J.K. Harvey. Some observations of the vortex breakdown phenomenon. J. Fluid Mech. 14, 585-592 (1962).

5. T. Sarpkaya. On stationary and travelling vortex breakdowns. J. Fluid Mech. 45, 545-559 (1971).

6. J.H. Faler and S. Leibovich. Disrupted states of vortex flows and vortex breakdown. Phys. Fluids 20, 1385-1400 (1977).

7. M.P. Escudier and N. Zehnder. Vortex flow regimes. J. Fluid Mech. 115, 105-121 (1982).

8. M.G. Hall. Vortex breakdown. Ann. Rev. Fluid Mech. 4, 195-218 (1972).

9. S. Leibovich. The structure of vortex breakdown. Ann. Rev. Fluid Mech. 10, 221-246 (1978).

10. J.J. Keller, M.P. Escudier and J. Bornstein. The physics of vortex breakdown. (1982). Submitted for publication.

11. J.J. Keller. Breakdown of a Rankine vortex. (1983). Submitted for publication.

12. G.K. Batchelor. An introduction to fluid dynamics. Cambridge University Press. (1967).

13. J. Bornstein and M.P. Escudier. LDA measurements within a vortex-breakdown bubble. Proc. Int. Symp. on Applications of Laser Doppler Anemometry. Lisbon, (1982).

14. J.J. Keller and M.P. Escudier. Theory and observations of wave on hollow-core vortices. J. Fluid Mech. 99, 495-511 (1980).

15. R.R. Long. Steady motion around a symmetrical obstacle moving along the axis of a rotating fluid. J. Meteor 10, 197-203 (1953).

16. H.B. Squire. Rotating fluids. In "Surveys in mechanics". 139-161, Ed. Batchelor and Davies, Cambridge University Press (1956).

A Contribution to the Problem of Vortex Breakdown

E. Krause
Aerodynamisches Institut der RWTH Aachen
Aachen, Germany

Summary

Associated with the breakdown process is the formation of a stagnation point on the axis of the vortex. This requires the deceleration of the axial velocity component, which must be enforced by a positive axial pressure gradient. The analysis presented here shows, how the pressure gradient along the axis of the vortex is influenced by the radial and azimuthal velocity components. An explicit expression for $\partial p/\partial x\,(x,0)$ can be obtained by integration of the momentum equation for the radial velocity component with respect to the radial and subsequent differentiation of the integral with respect to the axial direction. In an order of magnitude analysis it is then demonstrated that for large Reynolds numbers one component of the frictional force in the azimuthal direction cannot be neglected. In order to obtain an estimate for the pressure gradient rigid body rotation is assumed for the vortex core, and a distribution similar to that of a potential vortex $w = kr^{-n}$, for the outer portion. The estimate shows that a positive axial pressure gradient can exist only, if the radial velocity component is positiv and if the exponent n is less than unity. It is also verified that a potential vortex cannot support an axial pressure gradient, that the pressure gradient in magnitude is directly proportional to the square of the maximum of the azimuthal velocity, referenced to the freestream velocity.

1. Introduction

In reference [1] S. Leibovich comments on the effects of the pressure gradients on vortex breakdown:
"Vortex breakdown is promoted by adverse pressure gradients (pressure increasing in the direction of flow). Pressure gradients may be impressed upon the vortex core by an acceleration of the outer flow (e. g. by shaping the walls of a confining tube); from pressure differences along the vortex core caused by a sudden expansion if the tube abruptly ends; or, in the leading-edge vortex, from the pressure rise associated with the trailing edge of a swept wing."

M. G. Hall summarizes in [2] (as quoted in [1]) the role of an applied pressure gradient: "When an adverse pressure gradient is increased, less swirl is required to maintain breakdown, or, if the same level of swirl is maintained, the breakdown is moved upstream".

It is this point which is investigated in this paper. The analysis was motivated by a numerical study, reported in [3] . In that study, it was assumed that the radial distribution of the axial, radial and azimuthal velocity components were known at some initial station. The equations of motion were simplified in the spirit of Prandtl's boundary-layer theory and integrated with an implicit finite-difference solution under the assumption of axisymmetric flow. The results of the integration showed that the axial velocity component approached zero with increasing distance from the initial station if certain specific initial distributions of the velocity vector were prescribed. For very small values of $u(x,r = 0)$, (u being the axial velocity component) the solution did not converge any more, yielding physically unrealistic results as in the vicinity of boundary-layer separation. In addition, it was found, that if a positive pressure gradient was superimposed in the axial direction for $r \to \infty$, the solution diverged at a point closer to the initial station than for the zero-pressure gradient flow. These results, although at least qualitatively known before the investigation [3] was carried out, for example, from Sarphaya's experiments [4] , were also implemented by R. Staufenbiel in his experimental studies of wing tip vortices [5]. By placing an annular diffusor about the vortex he showed that he could locally break the vortex at any arbitrary position downstream from the wing. These observations as well as the comments made by S. Leibovich and M. G. Hall and the results of the numerical studies reported in [3] ,stipulated the question, as to whether or not this behaviour of the flow could not directly be confirmed by inspection of the governing equations, put into a suitable form. Despite of the rather large body of literature (see, for example, the literature survey in S. Leibovich's review on vortex breakdown [1]) such an investigation was - to the author's knowledge - not reported before. The development of an analysis which shows the dependence of the pressure gradient along the axis of the three velocity components is given in the following.

It must be clear from the beginning, that the analysis does not intend to integrate the equations of motion in order to obtain a solution to the problem of vortex breakdown. Because of its highly non-linear character such a goal cannot be achieved without efforts; instead it is intended to extract general information from the governing equations in order to explain the overall behaviour of the flow and find out what simplifications are admissable upstream of the point of vortex breakdown.

2. Analysis

The flow upstream of the point of breakdown is assumed to be incompressible, steady and axisymmetric. The assumption of steady flow conditions is confirmed by experiments, see for example [2]; the assumption of axisymmetric flow implies that the azimuthal velocity component is essentially smaller than the axial component. As is also known from experiments the core of the vortex does, under such conditions, not change its diameter substantially, indicating that the radial velocity component is small and that the highest order derivatives in the axial direction can be neglected. It needs not be emphasized, that these assumptions become invalid downstream from the point of breakdown, as was, for example, also confirmed in [3], in addition to prior experimental evidence, reported in [1] and elsewhere.

With the omission of the highest order terms in the axial direction, describing the corresponding components of the frictional force per unit volume, and the terms describing the variation in the azimuthal direction, the governing equations read:

Continuity equation $$\frac{\partial}{\partial x}(ru) + \frac{\partial}{\partial r}(rv) = 0 \qquad (2.1)$$

Radial momentum equation

$$u\frac{\partial v}{\partial x} + v\frac{\partial v}{\partial r} - \frac{w^2}{r} = -\frac{1}{\varrho}\frac{\partial p}{\partial r} + \nu\left[\frac{\partial}{\partial r}\left(\frac{1}{r}\frac{\partial}{\partial r}(rv)\right)\right] \tag{2.2}$$

Azimuthal momentum equation

$$u\frac{\partial w}{\partial x} + v\frac{\partial w}{\partial r} + \frac{vw}{r} = \nu\left[\frac{\partial}{\partial r}\left(\frac{1}{r}\frac{\partial}{\partial r}(rw)\right)\right] \tag{2.3}$$

Axial momentum equation

$$u\frac{\partial u}{\partial x} + v\frac{\partial u}{\partial r} = -\frac{1}{\varrho}\frac{\partial p}{\partial x} + \nu\left[\frac{1}{r}\frac{\partial}{\partial r}\left(r\frac{\partial u}{\partial r}\right)\right] \tag{2.4}$$

All quantities have the usual meaning, with u, v, and w being the axial, radial, and azimuthal velocity components, respectively.

Equs. (2.1) - (2.4) are next rewritten in dimensionless form. In accord with the assumption stated above, it is justified to assume that the core radius R is much smaller than the distance L between the point of initiation and of breakdown of the vortex, i. e., $R \ll L$; consequently, the order of magnitude of v/u_∞ is $\epsilon = R/L$. The reference velocity for the azimuthal velocity component can be chosen arbitrarily. It can therefore be expressed in terms of the undisturbed axial velocity components u_∞, say $w_R = \alpha u_\infty$, where the subscript R denotes the reference velocity, and α some factor, either smaller or larger than unity. With the pressure normalized with ϱu_∞^2 the nondimensionalized equations read

$$\frac{\partial}{\partial x}(ru) + \frac{\partial}{\partial r}(rv) = 0 \tag{2.5}$$

$$\left(u\frac{\partial v}{\partial x} + v\frac{\partial v}{\partial r}\right)\epsilon^2 - \frac{\alpha^2 w^2}{r} = -\frac{\partial p}{\partial r} + \frac{1}{Re}\left[\frac{\partial}{\partial r}\left(\frac{1}{r}\frac{\partial}{\partial r}(rv)\right)\right] \tag{2.6}$$

$$u\frac{\partial w}{\partial x} + v\frac{\partial w}{\partial r} + \frac{vw}{r} = \frac{1}{Re\,\epsilon^2}\left[\frac{\partial}{\partial r}\left(\frac{1}{r}\frac{\partial}{\partial r}(rw)\right)\right] \tag{2.7}$$

$$u\frac{\partial u}{\partial x} + v\frac{\partial u}{\partial r} = -\frac{\partial p}{\partial x} + \frac{1}{Re\,\epsilon^2}\left[\frac{1}{r}\frac{\partial}{\partial r}\left(r\frac{\partial u}{\partial r}\right)\right] \tag{2.8}$$

In the system of equations, Equs. (2.5) - (2.8), all variables are now dimensionless quantities, with v/u_∞ stretched by R/L.

Equ. (2.6) is now integrated with respect to r; there results

$$p(x,0) = p(x,\infty) + \int_0^\infty \left[\left(u\frac{\partial v}{\partial x} + v\frac{\partial v}{\partial r}\right)\epsilon^2 - \frac{\alpha^2 w^2}{r}\right]dr - \frac{1}{Re}\int_0^\infty \frac{\partial}{\partial r}\left(\frac{1}{r}\frac{\partial}{\partial r}(rv)\right)dr \tag{2.9}$$

By making use of the continuity equation, the last equation can be casted into the following form:

$$p(x,0) - p(x,\infty) = \int_0^\infty \left[\left(u^2\frac{\partial}{\partial x}\left(\frac{v}{u}\right) - \frac{v^2}{r}\right)\epsilon^2 - \frac{\alpha^2 w^2}{r}\right]dr + \frac{1}{Re}\left(\frac{\partial u}{\partial x}(x,\infty) - \frac{\partial u}{\partial x}(x,0)\right) \tag{2.10}$$

From Equ. (2.10) it is clear that the vortex can exist only as long as the right-hand side remains negative. Vice versa, if the pressure difference and the gradients of the axial velocity component tend to zero, the azimuthal velocity component must vanish.

If the flow along the axis is to approach a stagnation point, the pressure along the axis must increase, i. e. $\partial p/\partial x\,(x,0) > 0$. An expression for the pressure gradient can be obtained by differentiating Equ. (2.10) with respect to the axial coordinate. With the definitions

$$\begin{aligned}(\Delta p)_r &= p(x,0) - p(x,\infty)\\ (\Delta u)_r &= u(x,0) - u(x,\infty)\end{aligned} \tag{2.11}$$

there results

$$\frac{\partial}{\partial x}(\Delta p)_r = \epsilon^2\int_0^\infty \left[2u\frac{\partial u}{\partial x}\frac{\partial}{\partial x}\left(\frac{v}{u}\right) + u^2\frac{\partial}{\partial x}\left(\frac{v}{u}\right) - \frac{2v}{r}\frac{\partial v}{\partial x}\right]dr - \alpha^2\int_0^\infty \frac{2w}{r}\frac{\partial w}{\partial x}dr - \frac{1}{Re}\frac{\partial^2}{\partial x^2}(\Delta u)_r \tag{2.12}$$

The axial gradient of the azimuthal velocity component can be replaced by Equ. (2.7):

$$\frac{\partial w}{\partial x} = -\frac{v}{ur}\frac{\partial}{\partial r}(rw) + \frac{1}{u\,Re\epsilon^2}\left[\frac{\partial}{\partial r}\left(\frac{1}{r}\frac{\partial}{\partial r}(rw)\right)\right] \tag{2.13}$$

With Equ. (2.13), Equ. (2.12) becomes

$$\begin{aligned}\frac{\partial}{\partial x}(\Delta p)_r = \epsilon^2\int_0^\infty &\left[2u\frac{\partial u}{\partial x}\frac{\partial}{\partial x}\left(\frac{v}{u}\right) + u^2\frac{\partial^2}{\partial x^2}\left(\frac{v}{u}\right) - \frac{2v}{r}\frac{\partial v}{\partial x}\right]dr - \frac{1}{Re}\frac{\partial^2}{\partial x^2}(\Delta u)_r\\ &- \frac{2\alpha^2}{Re\,\epsilon^2}\int_0^\infty \left[\frac{w}{u}\frac{1}{r}\frac{\partial}{\partial r}\left(\frac{1}{r}\frac{\partial}{\partial r}(rw)\right)\right]dr + 2\alpha^2\int_0^\infty \frac{v}{u}\frac{w}{r^2}\frac{\partial}{\partial r}(rw)\,dr\end{aligned} \tag{2.14}$$

If the order of magnitude assumptions stated earlier, namely

$$\alpha < 1 \quad , \quad \varepsilon^2 << 1 \quad , \quad Re >> 1 \quad , \quad Re\,\varepsilon^2 = O(1) \tag{2.15}$$

are introduced in Equ. (2.14), there is finally obtained

$$\frac{\partial}{\partial x}(\Delta p)_r = -\frac{2\alpha^2}{Re\,\varepsilon^2}\int_0^\infty \left[\frac{w}{u}\frac{1}{r}\frac{\partial}{\partial r}\left(\frac{1}{r}\frac{\partial}{\partial r}(rw)\right)\right]dr + 2\alpha^2\int_0^\infty \left(\frac{v}{u}\frac{w}{r^2}\frac{\partial}{\partial r}(rw)\right)dr \tag{2.16}$$

Equ. (2.16) shows that to zeroth order the pressure gradient along the axis is influenced by both, convectional and viscous terms, represented by the two integrals on the right hand side of Equ. (2.16). In fact, if the radial velocity component is assumed to be a slowly varying function of the axial distance x, and if v is close to zero initially, the second integral can completely be neglected. Then the increase of the pressure in the axial direction is solely built up by viscous forces (in the frame of the order of approximation considered here). Note that the factor $1/(Re\,\varepsilon^2)$ could could have been absorbed by either setting it equal to unity or by coordinate stretching. It was left in the equations in order to indicate the contribution of the viscous forces.

The influence of the first-order terms is contained in Equ. (2.14). The order of magnitude requirements, given by Equ. (2.15) are identical with boundary layer assumptions. If the term multiplied by ε^2 is maintained in the approximation, also terms of order 1/Re must be carried along. The first order terms cause an increase of the pressure along the axis, if the first integral in Equ. (2.14) is positive, and the second term is negative. The assumptions given by Equ. (2.15) become invalid in the immediate vicinity of the stagnation point, i. e., the point where the breakdown is initiated.

Hall's observation [1] , quoted in the introduction, is clearly confirmed through Equ. (2.16): The pressure gradient on the axis can be enforced either by a certain distribution of the azimuthal velocity component or by a pressure gradient imposed on the outer flow, i, e.:

$$\frac{\partial p}{\partial x}(x,0) = \frac{\partial p}{\partial x}(x,\infty) - 2\alpha^2\left[\frac{1}{Re\,\varepsilon^2}\,I_1 - I_2\right] \tag{2.17}$$

The expressions I_1 and I_2 designate the two integrals given in Equ. (2.16). If the pressure gradient on the axis is required to be positive, the right hand side of Equ. (2.17) must be greater than zero. This can be enforced either by certain distributions of the azimuthal velocity components which are such that the bracketed term in Equ. (2.17) is negative, while $\partial p/\partial x\,(x,0)$ is zero, or for a non-vanishing positive pressure gradient the bracketed term can be smaller in magnitude. In other w ords, Hall's statement can be casted into the following form. If $\Delta p(0)$ is the pressure difference along the axis necessary to cause breakdown, then

$$\Delta p(0) = \Delta p(\infty) - 2\alpha^2\left[\frac{1}{Re\,\varepsilon^2}\int I_1\,dx - \int I_2\,dx\right] = \text{constant} \tag{2.18}$$

In Equ. (2.18) $\Delta p(\infty)$ is the pressure difference imposed on the external flow in the axial direction; the integration has to be extended over the length L, the distance between the point of initiation and of breakdown of the vortex.

In order to investigate the conditions to be satisfied for breakdown, an estimate of the integrals is given in the next section.

3. Estimate of the Axial Pressure Gradient

Since it is impossible to extract further information from the integrals I_1 and I_2, additional assumptions must be introduced. The simplest assumption which can be made for the azimuthal velocity component near the axis is that the flow behaves like a rigid body, i. e., in dimensionless variables w = r, at least for $r \le r_1$, where r_1 is the dimensionless radius up to which rigid body rotation prevailes. The first integral I_1 yields zero for $r \le r$, while the second, I_2, is

$$\int_0^\infty \left(\frac{v}{u}\frac{w}{r^2}\frac{\partial}{\partial r}(rw)\right)dr = 4\alpha^2\int_0^{r_1}\frac{v}{u}\,dr \tag{3.1}$$

In order to obtain an estimate of the integrals I_1 and I_2 for the outer portion of the vortex, a distribution of the form

$$w = k r^{-2n} \quad , \quad n > 0 \tag{3.2}$$

is assumed for the azimuthal component. The parts of the integrands containing w can then be evaluated by means of Equ. (3.2). There is obtained

$$\begin{aligned} \frac{w}{r}\frac{\partial}{\partial r}\left(\frac{1}{r}\frac{\partial}{\partial r}(rw)\right) &= (n^2-1)\,k^2 r^{-(2n+3)} \\ \frac{w}{r^2}\frac{\partial}{\partial r}(rw) &= -(n-1)\,k^2 r^{-2(n+1)} \quad , \end{aligned} \tag{3.3}$$

so that the pressure gradient along the axis can be written as

$$\frac{\partial}{\partial x}(\Delta p)_r = 4\alpha^2\int_0^{r_1}\left(\frac{v}{u}\right)dr - 2(n-1)\,\alpha^2k^2\int_{r_1}^\infty\left(\frac{v}{u}\right)r^{-2(n+1)}\,dr - 2(n^2-1)\,\frac{\alpha^2k^2}{Re\,\varepsilon^2}\int_{r_1}^\infty\frac{1}{u}\,r^{-(2n+3)}\,dr \tag{3.4}$$

According to Equ. (3.4) the magnitude of the radial velocity component v and the exponent n, the radial decay of the azimuthal velocity, determine the sign of the pressure gradient. Note that the ratio v/u could be expressed by the continuity equation and the axial momentum equation

$$\frac{v}{u} = \frac{1}{r}\int_0^r \frac{\partial p}{\partial x}\frac{r'}{u^2}\,dr' - \frac{1}{Re\,\varepsilon^2 r}\int_0^r \frac{1}{u^2}\frac{\partial}{\partial r'}\left(r'\frac{\partial u}{\partial r'}\right)dr' \tag{3.5}$$

Then, the pressure gradient appears also on the right-hand side of Equ. (3.4), and the sign is basically determined by the second integral in Equ. (3.5), which is more complicated than Equ. (3.4). No use is therefore made of Equ. (3.5).

Although Equ. (3.2) is restricted to a certain class of azimuthal velocity profiles, it could be extended to fit arbitrary profiles by choosing n variable and extending the last two integrals in Equ. (3.4) only over finite radial strips. This would yield a sum, in which in the exponent n would be constant only for every single strip. In the limit the sum could be replaced by an integration over the radial coordinate. In order to keep the analysis as simple as possible, this step is not introduced here. All important conclusions can be obtained from Equ. (3.4).

The influence of the inner part of the vortex, for which rigid body rotation is assumed is completely determined by the radial velocity component: If v is positive, then the first integral in Equ. (3.4) is always positive, while the opposite is true for a negative radial velocity component. The second expression in Equ. (3.4) depends on both, the exponent n of the radial decay for the azimuthal velocity component, and on the radial velocity. The following cases can be distinguished:

Case 1:
The radial velocity component is positive and n is equal to one, so that the radial distribution of the azimuthal velocity component at every station x corresponds to that of a potential vortex. Of the three expressions on the right-hand side of Equ. (3.4) only the first is different from zero. The vanishing of the two latter expressions implies that a potential vortex cannot support an axial pressure gradient. For a positive radial velocity component the pressure gradient is also positive and vortex breakdown must occur. For a negative radial velocity component the axial flow is being accelerated. The magnitude of the axial velocity component is essential for the pressure gradient: If two vortices are compared with different initial axial velocity profiles, the one with the larger axial velocity component will encounter breakdown further downstream than the vortex in which the axial velocity is smaller.

Case 2:
The exponent n is smaller than one. The azimuthal velocity component decays less than that of the potential vortex. If, as before, the integrals containing the radial velocity component are positive, all three expressions in Equ. (3.4) are positive so that the pressure gradient is larger than under case 1. Vortex breakdown must occur closer to the point of initiation of the vortex. If the first two integrals are negative, breakdown is delayed. In fact it may not occur at all.

Case 3:
The exponent n is larger than one. The azimuthal velocity component has a steeper radial decay than that of the potential vortex. The last two expressions in Equ. (3.4) are now negative if the second integral (containing v) is positive. Vortex breakdown is delayed, and does not occur if also the first integral is positive, i. e.

$$(n-1)k^2\int_{r_1}^{\infty}\frac{1}{u}r^{-2(n+1)}\left(v+\frac{(n+1)}{Re\,\varepsilon^2 r}\right)dr \;<\; 2\int_0^{r_1}\left(\frac{v}{u}\right)dr \tag{3.6}$$

If the first two integrals are negative, vortex breakdown is possible only if

$$(n-1)k^2\left|\int_{r_1}^{\infty}\left(\frac{v}{u}\right)r^{-2(n+1)}\,dr\right| \;>\; 2\left|\int_0^{r_1}\left(\frac{v}{u}\right)dr\right| + (n^2-1)\frac{k^2}{Re\,\varepsilon^2}\int_{r_1}^{\infty}\frac{1}{u}r^{-(2n+3)}\,dr \tag{3.7}$$

Also note, that the factor α^2, the ratio of the maximum azimuthal velocity and the freestream velocity can be included in the nondimensionalization of the pressure, so that p is referenced to $\rho\alpha^2 u_\infty^2$, or α^2 can be absorbed by defining a new coordinate $x = \alpha^2 x$. Then from the above relations, in particular Equ. (2.18), it is clear that the length L between the point of initiation and of breakdown of the vortex is inversely proportional to the square of the maximum azimuthal velocity and directly proportional to the square of the freestream velocity u_∞. This means that vortex breakdown can be delayed by increasing the former and decreasing the latter.

4. Concluding Remarks

By casting the governing equations into a suitable form, it could be shown, how the pressure gradient along the axis of a vortex can be expressed by integral relations, containing the radial, axial, and azimuthal velocity components, and radial derivatives of the azimuthal velocity components. With simple assumptions for the radial distribution of the azimuthal velocity component it was demonstrated that not only inertia forces but also viscous forces contribute to the initiation of the breakdown process, which requires $\partial p/\partial x\,(x,o)$ to be positive. If the radius of the core is increasing in the direction of the axial flow, i. e. the radial velocity is always positive, breakdown must eventually occur. The analysis also shows, that the outer portion of the vortex cannot support a pressure gradient along the axis, if the radial distribution of the azimuthal velocity component is equal to that of a potential vortex; that a positive pressure gradient $\partial p/\partial x\,(x,o)$ results, if the radial decay of the azimuthal velocity components is less steep than that of the potential vortex for positive radial velocity components, and that an increase of the initial axial velocity component delays breakdown as does a decrease of the maximum azimuthal velocity component. The results given in this analysis a valid for large Reynolds numbers with small core radii. Extension to large core radii should be possible.

5. Literature

[1] S. Leibovich: "The Structure of Vortex Breakdown". Ann. Rev. Fluid Mech., 10, 221-246, 1978.

[2] M. G. Hall: "Vortex Breakdown". Ann. Rev. Fluid Mech., 4, 195-218, 1972.

[3] X. Shi and E. Krause: "Numerische Untersuchung des Aufplatzens eines Wirbels". Paper presented at the GAMM Tagung 1983. Submitted for publication.

[4] T. Sarpkaya: "On Stationary and Travelling Vortex Breakdown". J. Fluid Mech., 45, 545-559, 1971.

[5] R. Staufenbiel: Private Communication 1982.

NUMERICAL SIMULATION OF VORTEX BREAKDOWN BY THE VORTEX-FILAMENT METHOD

Y. Nakamura, A. Leonard, and P. R. Spalart
NASA Ames Research Center, Moffett Field, California 94035, U.S.A.

SUMMARY

The vortex-filament method was applied to the simulation of vortex breakdown. The principal vortex region was represented by multiple filaments, and an axial velocity component was induced by a spiral winding of the filaments. First, an accuracy check was performed for a cylindrical swirling flow with simple analytical expressions for the axial and theta velocities. The result suggests that the flow field can be simulated to any accuracy by increasing the number of filaments. Second, an axisymmetric-type vortex breakdown was simulated, with experimental data serving as upstream conditions. The calculated axial- and theta-velocity contours show the breakdown of the vortex, including a rapid change in the vortex core, followed axially by a recovery zone and then a second breakdown. When three-dimensional initial data are used the second breakdown appears to be of the spiral type in correspondence with experimental observations. The present method can easily be used to simulate other types of vortex breakdown or other vortex flows with axial velocity.

1. INTRODUCTION

The phenomenon of vortex breakdown is not only of fundamental interest, but is of considerable importance in aerodynamics as well. For example, vortex breakdown over a wing usually affects the aerodynamic performance of that wing. In fact, one of the first experimental studies of vortex breakdown was Peckham and Atkinson's investigation (Ref. 1) of flow over a delta wing. At high incidence they observed breakdown (usually defined as an abrupt change along the vortex axis with a limited region of flow reversal) of the pair of vortices formed at the leading edge of a delta wing. Since then many other experiments of vortex breakdown have been carried out. Those studies revealed three basic patterns of breakdown: axisymmetric, spiral, and double-helix. Flow visualizations by Sarpkaya (Ref. 2) show these patterns in water. He systematically measured the relationship between Reynolds number, the position of breakdown, the pattern of breakdown, and the amount of swirling. Lambourne and Bryer's study of flow over a delta wing (Ref. 3; see also Ref. 4) clearly shows two different patterns of vortex breakdown, axisymmetric and spiral, occurring at the same time. Recently, Faler and Leibovich proposed a more detailed classification scheme for vortex breakdown based on extensive observations (Ref. 5) and obtained measurements of velocity profiles using a laser Doppler velocimeter (Ref. 6). Escudier and Zehnder (Ref. 7) have proposed a simple criterion for vortex breakdown, using extensive flow-visualization data. See Hall (Ref. 4) and Leibovich (Ref. 8) for a review of these studies, as well as theoretical efforts on vortex breakdown.

On the theoretical side, Benjamin's finite transition theory (Ref. 9) proposes that the breakdown of swirling flow corresponds to the transition from supercritical to subcritical flow in a hydraulic jump in open-channel flow. On the other hand, Ludwieg (Ref. 10) proposed an instability theory for swirling flows in which vortex breakdown is attributed to the growth of instability waves on the vortex core by increasing helical interference vortices.

In an attempt to treat vortex breakdown numerically, Hall (Ref. 11) derived a boundary-layer-like equation and solved it by a marching method. This scheme assumes axisymmetric, steady flow and can treat an arbitrary upstream flow field. Since the equation itself is parabolic, there is some dispute over whether this type of equation is valid for sudden changes in flow structure. More recently, Grabowski and Berger (Ref. 12) solved the Navier-Stokes equations, using Chorin's artificial compressibility method, to simulate axisymmetric vortex breakdown. This scheme also assumes steady flow and appears to be limited to low Reynolds numbers.

It is clearly desirable to attack the vortex-breakdown problem numerically with a three-dimensional capability. According to detailed observations, even an axisymmetric-type vortex breakdown includes three-dimensional motion. In this paper, we present the result of numerical simulations of vortex breakdown, using the three-dimensional vortex-filament method developed by Leonard (Ref. 13). In particular, we have studied the axisymmetric breakdown. Our present results are for both axisymmetric and three-dimensional initial data. It is our view that the primary role of Reynolds number is in shaping the internal structure of the vortex core upstream of the breakdown. As shown below, the upstream conditions can be duplicated by proper choice of the filament geometry and strength. The process of breakdown occurs rapidly and is therefore dominated by nonlinear inviscid phenomena, well described by the dynamics of the vortex-filament method. In a similar approach, Del Prete (Ref. 14) modeled vortex breakdown using the vortex method. However, she used only parallel longitudinal vortex filaments upstream – with no axial velocity component – interacting with a vortex ring to produce a structure suggestive of vortex breakdown.

Although this report is concerned with the simulation of vortex breakdown, the method used can treat any system of vortices with or without axial velocity distribution and, for example, should be capable of simulating in detail the merging process of aircraft wake vortices.

2. NUMERICAL METHOD

The vortex-filament method was developed by Leonard (Ref. 13) and successfully applied to the wake-vortex interaction problem behind large jet aircraft (e.g., B-747) and to the spot-like disturbance in a laminar boundary layer. This method seems well suited to the simulation of vortex breakdown, in that computational elements are required only for the vorticity-containing fluid in and near the flow region where vortex breakdown is occurring. Furthermore, in the vortex filament method rapid changes in the flow pattern with three-dimensionality can be represented with minimal error due to numerical diffusion. The vortex-filament method is generalized from the two-dimensional vortex-blob method to three dimensions by assuming that the vorticity field is represented by a collection of tubes or filaments of vorticity defined

by the space curves $[\mathbf{r}_i(\xi,t),\ i = 1, 2, \ldots, L]$, where ξ is a parameter along the curve and L is the number of the vortex filaments. The vortex-filament method does not have a singular vorticity distribution inside the vortex filament as does the classical point-vortex method.

The dynamics of these filaments, consistent with the theorems of Helmholtz and Kelvin, is given by

$$\frac{\partial \mathbf{r}_i(\xi,t)}{\partial t} = -\frac{1}{4\pi}\sum_{j=1}^{L}\Gamma_j\int\frac{(\mathbf{r}_i - \mathbf{r}_j)\times(\partial\mathbf{r}_j/\partial\xi')s(|\mathbf{r}_i - \mathbf{r}_j|,\sigma_i,\sigma_j)d\xi'}{|\mathbf{r}_i - \mathbf{r}_j|^3} \tag{1}$$

The "s" function included in this equation is related to the vorticity distribution inside a vortex filament. Leonard (Ref. 13) gave two particular choices of the function "s." In this paper we use the so-called "scheme C," which is of the form

$$s(y,\sigma_i,\sigma_j) = \frac{1}{[1 + \alpha(\sigma_i^2 + \sigma_j^2)/2y^2]^{3/2}} \tag{2}$$

where the choice $\alpha = 0.413$ for a Gaussian distribution of vorticity within the core yields the correct speed of a single vortex ring.

In vortex-flow simulations, the following two flow representations are possible:

1. Single filament to represent each physical vortex

2. Multiple filaments to represent each physical vortex

The first method was used for test problems which are not described here. These are the interaction of four vortex rings and the interaction of two pairs of wake vortices that cross at a right angle with some clearance. The results were successful and convincing. In particular, the first case produced results very close to those of experiment (Ref. 15). These preliminary results were encouraging for the application of this method to vortex breakdown. However, the single-filament representation is appropriate only when the internal structure is not of major importance. The multiple-filaments representation has to be considered when the internal structure, including axial flow, has a significant effect on the dynamics. In this paper we use the latter representation to simulate vortex breakdown. If this method proves successful and if a detailed procedure is established, many new applications to practical flows dominated by vortices may be attempted.

3. ACCURACY CHECK OF THE VORTEX-FILAMENT METHOD

We first performed an accuracy check for the three-dimensional vortex-filament method. A flow with a simple analytical expression was chosen, and its vorticity was represented by vortex filaments. Then the velocity field induced by the filaments was compared with the idealized field. This method has two numerical parameters: the core radius and the initial spacing between the vortex filaments. The accuracy is expected to improve when the number of the filaments used is increased, which makes the average distance between neighboring vortex filaments smaller. It is also interesting to estimate the relation between the optimum core radius and the average distance. We did a similar study in two dimensions, with Gaussian cores (see Ref. 16). The results suggested the relation $\sigma \sim \delta^{0.875}$, where σ is the core radius and δ is the average distance. This means that the core radius should tend to zero more slowly than the average distance does.

For the test, it is convenient to choose a flow in which the vorticity sharply declines with the distance from the axis. The following expressions, often used for unbounded swirling flow, satisfy these requirements:

$$V_x = a_1 + a_2\exp(-a_3r^2) \tag{3}$$

$$V_\theta = \Gamma_0[1 - \exp(-b_1r^2)]/r \tag{4}$$

$$V_r = 0 \tag{5}$$

where V_x is the axial-velocity component, V_θ the theta velocity, and V_r the radial velocity. The values actually used for the parameters are

$$a_1 = 0.95\ ,\quad a_2 = 1.55\ ,\quad a_3 = 10\ ,\quad b_1 = 10.9\ ,\quad \text{and}\quad \Gamma_0 = 0.825$$

which approximate those obtained in an experiment inside a pipe (private communication, Uchida et al., Nagoya Univ.), as shown in Fig. 1. We are not concerned with the wall region where, of course, the idealized velocity does not match the experimental velocity because we are simulating an unbounded flow. The measurements were obtained by a laser Doppler velocimeter for axisymmetric vortex breakdown at a Reynolds number of 2300. Figure 1a shows the axial velocity component of Eq. (3) which is high near the axis and approaches 0.95 (potential flow) as the radius increases. Needless to say, this profile includes the axial flow inside the vortex. Figure 1b shows the theta velocity, with almost rigid rotation near the axis and a maximum value at $r = 0.34$. Beyond this point the profile becomes proportional to $1/r$ and represents a potential swirling flow for larger values of the radius. Figure 2 shows the theta-vorticity distribution, which was calculated from the axial velocity by the relation $\omega_\theta = -dV_x/dr$, assuming a cylindrical flow. At $r = 0.22$, the theta vorticity has a maximum value. Figure 3 shows the axial-vorticity distribution, which was calculated from the theta velocity by the relation $\omega_x = d(rV_\theta)/dr/r$, assuming a cylindrical flow. This is a Gaussian distribution. Figure 4 shows the distribution of the circulation, which is calculated by the expression

$$\Gamma = 2\pi r V_\theta \tag{6}$$

This has a familiar pattern of positive curvature near the x-axis approaching a constant value at infinity. Figure 5 shows the magnitude of the vorticity vector as a function of r. The deflection angle of the vorticity from the x-axis is also shown (dashed line); it increases monotonically with radius. Figure 6 shows a three-dimensional picture of the vorticity vector along the radial direction. It can be seen that the vorticity maintains a moderate deflection angle for all radii.

We now discuss the problem of discretizing the idealized vorticity field with helical vortex filaments. The circulation and helicity of each filament as well as their distribution in space must be chosen to represent the idealized vorticity field as well as possible. We divided the circular cross section radially into a number of zones or rings. Each radial zone in turn contains a number of filaments distributed uniformly in the azimuthal direction. In the present simulation we used more filaments per unit area near r = 0 where the vorticity is maximum. Using a nonuniform radial distribution of filaments allowed us to obtain a more accurate representation of the idealized flow.

First, we discuss the method used to obtain the filament circulations. For simplicity of analysis, we assume infinite, straight vortex filaments with axes in the x-direction, distributed continuously along the circumference of each ring at the radii r_i. We have the following expression for the axial vorticity produced by one of these cylindrical shells of vorticity

$$\omega_{x_i} = \Gamma_{x_i} \int_{-\infty}^{\infty} \int_0^{2\pi} \gamma r_i \, d\theta \, dx' \tag{7}$$

where Γ_{x_i} is the circulation per unit circumference, and γ is the distribution function of vorticity inside a filament which is calculated from Eq. (2) as follows:

$$\gamma(y) = (ds/dy)/4\pi y^2 = (3\alpha\sigma^2/4\pi)[y^2 + \alpha\sigma^2]^{-5/2} \tag{8}$$

Equation (7) with substitution of Eq. (8) may be integrated analytically to obtain

$$\omega_{x_i} = \Gamma_{x_i}\psi_i = \Gamma_{x_i} \frac{2\alpha\sigma_i^2 r_i (r_i^2 + r^2 + \alpha\sigma_i^2)}{([(r_i + r)^2 + \alpha\sigma_i^2][(r_i - r)^2 + \alpha\sigma_i^2])^{3/2}} \tag{9}$$

We determine the optimum circulation distribution Γ_{x_i} for given axial vorticity distribution by minimizing the square error with the total circulation fixed. This leads to the following expression for the H function

$$H = \int_0^{\infty} \left(\omega_x - \sum_i^N \Gamma_{x_i}\psi_i\right)^2 dr + \lambda\left(\sum_i^N 2\pi r_i \Gamma_{x_i} - C\right) \tag{10}$$

where C is the total circulation. Differentiating H with respect to the Γ_{x_i} and λ yields the following simultaneous equations for Γ_{x_i}:

$$\left.\begin{aligned} 2\sum_i^N \int_0^{\infty} \psi_i(r)\psi_k(r)dr\Gamma_{x_i} + \lambda 2\pi r_k &= 2\int_0^{\infty} \omega_x \psi_k(r)dr, \quad k = 1,2,\ldots,N \\ \sum_i^N 2\pi r_i \Gamma_{x_i} &= C \end{aligned}\right\} \tag{11}$$

Solving Eqs. (11), we obtain the optimum circulation distribution Γ_{x_i} for each ring. If N_i is the number of filaments placed in the ith ring then the circulation of each of these filaments is given by

$$\Gamma_j = 2\pi r_i \Gamma_{x_i}/N_i \tag{12}$$

The next step is to determine the angle each helical filament makes with the x-axis, the deviation angle. For this purpose we assume that the theta component of vorticity is distributed continuously and uniformly along the x-direction with Γ_{θ_i} circulation per unit axial length for the ith ring. Again, using Eq. (8) we find that the ith ring of distributed theta vorticity contributes to the theta vorticity component as follows

$$\omega_{\theta_i} = \Gamma_{\theta_i} \frac{4zr_i^2\alpha\sigma_i^2}{[(r_i^2 - r^2)^2 + 2\alpha\sigma_i^2(r_i^2 + r^2) + \alpha^2\sigma_i^4]^{3/2}} \tag{13}$$

The same minimization procedure used above was used to determine the optimum Γ_{θ_i} except that total vorticity constraint is not imposed in this case. Finally the deviation angle from the x-axis of each filament in ring i was determined by

$$\tan \alpha_j = \Gamma_{\theta_i}/\Gamma_{x_i} \tag{14}$$

By using the circulations and deviation angles for each ring, we calculated the induced velocity at a cross section using the following expressions:

$$\left.\begin{aligned} V_x &= -(1/4\pi)\sum_{j=1}^{L}\Gamma_j\int_{-\infty}^{\infty} a_jR_j[r\sin(a_jx' + \hat{\theta}_j) - R_j]/F\,dx' \\ V_y &= \sum_{j=1}^{L}(V_y'\sin\hat{\theta}_j - V_z'\cos\hat{\theta}_j) \\ V_z &= \sum_{j=1}^{L}(V_y'\cos\hat{\theta}_j + V_z'\sin\hat{\theta}_j) \end{aligned}\right\} \qquad (15)$$

where

$$F = [x'^2 - 2yR_j\cos(a_jx') - 2zR_j\sin(a_jx') + R_j^2 + \alpha\sigma_j^2 + r^2]^{3/2}$$

$$V_y' = -(1/4\pi)\Gamma_j\int_{-\infty}^{\infty}[z\sin\hat{\theta}_j - y\cos\hat{\theta}_j - R_j\sin(a_jx') + a_jR_jx'\cos(a_jx')]/F\,dx'$$

$$V_z' = -(1/4\pi)\Gamma_j\int_{-\infty}^{\infty}[-y\sin\hat{\theta}_j - z\cos\hat{\theta}_j + R_j\cos(a_jx') + a_jR_jx'\sin(a_jx')]/F\,dx'$$

$$p_j = 2\pi/\lambda_j\ , \qquad \hat{\theta}_j = \theta_j - \theta$$

(R_j,θ_j) and (r,θ) are the coordinates of the filament and the point where the induced velocity is required, respectively, and p_j is the filament pitch. These expressions are obtained by transforming the original expressions of the induced velocities, written in the Cartesian coordinates, using the relations representing the spiral shape of the filaments.

As our first test of our discretized vorticity field we calculated the distribution of the induced, unperturbed axial and theta velocity components of the upstream flow, which for the test extended over the entire x-axis. The actual integration was performed numerically from -10 to 10 using Simpson's rule with a spacing of 0.04 for x. Four rings were used radially with radii at 0.06, 0.18, 0.30, and 0.42 with 6, 6, 8, and 8 filaments in the respective rings. The core radius σ of each filament was 0.16. The results along the z-axis are depicted in Fig. 7 and show very good agreement. To check for uniformity in the azimuthal direction we obtained contour plots of the induced velocity field in a plane normal to the x-axis. These are shown in Fig. 8 along with corresponding contours of the idealized field. Generally we obtained a very good representation of the idealized field with a tendency to slightly underestimate idealized values.

4. SIMULATION OF VORTEX BREAKDOWN

For conditions upstream of vortex breakdown we assumed the idealized flow from above and therefore we used the filament parameters determined above. There might be some dispute over the difference between the experimental flow inside the pipe and the unbounded flow assumed for the simulation. As mentioned above, stable vortex breakdowns are produced inside the pipe with a divergent wall or without. Although some differences might exist between the two configurations, we assume the essential ingredients remain for vortex breakdown in unbounded flow. Experimentally, vortex breakdown is easily observed in a pipe at moderate Reynolds number which makes quantitative measurements less difficult.

In its present form the vortex filament method does not explicitly include the effect of viscous diffusion. Therefore, we cannot say anything about the effect of Reynolds number on the breakdown process itself. We assume this process to be dominated by nonlinear inviscid effects. However, the upstream profiles within the vortex depend on Reynolds number as well as the vane angles which control the amount of swirling. However, by shaping the vortex filaments upstream of breakdown we can reproduce any desired velocity (and hence vorticity) profiles. In this sense we can follow changes in Reynolds number, and in the present simulation we attempt to simulate a vortex breakdown occurring at an experimental Re = 2300.

For numerical purposes, we divided the flow domain into four axial subregions (Fig. 9). For simplicity just one filament is shown. Regions I, II, and IV have predetermined filament geometries. Only in region III is the flow simulated fully. Regions I, II, and IV are constructed to provide high-quality boundary data for region III. Regions I and IV consist of straight, semi-infinite filaments that induce a swirl component on the filaments in region III. Here, analytical expressions were used for the induced velocity. For example, if one of these semi-infinite filaments, parallel to the x-axis, extends from (x_0, y_0, z_0) to minus infinity, the analytical induced velocity is as follows:

$$\left.\begin{aligned} V_x &= 0 \\ V_y &= -(\Gamma/4\pi)(z - z_0)F \\ V_z &= (\Gamma/4\pi)(y - y_0)F \end{aligned}\right\} \qquad (16)$$

where

$$F = \{(x_0 - x)/[(x - x_0)^2 + (y - y_0)^2 + (z - z_0)^2 + A]^{1/2} + 1\}/[(y - y_0)^2 + (z - z_0)^2 + A]$$

$$A = \alpha(\sigma_i^2 + \sigma_j^2)/2$$

Region II consists of spiral or helical filaments which rotate and translate with fixed, predetermined velocities. The filaments in this region also induce velocity on the filaments in region III. Filament geometries and strengths in region II were determined as in the previous section. Thus the filaments in region III move according to an induced velocity from the filaments of region III as well as all other regions, using the dynamic equation, the Biot-Savart Law.

A Runge-Kutta fourth-order scheme was used for time-integration. Special attention was given to the filaments of region II. Because the Runge-Kutta scheme requires four different substeps to obtain the final solution at each time-step, we must use three different geometries other than the "exact geometry" to simulate precisely the Runge-Kutta errors that are being made in the upstream part of region III. Both the radius and phase angle were precalculated for each substep and stored in the program.

At each time-step node points were redistributed and, if necessary, added to each filament to maintain a nearly constant distance between points. This was accomplished by using a parametric spline fit to obtain the space curve defining a given filament.

At present we have insufficient knowledge about the initial disturbance necessary to produce vortex breakdown. Each type of vortex breakdown might need a different initial perturbation. At least it might be natural to consider that the three-dimensional type breakdown will need a three-dimensional disturbance. Preliminary axisymmetric calculations showed that a small amplitude disturbance on a vortex with no axial flow resulted only in weak traveling waves, but a large amplitude disturbance causes breakdown similar in appearance to wave-breaking. Experimentally, vortex breakdown is sometimes very sensitive to a disturbance in that a change in breakdown pattern occurs even if the same upstream conditions are maintained. In this report we present results for two initial disturbances. Case I had an axisymmetric disturbance and Case II had a three-dimensional disturbance.

The top function ($t = 0$) in Fig. 10a shows the initial geometry of the vortex filaments used for Case I and represents a large amplitude disturbance. The region of full simulation (region III) extends over the range $0 < x < 5$. In $0 < x < 3$, the helical geometry of the upstream flow was used, but in $3 < x < 4$, the helices gradually reverse pitch and the pitch was elongated by a factor of 1.4 in this decelerating region. In $4 < x < 5$, straight filaments were used.

Figure 10 also shows the time variation in the vortex filaments. The time-step was 0.2. A uniform axial velocity of 0.4 (potential flow) was added to that induced by the vortex filaments. This value was chosen after the results of preliminary runs were available, giving us an estimate of the speed of the disturbance. If this flow component is not chosen with some accuracy the disturbance will rapidly move toward one of the computational boundaries. However, this value does not play an essential part in flow pattern, because this is just the moving frame through which we see the phenomenon. Alternatively, one could continually adjust the free-stream component during the simulation to keep the disturbance centered. During the first few time-steps, a remarkable vortex swelling can be seen in the downstream region where the initial disturbance had a flow reversal ($t = 1$). This swelling moves downstream ($t = 2$). At later times these vortex filaments are elongated in the axial direction and in particular the filaments in the third ring appear almost parallel to the x-axis ($t = 2$ and $t = 3$). Just downstream of this region a narrow region with small pitch can be observed ($t = 3$). A central region which appears devoid of filaments due to the elongation and straightening of the filaments can also be seen at $t = 6$ in the middle of the picture. This region moves upstream and is a manifestation of the axisymmetric vortex breakdown. On the other hand, at $t = 4$ the filaments in the second and third rings show disorder just downstream of the center of the picture, followed by a contraction toward the x-axis near the downstream boundary. In contrast with this, the filaments in the outermost ring show slight expansion near the downstream boundary with some contraction upstream. At later times the outermost filaments establish a wavy pattern downstream of the first expansion. At $t = 6$ most filaments have become very disordered near the downstream boundary. Just upstream of this expansion the filaments of the second and third rings have become "untied" and elongated in the axial direction. Another interesting feature is that the filaments in the innermost ring contract to $r = 0$ at the station where the outer filaments show the expansion at $t = 2$. This region of contraction has a long axial extent by $t = 3$ and then moves downstream with time.

In Case II we added a three-dimensional perturbation to the initial disturbance as shown in Fig. 10b ($t = 0$). The perturbation was caused by adding a radial displacement to each filament which was a sinusoidal function of theta (wavenumber = 1) and was nonzero and sinusoidal in x for $3 < x < 4$. It can be seen that differences in the filament configurations between Case I and Case II persist in time but remain confined to the downstream end of the computational domain.

Figure 11 shows the contours of axial velocity. Solid lines denote positive values and dashed lines negative values. Figure 11a shows Case I. Initially ($t = 0$), a downstream region of low axial velocity is shown as expected from the initial geometry of the filaments. By $t = 1$ this low-velocity region has gone through the downstream boundary and cannot be seen. Instead a high-velocity region appears. Between $t = 1$ and $t = 2$ this high-velocity region enlarges and moves downstream. At later times we see the development and enlargement of a low-velocity region upstream of the high-velocity region. Meanwhile, the peak velocity in the high-speed region is decreasing. At $t = 7$ and $t = 8$ we see another interesting feature. Near the downstream boundary another low-velocity region appears. Apparently, a second breakdown is occurring near the downstream boundary. Experimentally it is very often observed that axisymmetric vortex breakdown is followed by a second breakdown of the spiral type. In the experiment used to determine the upstream conditions a clear spiral-type vortex breakdown was observed. However, the axisymmetric initial disturbance for Case I only leads to axisymmetric flow.

Next, we discuss Case II (Fig. 11b), having a three-dimensional initial disturbance. Generally, Case II shows a pattern similar to that of Case I. However, we again see that three-dimensionality remains at later times, but only near the downstream boundary. As seen at $t = 5$ and later, the contours in the first breakdown are very similar to those in Case I and appear axisymmetric. But the second breakdown is distorted, not axisymmetric, and appears to be rotating around the x-axis (as seen in the downstream region at $t = 7$ and 8). This is suggestive of a vortex breakdown of the spiral type.

Figure 12 shows the theta velocity contours. For Case I at $t = 0$, the contours show no disturbance in the theta velocity because the filaments are distorted initially only in the theta direction. At $t = 1$, swelling of contour lines can be seen in the region of the initial perturbation. At $t = 2$ an interesting phenomenon appears downstream. Another swelling after the first swelling can be seen near the downstream boundary. At this time the swelling of the filaments near the x-axis seen at $t = 1$ has disappeared. The contours at $t = 3$ are similar to those at $t = 2$. Between $t = 2$ and $t = 4$ the axial position of the maximum swelling of the level 3 contour clearly moves upstream. After $t = 6$ the first swelling spreads to the contours near the x-axis. The first and the second swellings correspond to the two breakdowns observed above.

For Case II (Fig. 12b) we see that at $t = 0$ the contour lines have a slightly crooked pattern for $3 < x < 4$ where the initial three-dimensional disturbance was imposed. At $t = 1$ we can see the clear three-dimensional wavy pattern inside the region of swelling. At $t = 2$ the three-dimensionality moves toward the downstream boundary and seems to disappear until $t = 7$. At $t = 7$ and $t = 8$ we clearly observe three-dimensionality near the downstream boundary and a comparison of the contours at these two times indicates a rotating disturbance. This is in contrast with the first breakdown whose contours appear to be nearly axisymmetric and agree well with those of Case I. We conclude that the complete pattern of an axisymmetric vortex breakdown followed by a breakdown of the spiral type was simulated by allowing for three-dimensionality.

5. CONCLUDING REMARKS

The vortex-filament method was applied to the numerical simulation of vortex breakdown, which is intrinsic to the longitudinal vortex. Generally, there are three types of vortex breakdown: axisymmetric, spiral, and double helix. In this paper we simulated the axisymmetric type of vortex breakdown. Generally, it is difficult to obtain information experimentally due to the sensitivity of breakdown to any perturbation. Calculated results should be helpful to understand this complicated phenomenon. The principal vortex region was represented by the multiple filaments. One filament is not enough to represent this complicated flow field. In particular, the present method can include axial flow which is often observed in physical vortices.

Vortex breakdown was simulated under the assumption of nonlinear, inviscid dynamics of vorticity using the three-dimensional vortex-filament method. Viscous effects are assumed to be important only in forming upstream velocity profiles. Upstream profiles were simulated accurately with helical vortex filaments by choosing pitch and circulation to minimize the error. First, an accuracy check was performed for a cylindical flow with simple analytical functions for the axial and theta velocities. This profile was the idealization for the experimental data used for the vortex-breakdown simulation. Comparison of the simulated results with the idealized flow suggests that the flow field can be simulated to any accuracy by increasing the number of the filaments.

Two cases, Case I and Case II, were calculated to simulate axisymmetric-type breakdown. In order to create a strong initial disturbance, the filaments in the downstream axial region were provided with a change in pitch. We used two kinds of initial disturbance to see their effect on vortex breakdown. Case I had an axisymmetric disturbance and Case II had a three-dimensional disturbance. Filament configurations and contour plots of velocity showed, for both cases, two simultaneous vortex breakdowns. One vortex breakdown was similar in both cases and was axisymmetric. The other vortex breakdown was axisymmetric for axisymmetric disturbances and three dimensional for three-dimensional disturbances. The latter case agrees with the experimental observations where an axisymmetric vortex breakdown is followed by a spiral-type breakdown.

Other types of breakdown (spiral and double-helix) should be possible to simulate by this method. The present method can also be applied to other vortex flows with axial velocity profile.

REFERENCES

1. Peckham, D. H. and Atkinson, S. A., "Preliminary Results of Low Speed Wind Tunnel Tests on a Gothic Wing of Aspect Ratio 1.0," Aeronautical Research Council C.P. No. 508, 1960.

2. Sarpkaya, T., "On Stationary and Travelling Vortex Breakdown," J. Fluid Mech., Vol. 45, 1971, pp. 545-559.

3. Lambourne, N. C. and Bryer, D. W., "The Bursting of Leading Edge Vortices – Some Observations and Discussion of the Phenomenon," Aeronautical Research Council R and M 3282, 1962.

4. Hall, M. G., "Vortex Breakdown," Annual Review of Fluid Mechanics, Vol. 4, 1972, pp. 195-218.

5. Faler, J. H. and Leibovich, S., "Disrupted States of Vortex Flow and Vortex Breakdown," Phys. Fluids, Vol. 20, 1977, pp. 1385-1400.

6. Faler, J. H. and Leibovich, S., "An Experimental Map of the Internal Structure of a Vortex Breakdown," J. Fluid Mech., Vol. 86, 1978, pp. 313-335.

7. Escudier, M. P. and Zehnder, N., "Vortex-Flow Regimes," J. Fluid Mech., Vol. 115, 1982, pp. 105-121.

8. Leibovich, S., "The Structure of Vortex Breakdown," Annual Review of Fluid Mechanics, Vol. 10, 1978, pp. 221-246.

9. Benjamin, T. B., "Theory of the Vortex Breakdown Phenomenon," J. Fluid Mech., Vol. 14, 1962, pp. 593-629.

10. Ludwieg, H., "Zur Erklärung der Instabilität der über Angestellten Deltaflügeln Auftretenden Freien Wirbelkerne," Z. Flugwiss., Vol. 10, 1962, pp. 242-249.

11. Hall, M. G., "A Numerical Method for Solving the Equations for a Vortex Core," Aeronautical Research Council R and M 3467, 1965.

12. Grabowski, W. J. and Berger, S. A., "Solutions of the Navier-Stokes Equations for Vortex Breakdown," J. Fluid Mech., 1976, pp. 525-544.

13. Leonard, A., "Vortex Methods for Flow Simulation," J. Comp. Phys., Vol. 37, 1980, pp. 289-335.

14. Del Prete, V., "Numerical Simulation of Vortex Breakdown," Lawrence Berkeley Laboratory Report 8503, Berkeley, Calif., 1978.

15. Oshima, Y. and Asaka, S., "Interaction of Multi-Vortex Rings," J. Phys. Soc. Japan, Vol. 42, 1977, pp. 1391-1395.

16. Nakamura, Y., Leonard, A., and Spalart, P. R., "Vortex Simulation of an Inviscid Shear Layer," AIAA Paper 82-0948, 1982.

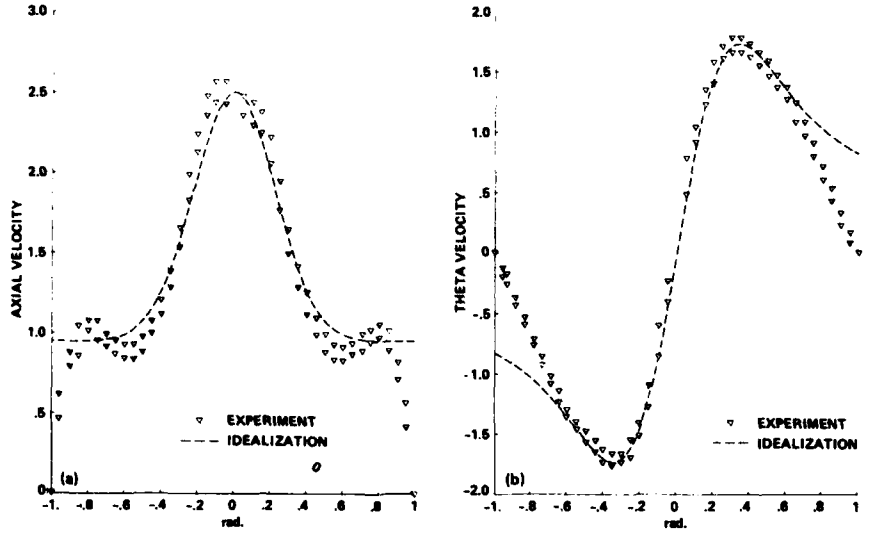

Fig. 1. Velocity profiles in the upstream region. (a) Axial velocity; (b) Theta velocity.

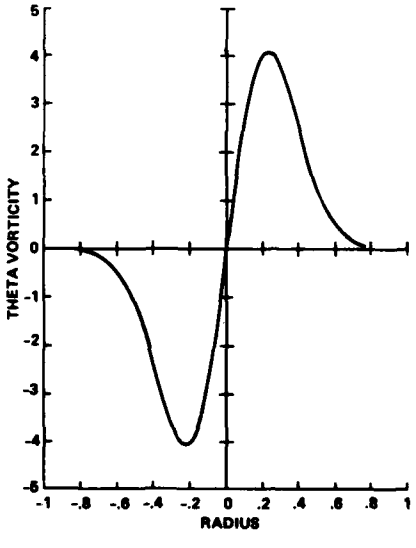

Fig. 2. Upstream theta vorticity.

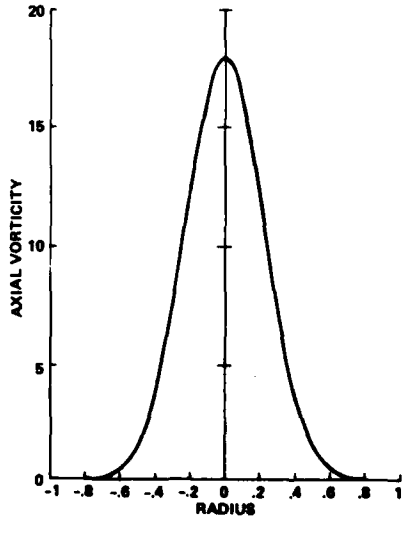

Fig. 3. Upstream axial vorticity.

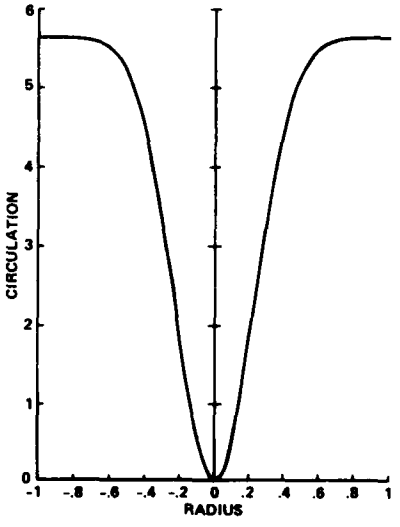

Fig. 4. Circulation.

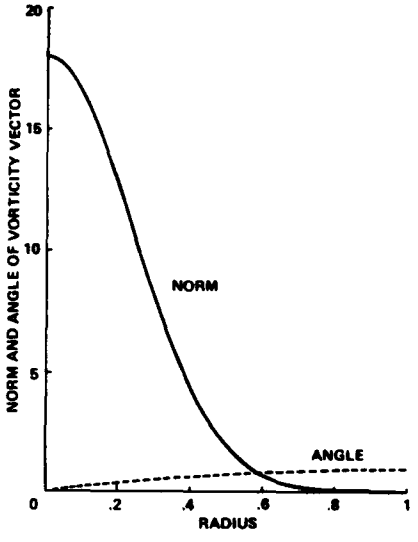

Fig. 5. Norm and angle of the vorticity vector of the idealization as a function of radius.

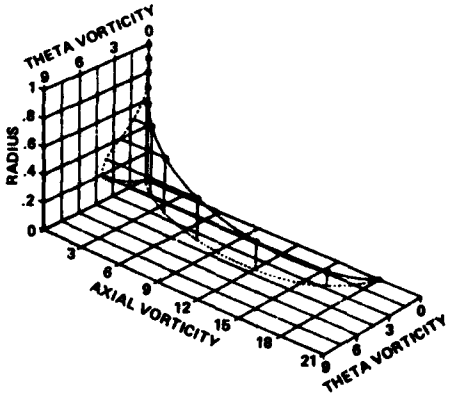

Fig. 6. Three-dimensional view of the vorticity-vector distribution.

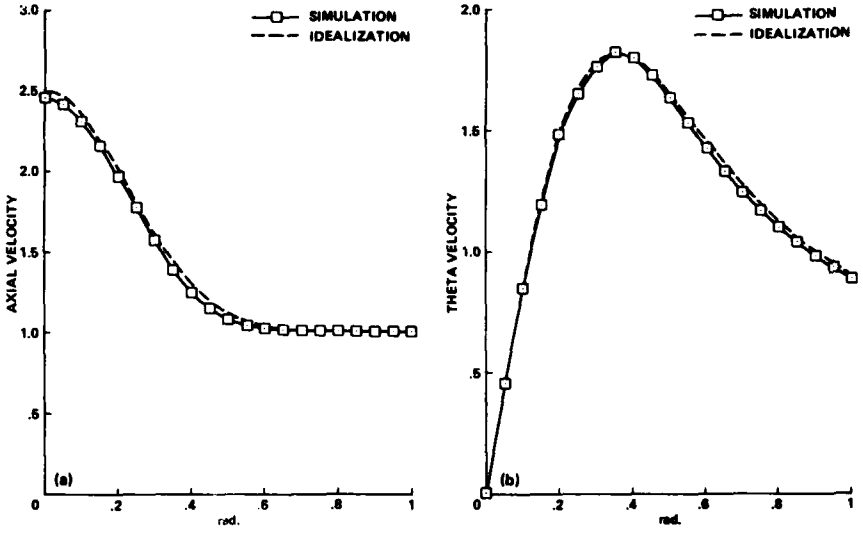

Fig. 7. Comparison between the calculat. velocity distribution along the z-axis and the idealization. (a) Axial velocity; (b) Theta velocity.

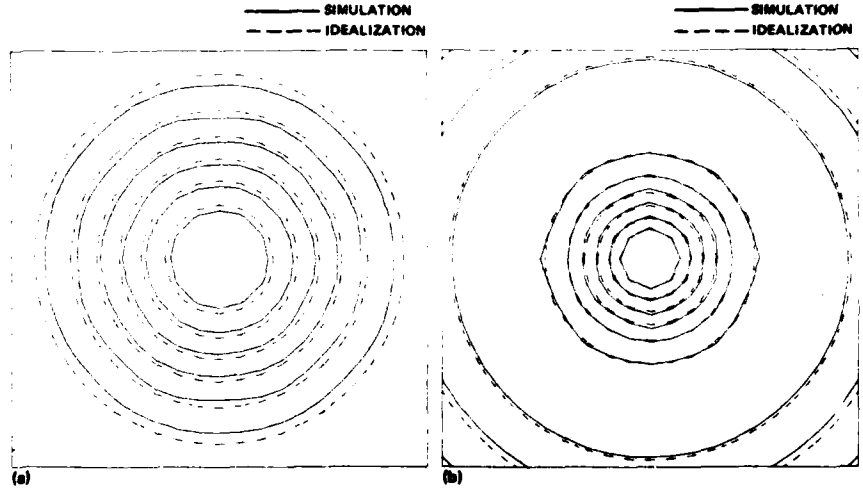

Fig. 8. Upstream velocity contours in a cross section. (a) Axial velocity; (b) theta velocity.

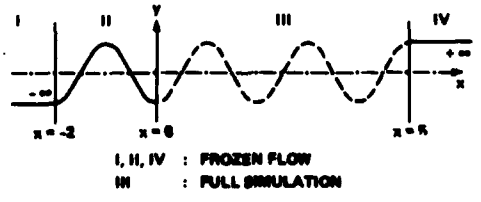

Fig. 9. Computational regions for filament to calculate induced velocity.

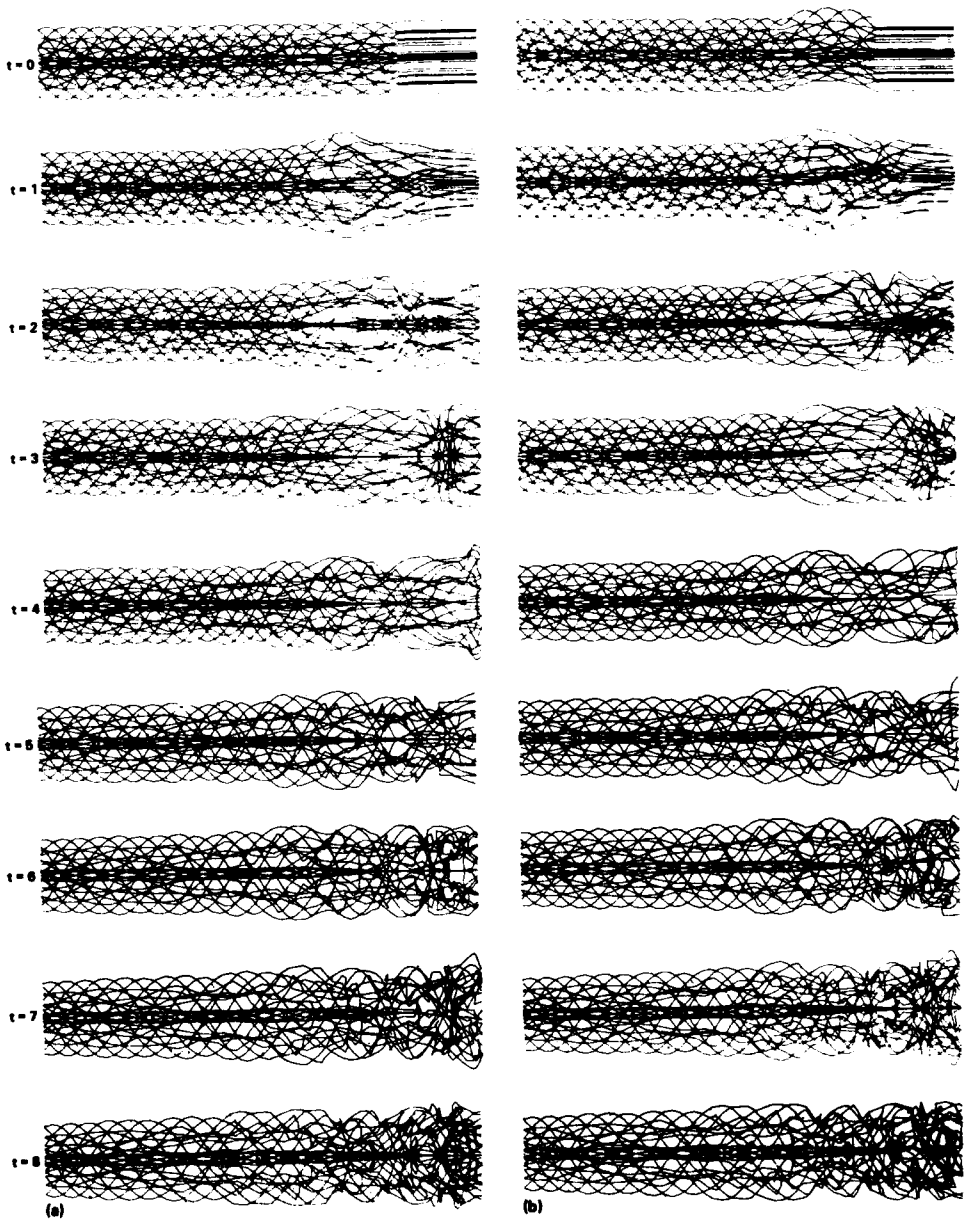

Fig. 10. Evolution of vortex filaments. (a) Case I; (b) Case II.

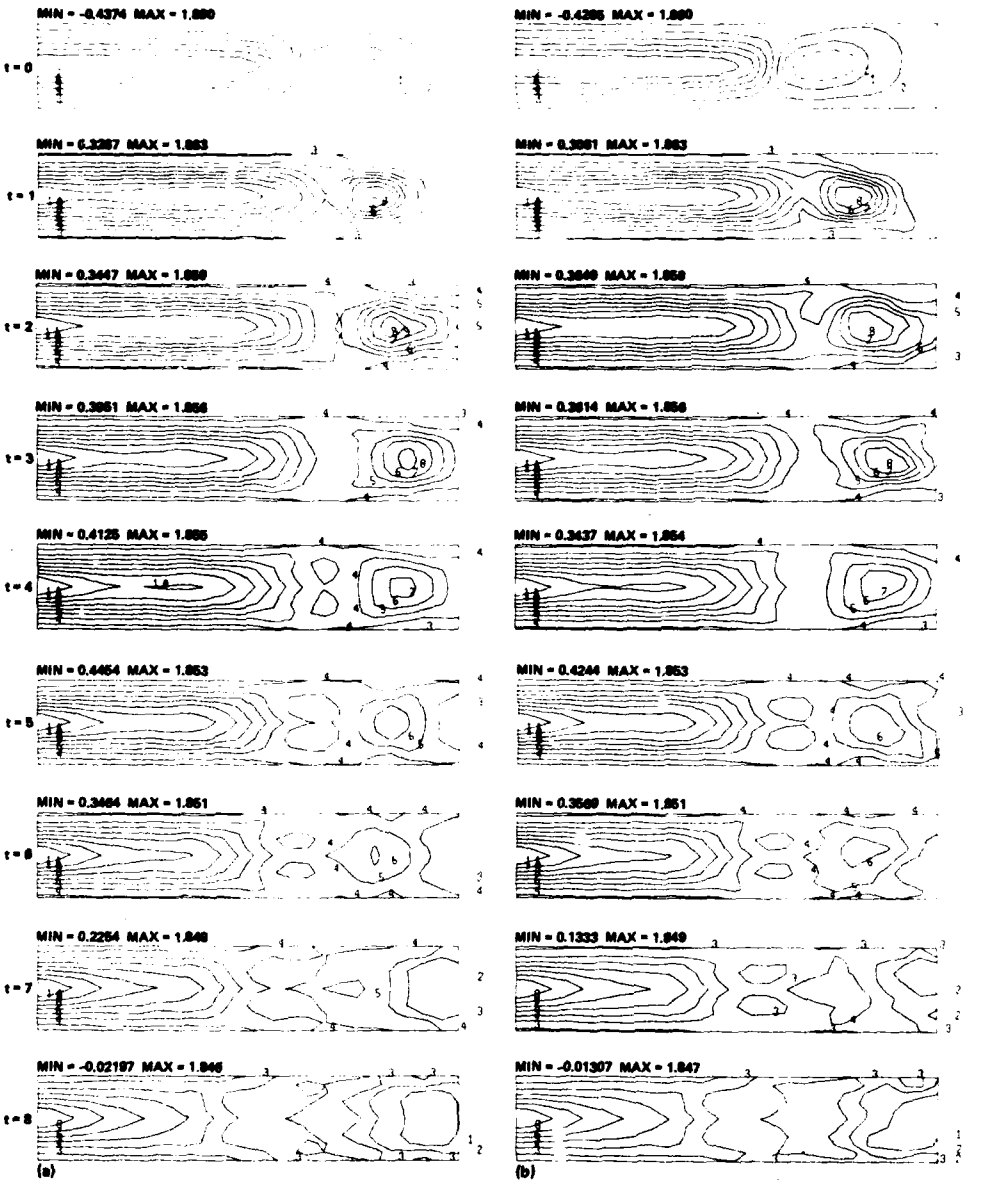

Fig. 11. Axial velocity contours. (a) Case I; (b) Case II.

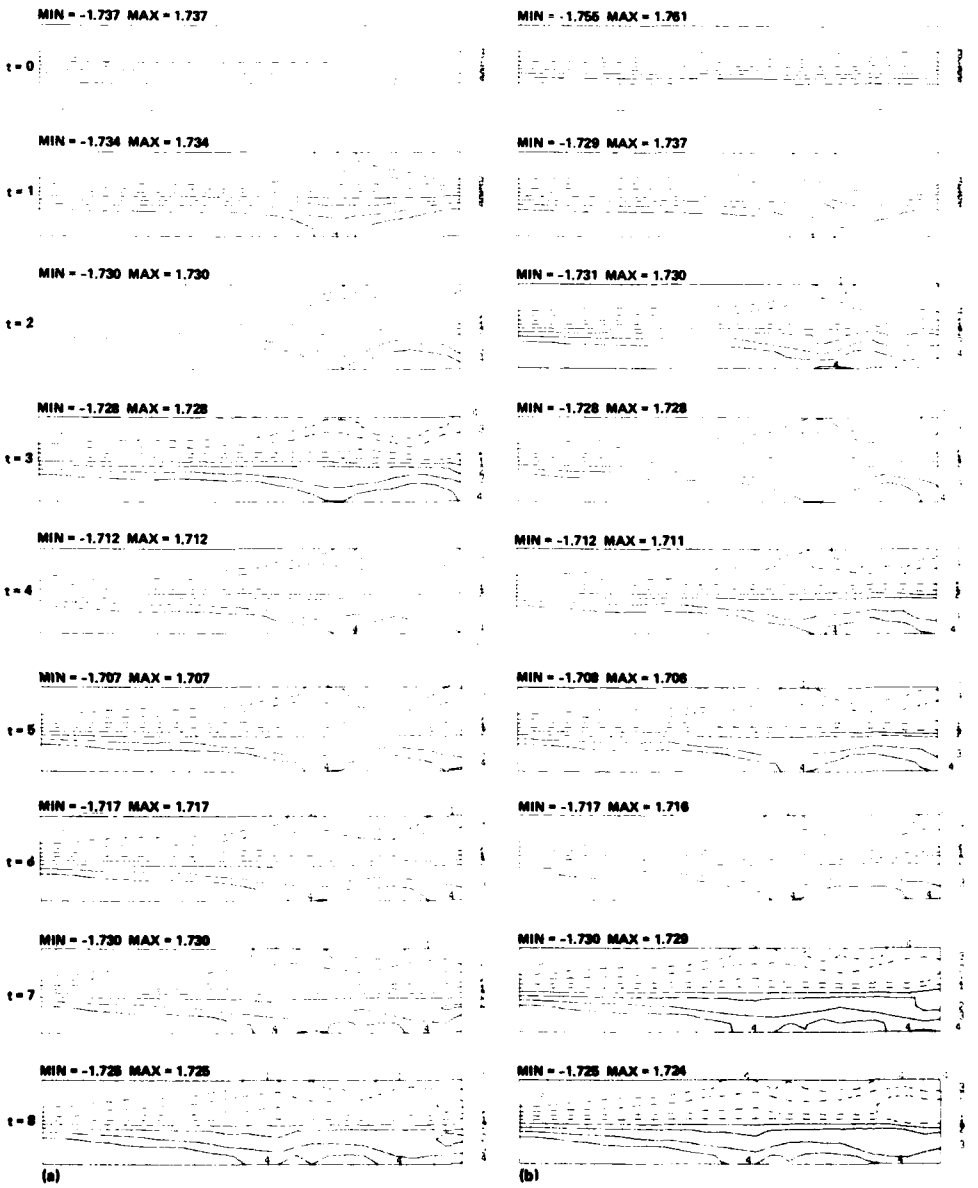

Fig. 12. Theta velocity contours. (a) Case I; (b) Case II.

ETUDES EXPERIMENTALES D'ECOULEMENTS TOURBILLONNAIRES SOUMIS A DES EFFETS DE GRADIENT DE PRESSION ADVERSE

par

J.L. SOLIGNAC et O.LEUCHTER

Office National d'Etudes et de Recherches Aérospatiales (ONERA)
92320 CHATILLON - FRANCE

RESUME

Le phénomène de destabilisation des tourbillons sous l'effet d'un gradient de pression adverse est étudié sur deux configurations différentes : la première est celle d'un tourbillon d'aile delta, la seconde est relative à un tourbillon engendré par un montage à deux ailettes en incidence opposée. L'étude comporte des visualisations par plan laser et des mesures locales de pression et de vitesse (par anémométrie laser). Des traits communs caractérisant l'éclatement sont mis en évidence sur les deux configurations (enroulement spiral du noyau et formation d'un bulbe de recirculation), mais aussi des différences en ce qui concerne l'intensité du phénomène d'éclatement et le caractère instationnaire, plus prononcés pour le tourbillon d'aile delta. Une brève exploitation des résultats de ce dernier a été effectuée dans le cadre des théories de Ludwieg et de Benjamin. Un critère d'éclatement a été recherché en fonction des paramètres intensité tourbillonnaire et gradient de pression adverse.

SUMMARY

The phenomenon of destabilization of vortex flows submitted to adverse pressure gradients is examined on two different configurations. The first concerns the leading-edge vortex of a delta wing, the second is generated by two blades set at opposite angles of incidence. The study comprises visualizations by the laser sheet technique and local measurements of pressure and velocity (by L.D.A.). Common features characterizing the vortex breakdown are evidenced for both configurations (helical distortion of the vortex core and formation of a recirculating bubble), but also differences concerning the intensity of the breakdown phenomenon and his instationary character, which is more pronounced for the vortex of the delta wing. A brief exploitation of the results concerning this configuration has been carried out in the context of the theories of Ludwieg and Benjamin. A breakdown criterion has been established depending on the parameters vortex strength and intensity of the adverse pressure gradient.

NOTATIONS PRINCIPALES

α	incidence de l'aile delta
K	circulation réduite
K_p	coefficient de pression
p	pression
P	densité de probabilité
q	pression dynamique
r	rayon vecteur compté à partir du centre du tourbillon
U,V,W	composantes de la vitesse moyenne suivant Ox , Oy , Oz .
u, v, w	composantes des fluctuations de vitesse

U_o vitesse de référence

V_t vitesse tangentielle

V_r vitesse radiale

x, y, z coordonnées :

Montage I : origine de x : bord de fuite de l'aile
origine de y : plan médian de la veine
origine de z : apex de l'aile

Montage II : origine du trièdre direct
à la pointe du corps central

Σ rapport de section A/A_c de la prise d'air (montage I)

ψ fonction de courant du mouvement projeté dans le plan méridien (paragraphe 6.2)

ρ masse spécifique

INDICES

o relatif aux conditions de référence amont

a relatif à l'axe du tourbillon

e relatif à l'écoulement extérieur

1 - *INTRODUCTION* -

Le phénomène de l'éclatement des structures tourbillonnaires enroulées retient l'attention des spécialistes depuis plusieurs décennies. Les premières observations faites sur les tourbillons confinés dans un canal [1] ou issus d'ailes delta [2],[3], [4] ont clairement mis en évidence l'effet déstabilisant d'un gradient de pression adverse pouvant conduire à la désorganisation complète du tourbillon et à son éclatement. En raison de l'intérêt renouvelé que porte aujourd'hui l'aérodynamique du vol à grande incidence à ce problème, diverses études fondamentales sur les écoulements tourbillonnaires ont été entreprises récemment à l'ONERA, sous l'impulsion des constructeurs aéronautiques et avec l'appui financier des services officiels français (DRET et STPA). L'objectif de ces recherches est multiple : il s'agit en premier lieu de préciser les circonstances dans lesquelles l'éclatement se produit et, compte tenu des connaissances encore trop fragmentaires sur ces phénomènes, d'en améliorer la compréhension physique. En second lieu il s'agit de recueillir des informations expérimentales détaillées sur la structure du champ moyen et de la turbulence permettant d'étayer, dans un stade ultérieur, les démarches d'une modélisation numérique de ces phénomènes. Dans cet esprit, deux études fondamentales sont menées parallèlement en écoulement incompressible portant plus particulièrement sur l'effet déstabilisateur d'un gradient de pression adverse appliqué de façon progressive à l'écoulement (par opposition à la recompression brutale par choc étudiée par ailleurs [5]). La première étude, centrée essentiellement sur l'analyse des conditions d'éclatement, utilise un tourbillon d'aile delta en incidence, alors que la seconde, davantage orientée vers l'analyse de la turbulence et sa modélisation, porte sur un sillage tourbillonnaire du type bout d'aile engendrée par un montage à deux ailettes mises en incidence opposée.

Les études expérimentales décrites dans le présent article ont largement bénéficié de l'avènement de techniques expérimentales nouvelles basées sur l'utilisation du laser. Ainsi, la technique de visualisation par plan de lumière laser (tomoscopie) a été utilisée avec succès sur les deux montages pour décrire qualitativement les phénomènes mis en jeu au cours du processus de destabilisation et de l'éclatement du tourbillon.

D'autre part, la technique de l'anémométrie laser, largement utilisée dans la présente étude, a permis d'effectuer des explorations détaillées du champ des vitesses moyennes et des fluctuations turbulentes, y compris dans les régions de recirculation du type bulbe caractérisant les configurations éclatées. Des moyens de mesure plus classiques, tels que les sondes de pression et l'anémométrie à fil chaud, ont également été employés.

Les résultats expérimentaux les plus significatifs obtenus à l'aide de ces techniques seront donnés après une description succincte des moyens d'essai et de mesure utilisés. Une présentation simultanée des résultats concernant ces deux configurations a été adoptée en général de manière à faire ressortir, au fur et à mesure de l'exposé, les traits communs ou, le cas échéant, les caractéristiques particulières propres à chacun de ces écoulements. Une discussion critique des résultats concernant l'éclatement sera ensuite effectuée à la lumière des diverses approches théoriques proposées dans la littérature. Dans ce contexte, on présentera l'ébauche d'un critère pratique basé sur des conditions limites d'existence de l'éclatement, dont la généralité reste cependant à établir.

2 - *MONTAGES EXPERIMENTAUX* -

2.1 - *Tourbillon d'aile delta (Montage I)* -

Une aile delta à bord d'attaque aigu placée en incidence dans un écoulement uniforme sert de générateur de tourbillon (Fig.1a). Ce dispositif possède l'avantage de représenter un cas réaliste de tourbillon rencontré en vol et de fournir de fortes intensités tourbillonnaires. Par contre, il n'évite pas la

distorsion de l'écoulement due au champ de l'aile qui affecte la symétrie de révolution, souhaitable pour schématiser les phénomènes.

L'aile est taillée dans une plaque de 4 mm d'épaisseur. Le biseau de bord d'attaque de 30° est situé à l'extrados de façon à conserver à la couche limite d'intrados qui décolle sur l'arête des caractéristiques de couche limite plane . La flèche est de 75° et l'envergure de 300 mm.

L'aile est montée en veine de façon qu'un seul des deux tourbillons d'apex soit absorbé par une prise d'air interne à la veine.

La fermeture des volets mobiles à l'arrière de cette prise d'air crée, en réduisant le débit capté, un gradient de pression adverse qui remonte vers l'amont avec une intensité croissante à mesure que la section minimale de la prise d'air diminue. L'évolution p(x) de la pression est caractérisée par le paramètre $\Sigma = A/A_c$, rapport de la section d'entrée A de la prise d'air à la section minimale Ac.

L'aile est mobile en incidence autour d'un axe vertical situé (aux 2/3 de la corde) de façon telle que le déplacement latéral du tourbillon reste peu sensible aux variations d'incidence (Δy = 16 mm au niveau du bord de fuite, pour une variation d'incidence de 10° à 30°).

2.2 - *Tourbillon du type bout d'aile (Montage II)* -

Le second montage utilise un générateur de tourbillon constitué par deux ailettes calées à des incidences opposées et fixées sur un dard cylindrique effilé placé dans l'axe de la veine d'essai (figure 1b). Celle-ci est de forme cylindrique, avec un diamètre de 300 mm. Les ailettes, de profil NACA 0012, ont une corde de 50 mm. Leur calage est en principe variable ce qui confère à ce montage la possibilité d'étudier des tourbillons de différentes intensités. Pour des incidences faibles (de l'ordre de 5° par exemple) on peut ainsi réaliser des configurations où l'effet de sillage provoqué par le dard prédomine (sillage tourbillonnaire). Dans la présente étude par contre, un calage élevé (12°) a été adopté en vue d'étudier une configuration présentant un caractère tourbillonnaire très prononcé. L'un des avantages de ce montage réside dans le fait que les nappes tourbillonnaires issues des ailettes s'enroulent en un vortex à double branche présentant des propriétés de symétrie et de stabilité intéressantes pour l'exploration du champ aérodynamique du tourbillon.

Le montage est installé dans un caisson permettant de créer dans la veine d'essai un gradient de pression positif au moyen d'une aspiration secondaire. Celle-ci a pour effet de diminuer la pression p_c du caisson qui s'exerce sur une portion limitée de la veine en provoquant ainsi, au sein de l'écoulement, un gradient de pression adverse commodément ajustable. L'intensité de ce gradient sera caractérisée par le coefficient de pression K_{p_c} .

La vitesse dans la veine est maintenue constante au moyen d'un col sonique situé en aval du caisson et relié à un réservoir à vide. Des conditions d'écoulement très stables peuvent ainsi être réalisées. La vitesse de référence U_o (vitesse dans la veine mesurée juste en amont du générateur) a été maintenue à une valeur constante de 32,5 m/s pour l'ensemble des essais.

3 - *INSTRUMENTATION* -

Sur chacune des configurations tourbillonnaires étudiées, deux modes d'investigation faisant appel chacun à la technique du laser ont été utilisés : il s'agit de la tomoscopie laser (visualisation par plan de lumière) d'une part et de l'anémométrie laser d'autre part. Par ailleurs, ces mesures ont été complétées par des mesures de pression (sondes de pression statique et sondes à 5 trous) et quelques mesures par anémométrie à fil chaud.

3.1 - *Visualisation par tomoscopie laser* -

La technique de tomoscopie laser qui consiste à illuminer l'écoulement au moyen d'une tranche de lumière laser très intense, a été mise au point à l'ONERA par la Division Optique de la Direction de la Physique Générale [6]. L'écoulement est rendu visible en l'ensemençant soit par un brouillard de vapeur d'eau condensée brutalement dans des vapeurs d'azote liquide, soit par des fumées de sulfite d'ammonium formées par la rencontre des gaz ammoniac et anhydride sulfureux au sortir de trous d'alimentation pratiqués dans la maquette.

Plusieurs modes de prise de vue ont été utilisés :

- instantanés en éclairage très bref (15 ns, laser à impulsion YAG 0,2 J/éclair, clichés Polaroïd 3000 ASA en noir et blanc et 400 ASA en couleur) ;

- cinématographie ultra-rapide (entre 900 et 3000 images/s, film 16 mm 400 ASA, éclairage continue par le laser 15 W du vélocimètre).

Des visualisations par éclairage diffus (temps de pose $\simeq$ 1/30 s) ont également été effectuées. Cette procédure simplifiée permet d'obtenir rapidement une vue de l'ensemble du tourbillon et de déterminer, en particulier, la position du point d'éclatement en fonction des paramètres de réglage(§ 7.4).

3.2 - *Anémométrie laser* -

Il s'agit d'un appareil bidirectionnel développé par la Direction de la Physique Générale [7] mesurant simultanément deux composantes du vecteur vitesse. La figure 2 en précise le schéma de principe : la source est un laser à argon ionisé du type Spectra Physics Modèle 171. Sa puissance maximale est de 15 W. Les deux couleurs utilisées sont le bleu (longueur d'onde 4880 Å) et le vert (5145 Å). Leur séparation est assurée par un jeu de lames dichroïques semi-transparentes. Les quatre faisceaux qui résultent de la traversée des deux diviseurs DB et DV sont focalisés pour constituer le volume de mesure dont le diamètre

utile est d'environ 300µm. Les rayonnements bleu et vert interfèrent dans le volume de mesure pour former deux systèmes de franges perpendiculaires dont l'inclinaison est réglée à ± 45° des axes horizontaux et verticaux.

Au cours de la présente étude, les interfranges étaient de 16,24µm pour le bleu et de 16,82µm pour le vert. Afin de permettre au système de détecter le signe de la composante de vitesse mesurée, les faisceaux traversent des modulateurs acousto-optiques (cellules de Bragg) induisant un défilement des franges dont la fréquence de modulation était de 2,5 MHz pour le bleu et de 3,75 pour le vert.

La partie réception est constituée de deux optiques collectrices indépendantes associées à des photomultiplicateurs précédés de filtres interférentiels assurant la discrimination des composantes bleue ou verte. L'ensemble fonctionne selon le mode diffusion directe de manière à bénéficier d'un rapport signal/bruit maximal. Les signaux délivrés par les photomultiplicateurs sont envoyés sur des compteurs DISA type 55L dont les sorties numériques sont connectées à un système d'acquisition par l'intermédiaire d'un numérisateur simultané.

Les parties émission et réception sont montées chacune sur une table motorisée permettant des déplacements identiques suivant 3 directions perpendiculaires avec une précision de 0,01mm. Les données relatives à la position du volume de mesure ainsi que les mesures proprement dites (valeurs des deux composantes de vitesse pour chaque particule validée) sont stockées sur bande magnétique en vue d'un traitement en différé. Certains résultats (vitesse moyenne, écart type) sont fournis en temps réel par le mini-ordinateur auquel est connecté l'anémomètre.

3.3 - *Autres moyens de mesure utilisés* -

Le champ de pression a été exploré, dans le cas du tourbillon d'aile delta, à l'aide de sondes à 5 trous. Celles-ci fournissent en principe les 3 composantes de la vitesse ainsi que la pression statique tant que l'inclinaison du vecteur vitesse sur l'axe de la sonde ne dépasse pas 40°. Ce type de sonde est par conséquent inadapté pour explorer des bulbes de recirculation.

Dans le cas du montage des ailettes, le champ de pression statique a été exploré à l'aide de sondes ONERA du type GG. Il s'agit de sondes en forme de dièdre, les orifices de prise de pression étant situés sur les deux faces du dièdre à une certaine distance en aval de l'arête. De par sa construction, cette sonde est particulièrement peu sensible à la direction de l'écoulement dans le plan de symétrie passant par l'arête de la sonde.

L'anémométrie à fil chaud a été également utilisée sur cette configuration dans le but d'effectuer des recoupements avec les mesures par anémométrie laser. Des chaînes standard du type DISA 55 M 01/05/10 ont été utilisées avec des sondes à 1 fil ou à 2 fils croisés.

4 - *CONDITIONS D'ESSAI* -

4.1 - *Montage d'aile delta* - (I)

Dans le cas du montage du tourbillon d'aile delta, les paramètres d'essai sont, pour une maquette donnée :

a) la position des volets (fig.1a) caractérisée par le rapport des sections $\Sigma = A/Ac$, en fonction duquel un gradient de pression plus ou moins intense s'établit dans la veine. Ce gradient caractérisé par l'évolution du coefficient de pression $Kp(x)$ est mesuré dans le plan des glaces de veine, à 470 mm du plan médian,

b) l'incidence α de l'aile qui commande l'intensité tourbillonnaire liée à la circulation de l'aile.

Un exemple d'évolution $Kp = f(x, \Sigma)$ est donné fig.3a ; dans la présente étude, on se limitera à l'analyse d'une configuration type réalisée pour $\Sigma = 2,2$ et $\alpha = 20°$ et dans laquelle l'éclatement se situe à 230 mm du bord de fuite de l'aile (courbe de référence en pointillé , fig.3a).

Pour les explorations transversales, quatre sections particulières ont été retenues (fig. 1a) :

① en amont de l'éclatement en x = 180 mm,
② au début du phénomène en x = 230 mm,
③ au sein du bulbe de recirculation, au voisinage du maximum de vitesse de retour, en x = 260 mm,
④ plus en aval dans le bulbe, en x = 350 mm.

L'origine des x est le bord de fuite de l'aile à l'incidence de 20°.

4.2 - *Montage des ailettes* - (II)

Pour les configurations du tourbillon engendré par les ailettes (à calage fixe), le seul paramètre d'essai est la pression du caisson p_c qui détermine le gradient de pression adverse au sein de l'écoulement. Les valeurs suivantes du coefficient de pression $Kp_c = (p_c - p_b)/q_o$ ont été adoptées dans la présente étude : - 0,05, - 0,10, - 0,15, - 0,20 et - 0,25. Dans le cas limite où aucune aspiration secondaire n'est effectuée dans le caisson (cas de "référence"), la valeur de Kp_c est voisine de 0. L'évolution de la pression statique p_e (exprimée par le coefficient de pression $Kp_e = (p_e - p_b)/q_o$), mesurée dans la partie saine de la veine à 80 mm de l'axe est précisée sur la figure 3b pour l'ensemble des valeurs du paramètre Kp_c. On voit que l'évolution de la pression est pratiquement linéaire au droit de la veine ouverte et que son gradient croît en intensité au fur et à mesure que la pression du caisson p_c diminue.

Contrairement au premier montage, où une seule configuration de recompression a été examinée, l'essentiel des résultats relatifs au deuxième montage sera présenté pour l'ensemble des 6 configurations de recompression de la figure 3b, mais seulement en une section, située à 200 mm en aval du générateur.

5 - RESULTATS -

5.1 - Visualisations -

La technique de visualisation par tomoscopie permet de décrire qualitativement les phénomènes mis en jeu au cours du processus de destabilisation :

une séquence filmée de la vue méridienne du tourbillon d'aile delta dans la région du point d'éclatement est représentée sur la figure 4*.

On note l'apparition de noyaux tourbillonnaires disposés en quinconce qui suggèrent l'existence de l'enroulement en spirale du noyau central du tourbillon, primitivement aligné avec l'axe en amont de l'éclatement.

La figure 5 montre une succession de vues instantanées obtenues au moyen du laser impulsionnel YAG sur le tourbillon issu des ailettes. Les clichés (a) à (f) sont disposés suivant des intensités croissantes du gradient de pression adverse repéré par le paramètre Kpc. Le processus de destabilisation se traduit, comme sur la figure précédente, par un enroulement en hélice du tourbillon initialement rectiligne. Ce processus commence par une légère ondulation du noyau central avec une faible hélicité (cliché (c)), alors que pour des recompressions plus intenses, l'éclatement s'établit plus brusquement, accompagné d'une rapide augmentation de l'hélicité (cliché (e) et (f)). En dépit des ressemblances évidentes entre les 2 configurations tourbillonnaires, on note pour le deuxième cas une destabilisation plus progressive et plus lente, alors que le tourbillon d'aile delta paraît se désorganiser nettement plus brusquement.

Un raisonnement simple basé sur la continuité du sens de rotation du noyau tourbillonnaire montre que seul un sens d'enroulement contraire au sens de rotation du tourbillon conduit à une décélération sur l'axe.

Sens de l'enroulement de la spirale

Les visualisations des plans transversaux présentées sur la figure 6 font clairement apparaître la structure feuilletée des tourbillons qui provient de l'enroulement des nappes tourbillonnaires issues des maquettes.

Dans le cas du tourbillon d'aile delta (figure 6a) le sillage d'intrados s'enroule à son extrémité en formant un contre-tourbillon adjacent au tourbillon principal.

Dans le cas du deuxième montage, (fig.6b) les sillages des ailettes s'enroulent pour former un tourbillon à deux branches, comme déjà remarqué plus haut. On retrouve d'ailleurs, lors des explorations transversales, la trace de ces sillages dans les profils de la pression d'arrêt, de la vitesse ou des grandeurs turbulentes.

Il convient de rappeler à propos de ces visualisations que l'élément traceur rend visible les zones rotationnelles [8] , (voir aussi [9] et [10]), donc en particulier les nappes tourbillonnaires issues des maquettes.

5.2 - Champ de pression -

Les figures 7a et 7b donnent, pour les deux configurations tourbillonnaires examinées, l'évolution longitudinale de la pression statique sur l'axe. Y sont rappelées, à titre de comparaison, les évolutions correspondantes de la pression dans l'écoulement extérieur. Pour le premier montage (aile delta), seule la configuration relative au paramètre $\Sigma = 2,2$ est présentée, alors que pour le second montage les mesures de pression ont été faites pour l'ensemble des valeurs du paramètre Kp_c

On note pour les deux configurations tourbillonnaires une amplification très importante du gradient de pression sur l'axe, par rapport à celui régnant dans l'écoulement extérieur. Il s'agit là d'un trait caractéristique de ce type d'écoulement, d'autant plus marqué que l'intensité tourbillonnaire est forte [11] . On observe en effet, sur l'axe du tourbillon d'aile delta (qui est plus intense) une dépression nettement plus accusée et une recompression plus brutale que dans le cas du sillage tourbillonnaire.

Quant à l'influence du paramètre Kp_c , on constate sur la figure 7b qu'une légère intensification de la recompression à l'extérieur du tourbillon conduit à une augmentation notable des pressions sur l'axe, par rapport à celle caractérisant la configuration de référence sans gradient extérieur ($Kp_c \simeq 0$) , où seuls les effets visqueux agissent. Simultanément, cette forte augmentation de la pression sur l'axe se déplace vers l'amont, bien que la recompression de l'écoulement extérieur reste localisée au droit de la portion de veine libre (voir figure 3b). Il s'agit là d'un phénomène de forte interaction caractérisant la sensibilité de la configuration vis à vis des perturbations venant de l'extérieur. (Une étude ultérieure devra préciser dans quelle mesure la présence de la sonde de pression peut intervenir dans ce processus d'interaction).

Les figures 8a et 8b précisent les évolutions radiales de la pression : il s'agit, pour le tourbillon d'aile delta (figure 8a) des mesures effectuées dans les 4 sections d'une même configuration avec éclatement (voir paragraphe 4.1), alors que pour le sillage tourbillonnaire (figure 8b) les mesures sont effectuées en une même section (x = 200 mm) pour les différentes configurations définies précédemment. Ces deux figures illustrent bien l'accroissement plus rapide de la pression sur l'axe par rapport à l'extérieur, soit en fonction

---

* Le film ayant été pris avec l'écoulement venant de la droite vers la gauche du photographe, le sens de rotation du tourbillon est ici inversé par rapport à ce qui est indiqué sur la figure 1a.

de x (fig.8a), soit en fonction de Kp_c (fig.8b). La disparition progressive de la dépression au centre du tourbillon, liée à la diminution du niveau de la vitesse tangentielle, traduit dans les deux cas la désorganisation progressive de la structure tourbillonnaire, conformément aux visualisations présentées plus haut (fig.5).

5.3 - *Evolution de la vitesse et de la turbulence sur l'axe du tourbillon* -

La vitesse moyenne et les taux de fluctuation axiale et transversale, présentés sur les figures 9a et 9b, ont été déterminés à l'aide de l'anémométrie laser.

Les résultats relatifs au tourbillon d'aile delta (fig.9a) montrent, à l'approche de l'éclatement, une brusque décélération de l'écoulement sur l'axe conduisant à la formation d'un bulbe, dont la réhabilitation en sillage est très lente. Corrélativement, le taux de fluctuation longitudinale augmente fortement au voisinage de l'éclatement, alors que le taux de fluctuation transversale présente une diminution sensible. Les histogrammes de la figure 10a mettent clairement en évidence le caractère intermittent des fluctuations longitudinales à l'approche de l'éclatement (section ②) responsable de la valeur élevée du taux des fluctuations $\sqrt{u^2}$. Les deux pics apparaissant sur l'histogramme des vitesses longitudinales U correspondent respectivement aux conditions amont (section ①) et aval (section ③). Quant à la composante verticale W, la forme particulière de l'histogramme à 2 pics en amont de l'éclatement (section ①) traduit l'existence de fluctuations transversales du noyau tourbillonnaire, compte tenu du fort gradient de vitesse tangentielle au voisinage de l'axe. Plus en aval, les histogrammes prennent progressivement des formes habituelles à 1 seul pic ce qui se traduit, pour les deux composantes, par une diminution des taux de fluctuation .

La figure 9b, relative au sillage tourbillonnaire issu des ailettes, est l'homologue de la figure 9a avec la différence que les mesures sont faites ici, comme plus haut pour la pression, à une abscisse fixe (x = 200 mm) en fonction du paramètre Kp_c, et non pas en fonction de x. Ainsi, au fur et à mesure que celui-ci diminue, le point d'éclatement se déplace vers l'amont en même temps que s'intensifie le processus de destabilisation. Les évolutions de la vitesse moyenne et de la turbulence sont analogues à celles de la figure 9a à l'exception de la forte augmentation de $\sqrt{u^2}$ qui n'est pas observée sur la figure 9b. Les histogrammes relatifs à la composante longitudinale U (figure 10b) montrent en effet l'absence des deux pics dans les configurations les plus destabilisées (Kp_c = - 0,1 et - 0,2), alors que pour la composante verticale W on retrouve les deux pics avant l'éclatement, semblables à ceux de la figure 10 a. Cette comparaison met donc bien en évidence l'existence de propriétés globales communes au deux configurations, mais aussi des différences, notamment en ce qui concerne le caractère instationnaire de l'éclatement, qui est plus prononcé dans le cas du tourbillon d'aile delta.

5.4 - *Evolutions transversales de la vitesse et de la turbulence* -

Les profils de vitesse longitudinale (U) et tangentielle ($V_t = W$) ainsi que les taux de fluctuation correspondants sont obtenus par explorations horizontales passant par l'axe du tourbillon. Les profils de vitesse moyenne U et W sont regroupés sur les deux figures 11a et 11b. Sur la première, relative au tourbillon d'aile delta, les profils sont donnés pour les 4 sections définies plus haut, alors que sur la seconde, relative au tourbillon des ailettes, figurent pour U et pour W les 6 profils correspondant aux diverses valeurs du paramètre Kp_c (section d'exploration x = 200 mm).

La destabilisation du tourbillon conduisant à l'éclatement se manifeste dans les deux cas de façon particulièrement nette en ce qui concerne le champ moyen par une diminution brusque de la vitesse U localisée près de l'axe et en même temps par une décroissance rapide du gradient radial de la vitesse tangentielle. L'éclatement a pour conséquence l'apparition d'une région à vitesse négative (bulbe de recirculation) au sein de laquelle la vitesse tangentielle devient très faible.(sections ③ et ④ dans le cas de la figure 11a, Kp_c =-0,2 et Kp_c = -0,25 dans le cas de la figure 11b).

Les ordonnées z mentionnées sur la figure 11a représentent la cote de la ligne d'exploration passant sensiblement au centre du tourbillon. Comme on le voit d'après l'ordonnée y du passage par zéro de la composante tangentielle W, l'axe du tourbillon subit aussi un décalage latéral en y, auquel correspond une légère incurvation de l'axe du tourbillon par rapport à la direction Ox. Ce décalage angulaire explique en partie de légères dissymétries sur les mesures de W .

Comme le montre l'histogramme de la figure 10a correspondant au point B (section ②), la vitesse moyenne correspondante U_B n'a qu'une faible probabilité d'existence et se présente comme la moyenne entre les valeurs U_A et U_C des états de vitesse stables en amont et en aval de la section ② , à l'opposé du tourbillon des ailettes, où la vitesse moyenne est de l'ordre de la vitesse la plus probable (voir figure 10 b).

Les profils transversaux des fluctuations de vitesse, regroupés sur les figures 12a et 12b, présentent également des caractères communs aux deux types de tourbillons, à savoir l'existence de deux pics pour la composante axiale dans les configurations les plus destabilisées et des évolutions plus plates pour la composante transversale qui présente d'ailleurs dans les deux cas des taux de fluctuation plus faibles que la composante longitudinale.

On notera cependant une différence essentielle entre les deux types de tourbillon : elle concerne, comme déjà remarqué au paragraphe précédent, les niveaux des fluctuations, notamment pour la composante longitudinale dans la zone d'éclatement et pour la composante tangentielle en amont de celle-ci. Les valeurs plus modérées des fluctuations observées dans la configuration du tourbillon des ailettes caractérisent vraisemblablement davantage la structure turbulente de cet écoulement, alors que les niveaux nettement plus élevés pour le tourbillon d'aile delta semblent être imputables en majeure partie à l'existence d'instabilités provoquant des mouvements organisés à grande échelle.

Comme la figure 12b le met très clairement en évidence pour le cas du tourbillon des ailettes, le processus de destabilisation engendre des champs turbulents intenses s'épanouissant rapidement dans le sens

transversal au fur et à mesure que le gradient de pression adverse augmente, comme on a pu le remarquer sur les visualisations de l'éclatement présentées figure 5.

6 - DISCUSSION DES RESULTATS -

6.1 - Symétrie de révolution -

Le mode de génération des tourbillons par enroulement de nappes tourbillonnaires issues des maquettes exclut en principe toute symétrie de révolution au sens strict du terme. L'expérience montre cependant, notamment dans le cas du générateur à ailettes, qu'à une distance raisonnable de celui-ci, les propriétés de symétrie axiale sont bien établies, même dans des situations de forte destabilisation. Tel est le cas de la figure 13, où sont comparés pour Kp_c =-0,20 des profils de vitesse longitudinale et du taux de fluctuation correspondant, obtenus à partir de deux explorations perpendiculaires, l'une dans le sens horizontal et l'autre dans le sens vertical. La congruence des profils est globalement très bonne, à l'exception des traces des sillages provenant des ailettes qui sont clairement visibles sur ces profils, mais qui n'apportent qu'une faible perturbation très localisée.

Grâce à l'hypothèse de symétrie de révolution, qui paraît donc raisonnablement bien justifiée dans le cas du tourbillon des ailettes, il est possible de relier la vitesse tangentielle V_t au gradient radial de la pression par l'intermédiaire de la relation d'équilibre radial

$$\rho \frac{V_t^2}{r} = \frac{\delta p}{\delta r}$$

On a ainsi calculé pour le cas de référence sans aspiration (pour lequel on disposait également de mesures effectuées par fil chaud) le profil de vitesse tangentielle à partir des mesures de pression statique. Ces résultats sont confrontés sur la figure 14. Malgré quelques écarts systématiques observés surtout dans la région visqueuse à proximité de l'axe (où les effets perturbateurs des sondes peuvent être éventuellement significatifs), l'accord entre ces différentes mesures paraît globalement satisfaisant.

Par opposition au sillage tourbillonnaire des ailettes, le tourbillon d'aile delta possède des propriétés de symétrie moins bonnes, de par la géométrie de son générateur qui n'assure pas la symétrie axiale dans les plans transversaux (voir profils de vitesse de la figure 11a). De plus, comme mentionné plus haut, l'écart angulaire entre l'axe du tourbillon et l'axe de la veine (Ox) peut contribuer à créer une dissymétrie des profils mesurés dans les plans transversaux. Ainsi, l'utilisation de la relation d'équilibre radial pour calculer la vitesse tangentielle a révélé, par comparaison avec les mesures directes de cette composante, des écarts plus importants que dans le cas du sillage tourbillonnaire des ailettes. Il a été admis néanmoins que la symétrie de révolution constitue une approximation valable pour exploiter les résultats à la lumière de théories ou à l'aide de schémas de calcul basés sur cette hypothèse.

6.2 - Evolution de la circulation -

L'hypothèse de la symétrie de révolution est implicitement contenue dans la formulation communément adoptée pour exprimer la circulation à partir de la vitesse tangentielle : $\Gamma = 2 \pi V_t r$.

Les évolutions radiales de la grandeur

$$K = \frac{V_t(r)}{U_o} r = \frac{\Gamma(r)}{2 \pi U_o}$$

sont présentées sur les figures 15a et 15b pour les deux types de tourbillons examinés. Elles se déduisent directement des profils $W(y)$ des figures 11a et 11b, en identifiant $W(y)$ à $V_t(r)$. La déformation progressive des évolutions $K(r)$, soit avec x (fig. 15a), soit avec Kp_c (fig.15b) reflète celle subie par les profils de vitesse tangentielle au cours du processus de destabilisation. Pour les deux configurations, la grandeur $K(r)$ tend vers une valeur constante loin de l'axe indiquant que l'écoulement est dans cette région du type "tourbillon potentiel". La différence entre les deux niveaux de K de part et d'autre de l'axe traduit une légère dissymétrie de l'écoulement. Celle-ci paraît plus accentuée dans le cas du tourbillon d'aile delta. On observe d'autre part que pour le tourbillon issu des ailettes, les évolutions de $K(r)$ à l'extérieur du noyau visqueux font apparaître un plateau de K intermédiaire correspondant à une portion de tourbillon potentiel. Cette particularité, qui est propre au type de générateur utilisé, est liée à la présence des nappes tourbillonnaires émises par les ailettes et à travers desquelles la grandeur K change de niveau. Le saut correspondant se décale vers l'extérieur au fur et à mesure que le tourbillon se destabilise, par suite d'un effet de déplacement croissant. L'introduction de la fonction de courant ψ définie par

$$\frac{\delta \psi}{\delta r} = r \frac{U}{U_o} \quad , \quad \frac{\delta \psi}{\delta x} = - r \frac{V_r}{U_o}$$

permet de regrouper approximativement sur une même courbe l'ensemble des profils de K , aussi bien pour le tourbillon d'aile delta que pour le tourbillon engendré par les ailettes (fig.15a et 15b, en bas). La grandeur $K(\psi)$ représente la moyenne entre les deux branches (y positif et y négatif) des figures 15a et 15b. Il convient de rappeler que dans l'hypothèse d'un écoulement permanent, axisymétrique et non visqueux la grandeur K ne dépend que de ψ [12]. Comme on peut le constater sur les figures 15a et 15b, cette hypothèse est assez bien vérifiée pour les deux tourbillons, sauf pour les configurations les plus destabilisées (Kp_c ≈-0,2 et -0,25) du tourbillon engendré par les ailettes, au voisinage de l'axe. Les valeurs moyennes de K relevées dans l'écoulement extérieur sont de 36 mm pour le tourbillon d'aile delta et 6,8 mm pour le tourbillon des ailettes.

6.3 - Comparaison des résultats en échelles normalisées -

D'après les résultats du paragraphe précédent, l'échelle propre du tourbillon peut être caractérisée par la valeur K_e que prend la quantité K à l'extérieur de la région visqueuse. Cette grandeur, qui ne fait intervenir que la vitesse axiale amont ainsi que la circulation du tourbillon potentiel auquel se raccorde le tourbillon réel, a en effet la dimension d'une longueur.

La figure 16 compare pour les deux tourbillons étudiés les évolutions longitudinales de la pression dans l'échelle réduite $\xi = x/K_e$. La figure 16a, relative à l'écoulement extérieur, montre que les gradients de pression sont en échelle réduite comparables entre eux. Le gradient $dK_p/d\xi$ relatif au tourbillon d'aile delta ($\Sigma = 2,2$) est en effet du même ordre que celui obtenu pour $K_{p_e} = -0,2$ dans le cas du générateur à ailettes. L'accroissement de la pression sur l'axe apparaît par contre nettement plus rapide dans le cas du tourbillon d'aile delta, ce qui implique un éclatement plus brutal, comme le montrent aussi les clichés de la figure 4 . Cette circonstance est à relier à la dépression plus accusée observée dans le cas du tourbillon d'aile delta (voir figures 7a et 8a), due essentiellement à la forme des profils de vitesse tangentielle. En effet, la différence des K_p sur l'axe et à l'extérieur s'exprime, en vertu de l'équilibre radial, par :

$$K_{p_a} - K_{p_e} = -\int_0^{\eta_e} \left(\frac{V_t}{U_0}\right)^2 \frac{d\eta}{\eta}, \quad \text{avec} \quad \eta = \frac{r}{K_e}$$

La figure 17b qui précise la forme des profils de vitesse tangentielle en coordonnées réduites, met clairement en évidence des niveaux de V_t/U_0 plus élevés pour le tourbillon d'aile delta, ce qui conduit, en vertu de la relation ci-dessus, à des écarts de pression entre l'axe et l'extérieur plus importants.

Quant à la forme des profils de vitesse (figures 17a et 17b) on note pour l'aile delta, l'allure caractéristique du tourbillon dit d'"Euler" [13] qui se traduit pour V_t par une évolution plus plate que celle du tourbillon potentiel et par un fort accroissement de U au voisinage de l'axe. Le tourbillon des ailettes par contre est caractérisé par un profil de vitesse longitudinale plus uniforme et par une vitesse tangentielle qui ne se raccorde au tourbillon potentiel qu'à l'extérieur de la nappe tourbillonnaire mise en évidence plus haut (figure 15b) et dont la trace est également visible sur le profil de U (fig.17a).

7 - *RECHERCHE DE CRITERES D'ECLATEMENT* -

Trois voies d'explication de l'éclatement se dégagent d'une bibliographie abondante sur le sujet:

1°) Une théorie dite de la "stabilité" [14] résulte de considérations d'équilibre local des nappes tourbillonnaires à partir desquelles peut être définie l'apparition éventuelle de zones d'instabilité qui viennent désorganiser la structure tourbillonnaire.

2°) Une théorie dite "théorie des ondes" [12] , [15] procède de l'analyse des conditions d'existence des ondes de perturbation et de leurs conséquences .

3°) Une troisième démarche [16, 17, 18, 19] plus pragmatique, consiste en l'élaboration de méthodes de calcul des écoulements tourbillonnaires dans le cadre de l'approximation quasi-cylindrique, qui est généralement adoptée pour représenter ce type d'écoulements en amont de l'éclatement. L'apparition de l'éclatement se présente comme une singularité dans le développement du calcul. C'est une circonstance analogue à celle que constitue le décollement lors du calcul des couches limites, circonstance qui oblige à renoncer au cadre des hypothèses simplificatrices de départ de la théorie de PRANDLT.

Les résultats expérimentaux ont donc été exploités tout d'abord en vue de vérifier le bien fondé de ces différentes démarches, ensuite dans le but de rechercher ou de valider certains critères d'éclatement.

7.1 - *Théorie de la stabilité (LUDWIEG)* -

En généralisant la condition de stabilité de Rayleigh : $d(V_t r)/dr > 0$, d'un fluide en rotation, au cas d'un écoulement soumis de plus à une vitesse longitudinale U , LUDWIEG [20] parvient à l'établissement des conditions de stabilité données par l'équation suivante qui dépend essentiellement des caractéristiques locales du profil de vitesse moyenne :

$$(1 - C_{\tilde{\psi}})^2 (1 + C_{\tilde{\psi}}) - (5/3 - C_{\tilde{\psi}}) C_{\tilde{z}}^2 > 0$$

$$\text{avec} \quad C_{\tilde{\psi}} = \frac{r}{V_t} \cdot \frac{\delta V_t}{\delta r}, \quad C_{\tilde{z}} = \frac{r}{V_t} \cdot \frac{\delta U}{\delta r}$$

Les points du profil moyen des vitesses, dans la section dans laquelle nous avons sensiblement localisé l'origine du phénomène ($x = 230$), ont été placés dans le diagramme des paramètres de LUDWIEG (fig.18). On voit effectivement qu'une partie des points représentatifs de ce profil se situe dans la zone d'instabilité. On observera d'ailleurs que cette zone est marquée par les fortes intensités de fluctuations, visibles sur la figure 12a, au voisinage de l'axe du tourbillon. Le critère de LUDWIEG apparaît ainsi beaucoup plus réaliste que celui proposé par HOWARD & GUPTA [21] , concernant les ondes de perturbation axisymétriques (fig.18).

7.2 - *Théorie des ondes de BENJAMIN [12]* -

On envisage la fonction de courant perturbée par une onde de faible intensité, stationnaire ou progressive. Nous nous limitons ici au cas stationnaire : $\psi = \psi_0 + F(r,x)\, e^{\gamma x}$.

L'équation des quantités de mouvement écrite dans le cadre des approximations quasi-cylindriques conduit pour F à la relation suivante : $\frac{\delta^2 F}{\delta r^2} - \frac{1}{r}\frac{\delta F}{\delta r} + \left[\gamma^2 - \frac{r}{U}\frac{\delta}{\delta r}\left(\frac{1}{r}\frac{\delta U}{\delta r}\right) + \frac{1}{r^3 U^2}\frac{\delta (V_t r)^2}{\delta r}\right] F = 0$

Le problème est un problème de valeurs propres pour γ , l'écoulement caractérisé par F étant : supercritique si toutes les valeurs propres de γ sont positives et subcritique si l'une au moins de ces valeurs propres est négative .

Selon le point de vue de BENJAMIN, l'éclatement du tourbillon fait passer d'un état supercritique à l'état subcritique conjugué. C'est ce que nous avons voulu vérifier à l'aide de nos résultats expérimentaux.

Comme le fait LEIBOVICH [22] pour des expériences concernant un tourbillon confiné dans un tube , on étudie le comportement de la fonction Fc qui provient de l'intégration de l'équation précédente pour $\gamma = 0$, à partir

des conditions aux limites pour $r = 0$: $Fc = 0$, $\frac{1}{r}\frac{\partial F_c}{\partial r} = 1$.

Si Fc devient négatif entre $r = 0$ et $r = r_e$, l'écoulement est subcritique, il est supercritique si Fc reste positif.

On constate ici que la section située en amont de l'éclatement ($x = 180$ mm) a bien les caractéristiques d'un état supercritique et que la section située un peu en aval ($x = 230$ mm) est subcritique (Fig.19).

Les idées de BENJAMIN se trouvent donc en accord avec les faits. Il est intéressant de voir aussi comment la fonction $A(r)$ $\quad A = -\frac{r}{U}\frac{\partial}{\partial r}\left(\frac{1}{r}\cdot\frac{\partial U}{\partial r}\right) + \frac{1}{r^3U^2}\cdot\frac{\partial(Vr)^2}{\partial r}$,

qui régit le comportement de la fonction Fc intervient par sa contribution essentielle au voisinage immédiat de l'axe.

7.3 - *Solutions quasi-cylindriques stationnaires : limite de validité de cette approximation* -

Deux études parmi les plus anciennes ont été choisies pour situer la nature du problème de l'éclatement dans le cadre de cette démarche [16], [17] .

Grâce à la simplicité des schémas proposés, des solutions analytiques représentent l'écoulement dans la section 2, à partir des données initiales dans une section 1 dont le paramètre caractéristique est le taux de rotation : $\tau = V_1/U_1$. Pour chacun des états 1 et 2, l'écoulement satisfait aux équations du mouvement avec l'hypothèse simplificatrice des écoulements quasi-cylindriques pour l'écriture de l'équation de l'équilibre radial.

L'état 2 se déduit de l'état 1 moyennant une recompression caractérisée par le paramètre $\chi = 1 - \left(\frac{U_2}{U_1}\right)^2$

Le calcul montre que dans le cadre de ces hypothèses il n'est pas toujours possible de trouver un rayon R_2 du noyau tel que les équations soient satisfaites entre les sections 1 et 2.

Ainsi, dans le plan des paramètres τ , χ (fig.20), on peut construire la courbe $(\mathcal{L})$ qui marque une limite au domaine d'existence des solutions quasi-cylindriques. De là vient l'idée simple d'utiliser cette courbe limite pour définir un critère d'éclatement.

On remarquera qu'en dépit des écarts qui peuvent s'expliquer par la différence des schémas de calcul proposés, les deux théories conduisent à des "critères" voisins.

7.4 - *Etude exploratoire des conditions d'éclatement* -

Pour préciser les conditions d'éclatement en fonction des paramètres mis en évidence au paragraphe précédent (intensité tourbillonnaire, gradient de pression adverse) une étude systématique a été entreprise sur le montage I (tourbillon d'aile delta). (La distance entre l'aile et la prise d'air était ici plus courte que dans les expériences décrites plus haut). Dans un souci de simplification on a adopté les paramètres de fonctionnement suivants : l'incidence α de l'aile, liée à l'intensité tourbillonnaire et l'ouverture des volets (paramètre Σ) déterminant la recompression dans la veine. On a ainsi obtenu, pour chaque couple (α , Σ), la position longitudinale x_E du point d'éclatement, dans la mesure où celui-ci se situe en amont de la prise d'air. Les valeurs de x_E , déterminées par voie optique, sont présentées sur la figure 21 en fonction de l'incidence α pour plusieurs valeurs de Σ . Les résultats font apparaître une limite, représentée par la courbe (L) sur la figure 21, au-delà de laquelle l'éclatement n'est plus observé .

Pour donner plus de généralité à ce résultat, la courbe limite (L) a été transposée dans le plan de deux paramètres plus directement liés à l'intensité tourbillonnaire d'une part et à la recompression d'autre part : pour le premier on a choisi la circulation Γ autour du tourbillon. Celle-ci est déterminée à partir de l'incidence α à l'aide de la théorie de POLHAMUS [23] (et partiellement contrôlée par mesure directe). Γ est normalisée par U_0 et R , rayon limite du tourbillon d'Euler : $\tau' = \Gamma/2\pi U_0 R$. Pour le second, on a choisi le gradient de pression lointain $\left(dK_p/dx\right)_E$ mesuré au droit du point d'éclatement, normalisé par la distance L_E du point d'éclatement à l'apex de l'aile : $\chi' = L_E\cdot\left(\frac{dK_p}{dx}\right)_E$.

La courbe $(\mathcal{L})$ définit donc dans le plan de ces deux paramètres la limite des possibilités d'éclatement, comme indiqué sur la figure 22. Elle présente une certaine analogie avec les courbes limites théoriques discutées plus haut (figure 20), dont la signification et le bien-fondé restent encore à préciser. De même, la généralisation de la limite d'éclatement mise en évidence dans la présente étude exploratoire devra faire l'objet de recherches expérimentales plus approfondies en vue de dégager des critères pratiques d'éclatement.

8 - *CONCLUSION* -

Une étude expérimentale des conditions de déstabilisation des tourbillons a été effectuée sur deux configurations tourbillonnaires de nature différente : l'une concerne le tourbillon d'apex d'une aile delta, l'autre s'apparente au tourbillon de bout d'aile, mais présente par rapport à celui-ci des propriétés de symétrie plus marquées, grâce à l'utilisation d'un générateur à deux ailettes. Alors que le premier montage engendre un tourbillon alimenté par la nappe issu du bord d'attaque de l'aile, le tourbillon engendré par le second montage se développe par enroulement en une spirale à double branche des deux nappes tourbillonnaires émises au bord de fuite des ailettes. Il en résulte une différence appréciable dans la structure interne du tourbillon, bien que le champ externe soit, dans les deux cas, du type "tourbillon potentiel". Ces différences se manifestent principalement dans la forme des profils de vitesse et se traduisent au centre du tourbillon par une survitesse axiale plus prononcée et par une évolution plus plate de la vitesse tangentielle dans le cas du tourbillon d'aile delta. Il en résulte une dépression sur l'axe plus accusée pour ce tourbillon, accentuée par le fait que son intensité tourbillonnaire est plus élevée.

L'étude de la destabilisation du tourbillon sous l'effet d'un gradient de pression adverse a été conduite sur ces deux configurations tourbillonnaires selon des objectifs légèrement différents : dans le cas du montage d'aile delta, qui est essentiellement destiné à l'étude des conditions d'apparition de l'éclatement et à l'établissement de critères pratiques, une configuration particulière de tourbillon éclaté a été analysée en plusieurs sections de l'écoulement. Dans le cas du montage à ailettes, qui est davantage destiné à l'analyse fine de la structure turbulente dans les vortex destabilisés, on a procédé à une étude plus systématique en faisant varier les conditions extérieures de déstabilisation, la plupart des mesures ayant été effectuées en une seule section.

En dépit des différences de structure interne des deux tourbillons, de nombreux traits communs caractérisant le processus de destabilisation se dégagent des deux séries d'essais : l'enroulement spiral du noyau tourbillonnaire, la formation d'un bulbe de recirculation pour les configurations éclatées, le brusque creusement des profils de vitesse longitudinale au voisinage de l'axe et la déformation concomitante des profils de vitesse tangentielle,... etc. Parmi les différences il convient de souligner, pour le tourbillon d'aile delta, l'évolution plus brutale de la destabilisation, les niveaux de fluctuation de vitesse sensiblement plus élevés, notamment dans les sections proches de l'éclatement, où le caractère instationnaire est très prononcé. Des études ultérieures faisant appel à la technique de l'échantillonnage conditionnel devront élucider la nature et l'origine de ces fluctuations.

Les configurations tourbillonnaires étudiées justifient l'hypothèse quasi-cylindrique, au moins avant l'éclatement. Les résultats relatifs au tourbillon de l'aile delta ont fait l'objet de quelques confrontations élémentaires avec des théories élaborées dans le cadre de ces hypothèses : la théorie de la stabilité met en évidence une zone instable au voisinage immédiat de l'axe. La théorie de BENJAMIN relative à l'état sub ou supercritique est bien confirmée par l'expérience. Enfin, la théorie des écoulements quasicylindriques suggère des critères d'éclatement en fonction des paramètres intensité tourbillonnaire et gradient de pression adverse dont le rôle fondamental est bien vérifié par l'expérience : une condition limite de l'existence de l'éclatement a été établie à partir des expériences, mais la généralisation de ce résultat reste encore à vérifier.

BIBLIOGRAPHIE

[1] HARVEY J.K -
Some observations of the vortex breakdown phenomenon.
J. Fluid Mech., Vol. 14, Part 4, 1962

[2] ELLE B.J. -
An investigation at low speed of the flow near the apex of thin delta wings with sharp leading edges.
ARC R & M 3176 (January 1958).

[3] WERLE H. -
Sur l'éclatement des tourbillons d'apex d'une aile delta aux faibles vitesses. Rech. Aéron. n° 74 (1960).

[4] LAMBOURNE N.C. and BRYER D.W -
The bursting of leading-edge vortices. Some observations and discussion of the phenomenon.
ARC R & M n° 3282 (April 1961).

[5] DELERY J. et HOROWITZ E. -
Interaction entre une onde de choc et une structure tourbillonnaire enroulée.
52 nd Meeting Fluid Dynamics Panel. AGARD ,Rotterdam 25-28 Avril 1983.

[6] P.PHILBERT, R.BEAUPOIL, J.P.FALENI -
Application d'un dispositif d'éclairage laminaire à la visualisation des écoulements aérodynamiques en soufflerie par émission de fumée.
Rech. Aérospatiale n° 1979-3, pp. 173-179.

[7] A.BOUTIER, J.LEFEVRE, C.PEROUZE, O.PAPIRNYK -
Operational two-dimensional laser velocimeter for various wind-tunnel measurements.
Communication 3ème réunion de Travail Internationale sur la Vélocimétrie Laser.
University - West Lafayette (Ind. U.S.A.) (11-13.7.1978).

[8] MICHALKE A., TIMME A. -
On the inviscid instability of certain two dimensional vortex type flows.
J. Fluid Mech. Vol.29, Part 4, 1967.

[9] PRANDTL L. -
Guide à travers la Mécanique des Fluides , Chap.2 § 11,
Dunod 1952

[10] VILLAT H. -
Leçons sur la théorie des tourbillons
Chap.3 - Gauthier-Villars 1930.

[11] HALL M.G. -
Vortex breakdown
Ann. Rev. Fluid Mech. 4, 195, 1972.

[12] BENJAMIN T.B. -
Theory of the vortex breakdown phenomenon.
J.Fluid Mech.,Vol,14, Part 4, 1963.

[13] HALL M.G.-
A theory for the core of leading edge vortex
J.Fluid Mech. Vol.11, Part.2, 1961
R.A.E. Report Aero 2644, 1960

[14] LUDWIEG H. -
Erklärung des Wirbelaufplatzens mit Hilfe der Stabilitätstheorie für Strömungen mit schraubenlinienförmigen Stromlinien.
Z.Flugwiss 13 (1965), Heft 12 pp 437 - 442.

[15] SQUIRE H.B. -
Analysis of the vortex breakdown phenomenon. Part.1.
Imp. Coll. of Sc. & Techn. U. London, Aeron.Dept.Rep.102, 1960.

[16] LAMBOURNE N.C. -
The breakdown of certain types of vortex.
ARC CP n° 915 (september 1965).

[17] SOUTH P.
A simple theory of vortex bursting.
National Research Council of Canada, Aeronautical Report LR 414, NRC 8290, 1964.

[18] HALL M.G. -
A new approach to vortex breakdown
Proceedings of the 1967 Heat Transfer and Fluid Mechanics Institute
(Stanford Univ. Press, 1967).

[19] RAAT J. -
Vortex development and breakdown
AIAA paper 75-881
AIAA 8th Fluid and Plasma Dynamics Conference, Hartford, Conn.,
June 16-18, 1975.

[20] LUDWIEG H. -
Ergänzung zu der Arbeit :
"Stabilität der Strömung in einem zylindrischen Ringraum".
Z.Flugwiss. 9 (1961) Heft 11 pp.359-361.

[21] HOWARD L.N., GUPTA A.S. -
On the hydrodynamic and hydromagnetic stability of swirling flows.
J.Fluid Mech.,Vol.14, Part.3, 1962.

[22] LEIBOVICH S. -
Vortex breakdown : experiment and theory
Rep. EFR-76-8, Cornell University, Ithaca, Dec.1976.

[23] E.C. POLHAMUS -
A concept of the vortex lift of sharp edge delta wings based on a leading edge suction analogy.
NASA TN D-3767 (décembre 1966).

REMERCIEMENTS - *Les auteurs tiennent à remercier MM. M.PHILBERT, R.BEAUPOIL et J.P.FALENI, qui ont réalisé les visualisations, ainsi que MM. C.d'HUMIERES et D.SOULEVANT qui ont exécuté les mesures au laser.*

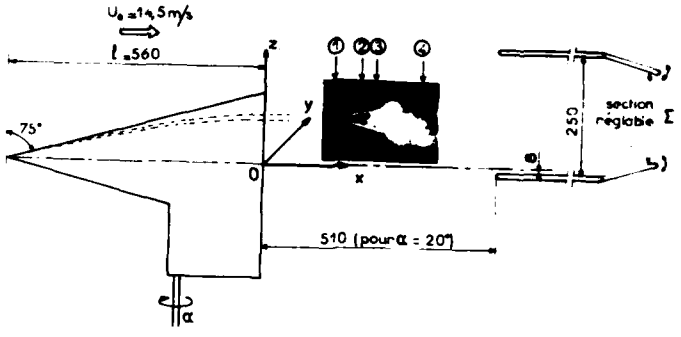

Fig. 1a - Montage expérimental I : tourbillon d'aile delta.

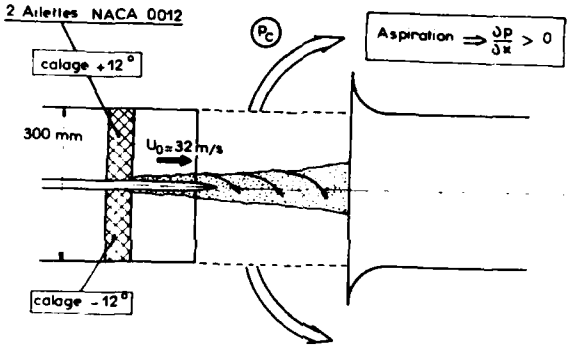

Fig. 1b - Montage expérimental II : tourbillon des ailettes.

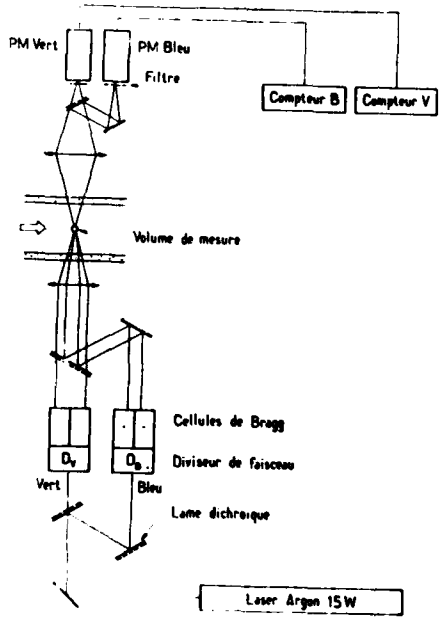

Fig.2 - Schéma de principe de l'anémomètre laser

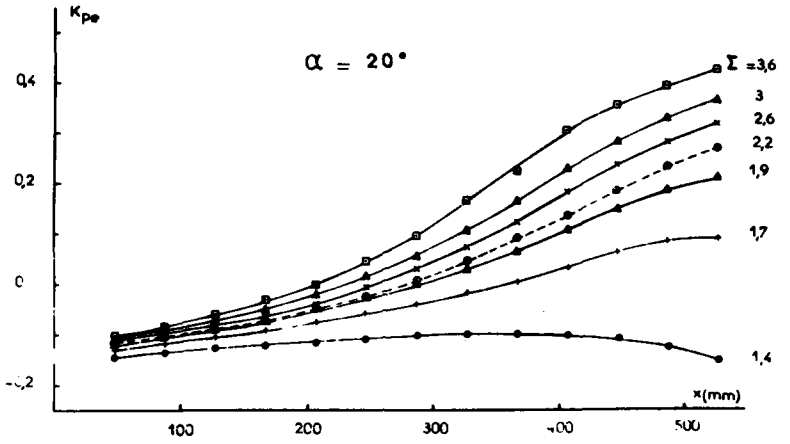

Fig. 3a - Evolution de la pression dans l'écoulement extérieur : Montage I (= 20°)

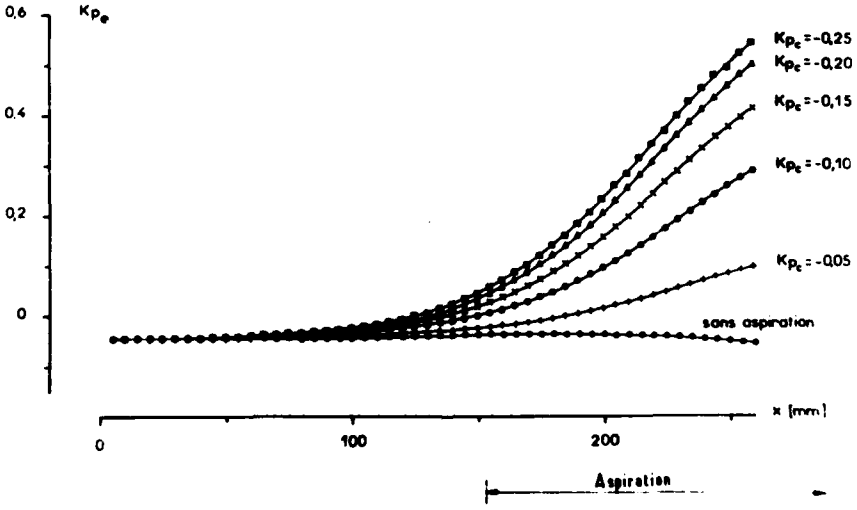

Fig. 3b - Evolution de la pression dans l'écoulement extérieur : Montage II

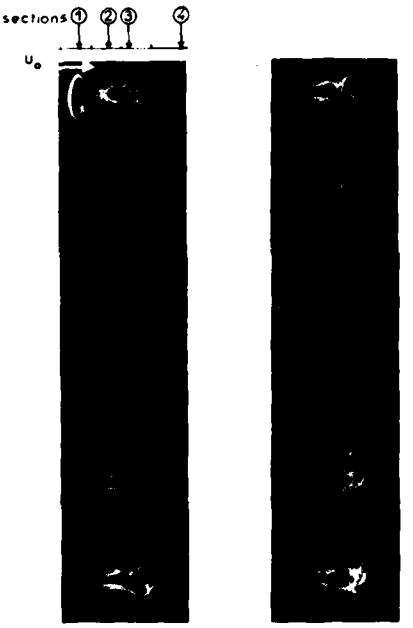

Fig. 4 - Vues méridiennes du tourbillon d'aile delta - séquence filmée.

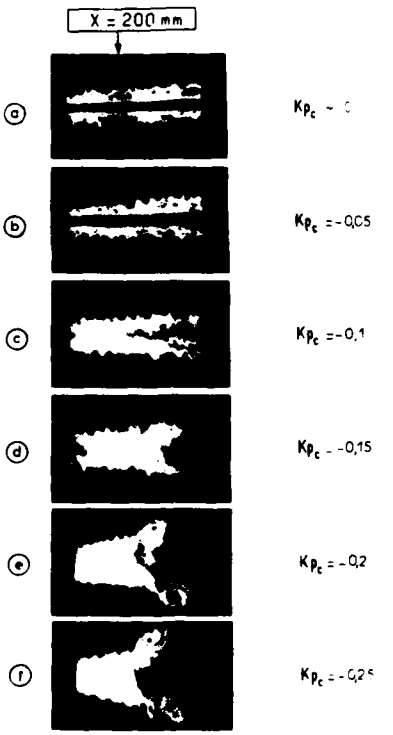

Fig.5 - Vues méridiennes du tourbillon des ailettes en fonction de K_{pc}

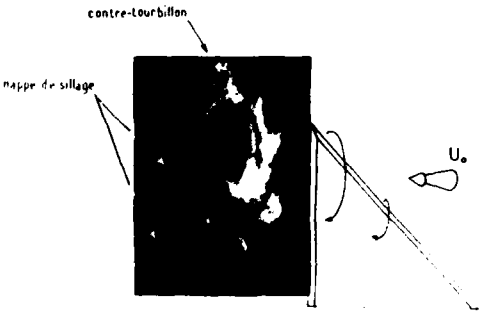

Fig.6a- Vue transversale du tourbillon d'aile delta.

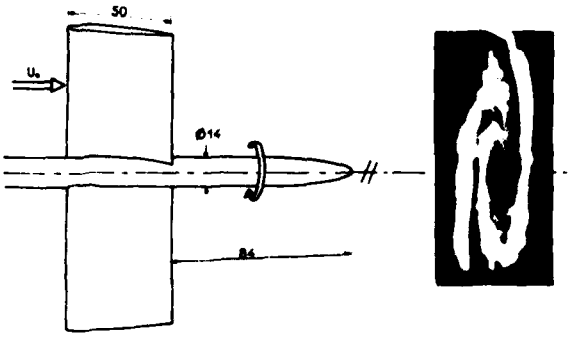

Fig.6b - Vue transversale du tourbillon des ailettes.

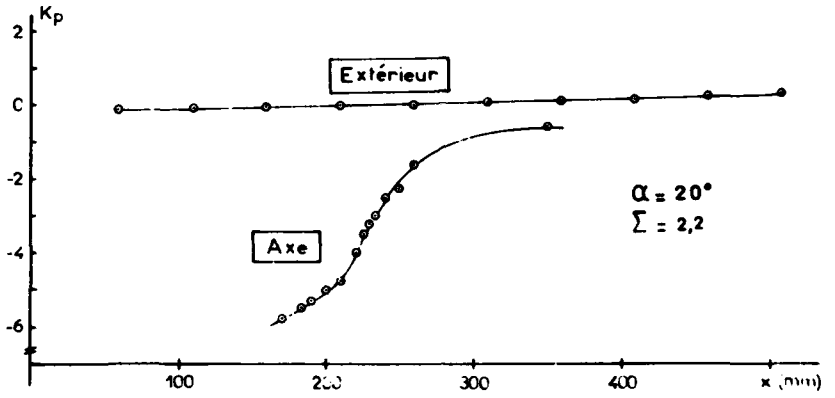

Fig. 7a - Evolution de la pression sur l'axe du tourbillon - Montage I

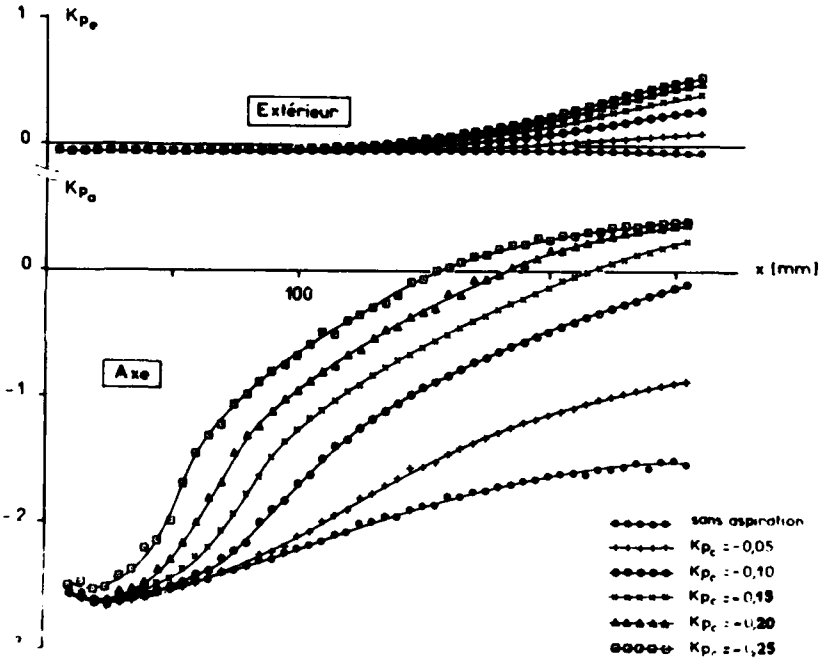

Fig.7b - Evolution de la pression sur l'axe du tourbillon : Montage II

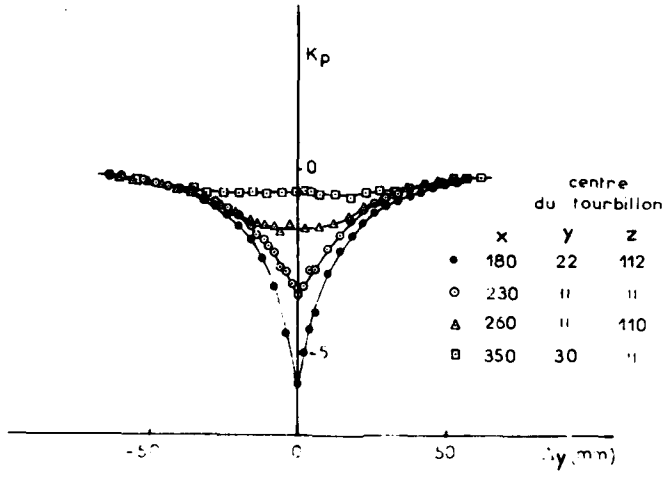

Fig.8a - Evolution radiale de la pression : Montage I

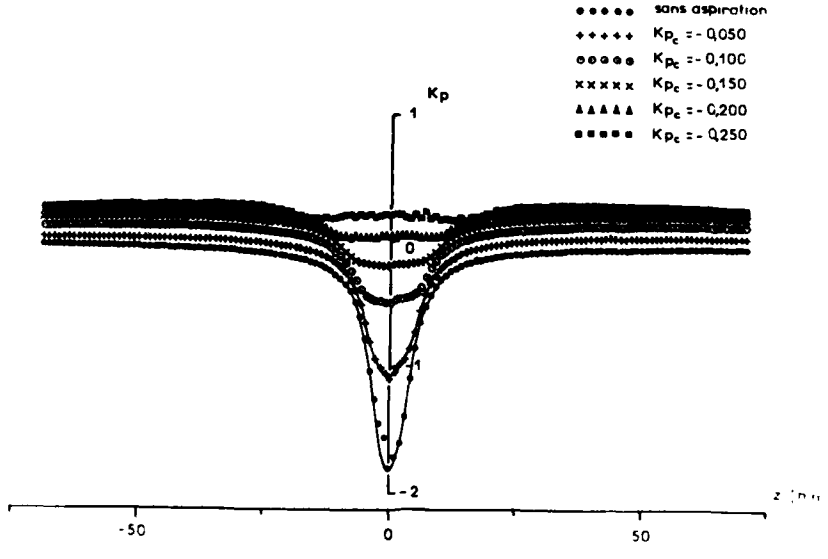

Fig.8b - Evolution radiale de la pression : Montage II

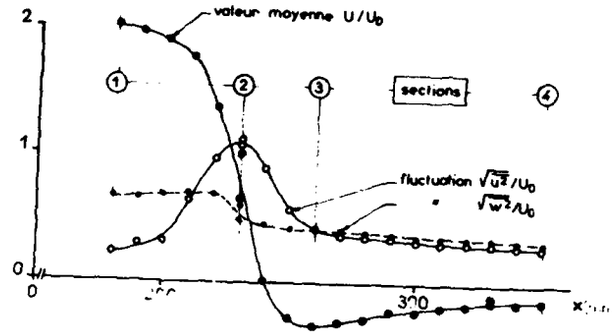

Fig.9a - Evolution, le long de l'axe, de la vitesse et des taux de fluctuation : Montage I

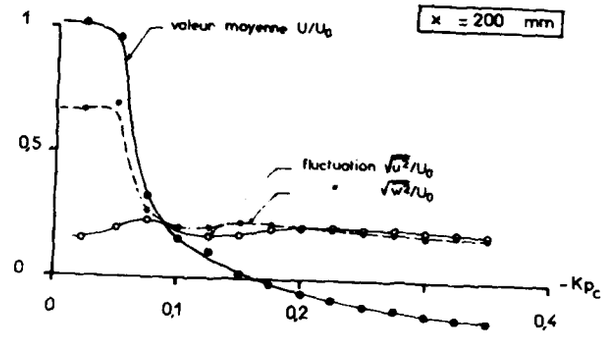

Fig.9b - Evolution, en fonction de Kpc, de la vitesse et des taux de fluctuation sur l'axe : Montage II

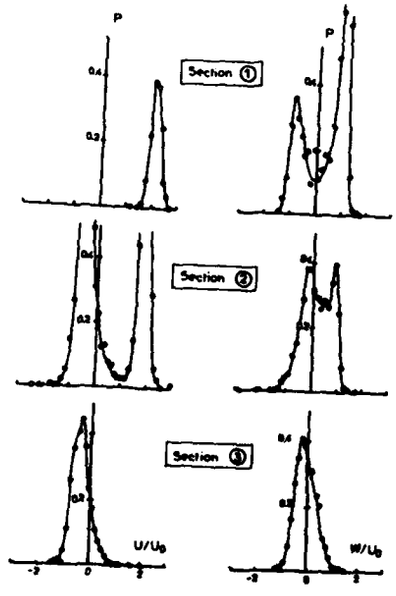

Fig.10a - Histogrammes des vitesses sur l'axe : Montage I

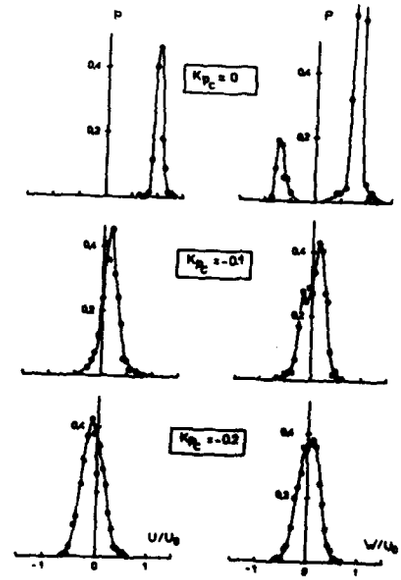

Fig.10b - Histogrammes des vitesses sur l'axe Montage II

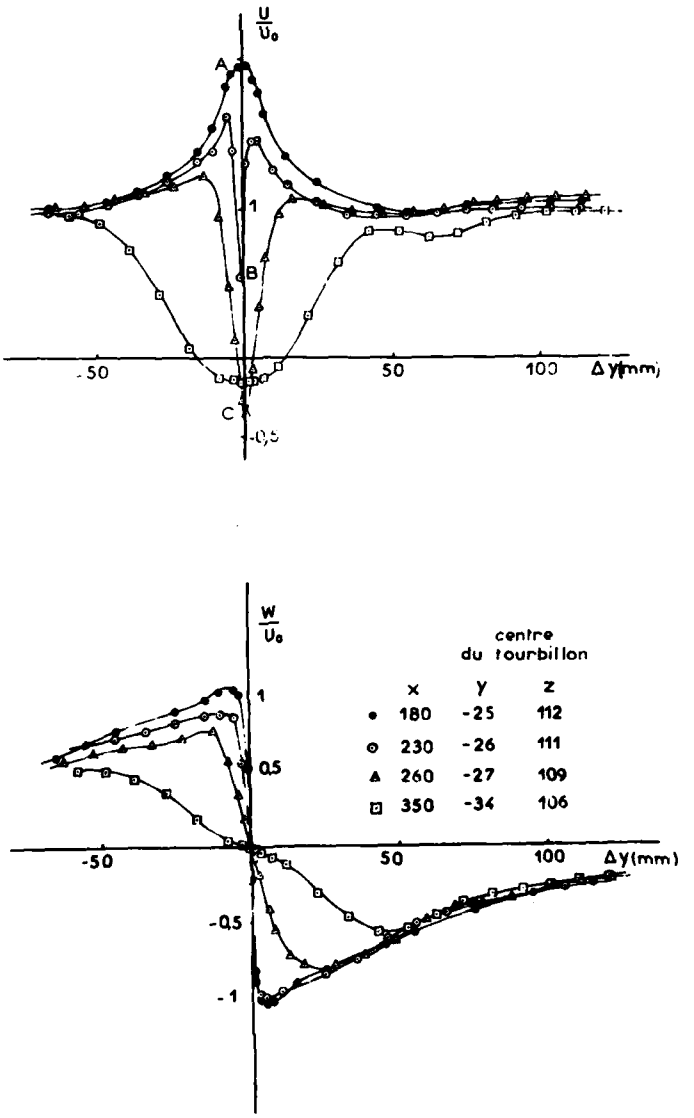

Fig.11a - Evolution radiale des vitesses moyennes - Montage I
Composantes axiale (en haut) et tangentielle (en bas)

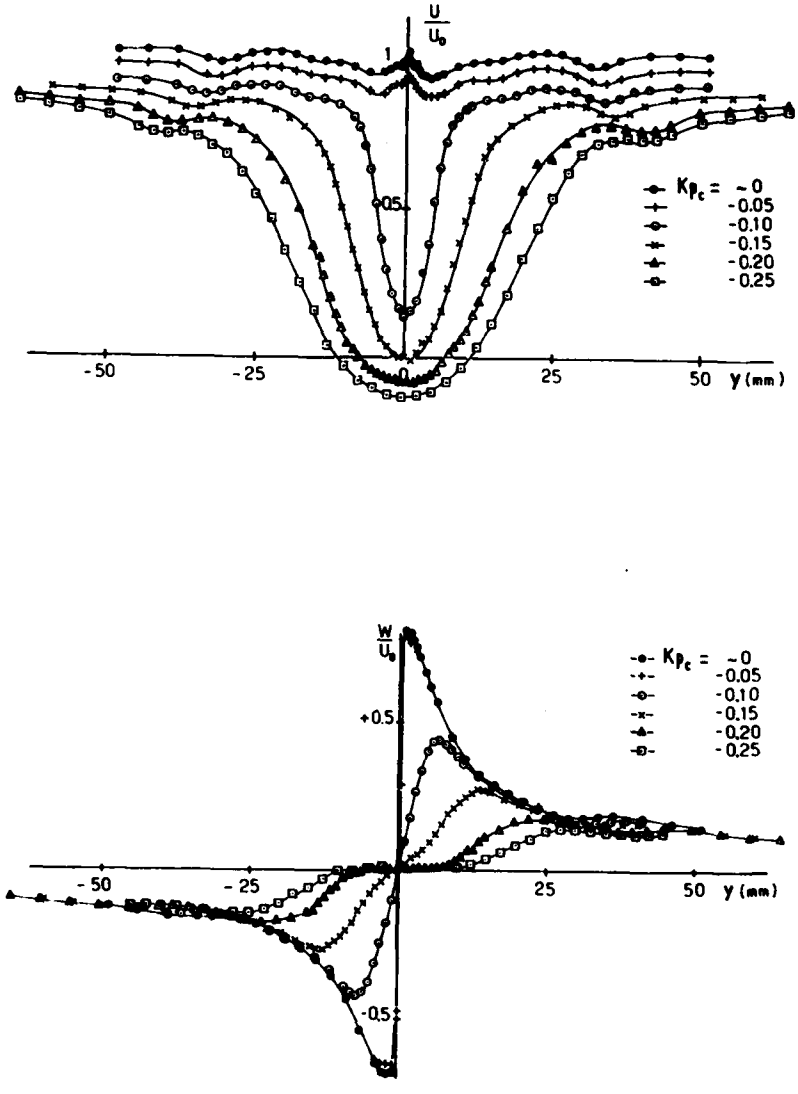

Fig.11b - Evolution radiale des vitesses moyennes - Montage II
Composantes axiale (en haut) et tangentielle (en bas)

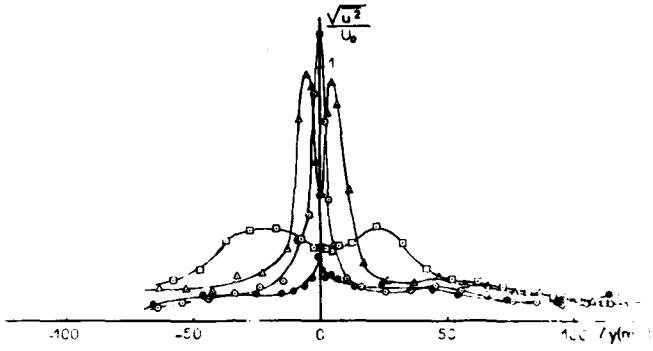

Fig.12a - Evolution radiale des fluctuations de vitesse : Montage I Composantes axiale (en haut) et tangentielle (en bas)

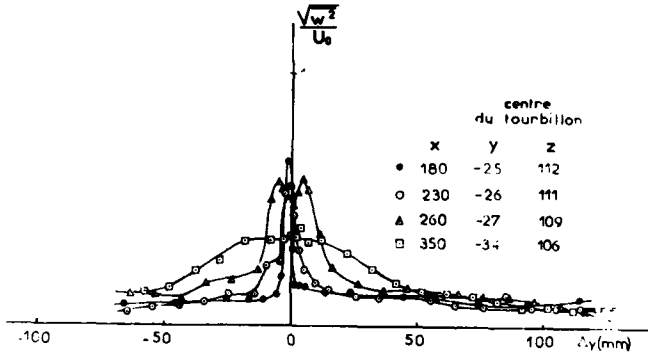

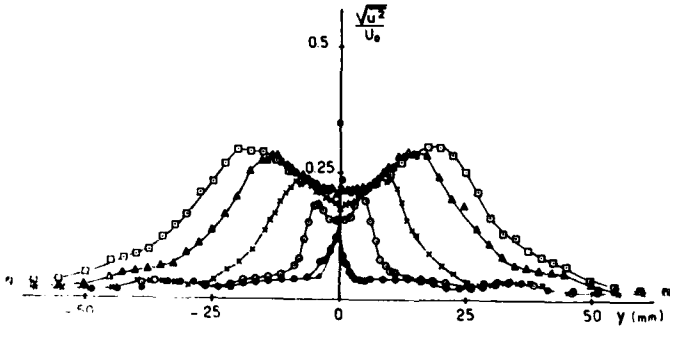

Fig.12b - Evolution radiale des fluctuations de vitesse : Montage II Composantes axiale (en haut) et tangentielle (en bas)

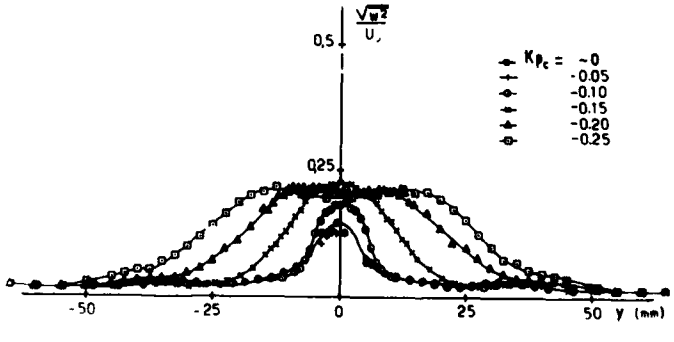

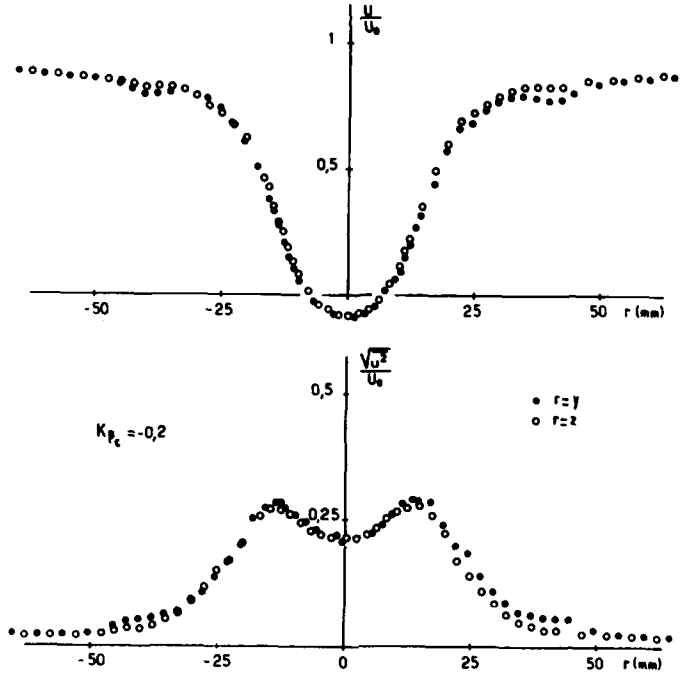

Fig.13 - Contrôle de la symétrie de résolution - Montage II

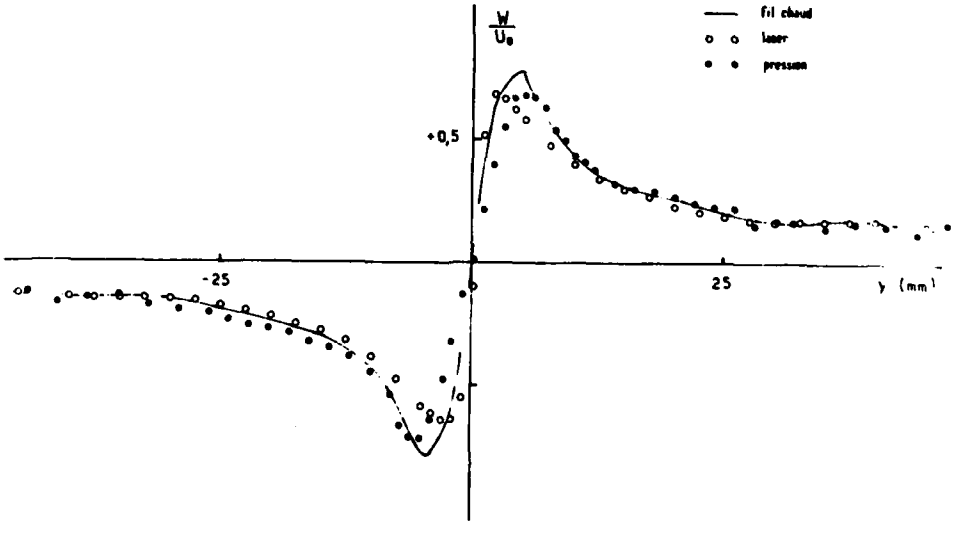

Fig.14 - Comparaison des méthodes de mesure sur le profil de vitesse tangentielle : Montage II (x = 250 mm).

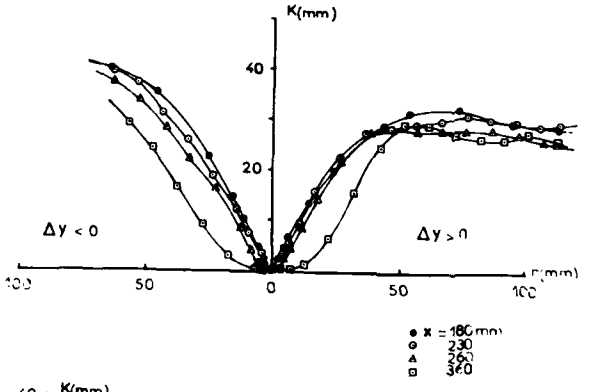

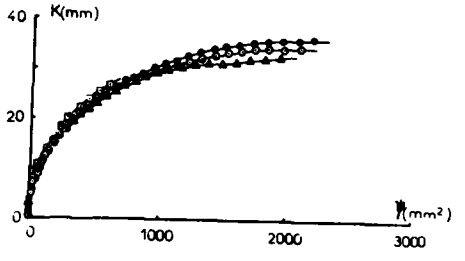

Fig.15a - Evolution radiale de la "circulation" K en fonction de Γ et de ψ : Montage I

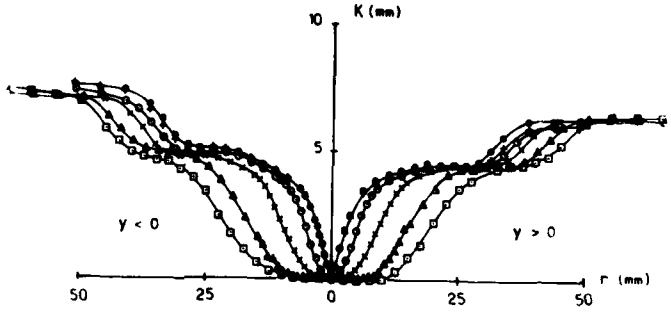

Fig.15b - Evolution radiale de la "circulation" K en fonction de Γ et de ψ : Montage II

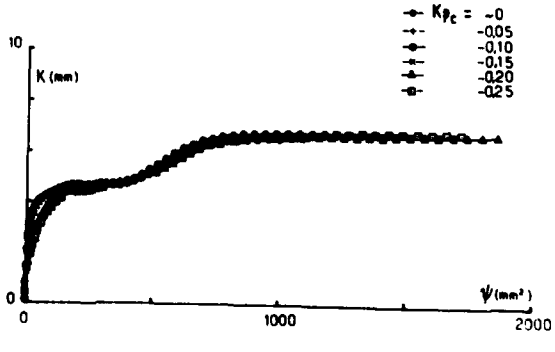

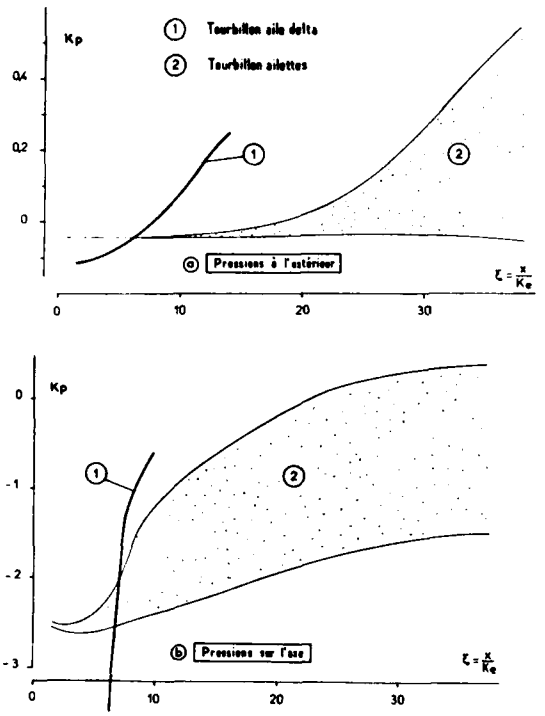

Fig.16 - Evolution longitudinale des pressions en fonction de l'abscisse réduite
a) à l'extérieur du tourbillon
b) sur l'axe du tourbillon

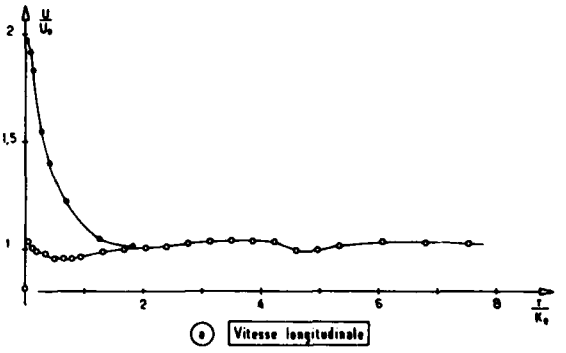

Fig.17 - Forme des profils de vitesse en coordonnées réduites
a) Vitesse longitudinale
b) Vitesse tangentielle

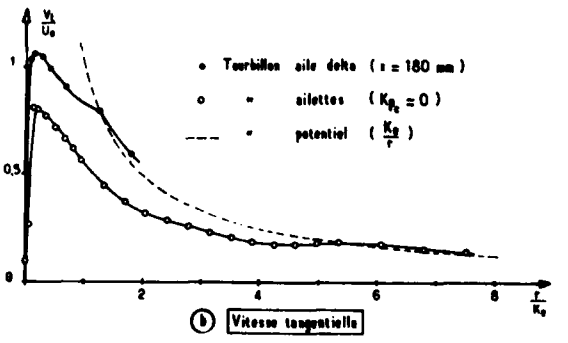

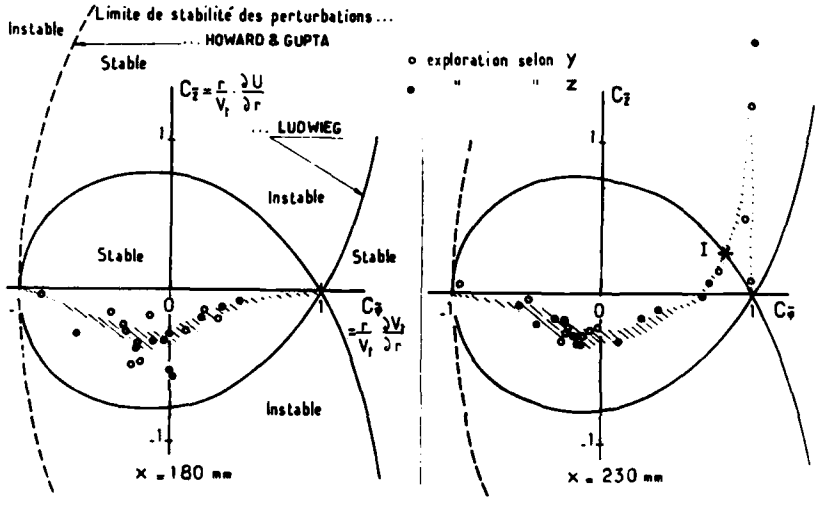

Fig.18 - Critère de stabilité de Ludwieg

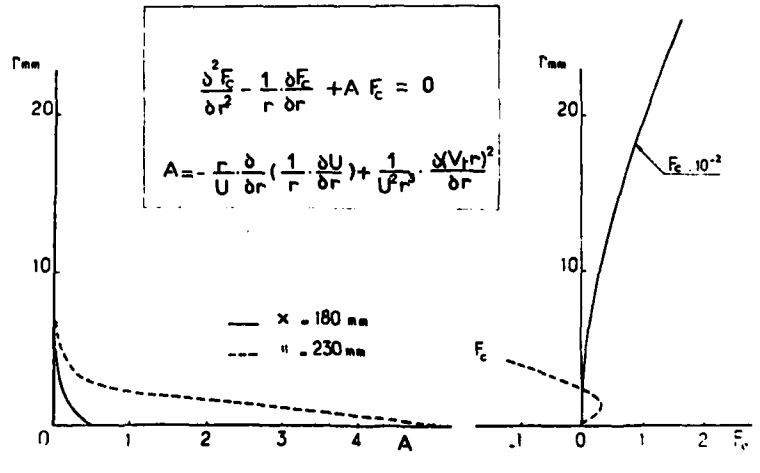

Fig. 19 - Fonction test de l'état critique (Benjamin).

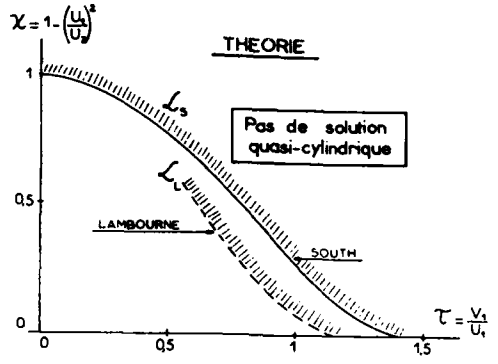

Fig.20 - Critères d'éclatement (solutions quasi-cylindriques)

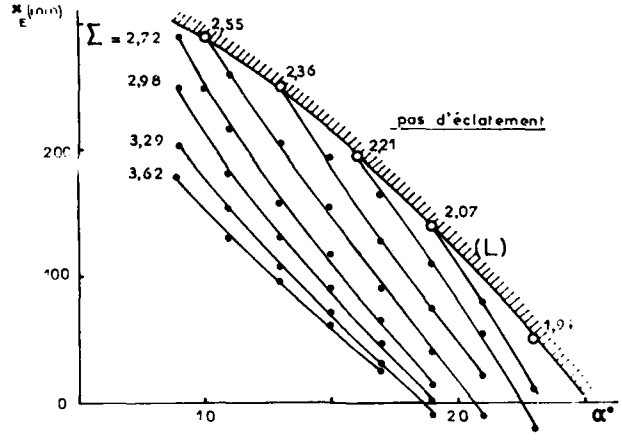

Fig.21 - Evolution de l'abscisse du point d'éclatement en fonction de α et de Σ

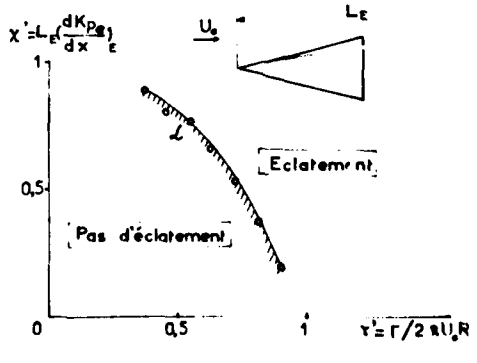

Fig.22 - Condition limite d'éclatement (expérience).

WAVES ON VORTEX CORES AND THEIR RELATION TO VORTEX BREAKDOWN

by

T.Maxworthy*, M.Mory and E.J.Hopfinger
Institut de Mécanique
(Laboratoire Associé au C.N.R.S.)
Université de Grenoble
B.P. n° 68
38402 St Martin d'Hères
France

SUMMARY

It was conjectured by Hopfinger, Browand and Gagne (1982) [1] that travelling, large amplitude "kink" waves, observed by them in rotating, turbulent fluid might be at the origin of vortex breakdown and small scale turbulence production. This observation motivated us to study such waves experimentally on isolated vortices under controlled conditions. Their characteristics are interpreted in terms of theories based on the localised induction equation. It is found that these kink waves remain stable and exhibit soliton interaction properties. Axisymmetric travelling waves on the contrary cause breakdown when their amplitude exceeds a certain magnitude. Benjamin's (1967) [2] theory was used to calculate the critical phase speed and the velocity perturbation inside a wave of finite amplitude. The theoretical results show that the axial velocity changes rapidly become large so that, according to instability considerations, growth of spiral disturbances is possible. Breakdown caused by axisymmetric waves and possibly by combined, axisymmetric and kink waves, is demonstrated experimentally.

1. INTRODUCTION

In a recent study of a turbulent flow field generated by an oscillating grid in a rotating tank, Hopfinger, Browand and Gagne (1982) [1] (from here on referred to as HBG) discovered the existence of intense vortices approximately aligned with the rotation axis. Vorticity intensification in these vortices was well over a factor of 10 and a variety of wave motions were observed upon them with frequent occurrences of vortex breakdown. An analysis of a selected "kink" wave disturbance by Hopfinger and Browand (1982) [3] showed that it was well described by Hashimoto's (1972) [4] vortex solitary wave theory which is based on the local induction equation. HBG gave these kinked solitary waves a central place in the dynamics of vortex breakdown and even in vortex intensification. If the latter is rather speculative, the possible relation of kink waves with vortex breakdown is an aspect worth investigating. This has also been recognised by Leibovich (1982) [5]. In particular the "loop" mode, not mentioned in previous studies, seems indicative of a kink wave event.

The study of wave motions on vortex cores is a venerable one and for many years relatively simple solutions for the helicoidal wave and plane sinusoidal wave have been known. The kinked soliton solutions on the contrary are quite recent (Hashimoto, 1972, Kida, 1981) [4, 6] and are just beginning to be examined for vortices with distributed vorticity [7]. More surprising is that only in the past few years has it been recognized that vortex flows are one class of fluid motion which can support axisymmetric solitary waves which are manifested by an increase in core diameter as the wave passes [2, 8, 9]. The theory of axisymmetric long waves which are the ingredients for a discussion of solitary waves are due to Squire [10] and Benjamin (1962) [11].

While some parts of this theoretical framework have been subject to a certain amount of experimental scrutiny, in particular standing axisymmetric waves on supercritical core flows, known from vortex breakdown phenomena (see for instance Reference 12), others have not.

In what follows, we study travelling kinked solitary wave motions and axisymmetric waves in the aim to determine their properties and their possible role in vortex breakdown of subcritical core flow. In Section 2 the apparatus and the vortex flow structure is described. The results for kink waves are presented in Section 3 and experimental and numerical results for axisymmetric waves are considered in Section 4. The relation of these waves with vortex breakdown is discussed in Section 5, including also turbulent flow conditions.

---

* Permanent address: Dept Mech. & Aerospace Eng., University of Southern California, Los Angeles, Ca 90089-1453.

2. THE VORTEX STRUCTURE

2.1 Vortex Generation Apparatus

The basic apparatus is identical to that used in H.B.G., except that the grid mechanism at the bottom of the tank was replaced by a plastic disc, and an apparatus to produce a single concentrated vortex was mounted within and around the tank (Fig.1). The latter consisted of a central suction tube of 1.4 cm diameter connected to a pump, flowmeter and discharge pipe all mounted outside the tank and fixed in the laboratory frame. The vortex was made visible either by injecting dye through a central hole in the bottom plate or by observing, photographically, small, neutrally buoyant particles circulating through the system. The latter were used to measure the axial and swirl velocity profiles within the vortex. The wave pattern and propagation speed were obtained from ciné films taken of the vortex, made visual by dye. After several initial trials, three flow conditions were chosen, all had the same clockwise tank rotation rate Ω of 1.5.1 rad/s with three different total suction flow rates 130, 180, 230 ltr/hr.

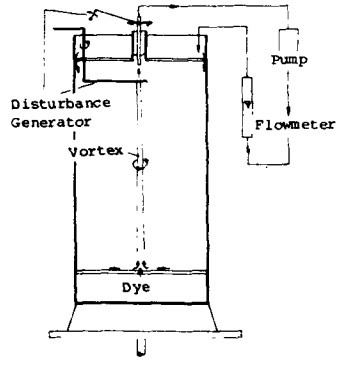

Fig.1 The apparatus. The suction tube above causes a convergence of vorticity. The vortex is disturbed by either shaking the suction tube, by cutting through the vortex with the disturbance generator or by suddenly stopping the suction for a short time

To produce isolated kink waves, a thin metal rod was swung horizontally so that it cut the vortex at either the top or the bottom or both in some cases for interaction studies. This had the effect of both, stopping the vertical flow in the cut section for an instant and also of bending the core. This is perhaps not the best method of producing solitary kink waves. A more adequate method but experimentally difficult to realize would be to oscillate the suction tube in just the right way to produce the required torsion. Axisymmetric waves were produced by suddenly reducing for a short duration the suction rate by pinching the plastic suction tube.

2.2 Undisturbed Flow Field

The undisturbed flow field of the vortex at the middle of the tank is shown in Figure 2 for the three cases considered. The vortices are relatively thick (3–4 mm radius) and the vortex diameter decreases only slightly with increasing flow rate. In a later series of qualitative tests, the core could be made much thinner by inserting a porous plate on the bottom of the tank and withdrawing fluid from the bottom boundary layer. This greatly modified the boundary layer eruption and vortex breakdown at the bottom of the tank and created a thinner initial core diameter as a bottom boundary condition on further core development (Maxworthy, 1973) [13]. However, this scheme gave a rather unsteady core, due to pore blockage and the small diameter of the porous plate and was not used in the reported wave experiments.

On Figure 2, we compare the experimental swirl velocity measurements for each case with the Burgers vortex (Equ.1a) and the axial velocity profiles with Turner's (1966) [14] model (Equ.1b).

$$V(r) = \frac{\Gamma}{2\pi}\frac{(1-e^{-\alpha y})}{\sqrt{2y}} \quad (a); \qquad W(r) = W_m(1-\beta y)e^{-\beta y} \quad (b) \qquad (1)$$

where Γ is the circulation, W_m is the maximum axial velocity, $y = r^2/2$ and α and β are parameters determined by adjusting the model to the experimental distribution (here the case 230 ltr/hr, $\alpha = 25$ cm^{-2}, $\beta = 4$ cm^{-2}.

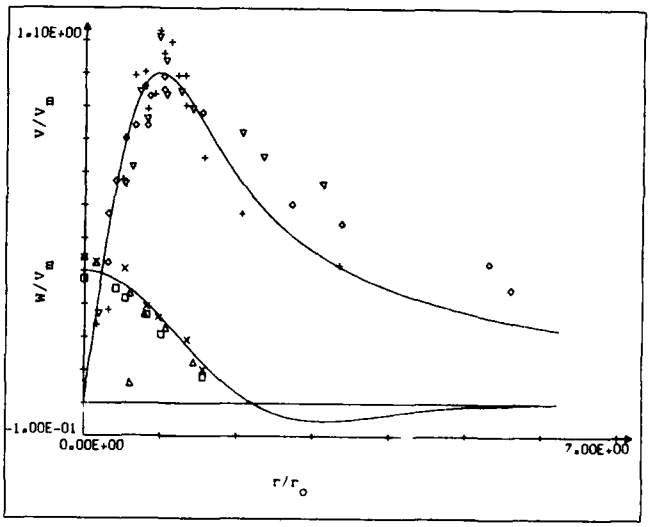

Fig.2 Undisturbed swirl and axial velocity profiles for the three cases considered in this paper, Ω = 1.51 rad s^{-1} ; ◇, □, flowrate Q = 130 ltr/hr, $V_T \simeq 58$ cm^{-1}, $W_m \simeq 25$ cm^{-1}, ▽, △, Q = 180 ltr/hr, $V_m \simeq 93$ cm^{-1}, $W_m \simeq 35$ cm^{-1}, +, x, Q = 230 ltr/hr, $V_m \simeq 132$ cm^{-1}, $W_m \simeq 60$ cm^{-1} ; ——, calculated from Equation 1 for case Q = 230 ltr/hr: $r_o \approx 0.32$ cm

A considerable amount of vorticity lies outside any reasonably defined core radius (e.g. the radius at which V is a maximum). However all of the theories to be used in our comparison with experiment assume that the core is thin compared to some reference length (e.g. the wave length of a typical disturbance) and that all of the vorticity is contained within it. Clearly with the observed vorticity distributions we should really calculate the radial modal response of the vortex to any particular input. However, this is beyond our present abilities and invariably severe simplifying assumptions must be made. At the heart of these lies the "localised induction equation", well described in Batchelor (1970, pg.509) [15], in which the induced velocity at any point on the vortex centre-line is supposed to be due only to the vorticity in these elements within a short distance (L) on either side of the point. The ratio of L to the core diameter, r_o , is always assumed to have some constant value, which as far as we know, has been estimated for vortex rings (with constant curvature), where it turns out to depend on at least the Reynolds number (i.e. effective vortex core diameter), and for kink-waves by HBG. Maxworthy and Hopfinger (1983) [16] were able to estimate this quantity and show how it varies, not only with the vorticity distribution, but also with the curvature of the filaments. In the range $0.05 \lesssim \kappa\, r_o \lesssim 0.2$, where κ is the curvature, the ratio L/r_o can be taken constant and for practical purposes ≈ 4 .

3. ISOLATED KINK WAVES

We have refrained from calling this section "solitary kink waves" because it now appears that the waves we can produce most readily are probably not yet solitary waves in the classical sense. They are still evolving during our observations and although they exhibit some of the features of solitary waves, in other ways they are different. We start our discussion with a description of the formation process. In the first method the suction tube was oscillated quickly through one cycle and the evolution of the resultant single kink followed photographically. In the present apparatus, such waves were of such small amplitude compared to the visible core size, for example, that it was impossible to obtain any useful information from them.

Alternatively, and first chronologically, the core region at either the top or bottom could be disturbed by rapidly cutting through the core with a thin, solid rod. This had effects which were different depending on the direction of propagation.

3.1 Wave Pattern and Wave Speed

When the core was cut near the top, the axial flow was cut-off briefly. This information was transmitted to the rest of the vortex by an axisymmetric solitary wave of expansion which depending on its amplitude, sometimes became unstable and produced growing spirals behind it. This axisymmetric wave had a high velocity and rapidly left the region

of the original disturbance. A second perturbation was created by the motion of the rod and this consisted initially of a single kink under most circumstances. At the same time as this kink began to propagate, the axial flow was reestablished by a wave of contraction or convergence from the suction tube, which also had a much higher velocity than that of the kink.

In Figure 3, we show the evolution of a typical kink of this type (a photograph of a kink wave is presented in Figure 8b). The chain-dotted lines join identical points on the pattern as it rotates slowly clockwise (in the sense of the vortex rotation) at 2.4/s in the frame of reference of the rotating tank. The forward part of the wave develops an extra twist indicating that the group velocity exceeds the phase velocity (as discussed in [16]. This effect confused interpretation of the wave pattern at first since if one follows the developing wave, the pattern appears to rotate in the wrong direction. Clearly our method of production is not optimal. This would require that we oscillate the suction tube in exactly the right way, with increasing then decreasing amplitude to put in the correct initial wave shape. This we have not been able to do in this set of experiments. When the wave interacts with the end wall, it goes through a phase advance as it does and reappears as a left-handed kink. We return to a more general discussion of such interaction in the next section.

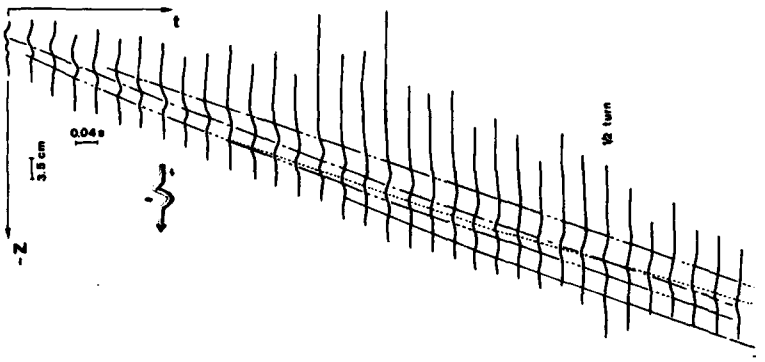

Fig.3 Evolution of an isolated kink wave running down the vortex core corresponding to conditions Q = 180 ltr/hr. The chain dotted lines represent the estimated trajectory of the wave envelope and the dotted line is the trajectory of a wave crest through the packet. The wave speed $C_g \simeq 33\ \text{cms}^{-1}$, maximum amplitude $a_m \simeq 0.49$ cm and torsion $\tau_0 \simeq 0.89\ \text{cm}^{-1}$.

Several waves like that shown in Figure 3 have been analysed using the results of Hashimoto (1972) [4] as interpreted by HBG. The wave (envelope) speed is given by

$$C_g = 2\tau_0 \frac{\Gamma_0}{4\pi} \ln \frac{L}{\sigma} \tag{2}$$

where τ_0 is the wave torsion, which for small a_m/λ is approximately equal to $2\pi/\lambda$, where a_m is the maximum radial displacement of the core centre line and λ the wavelength of the central kink so that

$$C_g \approx \frac{\Gamma_0}{\lambda} \ln \frac{L}{\sigma} . \tag{3}$$

However the wave peaks move at a different speed because in a frame of reference moving with the wave envelope the wave pattern rotates which shows up in a translation of the peaks without translation of material elements of the core. The rotation rate of the vortex filament is given by

$$\omega_p \approx \frac{\pi}{\lambda^2} \Gamma_0 \ln \frac{L}{\sigma} . \tag{4}$$

The maxima and minima then appear to move at a speed

$$C_p \approx \frac{\Gamma_0}{2\lambda} \ln \frac{L}{\sigma} . \tag{5}$$

With Equations (3) and (4) the parameter introduced by HBG and Hashimoto becomes

$$\frac{C_g}{\omega_p a_m} \sim \frac{\lambda}{\pi a_m} = T \,. \qquad (6)$$

Experimentally we can verify Equation (6) which does not depend on a knowledge of the induction length L. For the wave shown in Figure 3 the pattern appears to rotate in the sense opposite to that given by induction at a rate 2.4 rad/sec*. This indicates that the wave envelope had a velocity only slightly larger than the phase velocity (individual peaks), an effect that was generally true. For the particular wave considered $a_m \simeq 0.49$ cm, $\lambda \simeq 6.8$ cm and $C_p \simeq 33\ \mathrm{cms}^{-1}$, hence $C_p/\omega_p a_m \simeq 28$. The theoretical value $T = \lambda/\pi a_m \simeq 5.3$. At least two reasons for this discrepancy can be suggested. First, it is likely that the observed disturbances have either not yet evolved into solitary waves or that perhaps they never do under the present experimental conditions. The latter idea is related to Lamb (1980, p.200) [17] who showed that for a more general induction equation than the localised induction equation it is possible to obtain filament waves which obey the modified KdV. equation. Such an equation is known to support breather solitons, i.e. ones in which the interior pattern changes during propagation. They have a form similar to the ones found in our experiments and may in fact be the waves we observe if the variation in wave induction velocity as a function of curvature is that which leads to the MKdV. equation.

It should be noted that the kink waves which could be generated on the isolated vortices in the apparatus shown in Figure 1, of which the wave shown in Figure 3 is a typical example, have considerably lower wave torsion and relative amplitude than the wave analysed by Hopfinger and Browand (1982) [3]. The localised induction assumption may therefore be even less valid than in the situation of Hopfinger and Broward. However, if we calculate the apparent induction length from Equation (5) using the experimental value of the phase speed obtained from Figure 3 we get $L/r_o \simeq 3.4$ a value close to that of HBG [16].

3.2 Interaction of Isolated Kink Waves

The isolated kink waves appear to have very unusual properties as one might expect if they are evolving into solitary waves. We have created interaction by producing waves simultaneously at the top and bottom of the tank and allowing them to propagate towards one another. As described in the previous section, such waves running downwards have not fully evolved into solitary waves while those propagating upwards often have an oscillating character, none-the-less, they too cause a phase shift in the oncoming wave although the effect on the waves is often hard to determine. Two typical interactions are shown in Figure 4 where we have attempted to pick out the wave trajectories for the forward part of the wave, both incoming and outgoing. The forward advance of the phase is quite clear although the experiments are too crude for us to be able to determine the dependence of the phase shift on the initial conditions. We only note that typically it is of the order of the central wavelength of the isolated kink wave, but since this was not varied over a large range, the possibility of a more complex relationship is an open question.

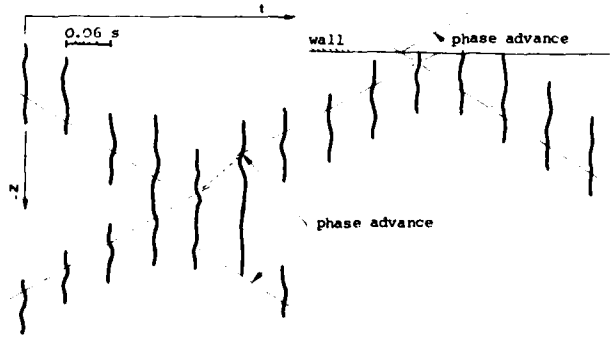

Fig.4 Interaction of kink waves produced at both ends of the tank.
Q = 180 ltr/hr. The phase *advance* by approximately only one wave length is clearly visible.

*The essential point here is not the actual value of the rotation rate which is difficult to determine to an accuracy better than ± 25%, but rather the fact that the apparent pattern rotation is in the sense of the core vorticity (phase speed < group velocity). While this result agrees qualitatively with Hashimoto's theory it contradicts the results of Leibovich and Ma [7].

4. AXISYMMETRIC WAVES

More is known about axisymmetric waves than any other despite the difficulties of measurement in rapidly rotating fluids where the insertion of a measuring probe completely disrupts the flow one wishes to measure. This is because they are directly and intimately related to the phenomenon of vortex breakdown which has many technical applications (e.g. Lambourne and Bryer, 1961) [18]. The most complete theoretical description we know of is due to Benjamin (1962, 1967) [2, 11] which has considerable experimental support in the work of Escudier, Bornstein and Zehnder (1980) [19], Escudier, Bornstein and Maxworthy (1982) [12] among others.

Essentially the view is that a weak vortex breakdown consists of a standing train of finite amplitude waves each of which closely approximates a "sech^2" solitary wave solution of the Korteweg de Vries equation. When the leading wave reaches a certain critical amplitude, the wake-like flow field created in its interior becomes unstable to spiral disturbances of negative wavenumber a point of view espoused by Escudier, Bornstein and Maxworthy [12] based on the work of Lessen, Singh and Paillet (1972) [20]. In any experiment, these invariably grow to become unstable finite amplitude spirals of small pitch rotating in a direction opposite to that of the basic rotation.

Clearly, by a simple Galilean transformation, these standing waves on vortices with supercritical axial velocity can be replaced by travelling waves on a subcritical flow of the type described in Section 2.2. In order to determine the change in vortex structure by travelling waves we use here Benjamin's theory to calculate the local change on vortices with axial flow. This is an extension of Pritchard's (1967) [8] work who calculated solitary wave motion on vortices without radial velocity gradients of the axial flow.

4.1 Long Wave Solution

The axisymmetric flow is described in cylindrical coordinates in terms of the circulation Γ (r, z, t) and the stream function Ψ (r, z, t). Γ and Ψ are expanded to the different orders of perturbation of the basic flow Γ_0 (r) and Ψ_0 (r, z).

$$\begin{aligned} \Gamma &= \Gamma_0 + \epsilon\Gamma_1 + \epsilon^2 \Gamma_2 + ... \\ \Psi &= \Psi_0 + \epsilon\Psi_1 + \epsilon^2 \Psi_2 + ... \end{aligned} \tag{7}$$

The equations of motion are written to the different orders in ϵ. To first order we look for solutions of the form

$$\begin{aligned} \Psi_1 (r, z, t) &= \varphi_1(r)\, e^{ik(z-ct)} \\ \Gamma_1 (r, z, t) &= \gamma_1(r)\, e^{ik(z-ct)} \end{aligned} \tag{8}$$

where φ_1 (r) satisfies the equations of motions (Benjamin, 1967) [2]

$$\varphi_{1yy} + \varphi_1 \left\{ -\frac{k^2}{2y} + \frac{\Gamma_0\Gamma_{0y}}{2y^2} \frac{1}{\{\Psi_{0y} - C\}^2} - \frac{\Psi_{0yyy}}{\{\Psi_{0y} - C\}} \right\} = 0 \tag{9}$$

$$\Gamma_1 = \frac{\Gamma_{0y}}{\Psi_{0y} - C} \Psi_1 \ . \tag{10}$$

Here $y = r^2/2$ for simplicity. Since we consider an unbounded flow, boundary conditions are chosen as follows:

$$\Psi(y = 0) = 0 \text{ and } \Psi_y(y) \to 0 \text{ as } y \to \infty .$$

The axial and azimuthal velocities W and V are given by:

$$\begin{aligned} W &= \Psi_y \\ V &= \frac{\Gamma}{\sqrt{2}_y} \end{aligned} \tag{11}$$

For any value of C, the Sturm Liouville System (9) has an infinite set of eigenvalues which are ordered $... < k_j^2 < ... < k_2^2 < k_1^2 < k_0^2$. If k_0^2 is negative, no axisymmetric wave propagates on the vortex core with the velocity of C^2. Long waves correspond to the critical point where $k_0^2 = 0$.

Analytical solutions for long waves are available when the axial flow has no radial gradient. Using a variational method we obtain the wave velocity C and the shape of the perturbation φ_1. In the presence of radial velocity gradients we have attempted to obtain a solution by a variational method but the results were unreliable. A numerical integration was therefore carried out.

We integrated the vortex flow shown in Figure 2 with the axial and azimuthal velocities, here denoted V_0 and W_0 given by Equation (1).

Although the basic flow contains a reverse flow for large values of y, this remains weak and can be neglected. Then lower and upper bounds for the phase speed of the wave can be obtained from (2) by application of the variational method

$$0 < | C - V_{om} | < W_{om} .$$

The value of the phase speed and the corresponding stream function for long waves is approached by using an iterative method to solve (2) numerically for different values of C. This was done for the vortex approximated by (1) with $W_{om} = 60\ cm.s^{-1}$, $\Gamma_0 = 65\ cm^2.s^{-1}$, $\alpha = 25\ cm^{-2}$, $\beta = 4\ cm^{-2}$ for both directions of wave propagation.

The results obtained for the speeds are as follows

$$\begin{aligned} C > 0 \quad & C = V_{om} + 0.93\, W_{om} \\ C < 0 \quad & C = -V_{om} + 0.93\, W_{om} . \end{aligned} \tag{12}$$

We considered only one case but the results we present here are likely to give a good estimation for the other two cases because the vortex core diameters are similar. Calculations for different cases are presently being carried out.

4.2 Solitary Waves

Here we consider the expansion of the stream function Ψ and the circulation Γ to second order. In analogy with the Korteweg de Vries equation and since we are interested in waves of permanent form, we use the coordinates y and $x = \epsilon^{1/2}(z - Ut)$ rather than y, z and t. The velocity of the solitary wave is taken as:

$$U = (1 + \epsilon\Delta) \tag{13}$$

where Δ is an unknown coefficient which will not appear explicitly later on. A solution for Ψ_1 is sought which has the form

$$\Psi_1 = \varphi_1(r)\, F(X) \tag{14}$$

The second order system which relates Ψ_2 and Γ_2 to Ψ_1 and Γ_1 gives the following condition for F:

$$A_1\, Fxx + B_1\, F + C_1\, F^2 = 0 \tag{15}$$

which is easily integrated as

$$F(X) = -\frac{3}{2}\,\frac{C_1}{B_1}\ \mathrm{sech}^2\left\{\frac{1}{2}\left(\frac{-C_1}{A_1}\right)^{1/2} X\right\} \tag{16}$$

A_1, B_1 and C_1 are integrals over the entire radius and depend only on known quantities Γ_0, Ψ_0 and C and φ_1.

A_1 and $-C_1$ remain positive for the two ways of propagation, indicating the existence of solitary wave solutions. But the sign of B_1 changes with the sense of propagation. The stream function Ψ_1 is then written for waves with positive and negative wave speeds.

$$\begin{aligned} C < 0, \quad \Psi_1 &= -\epsilon\,\varphi_1(y)\,\mathrm{sech}^2\{\alpha_1 \epsilon^{1/2}(z - Ut)\} \quad \alpha_1 = \left(\frac{-B_1}{6A_1}\right)^{1/2} \\ C > 0, \quad \Psi_1 &= \epsilon\,\varphi_1(y)\,\mathrm{sech}^2\{\alpha_1 \epsilon^{1/2}(z - Ut)\} \quad \alpha_1 = \left(\frac{B_1}{6A_1}\right)^{1/2} . \end{aligned} \tag{17}$$

The circulation Γ_1 is calculated from Equation (10) which immediately indicates that for waves of identical amplitude (same ϵ) the maximum of the induced perturbation Γ_1 is much larger when the wave propagates opposite to the axial vortex flow (negative sense).

Since surfaces of equal circulation and surfaces of equal pressure coincide this results in an expansion of the vortex core which is much larger when C is negative. More precisely, the distorsion of the vortex core by the wave is written as

$$r(z - Ut) = r_0 \left(1 + \frac{\int_0^{r_0^2/2} \frac{C_0 \Gamma_1}{y}\, dy}{C_0^2(r_0)}\right) \tag{18}$$

where r_0 is the radius of the vortex core.

In Figure 5 (a) – (b) we show schematically the flow configuration for negatively and positively propagating solitary waves in a frame moving with the wave. When $C > 0$ (Figure 5 (a)) the solitary wave disturbance tends to increase locally the axial velocity hence increasing the azimuthal vorticity or radial shear stress. A negatively propagating wave (Figure 5 (b)) may on the contrary lead to flow reversal (a change from a jet to a wake axial velocity profile).

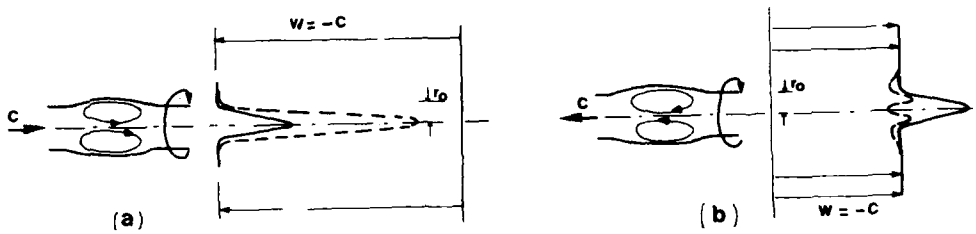

Fig.5 Schematic of critical flow conditions and perturbation induced by a passing solitary wave.
(a), wave travelling in the sense of the axial flow in the vortex ($C > 0$),
(b), wave travelling opposite to the vortex flow ($C < 0$).
- - - - - , axial velocity distribution in interior of solitary wave.

For a maximum distortion of 20% of the vortex core ($(r_m - r_0)/r_0 = 0.2$) and for a wave propagating opposite to the vortex flow we calculated the corresponding value of ϵ from Equation (18) using Equations (17) and (10). This value was then used to compute the shape of the vortex core when the wave propagates in the same way as the vortex flow. The shapes of the vortex core are plotted on Figure 6. The amplitude of the bump is shown to be larger for waves propagating in the negative direction.

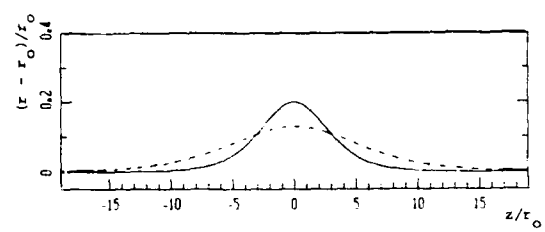

Fig.6 Calculated perturbation of vortex core boundary on passage of a solitary wave:
$(r_m - r_0)/r_0 = 0.20$ for negatively propagating wave and some parameter ϵ for both wave propagation directions.
——, negatively propagating wave, - - - - , propagation in positive sense.

We performed also calculations of the azimuthal and axial velocity field in the centre of the solitary wave using the same value of ϵ as in Figure 6. It is seen from Figure 7 (a) – (b) that the effect on the axial velocity of the passage of a solitary wave with relatively small amplitude (20% or less change in core radius) is considerable. For positive propagation (Figure 7 (a)) the flow becomes nearly critical and for negative propagation a wake flow (reversal of azimuthal vorticity) with large radial velocity gradients is established. Passage of axisymmetric solitary wave of relatively small amplitude can therefore cause the vortex to become locally unstable to spiral disturbances [20].

Although the disturbance of the vortex core is small, the corresponding perturbation for the stream function is not of weak amplitude. This raises the question of the validity of the application of Benjamin's perturbation method. A large amplitude model would be without any doubt more accurate to describe the kind of wave we are interested in. Such an attempt was made recently by Leibovich [5] but the effort required to establish such a model is considerable. Therefore, the model approximation based on a small perturbation parameter was used which is, in any case, a good approximation of the important mechanisms involved in vortex breakdown.

AD A135 157 AERODYNAMICS OF VORTICAL TYPE FLOWS IN THREE DIMENSIONS: CONFERENCE PROCE..(U) ADVISORY GROUP FOR AEROSPACE RESEARCH AND DEVELOPMENT NEUILLY.. JUL 83

6/6

UNCLASSIFIED AGARD-CP-342 F/G 20/4 NL

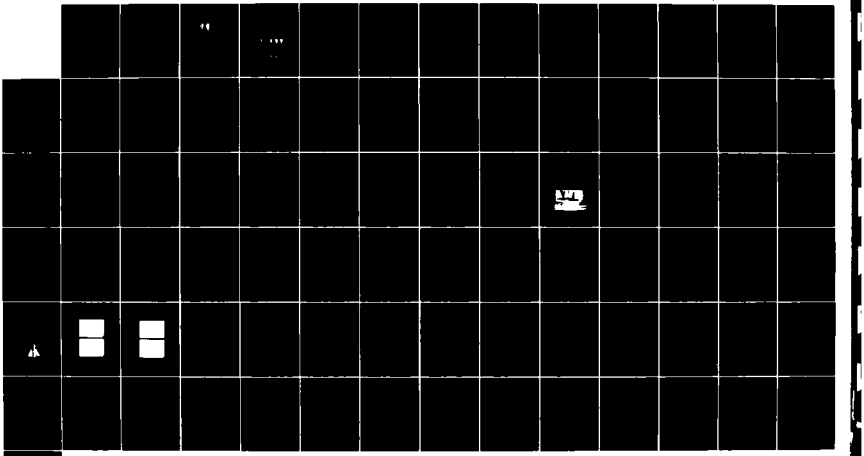

END
DATE FILMED
1 84
DTIC

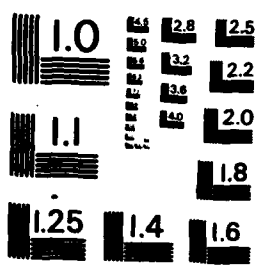

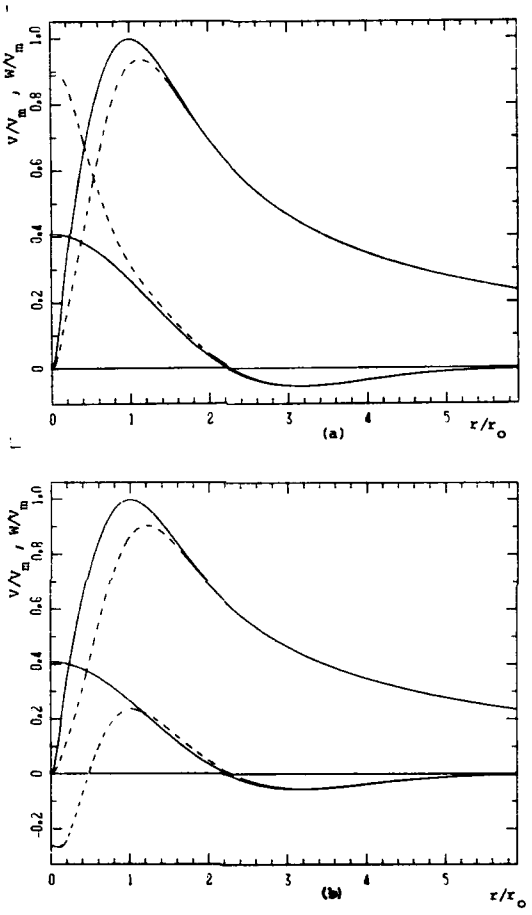

Fig.7 Calculated velocity distributions inside a solitary wave indicated by dashed lines:
(a), positive sense of propagation and $a_m/r_o \simeq 0.13$, (here $a_m = r_m - r_o$);
(b), negative sense of propagation with $a_m/r_o = 0.20$;
the parameter ϵ is the same in (a) and (b); ——, undisturbed vortex flow.

4.3 Experimental Results on Axisymmetric Waves

In Figure 8 (a) – (b) we show an axisymmetric wave travelling on a vortex with Q = 230 ltr/hr in the opposite sense to the core flow. The time interval in 8 (a) is 0.2 s and in 8 (b) 0.25 s. Figure 8 (a) is a nice example of solitary wave development out of a large initial disturbance. Figure 8 (b) on the other hand shows unstable conditions with a vortex breakdown region behind the wave. The latter wave has been produced by cutting through the vortex and this is why the axisymmetric wave is followed by a kink-wave.

The wave speed calculated from Equation (12) is for the condition corresponding to Figure 8 (V_m = 132 cms^{-1} and W_m = 60 cms^{-1}) C = 76 cms^{-1}. The measured speeds are respectively for Figure 8 (a) and (b) 83 cms^{-1} and 81 cms^{-1}. We have not succeeded at present to determine the wave speed with better accuracy and it seems unlikely

that any amplitude dependence of the wave speed can be established. For one thing the amplitude is already relatively large when the wave can be followed on movie pictures and vortex breakdown occurs for somewhat larger perturbations. Furthermore the vortex is always subjected to weak disturbances, caused either by dye injection or by vortex breakdown inside the suction tube which affect the vortex structure. The scatter in the experimental points in Figure 2 is to some extent indicative of the unsteady character of the vortex.

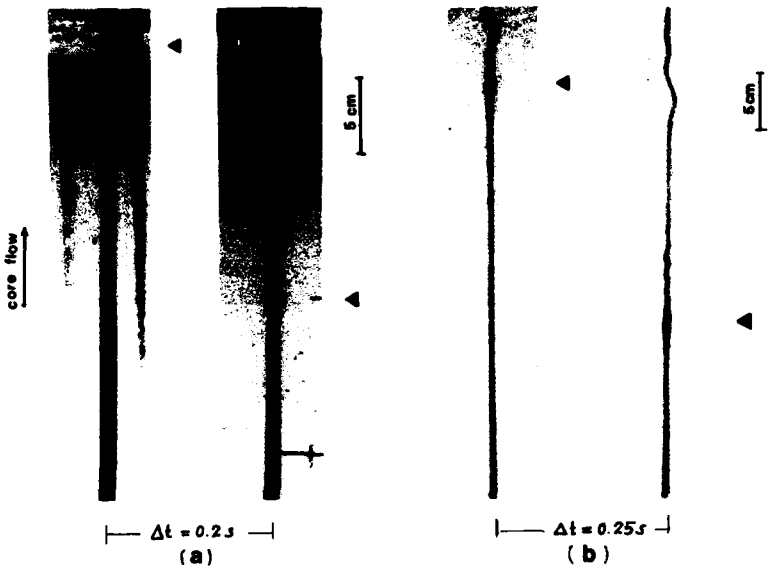

Fig.8 Photographs of axisymmetric waves on vortex characterised by Q = 230 ltr/hr.
(a) developing stable solitary wave, (b) unstable wave.

The core diameter determined from the dyed region in Figure 8 corresponds, within experimental error, to the vortex core size $2r_0$ which defines the radius characterized by $V = V_m$. Figure 8 (a) also shows that the vortex has a taper with the radius increasing in the direction opposite to the flow. This causes the relative amplitude of negatively propagating waves to decrease more rapidly than would be expected from viscous dissipation alone.

Various methods were tried to produce axisymmetric waves at the end opposite to the suction tube which would propagate in the positive sense. The only technique with reasonable success was to cut the vortex by a rod which produced an axisymmetric wave followed by a kink wave. The wave front was however less well defined than that of waves produced near the suction tube (see Figure 9) and any determination of wave propagation speed remained fruitless. The analysis shows (see Figure 6) that positively propagating waves have smaller amplitudes and this explains part of the difficulty encountered experimentally.

5. VORTEX BREAKDOWN CONDITIONS AND CONCLUDING REMARKS

5.1 Breakdown on Isolated Vortices

In Section 4 we showed that travelling axisymmetric solitary waves of relatively small amplitude on subcritical core flow can bring about locally unstable flow conditions. In particular, a wave moving with $C > 0$ causes the swirl parameter $q = V_m/W_m$ to decrease from 2.4 to about 0.7 when the wave amplitude, referred to the core radius, is $a_m/r_0 \simeq 0.18$. With this value of the swirl parameter spiral modes could just about grow according to the stability criteria obtained by Lessen, Singh and Paillet [20]. A wave propagating opposite to the core flow changes the jet-like profile into a wake (Figure 7 (b)) which remains subcritical but has a large radial velocity gradient. For a relative wave amplitude of 0.28 , the maximum gradient of the axial core velocity inside the wave is of the same order as the gradient inside the wave with positive C and $a_m/r_0 \simeq 0.18$ (Figure 7). It is therefore plausible that the wake profile caused by a

wave with $a_m/r_0 = 0.28$ is also near to marginal stability. More definite conclusions would require a stability analysis. It might be possible to use the stability criterion recently obtained by Leibovich and Stewartson (1983) [21]. We should point out however that both instability studies [20, 21] are valid for steady flow conditions which are not strictly speaking satisfied by travelling waves.

Figure 8 (b) shows a case of local vortex breakdown in the wake of an axisymmetric solitary wave creating tightly wound helices and turbulence. It would be a fruitless task to try to determine a wave amplitude criterion for vortex breakdown from the present experiments but Figure 8 (a) would indicate that a wave with $C < 0$ and $a_m/r_0 \approx 0.25$ is still stable. Considering the uncertainties in the experiments and in the determination of stability criteria, observations are consistent with the above discussions.

The isolated kink waves are observed to be stable entities which do not cause disruption of the vortex core (see for instance the kink in Figure 8 (b)). Even when they interact quite violently the core remains unbroken. When a kink wave is formed by disrupting the core, the latter reforms through the propagation of a wave of contraction from the suction tube which then reconcentrates the disrupted vortex lines. As the kink waves propagate they appear to have no effect upon the core flow. There exists the possibility that kink waves with larger torsion and larger curvature would be less stable. In the turbulent flow system investigated by HBG, for instance, torsion and curvature were considerably larger than what could be obtained on the isolated vortices and this could explain why HBG seemed to be able to relate vortex breakdown to kink wave dynamics (see however Section 5.2).

It has been speculated recently by Leibovich [5] that the nonlinear interaction between axisymmetric and non-axisymmetric waves might be the most favourable ground for breakdown. A possible case of interaction of different wave types is shown in Figure 9. The vortex has been cut on both sides which generates an axisymmetric wave followed by a kink wave. The waves propagate toward each other and strong interaction takes place which results in breakdown and turbulence production. The vortex rapidly reforms behind the wave disturbances by waves of contraction.

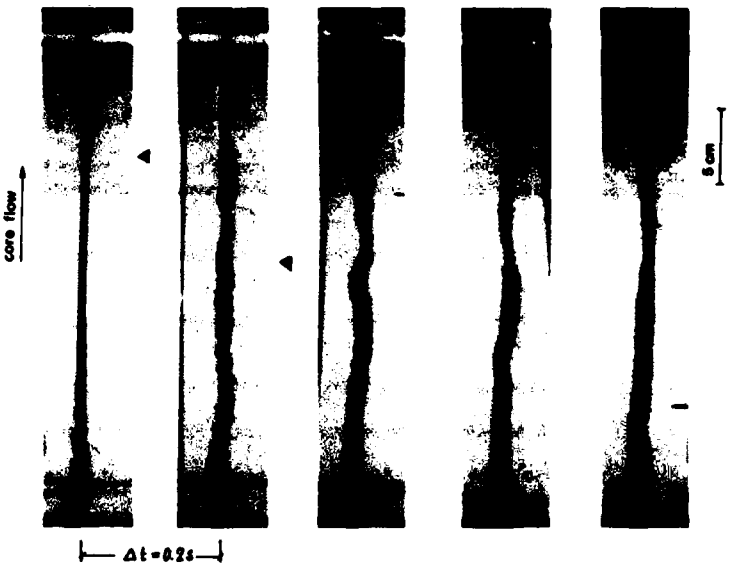

Fig.9 Photographs of a wave interaction and vortex breakdown on a vortex corresponding to Q = 130 ltr/hr. The time interval is 0.2 s and the axisymmetric wave with $C < 0$ is marked by arrows on the first two frames.

5.2 Waves in Turbulent Rotating Fluids

Here we reexamine the results of HBG, noting, among other things, the preponderance of unstable axisymmetric waves, and add some extra observations to emphasize this point. The critical observation here is that any disturbance which tends to cut-off or reduce the axial flow in the vortex core creates an axisymmetric type of solitary wave which may or may not become unstable, depending on its amplitude. In the experiments of HBG, the axial flow in the cores was downward into the mixed region. At frequent intervals this axial flow was cut-off completely by the turbulent motion in the mixed layer and this information was transmitted along the core to the rest of the fluid by a wave of such large amplitude that it was invariably unstable. Such a wave can be clearly seen in HBG (Figures 16 (c) and (12)). Due to the asymmetry of this process the most unstable waves propagate against the axial flow i.e. upwards, while the downward propagating ones which are usually not visible in the visualisation, cause little disruption. The axial flow into the mixed layer is maintained and this causes a wave of contraction upwards into the disturbed region which reestablishes the axial flow.

In the turbulent system, generation of waves is random and varying in amplitude and form so that axisymmetric and kink waves are produced simultaneously. On the average 5 kink or helicoidal waves exist on a vortex in the system studied by HBG and from a re-examination of the film taken by HBG it is clear that the vortex core supports at least an equal number of axisymmetric waves. It is therefore difficult to determine the cause of vortex breakdown in the interior of the fluid, that is, further away from the mixed layer. What seemed to HBG a clear case of kink-wave interaction breakdown (their Figure 16 (a) and perhaps 16 (b)) may actually be caused by nonlinear interactions of different types of waves. Hopefully, future theoretical and experimental studies will help to clarify the cause and mechanisms of breakdown due to travelling waves.

REFERENCES

1. Hopfinger, E.J. Browand, F.K. Gagne, Y. — *Turbulence and Waves in a Rotating Tank*, J. Fluid Mech. 125, pp.505-534, 1982.
2. Benjamin, T.B. — *Some Developments in the Theory of Vortex Breakdown*, J. Fluid Mech. 28, pp.65-84, 1967.
3. Hopfinger, E.J. Browand, F.K. — *Vortex Solitary Waves in a Rotating, Turbulent Flow*, Nature 295, pp.393-395, 1982.
4. Hashimoto, H. — *A Soliton on a Vortex Filament*, J. Fluid Mech. 51, pp.477-485, 1972.
5. Leibovich, S. — Wave propagation, instability and breakdown of vortices, in *Vortex Motion*, H.G. Hornung, E.A. Müller (eds.), Friedr, Vieweg und Sohn, Braunschweig/Wiesbaden, 1982, pp.50-67, 1982.
6. Kida, S. — *A Vortex Filament Moving Without Change of Form*, J. Fluid Mech. 112, pp.397-409, 1981.
7. Leibovich, S. Ma, H.Y. — *Soliton Propagation on Vortex Cores and the Hashimoto Soliton*, to be published in J. Fluid Mech., 1983.
8. Pritchard, W.G. — *Solitary Waves in Rotating Fluids*, J. Fluid Mech. 42, pp. 61-83, 1970.
9. Leibovich, S. — *Weakly Non-Linear Waves in Rotating Fluids*, J. Fluid Mech. 42, pp.803-822, 1970.
10. Squire, M.B. — *Analysis of the "Vortex Breakdown" Phenomenon, Part I.* Miszellanen der Angewandten Mechanik. Akademie/Berlin, pp.306-312, 1962.
11. Benjamin, T.B. — *Theory of the Vortex Breakdown Phenomenon*, J. Fluid Mech. 14, pp.593-629, 1962.
12. Escudier, M.P. Bornstein, J. Maxworthy, T. — *The Dynamics of Confined Vortices*, to be published in Proc. Roy. Soc., 1983.
13. Maxworthy, T. — *On the Structure of Concentrated, Columnar Vortices*, Astro. Acta 17, pp.363-374.
14. Turner, J.S. — *The Constraints Imposed on Tornado-Like Vortices by the Top and Bottom Boundary Conditions*, J. Fluid Mech. 25, pp.377-400, 1966.

15. Batchelor, G.K. — *An Introduction to Fluid Dynamics*, Cambridge University Press, Cambridge, p.509, 1967.

16. Maxworthy, T.; Hopfinger, E.J. — *Turbulence in Rotating Fluids: Finite-Amplitude Wave Motions on Vortex Cores*, to appear.

17. Lamb, G.L. — *Elements of Soliton Theory*, Wiley Interscience Publication, John Wiley & Sons, New York, pp.190-200, 1980.

18. Lambourne, N.C.; Bryer, D.W. — *The Bursting of Leading Edge Vortices – Some Observations and Discussions of the Phenomenon*, Aeronaut. Rec. Counc. R. & M. 3282, pp.36.

19. Escudier, M.P.; Bornstein, J.; Zehnder, N. — *Observations and L.D.A. Measurements of Confined Vortex Flow*, J. Fluid Mech. 98, pp.49-63, 1980.

20. Lessen, M.; Singh, P.J.; Paillet, F. — *The Stability of a Trailing Line Vortex. Part 1. Inviscid Theory*, J. Fluid Mech. 63, pp.753-763, 1974.

21. Leibovich, S.; Stewartson — *A Sufficient Condition for the Instability of Inviscid Columnar Vortices*, to be published in J. Fluid Mech., 1983.

ACKNOWLEDGEMENTS

The authors wish to thank S.Layat for experimental assistance and P.Pegon for numerical advice. Discussions with F.K.Browand were of crucial importance. Financial support by the D.R.E.T. under contract number 82-468 and by the O.N.R., contract number N 00014-82-K-0084 is acknowledged.

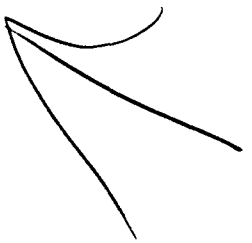

VORTICAL FLOW MANAGEMENT FOR IMPROVED CONFIGURATION AERODYNAMICS - RECENT EXPERIENCES

Dhanvada M. Rao
Vigyan Research Associates, Inc.
28 Research Drive
Hampton, VA 23666, U.S.A.

SUMMARY

This paper reports recent progress in vortex-control applications for alleviating the adverse consequences of three-dimensional separation and vortical interactions on slender body/swept wing configurations. Examples include: helical separation trip to alleviate the side force due to forebody vortex asymmetry; hinged strakes to avoid vortex breakdown effects; compartmentation of swept leading-edge separation to delay the pitch-up instability; under-wing vortex trip and vortex flaps for drag reduction at high lift; and an apex-flap trimmer to fully utilize the lift capability of trailing-edge flaps for take off and landing of delta wings. Experimental results on generic wind-tunnel models are presented to illustrate the vortex-management concepts involved and to indicate their potential for enhancing the subsonic aerodynamics of supersonic-cruise type vehicles.

NOMENCLATURE

C_L	Lift coefficient	C_Y	Side force coefficient
C_l	Rolling moment coefficient	C_t	Local leading-edge thrust coefficient
C_{l_β}	Lateral stability derivative, $\partial C_l/\partial\beta$	L/D	Lift-to-drag ratio
C_m	Pitching moment coefficient	α	Angle of attack
C_n	Yawing moment coefficient	β	Angle of sideslip
C_{n_β}	Directional stability derivative, $\partial C_n/\partial\beta$	δ	Control deflection angle
C_p	Pressure coefficient	η	Spanwise coordinate normalized by semi-span

1. INTRODUCTION

The expanding flight and maneuvering envelopes demanded by recent tactical aircraft design studies have resulted in a growing awareness of the need to understand and to work with massive three-dimensional separations and the associated vortical flows. Slender bodies and highly-swept wings in combination generate a kaleidoscope of complex vortex systems through the angle of attack range, whose implications increasingly concern the configuration aerodynamicist. Equally, they offer an unique opportunity for utilizing the energy and persistence of these vortical structures in innovative ways to engineer the aerodynamic characteristics for improved flight capability and extended operational limits.

This paper is a progress report of continuing research at NASA Langley Research Center, aimed at conceptualizing practical means of vortex-flow manipulation to upgrade the subsonic performance, stability and control characteristics of the new generation supersonic-cruise tactical aircraft. Selected examples from recently published results of this work will be presented, to indicate the broad scope of the problem areas being addressed with the underlying theme of re-structuring a problematical separated flow condition through artificially-generated vortex systems, as opposed to the conventional approach of suppressing flow separation. Only the basic concepts and their experimental evaluation can be discussed within the present space limitations; additional results indicating the scope of applications of the concepts can be found in the referenced literature. This paper complements a preceding NASA Langley paper (ref. 1).

2. HELICAL TRIPS

The onset of asymmetry in the forebody vortices at high angles of attack produces an abrupt side force (and yawing moment) which can be highly adverse to the aircraft handling characteristics at maneuvering limits. This asymmetry is believed to arise from an unstable interaction between the counter-rotating primary vortices when they are in close proximity to each other, but away from a solid boundary. While research continues for a better understanding of the basic fluid mechanism involved and to predict the onset and magnitude of side force, it is of interest to devise practical means to eliminate or control the phenomenon which can be a limiting factor in high-alpha maneuvering of aircraft and missiles. A passive, add-on device is preferred which will alleviate the side force on any given forebody shape without inducing undesirable side effects on performance or stability. The well known nose strakes generate vortex systems of their own which, in a manner not yet fully understood, force the forebody wake to remain symmetrical to higher angles of attack. However, experience with nose strakes shows that their effectiveness is highly dependent on the forebody shape and therefore a trial-and-error development of the optimum strake is required for every new application; they also frequently produce adverse changes in the lateral-directional characteristics at high angles of attack. Nose-radome mounted strakes in addition are likely to interfere with radar performance. Nevertheless, the low drag penalty and ease of installation are positive advantages that motivate the search for more universally applicable forms of nose strakes, which are also free of the adverse side effects mentioned above.

The helical-trip device (fig. 1) represents an approach that is conceptually different from the conventional strakes: it seeks to prevent the formation of a coherent vortex pair from forebody separation and thus to eliminate the possibility of asymmetry altogether. The means adopted for this purpose was suggested by the mechanism of suppression of the alternate vortex shedding from cylinders in cross-flow, ref. 2 . The helical trips were accordingly devised to force separation at varying peripheral locations along the forebody length to generate a non-uniform feeding sheet and thereby impede the roll-up into concentrated vortex cores, while maintaining a "mirror-image" symmetry of trips with respect to the pitch plane to avoid any direct trip-induced side force. The selected helix orientation placed the trip nearly transverse to the boundary-layer flow at high angles of attack, thus making it more effective in provoking separation.

The concept was evaluated on a series of wind-tunnel force models ranging from basic axi-symmetric bodies (cone- and ogive-cylinders), through fuselage shapes with vertical and horizontal oval cross-section, to wing/fuselage/tail combinations representing a generic fighter configuration (ref. 3). The results shown in fig. 2 are supportive of the helical trip concept:

i) straight side-trips (B) do not appreciably change the basic fuselage side force characteristics (A);
ii) helical trips (C), made from the same wire material as (B), suppress the side force up to the highest alpha;
iii) inverted helical trips (D), obtained by rolling the forebody through 180°, totally lose their capability (since they are now approximately parallel to the boundary layer flow);
iv) truncated helical trips (E), possibly to further reduce radar interference, basically remain effective; and
v) 50-percent reduction in helical trip diameter (F) does not degrade the trip capability until approaching the highest alpha.

Since the trip height will be scaled with the boundary-layer thickness, in full-scale applications the relative trip size will be much smaller than the size tested on the wind tunnel models. It is noteworthy that on all the test bodies, the very first helical trip application was effective, no subsequent adjustment being required of the initial trajectory shape used. This lack of sensitivity to the trajectory shape is consistent with the helical-trip hypothesis, apart from being an advantage in practical applications.

Helical trips were further evaluated during a NASA Langley study of forebody shape effects on the lateral/directional as well as longitudinal stability at high angles of attack of a contemporary fighter configuration with extended forebody (ref. 4). The helical-trip effectiveness results presented in fig. 3 show that the high-alpha yawing moments were alleviated generally without degrading the lateral-directional stability characteristics. A further consideration (ref. 4) was the yaw-induced pitching moment during high-alpha maneuver when the pitch-down authority of the longitudinal controls may become marginal. A direct comparison of conventional nose-strakes and helical trips (fig. 4) shows that whereas the addition of strakes results in an adverse nose-up moment in sideslip, helical trips actually produce a favorable trend relative to the "clean" forebody. These results serve to emphasize the basic difference between the two devices: the helical trips achieve side-force suppression by disrupting the forebody vortices thus avoiding the undesirable vortex-triggered side effects, as opposed to vortex intensification by the conventional nose strakes.

3. HINGED STRAKES

Wing strakes are highly-swept root extensions of the leading-edge whose function is to generate strong vortices at high angles of attack in order to re-energize the stalling flow over the wing and thereby improve the maximum-lift capability. The strake vortices generally have sufficient lateral separation to preclude the unstable mutual interaction associated with forebody vortices; however, they individually are subject to the well-known breakdown phenomenon. When vortex breakdown occurs over the wing, an abrupt loss of its beneficial influence leads to stall, pitch-up and roll/yaw disturbances. Being a dynamic phenomenon, vortex breakdown also instigates buffet and associated undesirable motions such as wing rock, noseslice etc. The expansion of wing wake following strake vortex breakdown degrades the effectiveness of aft-tail surfaces, and may result in serious loss of controllability. Automatic limitation of the angle of attack envelope in order to stay below the vortex-breakdown boundary restricts the maneuver potential of the vehicle and is not a preferred solution. The hinged-strake concept was devised as a means to suppress the strake vortices and thus to eliminate the vortex-breakdown boundary altogether; in addition, articulated strakes offered the possibility of improving post-stall maneuverability when the control power of conventional surfaces has degraded.

The hinged strakes, structurally separate from the wing, are attached to the fuselage through longitudinal hinges (fig. 5). In the normal co-planar position the strakes function conventionally. At high angles of attack approaching vortex breakdown, however, they may be rotated downwards to an anhedral angle. Increasing anhedral not only decreases the strake projected planform area but also the normal force coefficient by reducing both the linear and the non-linear contributions (ref. 5), thus providing an effective control over the strake loading as well as on its vortex characteristics. Examples of strake anhedral effects on the high-alpha aerodynamics of a generic fighter configuration (fig. 6) will be presented through some results of a low-subsonic wind tunnel study (ref. 7). In order to highlight the anhedral effects, relatively large strakes (of exposed area = 26.6% of wing reference area) were selected for this investigation.

The lift and pitching-moment characteristics of the wing/fuselage/vertical fin configuration (without a horizontal tail) having strakes at 30 deg. anhedral are shown in fig. 7, in comparison with planar strake data (ref. 6). The onset of vortex breakdown with the planar strake is evidenced by a peaking of C_L accompanied by pitch-up and lateral/directional disturbances as the angle of attack approaches 30 degrees. These vortex breakdown effects can be seen to be greatly alleviated with the anhedral strakes. Suppression of vortices coupled with the reduced projected area of anhedral strakes inevitably penalizes the maximum lift relative to planar strakes of equal surface area. However, when compared with data for planar strakes of smaller i.e. 16.5% area (ref. 6) where pitch-up limits the usable C_L to 1.2 approx. (at α = 19 deg.),

the anhedral strakes are seen as an improvement with a maximum C_L of 1.5 (at α = 42 deg.) free of pitch-up. Thus, hinged-strakes of suitably increased size in an anhedral setting can allow high-alpha maneuvering free of vortex breakdown problems and without sacrificing the maximum lift capability of the conventional fixed strakes.

The planar-strake vortex effects also cause non-linearity in the restoring moment characteristics of the horizontal tail, as indicated in fig. 8. In the low-alpha range, addition of planar strakes to the strake-off configuration reduces the horizontal-tail effectiveness due to increased downwash behind the wing. Vortex breakdown and associated reduction in the downwash then leads to a rapid increase in $\Delta C_{m,HT}$ slope around α = 30 degrees. An absence of this non-linearity in the hinged-strake data, which closely duplicates the strake-off characteristics, is further evidence of vortex suppression due to strake anhedral. As a result, up to 50% increase in horizontal-tail effectiveness is obtained in the mid-alpha range by employing anhedral rather than planar strakes.

Effective pitch-down capability is important for a positive and rapid recovery from extreme nose-high attitudes during post-stall maneuvering, an area where aft-tail pitch controls are usually found lacking due to wake effects. On the other hand, the strake loading not only continues to increase to high angles of attack but also acts well forward of the aircraft c.g. Consequently, the use of hinged strakes for pitch recovery appears worth considering. The incremental nose-down moment due to symmetrically articulated strakes at 30 deg. and 45 deg. anhedral is shown in fig. 9, together with strake-off data which may be supposed to represent the limiting case of 90 deg. anhedral. Also shown for comparison is the result taken from ref. 8 for an aft-tail fighter configuration with maximum nose-down stabilator deflection, which displays the typical loss of effectiveness starting at α = 25 deg. Evidently the hinged strakes can provide a powerful and fully controlled nose-down moment for recovery from very high angles of attack.

Considering now the asymmetric articulation mode, e.g. only the right-hand strake deflected, a positive rolling moment is obtained due to the larger lift on the left-wing panel which is still under the influence of the planar-strake vortex. As shown in fig. 10, the rolling moment coefficient increases quadratically with angle of attack for a given strake deflection until the onset of the planar-strake vortex breakdown, i.e. α = 28°. Up to this angle of attack, the induced yawing moment (resulting from the forebody side-force generated by the right-strake deflection) is favorable. After vortex breakdown the rolling moment rapidly decreases and the yawing moment becomes adverse; however a substantial roll power is still available at high angles of attack in comparison with the conventional ailerons. Also shown in fig. 10 are the results for another vortex-related roll control concept viz. spanwise blowing on one wing panel (ref. 9). Although the rolling moment characteristics in this case are very similar to the asymmetrically deflected hinged strake, the induced yaw unfortunately is adverse and equal in magnitude to the rolling moment throughout the alpha range.

4. 'COMPARTMENTATION' OF SWEPT LEADING-EDGE SEPARATION

The predilection for early separation off highly-swept leading edges offers a rewarding field for the application of vortex flow control concepts. From the onset of leading-edge separation, a rapid collapse of leading-edge suction with increasing angle of attack aggravates the lift-dependent drag; with the progressive inboard movement of leading-edge vortices the tip sections lose the benefit of vortex lift resulting in pitch instability, which is of special concern in relaxed static stability applications to tail-less configurations.

This section deals with a leading-edge 'compartmentation' concept which aims to restrain the inboard spread of separation by means of fixed leading-edge devices. The swept leading edge is divided into aerodynamically isolated compartments, each having attached flow at its inboard end while the growth of leading-edge separation is confined to the compartment span. Consequently, at a given angle of attack the scale of separation averaged over the span is reduced in comparison with the original wing. At the same time, the vortex migration out of the tip region is retarded thus improving the tip lift characteristics. The postulated compartmentation of the leading-edge separation is sketched in fig. 11.

The compartmentation concept was evaluated in low-subsonic tests on 60-deg. and 74-deg. delta wing models. The leading-edge devices used for the purpose were fences, chordwise slots and pylon-type vortex generators. The pressure-instrumented leading edge on the 60 deg. delta model allowed the compartmentation effect to be monitored via the spanwise distribution of leading-edge pressure coefficient ($C_{P,L.E.}$), as illustrated in fig. 12. With the basic wing leading edge substantially separated at α = 18.7 deg., the fence as well as the slot reduce the separation outboard of their location as indicated by the raised leading-edge suction levels, the fence showing a stronger effect than the slot at this high angle of attack. Further compartmentation of the leading edge by means of three equally-spaced slots is shown in fig. 13. The increased average leading-edge suction level due to multiple compartmentation results in drag reduction above α = 11 degrees (when the basic wing has become significantly separated), which is reflected in the L/D comparison of fig. 14A. At a given C_L however the L/D is hardly improved (fig. 14B), because suppression of leading-edge separation also reduces the vortex lift, which must be compensated by increasing the angle of attack resulting in a drag increment. This is an intrinsic limitation on the use of leading-edge separation control (regardless of the means employed) for L/D improvement on wings where leading-edge vortices contribute significantly to lift.

The second purpose of compartmentation, i.e. to retard the inboard migration of the leading-edge vortex, is illustrated for the same three-slot configuration in fig. 15, which plots the upper-surface pressure coefficient at a representative tip location versus angle of attack. The compartmentation effect increases the angle of attack corresponding to the vortex passage over the reference point (as identified by the -Cp peak) from 12.5 deg. on the basic wing to 19.5 deg. with the slots. The later departure of the vortex from the tips is directly reflected in a delayed pitch-up observed in pitching-moment characteristics, fig. 15. Additional information and data on the performance of other slot and fence arrangements on the 60-deg. delta model will be found in refs. 10-12.

The pylon-type vortex generator (PVG) resembles a scaled-down pylon projecting down and forward from the leading edge (fig. 16). This arrangement was intended to exploit the prevailing sidewash near the swept leading edge for generating a streamwise vortex off the top edge of the pylon, the vortex rotation being such as to induce a downwash on the outboard side. The increasing sidewash with angle of attack intensifies the vortex, resulting in augmentation of downwash which will tend to keep the leading edge attached adjacent to and outboard of the PVG location (fig. 17). Thus the compartmentation effect should be maintained to high angles of attack when the previous devices (fence and slot) begin to fail.

The persistence of the compartmentation due to pylon vortex generators may be judged by the 60 deg. delta spanwise leading-edge pressure distribution at 22.5 deg. angle of attack (the maximum of the test) with three equi-spaced devices, fig. 18, in comparison with a three-slot arrangement. The corresponding pitching-moment characteristics, fig. 19, show a strong stabilizing influence due to the vortex generators. A further demonstration of the pylon effectiveness in improving the longitudinal stability of 74 deg. delta wing is shown in fig. 20, this time in comparison with fences (ref. 13). It should be stressed that the PVG arrangements employed in these tests were by no means optimum, and that more efficient spanwise locations might be found for specific planforms.

5. UNDERWING VORTEX TRIP

While compartmented-separation is found to be an effective means of improving the longitudinal stability of highly-swept configurations, its potential for drag reduction at high angles of attack may be limited on thin, small-radius leading edges typical of supersonic cruise wings. At the same time, the cruise drag penalty of multiple fixed devices may be unacceptable. Alternatively, for retractable systems light weight and short travel are important considerations to allow rapid actuation during high-speed tactical maneuvers. These requirements, as well as the need for effective leading-edge thrust capability on thin wings to high angles of attack, appear to be met by the underwing vortex trip, fig. 21. This flap-like device opens to create a forward-facing cavity under the leading edge. Forced separation at the sharp forward edge of the flap feeds a spanwise spiralling vortex situated at the mouth of the cavity. The vortex suction acting over the cavity frontal area produces thrust all across the cavity span. An optimally placed vortex will induce the outer flow to turn parallel to the upper surface thus remaining attached on the wing, regardless of the leading-edge radius. The adjustable flap will allow control of the vortex position as a function of angle of attack, in order to maximize the thrust effectiveness over the alpha range.

For simplicity during a preliminary investigation of the concept, the underwing vortex trip was simulated by means of a thin, swept flat plate secured to the bottom surface of the 60-deg delta model (ref. 10-12). This plate projected parallel to the wing plane and terminated directly below the leading edge, leaving a gap between the plate and the wing lower surface (see sketch in fig. 22). While this fixed geometry restricted the scope of the investigation to a single (and not necessarily optimum) trip position, the results still are of interest as they reveal the mechanism underlying the drag-reduction capability of the concept.

A set of chordwise pressure distributions around the leading edge at the highest angle of attack of the test (i.e. α = 22.5 deg.) presented in fig. 22 show the vortex-trip induced suction replacing the positive pressure region on the lower surface of the basic wing leading edge (shaded area). The spanwise distribution of the local thrust coefficient obtained by integrating these pressure distributions show that the thrust with the vortex trip is more than twice that on the basic leading edge, fig. 23. The effect on L/D is shown in fig. 24, which also indicates the theoretical boundaries for the delta wing assuming 100-percent leading edge thrust (fully-attached flow) and 0-percent thrust (fully-separated vortex flow). In comparison with the lower boundary, it is seen that the basic wing retains a fair degree of residual thrust even after separation due to the relatively blunt leading edges (see fig. 23); consequently the L/D-increment due to the vortex trip appears rather small. However, since the leading-edge radius is irrelevant to its aerodynamic mechanism, the vortex trip should function equally well under a sharp leading edge given an equivalent frontal area of the cavity. Therefore, the L/D-increment relative to the zero-thrust boundary should be a fairer assessment of the vortex-trip capability. While the present results serve to verify the basic hypothesis of the concept, further studies on a thin wing whith variable trip deflection will provide a better indication of the drag-reduction potential of vortex trips at high lift coefficients.

6. VORTEX FLAPS

Unlike the conventional leading-edge flaps for maintaining attached flow at high angles of attack, the vortex flap is designed to operate with separation on its upper surface. When employed on a highly swept wing the three-dimensional separation is stabilized by a spanwise-spiralling vortex, whose concentrated suction acting on the forward-sloping flap surface generates a thrust component (fig. 25). While it may also serve in the conventional sense at the lower angles of attack (or on less-swept leading edges) where attached flow is feasible, the unique ability of the vortex flap to function effectively under an organized and stable separated flow renders it less sensitive to off-design conditions. This feature is particularly advantageous on slender wings which operate through a large angle-of-attack range and have a pronounced spanwise variation in the leading-edge upwash. In addition, the vortex-induced re-attachment at or near the hinge line helps to suppress hinge-line separation which can be a limitation with the conventional leading-edge flaps.

Since the first experimental demonstration of the drag-reduction potential of the vortex flap concept (ref. 14), a sizeable data base has been generated (refs. 15-26). In this section, some recent results from on-going research at Langley will be presented to support a discussion of area-efficient vortex flaps.

Originally conceived for use on supersonic transports to allow approach and landing with reduced engine thrust (for airfield noise alleviation), the vortex flap was to be deployed (Kreuger fashion) from

a nested position on the wing under-surface, i.e. in an area-extending mode, (fig. 25). Currently, there is considerable interest in combat aircraft applications of the vortex flap to improve the sustained-g performance in high-speed maneuver. For such applications a rapid-deflection capability as with the conventional leading-edge flaps would obviously be more desirable. However, the integration of vortex flaps with their relatively large chord is structurally difficult within a slender wing planform and also leads to an aerodynamic performance penalty. As an illustration of the aerodynamic problem, two sets of L/D results with vortex flaps of nearly equal area and at 30 deg. deflection on a 74 deg. delta wing are compared in fig. 26: one pertaining to "extending" flaps where the basic wing reference area (i.e. excluding flaps) is used (ref. 14), and the other for "integral" flaps where the reference area includes the flaps (unpublished Langley data). Although in both cases the vortex flaps generated nearly the same aerodynamic thrust (as confirmed by their axial force characteristics, not shown), the L/D increments are far less in the "integral" case. This is because for a given lift coefficient, say C_L = 0.5, a higher angle of attack is needed with integral flaps (viz. 16.5 deg. versus 14.6 deg. for extending flaps), and the consequent drag increase significantly penalizes the L/D improvement. Although trading vortex lift for thrust is central to the vortex flap concept, with integral flaps not only the vortex lift but also some linear lift is lost on slender wings (ref. 5), whereas the additional area provided by extending flaps is able to largely compensate for the loss of linear lift.

The above example serves to emphasize the importance of reducing the integral vortex flap area without unduly sacrificing its thrust, for obtaining useful L/D improvements. The possibilities in this regard are suggested by the spanwise variation in flap thrust contribution as determined by the vortex development. A typical case is illustrated in fig. 27, where the upper-surface pressure distributions at five spanwise stations on the 74 deg. delta wing are used to infer the local aerodynamic loading and the associated flow patterns. Flap deflection is seen to lower the suction level inboard of the hinge line well below the planar wing levels throughout the span, which coupled with the smaller effective wing area is responsible for a marked lift reduction. The varying average suction level on the flap upper surface indicates a wide-ranging thrust effectiveness at the different stations. In particular, at station (A) a largely attached flow is obtained inboard of a localized leading-edge vortex (which lies just outside the first pressure tap), thus the flap chord here contributes negligible thrust. The flap utilization is improved considerably, however, at stations (B) and (C) where the vortex has expanded to nearly match the flap chord. Thereafter, continued vortex enlargement progressively drives the peak suction and the re-attachment inboard across the hinge line, stations (D) and (F) indicating successive reductions of the flap thrust as well as increasing drag due to spreading of the vortex suction foot-print onto the wing. A planview projection of the suction peak and re-attachment positions inferred from the upper-surface pressure distributions in fig. 27 graphically presents the vortex track and its expansion down the wing. A large, obviously unproductive region of this flap (shaded area) may be eliminated by means of a gothic-shaped apex. Further, by a suitable re-structuring of the vortex to delay its inboard migration, the thrust contribution of the outer regions of the flap may be improved.

A preliminary trial of the above qualitative ideas was included in a recent Langley test program, (ref. 24), using a 58 deg. delta wing/fuselage model originally fitted with a constant-chord vortex flap (fig. 28, A), which also shows the successive modifications of the original flap. The corresponding L/D characteristics, fig. 28, B attest to the improvements accompanying the flap modifications (at a constant deflection of 40 deg.). A relatively small alteration of the apex from its original low-sweep to the gothic shape improves the vortex initiation and renders the apex region more thrust effective, leading to a striking increase in L/D up to C_L = 0.6. Introduction of a snag was intended to arrest the flap vortex at a part-span discontinuity and, with the help of a counter-rotating snag vortex, to retard its inboard migration. At the same time, the flap chord inboard of the snag was substantially reduced to match the much smaller vortex in this region. These modifications to the flap shape further improved the L/D up to C_L = 0.6. An alternative approach (to the snag) considered for maintaining the thrust effectiveness of outboard flap region was to strengthen the vortex feeding sheet at a part-span position by a local sweep reduction, which was simply obtained by removing the snag. The results show that the L/D improvement at higher lift coefficients was retained with the final shape, while achieving a 25% flap area reduction relative to the original constant-chord flap. The pitching-moment characteristics (fig. 28, C) associated with these flap modifications for L/D improvement show simultaneous benefits in the longitudinal stability, which is an equally important consideration in maneuvering applications.

At this writing, an aggressive program to explore further refinements of the basic vortex flap concept (refs. 25, 26) and to develop design tools is in progress at NASA Langley and within the industry, and it is likely that the next generation tactical aircraft designs will utilize advanced forms of leading edge vortex manipulation concepts.

7. APEX FLAP

The restriction on angle of attack to ensure adequate forward view as well as to avoid tail scraping on slender wing aircraft, denies access to the non-linear lift and consequently limits the lift capability during take off and landing. The lift contribution of trailing-edge flaps on such aircraft also is generally limited by the available trim power, particularly on tail-less configurations. Augmentation of the trim capability by using canard surfaces must accept a supersonic drag penalty; on the other hand, retractable canard devices are mechanically complex and cannot usually be deployed during high speed maneuvering.

Lift enhancement on highly swept wings at low angles of attack by means of forced vortices has been considered, two such concepts being the inverted vortex flap (ref. 23) and the upper vortex flap (ref. 25), fig. 29. Wind tunnel tests with these devices indicate a lift-increment potential of ΔC_L = 0.06 on a 74-deg. delta wing; even this modest lift increase requires quite large vortex-generating flaps, approaching 25% of the wing area. Apart from practical considerations, these large flaps produce drag levels that may be excessive during take off.

This section discusses an apex flap concept for delta wings which also relies on forced vortices, fig. 29. The apex flap however is intended primarily as a controllable lifting trimmer (like a canard) to permit the full utilization of trailing-edge flap potential at low angles of attack. The undeflected

apex flap becomes an undistinguishable part of the high-speed wing configuration and therefore incurs no cruise-drag penalty. Since the apex flap generates a large amount of vortex lift well forward of the center of gravity, a relatively small flap area (viz. 10% or less of the wing) can provide a powerful trim effect, in addition to its own direct lift. The possibility of obtaining some additional lift from the induced suction of the apex vortices passing over the main wing surface lends further interest to apex flap concept.

A basic study was performed on a 74 deg. flat-plate delta wing, incorporating a transverse hinge line at 25% center chord to obtain a 6% area apex flap and also trailing-edge flaps of comparable area (ref. 27). Flow visualizations revealed three basic vortex-patterns as sketched in fig. 30 in the order of increasing angle of attack with constant apex flap deflection; most frequently encountered was the 'merged' vortex pattern, probably due to the high leading-edge sweep of the subject wing.

The apex-flap trim capability is indicated by comparing the opposing pitching-moment increments generated by the apex and the trailing-edge flaps, fig. 31, according to which an almost-trimmed condition is achieved fortuitously with equal deflections of the two flaps up to α = 20 degrees. The trimmed-lift curve generated by the 20 deg/20 deg. flap combination (fig. 32) allows a 4 deg. reduction in angle of attack (or a ΔC_L = 0.12) relative to the planar wing. As shown in fig. 32, this trimmed configuration incurs no L/D penalty at $C_L \geq 0.5$ in comparison with the planar wing.

Above 20 deg. deflection the trailing-edge flap ΔC_m curve (fig. 31) indicates a progressive loss of its effectiveness (due to extensive flow separtion on the flap as confirmed by oil flow), whereas the apex-flap moment increment continues unabated to nearly 30 deg. deflection. Thus, the trimmed-lift increment shown in fig. 32 is limited not by the apex flap but rather the trailing-edge flap. The excess trim capability of the apex flap might therefore be further exploited for instance, by controlling the trailing edge flap separation and thus extending its effectiveness to higher deflection angles. A potential flow calculation of the trailing-edge flap characteristics gives the upper-limit of improvement if attached flow were maintained up to δ = 30 deg., fig. 33. The corresponding C_L (trim) curve, using apex-flap experimental ΔC_m data, then indicates a substantial improvement at low alpha, fig. 34.

The apex flap lift coefficient based on apex area, deduced from the measured axial-force increment due to flap deflection, at various deflection angles is plotted versus the apex angle of attack relative to free stream ($\alpha + \delta$) in fig. 35. For comparison, lift data for a 74 deg. delta wing (ref. 28) is also given, which shows the vortex breakdown effect at α = 35 deg. Contrary to the expectation of an earlier vortex breakdown at the hinge line, the apex lift curves do not indicate any evidence of it even with the ($\alpha + \delta$) approaching 60 degrees. Smoke visualizations of the apex vortices in the hinge-line plane also did not show the typical characteristics associated with vortex breakdown up to the extreme apex flap deflection and angle of attack. A satisfactory explanation of this observation is lacking; however, the sustained aerodynamic effectiveness of the apex flap makes it a potentially powerful control surface for high alpha applications. As such, further investigation of the concept and its integration into fuselage-wing configurations appears worth pursuing.

8. CONCLUDING REMARKS

A number of vortex-control devices were conceptualized and investigated experimentally as possible solutions to a range of high-alpha aerodynamic problems of slender and highly-swept configurations. Specifically, forebody side force triggered by vortex asymmetry, post-stall maneuvering limitations due to strake vortex breakdown, pitch-up resulting from the migration of leading-edge vortices away from the tips, excessive lift-dependent drag due to loss of leading-edge suction and vortex lift, and lift limitation at take off and landing were addressed. In each case a practical approach was demonstrated for vortex manipulation to eliminate the problem or to reduce its severity. While the devices described in this paper are interesting in themselves, the experience of formulating certain hypotheses relating to vortex behaviour and putting them to test has proved valuable towards refining our insights into the relatively new field of vortex aerodynamics.

REFERENCES

1. Lamar, J. E. and Campbell, J. F.; "Recent Studies at NASA-Langley of Vortical Flows Interacting with Neighbouring Surfaces." 1983, AGARD Symposium on Aerodynamics of Vortical Type Flows in Three Dimensions, Paper No. 10.

2. Naumann, A., Marsbach, M. and Kramer, C.; "The Conditions of Separation and Vortex Formation Past Cylinders," 1966, AGARD CP4, pp. 547-574.

3. Rao, D. M.; "Side Force Alleviation on Slender, Pointed Forebodies at High Angles of Attack." J. Aircraft, Vol 16, No. 11, Nov. 1979.

4. Carr, P. C. and Gilbert, W. P.; "Effects of Fuselage Forebody Geometry on Low-Speed Lateral-Directional Characteristics of Twin-Tail Fighter Model at High Angles of Attack." 1979, NASA TP 1592.

5. Kuchemann, D.; "The Aerodynamic Design of Aircraft." Pergamon Press, 1978.

6. Luckring, J. M.; "Subsonic Longitudinal and Lateral Aerodynamic Characteristics of a Systematic Series of Strake-Wing Configurations." 1979, NASA TM 78642.

7. Rao, D. M. and Huffman, J. K.; "Hinged Strakes for Enhanced Maneuverability at High Angles of Attack." J. Aircraft, Vol 19, No. 4, April 1982.

8. Nguyen, L. T., Gilbert, W. P. and Grafton, S. B.; "Control Considerations for CCV Fighters at High Angles of Attack." 1979, AGARD CP 262, Paper No. 11.

9. Erickson, G. E. and Campbell, J. F.; "Improvement of Maneuver Aerodynamics by Spanwise Blowing." 1977, NASA TP 1065.

10. Johnson T. D., Jr. and Rao, D. M.; "Experimental Study of Delta Wing Leading-Edge Devices for Drag Reduction at High Lift." 1982, NASA CR 165846.

11. Tingas, S. A. and Rao, D. M.; "Subsonic Balance and Pressure Investigation of a 60-Deg. Delta Wing with Leading-Edge Devices." 1982, NASA CR 165923.

12. Rao, D. M. and Johnson, T. D., Jr.; "Investigation of Delta Wing Leading-Edge Devices." J. Aircraft, Vol. 18, No. 3, March 1981.

13. Rao, D. M. and Johnson, T. D., Jr.; "Subsonic Pitch-Up Alleviation on a 74-Deg. Delta Wing." 1981, NASA CR 165749.

14. Rao, D. M.; "Leading-Edge Vortex Flap Experiments on a 74-Deg. Delta Wing." 1979, NASA CR 159161.

15. Rao, D. M.; "Exploratory Subsonic Investigation of Vortex Flap Concept on Arrow Wing Configuration." 1979, NASA CP 2108.

16. Rao, D. M.; "Leading-Edge Vortex Flaps for Enhanced Subsonic Aerodynamics of Slender Wings." 1980, ICAS 12th Congress, Paper 80-13.5.

17. Smith, C. W., Campbell, J. F. and Huffmann, J. K.; "Experimental Results of a Leading-Edge Vortex Flap on a Highly Swept Cranked Wing." 1980, NASA CP 2162.

18. Lamar, J. E. and Campbell, J. F; "Design Related Study of Transonic Maneuvering Slender Wings Having Vortex Flow." 1980, NASA CP 2162.

19. Yip, L. P. and Murri, D. G.; "Effect of Vortex Flaps on the Low-Speed Aerodynamic Characteristics of an Arrow Wing." 1981, NASA TP 1914.

20. Schoonover, W. E., Jr. and Ohlson, W. E.; "Wind Tunnel Investigation of Vortex Flaps on a Highly-Swept Interceptor Configuration." 1982, ICAS 13th Congress, Paper 82-6.7.3.

21. Frink, N. T.; "Analytical Study of Vortex Flaps on a Highly Swept Delta Wing." 1982, ICAS 13th Congress, Paper 82-6.7.2.

22. Marchman, J. F.; "Effectiveness of Leading-Edge Vortex Flaps on 60- and 75-Deg. Delta Wings." J. Aircraft, Vol. 18, No. 4, April 1981.

23. Marchman, J. F.; "The Aerodynamics of Inverted Leading Edge Vortex Flaps on Delta Wings." 1981, AIAA Paper 81-0356.

24. Frink, N. T., et al; "Vortex Flow Re-attachment Line and Subsonic Aerodynamic Data for Vortex Flaps on 50-Deg. to 74-Deg. Delta Wings on Common Fuselage." 1983, NASA TM 84618.

25. Rao, D. M.; "Upper Vortex Flap - A Versatile Surface for Highly Swept Wings.: 1982, ICAS 13th Congress, Paper 82-6.7.1.

26. Rao, D. M.; "Segmented Vortex Flaps." 1983, AIAA 21st Aerospace Sciences Meeting, Paper 83-0424.

27. Buter, T. A. and Rao, D. M.; "Experimental and Computational Investigation of an Apex Flap Concept on a 74° Delta Wing." NASA CR 166080, 1983.

28. Wentz, W. H., Jr.; "Effects of Leading-Edge Camber on Low Speed Characteristics of Slender Delta Wings." 1972, NASA CR 2002.

ACKNOWLEDGEMENT

The sustained encouragement and cooperation received by the author from colleagues at NTF Aerodynamics Branch, as well as the material support of Transonic Aerodynamics Division, NASA Langley Research Center, are gratefully acknowledged.

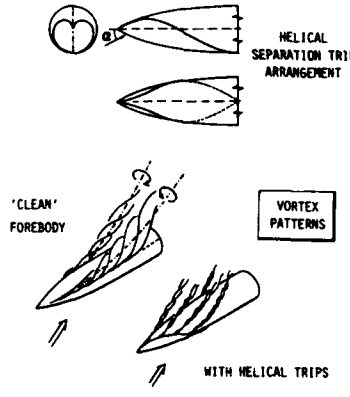

Fig. 1. Helical trip concept

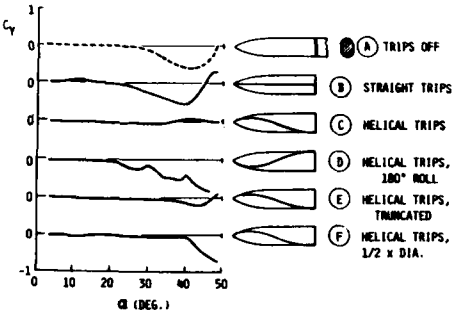

Fig. 2. Basic fuselage side force characteristics with helical and modified trips

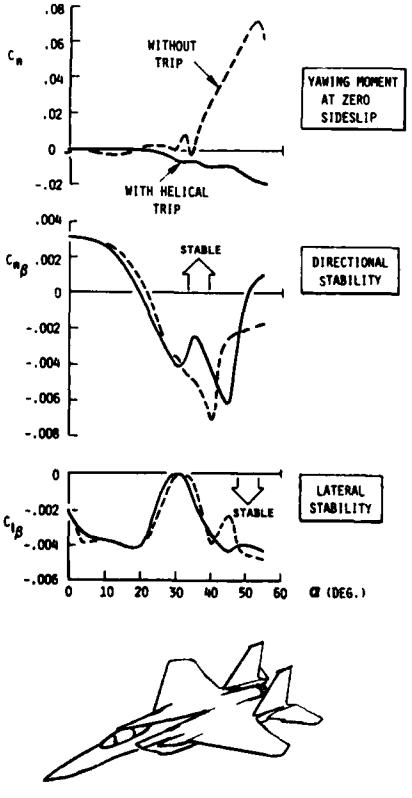

Fig. 3. Helical trip effectiveness on a fighter configuration (ref. 4)

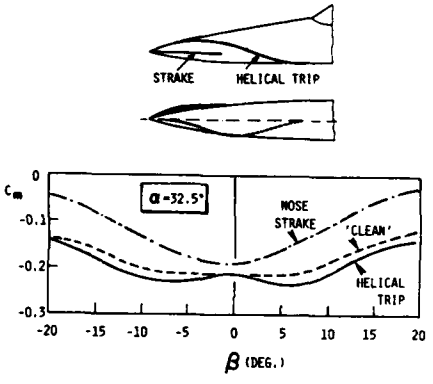

Fig. 4. Helical-trip and nose-strake effects on sideslip-induced pitching moment (fighter configuration, ref. 4)

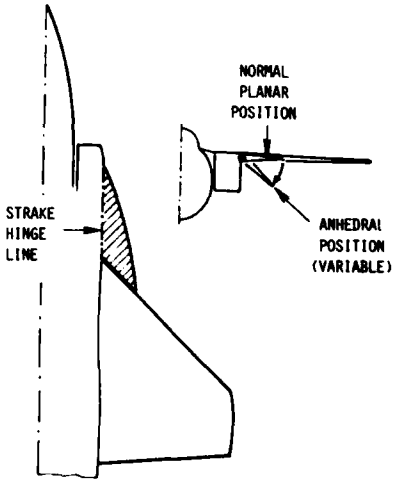

Fig. 5. Hinged strakes, shown in a hypothetical installation

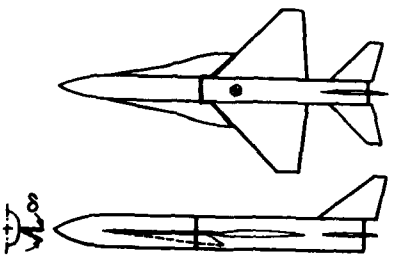

Fig. 6. Generic fighter model for hinged strake investigation

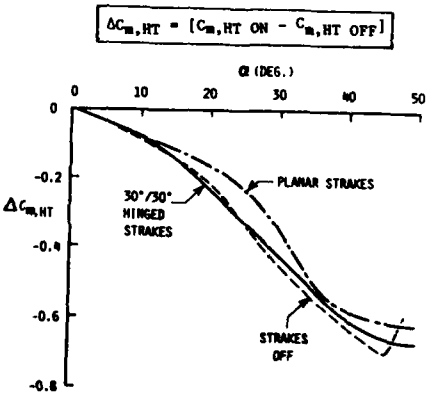

Fig. 8. Horizontal tail (HT) effectiveness with planar and anhedral strakes

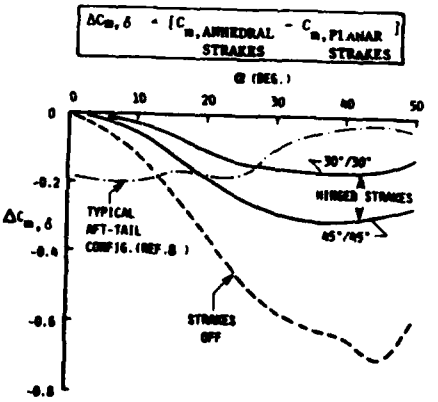

Fig. 9. Nose-down moment by anhedralling hinged strakes from planar position

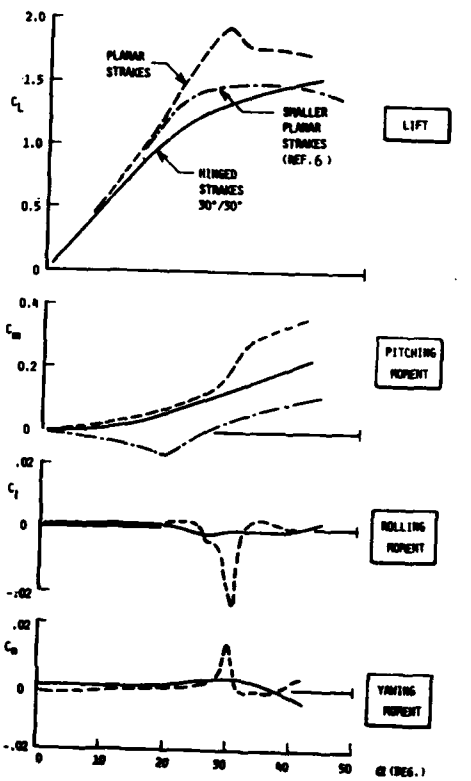

Fig. 7. Aerodynamic characteristics with planar and anhedral strakes

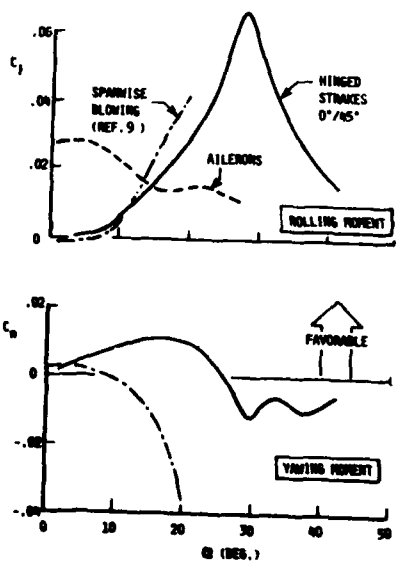

Fig. 10. Rolling moment and induced yaw due to asymmetric anhedral

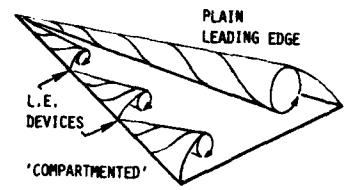

Fig. 11. 'Compartmentation' of swept leading edge separation

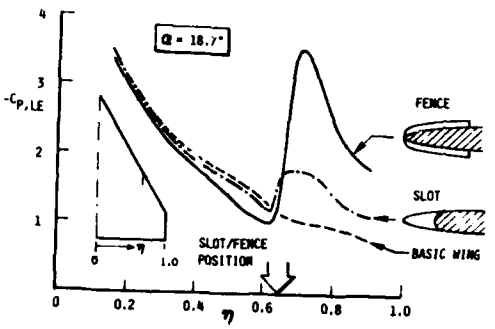

Fig. 12. Spanwise leading-edge pressure distribution with a slot or a fence

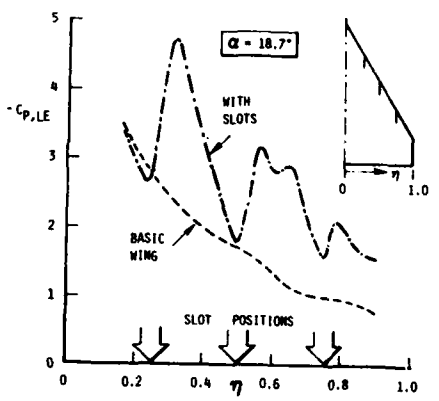

Fig. 13. Spanwise leading-edge pressure distribution with three slots

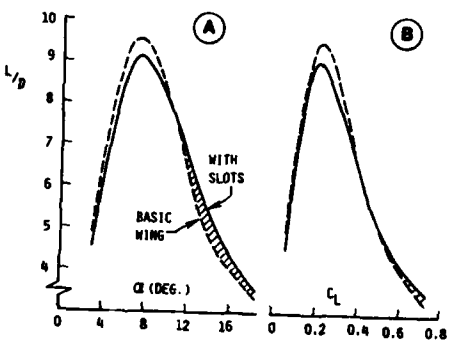

Fig. 14. Lift/drag ratio improvement with three slots

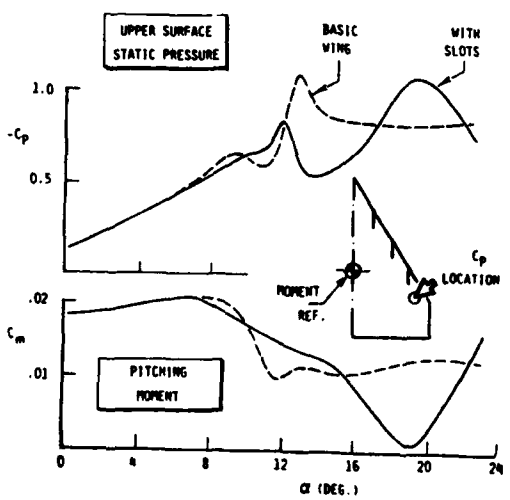

Fig. 15. Effect of three slots on upper-surface static pressure in tip region, and resulting pitching moment characteristics

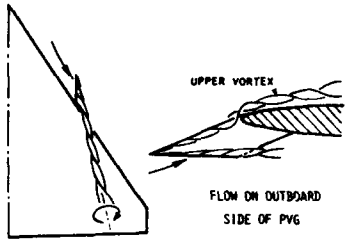

Fig. 16. Pylon vortex generator concept

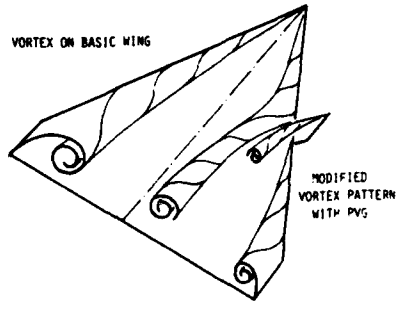

Fig. 17. Suggested leading-edge compartmentation mechanism of pylon vortex generator

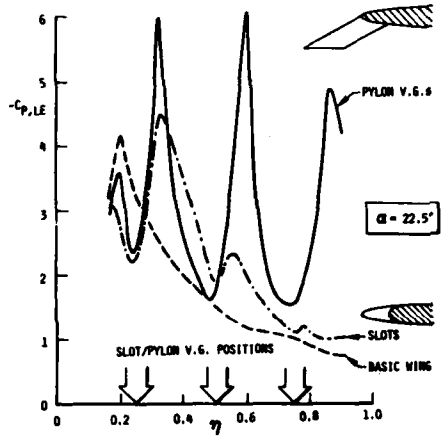

Fig. 18. Spanwise leading-edge pressure distribution at highest angle of attack with three PVGs

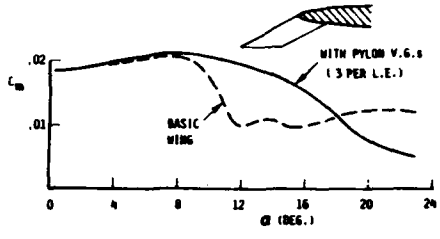

Fig. 19. Pitching-moment characteristics of 60-deg. delta with three PVGs

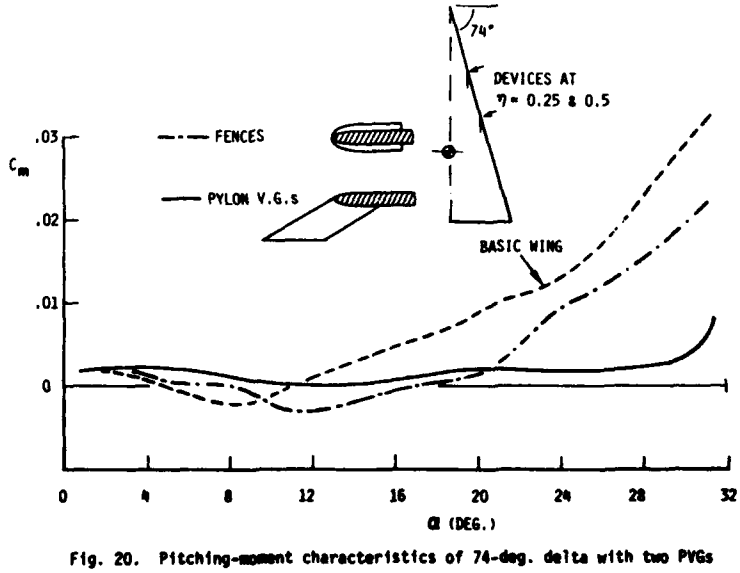

Fig. 20. Pitching-moment characteristics of 74-deg. delta with two PVGs

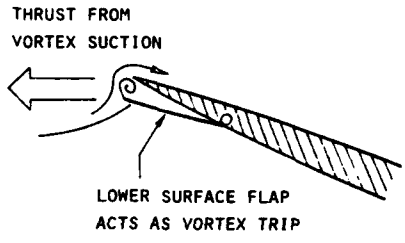

Fig. 21. Under-wing vortex trip concept

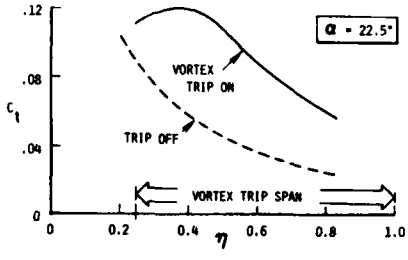

Fig. 23. Local leading-edge thrust distribution at highest angle of attack, showing effect of vortex trip

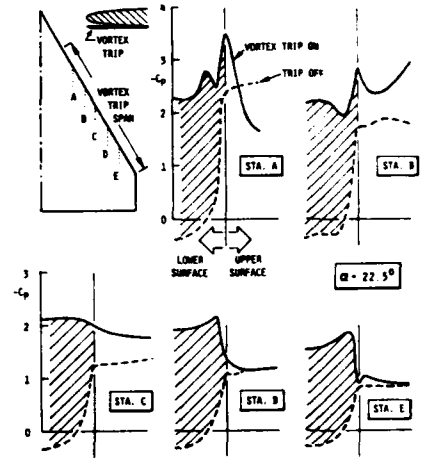

Fig. 22. Pressure distributions around leading edge at various semi-span stations, showing effect of vortex trip

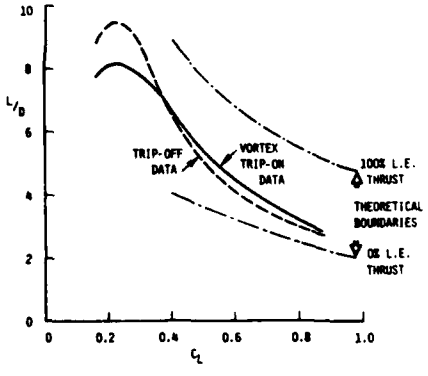

Fig. 24. Lift/drag ratio improvement due to vortex trip on 60-deg. delta

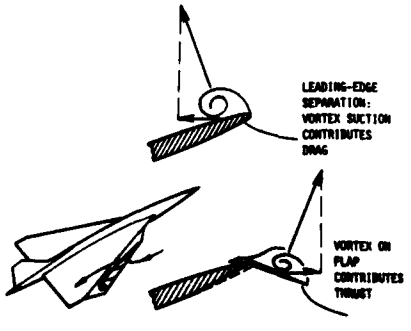

Fig. 25. Vortex flap concept

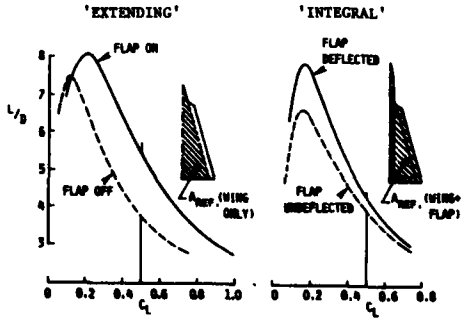

Fig. 26. Lift/drag ratio improvement due to 'extending' and 'integral' vortex flaps

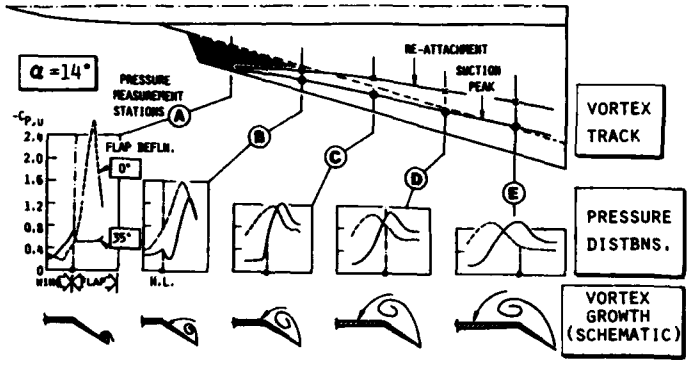

Fig. 27. Upper-surface pressure distributions at various spanwise stations showing vortex development

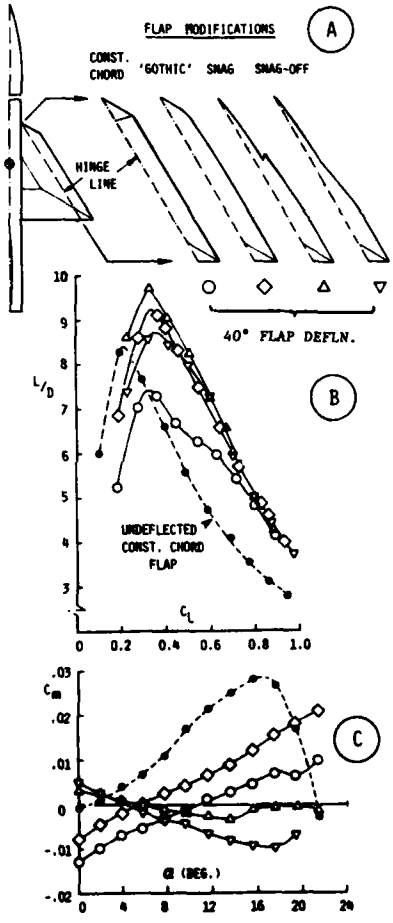

Fig. 28. Vortex flap modification effects on lift/drag ratio and pitching-moment characteristics

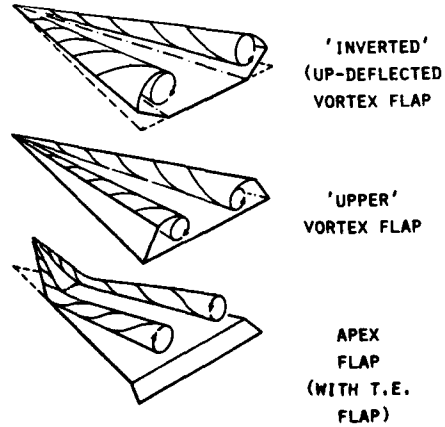

Fig. 29. Forced-vortex concepts for lift increase at low angles of attack

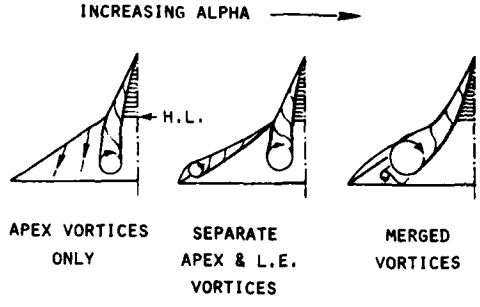

Fig. 30. Observed vortex patterns with deflected apex flap

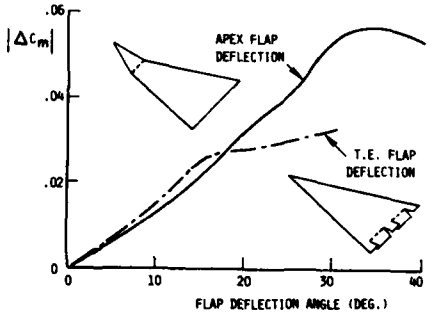

Fig. 31. Pitching-moment increments due to apex flap and trailing-edge flap

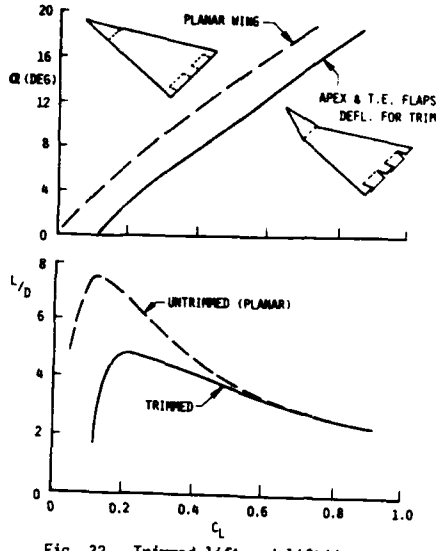

Fig. 32. Trimmed-lift and lift/drag ratio characteristics with apex flap and trailing-edge flap

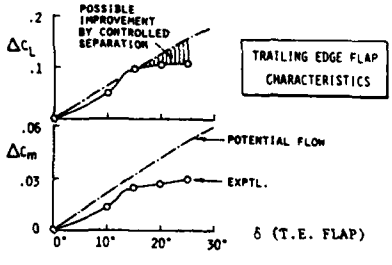

Fig. 33. Possible additional lift by maintaining attached flow on trailing-edge flap

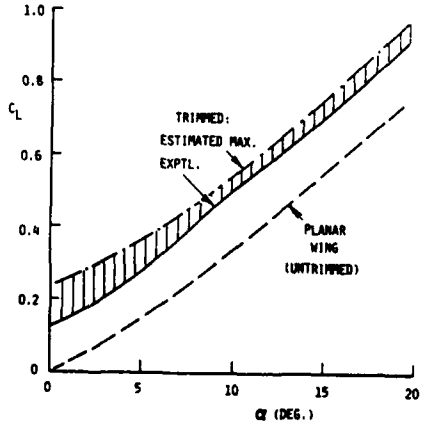

Fig. 34. Possible trimmed-lift increase with apex flap and unseparated trailing-edge flap

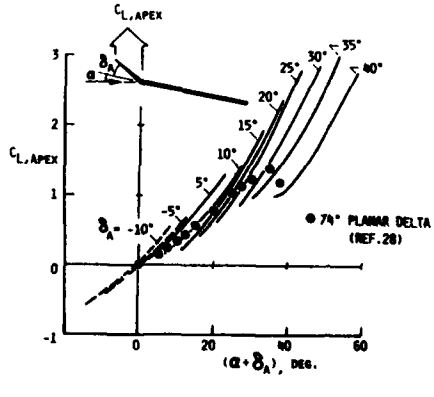

Fig. 35. Apex flap lift characteristics

THE EFFECTS OF WING TIP DEVICES ON

(a) THE PERFORMANCE OF THE BAe JETSTREAM

(b) THE FAR-FIELD WAKE OF A PARIS AIRCRAFT

J. J. Spillman, *Professor of Applied Aerodynamics*,
Cranfield Institute of Technology,
Cranfield, Bedford
MK43 0AL, England

And

M. J. Fell, Aerodynamicist,
British Aerospace PLC, Woodford
Chester Road,
Woodford, Bramhall
Stockport, Cheshire,
SK7 1QR, England

The first part of this joint paper discusses the techniques used in the design and wind tunnel testing of winglets and wing tip sails for a model of the BAe Jetstream. An analytical design procedure for the winglets and an empirical one for the sails are compared. The windtunnel tests highlight not only the problems of trying to measure small drag changes, but also the difficulties and dangers of low Reynolds number tests associated with small tip devices. The results show that significant reductions in drag can be achieved with these devices and their relative merits are discussed.

The second part describes flight tests made with an instrumented Jetstream aircraft flying across the wake of a Paris aircraft with and without sails mounted from its tip tanks. Vertical velocities and normal accelerations were measured in the wake of the Paris at various distances behind it. The results show that when sails are fitted the peak disturbances which occur 400m to 700m behind the aircraft are reduced significantly. However, sails seem to reduce the rate of decay of the vortices in the farfield and at distances greater than 700m. Larger disturbances were measured with the sails fitted, although these were small compared to the peak values.

THE EFFECTS OF WING TIP DEVICES ON THE PERFORMANCE OF THE BAe JETSTREAM

M. J. Fell — Aerodynamicist, British Aerospace PLC

and

J. J. Spillmann — Professor of Applied Aerodynamics, Cranfield Institute of Technology,

SYMBOLS USED

C_L Lift coefficient
C_{L_t} Local lift coefficient
α Incidence

1. INTRODUCTION.

The formation of a strong tip vortex has an undesirable effect on the drag of a lifting surface. Firstly, it induces a strong downwash field locally which increases the vortex drag and secondly introduces a strong cross flow around the tip causing separation on the top surface. Tip devices seek to remove these effects. Sails unwind the tip vortex and in doing so experience a thrust, like stators behind a fan. Their nose to tail arrangement gives them the ability to carry high lift coefficients, in the manner of cascades or slotted aerofoils. Winglets, or tip fins attenuate the tip vortex by dissipating the shed vorticity along their length, thereby reducing the downwash induced at the wing tip region.

Similar effects are attainable with wing tip extensions but the advantage of winglets and sails is that the drag reduction, for a given increase in wing root bending moment, is greater. This is because winglets and sails utilise the sidewash effectively. In addition the extra loading due to a winglet configuration is primarily a side force and the bending moment increase due to sails can be controlled by their incidence. Over the majority of the incidence range tip devices which extend the span will increase wing root bending moment. There is little prospect for reducing this by cropping the wings on an existing aircraft as this would generally encroach upon the area already occupied by the aileron. Tip devices tend to be viewed with scepticism since in general any addition to an aircraft can be expected to increase the drag. This is indeed true for tip devices at low lift coefficients, but because they reduce the lift dependent drag, the overall drag is reduced at higher incidence.

In order to assess these effects, it was proposed that a 1/10th scale model of a BAe Jetstream (Figure 1) should be tested at Cranfield Institute of Technology in the 8' x 6' low speed wind tunnel with sails and winglets. The first objective of the tests was to demonstrate a measurable drag reduction for a Jetstream fitted with tip devices over the range of operational lift coefficients. The second objective was to estimate the increase in wing root bending moment due to either device in order to compare their relative merits with simple tip extensions. In the past this had been done with wing only half models with encouraging results, but an estimate for the complete aircraft configuration was highly desirable.

2. MODEL AND TUNNEL

A 1/10th scale model of the British Aerospace Jetstream shown in Figure 2 was modified to allow the wing tips to be fitted with winglets, sails or normal tips. Whilst the full scale aircraft can only be changed outboard of the aileron if a major redesign of the wing and control system is to be avoided, the wooden model required a break joint further inboard to obtain an adequately strong joint. Details of the joint position are given in the drawing of the standard tip fitting shown in Figure 3. The brass junction plates were contoured to the local wing section and screwed onto the tip of the main part of the model. The standard tips each extended 33mm beyond their break joints giving the model an overall span of 1.585m and a wing plan area of $0.2508m^2$. Figure 4 shows an alternative tip with an end body of revolution whose diameter was equal to the maximum thickness of the local section. This body was mounted such that its centreline was parallel to the fuselage centreline in plan view and co-axial with the wing tip chord line when viewed from wing tip to root. Four small sails either of symmetrical untwisted or of cambered and twisted form could be mounted from each wing-tip body. Each sail had a span of 25mm, a mean chord of 11mm, and a taper ratio of 0.57 and was mounted at 15° less dihedral than the sail in front. The arrays were set such that the third sail from the front was in the plane of the wing, that is at a dihedral of 7° to the horizontal in normal level flight. In plan view the root leading edge of each sail was 4mm behind the root trailing edge of the sail in front. The trailing edge of the rear sail had the same fore and aft position as the trailing edge of the tip section of the wing inboard of the body of revolution. Each sail could be pivoted about an axis normal to its tip body centreline to enable its tip chord line to be set at an angle to the tip body axis which could be varied from -10° to +5° in 5° increments. When these tips were fitted the model had an overall span of 1.619m. and a wing area of $0.2529m^2$ when developed onto a horizontal plane.

The third form of tip tested was the winglet whose geometry is given in Figure 5. Just beyond the break joint the chord of the wing was reduced rapidly and at about the position of the tip of the plain

wing the winglet surface bent upwards to give the outer part a dihedral of 70° to the horizontal. Complex curvature of the surface at the kink gave the sections just outboard of the bend a slight outward cant. The canted part of the winglet had a projected root chord of 46mm, a tip chord of 15mm and a vertical height above the wing-tip chord line of 100mm. With winglets fitted to both tips the model had an overall span of 1.639m and an area of 0.256m^2 when developed onto a horizontal plane. The developed areas given are equivalent to total plan areas of planar wings whilst the spans are actual overall spans as seen in plan view.

Details of the profiles and sections of the sails and winglets are not given because their small size made it impossible to do more than give a close approximation to the geometries specified. The winglets were made to templates cut to the sections specified and are thought to be reasonably accurate but the uncambered sails, shown in Figure 4, had sections which appeared to be typical of symmetrical 12% thick aerofoil form. The other sails had strongly cambered root sections and uncambered tip sections. Figure 4 shows that whilst their leading edges were curved in front elevation their trailing edges were straight, giving their noses distinct droops at the root stations.

The tests were made in the 2.44m (8.0 ft) by 1.83m (6.0 ft) low speed wind tunnel at Cranfield at a wind speed of approximately 58m/sec (190ft/sec) giving a mean chord Reynolds number of 6.37 x 10^5 for the wing, 1.24 x 10^5 for the winglets and 4.65 x 10^4 for the sails. Because of these low Reynolds number transition wires were fixed at 10% chord behind the leading edge of the wings on both top and bottom surfaces and the leading edges of winglets and sails were covered with ballotini spheres of 0.18mm (0.007") diameter from 5% to 10% chord on top and bottom surfaces to give as even a cover as could be achieved.

Overall forces and moments were measured on a virtual centre, Warden balance and corrected for tare, blockage and tunnel wall effects.

3. DESIGN OF TIP DEVICES

3.1 DESIGN PHILOSOPHY FOR WING TIP SAILS

References 1 and 2 have shown the swirling nature of the flow about the wing tip. If small lifting surfaces are placed in this flow they can experience a resultant force which has a component into the free stream direction. Since the swirl varies with distance from the wing tip, these surfaces, called sails, have to be twisted along their span in order to obtain a near uniform incidence distribution which will only give optimum spanwise conditions at one wing incidence. The change in local incidence at the root of the sails close to the wing tip surface is about four times any change in wing incidence so that, at high wing incidences, the flow over the root top surface of the sail is likely to separate. To minimise this effect the root section should have positive camber and be set at as low an incidence to the wing tip chordline as can be allowed without inducing a negative lift on the sail at the lowest operational incidence of the wing. Thus the camber and twist distribution of the sails and their rigging angle on the tip is a compromise between good performance in cruising flight and unstalled behaviour at lower flight speeds. At first thought the use of camber and twist suggests that sails are liable to adverse Mach number effects. However they are shaped in this way to avoid excessive local speeds and adverse pressure gradients being induced by the naturally swirling flow and therefore should not suffer adverse effects due to compressibility if designed correctly.

Since the swirling motion is greatest near the tip trailing edge this is the best fore and aft position. However adding more sails forward of this position increases the total thrust available and reduces the incidence range experienced by the rear sail. Thus three or four sails have been found desirable extending forward to about 30% chord (Reference 1). Whilst downwash interference between them is desirable to limit their overall ranges of incidence, wake interference is not, and for this reason successive sails are mounted at about 15° dihedral difference, the front sail having the greatest dihedral so that its wake passes well above the subsequent sail. It has been found from previous experiments that the sail spans should be about a quarter of the wing tip chord and have root chords about one sixth of the wing tip chord. Ideally their root settings, camber and twist distributions should each be different but difficulty of manufacture has suggested that for these tests they should be the same for all sails.

3.2 DESIGN METHODS FOR WINGLETS

In designing the winglets, the principal methods used were a subsonic panel program developed by J. C. Newling (Reference 3) and a vortex drag analysis program (Reference 4) based on the methods of J. A. Blackwell (Reference 5) and R. T. Jones (Reference 6). The panel method gives a good estimation of lift from the integration of panel pressures. The accuracy of the drag is dependent upon the panel spacing, therefore it is normal practice to evaluate the vortex drag from the panel method load distribution using the vortex drag analysis program. In addition the same program will produce an optimised lift distribution which can be compared with the actual distribution obtained from the panel method in terms of local loading and vortex drag. There are,however,limitations to the accuracy of Treffts plane drag analysis for non planar wings. Cancellation of 'X' dependent terms, as per Munk's stagger theorem, is not exact for non-planar configurations, but due to the nature of the formulation the errors for a winglet type configuration are small.

Previous parametric studies had indicated what length and cant angle would be practical for winglets to achieve a worthwhile drag reduction. The winglet chord distribution follows from the anticipated maximum load required. A large winglet will give a large drag reduction at a high wing lift coefficient, but the wing lift coefficient, below which the device increases drag, will be higher due to the increased profile drag.

Once the planform and cant angle have been chosen, the winglet root incidence and twist distribution are obtained as follows. A panel method model of the wing with the winglet at some initial setting is

run at a design lift coefficient. The lift distribution obtained is compared with an optimised lift distribution from the vortex drag analysis program and a twist correction is applied using the approximation

$$\Delta\alpha = \left(\frac{C_{L_{optimised}} - C_{L_{panel\ method}}}{\text{Lift curve slope}} \right)$$

This is an iterative process and is fully described in Reference 7.

A relatively large winglet span of 12% of the wing semispan was chosen to give a measurable drag reduction and was optimised for a wing lift coefficient lift of 0.7. A 13% thick ARA 'D' section was chosen for the winglet which was modelled, using a panel method on the tip of Jetstream wing. The wing planform, twist and sectional variation were represented but the nacelle and fuselage were not. Initially the winglet was toed out by 2° to offset the camber. Using the design procedure outlined above the winglet twist converged after 2 iterations. The blend region between the wing and winglet was designed 'by eye' to reduce the design costs and is therefore not necessarily the optimum shape. The only major constraint on the blend region was that the wings remain unchanged inboard of the aileron tip.

4. TESTING

Six component forces and moments were taken for three types of configuration.

(a) Standard wing tips

(b) Tip devices on both wing tips

(c) One Standard tip and a tip device on the other.

The change in drag was calculated from (a) and (b). Differences in rolling moment between configurations (a) and (c) gave an estimate of the increase in wing root bending moment. This technique relied heavily upon the repeatability and accuracy of the results, which for the rolling moments were disappointing considering the small differences sought.

Initially transition was fixed with 'pinked' tape, but flow visualisation on the wing showed that the flow over the inboard half of the wing was completely turbulent whereas that over the outboard half showed transition at 50% chord (Reference 8 describes this in more detail). Since this would cause an unrepresentative lift distribution, a different means of fixing transition was employed. Ballotini of 178μm(0.007") diameter were used to fix transition on the tips but these were impractical on the rest of the model as it would need to be de-rigged in order to apply them. Consequently a wire trip was chosen but the smallest diameter available was 230μm(0.009"), in retrospect it appears to have 'over fixed' the transition causing the trailing edge separation to move forward: this had the effect of increasing the drag and decreasing the lift. Wire of about 150μm (0.006") diameter may have been sufficient. As forced transition can reduce the local CLmax, the results near the stall are unreliable.

In the first set of tests with the tailplane on, the elevators were at zero deflection. Since the lift and drag due to the tailplane were unrepresentative of trimmed flight it was excluded from the second set of tests.

5. RESULTS

The lift curve slopes are presented in Figure 6. $\frac{\partial C_L}{\partial \alpha}$ for the tail off is 4.75 compared with 5.34 for the panel method wing alone. Considering that the figure of 4.75 includes the lift due to the fuselage and nacelles, it is quite low by comparison. The effect of the fuselage and nacelles on the lift is manifest in the large shift in zero lift angle from -5° to -3.5° body incidence. Evidently there was a large loss of wing lift and this was directly attributable to the low Reynolds number and transition fixing. Flow visualisation revealed areas of separation aft of the flap shroud and on the wing close to the fuselage and nacelle at the higher incidences.

Drag polars for the Jetstream with standard tips are shown in Figure 7. Minimum drag coefficient is at a C_L of 0.2 which for the tail off configuration occurs at a body incidence of approximately -1°. As can be seen the untrimmed tailplane has a significant effect on the drag polar. Comparison of the tail on transition free and tail on transition fixed results gives an indication of the Reynolds number related effects on the profile drag.

The results for the testing of winglets and various different sail configurations have been corrected for tares and are presented in Tables I and II. The coefficients are based on the original wing area and span, and have been interpolated back to the same lift coefficiients since the uncambered sails and winglets increased $\frac{\partial C_L}{\partial \alpha}$ by 0.1 and 0.18 respectively, without changing the zero lift incidence. Figure 8 shows the incremental drag variation with lift for winglets and for the best sails. The effects of varying the sail settings are illustrated and discussed in detail in Reference 9. A similar trend is shown in the results for either device with the winglet performing better than sails above a lift coefficient of 0.5 and worse below. With the exception of the uncambered sails at -10°, the sail configurations appear to have stalled at high incidences. Flow visualisation showed separation on the roots of the uncambered sails at most incidences, particularly the fore sail. The cambered sails showed separations at all incidences. One would expect better flow behaviour at higher Reynolds number which would improve their performance.

Variation of rolling moment due to the devices with lift is presented in Figure 9. There is a significant scatter of the results with identical devices on either tip but despite this one can clearly see a rolling moment increment due to the -5° uncambered sails and a marginally greater rolling moment increment due to a winglet. The lift coefficients at which the sails and winglet produce zero rolling moment increment are approximately 0.18 and 0.08 respectively, which are the lift coefficients at which the tip devices induce no nett load on the device and wing.

6. ANALYSIS AND DISCUSSION

Results from the panel method model described in Section 3.2 yield the following theoretical vortex drag reductions and wing root bending moment increases.

Lift coefficient	0.5	0.7
Vortex drag reduction	7.2%	8.3%
Wing root bending moment increase	3.2%	3.6%

The actual values have been added to Figures 8 and 9. Since there is a large difference between the lift coefficients of the panel method model and the wind tunnel model at the same incidence, it is unclear whether the two drag reductions should be compared at the same lift coefficient or at the same incidence; the true effect is probably somewhere in between. Therefore the panel method results are also shown at the same incidence as the wind tunnel model, and it can be seen that the gradient of experimental drag increment upon lift coefficient due to winglets is between the gradients of the two theoretical curves.

At the lift coefficients when the tip devices induce no nett load the drag increment for the winglet is roughly 15 counts and the drag increment for the -5° uncambered sails is somewhere between 10 and 15 counts. Allowing for the low Reynolds number and transition fixing on the sails and winglets, profile drag coefficients, based on their own areas, of 0.05 and 0.04 respectively are not unreasonable. As the area ratio of the wing to the combined sails is 1:0.008 their profile drag would give 4 counts, which is only a third of the measured drag increment and indicates poor flow behaviour at the tip. Similarly the area ratio of wing to the two winglets is 1:0.021 giving a profile drag estimate of 8½ counts which is slightly over half the measured drag increment. Flow visualisation showed small areas of separation at the winglet root but not as extensive as that on the sails.

If these separations disappeared at flight Reynolds number, the profile drag increment for winglets and sails would be approximately 5 counts and 2 counts respectively. Therefore the sails could reduce drag above a lift coefficient of 0.2 and the winglets would start to reduce drag at a lift coefficient of 0.4.

7. CONCLUSIONS

1. The tests clearly showed that winglets and sails can produce reasonable drag reductions. However the reductions obtained were disappointing compared with the theoretical predictions and results from previous half wing tests. The loss of lift and high drag were characteristic of separated flow and it is hoped these effects would disappear at higher Reynolds number. Due to the small size of tip devices in relation to the aircraft, a significantly larger model and faster tunnel would be required to take this investigation further and it may even prove more cost effective to flight test the devices, despite the difficulties of measuring drag in flight.

2. The overall profile drag and in particular the drag increments due to the tips were very high. In retrospect more time could have been spent investigating transition fixing on the model.

3. The results suggest that at flight Reynolds number, sails could reduce drag above a lift coefficient of 0.2 and provide a worthwhile drag reduction over the normal lift coefficient range provided they did not stall. The winglets would start to reduce drag at a lift coefficient of 0.4 and give larger drag reductions at high incidence but would give a small penalty at maximum cruise speed. A shorter winglet, optimised at a lower lift coefficient, would have given less drag reduction at high incidence but would break even at a lower lift coefficient. If the tests were repeated a shorter winglet would be chosen.

REFERENCES

1. Spillman J. J. — The use of wing tip sails to reduce vortex drag
The Aeronautical Journal Vol 82 No. 813 September 1978

2. Yip L. P. Shubert G. L. — Pressure distributions on a one by three metre semispan wing at sweep angles from from 0° to 40° in subsonic flow.
NASA TND-8307 December 1976

3. Newling J. C. — A 3D panel method for computing flows around wings
BAe-MAE-R-FDM-0105

4. Fell M. J. — A method for predicting the performance of non-planar wings
BAe-MAE-R-FDM-0020 January 1978

5. Blackwell J. A. A Numerical method to calculate the induced drag or optimum loading for arbitrary non planar wings
NASA SP 405 May 1976

6. Jones R. T. The spanwise distribution of lift for minimum drag of wings having a given bending moment
NACA TN 2249 December 1950

7. Renshaw M.
Fell M. J. A review of studies into wing tip winglets undertaken at BAe Woodford
BAe-MAE-R-FDM-0052 September 1979

8. Fell M. J. Wind Tunnel testing of Sails and Winglets on a 1/10 scale model of a Jetstream
BAe-MAE-R-FDM-0084 May 1981

9. Spillman J.J. A Wind tunnel comparison of the effects of fitting sails and winglets to the wing tips of a model Jetstream aircraft
Co A Memo 8205 March 1982
Cranfield Institute of Technology.

TABLE I.

TAIL-ON RESULTS

Note:- All results given are counts i.e. coefficient x 10^4

		Lift Coefficient		0	0.1	0.2	0.3	0.4	0.5	0.6	0.7	0.8
		Standard Tips	C_D	541	525	518	526	548	577	622	696	796
			C_L	-47	-50	-50	-52	-56	-61.5	-63	-66	-58.5
BOTH TIPS	SAILS	Winglet	C_D	555	540	531	535	552	578	617	687	783
			C_L	-49.5	-51.5	-51.5	-52	-58.5	-64	-71	-72	-65.5
		-5° Uncambered	C_D	551	533	526	532	547	577	620	691	794
			C_L	-49.5	-52.5	-58	-60	-70.5	-68.5	-74.5	-73.5	-67
		-5° Cambered	C_D	554	539	536	541	557	582	629	698	794
			C_L	-51.5	-51	-53	-57.5	-62.5	-64.5	-66	-68.5	-59.5
		-10° Uncambered	C_D	550	540	533	534	552	581	624	691	785
			C_L	-49.5	-54	-51.5	-55	-57.5	-66	-68.5	-77	-71.5
		-10° Cambered	C_D	563	547	544	546	563	587	629	698	790
			C_L	-51	-54.5	-54.5	-56.5	-57.5	-66	-66	-71.5	-62.5
STARBOARD TIP ONLY		Winglet	C_D	549	540	532	532	549	578	622	694	795
			C_L	-42.5	-46	-57.5	-63	-71.5	-79	-87	-95	-91
	SAILS	-5° Uncambered	C_D	550	529	526	531	550	577	622	693	788
			C_L	-33	-37	-49.5	-57	-63	-78	-84	-93.5	-88
		-5° Cambered	C_D	549	535	534	540	556	582	623	699	811
			C_L	-44	-52	-60	-72.5	-78	-84	-92	-96.5	-88
		-10° Uncambered	C_D	542	532	529	533	550	580	622	693	795
			C_L	-31.5	-49	-49	-58.5	-65.5	-75	-83.5	-96	-94
		-10° Cambered	C_D	551	539	535	541	554	583	627	695	803
			C_L	-41	-47	-54	-60.5	-68	-74.5	-77	-87.5	-82

TABLE II

TAIL-OFF RESULTS

Note:- All results given are counts i.e. coefficient x 10^4

		Lift Coefficient		0	0.1	0.2	0.3	0.4	0.5	0.6	0.7	0.8
		Standard Tips	C_D	490	476	469	476	493	528	593	688	922
			C_L	-35	-42.5	-42.5	-49	-52	-57	-62	-47	-66.5
BOTH TIPS		Winglet	C_D	516	497	490	491	501	529	581	673	872
			C_L	-37.5	-39.5	-42.5	-44.5	-49	-55	-59	-49	-47
	SAILS	+5° Uncambered	C_D	503	491	485	492	511	548	606	700	907
			C_L	-38	-45.5	-47	-52	-55	-54	-61.5	-50	-62
		0° Uncambered	C_D	493	484	479	482	501	532	595	691	882
			C_L	-43	-50	-54	-62.5	-61.5	-68	-72	-55.5	-71.5
		-5° Uncambered	C_D	503	492	487	488	503	532	594	689	874
			C_L	-40.5	-44	-48	-54.5	-58.5	-64.5	-67	-51.5	-60
STARBOARD TIP ONLY		Winglet	C_D	508	493	483	488	502	536	590	684	872
			C_L	-33	-42.5	-54	-67	-76.5	-97.5	-101	-95.5	-108
	SAILS	+5° Uncambered	C_D	500	481	481	483	501	535	595	690	895
			C_L	-41	-54	-66.5	-76.5	-81.5	-89.5	-98.5	-90	-108
		0° Uncambered	C_D	493	478	473	480	497	531	591	688	909
			C_L	-32	-39	-53.5	-61	-72.5	-81.5	-90.5	-78	-95
		-5° Uncambered	C_D	500	483	477	482	494	525	590	688	894
			C_L	-33	-33	-47	-56	-68.5	-80.5	-89.5	-78.5	-96.5

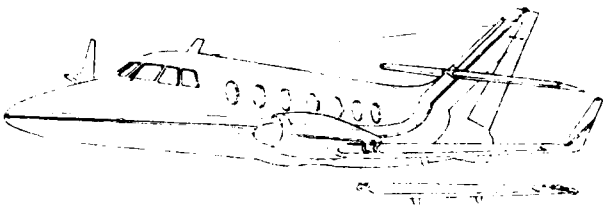

BAe. JETSTREAM WITH WINGLETS AND SAILS

FIGURE 1

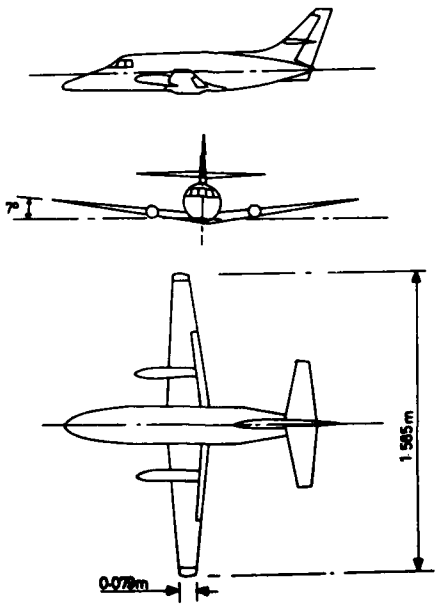

GENERAL ARRANGEMENT OF THE JETSTREAM MODEL.

FIGURE 2

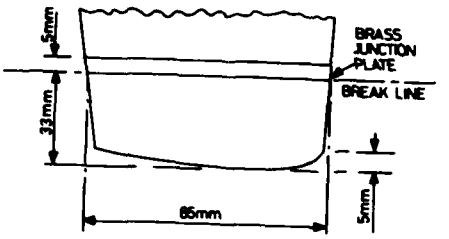

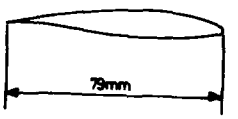

SECTION ON WING TIP CHORD

STANDARD TIP

FIGURE 3

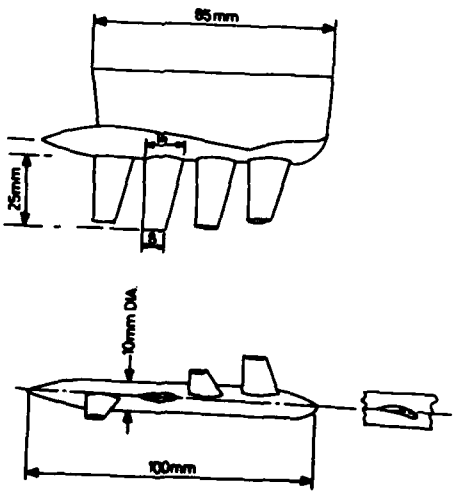

UNCAMBERED CAMBERED

SAILS SHOWN AT ZERO SETTING TO THE BODY AXIS. DIHEDRAL DECREASE IS 9° BETWEEN EACH SAIL.

WING TIP WITH SAILS

FIGURE 4

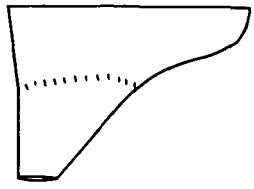

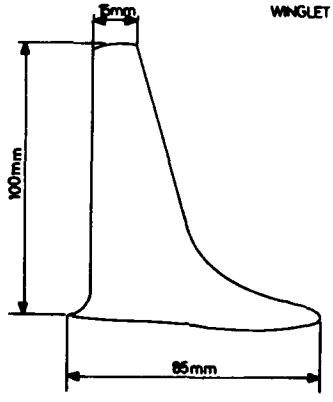

WINGLET TIP

FIGURE 5

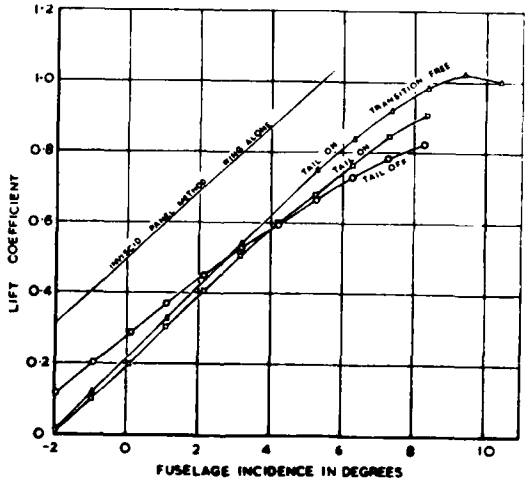

VARIATION OF LIFT WITH INCIDENCE

FIGURE 6

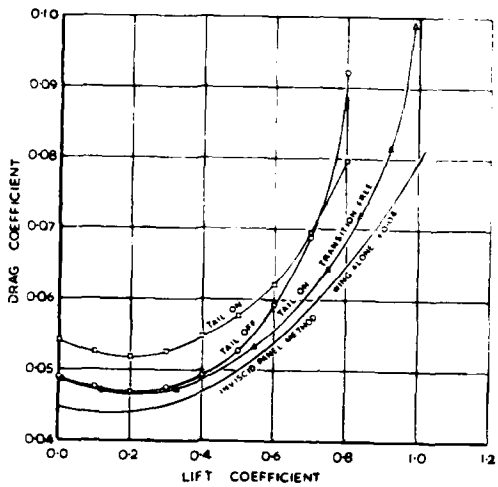

VARIATION OF DRAG WITH LIFT

FIGURE 7

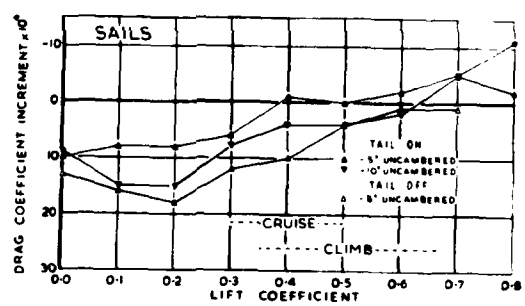

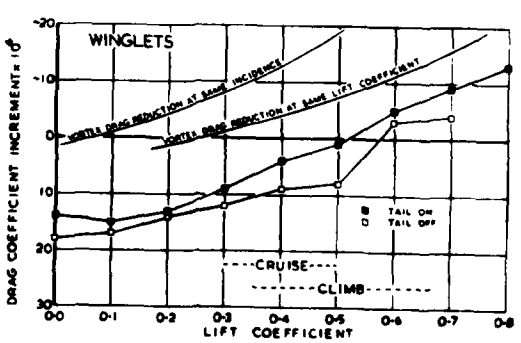

DRAG INCREMENT DUE TO TIP DEVICES

FIGURE 8

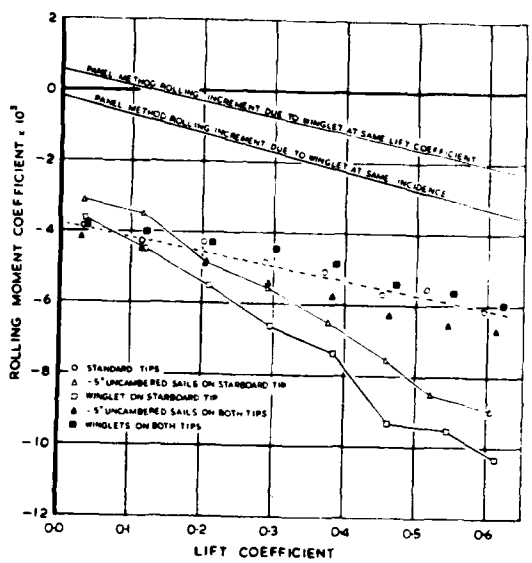

VARIATION OF ROLLING MOMENT WITH LIFT

FIGURE 9

THE EFFECT OF WING TIP DEVICES ON THE FAR-FIELD WAKE OF A PARIS AIRCRAFT.

J J SPILLMAN

PROFESSOR OF APPLIED AERODYNAMICS
CRANFIELD INSTITUTE OF TECHNOLOGY
BEDFORD, MK43 OAL
ENGLAND

1. INTRODUCTION

Studies made of the flow about the wing-tip of a windtunnel model showed that the vortex-type flow generally associated with the rolled-up vortex sheet well behind the tip existed just behind the trailing edge and seemed to be forming over the top of the wing-tip itself. As a result small cambered aerofoils were attached to the wing-tip to redirect the flow locally in such a way that each experienced a force with a significant thrust component. The effect is similar to that generated by the sail of a close-hauled yacht; consequently these small tip extensions were called sails. Reference 1 describes the original windtunnel and the preliminary flight tests of sails mounted from the tip tanks of the Paris aircraft of the Cranfield Institute of Technology. These initial tests showed that a considerable reduction in the lift-dependent drag resulted from fitting the sails but there was a marked scatter in the results which detracted from their credibility.

Subsequently, the Science Research Council has given Cranfield a grant for further research on sails. The first part of this programme was to extend the flight tests made on the Paris in two ways, firstly to measure engine characteristics in steady level flight to obtain drag and fuel consumption comparisons and secondly to fly another aircraft across the wake of the Paris to measure the effect of sails on the decay of the trailing vortex system. Reference 2 reports on the first of these investigations which showed a 4% reduction in fuel requirements for cruising flight whilst this note describes the wake explorations.

2. TEST AIRCRAFT AND PROCEDURE

The sails were fitted to the tip tanks of the Paris aircraft G-APRU at an early stage in the research programme aimed at drag reduction, described in reference 1, because it was felt that it was essential to confirm their drag reducing properties at flight Reynolds numbers. As a result their configuration was not an optimum for drag reduction but it was thought that their effect on the flow about the wing tips was sufficiently significant to justify their use without modification for the research into the effects of sails on wake behaviour.

Figures 1 and 2 show the general arrangement of the Paris with sails whilst details of the sail geometry are shown in Figure 3. The aircraft was standard apart from the addition of the sails and the fitting of a simple system to allow diesel oil to be introduced into the jet pipe of the port engine to create a dense smoke trail.

The Jetstream flying classroom G-AXUI of the College of Aeronautics was used to traverse the wake of the Paris. An ultra-violet light sensitive paper-tape recorder, running at 30mm/sec., was used to obtain the time histories of the deflection of a pitch vane, mounted on the end of the stiff nose boom, and the normal acceleration at the centre of gravity of the aircraft. The instruments were calibrated in the laboratory prior to the flight tests.

The Paris was flown straight and level at 120 knots at 1500m altitude and the Jetstream was positioned to make a transverse pass across its wake. As the pilot of the Jetstream began to broadcast a count-down, the recorder was started and at the zero count the recorder was time marked and the smoke generator on the Paris switched on. Smoke became visible from the Paris port engine 1.5 seconds later and the Jetstream was flown to pass through the end of the smoke trail. As it penetrated the wake it experienced a sudden jolt which lasted too short a time to affect its bank angle or heading. After penetration the recorder was stopped and both aircraft turned through 90° towards each other to start another traverse. Thus the two aircraft flew a criss-cross path, the programme being controlled by the Jetstream pilot to vary the times between smoke on and penetration between five and forty seconds. After a little practice it was possible to get this period to within a few seconds of that required without too violent an an initial manoeuvre and with the Jetstream in almost straight and level flight at penetration. Although it was necessary to vary the penetration speed between 95 and 155 knots, in most cases it was between 120 and 130 knots. By switching on the smoke for only about 5 seconds it was possible to get up to forty passes before the Paris had to return to Cranfield to replenish the diesel oil. Some experience of this technique was obtained when the Paris was used as the aircraft

penetrating the wake of the Handley Page 115 experimental aircraft.[3]

As the Jetstream approached the smoke trail it appeared to be two to three metres from top to bottom and to have a distinct rotational motion although details like its cross-sectional shape could not be discerned in the 0.15 seconds it took to penetrate the wake. Occasionally the pilot said the pass was slightly high or low but on most traverses he was confident that the nose probe passed through the central third of the smoke trail depth. It was obvious to the Jetstream crew that there was a considerable variation in the intensity of the jolt and that it could not be predicted with any confidence. This impression was confirmed by the wide scatter of the readings.

3. TEST RESULTS AND DISCUSSION

Figure 4 shows typical trace patterns for the vane deflection and the normal acceleration. With a big jolt the vane deflected upwards initially, then very strongly downwards, started to return to zero but then got a second downward pulse rapidly followed by a strong upward pulse taking the reading well into the positive settings before returning to an almost steady value near that recorded before the disturbance. The relative values of the first and second upward and downward peak readings varied, on most occasions the first peaks both positive and negative gave the greater values. When the jolt was small the vane signal degenerated into a simple down and return deviation as shown in Figure 4b. Of the 75 penetrations made without sails 15 gave bigger first peaks, 7 equal peaks, 6 bigger second peaks, 38 only one negative peak and 9 were difficult to interpret in this way. With sails the 85 penetrations recorded showed 27 with bigger first peaks, 10 with equal peaks, 13 with bigger second peaks, 29 with only a single negative peak and 6 were difficult to classify. These numbers indicate that more of the signals obtained with sails showed a double peak in the downward deflection of the vane.

The vane signals showed the upward and downward velocity perturbations which one would expect from a traverse through a pair of vortices somewhat as shown in Figure 5. The time over which the Jetstream experienced a downward velocity was about 0.13 seconds which suggests that the cores of the vortices were eight to nine metres apart. It is clear from this figure that unless the aircraft passed very close to the vortex cores it will not have been subjected to the greatest vertical velocities. The fact that on most of the traces the vane deflection pattern was not symmetrical about the time corresponding to the middle of the penetration suggests that a slight upward or downward aircraft path relative to the transverse axis of the wake occurred on most occasions. This could have been due to the Jetstream manoeuvring to get into position or some asymmetry in the wake formation and development may have caused it to tilt off a horizontal axis. Whatever the cause it seems clear that in aiming generally at the centre of the smoke trail, and therefore presumably the centre of the port vortex, the aircraft was not positioned accurately enough to consistently measure the maximum perturbation velocities and this is the prime reason for the large scatter in the values recorded.

The maximum negative normal acceleration always occurred about 0.13 seconds after the mid-time of the downward vane deflection. This is primarily because the vane was about eight metres ahead of the aircraft centre of gravity, but may also be affected by the different response characteristics of the instruments. Whilst the record of the vane deflection shows that it was well damped after the disturbance, the accelerometer record shows clearly that, subsequent to the initial disturbance, there was a damped oscillation at a frequency of about 6HZ, which lasted until the aircraft was well clear of the wake of the Paris. It is probable that this was a result of the excitation of the fundamental bending of either the wing or the fuselage, probably the former.

The overall time of the vane deflection on all the traces was approximately the same, irrespective of the magnitude of the signal, as one would expect if the aircraft height varied only slightly relative to the centres of the vortices. There was some evidence from the traces which suggested that the distances apart of the vortices remained nearly constant for up to 1500m behind the Paris but at greater distances the signals became more irregular and spread out although this was not obvious when looking at the smoke trails.

The maximum vane deflections both positive and negative, have been converted to give the local maximum upward and downward vertical velocities measured in the wake by assuming that the vane angle in radians was equal to the ratio of vertical velocity to Jetstream penetration velocity. The normal acceleration readings have been corrected for variation in penetration speed by assuming that the normal acceleration due to a given wake form would increase linearly with penetration speed. The distance of penetration behind the Paris was calculated by subtracting 1.5 seconds from the recorded time between the initial time mark and that corresponding to the centre of the wake disturbance to allow for the delay in the appearance of the smoke, and multiplying the resulting increment in time by the flight speed of the Paris, which was always 120 knots. The results have not been corrected for any variation in weight due to fuel usage. Since the maximum variations in Jetstream and Paris weights possible during the tests were about 4% and 13% respectively it was felt that any correction would have a negligible effect on the overall trends in view of the very large variation in results at any particular separation distance between the aircraft. Again an accurate assessment of the aircraft weight would be difficult since the recorder was not left running all the time.

Figure 6 compares the maximum upward vertical velocities experienced by the Jetstream from the peak vane deflection measurements with and without sails whilst Figure 7 compares the maximum downward vertical velocities experienced with and without sails and Figure 8 shows the maximum normal acceleration values experienced by the Jetstream with and without sails, all plotted against the distance between the two aircraft at penetration. It is immediately apparent that the scatter in the results is huge. Fortunately the large number of passes made both with and without sails allows some general conclusions to be drawn from the average and bounding values, which are shown as full and dashed lines respectively on these figures. The results all show that the disturbances increased in magnitude with initial increase in the distance behind the Paris, reaching maximum values at 400m. to 500m. when sails were not fitted and 650m. to 700m. when sails were fitted. Beyond these distances the intensity of the disturbances decreased, progressively more slowly as distance increased. In all cases the aircraft with sails gave lower peak disturbance values. It is interesting to note that the wake penetrations giving the boundary points for maximum disturbances were not always the same for the three forms of disturbance shown in Figures 6, 7 and 8. The ratios of maximum disturbances measured without sails to those measured with sails are in the ratio of 1 to 0.89, 1 to 0.75 and 1 to 0.72 for the upward velocities, downward velocities and normal accelerations respectively. Somewhat surprisingly, the rate of decay of these maximum disturbances with distance behind the Paris was significantly lower when sails were fitted. Thus 1500m. behind the Paris the greatest upward velocity, downward velocity and normal acceleration without sails were respectively 43%, 50% and 42% of the values measured with sails.

The average values of the disturbances, shown as full lines in Figures 6, 7 and 8, with and without sails did not vary significantly for distances up to 700m. behind the Paris. Beyond this distance the lower rate of decay of the disturbances with increase in distance which occurred when sails were fitted made the average values at a kilometre or more much greater. The figures suggest that there is little chance of an aircraft which penetrates the wake two kilometres behind the Paris experiencing a measurable disturbance when sails are not fitted but a good chance of a slight bump when sails are fitted.

In order to get a clearer understanding of the effect of sails on the wake of the Paris, in the distance band associated with the maximum disturbances, that is 400m. - 800m. behind it, the results have been put into nine equal interval classes of intensity, Class 1 being the lowest disturbance group. The number of results in each size class, expressed as a percentage of the total number of results, is plotted against class size in Figure 9. With the relatively small numbers in each size class it is not surprising that each set of results shows some scatter but the averages of the results of the three ways of judging the magnitude of the disturbance show quite clear trends. Without sails there are far more results in the low size class but after a rapid decrease in numbers with increase in size class the curve levels off and suggests that with more results available some values in classes above the maximum measured would have been obtained. The variation with class size of the results obtained with sails is quite different, there is almost a constant number in the size classes up to 5 and then the number of results in the higher classes falls rapidly to zero in class 9 for all three types of assessment.

The average results from Figure 9 have been used to show the probability of getting a result at or less than a given level of disturbance. Figure 10 shows that when sails are fitted there is a greater chance of another aircraft flying through the wake 400m. to 800m. behind the Paris experiencing a moderate sized disturbance as it passes through the wake of the Paris but that there is a considerably lower chance of getting a severe disturbance and no chance of getting the most severe values which can be encountered behind the Paris without sails.

The theory of Squire[4] as used by Bisgood, Maltby and Dee[3], predicts that the strength of the disturbance due to a vortex should vary inversely as the square root of time, that is distance from the generating aircraft. Logarithmic plots of the enveloping and mean curves of figures 4,5 and 6 showed no consistent linearity. This is not surprising in view of the large scatter in the basic results. As a result further comparisons with theory have not been made.

In order to make a better assessment of the effect of sails on wake roll-up and decay it is planned to repeat these experiments using a much more sensitive instrumentation system which will measure vertical and in-line-of-flight velocities at a rate of 100 per second during the wake traverses. This will allow the peak radial velocities and the positions of the vortex cores to be evaluated. In this way it is hoped to obtain measurements of peak radial velocities and hence estimates of peak disturbance conditions for at least 85% of the traverses made. It is hoped that in this way sufficient data will be obtained to assess the behaviour of the wake behind the Paris and the changes which result when devices like sails are fitted.

CONCLUSIONS

a) The intensity of the disturbance experienced by a Jetstream aircraft passing transversely through the wake of a standard Paris aircraft was a maximum when the traverse was made 400m.behind it. This distance increased to 700m. when sails were fitted to the wing tip tanks of the Paris. This suggests that the sails delayed the complete roll-up of the vortex sheet from 6.5sec. to 11.3sec. after it left the aircraft.

b) The peak intensities likely to be experienced by aircraft flying through the wake of the Paris at distances 400m. to 700m. behind it are about 25% less when sails are fitted to the Paris tip tanks.

c) Analysis of all tests made between 400m. and 800m. behind the Paris suggest that there was a greater chance of a traversing aircraft experiencing a moderate disturbance when sails were fitted but a lower chance of getting a really severe disturbance than without sails.

d) Sails reduced the decay rate of the trailing vortices. This effect together with the delay in complete roll-up of the vortices meant that at distances greater than 700m. behind the Paris with sails, the traversing aircraft experienced greater disturbances than when sails were not fitted. At a distance of two kilometres, or a time of about 30 seconds after leaving the aircraft the wake of the Paris without sails gave a negligible disturbance to a traversing aircraft whilst the disturbance caused by the Paris with sails was likely to be of measurable size.

e) The considerable variation in the size of the disturbances experienced by the traversing aircraft at nominally the same conditions suggest that it was not passing exactly through the centres of the rolled-up vortices on each occasion. Apparently slight errors in height were sufficient to reduce the intensity of the disturbance experienced. Because of this even the 160 traverses for which measurements were made were insufficient to give the maximum levels of disturbances likely to be experienced by a traversing aircraft to a high level of confidence. This is probably the reason why an analysis of the variation of the enveloping and mean disturbance levels with distance did not yield any consistent trend in the rates of decay of the vorticity.

f) To enable more accurate results to be obtained it is essential to measure the disturbances in much greater detail, increasing the sensitivity of the instrumentation and particularly the time scale of the recordings. It is proposed that further tests are made using a system in which both velocity perturbations in both the vertical and in-line of flight directions are measuredat 0.01 second intervals. This should allow the peak radial velocities and positions of the vortex cores to be calculated from the readings taken during the traverses.

REFERENCES

1. SPILLMAN J.J. The use of wing-tip sails to reduce vortex drag. The Aeronautical Journal. Royal Aeronautical Society, Vol.82 No.813.Sept.1978.

2. SPILLMAN J.J. RATCLIFFE, H.Y. MCVITIE. A. Flight experiments to evaluate the effect of wing-tip sails on fuel consumption and handling characteristics. The Aeronautical Journal. Royal Aeronautical Society. Vol. 83, No. 823, July, 1979.

3. BISGOOD P.L. MALTBY R.L. DEE F.W. Some work on the behaviour of vortex wakes at the Royal Aircraft Establishment. RAE Tech.Memo Aero 1244. 1970.

4. SQUIRE H.B. The growth of a vortex in turbulent flow. British Aeronautical Research Council Paper 16666. 1954.

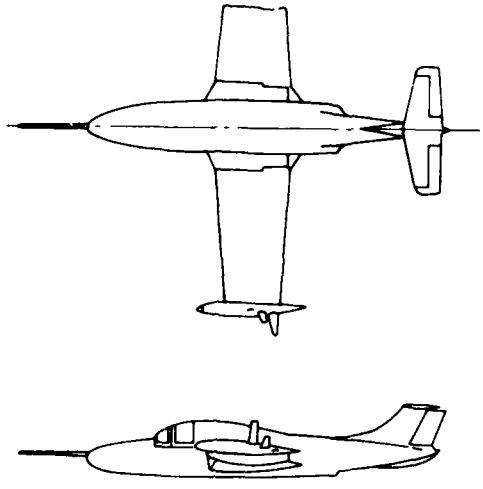

GENERAL ARRANGEMENT OF PARIS WITH SAILS

FIGURE 1

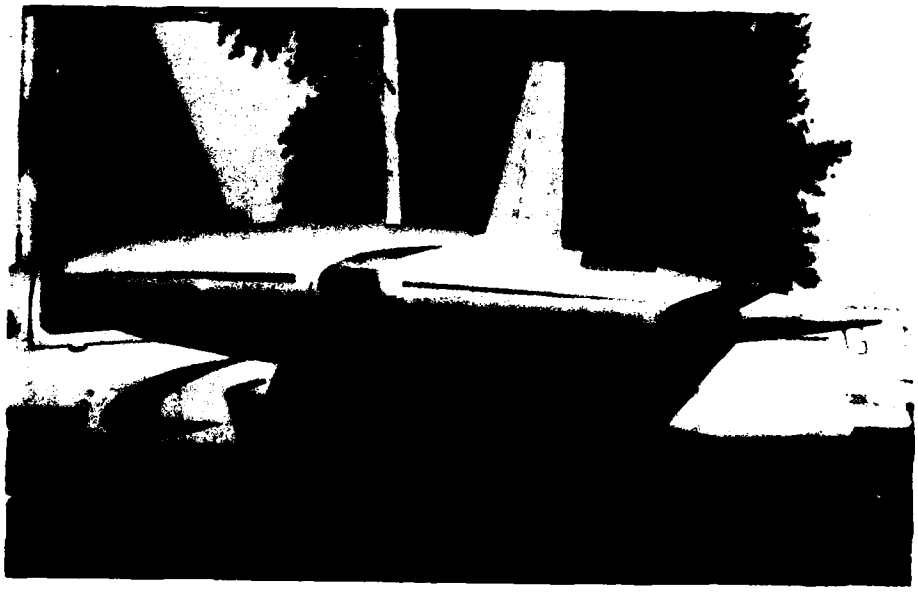

WING-TIP SAILS ON PARIS FIGURE 2

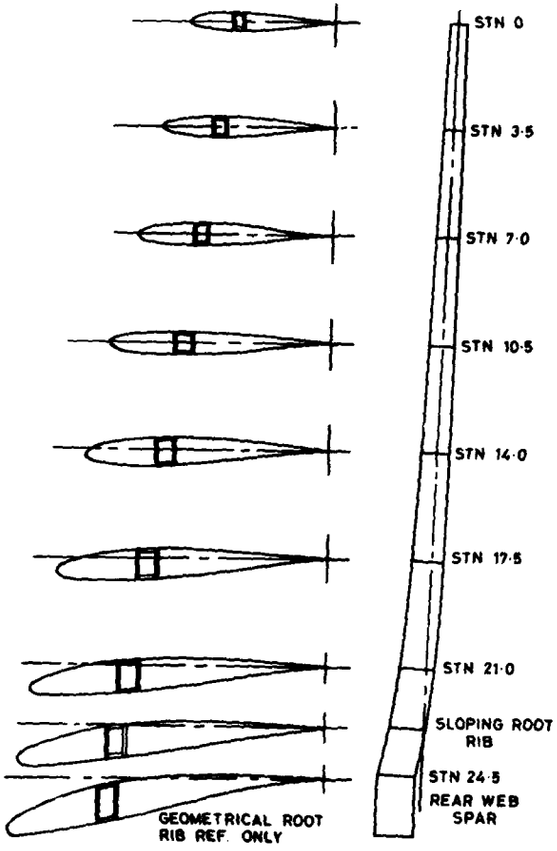

AIRCRAFT SAIL GEOMETRY

FIGURE 3.

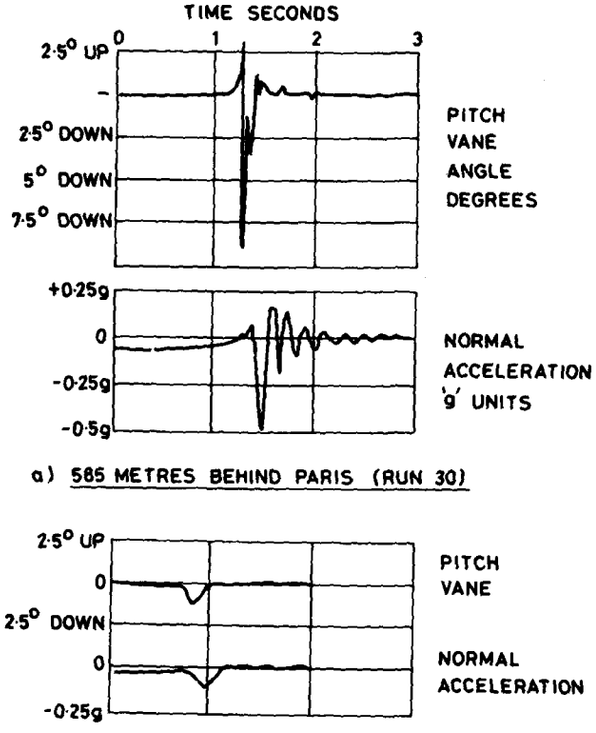

TYPICAL VANE ANGLE AND ACCELERATION TRACES

FIGURE 4

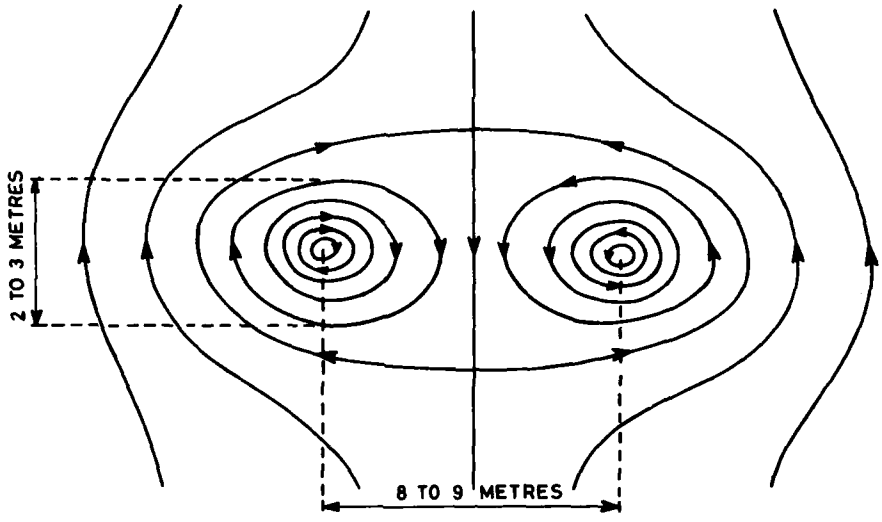

SCHEMATIC DIAGRAM OF THE FLOW IN THE WAKE

FIGURE 5

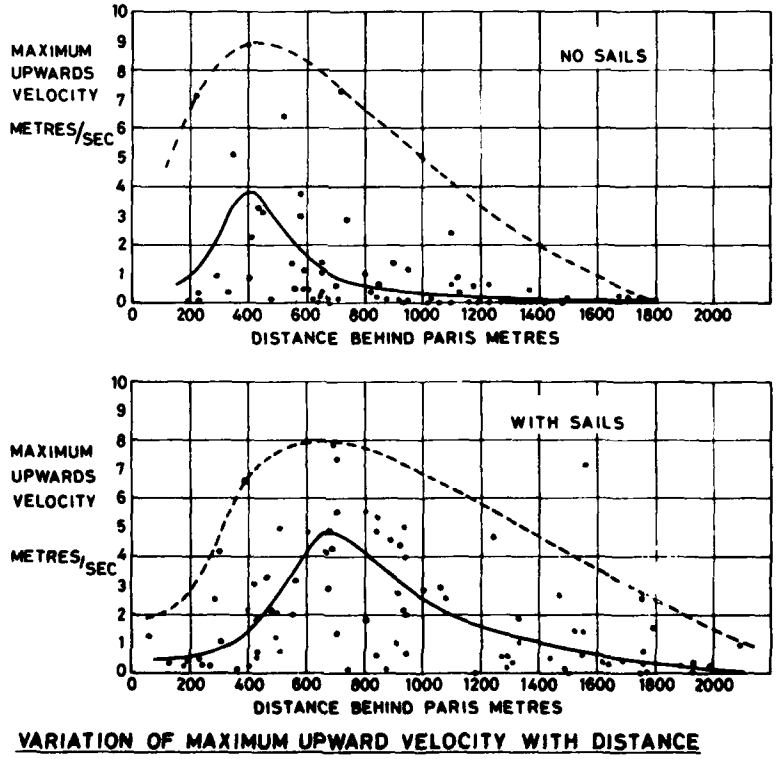

VARIATION OF MAXIMUM UPWARD VELOCITY WITH DISTANCE BEHIND PARIS

FIGURE 6

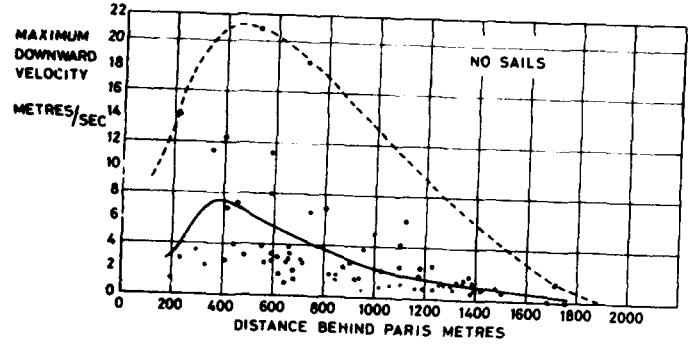

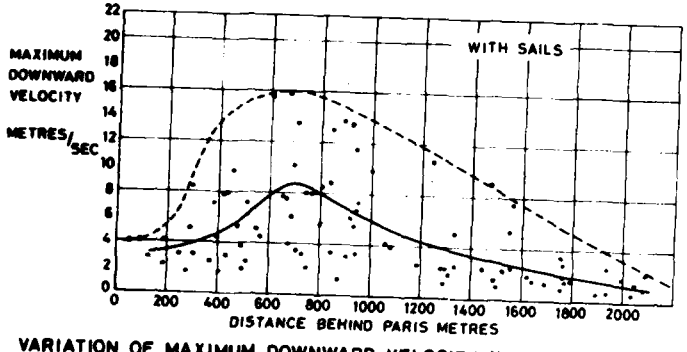

VARIATION OF MAXIMUM DOWNWARD VELOCITY WITH DISTANCE BEHIND PARIS

FIGURE 7

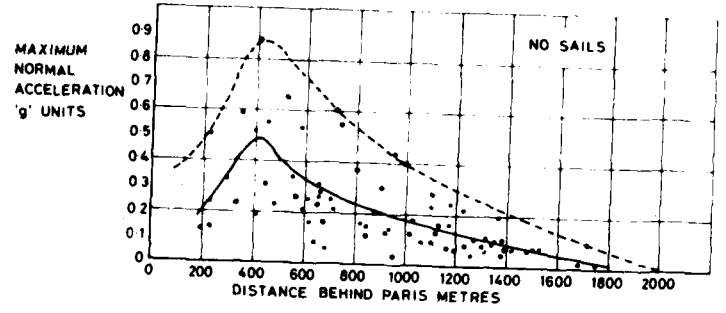

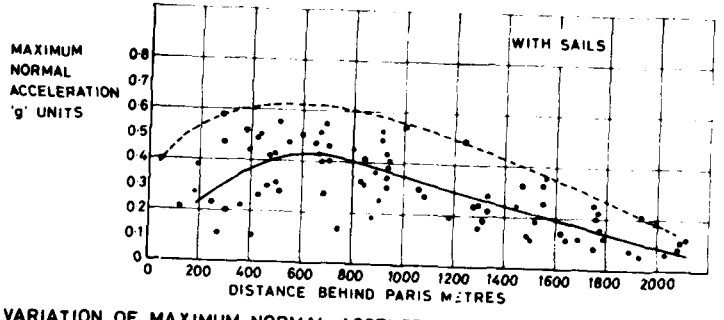

VARIATION OF MAXIMUM NORMAL ACCELERATION OF JETSTREAM WITH DISTANCE BEHIND PARIS

FIGURE 8

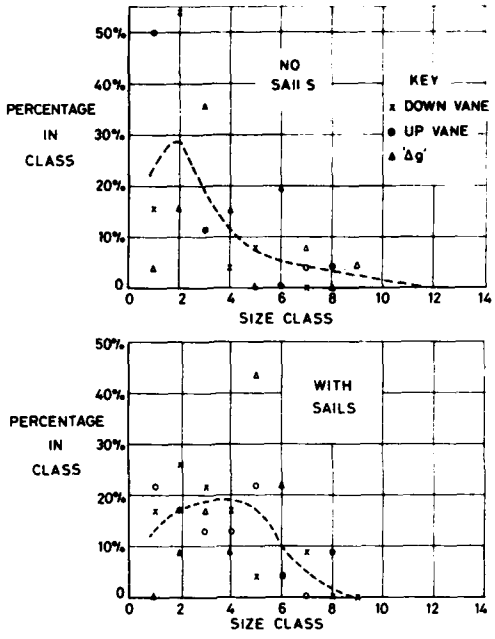

DISTRIBUTION OF DISTURBANCES MEASURED
400m - 800m BEHIND THE PARIS

FIGURE 9

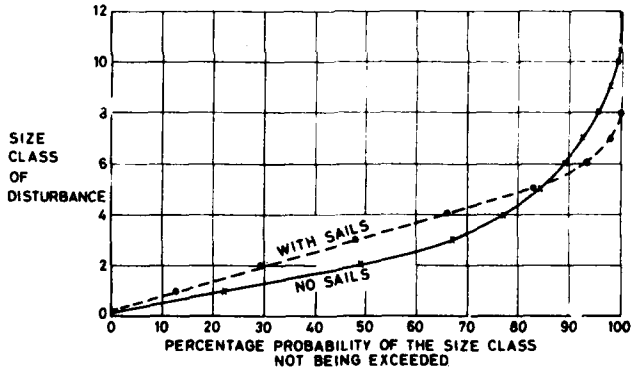

THE EFFECT OF SAILS ON THE PROBABILITY OF A FOLLOWING AIRCRAFT
400m - 800m BEHIND RECEIVING A DISTURBANCE OF A GIVEN SIZE

FIGURE 10

BOUNDARY LAYER SEGMENTATION ON SHARP HIGHLY SWEPT LEADING EDGES AND ITS EFFECTS ON SECONDARY VORTICES

by

A.Baron and Prof. S. De Ponte
Politecnico di Milano
Dipartimento di Ingegneria Aerospaziale
Via Golgi 40
20133 Milan, Italy

ABSTRACT

In lifting conditions, the vortical flow on a sharp highly swept leading edge is characterized by a strong adverse pressure gradient acting from the centerline of the wing towards the leading edge, which produces boundary layer separation. A secondary vortex grows and brings to lift loss and to drag rise.

The reduction of this secondary vortex may be obtained by means of a slot, which divides the boundary layer in two parts, as in usual slotted flaps. In the present work, the effect of a single slot on a delta wing model has been investigated experimentally, in order to verify the correctness of the basic principle of operation.

In the first part of this research, pressure measurements have been performed on an unslotted delta wing model, which enabled to determine the location of the secondary separation line, as a function of the angle of attack. A slotted delta wing model was then built and tests were carried on, showing a remarkable shift of the location of the secondary separation line. In addition, the secondary vortex flow was investigated by means of a tracing gas technique, based on the injection of Helium on the upper surface of the wing and measurements of its concentration in the flow downstream.

As a conclusion, boundary layer segmentation appears to be a useful tool in preventing large secondary separations and allows higher lift coefficients to be obtained. It is reasonable to suppose that results similar to those reached for this delta wing could be expected also for conventional highly swept wings.

NOTATION

b	local wing semi-span	(mm)
c	wing root chord	(mm)
c_p	pressure coefficient	
x	chordwise coordinate from apex	(mm)
z	spanwise coordinate from the root	(mm)
α	angle of attack	(degrees)

1 - INTRODUCTION

Secondary vortices on highly swept leading edges, as on delta wings, are responsible for a significant decrease in lift and increase in drag. Furthermore, the suppression of secondary vortices permits to verify experimentally the accuracy of numerical prediction methods, based on potential flow theory. These predictions in fact are not comparable with experiments, in the high angle of attack range, where secondary separation is usually present, without complex three-dimensional boundary layer calculations.
A further reason for investigation on secondary separation is to evaluate its effects, if some, on the breakdown of the primary vortex, at high angle of attack.
Any means of boundary layer control, as suction or blowing, may be useful for secondary separation suppression, but are generally rather difficult to be used on thin wings, due to ducting problems. It appears easier, in order to remove the secondary separation and the associated secondary vortices, to slot properly the leading edge of the wing, thus distributing the necessary pressure recovery in two, or more, boundary layers.
Taking into account that the spanwise flow on a swept leading edge is directed outwards, the slot (or slots) may be regarded as a usual trailing edge flap, which produces a flow with a cross component directed towards the leading edge.
The slot width should allow the maximum lift condition shown by Ljungstrom to be verified, i.e. the boundary layer on the flap and the wake of the main wing should merge

at the leading edge. This should be regarded as a first design criterion, although such a condition, in highly three-dimensional flows, must be verified by means of a proper series of tests.
This research was intended to make a preliminary analysis of the effect of this kind of slots on a delta wing, and confirmed the correctness of the principle of boundary layer segmentation. As first step, it was necessary to find the location of the secondary separation line, at a "design" angle of attack. Of course the blowing slot must be located upstream this line, directed towards the leading edge, in order to succesfully prevent separation effects. In the actual experimental investigation, a first series of tests was performed, in order to determine both "design" angle of attack and secondary separation line location, using an unslotted delta wing model. As "design" angle of attack, the one giving the maximum overall lift on such a model, was chosen, as it seemed to be a reasonable starting point. On the basis of the results so obtained, a new slotted wing was constructed, having the same geometry (except for the slot), and it was tested as illustrated in the following.

II - TESTING EQUIPMENT AND METHODOLOGIES

II-1 The delta wing models

The experimental research was carried-out using two delta wing models having the same geometry (swept angle 60 degrees, maximum thickness 16 mm, semi-span 404 mm, and root chord C=700 mm), but with a slot on the second one, able to control the boundary layer on the upper surface, near the leading edge of the wing (see Fig.1). For ease of construction, the wing was not conical, but it consisted of two parallel planes, connected by the surface of a circular cylinder passing through the leading edge and tangent to the upper plane, as shown in figure 1. This departure from conical geometry was nevertheless rather small and seemed not compromise significantly the hypotesis of conical flow. The first model permitted to determine, with a preliminary series of pressure measurements, the position of the secondary separation line on the upper surface of the wing and, therefore, the location of the slot on the second model, of more complex construction. Such a position, at given wing geometry, is of course a function of the angle of attack. In order to carry-out the tests in meaningful conditions, an angle of attack of 25 degrees was selected. At this angle, a sufficiently strong secondary separation was noticed, while the flow still presented an organized vortical structure, not yet affected by significant bursting phenomena. The second wing model was composed by a fixed part and by a movable leading edge, among which a slot of conical geometry was obtained, in order to segment the boundary layer on the upper surface of the wing (see Fig.1). The width of the slot could be varied with relative movements of the two elements, either in the plane of the wing, or in direction perpendicular to it. This permitted to control the flow in the slot modifying in the least possible way the overall geometry of the wing, with respect to that of the unslotted model. It was also possible to rotate the movable leading edge, in a similar way as it can be done in conventional trailing edge flaps. As the purpose of this preliminary work was to state, in principle, the effectiveness of boundary layer segmentation, neither the slot width nor the slat deflection were changed systematically. The optimization of these parameters will be investigated in future research.

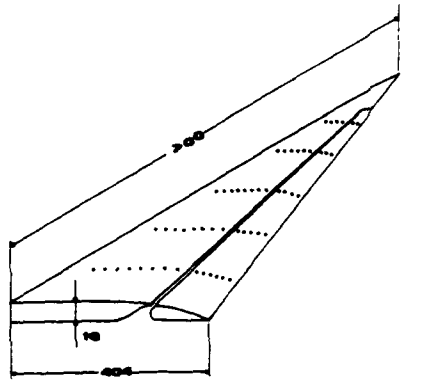

Fig. 1
GEOMETRY OF THE DELTA WING HALF MODEL AND LOCATION OF PRESSURE TAPPINGS.

II-2 Pressure measurements

The presence of secondary separation and the effect of boundary layer segmentation on the leading edge of the wing have been at first investigated by means of pressure

measurements and, afterwards, by means of measurements of concentration of a tracing gas (Helium). On the wing models a series of 120 pressure tappings, placed on five stations along the chord (respectively at 33, 46, 57, 71 and 83 per cent of the root chord) were made. The measurement stations are perpendicular to the wing center-line. Measurements of pressure coefficients were performed by means of a Scanivalve system, controlled by a microcomputer capable of automatic data processing and plotting. Each measurement was repeated several times and the values on the diagrams are average values between a minimum of 10 and a maximum of 50 readings per point. The number of readings was determined, time by time, according to the values of standard deviation required (10^{-3} approx.). This permitted to achieve a good repeatability of measurements and allowed to limit the influence of random pressure fluctuations. In particular, for the comparison between the pressure distributions at "design" angle of attack, 50 readings per point were always carried-out.
The wing models were fixed on the center-line to a disc connected to an electromechanical device able to change the angle of attack of the wing.

II-3 The tracing gas technique

The development of a vortical flow can be followed by injecting in it a tracing gas (Helium, in the present case) and detecting its concentration at different locations in the flow field, downstream the injection point (2). This technique has already been succesfully applied to the study of the rolling-up of the viscous sheet produced by low aspect ratio rectangular wings, as vortex generators (3). The results so obtained were in good agreement with those resulting from potential theory calculations. An example of such an application is shown in figure 2. In the lower part of this figure, the distribution of Helium concentration, corresponding to the B station, is reported. In the upper part of the same figure, the comparison between the shape of the wake, determined numerically, and the position of the peaks of Helium concentration, resulting from several measurements similar to the one of station B, is presented (4). The concentration of the tracing gas was measured by means

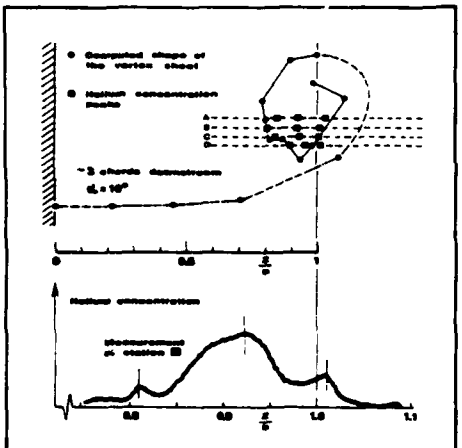

Fig. 2
HELIUM CONCENTRATION MEASUREMENTS ON THE VORTEX SHEET OF A RECTANGULAR WING OF 1.2 ASPECT RATIO.

of a special hot-wire anemometric probe, designed for this purpose, which is schematically shown in Figure 3. The operating principle of such device is based on the varaiation of specific heat of air-Helium mixtures, as a function of relative concentration of the two gases. In this case, the two hot-wire probes are used, at known velocity, to determine the concentration of the tracing gas in the mixture, according to the measurement of the specific heat.
In one of the two channels, where the probes are located, the mixture of unknown composition is sucked from the measurement point, while in the other channel, pure air (at same temperature) is sucked. The measurement of the concentration is therefore obtained comparing the signals supplied by the two probes. It is not then an absolute value, as it happens in other similar systems. In order to obtain a measurement independent from the

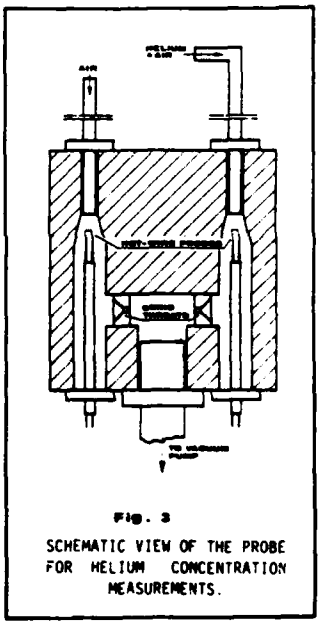

Fig. 3
SCHEMATIC VIEW OF THE PROBE FOR HELIUM CONCENTRATION MEASUREMENTS.

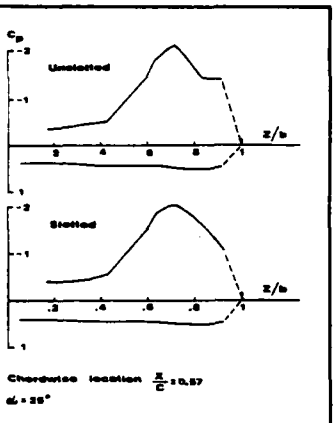

Fig. 4
BOUNDARY LAYER SEGMENTATION EFFECTS ON PRESSURE RECOVERY.

speed inside the channels, two sonic throats are placed, downstream. The speed of sound is a function of the molecular masses and of the number of atoms which constitute the molecules of the sucked mixtures, and therefore, of the tracing gas concentration. This implies an increase in the sensitivity of the instrument. The maximum sensitivity is obtained when the tracing gas is monoatomic and with low molecular weight. Among commercial gases, Helium has been chosen, as it presents also the advantage of being an inert gas not dangerous to handle.

In the present application of the tracing gas technique, Helium was injected on the upper surface of the wing, close to the slot location, at 57% of the root chord. This location corresponds to the third chordwise station where the pressure measurements have been performed. The Helium concentration was measured in a region covering the whole extension of the slat, located at 71% of the root chord. This position corresponds to the fourth chordwise station where measurements of pressure have been carried on. The spanwise track of the probe was parallel to the lower surface of the wing. Measurements were repeated for both the slotted and unslotted configurations.

The tracing gas technique is particularly suitable for the study of vortical flows, as the effect of a moderate suction through the probe compensates for the deceleration due to its presence, and therefore does not promote vortex bursting.

III - RESULTS

III-1 Pressure measurements

On the basis of the pressure measurements carried out on the two delta wing models, it can be stated that boundary layer segmentation allows a considerable displacement of the secondary separation line. A significant pressure recovery is obtained near the leading edge of the wing, as shown in figure 4. This appears clearly also from the examination of figures 5, 6 and 7, in which the pressure distributions on the wings are reported, at an angle of attack of 25 degrees, chosen as "design" condition. Please note that for clearness of representation, and due to the lack of pressure tappings near the leading edge of the wing, the pressure distributions on the upper and lower surfaces of the wing have been arbitrarily closed, assuming a zero value for both of them on the leading edge.

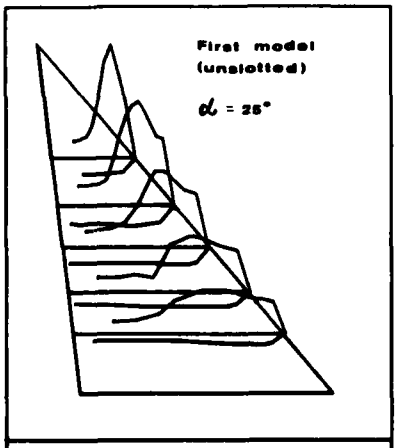

Fig. 5
PRESSURE DISTRIBUTION ON THE UNSLOTTED DELTA WING MODEL AT "DESIGN" ANGLE OF ATTACK.

As it can be noted, the secondary separation line, which was located at about 80% of the local semispan, in most part of the wing, has moved, in the first three stations along the chord (X/C=0.33, 0.46 and 0.57), beyond the last measurement point along the span, situated approximately at 95% of the local span (Fig. 7). Also in the stations more downstream (X/C=0.71 and 0.83) a similar result has been obtained, even if slightly weaker. This is probably due to the onset of vortex breakdown phenomena which have reduced the effectiveness of boundary layer segmentation. Anyhow, the secondary separation seems to be located, also in this region, over 85% of the local chord. This result has been also confirmed by a series of flow visualizations, which has permitted to find out the region of separated flow on the slat. While without boundary layer control, flow separation is present on the whole surface of the slat, that is 20% of the local span, in

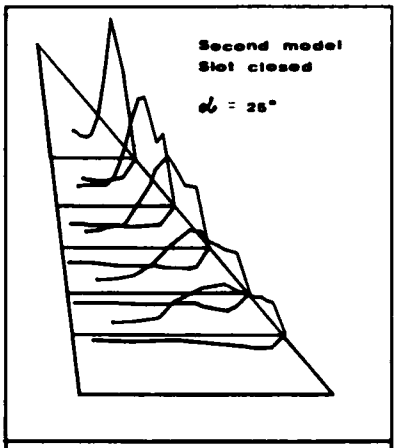

Fig. 6
PRESSURE DISTRIBUTION ON THE DELTA WING MODEL WITH CLOSED SLOT. AT " DESIGN " ANGLE OF ATTACK.

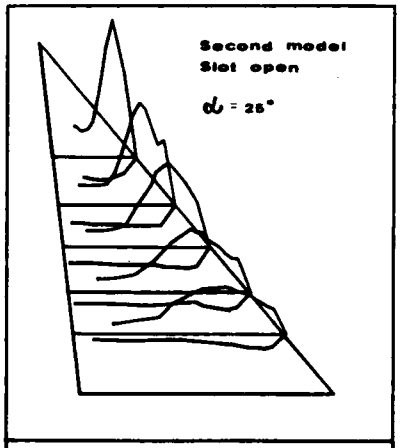

Fig. 7
PRESSURE DISTRIBUTION ON THE DELTA WING MODEL WITH OPEN SLOT, AT "DESIGN" ANGLE OF ATTACK.

proximity of the leading edge, such region is reduced to about one third when boundary layer segmentation is applied.

From the results of the tests, it has also appeared that the internal geometry of the slot, besides its position, is a critical parameter of great importance. An example of unsufficient pressure recovery produced by flow separation in the slot, due to a wrong positioning of the same, is illustrated in figure 8. To this respect, it has to be noted that the not exactly conical wing geometry, implies radii of curvature of the slat nose, which are unfavorable in proximity of the apex of the wing. This can be anyway a limitation present in many practical applications when radii of curvature, suitable to avoid separation inside the slot, have to be obtained on low thickness wings.

As far as the influence of secondary separation on the primary vortex bursting is concerned, it can be said that, at least in the test conditions examined, it is completely negligible. This is evident not only on the after part of the wing, at

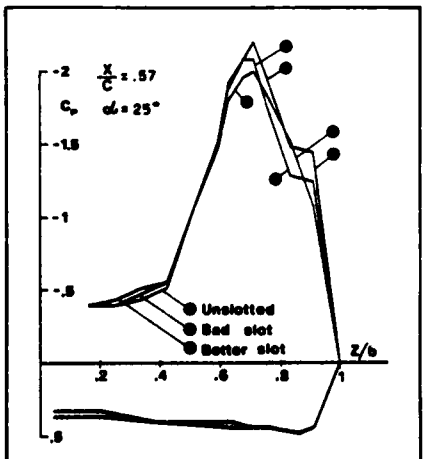

Fig. 8
THE EFFECT OF THE SLOT GEOMETRY ON PRESSURE RECOVERY.

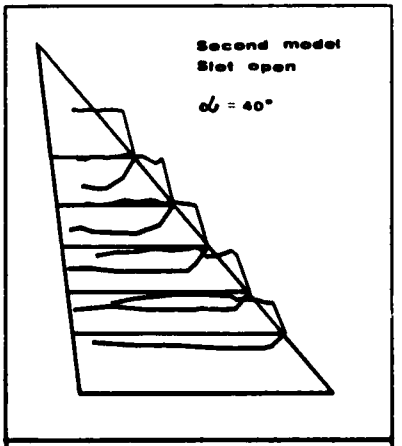

Fig. 9
PRESSURE DISTRIBUTION ON THE DELTA WING MODEL WITH OPEN SLOT. AT HIGH ANGLE OF ATTACK.

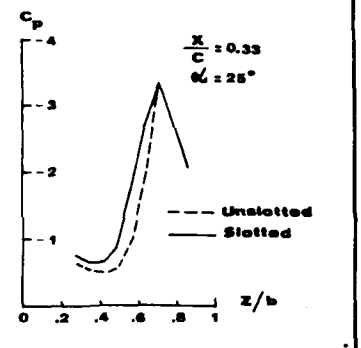

Fig. 10

THE EFFECT OF BOUNDARY LAYER SEGMENTATION ON PRESSURE DISTRIBUTION IN THE FORWARD PART OF THE WING.

low angles of attack (25 degrees), as indicated on figure 7, but also on the whole wing at higher angles (40 degrees, Fig. 9).
The effect of the reduction of secondary separation on the normal force coefficient of the wing, is considerable especially in the front region of the wing, as shown in figure 10. This effect is accompanied by the displacement of the center of pressure towards the centerline of the wing. This last effect can contribute in a sensible way to the reduction of structural stresses on the wing. In the test conditions examined, such effects become weaker in the rear part of the wing. This is probably due to the onset of primary vortex bursting. Also to this respect, it is possible that the not perfect conicity of the wing plays a not negligible role, which does not permit to evaluate in a deeper way the effect of boundary layer segmentation on the normal force coefficient of the wing. Unfortunately, also the available numerical methods (5), which generally neglect the thickness of the wing, are not suitable for a comparison of this kind with experiments.

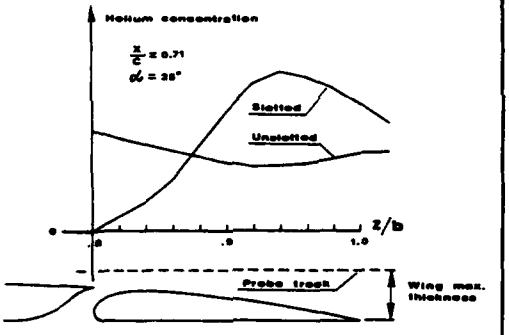

Fig. 11

HELIUM CONCENTRATION DISTRIBUTION ON THE DELTA WING.

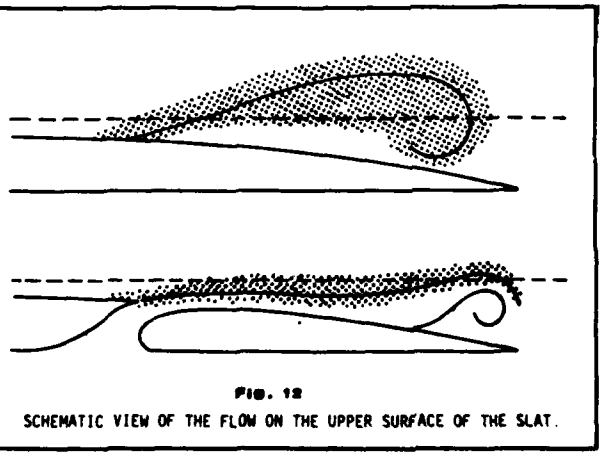

Fig. 12

SCHEMATIC VIEW OF THE FLOW ON THE UPPER SURFACE OF THE SLAT.

III-2 The measurements of Helium concentration

The analysis of the tracing gas concentration profiles confirms the displacement of the secondary separation line and the reduction in the dimensions of the related secondary vortex. Unlike the measurements reported in figure 2, the presence of not negligible turbulence levels, did not allow to detect concentration peaks corresponding to the rolling-up of the vortex sheet. Anyway, figure 11 shows that, while with closed slot an almost constant concentration distribution is present, with open slot such a distribution is strongly modified. Almost no concentration is measured in correspondence of the slot location, while a maximum is present close to the leading edge, at about two thirds of the span of the slat. The presence of a turbulent separation, in case of closed slot, produces, without any doubt, a stronger diffusivity of the gas, and gives reason of the absence of strong concentration peaks. In case of open slot, on the contrary, a concentration peak is detected, due to the presence of a small secondary vortex, as shown in the schematic view of figure 12. In this case, the reduction to zero of

the Helium concentration, in correspondence of the slot, is due to the fact that it flows in the boundary layer attached to the wing surface, below the measurement section.

IV - CONCLUSIONS

According to the results of the present research, it can be concluded that it is possible to reduce, if not suppress, the secondary separation region on highly swept leading edges, by means of a proper boundary layer segmentation.
Boundary layer segmentation has proved to be an effective means of separation control, also in strongly three-dimensional flows.
One of the limits of the present research derives essentially from technological problems, which have not permitted to measure the pressures in points situated very close to the leading edge of the wing, as it would be desirable in further development of the researches.
Another limit is due to the preliminary aspect of this work, during which optimization of the slot geometry has not been attempted. This has resulted, on the contrary, to be a foundamental parameter. A deeper study of the flow inside the slot seems to be therefore essential, in order to evaluate the actual applicability of this technique. Of course such a research requires to determine some characteristic parameters of the boundary layer, and has to be performed with more complex methodologies.
Due to the turbulence associated to the secondary separation, the results obtained by means of the tracing gas technique have revealed a more difficult interpretation in case of secondary vortices than in case of primary ones. The tracing gas technique can be therefore more useful in case of laminar separations, even if also in the present case, it has permitted to determine clearly the different phenomenologies associated to the presence or not of boundary layer control.
Besides, the applications of boundary layer segmentation to the control of three-dimensional separations, are not limited to delta wings, as examined in the present research, but can reasonably be extended to many other cases, not only in the aeronautical field.

REFERENCES

(1) B.L.G. LJUNGSTROM, "Experimental High-Lift Optimization for Multi-element Airfoils", AGAHD-CP-143, 1974.
(2) S.E. DE PONTE, "Road Tunnel Pollution and Ventilation Study", VonKarman Institute for Fluid Dynamics PR-70-267, 1970.
(3) M. COPPI, "Analisi sperimentale della scia di un generatore di vortici", thesys, Politecnico di Milano, 1979.
(4) A.BARON, S. DE PONTE, "Analisi della circolazione prodotta da un generatore di vortice, to be published on l'Aerotecnica Missili e Spazio, 1983.
(5) J.H.B. SMITH, "Inviscid Fluid Models, Based on Rolled-up Vortex Sheets, for Three-dimensional Separation at High Reynolds Number", AGARD-LS-94, 1978.

ACKNOWLEDGMENT

The authors acknowledge the support of Mr. P. Leveghi and Mr. C. Mazzucchelli, who carried on part of the experimental work.

AUGMENTATION OF FIGHTER-AIRCRAFT PERFORMANCE BY SPANWISE BLOWING OVER THE WING LEADING EDGE

Arnan Seginer
NASA Ames Research Center
Moffett Field, California 94035, U.S.A.

and

Meir Salomon
SAL Engineering
Haifa, Israel

SUMMARY

Spanwise blowing over the wing and canard of a 1:35 model of a close-coupled-canard fighter-airplane configuration (similar to the Kfir-C2) was investigated experimentally in low-speed flow. Tests were conducted at airspeeds of 30 m/sec (Reynolds number of 1.8×10^6 based on mean aerodynamic chord) with angle-of-attack sweeps from -8° to 60° and yaw-angle sweeps from -8° to 36° at fixed angles of attack 0°, 10°, 20°, 25°, 30° and 35°. Significant improvement in lift-curve slope, maximum lift, drag polar and lateral/directional stability was found, enlarging the flight envelope beyond its previous low-speed/maximum-lift limit. In spite of the highly swept (60° leading edge, the efficiency of the lift augmentation by blowing was relatively high and was found to increase with increasing blowing momentum on the close-coupled-canard configuration. Interesting possibilities of obtaining much higher efficiencies with swirling jets were indicated.

LIST OF SYMBOLS

C_D drag coefficient, including jet thrust

C_L lift coefficient, including jet thrust

$C_{L_{max}}$ maximum-lift coefficient, including jet thrust

ΔC_L lift increment due to blowing, including jet thrust

C_N yawing-moment coefficient, including jet thrust

C_R rolling-moment coefficient, including jet thrust

C_Y side-force coefficient, including jet thrust

C_μ jet-momentum coefficient, equal to the product of the jet mass flux and its exit velocity normalized by the free-flow dynamic pressure and the wing-planform area

Re Reynolds number

α angle of attack

ψ yaw angle

Subscripts

B relative to the body frame of reference

c on the canard

T net aerodynamic coefficient corrected for jet thrust

w on the wing

1. INTRODUCTION

One of the persistent goals in the design of advanced tactical fighter aircraft has been the generation of additional usable lift. It is required for improved maneuverability (this is also true for the new generation, highly maneuverable air-to-air missiles) and for good low-speed performance in takeoff and landing. Since the limits of conventional linear-lift have been reached, current modern designs use nonlinear, or vortex lift, which is characteristic of slender wings and of moderately swept wings with sharp leading edges. The leading-edge-vortex phenomenon has been understood for many years (e.g., Ref. 1). At moderate to high angles of attack the flow separates from the leading edge. The favorable spanwise pressure gradient causes the separating vortex sheet to reattach behind the leading edge and to roll up into a steady vortex over the leading edge (Fig. 1). The high velocities and low pressures induced on the wing under the vortex produce the additional lift. Polhamus, in his well-known Suction-Analogy (Ref. 2), estimated the maximum lift that can be obtained in this way. The influence of the vorticity, shed from the leading edge, on the whole flow field and on the aerodynamic characteristics of an aircraft or missile configuration can be computed by a nonlinear vortex-lattice method (Ref. 3).

The use of vortex lift is limited by vortex bursting or breakdown, which is characterized by a sudden expansion of the vortex about a rapidly decelerating core, with subsequent vortex disintegration and loss

of the orderly vortical flow. As the angle of attack is increased, the point of vortex breakdown moves upstream, causing loss of lift and, finally, stall (Ref. 4).

While leading-edge vortices on slender highly swept wings are stable at moderate to high angles of attack, moderately swept wings that are in common use on fighter aircraft suffer from vortex breakdown at low angles of attack (e.g., Fig. 3 of Ref. 5), or sometimes do not produce leading-edge vortices at all (Ref. 6). Consequently, Kuchemann (Ref. 7) suggested a compromise between the contradictory requirements of fighter wings by combining coiled vortex sheets originating from the inboard parts of the wing with conventional attached flow over its outboard parts. This led to a hybrid wing design including concave double-delta wings, straked wings, or close-coupled-canard configurations (Ref. 8). In these designs a vortex emanating from the inboard elements (slender delta, strakes, or canard) produces a leading-edge vortex on the moderately swept outer part of the wing or stabilizes an existing one. These devices are essential for the nonlinear lift of moderately swept wings (Ref. 6), and also work in delaying the vortex breakdown of highly swept wings to still higher angles of attack (e.g., the Swedish Viggen aircraft, Ref. 9, or the Israeli Kfir-C2 aircraft).

Although much has still to be learned about the basic mechanism of the vortex breakdown (Ref. 10), Cornish's description of the fluid-mechanic processes involved (Ref. 11) enabled him to apply vortex control in subsonic flow by blowing a high-velocity jet down its core. There is still some disagreement about why and how this method works. Cornish thought that the low-speed, highly vortical core was removed through entrainment by the high-speed jet. Dixon's observations (Ref. 12) indicated that the jet and the vortex did not mix until the jet had expended most of its energy. These observations were strengthened by later experiments with hot jets on large-scale vectored-engine-over-wing (VEO-Wing) STOL configurations (Refs. 13-15). Dixon's contention was that the jet acted as a barrier to the downstream motion of the leading-edge vortex and that vortex control was a function of the spanwise entrainment of the free-stream flow.

In spite of the disagreement concerning the nature of the phenomenon, the feasibility and potential benefits of spanwise-blowing (SWB) in low-speed flow were proven by the results of many experimental programs. Dixon pioneered the SWB with his flat-plate experiments (Ref. 16) and was closely followed by Cornish's SWB over a flap (Ref. 11) and Poisson-Quinton's SWB over wings (Ref. 17). The investigation developed further by testing many wing planforms and configurations (Refs. 5, 6, 8, 18, 19), and some research aircraft configurations (Refs. 8, 13, 14, 15, 20, 21). All these investigations (and many more not mentioned here) concluded that SWB generates significant lift increments and improves the drag polars at high angles of attack, with no loss (and in some cases a slight improvement) in longitudinal static stability, and usually with a significant improvement in lateral/directional stability and a delay in the departure conditions (e.g., Ref. 8). Comparisons with other high-lift devices have led to the conclusion that SWB is more effective at high angles of attack (e.g., Refs. 5, 8) and may be an alternative to mechanical flaps or strakes.

The efficiency of SWB is also in question. It is addressed in most of the investigations as the ratio, $\Delta C_L/C_\mu$, between the lift-coefficient increment (ΔC_L) and the thrust coefficient of the spanwise jet (or jet-momentum coefficient, C_μ, which is the jet contribution to the lift when vectored vertically downwards). This ratio (rather than the ratio of the negative drag increment at a given α to the jet-momentum coefficient) is used because the main aim is to increase $C_{L_{max}}$. This efficiency is higher than 1.0 at angles of attack that are typically higher than 10°. The highest efficiencies are reported at the lowest blowing rates (Ref. 19) because of the small C_μ in the denominator. As the blowing rate is increased, the efficiency decreases because of the diminishing lift increments (Ref. 8). The goal of the highest possible maximum lift ($C_{L_{max}}$) would therefore mean a low-efficiency, high blowing rate. Furthermore, the evaluation of SWB potential improvements in overall aircraft performance should also account for the loss in thrust from bleeding off engine air for the SWB. Several investigators have subtracted the thrust of the jet from the engine thrust and have come up with very promising results. Campbell (Ref. 19) concluded that SWB increases the specific excess power at load factors above 1.0 and allows higher load factors to be attained before reaching the lift limit. Dixon, Theisen, and Scruggs (Ref. 22) estimated that the A-7 Corsair II aircraft could substitute SWB for all of its high-lift devices at a cost of only 15% of its thrust. Staudacher et al. (Ref. 8) were also optimistic for the low-speed region, where the flight envelope was limited by the attainable maximum lift (that could be improved by SWB) while excess thrust was available. Erickson (Ref. 23) was less optimistic when he found a 27% reduction in thrust of the F-5E at the relatively low blowing rate of 0.012, and a corresponding reduction in specific excess power available for maneuvering. One should, however, heed Erickson's remarks that SWB may be practical when used with new and suitable engines. An example of such innovative thought is the VEO-Wing concept (Refs. 13-15), where up to 16% of the engine exhaust was diverted to the SWB system.

Erickson's investigation of an existing fighter configuration (Ref. 23) is of particular interest because it provides information about the effects of SWB on its overall high-angle-of-attack aerodynamic characteristics. This is an area of ongoing interest, as can be evidenced by the NASA/DFRC-LaRC F-4C flight-test program. Therefore, for the present investigation it was decided to test existing fighter-airplane configurations at the Technion, Israel Institute of Technology (IIT). The aircraft chosen for this test was the basic low delta-wing airframe of the Dassault Mirage-IIIC that closely resembled the IAI Kfir-C1, and when equipped with a canard resembled also the configuration of the IAI Kfir-C2.

Whereas most of the configurations tested in the previously discussed references had moderately swept wings, this configuration had a 60° swept delta wing. The highly swept wing was chosen for obvious practical reasons, although it was known (Refs. 18, 19) that SWB is more efficient on wings of lower sweep; highly swept leading edges generate a sizable amount of natural vortex lift that usually could not be increased by SWB. Blowing only increased the maximum lift. Lift augmentation throughout the angle-of-attack envelope that was measured in the present investigation was, therefore, unexpected and the investigation concentrated on delaying the vortex breakdown and on increasing the maximum lift. Because this aircraft (like many others) was limited in high-lift maneuvers by lateral/directional stability and control considerations rather than by stall, special attention had to be paid to its stall-departure characteristics. The first stage of the investigation was conducted in a low-speed wind tunnel, and it is assumed that the low-speed data presented here are indicative of lift and drag augmentation at speeds up to the

critical Mach number (Ref. 20). Furthermore, at the low-speed end of the flight envelope aircraft are usually limited by their maximum lift, while they still have ample excess power. It is, therefore, in this speed regime that the spanwise blowing can most effectively improve maneuverability. Improving maneuverability in the transonic speed range would also be desirable, but vortex stabilization by SWB from the fuselage would require impractical blowing rates (Ref. 8). Transonic performance can be improved by local blowing from the wing (Ref. 24) but that is a result of shock-induced-separation control rather than vortex stabilization. Therefore, transonic testing would have to be done at a later stage.

In addition, the investigation includes a comparison of SWB with the effects of the canard, asymmetric blowing (to study the effects of a malfunctioning blowing system), and blowing of swirling jets (to evaluate the various theories on the SWB mechanism).

2. EXPERIMENTAL APPARATUS AND TESTS

2.1 The Model

The model used in this study (Fig. 2) is a 1:35-scale metal-reinforced plastic replica of the aircraft with the twin inlets faired over. The model has a low delta wing with a relatively sharp leading edge that has a conical droop and is swept back 60°. The basic model (no canard) is designated as Configuration A in the following discussion. The same model can also be equipped with a canard mounted on the engine inlets at a height of 0.31 local fuselage diameter above the wing. The canard has a leading-edge sweep angle of 45° and a span of 44% of the wing span (fuselage included). The model with the canard is designated as Configuration B.

Four convergent steel nozzles were installed in the model, two on each side of the fuselage, one above the wing and one above the canard. The wing nozzles (2.3 mm in diameter) issued a jet parallel to the wing leading edge. Their location, one diameter above the wing surface and 10% of the root chord from the leading edge, was determined by preliminary tests on a larger model (not reported). The effects of the vertical position on the blowing were rather small. The axial location had a somewhat stronger influence, with the blowing becoming more effective as the nozzles were moved aft. The location used in the present experiments was the farthest aft that was consistent with the structure of the inlets of the existing aircraft. The canard nozzles had a 1.3 mm diameter and their location relative to the canard was similar to the location of the wing nozzles relative to the wing.

2.2 The Blowing System

Compressed air at pressures up to 8 atm was supplied to the model's nozzles from the laboratory's low-pressure system through flexible hoses along the model sting-support, and through stainless steel tubes inside the model. Air could be blown from any single nozzle when asymmetric blowing was investigated; or from all four nozzles simultaneously, or separately from the wing or canard nozzles only. Swirling jets were obtained from the same nozzles by inserting drill bits because good swirl nozzles could not be manufactured due to their small size. Swirl direction was controlled by using right- or left-hand bits. The inserts reduced the nozzle cross-section area by about 75%. It is not known how much swirl was actually imparted to the jets by this method.

2.3 Wind Tunnel and Instrumentation

The tests were conducted in the 1 m × 1 m (3-m long) test section of the low-speed atmospheric wind tunnel of the Aeronautical Research Center, Technion, IIT. Airspeed in all of the tests was 30 m/sec with a corresponding Reynolds number of $\sim 1.8 \times 10^6$/m or 1.8×10^5, based on the mean aerodynamic chord.

The model was mounted on a six-component internal strain-gage sting balance, and the data were acquired and reduced to aerodynamic coefficients by an NEFF620/Elbit-CR 17 data-acquisition/computer system. Forces were conventionally normalized by the free-stream dynamic pressure and the wing area; moments, measured relative to a reference point at 48% of the root-chord, were normalized with the mean aerodynamic chord. The longitudinal aerodynamic coefficients were computed in the wind frame of reference whereas the lateral coefficients were computed and presented in the body frame of reference.

2.4 Force Tests

The longitudinal aerodynamic coefficients were measured at 0° yaw angle during angle-of-attack sweeps from -8° to 60°, and the lateral coefficients were measured during yaw-angle sweeps from -8° to 36° at fixed angles of attack of 0°, 10°, 20°, 25°, 30°, and 35°. Blowing stagnation pressures were 4, 6, and 8 atm for the wing and 4 and 6 atm for the canard, corresponding to jet-momentum coefficients of 0.05, 0.07, and 0.09 on the wing, and 0.016 and 0.022 on the canard. In the asymmetric-blowing tests on one wing only, the jet-momentum coefficient was 0.025, 0.035, and 0.045, and in the swirling-jet experiments it was ~0.012 (for a blowing pressure of 4 atm).

Before beginning the wind-tunnel tests, all the nozzles were plugged and the air-feed and blowing systems were pressurized to ensure that the balance was not affected by stiffening of the air hoses and tubes. The nozzles were then unplugged and the direct contributions of the jets to the lift and the thrust were recorded without flow in the tunnel, later to be subtracted from the values measured with flow in the tunnel. The results presented here for Configuration A are net aerodynamic results corrected for the contributions of the jet momentum. The results for Configuration B were not corrected the aerodynamic coefficients include the contributions from the jets; these contributions are presented so that the results with thrust removed can be calculated. The correction for the thrust contributions is the aerodynamicist's way of evaluating the net aerodynamic effects of SWB, but since the actual aircraft experiences the total lift and drag, these are shown for Configuration B. The thrust loss should also be taken into account but must be measured on the actual engine (Ref. 23). It is interesting to note that the thrust resulting from the jets was larger than the streamwise component of the jet momentum, possibly because of suction over the leading-edge droop.

2.5 Flow-Visualization Tests

Some flow-visualization tests were conducted using a helium bubble generator. Bubbles are generated by blowing a helium-air stream through a liquid detergent. The bubbles are filtered so that only the neutrally buoyant bubbles are injected into the wind tunnel through a nozzle and follow the air-flow streamlines. The bubbles reflect the light of a high-intensity spotlight and can be seen against the dark background of the black-painted model and wind-tunnel walls. Flow visualization was used to study the characteristics of the flow over the wing and the canard and to correlate them with the force measurements. An example is presented in Figs. 3 and 4 where the model is at an angle of attack of -35°. The streamlines over a section of the wing leading edge are shown in Fig. 3a without blowing ($C_\mu = 0$). The flow is separated from the leading edge onwards. There is no observable orderly pattern and some reversed flow can be seen. When the spanwise blowing ($C_\mu = 0.07$) is turned on (Fig. 3b), the flow is seen to reattach behind an orderly vortex. The vortex core is clearly defined with its breakdown occurring somewhere over the trailing edge. Figure 4a shows the flow over the canard under the same conditions without blowing. The canard does not seem to have any effect on the flow field. In fact, the local flow seems to be separated from the canard and the wing. When air is blown over the canard and the wing ($C_{\mu_C} = 0.022$, $C_{\mu_W} = 0.07$), a vortex is formed over the canard, and the flow over the vortex turns downward and reattaches to the wing (Fig. 4b).

3. RESULTS AND DISCUSSION

3.1 Configuration A

Symmetric blowing. The effects of blowing on the lift coefficient (corrected for the jet contribution) are shown in Fig. 5. Contrary to previous experience with wings of high sweep angles (Refs. 18, 19), blowing not only increases the maximum-lift values, but also increases the lift-curve slope. The slope increment at low angles of attack ($\alpha < 12°$) was small but unmistakable and was probably due to an increased effective camber (Ref. 19). At higher angles of attack there was an appreciable increase in the slope and the maximum-lift coefficient was increased from 1.37 to 1.67. The angle of attack for maximum lift was increased by only about 1°, from 34° to 35°. An increase in the jet-momentum coefficient from $C_\mu = 0.05$ to $C_\mu = 0.07$ had a small effect, and was unjustifiable as far as efficiency was concerned.

Figure 6 presents the improvement in the drag polar after subtraction of the thrust of the jets. There was a slight decrease in the zero-lift drag, possibly because of some increase in leading-edge suction, and although the drag for any other given angle of attack was higher with blowing than without blowing, there was a significant reduction in drag for any given lift coefficient. Blowing had no effect on the longitudinal static stability except for extending the stable region (not shown) to the new $C_{L_{max}}$ without pitchup (e.g., Refs. 8, 21, 23).

Asymmetric blowing. The effects of asymmetric blowing had to be investigated in order to assure that the control surfaces could cope with the asymmetric loads on the airframe in the case of a malfunction. The effects of blowing over the left wing only are shown in Figs. 7-10. The previous blowing coefficients of 0.05 and 0.07 were halved to 0.025 and 0.035 and the lift increments resulting from blowing were lower than with symmetric blowing, but by less than 50% (Fig. 7). Increasing the blowing pressure to 8 atm and the blowing coefficient to $C_\mu = 0.045$ brought the $C_{L_{max}}$ back to the value of 1.65, almost the value achieved with $C_\mu = 0.07$. This gives some insight into the effects of blowing rate, and it seems that $C_\mu = 0.045 \pm 0.05$ is the maximum needed. Interestingly, the asymmetric blowing increased the angle of attack of maximum lift to $\alpha = 38°$.

Asymmetric blowing had no detrimental effects on the lift. No new effects on the drag or the pitching moment were expected or observed. On the other hand, effects on the lateral aerodynamic coefficients were expected, but the measured side force (thrust not removed) (Fig. 8) was small and probably attributable to the jet thrust. The small asymmetry of the side force was also observed without blowing and must have been the result of some model asymmetry. The sudden dip in the side force at $32° < \alpha < 58°$ and the sign reversal at still higher angles of attack, that are apparently the result of asymmetric separation and vortex shedding from the fuselage, were not affected by the blowing.

The trend of the uncorrected yawing moment (Fig. 9) is similar to that of the side force. The additional moment resulting from blowing is not large and can be controlled by the rudder. The effect on the corrected rolling moment was more significant (Fig. 10). Blowing over the left wing only and increasing its lift had a dramatic effect at angles of attack above 12°, when it generated a strong positive rolling moment. This continued up to $\alpha = 40°$, when the moment was drastically reduced. The moment was not too large for the ailerons to handle; moreover, such an effect could be used for rapid roll control as an aid to the ailerons. The sudden dip in the rolling moment at $\alpha > 32°$ without blowing, or at $\alpha > 36° \pm 40°$ with blowing, is again related to the asymmetric separation on the nose.

Swirling jets. As stated before, it was Cornish's contention (Ref. 11) that the jet's function was to flow down the core of the vortex and, acting like a spanwise line sink, remove by entrainment the low-velocity high-vorticity core flow. Later experiments showed, however, that the jet and the vortex did not mix (Refs. 13-15). Dixon (Ref. 12) on the other hand, believed that the leading-edge-vortex breakdown phenomenon was a result of its helix angle becoming less than 42°, or a result of the ratio of the vortex swirl velocity to the axial velocity becoming greater than 1.12. This happened when the vortex began to turn downstream. Dixon reasoned that SWB prevented or delayed the vortex breakdown by acting as a barrier and correlated the effectiveness of SWB with its spanwise entrainment of free-stream flow. Increasing the SWB effects should therefore result from improved mixing of the jet with the free stream and would also require the longest possible spanwise reach of the jet.

Several experiments were conducted with swirling jets to test these concepts. The swirl of the jet could have several effects. Diverting some of the jet's axial momentum into its circumferential flow should shorten its active length and, therefore, reduce its effectiveness as a barrier. On the other

hand, swirl should improve its entrainment characteristics and thus its effectiveness. Also, since the vortex and jet cores have a common boundary, the jet's swirl should, according to Dixon (Ref. 12), reduce the vortex helix angle and, therefore, destabilize the vortex when they are counterrotating, and, conversely, stabilize the vortex when they are corotating.

Three different swirling-jet experiments were conducted, one with positive swirl (the jets on both wings corotating with the leading-edge vortices), a second with negative swirl (both jets counterrotating), and a third with negative swirl on the right wing and positive swirl on the left. The results were surprising. In spite of the much lower jet-momentum coefficient ($C_\mu = 0.012$) resulting from the reduced nozzle cross-section area, a maximum-lift coefficient of $(C_{L_{max}})_T = 1.67$ was obtained (Fig. 11), essentially equal to the one corresponding to axial blowing with $C_\mu = 0.50$ (Fig. 5). The highest lift was obtained with the positive swirl, but the differences, due to swirl direction, are too small to be significant. The same is also true for the drag polar (Fig. 12).

Before drawing any conclusions from these results, one has to remember that the jet was not truly swirling, but rather made of two discrete jets emerging from the drill-bit grooves at cross angles. It is, therefore, impossible to speculate about the effects of swirl on the stability of the vortex. It can be safely assumed, however, that the two jets improved the mixing and entrainment of the free-stream flow, resulting in the dramatic increase in the lift.

Lateral aerodynamics. The side force acting on the basic model (measured in the body frame of reference) increased with yaw angle and became more nonlinear with increasing angle of attack (Fig. 13). The side force also increased with increasing jet momentum, smoothing the curves and apparently preventing local separations. The stronger effect of the SWB was on the yawing moment (Fig. 14). At the lower angles of attack ($\alpha \leq 20°$) the SWB had little effect (Fig. 14a), whereas it stabilized the configuration at the higher angles of attack ($20° < \alpha \leq 30°$) up to high yaw angles, where without blowing it was unstable (Fig. 14b). In fact, only at $\alpha = 35°$ did blowing fail to stabilize the configuration. This is a good example of an airframe that was not limited in angle of attack ($\alpha < 25°$) by stall, which started only at $\alpha = -34°$, but by lateral/directional instability, which was postponed by blowing to $\alpha > 30°$.

3.2 Configuration B

SWB over the wing only. The canard itself increased the natural vortex lift of the wing by intensifying and stabilizing its vortex, as can be seen in the increased lift curve slope (solid curve in Fig. 15) and in the maximum lift ($C_{L_{max}} = 1.63$). Blowing over the wing only on Configuration B further increased the vortex lift (Fig. 15, jet thrust not removed). The slope of the lift curve was increased above $\alpha = 8°$ and the maximum lift was increased to 1.66 and 1.74 with blowing rates of $C_\mu = 0.05$ and 0.07, respectively (Fig. 15). As a result of the increase in natural vorticity, induced by the canard, the efficiency of the blowing on this configuration was lower than without a canard (Fig. 5). Without a canard $\Delta C_L/C_\mu = 0.28/0.05 = 5.60$ and $\Delta C_L/C_\mu = 0.3/0.07 = 4.29$, whereas with a canard $\Delta C_L/C_\mu = 0.03/0.05 = 0.60$ and $\Delta C_L/C_\mu = 0.11/0.07 = 1.57$. Surprisingly though, the efficiency of SWB with the higher blowing rate was in this case higher than the efficiency of SWB with the lower momentum coefficient. Obviously, if one is willing to pay the price, SWB can increase the maximum lift already obtained by high-lift devices, but at reduced efficiency. The effect of blowing over the wing only on the drag polar of Configuration B (Fig. 16) is similar to that of Configuration A, namely, an increased lift for a given drag or a reduced drag for a given lift.

SWB over both wing and canard. Blowing over both lifting surfaces increased the lift curve slope and the maximum lift more than did SWB over the wing alone (Fig. 17). With a total jet-momentum coefficient of $C_\mu = 0.066$ ($C_{\mu_w} = 0.05$ plus $C_{\mu_c} = 0.016$) the maximum-lift coefficient was increased to $C_{L_{max}} = 1.78$ with an efficiency of $\Delta C_L/C_\mu = 0.15/0.066 = 2.27$, and with $C_\mu = 0.092$ ($C_{\mu_w} = 0.07$ plus $C_{\mu_c} = 0.022$) $C_{L_{max}}$ was increased to 1.91 with an efficiency of $0.28/0.092 = 3.04$. This is also surprising, because not only was the efficiency higher with the higher jet momentum, but it was even higher than it was with blowing over the wing alone with a lower jet momentum coefficient. Figure 17 also shows the direct lift of the jets so that the pure aerodynamic lift increments resulting from blowing could be evaluated. These were $\Delta C_L = 0.11$ and 0.21, respectively, for the above-mentioned cases with thrust removed and $\Delta C_L = 0.15$ and 0.25, respectively, with thrust included.

Figure 18 shows the improvement in the drag polar without removing the thrust. The static thrust of the jets is also shown. If the thrust was subtracted from the drag, the zero-lift drag would be slightly reduced by the blowing and the lift-to-drag ratio would still be improved for all angles. With direct jet contributions included, the lift-to-drag ratio for $C_D = 1.0$ was increased from $L/D = 1.58$ to $L/D = 1.73$ and $L/D = 1.83$ for the two blowing rates presented. At the maximum lift the corresponding values of this ratio were $L/D = 1.58$ and 1.65, respectively, whereas L/D was only 1.46 without blowing.

Lateral/directional stability. With blowing over both lifting surfaces, the lateral/directional characteristics of the configuration had to be tested again. As was the case with Configuration A, SWB smoothed the curves of the side force versus yaw angle up to an angle of attack of 30° (Fig. 19). It maintained a monotonously increasing side force, apparently by preventing asymmetric-vortex breakdown and local separations and rapid shifts of the lateral center of pressure. The SWB lost its influence on the side force only at $\alpha = 35°$.

The effect of blowing on the yawing moment is shown in Fig. 20. Without blowing, the configuration was gradually losing its lateral stability at lower yaw angles when the angle of attack was increased (Fig. 20a), until at $\alpha = 25°$ it was too unstable for practical purposes (Fig. 20b). SWB increased the stability at the lower angles of attack (Fig. 20a) and stabilized the configuration at $\alpha = 25°$ and 30° up to yaw angles of 30° ± 32°. At an angle of attack of 30°, the higher blowing rate was required on both wing and canard for stabilization, but even this rate was insufficient for stabilization at $\alpha = 35°$. In summary, like Configuration A, Configuration B was also limited in angle of attack by lateral/directional

instability rather than by stall. Spanwise blowing increased the flight envelope and improved performance by stabilizing the configuration and increasing the available lift.

3.3 Comparison of SWB with the Canard

Figures 21 and 22 summarize the results of this investigation. Lift and drag results, with and without the canard, are compared with and without blowing. All the results are with thrust removed. Spanwise blowing with a jet-momentum coefficient of $C_\mu = 0.05$ (a lower one will probably also do) gives about the same lift characteristics as the canard (Fig. 21, circles vs dashed line), both in lift-curve slope and in maximum lift, and with a much lower drag (Fig. 22). The canard increases the drag for a given lift coefficient whereas the SWB reduces it. Furthermore, while SWB can be turned on or off as required and can thus conserve energy during most phases of a mission profile, the penalty of increased drag and additional deadweight of the canard persists throughout the flight envelope, even when the canard is not needed. The lateral/directional effects of SWB are also much better than effects of the canard (not shown); it enables the airframe to fully exploit its maximum lift without additional stabilizing aids like the wing-leading-edge sawtooth or the mustache on the Kfir-C2 aircraft. The lift curve and drag polar of the close-coupled-canard of Configuration B, with SWB over both wing and canard, are shown in Figs. 21 and 22 for overall comparison. The additional gains in both lift and lift-to-drag ratio are impressive.

4. CONCLUSIONS AND RECOMMENDATIONS

1. Spanwise blowing on Configuration A over the highly swept (60°) delta wing with a conically drooping leading edge increased the maximum lift and the slope of the lift curve. The efficiency of increasing the maximum lift (5.60 for $C_\mu = 0.05$ and 4.29 for $C_\mu = 0.07$) was higher than previously reported for similar delta wings (Ref. 21) and almost as high as efficiencies found on the moderately swept wings (45° and 32°) of Refs. 8, 19, and 20.

2. SWB over this wing significantly improved the lift-to-drag ratio.

3. Asymmetric blowing did not pose a control problem, but could be used to augment the roll response of the aircraft.

4. The efficiency of the SWB was quadrupled using swirling jets, without any additional penalty. The use of swirling jets has to be further investigated, as well as the possible use of more than one jet to improve mixing and entrainment.

5. SWB increased the lateral/directional stability of Configuration A at low angles of attack and stabilized it in its naturally unstable region of $25° < \alpha < 30°$, thus enabling it to exploit its full maximum-lift capability.

6. SWB over the wing of Configuration A achieved the same lift augmentation (thrust removed) as did the canard, but at a much lower drag.

7. SWB on Configuration B, over the wing only, further improved both the lift curve and the drag polar, but at a lower efficiency than with SWB on Configuration A (without a canard).

8. SWB on both wing and canard of Configuration B augmented the lift and improved the drag polar more than did blowing on the wing alone. The efficiency of SWB over both lifting surfaces was higher than that of blowing over the wing only.

9. In both cases of blowing on Configuration B, the blowing efficiency increased when the jet momentum was increased, contrary to past and present experience with blowing over wings alone.

10. Configuration B was stabilized by SWB up to high yaw angles at angles of attack up to 30°, and could therefore use the maximum lift that could not be reached previously because of lateral/directional instability.

11. SWB on Configuration B has to be investigated in high-subsonic-speed flows where Ref. 20 reported lift augmentation of the order found in the low-speed experiments. Supercritical transonic testing is also needed to find out if the same blowing system, with reasonable momentum coefficients, could achieve the shock-induced-separation control reported in Ref. 24.

12. As a result of Erickson's comments (Ref. 23) about the feasibility of practical application of SWB with engines designed for high bleed rates and low sensitivity of thrust loss to engine bleed, and the success of SWB with the VEO-wing concept, further investigation is recommended concerning the possibility of bleeding the engine combustion products downstream of the turbine instead of bleeding the compressor air. This would require longer and heat-insulated piping but will affect the thrust to a much lesser degree. The hot gases may also be used to preheat the fuel, thus compensating for the remaining thrust loss.

REFERENCES

1. Stanbrook, A. and Squire, L. C., "Possible Types of Flow at Swept Leading Edges," The Aeronautical Quarterly, Vol. 15, Feb. 1964, pp. 72-82.

2. Polhamus, E. C., "Predictions of Vortex-Lift Characteristics by a Leading-Edge Suction Analogy," Journal of Aircraft, Vol. 8, April 1971, pp. 193-199.

3. Rusak, Z., Wasserstrom, E., and Seginer, A., "Numerical Calculation of Nonlinear Aerodynamics of Wing-Body Configurations," AIAA Journal, to be published June or July 1983.

4. Wentz, W. H., Jr. and Kohlman, D. L., "Wind Tunnel Investigations of Vortex Breakdown on Slender Sharp-Edged Wings," NASA CR-98737, 1969.

5. Erickson, G. E., "Effect of Spanwise Blowing on the Aerodynamic Characteristics of a Half-Span 50°-Swept Cropped Delta Wing Configuration," AIAA Paper 79-1859, AIAA Aircraft Systems and Technology Meeting, New York, N.Y., Aug. 1979.

6. Clarke, K. P., "Lift Augmentation on a Moderately Swept Wing by Spanwise Blowing," Aeronautical Journal, Vol. 80, Oct. 1976, pp. 447-451.

7. Kuchemann, D., "On the Possibility of Designing Wings that Combine Vortex Flows with Classical Airfoil Flows," RAE Tech. Memo. Aero. 1363, Oct. 1971.

8. Staudacher, W., Laschka, B., Poisson-Quinton, P., and Ledy, J. P., "Effect of Spanwise Blowing in the Angle-of-Attack Regime $\alpha = 0 \div 90°$," Proceedings of the 11th Congress of ICAS, Vol. 1, Sept. 1978, pp. 85-95.

9. Behrbohn, H., "Basic Low-Speed Aerodynamics of the Short-Coupled Canard Configuration of Small Aspect Ratio," SAAB, Sweden, TN-60, July 1965.

10. Leibovich, S., "The Structure of Vortex Breakdown," Annual Review of Fluid Mechanics, Vol. 10, 1978, pp. 221-246.

11. Cornish, J. J., III, "High Lift Applications of Spanwise Blowing," ICAS Paper No. 70-09, 7th Congress of ICAS, Rome, Italy, Sept. 1970.

12. Dixon, C. J., "The Mechanism of Vortex Control by Spanwise Blowing and Wing Geometry," Lockheed-Georgia Co., Marietta, Ga., Engineering Report LG78-ER-0187, June 1978.

13. Leavitt, D. L., Whitten, P. D., and Stumpfl, S. C., "Low Speed Aerodynamic Characteristics of a Vectored-Engine-Over-Wing Configuration," AIAA Paper 78-1081, AIAA/SAE 14th Joint Propulsion Conference, July 1978.

14. Falarski, M. D., Dudley, M. D., and Howell, G. A., "Analysis of Data from a Wind Tunnel Investigation of a Large-Scale Model of a Highly Maneuverable Supersonic V/STOL Fighter: STOL Configuration," AIAA Paper 81-2620, AIAA/NASA Ames Research Center V/STOL Conference, Dec. 1981.

15. Howell, G. A., "Test Results of Chordwise and Spanwise Blowing for Low-Speed Lift Augmentation," *Proceedings of the 13th Congress of ICAS and AIAA Aircraft Systems and Technology Conference*, Vol. 2, Aug. 1982, pp. 1222-1234.

16. Dixon, C. J., "Lift Augmentation by Lateral Blowing Over a Lifting Surface," AIAA Paper 69-193, AIAA/AHS VTOL Research, Design and Operations Meeting, Feb. 1969.

17. Poisson-Quinton, P., "Contrôle du D'ecollement D'use Surface Portante par un Jet Transversal," Intervention au 7 iem Congress ICAS, Rome, Sept. 1970.

18. Bradley, R. G. and Wray, W. O., "A Conceptual Study of Leading-Edge-Vortex Enhancement by Blowing," Journal of Aircraft, Vol. 11, Jan. 1974, pp. 33-38.

19. Campbell, J. F., "Augmentation of Vortex Lift by Spanwise Blowing," Journal of Aircraft, Vol. 13, Sept. 1976, pp. 727-732.

20. Bradley, R. G., Whitten, P. D., and Wray, W. O., "Leading-Edge-Vortex Augmentation in Compressible Flow," Journal of Aircraft, Vol. 13, Apr. 1976, pp. 238-242.

21. Anglin, E. L. and Satran, D., "Effects of Spanwise Blowing on Two Fighter Airplane Configurations," AIAA Paper 79-1663, AIAA Atmospheric Flight Mechanics Conference, Aug. 1979.

22. Dixon, C. J., Theisen, J. G., and Scruggs, R. M., "Theoretical and Experimental Investigations of Vortex Lift Control by Spanwise Blowing, Vol. 1, Experimental Research," Lockheed-Georgia Co., Marietta, Ga., Engineering Rept. LG73-ER-0169, Sept. 1973.

23. Erickson, G. E., "Effect of Spanwise Blowing on the Aerodynamic Characteristics of the F-5E," Journal of Aircraft, Vol. 16, Oct. 1979, pp. 695-700.

24. Dixon, C. J., Dansby, T., and Poisson-Quinton, P., "Benefits of Spanwise Blowing at Transonic Speeds," Proceedings of the 11th Congress of ICAS, Vol. 1, Sept. 1978, pp. 72-84.

ACKNOWLEDGMENT

The first author is a National Research Council Research Associate, on leave from the Department of Aeronautical Engineering, Technion-Israel Institute of Technology, Haifa, Israel.

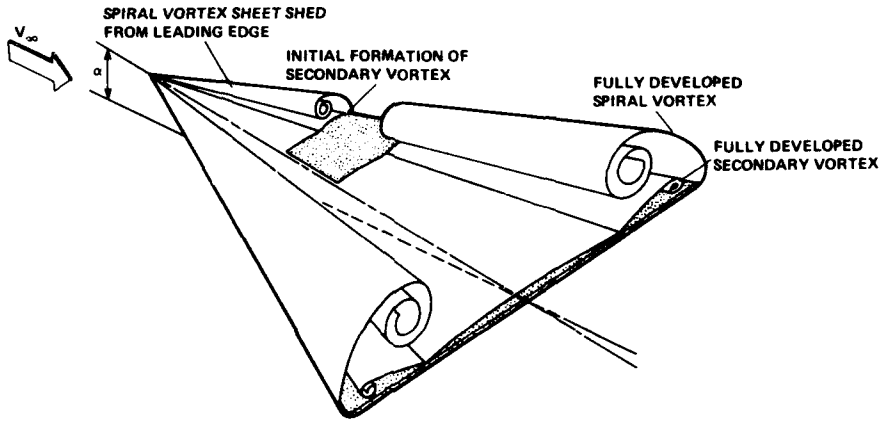

Fig. 1. Sharp leading-edge-induced vortical flow field.

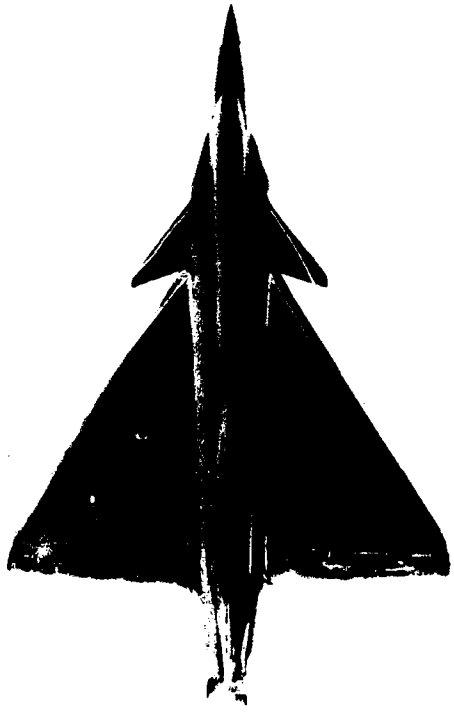

Fig. 2. Aircraft model – Configuration B.

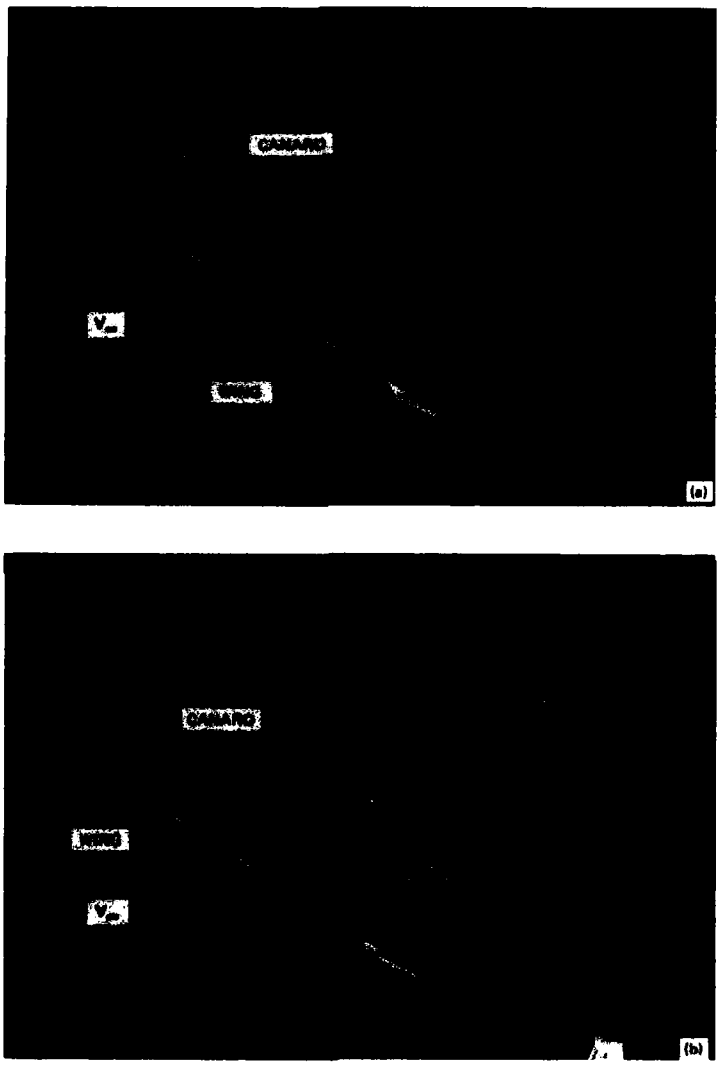

Fig. 3. Main-wing vortex breakdown and stabilization. (a) Breakdown. (b) Stabilization by SWB.

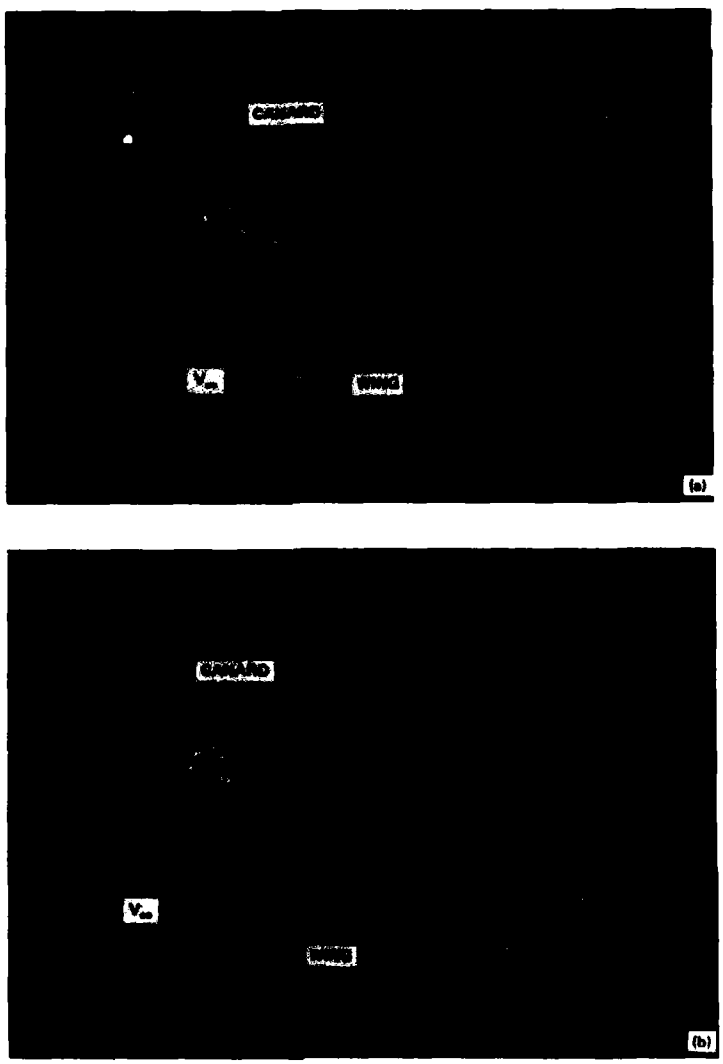

Fig. 4. Canard-vortex breakdown and stabilization. (a) Breakdown. (b) Stabilization by SWB.

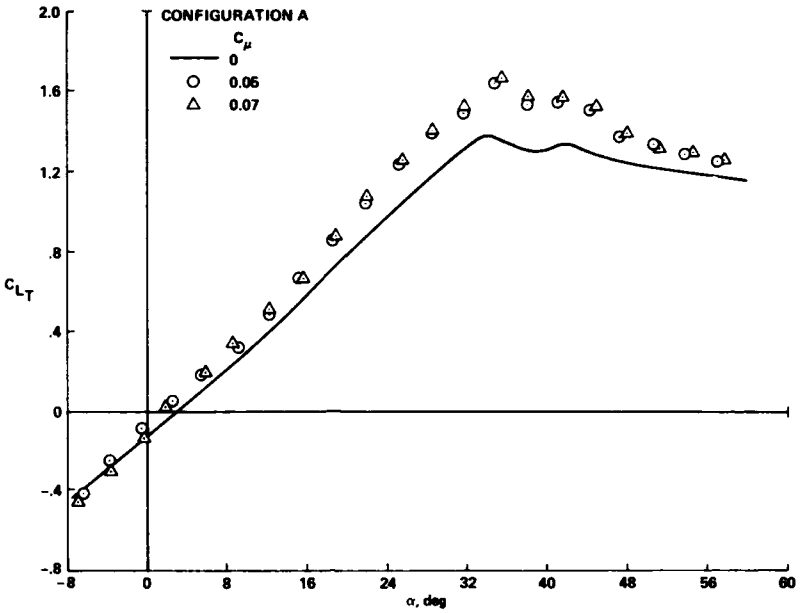

Fig. 5. Configuration A – lift augmentation.

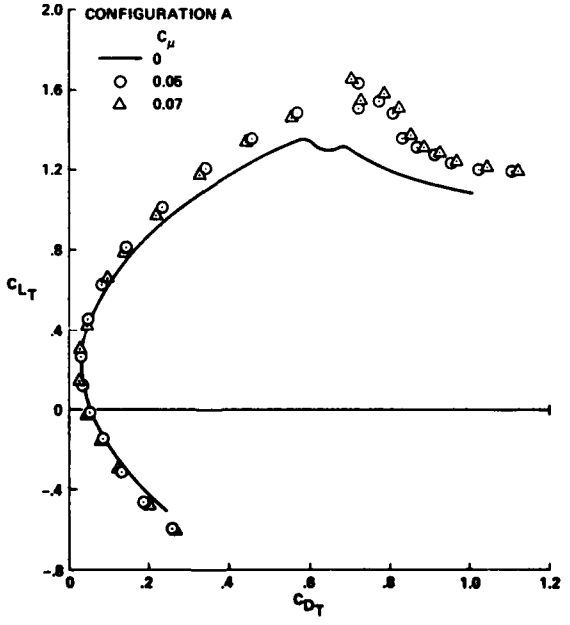

Fig. 6. Configuration A – drag polar.

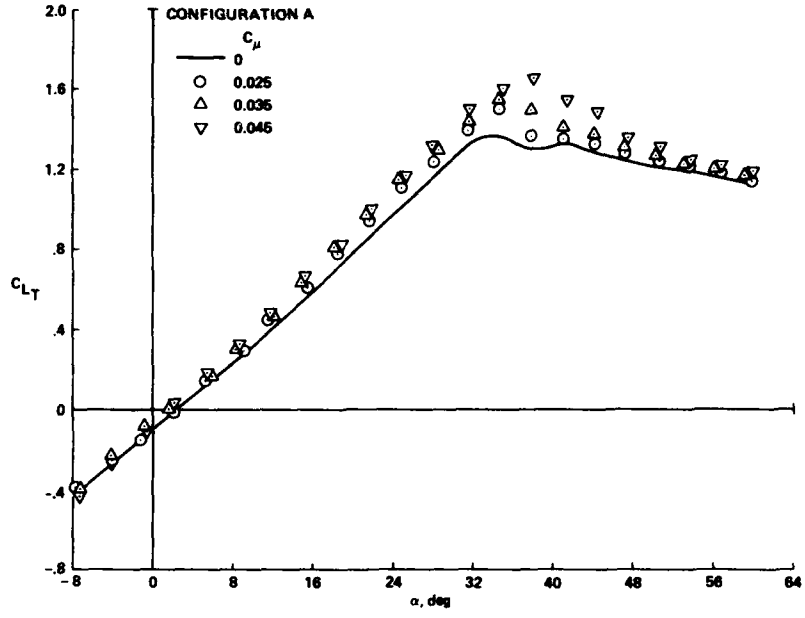

Fig. 7. Lift augmentation – left wing SWB only.

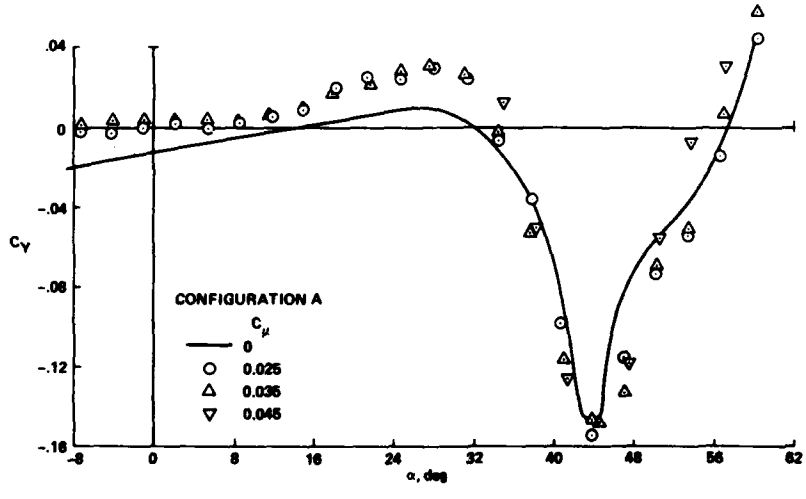

Fig. 8. Side force induced by left wing SWB.

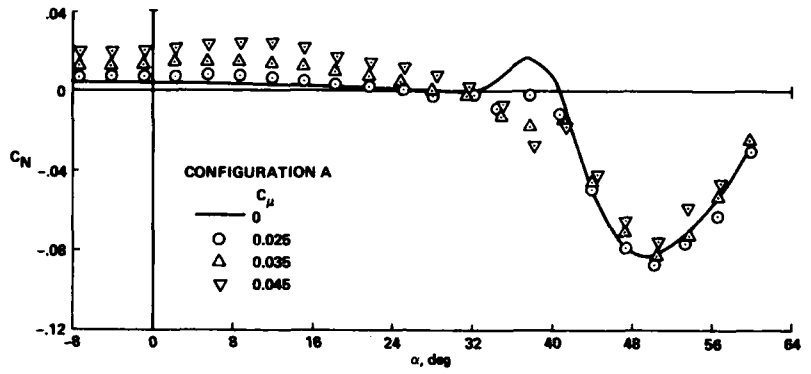

Fig. 9. Yawing moment induced by left wing SWB.

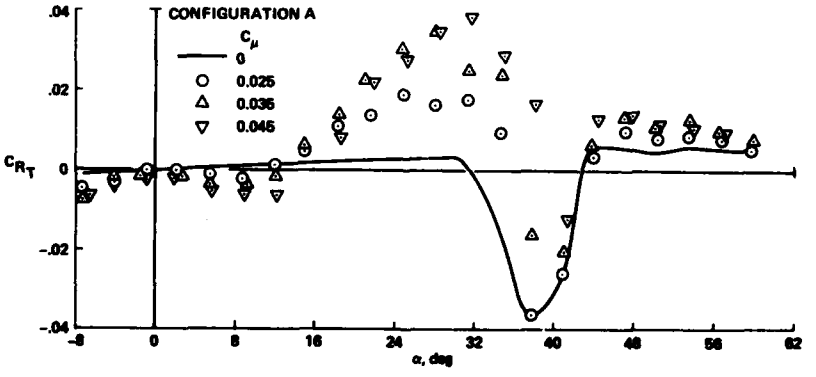

Fig. 10. Rolling moment induced by left wing SWB.

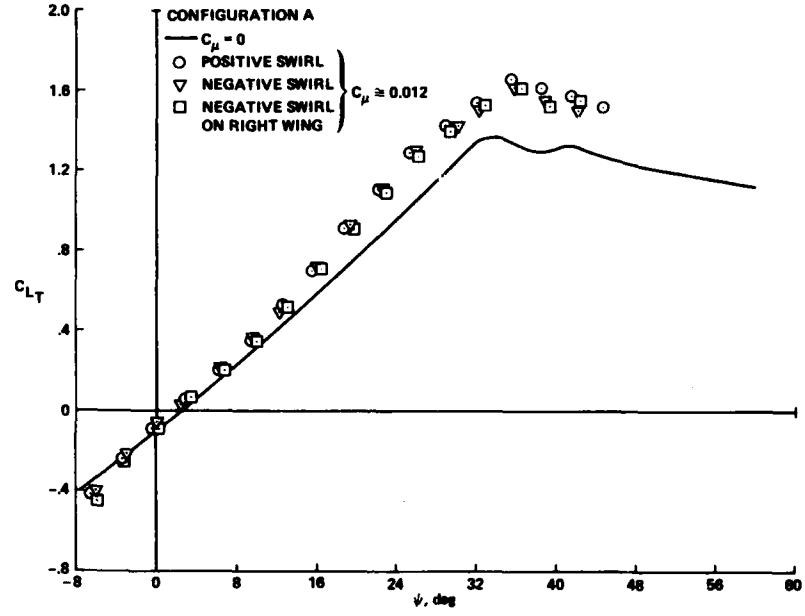

Fig. 11. Lift augmentation – swirling jet SWB.

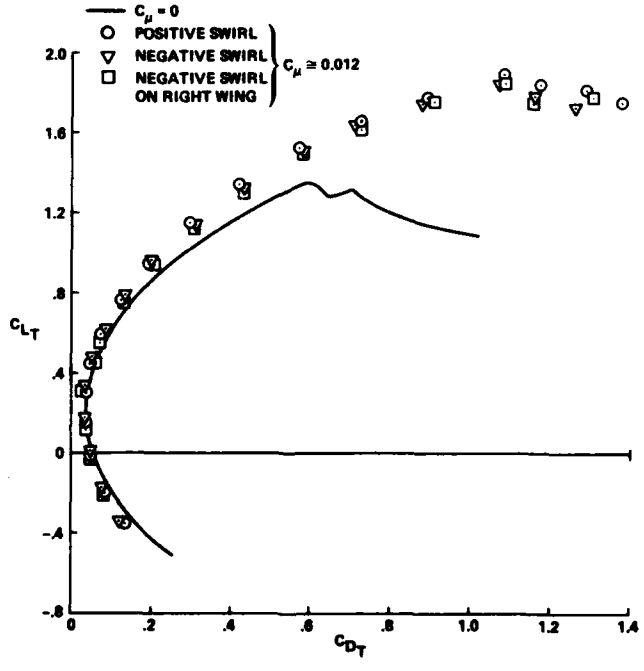

Fig. 12. Drag polar – swirling jet SWB.

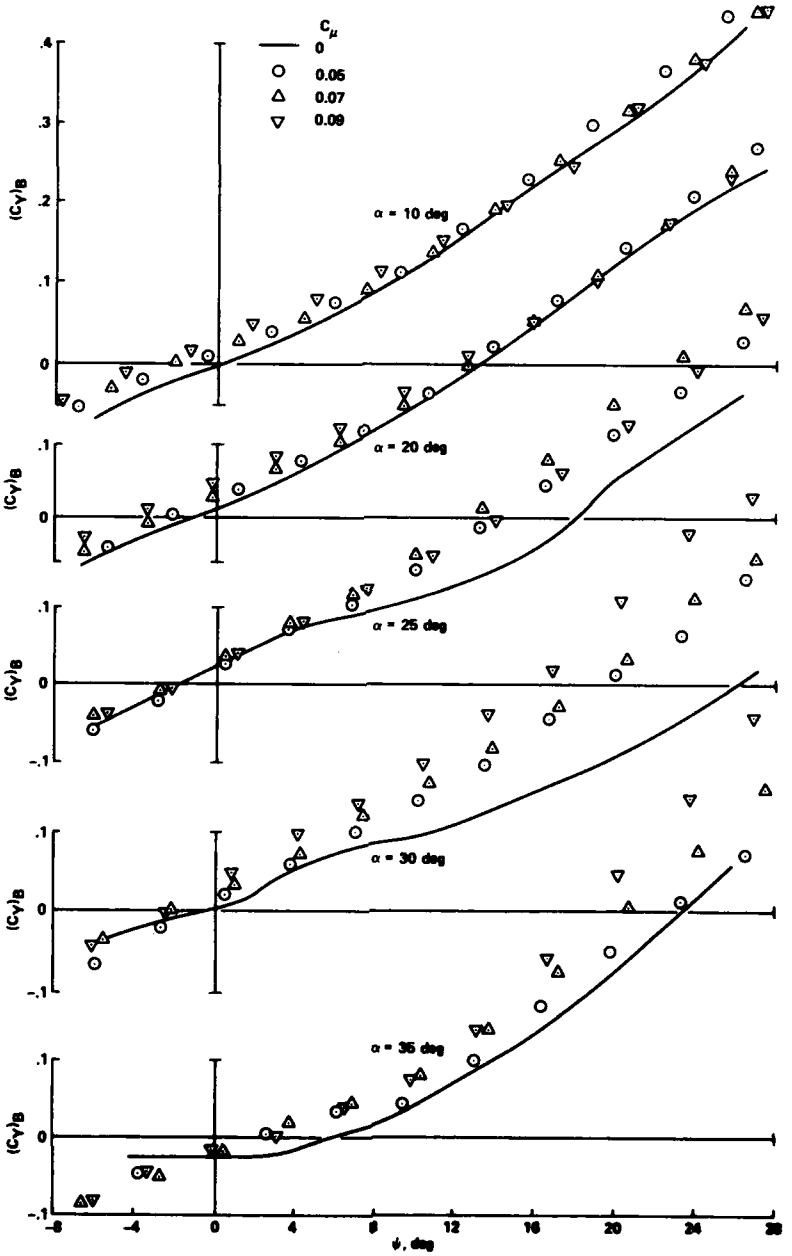

Fig. 13. Configuration A – lateral stability, side forces with SMB.

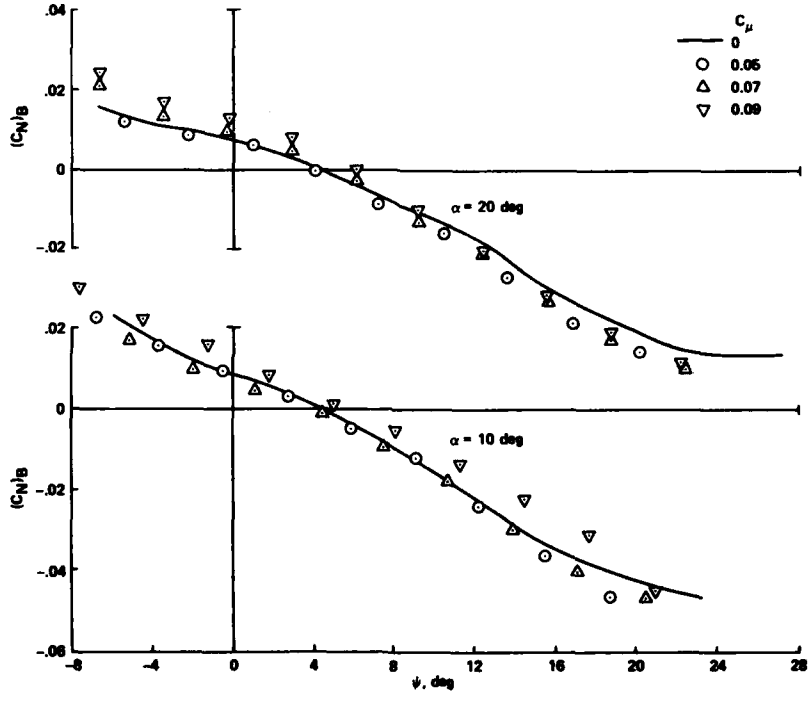

(a) α = 10° and 20°.

Fig. 14. Configuration A – lateral stability, yawing moments with SWB.

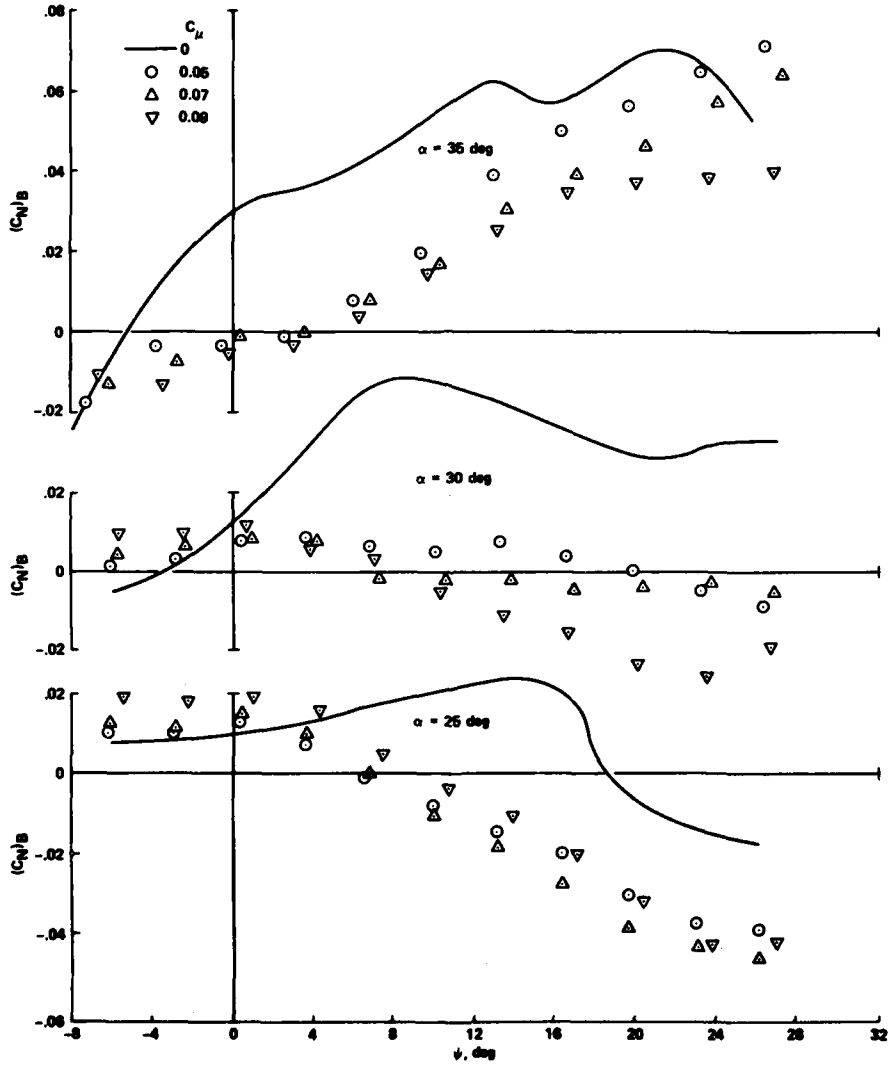

(b) α = 25°, 30°, and 35°.

Fig. 14. Concluded.

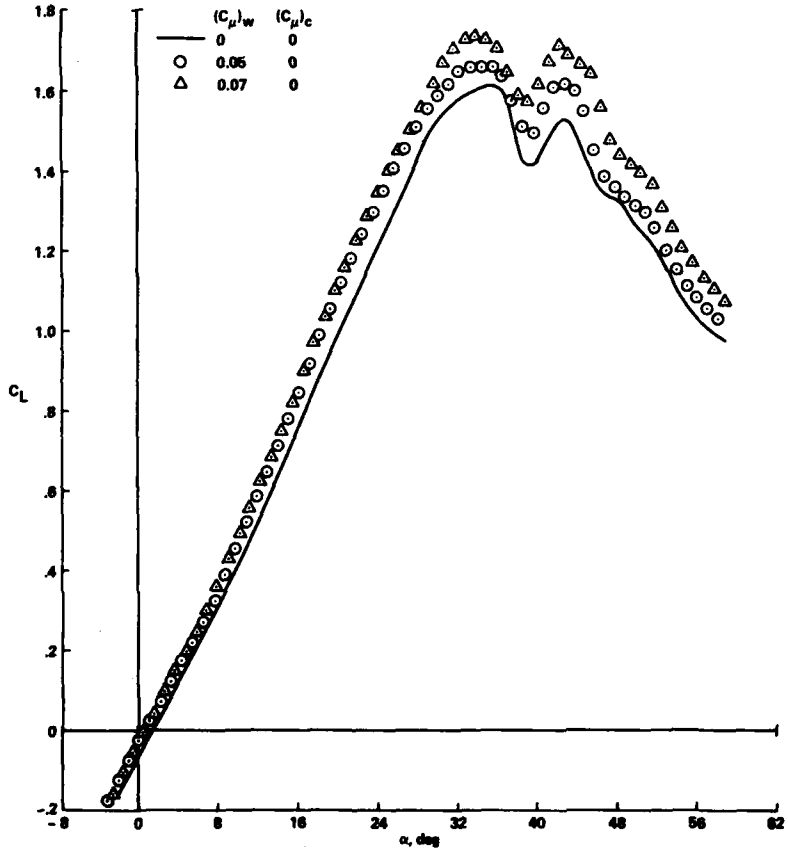

Fig. 15. Configuration B – lift augmentation by SWB over the wing only.

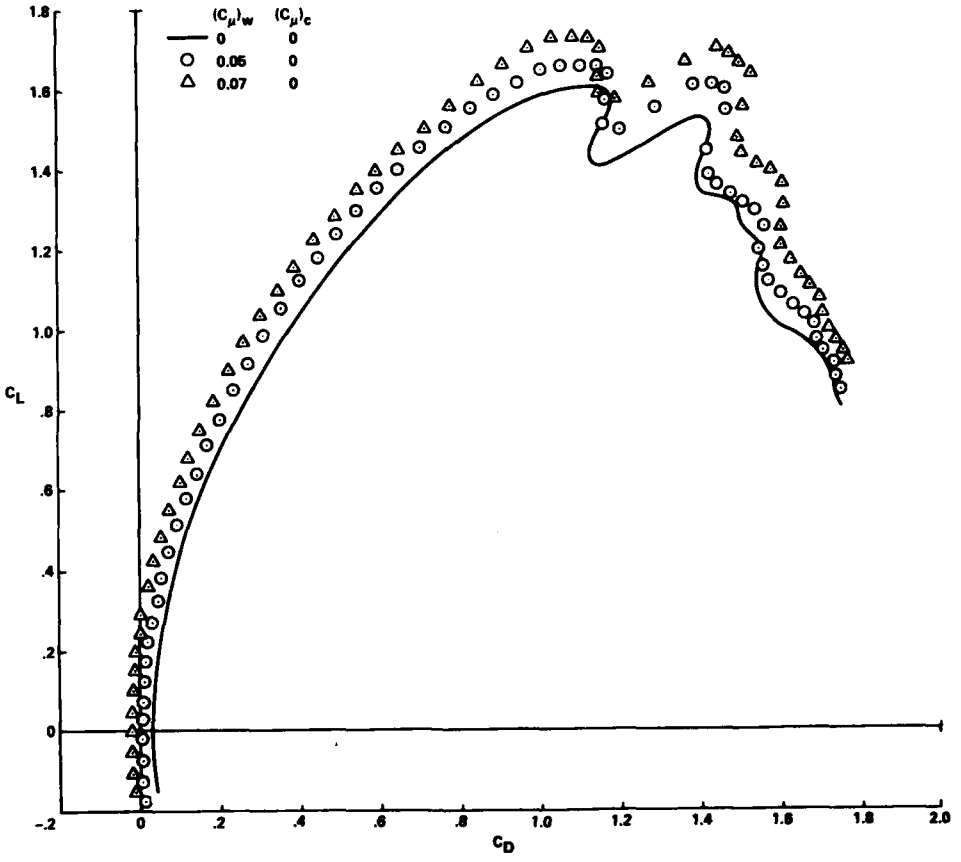

Fig. 16. Configuration 8 – drag polar by SWB over the wing only.

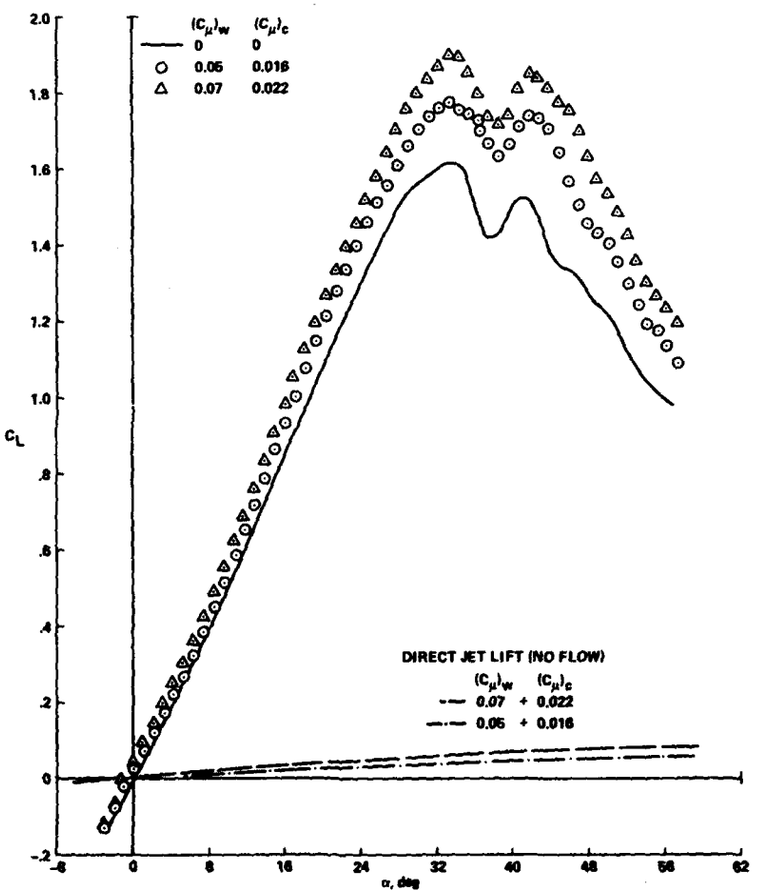

Fig. 17. Configuration B – lift augmentation by SWB over both wing and canard.

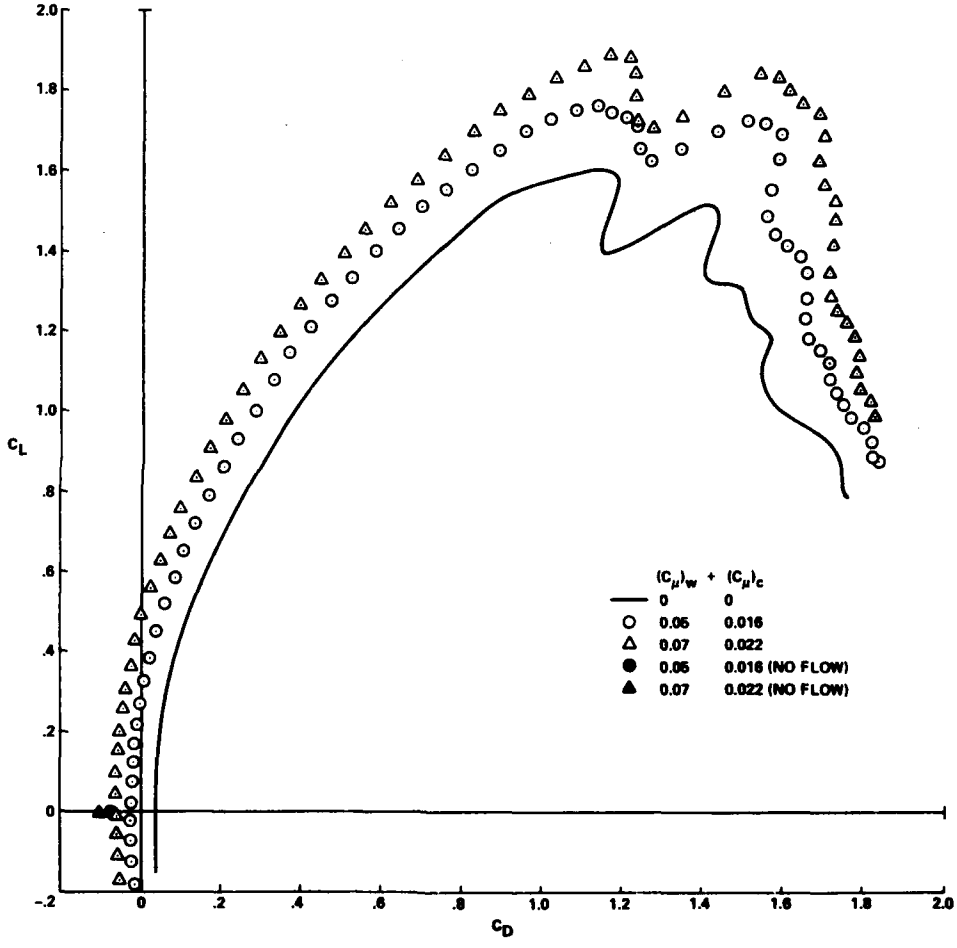

Fig. 18. Configuration B – drag polar by SWB over both wing and canard.

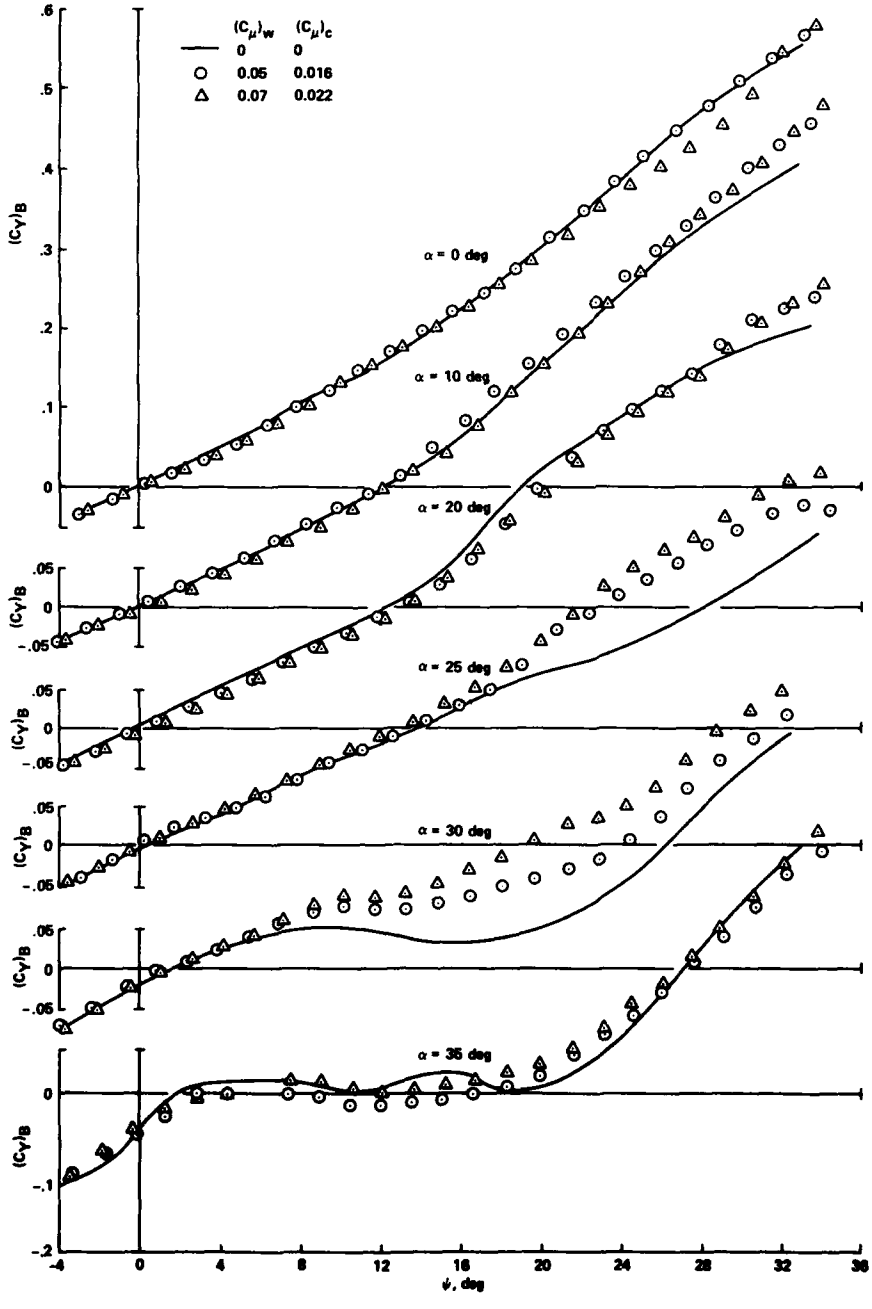

Fig. 19. Configuration B – side forces by SWB over both wing and canard.

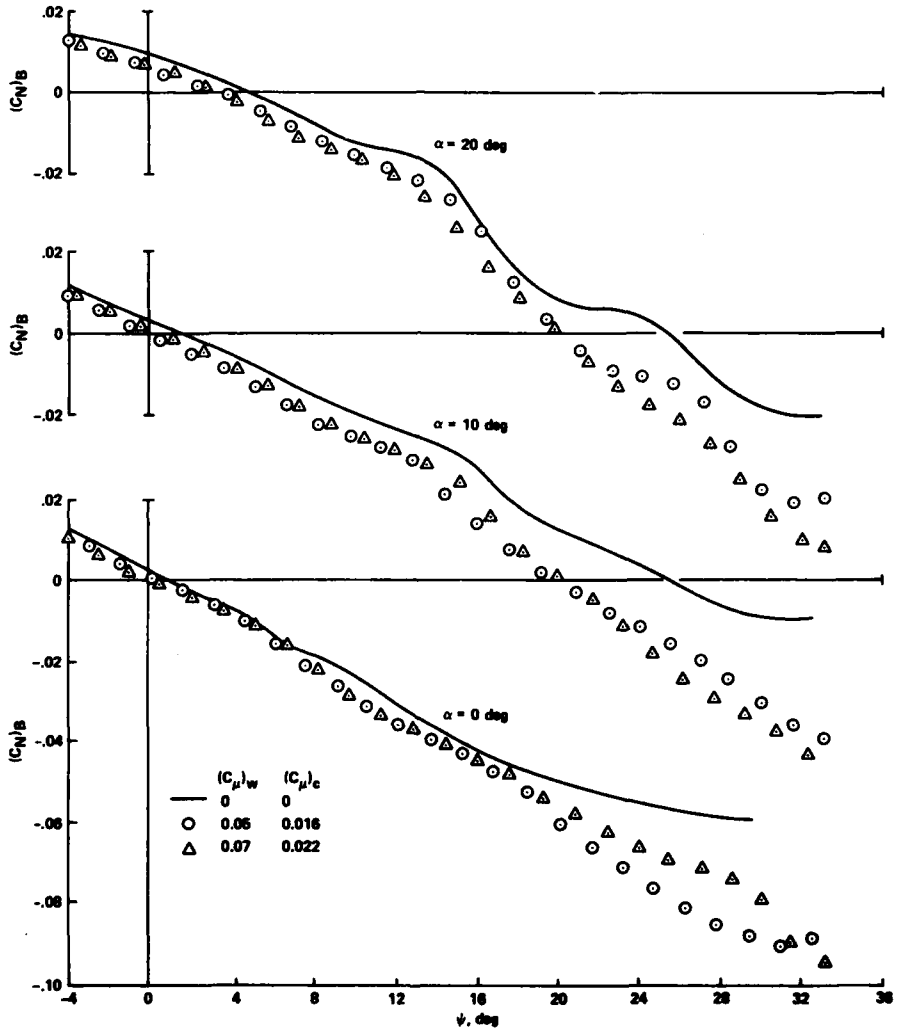

(a) α = 0°, 10°, and 20°.

Fig. 20. Configuration B – yawing moments by SWB over both wing and canard.

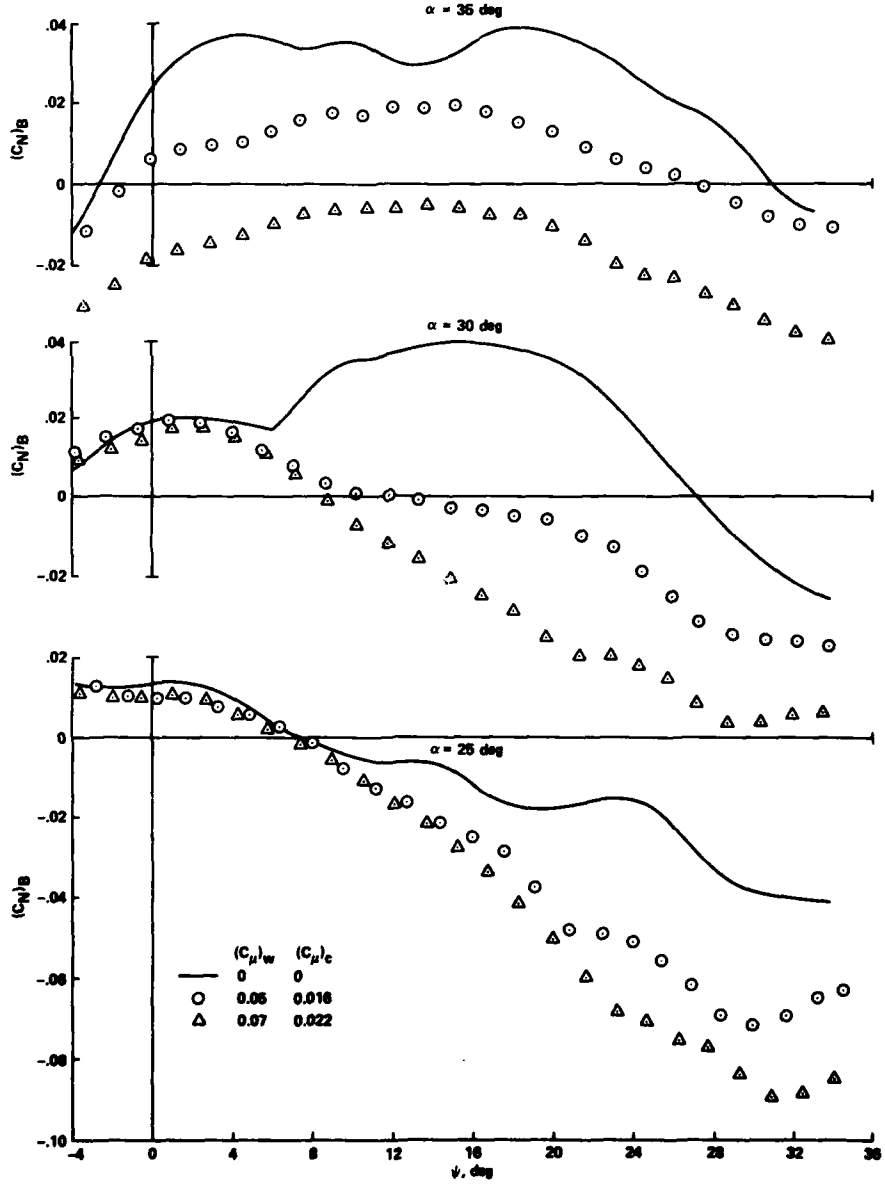

(b) α = 25°, 30°, and 35°.

Fig. 20. Concluded.

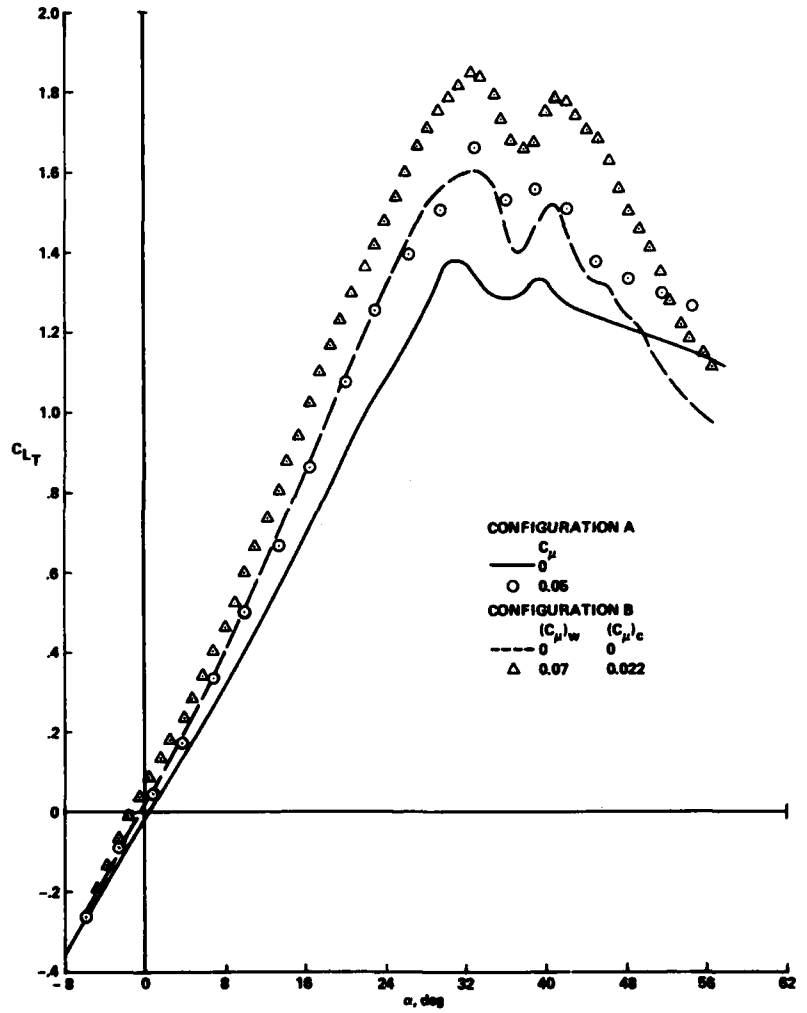

Fig. 21. Lift augmentation – canard versus SNB.

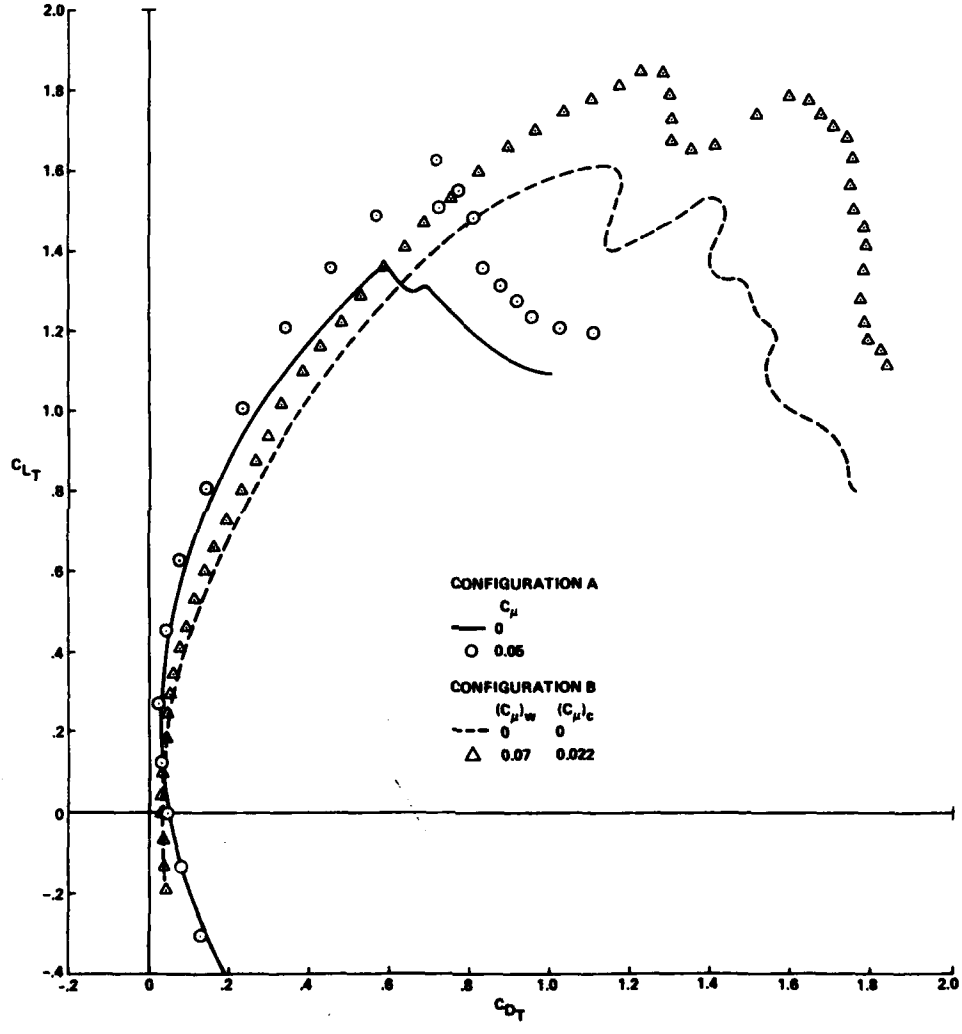

Fig. 22. Drag polar – canard versus SMB.

FLUID DYNAMICS PANEL

Symposium on Aerodynamics of Vortical Type Flows
in Three Dimensions

Prof. Young

The first thing I would like to do is to ask Mr. Jeremy Smith to present a summary of what he sees as the main highlights of the meeting. He has very kindly agreed to do this. Then we will open the discussion to anyone who wishes to make any particular point or comment on the meeting or perhaps ask a final question of any of the lecturers who are still here.

But just before I get Mr. Smith to speak, I would like to show you a viewgraph which was given to me by David Peake; which, if you needed any justification for having sat here for several days and listened to the various lectures, will provide that justification.

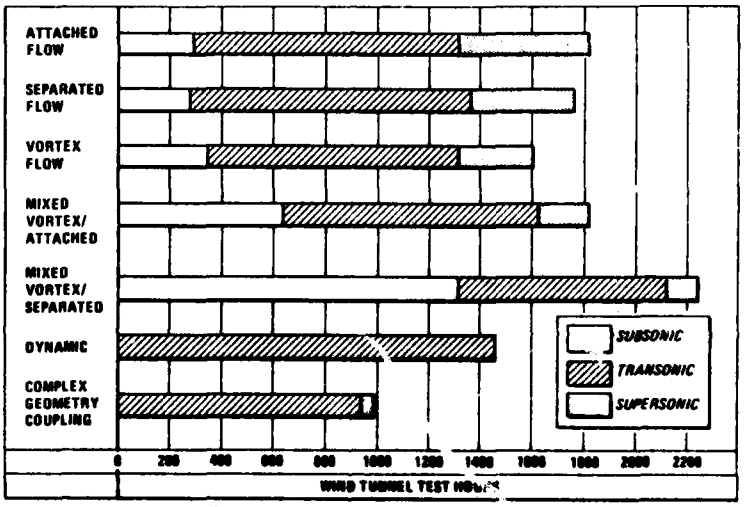

Breakout of F-16 Wind Tunnel Testing by Flow Field Complexity.

What this shows is a breakdown (they call it a breakout) of the number of windtunnel test hours devoted to the F16, and it is broken down according to various aspects of the flow fields. You'll see seven different aspects which were considered, of which the three middle are all involving vortex flows of one kind or another. The different shadings as you see from the key refer to subsonic, transonic and supersonic speeds. Of course, the transonic regime in most cases plays a very dominant part. But the point I want to make is that those three central bars, referring to vortex flow, mixed vortex and attached and mixed vortex seperated, actually comprise half the total windtunnel test hours that have been devoted to this aircraft. So the importance of vortex flows in the flow regime of main concern is very clearly brought out by this chart. Now I will ask Jeremy Smith to give you his views as to what are the main points that have emerged from this meeting.

Mr. J.H.B. Smith

Thank you Prof. Young. I haven't made a great attempt to fish out what seemed to be the really most important things. I have fished out the things that seemed to me to be interesting and attractive. Since I have to write a technical evaluation report later, perhaps I'll try and attend to the things that are really important in that.

Let me say first that I think that this has been a very successful conference. The arguments seemed to start quite early on the first day and I felt at the time that that was a good sign, and I think that the same spirit has been kept up. We were very well served by at least four of the invited speakers; David Peake produced an excellent collection of pictures to remind us in that international pictorial language what it was we were here to discuss. John Lamar introduced us to a most impressive volume of work which has been proceeding recently in and around Langley, much of which was certainly new to me. Harry Hoeijmakers gave us an invigorating gallop over the extraordinarily extensive landscape of calculation methods; quite clearly the collection of references in his paper, as in the case of John Lamar's paper, will be extremely useful to everyone in the field. Sidney Leibovich made an extremely gallant attempt to encapsulate the essence of vortex breakdown in 40 minutes.

I think that the general standard of presentation was good. I guess that every speaker was understood by at least someone in the audience, and perhaps a few people managed to understand all the speakers. I wasn't among them. The slides were good on the whole, and of course, they had to be pretty good if you were trying to read them off the ceiling or off the backs of the heads of the people in front of you. I think that we should be very grateful to all our speakers, and, of course, we should also be very grateful to the interpreters. The balance between presentations and questions was also good, I thought, about

right. As usual, there was a lack of time for discussion on topics which had been covered by a group of papers, and for authors and questioners to express second thoughts on subjects. Most of us will have had some fairly intensive private discussions in various places over the last few days. The only time that we have a chance to bring out the results of these discussions is when I stop talking in a minute or two. So, I propose to stop before very long and ask you to continue the discussion. Before doing that, I am supposed to remind you a little of what has happened. As I say, I can do no more than draw attention to things I found particularly striking.

First of all, a comment about topology. Actually, not about topology, but about my assessment of the value of looking at the topology of different sorts of streamlines. First of all, conical streamlines only exist for conical flow; obvious statement. Body and vortex sheet are streamlines, the streamlines tend to the radial direction as you go a long way away from the body. I believe conical streamlines have some value. Now, about cross flow streamlines, they always exist. The body and the vortex sheet are not usually streamlines. They tend to the vertical direction at a large distance from the cross section, and my assessment is that they have no value. Unfortunately, David Peake, who might like to argue the points, has left. My final remark is that any topological characterization of the fully three-dimensional flow would be very useful. I wish Dr. Vollmers and his colleagues all success.

On this theme of appreciating the structure of three-dimensional flows there is no doubt that technical developments have helped a lot. I think that Dr. Verhaagen's work with the laser illuminated smoke was particularly helpful. Computer graphics help in appreciating numerical results, and here I would instance Dr. Rizzi's contour plots in their correct spatial orientations, and Dr. Hoeijmakers' computer animation of his calculations. However, technical developments also sometimes distance us from what is really going on. I felt that I understood more of what Dr. Strange was telling us about trailing vortices from the photographs she showed than I did from the composite picture based on the conditional sampling technique. The second example, the controversial results which Dr. Wendt presented on compressible leading edge vortices, seemed to me just a little less certain because of the laser technology which was involved in obtaining them. The same sort of thing applies in the computing field. We have to learn whether such things as artificial viscosity and local time marching are or are not coming between us and the physics.

I think that we were all impressed by the agreement between the vortex breakdown boundaries which were measured and computed by Messieurs Delery and Horowitz. After the session on vortex breakdown, I felt a little confused and sought reassurance on some fundamental points. It seems to be agreed that breakdown, at least in the aeronautical context, is still an inviscid phenomenon. The frequent appearance of Reynolds number on the screen in the course of the presentation seems to be incidental and not fundamental to the subject. It also seems possible that unsteadiness is an important part of vortex breakdown. That seems significant because we are being offered calculations by time-dependent Euler methods of flows over delta wings, and one could imagine a situation in which a sufficiently fine mesh was employed, so that the method which calculates the development of the vortex might also calculate its breakdown.

Two things stood out for me in John Lamar's paper. First, the large change in pressure distribution on the TACT F-111 between the Reynolds numbers of 20 and 40 million. Second, the appearance of the two calculated vortex sheets on the double-delta wing. Dr. Erickson's paper made me realize how far we still are from explaining the forces and moments on aircraft at high angle of attack in terms of fluid mechanical ideas. I felt a little more hopeful about the missile flow fields that Mr. Peckham presented. They looked hard, but not impossibly so. I was intrigued by Dr. Vollmers' displacement tensor and his use of eigen-vectors but I do not claim yet to have understood it. The most significant thing for all of us is probably the emergence of methods for solving the Euler equations which represent regions of vortical flow over wings. These regions occur where we should expect to see them and induce surface pressures which can be like those measured. What we need to see is that the results are reasonably independent of such non-physical parameters as mesh size and artificial viscosity. We also need to convince ourselves that the reduction in total pressure in the vortical region is not important or else find ways to avoid it. The ideas of Dr. Steinhoff for incorporating vortex filaments and particularly vortex sheets into a potential flow seem very attractive. Essentially he seems to have managed to divorce the vortex elements from the computing grid. I hope that what you have heard this morning is still sufficiently fresh in your memory that you do not need me to remind you of it. What I have tried to do is to remind you of some of the unresolved questions and to provoke some discussion. First of all, does anyone feel that he has an answer to any of the mysteries that have been exposed to us.

Prof. Young

I think Jeremy is being particularly modest in not referring to his own excellent review paper; I will fill that gap and say how much I enjoyed that paper, and I am sure that everybody did.

After that very pertinent and valuable review of what has gone on in the past few days, I would like now to have any questions, comments or contributions from you. Has anyone got any point that they wish to make or comment on the meeting as a whole?

Dr. Poll

I should like to address the question of the F-111 results which seem to have impressed you so greatly. After Mr. Lamar's paper, I did comment that 'you pick a length and you get a Reynolds number - if you pick a length which is big, you get a number which is big.' On the F-111, the 20 million and the 40 million are mean chord Reynolds numbers, had they taken the fuselage length, then you could have had 80 million, which is an even bigger number! However, to account for the disappearance of the vortex flow, one ought to take a Reynolds number based on a more relevant length scale - such as the leading edge diameter. The tiny picture which is in John Lamar's paper just gives you enough information to make some estimates. Doing a quick calculation on the back of an envelope, you find that, based on leading edge diameter, the Reynolds numbers are 1×10^5 to 2×10^5 and these numbers lie in the critical region for the three-dimensional boundary layer transition mechanisms with which some people will be familiar. In fact, they precisely bracket the range in which transition induced scale effects are known to occur. Therefore,

it is really of no surprise to me that if you switch off the primary separation sheet for any reason, then the vortex flow immediately collapses. So be very careful when you define Reynolds numbers. Some of these effects are boundary layer phenomena, and they are feeding directly into shear layer phenomena.

Mr. J.H.B. Smith

Ian, what estimate of the leading edge radius did you use to make that estimate of the local Reynolds number, because some people here may know what it is?

Dr. Poll

It is on the picture in John Lamar's paper; there is a little picture of the leading edge radius with the pressure distribution. It is about an inch if I may use Imperial terms.

Dr. McCroskey

That is a good point that has just been made about not necessarily assuming flows are at high Reynolds number just because there is some length that is large in the body in question. On the other hand, I think that it points out the problems that one might encounter in trying to do scale models of this sort of flow. Considering the sort of arguments that you are making about the relevant Reynolds numbers obtained in the aircraft, think what these values must be in the small-scale water tunnel and wind tunnel models. Then one wonders what relevance they have indeed to the flight measurements.

Mr. J.H.B. Smith

My reaction to that would be that it would depend very much on what sort of leading edge sweep one was dealing with. I think that the transition phenomena that Dr. Poll was talking about are effecting things on rather lower angles of sweep, perhaps, than a lot of the work done in water tunnels.

Dr. Murman

I would like to just put in the request for those of us who are going to be involved in the computational activities for the establishment of some good data sets for comparison of computational methods. I know the delta wing which Art Rizzi showed has been selected as one of the data sets for the AGARD working group, but perhaps there are others that people would like to suggest that will help in the future years sorting out and validating the computational methods.

Mr. J.H.B. Smith

Would Dr. Yoshihara like to comment on that as Chairman of the Working Group?

Dr. Yoshihara

I think that with perhaps just 6 months left of the working group, I certainly would not entertain additional models, but I think you have a very good point; we really lack good data sets.

Dr. Schmidt

Just to add a comment to what you mentioned earlier about the inviscid behavior of the vortex breakdown. I think that you might be aware that at the AIAA conference in January we gave some first results in three dimensions on this vortex breakdown phenomenon based on the Euler solution. In this case, we have about 100 points on the surface in x-direction so that the resolution was fairly dense in the x-direction, but not fine enough, we must admit, to give definite statements in the other direction. So there are some first indications that this might happen, what you were saying, but it is not decisive for the moment.

Mr. J.H.B. Smith

I was mentally comparing the sort of mesh that you have in three dimensions with the sort of mesh which M. Delery had in his axi-symmetric flow.

Mr. McRae

Not wishing to belittle in any way the gallant efforts of all the speakers, but there is one problem, which is a very practical problem, that we have heard nothing about, and that is what the criterion is, probably in terms of separation line sweep and other conditions, perhaps Reynolds number, which separate the regimes of ordered vortex flow downstream of the separation from chaotic flow with high buffeting levels.

Mr. J.H.B. Smith

It would be a rash man that inserted a figure at this moment, wouldn't it?

Prof. Young

The papers on the stability and breakdown of vortices did give some indication of criteria that are beginning to emerge. I agree with you that I don't think at this stage one could say that there was anything that clearly would be applicable in general terms. The available criteria would be applicable only to the kind of vortices considered. Certainly for many aeronautical problems, we are faced with vortices which are half immersed in non potential flows, in bits of boundary layer and in wider ranging vortical flows, and presumably their stability and breakdown will be much more complex than in the kind of models that have been considered so far.

I don't know whether Prof. Leibovich is here to add anything to that.

However, I would think that even so it is worth examining the available criteria to see whether any look relevant to the particular problem with which you are concerned.

Dr. Escudier

I would like to comment on your remark about the apparently unsteady nature of vortex breakdown. We have the view that vortex breakdown itself is not an unsteady phenomenon since the flow downstream of the breakdown regime is subcritical, it can support waves. Most vortex breakdown flows, especially in external situations (flows over wings, and so on) find themselves embedded in flows which are highly turbulent. This unsteadiness can propagate through the subcritical flow up into the breakdown regime and give the appearance of unsteadiness. But it is a feedback.

Mr. J.H.B. Smith

I don't want to enter into an argument about vortex breakdown, because I am not qualified, but Prof. Leibovich did suggest that the unsteady processes downstream of the breakdown were perhaps necessary to establish the energy balance of these upstream moving disturbances. I think, I guess like most of the subject, it is an unresolved question. I was merely suggesting that if we didn't find it in a steady calculation, perhaps we should not be too downhearted. We should introduce the possibility of unsteadiness, and I was associating that with the fact that a lot of our calculations are time dependent now, and so we might have this advantage for nothing. But, I certainly take your point, it is by no means certain that it is necessary.

Dr. Richey

There are a couple of areas that I don't think have been discussed too much in the meeting. They might be worthy of some consideration. One is the effect of stores or weapons on vortex flows. One wonders about the contamination of the vortex lift on the upper surface of a wing due to unusual shaped store configurations on the bottom of the wing. The paper this morning by Dr. Rao which discussed a device which stuck out in front of the wing was interesting in this regard, and perhaps turning the coin around, one might be able to configure a store pylon which would have a favorable effect on vortex flows. In the second area, concerning combat aircraft which manoeuvre very rapidly, one has to wonder and be concerned about hysteresis effects. Does the vortex flow reattach? How does the vortex flow set up as the pilot pitches the nose around at 30^{o}, 40^{o}, 50^{o} per second and rolls rapidly, changing and pointing the velocity vector? How can we be sure that these manoeuvres are controllable and useful? High lift by itself is no good by itself unless we can control it and prevent undesirable flight characteristics such as departure and spin. I think that the research should give some consideration to oscillatory and dynamic derivatives as we pursue these very interesting effects.

Mr. J.H.B. Smith

I think that that is a very real point and a real warning, because it is not easy, in fact it is almost impossible, to check these dynamic effects in windtunnel testing. They obviously are dependent on the particular manoeuvres that the aircraft is performing. Even if you can reproduce these manoeuvres in the windtunnel, there are still far too many of them to cover properly in a systematic series of tests. That consideration is the one which always led Dietrich Küchemann to insist that we should never have any unnecessary pair of vortices. He would always say that one pair of vortices is all right. If you can manage to get what you need with one pair of vortices, then don't introduce any more. I think that it is a very important principle. I think that forebody vortices and split wing vortices represent, in the end, trouble from just these issues of dynamic stability.

Prof. Seginer

I just wanted to add to Dr. Richey's comment that as far as I know the only program to test that was the F4 with blowing. There is a program ongoing at Dryden, except that I understand that the funding of that program is fluctuating. Maybe someone could influence the authorities to push that program.

Mr. J.H.B. Smith

Could we return to science?

Dr. Hornung

I would like to ask Jeremy Smith a question. Are you continuing with that work with the second family?

Mr. J.H.B. Smith

Not at the moment. There is nothing going on at present. I hope to get somebody else to continue with the work, but one has to make a decision in the light of the situation at the time, and I would be interested in pursuing it in any way that we could.

Dr. Hornung

We would also be interested.

Mr. Bore

Dr. Richey has introduced the topic of real things on real airplanes, and perhaps I would like to call to the attention of the workers in this vortex field some other real things on which perhaps they can produce some answers at another meeting in the future. Such things as proper rules for vortex generator arrays for controlling boundary layers; the interaction of vortices from various leading edge fences which can do some marvellous things at certain times, only we are not quite sure how and why. Various things like that could merit some attention. Another thing which struck me during the meeting was the absence of discussion of one thing that exercised us over recent years, which was the opposite to vortex breakdown, that is, vortex formup on a flow going into air intakes; something which I was addressing very recently indeed. It is a strange thing that there you find that you have uniformly distributed vorticity approaching your air intake and then magically sometimes it forms itself up into a discrete vortex which can now go and attach itself to the ground and throw up stones which might enter your engine. So it seems to me that that is very much the inverse of vortex breakdown. Anyway, I will leave those thoughts for future workers.

Prof. Young

It is almost time to close the meeting. I would just like to add one comment to the various points that have been raised. I hope that the people concerned with preparing theoretical models of these complex flows that we have been considering will try as hard as they can to bring in viscous effects because their absence seems to me to be a major weakness of many of the theoretical computing methods that have been developed to date. We saw how important secondary separations were, but they could not be modelled or were not modelled in the inviscid pictures that we were presented with.

Nonetheless, I think that this meeting has been a very valuable one, and judging by your response, it has excited your interest continuously. As Chairman of the Program Committee, I would like to say how much I enjoyed the meeting and how grateful I am to the various people who presented papers, in particular those who presented the key review papers, including Jeremy's final summing up which you have just heard. I will hand over now to M. Monnerie, the Chairman of the Panel.

M. Monnerie

I would not like to prolong this session which has already been a lengthy one, and I do not want to delay those of you who have trains and planes to catch. However there are two things that remain to be done before I release you. I would like first to give our thanks to all those who have put in all their efforts for the symposium to occur in the best of conditions and to be as interesting as possible:
- First of all, our Dutch hosts and especially Prof. Gerlach who welcomed us on Monday morning; the coordinator Mr. Bleeker and his secretary, Mrs. Fadeggon.
- Then, for the scientific part, the Program Committee and its Chairman Prof. Young, the authors and the lecturers.
- The people who helped us solve our communication problems, the interpretors and technicians in charge of the sound equipment.
- Lastly the one who is the central point for the work of the Fluid Dynamics Panel. Mr. Rollins, with his secretary Miss Rivault, has succeeded in optimizing a system whose operation is even more complex and unpredictable than a vortex system created by a high angle of attack plane, and we owe very much to him.

The second thing I have to do is to give you a few indications on the future activities of the Fluid Dynamics Panel.

As regards the year 1983, I would like to mention first briefly the lecture series organized next week at the von Karman Institute on the problem of transonic Aerodynamic Interactions. It will convene about 10 international experts and ought to be very interesting. It will also be given from the 16th to the 20th May in the U.S.
Then at the end of September in Turkey we will have our Autumn meeting with a Symposium on Windtunnels and Test Techniques. The program has just been published and is available at the desk when you go out of the room.
I would like to mention to finish with, that from the 10th to the 13th of October 1983, there will be a symposium organized in Brussels by the Flight Mechanics Panel on the Technology for Supersonic Cruise and Manoeuvre, and, of course, a lot of aerodynamics will be discussed in that syposium.

As regards 1984, the Fluid Dynamics program will be the following:
- from the 26th to 30th March at the von Karman Institute; lecture series on Stability and Control of Laminar Flows,
- from the 14th to the 18th May at von Karman Institute and the 4th to the 8th of June at NASA, Ames, a series of conferences on VSTOL Aerodynamics,
- from the 21st to the 24th of May in Brussels, a Symposium on the Improvement of Aerodynamic Performance through Boundary Layer Control and High Lift Devices.
- Finally, from 1st to 4th October, in Toronto Canada, a Symposium on Aerodynamics and Acoustics of Propellors.

This time I have really finished with my closing words, and I would like to say goodbye and have a nice trip home and I hope to meet you at one of the events that I have just mentioned. I declare this meeting closed.

REPORT DOCUMENTATION PAGE			
1. Recipient's Reference	2. Originator's Reference AGARD-CP-342	3. Further Reference ISBN 92-835-0334-1	4. Security Classification of Document UNCLASSIFIED

5. Originator	Advisory Group for Aerospace Research and Development North Atlantic Treaty Organization 7 rue Ancelle, 92200 Neuilly sur Seine, France
6. Title	AERODYNAMICS OF VORTICAL TYPE FLOWS IN THREE DIMENSIONS
7. Presented at	

8. Author(s)/Editor(s)	9. Date
Various	July 1983
10. Author's/Editor's Address	**11. Pages**
Various	576

12. Distribution Statement	This document is distributed in accordance with AGARD policies and regulations, which are outlined on the Outside Back Covers of all AGARD publications.

13. Keywords/Descriptors

Fluid flow	Wings
Vortices	Trailing edges
Boundary layer separation	Aerodynamics

14. Abstract

Associated with flow separations we frequently find vortical type flows. A familiar and classic example is the trailing vortex system behind a lifting wing where the separation occurs at the trailing edge. With the use of large sweep angles, we have become increasingly familiar with vortical flows associated with separations forward of the trailing edge. A feature of such flows in three dimensions is that they are frequently well ordered with a defined stable structure and designers have increasingly sought to exploit them in meeting the growing speed and manoeuvre demands on modern aircraft.

The Symposium provided a "state of the art" review, both experimental and theoretical, of such flows and the scope of current research in five main session: I – Fundamentals, Generation and Structure of Vortical Flows; II – Interaction of Vortical Flows with Surfaces; III – Modelling and Computing; IV – Stability and Breakdown of Vortical Flows; V – Control and Exploitation of Vortical Flows.

At the close of the meeting a short discussion of summary remarks was recorded and is included in the volume.

Papers were presented and discussions held at the Fluid Dynamics Panel Symposium held at Rotterdam, Netherlands, 25–28 April 1983.

increasingly sought to exploit them in meeting the growing speed and manoeuvre demands on modern aircraft.

The Symposium provided a "state of the art" review, both experimental and theoretical, of such flows and the scope of current research in five main sessions: I – Fundamentals, Generation and Structure of Vortical Flows; II – Interaction of Vortical Flows with Surfaces; III – Modelling and Computing; IV – Stability and Breakdown of Vortical Flows; V – Control and Exploitation of Vortical Flows.

At the close of the meeting a short discussion of summary remarks was recorded and is included in the volume.

Papers were presented and discussions held at the Fluid Dynamics Panel Symposium held at Rotterdam, Netherlands, 25–28 April 1983.

ISBN 92-835-0334-1

increasingly sought to exploit them in meeting the growing speed and manoeuvre demands on modern aircraft.

The Symposium provided a "state of the art" review, both experimental and theoretical, of such flows and the scope of current research in five main sessions: I – Fundamentals, Generation and Structure of Vortical Flows; II – Interaction of Vortical Flows with Surfaces; III – Modelling and Computing; IV – Stability and Breakdown of Vortical Flows; V – Control and Exploitation of Vortical Flows.

At the close of the meeting a short discussion of summary remarks was recorded and is included in the volume.

Papers were presented and discussions held at the Fluid Dynamics Panel Symposium held at Rotterdam, Netherlands, 25–28 April 1983.

ISBN 92-835-0334-1

increasingly sought to exploit them in meeting the growing speed and manoeuvre demands on modern aircraft.

The Symposium provided a "state of the art" review, both experimental and theoretical, of such flows and the scope of current research in five main sessions: I – Fundamentals, Generation and Structure of Vortical Flows; II – Interaction of Vortical Flows with Surfaces; III – Modelling and Computing; IV – Stability and Breakdown of Vortical Flows; V – Control and Exploitation of Vortical Flows.

At the close of the meeting a short discussion of summary remarks was recorded and is included in the volume.

Papers were presented and discussions held at the Fluid Dynamics Panel Symposium held at Rotterdam, Netherlands, 25–28 April 1983.

ISBN 92-835-0334-1

increasingly sought to exploit them in meeting the growing speed and manoeuvre demands on modern aircraft.

The Symposium provided a "state of the art" review, both experimental and theoretical, of such flows and the scope of current research in five main sessions: I – Fundamentals, Generation and Structure of Vortical Flows; II – Interaction of Vortical Flows with Surfaces; III – Modelling and Computing; IV – Stability and Breakdown of Vortical Flows; V – Control and Exploitation of Vortical Flows.

At the close of the meeting a short discussion of summary remarks was recorded and is included in the volume.

Papers were presented and discussions held at the Fluid Dynamics Panel Symposium held at Rotterdam, Netherlands, 25–28 April 1983.

ISBN 92-835-0334-1

AGARD Conference Proceedings No.342 Advisory Group for Aerospace Research and Development, NATO AERODYNAMICS OF VORTICAL TYPE FLOWS IN THREE DIMENSIONS Published July 1983 576 pages Associated with flow separations we frequently find vortical type flows. A familiar and classic example is the trailing vortex system behind a lifting wing where the separation occurs at the trailing edge. With the use of large sweep angles, associated with separations forward of the trailing edge. A feature of such flows in three dimensions is that they are frequently well ordered with a defined stable structure and designers have P.T.O	AGARD-CP-342 Fluid flow Vortices Boundary layer separation Wings Trailing edges Aerodynamics	AGARD Conference Proceedings No.342 Advisory Group for Aerospace Research and Development, NATO AERODYNAMICS OF VORTICAL TYPE FLOWS IN THREE DIMENSIONS Published July 1983 576 pages Associated with flow separations we frequently find vortical type flows. A familiar and classic example is the trailing vortex system behind a lifting wing where the separation occurs at the trailing edge. With the use of large sweep angles, associated with separations forward of the trailing edge. A feature of such flows in three dimensions is that they are frequently well ordered with a defined stable structure and designers have P.T.O	AGARD-CP-342 Fluid flow Vortices Boundary layer separation Wings Trailing edges Aerodynamics
AGARD Conference Proceedings No.342 Advisory Group for Aerospace Research and Development, NATO AERODYNAMICS OF VORTICAL TYPE FLOWS IN THREE DIMENSIONS Published July 1983 576 pages Associated with flow separations we frequently find vortical type flows. A familiar and classic example is the trailing vortex system behind a lifting wing where the separation occurs at the trailing edge. With the use of large sweep angles, associated with separations forward of the trailing edge. A feature of such flows in three dimensions is that they are frequently well ordered with a defined stable structure and designers have P.T.O	AGARD-CP-342 Fluid flow Vortices Boundary layer separation Wings Trailing edges Aerodynamics	AGARD Conference Proceedings No.342 Advisory Group for Aerospace Research and Development, NATO AERODYNAMICS OF VORTICAL TYPE FLOWS IN THREE DIMENSIONS Published July 1983 576 pages Associated with flow separations we frequently find vortical type flows. A familiar and classic example is the trailing vortex system behind a lifting wing where the separation occurs at the trailing edge. With the use of large sweep angles, associated with separations forward of the trailing edge. A feature of such flows in three dimensions is that they are frequently well ordered with a defined stable structure and designers have P.T.O	AGARD-CP-342 Fluid flow Vortices Boundary layer separation Wings Trailing edges Aerodynamics

AGARD
NATO ⊕ OTAN
7 RUE ANCELLE · 92200 NEUILLY-SUR-SEINE
FRANCE
Telephone 745.08.10 · Telex 610176

DISTRIBUTION OF UNCLASSIFIED AGARD PUBLICATIONS

AGARD does NOT hold stocks of AGARD publications at the above address for general distribution. Initial distribution of AGARD publications is made to AGARD Member Nations through the following National Distribution Centres. Further copies are sometimes available from these Centres, but if not may be purchased in Microfiche or Photocopy form from the Purchase Agencies listed below.

NATIONAL DISTRIBUTION CENTRES

BELGIUM
Coordonnateur AGARD – VSL
Etat-Major de la Force Aérienne
Quartier Reine Elisabeth
Rue d'Evere, 1

CANADA
Defence Scien
Department o
Ottawa, Ontar

DENMARK
Danish Defen
Østerbrogade
Copenhagen

FRANCE
O.N.E.R.A. (I
29 Avenue de
92320 Châtil

GERMANY
Fachinforma
Physik, Math
Kernforschu
D-7514 Eggs

GREECE
Hellenic Air
Research and
Holargos, Athens

ICELAND
Director of Aviation
c/o Flugrad
Reykjavik

ITALY
Aeronautica Militare
Ufficio del Delegato Nazionale all'AGARD
3, Piazzale Adenauer

(ARGE)

UNITED KINGDOM
Defence Research Information Centre
Station Square House
St. Mary Cray
Orpington, Kent BR5 3RE

UNITED STATES
National Aeronautics and Space Administration (NASA)
Langley Field, Virginia 23365
Attn: Report Distribution and Storage Unit

THE UNITED STATES NATIONAL DISTRIBUTION CENTRE (NASA) DOES NOT HOLD STOCKS OF AGARD PUBLICATIONS, AND APPLICATIONS FOR COPIES SHOULD BE MADE DIRECT TO THE NATIONAL TECHNICAL INFORMATION SERVICE (NTIS) AT THE ADDRESS BELOW.

2 2434 S02672DS
DEPT OF DEFENSE
DEFENSE TECHNICAL INFORMATION CENTER
ATTN: DTIC-DDA-2
CAMERON STATION BLDG 5
ALEXANDRIA VA 22314

PURCHASE AGENCIES

Microfiche or Photocopy	*Microfiche*	*Microfiche or Photocopy*
National Technical Information Service (NTIS) 5285 Port Royal Road Springfield Virginia 22161, USA	Space Documentation Service European Space Agency 10, rue Mario Nikis 75015 Paris, France	British Library Lending Division Boston Spa, Wetherby West Yorkshire LS23 7BQ England

Requests for microfiche or photocopies of AGARD documents should include the AGARD serial number, title, author or editor, and publication data. Requests to NTIS should include the NASA accession report number. Full bibliographical references and abstracts of AGARD publications are given in the following journals:

Scientific and Technical Aerospace Reports (STAR) published by NASA Scientific and Technical Information Facility Post Office Box 8757 Baltimore/Washington International Airport Maryland 21240, USA

Government Reports Announcements (GRA) published by the National Technical Information Services, Springfield Virginia 22161, USA

Printed by Technical Editing Service Limited
18 Chapel Street, Shirley, Solihull
West Midlands

END

DATE
FILMED

L 84

DTIC